AD-A009 847

PROCEEDINGS OF THE INTERNATIONAL SYMPOSIUM ON AIR BREATHING ENGINES (2ND), HELD IN RANMOOR HOUSE, SHEFFIELD UNIVERSITY ON 24TH-29TH MARCH 1974

Sheffield University

Prepared for:

Office of Naval Research

March 1974

DISTRIBUTED BY:

NTIS
National Technical Information Service
U. S. DEPARTMENT OF COMMERCE

NR-094-371
N00014-74-C-0290

149075

AD A009847

I.C.A.S.

SECOND INTERNATIONAL SYMPOSIUM ON AIR BREATHING ENGINES

24th/29th March 1974
SHEFFIELD, ENGLAND

D D C
RECEIVED
MAR 15 1975
A

PROCEEDINGS

Reproduced by
NATIONAL TECHNICAL
INFORMATION SERVICE
US Department of Commerce
Springfield, VA. 22151

DISTRIBUTION STATEMENT A
Approved for public release;
Distribution Unlimited

Best
Available
Copy

FOREWORD

2nd I.S.A.B.E. held in Ranmoor House, University of Sheffield

24th-29th March 1974

President of the Symposium: Air Cdre. F.R. Banks, CB, OBE,
HonCGIA, CEng, HonFRAeS,
RAF (Ret'd).

At the successful first meeting of I.S.A.B.E. in Marseilles it was resolved to renew the Symposium in 1974 and the task was entrusted to Dr. J.P. Gostelow, University of Cambridge and Dr. J. Swithenbank, University of Sheffield, at whose request the Royal Aeronautical Society undertook to organise I.S.A.B.E. II. A British organising committee was set up by the Society early in 1973. In October 1973 the organising committee submitted its proposals for the Symposium to a special meeting of the International Committee of I.S.A.B.E. held in Sheffield at which the main arrangements were agreed.

At the first I.S.A.B.E. meeting in Marseilles it was felt by many of the people attending or concerned with its inception that it would be an advantage on future occasions for an international specialist meeting of this type to be co-ordinated with other allied activities in the international aeronautical field. An international meeting to discuss this aspect was held at the Royal Aeronautical Society in December 1972 at which it was agreed that this could be best achieved by incorporating I.S.A.B.E. within the activities of the International Council of the Aeronautical Sciences (I.C.A.S.). Confirmation of the sponsorship of I.S.A.B.E. by I.C.A.S. was received in the Spring of 1973.

At the business meeting held during I.S.A.B.E. II under the chairmanship of Dr. A.M. Ballantyne, Member of the Council of I.C.A.S., it was agreed by the delegates that this should be the pattern for future meetings of I.S.A.B.E. and that on future occasions I.C.A.S. should request the appropriate national aeronautical body to undertake the organisation of the Symposium.

I.S.A.B.E. II (Sheffield 1974), held under the distinguished presidency of Air Cdre. Banks, was attended by about two hundred delegates from nearly twenty countries. Forty six papers were presented and are reproduced in this volume of the Proceedings.

cont/..

DDC
MAR 5 1975
A

We were to have been honoured by the presence of Professor Maurice Roy, Honorary President of I.C.A.S. but as, unfortunately, Professor Roy could not attend he sent the following message of goodwill to the Symposium.

"Last year I had the pleasure to inaugurate by a special lecture the meeting of I.S.A.B.E. I, organised in Marseilles by the Director of the Institute of Fluid Mechanics in this city of South France, my colleague and friend, Professor J. Valensi.

This year I welcomed with a great pleasure as I.C.A.S. Honorary President the very kind invitation of the Organising Committee of I.S.A.B.E. II to say a few words during the Banquet, firstly expressing the regret of the I.C.A.S. President, Dr. J.J. Green to be unable to be here and secondly expressing the interest of the scientific and aeronautical community of I.C.A.S. for this second I.S.A.B.E. meeting and the best wishes of the same I.C.A.S. for the full success of the Sheffield meeting.

Unfortunately one unforeseen commitment has oblig recently to stay in Paris at the same time. Permit me consequently to express to all of you my very deep and sincere regret of being unable to attend as contemplated this Sheffield meeting.

Permit me also to say that the location of I.S.A.B.E. II in the vicinity of a long world-famous centre of research, development and production of air-breathing engines and jet engines appears to me a very significant and favourable choice for the wished success of this second I.S.A.B.E. meeting.

Finally permit me to thank again the Organisers for their very kind invitation to me and say my best personal regards to all of you."

In conclusion the organisers would like to acknowledge the financial grants by the U.S. Army, Air Force and Navy agencies to Sheffield University as contributions towards the running of the Symposium.

R.R. JAMISON
Chairman,
I.S.A.B.E. Organising Committee

Organising Committee

Dr. R.R. Jamison, Chairman
Dr. J.P. Gostelow
Dr. J. Swithenbank
Mr. M.G. Farley
Miss Maureen Michael) RAeS Conference
Miss Rosemary White) Secretaries

CONTENTS PAGE

List of Delegates

1. The CF6-6 Engine - The First Million Hours
   - Paul C. Setze, General Electric Co., USA

2. Hydrogen as a Turbojet Engine Fuel - Technological, Economical and Environmental Impact
   - D.T. Pratt, K.J. Allwine and P.C. Malte, Washington State University, USA

3. Performance Problems Related to Installation of Future Engines in Both Subsonic and Supersonic Transport Aircraft
   - W.C. Swan, Boeing Commercial Airplane Company, USA.

4. Feederliner Engine Installation - Trends and Problems
   - D.H. Tipper, Hawker Siddeley Aviation, UK

5. Exhaust Emissions Under Simulated Flight Conditions
   - A.K. Forney, Department of Transportation, USA

6. The Use of a Rotating Arm Facility to Study Flight Effects on Jet Noise
   - W. Smith, Rolls-Royce (1971) Ltd., Bristol, UK

7. Life Enhancement of Turbine Blades
   - R.V. Narayana Murthy, Dte. of Aero. (R&D), India

8. The Influence of Air-Precooling before Compression in Air-Breathing Engines of a Space-Launcher
   - H. Kunkler, Technical University, Aachen, West Germany

9. Composite Propulsion Systems for an Advanced Reusable Launch Vehicle Application
   - Joseph G. Bendot, The Marquardt Company, USA

10. An Examination of Injector/Combustor Design Effects on Scramjet Performance
    - Griffin Y. Anderson, NASA Langley Research Center, USA.

11. Some Problems Concerning Optimal Ducted Rocket Engine with Secondary Burning
    - V.A. Sosounov, USSR

12. Ramjet Engines: Highlights of Past Achievements and Future Promise
    - E.T. Curran and F.D. Stull, Wright-Patterson Air Force Base, USA

13. Etude de l'Ecoulement dans un Ejecteur Transsonique
    - J.M. Hardy and L. Dutouquet, S.N.E.C.M.A., France.

14. A Numerical Method for the Solution of Three-Dimensional Internal Flows
    - R. Camarero, University of Sherbrooke, Canada.

15. Investigation of Separated Flow over Bodies of Revolution in Supersonic Intake Ducts
    - N.N. Zakharov, USSR

16. Three-Dimensional Wave Interactions in Supersonic Intakes
    - R.K. Nangia, British Aircraft Corp. Ltd., Filton, UK

17. Mixed Compression Air Intakes for Operation at Mach 2.2.
    - A.J. Brooks and G.J. Dadd, National Gas Turbine, Est., UK

18. Recompression par Chocs dans une Prise D'Air Supersonique en Presence D'Un Piege a Couche Limite
    - G. Meauze, O.N.E.R.A., France

19. Noise Generation by Steady and Unsteady Flow Distortions
    - J.S.B. Mather, University of Nottingham and M.J. Fisher, Institute of Sound and Vibration Research, UK

20. Contribution a L'Etude du Bruit de Jets en Vol
    - G. Richter and C. Schmidt, S.N.E.C.M.A., France.

21. Inlet Distortion and Blade Vibration in Turbomachinery
    - Y. Tanida, University of Tokyo, Japan

22. Experimental Investigation of a Transonic Axial Flow Compressor Stage with Steady State Distorted Inlet Flow
    - M. Lecht and H. Weyer, D.F.V.L.R., Germany

23. Experimental Investigation of the Performance of Short Annular Combustor-Dump Diffusers
    - A. Klein, K. Kotheder and M. Rohlffs, Motoren- und Turbinen-Union Munchen GmbH, Germany

24. Dynamic Flow Distortion in Subsonic Air Inlets
    - J.R. Jones and W.M. Douglass, Douglas Aircraft Company, USA

25. Directional Effects in 3-D Diffusers
    - H. Viets, Wright-Patterson Air Force Base, USA

26. Some Aerodynamic Design Considerations for High Bypass Ratio Fans
    - L.H. Smith, General Electric Co., USA

27. A Comparison of Theoretical and Experimental Investigations of Two Different Axial Supersonic Compressors
    - H. Simon and D. Bohn, Technical University, Aachen, Germany

28. The Influence of Viscous Interactions on the Flow Downstream of an Axial Compressor Stage
    - R.C. Lockhart and G.J. Walker, University of Tasmania, Australia

29. Turbine Cooling - A Review of the Various Interface Problems
    - A. Moore, Rolls-Royce (1971) Ltd., Bristol, UK

30. Film Cooling of Turbine Blades
    - M. Saarlas, U.S. Naval Academy, USA

31. Aerodynamic and Heat Transfer Interactions in High Temperature Turbines
    - J.R. Fagan, D.J. Helton and D.A. Nealy, Detroit Diesel Allison Division of GMC, USA

32. Linearized Three-Dimensional Potential Flow Through a Rectilinear Cascade of Blades
    - A.F. de O. Falcao, Universidade Tecnica de Lisboa, Portugal

33. Design of Blade Sections for Axial-Flow Compressors
    - D.A. Frith, Aeronautical Research Laboratories, Australia

34. The Chord-Wise Pressure Distribution on a Rotating Axial-Flow Compressor Blade
    - H.L. Moses and W.F. O'Brien, Virginia Polytechnic Institute and State University, USA

35. Combustor Modelling
    - I. Poll, R. Payne, J. Swithenbank and M.W. Vincent, University of Sheffield, UK

36. Heat Transfer Measurements on Advanced Combustor Liner Cooling Systems
    - D. Wahl, G. Kappler and J. Schmidt, Motoren- und Turbinen-Union Munchen GmbH, Germany

37. The Design and Development of an Advanced Annular Combustor for Civil Application
    - A.B. Wassell and J.E. Bradley, Rolls-Royce (1971) Ltd., Derby, UK.

38. Pyrogenic Ignition Systems for Afterburners
    - S. Subrahmanyam, G.K. Murthy and P.A. Paranjpe, National Aeronautical Lab., India.

39. Visualisation par Strioscopie dans un Diffuseur de Compresseur Centrifuge Supersonique
    - Y. Ribaud and P. Avram, O.N.E.R.A., France

40. Trace des Aubages de Turbine Transsoniques par la methode de L'Hodographe
    - G. Karadimas, S.N.E.C.M.A., France

41. A Statistical Method for the Analysis of Rig Traverse Measurements on Annular Combustion Chambers
    - D.C. Dryburgh, Rolls-Royce (1971) Ltd., Derby, UK

42. Optical Temperature Measurements in a Continuous Flow Combustion Chamber
    - A. Coghe, U. Ghezzi, S. Pasini, Politecnico di Milano, Italy.

43. Some Aspects of Digital Control Systems Applied to Aircraft Powerplants
    - J. McNamara, E. Roberts and C.G. Legge, Rolls-Royce (1971) Ltd. Bristol, UK

44. Telemetry of Engine Rotor Test Data
- A.J.S. Pratt, Rolls-Royce (1971) Ltd., Derby, UK

45. Utilisation de la Methode des Analogies Hydrauliques pour l'Etude d'un Diffuseur Supersonique pour Compresseur Centrifuge
- H. Miton and J. Valensi, Institut des Fluides Mechaniques, Marseille and J. Plotkowiak, Hispano-Suiza Div., SNECMA, France

46. The Design and Development of the GEM Engine
- R.M. Heathcote and C.E. Payne, Rolls-Royce (1971) Ltd., Leavesden, UK

6<

LIST OF DELEGATES

AHRENDT, H. - D.F.V.L.R., Germany
ALDRUBY, Dr. M.I. - Baghdad University, Iraq.
ALLARD, P. - Aerospatiale, France
ALVARO-FERNANDEZ, F. - Inst. Nacional de Tecnica Aerospacial, Spain
ANDERSON, G. - NASA Langley Research Center, USA
ASHWOOD, P.F. - N.G.T.E., Pyestock, UK

BAGLEY, J.A. - RAE Farnborough, UK
BALDWIN, G.G. - Daniel Doncaster & Sons Ltd.
BALLANTYNE, Dr. A.M. - I.C.A.S.
BANKS, Air Cdre. F.R. - Symposium Chairman
BARNES, C.S. - R.A.E. Bedford, UK
BELDING, Dr. J.A. - Naval Air Systems Command, USA
BENDOT, J.G. - The Marquardt Co., USA
BENNETT, H.W. - Rolls-Royce (1971) Ltd., Derby, UK
BERNIER, J. - Aerospatiale, France
BILLIG, F.S. - Johns Hopkins Univ., USA
BOHN, D. - Aachen Technical Univ., Germany
BOLTON, Dr. M.S. - University of Sheffield, UK
BORD, A.D. - Aerospatiale, France
BOTTOMS, H.S. - Lucas Aerospace Ltd., Birmingham, UK
BRADLEY, J.E. - Rolls-Royce (1971) Ltd., Derby, UK
BRAIG, W. - Univ. of Stuttgart, Germany
BREUGELMANS, Professor F.A.E. - Von Karman Inst., Belgium
BROOKS, A.J. - N.G.T.E., Pyestock, UK
BUBB, Dr. J.E. - Consultant, USA
BUGG, S.L. - Ministry of Defence, UK
BUHLER, Professor R.D. - University of Stuttgart, Germany

CAMARERO, Prof. R. - Univ. de Sherbrooke, Canada
CANNAVO, R. - SNECMA, France
CARRIERE, P. - ONERA, France
CARTER, E.C. - Aircraft Research Association, Bedford, UK
CHAPPELL, M.S. - National Research Council, Canada
CHIANG Kuo-fang - The Research Inst. of Mechanics, China
COOPER, P.J. - British Aircraft Corp., Warton, UK
CREASEY, R.F. - British Aircraft Corp., Warton, UK
CRESSWELL, R.A. - Rolls-Royce (1971) Ltd., Bristol, UK
CUMPSTY, Dr. N.A. - University of Cambridge, UK
CURRY, J.J. - Office of Naval Research, USA

DADD, G.J. - N.G.T.E., Pyestock, UK
DALEY, Col. D.H. - United States Air Force Academy, USA
DENNING, R.M. - Rolls-Royce (1971) Ltd., Bristol, UK
DE VILLIERS, P.V. - Cranfield Inst. of Technology, UK
DOUGLASS, W.M. - Douglas Aircraft Co., USA
DRYBURGH, D.C. - Rolls-Royce (1971) Ltd., Derby, UK

7<

EL'EHWANY, Dr. A. - Ainshamps University, Cairo, Egypt
EL'MAWLA, Dr. A. - Faculty of Engineering, Cairo, Egypt
ENGL, E. - Messerschmitt-Bolkow-Blohm, Germany
ESENWEIN, F.T. - L.T.V. Aerospace Corpn., USA

FAGAN, J.R. - Detroit Diesel Allison Div., General Motors, USA
FAGE, E. - Ste ASTECH sarl, France
FAHMI, Dr. G.J.S. - Baghdad University, Iraq
FALCAO, Prof. A.F. de O. - Universidade Tecnica de Lisboa, Portugal
FARLEY, M.G. - Rolls-Royce (1971) Ltd., Leavesden, UK
FLETCHER, Prof. R. - Cranfield Inst. of Technology, UK
FORNEY, A.K. - Dept. of Transportation, USA
FRAENKL, W. - IABG, Germany
FREUND, Col. B.L. - European Research Office, USA
FRITH, D.A. - Aeronautical Research Labs., Australia
FUNKE, R. - D.F.V.L.R., Germany

GARCIA, J.O. - Inst. Nac. de Tecnica Aerospacial, Spain
GEHLHAR, B. - D.F.V.L.R., Germany
GOLDSMITH, H.A. - British Aircraft Corpn., Filton, UK
GOSTELOW, Dr. J.P. - S.R.C. Turbomachinery Lab., Cambridge, UK
GREEN, D.R. - Solartron Electronic Group, Farnborough, UK
GUPTA, Dr. A.K. - University of Sheffield, UK
GUYOT, A. - Aerospatiale, France

HADWIN, R.L. - Hawker Siddeley Aviation, Brough, UK
HANSEN, P.L. - Volvo Flygmotor, Sweden
HARDY, J.M. - SNECMA, France
HARRIS, A.E. - Aircraft Research Association, Bedford, UK
HEATHCOTE, R.M. - Rolls-Royce (1971) Ltd., Leavesden, UK
HEMM, Co., R.V. - European Office of Aerospace Res. & Dev., USA
HENNECKE, Dr. D.K. - MTU-Munchen, Germany
HILL, Professor P. - Queen's University, Canada
HOLL, R. - Ministry of Defence (PE), UK
HOLLAND, P.J. - Lucas Aerospace Ltd., Bradford, UK
HYDE, J.A.C. - GEC Gas Turbines Ltd., UK

ISAAC, J.J. - Cranfield Inst. of Technology, UK
ITOH, M. - Ishikawajima-Harima Heavy Industries, Japan

JACQUES, Dr. M.T. - University of Leeds, UK
JAMISON, Dr. R.R. - Rolls-Royce (1971) Ltd., Bristol, UK

KAPPLER, Dr. G. - MTU-Munchen, Germany
KARADIMAS, G. - SNECMA, France
KIOCK, Dr. R. - D.F.V.L.R., Germany
KLEIN, A. - MTU-Munchen, Germany

KOLIAZHNOV, V.V. - USSR
KOLODOCHKIN, V.P. - USSR
KRAMER, P. - University of Stuttgart, Germany
KRIER, Dr. H. - University of Illinois, USA
KUNKLER, Dr. H. - Aachen Technical University, Germany

LANGWORTHY, R.A. - Eustis Directorate, US Army
LECHT, M. - D.F.V.L.R., Germany
LEGGE, C.G. - Rolls-Royce (1971) Ltd., Bristol, UK
LI Chih-kuang - Chinese Aeronautical Society
LIU Shou-hsi - The Research Inst. of Mechanics, China
LOCK, D. - British Aircraft Corp., Warton, UK
LORD, M.J.H. - Doncasters Monk Bridge Ltd., Leeds, UK
LORENZETTO, G. - Cranfield Inst. of Technology, UK

MCCARTHY, P.J. - Lucas Aerospace Ltd., Birmingham, UK
MCGREGOR, Dr. I. - RAE Bedford, UK
MCNAMARA, J. - Rolls-Royce (1971) Ltd., Bristol, UK

MATHER, Dr. J.S.B. - University of Nottingham, UK
MATTHEWS, Capt. D.W.B. - Canadian Forces
MATTON, Prof. G. - Ecole Nationale Polytechnique, France
MEAUZE, G. - ONERA, France
MELVILLE, J.E. - Rolls-Royce (1971) Ltd., Derby, UK.
MERLE, K.F.A. - Doncasters Monk Bridge Ltd., Leeds, UK
MEYER, Dr. J. - KWU, Germany
MILBURN, Col. R. - U.S. Embassy, UK
MILFORD, C.M. - Hawker Siddeley Aviation, Kingston, UK
MILLER, Prof. R.H. - National Academy of Science, USA
MITON, Dr. H. - Inst. des Fluides Mechaniques, Marseille, France
MIYAZAWA, K. - Ishikawajima-Harima Heavy Industries Ltd., Japan
MOORE, A. - Rolls-Royce (1971) Ltd., Bristol, UK
MORISHITA, Y. - Ishikawajima-Harima Heavy Industries Ltd. Japan
MURTHY, Prof. S.N.B. - Purdue University, USA

NAMBA, Prof. M. - Kyushu University, Japan
NANGIA, Dr. R.K. - British Aircraft Corp., Filton, UK
NICHOLAS, D.J. - Rolls-Royce (1971) Ltd., Derby, UK
NORMAN, P.A. - Rolls-Royce (1971) Ltd., Leavesden, UK

O'BRIEN, Professor W.F. - Virginia Poly. Inst. and State University, USA
OHTSUKA, M. - Ishikawajima-Harima Heavy Industries Ltd., Japan
OLSSON, Dr. U. - Volvo-Flygmotor, Sweden
OVERLI, J. - University of Trondheim, Norway

9<

PARANJPE, Dr. P.A. - National Aero. Lab., India
PARKER, R.W. - British Aircraft Corp., Filton, UK
PASINI, S. - Politecnico di Milano, Italy
PATTON, J.R. - Office of Naval Research, USA
PAYNE, C.E. - Rolls-Royce (1971) Ltd., Leavesden, UK
PAYNE, R. - University of Sheffield, UK
PEACOCK, R.E. - Cranfield Inst. of Technology, UK
PENDLEBURY, E.M. - CIBA-GEIGY (UK) Ltd., UK
PERKINS, Dr. H.J. - Ruston Gas Turbines Ltd., Lincoln, UK
PERSSON, Y. - Air Material Dept., Sweden
PIVKO, Dr. S. - University of Belgrade, Yugoslavia
POLL, D.I.A. - Hawker Siddeley Aviation, Kingston, UK
POLL, Dr. I. - University of Sheffield, UK
PRATT, A.J.S. - Rolls-Royce (1971) Ltd., Derby, UK
PRATT, Professor D.T. - Washington State University, USA

RAILLY, Professor J.W. - University of Birmingham, UK
RAO, K.V. - Cranfield Inst. of Technology, UK
REESE, Professor B.A. - Purdue University, USA
REFORD, F.S. - Rolls-Royce (1971) Ltd., Glasgow, UK
RIBAUD, Y. - ONERA, France
RICHTER, Dr. G. - SNECMA, France
ROACH, C.D. - U.S. Army, West Germany
ROBERTSON, A.M. - Southall College of Technology, UK
ROBINSON, P. - Hawker Siddeley Aviation, Kingston, UK
ROBINSON, P.J. - Rolls-Royce (1971) Ltd., Derby, UK.

SAARLAS, Dr. M. - U.S. Naval Academy, USA
SAKURAI, Dr. T. - Mech. Eng. Res. Labs., Japan
SANCHEZ-TARIFA, Prof. C. - Inst. Nac. de Tecnica Aerospacial, Spain
SCHAFFLER, A. - MTU-Munchen, Germany
SHARPF, R.L. - European Research Office, USA
SCHMIDT, C. - SNECMA, France
SCHOLZ, Professor N. - MTU-Munchen, Germany
SCHOTTLE, U. - Univ. of Stuttgart, Germany
SCHUMAKER, Major K.H. - Office of Aerospace Res. & Dev., USA
SETZE, P.C. - General Electric Co., USA
SILLS, T.D. - Rolls-Royce (1971) Ltd., Derby, UK
SMITH, L.H. - General Electric Co., USA
SMITH, M. - Ministry of Defence (PE), UK
SMITH, T. - Lucas Aerospace Ltd., Birmingham, UK
SMITH, W. - Rolls-Royce (1971) Ltd., Bristol, UK
SMYTH, R. - VFW-Fokker, Germany
SOBERS, B. - Naval Air Systems Command, USA
SPARKS, B.-Lucas Aerospace Ltd., Birmingham, UK
STARKE, J. - T.U. Braunschweig, Germany
STEVENS, Dr. S.J. - Univ. of Technology, Loughborough, UK
STITT, I.S.D. - Marconi-Elliott Avionic Systems, Rochester, UK
STULL, F.D. - Wright Patterson Air Force Base, USA
SWAN, W.C. - Boeing Commercial Airplane Co., USA
SWINDLEHURST, Wg. Cdr. P. - Ministry of Defence (Air Force) UK
SWITHENBANK, Dr. J. - University of Sheffield, UK
SYRED, Dr. N. - University of Sheffield, UK.

TAKAHARA, K. - National Aero. Lab., Japan
TANIDA, Professor Y. - University of Tokyo, Japan
TIPPER, D.H. - Hawker Siddeley Aviation, Hatfield, UK
TIPPETTS, Dr. J.R. - University of Sheffield, UK

UTTERBACK, J.C. - L.T.V. Aerospace Corpn., USA

VALENSI, Professor J. - Inst. des Fluides Mechaniques,
Marseille, France
VIETS, H. - Aerospace Research Labs., USA

WAHL, D. - MTU-Munchen, Germany
WALKER, Dr. G.J. - University of Tasmania, Australia
WANGLIE, Cdr. E.E. - Office of Naval Research, USA
WARNE, E.H. - Lucas Aerospace Ltd., Bradford, UK.
WASSELL, A.B. - Rolls-Royce (1971) Ltd., Derby, UK
WELLER, C.E. - Hawker Siddeley Aviation, Kingston, UK
WELLS, C. - Doncasters Monk Bridge Ltd., Leeds, UK
WEYER, H. - D.F.V.L.R., Germany
WHITE, C. - Ministry of Defence (PE), UK
WIDING, K.A. - Aero. Res. Inst., Sweden
WINTERFELD, Dr. G. - D.F.V.L.R., Germany
WRIGHT, G.H. - Rolls-Royce (1971) Ltd., Bristol, UK
WU Chung-hua - Research Inst. of Mechanics, China
WURZ, Dr. D. - Univ. of Karlsruhe, Germany

YAMAGUCHI, N. - Mitsubishi Heavy Industries Ltd., Japan
YARKER, A. - Rolls-Royce (1971) Ltd., Derby, UK
YU Shen, - Research Inst. of Mechanics, China

ZETTERSTROM, K-A, - Volvo-Flygmotor, Sweden.

11<

THE CF6-6 ENGINE - THE FIRST MILLION HOURS

Paul C. Setze

Aircraft Engine Group - General Electric Co. (USA)

INTRODUCTION

The initiation of high by-pass ratio turbofan engines, of which the CF6-6 is an example, into commercial airline service, provided many new dimensions in operating characteristics and maintenance technology for the airlines of the world. The very physical size of these engines, the amount of energy stored in their rotating components, the temperature and pressure levels at which they operate, all required new techniques and new philosophies on the part of the engine operators.

The high by-pass ratio turbofan engine offers the user airlines many advantages over the previous generation of commercial transport engines. One of the most outstanding of these advantages is its much superior fuel economy. Other major advantages include: 1) better thrust to weight ratio, 2) ease of maintenance, and 3) easy thrust growth. The significant improvement in cruise fuel consumption and engine thrust to weight obtained with this new generation of engines is shown graphically on Figure 1.

This paper traces the General Electric CF6-6 engine from its initial conceptual stages through the first one million hours of commercial airline service; achieved approximately two and one half years after initial service introduction of the engine. From the time of the first design layouts, the CF6-6 was designed specifically for commercial airline service. Although the CF6-6 is derived from the military TF39 engine (the powerplant for the Lockheed C5A military cargo/transport), many changes were incorporated to increase the suitability of the engine for airline service.

The desired high thermodynamic cycle efficiencies require high temperatures and pressures which in turn required the development of new high temperature materials and cooling techniques. Also required were new design techniques to maintain these high pressures in structures that were of sufficiently low weight to make the engine competitive in the evolving commercial environment of the late 1960's. These engines also require tighter tolerances and closer clearances of rotating parts because leakage of air at these high pressures represents a more significant effect on the overall cycle performance than does the leakage of air at the lower pressure levels of the previous generation of jet engines. These new materials, new design techniques, new tolerances and new clearance levels required a lot of rethinking on the part of the airlines with regard to maintenance philosophies and practices.

The introduction of these families of engines altered the concept of maintenance being conducted on a fixed overhaul time to maintenance based on engine condition. This means the engines are flown until inspection or measured performance shows that a part requires maintenance. At that time the engine or part is removed and appropriate maintenance performed. With this new concept of maintenance intervals, introduction into a system designed around fixed overhaul times required new planning on the part of the airlines in order to accept these engines into their existing maintenance systems.

Once certified, introduction of the CF6-6 engine into initial service went very smoothly. Only major technical problem, to be detailed later, occurred during the first year of operation. Immediate action to resolve the problem was initiated and retrofit programs established and implemented. The entire (then) existing fleet of two hundred and sixty engines was retrofitted in approximately four months without a single aircraft departure delay due to lack of an engine. Cycle performance of the engine in service has truly been excellent. Deterioration as measured in terms of increases in specific fuel consumption or exhaust gas temperature has met all expectations. Mechanical performance has also exceeded expectations. Life limiting components, as shown by initial service, have been identified and at the present time all user airlines have programs underway to introduce improved components that will result in further increases in engine life and reliability in airline service.

INITIAL CONCEPT AND DESIGN

The CF6-6 engine as originally envisioned in 1966-67, was to be a 30, 000 pound thrust class engine for a three engine airbus concept being studied by a number of airframe manufacturers. During the initial airframe studies and concurrent discussions with the airlines, the size and gross weight of the aircraft continued to grow until the thrust requirements approached 40, 000 pounds. By this time the aircraft thrust requirements were sufficiently defined so that the final engine requirements and specifications could be established. All data at this time indicated that the proper thrust level for the CF6-6 engine was approximately 40, 000 pounds or 33% larger than originally envisioned.

With the thrust level established, it was then possible to define an engine optimized for commercial airline service within a number of specific design requirements. These requirements were established for the following areas: 1) engine weight, 2) fuel consumption at takeoff, 3) climb and cruise thrust ratings, 4) performance deterioration (based upon increase in specific fuel consumption and exhaust gas temperature), 5) maintainability, 6) installation ease and interface definitions, 7) operational characteristics, 8) growth capability and 9) operating cost. Once established, these requirements were collected and reviewed for inconsistencies. The engine preliminary design thus resulted. This preliminary design was based in large part upon the technology derived from the TF39 engine, which at the time the CF6-6 program was initiated, was conducting early flight tests in the Lockheed C5A. Detail discussions were held with potential airline users of the CF6-6 to incorporate into the design requirements that the airlines required in an engine scheduled for use in the 1970's.

At the time the design requirements were formulated, it was felt that the key to providing a successful engine for airline service revolved around improvements in fuel consumption, maintenance ease and increased parts life. From a marketing standpoint the airlines would expect significantly more extensive warranties on the engine and parts than had heretofore been provided. This made necessary the establishment of stringent requirements on both parts life and engine maintenance costs. The component lives that were established as requirements are shown in Table 1. It was necessary to meet these requirements in order to obtain the level of reliability and operating costs that were established as primary goals for the engine.

TABLE 1

TYPICAL COMPONENT LIFE REQUIREMENTS

Component	Life Requirement	Expected Life In Service
H.P. Comp. Rotor	30,000 cycles	30,000 cycles
H.P. Turb. Rotor	25,000 cycles	6,300/27,000 cycles*
Fan Rotor	30,000 cycles	24,000 cycles
Combustor	15,000 cycles	2,000/8,000 cycles*
HPT Static Parts	12,000 cycles	12,000 cycles
Frames	35,000 cycles	35,000 cycles
HPT Blades	12,000 cycles	8,000 cycles

*Design/Rework defined to obtain improved life shown.

The initial design parameters for the CF6-6 are shown in Table 2 compared to similar parameters for engines that were designed and that entered service in the late 1950's and 60's. An additional column shows what was actually achieved by the CF6-6 at the time of certification and also represents the average performance of production engines shipped to date.

TABLE 2

CF6-6 DESIGN PARAMETERS

Parameter	CJ805-23 Certified 1960	CF6-6 Requirement	CF6-6 Actual
Takeoff Thrust-lbs.	16,100	40,000	41,300
Takeoff SFC-lbs/hr/lb	0.56	0.354	0.348
Cruise SFC-lbs/hr/lb	0.92	0.633	0.62
Thrust/Weight-lbs/hr	4.1	5.2	5.4
Acceleration Time-sec	6	5	4.1
Fan Stall Margin-%	15	16	15
EGT Margin-°C	10	20	63
Takeoff Noise-EPNdb*	110	106	99
Side Line Noise-EPNdb*	111	107	96
Approach Noise-EPNdb*	112	107	102

* For CJ805-23 in CV990 Aircraft at 253,000 lb. gross weight.
For CF6-6 in DC10-10 Aircraft at 430,000 lb. gross weight.

Improved fuel consumption was the primary reason for going to the high by-pass ratio concept and was therefore a primary goal in the initial design. The next objective was to provide the airlines with an engine that could be easily maintained both installed in the aircraft and in the airline maintenance shop. In order to assure that this objective was met, the airlines who had purchased the CF6-6, were made a part of the design and development team. The airlines assigned personnel from their maintenance and engineering departments to work with the CF6-6 design engineers and requirements engineers to arrive at a number of the concepts that eventually were put into the final engine design. This design and development team met quarterly throughout the development program to report progress and problems, and to assure that the airline needs were being both understood and incorporated into the design of the CF6-6. The engine that resulted is shown on Figure 2. It consists of a single stage fan of 86.4 inches in diameter with an overall pressure ratio of 1.6 at takeoff power. Attached to the fan disk is a single booster stage that supercharges the air entering the core. The core engine consists of a 16 stage high pressure compressor with 6 stages of variable stators and variable inlet guide vanes, a full annular combustor with thirty pressure atomizing fuel nozzles, a 2 stage air cooled high pressure turbine and a 5 stage tip shrouded low pressure turbine. The turbine thrust reverser attaches to the turbine rear frame as part of the basic engine assembly.

In keeping with the concept of providing an engine that was easy for the airlines to maintain, two major features were incorporated into the engine. The first of these is the modular concept that permitted major engine modules to be changed either on the wing or in the maintenance shop with a minimum expenditure of labor required. Once exchanged, the removed module could then be disassembled for the required repair.

The basic modules of the engine (see Figure 3) consist of the fan module, the core module, which includes the high pressure compressor and combustor, the casing of which forms the compressor rear frame, the high pressure turbine module, the low pressure turbine module which includes the turbine mid and rear frames, and an accessory module. Any or all of these modules can be replaced in a very short period of time so that the module requiring repair can be maintained as a separate component. Complete module interchangeability between engines is possible.

The second of these features involved the mounting of the fan thrust reverser on the aircraft pylon rather than on the engine. The reverser is attached to the pylon with hinges and is split along the bottom centerline permitting the reverser to be unlatched along the bottom. By swinging it upward, there is complete accessibility to the engine on the wing (see Figure 4) which also allows removal from the aircraft while leaving the fan thrust reverser installed. This concept alone has reduced the amount of labor required to maintain the CF6-6 engine in service by approximately 5 to 7 percent.

The requirement pertaining to performance deterioration in service was aimed at achieving long time on-the-wing performance. The specific requirement was to establish adequate margins for fuel consumption and exhaust gas temperature (see Table 2) on new engines as shipped from the factory and repaired engines as they leave the maintenance shop. This also established the requirement for component design details and efficiency levels that would be relatively insensitive to the normal in service "wear and tear". Because of its on-condition maintenance concept, provisions are in the engine to permit ease of inspection during periodic preventive maintenance so that it could be determined when a part was deteriorating to the point where removal of the engine or the module containing the part might be necessary to perform maintenance. For example, internal parts of the engine are inspected by means of a borescope through borescope ports which are strategically located at every stage in the compressor, at several locations in the combustor and at every stage in the high pressure and low pressure turbine. Borescope inspection of all major engine components assures the engine is capable of maintaining its in-service status and will provide good operational reliability until the next scheduled inspection.

CERTIFICATION PROGRAM

The certification test program (see Figure 5) included over 3,000 factory engine test hours. Certification of the engine occurred in September 1970. This test program is continuing today and is meeting a commitment to the airlines to stay two years ahead of the high cycle engine in service with an engine in the factory test fleet.

The airline personnel assigned to the development program also played a part in the creation of our factory engineering test and certification plans. Previous experience with the CJ805 and other commercial and military engines and experience brought by the airline customers indicated that parts life in the field was more dependent on the number of flight cycles than it was on the number of flight hours. For that reason, a simulated airline cycle was defined that was used during most of the factory endurance testing in order to best describe in the factory, types of experiences that would be seen when the engine went into airline service. This cycle, which consists of operating the engine at various power settings used in a single typical airline flight, is shown on Figure 6. This cycle, which takes approximately fifteen minutes, simulates one complete airline flight. Such testing has proven to be very accurate in determining problems on the engine that are cyclic oriented, as most in-service problems are.

During the certification program, flight testing of the CF6-6 engine was accomplished with the DC10 series 10 nacelle design mounted on the in-board pylon of a Boeing B-52 aircraft (see Figure 7). This program completed 143 flight test hours and provided invaluable data for the certification program on engine inflight operation and performance.

Prior to certification the engine initiated flight test on the McDonnell Douglas DC10 series 10 aircraft in July 1970. This flight test program covered more than 1,500 flight test hours or 4,500 engine hours. From an engine operational standpoint, the flight test program was essentially uneventful. Very few problems were discovered that required any modification to the engine during this phase of the program.

In addition to the amount of factory test hours indicated earlier, a number of other tests were conducted prior to certification to assure that upon introduction into service, a high level of reliability would be obtained. These tests included component test of: 1) gearbox; 2) major control and accessory components; 3) combustor and 4) heat transfer tests on the turbine cooling systems. Results of these tests were submitted to the FAA in support of the certification program.

An integral part of the certification and follow-on component improvement program was to develop procedures for the repair of engine components for use when the engine entered airline service. Throughout the development program, parts from engines that had run significant endurance hours or cycles were sent to the repair development shop for the development of repair procedures. Parts were then repaired following these procedures and reinstalled in endurance engines to continue on the evaluation and test program.

INITIAL SERVICE EXPERIENCE

Initial service experience with the CF6-6 engine was probably the best ever achieved for a new commercial production engine. First revenue service started in August 1971 with American and United Airlines. Through the first 80,000 flying hours there were no major problems. The in-flight shutdown rate and premature removal rate was outstanding and the engine generated broad airline acceptance.

A major problem occurred in mid-1972 after about 80,000 hours. The problem was the result of an oil fire in the turbine mid-frame or "C" sump section of the engine. The cause was attributed to a loss of oil scavenge from the sump which permitted oil to leak into a high temperature area in the frame surrounding the sump causing it to ignite. This burning oil overtemperatured the structure of the low pressure turbine rotor and in two instances caused sections of the aft portion of the engine to become separated during flight.

An accelerated engineering investigation of this problem revealed that a feature incorporated into the engine to improve the maintainability of the turbine mid-frame was the cause. A flange had been placed in the scavenge line from the C sump. This flange, because of restricted space inside one of the turbine mid-frame struts, was not adequate to provide good sealing during all engine operating conditions. The scavenge line was surrounded on the outside by high pressure air, and when the flange leaked high pressure air entered the line starving the oil scavenge flow and causing the sump to flood. Flooding of the sump permitted oil to pass through the seals and enter the high temperature cavity in the frame and ignite. Several design changes were introduced when the cause of the problem was determined to assure that the problem would never occur again. These design changes included not only the elimination of the flange in the scavenge line, but also the addition of lower temperature air in the cavity surrounding the sump so that even if the sump did leak oil, the temperature would be low enough to preclude a fire.

A retrofit of this package of fixes was initiated in November 1972, just 6 months after the first incident occurred, and was completed on the entire fleet of DC10 aircraft by the end of March 1973. This retrofit was accomplished without a single delay or cancellation of a revenue flight due to lack of engines.

Performance of the engine in this area since the introduction of these changes has been flawless. In over 700,000 flying hours, not a single repeat of this problem has occurred. Once this problem was solved, service experience with the engine continued to be quite good.

CURRENT EXPERIENCE

At the present time the average age of the 284 CF6-6 engines in service is about 4,000 hours. The age and cycle distribution are shown on Figures 8 and 9. As the in-service engines increased in age, some problems associated with high time could be seen. The most severe of these problems was combustor dome and inner shell life. Experience has shown that these parts have an average in-service life of between 2500 and 3500 hours, below the age considered necessary for satisfactory in-service life. As the first signs of combustor distress appeared, a program was initiated to improve the inner shell and dome of the combustor. This program, completed in early 1973, involved material and structural modifications and was packaged with several other changes to improve life. Airline agreement was obtained to introduce these changes starting in late 1973. Incorporation of these changes is currently underway and should be completed by early 1975. It is expected that, when completed, these changes will solve all identified problems that might cause premature engine removals in a time of less than 4,000 hours, thus continuing the high level of reliability for the engine in service.

A continuing repair development program in cooperation with the airlines is proceeding according to plan. In service, parts are not always wearing out in exactly the same manner as the initial factory development program predicted. With the assistance of the airlines, repair procedures are being developed and the repaired parts reinstalled in service engines. This program to date has been extremely successful and will ultimately show a significant reduction in overall engine operating costs to the airlines.

A number of inspections are required to be conducted by each airline to assure the FAA that the engine and airline is capable of going "on-condition". These "threshhold inspections", as they are called, were conducted at 500, 1500 and 3000 hours by each major airline user. The CF6-6 has passed each of these inspections with ease, and the FAA has approved the engine for a complete on-condition maintenance program without any fixed overhaul time for either the engine or any of its components.

The engine entered airline service with life limits established for only five parts that were below the design requirements. In each of these cases, the parts were limited by low cycle fatigue based on factory test experience. Factory testing after certification revealed a life problem of a low cycle fatigue nature on two other parts and as a consequence, life limits were placed on these parts as well. Design changes to improve the low cycle fatigue life of each of these parts are now available and in each case involve a rework of the existing part rather than replacement. Programs have been agreed to with each airline to remove these parts prior to the time that the life limit is reached. Upon removal the parts are reworked and placed back in service. In each case, the part returned to service will meet its initial design objectives in terms of low cycle fatigue life. Referring back to Table 1, the last column shows component lives actually demonstrated either by factory test or achieved in service to date. The components that are indicated to have less than the objective lives in actual service, have modification programs underway to retrofit field engines. These components, shown in the table, are indicated by an asterisk.

A program is underway to inspect high time engine parts as they come into the airline maintenance shops to allow the early identification of problems. This will permit the solution to be available prior to the time that a marked increase in failure rate occurs.

Since passing the 4,000 hour point in service life, no new problems have occurred that were not seen prior to this time. Although it is inconceivable that this trend will continue, it leads to optimism regarding the continued service experience with the engine. As the engines have grown older, the premature removal rate has increased, but it is anticipated that with introduction of the modifications discussed earlier, this trend will be reversed and the engine will level out at a very acceptable premature removal rate.

IN SERVICE PERFORMANCE

With respect to engine performance, the average engine as shipped new from the factory exceeds its guaranteed performance levels by the amount shown in Table 3.

TABLE 3

ACTUAL CF6-6 PERFORMANCE

	Guarantee	Actual	Margin
Takeoff Thrust-lbs.	38,900	40,100	3.1%
Takeoff SFC-lbs/hr/lb	0.357	0.352	1.5%
Max. Cont. SFC-lbs/hr/lb	0.355	0.348	2.8%
Exhaust Gas Temp.-^{o}C	--	840	65

The CF6-6 engine uses fan speed as a measure of thrust being produced. As the engine deteriorates in service exhaust gas temperature (EGT) rises at constant fan speed. When EGT reaches the limit established for the CF6-6 (915°C) the engine must be removed from the aircraft and maintenance performed to recover the performance lost. In service experience to date with respect to performance deterioration has been quite good during the first million flying hours. Figures 10 and 11 show the amount of performance deterioration with respect to cruise fuel flow and exhaust gas temperature margins that have been observed to date. With the exhaust gas temperature margins being obtained on new engines as they are shipped from the factory, experience shows that for the average engine the exhaust gas temperature limit will not be exceeded during the first 4,000 - 6,000 hours of on-wing operation. Similarly, fuel flow is deteriorating at about the same rate. As expected, the most rapid deterioration occurs during the first 1,000 to 1,500 hours of operation after which the rate of deterioration levels off considerably. The deterioration that occurs during the first 1,000 to 1,500 hours of operation is the result of the rotating parts wearing in, seals opening up and clearances are increasing. After this point, the clearance increase and wear rate slows significantly.

Currently underway is a program with the airlines on performance recovery aimed at determining which components contribute most to performance deterioration in service and what modifications to these components should be made during routine maintenance to recover the performance lost in service. It appears the major contributor to performance loss is the high pressure turbine, with the high pressure compressor being a lesser contributor. Engines are being tested after significant airline service to determine which parts of these components are the primary cause of the performance deterioration. As a result of this program procedures for module repair that recover lost performance will be established.

AIRLINE PRACTICES

As shown earlier, the engine was designed for the replacement of major engine modules with the engine installed in the aircraft. Airline preference to date has been to remove an engine from the aircraft and perform the module replacement in the maintenance shop rather than perform the change on the wing. The major reason for this has been aircraft scheduling in revenue service. A number of very successful replacements of both fan modules and low pressure turbine modules have been accomplished on the wing, however. The time required to accomplish these module exchanges has been well within the time initially predicted for module replacement.

All of the CF6-6 features to simplify periodic maintenance have done the job for which they were intended. The airlines make maximum use of borescope and other inspection features. As a consequence, the on-condition maintenance program has proceeded without any problems. The engine has proven itself to be extremely simple to maintain with a very low maintenance labor requirement.

One problem observed to date is that the airlines tend to let the engine mechanical deterioration go beyond the most economical point for the performance of maintenance. As an example, scheduled borescope inspections of the combustor show the first signs of distress very clearly, and the deterioration rate is well established. However, it has been the tendency of the airlines to continue to keep the engine in service until the combustor deterioration reaches a point where secondary damage (usually in the turbine section) occurs. This results in a much more expensive failure in terms of labor and parts replacement costs than would have occurred if the airlines had removed the engine for combustor replacement sooner. Programs are currently underway with the airlines to work out in detail their on-condition maintenance program to assure that the most economical operation of the engine is the end result.

FUTURE DIRECTIONS

With todays emphasis being placed on the energy shortage and the resultant desirability to obtain better fuel consumption, there is currently underway component improvement programs that will further improve the fuel consumption margin obtained with new engines c engines that receive major maintenance in airline shops. Once these improvements are incorporated, further reductions in engine fuel consumption, both during initial operation and after maintenance actions are expected.

CONCLUSIONS

In general, the introduction of the CF6-6 into commercial airline service and its operation through the first one million flight hours has proceeded smoothly. It is felt the reason for this was initial design requirements aimed directly at commercial service and close coordination with the airlines during the initial design and development program. The concept of on-condition maintenance is working and although both the engine manufacturers and the airlines have a lot to learn regarding the operation and maintenance of high by-pass ratio turbofan engines, the inherent advantages of these engines have resulted in meeting the expectations of both the manufacturers and the users.

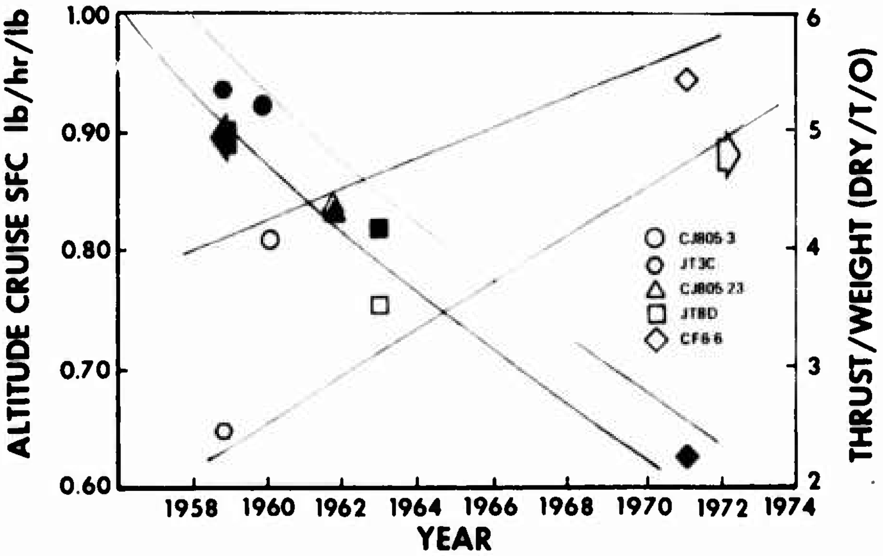

Figure 1 Commercial Engine Fuel Consumption & Thrust/Weight Trends

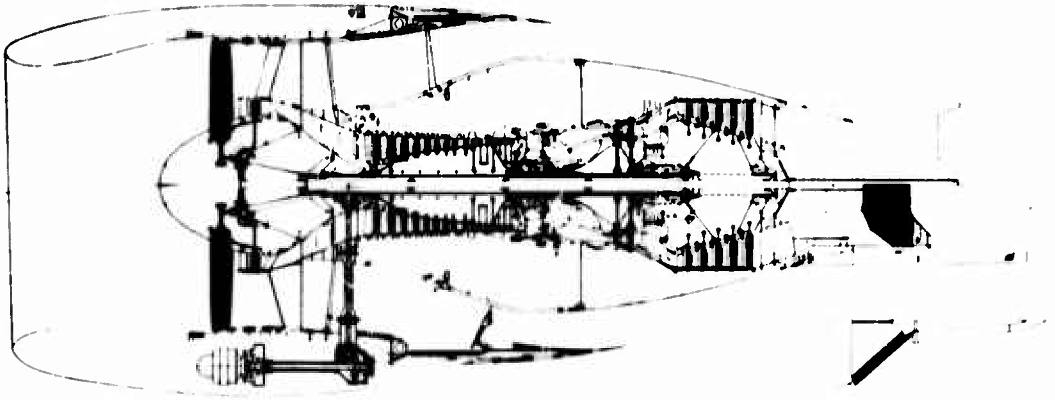

Figure 2 CF6-6 Engine Cross-section

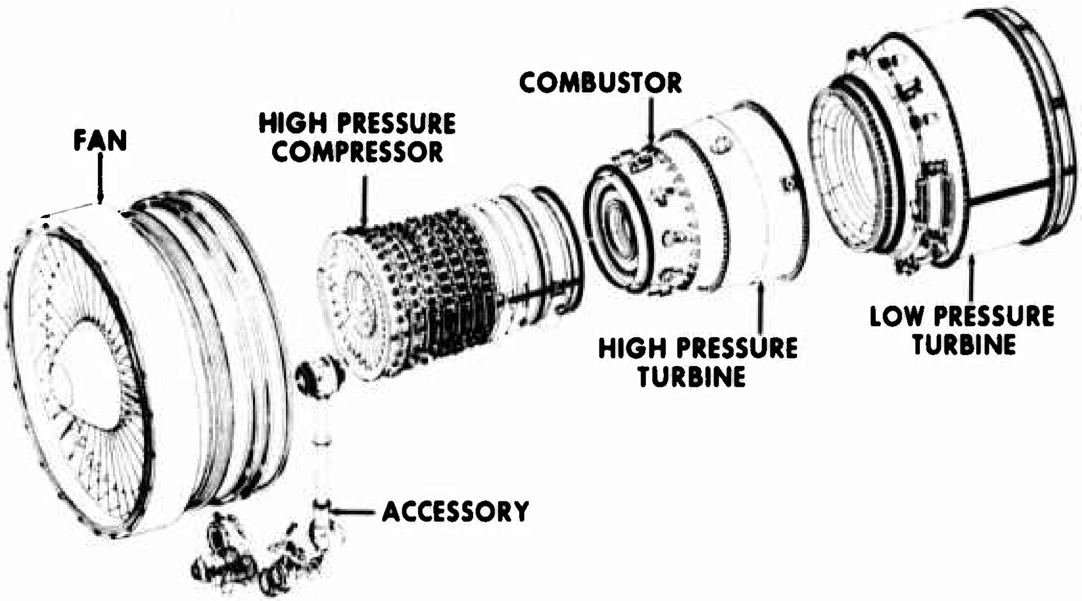
COMBUSTOR
FAN
HIGH PRESSURE COMPRESSOR
LOW PRESSURE TURBINE
HIGH PRESSURE TURBINE
ACCESSORY

Figure 3 CF6-6 Engine Modules

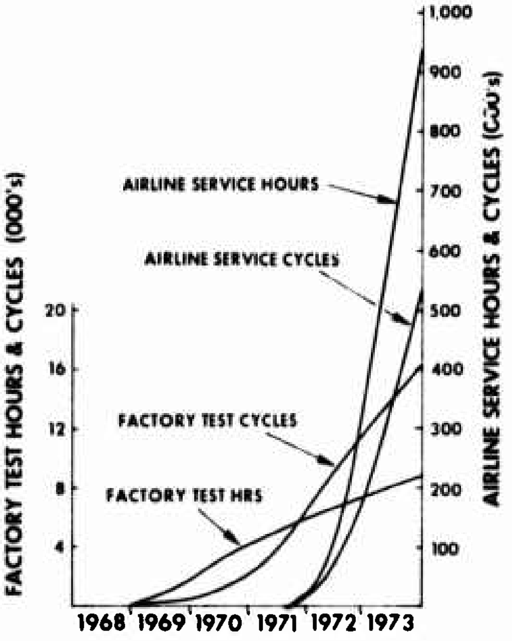

Figure 4 Accessibility of CF6-6 Engine Installed in Nacelle

Figure 5 Service Time and Cycles Factory Test and Airline

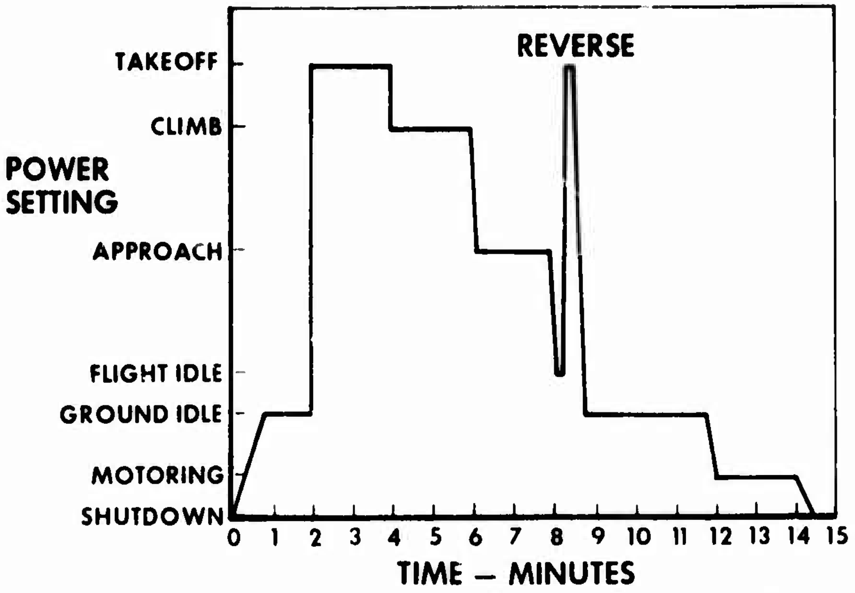

Figure 6 Simulated Airline Cycle Used for Factory Endurance Testing

U.S. AIR FORCE

Figure 7 CF6-6 Engine Mounted on Pylon of B52 Flight Test Aircraft

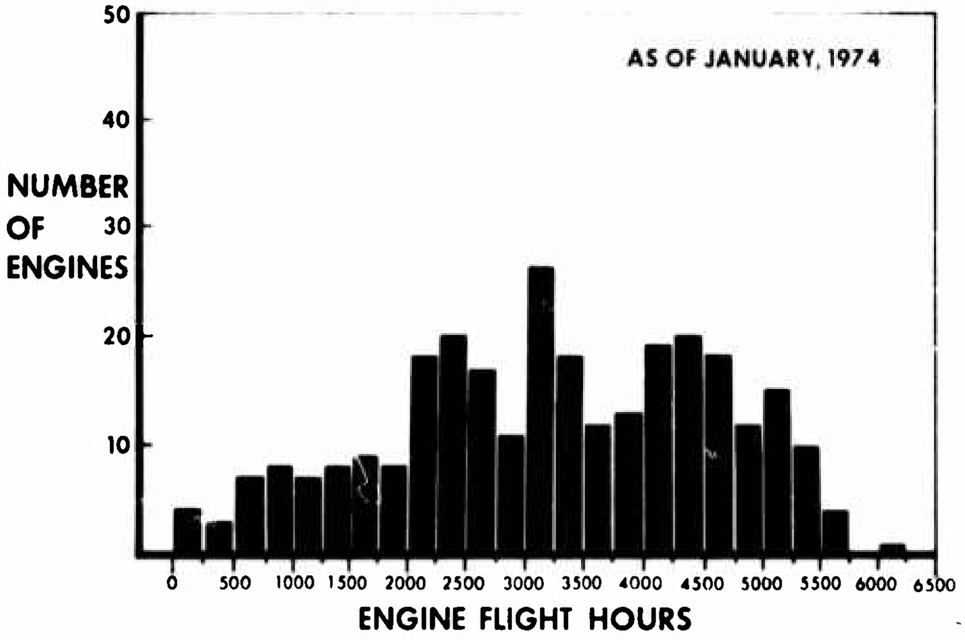

Figure 8 Engine Age Distribution in Service

1 - 2

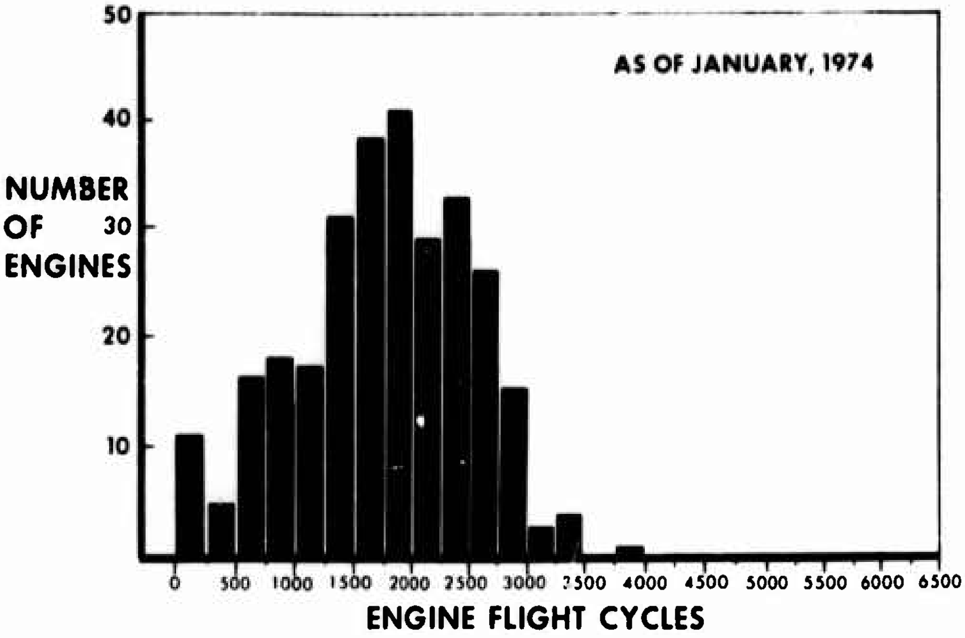

Figure 9 Engine Cycle Distribution in Service

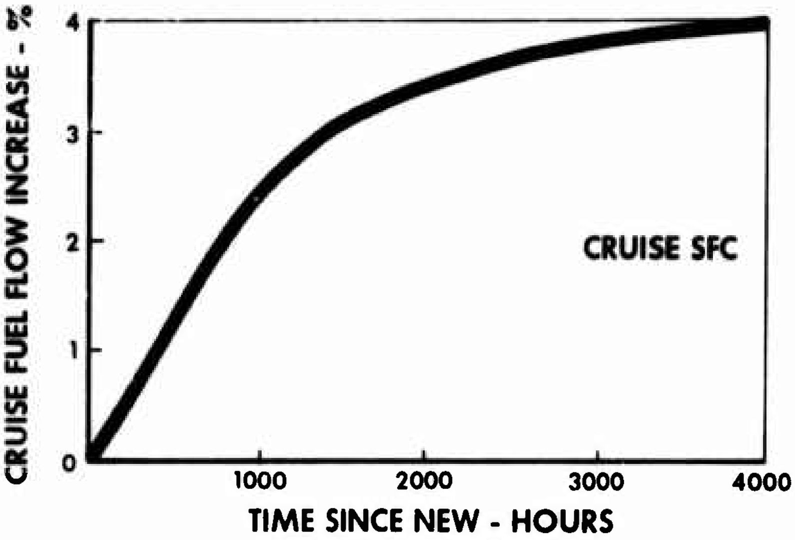

Figure 10 CF6-6 Fuel Flow Increase in Service

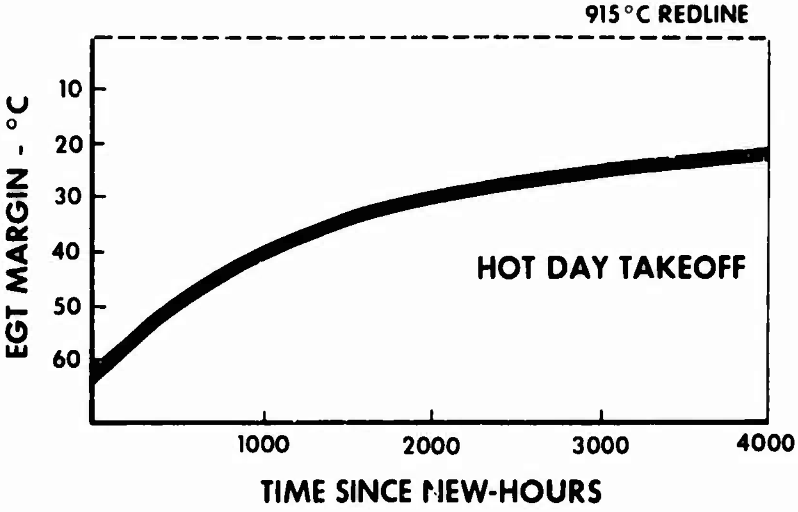

Figure 11 CF6-6 Exhaust Gas Temperature Increase in Service

HYDROGEN AS A TURBOJET ENGINE FUEL--
TECHNOLOGICAL, ECONOMICAL AND ENVIRONMENTAL IMPACT

D.T. Pratt, K.J. Allwine and P.C. Malte
Washington State University, Pullman, Washington, USA

Abstract

The present energy crisis has created an increased level of concern with respect to availability of petroleum fuels within the next decade. This consideration, together with the fact that turbojet engines are a significant and increasing contributor of NO_x and other pollutants, led to a critical examination of the technological, economic and environmental considerations of using hydrogen (LH2) as a jet engine fuel. In addition to reviewing U.S. literature on technological and economic considerations, an assessment is made of combustion and pollutant kinetics of hydrogen in supersonic and hypersonic aircraft engines, by means of a perfectly-stirred reactor model. Conclusions are drawn concerning the short, mid-term and long-range possibilities of adapting aircraft to hydrogen fuel.

Introduction

The motivation for examining the technological, economical and environmental impact of hydrogen (specifically liquid hydrogen, LH2) as an alternative fuel for jet aircraft arises primarily from four considerations:

1. Decreasing availability and increasing cost of hydrocarbon fuels.
2. The quest for an environmentally "clean" fuel.
3. Anticipation that the present fossil fuel economy may eventually be superseded by a nuclear-based energy economy.(1)
4. The need for fuels with desirable properties for future hypersonic commercial aircraft.(2)

For purposes of this paper, no attempt has been made to address these issues on a worldwide basis; only U.S. sources of information have been utilized.

Air Transportation and the Energy Crisis

Within the United States, air travel is the major passenger carrier between cities. In 1970, the airlines accounted for 77% of U.S. intercity revenue passenger miles; and airlines now carry more than 91% of transatlantic passengers.(3) Tremendous growth has been predicted in interurban (80-800 km), long-haul (domestic) and general aviation, as shown in Table 1. The largest potential of all is anticipated for air cargo, in spite of its low energy efficiency. Also by 1985, there will be a need for larger aircraft carrying about 800-1000 passengers, and the free world air carrier fleet will have grown from 5100 to 8300 aircraft.(4)

	Enplaned Passengers (millions)	
	1969	1985
Intraurban (0-80 km)	13	38
Interurban (80-800 km)	81	331
Long-Haul Domestic	75	334
Long-Haul International	13	75
General Aviation	219	394

	Cargo Originating Tons (millions)	
	1969	1985
Air Cargo	3	34

TABLE 1. Air Transportation in the United States. 1969 Actual Demand, 1985 Projected Demand. (Ref. 4)

In 1970, aircraft consumed 13% of the total energy used in the U.S. transportation sector, and by 1985 that figure is expected to be about 18%. Table 2 shows the energy consumption in 1970 and projected 1985 figures for aircraft, total transportation and total U.S. energy consumption.(5)

10^{18} J/year

	1970	%*	1985	%*
Aircraft Total	2,3	3,2	5,4	3,8
Transportation Total	17,7	24	30,4	22
United States Total	73,3	100	141,2	100

*Percent of total U.S. consumption

TABLE 2. Aircraft Energy Consumption in the United States in 1970, and Projected in 1985. (Ref. 5)

During the early part of 1973, jet fuel shortages began to disrupt the operations of some airlines.(6) During the latter half of 1973, international conflict and resultant oil price increases and supply reductions seriously affected the availability of fuels manufactured from the middle distillate fraction of oil (home heating fuel, gasoline, diesel and jet fuel.) The present "energy crisis" is of course symptomatic of a larger disease: the ever-increasing demand in the U.S. for energy of all kinds; total consumption increased from 35×10^{18} J/y in 1950 to 45×10^{18} J/y in 1960, and skyrocketed to 72×10^{18} J/y in 1972.(7,8) Table 3 indicates the distribution of energy sources in the U.S.; it is clear that even with increased imports of oil, coal and nuclear energy will occupy a larger position in the future U.S. energy picture.

ENERGY SOURCE	10^{18} J/year			
	1970	1975	1980	1985
Domestic Oil	23,9	24,5	25,2	25,0
Import Oil	6,5	14,9	23,1	31,7
Domestic Natural Gas	23,8	21,7	19,3	15,4
Import Natural Gas	1,1	1,7	4,0	6,2
Syngas	----	0,4	0,7	1,1
Coal	13,8	18,0	22,7	28,6
Hydroelectric	1,9	2,7	2,9	2,9
Nuclear	0,4	3,6	9,5	19,8
Geothermal	----	0,5	0,7	0,9

TABLE 3. United States Projected Energy Demand by Source Through 1985. (Ref. 7)

The shift from dependency on fossil fuels is inevitable, and alternate fuels for aircraft must be developed. It is doubtful that storage batteries and motors or nuclear power will ever be widely applicable to aircraft, so a liquid synthetic fuel appears to be an attractive possibility. Liquid hydrogen (LH2) has a high energy-to-weight ratio and burns cleanly with no carbon monoxide and no unburned hydrocarbons, but with some nitric oxide which can be controlled to very low levels by properly designed combustors. If hypersonic (above Mach 3,5) turbojet aircraft are developed for air transportation systems in the future, LH2 is clearly the most suitable fuel.(9)

Hydrogen Economy

In the "hydrogen economy" concept, all of the energy required by the economy is generated in central power stations, with hydrogen as the primary mechanism for transporting energy. Nuclear energy (fission and eventually fusion) is expected to become the primary source of energy with support from solar, geothermal and hydroelectric sources.

One proposed scheme envisions offshore nuclear plants of 50 GW generating capacity electrolyzing sea water to form hydrogen and then piping the liquified hydrogen to distribution centers to be used as a fuel for transportation, industrial and home applications, or for conversion back into electricity by fuel cells or by conventional steam power plants.(10)

Hydrogen has a history of use in the U.S. space program and in industrial applications. Several large electrolyzer plants exist now for supplying hydrogen to the ammonia and fertilizer industries. Pipelines carrying hydrogen over distances of up to 80 km are in operation in the Houston, Texas area. In the Ruhr area of Germany a hydrogen delivery pipeline network extends for 210 km. Much of this network has been in continuous operation since 1940.(11)

Liquid Hydrogen as a Jet Engine Fuel

Properties of LH2 are compared with a conventional hydrocarbon jet fuel, JP-4, in Table 4.

Property	LH2	JP-4
Density (g/cm^3)	0,0708	0,773
ΔH_c (kJ/g)	121,4	42,9
ΔH_c (MJ/1)	8,58	33,16
Freezing Pt. (°C)	-259,20	-60
Boiling Pt. (°C)	-252,77	121/288

TABLE 4. Thermochemical Properties of Liquid Hydrogen and JP-4. (Ref. 13 and 14)

In 1956, Pratt and Whitney Aircraft successfully ran a converted J57 jet engine on LH2.(12) The excellent mixing and combustion characteristics of hydrogen were exhibited in single-can burners with simple axial tube injection. Acceptable burner can discharge temperature profiles (pattern factors) and combustion efficiencies (99+ %) could be obtained with about one-quarter the axial length required for hydrocarbon fuels. The very wide flammability limits of the hydrogen-air mixtures permitted stable engine operation with a combustion chamber temperature rise of less than 110°C. The excellent heat transfer characteristics permit long combustion-chamber life and satisfactory operation of gears and bearings without conventional lubrication.

In 1957, NASA's Lewis Research Center installed an LH2 fuel system on a B-57 airplane and successfully operated one of its J65 turbojet engines at a flight speed of Mach 0,72.(2) A ram air heat exchanger was used to gasify the LH2 and helium was used to pressurize the fuel tank and purge the fuel system. Though not measured during flight, ground tests showed that the specific fuel consumption of the J65 engine using JP-4 fuel was 2,73 times that when hydrogen was used, in good agreement with the ratio of the heat of combustion of the two fuels.

Future air transportation looks toward aircraft of supersonic transport size flying at Mach 6. At these hypersonic speeds, a fuel is required which has both a very high energy content for engine performance and a heat-sink capacity sufficient to cope with the thermal environment experienced at hypersonic speeds. Liquid hydrogen has about 30 times the heat-sink capacity of JP-4, since JP-4 cannot be heated beyond 190°C.(2) An optimum range study for hypersonic flight(2) revealed that a Mach 3 LH2-fueled airplane has a greater range than a JP-fueled aircraft by more than 30 percent.

Of course, disadvantages also exist, primarily the problem of in-flight LH2 storage. Since LH2 has about one-quarter the energy per unit volume of JP-4, it requires four times the volume for the same total energy content. The cryogenic nature of LH2 adds to the problem of building lightweight fuel tanks for aircraft use. Wing tanks do not appear to be feasible. A recent study of LH2 feasibility for aircraft suggested that the upper-lounge lobe of a Boeing 747 "jumbo jet" could be extended the full length of the fuselage to provide a $6,8 \times 10^5$ litre fuel tank.(1)

Production and Cost of Liquid Hydrogen

If all of the U.S. fuel requirements for airplanes in 1970 had been supplied by LH2, a production capacity of $52,8 \times 10^3$ t/d (metric tons per day) would have been required. The total LH2 production capacity in the U.S. at that time was 136 t/d with the largest plant having a production capacity of 54 t/d.(13) Using existing liquification technology, plants having a capacity as large as 227 t/d could be built.(15) However, a single HST flying 8046 km (5000 miles) a day at Mach 6 would consume 91 t/d (3.4 million gallons/day) of LH2.(16) Obviously, the U.S. LH2 production capacity will have to increase significantly if LH2 is to become marketable as a jet fuel.

The most economical method of producing LH2 at present is by steam reforming with hydrocarbons, which costs about 0,18 \$/kg. The cost of producing LH2 by electrolysis in 1971 (not including marketing and distribution) was about 0,44 \$/kg. However, with production geared to the HST system, an electrolytic LH2 plant with a capacity of 2268 t/d could be competitive.(13) According to Peterson and Waters(17), the cost of LH2 will be about 0,33 \$/kg ($2,7 \times 10^{-9}$ \$/J) early in the introduction of the hypersonic fleet. The early 1973 cost of jet fuel delivered at the aircraft was about 0,05 \$/kg or $1,3 \times 10^{-9}$ \$/J.(6) Figure 1 shows the relative energy cost of LH2 compared to jet fuel during the past ten years.(2)

Transportation, Handling, and Storage of Liquid Hydrogen

The transportation, handling, and storage technologies for LH2 are well developed and little further technological development is necessary for safe and efficient handling of significantly greater amounts of LH2.

Transporting of LH2 is done by highway transport and railroad tankers. In the U.S., highway transports of 50 x 10^3 litre (13000 gal) capacity are commonplace and some special 75 x 10^3l highway transport trailers have been built.(18) Railroad tankers with 100 x 10^3l capacity and some with 130 x 10^3l capacity are in common use. Boil-off losses of 0.25% per day can be expected from the 50 x 10^3 litre capacity highway transports, with less for the larger vessels.

Vacuum-jacketed transfer lines for LH2 have been built with inside diameters of from five to fifty centimeters and lengths up to a few thousand meters. Operating pressures in these lines are as high as 138 bar (2000 psi). At the Nuclear Rocket Development Station in Nevada, LH2 has been transferred at rates up to 133 x 10^3 l/min(35000 gal/min).(18) At this transfer rate, 1,6 hours would be required to deliver the LH2 fuel to an HST for one 8000 km flight using one delivery line.

Also at the Nuclear Rocket Development Station in Nevada, vacuum-jacketed, perlite-insulated LH2 storage vessels have been built with capacities of up to nearly two million litres.(18) Boil-off for such dewars is of the order of 0,05% per day; the holding time is greater than 5 years. The cost of dewars of this size is roughly 0,50 $/l capacity. No further developments would be required to build dewars of this type up to eight or nine million litre capacity. For non-vacuum jacketed storage, dewars of up to tens of millions of litres capacity should be capable of being fabricated by current techniques.

Aircraft Liquid Hydrogen Fuel Tanks

As already mentioned, onboard storage of fuel LH2 is a problem due to its cryogenic nature and its low energy per unit volume. The wide flammability limits of hydrogen also present a serious problem. Witcofski of the U.S. NASA-Langley Research Center assessed the fuel containment problem as related to an HST as follows:(2)

> "Containment of the liquid hydrogen fuel requires consideration of safety aspects as well as minimization of the heat transfer to the fuel. Because of the wide flammability range of LH2, the space between the tank wall and the outer skin of the airplane will likely by purged with an inert gas, such as nitrogen.
>
> Unless the purge gas is prevented from coming into contact with the cold tank wall, cryopumping will result, causing high heat transfer to the fuel. Attempts to construct flight weight, vacuum-tight shells around the tanks have proved unsuccessful. If the fuel tanks are

> housed with a 'hot structure' airplane, two layers of external tank insulation might be used."

Witcofski also discussed the use of slush hydrogen (50% liquid/ 50% solid) as a means of decreasing fuel volume (14% reduction compared to LH2) and significantly reducing in-flight fuel boil-off.

One proposal for subsonic aircraft is the addition of cryogenic outboard wing tanks which, as a safety measure, could be released if necessary.(10) Further research is definitely needed in this area, and whatever finalized tank design is arrived at will dictate what LH2 production storage and distribution facilities will be required.

Safety of Liquid Hydrogen Use

Public skepticism concerning the safety of hydrogen, due in part to the widely publicized explosion of the dirigible "Hindenburg" in the 1930's, must be overcome before hydrogen will have public acceptance as a jet engine fuel. Large segments of the public are probably unaware that synthetic fuel gases designated "producer" gas, "manufactered" gas, "oil" gas, "water" gas, and "town" gas, commonly containing from 15-85% hydrogen, were formerly distributed to residences in cities in many countries with relative safety.(18) Gaseous hydrogen has also been used safely for years in chemical processing, heat treating, and the food processing industry.(19) Large quantities of LH2 have been used safely in the U.S. space program.

Following is a comparison of some properties of hydrogen and its dangers relative to methane:(18)

1) Hydrogen's shorter quenching distance makes it more dangerous than methane (0,06 cm vs. 0,25 cm). (Quenching distance is the distance between surfaces that will just permit a flame to pass without being cooled to extinction.)

2) Hydrogen's lower ignition energy makes it more dangerous than methane (0,02 mJ vs. 0,3 mJ).

3) Both hydrogen and methane are non-toxic.

4) Hydrogen has a higher diffusivity than methane (0,634 cm/sec vs. 0,20 cm/sec) which causes it to leak faster, but also to dissipate faster.

5) Hydrogen has a wider explosive range in air (4-75%) compared to methane (5-15%), but the lower explosive limit is the one which must be avoided, and this is essentially the same for both fuels.

6) Hydrogen has a higher ignition temperature than methane (858 K vs. 811 K) which makes hydrogen less dangerous than methane.

7) Hydrogen does not produce the toxic combustion products carbon monoxide and smoke.

The handling of liquid hydrogen for expanded commercial application will not be difficult as long as existing safety standards, regulations, and specifications are followed.(19) The extremely low temperature handling and potential leakage problems are recognized; equipment can be designed and personnel trained accordingly.(20) It is interesting to note that a spill of 2 x 10^3 litre (500 gallons) of LH2 in an unconfined area will diffuse to a non-explosive mixture in about one minute.(19)

Combustion and Pollution Characteristics of Hydrogen

The reduced environmental impact of jet aircraft fueled with LH2 results because hydrogen is the "cleanest burning" of all chemical fuels. A LH2-fueled aircraft would emit no carbon monoxide, no carbon dioxide, no particulate matter, and no unburned or partially burned hydrocarbons. It will be shown presently that oxides of nitrogen NO_x (NO and NO_2) can be significantly reduced since hydrogen can be stably burned at extremely lean fuel/air ratios in turbojet combustors. Formation of ammonia, NH_3, the other possible pollutant resulting from hydrogen/air combustion, is not chemically favored under fuel-lean conditions.

LH2-fueled aircraft would significantly reduce urban/near-airport pollutant loadings. Airports are now known to be significant and concentrated area sources of pollutant emissions,(21) due to aircraft taxi, takeoff, and landing approach operations.

A potential environmental/health danger connected with world-wide SST operations involves the possibility of stratospheric ozone depletion due to reaction with aircraft-emitted NO_x.(22) Depletion of stratospheric ozone would cause increased amounts of hazardous short-wavelength radiation to reach the earth's surface. Therefore, the major reduction in NO_x emissions achievable with LH2 should have an important impact on the environmental acceptability of stratospheric commercial flight. Low NO_x emissions can be achieved by injection of prevaporized LH2 into a well-stirred, near-homogeneous combustor primary zone. Due to the wide flammability limits of hydrogen, it can be stably burned at far lower fuel/air ratios and correspondingly lower flame temperatures than conventional jet fuels. Intense back-mixing and turbulent stirring in the combustor primary zone, together with hydrogen's high diffusivity, further minimize NO_x formation by eliminating fuel-rich hot spots. Pre-mixing of fuel and air could achieve even further homogeneity, but it will probably not be necessary.

Figure 2 presents measurements made by the authors of temperature and NO_x concentrations resulting from hydrogen-air combustion in a 67,4 cm^3 volume laboratory jet-stirred reactor, which features the intense turbulent backmixing required for steady-flow, fuel-lean, low NO_x combustion.(23)

In Fig. 2, the increase of temperature and NO_x with increasing $\dot{m}/V$ (decreasing residence time, $\tau = \rho V/\dot{m}$) indicates mixing controlled combustion while decreasing T and NO_x with increasing $\dot{m}/V$ indicates chemical-kinetically controlled combustion. The highest value of $\dot{m}/V$ measured for $\Phi = 0,310$ corresponds to incipient blowout; blowout was not achieved at $\Phi = 0,575$ due to temperature and fuel supply system limitations.

In addition to a well-stirred primary zone, a conventional turbojet combustor must have a secondary zone following the primary zone to ensure complete combustion, improve the uniformity of the temperature profile entering the turbine, and to cool (by dilution) the product gases to allowable turbine inlet temperatures (ca. 1250 K for non-cooled blades). The relatively slow kinetics of NO_x formation cause the NO_x to be largely "frozen" in the secondary zone so that NO_x concentrations in the exhaust are reduced below primary zone values due to dilution alone, and therefore may exceed equilibrium values based on local temperature and pressure by orders of magnitude.

With hydrogen as a fuel, however, a secondary zone may not be necessary; the primary zone may be operated at the overall or exit value of uniform fuel/air ratio, thus enabling low flame temperatures equal to the turbine inlet temperature (and correspondingly low NO_x concentrations) throughout. In addition, hydrogen/air kinetics are so rapid compared to hydrocarbon/air kinetics that combustion efficiencies greater than 99% may be achieved in the primary zone for residence times as low as five milliseconds.

In Fig. 3, results of computer calculations are shown for the intensely stirred primary zone of a hypothetical turbojet combustor at typical SST cruise conditions: Mach 2,7 flight at 20km altitude,(24) assuming an 88% efficient inlet diffuser, and compressor pressure ratio of 13,5.(25) These calculations employed the adiabatic perfectly-stirred reactor (PSR) calculational model(23) with the hydrogen/oxygen combustion kinetic mechanism of Jenkins et al.(26) and two NO_x formation kinetic mechanisms: Zeldovich NO_x kinetics, and an NO_x formation mechanism including N_2O production and decomposition.(27) Comparison of Figs. 2 and 3 for similar temperatures and residence times or $\dot{m}/V$ values, at low fuel/air equivalence ratios, shows much higher NO_x for the computer predictions. This is due to the increase in NO_x with increased pressure from 0,93 bar (Fig. 2) to 16 bar (Fig. 3). Also shown in Fig. 3 are the predicted combustion temperatures for a range of fuel/air equivalence ratios from 0,1 to 0,6. For the range of residence times plotted, reactor blowout was not approached, and consequently the predicted combustion temperatures were always very close to the corresponding equilibrium adiabatic flame temperatures shown. At $\tau = 10$ msec, combustion efficiency was 99%, while at $\tau = 1$ msec, this decreased to 96%.

At $\Phi = 0,2$ and for $\tau = 5$ msec (typical conventional turbojet combustor primary zone residence time), Fig. 3 shows NO_x ~80 ppm. Dilution with air (1100 K temperature) to reach a turbine inlet temperature of 1250 K then yields a combustor emission of approximately 20 ppm NO_x. If the combustor primary zone residence time is reduced to 1 msec by shortening the primary zone length, stable, efficient combustion of hydrogen still obtains, and NO_x emissions at combustor exit are reduced to 13 ppm. On the other hand, if a higher fuel/air equivalence ratio of $\Phi = 0,6$ is used, which gives a primary zone temperature of 2470 K, (typical of current combustors), then for a 5 msec primary zone residence time and with dilution to a turbine inlet temperature of 1250 K, the NO_x emission is about 900 ppm.

The extreme nonlinearity shown in the NO_x predictions of Fig. 3 is due in part to the fact that at combustion temperatures below 2000 K, the N_2O kinetic mechanism for NO_x formation dominates, while above 2000 K the Zeldovich kinetics control NO_x formation. Another reason for this nonlinearity is non-equilibrium combustion: super-equilibrium concentrations of oxygen atoms, and other combustion radicals (OH and H), are predicted by the PSR model, even though essentially equilibrium flame temperatures are calculated. Oxides of nitrogen formation for intensely stirred combustion is dependent on the first or second power of O-atom concentration. However, for an actual intensely stirred combustor, such as required for a homogeneous (no hot spots) turbojet combustor primary zone, O-atoms cannot at this time be predicted accurately, due to the lack of quantitative knowledge of the interaction between chemical kinetics and turbulent mixing. The PSR analysis likely predicts maximum NO_x levels, since maximum super-equilibrium O-atom concentrations--an order of magnitude above corresponding equilibrium concentrations--are predicted. For example, PSR calculations corresponding to the data shown in Fig. 2 give NO_x concentrations greater than measured by a factor of 2 to 4. However, this comparison between theory and experiment also indicates that non-equilibrium combustion phenomena (i.e., super-equilibrium O-atoms) are indeed mainly responsible for the measured NO_x levels. While the PSR predictions in Fig. 3 may be two to four times greater than actually occurring, the trends shown are probably correct. The NO_x predictions of Fig. 3 show the advantage of using a fuel such as hydrogen which can be burned stably, with good combustion efficiency, at very fuel-lean conditions and short residence times in a homogeneous turbojet combustor primary zone.

Conclusions

The future of liquid hydrogen LH2 as a jet engine fuel depends on the following interrelated factors:

1) The role of airplanes in future transportation systems...whether or not to build SST's and HST's.

2) Detailed research and development efforts concerning cryogenic fuel tanks, slush hydrogen, liquid hydrogen handling and storage, ground operations, and production volume geared to airlines.

3) Continued environmental problems due to combustion of hydrocarbon fuels.

4) Public acceptance of hydrogen as a safe fuel.

5) Fuel economics, actions of governments, and future energy developments.

6) Airlines' interest in searching for alternate jet fuels.

It is doubtful that liquid hydrogen will be in widespread use as a jet fuel prior to 1985. Even if the price/supply ratio for LH2 becomes favorable by 1985, significant structural changes in aircraft will be necessary to accommodate onboard storage of LH2; LH2-fueled aircraft will necessarily be a new or modified generation of aircraft. Aircraft under development at the present time would be expected to be in service until 1990 or 2000. But as rapidly as the fuels situation is changing at the present time, these aircraft may become obsolete within their useful lifespan of 15 to 25 years if they are designed solely for conventional jet fuel.

Acknowledgments

This work was supported in part by a National Institutes of Health grant to the Washington State University Graduate School (PCM), an Environmental Protection Agency Air Pollution Traineeship (KJA), the Washington State University Computing Center, and a grant from the General Motors Research Center, Warren, Michigan.

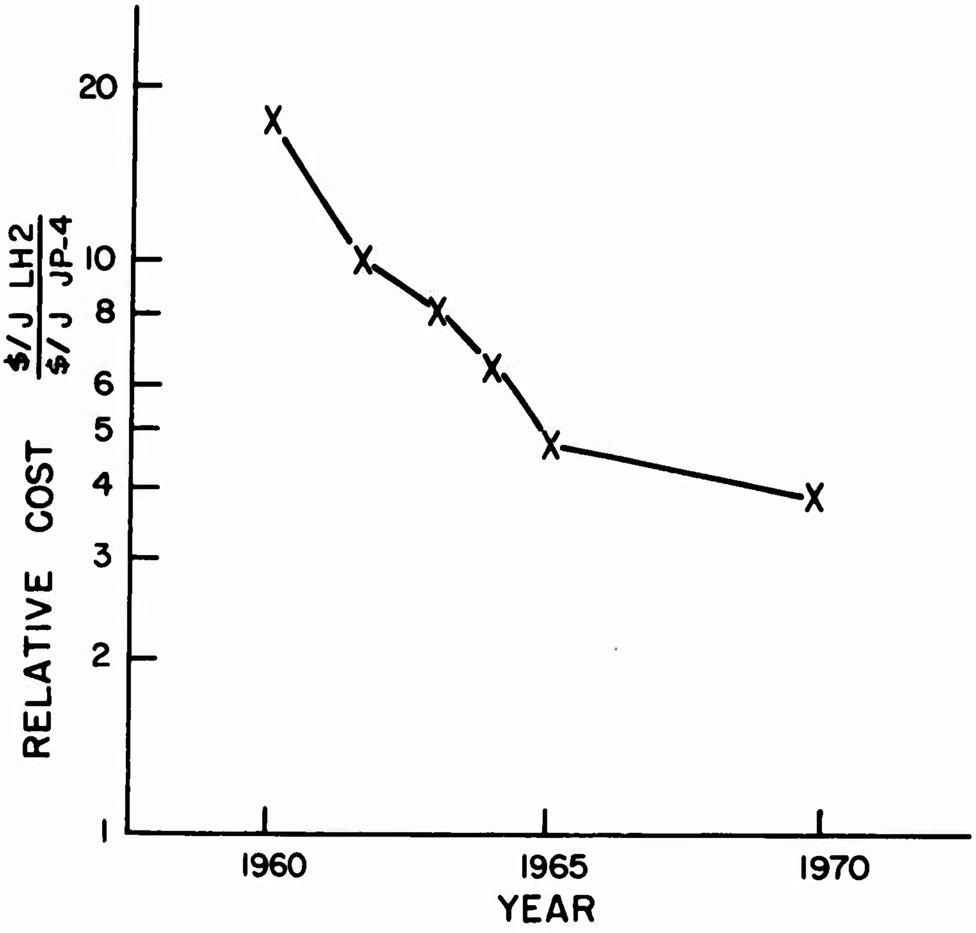

FIGURE 1. Relative energy cost of liquid hydrogen compared to conventional hydrocarbon jet fuel. (Ref. 2)

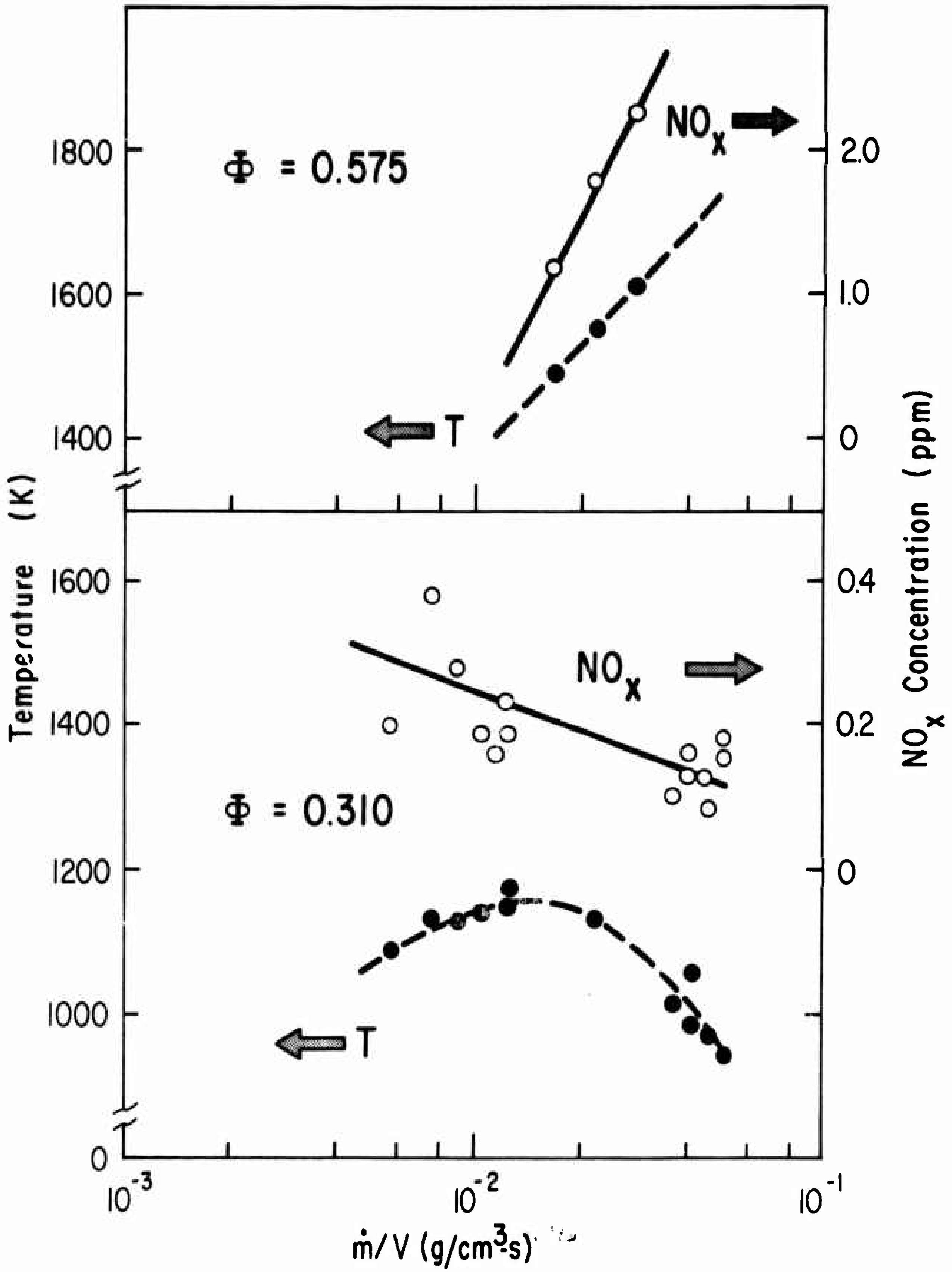

FIGURE 2. Temperature and NO_x concentrations for hydrogen/air combustion in a laboratory jet-stirred reactor for varying reactant mass flow rate per unit volume. P = 0,93 bar, fuel/air equivalence ratios Φ = 0,310 and 0,575. Premixed fuel/air inlet temperature T* = 300 K.

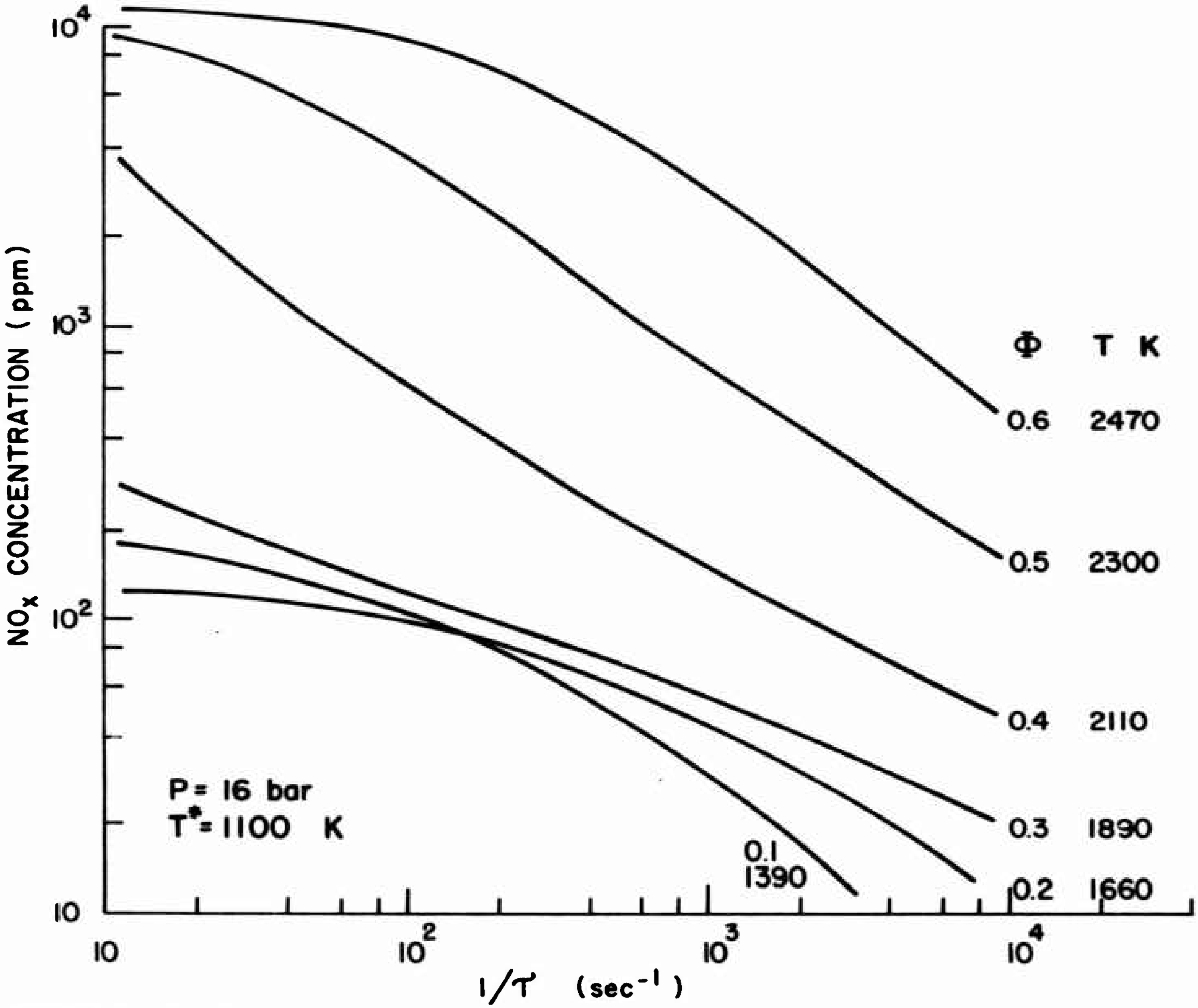

FIGURE 3. Predicted NO_x concentration variation with reciprocal residence time in combustor primary zone, modelled as an adiabatic, perfectly-stirred reactor: SST cruise conditions - Mach 2.7 at altitude 20 km.

REFERENCES

1. GOODMANSON, L.T. Boeing Commercial Airplane Company, Seattle, Wash., USA, private communication, December 1973.

2. WITCOFSKI, R.D. Potentials and Problems of Hydrogen Fueled Supersonic and Hypersonic Aircraft. Proceedings of the 7th Intersociety Energy Conversion Engineering Conference, San Diego, California, pp. 1349-1354, September 1972.

3. TIPTON, S.G. The Role of Air Travel in Transportation Systems. Traffic Quarterly, pp. 563-574, October 1971.

4. CARD Report Outlines 1985 Aircraft Goals. Automotive Engineering, Vol. 79, No. 10, pp. 38-41, October 1971.

5. SATRE, W.J. Energy Utilization--Today and the Future. Proceedings of the Energy Facts for Concerned Citizens Conference, Boise, Idaho, presented by The Colleges of Engineering of the University of Idaho and Washington State University, April 1973.

6. YAFEE, M.L. More Jet Fuel Pinches Expected. Aviation Week and Space Technology, pp. 19-20, January 22, 1973.

7. Energy 'Demand' Studies, An Analysis and Appraisal. Committee on Interior and Insular Affairs of the U.S. House of Representatives, 92nd Congress, 2nd session, September 1972.

8. McKETTA, J.J. Graphical View of Energy Supply and Demand. Chem. Eng. Prog., Vol. 68, pp. 24-28, October 1972.

9. BURNHAM, Frank. After SST: A Hypersonic Aircraft. American Aviation, pp. 36-37, July 22, 1968.

10. WILLIAMS, L.O. The Cleaning of America. Astronautics and Aeronautics, pp. 42-51, February 1972.

11. GREGORY, D.P. and WURM, J. Production and Distribution of Hydrogen as a Universal Fuel. Proceedings of the 7th Intersociety Energy Conversion Engineering Conference, San Diego, California, pp. 1329-1334, September 1972.

12. MULREADY, R.C. Liquid Hydrogen Engines. Chapter 5, Technology and Uses of Liquid Hydrogen, Pergamon Press, MacMillan Co., New York, 1964.

13. JONES, L.W. Liquid Hydrogen as a Fuel for the Future. Science, Vol. 174, No. 4007, pp. 367-370, October 22, 1971.

14. HAZARD, H.R. Gas Turbine Fuels. Chapter 4, Gas Turbine Engineering Handbook, Vol. II, Editor, John W. Sawyer, Gas Turbine Publications, Inc., Stamford, Connecticut, 1972.

15. TANNER, E.C. and HUSE, R.A. A Hydrogen-Electric Utility System with Particular Reference to Fusion as the Energy Source. Proceedings of the 7th Intersociety Energy Conference, San Diego, California, pp. 1323-1328, September 1972.

16. GREGORY, D.P., NG, D.Y.C. and LONG, G.M. The Hydrogen Economy. Chapter 8, Electrochemistry of Cleaner Environments, John O'M Bockris, Editor, Plenum Press, New York, 1972.

17. PETERSEN, R.H. and WATERS, M.H. Hypersonic Transports--Economics and Environmental Effects. J. Aircraft, Vol. 10, No. 6, pp. 334-341, June 1973.

18. BARTLIT, J.R., EDESKUTY, F.J. and WILLIAMSON, K.D.Jr. Experience in Handling, Transport and Storage of Liquid Hydrogen--The Recyclable Fuel. Proceedings of the 7th Intersociety Energy Conversion Engineering Conference, San Diego, California, pp. 1312-1315, September 1972.

19. MARTIN, F.A. The Safe Distribution and Handling of Hydrogen for Commercial Application. Proceedings of the 7th Intersociety Energy Conversion Engineering Conference, San Diego, California, pp. 1335-1341, September 1972.

20. Liquefied Hydrogen Safety--A Review. American Society of Safety Engineers Journal, pp. 18-23, May 1969.

21. GEORGE, R.E., NEVITT, J.S. and VERSSEN, J.A. Jet Aircraft Operations: Impact on the Air Environment. Journal of the Air Pollution Control Association, Vol. 22, No. 7, pp. 507-515, July 1972.

22. FERRI, A. Better Marks on Pollution for the SST. Astronautics and Aeronautics, Vol. 10, No. 7, p. 37, 1972.

23. BOWMAN, B.R., PRATT, D.T. and CROWE, C.T. Effects of Turbulent Mixing and Chemical Kinetics on Nitric Oxide Production in a Jet-Stirred Reactor. Proceedings of the 14th Symposium (International) on Combustion, The Combustion Institute, Pittsburgh, Pa., 1972.

24. SWIKART, J.M. Our SST and its Economics. Astronautics and Aeronautics, Vol. 8, No. 4, p. 30, 1970.

25. TAYLOR, E.S. Evolution of the Jet Engine. Astro and Aero, Vol. 8, No. 11, p. 64, 1970.

26. JENKINS, D.R., YUMLU, V.S. and SPALDING, D.B. Combustion of Hydrogen and Oxygen in a Steady-Flow Adiabatic Stirred Reactor. Eleventh Symposium (International) on Combustion, The Combustion Institute, Pittsburgh, Pa., pp. 779, 1969.

27. MALTE, P.C. and PRATT, D.T. Oxides of Nitrogen Formation for Fuel-Lean, Jet-Stirred Carbon Monoxide Combustion. Paper 73-37, WSS/Combustion Institute, Fall Meeting, El Segundo, California, October 1973.

1

PERFORMANCE PROBLEMS RELATED TO INSTALLATION OF FUTURE ENGINES IN BOTH SUBSONIC AND SUPERSONIC TRANSPORT AIRCRAFT

Walter C. Swan
Director of Technology, Boeing Commercial Airplane Company

1.0 Introduction

The requirement for variable-cycle engines has been abundantly clear to many airframe system designers for years. It is the next logical step in aircraft development in a long series of variable-geometry aircraft features which have occurred since the Wright brothers' first flight. The designers have solved problems of previous aerodynamic configurations for several special flight conditions through the use of variable flaps, leading-edge devices, ailerons, flaperons, elevons, spoilers, sweep, camber, and even variable dihedral. Similar variable or adjustable features have been provided to empennage components, landing gears, and flight cabs. In most cases, these added complexities have been conceived to solve problems in either performance, ride quality, or handling quality at selected operating points in the aircraft mission.

The advent of the multimission aircraft, in both the military and the commercial fields, is now forcing the designer to consider additional means of better matching the important multiple uses of the vehicle. This paper draws particular attention to concepts for variable-geometry engines and the potential that such concepts may provide for further improvement and refinement of multimission aircraft. The principal goal of any variable-cycle engine concept is to improve the total range or the flexibility of a given multimission aircraft, while reducing weight and cost, to perform a prescribed mission range. In accomplishing this goal, the propulsion system concept must be treated as an entity, including the intake and exhaust system, such that reduced weight, drag, and complexity of these latter components may be traded for increased weight and complexity of the variable cycle.

Certain secondary benefits of variable-geometry engines may offer unique solutions to other aircraft problems which are not normally thought of in multimission considerations. For example, these same variable-cycle concepts may provide outstanding solutions to aircraft center-of-lift control on V/STOL aircraft during landing and takeoff. As another example, the noise near airport boundaries may be significantly reduced through an alternate engine cycle on landing and takeoff.

This paper uses the supersonic transport and the noise-sensitive commercial STOL aircraft to illustrate the potential for performance improvements obtainable with a variable-cycle engine. Several alternative concepts of variable-cycle engine configurations, which should be investigated to define the benefits to such vehicles, are described. Finally, a few provocative thoughts will be presented on how to accomplish such an engine development. With the present world fuel shortage, the tremendous potential for a reduction in energy consumed per seat-mile should offer incentive for an assault on new approaches to variable-cycle engine design.

2.0 The Multimission Problem

The airframe and engine designer each attempts to maximize performance at minimum cost and weight when configuring his respective components of the aircraft system. Characteristically, the airframe designer attempts to maximize the aerodynamic efficiency lift/drag while the engine specialist maximizes the propulsive efficiency the flight velocity/specific fuel consumption (V/SFC). Each tries also to optimize the weight of his respective components.

Problems often exist as to territorial rights concerning design responsibility, which causes bookkeeping systems and data validation processes to go astray.

When the aircraft is designed for a single mission, the problem is bad enough, but when more than one mission is demanded for the vehicle, then real technical and territorial problems result. As airport noise constraints get tougher, the single-mission problem becomes a dual one, because noise goals and cruise objectives are no longer compatible.

Consider only the cruise propulsion system for the moment. Figure 1 illustrates the alternatives available through changes in cruise Mach number for the multimission vehicle. Shown are representative desires of engine configuration, intake, and nozzle over the speed spectrum of interest for aircraft today. If one wanted to cruise at Mach 0.80 for long range, but also wanted to fly at Mach 2.20, one readily sees that the desire is for a moderate bypass ratio (5-8) turbofan with a pitot intake and a fixed convergent nozzle at the low speed. At the higher speed, one might want an augmented turbofan or turbojet, depending on the vehicle configuration, and would want an external compression intake and some form of variable convergent-divergent or ejector nozzle. Thus, many of our mixed mission aircraft today have very complex variable-geometry intakes and nozzles, which are often a source of many unpredictable drag, weight, operational, and maintenance headaches. Until now, the engine has been pretty much left alone, except for reheat options. The picture gets much more complex as the split in range at the different speeds varies, as the cruise altitude for each speed is changed, and when considerations for reserves, loiter, in-flight refuel, climb rates, field lengths, noise goals, and other primary or secondary mission objectives are added.

3.0 The SST Opportunity

As one example of the opportunity for variable-cycle engines, the former Boeing SST will be used to illustrate the complication of the design integration exercises required and to indicate the benefits from one such variable-cycle engine concept.

Figure 2 illustrates the Boeing B2707-300 SST, which was a 750,000-lb vehicle design to fly from Paris to New York with 300 passengers. The design mission is shown in Figure 3. The aircraft had four General Electric GE4 turbojet engines, each housed in a carefully contoured pod at the aft end of the cambered and twisted double-delta wing planform. The aircraft and engine configuration were matched to meet noise goals approaching FAR 36 at the airport, operate from 12,000-ft fields, climb and cruise subsonically at Mach 0.90 at least 200 miles to avoid sonic booms, then climb to a cruising altitude of 60,000 ft at a Mach number of 2.70. It would fly the Atlantic at that speed, descend to 35,000 ft, and cruise again at Mach 0.90 for 200 miles to its destination. This vehicle would have been used by the airlines as a multimission vehicle, because subsonic cruise would have been required over inhabited land masses and for a variety of mixed missions on selected airline intercontinental routes.

Figure 4 illustrates the physical differences between the SST propulsion pod and a modern subsonic transport pod. Note that the SST intake is three diameters in length as opposed to less than one diameter for the subsonic intake. The complications of this intake and its influence on weight will be discussed later. The SST exhaust system is also much longer and more complex than the subsonic jet. Shown in Figure 4 is a convergent-divergent SST nozzle with a multitube stowable suppressor, which was one concept under development at the time of the SST program termination. A main point to be emphasized here is the tremendous number of complications and weight problems which were involved in the intake and exhaust systems to "condition" the environment for the engine.

Figure 5 shows a comparison of the pressure recovery variation with Mach number of the simple pitot intake and the SST intake. The recovery of the pitot intake is great at subsonic speeds but poor at higher supersonic speeds due to normal shock losses. While the SST intake was 2% poorer than the pitot intake at subsonic speeds, it did achieve 92% recovery at Mach 2.70. Performance of the pitot intake at Mach 2.70 is very poor, and this is why the intakes must be different.

Figure 6 shows the engine airflow demand curve as a function of flight Mach number for a climb at full power to supersonic cruise. Superimposed is the intake capture flow capability that was achieved after many variable-geometry features were added to match the engine over the flight envelope. It is seen that complete matching of this high-performance intake to the engine demand curve at all flight speeds and altitudes was impossible to obtain. With the intake fully started at Mach 1.60, overboard spillage and internal bypass of air was necessary. With the intake unstarted below Mach 1.60, it was necessary to resort to movable throat doors in combination with the translating plug in order to avoid starving the engine of flow. In general, weight and complexity were added to minimize spillage and bypass drag. Note, however, that the reduced power setting at subsonic cruise still causes considerable spillage and bypass drag.

Some attempt was made by General Electric to get high flow in the engine at Mach 2.70 cruise and to spool down the engine during transonic climb to assist in this intake-engine match solution. But basically this was a fixed-geometry engine whose pumping characteristics were tied to throttle movement and nozzle position.

Figure 7 shows the complication of the SST intake, including translating centerbody, throat doors, bypass doors, takeoff doors, and secondary flow valves. All of these devices were needed to match this fixed-cycle engine.

Figure 8 shows a buildup of the drag increments for the intake portion of the SST propulsion system in both the started (above Mach 1.60) and unstarted (below Mach 1.60) modes. Note that the drag is maximum in the transonic region where large amounts of centerbody spillage and normal shock spillage dominate the drag picture. With some form of variable geometry in the engine, both the centerbody and normal shock spillage terms could be reduced. Similarly, during the climb to supersonic speed, additional drag due to centerbody spillage, bypass spillage, and bypass door leakage could be reduced or eliminated through engine cycle modification. The net effect of these intake drag increments is expressed as an airplane drag increment in Figure 9. The interference drag imposed on the wing due to overboard spillage is not included.

Turning to the exhaust system of the SST, Figure 10 shows one proposed nozzle concept that was designed to meet FAR 36 noise rules at the airports. It is shown here to note the effect of reduction in jet noise, on exhaust systems weight and complexity, and the multimission requirements of good nozzle performance at subsonic as well as at supersonic speeds.

Figure 11 shows the gross thrust coefficient as a function of flight Mach number for an SST-type nozzle compared to a simple convergent nozzle. In both cases, the top line represents the internal performance, and the bottom line shows the gross thrust coefficient when external boattail and separation drag are included, such as would be measured on a wind tunnel balance. As expected, the simple nozzle offers a distinct advantage up to cruise speeds of Mach 1.00, but has no place on an SST which must cruise at Mach 2.70.

Of particular interest in Figure 11 is the fact that subsonic aircraft usually cruise at less than maximum available thrust, and therefore the gross thrust coefficient usually improves at lower power settings because underexpansion losses are reduced. This is the predominant loss in the simple nozzle at high speeds. However, the SST nozzle can operate as a C-D nozzle to eliminate the underexpansion loss, but it requires a larger boattail angle at the reduced power because of the reduced nozzle pressure ratio, expansion ratio, and airflow.

Figure 11 illustrates the need to increase the volume flow in the exhaust nozzle (at constant thrust) to fill up the nozzle base and to operate at more favorable boattail angles with the C-D nozzle. Some form of variable geometry in the engine could help solve this problem. Figure 12 shows the isolated pod boattail drag of the SST nozzle, and it also shows the drag reduction that is possible if the engine volume flow could be adjusted to allow a more favorable ejector flap position. This drag estimate does not include the unfavorable interference wing drag that results from the present boattail angles or the influence of intake spillage and overboard bypass on boattail separation at the subsonic cruise conditions.

Figure 13 shows the buildup from bare engine to fully installed SFC at Mach 0.90, for the typical subsonic and supersonic installations. Losses that are not throttle sensitive (e.g., skin friction drag) are normally included in the airplane drag polar; however, this item is included in Figure 13 to show its relative magnitude. The striking thing is that the installed SFC of the subsonic pod is 50% lower than that of the supersonic pod. Although the major difference is due to the engine cycle, the supersonic nacelle also suffers by the off-design losses of the intake and exhaust system. Anything that can be done to make the intake and nozzle flow full could improve the subsonic SFC of the SST. It must be remembered that there are subsonic legs in the SST mission, and reserves are based on subsonic cruise to alternate fields. Based on this comparison, a reduction in subsonic SFC of 50% is theoretically possible; however, a practical variable cycle with supersonic nacelle could probably achieve 30% reduction–which is significant.

Thus far, the emphasis has been on opportunities for improved drag and fuel consumption, although it has been noted that the weight of both the intake and nozzle for the SST appears to be a large percentage of the total propulsion system weight. Figure 14 shows the relative weight of the subsonic and supersonic propulsion pods expressed as a percentage of the bare engine weight. It is seen that the intake and exhaust system combine to double the engine weight on an SST, while they only represent about a 20% increment on the subsonic installation. The hardware elements provided in the SST installation that are necessary to accommodate the requirements of the fixed turbojet engine cycle are shaded in Figure 14. If the engine cycle were variable, over 60% of the excess weight for installation could be offered as a trade for increased engine weight.

Table 1 lists the equivalent weight that could be saved on the SST with a variable cycle. This staggering total of 61,000 lb is equivalent to the entire design payload of the SST. These items include some of the major benefits of variable cycle on the SST, such as improvements in weight or reductions in complexity of the nacelle, subsonic SFC, and noise. Figure 15 shows the actual weight breakdown of the SST components, including trip fuel and reserves, to show the relative importance of subsonic fuel, climb fuel, and pod weight.

The multimission capability of the SST could be improved with the variable-cycle engine as shown in Figure 16. Only the change in subsonic SFC was considered in this comparison. Design gross weight, OEW, payload, and fuel capacity were held constant for both engines. This figure shows that the total range decreases for the turbojet if the subsonic portion of the mission is increased. With the variable-cycle engine, the total range would increase as the subsonic range fraction increased. On an all-subsonic mission, the variable engine would fly 4800 nmi as opposed to 3000 nmi for the turbojet.

It is realized that these data simply indicate the potential gain. Any variable-cycle engine will probably eat into this group of offered items because it will occupy more volume than the present turbojet and may be heavier. But this type of challenge should serve to excite the inventive engineer.

4.0 Quiet Commercial STOL Transport

A second example where the variable-cycle engine may come into existence is now discussed.

Continued study of the commercial short takeoff and landing (STOL) transport suggests that it will only come into existence if it can be done economically in competition with CTOL aircraft. At the same time, the STOL aircraft must provide a much smaller noise footprint area for the same payload-range than its CTOL competitor. It is this potential for noise reduction which will allow the STOL civil transport to replace the CTOL aircraft in the short-haul market. Commercial STOL will be intercity transportation under 500 miles in range. The same aircraft should also be capable of flying ranges up to 1000 miles under CTOL rules in as economical a manner as competing CTOL vehicles.

The short-haul passenger is willing to pay some increased ticket price over an equivalent CTOL ticket, in exchange for a more convenient airport location; but he will not pay a large excess over that for a ticket on a train plus that for connecting ground transportation when considering the time saved.

With the prospects of a fossil fuel shortage extending for many years, much of the intercity travel now accomplished by automobiles may be competed for by the train, bus, and the short-haul aircraft. Hence, energy consumption per seat-mile and pollution consequences will probably determine which mode survives.

Present thinking on STOL transports leaves much to be desired, both in terms of operating economics, fuel consumed, and aircraft complexity. Figure 17 illustrates several powered lift concepts currently under consideration for STOL transports. Externally blown flap (EBF) and the internally blown flap (IBF) concepts tend to employ very high bypass ratio fixed or variable pitch fans at 8-15 bypass ratio. These engines are chosen to minimize flap interaction noise caused by the primary nozzle efflux. Such engines, as now conceived, are very large in diameter per unit of static thrust and produce very poor climb and cruise thrust due to their poor lapse ratio. Installing four such engines under a wing probably requires a high-wing configuration. Problems with wing flutter, cabin interior noise, ability for passenger egress, and tail interference with inboard engine efflux become some of the unsatisfactory consequences of the large engine, wing mounted installations. Perhaps the reduced climb and cruise thrust of such large fixed cycle engines may be tolerable because it may become necessary to trade flight speed for trip fuel in the present fuel crisis.

Vectored thrust concepts may be a very efficient means of obtaining good powered lift, but the same problems with noise exist as with the IBF and EBF concepts.

The upper-surface blowing (USB) concept offers some improved opportunity for low noise due to wing shielding, and perhaps the engine diameters can be smaller (bypass 5-8) for the same noise footprint as the IBF and EBF concepts. In this type of configuration, the cabin noise for low-wing configuration and wing trailing-edge shear noise are still possible problems. Intake noise may become the dominant noise source as lower exhaust noise occurs, and some increased drag penalty must be paid for this engine location because of the increased nacelle length.

The augmentor wing (AW) concept requires large internal airflow through the strut and wing. As a propulsive lift concept, it depends on an ejector flap to offer the propulsive lift. A real attraction of this concept is that it offers a possibility for very low noise. The power jet flap (PJF) is an alternative arrangement of the augmentor wing.

Figure 18 shows the relative noise capability of a series of competitive airplane designs using each of these lift concepts. The sideline noise of a Boeing 727 aircraft at 500 ft is approximately 113 PNdB to indicate why STOL is being given consideration for operation at many current general aviation airports of 3000-5000 ft in length.

Figure 19 shows a comparison of the low-speed lift/drag polars of the various concepts based on Boeing wind tunnel tests. It shows that all concepts are quite competitive for short-field operations with USB and AW concepts offering the best promise for minimum noise contours.

Figure 20 indicates current estimates of the payload/gross weight ratio and sideline noise as a function of operating field length for each of these competing configurations, based on Boeing systems studies. Also included are the effects of off-loading payload on both 727 and 737 airplanes to meet the requirements for shorter field lengths than are currently in use. Illustrated also are the effects of resizing the bodies of a 727 and a 737 to operate at reduced payload at full load.

The importance of Figure 20 is the tremendous disparity between the payload/gross weight ratio of all STOL aircraft and optimum current CTOL aircraft. At the same operating range, speed, and payload, the direct operating costs (DOC) are proportioned to aircraft payload/gross weight ratio. Hence, it is readily seen that STOL as currently understood is too expensive to be competitive. The primary problem stems from engine diameter, engine weight, nacelle drag, and poor thrust lapse rate.

For STOL to offer an economic challenge to CTOL, there must be created some form of variable-geometry engine that reduces the diameter per unit of static thrust and one wherein the climb and cruise thrust can be augmented to meet the demands of speed and range. The turboprop is not the solution, particularly as aircraft get larger. To date, little attention has been given to the use of multicycle engines for STOL. Figure 21 shows the influence of bypass ratio on cruise fuel consumption and climb thrust per pound or airflow for fixed-geometry turbofans. Also shown are recent estimates of the potential for variable geometry.

5.0 Concepts of Variable-Cycle Engines

While the engine industry for years has been employing variable stators to regulate the flow capacity of compressors, and more recently has developed some variable-stagger turbine components to regulate the pumping characteristics of turbojet and turbofan engines, the promises of large variations in cycle or pumping characteristics have not been realized to any great extent with this concept. On the SST, several attempts were made by the General Electric Company to get high and low flow in certain phases of the flight envelope with variable-turbine area, but only small gains were indicated, and hence these efforts were abandoned.

It is suggested that efforts to increase the flexibility of such gas generator parts should continue. Variation in the combustor arrangement and number of burning zones could also be exploited to improve the thermal efficiency at off-design conditions. But besides this type of activity, a bold approach to variable-cycle engine concept development needs to be taken. Figure 22 illustrates a few of many concepts that may fulfill the goals suggested in this paper. The configurations shown include most of the known types of variable devices such as series and parallel arrangements of gas generators, fans that employ airflow valves, common turbines, common fans, and in some cases common shafts. Each concept offers different degrees of flexibility which could be expanded to cover increased numbers of design-point operating conditions. The volume occupied by each concept becomes important only in the way it affects the shape and hence the drag of the aircraft for the desired multimission capability. The weight of such composite engines will, of course, be greater than that of the current fixed cycles, and there may be operating restrictions which may rule out their use. But equivalent weight savings in other parts of the aircraft may more than offset the weight of the variable device. In the SST example, this amounted to 20% of the baseline operating empty weight when a fixed cycle is replaced with a variable cycle.

6.0 How Does This Get Done?

The most difficult question is not whether variable-cycle engines are worth studying, or whether variable concepts can be evaluated, but how does industry get started doing the job. It should be clear that for any variable-cycle propulsion system to be developed beyond the concept stage, reasonble proof of a concept must be demonstrated to the satisfaction of the customers. This requirement alone forces industry, in cooperation with its customers' governments and others, to develop more satisfactory methods for sorting out thrust, drag, weight, and lift on such integrated aircraft-engine systems. Fortunately, such work is going on, at least in the United States, and much will be gained by this effort. Having accepted that adequate evaluation methods will exist, a very important new ingredient in the evolutionary process of engines and aircraft needs to be introduced.

In the commercial business today, when an airframer wants an engine, he issues a specification that defines the thrust, SFC, and weight goals but little else in the way of restraints to the engine manufacturer. The engine company will look at that specification as one of many uses for his products, and the process of trading goes on. In the end, the engine offered is a compromise between what the airframer wanted and what many other customers wanted. It gets more complicated by the different mounting systems, accessory locations, kinds of cowling, and often whether the engine is wing mounted, aft-body mounted, and even whether the wing has a pivot. Since commercial engine development usually follows some military development program, the time lapse between engine start and airplane start is not too critical. In the military arena, a somewhat similar situation exists, but there is now a third party that must be satisfied. It is not believed possible that an outstanding variable-cycle engine can be conceived and developed to achieve its full promise in the present environment employed in engine development.

The author would like to suggest for consideration two alternative methods, which are summarized in the concluding remarks. The first of these is teaming. It simply means that for the purpose of a given mission task, a joint venture is undertaken so that the general arrangement of the airplane and the propulsion system can be controlled under one roof. This approach would not be in conflict with engine component development or gas generator upgrading such as are currently being done by the engine manufacturers. The variable-cycle concepts and other engine development programs would use such technology as building blocks. This teaming method of airframe system concept selection and development can work with the highest possible efficiency in the use of both companies' resources.

For those who object to teaming as being anticompetitive, an alternative is to encourage both airframers and engine companies to know as much about each other's business as is necessary for conceptual evaluations. We should encourage the engine manufacturer to develop expertise in airframe design, at least to the point where he can explore engine cycle arrangements in a meaningful, mission-oriented manner. Today this is far from being done. Concurrently, encouragement should also be given to the airframer to develop his expertise in engine configurations, at least to the point where he can conceive meaningful engine-airframe arrangements.

This latter approach is taken today by the airframer in selecting most of the other aircraft subsystems, but it is not in general use for the propulsion system. It is realized that either of these methods may conflict with the established thinking of many of our leading authorities, but until some similar plan is found acceptable within the industry, governments, and/or airlines, it is doubtful that the full promise of the variable-cycle engine will be realized.

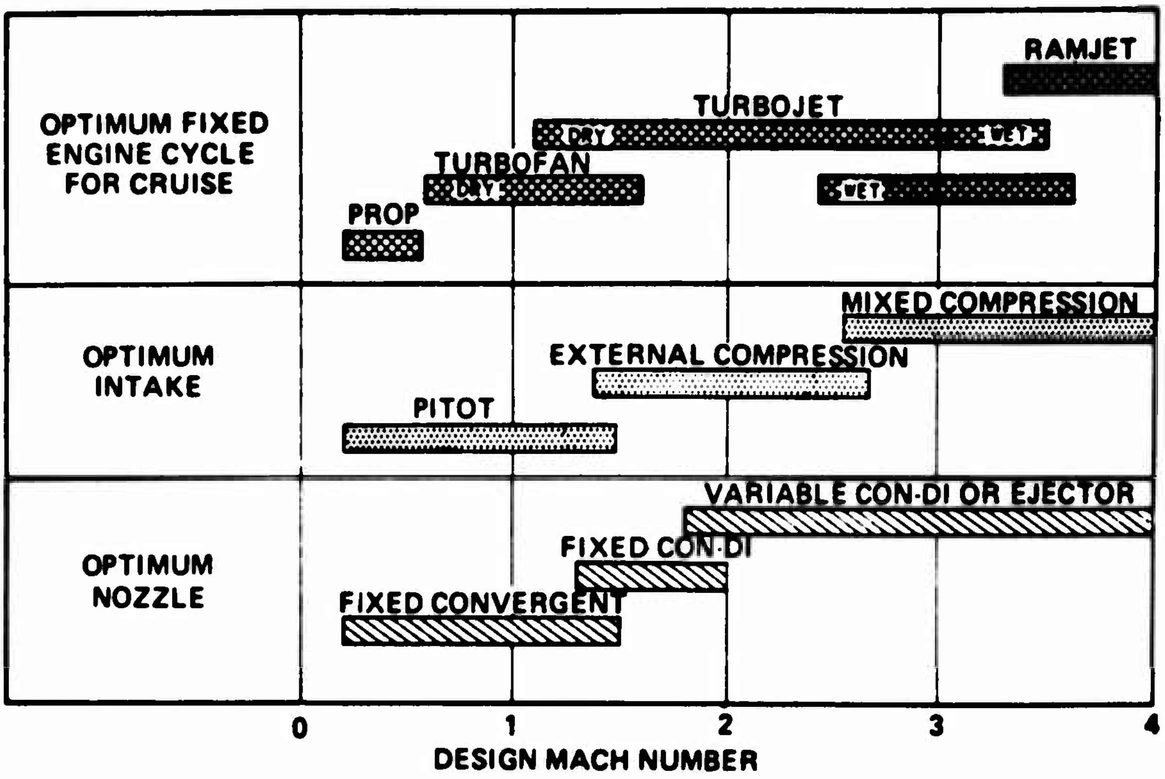

Figure 1. Effect of Cruise Speed on Propulsion Systems

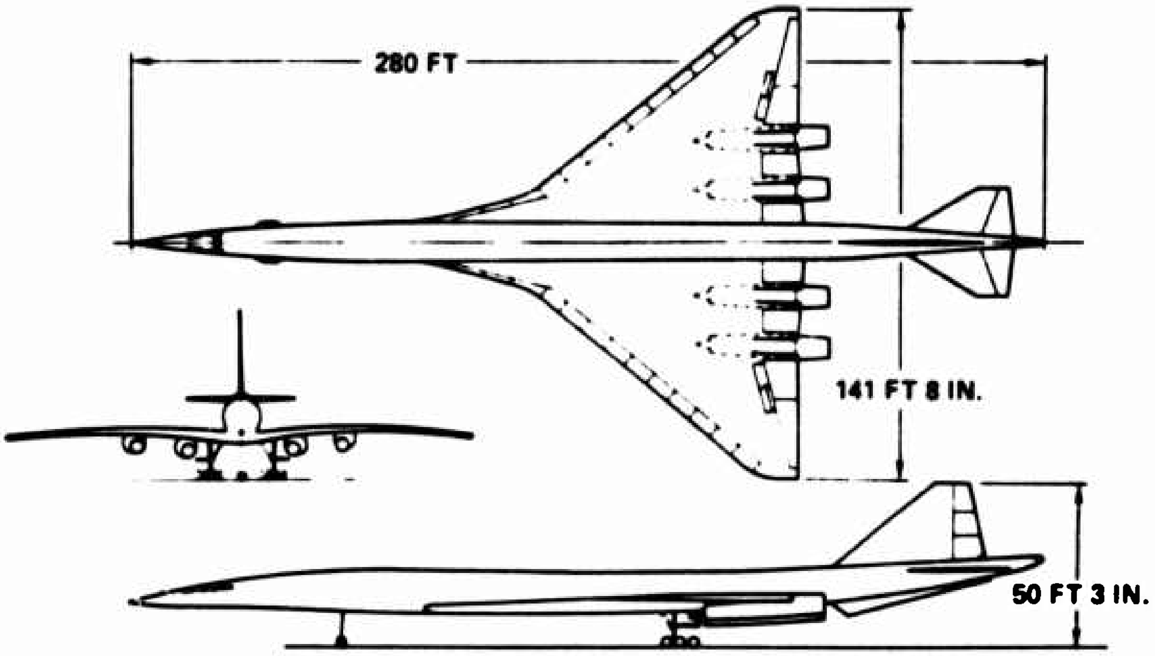
280 FT
141 FT 8 IN.
50 FT 3 IN.

Figure 2. An Example: the SST

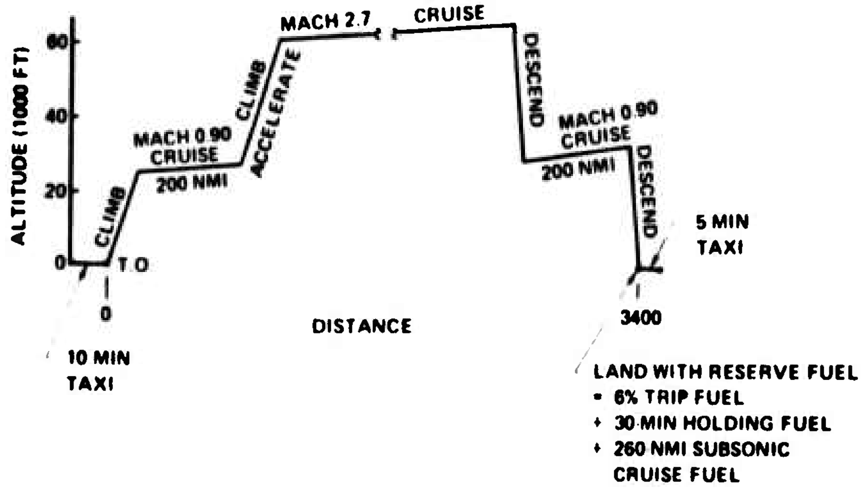

Figure 3. SST Design Mission

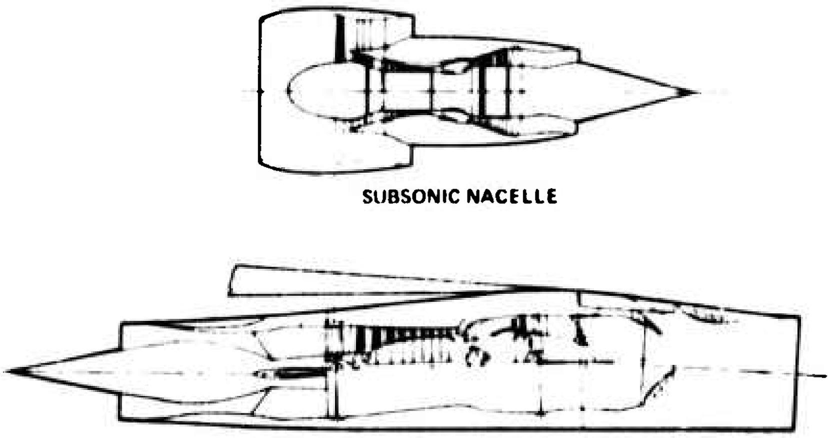
SUBSONIC NACELLE

SST NACELLE

Figure 4. Comparison of Subsonic and Supersonic Nacelles

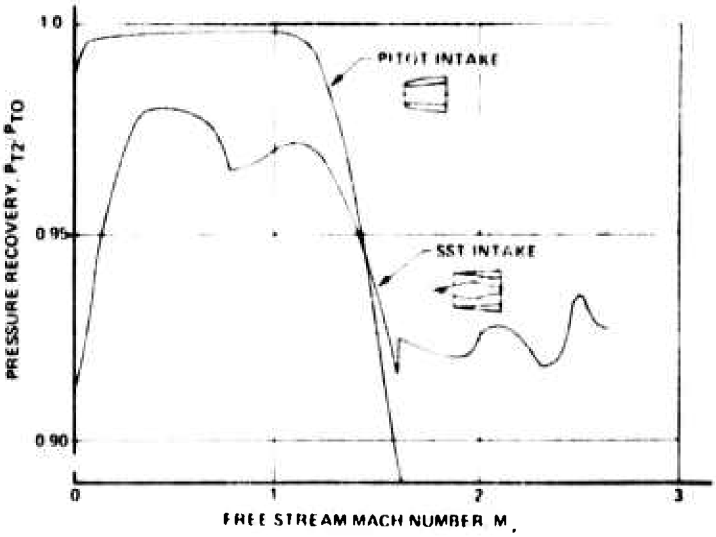

Figure 5. Intake Pressure Recovery Comparison

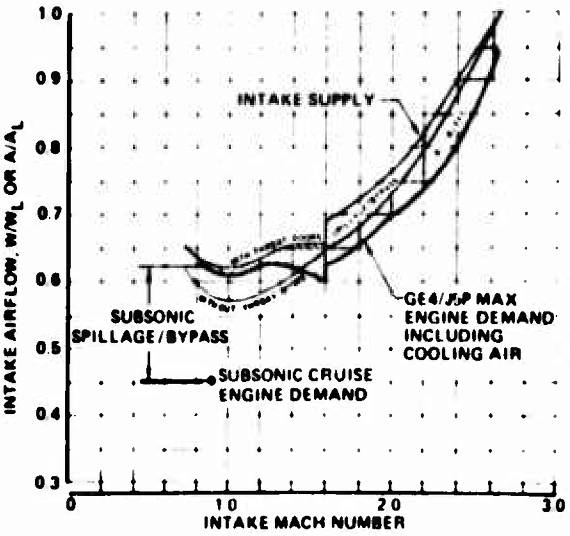

Figure 6. SST Intake Swallowing Capability

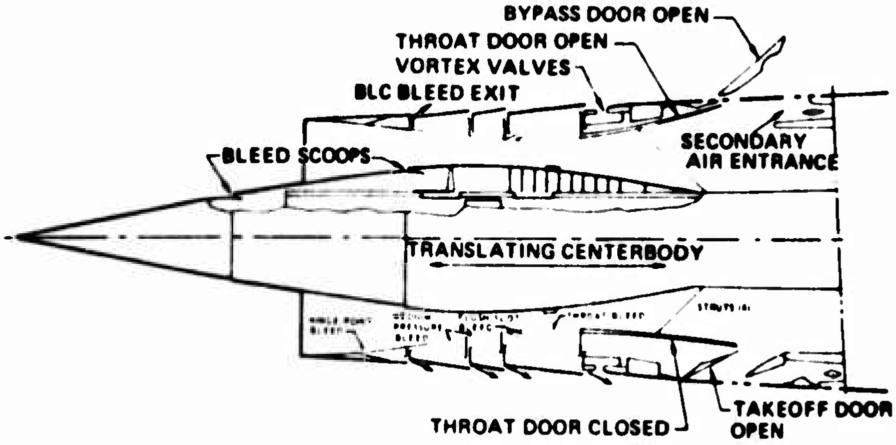
BYPASS DOOR OPEN
THROAT DOOR OPEN
VORTEX VALVES
BLC BLEED EXIT
BLEED SCOOPS
SECONDARY AIR ENTRANCE
TRANSLATING CENTERBODY
THROAT DOOR CLOSED
TAKEOFF DOOR OPEN

Figure 7. SST Intake Systems

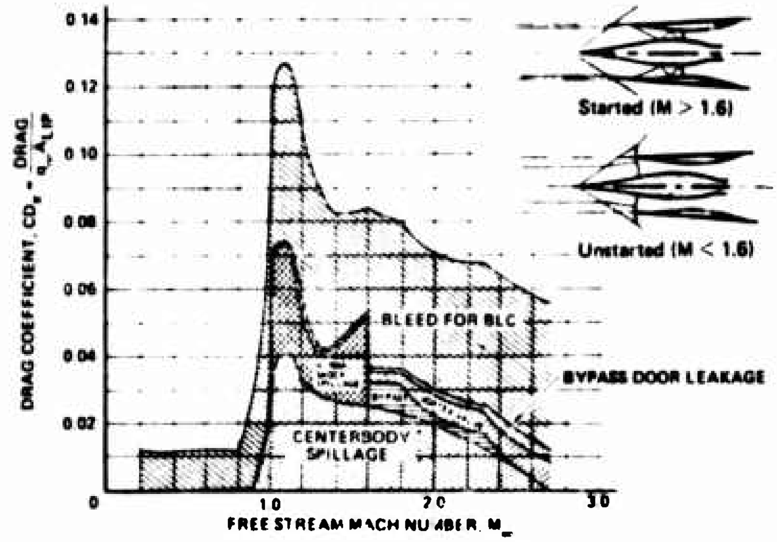

Figure 8. SST Intake Drag Buildup at Full Engine Power

50<

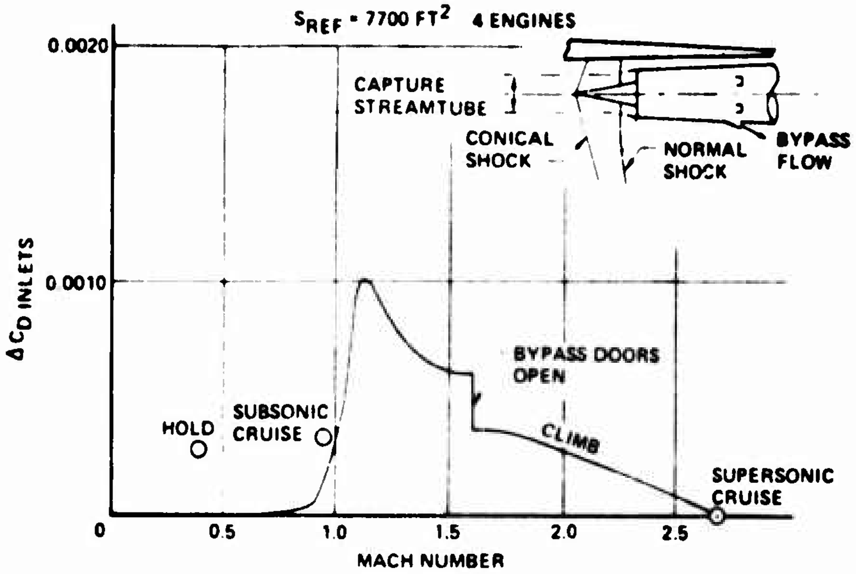

Figure 9. Intake Spillage and Bypass Drag

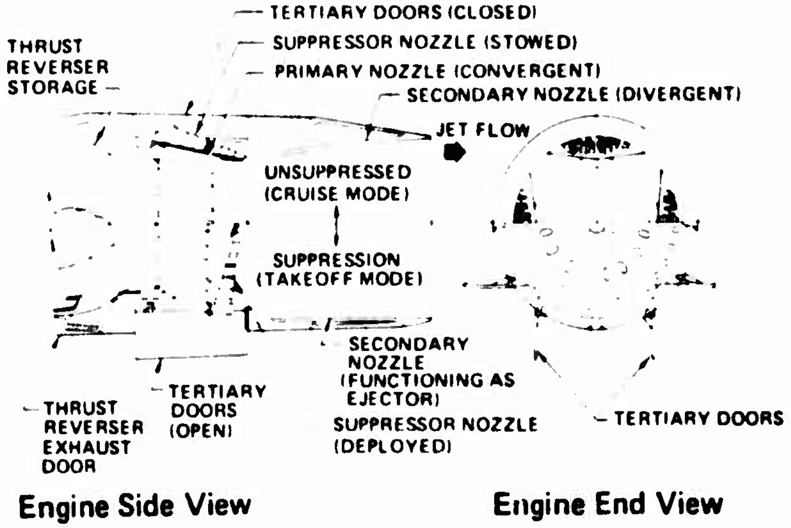
TERTIARY DOORS (CLOSED)
SUPPRESSOR NOZZLE (STOWED)
PRIMARY NOZZLE (CONVERGENT)
SECONDARY NOZZLE (DIVERGENT)
THRUST REVERSER STORAGE
JET FLOW
UNSUPPRESSED (CRUISE MODE)
SUPPRESSION (TAKEOFF MODE)
SECONDARY NOZZLE (FUNCTIONING AS EJECTOR)
SUPPRESSOR NOZZLE (DEPLOYED)
TERTIARY DOORS (OPEN)
THRUST REVERSER EXHAUST DOOR
TERTIARY DOORS
Engine Side View
Engine End View

Figure 10. SST Exhaust System

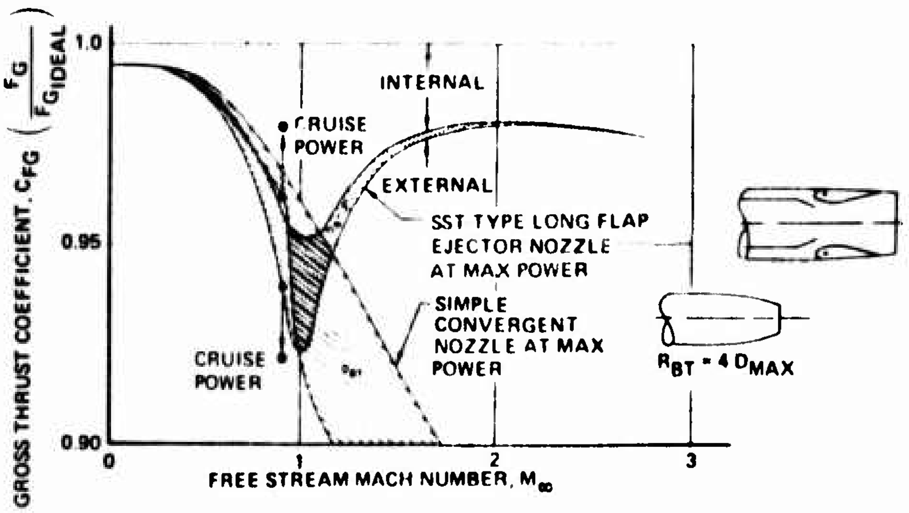

Figure 11. Nozzle Performance Comparison

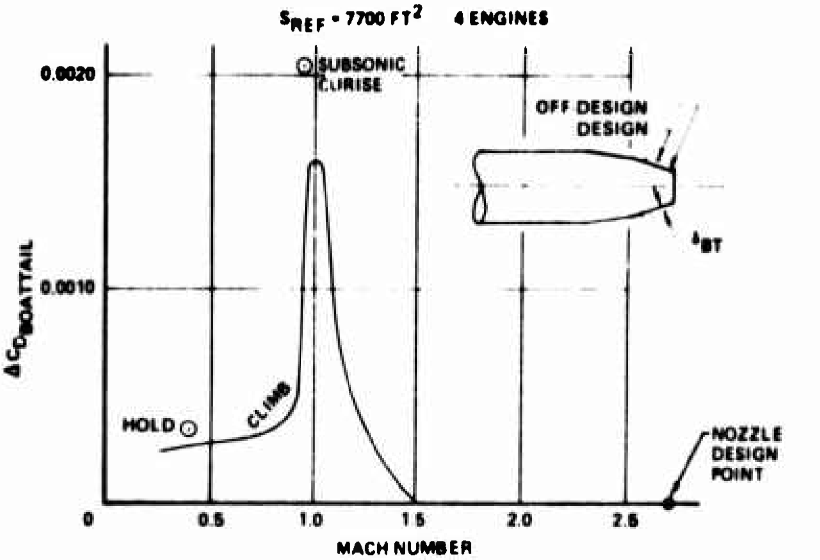

Figure 12. Incremental Boattail Drag

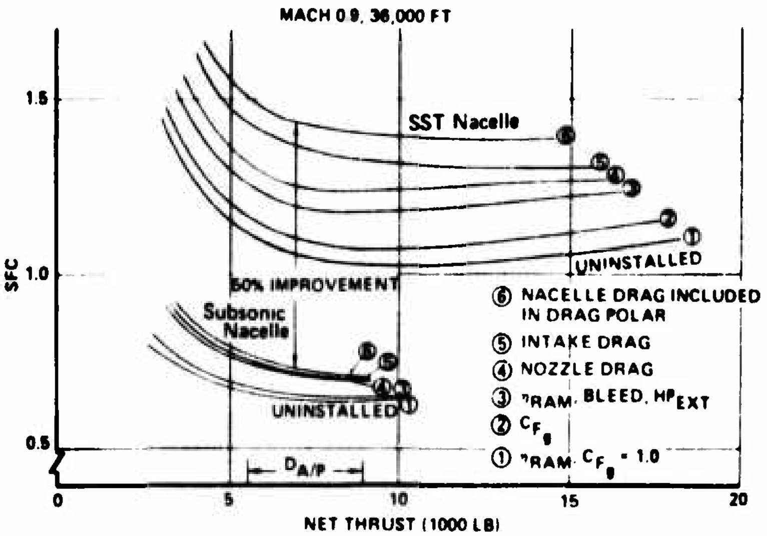

Figure 13. Subsonic SFC Installed Comparison

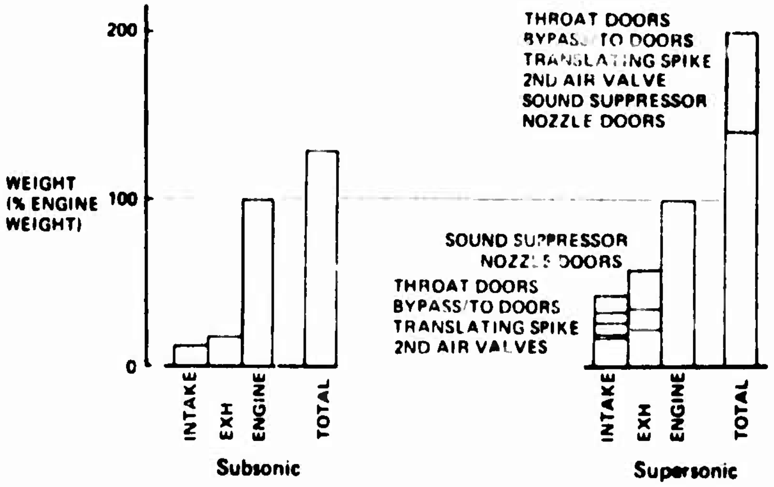

Figure 14. Nacelle Weight Comparison

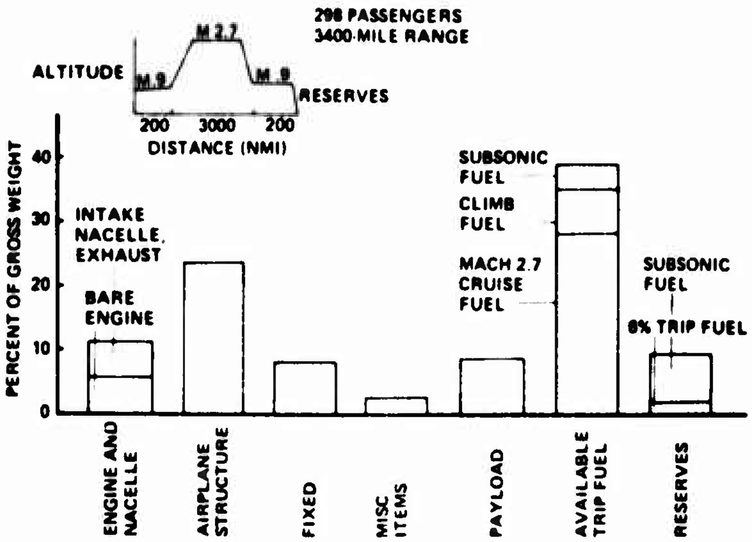

Figure 15. SST Weight Breakdown

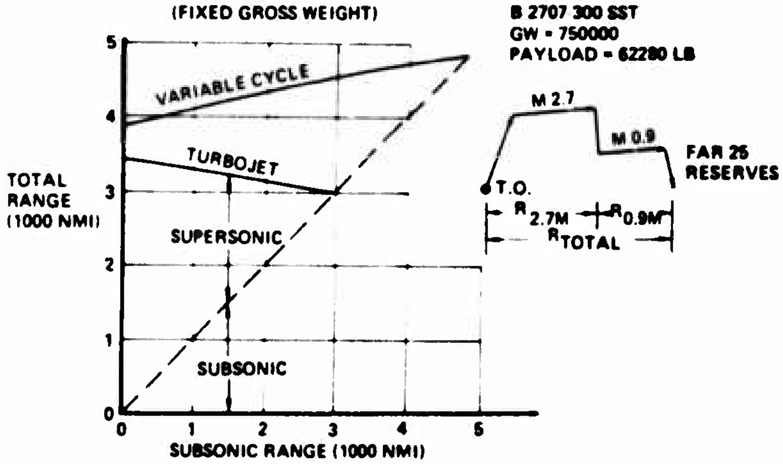

Figure 16. Effect of Subsonic Range on Total Range of the SST

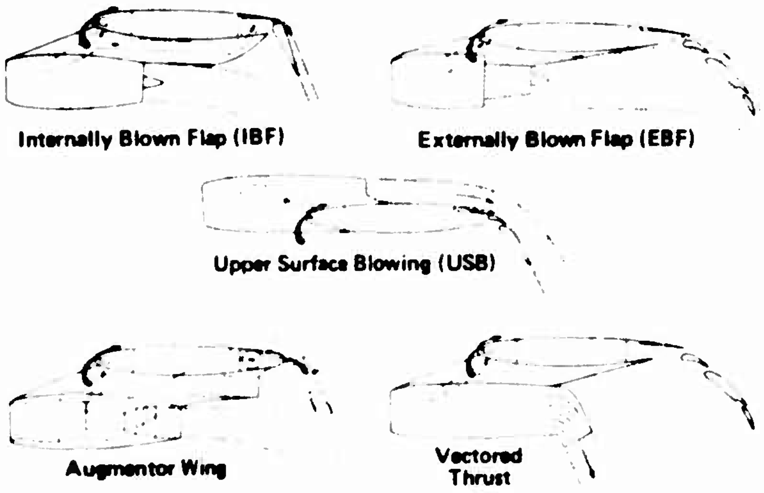
Internally Blown Flap (IBF)
Externally Blown Flap (EBF)
Upper Surface Blowing (USB)
Augmentor Wing
Vectored Thrust

Figure 17. Powered-Lift STOL Concepts

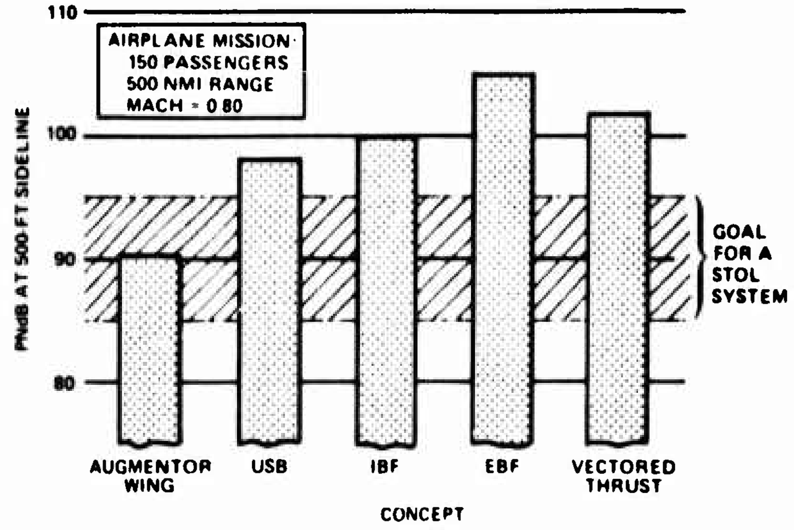

Figure 18. Comparative Noise Levels for Various Powered-Lift Concepts

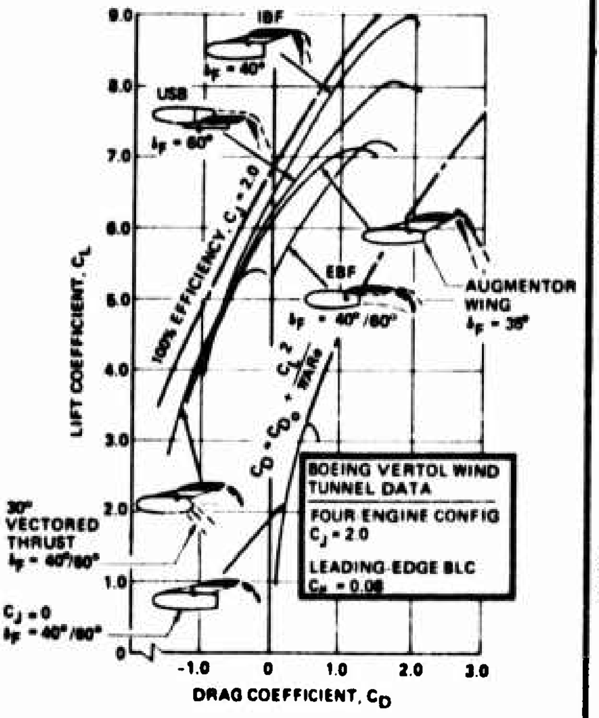

Figure 19. Drag Polars for Various Powered-Lift Concepts

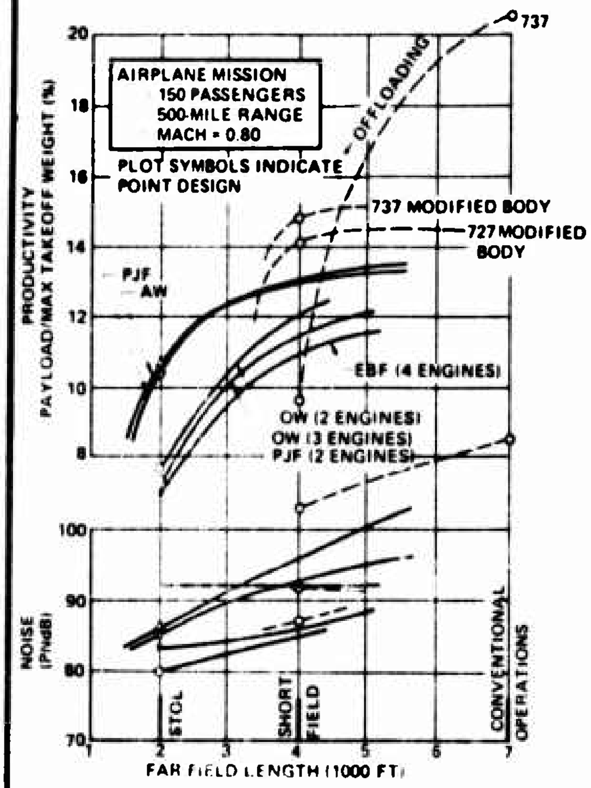

Figure 20. Performance Summary—Noise and Field Length Objectives vs Productivity

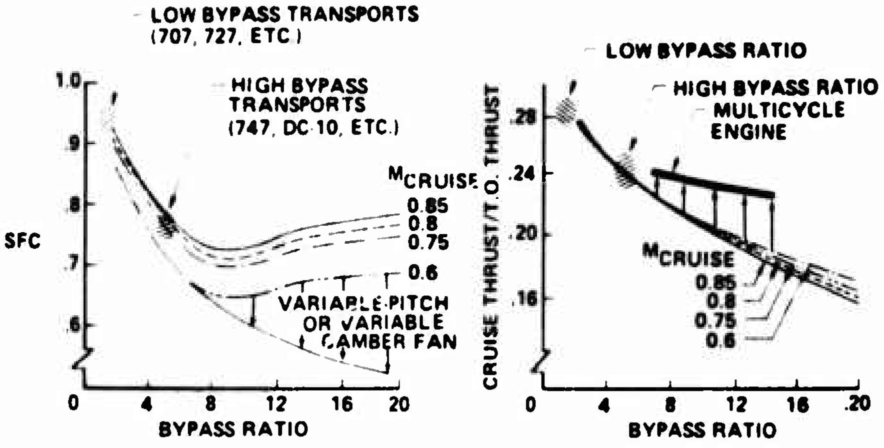

Figure 21. Engine Cycle–Effect of Bypass Ratio

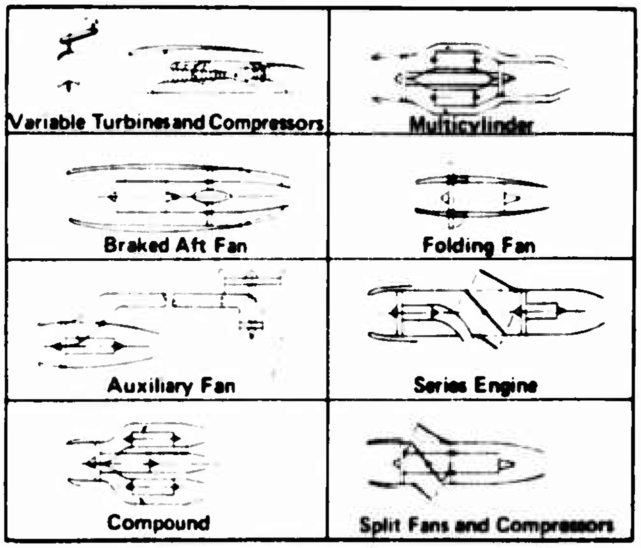
Variable Turbines and Compressors
Multicylinder
Braked Aft Fan
Folding Fan
Auxiliary Fan
Series Engine
Compound
Split Fans and Compressors

Figure 22. Some Variable Cycles

Table 1. The Potential

ITEM	EQUIVALENT UNCYCLED WEIGHT IMPROVEMENT
REDUCE MISSION RESERVES BECAUSE OF IMPROVED OFF DESIGN SFC	15,000 LB
BETTER BARE ENGINE SFC ON 400 NMI SUBSONIC MISSION LEGS	14,000
ELIMINATE INTAKE COMPLEXITY	7,000
NOZZLE MOVING DOORS	5,000
SOUND SUPPRESSOR	9,000
DRAG EQUIVALENT OF SUPPRESSOR	6,000
OFF-DESIGN INTAKE DRAG	2,000
OFF-DESIGN BOATTAIL DRAG	3,000
	TOTAL 61,000 LB > 300 PASSENGERS

FEEDERLINER ENGINE INSTALLATION - TRENDS AND PROBLEMS

D.H. Tipper

Hawker Siddeley Aviation Limited, Hatfield, England.

In this paper, I shall be discussing the influence of the feederliner type of operation on powerplant choice and installation. I hope to illustrate some of the reasons why an aircraft manufacturer's attitude and approach may differ from those for longer range aircraft and subsequently to describe some of the problems of installation and operation that are emphasised by this type of operation.

To start at the beginning - what is a feederliner? I intend to use the term to describe an aeroplane whose main purpose is transport between major airports and the surrounding communities. It will operate, therefore, into conventional airports at both ends of the spectrum - from a small town field with the minimum of aids and 3000-4000 ft. of runway into the big international airports. It is not intended for city centre operation or any form of mass transit.

The type of feederliner that I shall talk about is turbofan powered and used where an air transport market has already been established by propellor-driven aircraft. Air transport's foothold in this type of market is, however, frequently precarious and even at this second stage, capital is likely to be scarce.

How then can the use of turbofan power consolidate the market? There are various reasons which, although no one is compelling, combine to give an unmistakable probability of steady, if not rapid, growth. The appearance of more attractive aircraft types, together with maturing markets can be expected to maintain a steady expansion of around 8% per annum. With this rate of growth, the total number of turbofan feederliners in service by 1982 (outside the Warsaw Pact countries and China) is estimated to be around 650 aircraft, after making allowance for the continued use of propellor aircraft and competition from new and secondhand aircraft designed for rather longer hauls (Figure 1).

The main reasons for projecting growth are speed and passenger appeal. As is illustrated by Figure 2, speed tends to advance in large steps and one does not have to look far to find the reason. On a stage of 100 n.m., 175 kt. increase of cruising speed has only brought 5 minutes saving of block time and it is only for the longer stages of this type of operation that substantial time savings are made (Figure 3).

Passenger appeal is hard to quantify and easy to deprecate. However, a small increase in passenger load factor will have a substantial influence on the profitability of the operation. One way in which passenger appeal can be quantified in through cabin noise and vibration and Figure 4 shows how the elimination of the propellor cuts the overall noise level. On the other hand, speech interference frequencies are adversely affected by increased airspeed and must be contained by the use of additional acoustic treatment. However, if the high frequency noise is contained, the absence of propellor noise and vibration has a marked passenger appeal and has long been seen as one of the benefits of turbojet or turbofan propulsion.

After a spate of re-equipment in the 60s, feeder airline fleets are, once again, growing old and, at a time when public surface transport is showing the effect of renewed interest and investment, operators may be expected to seek a vehicle which can show as many tangible benefits as possible over its predecessors. The turbofan can provide the answer.

I forecast earlier that the size of the market will be 100×10^9 seat miles by 1982. For comparison the whole airline industry is forecast to generate 1200×10^9 seat miles in that year and, taken together with the need for high frequency of service, the feederliner will clearly be a comparatively small aeroplane; 70-90 seats being forecast as appropriate for the 1980 period (Figure 5). Such an aeroplane will need a total installed thrust of around 8500 to 9000 lb. to cruise at 20000 ft., 0.7 Mach No. and will consequently have available a total thrust at take-off between 20000 lb. and 27000 lb. according to bypass ratio.

I have already noted that feeder airlines are often short of capital. Is it possible to keep the price down by choosing low cost systems and by keeping the number of systems in the aeroplane to a minimum?

The engines may contribute between 15 and 30% of the price of an aeroplane - more if spares holdings are taken into account - furthermore they contribute a considerable share of the engineering costs. So, should we be seeking a cheap engine with correspondingly low engineering costs?

The answer that Figure 6 gives is encouraging. If SFC can be reduced by one third from the datum level, then it will only be worthwhile if the engine costs (first cost and engineering) do not exceed the datum level by more than 57% for a 100 n.m. stage or by 65% for a 400 n.m. stage.

The reason for this is, of course, the relatively small contribution of fuel cost to the total when compared with longer stages - even the small change from a 100 n.m. stage to one of 400 n.m. has shown quite a substantial movement of the threshold.

Clearly, such a point cannot be made without mention of the energy crisis. Are we at a step change in one contribution to general inflation or are we at a turning point? I do not propose to answer that question but Figure 7 shows the contribution of fuel (at 22 ¢ per US gallon) and of the engine, to direct operating cost. Even if the price of fuel doubles yet again, the incentives for an engine designed for low capital and engineering costs remain strong.

How does this ideal correspond with actual possibilities? Figure 8 shows, for typical cruise operating conditions, a broadly constructed envelope of achievable SFC as a function of bypass ratio and overall compression ratio. Also shown is an envelope which contains the currently available engines within a surprisingly small range of SFC and large range of bypass ratio. This SFC standard was used as the datum level in Figure 7 and it is a standard about one third inferior to the best current engines regardless of bypass ratio.

How much would the minimum SFC engine cost, if someone could be found to build it? Bearing in mind the relatively small size of the market (in monetary terms if not in terms of number off) and the great significance of price, it is not surprising that there has not been the rush to satisfy this market that occurred in the over 40000 lb. thrust category.

The lesson that I see here is that this market is no place for highly specialised engines and instead can be expected to rely, as at present, on developments or adaptions of engines developed for other roles.

In illustration of this point, I would mention the three engines currently in the field - one developed for medium range airliners, one developed from a combat aircraft engine project and one developed from a helicopter turboshaft.

If, for the moment, one sets aside the differences of thrust of these engines - Spey, M45H and ALF 502 - there is a striking variation of bypass ratio. The reasons for this are largely historical, but the consequences are worth closer examination. Perhaps the greatest impact is on noise.

Only flyover noise is significantly affected by factors peculiar to the feederliner. In this case, high installed thrust/aircraft weight ratio will result from the need to operate from runways 3-4000 ft. long and it is evident from Figure 9 that the consequent increase of height at flyover confers a benefit of perhaps 5 dB. The self cancelling effect of any thrust loss due to silencing is also evident.

By comparison, airframe changes - except possibly noise shielding if this can be achieved without marked loss of efficiency - offer comparatively little as can be seen from the lower plot on Figure 9. Major aerodynamic developments are implied by the 20% improvement of drag/weight ratio shown and yet the reduction of flyover noise is relatively small. Nor is the high maximum lift coefficient desirable for take-off in 3-4000 ft. of any significance since it is more or less exactly offset by poorer climb gradient. Thus, the chief factors in flyover noise are the intrinsic noise level of the engine and its installation and the ratio of installed thrust to aircraft weight.

The former of course also dominates sideline noise and Figure 10 shows the well known effect of reducing jet velocity with increasing bypass ratio. (Forward arc noise decreases as well due to the presence of a contribution from the exhaust when the exhaust velocity is high) - Increasing bypass ratio from one to six reduces peak noise level by around 12 dB and the observer will notice only one peak as the aeroplane passes.

In contrast, the landing approach is made along a fixed flight path at around 40% take-off thrust, a condition at which intake noise dominates. It is also the condition at which an acceptable noise level is proving most difficult to achieve. We see from Figure 11 that due to the dominance of intake noise, the advantages of high bypass ratio are greatly decreased at low thrust and are in fact very small if a 6° glideslope is used instead of the customary 3°.

So, noise considerations lead to quite conventional conclusions and I shall dwell upon them no further except to remark that the advantages of high bypass ratio might be largely lost if rapid progress was made in the control of jet noise.

However, the use of high bypass ratio results in a number of aircraft design and operating problems (Figure 12). As bypass ratio increases so does airflow and the frontal area and weight of the engine. Each type of installation has its particular problems and all these are aggravated by greater bulk and weight.

The lifting efficiency of a wing is sensitive to gaps in the high lift devices - to make room for nacelles or jets for instance - and to obstructions in the high speed flow above the wing. High efficiency is most readily achieved by mounting the engine well below the wing, thus allowing continuous slats and flaps to be used and operate in the most favourable conditions.

A feederliner will be expected to be able to operate from poorly prepared aerodromes which are not free of debris. Prevention of vortices between the intake and the ground, which are capable of lifting substantial pieces of debris, is most simply achieved by keeping the intake bottom lip well clear of the ground.

On a wet runway, the nosewheels will project two powerful jets of spray upwards and outwards. Tyre shaping can influence the direction of the jets to keep them clear of the intakes of rear mounted engines but otherwise, the engines should be widely spaced.

To achieve its desired take-off performance, the feederliner has a relatively low take-off speed and relatively high thrust/aircraft weight ratio. At low speed, rudder power is poor and thus the moment of asymmetric thrust, after the failure of one engine, must be minimised either by close spacing or by the use of three or four engines.

Although fuel economy is not a primary objective, as has already been seen, nor is fuel wastage and the installed drag of the engines should be minimised. Although much can be done by careful detail design, this is most easily achieved either by burying the engines or mounting them below and ahead of the wing leading edge.

Minimum installed weight is best achieved by compact installation and this will usually mean a pylon mounted pod.

Minimum noise, however, may modify this last consideration since long acoustically treated ducts are desirable - the use of noise shielding will, of course, have much further reaching consequences.

Although location of the intake above and behind the wing leading edge will greatly reduce the range of approach flow angles, the wake of the wing when stalled is hard to avoid. Long curved ducts or fuselage wakes also create pressure distortion at the engine face and these factors make an intake position ahead of the wing leading edge most attractive.

If the engines are widely spaced across the span, ample ground clearance must be provided for the crosswind landing case.

Finally, but not least important, maintenance and servicing, especially at outstations, will be quicker and cheaper if the necessary operations can be performed by a man standing on the ground - an objective most easily achieved if the engine is underwing mounted.

None of the problems that I have listed here is sufficiently intractable to prevent the use of a particular layout, as the diversity of existing airliners illustrates. But as the engine becomes bulkier, the options become fewer and the aircraft designer is likely to look back with regret to the palmy days of turbojets and bypass ratio one - at least occasionally.

As well as affecting aircraft layout, the type of engine chosen will also affect the systems. High propulsive efficiency means high idling thrust and this leads to two points of difficulty (Figure 13). At bypass ratios of six or more, depending on the installed thrust to aircraft weight ratio, ground idling thrust may exceed that required for taxying with consequent excessive braking, brake heating and wear.

High flight idle thrust increases distance in the landing flare and the touchdown speed and when it is realised that 100 ft. increase in landing distance required can result from 7% increase of the ratio of flight idle to take-off thrust and reduce the payload carried into a limiting runway by 15 to 20% it is clearly no small matter.

The question of idling thrust, would, perhaps, not matter quite so much if reverse thrust was available. However, I have already stressed the importance of reducing capital and engineering costs to a minimum and a reverser will cost about 15 to 20% of the price of the engine on which it is mounted as well as increasing weight and drag. Maintenance costs for a thrust reversal system result not only from the system itself but from the additional engine cycles involved and the risk of ingestion damage, which is always present and which assumes additional importance in rough field operations.

For these reasons, which are well known but which are amplified in their importance by our particular requirements, the reduction of idling thrust should be a major objective in future engine design.

Reduction of costs through simplicity has been a recurring theme in this paper and another way in which it shows up is in the supply of auxiliary power. The simplest way to extract energy from an engine is by airbleed from the compressor and the hot air thus provided is also an ideal medium for air conditioning and ice protection. However, the use of high bypass ratio results in less core airflow for a given installed thrust (Figure 14). Thus, for instance, if it is desirable to bleed 5% core airflow from an engine with bypass ratio 1.0:1 then, for equivalent performance, an engine with a bypass ratio of 6.0:1 must be bled of 9% of its core airflow. High available bleed percentages allow the use of lower thrust settings for descent - so long as sufficient bleed pressure is available - and the availability of a high rate of descent is increasingly necessary as airspace becomes more crowded.

I started by giving the reasons for preferring a turbofan engine for future feederliners. I went on to advocate the tempering of fuel economy with a broader operating economy and to discuss the current noise advantage possessed by the high bypass ratio turbofan before coming to the difficulties of aircraft design that are increased by such engines. I will conclude by listing the main conclusions.

1. Design for low capital and engineering cost, even at the cost of substantial SFC penalties.

2. A bypass ratio of around 6:1 is valuable for noise reasons. But many constraints are placed on aircraft design and operation and intermediate bypass ratios - say 4 or 5 to 1 - remain attractive if sufficient progress is made in the reduction of jet noise.

3. It is desirable to develop engines that are capable of operating at substantially lower idling thrust and higher bleed airflow percentages than are possible at present.

These views are, of course, those of someone with the viewpoint of an engine user. To the engine designer, I would echo the question put by Alice to the Cheshire Cat, "Would you tell me please, which way I ought to go from here ?"

I would like to thank the Directors of Hawker Siddeley Aviation for permission to give this paper and to my colleagues at Hatfield without whose help it would not have been possible. The views expressed are, however, my own.

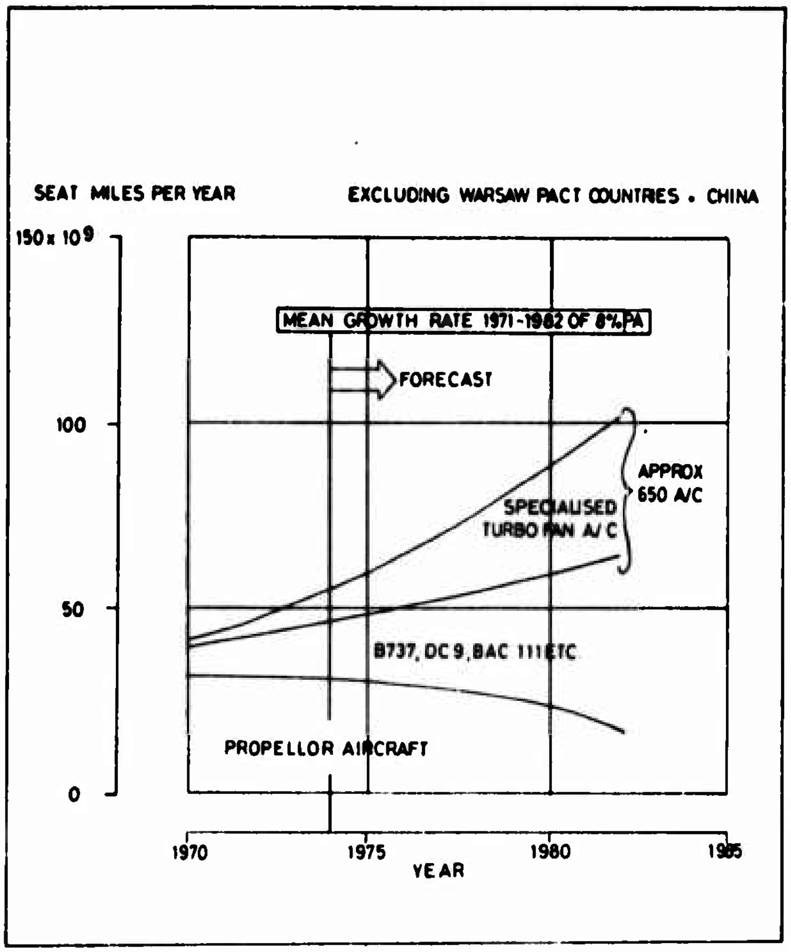

COMPOSITION OF WORLD FEEDER FLEETS

FIG.1

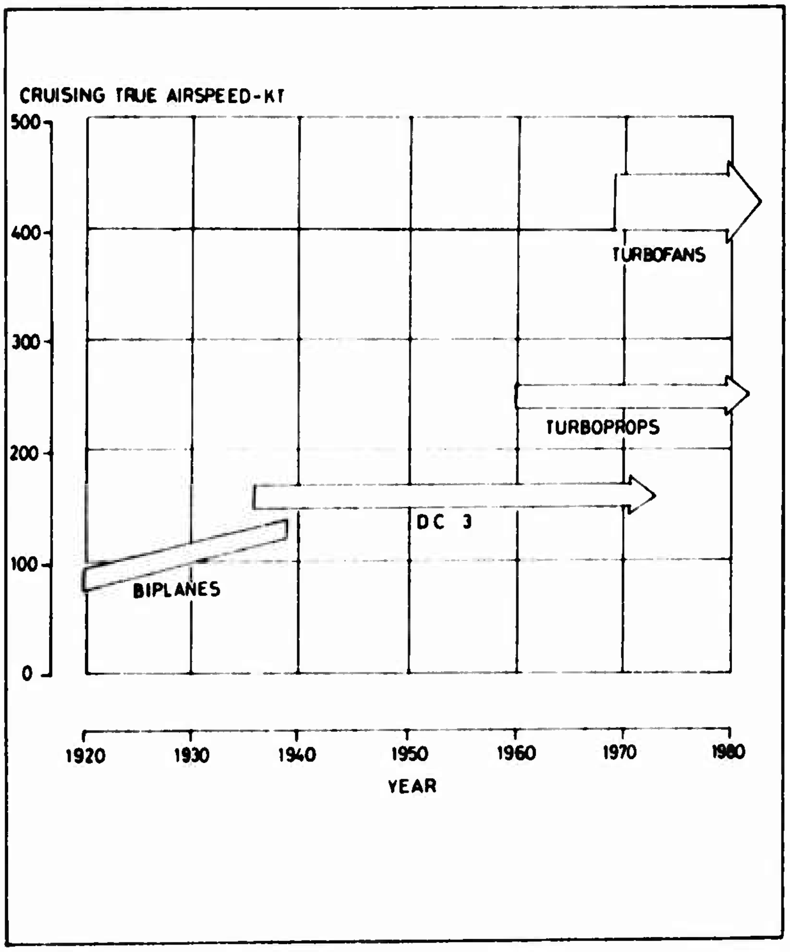

CRUISING SPEED

FIG.2.

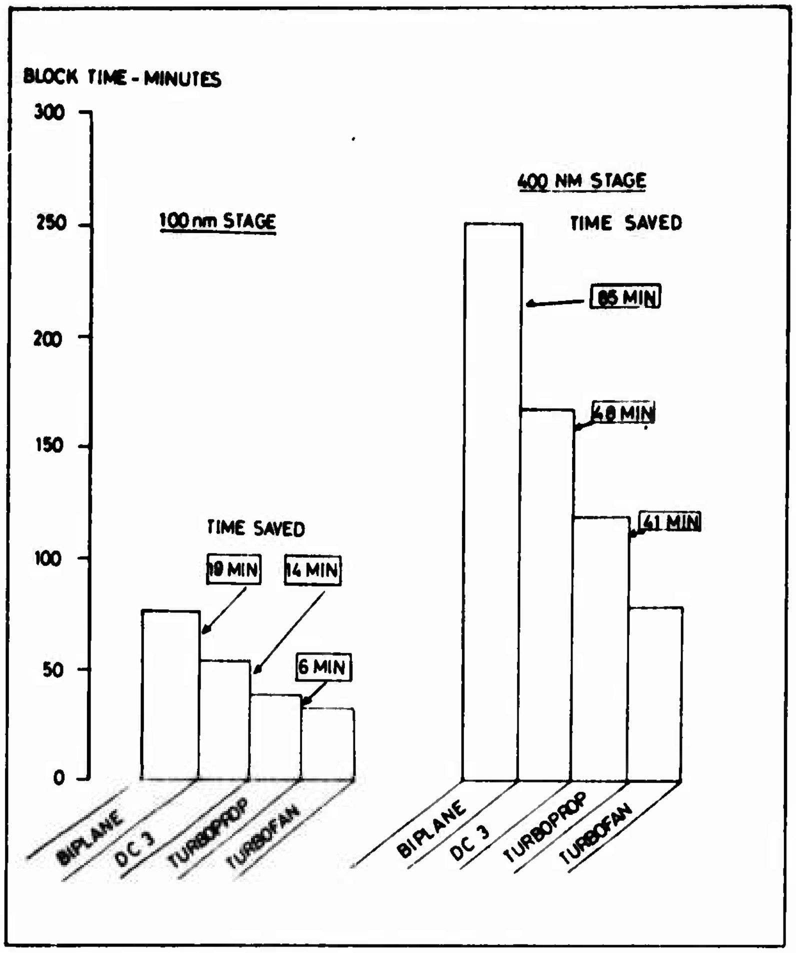

BLOCK TIME - TIME SAVED BY TECHNICAL ADVANCES

FIG.3.

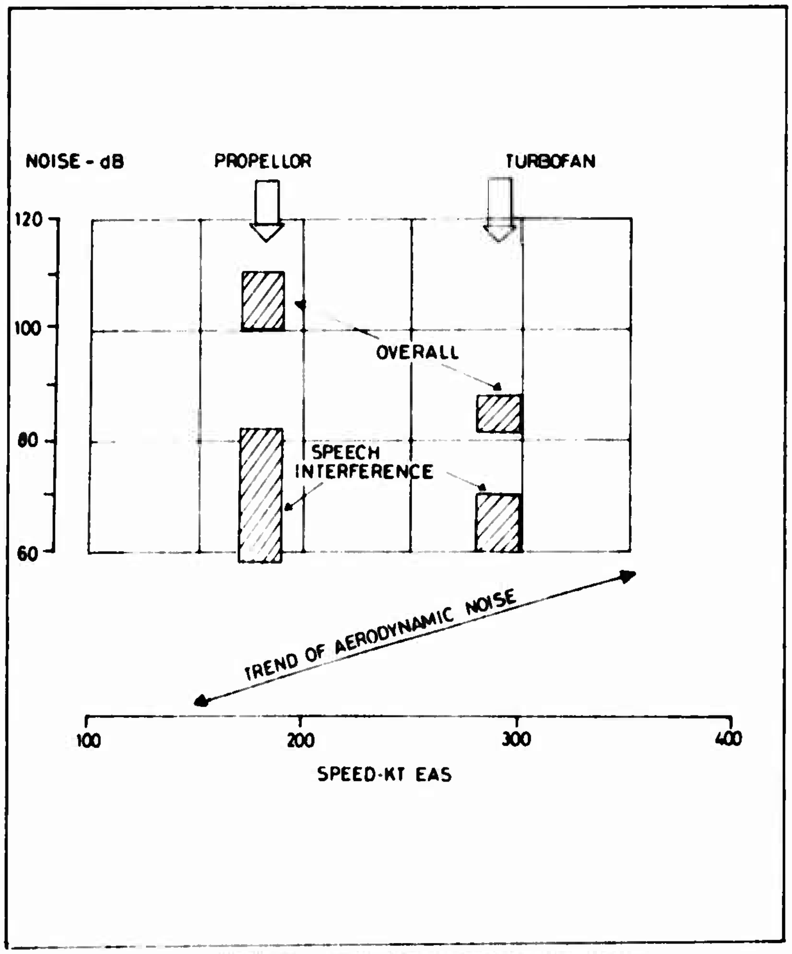

CABIN NOISE - COMPARISON OF PROPELLOR AND TURBOFAN

FIG.4.

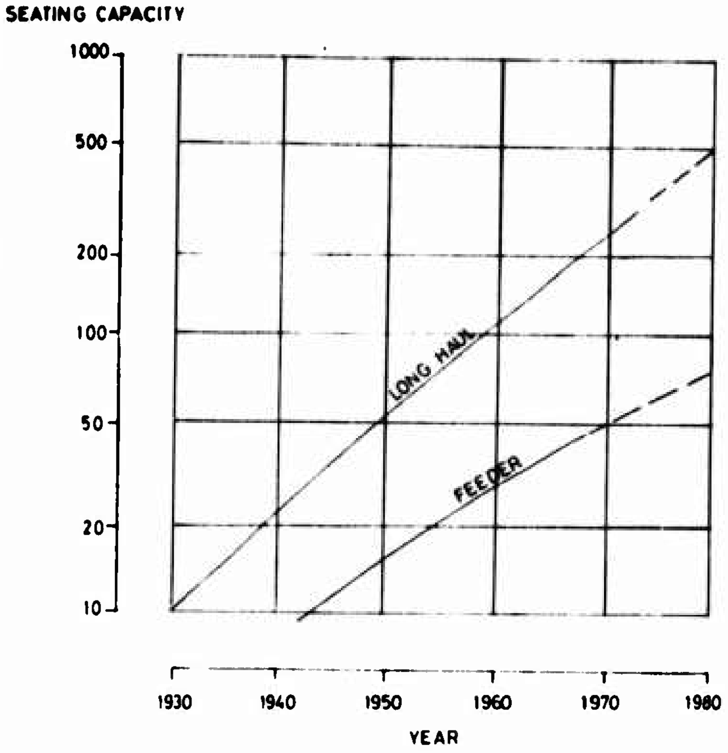

AIRCRAFT SIZE

FIG.5.

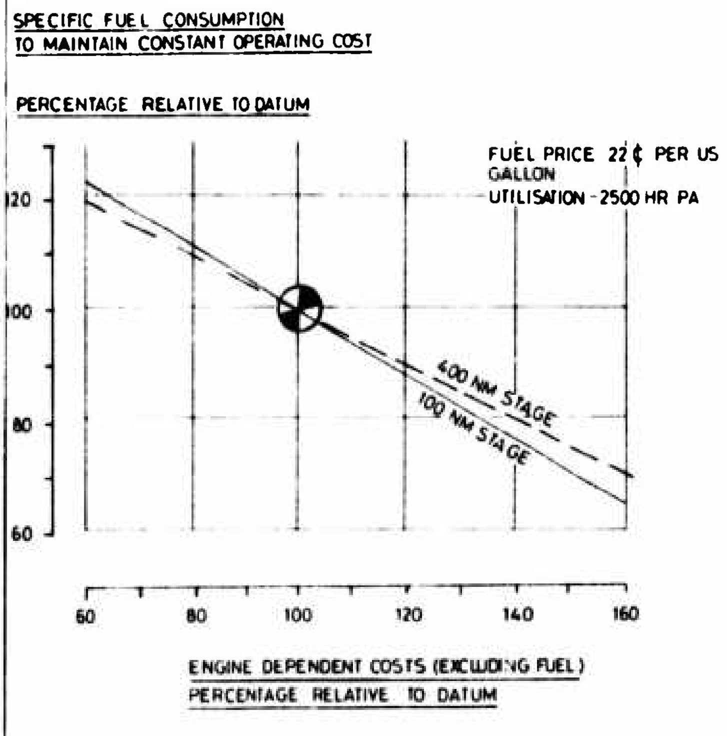

RELATIONSHIP BETWEEN ENGINE DEPENDENT COSTS AND SFC

FIG.6.

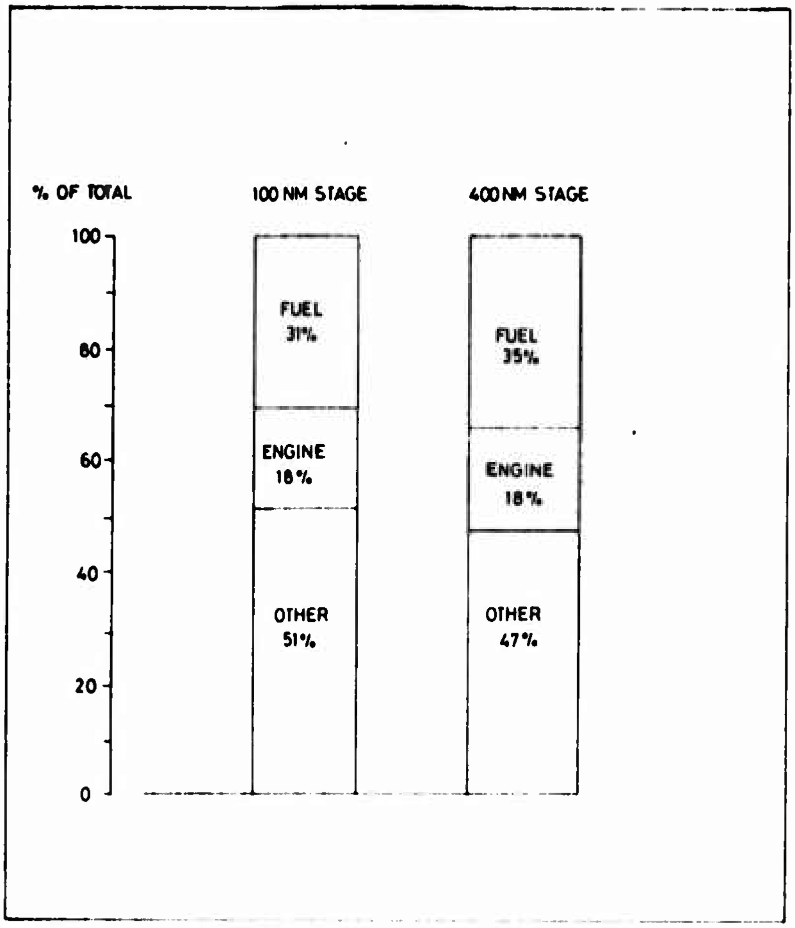

BREAKDOWN OF OPERATING COSTS

FIG.7.

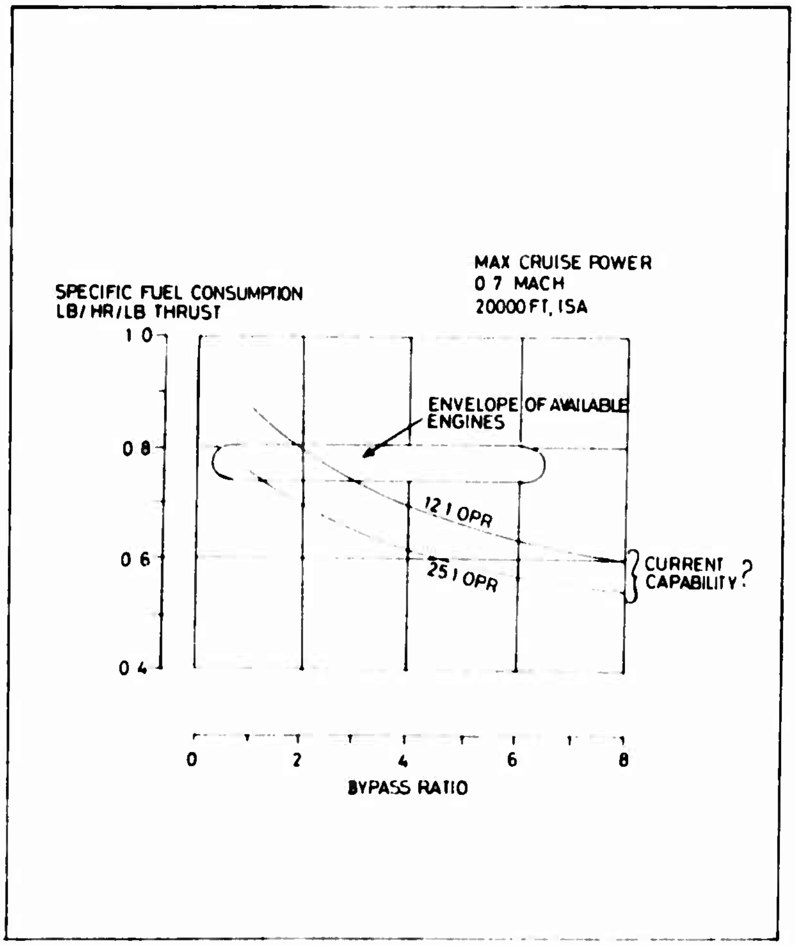

AVAILABLE AND ACHIEVABLE SFC

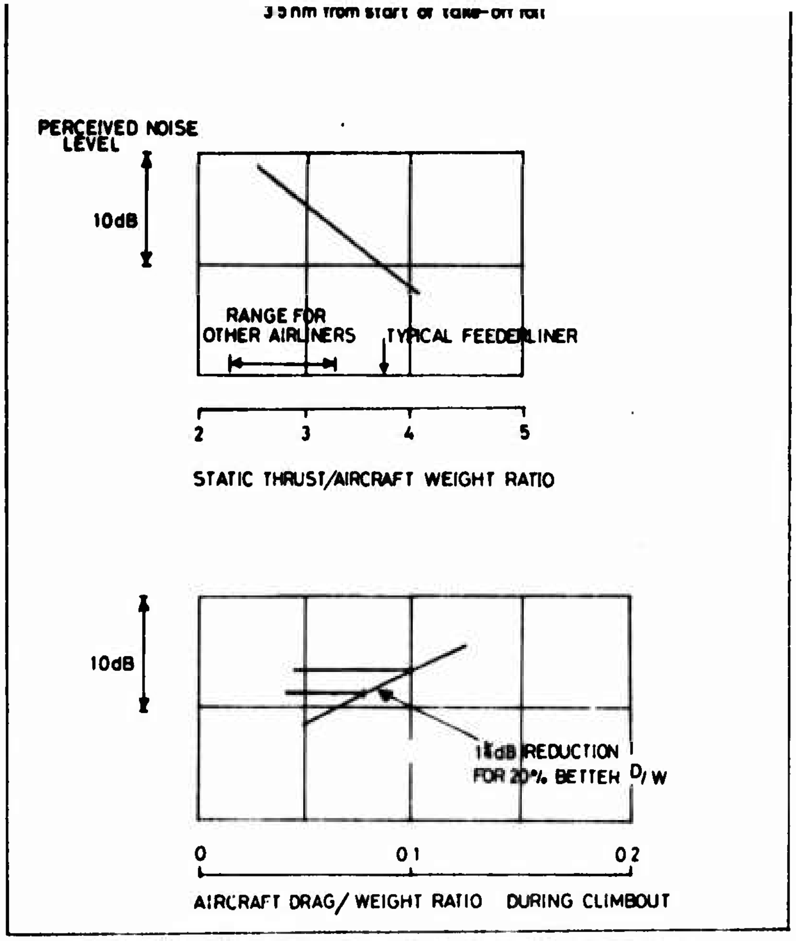

FLYOVER NOISE - EFFECT OF VARYING THRUST/WEIGHT AND DRAG/WEIGHT RATIO

FIG.9.

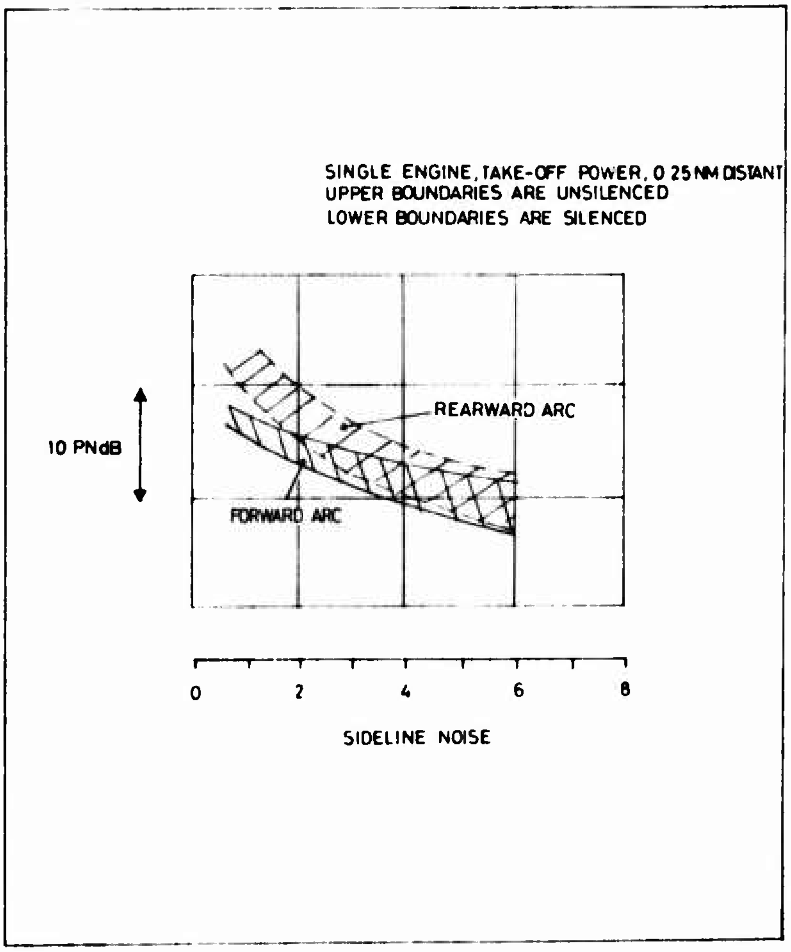

SIDELINE NOISE

FIG.10.

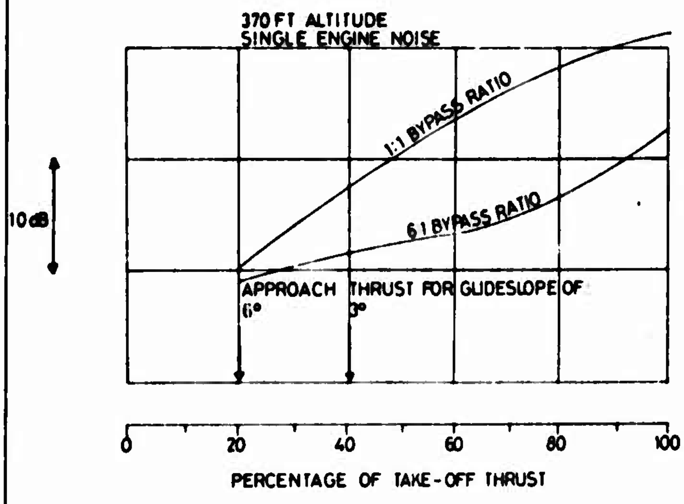

APPROACH NOISE - EFFECT OF REDUCING THRUST

FIG.11

REQUIREMENT	INTERPRETATION	MOST DIRECT SOLUTION
HIGH C_{LMAX}	HIGH LIFT DEVICES CONTINUOUS ACROSS SPAN. CLEAN WING UPPER SURFACE.	UNDERWING ENGINE ON LONG PYLONS.
FREEDOM FROM VORTEX INGESTION OF DEBRIS	INTAKE BOTTOM LIP WELL CLEAR OF GROUND - SAY $H/D > 2$	HIGH WING, or OVERWING ENGINES or REAR FUSELAGE ENGINES
FREEDOM FROM NOSEWHEEL SPRAY	ENGINES EITHER CLOSELY OR WIDELY SPACED TO AVOID SPRAY PLUME	REAR FUSELAGE ENGINES or WIDELY SPACED ON WING
LOW MINIMUM CONTROL SPEED, ONE ENGINE FAILED	SMALL MOMENT OF ASYMMETRIC THRUST	CLOSELY SPACED ENGINES or THREE or FOUR ENGINES
LOW INSTALLED DRAG	ENGINES LOCATED IN REGION OF ACCELERATING FLOW or NOT AFFECTING AIRCRAFT PROFILE	ENGINES BELOW AND AHEAD OF WING LEADING EDGE or BURIED ENGINES
LOW INSTALLED WEIGHT	COMPACT INSTALLATION	ENGINES IN PODS
MINIMUM NOISE	LONG INTAKE AND EXHAUST DUCTS, ACOUSTICALLY LINED	MAY OFFSET DISADVANTAGES OF INSTALLATIONS THAT ARE NOT COMPACT
FREEDOM FROM INTAKE PRESSURE DISTORTION	NO WAKES ENTERING INTAKE, OPTIMUM LIP AND DUCT SHAPES.	ENGINES BELOW AND AHEAD OF WING LEADING EDGE IN SIMPLE PODS.
GROUND CLEARANCE IN CROSSWIND LANDING	PODS REMAIN CLEAR OF GROUND WITH AIRCRAFT BANKED.	AVOID LONG PYLONS ON LOW WING.
ACCESSIBILITY	ROUTINE SERVICING BY MAN STANDING ON THE GROUND.	UNDERWING ENGINES

INFLUENCE OF THE ENGINE ON AIRCRAFT LAYOUT

FIG.12

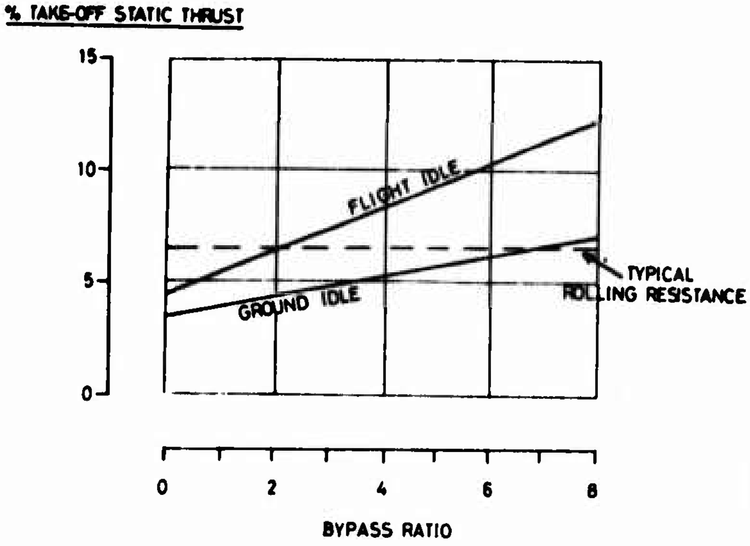

IDLING THRUST

FIG.13

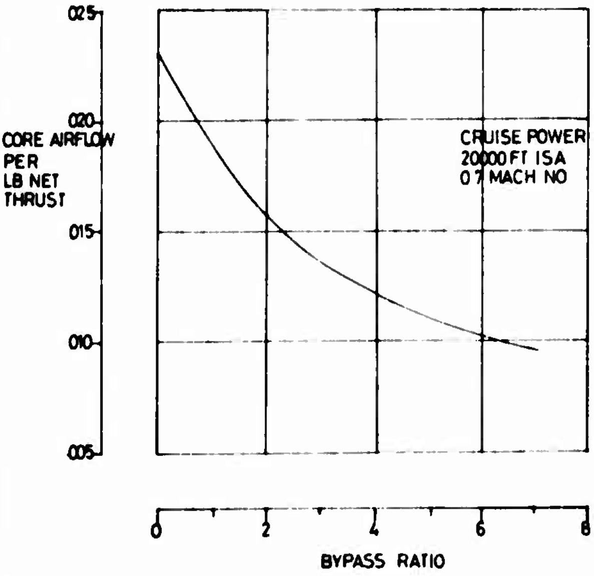

VARIATION OF CORE AIRFLOW WITH BYPASS RATIO

FIG.14

EXHAUST EMISSIONS UNDER SIMULATED FLIGHT CONDITIONS

A. K. Forney

U.S. Department of Transportation, Washington, D. C.

Introduction

At the First International Symposium on Air Breathing Engines, held at Marseilles in June 1972, Dr. Alan J. Grobecker(1) described the Climatic Impact Assessment Program (CIAP) being conducted by the U.S. Department of Transportation (DOT). At that time, Dr. Grobecker gave the CIAP objective as: "To assess, by a report in 1974, the impact of climatic changes resulting from perturbation of the upper atmosphere by the propulsion effluents from all elements of a world fleet of high-altitude aircraft, as projected to 1990." Measurement of engine exhaust emissions under simulated flight conditions has been included in the CIAP effort. The purpose of this paper is to review some of the results of two of those tests.

Before I proceed to the main purpose of the paper, there is one item I would like to call to your attention. Many studies and experiments of various kinds have been completed for CIAP since June 1972. We have learned much, and CIAP has been changed in many of its details. One of these changed details is its objective. It now is: "In order to determine regulatory constraints on flights in the stratosphere such that no adverse environmental effects result, DOT/CIAP will assess, by 1974 report, the impact of climatic changes resulting from propulsion effluents of vehicles in the stratosphere, as projected to 1990."(2)

To those of you involved in the design of engines that may be required to have certification in the United States, the inclusion of the words "regulatory constraints" may have some significance. Of course, I cannot say when, or even if, the Federal Aviation Administration (FAA) is going to issue Federal Air Regulations relating to engine exhaust emissions under cruise conditions. It appears to me, however, that the mere fact that the U.S. Department of Transportation, the parent department of the FAA, has made this change in the CIAP objective is worthy of serious consideration by engine designers and manufacturers. Many of you know that the U.S. Environmental Protection Agency (EPA) has already issued standards for aircraft engine emissions at low altitude. You also know that the FAA has issued a Notice of Proposed Rule Making (NPRM) that will probably lead to a regulation to enforce some, and eventually all, of the EPA standards. I believe you will agree that regulation of emissions during cruise will not appear a big step in the minds of regulatory people, once low altitude emission regulations are in effect. Therefore, I recommend that everyone concerned with engine design face this situation now and not wait until we are presented with proposed regulations. By beginning to address this problem now, we can help ensure that the regulations are intelligently applied when, and if, they become necessary.

At the time CIAP was started, the only engine exhaust emission data available had been obtained under sea level static conditions. Consequently, we felt it necessary to obtain data under simulated flight conditions. Further, we were interested in many more substances than were the people who had been making the sea level measurements. We were interested in as many of the species that take part in stratospheric chemistry as we could measure. In fact, we were interested in many more than we thought we could measure.(3) What actually happened, however, is that we were able to measure and get usable data on only a few of the species we thought we could measure. Measurement of chemical species in the exhaust of an engine in an altitude test cell turns out to be more difficult than making measurements in a chemistry laboratory.

This paper will review a portion of the results of tests on a YJ93-GE-3 engine in an altitude test cell and a J85-GE-5 engine in a propulsion wind tunnel. Both these tests and the instrumentation used have been described in published papers.(4,5,6,7) Consequently, I will omit those details and address only the results of the tests.

CIAP has progressed to the point where we believe we can state with conviction that, based on the best knowledge we have today, some of the products in the engine exhaust will have no adverse effect when injected into the stratosphere in the quantities we have estimated. On the other hand, we must also state that there is still some question about other products. It appears, as of today, that the carbon dioxide, carbon monoxide, unburned hydrocarbons, carbon particulates, oxygenates, and water vapor will have no adverse effect. I want to emphasize the word "today" in that sentence because there are still many unknowns in the chemistry and physics of the stratosphere, but our knowledge is increasing rapidly and the picture changes frequently. Unhappily, however, the oxides of sulfur and nitrogen cannot today be dismissed so easily.

Aviation kerosene has a low sulfur content, but not so low that it can be neglected by CIAP. However, a recent study shows that the cost to reduce the amount of sulfur in the fuel to a value well below present levels is not prohibitive, provided that it is determined a reduction is necessary.(8)

It is to the oxides of nitrogen that I plan to devote the major thrust of this paper. It is these oxides which present the greatest challenge to the engine designer.

Analysis of Results

Several points can be observed from Figure 1. First, the NO_x emission index decreases significantly in changing from military power to afterburning power, showing that the afterburner forms only a small amount of NO_x. Second, increasing flight Mach number at constant altitude increases the emission index. Third, increasing altitude at constant Mach number decreases the emission index.

There are several reasons why the afterburner forms only a small amount of the oxides of nitrogen. First, the air entering the afterburner has been vitiated by the exhaust products of the main combustion chamber. Consequently, the peak flame temperature is lower in the afterburner than for the same temperature and pressure conditions in the primary combustor. Second, the pressure level in the afterburner is lower than in the primary combustor. Third, the residence time in the afterburner is probably shorter than in the main combustion chamber. All three of these factors lead to lower NO_x formation. In no instance, however, was the total NO_x in reheat less than in military power for the conditions tested.

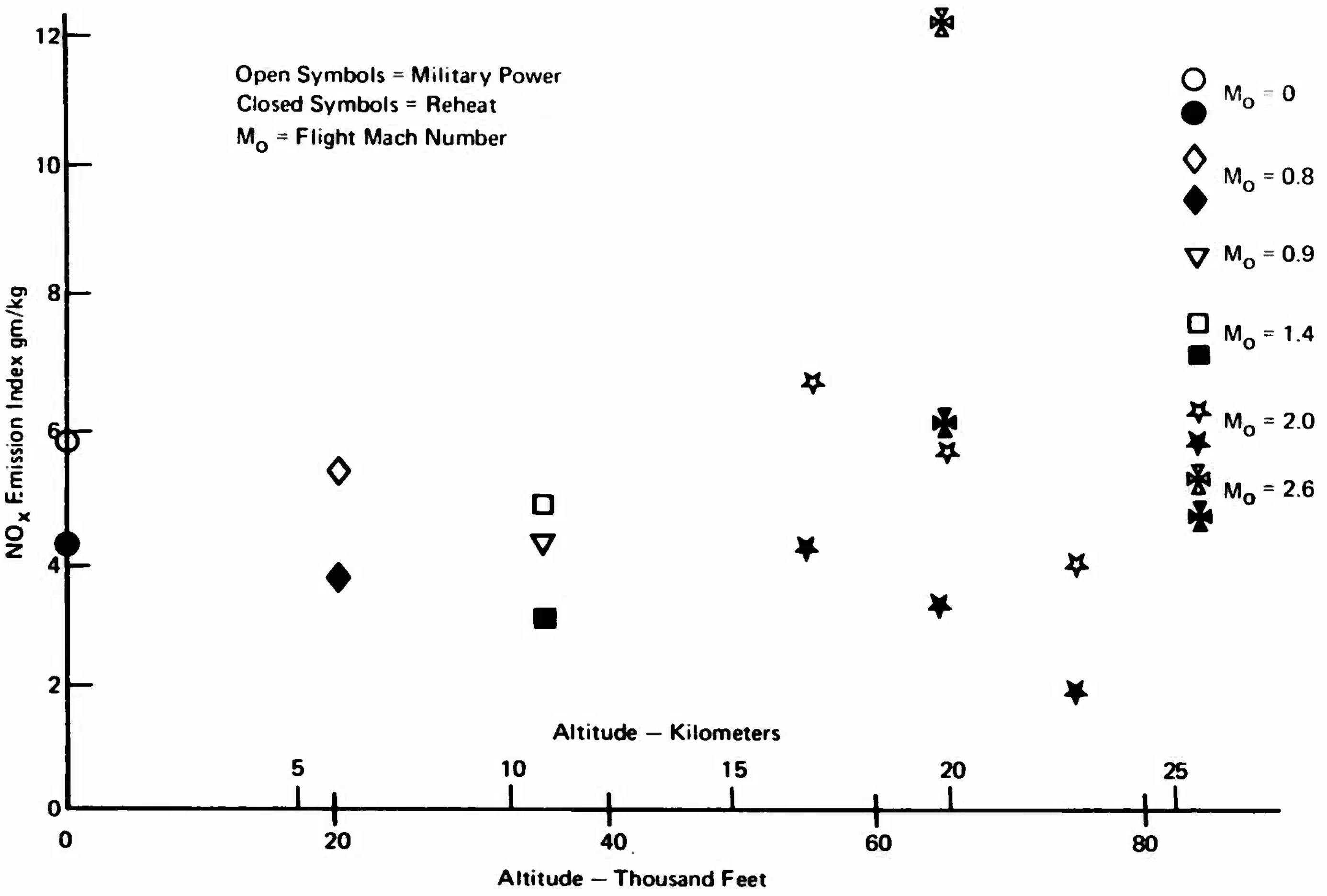

Figure 1. Effect of Reheat on NO$_x$ Emission Index

The increasing emission index with increasing Mach number at constant altitude can be seen for the 10.7 km (35,000 feet) and the 19.8 km (65,000 feet) altitudes of Figure 1. In each case, the main combustion chamber inlet temperature and pressure increased with the increased Mach number. Both these factors cause the NO_x emission index to increase.

The three Mach 2.0 sets of data points clearly show that the effect of increasing altitude at constant Mach number results in reducing the NO_x emission index. The constant Mach numbers resulted in essentially a constant main combustion chamber inlet temperature, but a reduced combustor inlet pressure with increasing altitude. Reducing the combustor inlet pressure reduces the NO_x emission index.

The emission index is, from its definition, related to fuel flow. The amount of NO_x in the exhaust, as measured by available instruments, a chemiluminescence instrument in this case, is measured as a concentration in parts per million by volume. It is interesting to observe what happens to the concentration when changing from a military to a reheat power setting. These effects are shown on Figure 2, where the NO_x concentration is shown against altitude for the same simulated engine conditions as for Figure 1, except there are no 6.1 km (20,000 feet) data points. Of the three effects of reheat observed on Figure 1, two are observed on Figure 2. These two effects are: first, the increasing NO_x with increasing Mach number at constant altitude (see the 19.8 km |65,000 feet| altitude data points); and, second, the decreasing NO_x with increasing altitude at constant Mach number (see the Mach 2.0, 16.8 km |55,000 feet|, 19.8 km |65,000 feet|, and 22.9 km |75,000 feet| data points). However, the third effect of reheat observed in Figure 1, that of decreasing emission index when changing from military power to reheat is not observed on Figure 2. In fact, the reverse is observed. That is, the NO_x concentration in parts per million increases when making this power setting change, except for the 22.9 km (75,000 feet), Mach 2.0 test point where there was no change in concentration. The fact that the NO_x concentration is greater in reheat, but the emission index is less, can be attributed to the great increase in fuel flow in reheat with only a small increase in NO_x formation by the afterburner.

You will recall that NO_x is the sum of NO and NO_2. It is of interest to observe the change in amount of NO_2 making up the NO_x when going from military power to reheat. This effect is shown on Figure 3. In every instance, the amount of NO_2 increases and, in some cases, very greatly.

For a long time, the chemical kineticists insisted that NO_2 should not be present in the exhaust in the quantities being measured by almost everyone. Their reasoning was that the destruction rate of NO_2 under the conditions existing in the exhaust was much greater than the formation rate. Recently, Dr. L. B. Anderson, et al(9) have published a paper explaining the presence of the NO_2. According to them, it is formed as the result of a reaction between HO_2 and NO when there are hydrocarbons present to suppress the hydrogen and oxygen atoms.

The results of the J85 tests in the propulsion wind tunnel confirm those presented on Figures 1, 2, and 3. Because the J85 test permitted measurement downstream of the engine, additional information was obtained. These results are shown on the next few figures.

Figure 4 shows the effect of reheat on NO_x emission index at the engine exit plane, approximately 5 meters (10 diameters) downstream and

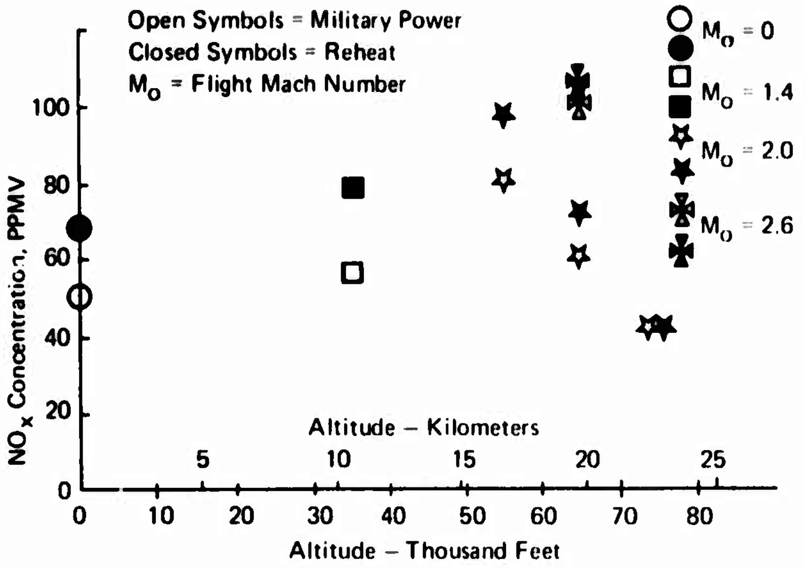

Figure 2. Effect of Reheat on NO_x Concentration

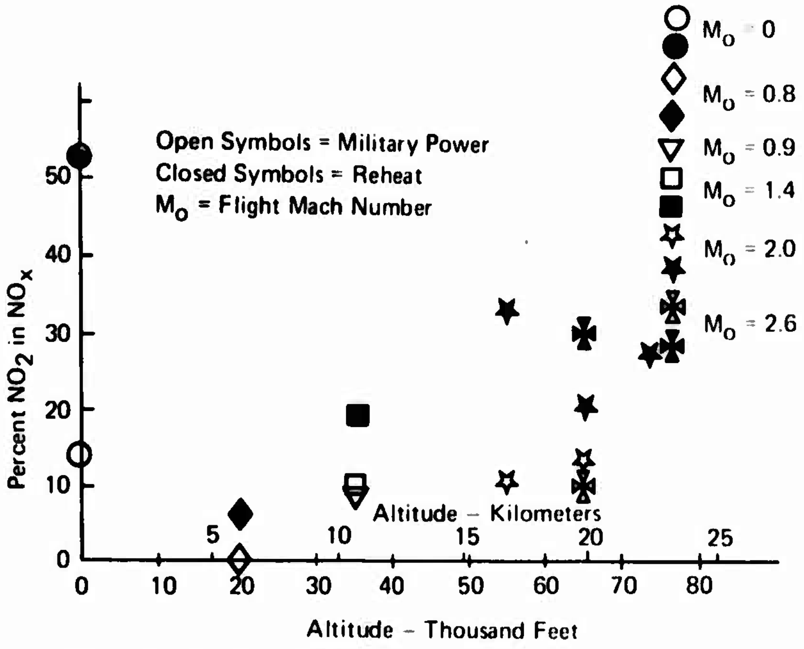

Figure 3. Effect of Reheat on Percent of NO_2 in NO_x

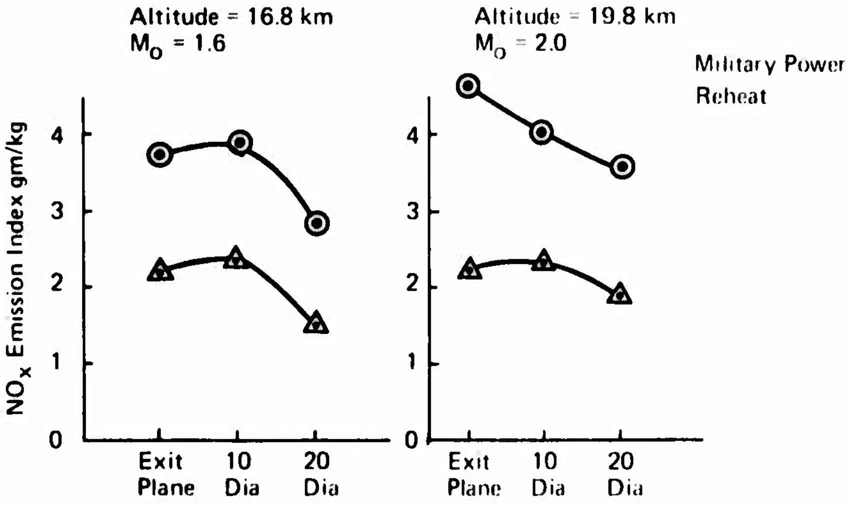

Figure 4. Change in NO_x Emission Index Downstream of Engine

approximately 10 meters (20 diameters) downstream for two different flight Mach numbers and altitudes. Again, the NO_x emission index decreased when the power setting was changed from military to reheat. Three of the four curves on this figure show a greater emission index at approximately 5 meters (10 diameters) than at the exit plane. This result confirms that observed by Diehl.(10)

Figure 5 shows the NO_x concentration for the same conditions of Figure 4. Again, the NO_x concentration increases when changing power setting from military to reheat, except for the Mach 2.0, 19.8 km (65,000 feet) data point at the engine exit plane. The sharp decrease in concentration downstream of the engine is expected. It results from the mixing of the exhaust with the air flowing around the engine.

Figure 6 again shows an increase in NO_2 when changing power setting from military to reheat. An interesting point to observe on this figure is the reducing percentage of NO_2 downstream of the engine. This phenomenon is attributed to the fact that the fuel (hydrocarbons) continues to burn. Accepting the explanation of Anderson, et al(9) the hydrocarbons disappear and are no longer present to suppress the hydrogen and oxygen atoms. The HO_2 and NO reaction does not take place so that the normal NO_2 destruction reactions take over and the NO_2 reduces the further one goes downstream. The only explanation for the two zero NO_2 points appears to be that frequently the concentration was below the capability of the instruments to measure it.

A secondary reason for conducting the engine tests was to attempt to obtain an empirical expression for converting NO_x emission index from one engine operating condition to another. Several different organizations, including the Arnold Research Organization (ARO), the General Electric Company, NASA Lewis Research Center, and Rolls Royce Bristol Engine Division, have developed such expressions. They are generally of the form

$$\frac{(EI_{NO_x})\ cond_1}{(EI_{NO_x})\ cond_2} = \frac{P_{cond_1}^{\frac{1}{2}}}{P_{cond_2}^{\frac{1}{2}}} \, \frac{e^{kT_{cond_1}}}{e^{kT_{cond_2}}}$$

Where: $(EI_{NO_x})\ cond_1$ = Measured NO_x emission index at one engine operating condition

$(EI_{NO_x})\ cond_2$ = The desired NO_x emission index at some other engine operating condition

P_{cond_1} = Combustor inlet pressure at the first engine operating condition

P_{cond_2} = Combustor inlet pressure at the second engine operating condition

k = Empirically derived constant

T_{cond_1} = Combustor inlet temperature at first engine operating condition

T_{cond_2} = Combustor inlet temperature at second engine operating condition

A comparison of these expressions with the measured values obtained at military power setting from the YJ93-GE-3 engine test is given on

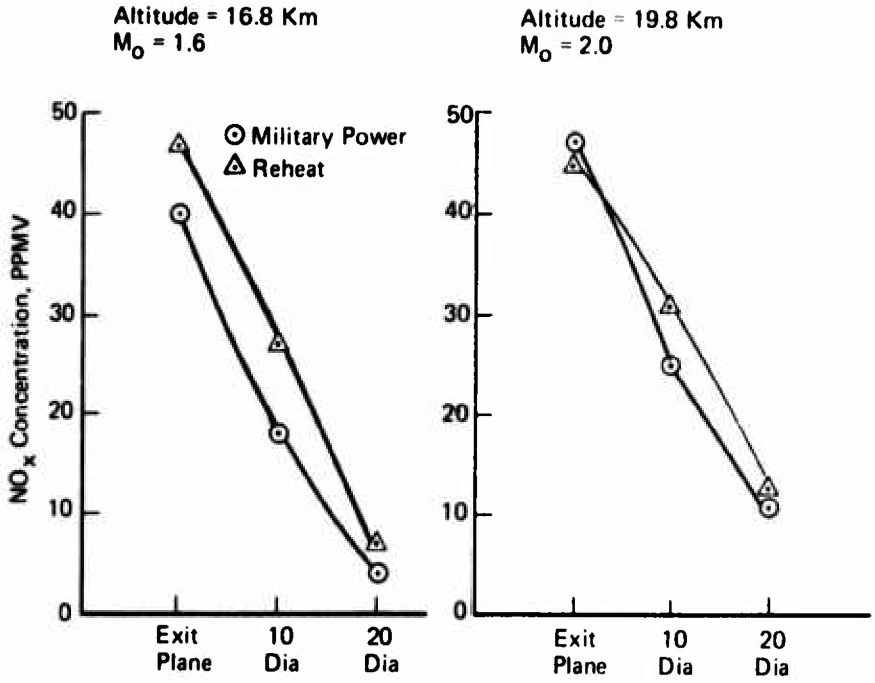

Figure 5. Change in NO$_x$ Concentration Downstream of Engine

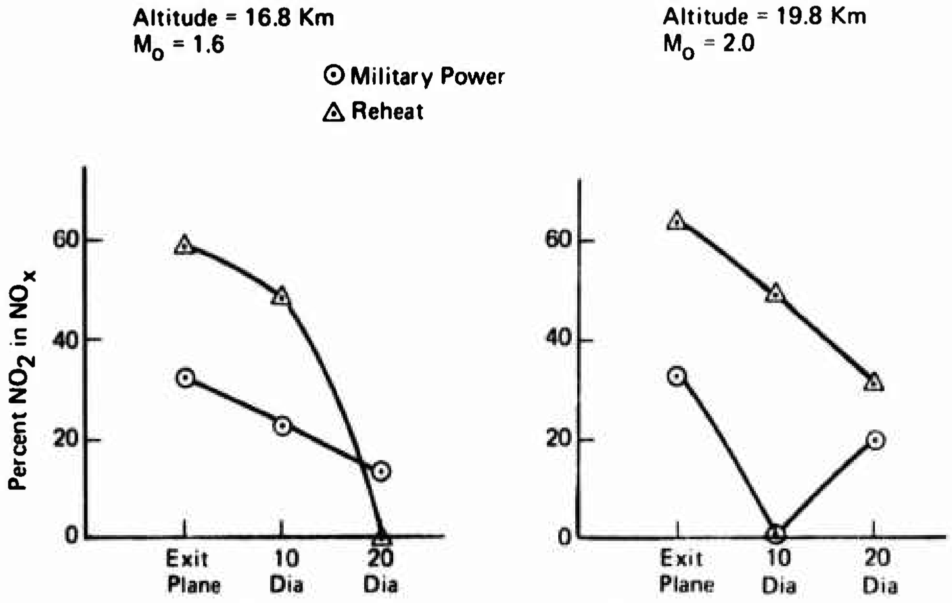

Figure 6. Change in Percent NO$_2$ in NO$_x$ Downstream of Engine

Figure 7. The measured value of 6 gm/kg for the engine at sea level static was used as the known value. The author made the calculations using the expressions developed by the organizations mentioned above and assumes full responsibility for any errors made in the use of the expressions.

Each of the expressions gives a fairly good representation of the measured values, except for the upper set at 19.812 km (65,000 feet). This set represents the Mach 2.6 flight condition. None of the expressions does as well at this condition.

Development of a suitable expression is worth some effort. Altitude testing of aircraft engines is expensive. If a suitable expression for converting sea level NO_x emission indices to flight conditions were available, it would enable one to use the large amount of sea level emission data now becoming available. Furthermore, it would eliminate any need, in the event of regulations on emissions at cruise, the specter raised in the introduction of this paper, for altitude production acceptance tests.

Instrumentation and Sampling Problems

In conclusion, I want to bring to your attention several problems encountered with the sampling system and the instrumentation during these tests. As an introduction to this subject, it is important to recognize that the instruments available for the measurement of chemical species in exhaust plumes of aircraft engines are essentially laboratory instruments. And, even in the laboratory, they are not as accurate as the test cell instrumentation normally used in measuring engine performance parameters, such as temperatures, pressures, rpm, fuel flow, etc.

The basic guide for the measurement of the gaseous emissions used for these tests was the Aerospace Recommended Practice (ARP) 1256,(11) prepared by Committee E-31 and issued by the Society of Automotive Engineers in the United States. This ARP requires an orifice close to the entrance of the gas sampling probe. The purpose of this orifice is to quench the gas sample and stop any further chemical reactions that might alter the sample. For these tests, the range of pressures at the probe inlet from reheat at sea level to military power at 22.9 km (75,000 feet) covered a wide range. In order to have the residence time of the gas sample in the 16.8 meters (50 feet) line between the probe and the instruments not exceed 2 seconds with low pressures at the probe, it was necessary to eliminate the orifice. The probe was water-cooled, but under some conditions the sample had traveled 1.5 meters (5 feet) down the line before it was cooled to the wall temperature required by ARP 1256. What effect the absence of the orifice had on the gas sample is not known. It was assumed to be small.

All of the instruments used for these tests were designed to operate with the sample gas at a pressure of one atmosphere. Frequently in these tests, the sample gas was below that pressure. Therefore, there were pumps in the sample line to raise the pressure. The pumps were insulated, but not temperature controlled to the temperature required by ARP 1256. What effect the pumps had on the sample is again unknown. And, again, it was assumed to be negligible.

The sampling arrangement employed a single traversing probe. The probe itself and the first few feet of the line were of Type 316 stainless steel. At this point, a 1.8 meter (6 feet) section of Teflon was inserted in the line to provide the flexibility required to permit the

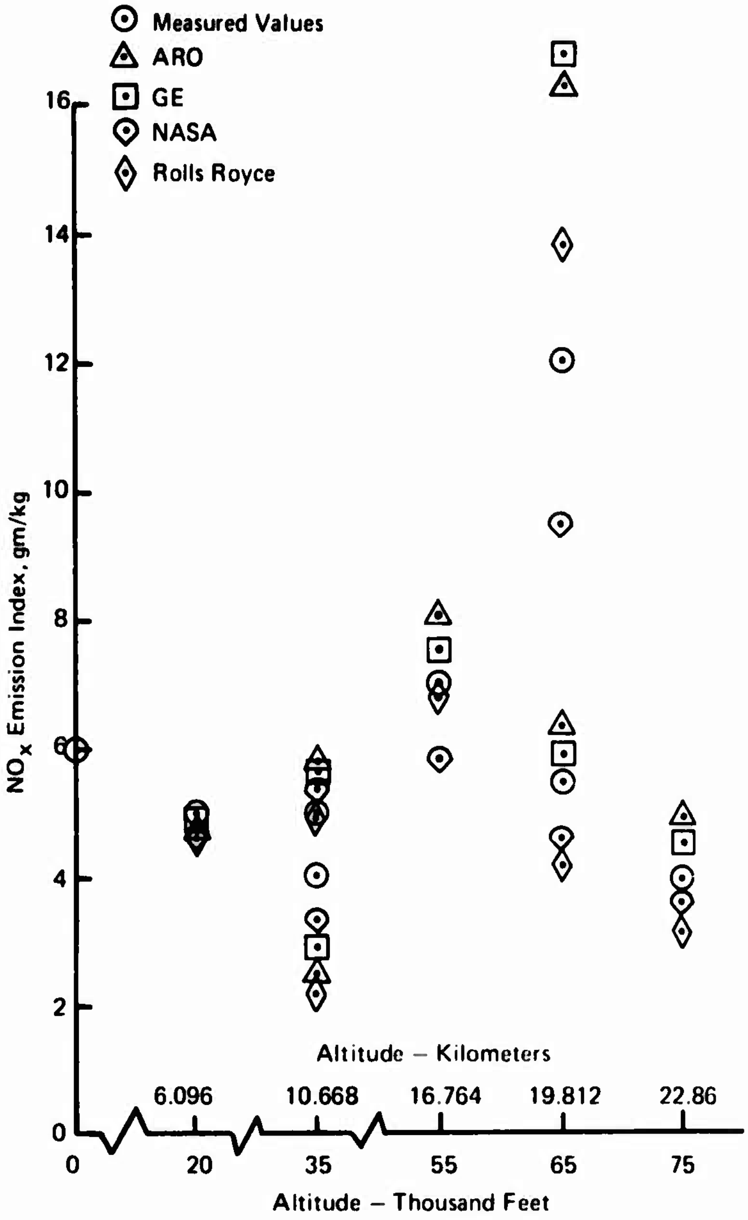

Figure 7. Comparison of Empirical Expressions

probe to traverse. Later, it was learned that Teflon absorbs NO_2. Investigation revealed this absorption to be very slow. It was therefore assumed that, with a maximum of 2 seconds residence time in the sampling line, of which only 1.8 meters (6 feet) were of Teflon, the NO_2 absorption was inconsequential.

Early examination of the NO_x emission data led to the conclusion that there might be some destruction of NO in the sampling line. This conclusion was based on an informal knowledge of the information later published by C. England, et al.(12) These data show that, at an equivalence ratio of 1.0, a stainless steel probe reads approximately 24 percent less NO than does a quartz probe. At an equivalence ratio of approximately 0.7, the two probes read the same value of NO. The measurements in these engine tests were made in the engine exhaust, not at the combustor exit. Consequently, equivalence ratios higher than 0.7 were never encountered. Again, it was assumed that any error from this source could be neglected.

It has been necessary for CIAP to address the problem of the oxides of sulfur, as mentioned in the introduction of this paper. Attempts to measure these species failed. A flame photometer was used to measure the oxides of sulfur on line. The instrument is regularly used to measure sulfur oxides in ambient air quality situations and is therefore considered to be a good instrument. The instrument never became operational, however, during these tests. At first, the instrument failed to indicate any sulfur oxides even in known calibration gases located approximately 3 meters from the instrument. When the calibration gas line was changed from stainless steel to Teflon, the instrument could then be calibrated. Apparently, the stainless steel tube originally used caused some reaction that prevented the sulfur dioxide calibration gas from reaching the instrument. It was concluded that, during engine tests, the long length of stainless steel sampling line caused this same reaction, thereby preventing any oxides of sulfur from reaching the instrument.

In addition to the flame photometer, two wet chemistry methods were used to measure the oxides of sulfur. The two methods are identified as the West and Gaeke Method, and the Hydrogen Peroxide Method. Sulfur oxide measurements were obtained by these two methods. However, these measurements account for only 60 percent of the sulfur known to be in the fuel. It is hypothesized, therefore, that the hot stainless steel probe located in the engine exhaust could have acted as a catalyst to convert SO_2 to SO_3, which would then convert to sulfuric acid. The sampling line was conditioned to 423°K in accordance with ARP 1256.(11) This temperature is below the boiling point of sulfuric acid. It is further hypothesized, therefore, that the sulfuric acid condensed on the walls of the sampling line or in the filter located ahead of the wet chemistry device to remove the particulates that may be present.

Finally, our sampling probe has been critized because it was not designed from the point of view of supersonic aerodynamics. The criticism is that there was probably a standing shock wave in front of the probe, so that the full temperature rise occurred across that shock wave. The concern is that this temperature rise may have altered the sample. This concern was discussed with the ARO engineers before the J85 engine test. Their position, as I understand it, is that the same temperature would have been attained within a few milliseconds regardless of the probe design. As a result, it is assumed that any effect of the standing shock can be neglected. It is recognized, however, that the shock pattern may influence the kinetics involved. Therefore, it is conceivable that the sample was altered by the probe design used.

These problem areas have been included to show people now beginning to make emission measurements some of the pitfalls to be avoided. In addition, it may cause persons with a knowledge of the chemistry involved to come forth with methods to eliminate the problems for us.

References

1. GROBECKER, A.J. Studies of Environmental Effects of Stratospheric Aircraft. First International Symposium on Air Breathing Engines, Marseilles, France, June 1972.

2. GROBECKER, A.J. International Efforts for the Assessment of the Effects of Stratospheric Pollution. IAMAP, Melbourne, Australia, January 1974.

3. FORNEY, A.K. Engine Exhaust Emission Levels. AIAA Paper 73-98, Washington, D.C., January 1973.

4. DAVIDSON, D.L. and DOMAL, A.F. Emission Measurements of a J93 Turbojet Engine. DOT Report No. FAA-RD-73-66, September 1973.

5. GERMAN, R.C., HIGH, M.D. and ROBINSON, C.E. Measurement of Exhaust Emissions from a J85-GE-5B Engine at Simulated High-Altitude, Supersonic, Free-Stream Flight Conditions. DOT Report No. FAA-RD-73-92, June 1973.

6. GRISSOM, J.L. Instrumentation and Measurement for Determination of Emissions from Jet Engines in Altitude Test Cells. AIAA Paper 72-1068, New Orleans, December 1972.

7. McGREGOR, W.K., SEIBER, B.L. and FEW, J.D. Concentration of OH and NO in YJ93-GE-3 Engine Exhausts Measured In Situ by Narrow-Line UV Absorption. Proceedings of the Second CIAP Conference, Cambridge, November 1972.

8. RICHARDSON, R.L. and PERALTA, B. The Refining of Turbine Fuels by Modern Hydrotreating. AIAA Paper No. 74-162, Washington, D.C., January 1974.

9. ANDERSON, L.B., MEYER, J.W. and McLEAN, W.J. Turbojet Exhaust Reactions in Stratospheric Flight. AIAA Journal, January 1974.

10. DIEHL, L.A. Measurement of Gaseous Emissions from an Afterburning Turbojet Engine at Simulated Altitude Conditions. NASA Technical Memorandum X-2726, March 1973.

11. SAE ARP 1256. Procedure for the Continuous Sampling and Measurement of Gaseous Emissions from Aircraft Turbine Engines.

12. ENGLAND, C., HOUSEMAN, J. and TEIXEIRA, D.P. Sampling Nitric Oxide from Combustion Gases. Combustion and Flame. 20, 439-442, 1973.

THE USE OF A ROTATING ARM FACILITY TO STUDY FLIGHT EFFECTS ON JET NOISE

W. SMITH - ROLLS-ROYCE (1971) LIMITED (B.E.D.)

1. INTRODUCTION

There is ample evidence that forward speed has a significant effect on both the generation and radiation characteristics of exhaust noise. This noise can be considered as a combination of jet mixing noise, nozzle based tailpipe noise, internal noise and turbine noise and its source level and in-flight characteristics are of prime importance in both turbojet and turbofan engines.

Although in-flight effects on jet and exhaust noise have been the subject of detailed study for some time, it is only recently that measurement techniques have permitted the systematic study of these effects with sufficient precision to enable meaningful conclusions to be drawn. These findings to date have been salutary in many respects - particularly in regard to the unpredictability of the flight performance of jet noise silencers. There clearly exists a need to pursue these studies further to the point where

i) reliable jet noise prediction methods have been established which can cover in-flight situations over a wide range of jet velocities, and

ii) sufficient in-flight/static comparisons have been made with different forms of jet and exhaust noise silencers to enable meaningful interpretations of static tests and optimisation studies in terms of the expected flight performance.

Several possible techniques are available by which the effects of forward speed on jet and exhaust noise might be studied, they include

a) Standard aircraft or flying test beds,

b) high speed taxying with a suitable aircraft

c) tracked vehicles on which an engine might be carried

d) high speed road vehicles suitable for carrying an engine

e) engines or models mounted in a wind tunnel

f) models mounted on the end of a rotating arm.

Each of the above has its own advantages and disadvantages, paramount among these being size limitations, installation and operating costs, overall timescales, installation problems, flexibility and forward speed capabilities.

One of the facilities which Rolls-Royce (1971) Ltd. at Bristol is evaluating in detail is the rotating arm rig which is used to study the effects of forward speed on jet noise and uses model exhaust systems of between 1/5th and 1/10th full scale. Models are mounted as a tip jet unit (which includes a combustion system) at the end of a 10m (32 ft.) wing. Compressed air is provided to the tip jet unit and the wing can be rotated at speeds up to 150 m/s (500 fps) using the propulsive force from the tip jet at conditions fully representative of turbojet engine exhaust conditions.

The main advantages of this facility are its ability to provide high forward speeds, its low operating costs and short programme timescales. The main disadvantages are nozzle weight limitations due to centrifugal effects,and the complex analysis techniques required due to the transient nature of the noise signal.

This paper describes the rig, together with its capabilities and limitations. The noise data acquisition and analysis techniques are outlined and results obtained from recent tests presented to indicate the repeatability and accuracy of the data; together with a comparison of a typical aircraft in flight measurement.

2. GENERAL DESCRIPTION OF THE FACILITY

The rig is essentially a single rotor blade and two stub arms, rotating in a plane 4.6 m above ground level (Fig. 1). A jet unit complete with combustion can and interchangeable test nozzle is mounted at the tip of blade at a radius of 10m. Compressed air, bled from two Avon Series 200 gas turbine engines situated in an enclosed engine house some 30m from the rig, is supplied to the rig via a main supply pipe in which is situated the air control valve and air flow meter. After passing up through the rotor head the air supply line is split into three 76 mm diameter pipes which carry the air through the wing section to the tip jet unit. The test nozzles are mounted to the tip unit by means of a quick break coupling to facilitate nozzle changes.

To enable the rotational speed of the tip unit to be varied at constant nozzle flow conditions, remotely controlled air brakes are installed above and below the wing at approx 9.2m radius. These brakes are essentially flat plates approximately 76mm x 560 mm in size, and are controlled by a closed circuit pneumatic system incorporating inflatable bags which adjust the brake angle and hence the rotor drag. The system is controlled remotely from the main rig control cabin.

3. TIP JET ASSEMBLY

The complete tip jet assembly consists of three sections, namely the nose unit, combustion chamber and test nozzle.

The nose unit is a fairing covering balance weights which are placed to maintain the chordwise balance of the whole tip assembly. These balance weights ensure that the centre of gravity of the tip unit, including the test nozzle, lies on the neutral axis of the wing, thus avoiding twisting the wing with consequent normal forces when in motion.

The combustion chamber which is located over the three air supply pipes in the wing is of a simple design consisting basically of a short flame tube with zonal intermixing holes. A high energy igniter and fuel metering atomiser positioned at the front of the chamber are surrounded by an outer casing. Fuel is supplied under pressure to the combustor unit, the method of pressurising depending on whether the model nozzle is to be tested under static conditions (i.e. with the wing tethered), or with the wing rotating. In the tethered mode the fuel is supplied by a Lucas high pressure pump direct to the combustor. In the spinning mode fuel is supplied to the rotor head and then through a rotating seal to a fuel line situated on the leading edge of the wing. Burner pressure is generated by the standing column of fuel in the supply line.

4. RIG INSTRUMENTATION

Rig instrumentation is provided in the tip unit with which to determine test nozzle stagnation conditions when the rig is in operation. Pressures are transmitted from the measurement stations in the tip unit via hypodermic tubes to 8 pressure transducers mounted in the rotor hub. The voltage output from these transducers together with the output from the thermocouples in the tip unit, are fed to a multichannel slip ring in the hub. The slip ring system is limited to 15 channels covering both wing services and temperature/pressure readout. Seven of the channels are used for services which include: high energy igniter (2), air brake control valve (2), air brake position indicator (1), common negative earth (1), and multi-plex switching (1). The remaining 8 channels are used for the pressure and temperature measurement and by using multi-plex switching there is a total capacity of recording 17 readings, of which 8 are pressures.

5. ROTOR SPEED LIMITATIONS

In the interests of mechanical integrity and operational safety the maximum rotational speed of the rotor is limited. This limit is calculated from the centrifugal acceleration of the tip jet unit and the known variation of hub stress with tip speed and mass.

The ultimate speed limit is bounded by:-

a) Maximum permitted under 'g' loading
= 3.3 revs/sec (200 rpm)

and b) The stress limit on the stub shaft counterbalance weight retention studs
= 45 Kg (100 lb) per arm

The stress on the retention studs is dependant on the actual mass required on the stub arms to effect complete balancing of the rig, and this mass is a function of the all-up-mass of the tip jet unit.

Thus having established the counterbalance mass required on the stub arms it is possible to ascertain the maximum rotational speed. This in effect results in practice in a maximum nozzle weight of approximately 15 Kg (33 lbs) over the normal operational range over which tests are performed.

6. ACOUSTIC DATA ACQUISITION

Two methods of noise recording are employed depending on whether the wing is tethered for static testing, or rotating for in-flight simulation.

6.1 Static Tests

Fig. 2 shows diagrammatically the rig and microphone arrangements for static nozzle noise recordings. Essentially the basic system uses a boom on which is mounted at 6m (20 ft.) radius a $\frac{1}{4}$ inch Bruel and Kjaer condenser microphone at nozzle centre line height and at normal incidence to the nozzle exit plane. The pivot point of the boom is positioned below the nozzle exit plane and an electric motor is used to drive the boom, at a rate of $\frac{1}{2}^{\circ}$ per second, over an angular range from 20° to 150° to the exhaust axis. Cams at 10° intervals are used as angular position indicators, a signal being recorded as the boom passes each cam. To minimise ground reflection interference effects, the boom is acoustically treated with acoustic foam wedges.

Additional microphones can be installed to suit any particular requirements of the test programme being carried out, and it is normal practice to utilise additional microphones at certain angles to examine the stability of the noise signal.

The signal from the microphone and the angular indicator is recorded on an Ampex FR 1300 multi-channel tape recorder, at a tape speed of 15 ins/sec.

6.2 In-Flight Recordings

The basic microphone positions used for recording in-flight measurements are shown diagrammatically in Fig. 3. A linear array of microphones is used although it will be shown when describing the analysis technique that only one microphone is needed to provide the complete angular range (20° to 150° to the exhaust axis), thus the additional microphones are only used for back-up purposes. All the microphones in the array are positioned in the plane of the wing at normal incidence relative to the nozzle exit plane when the wing is in the position as shown in Fig. 4. A microphone is also positioned at a distance of 3.8m above the axis of rotation of the rig, this being used to examine the stability of the noise throughout the test and can also be used to carry out narrow band analysis as the angle relative to the jet is a constant 90°.

To give an accurate reading of the nozzle position relative to the microphones while the wing is rotating, a master pulse signal, together with 120 intermediate pulses (3° increments) is recorded during each revolution of the rotor.

Again to minimise ground reflection interference effects the measurement surface between the rig and microphones is covered with acoustic treatment.

The signals from the microphones and the rotor positional transducers are recorded on an Ampex tape recorder using a tape speed of 60 ins/sec. This high tape speed is required for the in-flight measurements as it is necessary to reduce the tape speed by a factor of 16:1 when analysing the data, the reason for this will be explained in the description of the analysis technique.

7. ACOUSTIC DATA ANALYSIS

Analysis of both static and in-flight measurements is carried out on a General Radio Type 1921, $\frac{1}{3}$rd octave parallel filter analyser. The method used to analyse each measurement mode however differs significantly.

7.1 Analysis of Flight Measurements

The principal problem encountered in the analysis of the flight recordings is the rapid variation of noise level with time. This is demonstrated clearly in Fig. 4 which shows the variation of overall noise with time at the "outboard" microphone for a rotor speed of 1.68 rev/sec. The problem resolves itself into finding a method of obtaining adequate statistical accuracy of noise level measurement over the frequency range of interest (200 Hz - 50 KHz) combined with adequate angular resolution of the noise field shape. These fundamental requirements have to be combined with the practical constraint of a minimum analyser averaging time of $\frac{1}{8}$ sec.

Fig. 4 shows that in $\frac{1}{8}$ sec. the rotor has turned through about 75°, a clearly unacceptable angular resolution. The solution adopted is to reduce the replay speed of the tape to 1/16 of the recording speed which then gives a resolution of about $\pm 2\frac{1}{2}^{\circ}$ of rotor movement equivalent to an acceptable resolution of about ±5° angle relative to the jet axis at a high rotor speed (Fig. 5). Noise levels are measured for 10 consecutive revolutions to increase the effective signal averaging time at 1/16 of recording speed to 1.25 secs ($\frac{1}{8}$ x 10 sec.) which gives a 95% confidence limit of about ±1dB at frequencies above 2500 Hz. The model scale factor is of order 10 so that when converted to full scale this accuracy is obtained at frequencies above 250 Hz. At lower frequencies the accuracy will deteriorate, but still yields a 95% confidence limit of ±1.5 dB at 125 Hz.

Timing of the analysis operation is clearly critical. Transducers on the rig rotor head produce a master pulse once per revolution and also a second set of pulses at every 3° of angular movement; these pulses are also recorded on the same tape as the noise. Triggering of the analyser is performed by a timing unit using these pulses as input and which makes allowance for the time taken by the sound to reach the microphone from the nozzle. The timing unit can be set to trigger the analyser at an instant corresponding to any specified angle to the jet axis of the noise emission.

7.2 Analysis of Static Measurements (rotor tethered)

Analysis of static noise recordings is carried out by more conventional methods. An integration period of 16 seconds is utilised for the recordings from the fixed microphones at each test condition. The polar traverse microphone recordings utilise the positional indicater signal from each cam to trigger the analyser, and a 1 second integration period is used at each angular position.

The ensuing data from the analyser, for both static and flight analysis, appears on punched paper tape. The computer applies microphone tape recorder frequency response, and atmospheric absorption corrections and prints out the third octave tabulations etc., at model scale and if required extrapolated full scale results.

8. NOISE RESULTS

One of the first features of the rig's performance to be examined was its ability to produce repeatable results, both statically and in-flight. This was achieved by installing a nozzle unit and recording its noise characteristics during repeated tests at given stagnation conditions. The tests were made both under static and flight conditions, the latter at a constant flight speed, over a period of several days. Fig. 6 shows the results of the static measurements, the data having been scaled to equivalent engine size and presented as a plot of perceived noise (PNdB) against angle to the jet axis (θ). This figure, shows seven separate noise measurements with a scatter, in general, better than ±1 dB. The corresponding flight measurements, which in this case only covers five separate results, are shown in Fig. 7. Although it can be seen that there is slightly more scatter compared with the static case, in general the scatter is no greater than ±1 dB, which compares favourably with that achieved from measurements carried out on aircraft.

With encouraging results showing that the rig was capable of producing repeatable noise data, it is now possible to look at a typical result from tests performed on a convergent nozzle, and examine the static to flight changes.

Fig. 8 presents the results of static and flight measurements from a convergent nozzle operating at a sub-critical pressure ratio, with a resulting jet velocity of 505 m/s (1660 fps), and for the flight case at a forward speed 71 m/s (232 fps). The results have been corrected to the same distance for comparison. The reductions in noise due to forward speed are seen to be largest at angles close to peak noise, and that above 90° to the jet there is no reduction. The reduction in noise at 30° (peak static noise angle) is approximately 5 dB which is equivalent to an eighth power dependance based on the relative jet velocity (difference between jet and flight velocities). This reduction in noise is thus in line with the prediction based on the static noise velocity dependance.

The ultimate evaluation of the rig's performance must be the ability to reproduce results which are compatible with full scale measurements from aircraft in-flight. This has been made possible by recent controlled measurements on the Viper 601, installed in the H.S. 125 aircraft, together with the corresponding static measurements. Fig. 9 shows comparisons, both statically and in-flight, of the engine's noise characteristics at a condition where jet noise is dominant, with those from scaled model measurements on the spinning rig, at identical jet velocities and forward speeds. The full scale results have been corrected to free field conditions and all the results extrapolated to a distance of 450 m for ease of comparison. It can be seen that both statically and in-flight the field shapes show very good agreement between the scale model and engine results. Both show small reductions at peak, and increases in the forward arc ($\theta > 70^\circ$) due to forward speed. This comparison is encouraging, and leads to greater confidence in the rig's ability to reproduce effects measured on full scale engines.

9. FUTURE WORK

During the past twelve months the rig has been extensively overhauled, instrumentation services improved, and a very detailed noise programme has recently commenced. This work will be aimed at evaluating in more detail the rig's capabilities, for besides fundamental noise studies on convergent nozzles to compare with existing data measured in a wind tunnel, programmes are to be carried out with models of silencer systems which have recently been evaluated at full scale.

10.0 CONCLUSIONS

The results presented in this paper have shown that the rotating arm as a flight simulation facility is capable of providing repeatable data for model exhaust nozzles. The results for a standard convergent nozzle system are compatible with in-flight measurements at full scale, and give confidence that this type of facility is a useful tool with which to evaluate meaningully and cheaply the in-flight acoustic performance of jet nozzle systems.

11.0 ACKNOWLEDGEMENT

The author gratefully acknowledges the assistance of colleagues at Rolls Royce (1971) Limited, Bristol Engine Division, in the preparation of this paper.

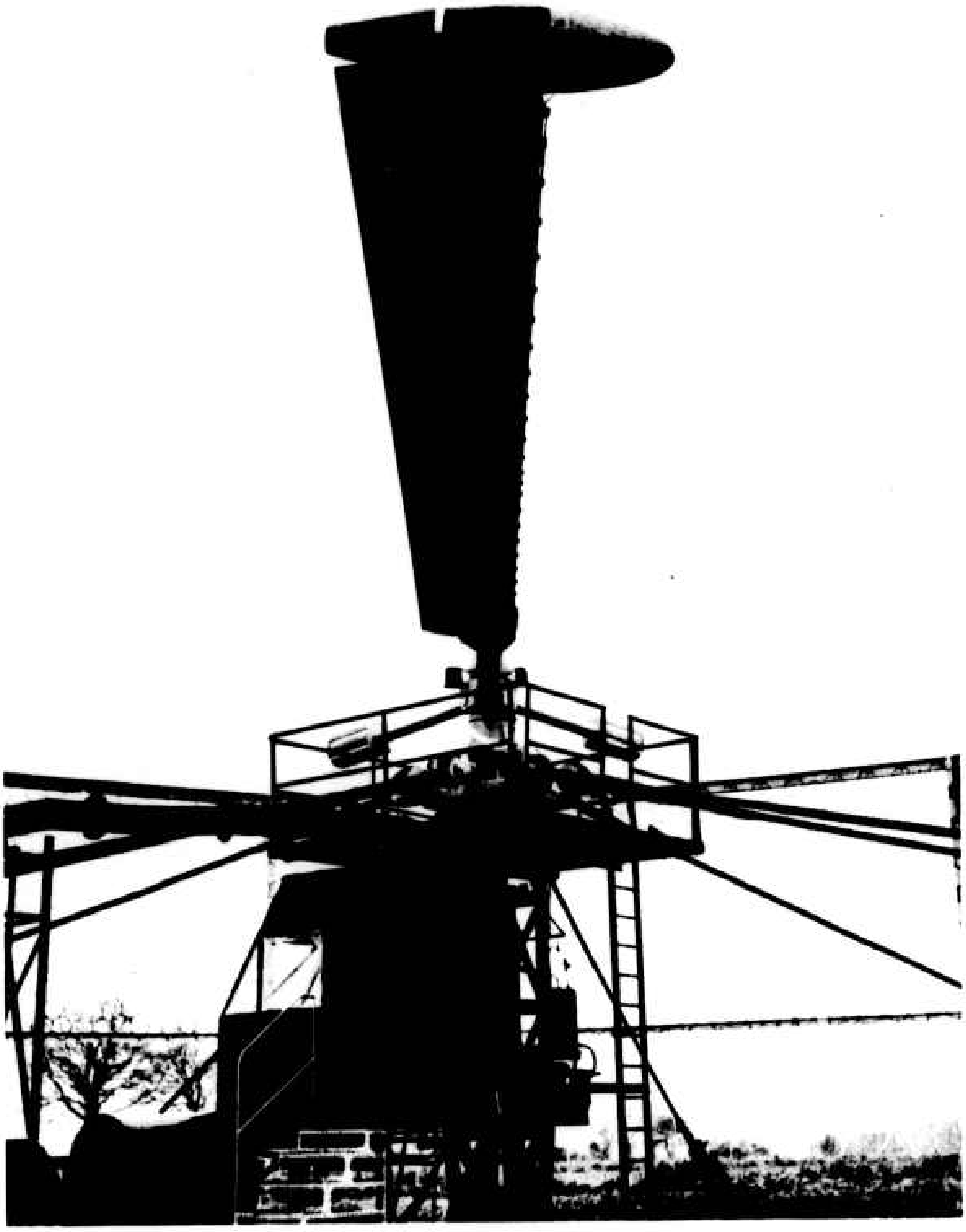

FIG. 1. GENERAL VIEW OF ROTATING ARM FACILITY

ROLLS-ROYCE (1971) LIMITED, BRISTOL ENGINE DIVISION, FILTON, BRISTOL. | L.J.D. MAR. 1974.

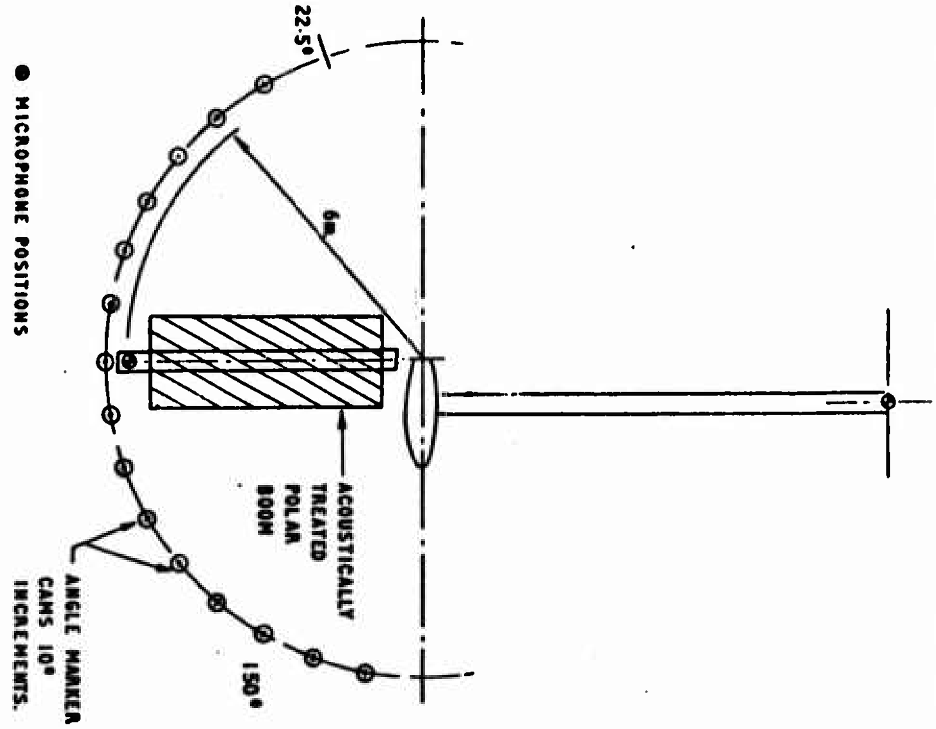
22.5°
6m.
ACOUSTICALLY TREATED POLAR BOOM
ANGLE MARKER CAMS 10° INCREMENTS.
150°
● MICROPHONE POSITIONS

ROLLS ROYCE FLIGHT SIMULATION FACILITY
STATIC NOISE MEASUREMENT SYSTEM.

FIG.2.

C D W Ltd 186

ROLLS-ROYCE (1971) LIMITED, BRISTOL ENGINE DIVISION, FILTON, BRISTOL. | L.J.D. MAR. 1974.

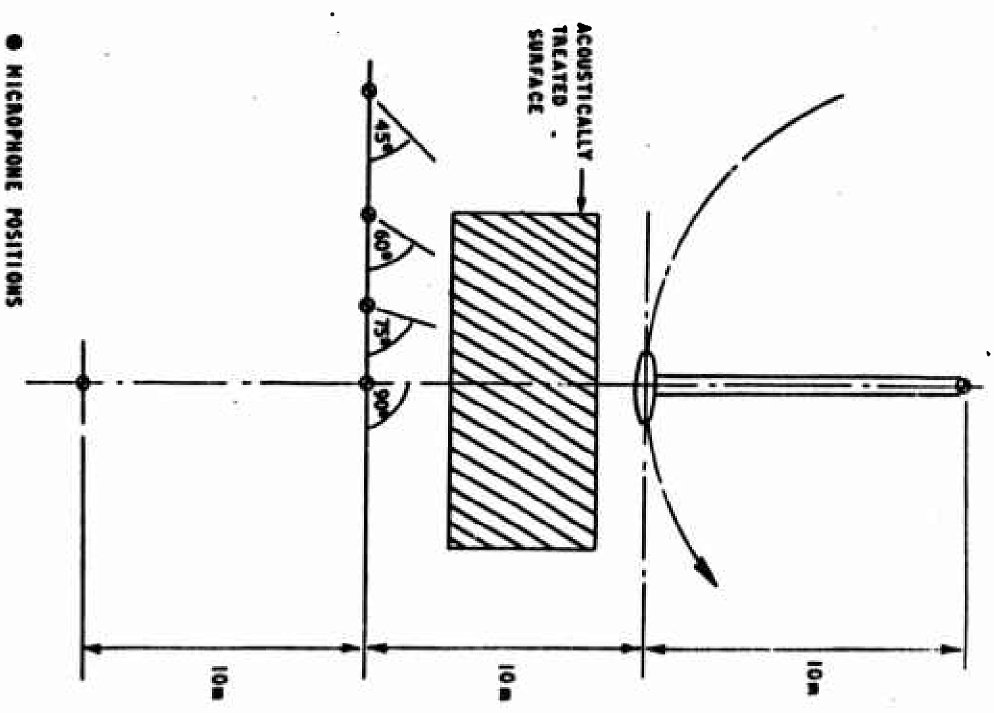
ACOUSTICALLY TREATED SURFACE
45°
60°
75°
90°
10m
10m
10m
● MICROPHONE POSITIONS

FLIGHT MEASUREMENT SYSTEM.

FIG.3.

C D W Ltd 186

ROLLS-ROYCE (1971) LIMITED, BRISTOL ENGINE DIVISION, FILTON, BRISTOL. L.J.D. MAR. 1974.

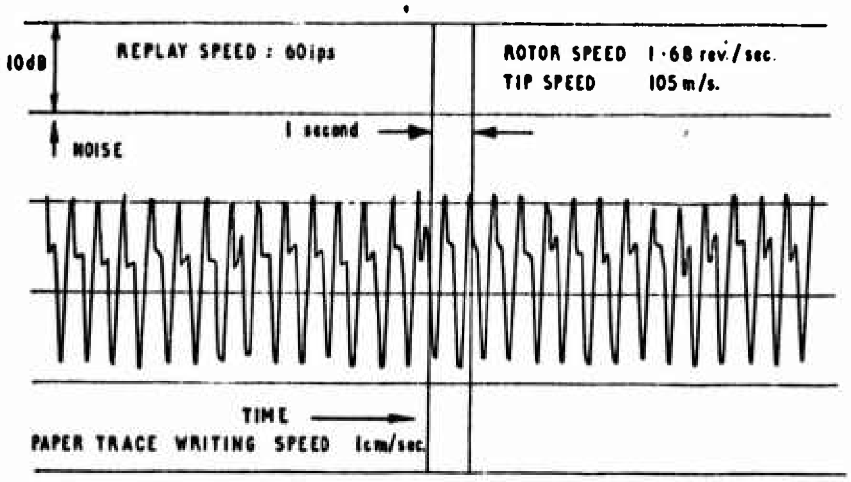

OVERALL NOISE vs TIME.

FIG.4.

C D W Ltd

ROLLS-ROYCE (1971) LIMITED, BRISTOL ENGINE DIVISION, FILTON, BRISTOL. L.J.D. MAR. 1974.

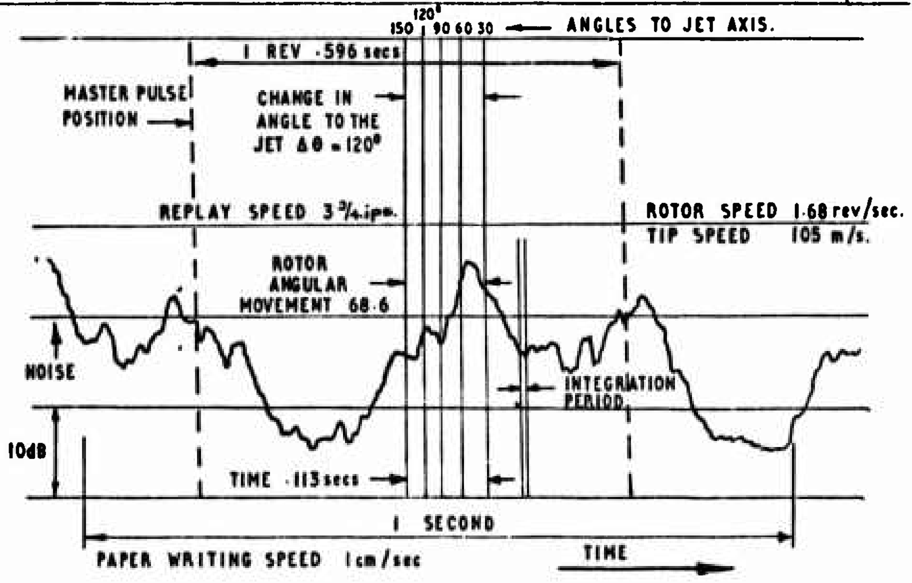

OVERALL NOISE vs TIME.

FIG.5.

C D W Ltd

ROLLS-ROYCE (1971) LIMITED, BRISTOL ENGINE DIVISION, FILTON, BRISTOL.

L.J.D. MAR. 1974

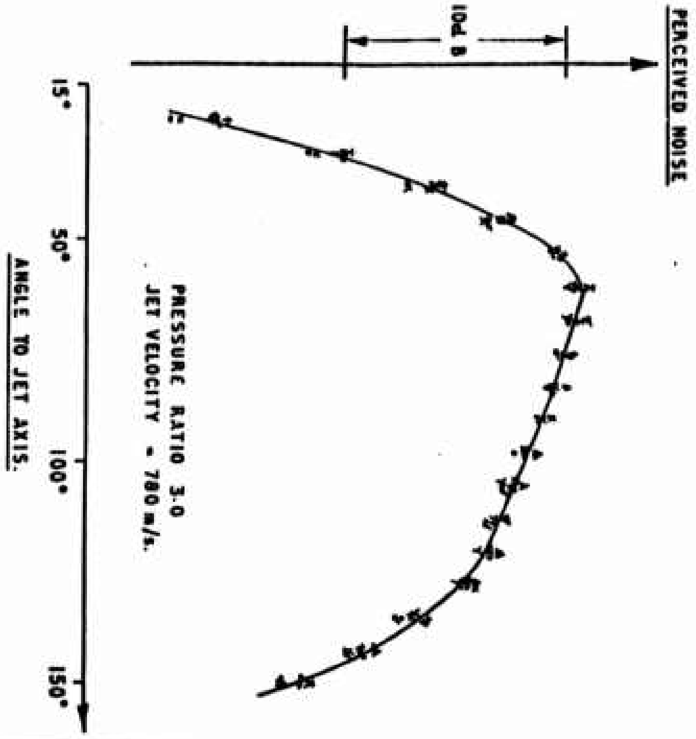

STATIC NOISE REPEATABILITY.

FIG.6.

C D W Ltd 18p

91

ROLLS-ROYCE (1971) LIMITED, BRISTOL ENGINE DIVISION, FILTON, BRISTOL

L.J.D. MAR. 1974

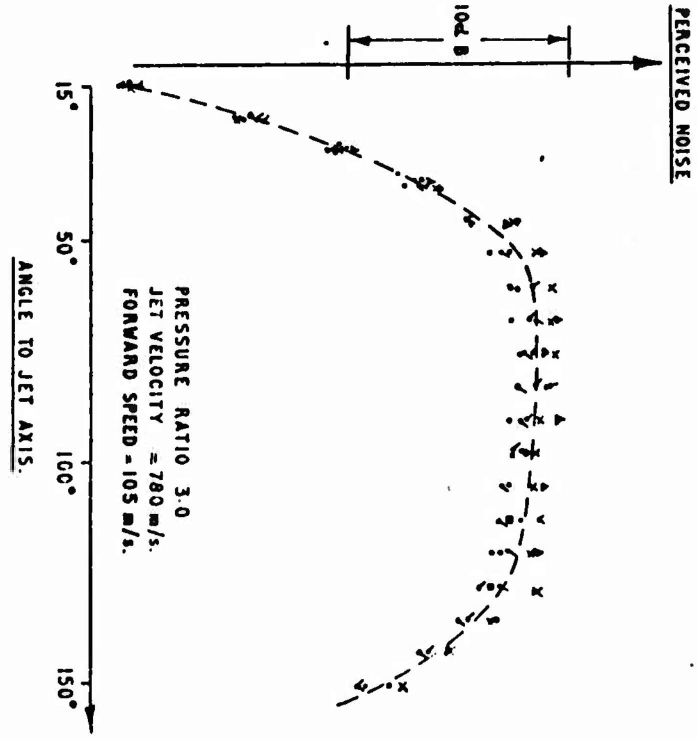

FLIGHT NOISE REPEATABILITY.

FIG.7.

ROLLS-ROYCE (1971) LIMITED, BRISTOL ENGINE DIVISION. FILTON, BRISTOL. L J D MARCH '74.

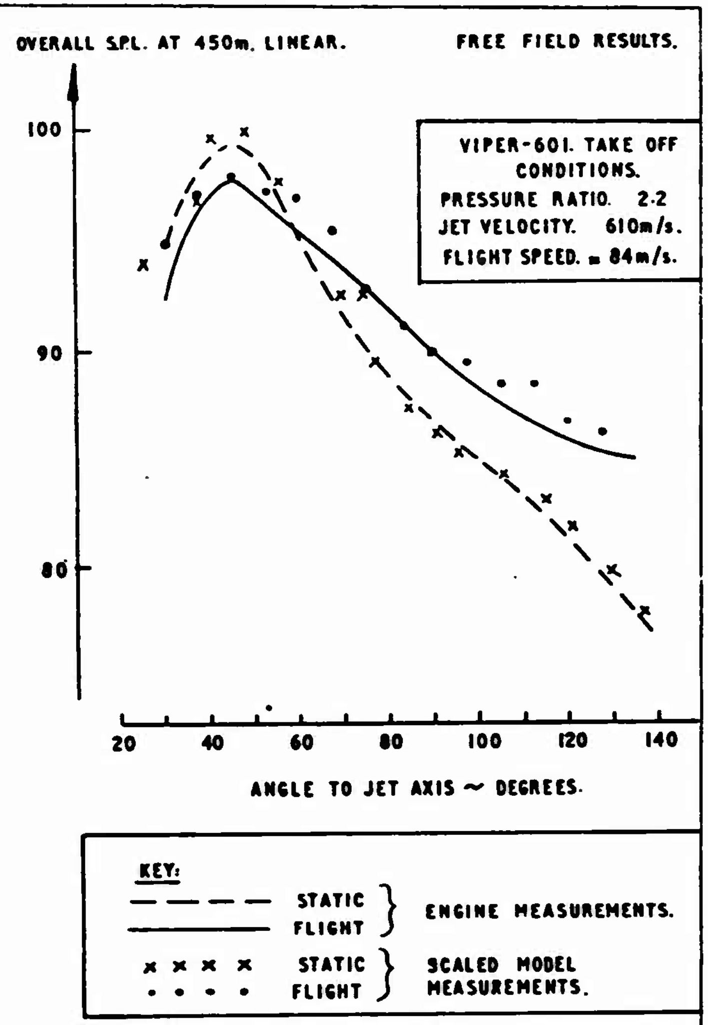

ENGINE vs SCALED MODEL RESULTS STATIC & FLIGHT.

FIG. 9.

ROLLS-ROYCE (1971) LIMITED, BRISTOL ENGINE DIVISION. FILTON, BRISTOL. L.J.D. MAR.1974.

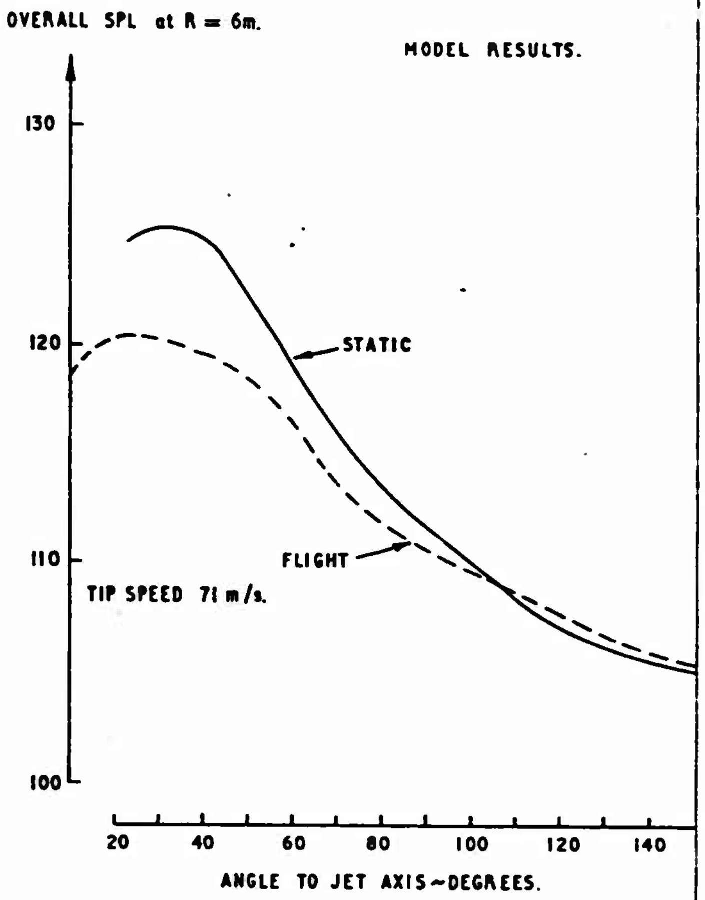

CONVERGENT NOZZLE. $P_J/P_\infty = 1{\cdot}83$ $T_J \triangleq 790°K$ $V_J \triangleq 505$ m/s

FIG. 8.

LIFE ENHANCEMENT OF TURBINE BLADES

R. V. Narayana Murthy

Introduction

Life of Nimonic 90 material turbine blades, fitted on engines manufactured in India under licence agreement had been restricted to 250 hours by the foreign collaborator. A few years back, the turnover of engines at the factory was greatly hampered due to a dearth of new sets of blades. Many sets of blades fitted on engines were nearing completion of the authorised life. These in turn affected to a great extent the operational programme. An investigation was therefore immediately undertaken to examine the possibility of enhancing the life of blades. The investigation involved a theoretical analysis followed by testing for creep on a few test specimens and an engine type test. Based on these exercises, the life of blades was enhanced to 300 hours for application on one of the marks of the engine and to 550 hours for a derated version. The investigation made in the absence of complete design details and sophisticated rig testing facilities benefited further utilisation of a large number of turbine blades, which otherwise would have been scrapped. The investigation also enabled to tide over the difficulties faced at the factory in meeting the production targets. Further a considerable amount of financial benefits was realised. Service experience on engines has been satisfactory and a number of blades have completed the increased life without any incident. It is felt that in an emergency a similar procedure could be adopted for enhancing the life of other highly stressed components of aero engines.

The purpose of this paper is to present in detail the investigation made here in connection with life development of turbine blades.

Theoretical Analysis

As a preamble to creep testing on test specimens and proving trials on test bed, a theoretical analysis was made by computing the stresses experienced at various stations along the blade height. Life of turbine blades is mainly limited by creep and fatigue characteristics. No design details apart from manufacturing drawings and engine performance figures were readily available. Stresses due to centrifugal force, gas bending moment and offset bending moment at maximum rating condition of the engine were calculated. These values were then compared with the stresses required for rupture of Nimonic 90 material in 500 hours at temperatures actually encountered by the blade.

Blade Stresses

The main loadings producing stress in a blade are due to :

(a) Tension caused by centrifugal force

(b) Bending resulting from blade lean

(c) Bending resulting from gas load

(d) Vibration

(a) Tension due to centrifugal force

Centrifugal stress of a turbine blade is given by the relation

$$f = \rho \omega^2 l r$$

where f = centrifugal stress
ρ = density of blade material
ω = angular velocity
l = length of blade
r = mean radius

The blade was divided into convenient sections and the centrifugal forces due to these sections were calculated. Sectional areas at various stations were measured by the aid of a planimeter. At these stations centrifugal stresses were computed by using the above formula.

(b) Bending resulting from blade lean

Blade profile invariably tapers from root to tip, and generally thickness at the tip is the minimum consistent with aerodynamic requirements. In general, centroids of sections at different radii do not lie on a radial line but are arranged to lean in the direction of rotation. Hence, a small element of the blade subjected to centrifugal force produces bending moment at the root. The blades under consideration had centroids of sections along the height offset in both axial and circumferential directions. The blade was divided into a number of elements by planes at right angles to the radius. Taking the centroid of root section as origin, offset in axial and circumferential directions at different stations was measured. Bending moments resulting from blade lean were then estimated for maximum engine rating condition.

(c) Bending resulting from gas load

Change of momentum of gas passing over blades provides the torque necessary for driving a turbine wheel. This force will not be a uniformly distributed load along the blade length but will vary from root to tip, depending upon the degree of reaction employed at various radii. In addition to the torque resulting from gas flow, each element of the blade is also subjected to a thrust load. Integrals of these forces along the blade length in the tangential and axial directions give an equivalent single circumferential force and thrust force acting at a radius which would induce in the root section the same stress as the actual loading due to the gas force. These forces and consequent bending moments were calculated from velocity triangles drawn for various sections of the blade by making the following assumptions :

(i) $Va_1 \; r^{\cos^2\alpha} =$ constant

(ii) $Vw_1 \; r^{\cos^2\alpha} =$ constant

(iii) $\alpha =$ constant along the height

where $Va_1 =$ axial velocity at entry to turbine rotor

$Vw_1 =$ whirl velocity at entry to turbine rotor

$r =$ radius

$\alpha =$ nozzle exit angle

(d) Stresses due to vibration

In engine operation, there will not be a uniform flow of gas through blade passages, but the flow will consist of a series of puffs of cyclic nature. This induces vibration in blades. For the present investigation, it was presumed that the designer would have ensured there would be no resonance of blades under all conditions of engine operation. Nevertheless, a variation of 20 per cent was allowed on the average steady gas bending stresses to account for stresses due to vibration and stress concentrations.

Resultant Stresses

The bending moments in the circumferential direction due to gas loads and centrifugal forces were added together as well as those for the axial direction. Thus two resultant moments were obtained in both circumferential and axial directions. The bending moments about principal axes were then calculated. The resultant bending stresses at leading and trailing edges and at back of the blade were then estimated using the relation :

$$\text{Stress at edge of blade} = \frac{x.M_{min}}{I\ min} + \frac{y.M_{max}}{I\ max}$$

where x = distance from minor principal axis to edge of blade

y = distance from major principal axis to edge of blade

I min, I max = moments of inertia about minor and major principal axes respectively.

M_{min}, M_{max} = bending moments about minor and major principal axes respectively.

Total Stresses and Theoretical Blade Life

The total stresses at various stations of the blade were obtained by algebraic addition of stresses resulting from centrifugal force, blade lean and gas loads. A check on total stresses to cater for vibration and stress concentrations revealed an adequate margin between total stresses and creep rupture strength of the blade material. The total stresses at maximum engine rating for ISA sea level static condition only were determined since the engines were not being operated by the service at other conditions such as Arctic sea level Mach1, Tropic sea level Mach1 and ISA 15.24 Km Mach 2. The total stresses computed are shown in Table 1 and the same are plotted in Fig. 1. The figure also indicates the stresses required to rupture Nimonic 90 material in 500 hours at temperatures actually experienced by the blade. Thermal paint technique was employed to determine the temperatures encountered by the blade in engine running conditions. It is observed that the most critical point is the back of the blade at root station. The total stress at this point is 237 MN/m^2, whereas the stress to rupture the blade in 500 hours at the same location is 386 MN/m^2. Considering the adequate margin in the magnitude of stresses it was concluded that the life of blades could be increased to 500 hours theoretically. Since blades of the same material were also being used on a derated version of the engine, a possibility of enhancing the blade life to more than 500 hours was envisaged for this application.

Test Results

The next part of the investigation comprised creep test on test specimens and type test on an engine.

Creep Test

A few turbine blades which had been earlier subjected to type test for 314 hours were selected for creep test. A tensile load of 9964 KN was applied on test specimens maintaining the temperature around them at 1023°K. The specimens withstood these loading conditions for 278 hours before rupture. The failure was believed to be not entirely due to creep but also due to high strain rate. Thus it may be observed that the sample blades withstood 314 hours of type test and 278 hours of creep test making a total of 592 hours prior to failure.

Type Test

Though Nimonic 90 turbine blades had earlier withstood type test conditions for 314 hours, further testing on an engine on test bed was programmed to obtain additional data on creep characteristics. An engine fitted with 65 blades which had earlier completed 314 hours of type test and the remaining 60 blades which had completed about 200 hours of run in service was selected for the purpose. The schedule for the test stipulated cyclic running of the engine conforming to the requirements laid down in D.Engg.R.D. Specification 2100. Each cycle of six hours comprised acceleration, deceleration, prolonged running at various engine rating conditions and at a number of speeds between idling and maximum. The type test of about 100 hours duration was satisfactorily completed and growth of the blades due to creep was found to be well within allowable limits.

Life Enhancement

From the foregoing, the following may be observed :

(a) The theoretical estimation indicates that the blade life can safely be increased to 500 hours for application on one of the marks of the engine and to more than 500 hours on a derated version.

(b) Test specimens from samples of blades which had undergone type test for 314 hours withstood a load of 99.64 KN at 1023°K for 278 hours.

(c) The growth of blades due to creep was well within limits even after more than 400 hours of running under type test conditions.

In view of the above, airworthiness authorities in India considered it reasonable to enhance the life of blades to 300 hours for the standard version engines and to 550 hours for the derated version without jeopardising airworthiness of engines.

Service Experience

One of the factors that restricted enhancing overhaul life of engines was the limitation imposed on life of turbine blades. The investigation resulted in increasing the overhaul life of one hundred and eighty-three standard version engines to 300 hours. Hitherto nearly thirty-six engines have completed the enhanced life without any incident. Of the remaining engines, though some have been prematurely returned from service for various reasons no engine has been withdrawn for failure of turbine blades.

Fifty-two derated version engines had been built with Nimonic 90 turbine blades. Since the overhaul life of these engines was about one-third the enhanced life of blades, a number of engines with original set of turbine blades could be immediately released for a second overhaul. Consequent to the enhancement of life of turbine blades, no case of turbine blade failure has been reported by the operators. However, on completion of 400 hours the condition of turbine blades on two engines received for second overhaul has not been very satisfactory. On most of these blades heavy corrosion and erosion were noticed. The extent of erosion may be seen from Fig. 2. This is probably due to the presence of certain additives in the aviation gasoline used in the derated engines. Further experience is awaited to probe the matter in greater detail.

Benefits of Life Extension

The present investigation which led to the enhancement of life of turbine blades enabled overcoming the difficulties experienced in meeting the production schedules at the factory and also in further utilisation of a large number of blades. Besides, on every engine a saving of about Rs. 20,000/- has accrued.

Conclusion

In the absence of full design details and elaborate rig testing facilities, the investigation enabled life enhancement of turbine blades with full confidence. In addition to pecuniary benefits to the tune of Rs.20,000/- on every engine, the investigation obviated a set-back in production targets at the factory and also tided over operational difficulties at the service units. It is felt that in an emergency a similar philosophy could be adopted for life development of other stressed components of aero engines. Obviously such an approach is not advisable where complete design calculations, rig testing facilities, development background, results of type test, flight trials and sampling checks at various stages of operation in service are available, for such details supplemented by service experience are always deemed imperative by airworthiness authorities in any life development programme.

Acknowledgement

The author is indebted to the officers and staff of Resident Technical Office(Engines), Directorate of Aeronautics and Aero Engine Factory, Hindustan Aeronautics Ltd., Bangalore for their valuable suggestions and help in preparing this paper. He also extends his gratitude to all who have contributed to the investigation.

TENSION + VE	125 BLADES/ROTOR	BLADE MATERIAL NIMONIC 90
RPM 10000 (100%)	I. S. A S.L STATIC	

BLADE STATION AND RADIUS IN CMS		STRESS MN/m^2					
		CENTRI-FUGAL	BENDING				TOTAL
			OFF SET		GAS		
			X-AXIS	Y-AXIS	X-AXIS	Y-AXIS	
A (ROOT) 26.5	LE	+ 167.0	-202.0	-21.85	+114.8	+20.55	+78.5
	TE	+ 167.0	-250.0	+29.4	+148.2	-27.6	+67.0
	B	+ 167.0	+162.0	-	- 92.0	-	+237.0
B 28.8	LE	+ 141.8	-115.0	-8.13	+ 64.0	+14.5	+97.17
	TE	+ 141.8	-165.0	+11.45	+ 92.0	-20.4	+59.85
	B	+ 141.8	+91.4	-	-50.8	-	+182.4
C (MEAN) 31.0	LE	+ 105.0	-64.7	+ 1.04	+34.15	+4.25	+ 79.74
	TE	+ 105.0	-52.5	-1.58	+27.8	-6.48	+ 72.24
	B	+ 105.0	+36.30	-	-19.23	-	+ 122.07
D 33.3	LE	+ 58.4	-65.2	-0.88	+35.1	+1.18	+ 28.6
	TE	+ 58.4	-75.5	+1.32	+40.75	-1.76	+ 23.21
	B	+ 58.4	+36.9	-	-20.00	-	+ 75.3
E 35.4	LE	0	0	0	0	0	0
	TE	0	0	0	0	0	0
	B	0	0	0	0	0	0

LE = LEADING EDGE, TE = TRAILING EDGE, B = BACK

TABLE 1. STRESSES AT VARIOUS STATIONS ALONG BLADE HEIGHT

100

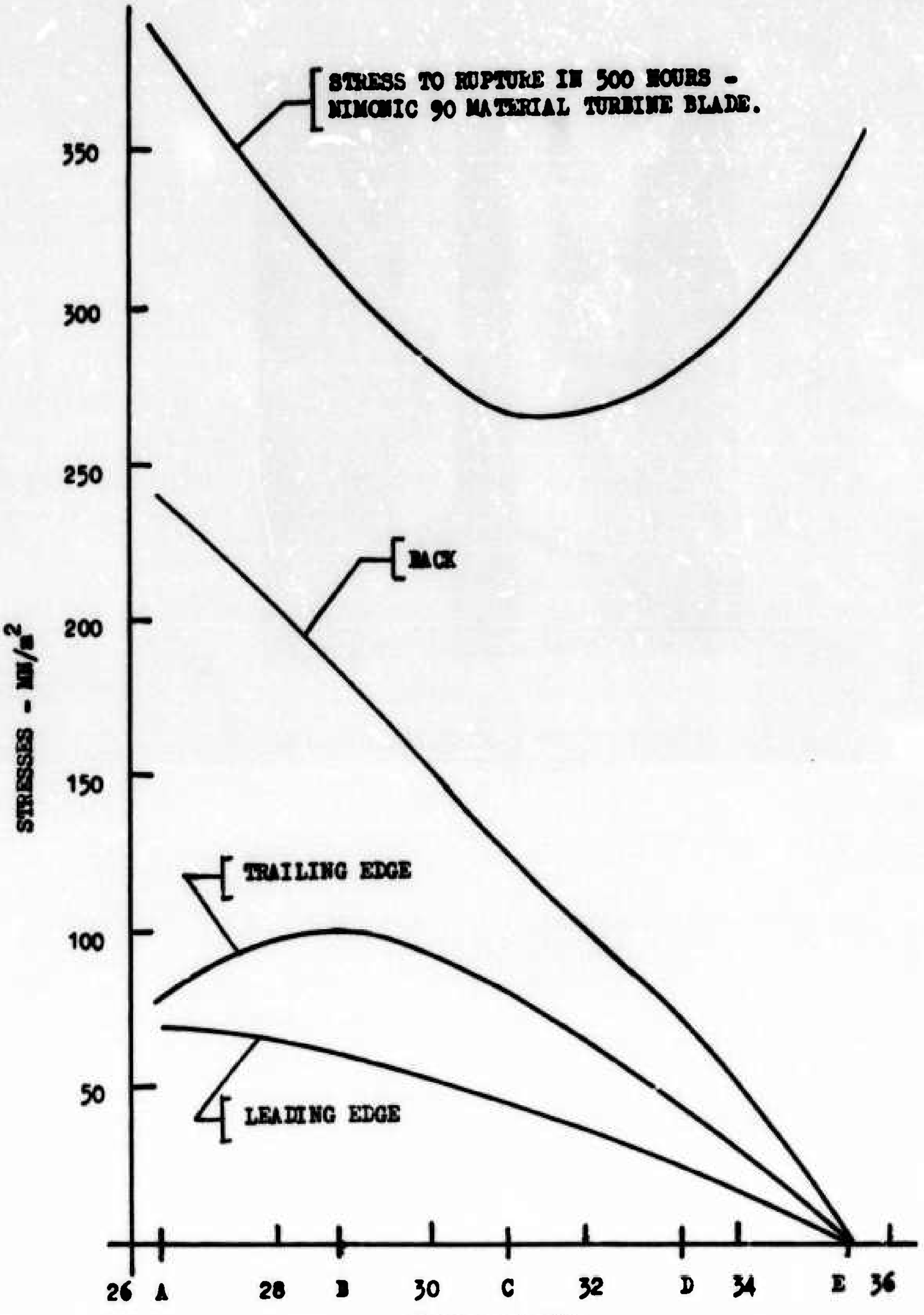

FIG. 1. ESTIMATED STRESSES ALONG BLADE HEIGHT.

101<

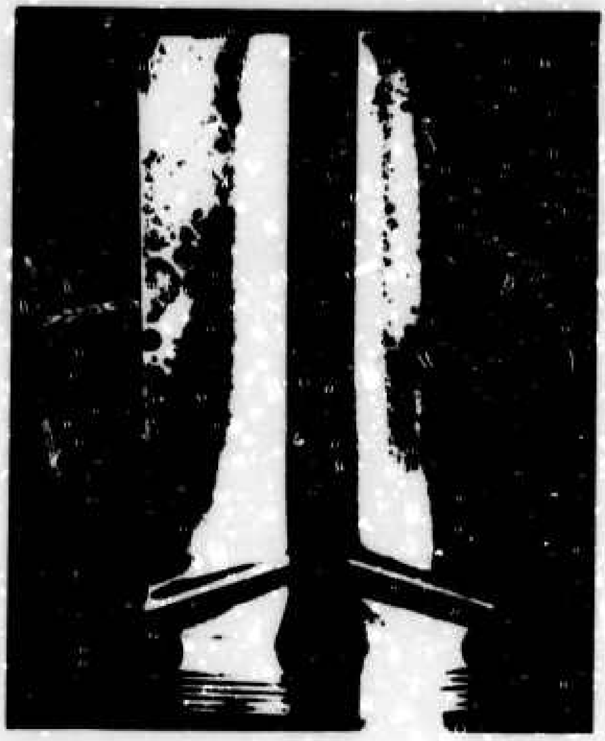

FIG. 2. CONDITION OF BLADE AFTER 400 HOURS.

THE INFLUENCE OF AIR-PRECOOLING BEFORE COMPRESSION IN AIR-BREATHING ENGINES OF A SPACE-LAUNCHER

H. Künkler ; Institute of Jet Propulsion and Turbomachines,
Technical University, Aachen. West Germany

1. INTRODUCTION

The cost of a mission in the earth orbit with a rocket driven launcher is considerably reduced when all the stages are designed for an aerodynamic landing at a predetermined place and when they can be reused several times (Space Shuttle System). An undisputed economy is to be expected, when a booster-stage for the overall flight schedule through the dense atmosphere is equipped with air-breathing jet engines and consistently utilised as an aerodynamic launcher. Besides the economy of the situation, other indirect advantages to be gained by using such aerodynamic booster-stages are:

- the free choice of launching sites and launching inclinations as a result of the high manoeuvrability of the booster-stage with relatively low fuel consumption. This advantage can have a very special significance for European space research.
- the unproblematic recovery of the booster-stage to the launching site.
- the reliability necessary for "space traffic" and the limiting of the accompanying acceleration.

In the current paper, the first topic to be discussed is the requirements of air-breathing engine systems. The limitations that one has to face in adapting air-breathing engines for space applications have been studied, the necessity of introducing changes in the air-breathing engine cycles and the possibilities for the variations of the thermodynamic processes have been compared and discussed. The influence of air precooling before compression on the overall performance of the air-breathing turbo engines has been specially investigated, particularly with reference to an air precooled conventional turbojet designed for this special application. A detailed quantitative comparison of this engine with other feasible concepts, against the background of technological advances, has been made for a special application in an aerodynamic booster-stage.

2. AIR-BREATHING ENGINES FOR SPACE-LAUNCHERS

2.1 Requirements

It can be accepted that a fully reusable aerodynamic space-launcher with a useful payload, that could be launched in a lower earth orbit, should consist of two stages. In order to reduce the work of the rocket-propelled "Orbiter" the horizontal take-off "Booster" equipped with a more economic air-breathing propulsion system must be designed for higher maximum flight Mach numbers, preferably over $M_\infty=10$.

For such high flight Mach number ranges, the Scramjet seems to be the only possibility. The boundary layer temperatures rise even in the case of such jet engines, above the range of $M_\infty=10$, to values of over T=4000 K. The high temperatures coupled with the large surface area require a very large amount of cooling. Even using liquid hydrogen (LH_2) as fuel, it could be seen that a larger quantity of liquid hydrogen is used for cooling than for the combustion itself. Taking into account the thermal problems associated with the vehicle body itself, at the present stage of technological development, the limiting maximum flight Mach number is still reduced, when an aerodynamic booster-stage is to be accelerated by air-breathing engines.

The essential advantages of an air-breathing jet engine over a rocket can only be fully recognized, when a jet engine system can be developed which covers the overall atmospheric flight Mach number range, from the start to the maximum flight Mach number. It should not be heavier than a conventional turbojet with reheat, which in the lower flight Mach numbers gives a comparable thrust. The specific fuel consumption of such jet engines should lie below that of conventional turbojets with reheat, and specially in the higher flight Mach number ranges (up to $M_\infty=7$) below the corresponding ramjet.

The jet engine dimensions required and consequently the engine mass depend essentially on the magnitude of specific thrust $F/\dot{m}_a$, that the turbojet achieves in the higher flight Mach number ranges. In order to avoid the unused thrust and the inlet drag in the lower flight Mach number ranges, the value of $F/\dot{m}_a$ with increasing flight Mach number must fall as little as possible.

To summarize, the following are the requirements of an air-breathing jet engine to be used in a space-launcher:

- sufficient starting thrust and sufficient thrust surplus in the transonic flight range;
- useful up to flight Mach numbers above $M_\infty=6$;
- higher specific thrust $F/\dot{m}_a$ mainly for higher flight Mach numbers;
- lower specific fuel consumption $\dot{m}_f/F$ over the total flight Mach number range;
- high thrust/weight ratio $F/(m_e.g_o)$ with uncomplicated and high reliability construction of the turbojet.

2.2 Propulsion Systems based on Conventional Aerospace Jet Engines

The flight Mach number range of the air-breathing turbo engines is limited by the permissible temperature at the compressor exit. Similarly, using the conventional turbine cooling methods with air from the compressor, the limit for the reheated turbojet is about $M_\infty=3.5$. Where it is possible to precool the turbine coolant by a process of heat exchange with the fuel or to utilize the fuel directly for blade cooling, it is to be expected that the flight Mach number range could be raised to $M_\infty=4.5$. Here the compressor exit temperature reaches a value of $T_{t2}=1200$ K which, for a compressor with uncooled blading, is, for technological reasons, considered the maximum permissible. The same limiting flight Mach number is also naturally valid for the Turborocket that has been for some time under experiment ①.

If the turbojets described above are used for the start and the initial acceleration in combination with a ramjet, their internal parts in the higher flight Mach number ranges must be hermetically screened against the through-flow; their external cover then must be cooled with fuel against heat exchange from the hot outer streams into the internal turbo engine.

2.3 Thermodynamic Process Possibilities for such Special Applications

This special application of employing air-breathing engines for accelerated launchers, results in the possibility of using liquid hydrogen as fuel. Apart from the fact that liquid hydrogen has a higher energy content per unit mass and is therefore economical when compared to other hydrocarbons (like ATK, JP4), it also acts as a heat sink, which can be used as a precoolant of the air before the compressor inlet:

- For the same pressure ratio, this leads to lesser compression work, and improves the specific thrust and specific fuel consumption.
- The reduction in temperature at the compressor inlet induces an increase

when an aerodynamic booster-stage is to be accelerated by air-breathing engines.

The essential advantages of an air-breathing jet engine over a rocket can only be fully recognized, when a jet engine system can be developed which covers the overall atmospheric flight Mach number range, from the start to the maximum flight Mach number. It should not be heavier than a conventional turbojet with reheat, which in the lower flight Mach numbers gives a comparable thrust. The specific fuel consumption of such jet engines should lie below that of conventional turbojets with reheat, and specially in the higher flight Mach number ranges (up to $M_\infty=7$) below the corresponding ramjet.

The jet engine dimensions required and consequently the engine mass depend essentially on the magnitude of specific thrust $F/\dot{m}_a$, that the turbojet achieves in the higher flight Mach number ranges. In order to avoid the unused thrust and the inlet drag in the lower flight Mach number ranges, the value of $F/\dot{m}_a$ with increasing flight Mach number must fall as little as possible.

To summarize, the following are the requirements of an air-breathing jet engine to be used in a space-launcher:
- sufficient starting thrust and sufficient thrust surplus in the transonic flight range;
- useful up to flight Mach numbers above $M_\infty=6$;
- higher specific thrust $F/\dot{m}_a$ mainly for higher flight Mach numbers;
- lower specific fuel consumption $\dot{m}_f/F$ over the total flight Mach number range;
- high thrust/weight ratio $F/(m_e.g_o)$ with uncomplicated and high reliability construction of the turbojet.

2.2 Propulsion Systems based on Conventional Aerospace Jet Engines

The flight Mach number range of the air-breathing turbo engines is limited by the permissible temperature at the compressor exit. Similarly, using the conventional turbine cooling methods with air from the compressor, the limit for the reheated turbojet is about $M_\infty=3.5$. Where it is possible to precool the turbine coolant by a process of heat exchange with the fuel or to utilize the fuel directly for blade cooling, it is to be expected that the flight Mach number range could be raised to $M_\infty=4.5$. Here the compressor exit temperature reaches a value of $T_{t2}=1200$ K which, for a compressor with uncooled blading, is, for technological reasons, considered the maximum permissible. The same limiting flight Mach number is also naturally valid for the Turborocket that has been for some time under experiment ①.

If the turbojets described above are used for the start and the initial acceleration in combination with a ramjet, their internal parts in the higher flight Mach number ranges must be hermetically screened against the through-flow; their external cover then must be cooled with fuel against heat exchange from the hot outer streams into the internal turbo engine.

2.3 Thermodynamic Process Possibilities for such Special Applications

This special application of employing air-breathing engines for accelerated launchers, results in the possibility of using liquid hydrogen as fuel. Apart from the fact that liquid hydrogen has a higher energy content per unit mass and is therefore economical when compared to other hydrocarbons (like ATK, JP4), it also acts as a heat sink, which can be used as a precoolant of the air before the compressor inlet:
- For the same pressure ratio, this leads to lesser compression work, and improves the specific thrust and specific fuel consumption.
- The reduction in temperature at the compressor inlet induces an increase

in mass flow rate. This allows for a similar thrust, smaller turbo engine dimensions, and thereby reduces weight.

- Finally the reduction in temperature at the compressor outlet allows a substantial increase in the flight Mach number range of the air-breathing turbojet engine - and this is the factor which really makes it worthy of serious consideration as a propulsion system for an aerodynamic space-launcher.

Precooling the compressor inlet air by means of fuels such as liquid methane or hydrogen, was proposed by Mordell as early as 1961 in the "Inverted turbojet". For the proposed utilisation of the special turbojet for a space-launcher, this is not suitable, since in the take-off and transonic flight ranges a totally insufficient thrust is developed.

The Texaco Experiment Inc.'s projected "Air Turbo Exchanger (ATE)", suffering from the same disadvantage, must likewise be rejected as a propulsion system for a booster-stage. Here the turbine is designed to operate only with fuel, essentially hydrogen. This hydrogen fuel is previously preheated in a heat exchanger located in front of the compressor.

An increase in thrust in the lower flight Mach number ranges is possible, when the hydrogen before its entry into the turbine is heated by reaction with an oxidiser. The flight load consumption of this turborocket with air precooling increases rapidly with the oxidiser. This is, however, something which has to be put up with in the lower flight Mach number range as, in the starting phase and climb, up to an altitude of about H_∞=10 km, the heat exchanger must not be operated with hydrogen, because of the icing dangers due to humidity in the lower atmosphere.

Besides the already stated limitations in their applications, the unconventional turbojet concepts mentioned have the disadvantage that in their technological specifications, they considerably deviate from the standards required of modern aeronautic turbojet construction.

On the other hand, because of their largely conventional construction, reheated turbojets with precooling of the air before compression (TJ+PC) appear particularly suitable as high speed propulsion systems for the very near future (Fig. 1). Even without air precooling, these turbojet types produce in the subsonic regions, for start and climb, a high amount of thrust with a reasonable fuel consumption. With precooling, in the entire flight Mach number range, already mentioned from the transonic phase right up to the maximum flight Mach number, this type of propulsion system offers a comparatively economical fuel consumption, as will be shown later.

As a result of the reduction in temperature at the compressor inlet, the mass flow inducted is higher and with that the thrust developed by the engine increases to such an extent, that although an addition in weight through the utilisation of a heat exchanger is involved, an economical thrust/weight ratio is achieved compared to the conventional reheated turbojet. The main advantage of precooling the air lies in the extending of the flight Mach number range, and though in reality the flight Mach numbers are higher, the conditions before the compressor remain with precooling as they would be for a lower Mach number without precooling.

The hydrogen used as fuel in the main and after -burners is heated in the opposed flow heat exchanger to a temperature in the vicinity of the flight stagnation temperature $T_{t\infty}$ (Fig.1). It is therefore possible that with increasing flight Mach numbers a continuously increasing heat capacity could be absorbed from the air stream. This would be carried in the heat exchanger because of a higher mean temperature difference between the distributed streams with increasing $T_{t\infty}$.

In spite of its higher flexibility a reheated bypass turbojet with air precooling (BTJ+PC) is not suited to the current application. As against the TJ+PC, the BTJ+PC has no added advantage as far as fuel consumption is concerned. A favourable improvement of the fuel consumption is achieved under certain operating conditions by a liquidization of the air stream and a fluid phase compression of the primary flow. The main disadvantage of such jet engine concepts and similar systems with air liquidising, apart from their less conventional construction, is that they develop an insufficient thrust for start and subsonic climb flights.

Besides the possibility, afforded by air precooling, of running turbojets up to such high flight Mach numbers that they can be employed as propulsion systems for the booster-stages of space-launchers, the special nature of the application also dictates the following necessity for the thermodynamic processes:

If by means of under-stoichiometric fuel supply one limits the allowable combustion chamber temperature to a technologically acceptable value of about $T_{tmax}=2400$ K, then the ramjet will cease to provide sufficient thrust beyond approximately $M_{\infty}=5{,}5\div6$. If the same maximum permissible combustion chamber temperature is maintained by combustion of a rich fuel flow, an increase in the jet velocity and thrust is obtained. The ramjet is now suited for over $M_{\infty}=7$. This is however, at the expense of an increase in the specific fuel consumption.

As in the case of a turbojet with air precooling the fuel stream is also the coolant stream, a rich fuel/air mixture not only involves an increase in the jet velocity but also increases the effect of precooling. This results in an increase of the jet thrust and also a comparable extension of the flight Mach number range over $M_{\infty}=6.5$.

The thrust increase results in an improvement of the thrust/weight ratio and also a shortening of the flight duration of the accelerated space-launcher. Even with an air-breathing engine with fuel-rich combustion (where it is assumed that the fuel consumption is naturally higher), an overall reduction in the amount of fuel can result.

3. SPECIAL REQUIREMENTS OF THE COMPONENTS AND CALCULATION METHODS EMPLOYED

In order to make a comparative study of the performance of the air-breathing jet engine systems for higher flight Mach number ranges, the calculation must as far as possible be based on realistic assumptions and calculation methods; otherwise a completely different picture could result.

Besides the real gas conditions of the working fluid, in both the low temperature and dissociation regions, the information about the momentary characteristics of all the components must be readily available for the computer. This especially applies to the operating conditions of the components. The realities and technical limitations should also be taken into consideration.

The special requirements of the supersonic inlet of the air-breathing jet engines for space-launchers arise from the unconventional higher maximum flight Mach numbers. The inlet should to be located under the wing; there, as a result of the established shock, the velocity hardly reaches a value of $M_o=4$, although the flight Mach number itself is of the order of $M_{\infty}=7$. The inlet is considered as a plane 4-shock inlet with a combined outer and inner compression. The problem of matching the inlet with the jet engine is solved by a limited variation of its geometry; in the case of the turbojet with air precooling, additionally by controlling of the intensity of precooling and by regulating the rotor speed. ③

The capacity of a jet engine with air precooling is dependent on the heat exchanger, and the work output of this has a decisive effect. For the calculation of its pressure loss, dimensions and weight, the measured data were based on the heat exchanger matrices ②, which were ideally suited for the present case. The matrices indicate a high ratio of heat exchange area/volume by a low weight. In spite of consequently reducing the high degree of heat exchange, a larger amount of hotter fluid was possible for a lesser volume and accompanying low pressure losses.

The computational consideration of the changes in pressure ratio, mass flow and efficiency of the compressors with the current entry conditions, was based on suitable characteristics. The gaseous fuel and the extremely short combustion length simplify the mixing process and make possible the adoption of a smaller combustion chamber volume. Because of the possibility of using a relatively small after-burner with hydrogen cooling, higher peak temperatures could be realised.

The reduced thrust nozzle sectional area remains approximately constant. The mixing of the bypass air in the thrust nozzle reduces, in the lower flight Mach number range, the drag of the inlet and also the outer drag of the thrust nozzle. The computation of the actual expansion was approximated in accordance with Bray's criterion.

4. PROJECT LAYOUT OF A TURBOJET WITH AIR PRECOOLING

In the following pages a project layout of a reheated turbojet with air precooling (TJ+PC) is presented, which is designed to drive the aerodynamic booster-stage of a space-launcher.

4.1 Assumptions

The aim of this project was to conceive an uncomplicated jet engine. The engine should be suitable for accelerating the booster-stage from start to a flight Mach number M_∞=7, as well as for an economical return. At the same time the technological specifications should, as far as possible, not exceed the achieved standards of present-day aerojet construction.

For the flight trajectory of the booster a path, which for an accelerated flight is relatively high (see Fig. 2), was chosen, the maximum pressure in the after-burner not exceeding 6 bar. Although the booster after start first followed the path shown by the dotted lines all the calculations, even those beneath H_∞=11 km, are based on the extended path, so that the curves calculated can more clearly be followed.

The heat exchanger is so located and regulated that the hydrogen, even in the higher flight Mach number range, is not heated beyond $T_{H2,max}$=1050 K. This means the hydrogen after emerging from the heat exchanger can even be used for an effective cooling of the after-burner and the thrust nozzle, without allowing the wall temperature to exceed 1200 K.

The inlet area of the compressor was taken as A_1=1 m^2 for all the calculations. In order to design the turbine as a single stage one, the compressor pressure ratio was limited to $(\pi_{tC})_{DP}$=7 at design point. As design point efficiencies for the compressor, turbine and thrust nozzle average standard values were taken.

The inlet temperature of the cooled turbine - T_{t3}=1800 K - lies within the average test standard operating conditions of today. The cooling air needed for the turbine cooling, obtained from the heat exchange with the fuel stream, has an intermediate temperature of T=500 K,so that T_{t3} could be maintained constant independent of the compressor exit temperature T_{t2}. The maximum peak temperatures in the after-burner could for the reasons mentioned be raised from the current standard temperatures by 300 K to about $T_{t\,max}=2400$ K.

In order to determine the influence of air precooling on the thrust/weight ratio, an estimation of the jet engine mass was made. During the heat exchanger calculations, the mass of the heat exchanger was obtained, and the jet engine mass itself was determined by a statistical method.

4.2 Conception of the Jet Engine

An overall view of the jet engine concept is shown in Fig. 15 a. The plane 4-shock inlet at flight Mach numbers lesser than $M_\infty=4$, inducts a larger amount of air than is needed by the turbojet. Therefore, in the lower flight Mach number ranges, a part of the inlet inducted air bypasses the turbo engine and, together with the exhaust gases, is expanded in the common thrust nozzle. The amount of bypass is controlled by the adjustable "cold" thrust nozzle. Above $M_\infty=4$, the air consumption of the turbojet engine exceeds the air supplied by the inlet. To avoid "supercritical" operation of the inlet and the accompanying high losses, the rotor speed must be continuously reduced.

After the air has passed the opposed stream heat exchanger, it is inducted into the 6-stage compressor. The smaller unit length of the compressor with the short combustion chamber, and the single-stage turbine, allow a very solid construction and simple bearings of the monolithic rotor. Behind the short after-burner in the convergent part the hot thrust nozzle is located, which forms a transition from a rotationally symmetric turbo system to a plane thrust nozzle of variable geometry.

4.3 Influence of Air Precooling on the Thermodynamic Process

The influence of air precooling on the value of the temperature T_{t1} at compressor inlet is shown in Fig. 3. During the start and at the beginning of the climb, because of the danger of icing in the heat exchanger, precooling of the air must be avoided. The dotted curve gives the variation of temperature T_{t1} at compressor inlet without air precooling. This is practically the same as the stagnation temperature $T_{t\infty}$. The drawn curves show the reduction in compressor inlet temperature as a result of precooling.

In order that the allowable maximum temperature in the after-burner does not exceed 2400 K, either the fuel/air ratio must, as the stagnation temperature increases, be continuously reduced (thin curve), or one must limit the combustion end temperature by a corresponding increase in fuel content (thick curve). For the two operating conditions, the differences in the temperatures are sketched (Fig. 3); these arise because of the different fuel streams and also because of the differences in the quantity of coolants. For the curve with $(\beta>\beta_{st})$ a kink is obtained around $M_\infty=5$, because there in the heat exchanger the liquid hydrogen has reached its maximum temperature.

The effect of precooling on the temperature T_{t2} at compressor exit is shown in Fig. 4. The technologically calculated limiting temperature which should be obtained at $M_\infty=4.5$ is first reached at about $M_\infty=7$.

In view of the reduction in the compressor inlet temperature, the reduced rotor speed $N/\sqrt{T_{t1}}$ and the corresponding mass rate of flow at compressor inlet increases. The noticeable increase of the engine air flow, which forms the main part of the thrust increase as a result of air precooling, is shown in Fig. 5.

The different specific thrusts likewise increase owing to air precooling, and this is directly due to the increase in compressor pressure ratio without corresponding increase in the turbine pressure ratio (p_{t3}/p_{t4}). This results in an increase of the overall pressure ratio p_{t4}/p_{t1E}

of the turbo unit (Fig. 6), where p_{t4} is the total pressure behind the turbine und p_{t1E} the total pressure at the end of the intake nozzle in front of the heat exchanger.

4.4 Analysis of the Characteristics of the Jet Engine

In order to eliminate the influences of the mounting aspects of the jet engine on the thrust, the engine is firstly considered without external assembly.

The variation of the thrust, based on air induction, $F/\dot{m}_a$ with and without precooling is indicated in Fig. 7. Because of the increasingly higher deviation of specific thrust, it is not essential for an undesirably large amount of air to be inducted, with higher flight Mach numbers. This would tend to increase the intake dimensions to an inexpedient extent.

Fig. 8 shows the variation of specific thrust, based on fuel consumption, $F/\dot{m}_f$ with flight Mach numbers. By air precooling with under-stoichiometric combustion, the specific thrust $F/\dot{m}_f$ increases on an average by nearly 10 %, but with over-stoichiometric ratios $F/\dot{m}_f$ falls to very low values. In this case, a greater thrust and an extension of the flight Mach numbers must be attained at the cost of higher specific fuel consumption. The overall drive mass for fulfilling the flight conditions need not be negatively affected by this.

Apart from the influence of air precooling on the amount of fuel mass that is needed for the driving phase, the effect of precooling on the thrust/weight ratio is decisively important. Fig. 9 shows the specific thrust variation, based on engine weight, against flight Mach numbers. The mass m_e for a turbojet engine with precooling (TJ+PC) considered along with the heat exchanger, is naturally greater than for an uncooled standard turbojet (TJ) because of the mass of the heat exchanger. Above flight Mach numbers M_∞=0.8, however, the higher thrust/weight ratio more than compensates for this apparent excess in mass.

5. OVERALL PERFORMANCES OF COMPARABLE JET ENGINE CONCEPTS

In the following section the performance values of the turbojet engine with air precooling and other comparable jet engine systems are discussed.

The jet engines under donsideration (Fig. 10) are the reheated Turbojet with air precooling (TJ+PC), the reheated Turborocket with air precooling (TR+PC) and the Ramjet (RJ) in combination with the turbojet engine (TJ) or the Rocket (R). The simple turborocket is less suited for such combinations.

The aim of the comparative study was to examine the jet engines that are best suited for use in an aerodynamic space-launcher, and to determine the mass of the total drive system (fuel and engine mass) for the entire trajectory of flight. To enable a fair comparison of the different jet engine systems, they were all analysed in accordance with the same system. The performance parameters will now be described, taking into account the inlet size, the wing mountings and also the jet engine drag in the external stream.

5.1 Comparison of Performance Values

As all the jet engine concepts already discussed are suited for the acceleration of a space-launcher in the envisaged flight Mach number range only with combustion at a fuel-rich stoichiometric ratio I shall restrict myself to plotting soleley the curves concerned.

Fig. 11 shows the variation of the specific thrust $F/\dot{m}_a$ for the flight Mach number range discussed. The reason why the performance curve of the turbojet with air precooling falls slightly below other jet engines at higher flight Mach numbers is that here the overall pressure ratio of the turbopart lies below unity.

The strong reduction in the specific thrust based on fuel rate for the TR+PC and the RJ+R in the lower flight Mach numbers is a result of the oxygen needed (Fig. 12). For comparison, the variation of the specific thrust $F/\dot{m}_f$ of an O_2/H_2 rocket which was driven with an optimum mixing ratio is presented.

The four jet engine systems compared have a geometrically similar intake and intake capture area A_E, a similar compressor inlet area A_1, a similar thrust nozzle exit area and the same peak temperature $T_{tmax}=2400$ K. The turbine inlet temperature of the turbojet at design conditions was $T_{t3}=1800$ K, while the turbine inlet temperature for the turborocket with air precooling varied between $600 \text{ K} < T_{t3} < 1200 \text{ K}$.

Fig. 13 presents the thrust variation of the individual jet engines. In these curves the nett thrusts are available after deduction of the jet engine drag, and those which are effectively available for propulsion of the craft, and whose drag is shown in the diagram, are presented. D_{cr}/n_e is the part of the drag of the craft which a single jet engine normally suffers. The drag curve D_{cr}/n_e vs M_∞ has been obtained for the quasistationary case of an unaccelerated horizontal flight of an aerodynamic space-launcher obtained by a take-off mass $m_{TO}=230\ 000$ kg in combination with a 2-stage O_2/H_2 rocket with a payload $m_u=12\ 000$ kg for an earth orbit of 200 km. Naturally the optimal dimensions for the discussed jet engine concepts are different.

Finally, Fig. 14 shows the drag variation of the compared jet engines. The high drag of the combination jet engines at low flight Mach numbers, is a result of the thermal blockage.

5.2 Comparison of the Total Drive Mass as Illustrated in the Case of a Space-Launcher

On comparison, the TJ+RC and the RJ+TJ are specially suited. For these propulsion systems, the total drive mass has been estimated and compared. The total drive mass consists of the installed engine mass and the total mass of fuel which would be needed for the acceleration of the booster stage up to the stage separation for the given flight trajectory.

Fig. 15 compares the sectional views of a TJ+PC and RJ+TJ. At intake the two systems look identical, but an apparent excess can be seen in the presence of a heat exchanger in the TJ+PC. On the other hand, in the RJ+TJ the following are the main excesses:

- the significantly larger after-burner;
- the flap system for the hermetic sealing of the turbo-part;
- the cooling of the total bypass channel including the external envelope of the turbo-part. On the other hand, the bypass channel of the TJ+PC in the higher flight Mach number range is not supplied, so that no excessively high temperatures or high pressures are reached.

The total excess in engine mass of the combination jet engine RJ+TJ can be clearly seen to be overcome with an TJ+PC.

In Fig. 16 the overall mass m_{ov}, namely, the installed engine mass m_e and the fuel mass m_f, which must be carried for acceleration to the flight Mach number M_∞ by the alternative utilisation of a TJ+PC and RJ+TJ, has been shown against M_∞. For the estimation of these curves the number of motors for the particular turbojet concepts, namely, the overall installed turbojet dimensions (A_{1ov}, A_{Eov}) were optimised to give the minimum overall engine plus fuel mass. Besides, the different optimum transition Mach numbers, namely the Mach numbers at which the combustion was switched over from a weak to a rich stoichiometric mixture, in the after-burner, were also taken into consideration.

As seen in fig. 16, the calculations show that in the case of a TJ+PC a comparably lower overall drive mass is possible. This is particularly notable, in view of the fact, that in every case of an uncertain assumption the TJ+PC were always decided against. The calculations were made as far as possible accurately with some limitations of course. The author is aware of the fact that it is not possible for him to make a complete calculation, because of the several limitations, namely, the multidimensionality of the flow, which could only be taken into account with correction factors, and also the operating conditions of some of the components were roughly estimated and taken into consideration.

6. CONCLUSIONS

It has been shown, in general, that air precooling before compressor inlet is a suitable way of extending favourably the flight Mach number range of an air-breathing turbo engine. Thereby it is possible without a ramjet combination to make the air-breathing engine attractive as propulsion system for an aerodynamic booster-stage, for the start and acceleration of the space-craft. Another definite advantage of the air precooling with regard to the development stage of the turbo engines, is that these need only a test facility of upstream Mach numbers $M_o=4$ to 4.5 to obtain conditions at flight of $M_\infty=7$.

As a special case, the reheated turbojet engine with air precooling serves the requirements of space-launchers very suitably. Another advantage of this special turbojet concept is that it fully utilises the current technological development facilities of conventional aircraft propulsion systems yet does not much exceed these requirements either. The problem faced is essentially the development of suitable heat exchanger matrices and, as experience indicates, such developments have already been made. However, besides the variable intake, owing to the strong temperature gradients the heat exchanger is likely to pose design difficulties. The thermal stresses by heat exchangers of conventional construction, however lie within the controllable range, because of the relatively elastic matrix.

Finally, it remains to be stated that a turbojet engine with air precooling, using liquid Methane as fuel and with air-rich combustion is eminently suited as a propulsion system for a supersonic transport (SST) with flight Mach numbers between $M_\infty=3$ to 5. With its relatively simple construction and an economical thrust/engine weight ratio, it offers a comparatively low specific fuel consumption.

7. REFERENCES

1 Lombard, A.A. and J.G. Keenan: The Turborocket for High Speed Air Breathing Vehicles
Paper, presented at the DGRR and WGLR Joint Annual Congress in Berlin, 1964, Rolls Royce, Derby

2 Kays, W.M. and A.L. London: Compact Heat Exchangers
McGraw Hill Book Company, New York, 1964

3 Künkler, H.: Zum Problem der Anpassung eines Einlaufs an ein Turbotriebwerk für extrem hohe Flug-Machzahlen
Zeitschrift für Flugwissenschaften, Dec. 1973

4 Lane, R.J.: Recoverable Air-Breathing Boosters for Space Vehicles
Journal of the Royal Aeronautical Society, June 1962

Symbols of Engine Systems

RJ	Ramjet
TJ	Turbojet engine
TR	Turborocket
R	Rocket
PC	Precooling (before compression)
$\beta > \beta_{st}$	Fuel-rich stoichiometric fuel/air ratio

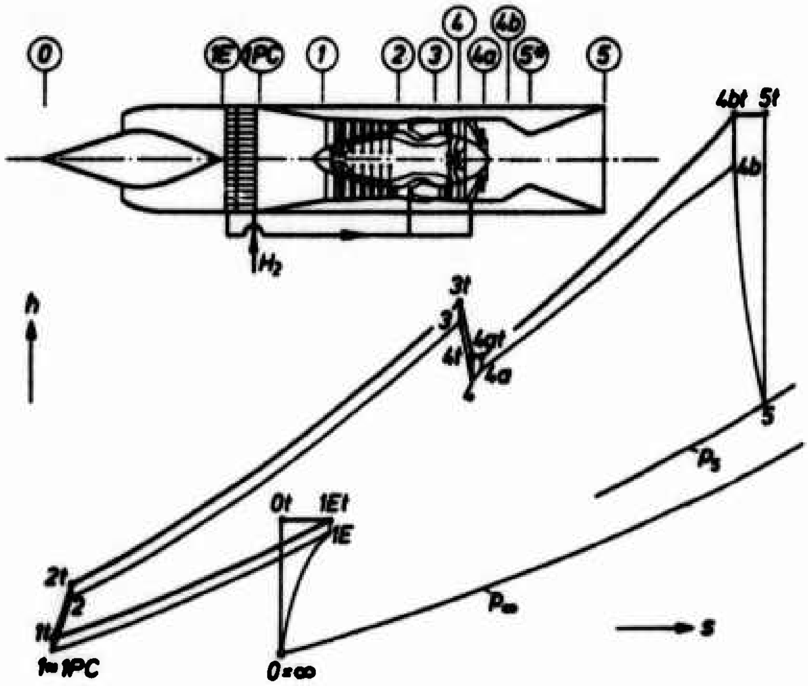
0
1E
1PC
1
2
3
4
4b
4a
5*
5
H_2
h
4bt
5t
4b
3t
3
4at
4t
4a
4
5
p_5
0t
1Et
1E
2t
2
1t
1=1PC
0=∞
p_∞
s

Fig.1: Thermodynamic Process of the TJ+PC

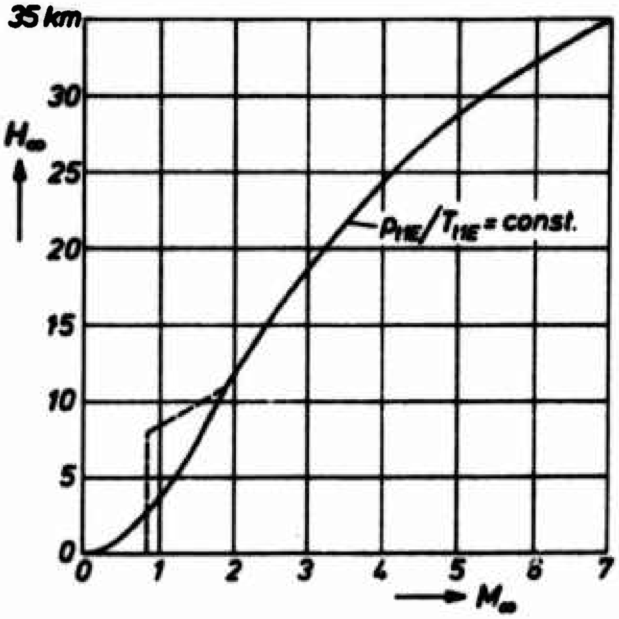

Fig.2: Flight Trajectory

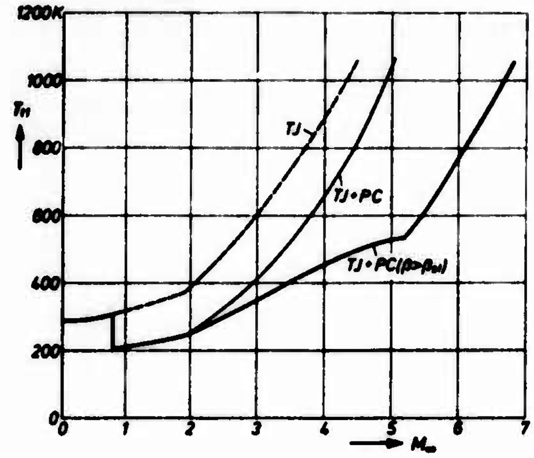

Fig.3: Influence of air precooling on the temperature at compressor inlet

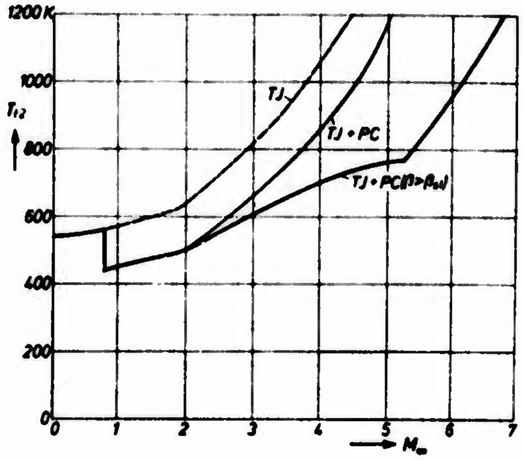

Fig.4: Influence of air precooling on the temperature at compressor exit

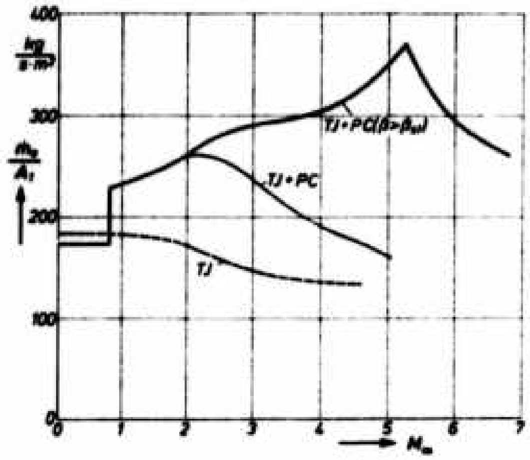

Fig.5: Influence of air precooling on the mass flow rate at compressor inlet

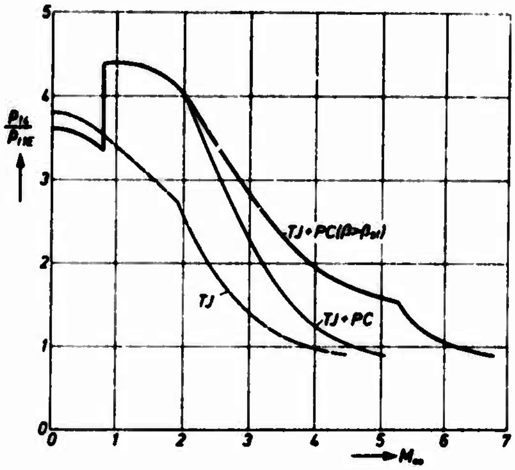

Fig.6: Influence of air precooling on the overall pressure ratio of the turbo-part

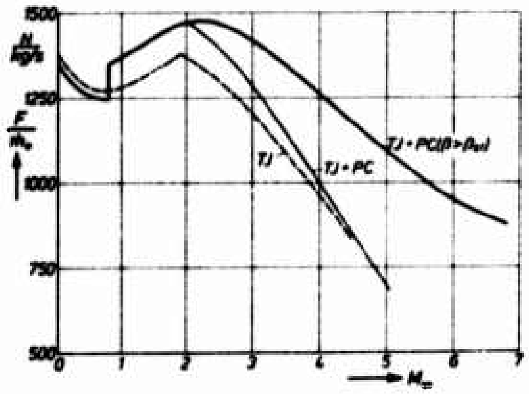

Fig.7: Distribution of the specific thrust (air basis) over the flight Mach number range

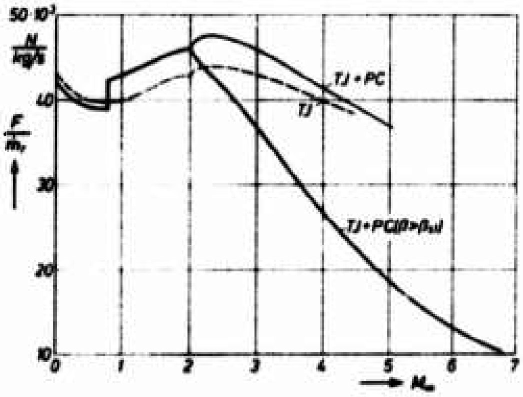

Fig.8: Distribution of the specific thrust (fuel basis) over the flight Mach number range

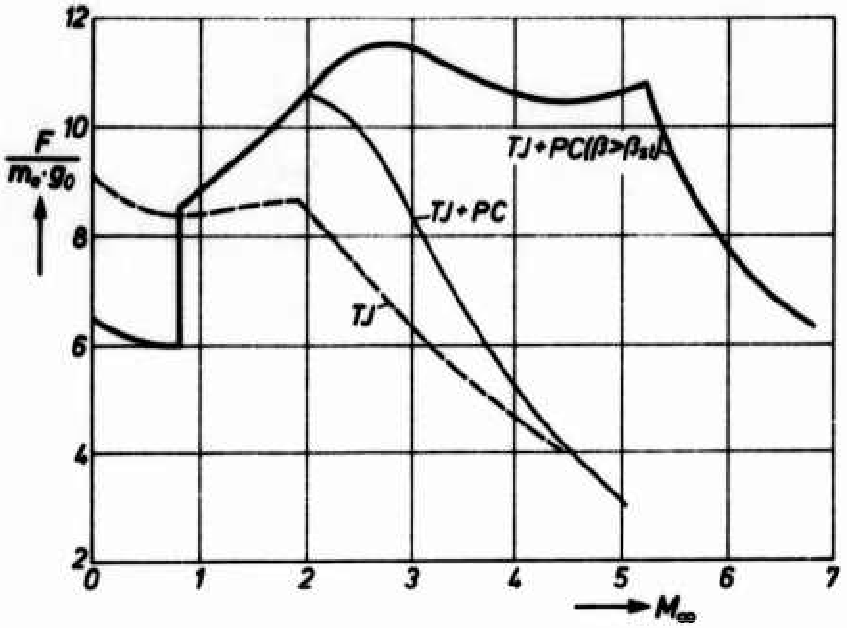

Fig.9: Distribution of the specific thrust (engine weight basis) over the flight Mach number range

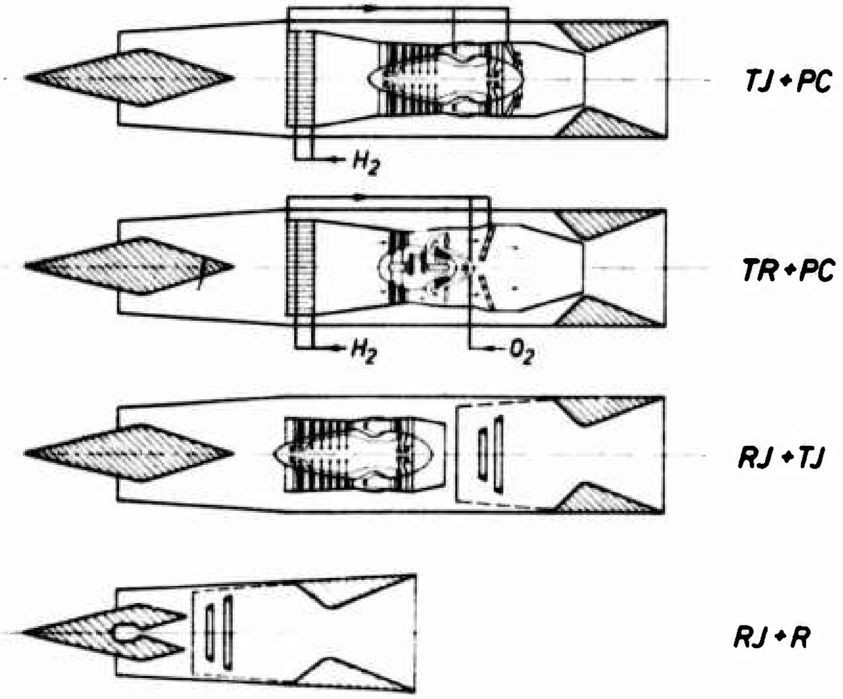
$TJ+PC$
H_2
$TR+PC$
H_2
O_2
$RJ+TJ$
$RJ+R$

Fig.10: Schematic of the compared turbo jet concepts

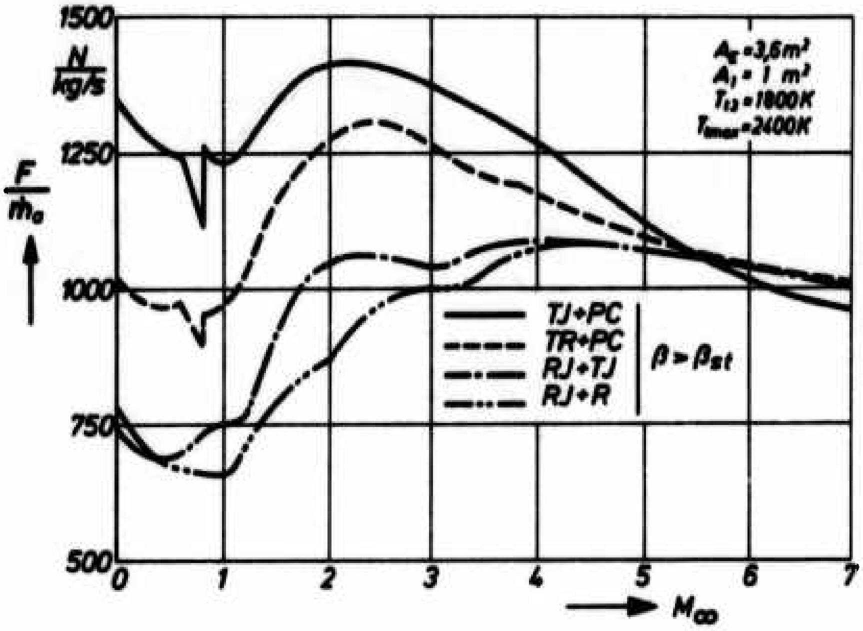

Fig.11: Variation of specific thrust (air basis) for the high Mach number turbo jet engines

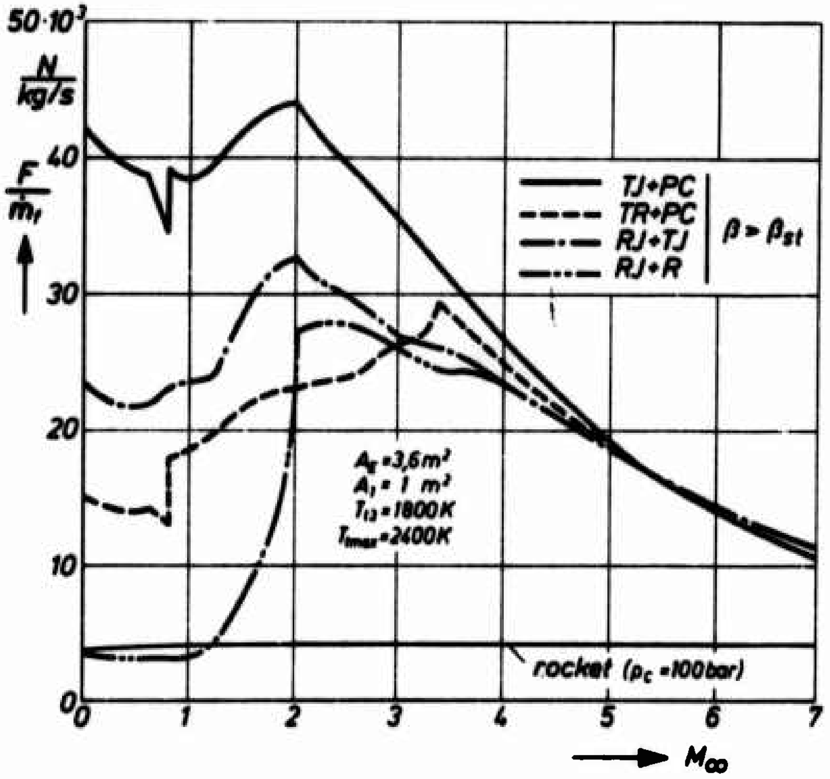

Fig.12: Variation of specific thrust (fuel + oxidiser basis) for the high Mach number turbo jet engines

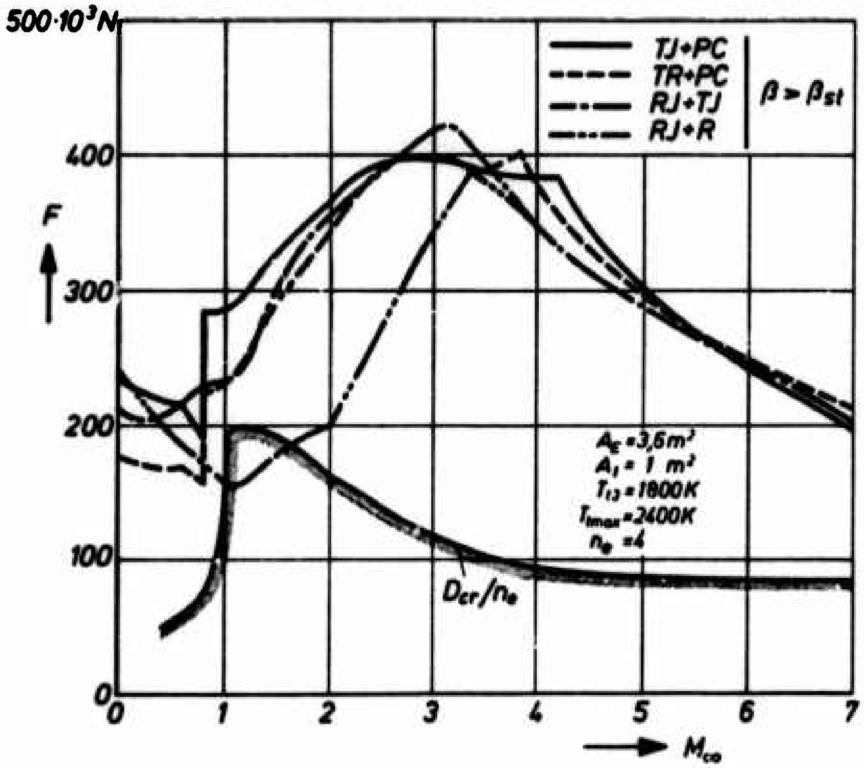

Fig. 13: Thrust distribution for high Mach number turbo jet engines

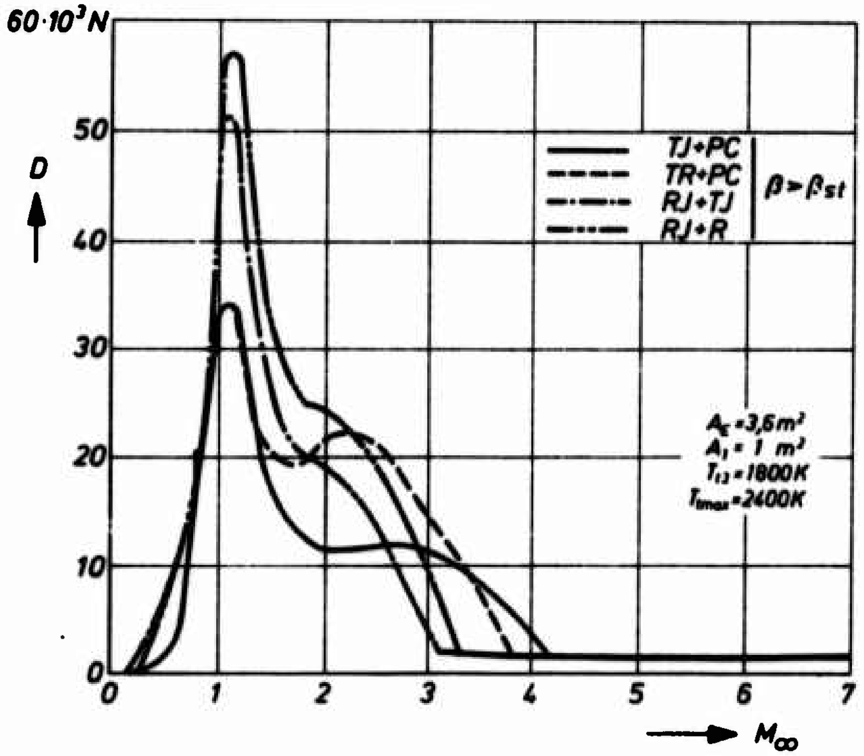

Fig. 14: Drag distribution for high Mach number turbo jet engines

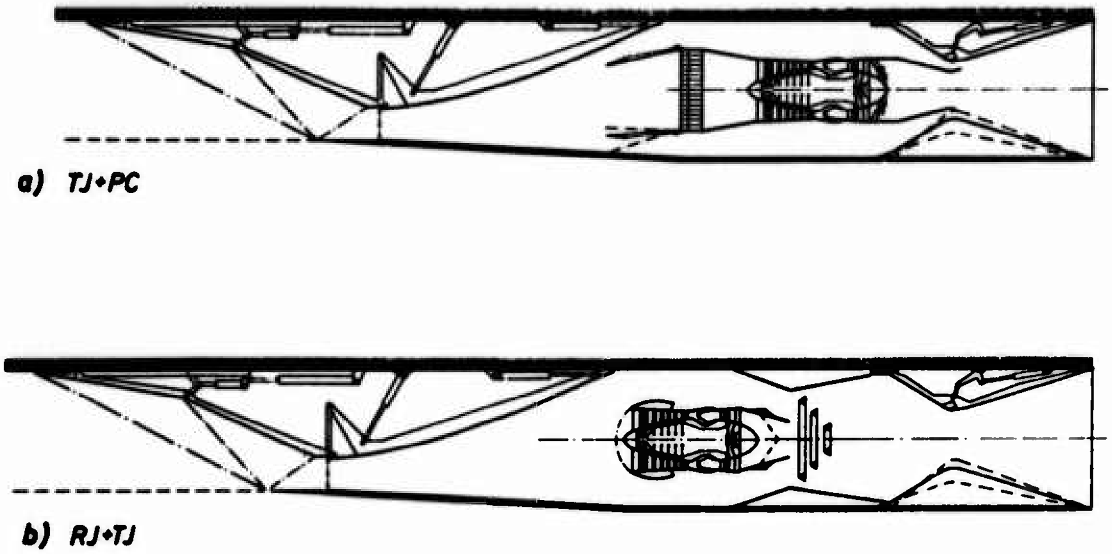
a) TJ+PC

b) RJ+TJ

Fig. 15: The overall layouts of the turbojet with air precooling and the ramjet combined with a turbojet

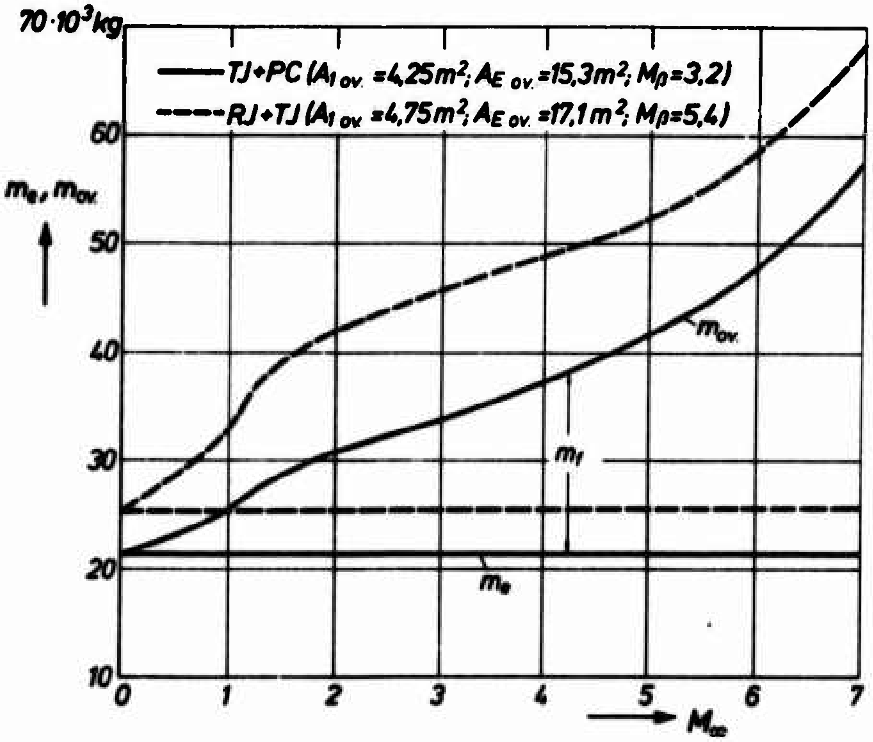

Fig. 16: Comparison of the overall drive masses

COMPOSITE PROPULSION SYSTEMS FOR AN ADVANCED REUSABLE LAUNCH VEHICLE APPLICATION

Joseph G. Bendot

The Marquardt Company, Van Nuys, California, U.S.A.

ABSTRACT

The composite engine combines the best features of airbreathing and rocket engines into a simple, integrated, highly flexible propulsion system. These propulsion systems feature multimodal operation capability with cycle process interactions between engine components. Increased engine performance results from this synergistic design approach. Examples of composite engines are the Ejector Ramjet (ERJ), Supercharged Ejector Ramjet (SERJ), SCRAMLACE and Ejector SCRAMJET. This class of engine is also frequently referred to as mixed cycle engines, rocket ramjet engines, and less frequently compound cycle engines.

This paper will summarize a detailed engineering study conducted to evaluate the potential of composite engines when applied to the first stage of a two-stage manned advanced reusable launch vehicle. Briefly, the launch vehicle mission/design constraints were as follows:

- Reusable vehicle, passenger/light cargo payload
- Two stage to 262 nautical mile (485 kilometer) orbit
- Horizontal takeoff and landing
- Hydrogen/Oxygen (rocket engine only) propellants
- One million pound (453600 kilogram) vehicle takeoff gross weight
- Full mission profile, liftoff to landing with 3 "g" acceleration limit (manned application).

Payload in orbit was the prime evaluation criteria.

A total of 36 composite engines were evaluated for this mission/application. In all cases considered, composite engines were clearly shown to be superior when compared to an advanced liquid rocket engine. Payload in orbit results are presented for the more attractive composite engines. In addition, vehicle payload performance as a function of vehicle staging velocity is presented. Typical staging velocities are Mach 8 to 10.

INTRODUCTION

Launch vehicles in which all components are fully reusable must eventually be developed if truly low cost space launch operations are to be achieved. The horizontal takeoff and landing airbreathing launch vehicle has inherent features which make it a prime candidate for future second generation shuttle systems.

The rocket engine is characterized by high thrust to weight ratio but at low specific impulse values. In contrast, true airbreathing engines are characterized by high specific impulse performance but engine weights are heavy, The composite engine combines the best features of rocket and airbreathing engines into simple integrated, highly flexible propulsion systems.

As suggested in Figure 1, a fully reusable launch vehicle (two stage to orbit mission), powered by composite engines, may offer major improvements in payload in orbit performance. This paper summarizes a detailed engineering study conducted to evaluate the potential of the composite engine.*

COMPOSITE ENGINE SYNTHESIS, DESIGN, AND OPERATION

The elemental propulsion systems which provide the basic building blocks for synthesizing composite engines are the familiar rocket and airbreathing systems, which are symbolically illustrated in Figure 2.

If it is desired to incorporate the features of both elements (rocket and airbreather) in a single vehicle, two approaches are obvious: the elements may be installed either separately or integrally. The former may be termed a combination propulsion system. Thus, to illustrate the contrast, combination propulsion systems incorporate two or more elemental engine types in a nonintegrated installation, i.e., with little or no direct physical or process interaction between engine types within the vehicle's propulsion complement.

If, however, the elements are physically integrated into a single propulsion system, having multimodal operation capabilities, with cycle process interactions between elements, the result is a composite propulsion system. Increased engine performance results from this synergistic design approach.

Marquardt approached the composite engine from the standpoint of expanding and developing the functions and operation of the basic ramjet cycle. Thus a clear initial goal was to provide the ramjet with low speed thrust capability such that it could accelerate under its own power to ramjet cruise conditions. The Ejector Ramjet is thus the most simple composite engine which integrates the rocket function and ramjet function into a single integrated engine (see Figure 3). The Ejector Ramjet engine has two operating modes: (1) Ejector Mode and (2) Ramjet Mode (high flight speed operation).

---

*This study was sponsored by the National Aeronautics and Space Administration (NASA) under Contract NAS7-377. Marquardt was supported in this study by the Lockheed-California Company and Rocketdyne.

Manned high supersonic/hypersonic speed aircraft will cruise on ramjet power. However, such aircraft also require low speed cruise/loiter capability at low specific fuel consumption. The Supercharged Ejector Ramjet (SERJ) engine meets these requirements. In this engine, a low pressure ratio fan/gas generator is integrated with the ejector primaries and ramjet/afterburner. The fan provides an additional pressure rise for the high thrust/acceleration Ejector Ramjet operating mode, or Fan Ramjet operation (i.e. augmented turbofan) for intermediate speed acceleration, or low speed cruise/loiter capability with the ejector and ramjet components inoperative, (Fan Mode). During ramjet operation, the fan may be allowed to windmill or be removed from the airstream. The windmilling technique has been experimentally demonstrated.

The Ejector Ramjet and SERJ engines can be designed for cryogenic (i.e. liquid hydrogen, liquid methane) or storable propellants. Advanced high performance composite propulsion systems which operate over a very wide flight speed range have been established by combining ramjet, Ejector Ramjet, SERJ, supersonic combustion and/or LACE engine technology. The Ejector SCRAMJET, RAMLACE, and SCRAMLACE engines are shown in Figure 4. Figure 5 illustrates the Supercharged Ejector SCRAMJET, Supercharged RAMLACE and Supercharged SCRAMLACE engines.

The basic LACE engine cycle uses the large cooling capacity of liquid hydrogen to liquefy air. Therefore, this basic engine cycle and its derivatives are limited to the use of liquid hydrogen fuel. The Supercharged Ejector SCRAMJET and Ejector SCRAMJET engines can be designed to operate on cryogenic fuels or storable propellants. The basic technology to develop these advanced engines has largely been demonstrated; however, development of these engines will be more costly and will require a longer development period than for either the Ejector Ramjet or Supercharged Ejector Ramjet engine.

Figures 4 and 5 described several composite engines which use the basic LACE engine as the ejector primary/rocket subsystem. These engines are RAMLACE, SCRAMLACE, Supercharged RAMLACE and Supercharged SCRAMLACE. The performance of these engines can be significantly improved if the cooling capacity of liquid hydrogen can be increased. One demonstrated approach is the use of slush hydrogen (super cooling) which lowers the hydrogen boiling point from 36°R (20°K) to approximately 25°R (14°K). The performance potential of this technique as applied to the RAMLACE engine is illustrated in Figure 6. In this composite engine application study, this cooling/improved performance concept was evaluated for the following engine designs:

Recylcled RAMLACE
Recycled SCRAMLACE
Recycled Supercharged RAMLACE
Recycled Supercharged SCRAMLACE

The ejector mixing and pumping (jet compression) offered by the ejector primary/rocket subsystem forms the heart of the Marquardt developed composite engine cycles. The kinetic energy of high pressure ejectors is used to induce airflow at low speed conditions and at all flight speeds to raise the total pressure level of the mixed air/primary system. As with all airbreathing engines, thrust and cycle efficiency increase as the cycle pressure ratio is increased.

The continuity, momentum and energy equations relate the aerothermodynamic properties of the fully mixed air-primary (i.e. mixer exit) to mixer entrance flow conditions. Experimental mixing data are in close agreement with predictions. However, the length required to achieve full mixing cannot be analytically predicted and, therefore, must be experimentally correlated.

Representative ejector/mixer performance in terms of total pressure ratio is presented in Figure 7 as a function of secondary/primary mass flow ratio or more simply engine airflow/ejector propellant flow ratio. Achievable ejector/mixer total pressure ratios are modest, therefore, the resultant improvement in engine performance is maximum at lower flight speeds.

Marquardt has conducted an intensive jet compression research program. Initial ejector primary propellants (fluids) included heated air, hydrogen/air and hydrogen/oxygen. Later tests included hydrocarbon fuels and hydrogen peroxide as the oxidizer. As a result of this work, the required mixer length was correlated as a function of the number of primary nozzles, the primary exit Mach number, air/primary flow rate ratio, primary/secondary total temperature ratio and mixer/primary geometry (see Figure 7). Efficient jet compression with short mixer lengths has been demonstrated.

The Ejector Ramjet engine cycle has been successfully demonstrated in several engine test programs. Initial small scale demonstrations were accomplished with hydrogen/air and hydrogen/oxygen ejector primary subsystems. Later, two 18-inch diameter Ejector Ramjet engine demonstration programs were conducted using hydrocarbon fuel/hydrogen peroxide propellants. A photograph of the second test engine is presented in Figure 8. Briefly these test programs demonstrated the following:

- Experimental thrust stand performance agreed within ± 5% of predicted performance.
- Both engine operating modes were demonstrated.
- Mode transitions were demonstrated.
- Ejector primary throttling was demonstrated.
- Afterburner throttling was demonstrated.
- Static and high flight speed operation were demonstrated.

Thus, the composite engine has been convincingly demonstrated in scale engine test programs.

The composite engine is characterized by its multi-operating mode capability and resultant mission flexibility. The flexibility of this class of engine is illustrated in Figure 9. Specifically, this figure describes the operating modes of the Supercharged Ejector SCRAMJET engine when used to power an advanced reusable launch vehicle. A single stage to orbit option is apparent.

Studies conducted by Marquardt and several major airframe companies have shown that while composite engine multimode operating flexibility is a valuable asset, the mission optimization process is complex and requires more effort than for single operating mode engines.

ADVANCED LAUNCH VEHICLE APPLICATION

Marquardt evaluated the performance potential of composite engines when applied to an advanced reusable launch vehicle. Briefly, the launch vehicle/mission design constraints were as follows:

- Reusable vehicle, passenger/light cargo payload
- Two-stage to 262 nautical mile (485 kilometer) orbit
- Horizontal takeoff and landing
- Hydrogen/oxygen (rocket engine only) propellants
- One million pound (453600 kilogram) vehicle takeoff gross weight
- Full mission profile, liftoff to landing and 3"g" acceleration limit.

Payload in orbit was the prime evaluation criteria.

A total of 36 composite engines were evaluated for this application/mission; however, the engines of primary interest have been reviewed in this paper. Study results were compared to "Very Advanced" rocket and Turboramjet engine performance.

The baseline composite engine fully reusable launch system is a two-stage, horizontal takeoff and landing, nested lifting body configuration. The first stage provides an aerodynamic pressure field for the inlets of the integrated propulsion system. The all-rocket second stage vehicle is fully recoverable and reusable and was established in a previous study program.* The design of this vehicle was not perturbed; rather, it was scaled in accordance with first stage capabilities.

An orbital launch system was defined for each composite propulsion system. Figure 10 describes a representative system. Specifically, the first stage of this launch vehicle is powered by SCRAMLACE engines. Figure 11 presents an artist's rendering of this vehicle.

In general terms, composite engines operate on ejector (primary rocket) mode from Sea Level Static to as high as Mach 2, where ramjet mode transition occurs. For engines employing the subsonic combustion mode, the maximum airbreathing Mach number is 8. For engines employing the SCRAMJET mode, the transition from subsonic to supersonic combustion occurs at Mach 6 and this high speed mode nominally continues to Mach 12. Specifically, engine operating modes/transition speeds were optimized in terms of minimum propellant plus engine weight for each composite propulsion system. Figure 12 illustrates the broad range of composite engine performance during ejector mode operation. Corresponding Sea Level Static Engine thrust to weight ratios are also presented.

---

*NASA Contract NAS8-11463

A stated objective of this study was to compare composite engine mission results with "Very Advanced" rocket engine propulsion. For this study, "Very Advanced" rocket engines were defined as follows:

Propellants	Liquid Hydrogen/Oxygen
Cycle	Fuel Rich Tap Off
Oxidizer/Fuel Ratio	6.5
Chamber Pressure	2000 psi (141 kg/cm^2)
Specific Impulse, Sea Level	375 sec.
Thrust/Weight Ratio	179

The results of the mission analysis study are presented in Figure 13 in terms of payload in orbit and system total dry/gross payload weight ratio. System cost effectiveness was specifically not an objective of this study. However, system total dry/gross payload weight ratio is a rough indicator of total system cost.

With these results, two composite engines were selected for further detailed study. An objective of this study was to conduct an assessment and evaluation of engine technology requirements. This resulted in the selection of the two composite engines; (1) the first engine should provide attractive payload in orbit performance yet only require near term technology for its successful development while (2) the second engine should provide near maximum payload in orbit performance recognizing major advances in engine technology would be required for its successful development. The selected engines were: (1) near term technology - Supercharged Ejector Ramjet engine and (2) advanced engine technology - SCRAMLACE engine.

These two engines and comparison "Very Advanced" rocket and Turboramjet engines were intensely studied. For example, optimum* launch vehicle staging velocity was defined (see Figure 14). In addition, study of the "Very Advanced" rocket powered vehicle was expanded. Specifically, three takeoff modes were evaluated:

1. Horizontal takeoff and landing (internal landing gear)
2. Horizontal takeoff and landing (rocket sled assisted takeoff)
3. Vertical takeoff.

Optimum staging velocities for these vehicles are also presented in Figure 14.

In the same format as previously presented, the results of this detailed study are presented in Figure 15. This figure compares the following engines:

- "Very Advanced" Rocket
- Supercharged Ejector Ramjet (SERJ)
- SCRAMLACE
- Turboramjet.

It should be noted that the payload in orbit values are the maximum from Figure 14.

---

*In terms of payload in orbit performance

These results indicate a more favorable position for the "Very Advanced" rocket engine particularly with the alternate takeoff modes. These results notwithstanding, the payload in orbit potential of the composite engine is clearly shown. The Turboramjet engine shows excellent growth potential; however, development of the Supercharged Ejector Ramjet engine could be accomplished for a fraction of the development cycle and cost of the Turboramjet engine.

Although the Ejector Ramjet engine was not evaluated in the detailed engineering study, its high performance/low development cost potential should be recognized. If first stage loiter is not established as a requirement, this conclusion becomes stronger. With this engine, development of rotating machinery is not required and this engine cycle has been convincingly demonstrated in several engine test programs.

124<

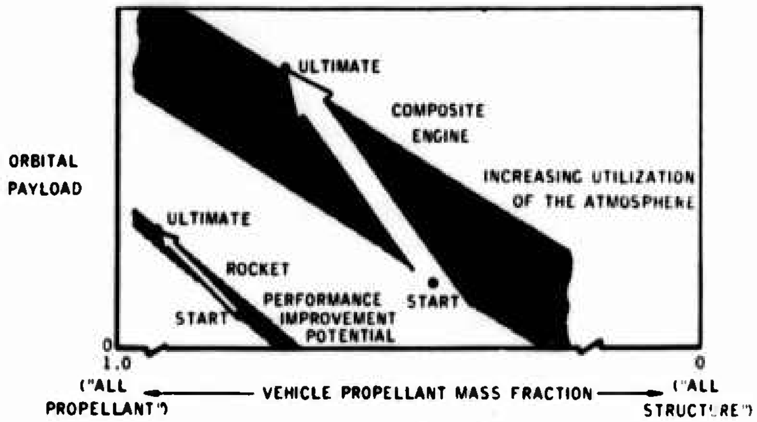

Figure 1. Reusable Launch Vehicle Performance - Composite Engine VS Rocket

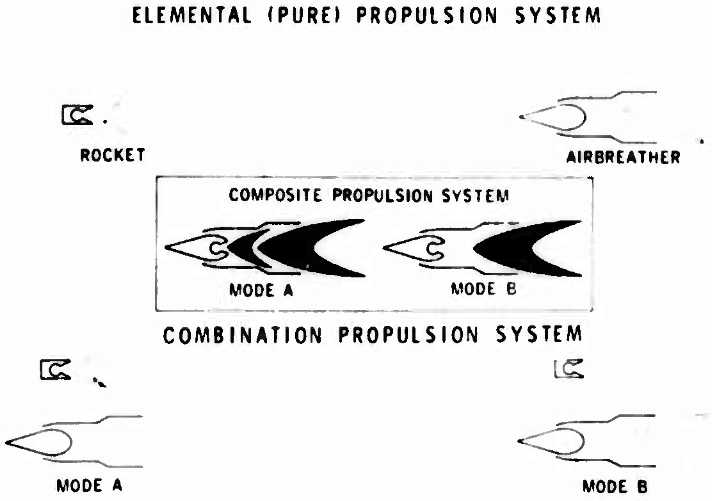
ELEMENTAL (PURE) PROPULSION SYSTEM
ROCKET
AIRBREATHER
COMPOSITE PROPULSION SYSTEM
MODE A
MODE B
COMBINATION PROPULSION SYSTEM
MODE A
MODE B

Figure 2. Propulsion Classes

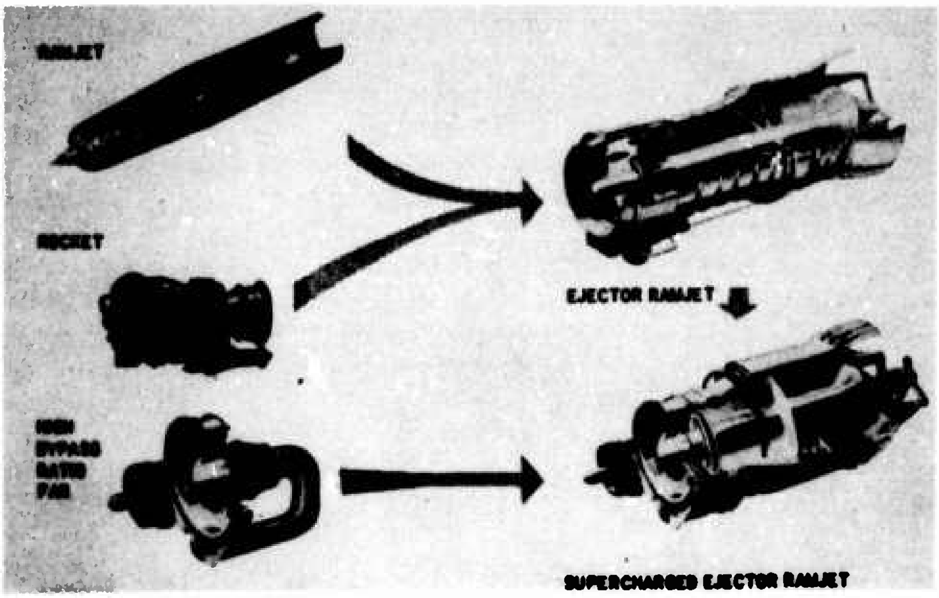
RAMJET
ROCKET
HIGH BYPASS RATIO FAN
EJECTOR RAMJET
SUPERCHARGED EJECTOR RAMJET

Figure 3. Gensis of The ERJ and SERJ Composite Engines

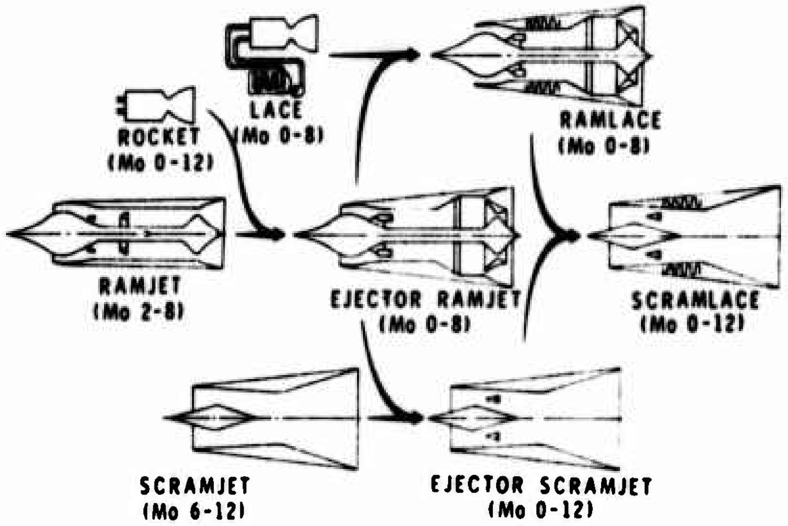
ROCKET
(Mo 0-12)
LACE
(Mo 0-8)
RAMLACE
(Mo 0-8)
RAMJET
(Mo 2-8)
EJECTOR RAMJET
(Mo 0-8)
SCRAMLACE
(Mo 0-12)
SCRAMJET
(Mo 6-12)
EJECTOR SCRAMJET
(Mo 0-12)

Figure 4. Evolution of Advanced Propulsion Systems

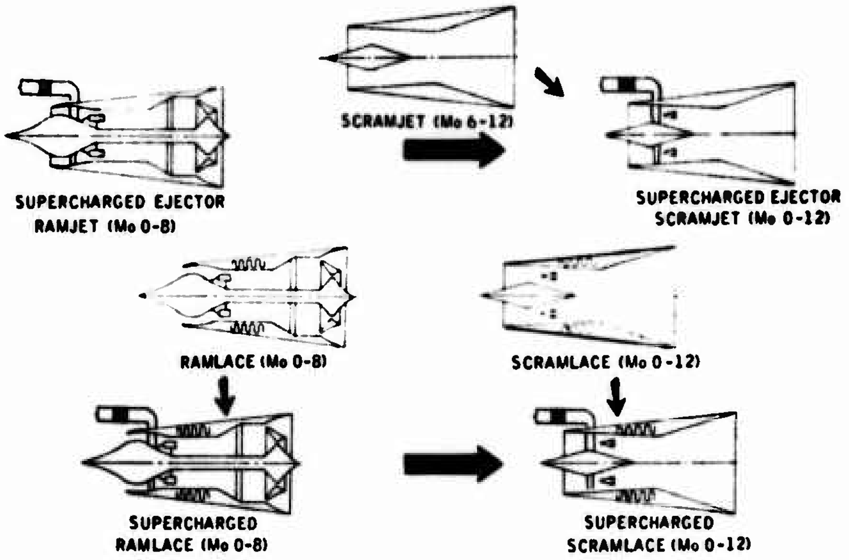
SCRAMJET (Mo 6-12)
SUPERCHARGED EJECTOR RAMJET (Mo 0-8)
SUPERCHARGED EJECTOR SCRAMJET (Mo 0-12)
RAMLACE (Mo 0-8)
SCRAMLACE (Mo 0-12)
SUPERCHARGED RAMLACE (Mo 0-8)
SUPERCHARGED SCRAMLACE (Mo 0-12)

Figure 5. Evolution of Advanced Propulsion Systems (Continued)

I_s IS FOR SEA LEVEL STATIC CONDITIONS

ϕ = NET ENGINE EQUIVALENCE RATIO

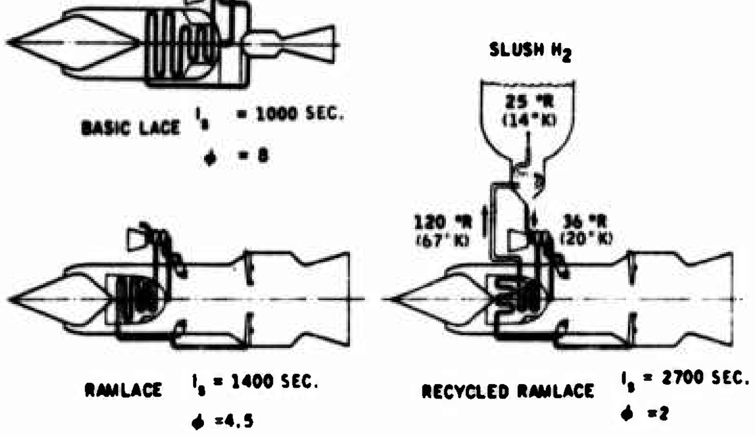
BASIC LACE
I_s = 1000 SEC.
ϕ = 8
SLUSH H_2
25 °R
(14°K)
120 °R
(67°K)
36 °R
(20°K)
RAMLACE
I_s = 1400 SEC.
ϕ =4.5
RECYCLED RAMLACE
I_s = 2700 SEC.
ϕ =2

Figure 6. Air Liquefaction Cycles

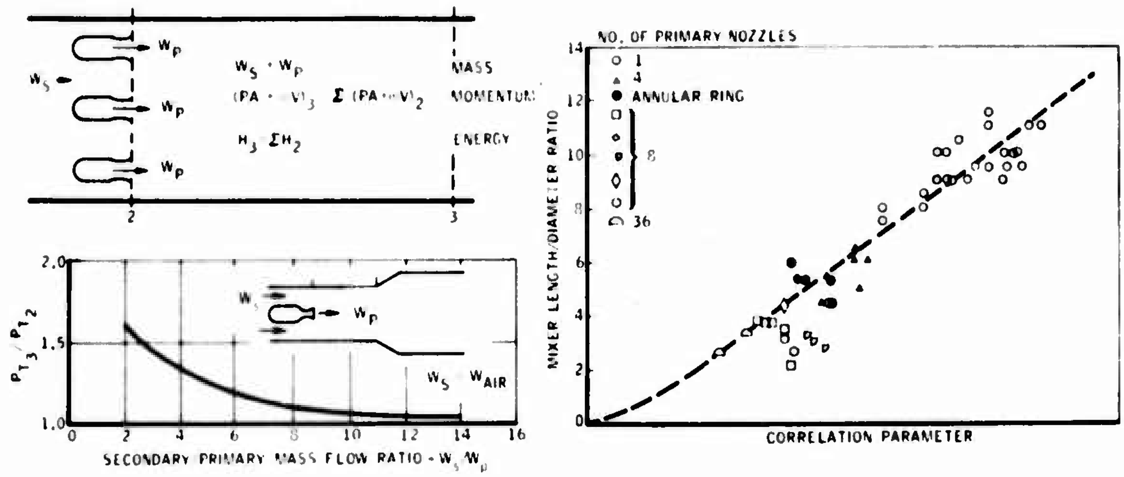

Figure 7. Ejector Mixing And Pumping

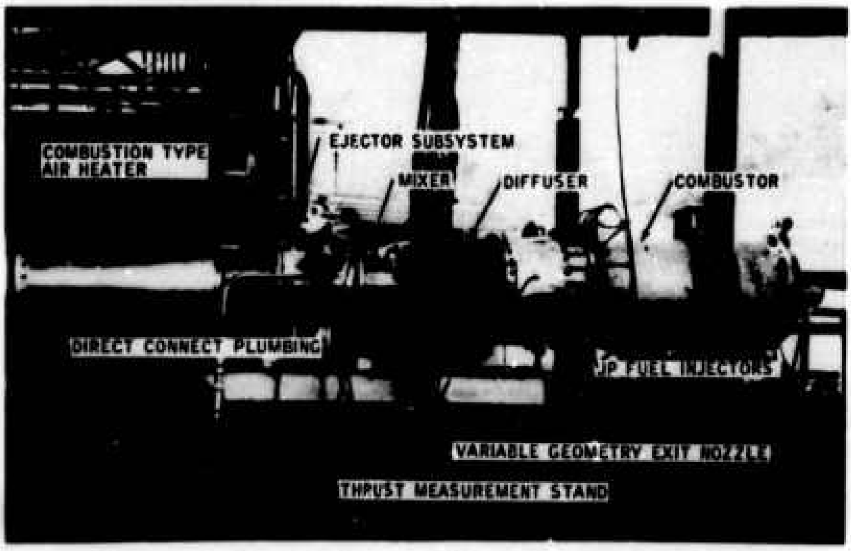
COMBUSTION TYPE AIR HEATER
EJECTOR SUBSYSTEM
MIXER
DIFFUSER
COMBUSTOR
DIRECT CONNECT PLUMBING
JP FUEL INJECTORS
VARIABLE GEOMETRY EXIT NOZZLE
THRUST MEASUREMENT STAND

Figure 8. Ejector Ramjet 18 Inch Engine Installation

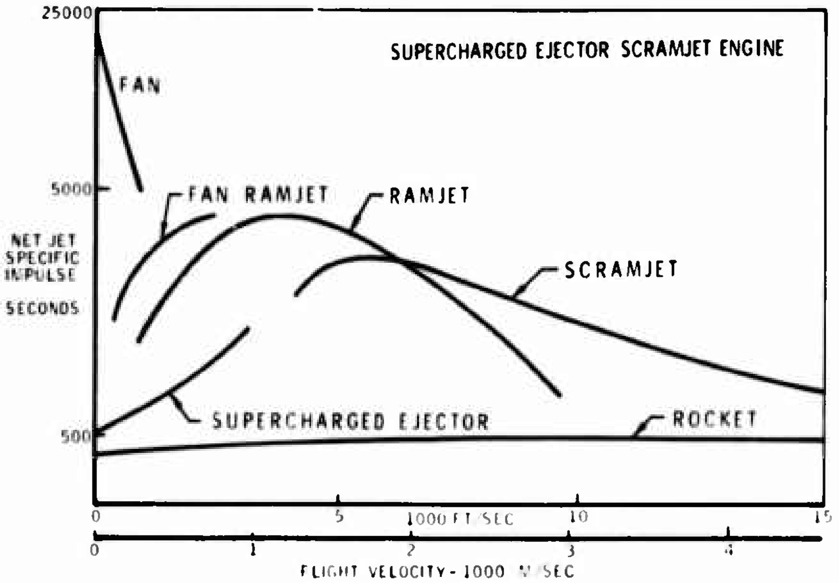

Figure 9. Composite Engine Multimode Operation

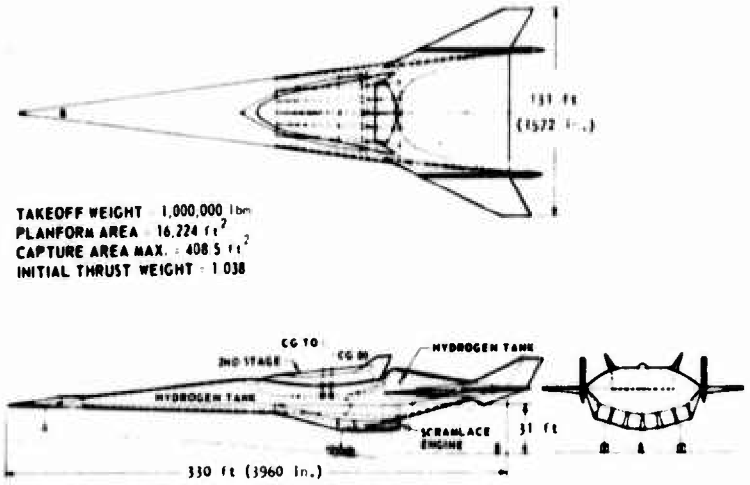
131 ft
(1572 in.)
TAKEOFF WEIGHT = 1,000,000 lbm
PLANFORM AREA = 16,224 ft²
CAPTURE AREA MAX. = 408.5 ft²
INITIAL THRUST WEIGHT = 1.038
CG TO
2ND STAGE
CG BO
HYDROGEN TANK
HYDROGEN TANK
SCRAMLACE ENGINE
31 ft
330 ft (3960 in.)

Figure 10. Baseline Reusable Launch Vehicle

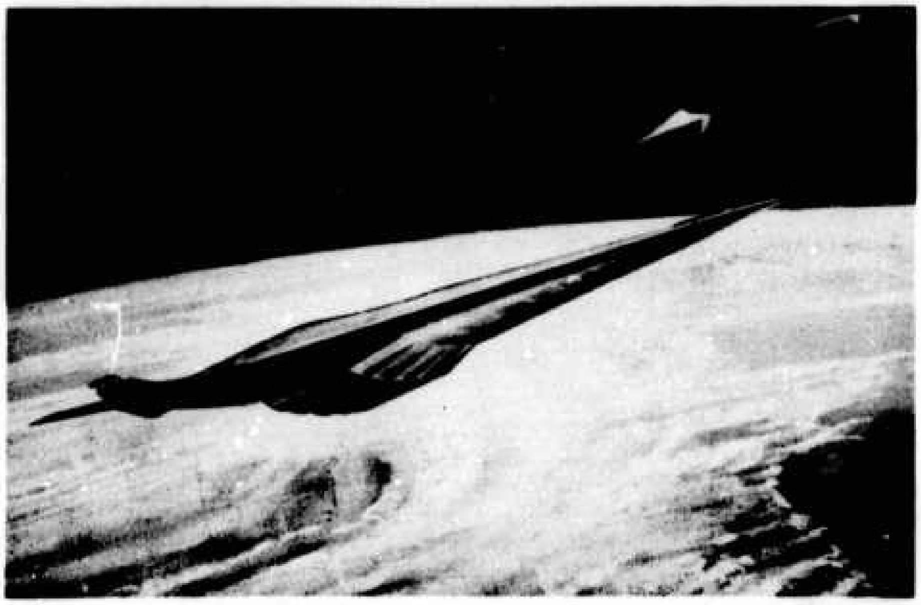

Figure 11. Airbreathing Launch Vehicle - Composite Engine Powered Booster / Rocket Powered Orbiter

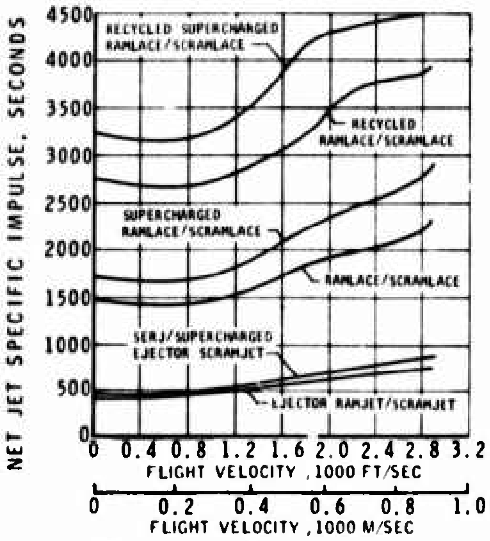

ENGINE	THRUST TO WEIGHT RATIO*
EJECTOR RAMJET	35.0
EJECTOR SCRAMJET	37.8
SERJ	24.9
SUPERCHARGED EJECTOR SCRAMJET	26.6
RAMLACE	18.7
SCRAMLACE	19.8
SUPERCHARGED RAMLACE	15.8
SUPERCHARGED SCRAMLACE	17.0
RECYCLED RAMLACE	14.2
RECYCLED SCRAMLACE	15.0
RECYCLED SUPERCHARGED RAMLACE	14.2
RECYCLED SUPERCHARGED SCRAMLACE	15.0

*SEA LEVEL STATIC CONDITIONS
THRUST = 250000 LB (113400 KG)

Figure 12. Engine Performance Comparison - Ejector Mode Operation

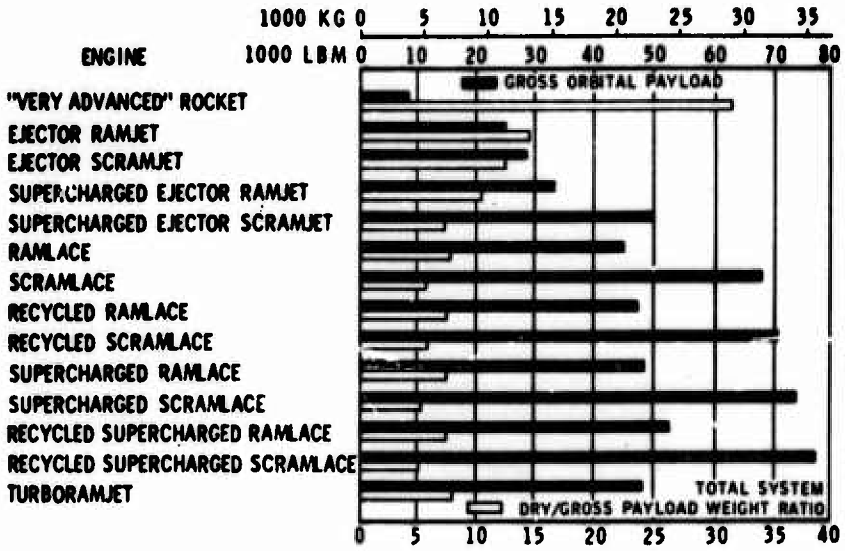

Figure 13. Payload in Orbit Performance Summary

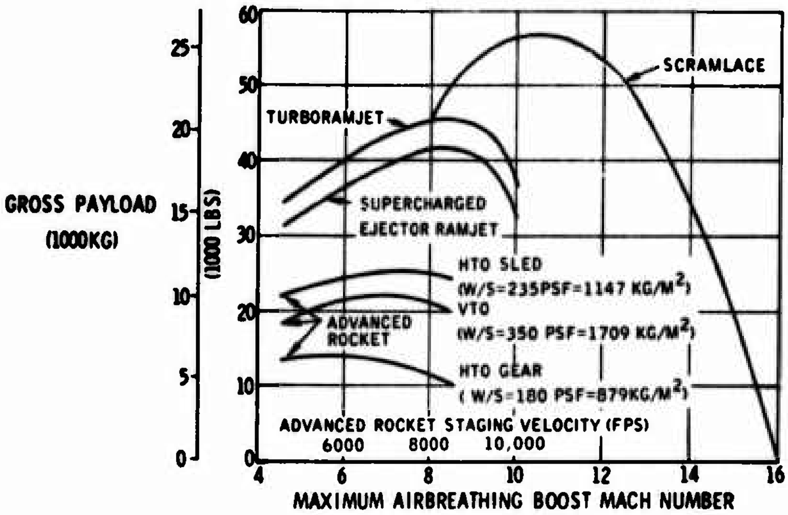

Figure 14. Payload in Orbit Vs. Launch Vehicle Staging Velocity

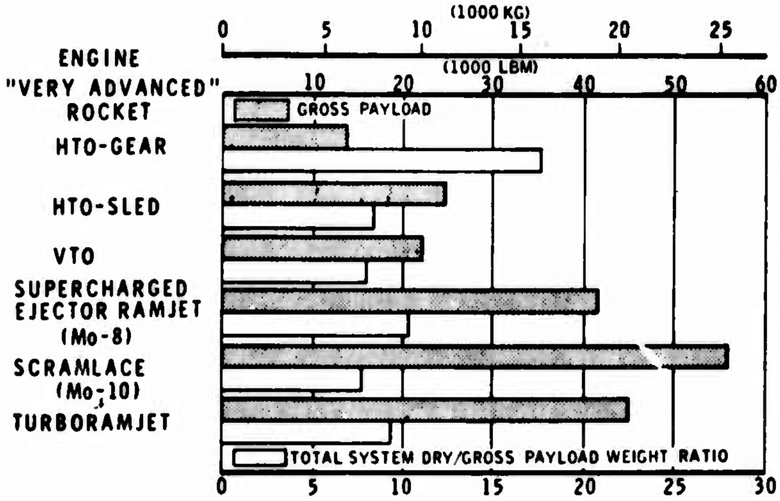

Figure 15. Payload in Orbit Performance Summary

AN EXAMINATION OF INJECTOR/COMBUSTOR DESIGN EFFECTS ON SCRAMJET PERFORMANCE

Griffin Y. Anderson
NASA Langley Research Center, Hampton, Virginia

INTRODUCTION

The feasibility and performance potential of the supersonic combustion ramjet (scramjet) was firmly established by experiments conducted with research scale engines in the 1960's.[1] The challenge in hypersonics for the 1970's is to evolve practical integrated engine-vehicle concepts suitable for a mission like the first stage of a space shuttle or for hypersonic cruise. A key element in achieving attractive system performance is the use of hydrogen fuel with its large heat sink to provide active cooling of both the engine and the vehicle.[2] Minimum engine heat load is a prerequisite so that adequate cooling will be available for the vehicle. Since the combustor contributes the bulk of the engine heat load, proper modeling of combustor heat load is of first importance.

Of course, the combustor and fuel injector design have other important influences on overall engine characteristics and performance. The injector must distribute the fuel to allow nearly complete mixing and chemical reaction within the combustor length provided. The maximum pressure in the engine generally occurs in the combustor and its level affects engine structural weight. Also, the wall pressure distribution and skin friction in the combustor can be significant factors in overall engine thrust. Since all these factors - heat load, combustion efficiency, maximum pressure, pressure distribution, and skin friction - are interrelated, the task of analyzing the flow in a scramjet combustor is a complex one.

Progress is being made toward development of numerical schemes to calculate supersonic combustion flow fields in detail. Reference 3 applied a "viscous-characteristics" analysis,[4] which accounts for lateral and axial pressure variation due to mixing and combustion, to the design of a two-dimensional slot injector which produces constant static pressure in the region of the supersonic flame. Reference 5 presents a calculation procedure which can be applied to three-dimensional supersonic combustion flow fields and is suitable for use with the newer models for turbulent transport (see paper 11 of Ref. 6). Ultimately, techniques such as these may evolve to the point where they can serve as design tools for scramjet combustors, and their development is being vigorously pursued. At present, however, numerical complexity, lack of well-established turbulence models, and uncertainty about the description of chemical reaction in turbulent flow makes less detailed approaches, such as a one-dimensional analysis, attractive for preliminary design studies.

Even with a one-dimensional treatment the task of analyzing a scramjet combustor of general shape is not straightforward. Only the special cases of a constant area duct or a duct shaped to give constant wall pressure can be treated simply, and these cases are not sufficiently general for engine design purposes. One way to treat more general geometry is to assume a pressure-area power law of the Crocco type.

$$pA^{\varepsilon} = \text{constant}$$

This approach has the advantage of providing direct means for determining combustor exit conditions for a given heat addition if the appropriate exponent is known and has been used successfully to model supersonic combustion results.[7,8] However, a single value of exponent may not be adequate for all regions of the combustor and proper qualitative modeling of the local heat flux in the combustion region is not achieved.[9]

Another approach for combustors of general shape[10] is to specify the amount of fuel reacted as a function of distance and compute the resulting (one-dimensional) flow properties step by step through the combustor. This technique has the advantage of allowing development of relations between fuel injector design and heat release distribution at the expense of some additional calculation. Also, better modeling of local conditions, including local heat flux, might be expected. The purpose of this paper is to explore the application of this scramjet combustor analysis technique to problems of practical interest. First, the relation between injector design and heat release distribution is reviewed. Then, data from direct-connect supersonic combustion tests using simple strut injectors are compared with calculations. Finally, the calculated performance of two distinctly different scramjet engine designs is compared.

SCRAMJET COMBUSTOR ANALYSIS

Relation Between Injector Design and Heat Release

Unlike many low-speed combustion problems, supersonic combustion flow fields are generally dominated by the momentum of the reactants. In the case of hydrogen as fuel and air as oxidizer, the momentum of the air stream entering the supersonic combustor largely determines the streamline pattern of the flow. Mixing and heat release cause significant changes in local static pressure; but because the flow is supersonic, relatively small streamline deflections are involved (generally on the order of a few degrees). At hypersonic flight speeds in cases of practical interest for propulsion, heat release is controlled by the rate of mixing of the injected fuel with the air stream.[11] A first step toward describing the supersonic combustion process is to develop means to model the accomplished mixing (and hence combustion) produced for a given combustor length in terms of injection geometry and conditions. As in most treatments of turbulent flow problems, considerable reliance on empiricism is necessary. Ultimately, more sophisticated treatment of the fluid dynamics and turbulence will be desirable for detailed design.

Parallel injection. The existence of an orderly streamline flow pattern seems particularly likely for parallel injection, and numerical procedures are widely available which can calculate detailed flow property distributions if an appropriate turbulent transport model can be supplied. While this is difficult in the general case, even fairly simple transport models can do an adequate job for a restricted class of flows.[6] For use in preliminary scramjet design studies an integral measure of accomplished mixing with length suitable for a one-dimensional analysis is most useful first rather than detailed fuel distribution profiles. Thus an accomplished mixing or "mixing efficiency" parameter, η_m, can be defined from the fuel distribution at any axial location as the amount of fuel that would react if complete reaction occurred without further mixing divided by the amount of fuel that would react if the mixture were uniform.[10] For high temperature flows with fast reactions which are nearly in local chemical equilibrium, mixing efficiency and combustion efficiency are equal.

Mixing efficiency results computed from profiles calculated with the theory described in Reference 12 for bounded multijet mixing are shown in Figure 1 for several parallel injection goemetries and arrangements. In all calculations shown in the figure the same jet and free-stream properties, initial step profiles, and turbulent eddy viscosity were used. The axial length scale for each case is nondimensionalized by the length for complete mixing, x_ℓ. The upper edge of the shaded band corresponds to uniformly spaced square arrays of circular jets while the lower edge represents two-dimensional slot injection. Rectangular arrays of circular jets with different aspect ratios fall in the shaded region between the curves for square arrays and slots. Changing the amount of injected fuel (as measured by equivalence ratio, ϕ) from 0.6 to 2 times stoichiometric has very little effect on the shape of the mixing efficiency distribution. Results of a single-jet calculation made with the theory described in Reference 13 are included in the figure for comparison.

Although equivalence ratio does not affect the dimensionless shape of the multiple jet curves in Figure 1, it does have an important influence on the length required for complete mixing. Figure 2 shows the relative length for complete mixing for slots and square arrays versus equivalence ratio. Reducing equivalence ratio to 0.6 decreases the length in which all the injected fuel is reacted by nearly a factor of 2. Increasing equivalence ratio to 2 decreases the length required to consume all the oxygen by a factor of 3. The effects are similar for slots and square arrays, but the most important conclusion to draw from Figure 2 is that an excess of either reactant substantially reduces the length required for sufficient mixing to allow complete reaction.

Perpendicular injection. Although considerable progress has been made by several groups[5-14] toward developing three-dimensional mixing calculation schemes which might be applied to cross-stream injection, at this time computed results for cross-stream injection comparable to the results for parallel injection shown in Figures 1 and 2 are not feasible. A series of experimental investigations with nonreacting flows has been carried out at the Langley Research Center of the NASA[15-17] to provide equivalent empirical information. Figure 3 shows the mixing efficiency results obtained in Reference 16 for a row of equally spaced perpendicular injectors. The principal difference between these empirical results for cross-stream injection and the computed results in Figure 1 for parallel injection is that some fuel is mixed immediately at the injector location with cross-stream injection. This result is physically reasonable since cross-stream injection causes a separated region with recirculation in the vicinity of the injectors. As pointed out in Reference 10, the amount of molecular level mixing accomplished near the injectors is likely to be somewhat less than the time mean fuel distribution measured in the experiments from which Figure 3 is derived. Therefore, an amount of reaction shown by the dashed line in Figure 3, somewhat below the mixing efficiency curve, is appropriate near the injectors.

Length for complete mixing. Of course the length for complete mixing, x_ℓ, is needed to apply the results shown in Figures 1 and 3. For parallel injection a mixing calculation for the appropriate conditions is used to estimate x_ℓ; the turbulent transport model chosen should be adapted to give good agreement with data from experiments at conditions similar to those of interest for engine design (see Ref. 18, for example). The effect of overall equivalence ratio on x_ℓ can be estimated from multiple jet calculations like those shown in Figure 2. For cross-stream injection x_ℓ is calculated from the data correlations developed in Reference 16.

Design for Controlled Heat Release

The distribution of heat release desired in a supersonic combustor changes with flight speed. At the lower end of the speed range (Mach 4 to 6) gradual heat release is required in a passage with increasing cross-section area in order to avoid thermal choking. At higher speeds (Mach 8 to 10) thermal choking is not a problem, and more rapid heat release in a passage with less increase in cross-section area can be utilized. One way to provide different heat release distributions at different flight speeds is to use fuel injectors at several axial locations and vary the distribution of fuel to the injectors with flight speed. Several research scale engines with small combustor height and wall fuel injection have used this approach successfully.[1] Another approach is to use injectors at one axial location which produce the appropriate mixing and heat release distribution over a range of flight speeds. In full-size engines which use fuel injection from struts to shorten the combustor, this technique is necessary since additional sets of strut injectors at downstream locations are not feasible.

In Reference 10 a combination of parallel and perpendicular injection was suggested to match heat release distribution to a given combustor geometry over a range of flight speed. At low speeds 70% of the fuel was injected parallel to the flow to take advantage of the nearly linear distribution of heat release produced near the injection point by parallel injection. At higher speeds all the fuel was injected perpendicular to the flow in order to achieve more rapid heat release to maximize engine thrust.

One-Dimensional Flow Model

The mixing efficiency distributions presented in Figures 1 and 3 can be used as fuel reaction distributions in a one-dimensional analysis to calculate flow properties in a supersonic combustor. This process is shown schematically in Figure 4. The analysis is based on the one-dimensional conservation equations for mass, momentum, and energy. Independent input parameters to the analysis are the geometry of the combustor, entering flow conditions, fuel injection distribution, fuel reaction distribution, wall skin friction coefficient, and wall temperature as indicated in Figure 4. Gas properties are handled with a partial reaction scheme which keeps equilibrium combustion products (produced by the reacted portion of the injected fuel) in thermal equilibrium with the injected fuel which is not reacted. With these parameters given, the conservation equations are used to calculate the flow properties along the combustor, stepwise, in a marching procedure starting from the combustor entrance. Thus, the calculation provides [illegible] property and wall heat transfer distributions with axial distance [illegible] the combustor.

COMPARISON WITH STRUT INJECTOR RESULTS

Substantiation of the simplified combustor analysis technique described in the preceding section must ultimately depend on comparison with experimental results. Comparisons of computed results with supersonic combustion data for perpendicular wall injection and for a single coaxial injector are presented in Reference 10 and show good agreement. In the case of strut injectors, no applicable data are available in the literature; so experiments were undertaken with some simple strut injector designs to provide data to test the technique. The apparatus is shown schematically in Figure 5. The strut is a 6° half-angle wedge oriented perpendicular to the test stream. The leading edge is water cooled but the body of the strut is cooled by the injector hydrogen fuel flow. Two configurations are shown for the downstream portion of the strut: a parallel injection configuration with five jets equally spaced along the rear face of the strut and a perpendicular injection configuration with four holes on each side immediately downstream of a small step. The purpose of the step is to isolate the upstream portion of the strut from the pressure rise caused by perpendicular injection and combustion. Details of the experiment are presented in Reference 19.

Figures 6 and 7 show photographs of the emission from the mixing-reacting flow fields produced by the injectors at test conditions simulating Mach 7 flight. The duct section downstream of the strut in Figure 5 was removed and the test stream exhausted as a free-jet to photograph the flow. The five parallel jets are clearly visible in Figure 6. Each jet is surrounded by a combustion region and the fuel-rich core of the jet appears as a dark streak. The bright regions downstream near the center of the flow are due to shocks caused by a mismatch in static pressure between the test jet and ambient air and to the shock waves and expansions from the wedge strut. In Figure 7 each of the four pairs of injectors produces a reacting zone that looks somewhat similar to a parallel jet in the plane of the strut. The dark streak or "jet core" disappears much sooner in the perpendicular injection flow field; also the emission intensity generated is much higher. Brighter emission results to a large extent from the higher pressure in the perpendicular injection flow field caused by reaction occurring at the point of injection (see Fig. 3). Of course the duct exit shock structure is also stronger, as is clearly evident by comparing Figures 6 and 7.

Wall static pressure distributions in the combustion duct downstream of the strut injectors are shown in Figures 8 and 9. Data for injection with and without reaction are compared with the corresponding computed pressure distributions. Data without reaction are obtained by conducting the experiment with hot test gas that does not contain free oxygen. The one-dimensional calculations provide a good representation of the data for the parallel injection strut as shown in Figure 8. A linear heat release with distance from the injector was used for the calculation since it is a good approximation to the early portion of the single-jet curve in Figure 1. The length for complete mixing (x_ℓ = 1.12 m) was calculated with a single jet theory[13] using the eddy viscosity model developed in Reference 20 with a value of the model constant equal to 0.01 as recommended in Reference 18. The fraction of injected fuel required to be reacted at the end of the duct is $\eta_c = 0.62$. For the equivalence ratio of the test ($\phi = 0.6$), apparently merging of the flow between adjacent jets has not affected the mixing rate, since gas sample measurements at the duct exit are consistent with this amount of reaction.

Agreement between data and theory in Figure 9 for the perpendicular injection strut is also good. The predicted pressure in the diverging portion of the duct is in excellent agreement with the data. The value of length for complete mixing for the one-dimensional calculations (x_ℓ = 0.6 m) is taken from the correlations in Reference 16. The measured pressure distribution in the constant area portion near the strut lies above the theory. This is expected since the theory does not account for shocks and separations which affect the pressure near the injectors.

The heat transfer to the walls of the combustion duct divided by the heat transfer with no reaction, Q/Q_o, is shown in Figure 10 plotted against the amount of fuel reacted at the end of the duct, ϕ_r, as inferred from the one-dimensional calculations. Data for perpendicular wall injection from the study of Reference 21 are included in the figure for comparison with the strut injection data. Uncertainty in the data is approximately ±0.5 and is due to the small coolant temperature rise. For moderate amounts of reaction ($\phi_r < 0.5$) the strut injection data and theory agree quite well, but for greater amounts of reaction the data lie above the predicted trend. If the enthalpy of the flow near the wall is taken as that corresponding to stoichiometric combustion products rather than the mean flow value, the predicted heat load is increased to more nearly the measured level. This higher local enthalpy at the wall is justified for the perpendicular injection strut (diamond symbol) because the fuel jets should penetrate from the strut to the combustion duct wall. The separation and shock waves in the region of the injector noted in the discussion of wall pressure data for the perpendicular injection strut (Fig. 9) also tend to increase the heat transfer above the level calculated with the one-dimensional analysis.

APPLICATION TO SCRAMJET PERFORMANCE EVALUATION

The usefulness of the combustor analysis technique described above is best demonstrated by application to the evaluation of scramjet performance potential at hypersonic speeds. Two engine designs are shown schematically in Figure 11; although quite different in appearance and concept, both designs produce high levels of internal thrust in the Mach 8 to 14 speed range. The first engine is a strut design similar to the scramjet module described in Reference 10. This engine is intended for careful integration with the undersurface of the vehicle on which it is installed. External drag is minimized by aligning the outside cowl surface with the local flow direction, and thrust is increased by using the vehicle base region for additional expansion of the engine exhaust. The design features an inlet with low internal contraction ratio (CR = 7) and multiple swept compression struts to allow self-starting without variable geometry at low supersonic flight Mach numbers. Fuel injection is in multiple planes from the aft portion of the struts, and the combustor has a relatively rapid increase in area near the fuel injectors.

The second engine is an axisymmetric design typical of several of the successful research scale engines discussed in Reference 1. Unlike the strut design, the axisymmetric design is intended for pod mounting outside the body volume of the vehicle on which it is installed. To keep the engine inlet within the compression field generated by the wing and body of the vehicle, the engine is located well aft. The cowl is made as thin as practical to reduce the slope of its external surface and minimize external drag. Also, since the engine nozzle is self-contained within the pod, its exit area must be limited to about two-thirds of the nozzle exit area available to the strut design in order to limit the external drag of the pod and maximize installed thrust. The inlet has variable geometry to allow starting and is intended to operate with high contraction ratio (CR = 14 to 20) in the Mach 8 to 14 speed range to maximize thrust. Downstream of the inlet throat the combustor has a nearly constant area section which is connnected by a diverging transition section to a second, larger constant area section that joins the exhaust nozzle. At hypersonic speeds fuel injection occurs near the inlet throat and combustion is largely completed within the constant area section there. The downstream portion of the combustor is provided for low-speed operation.

In both engines at high Mach numbers fuel is injected across the oncoming flow so a mixing efficiency distribution like that shown in Figure 3 is appropriate. The length for complete mixing estimated with the correlations of Reference 16 is $x_\ell/G = 48$ for the strut design and $x_\ell/G = 36$ for the axisymmetric design, where G is the gap between struts and inlet throat height for contraction ratio 14, respectively. The larger value can be achieved with a range of injector spacings, and the smaller value is near the minimum achievable for cross-stream injection from one wall. Combustor cross-section area distributions for both engines are given in Table 1. Note that the combustor exit areas match within 10%, and the strut design, although longer, has less wetted area in its combustor than the axisymmetric engine.

Computed combustor pressure distributions for the two designs are compared in Figure 12 for Mach 10 flight and stoichiometric combustion. For the axisymmetric design, wall pressure rises rapidly to a peak nearly four times the entrance pressure and approaches the pressure level for constant area combustion. Diverging area near the injectors in the strut design limits the peak pressure rise to about twice the entrance pressure. Of course the combustor entrance pressure for the axisymmetric design is higher (four times higher) than the strut design because the inlet contraction ratio is higher (16 versus 7), so that the actual peak pressure in the axisymmetric design would be eight times the peak in the strut design. Increasing the length for complete mixing for the axisymmetric design reduces wall pressure somewhat but also reduces thrust.

For combustor designs with large area changes from entrance to exit, the integral of the pressure on the combustor wall is a significant contribution to the overall engine thrust. Figure 13 illustrates this point for the axisymmetric design where engine thrust relative to engine thrust with constant area combustion is plotted against flight Mach number. Stoichiometric fuel-air ratio and nozzle flow in chemical equilibrium are assumed for all calculations. The hatched band represents engine thrust computed using the integral of wall pressure distributions like that shown in Figure 12. A constant value of one represents constant area combustion. If the mean pressure in the combustor is assumed to be the average of the entrance and exit pressures, thrust performance (shown by the line labeled $K = 1$) which is substantially in error results. In this example, thrust with $K = 1$ actually exceeds thrust with constant area combustion above Mach 13 which is not thermodynamically possible. Of course, the amount of error depends on the details of the geometry and heat release, but the effect can be of considerable importance.

If a fixed geometry configuration like the strut design is under consideration, it is possible to construct a simple correlation to model the combustor wall pressure integral factor, K. Figure 14 presents the combustor wall pressure integral factor for the strut design plotted against a heat release parameter, ϕ/M_o^2, which is an approximate dimensionless measure of the stagnation enthalpy change of the combustor heat addition. For Mach 4 and 6, a combination of perpendicular and parallel injection are used as described in Reference 10. For higher speeds, all perpendicular injection is used. The symbols represent flight along a given trajectory at a particular angle of attack for the vehicle; the top and bottom of the vertical bars represent flight at 4° lower and higher angle of attack, respectively, along the same trajectory. The variation shown in Figure 14 can be correlated as follows:

$M_o < 7$ (mixed parallel and perpendicular injection)

$$K = 0.25 + \left(0.09 + 6.88 \frac{\phi}{M_o^2}\right)(M_2 + 0.6)$$

$M_o > 7$ (perpendicular injection)

$$K = 0.05 + 1.98\ (M_2 + 0.6)\left(\frac{\phi}{M_o^{\,2}}\right)^{0.442}$$

Both equations are restricted to $0.5 \leq \phi \leq 2$ and the geometry of the strut combustor design. The variation in vehicle angle of attack noted above appears through the effect of inlet throat Mach number, M_2, in these equations. A correlation of this type is useful in mission studies because accurate parameteric thrust performance estimates can be made directly in an engine cycle calculation without making a separate combustor calculation for each condition of interest.

The wall static pressure distributions in Figure 12 also imply differences in heat load between the axisymmetric and strut designs. Figure 15 presents the relative combustor heat load for the two designs as a function of flight Mach number. The axisymmetric design has two to three times the heat load of the strut design over the entire speed range. This result is principally due to the higher inlet contraction and near constant area combustion of the axisymmetric design; the low speed combustor accounts for only about 10% of the heat load. The overall engine cooling requirement at Mach 8 is approximately 1.8 times the fuel for stoichoimetric combustion for the axisymmetric design compared to 0.7 for the strut design. Clearly this high combustor heat load makes the high inlet contraction of the axisymmetric design impractical.

Another important parameter for engine design is peak local heat flux which affects the choice of cooling approach, structural complexity, and engine operating cycle life. Figure 16 presents the peak heat flux in the combustor for the axisymmetric and strut designs. Peak heat flux for the axisymmetric design is considerably above that for the strut design due primarily to differences in mass flow per unit area between the two designs. In fact, the heat flux for the axisymmetric design in the Mach 12 to 14 speed range is well beyond the level that can be handled with regenerative cooling. Again high inlet contraction and near constant area combustion, which tend to give higher thrust performance, make the axisymmetric design impractical from a cooling standpoint.

The installed specific impulse (i.e., internal impulse minus external drag) of the two designs is compared in Figure 17. The impulse of the axisymmetric design is the same as the strut design at Mach 8; higher inlet contraction ratio increases internal performance to compensate for higher external drag of the axisymmetric engine installation. At Mach 14 even with higher inlet contraction ratio, the installed impulse of the axisymmetric design is somewhat less than the strut design because of the limited nozzle expansion available in the pod installation. However, based on the results shown in Figures 15 and 16, this impulse is unrealistic because the axisymmetric design cannot be cooled with such high inlet contraction. If inlet contraction is reduced to 10 to allow cooling, as shown by the lower curve in Figure 17, the strut design produces considerably better impulse at the higher Mach numbers.

CONCLUDING REMARKS

A simplified one-dimensional treatment of fuel injection for supersonic combustor performance analysis has been presented. Results giving representative mixing efficiency variations for both parallel and cross-stream injection were presented and approximate means of estimating the length required for complete mixing were indicated. Comparisons of supersonic combustion data for strut fuel injection were made with results calculated by the one-dimensional analysis technique. Good agreement was found between calculated results and the measured wall pressure distributions and combustion duct heat load. Application of the analysis technique was demonstrated by comparing results obtained for a multistrut and an axisymmetric engine design. High inlet contraction ratio and constant area combustion, which were used in the axisymmetric design to overcome the limited nozzle exit area and high external drag of its podded installation, were shown to result in unacceptably high combustor cooling requirements and peak heat flux levels in the combustor. When engine cooling performance is considered along with thrust performance, the need for an integrated, low external drag engine installation with moderate inlet contraction ratio is readily apparent.

REFERENCES

1. HENRY, JOHN R., and McLELLAN, CHARLES H.. The Air-Breathing Launch Vehicle for Earth-Orbit Shuttle - New Technology and Development Approach. AIAA Paper No. 70-269, February 1970. Also Journal of Aircraft, Vol. 8, No. 5, May 1971.

2. BECKER, JOHN V. New Approaches to Hypersonic Aircraft. Paper presented at Seventh Congress of the International Council of the Aeronautical Sciences (ICAS) (Rome, Italy), September 1970.

3. AGNONE, A. M. Development of a Two-Dimensional Tangential Fuel Injector with Constant Pressure at the Flame. NYU 72-25, New York University, September 1972. (Available as NASA CR-112302.)

4. DASH, S. An Analysis of Internal Supersonic Flows with Diffusion Dissipation and Hydrogen-Air Combustion. ATL TR 152, Advanced Technology Laboratory, Inc., May 1970. (Available as NASA CR-111783.)

5. PATANKAR, S. V., and SPALDING, D. B. A Calculation Procedure for Heat, Mass and Momentum Transfer in Three-Dimensional Parabolic Flows. International Journal of Heat and Mass Transfer 15, 1787-1806, October 1972.

6. Free Turbulent Shear Flows, Vol. I - Conference Proceedings. NASA SP-321, 1972.

7. BILLIG, FREDERICK S. Eleventh Symposium (International) on Combustion. The Combustion Institute, 1967, p. 755.

8. BILLIG, F. S., and DUGGER, G. L. Twelfth Symposium (International) on Combustion. The Combustion Institute, 1969, p. 1125.

9. BILLIG, FREDERICK S., and GRENLESKI, S. E. Heat Transfer in Supersonic Combustion Processes. Paper presented at Fourth International Heat Transfer Conference (Varsailles, France), August 1971.

10. HENRY, JOHN R., and ANDERSON, GRIFFIN Y. Design Considerations for the Airframe-Integrated Scramjet. NASA TM X-2895, 1973.

11. FERRI, A. Mixing-Controlled Supersonic Combustion. Annual Review of Fluid Mechanics, Vol. 5, 1973.

12. ALZNER, EDGAR. Three-Dimensional Mixing of Jets. ATL TR 150, Advanced Technologies Lab., Inc., July 1970. (Available as NASA CR-111782.)

13. Diffusion Controlled Combustion for Scramjet Application. Technical Report 569, Gen. Appl. Sci. Lab., Inc., December 1965. HOPF, H., and FORTUNE, O. Part II - Programmer's Manual. (Available as NASA CR-66714.)

14. BAKER, A. J., and ZELAZNY, S. W. A Theoretical Study of Mixing Downstream of Transverse Injection into a Supersonic Boundary Layer. Report 9500-920263, Bell Aerospace Company, 1972. (Available as NASA CR-112254.)

15. ROGERS, R. CLAYTON. A Study of the Mixing of Hydrogen Injected Normal to a Supersonic Airstream. NASA TN D-6114, 1971.

16. ROGERS, R. CLAYTON. Mixing of Hydrogen Injected from Multiple Injectors Normal to a Supersonic Airstream. NASA TN D-6476, 1971.

17. McCLINTON, CHARLES R. The Effect of Injection Angle on the Interaction Between Sonic Secondary Jets and a Supersonic Free Stream. NASA TN D-6669, 1972.

18. BEACH, H. LEE, JR. Supersonic Mixing and Combustion of a Hydrogen Jet in a Coaxial High-Temperature Test Gas. AIAA Paper No. 72-1179, November-December 1972.

19. ANDERSON, GRIFFIN Y., and GOODERUM, PAUL B. Exploratory Tests of Two Strut Fuel Injectors for Supersonic Combustion. NASA TN D-7581.

20. EGGERS, JAMES M. Turbulent Mixing of Coaxial Compressible Hydrogen-Air Jet. NASA TN D-6487, 1971.

21. ROGERS, R. CLAYTON, and EGGERS, JAMES M. Supersonic Combustion of Hydrogen Injected Perpendicular to a Ducted Vitiated Airstream. Paper presented at the AIAA/SAE Ninth Propulsion Conference (Las Vegas, Nevada), November 1973.

TABLE 1. COMBUSTOR GEOMETRIES FOR ONE-DIMENSIONAL ANALYSIS OF ENGINE CONFIGURATIONS

Strut Design		Axisymmetric Design	
x/H	A/A_{cowl}	x/H	A/A_{cowl}
0	0.14	0	$1/(6 + M_o)$
0	.17	.37	$1/(6 + M_o)$
.3	.35	.70	0.68
1.9	.60	1.05	.68
		1.36	.64
x_ℓ/H	1.88		0.6
x_ℓ/G	48		36
A_{wall}/A_{cowl}	8.1		11.6

H ≡ inlet cowl height (or diameter)

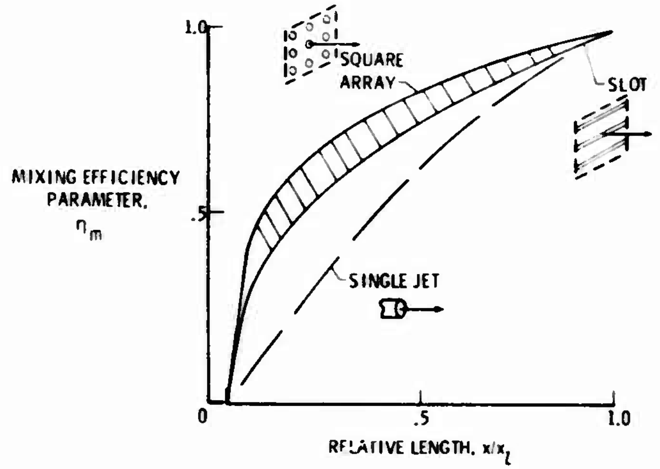

Figure 1. Mixing efficiency distribution for parallel injection.

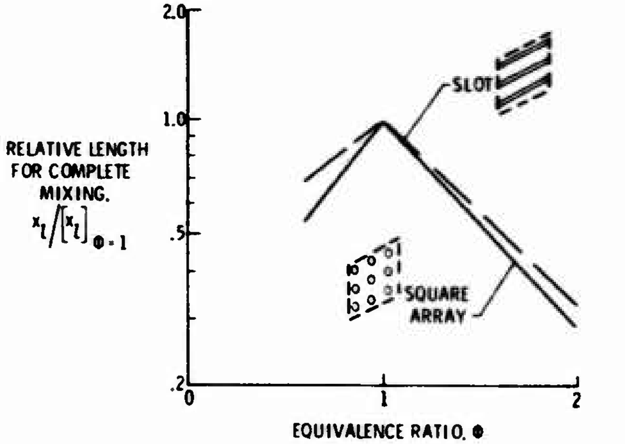

Figure 2. Effect of equivalence ratio on length for complete mixing with parallel injection.

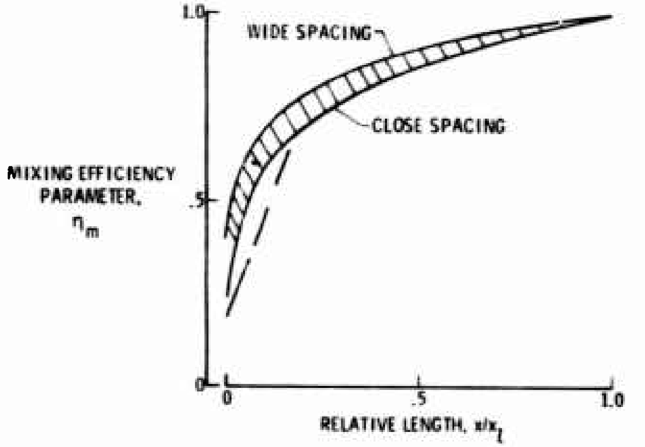

Figure 3. Mixing efficiency distribution with perpendicular injection.

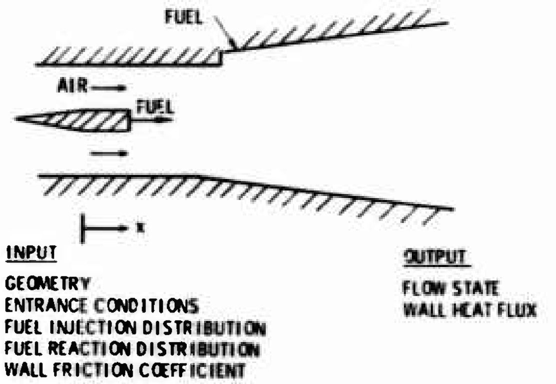
FUEL
AIR
FUEL
x
INPUT
GEOMETRY
ENTRANCE CONDITIONS
FUEL INJECTION DISTRIBUTION
FUEL REACTION DISTRIBUTION
WALL FRICTION COEFFICIENT
OUTPUT
FLOW STATE
WALL HEAT FLUX

Figure 4. Schematic of flow model for one-dimensional analysis.

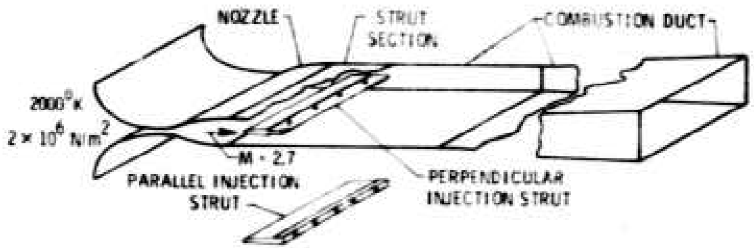
NOZZLE
STRUT SECTION
COMBUSTION DUCT
2000°K
2 × 10⁶ N/m²
M = 2.7
PARALLEL INJECTION STRUT
PERPENDICULAR INJECTION STRUT

Figure 5. Schematic of supersonic combustion apparatus with strut fuel injectors.

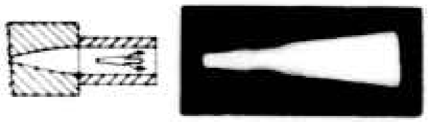

(a) SIDE VIEW

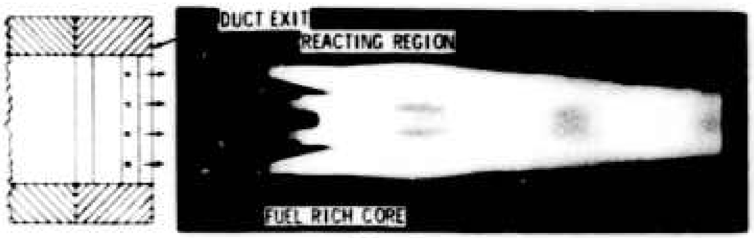
DUCT EXIT
REACTING REGION
FUEL RICH CORE

(b) TOP VIEW

Figure 7. Flame photograph - perpendicular injection strut.

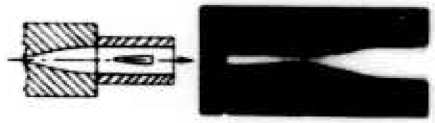

(a) SIDE VIEW

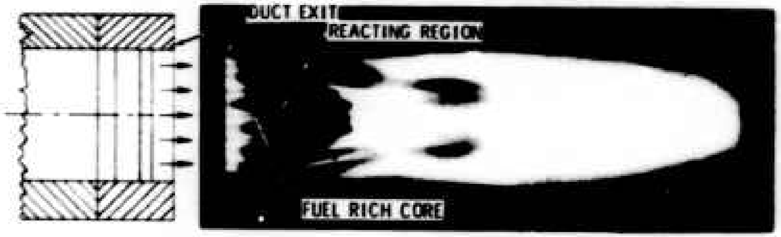
DUCT EXIT
REACTING REGION
FUEL RICH CORE

(b) TOP VIEW

Figure 6. Flame photograph - parallel injection strut.

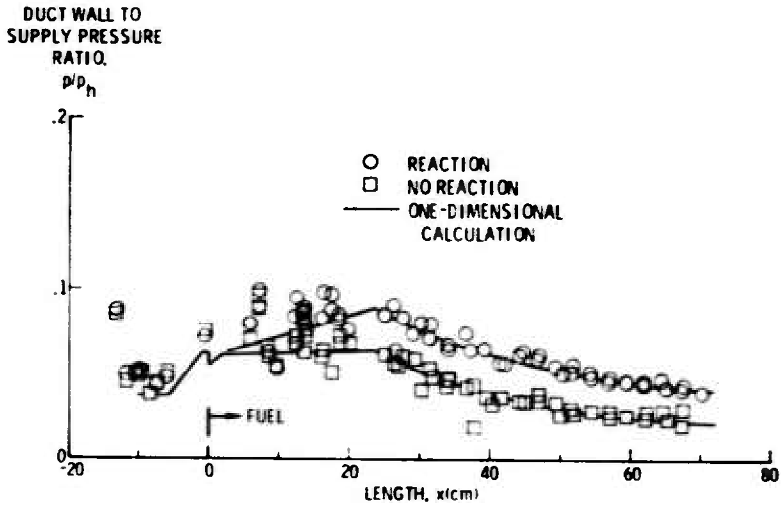

Figure 8. Duct wall pressure with the parallel injection strut (equivalence ratio = 0.6).

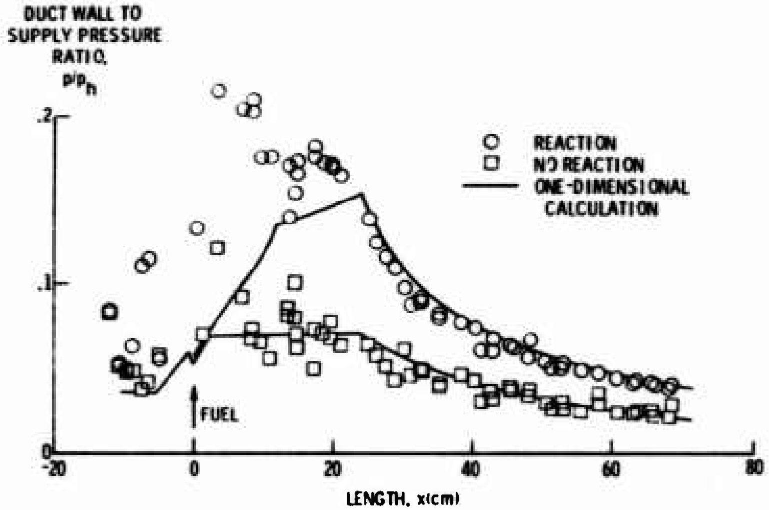

Figure 9. Duct wall pressure with the perpendicular injection strut (equivalence ratio = 0.6).

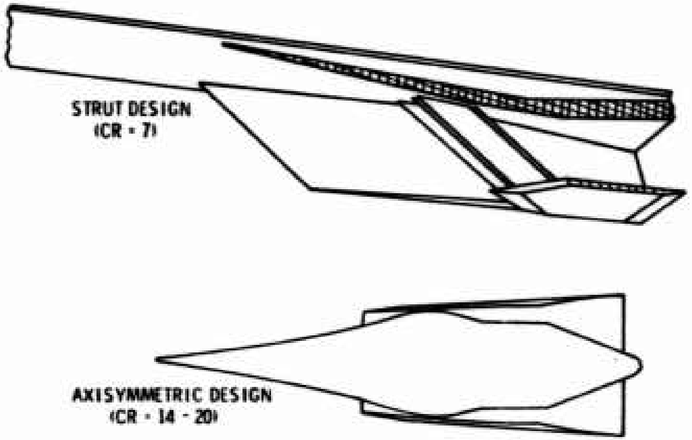
STRUT DESIGN (CR = 7)
AXISYMMETRIC DESIGN (CR = 14 - 20)

Figure 11. Scramjet engine configurations.

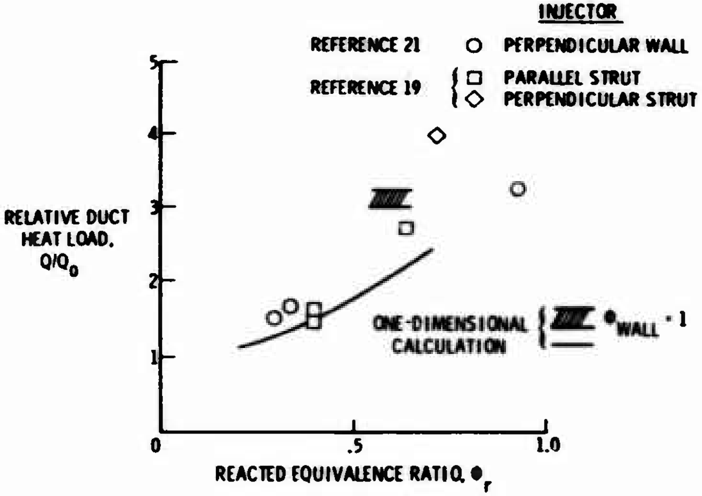

Figure 10. Combustion duct heat load.

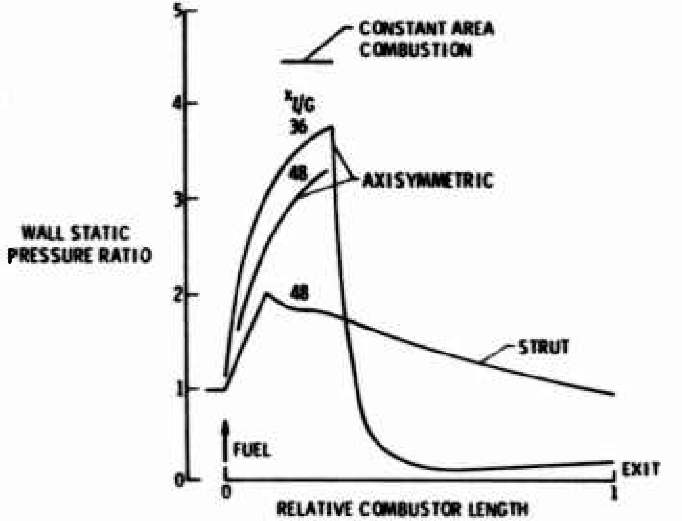

Figure 12. Combustor wall pressure distributions for Mach 10 flight with stoichiometric combustion.

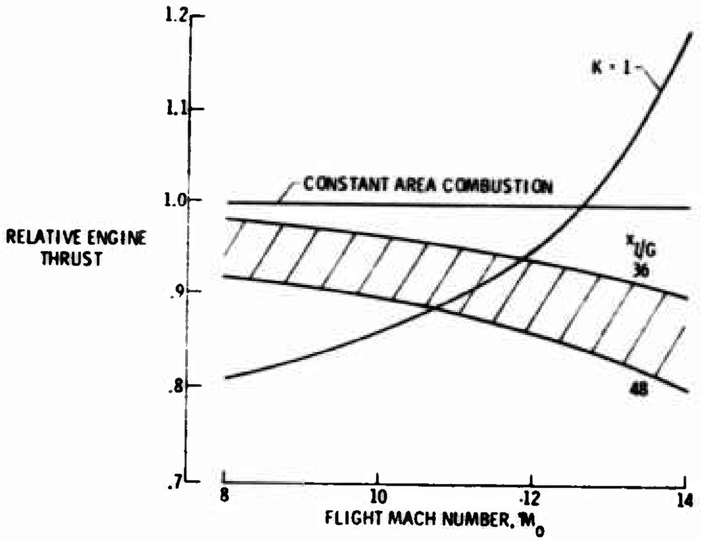

Figure 13. Relative engine thrust for axisymmetric design (stoichiometric combustion and nozzle expansion in chemical equilibrium).

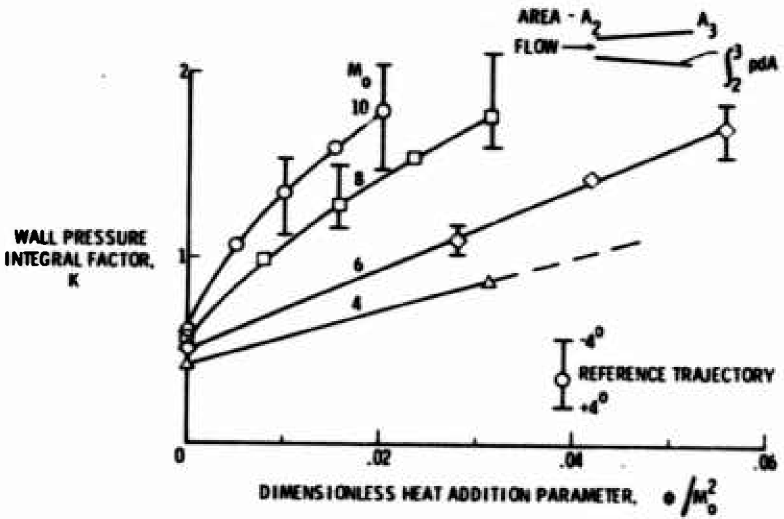

Figure 14. Correlation of wall pressure integral factor for strut design.

$$K \equiv \left[\int_2^3 pdA\right] \Big/ \left[\frac{1}{2}(p_3 + p_2)(A_3 - A_2)\right]$$

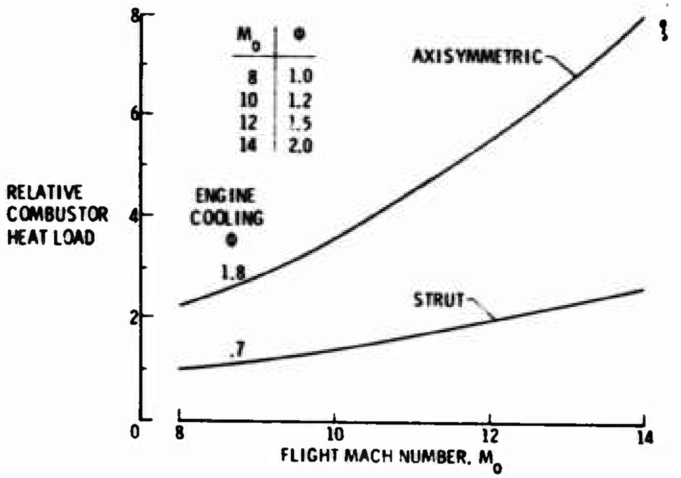

Figure 15. Relative combustor heat load.

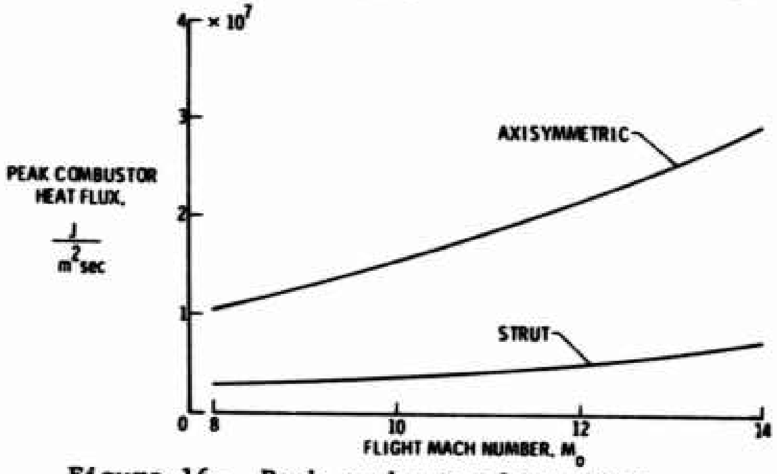

Figure 16. Peak combustor heat flux (flight dynamic pressure = 10^5 N/m^2).

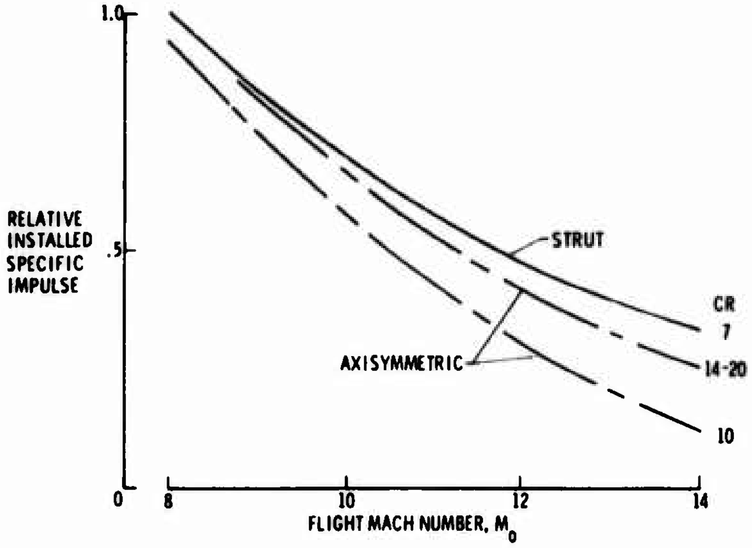

Figure 17. Relative installed specific impulse.

SOME PROBLEMS CONCERNING OPTIMAL DUCTED ROCKET ENGINE WITH SECONDARY BURNING

V.A.Sosounov

Utilization of atmosphere air as an oxidizer in space-vehicle engines significantly increases their economy as compared with pure rocket systems. Russian scientist, one of the pioneers of the rocket techniques F.A.Tsander [1] , more than once turned to this idea.

Considerable increase in specific impulse is achieved when using a ducted rocket engine (DR), where the rocket engine functions as the generator of fuel-rich combustion products, exhausting under pressure into ramjet chamber.

Processes of mixing (ejection) and combustion in the ducted rocket engine may be divided or they may occur simultaneously in the single after/burning chamber [2] . This paper concerns the engines with combined processes of mixing and combustion (Fig.1). The specific impulse of the engines of this group may be considerably higher than that of the rocket engines, reaching 10 000-12 000 N. s/kg when using conventional hydrocarbon fuels [3] .

As well as in the rocket engines solid, liquid and hybrid propellants can be used in the ducted rocket engines [3] . Use of liquid propellant allows to optimal inflight control of air-fuel ratio and also the propellant composition that is the fuel-oxidizer ratio. The solid propellant provides less opportunities of controlling. In such a case it is possible to program a desirable changing in fuel flow rate and propellant composition during flight time by choice of the solid-propellant charge construction.

The DR can include variable-geometry units (an air intake, a jet nozzle, gas generator nozzles) or it may be of more simple design with uncontrolled elements of the air-gas tract [2].

In general the DR efficiency is defined by two main factors: the ejection air-pumping effect of the rocket propellant and heat release at primary and secondary fuel burning. The both factors depend, first of all, on the propellant composition. At the high relative oxidizer flow rate corresponding to the high specific impulse of the gas generator I_g, the stoichiometric coefficient by air L_0 and the full heat capacity of fuel H_u (reburned in air) have the minimal values. In this case at the reduced specific impulse the frontal thrust of the DR will be the largest. With decreasing the oxidizer flow rate in the gas generator fuel parameters H_u and L_0 increase and the specific impulse of the DR becomes higher, but the frontal thrust goes down because of degradating ejection action of the propellant (I_g reduces) and decreasing the maximal heating temperature of the air.

At the given fuel-in-air burning efficiency η_b the frontal thrust R_f and the specific impulse of the DR are defined by the following factors:

1) - flight conditions (P_∞ , T_∞ , M_∞);
2) - an air intake characteristics;
3) - the propellant composition (H_u, L_0, I_g);
4) - air/ fuel equivalent ratio ($\alpha = m_a / (L_0 m_g)$)
5) - relative nozzle areas (f_g^* , f_g / f_g^* , f_e^* , f_e / f_e^*).

The analysis of parameters and characteristics of the ducted rocket engine at η_b = const offers no difficulty and it is studied theoretically rather well [2] [6] .

In particular, in such a way on the base of minimum quantity of experimental data on the hydraulic resistance of the DR combustor the influence of the ejection effect can be evaluated under different operating conditions. Specifically, one may show that the low efficiency of the ejection air-pumping decreases the effectiveness of DR using immediately from the start. In the range of flight speeds corresponding to M=0-1 the specific impulse of the ducted rocket is lower as compared with the pure rocket , especially when taking into consideration the real losses of the total pressure in the uncontrolled inlet.

In the case when the DR is used as the main engine at $M > 1{,}5 - 2$, where the ducted rocket is the most effective, and at the starting phase from M=0 to M=1,5-2 the acceleration is accomplished by the special rocket booster, the ignition of the ducted rocket from start is expedient. By this the additional resistance that would arise at the air flowing through the inoperative ducted rocket is eliminated and at the same time the total efficiency of the power plant is increased.

The organic feature of the ducted rocket as compared, f.e., with the conventional ramjet is a strong dependence of the fuel burning efficiency in the air-combustion chamber on the conditions of fuel and air flowing in it, on its geometry. As a result the value of η_b is the function almost of all the above parameters defining the thrust and the specific impulse of the engine and moreover it depends upon the relative length of the combustion chamber and the number of the gas generator nozzles. This specific feature, that is usually put out of account in the general theory of the ducted rockets [2] [6] , may strongly affect the selection of the scheme, propellant, engine parameters and its characteristic behaviour.

In comparison with the rocked engines the DR's have a somewhat heavier construction and the advantage of their installating is possible only when the economy of the fuel mass overlaps the increase in the construction mass. The large share of the DR mass falls on the air combustion chamber. The chamber length increasing, the secondary fuel burning efficiency becomes higher, the required propellant reserve becomes lower but the construction gets heavier. Thus, one of the most principal problems in DR designing is the choice of the optimal length of the chamber at which the total mass of the propellant and the engine construction will be the least.

In view of a great number of parameters which can be chosed or controlled the problems of finding the optimal DR tract dimensions and the operating modes become of great importance. This paper on the example of the most simple scheme of the DR with uncontrolled geometry, of the intake and the nozzle deals with some problems and trends of such an optimization with taking into consideration the efficiency of the secondary fuel burning in the air combustion chamber.

The products of the primary burning of various propellants in the DR gas generators may consist of combustible and incombustible gaseous components (f.e., H_2, CO, CO_2, CH_4, etc.), and also they may include condensed combustible and incombustible particles (soot, metals, oxides and others). Solid particles form certainly during the primary burning of solid fuels in the DR generator, which are characterized by a comparatively low oxidizer content (f.e., ammonium perchlorate - 30-50%, organic binder - 10-15% and a high metal content (aluminium, magnesium, boron and etc.) up to 40-60% [3] .

If one does not study the case when in the products of primary burning are present slowly burning particles (f.e., boron, aluminium, etc) [7] , then the process of secondary burning, in general, will be limited by turbulent diffusion mixing of a fuel jet with air [6] . This is indirectly evidenced, f.e., by the proportionality of the visible flame length to the nozzle diameter as observed during out - of - engine experimental investigations of the gas generator having two nozzles of different diameters (fig.2). That is why in some cases the model of a quasi-gaseous diffusion flame propagating in the turbulent jet of products of the fuel primary burning (in general, two-phase) may be assumed as a basis of the fuel secondary burning analysis in the DR air duct.

The said method of the analysis results in two conclusions:

1. Process modelling in the DR is available by means of geometrical similarity conservation of the air duct.
2. Direct comparison of the process efficiency in one- and multi-nozzle engines is possible providing the equality of their combustion chamber equivalent lengths and relative areas of the nozzles in their air-gas tract (fig.2).

By the chamber equivalent length one assumes the relative chamber length of the multi-nozzle DR expressed through the calibres of the one-nozzle engine that is equivalent to the multi-nozzle one:

$$\bar{L}_{eq} = \frac{L_b}{D_{eq}} = \frac{L_b}{D_b}\sqrt{\frac{N}{1-\bar{d}^2}} \quad , \qquad (1)$$

where N - is the number of nozzles of the gas generator; $\bar{d} = d/D_b$.

By means of designing a multi-nozzle gas generator (at the cost of complication of its construction and, apparently, of some mass penalty) there opens an opportunity to significantly reduce the length and to lighten the combustion chambers of the DR without decreasing fuel burning efficiency. The chamber equivalent length at the given engine air flow is reduced in inverse proportion to the square root of the number of nozzles. The possibility of reducing the chamber length of the DR by means of increasing the number of the gas generator nozzles was more than once discussed in literature [6] . The experimental data shown in fig.2 confirm the practical identity of the burning processes in one- and multi-nozzle models at $\bar{L}_{eq}$ = idem.

The air chamber length required for complete fuel burning is defined by the length of the diffusion flame formed in the jet of the fuel primary burning products which depends on the fuel type, the engine operating mode, the relation of diameters of the chamber, the jet nozzle and the gas generator nozzle. The intensity of mixing the unburning gaseous turbulent jet with the open air stream is determined by the values of speed and density ratios: V_a/V_g, ρ_a/ρ_g [5] . The length of the open flame L_f will be further dependent on the stoichiometric coefficient of the fuel by air which defines the relative amount of air that must diffuse towards the jet axis at the end of the flame [4] :

$$\bar{L}_f = f(V_a/V_g \, , \rho_a \, , \rho_g \, , L_0). \qquad (2)$$

The space limitation of the DR combustor, in its turn, affects the diffusion flame. This effect, in general, is due to the presence of the longitudinal pressure gradient in the chamber and the fixed air flow rate in it.

It is appropriate for the analysis to choose three typical operating mode ranges of the ducted rocket engine: $\alpha < 1$, $1 < \alpha < \tilde{\alpha}_f$ and $\alpha > \tilde{\alpha}_f$, where $\tilde{\alpha}_f$ - is the mean air/fuel equivalent ratio in the turbulent jet at the end of the flame (fig.3). Assuming here the concentration distribution as in the usual turbulent jet one obtains $\tilde{\alpha}_f = 2,5+1,5/L_o$. When $L_o > 1,5$ the value $\tilde{\alpha}_f$ is within narrow limits: from 3,5 to 2,5. At $\alpha < 1$ the flame front is confined to the chamber walls, and at $\alpha > 1$ it lies in its axis (by the flame front in a jet the line $\alpha = 1$ is conventionally assumed). At $\alpha < \tilde{\alpha}_f$ the external boundaries of the turbulent jet of the burning fuel reach the chamber walls prior to the flame burning completion on the jet axis.

The fixed airflow rate in the DR chamber leads to the notable flame extension at low air/fuel equivalent ratios, namely when $\alpha < \tilde{\alpha}_f$. On the theory at $\alpha \rightarrow 1$ the flame length goes into infinity because all the air is to be mixed with the fuel.

At $\alpha > \tilde{\alpha}_f$ the space limitation of the DR chamber has a rather slight influence on the diffusion flame length. In this region of the engine operating modes the flame length $\bar{L}_f$ practically remains unchangeable(by α).

The most frequently used regimes of the ducted rocket engine operation correspond to $\alpha < \tilde{\alpha}_f$ (including $\alpha < 1$).

The feature of the diffusion burning process in the DR combuster is the mutual relation between the flow parameters in the inlet and exit sections of the chamber, as the jet nozzle and the gas generator nozzle operate in the "choking" regime. In this connection the fuel mixing conditions and the flame length are fully defined by the engine operating mode (air/fuel equivalent ratio α and the air intake stagnation temperature T_{si}), the fuel type (L_o, I_g^*), nozzle throat areas (f_e^* and f_g^*):

$$\bar{L}_f = L_f / D_{eq} = f(\alpha, T_{si}, L_o, J_g^*, f_e^*, f_g^*). \qquad (3)$$

The qualitative nature of the effect of these parameters on the flame length, found in evaluating by the semiempirical theory for the group of similar fuels is shown on the right graph in fig.4. The air/fuel equivalent ratio influence on the flame length in the regions $\alpha > 1$ and < 1 is qualitatively contrary. Increase of α in the region $\alpha < 1$

results in incrementing of $\bar{L}_f$, and in the region of $\tilde{\alpha}_f > \alpha > 1$ it results in decreasing the flame length. The value $\bar{L}_f$ is lower in the event of greater differences in speed and density of the air and fuel flows in the chamber, because in this case the conditions of flow mixing become more favourable [5] . This fact, in general, explains the influence of such parameters as T_{si}, I_g^*, f_e^* , f_g^* . The noticeable increase in the flame length is evident at the air temperature rising T_{si} (that is, when the flight Mach number becomes higher). This feature may be illustrated with the experimental data on gas burning in unmoved air of different temperatures shown on the left graph in fig.4 [4].

The efficiency of fuel reburning in the air chamber of the DR will depend on the relation of the real chamber length and the diffusion flame length in the fuel jet that is typical for the given parameters of the engine and fuel. The total efficiency of the propellant burning in the engine can be obtained through the ratio of real heat release to the maximum possible one at combustion of one mass unit (kg.) of fuel Q_{max} which in the case of $\alpha \geq 1$ is equal to its full heat capacity H_u, and in the case of $\alpha < 1$ it is approximately defined by the equation

$$Q_{max} \approx (H_u - Q_g)\alpha + Q_g \quad , \qquad (4)$$

where Q_g - heat released at combustion of one kilogram of propellant in the gas generator.
When $\alpha < 1$ the value Q_{max} decreases as compared with H_u due to the lack of air required for complete fuel combustion. In the course of the experiment the real heat release in the combustion chamber and the value η_b are indirectly determined by the flow impulse in the jet nozzle (that is, by the stand-thrust of the engine). Therefore the experimental data on the fuel burning efficiency include not only the losses due to fuel unburning but also the losses related to the nozzle flow irregularity, nonequilibrium flow of the condensed and gaseous phases, heat leakage in the walls and etc.

It is in order to introduce the concept of the fuel reburning efficiency in the air combustion chamber, which is approximately (providing the absolute efficiency of burning in the gas generator) is expressed through the total burning efficiency:

$$\eta_{rb} = \frac{\eta_b - \bar{Q}_g}{1 - \bar{Q}_g}, \quad \left(\bar{Q}_g = \frac{Q_g}{Q_{max}} \right) . \qquad (5)$$

The analysis of the reburning efficiency seems to be more appropriate as the value η_{rb} for all the fuels in principle may change within the same limits (from 0 to 1). But the value of the total fuel burning efficiency η_b changes within the limits from $\bar{Q}_g$ to 1, while $\bar{Q}_g$ depending on the fuel type.

One may presume that there exists the universal relation of the similar fuel reburning efficiency with the length of the ducted rocket air combustion chamber in the following form:

$$\eta_{rb} = f\,(\bar{L}_{eq} / \bar{L}_f) \ ,$$

where η_{rb} - experimental data on the effective reburning efficiency obtained for different equivalent lengths of the combustion chamber L_{eq} at different operating modes; $\bar{L}_f$ - the flame length (relative to the equivalent diameter of the combustion chamber), that was estimated by the equation (3) for the given experimental conditions.

It is possible to introduce the concept of the corrected length of the ducted rocket engine combustion chamber

$$\bar{L}^o_{eq} = L_{eq} \, (\bar{L}^o_f / \bar{L}_f) \ , \qquad (6)$$

where $\bar{L}^o_f$ - estimated flame length for "standard" conditions ($\tilde{\alpha}_f$, T^o_{si}) in a "standard" engine (f^{*o}_e , f^{*o}_g) with a "standard" fuel (L^o_0 , J^{*o}_g). Then $\eta_{rb} = f\,(\bar{L}^o_{eq})$ (7)

The value $\bar{L}^o_{eq}$ (6) and consequently η_{rb} rise both with increasing the equivalent length of the combustion chamber (1) and with decreasing the flame length (3). Thus, the experimental relation (7) allows to integrate in one analysis geometric parameters of the combustion chamber and nozzles, typical parameters of fuel and operating modes of the DR.

The results of the flame length estimation show that for a characteristic region of changing parameters and flight conditions of the ducted rocket engine the functional dependence (3) may be expressed through an approximate relation in the appropriate form for subsequent use in equations (6) and (7):

$$\frac{\bar{L}_f^{\circ}}{\bar{L}_f} \approx \left(\frac{\tilde{\alpha}_f}{\alpha^{\nu}}\right)^{\beta} \left(\frac{T_{si}^{\circ}}{T_{si}}\right)^{\gamma} \left(\frac{L_o^{\circ}}{L_o}\right)^{\delta} \left(\frac{J_g^{*\circ}}{J_g^{*}}\right)^{\varepsilon} \left(\frac{f_e^{*\circ}}{f_e^{*}}\right)^{\varkappa} \left(\frac{f_g^{*\circ}}{f_g^{*}}\right)^{\lambda} , \qquad (8)$$

where $\nu = 1$ when $\alpha > 1$ and $\nu = -1$ when $\alpha < 1$.

Experimental investigations carried out with considerable variation of fundamental parameters ($\alpha, T_{si}, L_o, J_g, f_e^{*}, f_g^{*}, f_g / f_g^{*}, L_b / D_b, N = var$), confirmed the availability of such generalized correlation (7) (fig.5). On the one hand, it indicates the validity of the theoretical flame model (8), and on the other hand, it allows to use it for estimation of the burning efficiency of the given fuel with accounting of flight conditions, chosen air-fuel ratio, geometry of the combustion chamber. With this analysis it is sufficient to evaluate the relative flame length change during the flight by the relation of the type (8) and to determine the change of the corrected chamber length through the expression (6).

The change of the total fuel burning efficiency in the DR depending on its operating mode and the flight speed representative for pure diffusion burning is shown on the right graph of fig.6. The characteristic dropping in the burning efficiency with flight speed increasing (growing in T_{si}) is explained, as it was said above, by the unfavourable effect of growing relative velocity of air entering the chamber and decreasing its density on the process of fuel-air mixing.

The level of the fuel burning efficiency may be improved by means of increasing the equivalent length of the combustion chamber. According to equation (1) it may be achieved by increasing the number of the gas generator nozzles N with their quite uniform distribution over the chamber section .

The increment of the number of the gas generator nozzles of the DR is limited by reasonable engineering considerations. If the number of the gas generator nozzle in a particular ducted rocket engine has been chosen then there is the possibility of optimization of the in-flight engine operating modes by choise of corresponding geometry of the combustion chamber (in particular the length) in order to obtain the minimum total weight of the fuel and the construction.

The characteristic dependences of the optimal calculated values of the air/fuel equivalent ratio α_{opt} on the flight Mach number of the fixed-gepmetry DR-boosters determined under the condition of the maximum increase of the rocket speed per mass unit of the consumped fuel at each point of the traectory are shown on the left graph of fig.6. The evaluation was carried out for two engines, the combustion chamber equivalent lengths of which differ as much as four times at M=idem. The change of the fuel burning efficiency and the specific impulse of these engines is also shown on the graph. The current values of the burning efficiency have been estimated through the above method with using the generalized experimental dependence (fig.5).

The effective specific impulse (with taking into account the air intake drag) has a characteristic maximum near by Mach number ~ 3 (see also [2]). At the beginning of acceleration at $M = 2 \div 2{,}5$ when the maximally available frontal thrust is required the values α_{opt} of the engine with fixed geometry decrease with the speed growing so that the maximally possible the intake total pressure recovery coefficient should be kept. The decrease in the fuel burning efficiency at near by unity $\alpha \doteq$ values, especially at the elevated temperature air stagnation T_{si} results that the values of α_{opt} at a certain flight speed begin to increase. At the sufficiently high flight speed and altitude ($M > 4 \div 5$) for receiving the required thrust excess it is necessary to transit into the operation mode region of $\alpha < 1$.

The described behaviour of the optimal DR operating mode with the flight speed occurs most strong at the low equivalent length of the combustion chamber at which the fuel burning efficiency proves to be far less and the influence of unfavourable factors ($\alpha = 1$, high T_{si}) grows (the left part of the generalized dependence, fig.5).

It is evident that due to the contrary effect of the relative chamber length on the burning process efficiency and on the construction weight for any required rocket speed increase by means of the suggested method it is possible to choose a certain optimal chamber length at which the total weight of the fuel and the construction would be minimal.

REFERENCES

I. Цандер Ф.А. Сравнение расхода топлива для случая, когда кислород берется из атмосферы и для случая, когда он запасен в ракете. /1925г/. - В кн.:"Проблема полета при помощи реактивных аппаратов". М, Оборонгиз, 1961, 261-266pp.

2. Зуев В.С., Макарон В.С. Теория прямоточных и ракетно-прямоточных двигателей. М., Машиностроение, 1971, 368p.

3. Алемасов В.Е., Дрегалин А.Ф., Тишин А.П. Теория ракетных двигателей. М., Машиностроение, 1969.

4. Аннушкин Ю.М., Сосунов В.А. Длина турбулентного газового пламени в неподвижном воздухе различной температуры. _ "Физика горения и взрыва", 1970, т.5, № 4, 495-503 pp.

5. Abramovich G.N., Yakovlevsky O.V., Smirnova I.P., Sekundov A.N., Krashennikov S.Y. An investigation of the Turbulent Jets of Different Gases in a General Stream. Astronaut. acta, 14, 1969, pp. 229-240.

6. High-Speed Aerodynamics and Jet Propulsion, vol.XII. Jet Propulsion Engines. Princeton Univ. Press, 1959.

7. Schadow K. Experimental Investigation of Boron Combustion in Air-Augmented Rockets.- AIAA Journal, vol.7 No.10, 1969, pp. 1870-1876.

Symbols

D, d - diameter,

F - area,

$f = F/F_b$ - relative area,

H_u - full heat capacity of fuel,

J - specific impulse of engine,

$J_g = V_g + RT_g/V_g$ - specific impulse of gas generator,

L - length,

L_0 - stoichiometric coefficient by air,

M - Mach number,

m - mass flow,

N - number of gas generator nozzles,

P - pressure,

Q_g - heat released in gas generator,

R - gas constant,

T - temperature,

V - speed,

$\alpha = m_a/(m_g \cdot L_0)$ - air/fuel equivalent ratio,

η_b - fuel burning efficiency,

η_{rb} - fuel reburning efficiency,

ρ - density.

Indices

a - air,

b - combustion chamber,

e - engine exit nozzle

f - flame end section,

g - gas generator nozzle,

i - inlet air parameters,

s - stagnation parameters,

* - nozzles throat,

0 - normal, corrected values.

Ducted Rocket with Secondary Burning

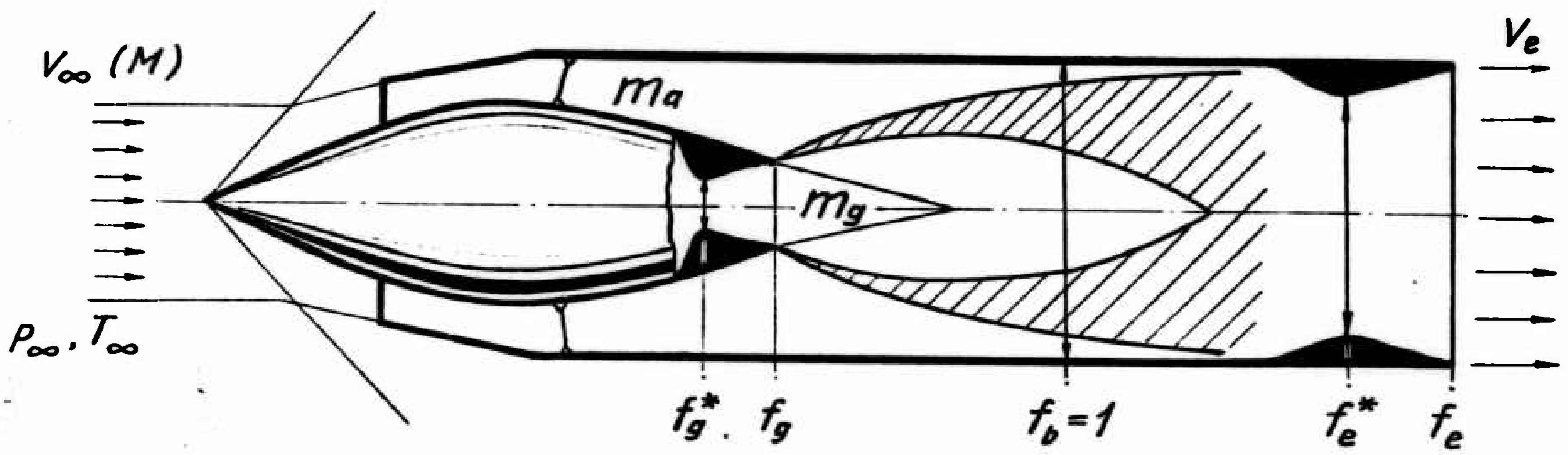
V_∞ (M)
p_∞, T_∞
m_a
m_g
V_e
f_g^*. f_g
$f_b=1$
f_e^*
f_e

Specific impulse – J = thrust / fuel mass flow

Specific impulse of gasgenerator – $J_g = V_g + RT_g / V_g$

Full heat capacity of fuel – H_u

Heat of primary burning – Q_g

Stoichiometric coefficient by air – L_o

Air/fuel equivalent ratio – $\alpha = m_a / (m_g \cdot L_o)$

Fig. 1

Reburning Process Scheme

Diffusion Flames

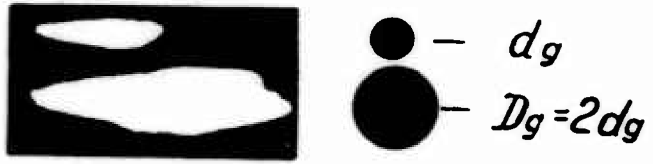

Reburning Efficiency

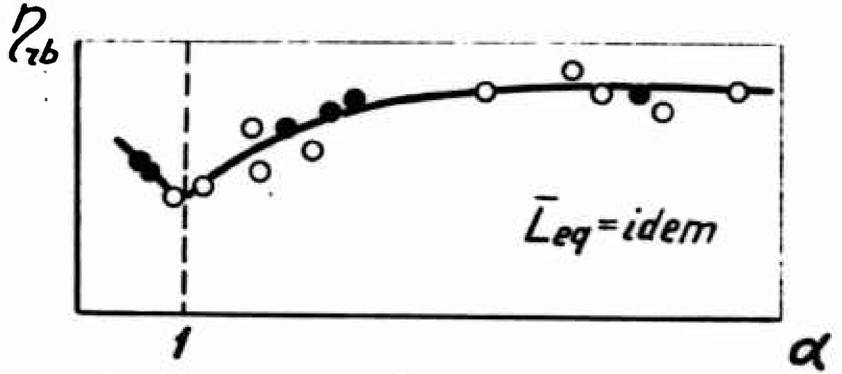

○ – one-nozzle model

● – multi-nozzle model

Chamber Equivalent Length

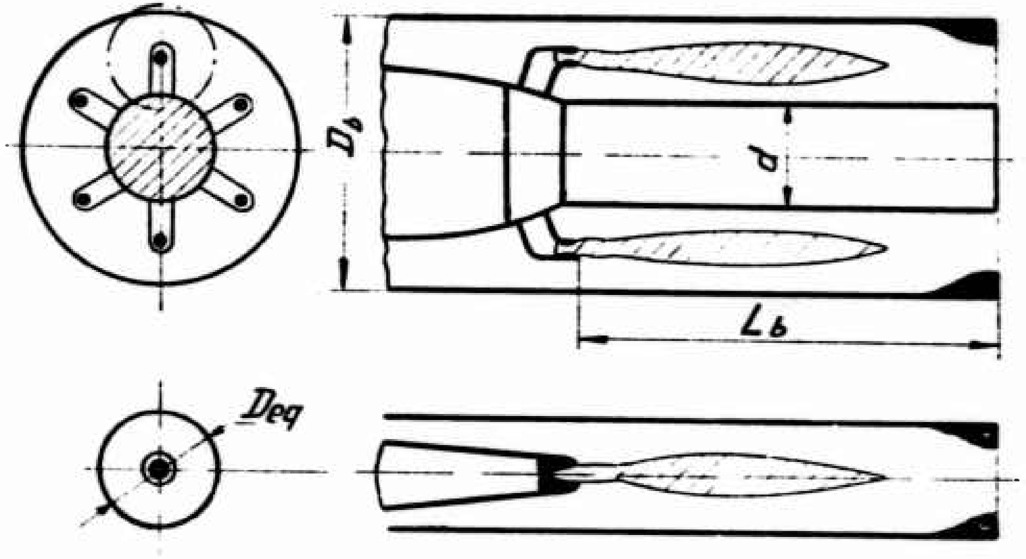

$$\bar{L}_{eq} = \frac{L_b}{D_{eq}} = \frac{L_b}{D_b}\sqrt{\frac{N}{1-\bar{d}^2}} \quad , \quad \bar{d} = \frac{d}{D_b}$$

Fig. 2

Flame Length in Ducted Rocket Chamber

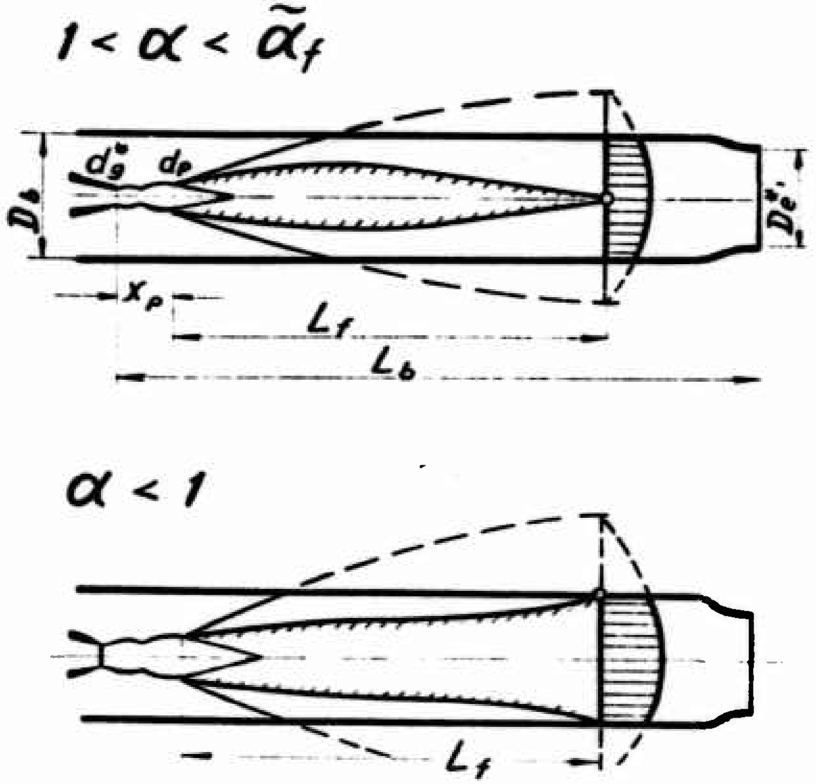

$1 < \alpha < \tilde{\alpha}_f$
d_g^*
d_p
D_b
D_e^*
x_p
L_f
L_b
$\alpha < 1$
L_f

Unlimited space

$\bar{L}_f = f\,(V_a/V_g,\ \rho_a,\ \rho_g,\ L_o)$

$\bar{L}_f \uparrow:\ V_a \longrightarrow V_g\ ,\ \rho_a \longrightarrow \rho_g\ ,\ L_o \uparrow$

Flame in duct

$\bar{L}_f = \frac{L_f}{D_{eq}} = f\,(\alpha, T_{si}, L_o, J_g^*, f_e^*, f_g^*)$

Mean air/fuel equivalent ratio

in jet at the end of flame

$\tilde{\alpha}_f \approx 2{,}5 + \frac{1{,}5}{L_o}\ ;\ \tilde{\alpha}_f = 3{,}5 \div 2{,}5\ ;\ L_o > 1{,}5$

Fig. 3

Diffusion Flame's Length

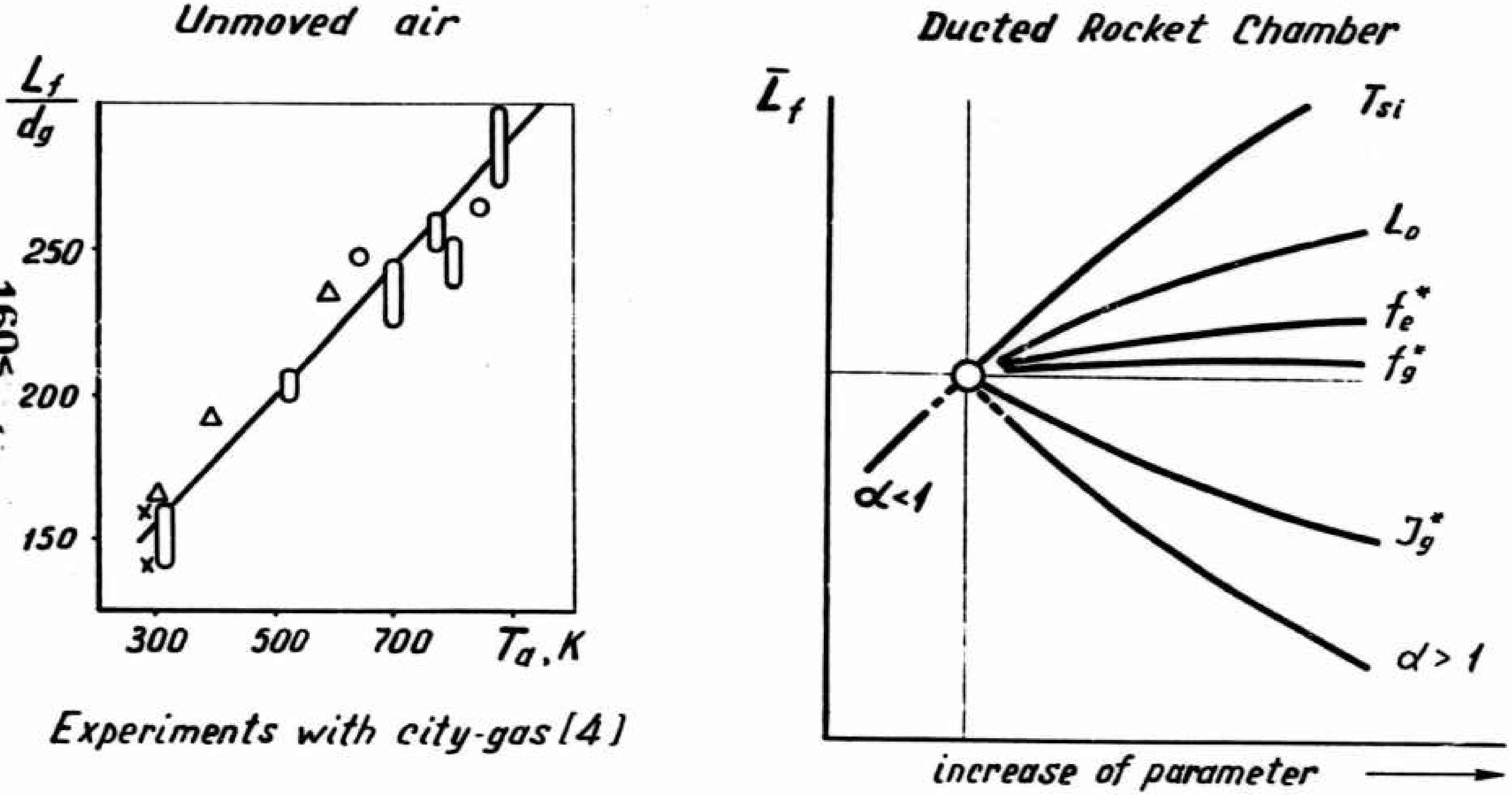

Fig. 4

Reburning Efficiency

Corrected length of chamber

$$\bar{L}^{o}_{eq} = \bar{L}_{eq}\,(\bar{L}^{o}_{f}/\bar{L}_{f})$$

$$\bar{L}^{o}_{eq}\uparrow : \bar{L}_{eq}\uparrow\,,\ \bar{L}^{o}_{f}\downarrow$$

161<

Approximation

$$\frac{\bar{L}^{o}_{f}}{\bar{L}_{f}} \approx \left(\frac{\tilde{\alpha}_{f}}{\alpha^{\nu}}\right)^{\beta}\left(\frac{T^{o}_{si}}{T_{si}}\right)^{\gamma}\left(\frac{L^{o}_{o}}{L_{o}}\right)^{\delta}\left(\frac{J^{*o}_{g}}{J^{*}_{g}}\right)^{\varepsilon}\left(\frac{f^{*o}_{e}}{f^{*}_{e}}\right)^{\varkappa}\left(\frac{f^{*o}_{g}}{f^{*}_{g}}\right)^{\lambda}$$

$\nu = 1$ by $\alpha > 1$; $\nu = -1$ by $\alpha < 1$

Generalized correlation

$\eta_{rb} = f(\bar{L}_{eq}/\bar{L}_{f})$ or

$\eta_{rb} = f(\bar{L}^{o}_{eq})$

Experimental data (models)

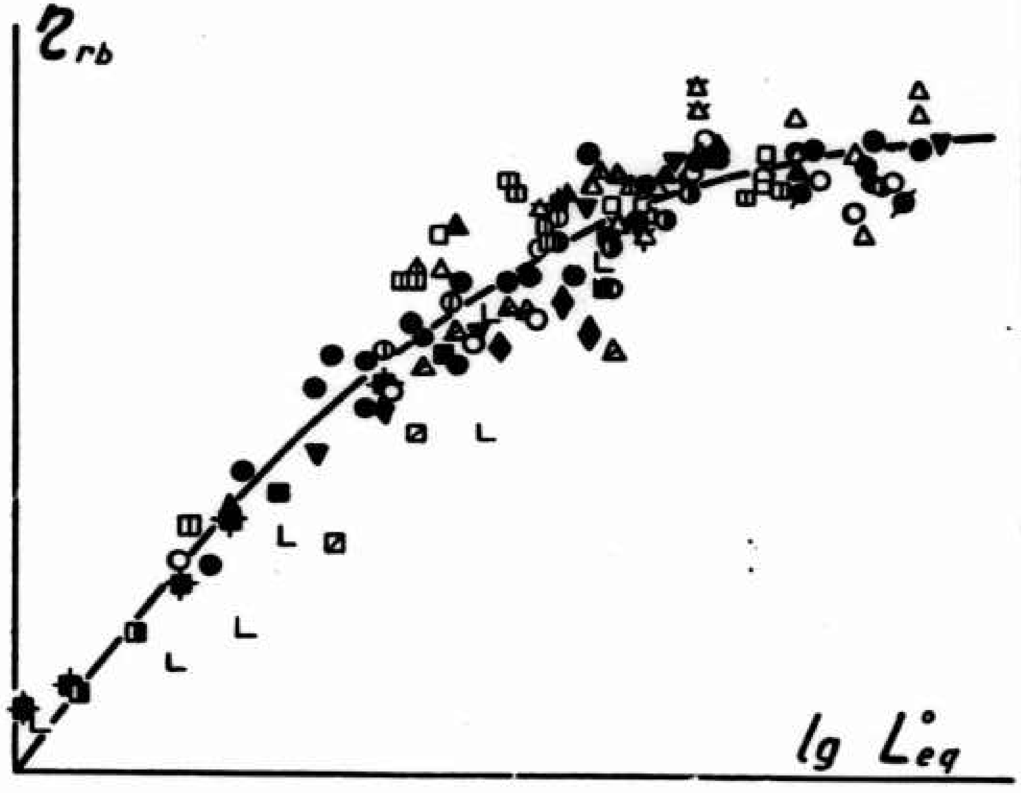

α, T_{si}, L_{o}, J^{*}_{g}, f^{*}_{e}, f^{*}_{g}, f_{g}/f^{*}_{g},
N, L_{b}/D_{b} = var.

Fig. 5

Ducted Rocket Optimization

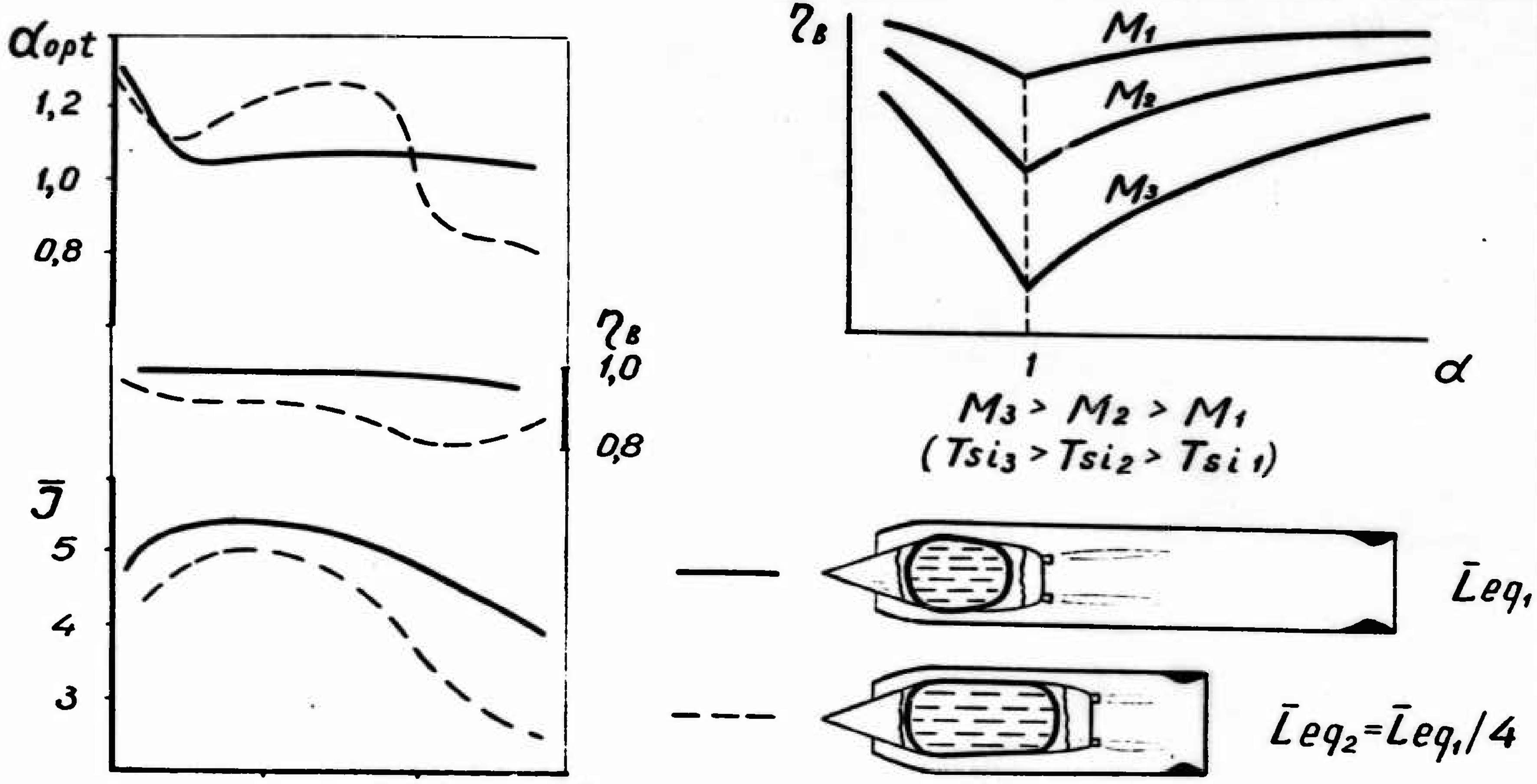

Fig. 6

RAMJET ENGINES: HIGHLIGHTS OF PAST ACHIEVEMENTS AND FUTURE PROMISE

Edward T. Curran
Frank D. Stull

Air Force Aero Propulsion Laboratory
Wright-Patterson Air Force Base, Ohio

INTRODUCTION

The aims of this paper are:

1. To review briefly the state-of-the-art of USAF ramjet engines and to survey ramjet engine hardware.

2. To illustrate the extensions to conventional ramjet technology that were achieved in the 1960's - but not necessarily flight tested.

3. To review high speed ramjet engine work and illustrate the potential of ramjet engines.

4. To review current ramjet technology efforts and their application to volume-limited systems.

FUNDAMENTAL TECHNOLOGY

Review of Flight Proven Ramjet Technology

A simple line diagram illustrating the ramjet operating cycle is shown in Fig. 1 and typical values of pressure and temperature at a given flight condition are shown. The gas flow through the engine is primarily along the centerline, and this type of engine, utilizing subsonic combustion, is usually referred to as a straight-flow-through or conventional ramjet engine.

During the 1950's and 1960's several countries developed ramjet engines and many significant advances were made in ramjet technology. An excellent review of ramjet progress prior to 1955 is given in an article by W. H. Avery, "Twenty-Five Years of Ramjet Development". This review, along with other significant papers in the ramjet field, can be found in ref. (1).

In the USA, two SAM systems were carried through to operational use, namely the Talos and Bomarc missiles. Ref. (2) gives the performance capability of Talos as a speed of Mach 2.5 and a slant range in excess of 65 miles, and that of the Super Bomarc MR CIM-10B as Mach 2.8 with a range of 440 miles and a maximum operational altitude of 100,000 ft.

The Bomarc is powered by two Marquardt RJ43-MA-7 engines. Development of this engine was carried out using the Lockheed X-7A test vehicle. This vehicle is illustrated in Fig. 2, and has flown at speeds in excess of Mach 4.0 using an advanced supersonic ramjet engine, the Marquardt RJ59. Regarding advanced engines, mention should also be made of the U.S. Navy engine, Typhon, which was a sequel to Talos. This engine was successfully flight tested and, together with the RJ59, is representative of some of the most advanced conventional supersonic ramjet engines developed to flight status in the USA.

Many other U.S. organizations participated in basic ramjet development. NACA, in addition to laying a sound technology foundation for ramjet components, also flew many ramjet test vehicles and a representative sample is shown in Fig. 3. Note the early use of a "roll-out" rocket booster in the ramjet combustor and the investigation of fuels other than simple hydrocarbons.

In Britain the conventional ramjet engine was developed for the SAM system "Bloodhound", which has proved to be an outstanding system and a successful export product. More recently another ramjet missile, the Sea Dart ship-to-air system, has appeared, which also utilizes a conventional ramjet.

In France a variety of conventional engines has been produced, including the Sirius series, the Vega, and the Stataltex. The Sirius II engine has found application in the twin engine Nord CT.41 target drone which operates in the region Mach 1.7 to 2.7. The Vega engine has a speed capability in excess of Mach 4.0, and the more advanced engine, the Stataltex (3), has flown to Mach 5. An advanced feature of this latter engine was the use of an ablative lined combustor and nozzle.

Summarizing, one can say that the conventional ramjet engine has been extensively flight proven to speeds up to Mach 5. In fact, well over 700 flights of conventional ramjet engines have been made in the USA in the last twenty years.

Typically, such engines have been axisymmetric, of fixed geometry, with spike type inlets, and the combustors have been predominately air-cooled. Most production engines have used simple hydrocarbon fuels although many advanced fuels have been demonstrated in flight. Corresponding fuel management systems were developed to yield reliable and consistent performance.

Although many vehicles were surface-launched, the X-7A program was predominately an air-launched program. Generally these engines were not called upon to operate over a wide range of speed and altitude - they were largely "cruise" engines. The main development problems of these engines were encountered in subsonic-diffuser/combustor compatibility, and in combustor durability. The former problem was often solved by the use of an aerodynamic grid located in the subsonic diffuser. The latter problem was primarily controlled by refined design of cooling air distribution systems. Air intake problems were minimized by installing the spike inlets at the nose of the vehicle and thus avoiding interactions with other missile components; angle of attack requirements were moderate.

In passing one should note that ramjet engines for subsonic flight were also successfully developed. These engines were simple, of light weight, and low cost; perhaps the most successful of these was the Marquardt MA-74 engine developed for the North American Redhead/Roadrunner target drone. Currently, the low cost and simplicity of subsonic flight engines make them eminently suitable for use in expendable vehicle systems.

Extensions to Flight Proven Technology

While the flight development of conventional engines was in progress, many schemes to improve the performance of fixed geometry engines were evaluated in ground test, and much supporting technology was generated.

Many of these developments were not carried into flight test because the demand for such technology did not materialize and, in the major switch from aeronautical research to space-oriented work, many promising developments were abandoned.

One of the most promising methods of improving engine performance is to employ variable geometry components and in particular variable geometry exhaust nozzles. Sting-mounted exhaust nozzles were tested by NACA and NGTE. Although these tests were successful, they were not carried into flight development. The NGTE air-cooled nozzle (4) provided wide area modulation and required only 4% of the main air flow for cooling when operated at stoichiometric conditions.

The related problem of variable intake geometry with its associated benefits of drag reduction and improved flow matching also received much attention. However, both variable geometry inlets and nozzles were not initially to find flight application in ramjets but in the development of supersonic turbojet systems.

A more fundamental and major problem for high speed engines was the high temperature durability of the combustor and exhaust nozzle. Combustor cooling by active and passive means was extensively investigated, although once again regenerative cooling technology was not carried into flight tests. High temperature exhaust nozzles were also investigated using refractory metals and alternative approaches such as film cooling have been tested.

Newer Concepts

During these active years of research, many new concepts for extending the performance and application of the basic ramjet engine were devised. These included:

1. The Hyperjet. This engine, devised by The Marquardt Corporation, used the translating inlet spike as a valve to shut off the air flow into the combustor at low speeds. The combustor was then operated in a rocket mode to give low speed thrust. Transition between rocket and ramjet operation was smooth and this engine system was successfully flight tested.

2. The Afterburning Ramjet. This system was investigated by Perchonok and Wilcox (5). The basic idea is to add a subsonic combustion afterburner behind the primary ramjet nozzle. The afterburner is operated to give a high boost thrust but is switched off during cruise when the engine operates solely on the primary combustor. The primary nozzle contraction ratio is chosen to yield good intake performance at cruise conditions.

3. The Ejector Ramjet (ERJ). The ejector ramjet concept is similar to the ducted rocket system. Static thrust is developed by ejecting either vaporized fuel or oxidizer through small rocket-type chambers into the main combustion system where the injectant is finally burned. Thus a low speed thrust capability is created at some penalty in propellant consumption. A more sophisticated version of the engine is the supercharged ejector ramjet (SERJ) in which a fan stage is used to increase the engine operating pressure ratio (6).

4. The Solid Fuel Ramjet (SFRJ). A relatively simple engine can be devised by utilizing solid fuel. Various fuel grain arrangements

are possible, and a boost fuel grain may be incorporated with the sustainer grain to yield an easily-handled propulsion system. Extensive flight testing of such engines has moreover been carried out and such systems in various forms are candidates for missile application. Since the fuel generation rate is primarily a function of the air mass flow rate through the engine, careful matching of the grain burn rate to the desired flight mission profile is necessary.

5. The Supersonic Combustion Ramjet (Scramjet). In the supersonic combustion ramjet the incoming air is not diffused to subsonic speeds, the flow remaining essentially supersonic through the engine. Thus intake losses are reduced but combustion losses are increased. The engine operates at much lower static pressure and temperature conditions compared to a conventional engine. Generally the scramjet is superior to the conventional engine at speeds in excess of about Mach 6.

RECENTLY ACQUIRED AND CURRENT TECHNOLOGY PROGRAMS

High Speed Propulsion

The advent of Sputnik and the rapid reorientation of aeronautical research, together with the conclusion of successful flight demonstrations of conventional ramjets, reduced emphasis on airbreathing engines for high speed aeronautical vehicles.

However, interest in high speed airbreathing propulsion was revived when a single stage-to-orbit vehicle (the Aerospace Plane) was conceived. Two airbreathing propulsion schemes were of prime interest, namely the air-collection system and the supersonic combustion engine. The latter had wider application including, for example, hypersonic cruise vehicles and hypersonic missiles. Hydrogen fuel was at that time the only fuel of interest for Aerospace Plane applications primarily because of its cryogenic nature, its intrinsic cooling capability, and its high specific impulse.

Conventional Engines

The need for a thrust chamber for the air-collection system led ultimately to the development of a subsonic combustion thrust chamber with flight capability in excess of Mach 6. This hydrogen-fueled regeneratively-cooled combustor and plug nozzle combination was developed and tested for structural integrity at conditions exceeding Mach 6 (100,000-120,000 ft.). An early version of this 18" dia. chamber is shown in Fig. 4 and the contoured tube wall construction will be noted. This chamber was designed for a maximum internal pressure of 250 psia and a maximum wall temperature of 2500°R; a combustion efficiency in excess of 90% was generally obtained. When integrated into an engine system the chamber was suitable for flight from Mach 3 to speeds in excess of Mach 6. The combustor tubes were fabricated from Hastelloy X, with a Rene 41 wrap, and over three hours of test time were acquired with the flight weight engine. This engine program was completed in 1969 and it represents one of the most advanced subsonic combustion engines developed under USAF sponsorship.

Supersonic Combustion Engines

Another area of high speed propulsion concerns the scramjet engine and it is well known that the U.S. Air Force sponsored a number of scramjet engine tests during the last seven years; the engines tested included the following:

1. Marquardt Dual Mode Scramjet
2. UARL Variable Geometry Scramjet
3. General Electric Component Integration Model (CIM) Scramjet
4. GASL Research Scramjet
5. GASL Flight Test Module Scramjet

These engines were hydrogen fueled and the performance levels theoretically predicted were, in general, substantiated. Experience was gained with a variety of spike inlets and inlets employing combined two-dimensional and three-dimensional flow fields. The combustors were primarily wall injection systems and staged combustor systems were utilized. Generally, good combustion efficiencies were demonstrated with stable operation in short combustors. Experience was also gained concerning potential problem areas such as unfavorable combustor-inlet interactions leading to inlet unstart, and reduced efficiency of combustion in divergent combustion chambers. It should also be noted that ground testing was restricted to the Mach 7 region because of facility limitations which existed at that time. However, such research engines confirmed the feasibility of scramjet operation and illuminated research required for further development.

Similar hydrogen fueled test engines have been sponsored by other U.S. organizations; for example, the hypersonic research engine (HRE) built for NASA by AiResearch. This engine has provided much data on the internal gas dynamics and on the durability of the regeneratively-cooled type of structure for a dual mode, axisymmetric engine. The HRE is a variable geometry engine designed to perform at speeds from Mach 4 to 8. Two versions of the engine were planned for test; a structural test model already tested at Mach 7 in a NASA, Langley facility and an Aerodynamic Integration Model which has undergone Mach 6 freejet testing at the Plumbrook facility of NASA, Lewis during 1973, and Mach 7 tests are planned in 1974.

In addition to sponsoring other hydrogen fueled scramjet studies, a significant amount of hydrogen engine research is being accomplished at the NASA, Langley center; some particularly interesting work is reported in ref. (7). The engine described, a rectangular module, is a pronounced three-dimensional shape resulting from the design requirements of fixed geometry, low wetted area in the combustor, flow spillage during starting, and vehicle installation limitations. Research work is proceeding steadily on this engine-vehicle concept.

It is apparent that scramjet engines employing dense storable fuels and flying at moderate hypersonic speeds are of more near term interest than hydrogen fuel systems, and work has been channeled into this area. Maintaining effective supersonic combustion at these lower speeds is more difficult because spontaneous ignition conditions are lacking, and hydrocarbon fuels are usually less easy to burn than hydrogen.

The application of supersonic combustion of hydrocarbon fuels to a vehicle designed for Mach 6, low level flight is discussed in ref. (8). The vehicle described utilizes aerodynamic interference to reduce wave drag and carefully controlled burning process to alleviate heating and structural loads. Once again the pronounced three-dimensional geometry of the inlet and nozzle gas flow paths is seen.

High Mach Number Scramjet Component Development

Testing of scramjet components poses a considerable problem in simulating flight test conditions at high Mach numbers. Continuous flow wind tunnels are not capable of supplying flow with high enough reservoir conditions required for high Mach number conditions ($M > 7$ or 8). Pebble bed blowdown tunnels are limited in the maximum temperature that they can supply. Arc-heated tunnels can provide the high enthalpies needed but are limited in pressure. Pulse facilities, on the other hand, can supply both the high temperatures and pressures needed but are limited to very short test times. Use of such facilities requires a different philosophy in component testing with extensive use of specialized instrumentation.

Considering the different types of pulse facilities, extensive use has been made of the shock tunnel in which useful test durations of from 5 to 20 milliseconds have been achieved. Various contractors have all utilized the shock tunnel in testing scramjet inlet concepts. Such tests have been conducted over a Mach number range of from 10 to 25. Fuel injector and combustor tests have also been carried out in such facilities over a velocity range of from 8000 to 14,000 ft/sec. Although test durations are very short, they are sufficient to permit efficient combustion of H_2 and air under the high temperature conditions associated with these high flight speeds. Elaborate and multiple instrumentation on one combustor model permitted combustion efficiency to be determined through five independent means. Correlation between the various techniques was very good. At Sheffield University a hypersonic shock tunnel was designed specifically for the intent of conducting supersonic combustion research.

Hot shot tunnels have also been utilized in testing scramjet components and can extend the useful test duration by over an order of magnitude over the shock tunnel. A disadvantage of the hot shot tunnel is that oxygen in the air is depleted and contaminants are released during the heating process. This is undesirable for testing combustors. As a result, most of the hot shot tests have been conducted with inlet and nozzle components.

Another type of pulse facility which has had limited use for testing scramjet components, but which appears attractive, is the gun tunnel. Its advantage over the hot shot is that the piston prevents mixing of the driver and driven gases. An extension of this concept leads to the light-gas gun in which a scramjet model is propelled to hypersonic velocities in free flight under controlled environmental conditions. General Motors Research Laboratories conducted experiments along these lines on a miniature scramjet model capable of burning fuel while in free flight.

Agreement between pulse facilities and steady state facilities has, in general, been good. Obvious limitations such as inlet starting, heat transfer, and structural considerations prevent the substantial development of a flight weight engine by using pulse facilities exclusively. However, such techniques can be used with confidence in the development of individual components from an aerothermodynamic point of view. In a series of inlet tests, which were conducted in two different steady state facilities, also in a shock tunnel, and in a hot shot facility, performance data obtained at a given Mach number was independent of the type of facility. When a slight problem of flow separation was encountered, the extent of this problem appeared more related to the test Reynolds number available, rather than the particular type of facility or actual Mach number at which test was conducted.

Pulse facilities have also been used, but to a more limited extent, to aerodynamically test small-scale scramjet engines. AEDC conducted a series of supersonic combustion tests using a double-oblique-shock scramjet model in a shock tunnel (9). Likewise, Douglas has tested both two-dimensional and axisymmetric scramjet engine models in their shock tunnel. In one series of tests involving modifications to a General Electric scramjet engine designed for much lower Mach number, reasonable performance (I_{sp} ~ 1300 sec) was demonstrated at flight Mach numbers greater than 9.

Low Speed Scramjet Engines

As the flight speed of a scramjet engine is reduced, the temperature of the air entering the combustor decreases and at some conditions will fall below the autoignition temperature of the fuel/air mixture being used. Likewise, reducing flight speed reduces the Mach number entering the combustor. Such a decrease has serious consequences on combustor operation. In the case of a constant area combustor, the amount of heat which can be added to the flow is limited by the attainment of sonic speed at the combustor exit. Any further attempt to add heat to this thermally-choked flow will result in shock wave formation upstream of the combustor and breakdown of the supersonic flow entering the combustor. Thus, as the flight speed is reduced, sustained combustion becomes more difficult and the amount of heat which can be added to the flow is reduced with a corresponding reduction in engine thrust. These problems, along with inlet-combustor matching, can be alleviated to some extent through the use of three-dimensional combustor designs involving complex flow fields (10,11).

An attractive alternate approach for providing scramjet engines with a lower Mach number capability is offered by the dual mode engine (12) in which both subsonic and supersonic modes of combustion are permitted within the combustor. The main feature of such an engine is that in principle the combustor is divided into two sections: one for supersonic combustion and the other for subsonic operation. The supersonic combustion section precedes the subsonic one and acts as the subsonic diffuser of the inlet during the subsonic combustion mode.

A water-cooled dual mode scramjet engine was developed and tested by The Marquardt Corporation in the 1964-68 time period. This was a fixed geometry two-dimensional Mach 3 to 8 engine incorporating highly swept-back features. Test results confirmed both the feasibility and practicability of combining subsonic and supersonic combustion into a single engine. The fuel system, consisting of several hydrogen axial fuel injector locations along with two ignitors, permitted stable combustion mode transitions to be made with high overall engine efficiency. Theoretical performance was achieved based upon the individual component efficiencies achieved earlier in detailed component tests.

Hydrocarbon Fuels

At the conclusion of the dual mode program and other successful hydrogen scramjet engine programs, Air Force interest shifted from large scramjet vehicles to small scramjet missile systems leaving the hydrogen scramjet area to NASA and their HRE and other programs. As a result, attention focused on the hydrocarbons and fuels with a high density impulse. Ignition delay and reaction times for gaseous hydrocarbons are much longer than for hydrogen, hence the problem of achieving high combustion efficiencies using these fuels proved more difficult than for hydrogen. Initially, attempts were made to simply modify existing hydrogen scramjet engines by lengthening the combustor section and using gaseous fuels such as methane and ethylene, but these met with only limited success. Subsequently, more detailed programs were initiated.

Many approaches were available for sustaining combustion of hydrocarbon fuels at the low Mach numbers where temperatures are well below the autoignition temperatures. These included the use of flameholders or other devices for stabilizing flames, highly reactive fuels, additives, and piloting systems.

Conventional flameholders which require immersion into the supersonic stream are not desirable, but techniques which utilize fuel injector configurations or wall recesses to provide stabilization through local recirculation zones show promise. Another approach is to use highly reactive fuels, or blends of reactive fuels with hydrocarbons. Reactive fuels that have been used at low temperatures include triethyl aluminum and pentaborane. Blends of such fuels with heavy hydrocarbons have been investigated extensively by the Applied Physics Laboratory. The effect of homogeneous additives on the autoignition has also received considerable attention in the U.S. (13) and in Germany (14). Nitric oxide or nitrogen dioxide was found to dramatically accelerate the ignition of gaseous hydrocarbons as well as hydrogen. n-propyl nitrate was found to decrease the ignition delay times of high density hydrocarbons by about two orders of magnitude.

Extensive effort has also been devoted to the development of piloting systems for use in scramjet engines employing liquid hydrocarbon fuels. The concept of a pilot is to provide a high temperature gas source, along with a large concentration of free radicals (15). Pilots are essentially hot gas generators and fall into two classes: those which use a portion of the main engine airflow for pilot oxidizer, and those which use a stored oxidizer. In addition, various geometric configurations are possible, such as recesses, cavities, wedges, cones, bumps, and impinging flush wall jets. Fig. 5 shows the region in which scramjet hydrocarbon combustion work has been conducted in regards to combustor inlet conditions. Good supersonic combustion efficiencies have been obtained using liquid hydrocarbon fuels in tests where suitable fuel injector/piloting systems have been developed.

An interesting extension of the piloting concept is to capitalize on the fact that free radicals in themselves are very effective in promoting ignition. Work has been conducted (16) oriented towards the photochemical enhancement of combustion in supersonic flows. Results from this work to date have shown that the absorption of ultraviolet radiation by molecular oxygen in the airstream creates photochemical effects that greatly improve the ensuing combustion characteristics compared to those normally initiated by thermal ignition alone.

Subsonic Combustion Ramjets for Missile Propulsion

Potential ramjet applications can be divided into three main areas:

1. Advanced surface-launched interceptor missile

2. Long range/low altitude air-to-surface missile
3. Multi-purpose air-launched missile systems

The first system considered is the surface-launched ramjet-powered interceptor missile: this has received major attention in previous years and little fresh discussion need be given here. It is apparent that modern ramjet technology could be applied to such systems to yield striking performance increases. An advanced conventional ramjet operating at hypersonic speeds could be used. The missile engine would probably be mounted in the flow field of the wing and, owing to wing precompression effects, a relatively small diameter engine would be adequate. Obviously, at these high speeds some form of combustor cooling would be essential and the various advantages of regenerative cooling, ablative cooling, or the use of a refractory metal structure would have to be considered.

For the second class of missile, long range at low altitude is sought. These specifications lead to a missile of high aerodynamic and propulsive efficiency, rugged structure, and efficient fuel packaging. This latter requirement leads to the use of high-energy dense fuels typified by boron-based compounds. A vast amount of research has been directed into this area over many years and the capabilities of such fuels are well documented (17).

The third ramjet system noted above is the multi-purpose class. This denotes a missile which may be used for air-to-air or air-to-surface roles; it may be launched at subsonic or supersonic speeds at various altitudes and it may have to conform to the constraints of either internal or external carriage. A typical approach to a low volume missile of this class is shown in Fig. 6.

It will be obvious that the unique feature of this engine is the dual use of the combustor for both ramjet operation and boost propellant, hence this engine is often referred to as the integral rocket/ramjet (IRR) system. Many other significant differences between this IRR engine and the conventional straight-flow-through engine are apparent. This radical change in configuration has far-reaching effects on component design, engine integration, and ground test requirements. To illustrate these effects, let us consider each component in detail.

Inlet

Considering first the induction system, the intake is now located adjacent to the missile body. It may be located well forward near the forebody or aft-mounted near the vehicle base. In any event, the inlet performance is distinctly affected by the presence of the forebody and severe coupling, particularly at angle of attack, may be anticipated. Conversely, the choice of inlet type and location significantly affects vehicle aerodynamic performance. Various inlet configurations are illustrated in Fig. 7. The actual inlet model design may also vary widely, as shown in Fig. 8. Note also that the subsonic diffusers associated with these systems may be very short and incorporate sharp turns and distinct changes of cross-section shape.

In addition to the usual requirements of high pressure recovery, low drag, and flow stability associated with inlets, it is also necessary to fabricate these small scale inlets precisely and yet cheaply; obviously, cost is a major factor when missile propulsion systems are being compared.

Of these candidate inlet configurations, the dual side-mounted (DSM) inlet is an attractive configuration. "Cheek" or "chin" inlets are more suitable where internal carriage constraints exist. It may well be possible to "fold" some inlet configurations and allow "pop-out" when the missile is launched, thereby easing these carriage constraints. An important consideration is the performance of the inlet at the high angles of attack likely to be attained during missile maneuvers; some inlet geometries, such as the DSM inlet, can be designed so that increased pressure recovery and mass flow capture is obtained with angle-of-attack increase in a preferred direction. The angle of attack now becomes a much more significant variable in determining the overall vehicle performance and flight mechanics, and this is a significant departure from conventional technology.

Combustor

Turning now to combustor technology, in Fig. 9 the IRR combustor configuration is compared to that of a conventional ramjet engine. Notice that because the chamber must be compatible with the boost grain requirement, it is not possible to use flame stabilizers or conventional air-cooled liners. Because of the large scale recirculation zones located near the walls of the combustor, severe thermal and flow stability problems may be anticipated. Precise control of fuel distribution is no longer possible because injectors are generally mounted at the end of the subsonic diffusers. Also, as it is difficult to air cool this type of combustor structure, ablative protection is a preferred system. Reviewing the combustor design in more detail, it will be evident from the inlet geometries shown in Fig. 8 that air will usually enter the combustor at an angle to the centerline, through one or more ports, which may lack symmetry and which may be located in either the head (or dome) region or in the combustor sidewall.

The primary problem is to maintain stable combustion at high efficiency and low pressure loss; volume is not necessarily critical as the combustor volume is often sized by the rocket grain requirements and often exceeds normal ramjet requirements. In early development much attention was given to parametric studies of various combustor geometries; these tests served to identify primary recirculation zones and establish fuel mixing and flame stability mechanisms. In early tests extensive use was made of flow visualization tests using both water and air flow models with various fuel simulants. In many geometries, very unsteady flows were anticipated and subsequently confirmed in practice, and several simple combustor geometries were eliminated. A typical flow pattern obtained with a single entry flow passage is shown in Fig. 10.

The geometries shown differ markedly from conventional ramjet combustors and consequently the extensive design background on gutter-type stabilizers and related bluff-body systems was of little direct use in preliminary designs. The design approach has concentrated more on calculating and controlling the fuel distribution into the various recirculation zones in the combustor; limited design flexibility exists in that only the type of fuel injectors and their spatial disposition in the diffuser ports or dome of the combustor can be varied. Of course, in the case of real difficulty, it is always possible to utilize variable geometry flameholding devices which can be stowed in the subsonic diffuser and deployed into the combustor region after rocket burnout.

As noted earlier, the preferred thermal protection is an ablative system. The ablative material must be compatible with the combustor wall and with the boost grain surface. It must be firmly anchored to the wall to resist erosion and must withstand the stresses of booster operation, of front face combustion gas loads, and of backside aerodynamic heating. Accurate charring models are required, together with sound thermochemical data, to enable the required ablator lining thickness to be determined.

Nozzle

The dual use of the combustor chamber in the integral rocket/ramjet has a major impact on exhaust nozzle design. Generally, differing throat areas and expansion ratios are required for the rocket and ramjet modes; also, some method of effecting mode transition is required. In principle, a simple VG nozzle could fulfill all requirements; in practice, two separate but concentric nozzles can be employed with mode transition being accomplished by explosively jettisoning the rocket nozzle.

The thermal loading is severe during both modes of operation. For the rocket mode an exhaust nozzle typical of solid propellant engine technology can be employed. However, for the ramjet mode the problem is more complex than using a conventional ramjet nozzle. Internal air cooling cannot usually be employed and a passively cooled nozzle must be used; also, external radiation must be minimized because vehicle controls or components are frequently packaged around the exhaust nozzle throat. Also, because of related volume limitations it is not possible to use massive amounts of thermal protection, and furthermore, it is undesirable to use ablative materials which permit dimensional changes. Consequently, the nozzle design area presents a severe, but not impossible, challenge.

Controls

A new problem introduced by the IRR configuration is the control of the transition process from rocket to ramjet operation. The transition sequence begins when the booster pressure decays; this fall in pressure permits the ram air pressure in the inlet ducts to blow in the inlet port covers. The port cover movement is allowed to trigger the booster nozzle explosive jettison device.

After a brief delay to clear the chamber of residual booster slivers, the ramjet fuel valves and ignitor are actuated. Precise timing is required to prevent excessive deceleration of the vehicle and avoid inlet unstart. Usually the time period required for transition is about 500 ms from inlet port blow-in to steady operation. Care must be taken to prevent discarded components, such as inlet port covers, from impacting on the thermal protection layer of the combustor and causing premature failure.

Another characteristic of the IRR which differs significantly from the conventional engine is the wide range of flight conditions under which the engine is required to operate. Ground launched conventional engines are usually boosted to a flight speed close to the cruise Mach number and off-design operation is limited. The IRR, however, may be air launched at a wide variety of speeds, both subsonic and supersonic, and at any altitude. This requirement demands a sophisticated energy management system with an unusually severe fuel modulation limit; this wide "turn-down ratio" requirement impacts all components from the basic system through to the fuel injectors.

Test Techniques

For axisymmetric, nose-inlet ramjet engines, the freejet test facilities required and associated test techniques are well understood.

However, unlike nose-inlet engines, the cruciform IRR geometries would require enormous quantities of air for interference-free simulation of the external streamtube enclosing the inlet configuration. An example of a technique to reduce airflow requirements to more reasonable levels has been explored by AEDC and is illustrated in Fig. 11. This so-called "jet stretcher" ducts air to the aft-mounted inlet such that the flow condition which the inlet experiences in-flight is simulated. The forebody nose shock "escapes" in front of the jet stretcher; the flight streamtube flow is extended back to the inlets by the jet stretcher, and shock disturbances from the facility do not impact the flow boundaries. Design procedures for these jet stretchers have been devised and these devices are successful for simulating flows corresponding to low incidence conditions.

Another test technique used successfully in many applications is the rocket sled test. Although proposed many years ago for scramjet testing, this technique has more recently been used for IRR development and is particularly attractive for aft-mounted systems. A typical layout of the sled train for an IRR test is shown in Fig. 12. The test engine is accelerated to, and sustained at, a given test condition by sets of solid rocket boosters. In this program, the ramjet vehicle was mounted on an existing rocket sled, suitably modified. Tests were aimed at simulation of low level flight in the Mach 2-3 regime, duplicating flight Mach number and Reynolds number. Operation at angle of attack is also possible. Obviously, care has to be taken to avoid interaction of ground-reflected shock waves with the aft-mounted inlets. Trackside initiators were used to control fuel flow sequence and ignition. Thus, it is possible to simulate ramjet engine boost, transition, and cruise with full recovery of the vehicle, and with a comprehensive pictorial and instrumental history of the test. It is also possible to utilize the sled as a launch stage for a flight test of the engine, the major advantage being the fact that successful engine ignition and operation can be confirmed prior to free-flight launch.

Engine Development

An early IRR vehicle developed under USAF sponsorship was the Low Altitude Supersonic Ramjet (LASRM); subsequently, a more refined IRR engine was developed for component evaluation and test and termed the CET engine. The U.S. Navy has sponsored the Air Launched Low Volume Ramjet (ALVRJ) vehicle discussed in ref. (18).

CONCLUSIONS

Conventional ramjet technology has been fully demonstrated to speeds of about Mach 4.0; advanced component technology needs to be fully validated in flight test.

Scramjet and dual mode engines have been tested at hypersonic speeds in various small scale engines and have demonstrated to be an effective propulsion system.

The low volume ramjet engine offers major improvements in missile performance now, and has considerable growth potential.

The ramjet propulsion cycle is an essential ingredient of all high speed airbreathing propulsion systems.

REFERENCES

1. DUGGER, GORDON L/EDITOR. AIAA Selected Reprints/Vol. VI, Ramjets. The American Institute of Aeronautics and Astronautics, June 1969.

2. Jane's All The World's Aircraft. 1960-1970 series.

3. MARGUET, R. Design and Flight Tests of a Mach Number 5 Experimental Ramjet. Pyrodynamics. Vol. 5, pp. 307-340, 1967.

4. CONSTANT, H. Pyestock's Contribution to Propulsion. Journal of the Royal Aeronautical Society. Vol. 62, No. 568, April 1958.

5. PERCHONOK, E. and WILCOX, F. A. Investigation of Ramjet Afterburning as a Means of Varying Effective Exhaust Nozzle Area. NACA RME52H27, 1952.

6. BREMA, A. Recent Advances in Mixed Cycle Engine Design and Application. 1st International Symposium on Air Breathing Engines, 19-23 June 1972.

7. HENRY, J. R. and ANDERSON, G. Y. Design Considerations for the Airframe-Integrated Scramjet. 1st International Symposium on Air Breathing Engines, 19-23 June 1972.

8. ROFFE, G., VISICH, M. JR., and RANLET, J. A Conceptual Design Study for a Low Altitude High Mach Number Vehicle. AFFDL-TR-71-48, September 1971.

9. OSGERBY, I. T., SMITHSON, H. K., and WAGNER, D. A. Supersonic Combustion Tests with a Double-Oblique-Shock Scramjet in a Shock Tunnel. AEDC-TR-69-162, February 1970.

10. FERRI, A. Review of Scramjet Propulsion Technology. AIAA Journal of Aircraft. Vol. 5, No. 1, 1968.

11. FERRI, A. and FOX, H. Analysis of Fluid Dynamics of Supersonic Combustion Process Controlled by Mixing. Twelth Sym. (Int.) on Combustion, 1969.

12. CURRAN, E. T. and STULL, F. D. The Utilization of Supersonic Combustion Ramjet Systems at Low Mach Numbers. RTD-TDR-63-4097. AIAA Summer Meeting, June 16-20, 1963.

13. SIMINSKI, V. J. and WRIGHT, F. J. The Effect of Homogeneous Additives on the Autoignition of Hydrocarbon Fuels. AIAA Paper 72-71. AIAA 10th Aerospace Sciences Meeting, January 17-19, 1972.

14. SUTTROP, F. Ignition of Gaseous Hydrocarbon Fuels in Hypersonic Ramjets. 1st International Symposium on Air Breathing Engines, 19-23 June 1972.

15. EDELMAN, R. B., SCHMOTOLOCHA, S. and SLUTSKY, S. Combustion of Liquid Hydrocarbons in a High Speed Air Stream. AIAA Paper 70-88. AIAA 8th Aerospace Sciences Meeting, January 19-21, 1970.

16. CERKANOWICZ, A. E. and McALEVY III, R. F. Photochemical Ignition and Combustion Enhancement in High-Speed Flows of Fuel-Air Mixtures. AIAA Paper 73-216. AIAA 11th Aerospace Sciences Meeting, January 10-12, 1973.

17. PINNS, M. L., OLSON, W. T., BARNETT, H. C. and BREITWIESER, R. NACA Research on Slurry Fuels. NACA Report 1388, 1958.

18. BELDING, J. A. and COLEY, W. B. Integral Rocket/Ramjets for Tactical Missiles. Astronautics & Aeronautics. Vol. 11, No. 12, December 1973.

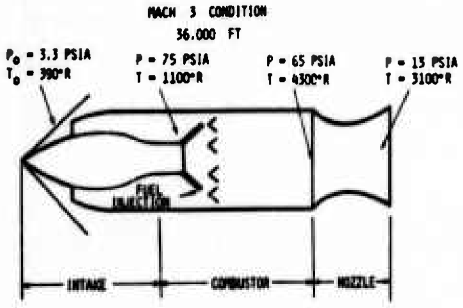
MACH 3 CONDITION
36,000 FT
P_0 = 3.3 PSIA
T_0 = 390°R
P = 75 PSIA
T = 1100°R
P = 65 PSIA
T = 4300°R
P = 13 PSIA
T = 3100°R
FUEL INJECTION
INTAKE
COMBUSTOR
NOZZLE

Fig. 1. Basic Ramjet Engine

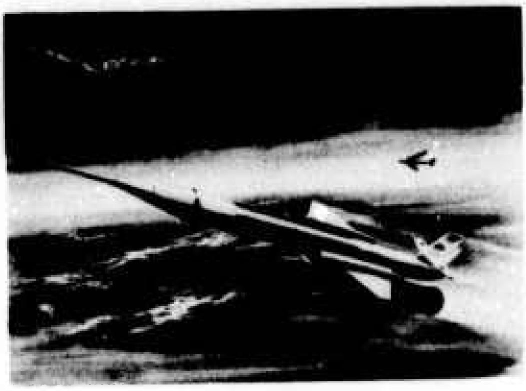

Fig. 2. Ramjet Installed on the X-7 Test Vehicle

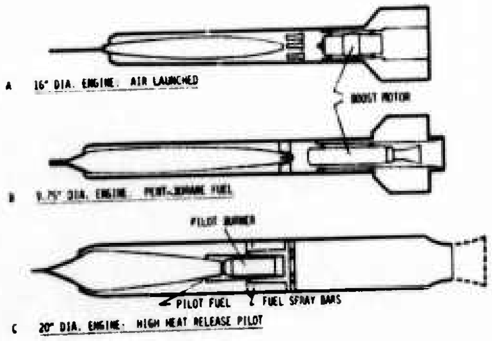
A 16" DIA. ENGINE: AIR LAUNCHED
BOOST MOTOR
B 9.75" DIA. ENGINE: PENT-BORANE FUEL
PILOT BURNER
PILOT FUEL
FUEL SPRAY BARS
C 20" DIA. ENGINE: HIGH HEAT RELEASE PILOT

Fig. 3. NACA/NASA Ramjet Vehicles

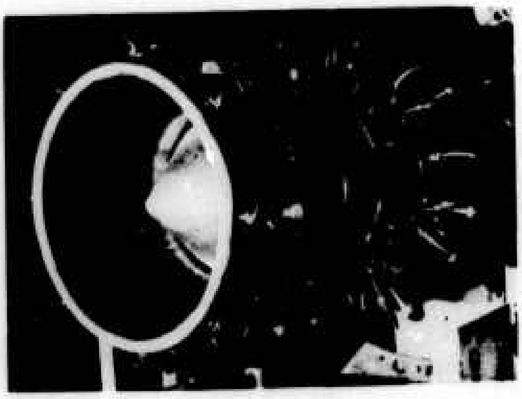

Fig. 4. Regeneratively Cooled Thrust Chamber

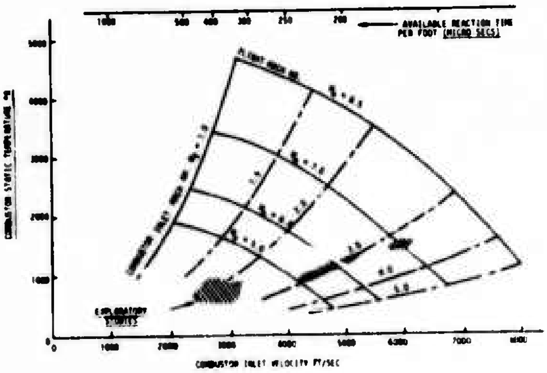

Fig. 5. Scramjet Hydrocarbon Combustion Work

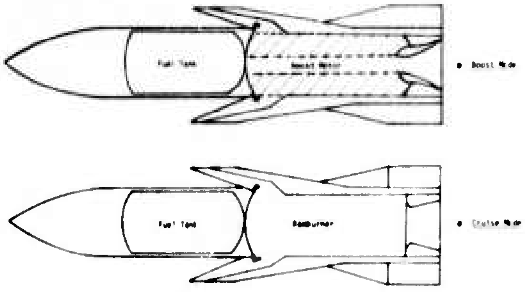
Fuel Tank
Boost Motor
Boost Mode
Fuel Tank
Ramburner
Cruise Mode

Fig. 6. Low Volume Integral Rocket/Ramjet

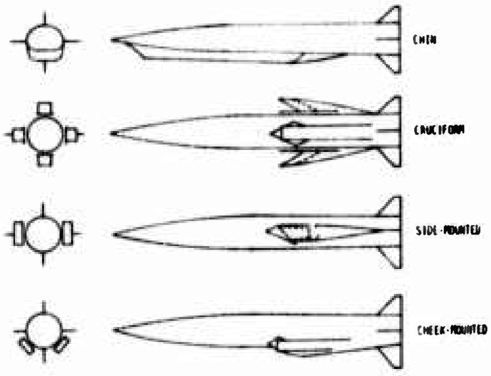
CHIN
CRUCIFORM
SIDE-MOUNTED
CHEEK-MOUNTED

Fig. 7. Missile Inlet Locations

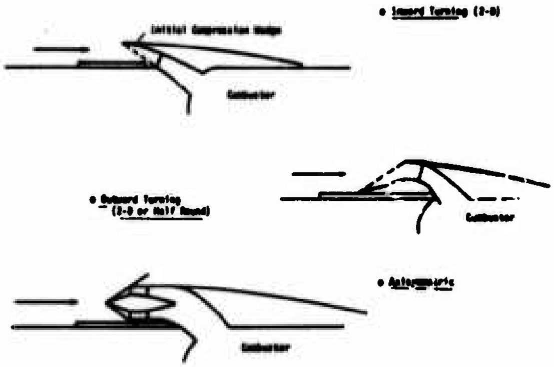
Inward Turning (2-D)
Initial Compression Wedge
Combustor
Outward Turning (2-D or Half Round)
Combustor
Axisymmetric
Combustor

Fig. 8. Inlet Module Types

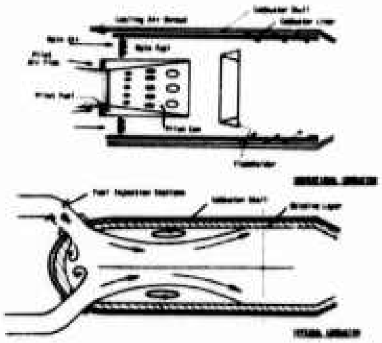

Fig. 9. Combustor Systems

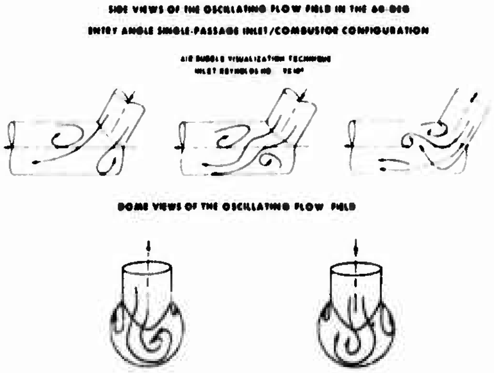
SIDE VIEWS OF THE OSCILLATING FLOW FIELD IN THE 60-DEG
ENTRY ANGLE SINGLE-PASSAGE INLET/COMBUSTOR CONFIGURATION
AIR BUBBLE VISUALIZATION TECHNIQUE
DOME VIEWS OF THE OSCILLATING FLOW FIELD

Fig. 10. Combustor Flow Visualization

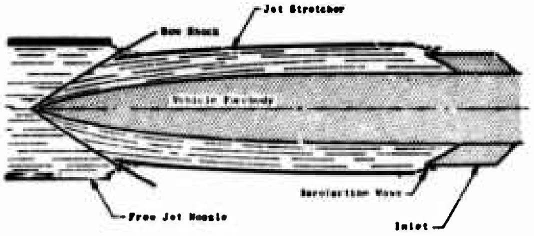
Jet Stretcher
Bow Shock
Vehicle Forebody
Free Jet Nozzle
Inlet

Fig. 11. Jet Stretcher

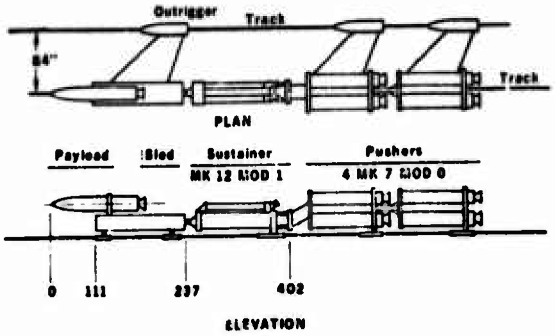
Outrigger
Track
84"
Track
PLAN
Payload
Sled
Sustainer
MK 12 MOD 1
Pushers
4 MK 7 MOD 0
0
111
237
402
ELEVATION

Fig. 12. Rocket Sled Test

ETUDE DE L'ECOULEMENT DANS UN EJECTEUR TRANSSONIQUE

J.M. HARDY et L. DUTOUQUET

SNECMA - Centre de VILLAROCHE

I. INTRODUCTION

La connaissance des coefficients de débit et de poussée des tuyères est nécessaire à la détermination des performances des moteurs et au dimensionnement des tuyères. La connaissance précise des domaines sonique et transsonique est indispensable au calcul des écoulements dans les tuyères convergentes-divergentes.

II. DESCRIPTION DES PHENOMENES PHYSIQUES

Dans une tuyère conique, l'écoulement ne peut être monodimensionnel, étant donné les conditions aux limites imposées par la géométrie. A la paroi se développe dans le canal une couche limite qui, du fait des gradients de pression, tend à se résorber dans le convergent. La réduction de débit qui lui est associée est responsable du $C_{D\delta}$. Les parois du convergent imposent à la ligne de courant pariétale une direction convergeant vers l'axe qui, associée aux conditions sur l'axe et à l'infini aval, est responsable d'importantes distorsions de vitesse en module et en argument dans le plan du col. Le coefficient de débit associé à ces hétérogénéités est noté C_{Dk}. On peut différencier deux types de fonctionnement de ces éjecteurs: le cas désamorcé qui correspond au domaine où C_D est fonction du taux de détente et le cas amorcé qui correspond au domaine où C_D est indépendant du rapport de détente.

Les conditions aux limites imposées à l'écoulement du fait de la géométrie sont au nombre de deux : α, demi-angle du convergent, et Σ, rapport du diamètre du col au diamètre du canal amont.

La figure 1 représente l'allure des "iso-Mach" dans un convergent infiniment étendu vers l'amont (M = 0), la seule contrainte étant la condition α. La figure 2 illustre l'allure des "iso-Mach" dans une tuyère où le Mach amont n'est pas nul. On notera les modifications importantes que ces lignes entraînent,en particulier l'existence d'un point d'arrêt.

III. DEFINITION DES COEFFICIENTS DE TUYERE

III.1. Coefficient de débit C_D

C_D est le rapport du débit réel traversant le convergent au débit isentropique monodimensionnel. Nous noterons C_{Dmax} la valeur de C_D en écoulement amorcé. Pour les taux de détente inférieurs à l'amorçage, il est commode de normaliser C_D par rapport à la valeur C_{Dmax} associée à la géométrie considérée.

III.2. Coefficient de poussée

Nous avons choisi comme poussée de référence la poussée absolue X_{GA}. Cette poussée sera rapportée au débit qui traverse la tuyère, soit $K_{TA} = X_{GA} / D_J \sqrt{T_J}$. Nous définirons alors un coefficient d'efficacité de tuyère : $\eta_{abs} = K_{TA} / K_{TA}^{*}$. Nous distinguerons deux définitions de ce coefficient : $\eta_{abs}^{*} = K_{TA} / K_{TA}^{*}(M=1)$ pour les taux de détente supérieurs à l'amorçage et : $\overline{\eta}_{abs} = K_{TA} / K_{TA}^{*}(\overline{M})$ pour les taux de détente inférieurs à l'amorçage, $\overline{M}$ étant le Mach mono-dimensionnel assurant le débit dans la section géométrique. Comme pour le coefficient de débit, nous normaliserons les valeurs de $\overline{\eta_{abs}}$, fonction du taux de détente, par rapport à la valeur de ce coefficient à l'amorçage. Notons que, pour les angles usuels et une gamme importante de taux de détente, $\frac{\overline{\eta_{abs}}}{\overline{\eta_{abs}}_{amorçage}} = 1$. Nous avons alors la relation : $\overline{\eta_{abs}}_{amorçage} = \eta_{abs^*} \cdot \frac{K_{TA^*}\ (M=1)}{K_{TA^*}\ (\overline{M})}$.

IV. ETUDE THEORIQUE DE L'ECOULEMENT

Nous avons abordé l'étude théorique de l'écoulement par diverses méthodes (BROWN, NORWOOD, FENAIN, Réf. 1-2-3-4) pour finalement adopter une méthode rigoureuse de description des écoulements proposée par M.FENAIN (ONERA), basée sur l'hodographe. Cette méthode relative aux écoulements bidimensionnels plans a été étendue aux écoulements de révolution par M.DUTOUQUET de la SNECMA. Cette méthode offre, en plus d'une formulation exacte des écoulements compressibles, de nombreux avantages : partie subsonique traitée dans un système original de coordonnées, utilisation d'un processus subsonique - supersonique couplé, ...

IV.I. Hodographe

La figure 3 représente l'hodographe d'un écoulement bidimensionnel supersonique non amorcé dans une tuyère. La figure 4 est relative à un écoulement amorcé.

La partie subsonique de l'hodographe est représentée dans le système argument - module normalisé du vecteur vitesse par rapport à l'angle de paroi et la valeur de V au col. La partie supersonique est représentée dans le système angle - nombre de pression de BUSEMANN (W).

On remarque que les segments I_a, I_a ; I_j, I_j et I_j, S représentent respectivement le point d'arrêt, la détente de PRANDTL-MEYER et la ligne sonique. Cette figure met en évidence la valeur du taux de détente amorçage $W = \frac{\alpha p}{2}$. En effet, la caractéristique montante S, I_j de pente - W coupe la détente de PRANDTL-MEYER I_j, I_j de pente + W en un point où $W = \alpha_p/2$

La figure 5 est relative à un écoulement de révolution. Dans ce cas, les caractéristiques ne sont plus des droites dans le plan de l'hodographe. En particulier, S T dite "frontière transsonique" interceptera la détente de PRANDTL-MEYER en un point I_j quand T sera sur la lèvre du convergent, différent du point I'_j correspondant à la caractéristique bidimensionnelle (figure 6). On peut toutefois remarquer, figure 5, que la droite S,I'_j joue un rôle important du fait du maillage choisi (schéma à 4 points). En effet, toute perturbation issue de D se répercute sur tous les points situés dans l'angle EDF et, par conséquent, sur la partie FS de la ligne sonique. Par contre, une perturbation issue d'un point situé dans l'angle ESW est sans effet sur la ligne sonique. SI_j est donc la ligne limite d'influence de l'écoulement aval sur l'amont. Ceci met en évidence le fait que le figeage de la ligne sonique est atteint pour un taux de détente inférieur à celui correspondant au figeage du domaine transsonique pour les écoulements de révolution, ce qui est bien recoupé par l'expérience.

IV.2. Résolution numérique

La méthode de résolution numérique ainsi que la formulation sont présentées conjointement par l'ONERA et la SNECMA dans la référence 5.

IV.3. Comparaison des écoulementsbi et tridimensionnels de révolution

IV.3.1. Ecoulement bidimensionnel de révolution

Les figures 7 et 8 présentent une comparaison des coefficients de poussée et de débit calculés pour des tuyères convergentes bidimensionnelles planes et de révolution. On peut remarquer que la méthode BROWN qui couple un écoulement subsonique plan et un écoulement supersonique de révolution donne des valeurs voisines de celles obtenues dans le cas d'un écoulement bidimensionnel plan.

IV.3.2. Ecoulement tridimensionnel de révolution

Les figures 9 et 10 montrent l'influence des deux paramètres géométriques Σ et α sur les coefficients de poussée et de débit. On voit, figure 9, que l'influence du Mach amont due à Σ est d'autant plus grande que l'angle est plus élevé. D'autre part, la figure 10 met en évidence l'intérêt de la corrélation $\eta_{abs}^{*} = f\ (C_D)$. On peut voir, en effet, qu'à C_{Dmax} donné l'influence de Σ est faible et, qu'en se reportant à la figure 8, les écarts entre écoulements bidimensionnel et tridimensionnel de révolution sont eux aussi faibles. On retiendra donc pour l'étude expérimentale cette corrélation.

IV.3.3. Influence de γ

Nous avons calculé les coefficients de débit et de poussée pour une tuyère conique de révolution pour diverses valeurs de γ . Nous pouvons remarquer dans le tableau ci-dessous que l'influence de ce terme est négligeable et que les valeurs expérimentales obtenues à $\gamma = 1,4$ peuvent être conservées pour l'étude des moteurs.

	$\alpha = 13°,5$		$\alpha = 40°$	$\Sigma = 0,72$
γ	C_D	η_{abs}^{*}	C_D	η_{abs}^{*}
1,4	0,9733	1,0088	0,9225	1,0189
1,3	0,9737	1,0092	0,9236	1,0202
1,2	0,9742	1,0096	0,9248	1,0216

IV.3.4. Importance des couches limites

Le calcul de la couche limite a été effectué par l'ONERA pour une série de convergents expérimentés à MODANE (Réf. 6). On en déduit que l'effet de couche limite est négligeable devant l'effet de distorsion de la ligne sonique.

IV.4. Recoupement théorie - expérience

IV.4.1. Tuyères amorcées

Sur la figure 11 nous présentons une confrontation théorie - expérience relative à des essais sur tuyères convergentes effectués à l'ONERA pour une valeur du Mach amont de 0,15 ($C_{Dk} = f\ (\alpha)$). La figure 12 met en évidence le bon accord théorie - expérience relatif au coefficient de poussée. Notons dans ce cas qu'il n'a pas été possible d'ordonner les résultats d'essais en fonction des valeurs de Σ et que la courbe théorique calculée pour $\Sigma = 0$ passe au mieux dans les points expérimentaux.

IV.4.2. Tuyères désamorcées

Dans ce cas nous avons également obtenu de bons recoupements théorie - expérience sur les évolutions de $\frac{C_D}{C_{Dmax}}$ et η_{abs} pour diverses valeurs de α et Σ . Les résultats des calculs théoriques comme les valeurs expérimentales nous ont montré que, pour l'étude des variations de $\frac{C_D}{C_{Dmax}}$, $\overline{\eta_{abs}}$ et $\frac{\eta_{abs}}{\eta_{abs\ amorcé}}$, les deux paramètres géométriques α et Σ peuvent être remplacés par C_{Dmax} .

V. ANALYSE DES RESULTATS EXPERIMENTAUX

Compte tenu de ce qui précède, nous retiendrons, pour analyser les résultats expérimentaux, la méthode suivante :

$$C_{Dmax} = f\ (\alpha \text{ et } \Sigma)$$

$$\eta_{abs}^{*} = f\ (C_{Dmax})$$

$$\frac{C_D}{C_{Dmax}} \text{ et } \frac{\overline{\eta_{abs}}}{\overline{\eta_{abs}}\ \text{amorcé}} = f\ (P_J/p_o \text{ et } C_{Dmax})$$

V.1. Coefficient de débit

Sur la figure 13 nous avons tracé le "tapis" représentant la corrélation $C_{Dmax} = f\ (\alpha \text{ et } \Sigma)$, déduit d'un ensemble de résultats expérimentaux de sources variées à diverses valeurs de Σ, d'études particulières de l'influence de Σ à angle donné et d'un ensemble de résultats de calcul théorique. Sur ce tapis figurent, à titre indicatif, quelques points de calcul théorique. Ce tapis peut être représenté par la formulation suivante :

$$C_{Dmax} = |0{,}995 - 0{,}095 \sin \alpha_p| \ . \ |1 + \Delta\ K\ (\alpha_p - 15°)|$$

$$K = 5{,}75\ \Sigma^4 - 5{,}61\ \Sigma^3 + 2{,}40\ \Sigma^2 - 0{,}21\ \Sigma - 0{,}85|\ 10^{-3}$$

$$\Delta = 0 \quad \text{si } \alpha_p < 15°$$

$$\Delta = 1 \quad \text{si } \alpha_p > 15°$$

taux de détente d'amorçage : $W_{amorçage} = \frac{\alpha_p}{2}$

La figure 14 donne la corrélation $\frac{C_D}{C_{D\ max}} = f\ (C_{Dmax} \text{ et } P_j/p_o)$

Cet ensemble permet la prédiction de C_D, donc le dimensionnement des tuyères dans tous les cas d'éjecteurs de moteurs.

V.2. Coefficient de poussée

Dans le cas des tuyères amorcées, la figure 10 représente la relation $\eta_{abs}^{*} = f\ (C_{Dmax})$ à retenir pour le calcul du coefficient de poussée. A C_{Dmax} donné, la valeur correspondante de η_{abs}^{*} peut être considérée comme indépendante de Σ pour les tuyères de réacteurs. La courbe représentative est donnée par la formule suivante pour $0{,}85 < C_{Dmax} < 1$

$$\eta_{abs}^{*} = 0{,}526 + 0{,}944\ (C_{Dmax}) - 0{,}12\ (C_{Dmax})^2 - 0{,}35\ (C_{Dmax})^3$$

Dans le cas des tuyères désamorcées, $\overline{\eta_{abs}}$ sera déduit de la relation:

$$\frac{\overline{\eta_{abs}}}{\eta_{abs}\ \text{amorçage}} = \eta_{abs}^{*} \cdot \frac{K_{TA*}\ (M = 1)}{K_{TA*}\ (\overline{M})}$$

avec $\overline{M} = f\ (1/C_{Dmax})$, ce coefficient étant pratiquement indépendant du taux de détente à géométrie donnée.

La figure 14 donne la variation du rapport

$$\frac{\overline{\eta_{abs}}}{\eta_{absam}} = f\ (P_J/p_o \text{ et } C_{Dmax})$$

pour les forts braquages de volets de tuyères et les faibles taux de détente. En dehors de ce domaine, $\dfrac{\overline{\eta}_{abs}}{\overline{\eta}_{abs\ amorcé}} = 1.$

VI. CONCLUSION

La synthèse théorie - expérience présentée ici résulte de sept années d'efforts aussi bien du point de vue expérimental que théorique. Elle nous permet de dimensionner les tuyères de tous les réacteurs actuels, l'étude théorique qui a été d'un grand intérêt pour la compréhension des phénomènes nous fournissant en plus les données transsoniques nécessaires au calcul des éjecteurs.

ANNEXE 1

ETUDE PARTICULIERE DE L'HODOGRAPHE

Dans le cas usuel, une tuyère est constituée d'un cylindre terminé par un cône. Sur la planche 2 sont présentés les hodographes correspondant à deux cas de fonctionnement pour une tuyère bidimensionnelle.

Figure 3 : supersonique non amorcé
Figure 4 : supersonique amorcé

La partie subsonique de l'hodographe est présentée dans des coordonnées module et angle normalisés du vecteur vitesse, la partie supersonique, nombre de pressions de Busemann et angle.

La ligne de courant sur la paroi $\alpha = 0$ subit un ralentissement du Mach infini à un Mach nul en Ia, puis en Ia à $M = 0$, elle subit un changement d'angle $\alpha = 0$ à $\alpha = \alpha_p$. Ensuite, à angle constant, elle s'accélère de $M = 0$ en Ia à $M = 1$ en I_J où elle subit une détente de Prandtl-Mayer jusqu'à la vitesse V_J (W_J) sur la figure. Les points anguleux Ia et I_J sont représentés sur l'hodographe par des segments de droite. La ligne sonique I_J, S est représentée dans le plan de l'hodographe par la droite I_J, S normale à l'axe des vitesses. La droite I_J, I_J représentant la détente de Prandtl-Mayer a pour équation $\alpha = -\alpha_p + W$, elle a donc une pente de 45°.

Si nous nous reportons à la figure 4, nous voyons que la dernière caractéristique issue de la détente au point anguleux I_J tombant sur la ligne sonique sera I_J, S; la pente de cette caractéristique est $\alpha = -W$. Toute détente en aval de cette caractéristique sera donc sans effet sur la ligne sonique. Le triangle I_J, I_J,S est donc isocèle et la valeur de W associée à ce point correspond à une déviation $\alpha_{amorçage} = \alpha_p/2$, soit un taux de détente d'amorçage correspondant au nombre de Busemann, $W_{amorçage} = \alpha_p/2$.

Sur les figures 5 et 6 sont présentées les parties supersoniques des hodographes correspondant à des écoulements de révolution. Dans ce cas, comme dans le cas bidimensionnel, la détente de Prandtl-Mayer est représentée par une droite à 45°. Mais les caractéristiques de l'écoulement, cette fois, ne sont plus des droites mais des courbes.

La figure 5 correspond à un écoulement à ligne sonique figée, mais à domaine transsonique non figé (ST frontière transsonique).

La figure 6 correspond à un domaine transsonique figé.

Si nous revenons à la figure 5, et que nous analysons le maillage utilisé pour la résolution numérique, maillage défini par des parallèles à I_{jet}, I_{jet} et SI_{jet}, nous voyons que, compte-tenu du schéma à quatre points utilisé pour la résolution des équations différentielles une perturbation du point D va se répercuter sur tous les points du maillage compris dans l'angle droit EDF (aval du point D) et par conséquent sur la partie de la ligne sonique FS modifiant ainsi le débit.

Par contre, une perturbation issue d'un point dans l'angle ESW sera sans effet sur la ligne sonique, ce qui revient à dire que SI jet est la ligne limite des influences de l'écoulement aval sur la ligne sonique; elle correspond à une caractéristique de l'écoulement plan de pente $\alpha = -W$. La valeur W_J associée à ce cas de figure correspond au taux de détente limite de figeage de la ligne sonique, donc de l'amorçage au sens du débit. Le taux de détente d'amorçage d'une tuyère convergente de révolution est donc donné par :

$$W = \alpha_p/2$$

Si, dans ce cas, la ligne sonique est figée, il n'en est pas de même de l'écoulement aval et, en particulier, de la caractéristique montante issue de S. En effet, en écoulement de révolution, les caractéristiques sont représentées sur l'hodographe par des courbes situées au-dessus de celle de l'écoulement plan (ST), ce qui fait que des perturbations se produisant entre T et I_{jet} influent sur le domaine transsonique de la tuyère et qu'il faut atteindre un taux de détente correspondant au cas de la figure 4 où le domaine transsonique est fermé sur I_{jet} pour ne plus avoir de dépendance des conditions aval.

On voit donc qu'en écoulement de révolution il existe un taux de détente de figeage du débit inférieur au taux de détente de figeage du domaine transsonique. Ceci est bien en accord avec les expériences relatives aux mesures de débit et avec l'analyse des interférogrammes faits par l'O.N.E.R.A.

Résolution numérique

La méthode est présentée dans la référence 5, la résolution numérique y est abordée. Les conditions aux limites dans le plan de l'hodographe étant parfaitement connues, le plan est alors discrétisé et les points singuliers éliminés par l'introduction de fonctions périodiques. Le retour au plan physique est fait par intégration (réf. 4, 5).

Dans le domaine subsonique, on a à résoudre un problème de Dirichlet, avec deux points singuliers et dans le domaine transsonique un problème de Tricomi avec un point singulier.

NOTATIONS

α : Angle

A : Section normale à l'écoulement

$\emptyset$: Diamètre

Σ : $\dfrac{\emptyset \text{ col}}{\emptyset \text{ canal}}$

T_j : Température génératrice

P_j : Pression génératrice

p_o : Pression statique d'échappement

V : Vitesse

W : Nombre de pression de Busemann

λ, μ : Coordonnées de Busemann

D : Débit

$C_{D\delta}$: Coefficient de débit dû à la couche limite

C_{DK} : Coefficient de débit dû à la distorsion de l'écoulement non visqueux

$\emptyset(M)$: $(p/P)\ A/A_c^* \ (1 + \gamma M^2) = f\ (M; \gamma)$

$\Delta(M)$: $\dfrac{D \sqrt{A_T}}{P\ A_c^*} = f\ (M \text{ et } \gamma)$

$\Sigma(M)$: $A/A_c^* = f\ (M \text{ et } \gamma)$

ϕ : Fonction de courant

A_c^* : Section critique du tube de courant

K_{TA} : $\dfrac{DV + Ap_o}{PA_c^*}$; $X_{GA} = DV + Ap_o$

$*$: Caractérise les valeurs isentropiques monodimensionnelles

g : Caractérise les grandeurs géométriques

X_{GA} : $DV_{col} + A_{col} \cdot p_o$: poussée absolue

LISTE DES REFERENCES

Réf.1 : "Compressible flow through convergent conical nozzles with emphases on the transonic region"
E.F.BROWN - Université de l'Illinois - 1968

Réf.2 : "Contribution à l'étude des coefficients de débit et de poussée des tuyères convergentes adaptées au propulseur"
Thèse C.N.A.M. - septembre 1971 - par J.P.MARECHAL

Réf.3 : "Two dimensional transonic gas jets"
R.E.NORWOOD - Theses Mechanical Engineering MIT

Réf.4 : "Méthodes numériques de résolution des problèmes d'écoulement mixte autour d'un profil"
M.FENAIN - O.N.E.R.A. 4/1285 AN - juillet 1969

"Application des méthodes de résolution hodographique à l'étude des jets et des profils supercritiques"
O.N.E.R.A. - Groupe sectoriel franco-soviétique - 1970

Réf.5 : "Congrés I.C.A.S. - Haïfa - septembre 1974
O.N.E.R.A. - S.N.E.C.M.A.
par MM.DUTOUQUET et FENAIN

Réf.6 : "Problème de mesure sur maquette de la poussée d'un arrière-corps d'avion supersonique"
par B.MAZURE - 38è réunion PEP AGARD - septembre 1971 - Sanderfjord (Norvège)

Réf.7 : "Transonic flow in conical convergent and convergent-divergent nozzles with nonuniform inlet conditions"
S.WEHOFER - W.C.MOGER - A.I.A.A. 70-635

Réf.8 : "N.G.T.E. Report 258"
Décembre 1963

Réf.9 : "Tuyère supersonique à double flux - méthode de calcul"
SFIM - 1967
Revue Française de Mécanique n° 24
J.M.HARDY - H.LACOMBE

Réf.10: "Etude théorique d'une tuyère convergente-divergente"
3è Symposium franco-soviétique - novembre 1969 - PARIS
J.M.HARDY (Publié dans Aéronautique et Astronautique n° 37)

Ecoulement infini radial

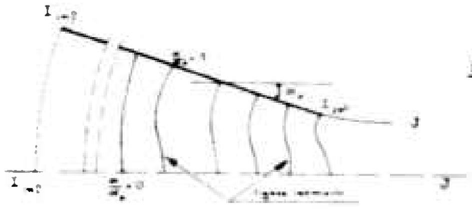
I
J
lignes isentropes

Figure 1

Ecoulement dans une tuyère

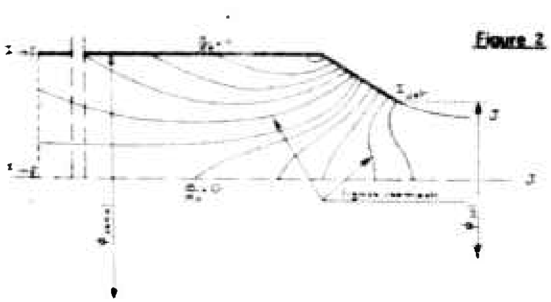
I
J
lignes isentropes

Figure 2

Hodographes correspondant à un écoulement bidimensionnel

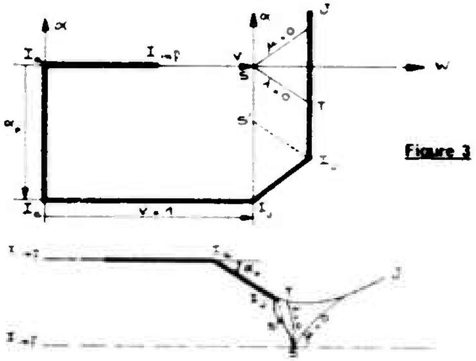
α
I
V
S
S'
T
W
J
v = 1

Figure 3

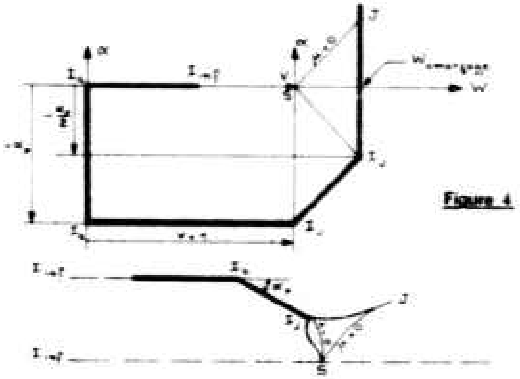
α
I
V
S
W
J
W émergent

Figure 4

Hodographes correspondant à un écoulement de révolution

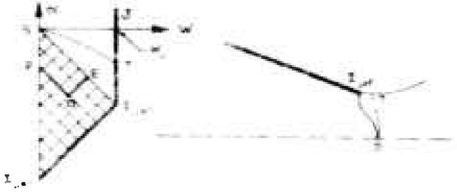

Figure 5

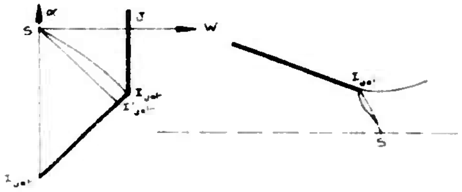

Figure 6

Comparaison entre les écoulements bidimensionnel et de révolution

III

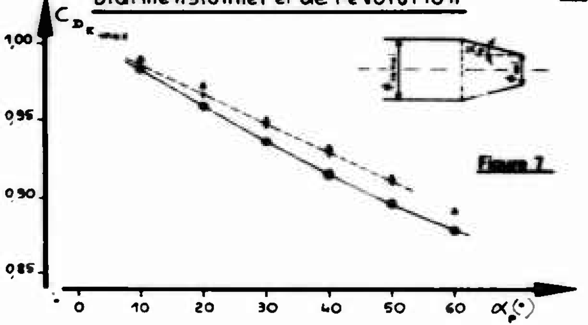

Figure 7

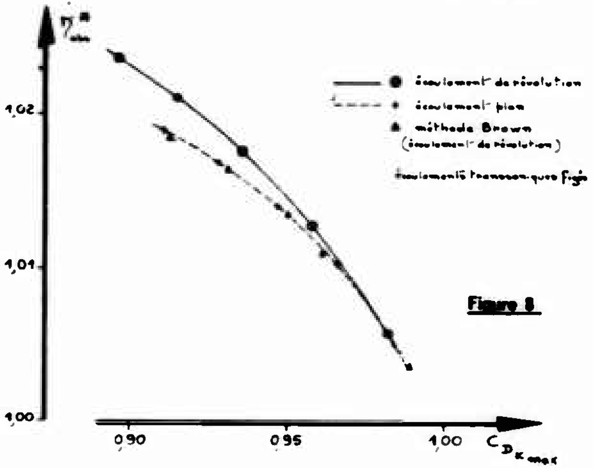

Figure 8

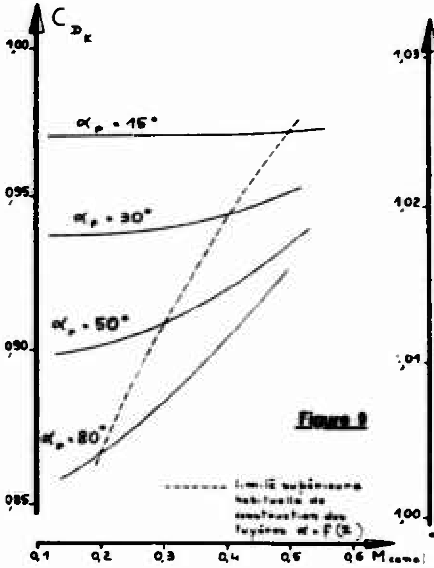

Figure 9

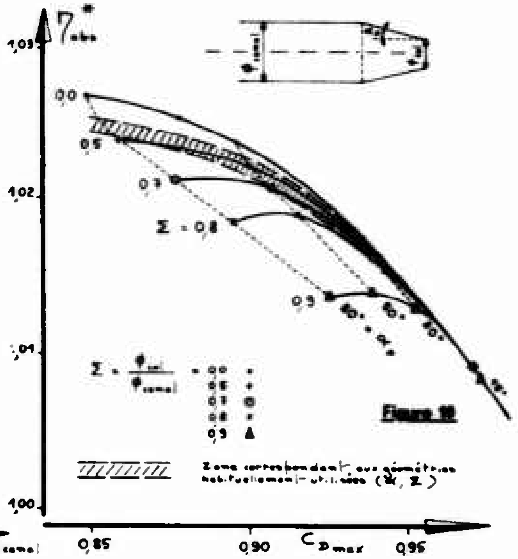

Figure 10

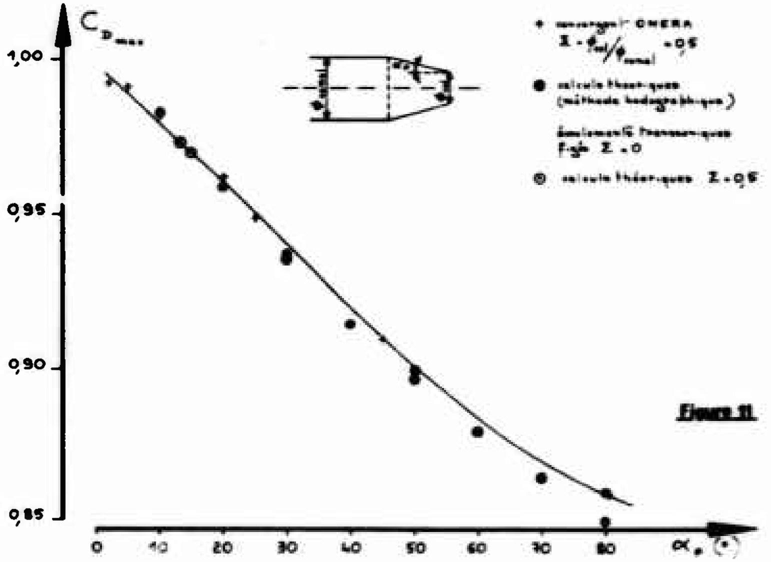

Figure 11

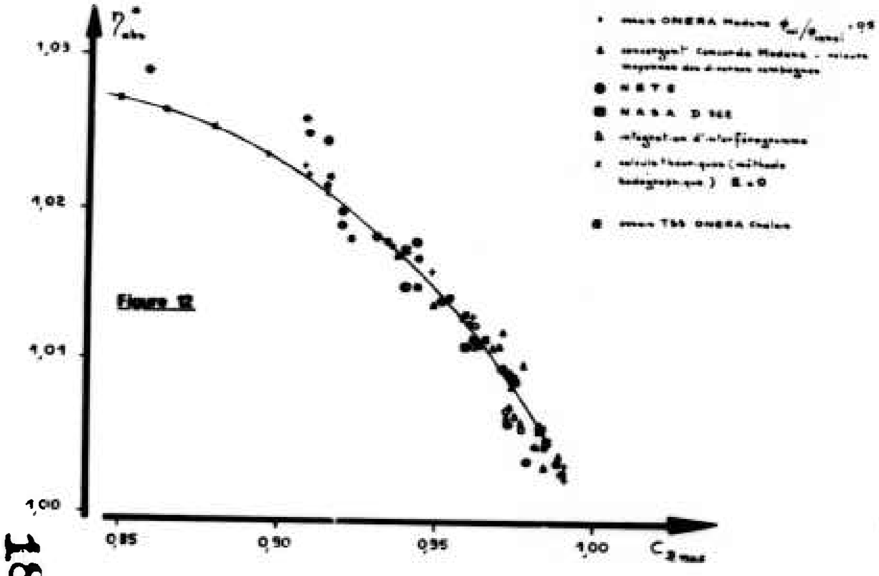

Figure 12

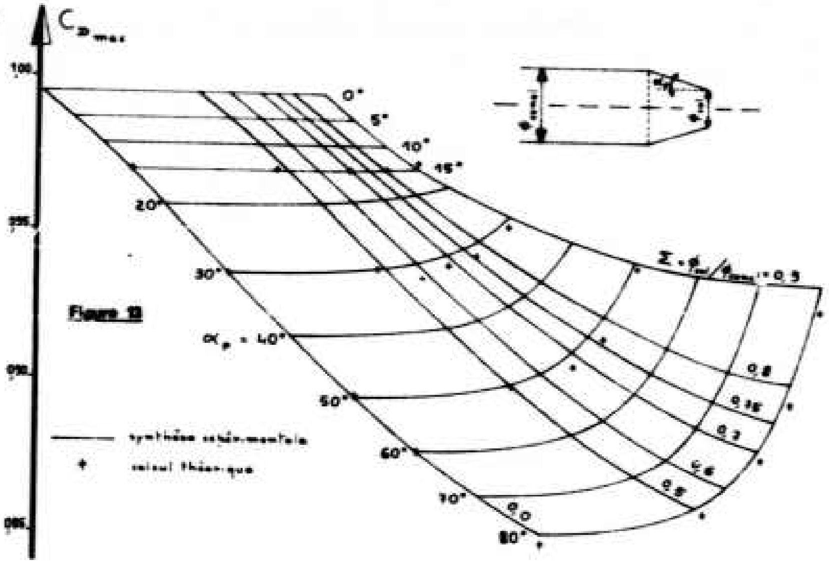

Figure 13

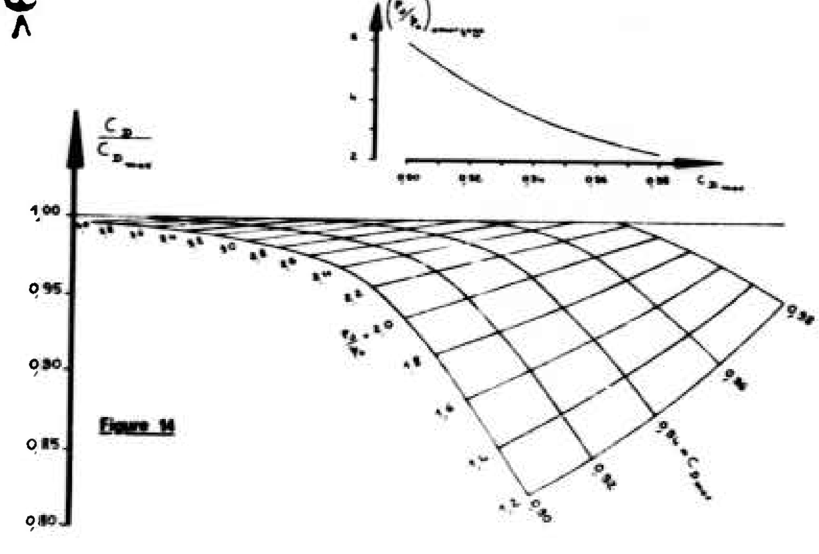

Figure 14

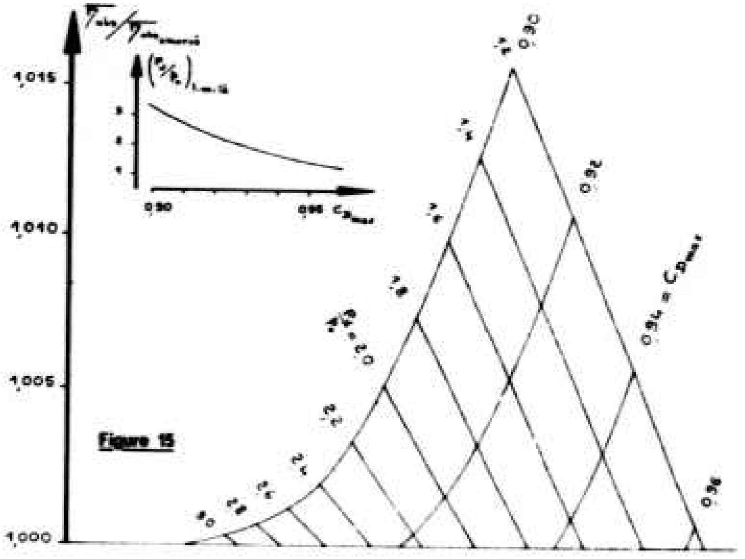

Figure 15

A NUMERICAL METHOD FOR THE SOLUTION OF THREE-DIMENSIONAL INTERNAL FLOWS.

R. Camarero

University of Sherbrooke, Dept. of Mech. Eng.

INTRODUCTION

In the design of high speed aircraft, it is of great importance to know the aerodynamic characteristics of various airframe components as these affect the overall flight performance of the vehicle. Particularly, a detailed knowledge of the external and internal flow field about open-nose components such as engine housings and inlets is essential to evaluate the external drag and the effectiveness of the compression process of the intakes. The flow fields over such surfaces have been the subject of numerous two-dimensional or axisymmetric analyses such as those by Meyer (1) and more recently by Lee (2) including boundary layer effects.

To study such problems in full generality, it is necessary to include three-dimensional effects as the inlet may be at an incidence to the freestream or simply because the shape is not axisymmetric. For such configurations the basic equations are highly nonlinear, and perturbations or other approximate methods based on the linearization of the equations are inadequate since the accuracy of the solutions thus obtained, as well as their range of validity are difficult to assess. The only other alternative is the use of numerical techniques, as analytical solutions are possible only under very restrictive conditions. Recent advances in computer technology as well as progress in the mathematics of approximation have made such computations both feasible and economical.

The aim of this paper will be to describe a numerical technique developped for the solution of inviscid internal and external three-dimensional supersonic flows past general ducted bodies at incidence.

PROBLEM FORMULATION

Supersonic flows about prescribed shapes are accurately described by the conservation equations of gas dynamics, plus an equation of state for the fluid and appropriate conditions on the boundaries. It is assumed that the flow is steady, inviscid, adiabatic, and that the fluid is a perfect gas. The assumptions are known to yield a good representation of the type of physical situation considered in this study. The basic equations written in symbolic form are:

Continuity: $$\vec{\Delta} \cdot (\rho \vec{V}) = 0 \qquad (1)$$

Momentum $$\vec{V} \cdot \vec{\Delta} \vec{V} + \frac{1}{\rho} \vec{\Delta} p = 0 \qquad (2)$$

Energy: $$\vec{V} \cdot \vec{\Delta} p - a^2 \vec{V} \cdot \vec{\Delta} \rho = 0 \qquad (3)$$

These equations constitute a system of five nonlinear partial differential equations in the five unknowns, p, ρ, v, w, and u. A particular solution is singled out from the infinity of possible solutions by imposing certain initial and boundary conditions. These constraints take the form of surfaces upon which the values of the variables are given (initial data) or surfaces where additional relations are to be satisfied. In the present problem these will be of two types; solid boundaries and shock wave surfaces.

A numerical method consists in replacing the continuous differential equations by a set of difference equations which apply at the nodal points of a grid. These difference equations are obtained by a process of discretization where the derivatives are approximated by means of finite differences.

There are basically two approaches. The first is the method of standard finite differences where the discretization is carried out initially, with the basic equations. For the other, the method of characteristics, the discretization is carried out after the basic equations have been transformed into an equivalent, but simpler, system of compatibility relations. The method of characteristics is based on the direction of propagation of pressure waves and thus will correctly represent the physical model at solid boundaries and shock wave surfaces. It is felt that such a scheme is a potentially more accurate method than one based on the standard finite differences. Furthermore stability criteria will be easier to satisfy.

METHOD OF CHARACTERISTICS

The method of characteristics has been successfully used to obtain numerous solutions to two-dimentional or axisymmetric supersonic flows. The extension to three dimensions poses no particular mathematical problem, but the practical implementation presents certain difficulties not encountered in the two-dimensional method. These arise from the more complicated geometry of the computation networks which are based on surfaces instead of lines. Interpolation and numerical differentiation are then more difficult and yield very involved algorithms. Thus, it is only recently that general three-dimensional solutions in gas dynamic have been attempted.

For hyperbolic systems of equations, such as those of gas dynamics, there exist surfaces along which the complete three-dimensional equations reduce to a simpler system which contains derivatives with respect to only two directions, instead of three. This represents a distinct advantage over the method of finite differences because only two derivatives need to be approximated.

These surfaces, and the directions within them are called characteristics and are obtained by means of a coordinate transformation of the basic equations (1), (2) and (3) as shown in the following section.

Through a point in space there exist an infinity of characteristic surfaces and this results in considerable freedom in the choice of a characteristic network. In practice, however, only two basic configurations have been used. These are the characteristic conoid which is the envelope of all characteristic surfaces through a point in space; and the two characteristic surfaces through a line in space formed as the envelope of all conoids issued from this line. A number of schemes based on these have been proposed by Thornhill (3) and Butler (4) and are discussed and compared in Ref.5 . In this study it is concluded that a modified scheme based on the reference plane method of Sauer (6) will yield the simplest and most efficient algorithm. This choice was reached on practical considerations such as ease of interpolation, accuracy of numerical differentiation, and the number of computations per step.

The reference plane method

The reference plane or near-characteristic network is a special type of characteristic scheme based on the characteristic surfaces associated with a coordinate curve. The compatibility relations are written along the curves of intersection between these surfaces and a streamwise coordinate plane. This results in a triangular network instead of a polygon for bicharacteristic schemes based on the characteristic conoid. The advantage is that there are fewer base points, but more importantly from the numerical aspect is that these are colinear, allowing the use of one-dimensional methods of interpolation. These are more efficient and more accurate than the bivariate methods required for interpolation over a surface as needed for bicharacteristic methods. Further as the characteristic surfaces are issued from a coordinate curve, the vertices of adjacent networks lie along this coordinate curve. Thus the numerical evaluation of derivatives is again a simpler process and potentially more accurate methods can be used. This is particularly important as these are a notorious source of error. (See Fig. 1)

Characteristic Relations

The scheme developed in the present study is based on the same formulation as that used by Katskova and Chushkin (7) with certain modifications in the numerical procedures. The first step in applying the method of characteristics is to find the characteristic directions and to transform the basic equations so that they reduce to a simpler set of compatibility relations along these directions. Before this is carried out, it will be convenient to transform the physical flow region, bounded by the shock wave and body surface, into a rectangular computational region. This results in a curvilinear coordinate system where both boundaries coincide with coordinate curves, thus general boundary conditions are more easily incorporated. This is accomplished by means of the following transformation.

$$\xi = (r - r_b) \ / \ (r_w - r_b) \tag{4}$$

The basic equations when written explicitly in terms of ξ, ϕ and x become:

$$\rho v \frac{\partial V}{\partial \xi} + \rho \frac{W}{r} \frac{\partial V}{\partial \phi} + \rho U \frac{\partial V}{\partial X} - \rho \frac{W^2}{r} + \frac{1}{\varepsilon} \frac{\partial p}{\partial \xi} = 0 \tag{5}$$

$$\rho v \frac{\partial W}{\partial \xi} + \rho \frac{W}{r} \frac{\partial W}{\partial \phi} + \rho U \frac{\partial W}{\partial X} + \rho \frac{VW}{r} + \frac{\mu}{\varepsilon} \frac{\partial p}{\partial \xi} + \frac{1}{r} \frac{\partial p}{\partial \phi} = 0 \tag{6}$$

$$\rho v \frac{\partial U}{\partial \xi} + \rho \frac{W}{r} \frac{\partial U}{\partial \phi} + \rho U \frac{\partial U}{\partial X} + \frac{\lambda}{\varepsilon} \frac{\partial p}{\partial \xi} + \frac{\partial p}{\partial X} = 0 \tag{7}$$

$$\begin{aligned} v \frac{\partial \rho}{\partial \xi} + \frac{W}{r} \frac{\partial \rho}{\partial \phi} + U \frac{\partial \rho}{\partial X} + \frac{\rho}{\varepsilon} \frac{\partial V}{\partial \xi} + \rho \frac{\mu}{\varepsilon} \frac{\partial W}{\partial \xi} + \rho \frac{\lambda}{\varepsilon} \frac{\partial U}{\partial \xi} \\ + \frac{\rho}{r} \frac{\partial W}{\partial \phi} + \rho \frac{\partial U}{\partial X} + \frac{\rho V}{r} = 0 \end{aligned} \tag{8}$$

$$\nu \frac{\partial p}{\partial \xi} + \frac{W}{r} \frac{\partial p}{\partial \phi} + U \frac{\partial p}{\partial X} - a^2 \left(\nu \frac{\partial \rho}{\partial \xi} + \frac{W}{r} \frac{\partial \rho}{\partial \phi} + U \frac{\partial \rho}{\partial X}\right) = 0 \qquad (9)$$

where $\varepsilon = r_w(\phi, x) - r_b(\phi, x) \qquad \lambda = -\xi \frac{\partial \varepsilon}{\partial X} - \frac{\partial r_b}{\partial X}$

$$\mu = -\left(\xi \frac{\partial \varepsilon}{\partial \phi} + \frac{\partial r_b}{\partial \phi} \right) /r \qquad \nu = (V + \mu W + \lambda U)/\varepsilon$$

A variable transformation for the above system

$$\bar{\xi} = f\ (\xi, \phi, x)\ ,\ \bar{\phi} = g\ (\xi, \phi, x) \text{ and } \bar{x} = h\ (\xi, \phi, x)$$

is sought such that in the new variables, derivatives with respect to $\bar{\xi}$, i.e. $\partial U/\partial \bar{\xi}$, $\partial V/\partial \bar{\xi}$, etc... do not appear. Then the surface $\bar{\xi} = f(\xi,\phi,x)$ is a characteristic surface. The details of this derivation are given in Camarero (5). This yields the following relations for the characteristic directions within the coordinate plane ϕ, i.e. the reference plane.

$$\frac{d\xi}{dX} = \frac{\nu}{U} \text{ and } \frac{d\xi}{dX} = \frac{\nu}{U} - \frac{1}{\varepsilon} \frac{\Gamma \pm \beta}{1 - U^2/a^2} \qquad (10) \qquad (11)$$

where $\beta = \sqrt{\frac{U^2}{a^2} \Gamma^2 - \left(1 - \frac{U^2}{a^2}\right)(1 + \mu^2)}$ and $\Gamma = (V + \mu W)/U$

These are known, respectively, as the stream or C^o - characteristic, and the wave or C^+ and C^- -characteristics. When written along these directions, Eqs. (5) to (9) become:

Along the stream characteristic, Eq. (10),:

$$VdV + WdW + UdU + dp/\rho = dX\ (VA_1 + WA_2 + UA_3)/U \qquad (12)$$

$$\Gamma dV + dU + dp/\rho U = dX\ (\Gamma A_1 + A_3)/U \qquad (13)$$

$$dp - a^2\, d\rho = A_5\ dX/U \qquad (14)$$

Along the wave characteristics, Eq. (11),:

$$dV + \mu dW - \Gamma dU \pm dp\beta/\rho U$$

$$= \frac{dX}{U} \left\{ A_1 + \mu A_2 - \Gamma A_3 + \frac{\Gamma \pm \beta}{1 - U^2/a^2} \left(A_3 - UA_4 - \frac{UA_5}{\rho a^2} \right) \right\} \qquad (15)$$

The coefficients A_1 to A_5 are defined by:

$$A_1 = -\frac{W}{r} \frac{\partial V}{\partial \phi} + \frac{W^2}{r} \qquad A_2 = -\frac{W}{r} \frac{\partial W}{\partial \phi} - \frac{WV}{r} - \frac{1}{r\rho} \frac{\partial p}{\partial \phi}$$

$$A = -\frac{W}{r} \frac{\partial U}{\partial \phi} \qquad A_4 = -\frac{1}{r} \frac{\partial W}{\partial \phi} - \frac{V}{r} - \frac{W}{r\rho} \frac{\partial \rho}{\partial \phi} \qquad A = -\frac{W}{r} \frac{\partial p}{\partial \phi} + a^2 \frac{W}{r} \frac{\partial \rho}{\partial \phi}$$

The problem thus reduces to the solution of Eqs. (12) to (15) instead of

Eqs. (5) to (9).

NUMERICAL TECHNIQUE

The application of the foregoing theory to practical numerical computations consists in the discretization of the characteristic relations, Eq. (12) to (15) and a reformulation of the initial boundary value problem as follows. On an initial spacelike surface $X = X_o$, the values of the variables are given at the nodes of a grid formed by the intersection of ϕ = constant and ξ = constant coordinate surfaces. It is required to find the solution, i.e. the values of the variables p, ρ, u, w, v at the nodes of a similar grid on an adjacent surface $X = X_o + \Delta X$. This is done by projecting a characteristic network from each node on the new surface to intersect the initial surface in a number of base points. The characteristic curves are approximated by straight line segments. The compatibility relations are then written as finite differences of the values at the end points of the appropriate segment of the network. This yields a system of algebraic equations which can be solved simultaneously for the variables at the vertex of the network. Using modified networks for boundary points, this procedure is carried out until the solution is available over an entire new surface, which then becomes the initial surface for the next step.

Field point

The network for the computation of a field point is shown in the adjoining diagram.

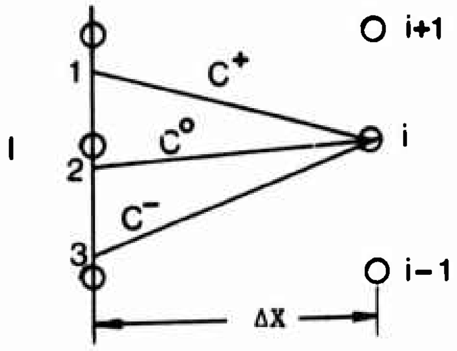

Field Point Network

The co-ordinates ξ_1, ξ_2 and ξ_3 of the base points 1, 2 and 3 are obtained from

$$\xi_{1,2,3} = \xi_i - \Delta X \left(\frac{d\xi}{dX} \right)_{1,2,3}$$

where ξ_i is the ordinate of the i-th node on a given ray and equals the value of the i-th root of the appropriate Tchebycheff polynomial as required by the proposed method of interpolation. The slopes of the corresponding characteristics are given by rewriting Eqs.(10) and (11) as:

$$\left(\frac{d\xi}{dX} \right)_1 = \frac{1}{\varepsilon} \left(\lambda - \frac{\Gamma U^2/a^2 + \beta}{1 - U^2/a^2} \right) \qquad (16)$$

$$\left(\frac{d\xi}{dX}\right)_2 = \frac{1}{\varepsilon}\,(\lambda + \Gamma) \tag{17}$$

$$\left(\frac{d\xi}{dX}\right)_3 = \frac{1}{\varepsilon}\left(\lambda - \frac{\Gamma U^2/a^2 - \beta}{1 - U^2/a^2}\right) \tag{18}$$

These are evaluated on the initial value surface at point I , which is the same node as the solution point. The compatibility relations, Eq. (12) - (15) are written as differences of the end points the segments of the network. This gives after some manipulations the following solution for the properties at a new point.

$$\begin{aligned}
p_i &= \rho U\,(K_1 - K_4)/2\beta \\
\rho_i &= \rho_2 + (p_i - p_2 - C_5\,dX)/a^2 \\
V_i &= V_2 - K_6 \\
W_i &= W_2 + dX\,C_6 - \mu K_6 \\
U_i &= U_2 + (p_2 - p_i)/\rho U + dX\,C_2 + \Gamma K_6
\end{aligned} \tag{19}$$

where

$$K_1 = dX\,C_1 + V_1 + \mu W_1 - \Gamma U_1 + \beta p_1/\rho U$$

$$K_2 = dX\,C_4 + VV_2 + WW_2 + UU_2 + p_2/\rho$$

$$K_3 = dX\,C_2 + \Gamma V_2 + U_2 + p_2/\rho U$$

$$K_4 = dX\,C_3 + V_3 + \mu W_3 - \Gamma U_3 - \beta p_3/\rho U$$

$$K_5 = dX\,C_5 + p_2 - a^2\rho_2$$

$$K_6 = \frac{K_1(\Gamma - \beta) - K_3(\Gamma + \beta) + 2\beta(K_7 + \mu\,dX\,C_6)}{2\beta(1 + \mu^2 + \Gamma^2)}$$

$$K_7 = -\Gamma dX\,C_2 + V_2 + \mu W_2 - \Gamma U_2 - \Gamma p_2/\rho U$$

and where

$$C_{1,3} = \frac{1}{U}\left\{A_1 + \mu A_2 - \Gamma A_3 + \frac{\Gamma \pm \beta}{1 - U^2/a^2}\left(A_3 - \mu A_4 - \frac{UA_5}{\rho a^2}\right)\right\}$$

$$\begin{aligned}
C_2 &= (\Gamma A_1 + A_3)/U \\
C_4 &= (VA_1 + WA_2 + UA_3)/U, \quad C_5 = A_5/U \\
C_6 &= (-\mu A_1 + A_2)/U
\end{aligned} \tag{20}$$

Body Point

For points lying on a solid boundary the interior point network is modified as follows

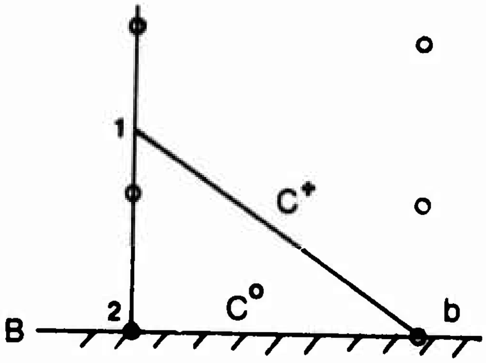

Body Point Network

The base point 1 is obtained by projecting the C^+-characteristic from the body point b . Its location on the initial value surface is given by:

$$\xi_1 = - \Delta X \left(\frac{d\xi}{dX}\right)_1$$

since $\xi_b = 0$. The slope of the characteristic is given by Eq. (16) evaluated at the corresponding body B, on the previous plane. The compatibility relations along one wave characteristic and the stream characteristic are written as finite differences, giving four relations. The fifth required to complete the system is obtained from the condition that the normal component of velocity at the wall be zero. This is expressed, after applying the transformation of Eq. (4) as:

$$V_b + \mu W_b + \lambda U_b = 0$$

The solution at the new body point is then obtained explicitly as

$$\begin{aligned} p_b &= \left[(1 + \mu^2 - \lambda\Gamma) K_1 + (1 + \mu^2)(\Gamma + \lambda) K_8 + \Gamma(\Gamma + \lambda) K_9\right] / K_{10} \\ \rho_b &= \rho_2 + (p_b - p_2 - C_5\, dX)/a^2 \\ V_b &= V_2 - K_{11} \\ W_b &= W_2 + dX\, C_6 - \mu K_{11} \\ U_b &= U_2 + (p_2 - p_b)/\rho U + dX\, C_2 + \Gamma K_{11} \end{aligned} \qquad (21)$$

where

$$K_8 = dX\, C_2 + U_2 + p_2/\rho U$$

$$K_9 = \mu dX\, C_6 + V_2 + \mu W_2$$

$$K_{10} = (1 + \mu^2 - \lambda\Gamma)\ (\lambda + \Gamma + \beta) + (\lambda + \Gamma)\lambda\Gamma$$

$$K_{11} = \left[\lambda K_1 - (\lambda + \Gamma + \beta)\ K_9 - \beta\lambda\ K_8\right] / K_{10}$$

Shock point

The second type of boundary that will be included is a shock wave for which the network is shown below.

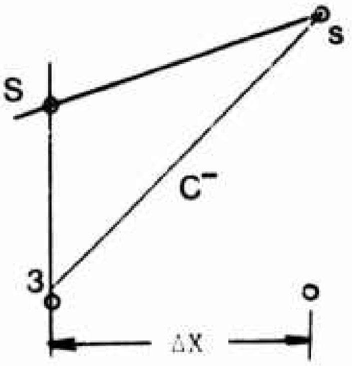

Shock Point Network

This consists of a single wave characteristic segment issued from the new location of the shock wave to intersect the initial surface in a base point 3. Unlike for a body point, the calculation of a shock point will be an iterative procedure since the shock shape is not known and must be found as part of the solution. This is obtained by matching the values of the flow properties behind the shock calculated from the Rankine-Hugoniot relations with those calculated from the compatibility relation along the wave characteristic. The iterative procedure consists of the following steps:

i) a shock slope is assumed and a new shock point is located;
ii) a C^--characteristic is projected from this point to the base point 3 whose ordinate is given by:

$$\xi_3 = 1 - \Delta X \left(\frac{d\xi}{dX}\right)_3$$

where the slope is evaluated from Eq. (18).
iii) the conditions behind the shock are evaluated using the Rankine-Hugoniot relations which, after the transformation of Eq. (4) become:

$$p_S = p_\infty - \rho_\infty U_{\infty n}^2 (F - 1) \qquad \rho_S = \rho_\infty / F \tag{22}$$

$$V_S = V_\infty + E \qquad W_S = U_\infty + \mu E \qquad U_S = U_\infty + \lambda E$$

where

$$F = \frac{\gamma - 1}{\gamma + 1} + \frac{2\gamma p_\infty}{(\gamma + 1)\rho_\infty U_{\infty n}^2}$$

$$U_{\infty n} \quad \frac{V_\infty + \mu W_\infty + \lambda U_\infty}{\sqrt{1 + \mu^2 + \lambda^2}} \qquad E = \frac{U_{\infty n}\ (F - 1)}{\sqrt{1 + \mu^2 + \lambda^2}}$$

iv) these values and the interpolated properties at point 3 are substituted into the compatibility relation Eq. (15) along the $\bar{C}$-characteristic.

v) the slope is changed, and Steps iii) to iv) are repeated until Eq. (15) is satisfied within a prescribed accuracy.

The prediction of a better estimate of the shock slope in Step v) is obtained using the Secant method. This is an iterative procedure where two initial values are extrapolated to yield the next improved estimate.

Initial Conditions

The method of characteristics is not self-starting and requires that a solution be specified on an initial space-like surface. This is usually a difficult problem in itself, but for the ducted bodies with an attached shock wave considered in this study, simple and accurate initial solutions are possible. This is because the shock wave is attached to the leading edge, and hence the flow field may be approximated locally by a number a two-dimensional wedge flows with a transverse velocity component, W_∞. Such flows are calculated within each reference plane using the oblique shock relations. It is noted, however, that the proposed numerical technique is not restricted to such flows, but can equally well be applied to blunt bodies by supplying the appropriate starting conditions.

Interpolation and differentiation

In the proposed technique, the solution is obtained at the nodes of a coordinate grid by issuing a network from each of these in the upstream direction. Thus, the base points of these networks will not coincide with the nodes of the previous plane. Consequently the values of the flow variables at the base points are obtained by interpolation. This manner of integrating the equations may appear disadvantageous compared to the schemes where the networks are projected downstream from the solution points of the previous step. In that instance the values at the base points are known exactly and no interpolation is required. It is discussed in Camarero (5), however, that such schemes are unstable, and that interpolation is precisely what is required to make them stable.

In the present study an interpolation procedure using Tchebycheff polynomials was devised. These polynomials have the property that they will yield a uniformly distributed error over the interval of interpolation so that equally accurate values are obtained near the end points as in the midrange of the interval. Furthermore, the maximum error will be the smallest compared to all other polynomials. This is achieved by spacing the nodes so that they coincide with the roots of the Tchebycheff polynomial whose order equals the number of nodes. Since the first and last roots do not coincide with the end points of the interval of a Tchebycheff polynomial, it was necessary to transform the polynomial so that these roots would coincide with the computational interval. The resulting algorithm is very efficient and simple, and is described in Ref. (5).

In all schemes using the method of characteristics it is required to evaluate derivatives. In the present problem, the flow properties are calculated explicitly by means of Eqs. (19), (21) and (22), where the derivatives $\partial U/\partial \phi$, $\partial V/\partial \phi$, $\partial p/\partial \phi$ etc, appear through the coefficient A_i's in the definitions of the C_i's in Eqs. (20).

Moretti (8) has used polynomial fittings which are then differentiated. These, however, oscillate between the nodes where they yield the largest error, and unfortunately this is precisely where the derivatives are required. Another method, used by Katskova and Chushkin (7), uses trigonometric series. These are well suited for variations which depart slightly from axisymmetric cases.

In the present technique, a procedure using spline functions was devised for the numerical evaluation of derivatives. Spline functions are a series of piece-wise polynomials which yield accurate and smooth derivatives. Furthermore, from a series of numerical experiments carried out in Ref.(5), it appears that cubic splines are relatively insensitive to truncation errors appearing in the data to be differentiated. This is particularly important in numerical techniques where the solution obtained at the nodes contain such errors.

NUMERICAL COMPUTATIONS

The various procedures for field and boundary points, the initial solution, interpolation and differentiation were incorporated into an overall algorithm for the computation of three-dimensional supersonic flows. The program has been coded in the Fortran IV-G language and the listing is given in Camarero (5).

The input data for a given calculation are the freestream Mach number, the angle of incidence, two intergers to determine the mesh size, the location of the initial solution, the maximum step size, a tolerance for the shock wave iteration, the angular position of the plane of symmetry, and other parameters for the output of the solution. The program can, without any alteration, compute internal and external flows. This is achieved by the sign of the angle of incidence; a positive value for internal flows and a negative value for external flows. This automatically generates the required changes in the program. The flow field may possess one, several or no planes symmetry. This is specified as input data by the angular location of the plane of symmetry. The width of the computational region is adjusted accordingly.

The step size of the integration procedure is regulated by an active procedure which determines the maximum allowable step size from the stability criterion at every step. The most restrictive point is used or a value specified as input data if the latter is smaller. The body shape is specified in a separate subroutine, supplied by the user for each case. This may be in the form of data points or as an analytic function.

The accuracy of a numerical procedure depends, for a given mesh size, on the order of the discretization process used to replace differentials. In the present program, these are first order accurate. Higher order accuracy can be obtained, but requires iterations for the solution of every point. As these can considerably increase the computing time, the first order explicit scheme was chosen.

The accuracy and the precision of the program was tested by computing flows over simple shapes such as cones and truncated cones. The number of nodes and reference planes were varied to determine the effect on the accuracy. It was found that a 7 x 7 grid, i.e. 7 nodes on 7 reference planes, resulted in a very good accuracy and that the improvement resulting when using a 9 x 9 grid was less than .5% . Further, comparison with the numerical solution of Katskova and Chushkin (7) shows that comparable accuracy can be obtained with the present method using a much coarser grid, i.e. 7 x 7 versus 25 x 7 for the method of Katskova and Chushkin. It was found, furthermore, that the essential features of a three-dimensional flow were preserved using as coarse a grid as 4 x 4. In that instance the error was of the order of 4%.

Similar agreement was obtained with the solution of the flow over elliptic cones at Mach 6. Figure 2 shows a comparison of the variation of the surface pressure coefficient with the experiments of Zakkay and Visich (9). The calculations were obtained using a 7 x 7 mesh at incidences of 0° and 10°, for an accentricity, $a/b = 1.39$. Figure 3 shows the variations of the surface pressure coefficient for a tangent ogive with a fineness ratio of 3 at an incidence of 5 degrees in a Mach 5.05 freestream, at various stations along the length of the body. These results agree very well with the experiments of Savin (10).

Internal Flows

The program was applied to the solution of internal three-dimensional problems using as a body surface a conically convergent duct with a tip angle of 15 degrees. The solutions were obtained using a 7 x 10 mesh at incidences of 5, 10 and 15 degrees to a Mach 4 freestream. The results are given in the isometric drawings of Fig. 5 to 7 which show the variation of the internal surface pressure with ϕ and X. Finally, a development of the shock wave surface is shown in Fig. 4 for $\alpha = 15$ degrees. It is seen that on the leeward side the wave is straight, i.e. it is a Mach wave. This is expected since the freestream is parallel to the body surface.

The program computes routinely at each step certain useful aerodynamic quantities, such as the normal and axial force coefficients whose variations are shown in Figs. 8 and 9 for the three incidences.

From Fig. 4, it is seen that the shock wave position on the windward side equals that on the leeward side at approximately $X = .93$, i.e. the shock wave collapses and intersect itself. There results a very complicated pattern of reflected and transmitted waves with possibly the appearance of a Mach disc. This problem has not been solved for the much simpler situation of axisymmetric flow, hence a solution for the three-dimensional flows is much less likely. The computation is terminated before this occurs and this constitutes a limitation of the method when applied to internal flows.

CONCLUSIONS

The end result of the present investigation is a computer program which can calculate flow fields past a great variety of body shapes under a wide range of conditions. The good agreement obtained with experimental measurements indicates that the solutions provide a realistic description of physical flows. These are obtained at a cost ranging from $3 to $40, depending on the grid size and the number of steps. The remarkable feature, is that even when using a coarse grid the essential nature of the flow is preserved.

The program generates its own initial data and different body shapes are easily specified. Thus making it a useful tool to the designer. A possible application would be to compute the inviscid flow field required for boundary layer calculations. Such solutions would also be useful to the experimentalist in the selection of the location of pressure taps on an experimental model.

The limitation to the method of characteristics is that the flow remain supersonic. However, the present program is further restricted to shapes with attached shock waves, and the flow can only be computed up to the point where the shock wave interacts with itself. The assumption of inviscid flow has been found to be adequate provided the Reynolds number is high and that boundary layer separation does not occur. The assumption of a perfect gas could easily be relaxed by using a different equation of state, presumably in tabular form.

The development of such a program is lengthly and involves a large amount of work. However, once the initial effort has been carried out, numerous solutions are obtained easily and inexpensively. In that respect, it is felt that such programs provide suitable alternatives to experiments.

REFERENCES

1. MEYER, R.F., "Perturbations of Simple Wedge Flow relating to Asisymmetric Hypersonic Intakes or Imploding Cylindrical Shocks", N.R.C. Aeronautical Report LR-496, 1968.

2. LEE, B.H.K., "Numerical Calculations of the Hypersonic Viscid-Inviscid Flow inside Simple Ducts of Circular Cross-section", Aeronautical Quarterly, Vol. 22, pp. 233-256, 1971.

3. THORNHILL, C.K., "The Numerical Method of Characteristics for Hyperbolic Problems in Three Independent Variables", Aero. Res. Council, Report and Memorandum No. 2615, 1948.

4. BUTLER, D.S., "The Numerical Solution of Hyperbolic System of Partial Differential Equations in Three Independent Variables", Proceedings of the Royal Society of London, Series A, Vol. 255, pp. 232-252, 1960.

5. CAMARERO, R., "Numerical Solutions of Internal and External Hypersonic Flows at High Incidence", M.E.R.L Report 73-5, Mech. Eng. Dept., McGill University, 1973.

6. SAUER, R., "Dreidimensionale Probleme der Charakteristiken Theorie Partieller Differentials Gleichungen", Z. Angew Math. Mech. Bd. 30, Nr. 11/12, 1950.

7. KATSKOVA, O.N. and CHUSHKIN, P.I., "Three-dimensional Supersonic Equilibrium Flow of a Gas around Bodies at the Angle of Attack", Zhurnal Vychislitel'Noy Mathematiki i Mathematicheskoy Fiziki, Vol. 5, No. 3, pp. 503-518, 1965. NASA TT F-9790, Translation.

8. MORETTI, G., "Three-dimensional Flow Field Analysis in Re-entry

Problems", Sixth Symposium on Ballistic Missiles and Aerospace Technology, Vol. IV, Ed. by C.T. Morrow et al, Academic Press, New York, 1961.

9. ZAKKAY, V., and VISICH, M. Jr., "Experimental Pressure Distribution on Conical Elliptical Bodies at $M_\infty = 3.09$ and 6.0", Pibal Report No. 467, Polytechnic Institute of Brooklyn, 1959.

10. SAVIN, R.C., "Application of the Generalized Shock-Expansion Method to Inclined Bodies of Revolution Travelling at High Supersonic Airspeeds", NACA TN-3349, 1955.

LIST OF SYMBOLS

a	speed of sound
B	point on body surface
C_n	local normal force coefficient
C_A	local axial force coefficient
I	field point
M	Mach number
p	static pressure
r	radial co-ordinate
S	point on shock surface
U, V, W	cylindrical velocity components
$\vec{V}$	velocity vector
X	axial distance

α	angle of incidence
γ	ratio of specific heats
δ_b	body surface angle
ξ	transformed radial co-ordinate
ρ	density
ϕ	circumferential co-ordinate

Subscripts

b	body point
n	normal component
i	field point
s	shock point
W	shock wave
∞	freestream conditions
1,2,3	base points of computational network

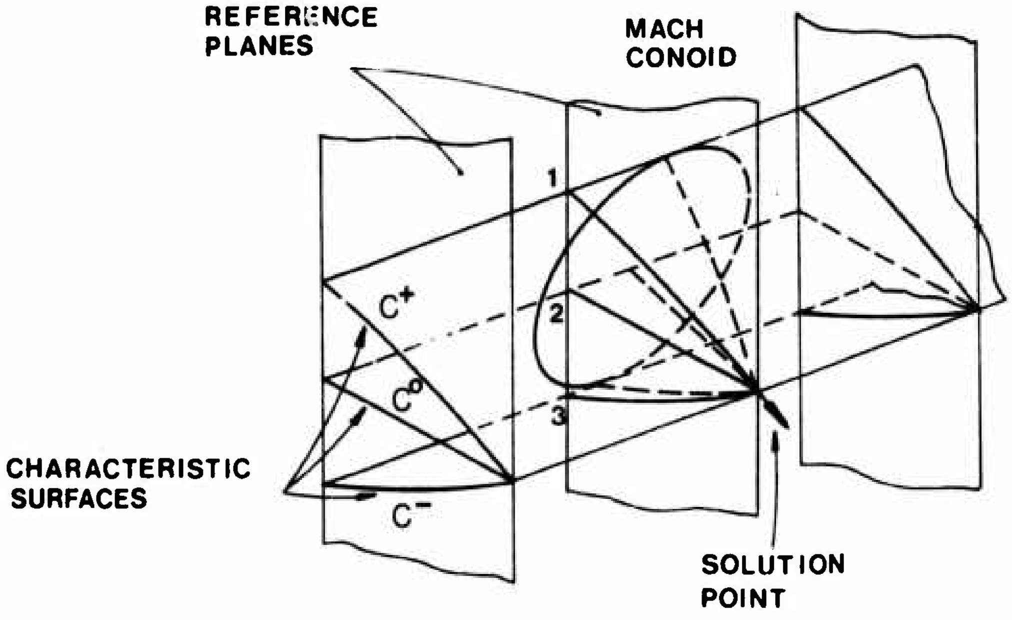

FIG. 1 Reference plane characteristic Network

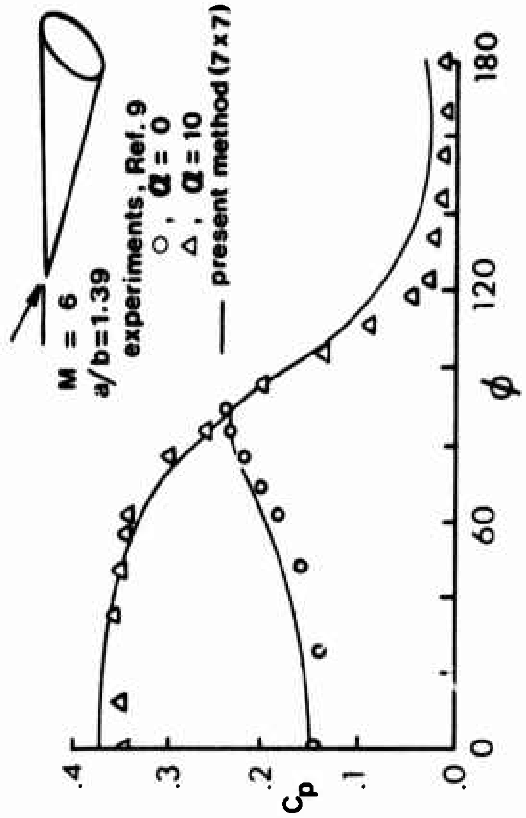

FIG. 2 Elliptic cone

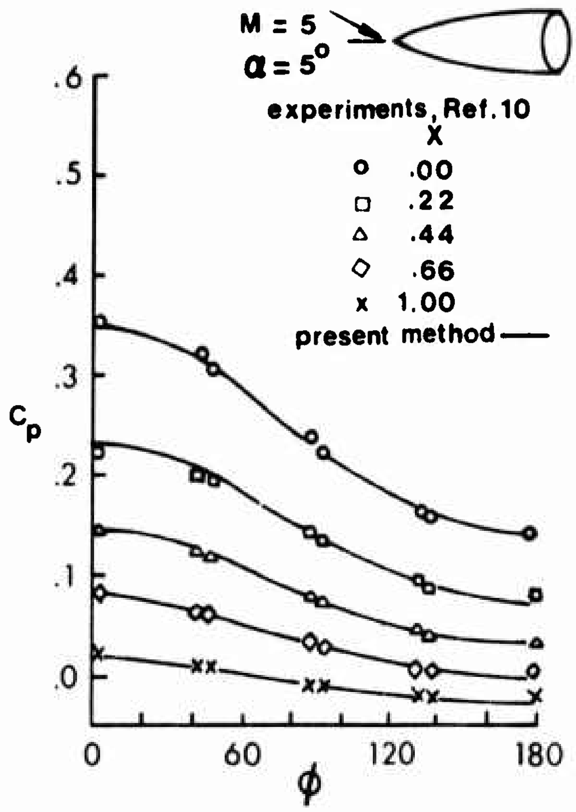

FIG. 3 Tangent ogive

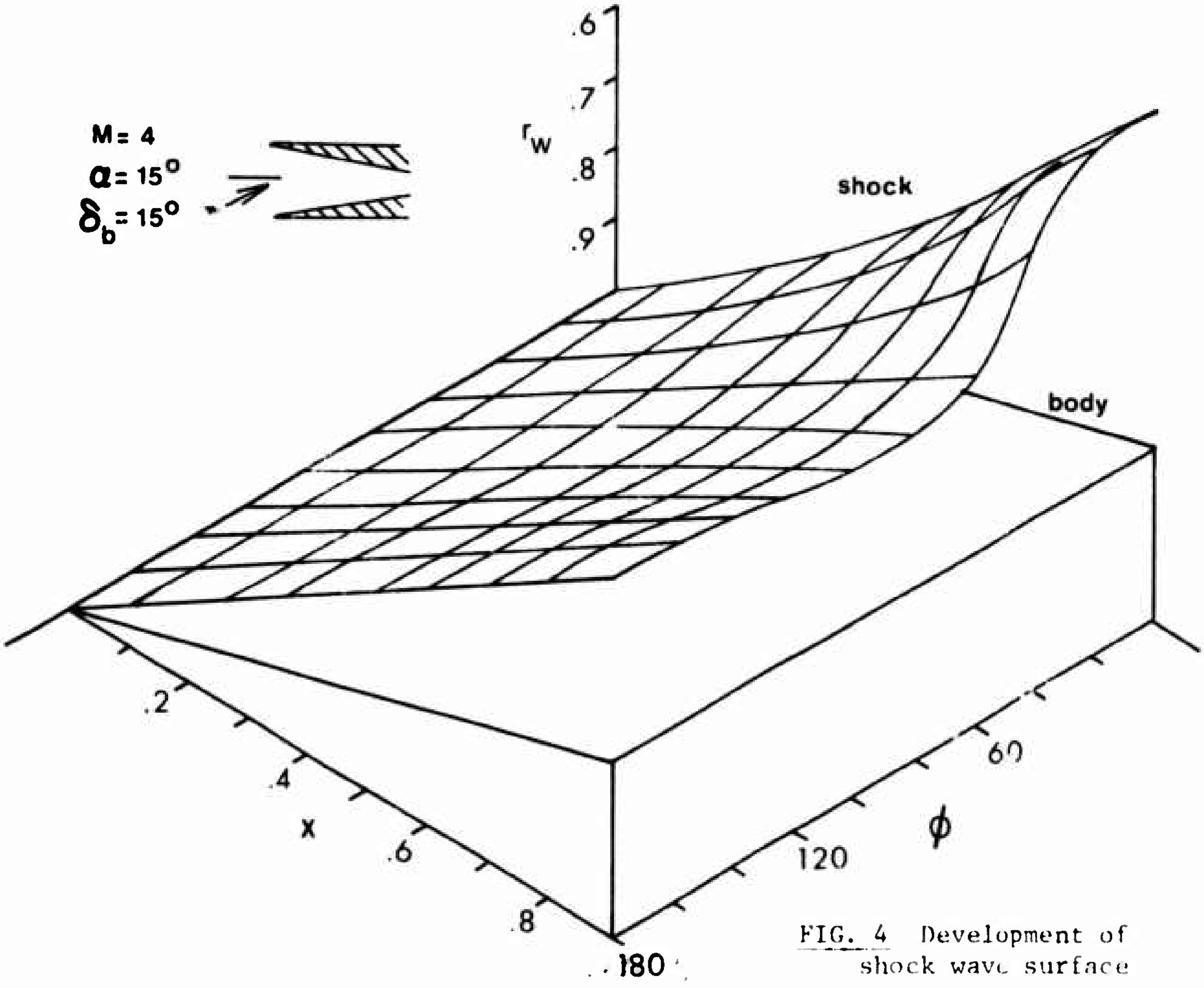

FIG. 4 Development of shock wave surface

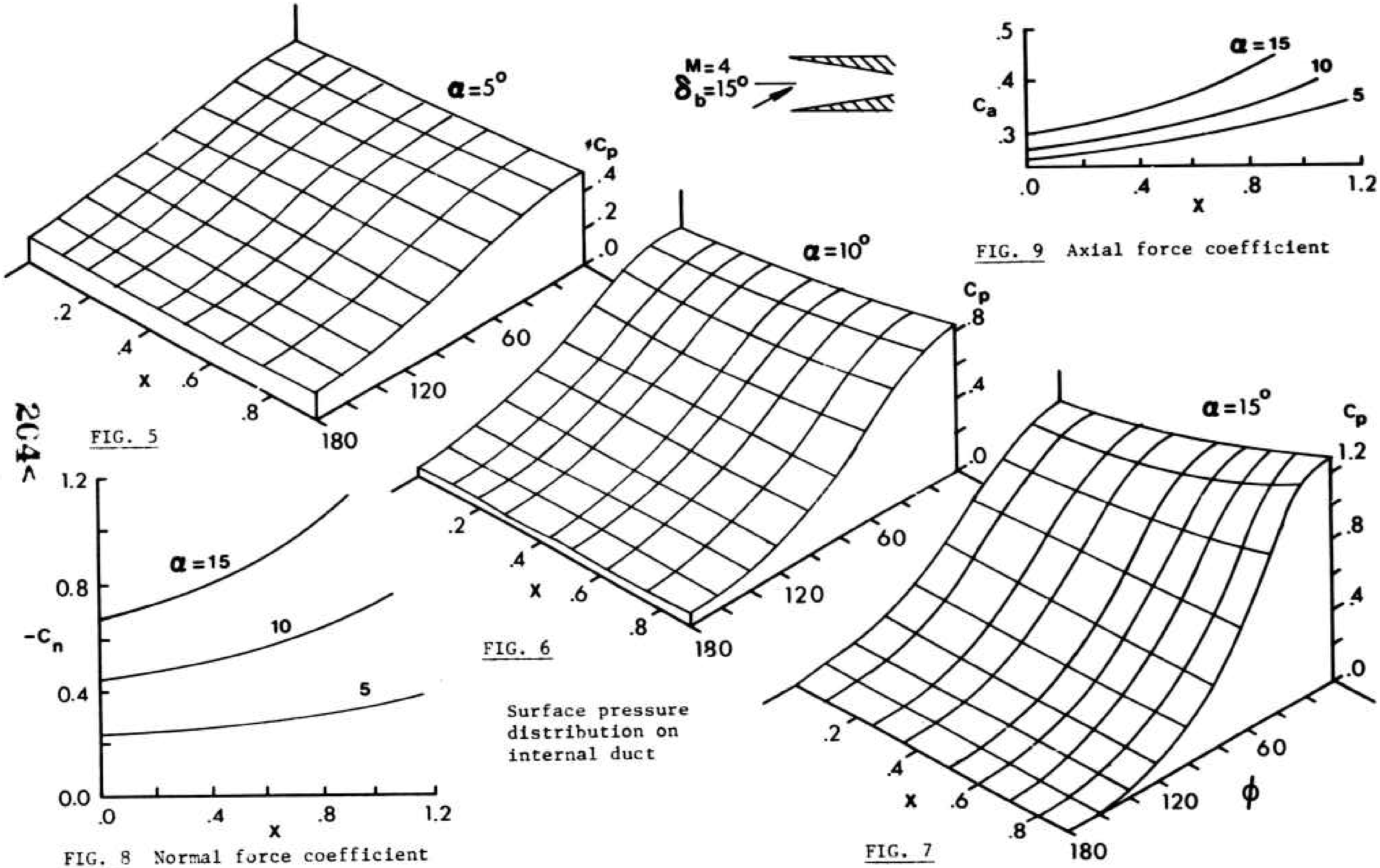

FIG. 5

FIG. 6

FIG. 7

Surface pressure distribution on internal duct

FIG. 8 Normal force coefficient

FIG. 9 Axial force coefficient

2C4<

INVESTIGATION OF SEPARATED FLOW OVER BODIES OF REVOLUTION IN SUPERSONIC INTAKE DUCTS.

Zakharov N.N.

Many works are devoted to the problem of separated flow. The authors of these works consider the conditions, under which separated flow is observed, and investigate the extention and configuration of separated regions. While investigating flows with separated zones, it is very important to study the methods of prevention the separation of boundary layer. The results of such investigations at low Mach and high Reynolds numbers and some experimental data at high Mach numbers and low Reynolds numbers for all kinds of influence on flow with separated zones are given in works (4-5).

The increase of Mach numbers of vehicles results in the considerable losses of their intake charecteristics, which are mainly caused by the increased influence of air viscosity. In this work the investigation of viscous supersonic flow was made on axial symmetric bodies representing a combination of an original cone with semi-angle $\beta_K=5^\circ$ and a flap, a generatrix of which in a meridional plane was formed along a circle arc smoothly matching with the cone or along the straight line (see the dash line on fig.I) inclined under angle α to the generatrix of the cone.

Besides, experiments on the models of axi-symmetrical intakes have been carried out.

Experimental research was made at the speeds of undisturbed flow corresponding to $M=6$. Reynolds number based on the parameters of undisturbed flow varied in the range of $Re=0.5X10^6-2.5X10^6$. The length of the cone generatrix to the matching point (fig. Ia) and that of the cone generatrix to the bending point of the central body (fig. Ib) were taken as charecteristic lengths. The conditions of the boundary layer flow were controlled by the temperature recovery factor on the surface of the body. The efficiency of the boundary layer control can be evaluated by the decrease of viscosity influence on the outer flow.

Outer flow disturbance is transmitted upstream along the subsonic sub-layer of the laminar boundary layer, which causes boundary layer thickening and at at significant disturbances its separation and outer flow distortion.

The problem of influencing boundary layer can be defined as a task of increasing its capacity to withstand high positive longgitudinal pressure gradients.

Static pressure distribution (refered to that on the cone) along the surface of the models with rectilinear generatrix of the flap and with the angle $\alpha=15^\circ$ (at the increase of surface cooling near separated zone) is shown on fig. 2.

The beginning of coordinates coincides with the bending point of the contour.

The dimension S in mm is countered along the surface of the body. These results correspond to Reynolds $Re = 0.5X10^{6}$. Numbers I,2,3 denote conditions (fig.2a) corresponding to different wall temperature ratio. The ratio of wall temperature and total flow temperature at the end of boundary layer. In the absence of wall cooling (curve I) in front of the flap a developed separated zone with the characteristic constant pressure level (the "plateau") is formed.

The increase of cooling intensity (fig. 2b) results in a monotonous decrease of the length of separated zone. At $T_w=0.15$ pressure distribution in front of the flap corresponds to practically unseparated flow. The decrease of size of separation zone is followed by the increase of pressure gradient in the region of flow reattachment. Numerous experimental research show (see reference 5) that the length of the separated zone on the adiabatic wall is determined by the values of M and Re numbers before the point of separation and "nonviscous" pressure value at the point of reattachment.

Development of separated zones on bodies with a curvilinear generatrix and in canals is characterized by the change of pressure P in the reattachment point with the change of the separated zone geometry.

That is why in these flows the influence on separated flow regions is stronger than on the bodies with rectilinear generatrixes in a free flow.

The character of the flow around the model with the curvilinear generatrix is shown on fig. 2b.

Pressure distribution in a meridional plane along the surface of the model is shown at the left (fig. 2b). Nondimensional pressure P is shown on a vertical axis. The distance measured along the axial symmetry of the body from the matching point of the cone and the curvilinear surface is shown on a horizontal axis. A solid line on fig.2 corresponds to pressure distribution calculated on modified Newton relation. A dash-and-dot line corresponds to pressure distribution calculated on Buseman equation and dashed one to that determined by the method of a normal wave. Curves of relative pressure (the ratio of pressure measured by Pitot tube and total pressure in a free flow) at the section of the beginning of pressure waves focussing ($X^{0}=1.9$) can be seen at the right (fig. 2b).

The pressure ratio after normal shock wave P^{0} is shown on a horizontal axis, the distance η in mm measured from the wall is shown on a vertical axis. The change of P^{0} for the ideal gas shown by a dash line (fig.2b). This was calculated on correlations on a simple wave. Sign 1 corresponds to experimental pressure values of the models shown on fig. 1a at

Re=0.5XIO^{6} with the extended separated zone on the surface. Sign 2 corresponds to experimental data when the surface is cooled.

One can see from the correlation of theoretical and experimental values of P and P^{o} that aerodynamic parameters at some temperature values of the wall correspond to an unseparated flow around the model. These values are close to the estimated data for the ideal gas.

The increase of the Reynolds number up to 2.5XIO^{6} also results in an unseparated flow around the curvilinear surface. Pressure distribution along the surface of the body at the value of Re=2.5XIO^{6} is shown on fig. 2b by sign 3. It coincides very well with the pressure distribution at Re=0.5XIO^{6} in case of cooling (T_w=0.I5). Temperature recovery factor r in the region of matching of conical and curvilinear surfaces was equal to 0.88, which proves that the flow regime in the boundary layer was transitional. Further increase of Reynolds number (Re > 2.5XIO^{6}) does not resultin a significant change in pressure distribution on the surface of the body. The supersonic flow in a canal with separated zones is illustrated on figs. 3 and 4. Pressure distribution along the central body in a meridional plane is shown on fig. 3 and fig.4 at the left.

The pressure ratio P is shown on a vertical axis. The distance measured along the axis of symmetry from the summit of the cone is shown on a horizontal axis.

At the right on figs. 3&4 one can see changes in the extention of the separated zone at different Reynolds numbers. The results of the investigation presented on fig. 3 are for laminar boundary layer.

The shock wave reflected from the cowling leads to a laminar boundary layer separation. Regions of the peak changes ofthe static pressure along the central body (fig. 3) nearly correspond to the regions of the reattachment of the flow. At Re=0.6XIO^{6} an extended separated zone with the point of flow attachment before the bending of contour is formed on a central body.

Pressure at the reattachment point P_+ is determined by the flow turning at $\omega=2(\beta_K+\theta_s)$ or $\omega\approx\beta_K+2\theta_s$ angle if the reattachment point is in front or behind the contour (a) bending point correspondingly.

For laminar flow the angle of the separated zone is determined by $\theta_s \sim Re^{-1/4}$. Thus at the increase of the value of Re number, pressure in an isobaric region and in the region of flowreattachment drops and the reattachment point moves downstream. At the same time the region of separated flow in front of the entrance plane monotonously changes with the Reynolds number increase. At Re= 2.88XIO^{6} the separated region is slowly moving downstream behind the contour bending.

If the boundary layer on the central body upstream of the intake entrance is not conserved laminar in the whole range of Reynolds, a nonmonotonous dependence l°(Re) is observed. With the increase of the Reynolds numbers separated zone decreases(fig. 4). At the same time the transition point in the intake canal begins moving upstream to the entrance plane. This flow is characterized by a symmetrical zone with non-curvilinear borders.

At $Re=0.9X10^6$ the transition point from one regime to the other reaches the intake entrance plane. With further increase of Reynolds number it begins influencing the outer flow in front of the entrance plane thus causing the extention of the separated zone.

The flow with an unsymmetrical separeted zone with curvilinear edge is characteristic of this range of Reynolds number change. At the turbulent flow on the conical surface of the central body separated zone begins to decrease. At the same time the separated zone becomes symmetrical

With further Reynolds number increase its insignificant change results in the sharp change of separated zone. At $Re=1.63X10^6$ separated zone moves behind the bending point of the central body of the model.

At the theoretical analysis of a supersonic intake starting in case of an ideal fluid the flow scheme with the normal shock wave is assumed.

However this scheme is significantly changed at the interaction of shock waves with influence on the boundary layer. Instead of a simple front shock wave, a shock wave in the form of   appears, which is further transformed into an inclined shock wave. It comes from the beginning of the separated zone to the frontedge of the intake cowling. The abovementioned phenomenon contributes to the following: for small semi-angles of the cone ($\beta_K=10^{\circ}$ to 12.5°) at high Mach numbers ($M=4.4$ to 5) and for laminar flow regime the throat area F_h which is necessary for intake starting (design flow in front of the entrance plane of the intake canal) decreases sharply at $1.5X10^6$ Re $2.4X10^6$ in comparison with F_h found at the assumption that the shock wave at the entrance and sonic speed in the throat exists (fig 3)

Central body cooling at the laminar flow regime in the boundary layer results in the decrease of the intake area at starting. Under these conditions the influence of the temperature factor T_w onF_h increases with Reynolds number decrease (fig. 5) .

The effect of heat exchange on starting and intake characteristics depends on the flow regime in the boundary layer. At the laminar boundary layer on the central body the extention of the separated zone in front of the entrance plane changes in proportion to temperature factor (fig. 6, sign 1,2). If transition from laminar to turbulent flow regime takes place on the central body near the separation point of the flow then the decrease of T_w leads to relamination of the boundary layer and to the increase of the separated zone before the entrance plane (fig. 6a, sign 3).

The analysis of the flow with a separated zone in a canal shows that the conservation of the linear size of separated zone is the condition of keeping its geometric similarity at Re and T_w

$$l^0(Re, T_w) = \text{constant}.$$

Let us assume that the pressure coefficient C_{p+} behind the region of the flow reattachment is proportional to the pressure coefficient of the throat behind the shock wave reflected from the cowling C_{ph}.

Then if one takes the approximated correlation for the linear size of the separated zone $l^0 = l/\delta^* \sim (C_{p+} - C_{p*})$ one can get the correlation between the Reynolds at starting and intensity of heat exchange T_w

$$\left[\frac{Re(\bar{T}_w)}{Re(1)}\right]^{\frac{3}{4}} - \left[\frac{Re(\bar{T}_w)}{Re(1)}\right]^{\frac{1}{4}} \varphi(M_H, \bar{T}_w) + \Psi(M_H, \bar{T}_w) = 0 \quad (1)$$

$$\varphi(M_H, \bar{T}_w) = \frac{a\bar{T}_w + b}{(1-\varepsilon)(a+b)} \bar{T}_w^{\frac{\nu-1}{2}}; \quad \Psi(M_H, \bar{T}_w) = \frac{\varepsilon}{1-\varepsilon} \frac{a\bar{T}_w + b}{a+b} \bar{T}_w^{\frac{3}{4}(\nu-1)}$$

$$a = 1 + \frac{K-1}{2} M_H^2; \quad b = \frac{13}{35} \frac{K-1}{2} M_H^2; \quad \varepsilon = \frac{C_{p*}(1, Re)}{C_{ph}};$$

$C_{p}*$ is the pressure coefficient in the region of the "plateau".

The calculation of $Re(T_w)/Re(1)$ values by the equation (1) for M=6 and ε =0 to 0.2 shows (fig.6, sign1) that starting Reynolds number in laminar flow regime decreases with the decrease of the temperature factor T_w.

Results of experimental investigations on intake models with the central bodies in the form of cones with the semiangle β_K=10° and F_h=0.210 to 0.454 are also demonstrated. Design data correspond to experimental ones.

The increase of the total turning angle of the flow (corresponding to the decrease of ε) reduces to a certain degree the influence of the temperature factor T_w on Reynolds number at starting.

At the transitional flow regime of separated zone the influence of wall cooling on Reynolds number at starting is rather weak if the regime does not change (fig. 6,sign2).

If the transition from the laminar to turbulent flow regime takes place on the central body near the point of flow separation, the decrease of temperature factor causes to decrease the Reynolds number at starting.

REFERENCES

I. CHAPMAN D.R., etc. Investigation of separated flow in supersonic and subsonic streams with emphasis on the effect of transition. NACA Rept., I958, No.I356.

2. ШЛИХТИНГ Г. Теория пограничного слоя. М. "Наука", 1969.

3. БОНДАРЕВ Е.Н. Отрыв пограничного слоя на конических телах.

Изв. Академии Наук СССР, МЖГ, 1969 №4

4. LEWIS J.E., KUBOTA T., LEES L. Experimental investigation of supersonic laminar two-dimensional boundary layer separation in a compression corner with and without cooling. AIAA Journal, I968, vol. 6, No. I.

5. ГРИНЬ В.Т., ЗАХАРОВ Н.Н. Экспериментальное исследование влияния тангенциального вдува и охдаждения стенки на течение с отрывом потока. Изв. АН СССР, МЖГ, 19719 №6.

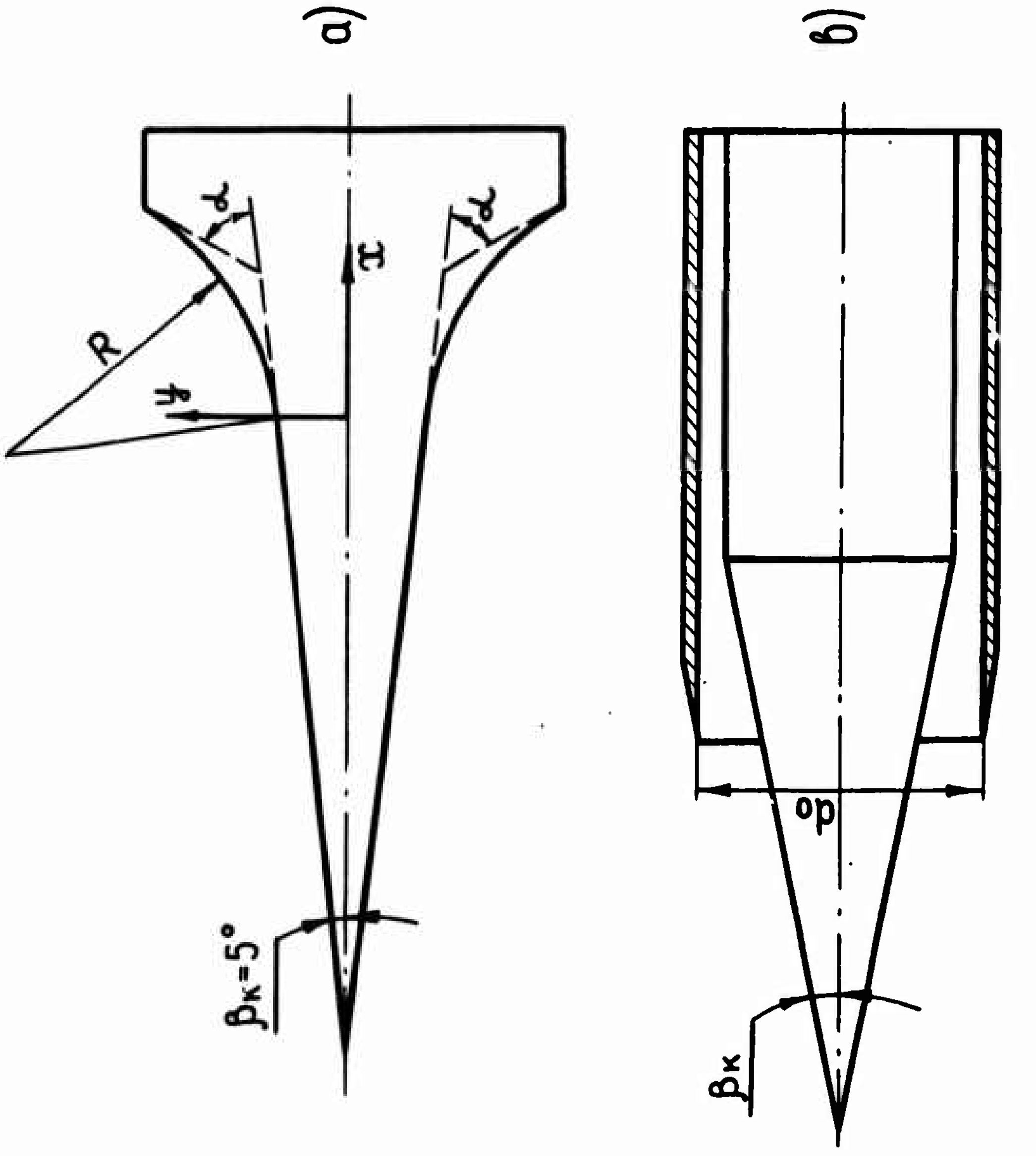
a)
b)
R
x
y
α
α
βк=5°
βк
d0

Fig. 1

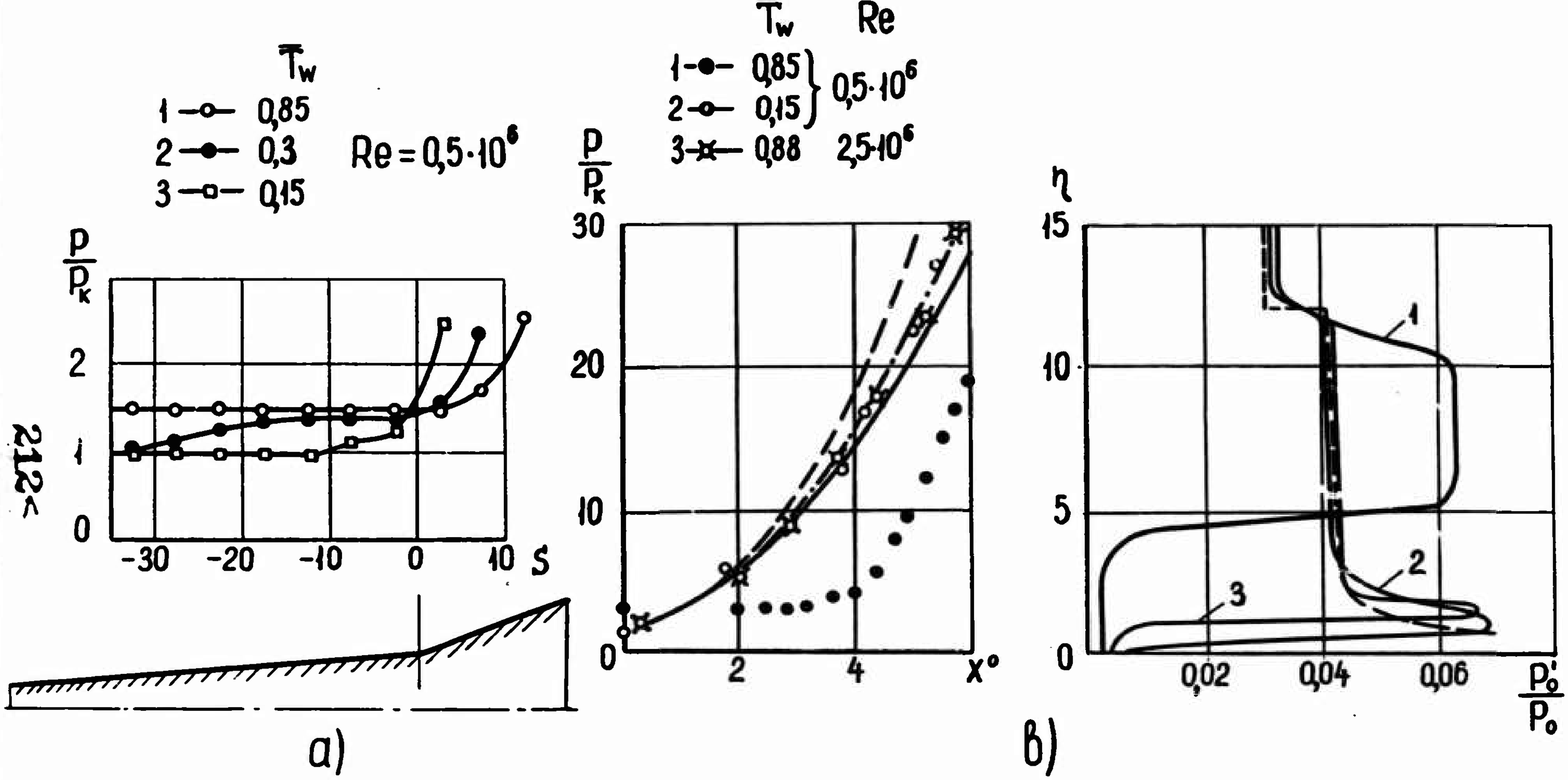
$\bar{T}_w$
1 —○— 0,85
2 —●— 0,3
3 —□— 0,15
Re = 0,5·10⁶
p/p_k
2
1
0
-30
-20
-10
0
10
S
a)
$\bar{T}_w$ Re
1-●- 0,85
2-○- 0,15 } 0,5·10⁶
3-☆- 0,88 2,5·10⁶
p/p_k
30
20
10
0
2
4
x°
η
15
10
5
0
0,02
0,04
0,06
p'_0/p_0
1
2
3
b)

Fig. 2

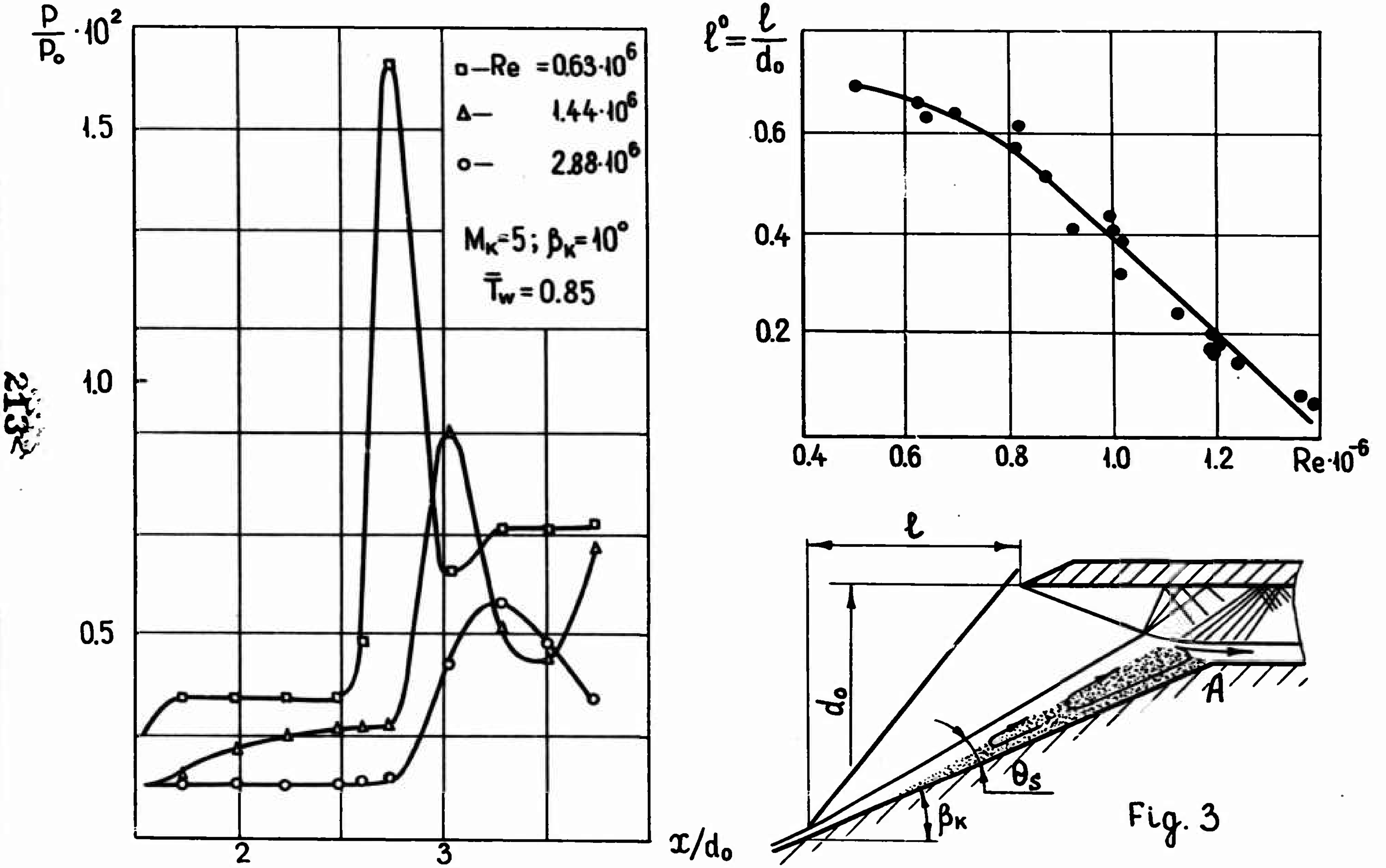
$\frac{p}{p_0} \cdot 10^2$
1.5
1.0
0.5
2
3
x/d_0
□—Re = 0.63·10^6
△— 1.44·10^6
○— 2.88·10^6
$M_K = 5;\ \beta_K = 10°$
$\bar{T}_w = 0.85$
$\ell^0 = \frac{\ell}{d_0}$
0.6
0.4
0.2
0.4
0.6
0.8
1.0
1.2
$Re \cdot 10^{-6}$
ℓ
d_0
A
θ_s
β_K

Fig. 3

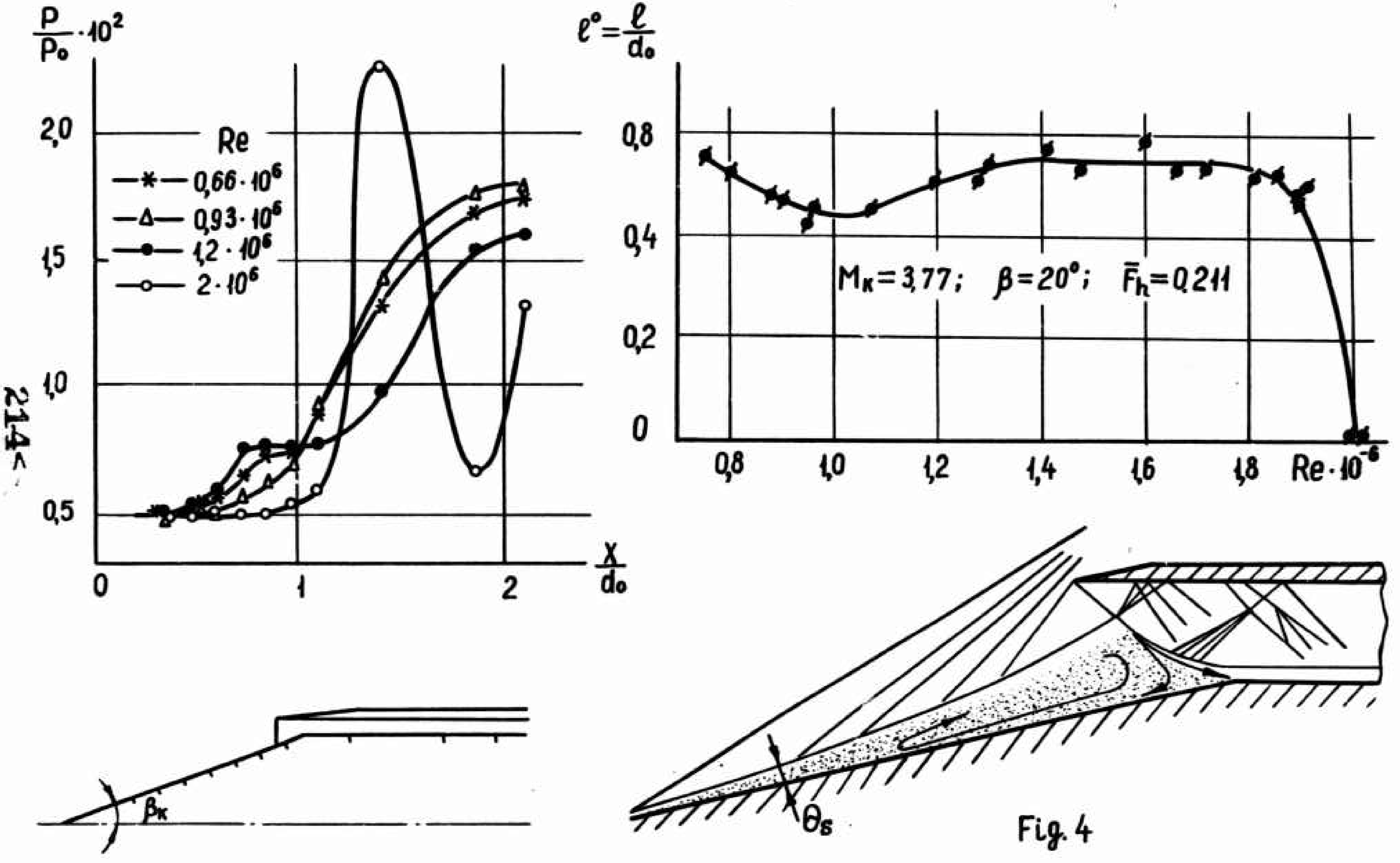
$\frac{P}{P_0}\cdot 10^2$
2,0
1,5
1,0
0,5
0
1
2
$\frac{x}{d_0}$
Re
0,66 · 10⁶
0,93 · 10⁶
1,2 · 10⁶
2 · 10⁶
$\ell^\circ = \frac{\ell}{d_0}$
0,8
0,4
0,2
0
0,8
1,0
1,2
1,4
1,6
1,8
Re · 10⁻⁶
$M_\kappa = 3{,}77$; $\beta = 20^\circ$; $\bar{F}_h = 0{,}211$
β_κ
θ_s

Fig. 4

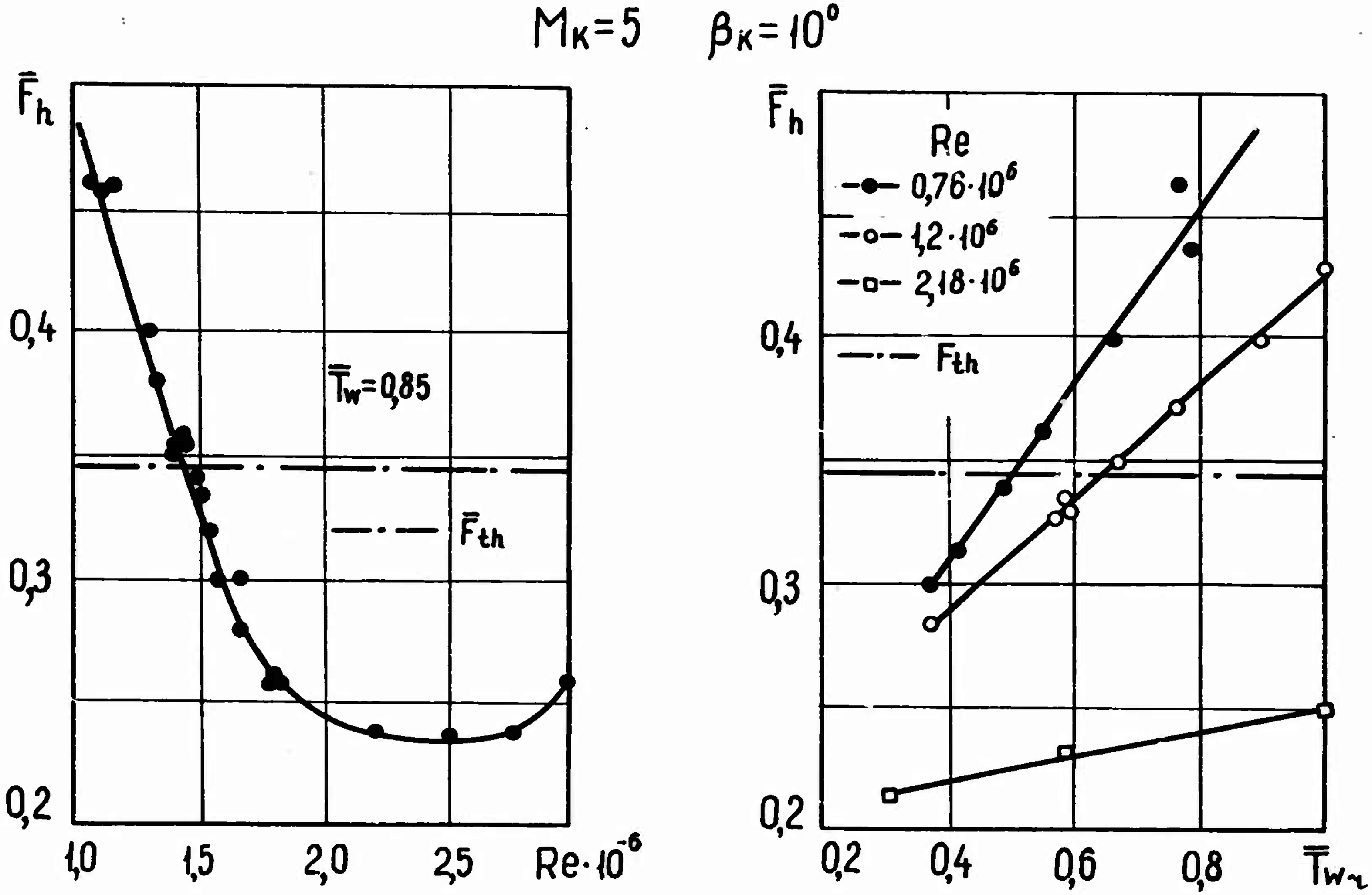
Mκ=5 βκ=10°
$\bar{F}_h$
0,4
0,3
0,2
1,0
1,5
2,0
2,5
Re·10⁻⁶
$\bar{T}_w$=0,85
$\bar{F}_{th}$
$\bar{F}_h$
Re
0,76·10⁶
1,2·10⁶
2,18·10⁶
$\bar{F}_{th}$
0,4
0,3
0,2
0,2
0,4
0,6
0,8
$\bar{T}_{w\sim}$

a) б)

Fig.5

$$\left[\frac{Re(\bar{T}_w)}{Re(1)}\right]^{3/4} - \left[\frac{Re(\bar{T}_w)}{Re(1)}\right]^{1/4} \phi(M_H, \bar{T}_w) + \psi(M_H, \bar{T}_w) = 0 \quad (1)$$

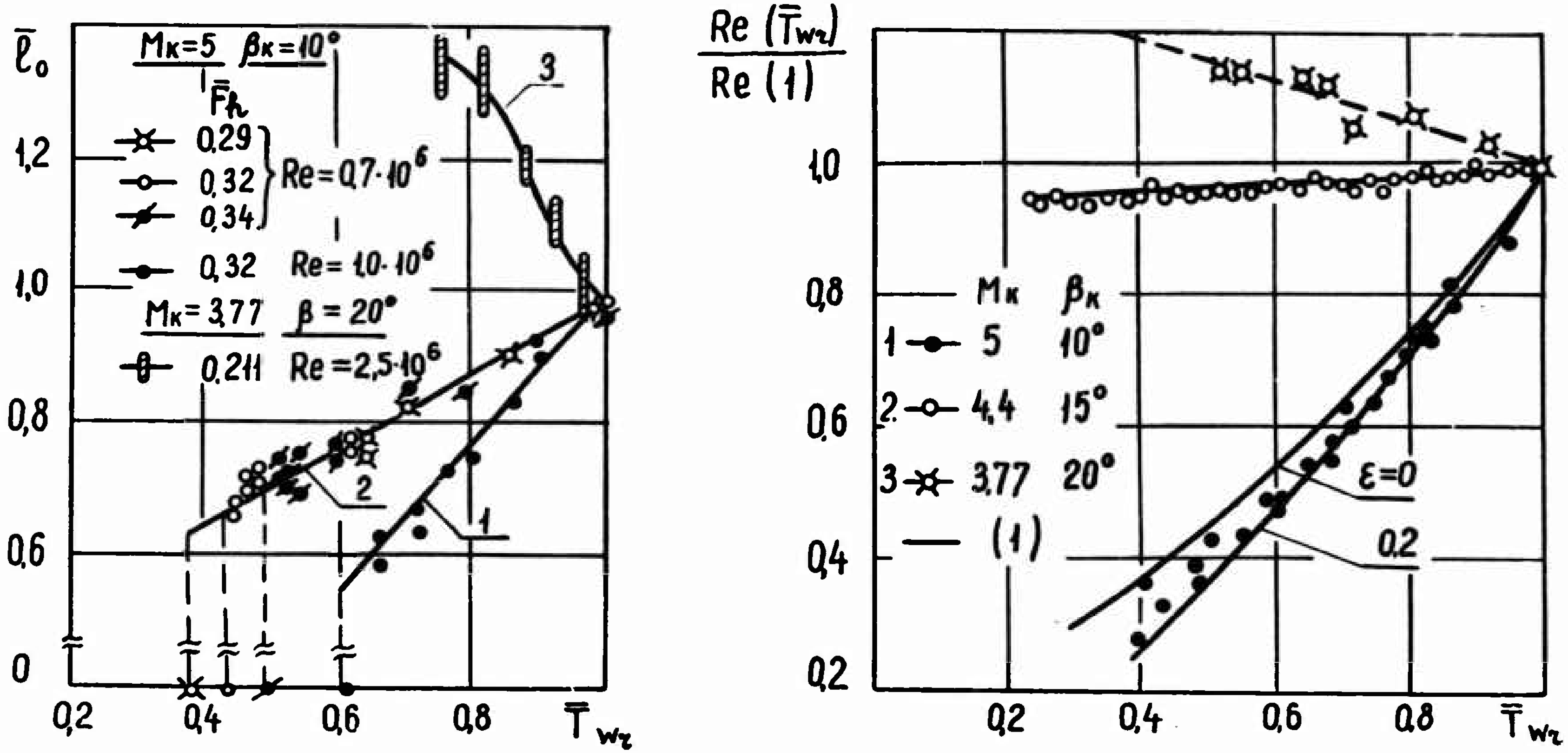

a)   в)

Fig.6

THREE-DIMENSIONAL WAVE INTERACTIONS IN SUPERSONIC INTAKES

R.K.Nangia

Aerodynamics Department, British Aircraft Corporation Limited,
Commercial Aircraft Division, Filton, Bristol, U.K.

SUMMARY

It is known that in intakes designed for supersonic flight, three-dimensional shock wave distortions and interactions are present. In general these effects are not easily avoided and may arise both in design and off-design conditions. Typical causes are intake location on the airframe and flow incidence or sideslip. Further complications also arise because of boundary layer.

This paper presents the results of an experimental programme designed to give better understanding of the simpler type of intake interactive flows. Models simulating free edge and corner flows were tested. The studies included fully compressive, "mixed" expansive-compressive, and fully expansive interaction flows. The interference wave structure was defined with the aid of surface statics and multi-tube pitot pressure rake measurements.

The application of this work to the design of air intakes for supersonic aircraft is discussed.

I. INTRODUCTION

Intakes designed on two-dimensional (2-D) principles are currently employed on a number of supersonic aircraft. In Fig. 1, a few typical installations, both fuselage side and underwing are illustrated. In some intakes the whole 2-D compression system is fully enclosed within the sidewalls, whilst in others, the sidewalls are either incomplete or begin downstream of the cowl-lip. The geometry of the basic 2-D compression system itself depends on the design Mach number of the intake (Fig. 2). For lower Mach numbers, external compression (i.e. ahead of the cowl) is used, whilst for higher Mach numbers, the current trend is towards the more efficient mixed type (i.e. external compression upstream of the cowl and internal compression downstream).

In this type of intake, interaction flows originate at the corners or free edges. These proceed downstream, expanding 'near conically' in cross-section and interfering with similar flows from other parts of the intake. Typical causes for these interactions are airframe intake interference and sideslip or incidence effects. The idealised 2-D shock structure is therefore not maintained either in "design" or "off-design" conditions. Korkegi(1) has reviewed some of the internal and external flow interactions. He has pointed out that in some cases, although regions of high compression or shock give rise to boundary layer flow separation and degradation of flow in an inlet, flow re-attachment can give rise to heat rates that far exceed those of attached boundary layer; this is particularly severe at hypersonic speeds.

To understand the complex flow structure in 2-D type intakes, a study of the simpler flows such as the corner flows and the free-edge flows on a wedge is a pre-requisite. The possibility of alleviating any adverse effects or preventing them at the onset can then be examined. Figs. 3 and 4 show the models necessary for study of such flows.

In Fig. 3, an assembly for investigating the conical corner flows is illustrated. In this model, the resulting interference flows may be classed as (i) Fully compressive, (ii) "Mixed", i.e. one surface producing compression and the other expansion, and (iii) Fully expansive, according to geometry. For the intakes, the flows of classes (i) and (ii) are more important, although the flows of class (iii) can arise in certain extreme off-design conditions particularly on fuselage side intakes.

Although many configurations are possible within these classes, most investigators have confined their study to the fundamental right-angled unswept compressive corner configuration of class (i). In this configuration, the interfering flow fields from the two plates are mutually perpendicular.

Fig. 4 shows a simple conical free edge model. The flows from both surfaces of the plate are matched across a free edge at some angle δ_T to the free stream. In the case of fuselage side intakes, this angle δ_T is related to aircraft incidence. This type of flow has received very little attention; although the effects can be very large, as will be seen later.

At this stage, it is useful to review the fundamental right-angled, unswept corner flows, since these give the first insight into the interference wave structure.

II. REVIEW OF FUNDAMENTAL WORK ON CORNERS

Experimental Considerations

Charwat and Redekeopp$^{(2)}$ investigated experimentally the unswept compression corner. They were mainly concerned with a 12.2° deflection model at Mach 3.17, although, limited results at other Mach numbers, wedge angles, and wedge intersection angles were also obtained. The Reynolds number of their tests was of the order of 0.75×10^7/m, and, ahead of the shock impingements, the boundary layer was laminar. They inferred a four-zone essentially conical interference wave structure (Fig. 5). The total extent of the interaction near the surface of the model was nearly twice that predicted by available small perturbation analyses. The zones identified were :-

Zone I - A region of conical flow bounded by a corner shock and two slip-surfaces (entropy waves or vortex sheets)

Zone II - A region of complex flow bounded by strong internal embedded ('inner') shocks

Zone III - An 'outer interaction region' characterised by a compression fan centered at the 'triple-shock' intersection point. The extent of this region was indicated from oil tests by the presence of an 'oil-accumulation' line

Zone IV - Undisturbed 2-D wedge flow

It is interesting to note that, for a typical 2-D intake, with the 'internal capture' area and cowl-lip located downstream of the two-dimensional wedge shock, the whole of the 'intake' flow field would be under the influence of the corner and lie wholly within Zones I and II of Fig. 5.

West and Korkegi(3) conducted tests on a 9.5^o unswept compression corner at Mach 3 through a Reynolds number range of 0.26 to 37×10^7/m. The main objective was to minimise the boundary layer displacement effects at high Reynolds number, and thus produce an improved indication of the inviscid shock structure. Fig. 6 summarises their work. It was found that Zone III although large at lower Reynolds numbers, did not extend as far as the 'triple-shock' intersection point. As the Reynolds number increased, the total extent of the interference decreased.

Theoretical Considerations

As far as calculation of the flow is concerned it is known that first and second order linear theories (Ref. 4) generally under-estimate the influence of corner flows, while the two-shock methods (Ref. 2) generally over-estimate the corner effects. Pike(5) and Goebel(6) have considered theoretical models of the inviscid compressive flow which require matching of pressure and flow direction only. The 'inner' (and 'outer') flow regions are not described, and, according to Korkegi(1) the uniqueness of this type of solution is open to some doubt.

Mikhaylov and Tamilov(7) have calculated a few corner flows at Mach 6 based on the three-dimensional finite difference scheme of Bohachevsky and Rubin(8). Both compression and expansion flow fields have been considered, but lack of sufficient detail in the original paper prevents any further discussion of their work.

More recently, Kutler(9) has presented an inviscid second-order shock-capturing finite-difference solution for the unswept intersecting wedges (Three-zone theoretical model - Fig. 7). His comparisons of the static pressure distributions and the wave structures for the configurations of Charwat and Redekeopp(2), and West and Korkegi(3) are shown in Fig. 8. The numerical results compare well with the high Reynolds number cases of the latter (Ref. 3)

To enable extension of this knowledge to 2-D sidewall type intakes of Fig. 1, it is necessary to include the effect of varying the leading edge sweepback of the sidewall. The sidewall field may be either in compression or expansion depending on the intake location on the aircraft and aircraft incidence or sideslip. Further, the interfering flow fields from the two plates will not be mutually perpendicular.

Similarly, it is important to understand the free edge flows for two-dimensional type intakes without sidewalls of Fig. 1.

With these objectives, an experimental programme using a series of corner flow and free edge models was started in 1969. The earlier work has been reported in Ref. 10, and the subsequent work will be published in due course. In this paper, brief details are presented of the experimental programme and the flow structure for the three types of corner flows and free edge flows.

III. EXPERIMENTAL PROGRAMME AND WAVE INTERACTION STRUCTURES

III.1 Models, Measurements and Testing

A series of 20.3 cm x 20.3 cm x 20.3 cm (8" x 8" x 8") right-angled corner flow models were built. In Fig. 9(a) to (c), three typical models are illustrated. The configurations were chosen from :-

base (or horizontal) plate leading edge sweepback $\phi_H = 0^\circ$
edge angle $\eta_H = 7.5^\circ$
surface deflection $\delta_H = 7.5^\circ$ (compression)

vertical plates leading edge sweepback $\phi_V = 0^\circ, 30^\circ, 45^\circ, 60^\circ$
edge angle $\eta_V = 4^\circ$
surface deflection $\delta_V = +7.5^\circ, +5^\circ, +2.5^\circ$ (compression)
$-2.5^\circ, -5^\circ$ (expansion)

The range of sweepback variation of the vertical plates included nominally supersonic and subsonic leading edges.

For studying free edge flows, three base plates with free edge angles $\delta_T = -7.5^\circ$ and -5° (cut-back) and $+5^\circ$ (cut-forward) were used.

Model testing at Mach 1.65, 2 and 2.8 was carried out in the 0.69 m x 0.76 m (26" x 30") supersonic wind tunnel at A.R.A. (Bedford). The main emphasis was on the Mach 2 testing. Typical test conditions were :-

Wind tunnel stagnation pressure - 1 Atmosphere
Reynolds Number 0.99×10^7/m (3.0×10^6/ft)

Surface static and pitot pressure measurements were made in a cross-flow plane 3.81 cm (1.5") downstream of the corner apex. Static tappings up to a maximum of 30 at 2.54 mm (0.1") pitch were provided in each plate. The pitot measurements were made with a traversing rake (2 to 4 banks of 30 to 50 tubes in each bank at 2.54 mm (0.1") pitch set parallel to the base plate (see Fig. 9(b) and (c)). This rake in its full configuration and through its complete movement covered an area approximately 10.4 cm x 10.4 cm (4" x 4") in the cross-flow plane. The wave structure was deduced from pitot pressure contours (steps of 0.01 in the ratio of local pitot pressure to the tunnel total pressure P/P_0).

As far as possible, the boundary layer on the model was made artificially turbulent by means of "transition" strips near the model leading edges.

III.2 Compressive Corner Flows (Class (i))

The Mach 2 compressive flows with variations of leading edge sweepback of the vertical plate ($\phi_V = 0^o, 30^o, 45^o$ and 60°), are illustrated in Figs. 10 and 11. Surface static and contours from pitot pressure distributions are both presented. Fig. 10 refers to tests with vertical plate compression $\delta_V = +7.5^o$ and Fig. 11 with $\delta_V = +5^o$. The horizontal base plate is unswept ($\phi_H = 0^o$) and produces compression $\delta_H = +7.5^o$ in all cases. It is observed that :-

(1) For the "symmetric" case - Fig. 10 (a), the shock structure confirms the pattern observed by West and Korkegi(3). The surface static pressure distribution illustrates a gradual merging of the wedge flow field with the corner flow field through the "inner" shock impinging on the turbulent boundary layer. The corner static pressure is approximately 1.5 times the undisturbed wedge static pressure i.e. about $10^o - 11^o$ effective compression is indicated. It may be mentioned in passing that slight asymmetries in the shock structure near the boundary layer are apparent; these are due to increased local interference when the lower bank of the pitot rake is in the proximity of the base plate.

(2) With δ_V decreasing, the corner influence on the wedge flow field decreases, e.g. for the unswept configuration of Fig. 11 (a) the corner static pressure is about 1.25 times the undisturbed wedge static pressure i.e. indicating about 9.5^o effective compression (see above).

(3) There is no shock impingement on the vertical plate for the configurations with $\phi_V = 45^o$ and 60°. The leading edge is effectively subsonic. On the base plate the impinging shock weakens as ϕ_V increases.

(4) The interference region decreases as ϕ_V increases.

(5) The corner static pressure decreases with increasing sweepback ϕ_V.

III.3 "Mixed" Corner Flows (Class (ii))

The Mach 2 "mixed" corner flows with variation of leading edge sweepback of the vertical plate ($\phi_V = 0^o, 30^o, 45^o$ and 60°) are illustrated in Fig. 12. The vertical plates produce expansion of $\delta_V = -5^o$ and the horizontal base plate is unswept ($\phi_H = 0^o$) and set at compression $\delta_H = +7.5^o$ in all cases. It is observed that :-

(1) The expansion contours were not purely expansive and showed a region of weak compression just upstream, due possibly to a finite radius at the plate leading edge.

(2) For the unswept configuration - Fig. 12(a), in the interference region, the base wedge shock is drawn nearer to the corner under the influence of the expansion flow from the vertical plate and the contours of the expanded flow move outwards under the influence of the wedge field. The static pressure distributions confirm these movements.

Thus, the static pressure jump corresponding to the shock impingement on the vertical plate is about 40% lower than the ideal 2-D base wedge shock location. The corner static pressure is about 0.78 of the wedge static pressure, i.e. only about 2° of effective compression.

(3) The pattern depends on the leading edge condition of the vertical plate. When the leading edge is supersonic, the wedge shock is deflected towards the corner under the influence of the expansion fan from the vertical plate. When the leading edge is subsonic, a "vortex" type flow field is present near the leading edge.

(4) Shock impingement on the vertical plate (indicated by a jump in the static pressure) is apparent for all sweepback angles. It is always lower than the 2-D shock location. For $\phi_V = 60°$ the impingement is almost 50% lower than the 2-D shock location. Furthermore the strength of the impinging shock appears to increase in strength with increasing ϕ_V.

(5) The interference region decreases as sweepback ϕ_V increases.

(6) The corner static pressure rises as the sweepback ϕ_V is increased.

III.3 "Expansive" Corner Flows (Class (iii))

Fig. 13 shows an example of Mach 2 "symmetric" flow, where both surfaces sweptback at $\phi_V = \phi_H = 12.5°$ are arranged to produce equal expansions of $\delta_V = \delta_H = -5°$. In the interference region both expansions are displaced nearer to the corner. The corner static pressure is approximately 0.79 of the "unperturbed" static pressure thus indicating that the effective expansion is about -8.8° in the corner. As mentioned earlier, this type of flow may arise in certain extreme off-design flow conditions on fuselage side intakes.

III.4 Free Edge Flows

Fig. 14 shows the wave structure and static pressure distribution on two 7.5° wedges. Fig. 14(a) refers to a wedge with cut-back edge ($\delta_T = -7.5°$) and Fig. 14(b) to a wedge with cut-forward edge ($\delta_T = +5°$). Static pressure distributions are compared in Fig. 14(c). As stated earlier, using such a model, the effect of incidence on a fuselage side intake can be simulated. From the wave structures it is noted that the wedge shock curves down under the influence of the free edge. The flow is far from two-dimensional. The static pressure distributions show that the extent of interference is larger than that predicted on the basis of Mach cones of either upstream flow or downstream wedge flow. The cut-forward edge gives nearer to 2-D conditions than the cut-back edge.

For the cut-back edge, the static pressure at the edge is about 0.75 of the wedge pressure i.e. indicating an equivalent compression of 1.7° only. For the cut-forward edge, the corresponding values are 0.84 and 4°. These values are comparable to those arising in "mixed" corner flows.

IV. WAVE STRUCTURES IN EMPIRICAL DESIGN OF 2-D TYPE SUPERSONIC INTAKES

The philosophy of intake design for sustained supersonic flight has been discussed in several papers (e.g. Rettie and Lewis(11), VanDuine, Rhoades and Swan(12) and Antonatos, Surber and Stava(13). An important requirement is that the flow presented to the engine, after being compressed be as free from distortion and at as high a recovery as possible. Performance requirements dictate that the external installation drag (spillage drag) should be as small as possible. This implies conditions close to shock on lip (i.e. maximum capture). It is implied that for 2-D type intakes, an important idea to be aimed for is to obtain a uniform (2-D) flow distribution downstream of the front-wedge (i.e. after the first stage of compression) in which the subsequent compression with hinged ramp and cowl-lip can also be designed to operate on 2-D principles.

It is easy to see that to maximise the capture area for a 2-D type intake the cowl-lip will lie just under the 2-D shock position. At Mach 2, the present results suggest a cowl-lip location at an angle of 38.45° and $\mathfrak{z}/x = 0.793$. Any departure from two-dimensionality and uniformity of flow will modify this criterion.

An attempt can be made to examine how the presence of a sidewall or free edge modifies the basic 2-D wedge flow field (i.e. the first stage of intake compression) and therefore also leads to the modification of the Mach number - capture area relationships. Whilst these effects may not be important at design conditions, when the sidewall or free edge influences may be small, they become important at off-design conditions such as sideslip or incidence (depending on how the intake is mounted) due to increased flow turning. For this demonstration and within the constraints of present experimental data, it must be assumed that the flow field is not subject to any additional effect due to another sidewall or a free edge.

Three capture areas (one larger than 2-D and the other two smaller) with the following geometry relationships are considered :-

Shock to cowl lip angle	$\mathfrak{z}/X$	$A_\infty/A_{\infty_{2-D}}$
30.75	0.598	0.7
36.20	0.732	0.86
40.75	0.863	1.08

The significance of using these capture areas and the relationships to cowl location may be aided by referring to Fig. 15(a) to (d). In Fig. 15(a), the cowl-lip locations correspond to varying capture areas A_∞, for a fixed length of the intake. In Fig. 15(b), the various cowl-lip locations show variation in the length of the intake required to keep the capture area A_∞ fixed. In both these cases decreasing $\mathfrak{z}/x$ implies increasing supersonic flow spillage along the span of the cowl lip. Fig. 15(c) and (d) show the effect on intake size (based on above $\mathfrak{z}/x$ values and square capture areas) with respect to the corner and free edge configurations.

In Fig. 16, for four corner configurations at Mach 2 ($\delta_H = +7.5^\circ$, $\phi_v = 45^\circ$ and 60°, $\delta_v = +5^\circ$ and -5°), the pitot tube pressures around the perimeter of the three capture areas have been plotted against the angular displacement from a datum through the centre of the capture area. To provide a reference, the pitot levels for $+7.5^\circ$ compressive flow, freestream at Mach 2, and -5° expansion are also indicated. Similar information for the two free edge flows ($\delta_T = -7.5^\circ$ and $+5^\circ$) at Mach 2 is presented in Fig. 17, only two capture areas ($z/x = 0.598$ and 0.732) have been considered.

From the corner configurations of Fig. 16, it is observed that :-

(i) The largest capture area ($z/x = 0.863$) includes part of the freestream for both compressive and mixed flow configurations and the distortion therefore indicated by the overall amplitude is very large.

(ii) In the case of compressive sidewall configuration, the pressure distribution around the perimeter is on the average higher than the ideal 2-D flow ($\delta_H = +7.5^\circ$).

(iii) On the expansion sidewall configuration the corresponding pressure distributions give a lower average, and distortion increases with increasing capture size, particularly near the cowl-lip region.

(iv) Increase in leading edge sweepback also reduces the amplitude of distortion.

Taking next the free edge flows (Fig. 17), it is noted that :-

(i) The average level of compression in the flow field is much less than the 2-D value ($\delta_H = +7.5^\circ$)

(ii) Cutting back at the free edge worsens the situation; adjacent to the edge a localised region of expansion is found.

It may be concluded from these illustrations that :-

(a) In the corner configuration, the vertical wall provides a sensitive means of controlling the average pressure level and the amplitude of distortion. This amplitude of distortion is less with a compressive sidewall.

(b) In the free edge situation, the average pressure levels are less than the 2-D levels and the cut-forward edge provides an improved flow field.

(c) Extension of the work to more complex configurations (i.e two sidewalls, hinged ramps, etc. - Fig. 18) is recommended.

(d) The non-uniform flow effects due to the airframe, particularly in a critical area such as the cowl-lip can be compensated to a large degree by the appropriate design of the front part of the intake. Further work could throw more light on this aspect of design. Extensions of theoretical methods to some realistic configurations would be a considerable advantage.

V. CONCLUDING REMARKS

It has been shown that, as a result of the location of a 2-D type intake on the airframe, combined with flow incidence or sideslip effects, the basic 2-D flow structure is subject to interaction from the corners or free edges. The main characteristics of the simpler interaction flows based on a series of experimental models have been described briefly.

A method of using this information in the empirical design of the corners and free edges associated with 2-D supersonic intakes has been illustrated. Further work in this field has been suggested.

It is hoped that the knowledge of the wave interaction structures will facilitate the development of satisfactory methods of calculation.

ACKNOWLEDGEMENTS

The author wishes to acknowledge the support given by the National Gas Turbine Establishment (Pyestock), the Aircraft Research Association (Bedford) and the British Aircraft Corporation (Filton) towards work presented in this paper. The opinions expressed are however, the author's own.

REFERENCES

1. KORKEGI, R.H., Survey of Viscous Interaction associated with High Mach Number Flight. AIAA J, Vol. 9, No. 5, pp 771-784 May 1971

2. CHARWAT, A.F. and REDEKEOPP, L.G. Supersonic Interference Flow along the Corner of Intersecting Wedges. AIAA J, Vol. 5, No. 3, pp 480-488. March 1967.

3. WEST, J.E. and KORKEGI, R.H., Supersonic Interaction in the Corner of Intersecting Wedges at High Reynolds Numbers. AIAA J, Vol. 10, No. 5, pp. 652-656, May 1972.

4. WALLACE J., and CLARKE, J.H., Uniformly Valid Second Order Solution for Supersonic Flow over Cruciform Surfaces. AIAA J, Vol. 1, No. 1, pp. 179-185, January 1963.

5. PIKE, J, Private Communication December 1970
The Flow past Flat and Anhedral Delta Wings with Attached Shock Waves. RAE TR - 71081, April 1971.

6. GOEBEL, T.P., A Theoretical Study of Inviscid Supersonic Flow along a Corner formed by Intersection of Two Wedges. Ph.D. Thesis, 1969, University of California, Los Angeles.

7. MIKHAYLOV, V.N. and TAMILOV, V.S., Supersonic Flow in a corner formed by Intersecting Plates. NASA-TT-F-14537, September 1972.

8. BOHACHEVSKY, J.O. and RUBIN, E.L. A Direct Method for Computation of Non-Equilibrium Flows with Detached Shock Waves. AIAA J, Vol. 4, No. 7, July 1966.

9. KUTLER, P., Numerical solution for the Inviscid Supersonic Flow in the Corner formed by two intersecting wedges. AIAA Paper 73-675, 1973.

10. NANGIA, R.K., Conical Interference Structure in Supersonic Streamwise Flows. Secondary Title - Wall Effects on the Front Wedge Flow Field in Supersonic Intakes. B.A.C. Filton/Aero/Rep/100, March 1972.

11. RETTIE, I.H. and LEWIS, W.G.E., Design and Development of an Air Intake for a Supersonic Transport Aircraft. J. of Aircraft, Vol. 5, No. 6 pp. 513-521, November-December 1968.

12. VanDUINE, A.A., RHOADES, W.W. and SWAN, W.C., Configuration Aspects of Propulsion Installation on Supersonic Transports. AGARD CP 71-71, 1971.

13. ANTONATOS, P.P., SURBER, L.E., and STAVA, D.J., Inlet/Airplane Interference and Integration. AGARD LS-53, 1972.

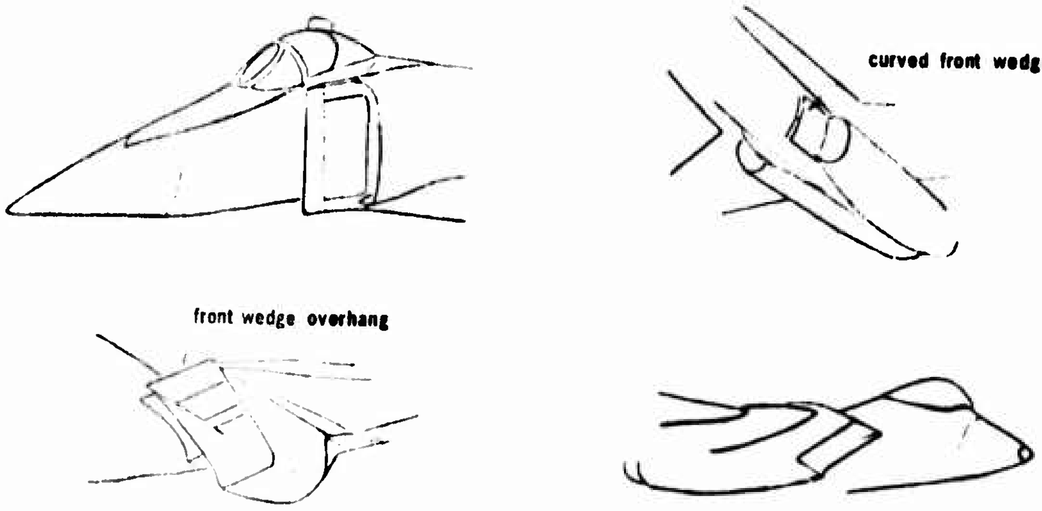
curved front wedge
front wedge overhang

Fuselage Side

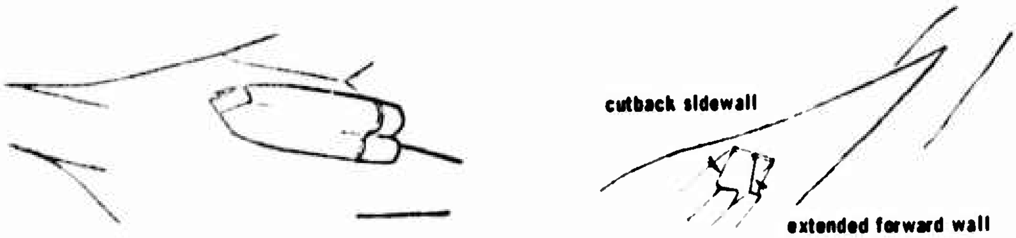
cutback sidewall
extended forward wall

Underwing

FIG. 1. TYPICAL INTAKE INSTALLATIONS ON SUPERSONIC AIRCRAFT

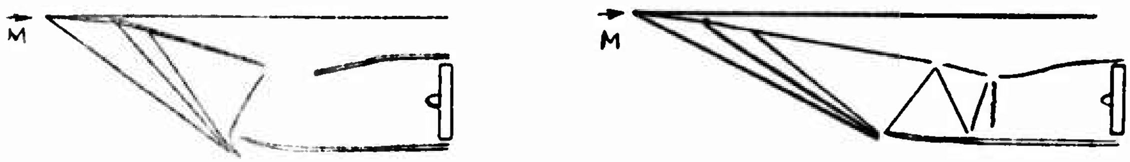

External Compression
(Lower Mach)

Mixed Compression
(Higher Mach)

FIG. 2. INTAKES DESIGNED ON TWO DIMENSIONAL PRINCIPLES

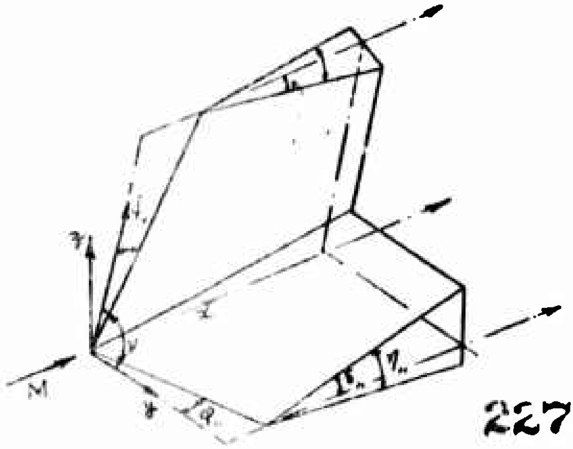

227<

FIG. 3. CORNER FLOW MODEL

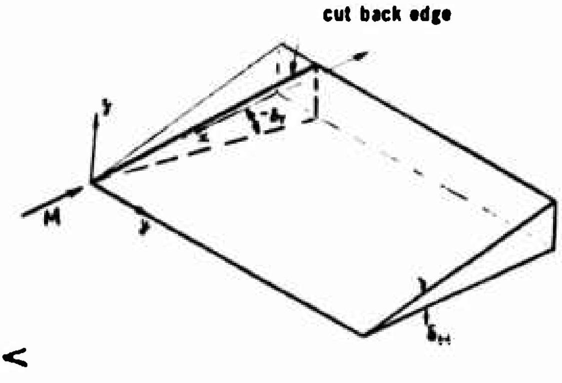
cut back edge
M

FIG. 4. FREE EDGE FLOW MODEL

(a) MODEL WITH UNSWEPT LEADING EDGES

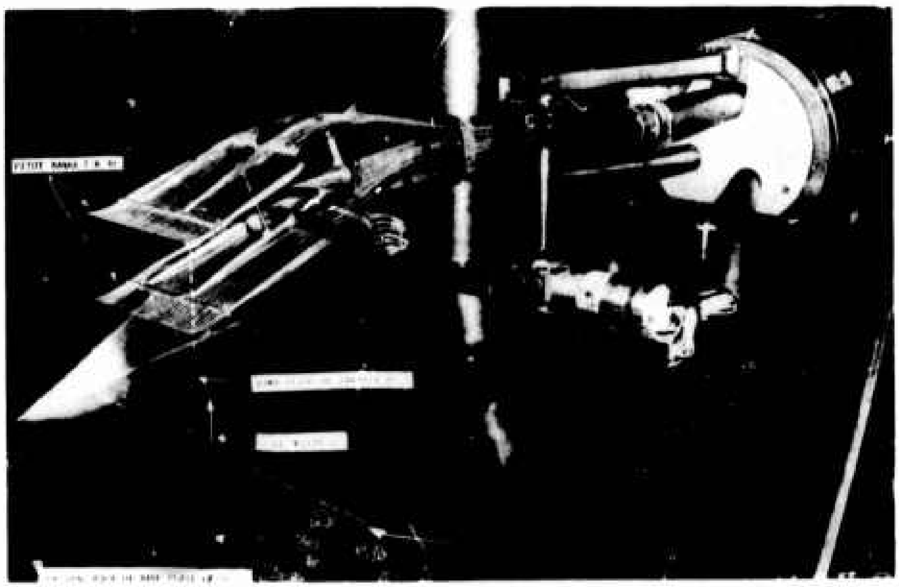

(b) ONE SWEPTBACK SIDEWALL MODEL WITH 2 - TIER RAKE

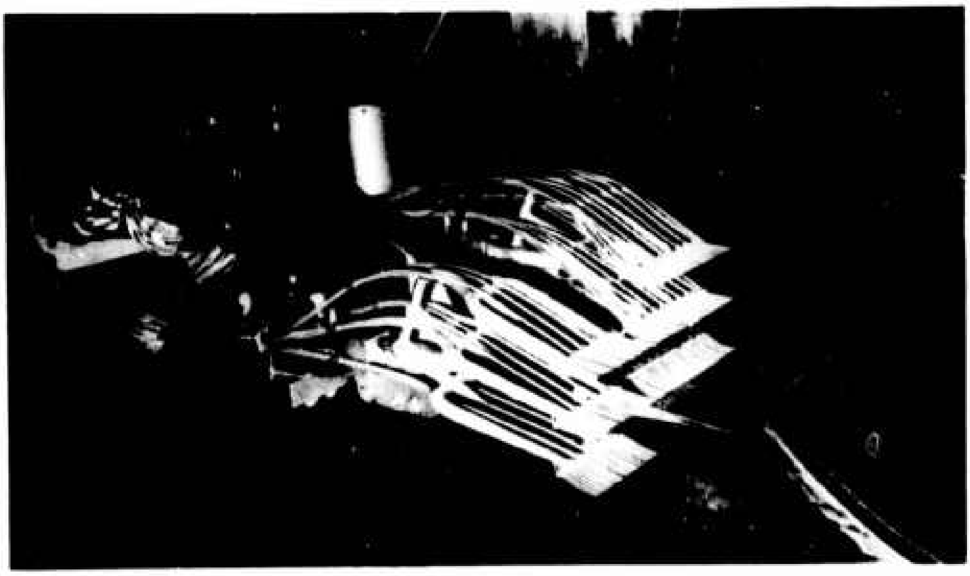

(c) FREE EDGE FLOW MODEL WITH 4 - TIER RAKE

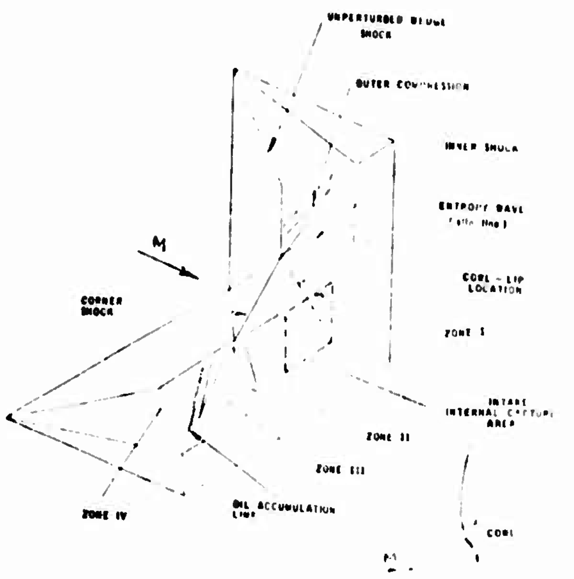
UNPERTURBED BLUNT SHOCK
OUTER COMPRESSION
INNER SHOCK
ENTROPY WAVE (slip line)
COWL - LIP LOCATION
ZONE I
INTAKE INTERNAL CAPTURE AREA
ZONE II
ZONE III
ZONE IV
OIL ACCUMULATION LINE
CORE
CORNER SHOCK
M

FIG. 5 WAVE STRUCTURE ACCORDING TO CHARWAT AND REDEKEOPP

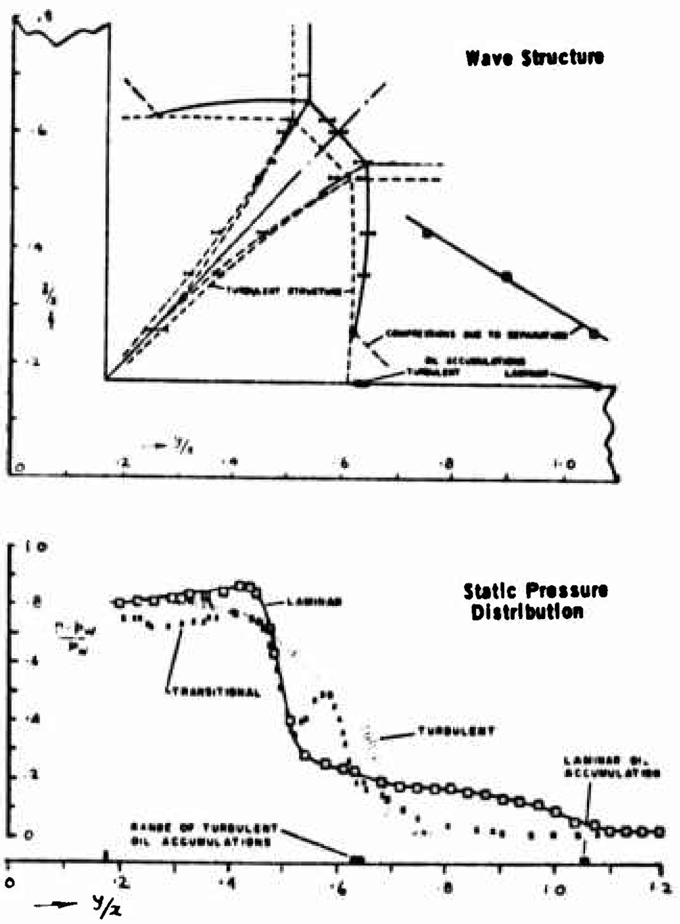

FIG. 6 SUMMARY OF THE EFFECTS OF REYNOLDS NUMBER ACCORDING TO WEST AND KORKEGI

$M = 3, \quad \delta_H = \delta_V = 9.5°$

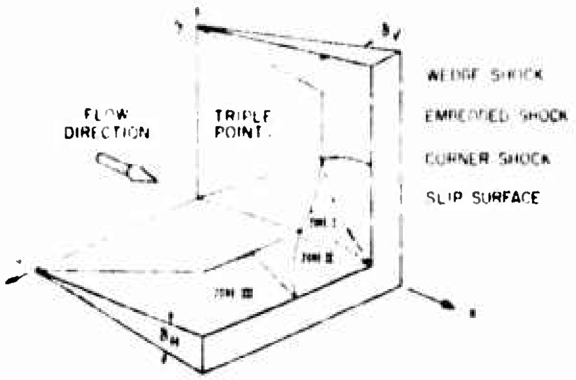
FLOW DIRECTION
TRIPLE POINT
WEDGE SHOCK
EMBEDDED SHOCK
CORNER SHOCK
SLIP SURFACE
ZONE I
ZONE II
ZONE III
δ_V
δ_H
y
z
x

FIG. 7. THEORETICAL MODEL OF KUTLER

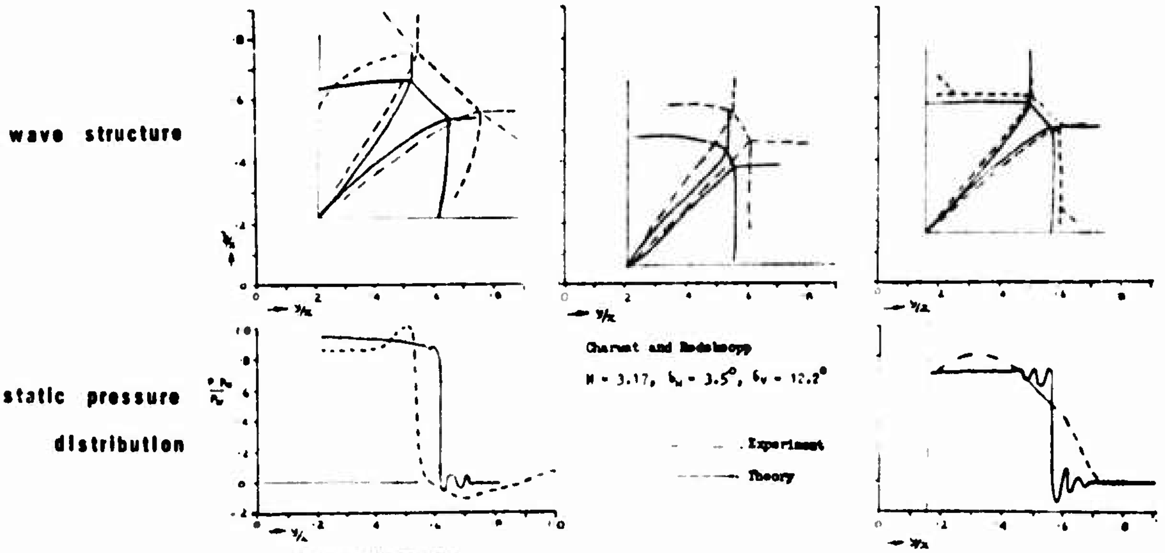

Charwat and Redekeropp
$M = 3.17, \ \delta_H = 3.5°, \ \delta_V = 12.2°$

Experiment
Theory

Charwat and Redekeopp
$M = 3.17, \ \delta_H = \delta_V = 12.2°$

West and Korkegi
$M = 3, \ \delta_H = \delta_V = 9.5°$

229<

FIG. 8. COMPARISONS BETWEEN THEORY OF KUTLER AND EXPERIMENTS OF CHARWAT AND REDEKEOPP AND WEST AND KORKEGI.

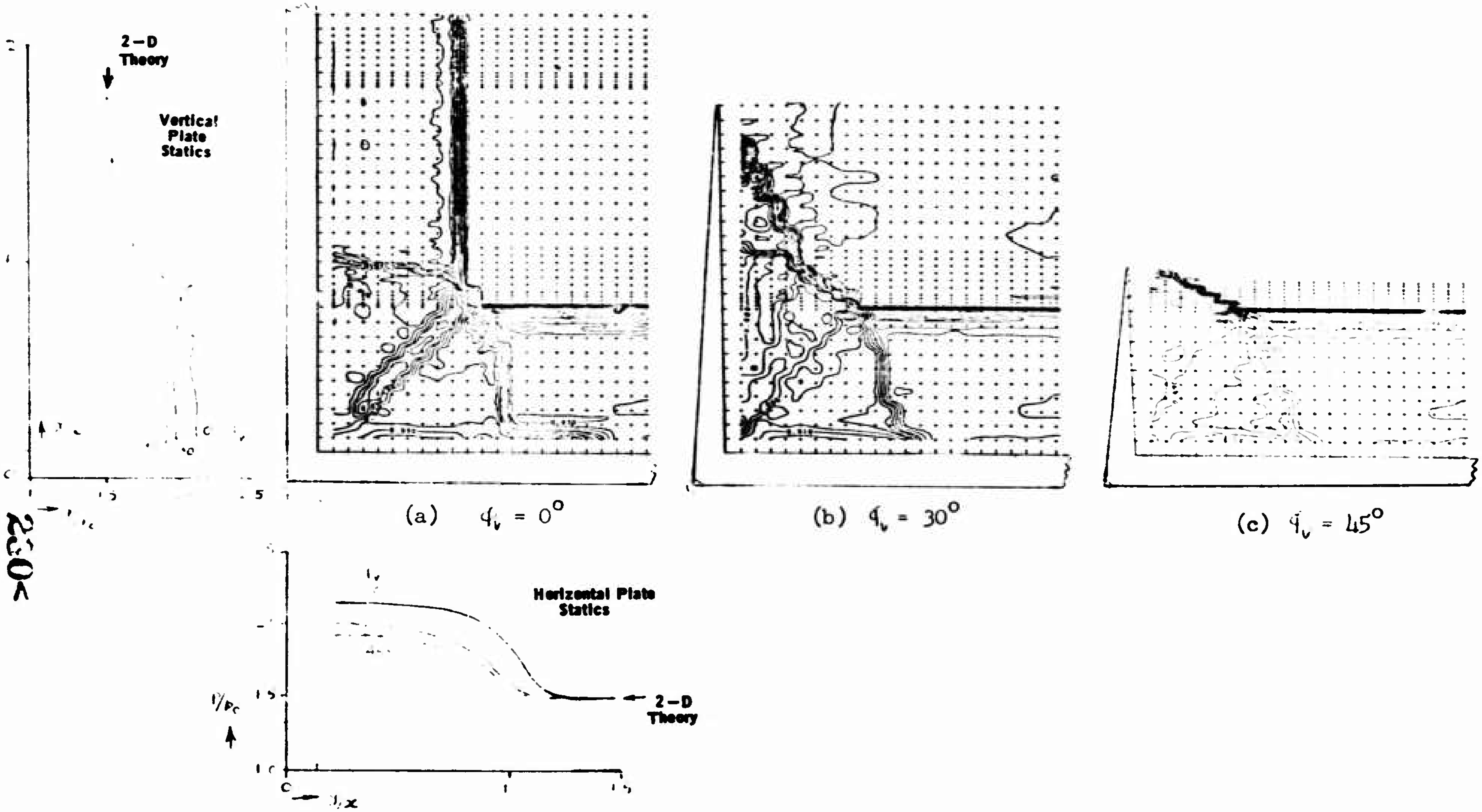

(a) $\phi_v = 0^\circ$ (b) $\phi_v = 30^\circ$ (c) $\phi_v = 45^\circ$

FIG. 10 COMPRESSIVE CORNER FLOWS

$M = 2, \ \phi_H = 0^\circ, \ \delta_H = +7.5^\circ, \ \delta_V = +7.5^\circ$

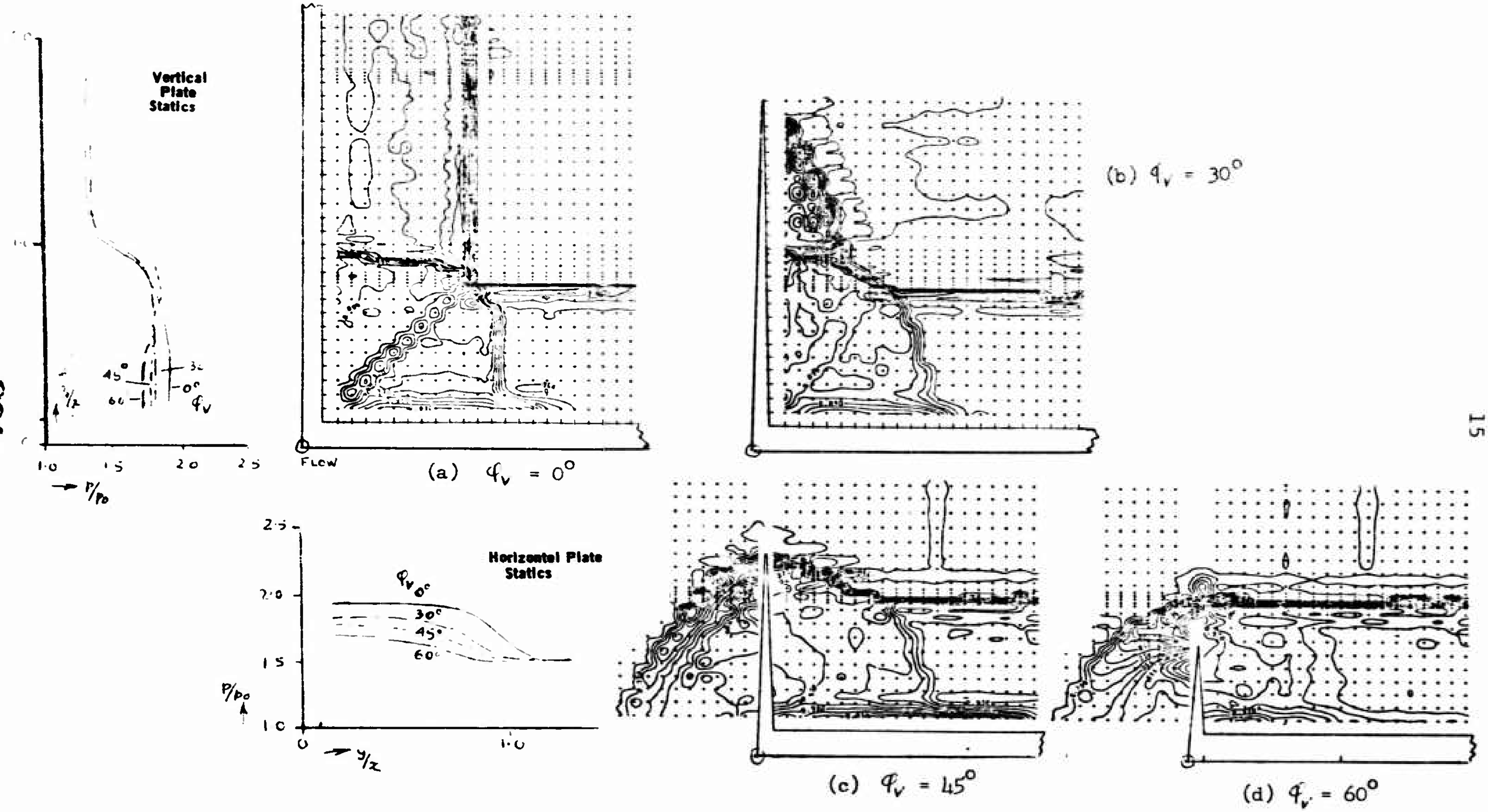

(a) $\varphi_v = 0^\circ$

(b) $\varphi_v = 30^\circ$

(c) $\varphi_v = 45^\circ$

(d) $\varphi_v = 60^\circ$

FIG. 11. COMPRESSIVE CORNER FLOWS

$M = 2$, $\varphi_H = 0^\circ$, $\delta_H = +7.5^\circ$, $\delta_V = +5^\circ$

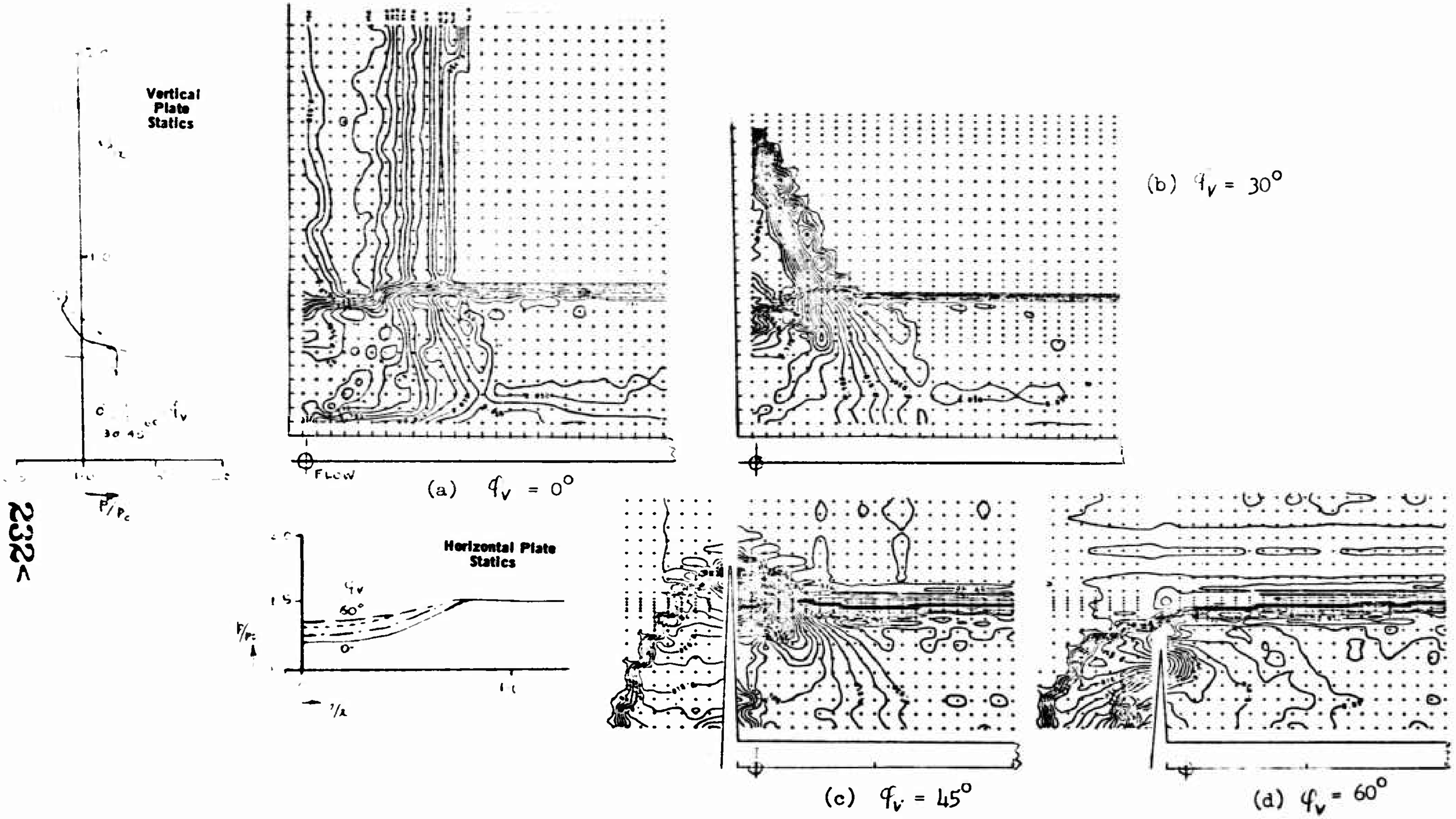

(a) $\varphi_V = 0^\circ$

(b) $\varphi_V = 30^\circ$

(c) $\varphi_V = 45^\circ$

(d) $\varphi_V = 60^\circ$

FIG. 12. ' MIXED ' CORNER FLOWS

$M = 2,\ \varphi_H = 0^\circ,\ \delta_H = +7.5^\circ,\ \delta_V = -5^\circ$

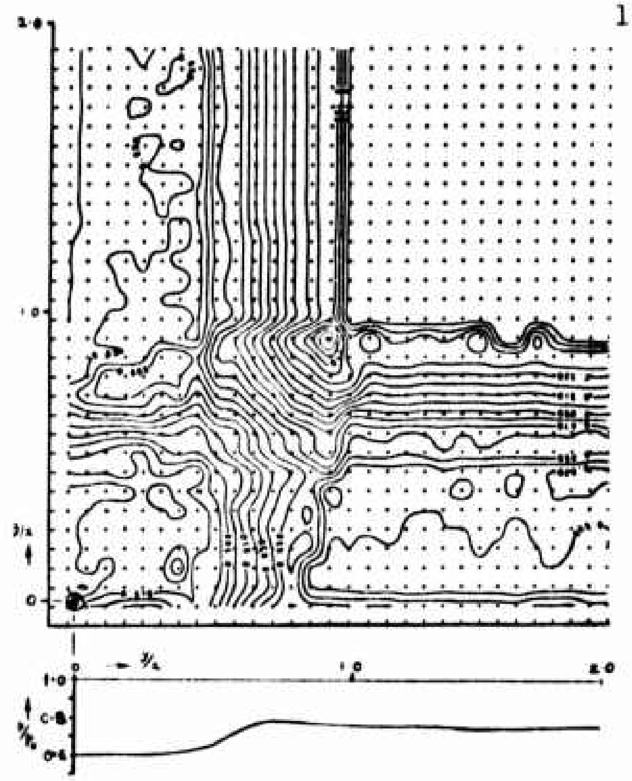

FIG. 13. EXPANSIVE CORNER FLOW

$M = 2,\ \phi_H = \phi_V = 12.5^\circ,\ \delta_H = \delta_V = -5^\circ$

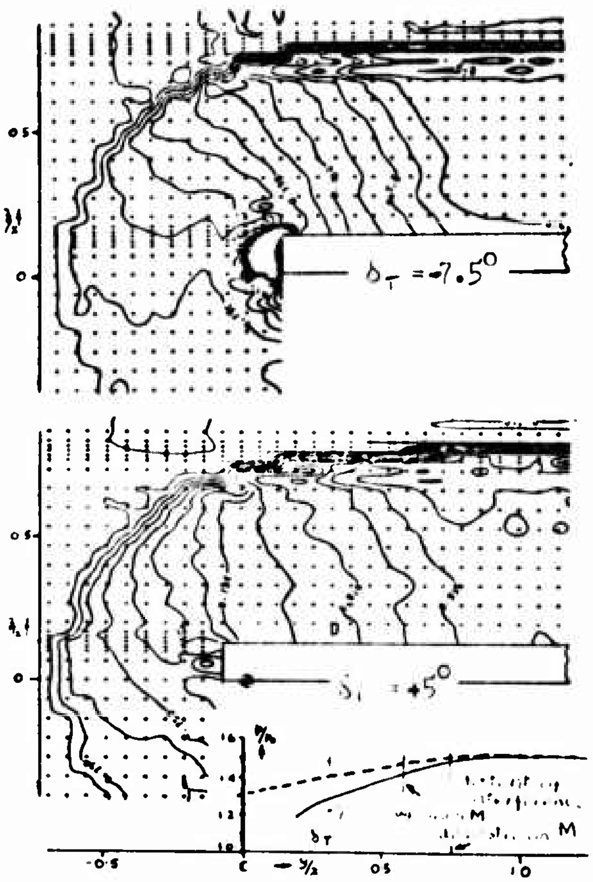

FIG. 14. FREE EDGE FLOWS

$M = 2,\ \phi_H = 0^\circ,\ \delta_H = +7.5^\circ$

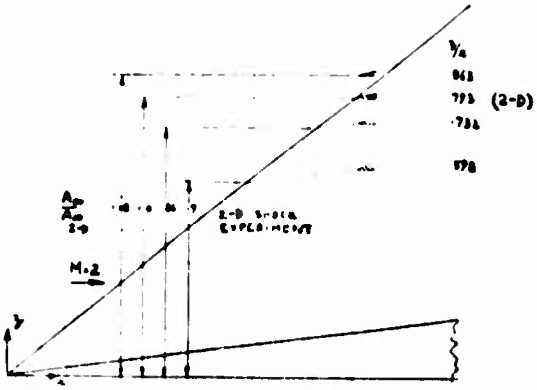
y/x
·863
·793 (2-D)
·732
·578
2-D SHOCK EXPERIMENT
M=2
y
x

(a) Intake Length Constant

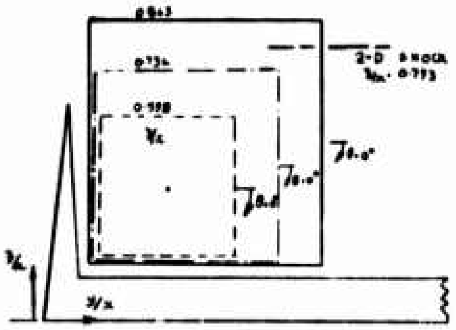
0·863
0·732
0·578
2-D SHOCK y/x = 0·793
z/x
y/x

(c) Capture Area on Corner Configuratuion

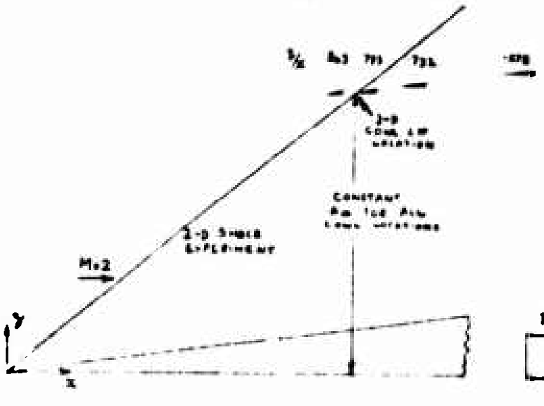
y/x
·863
·793
·732
·578
2-D COWL LIP LOCATION
CONSTANT
2-D SHOCK EXPERIMENT
M=2
y
x

(b) Capture Area A_∞ Constant

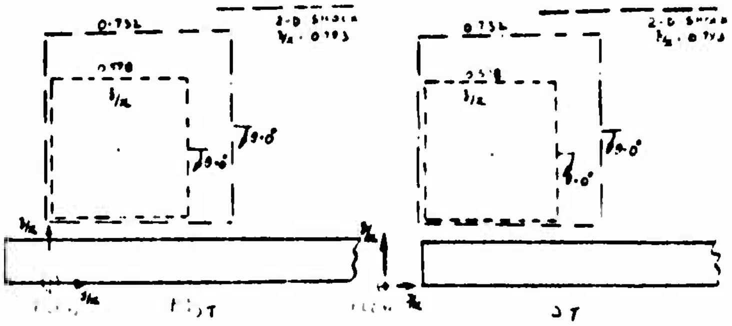
0·732
2-D SHOCK y/x = 0·793
0·578
y/x
0·732
2-D SHOCK y/x = 0·793
0·578
y/x
δ_T
δ_T

(d) Capture Area on Free Edge Configurations

FIG. 15. INTAKE CAPTURE AREA AND COWL LIP LOCATIONS

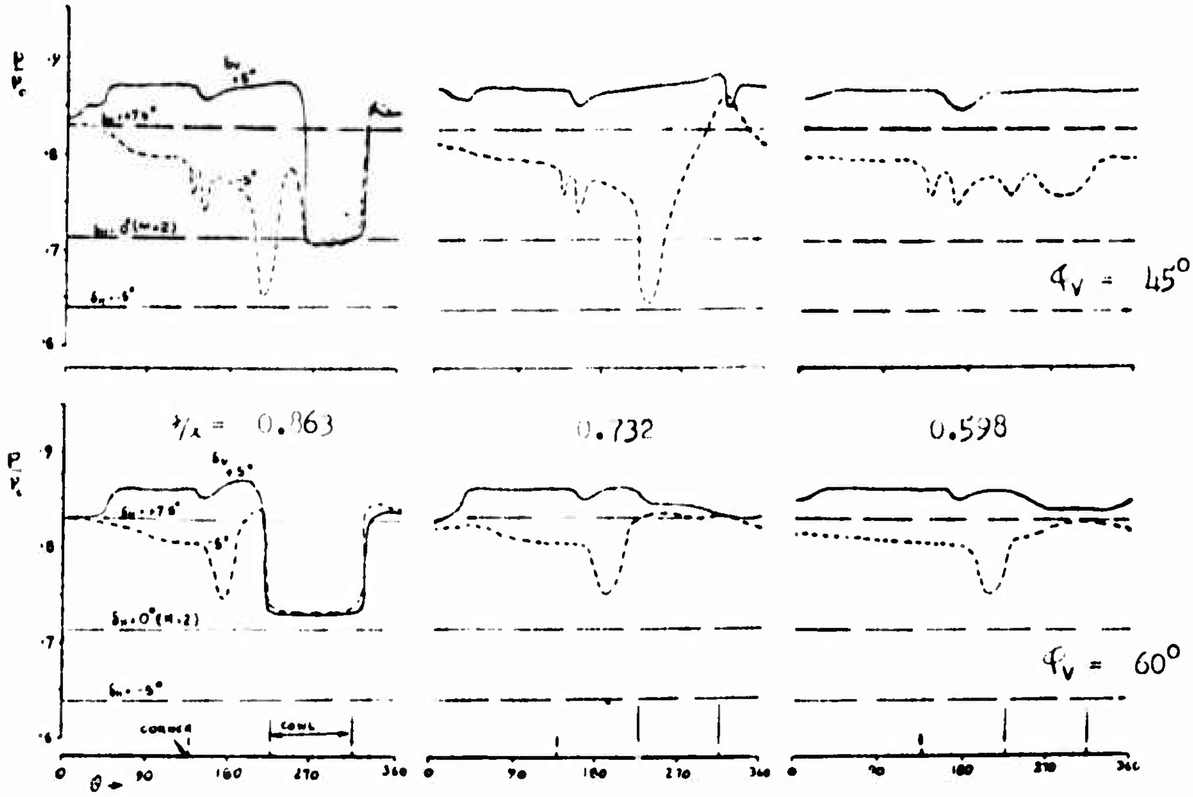

FIG. 16. PITOT PRESSURE AROUND SQUARE CAPTURE AREAS FOR CORNER CONFIGURATIONS

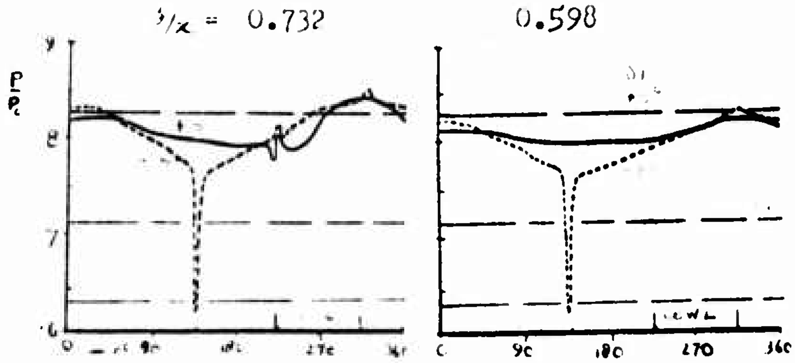

FIG. 17. PITOT PRESSURE AROUND SQUARE CAPTURE AREAS FOR FREE EDGE CONFIGURATIONS

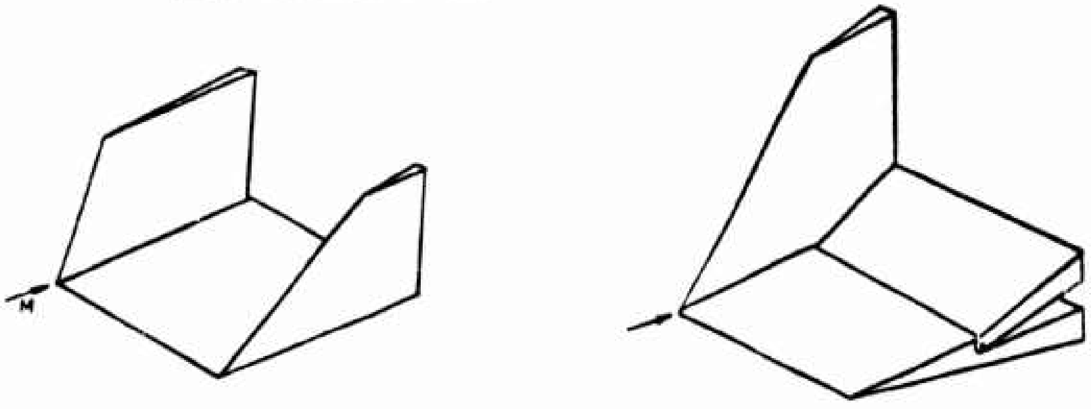

2 – Sidewall Model

Hinged – Ramp model

FIG. 18 EXTENSION OF WORK

RRATA TO PAPER ENTITLED 'MIXED COMPRESSION AIR INTAKES
OR OPERATION AT MACH 2.2' by A J BROOKS AND G J DADD

age	**Line** (lines include titles and equations but not tables)		
	10	Below equation, should read	C_{DI}/C_I C_{DI}/C_D
	22	Below table, should read	Build (b) Build (c)
	33	Fifth word, should read	off aft
)	11	(right hand data column) should read	$C_{LC} = 0.003366$ $C_{LC} = 0.00366$

MIXED COMPRESSION AIR INTAKES FOR OPERATION AT MACH 2.2

A. J. Brooks and G. J. Dadd

National Gas Turbine Establishment. U.K.

Summary

Model tests on a series of mixed compression intakes, at conditions equivalent to Mach 2.2 flight, led to the development of an intake bleed arrangement which permitted continuous operation over an adequate mass flow range and with acceptable engine flow distortion levels. An analysis method was developed for comparing intakes in terms of their effects on payload. This was used to demonstrate a payload performance improvement of 5½ per cent for the best model tested, relative to typical external compression intakes, with a potential for a further 2 per cent improvement following further development.

Introduction

Air intakes for supersonic aircraft are required to diffuse the incoming air from a Mach number equal to that of the aircraft, to one acceptable to the engine, typically about 0.4 to 0.5. In slowing the incoming air the intake raises its static pressure, and since at Mach 2 this compression is of the same order as that achieved by the compressor, the intake can make a significant contribution to the overall cycle efficiency.

The supersonic part of this diffusion process may take place entirely within the intake; this is referred to as internal compression. If the supersonic diffusion takes place over an unenclosed ramp or cone with a normal shock wave at the duct entry, then the intake is of the external compression type. Where the diffusion process takes place partly over an unenclosed body and is completed in a convergent duct the intake is described as a mixed compression intake.

The internal compression intake is theoretically the most efficient, but the problems of operation away from its design point make it an impractical proposition. The external compression type was chosen for Concorde. This choice was well justified by its ease of control and generally good levels of performance. The mixed compression intake is generally regarded as more complex and has control problems but offers a potentially lower installed drag than the simpler external compression type. The drag reductions offered by the mixed compression intake arise from the reduced inclination of the cowl to the free stream direction as compared with the external compression type (Figure 1). However, surfaces inclined to the free stream produce not only drag, but lift, and in considering intake optimisation this term must also be remembered.

A research programme has been undertaken at the National Gas Turbine Establishment to study the operating problems and the performance of the mixed compression intake at Mach 2.2. Model tests and a theoretical investigation were used for this study. To provide a focus for the research, the Concorde mission and the performance of the pre-production aircraft were selected as a basis for design and assessment of intake performance. This was designated the "reference" intake. The results are however, applicable to other aircraft designed for this speed range.

The experimental programme

Tests were carried out in the 12 in. Intake Test Facility[1] at NGTE on models which were approximately 1/15th scale representations of a single isolated intake (Figure 2). In order to obtain the correct Reynolds number the tests were run at elevated pressure. An inlet local Mach number of 2.1 was used to correspond to conditions in the underwing flow field at a flight Mach number of 2.2.

A series of interchangeable parts enabled various builds, as shown on Figure 3, to be tested. An internal cowl angle of 5^0 was common to all builds. The sidewalls extended in a straight line from ramp tip to cowl lip with no cutback on the leading edge, and in order to assist schlieren viewing of the flow, no representation of the splitter plate was made. The overall length and the subsonic diffuser were representative of the Concorde design, as was provision for removing bleed air from the throat region to control the ramp boundary layer.

The factors studied were intake pressure recovery, the bleed quantity and bleed pressure recovery (which together define the internal aerodynamic efficiency of the intake) and the non-uniformity (DC_{60}) of the engine face flow.

Intake pressure recovery was measured by a pitot rake at the engine face plane. An axially translatable calibrated plug was used to control and meter the representative engine flow.

The first mixed compression build tested is shown on Figure 3(a). The supersonic ramp extended right across the bleed slot as a distributed bleed area. The performance of this build, shown in Figure 5(a), shows a slight increase in intake pressure recovery over that of the reference intake. The engine face pressure distribution was also better than that of the external compression intake at this Mach number. The bleed pressure recovery however was low, about 0.26 with approximately 6 per cent bleed at the exit point. But no mass flow variation was possible; reduction of flow from the peak recovery condition brought on an 'unstart' (sudden expulsion of the normal shock) in the manner typical of intakes having some internal compression.

Standard atmospheric variations at a typical cruise altitude[2] show that a 5^0C change in ambient air temperature could be encountered in 0.03 nautical miles. At Mach 2.2 this implies a change of 0.027 Mach number or around 3 per cent of engine flow in 0.08 seconds. So an intake should ideally be able to accommodate, say, 5 per cent drop in engine flow from that at its operating point. If unstart is to be avoided a conventional mixed compression intake such as this first build would have to cruise very supercritically, with associated loss in pressure recovery and worsening of distortion levels at the engine face. A fast-acting control system to by-pass or dump the excess flow is a possible means of avoiding unstart, but imposes further complication and weight. An alternative solution is to operate the intake with a higher-than-optimum ramp angle. By this means the effects of unstart can be reduced or eliminated completely. Disadvantages of this solution are again a drop in performance, and a need to re-size the intake to obtain the desired flow at the new operating point.

In an effort to produce a mixed compression inlet not suffering from these problems an intake incorporating the 'free boundary' principal was made, (Figure 3(b)). At the operating point it had a conventional mixed compression shock pattern, but the ramp terminated at about the plane of the cowl lip. The 'free boundary' between the trailing edge of the front ramp and the leading edge of the rear ramp defined the internal geometry. Any reduction in engine flow caused the normal shock to move forwards, the increase in static pressure across the shock deflecting the free boundary to form a local 'effective' throat in which the normal shock could be positioned stably. The excess air spilled into the bleed system, and continuity was maintained without disturbing the upstream shock system.

The results from this first test of an intake featuring the free boundary were very promising. Unstart was eliminated and reasonable performance levels were measured (Figure 5(b)). A peak pressure recovery of 91 per cent was obtained, at which condition the DC_{60} was 0.14. A flow reduction of just over 4 per cent was possible between this point and the critical condition - here quite conventionally described as that point beyond which any further flow reduction causes detachment of the cowl shock. Since stable sub-critical operation was also possible with at least a further 4 per cent reduction in engine flow this "control bleed" margin would be acceptable. In the region between the operating point and critical, the pressure recovery fell slightly to 90 per cent and the DC_{60} remained at a very low level with a minimum value of 0.07. Schlieren photographs of the intake flow (Figure 6) at various points on the operating range help to explain these performance characteristics. In the first photograph 'A' on Figure 5 the intake is running with the design shock pattern. A local expansion fan is evident, emanating from the part of the oblique cowl shock where the free boundary turns back towards the diffuser tip. Downstream of this expansion the increased local Mach number causes a local increase in the strength of the normal shock and therefore introduces extra losses in this region leading to the poor recovery and DC_{60}. Photograph 'B' taken at the maximum recovery condition shows how the increased pressure in the bleed plenum has modified the cowl shock from a weak to a strong oblique shock over approximately half the duct height. The local re-expansion is now weaker and although the normal shock is not as strong as the previous case the overall recovery is reduced. In the third photograph, 'C', the cowl shock is all strong oblique, the local expansion and recompression are noticeably smaller and the distortion is at a minimum, although this is achieved at the expense of pressure recovery as one less shock is involved. A problem with this first design was that the bleed flow at the operating point was high at 7.8 per cent. The bleed recovery was again low, about 30 per cent of the free stream total pressure at the operating point. This is thought to have been primarily due to mixing within the bleed system of air with lower static pressure from upstream of the cowl shock.

In an attempt to reduce bleed flow at the operating point, the diffuser ramp was extended forwards to the intersection of the cowl internal shock and a line projected from the ramp surface (Figure 3(c)). This modification gave nearly 1 per cent higher pressure recovery with about 1 per cent less bleed, but DC_{60} was higher particularly in the transitional region between the operating point and critical (Figure 5(c)).

Schlieren photographs showed that the distortion over the operating range originated from interaction of shock waves on the ramp side. A small region of distributed bleed was introduced at the tip of the rear ramp in an effort to raise the recovery in this region (Figure 3(d)). This produced a further increase of about ½ per cent in pressure recovery and a definite improvement in distortion levels. A small (½ per cent) increase in bleed flow in the right place brought about this improvement (Figure 5(d)).

An additional test of this build was carried out at an inlet local Mach number of 2.0 (corresponding to Mach 2.1 flight) and a reduced bleed exit area. The pressure recovery at 0.93 was not quite as good as had been obtained previously, but the bleed flow was reduced to 4 per cent with a bleed recovery of 0.3. Control bleed margin was reduced to 2 per cent, but since the characteristic was continuous, stable subcritical operation was possible and therefore this intake could be operated satisfactorily.

The success of the provision of two regions of bleed led to the idea that if these could be kept separate, the 'performance' bleed taken from downstream of the normal shock should maintain a higher pressure recovery than if all the bleed flows were mixed at the lower levels of pressure ahead of the cowl shock. This higher energy stream could be used as in the present installation as secondary nozzle flow and engine bay cooling air, whilst the lower energy air could be discharged overboard locally (through suitable orifices). This scheme has the advantage that the 'performance bleed' passed through to the nozzle should be essentially constant flow, whilst the 'control' bleed varied with extra 'internal spillage' to accommodate engine flow variations. The higher secondary pressure could offer further performance gains by increased nozzle secondary thrust. The second ramp tip was also blunted to minimise the effects of varying flow direction at this point as it is essentially in a subsonic flow region. Figure 4(e) shows details of this configuration. The performance of this build showed further slight improvements in peak recovery and in operating margin (Figure 5(e)). The anticipated improvement in bleed recovery from the aft bleed region was not observed, perhaps due to the difficulty of engineering the bleed passages and the sealing between the two zones, at the small scale of the model.

Theoretical investigation

As has been shown, changes in intake design affect the intake pressure recovery, bleed flow and recovery, and lift and drag, sometimes improving one factor at the expense of another. It is not immediately obvious how to decide which intake design is best for the aircraft. A theoretical analysis was therefore undertaken to enable the effects of these changes to be assessed by expressing them in the form of perhaps the most significant index of merit: Payload.

Both range and payload represent bases for making intake comparisons and both, in the strictest sense, should involve the complete flight profile in their assessment. However since typically 50 per cent of total fuel load (including reserves) is used by a supersonic transport in the cruise condition during 70 per cent of the total mission time, optimisations made for the cruise condition are unlikely to differ much from those made for the complete mission. Since fuel at take-off represents a major proportion of total aircraft weight whereas payload represents only a minor proportion at all times during the mission, payload changes for a fixed range are far more sensitive to intake alterations than are range changes at constant payload. For these reasons payload at the cruise condition was chosen as an index for intake comparison.

It is convenient to start by defining a datum payload P_D which the aircraft could carry on its fixed range mission, if the intakes were isentropic, taking zero bleed, and had zero lift and drag. It is shown in Appendix I that the actual payload P_I is given by

$$P_I = \frac{P_D}{\left(1 + \left(\frac{1 - \eta_I}{\eta_I}\right)\phi_{REC} + \frac{C_{DI}}{C_D}\,\phi_D - \frac{C_{LI}}{C_L}\,\phi_L\right)} \qquad \ldots.(1)$$

Where η_I is the intake recovery, C_{DI}/C_L and C_{LI}/C_L are respectively the proportions of total drag and lift which are associated with the intake and the ϕs are the appropriate performance exchange rates. In order to go further it is necessary to select a particular design for which the numerical exchange rates can be calculated. The Concorde pre-production aircraft is an obvious reference for which these values are quoted in Appendix I.

Any subsequent intake designs may be compared by substituting either predicted or experimentally measured values of η_I, C_{DI}/C_D and C_{LI}/C_L in Equation (1) above.

The payload ratios for the intakes shown in Figure 3 at the design condition and calculated from experimental results are tabulated below.

Reference (External compression)	0.732
Build (a)	0.744
(b)	0.734
(c)	0.740
(d)	0.726
(e)	0.772

It can be seen that Build (b) showed the best performance with an improvement of some 4 per cent in datum payload over the reference level. This approximates to a 5½ per cent increase of reference payload.

It is felt that an index such as payload ratio incorporating the other interrelated factors could usefully become a standard parameter for intake testing and analysis.

In order to avoid an extensive experimental investigation of the effect of cowl angle on intake performance, further analysis was undertaken to predict optimum cowl and ramp angles. Additional assumptions were necessary; these were:-

1. That the bleed system of Build (e) (the best tried) taking 3 per cent flow in each stream at the local

static pressure prevailing at the extraction points would produce a viscous efficiency η_V equal to that of the reference intake.

2. That engine face recovery could be expressed as the product of shock recovery and viscous efficiency; the former varying against cowl angle and ramp angle according to Figure 7 while the latter, in keeping with assumption (1) above, was constant.

3. That losses associated with the bleed system could be expressed as a proportion of aircraft drag - the variation of which is shown against bleed recovery and mass flow fraction in Figure 8.

4. That cowl lift and drag were independent of ramp angle but varied according to Figure 9 with cowl angle.

5. That pre-entry drag and lift were constant at the levels quoted for the reference aircraft.

With these assumptions, the results of the analysis are shown in Figure 10 which indicates that the initial selection of a 5° cowl angle for the experimental model was quite appropriate. The best experimental performance has been achieved when operating at 15° ramp angle which is also consistent with the analysis though actual levels of payload ratio P_I/P_D are not. A detailed examination of the factors contributing toward payload in Equation (1) has shown the experimental shortfall to be due to two effects. These are that the same viscous efficiency as the reference intake has not been achieved and the second stream of the two-stream bleed system has been recovered at a pressure less than the assumed level. In retrospect the first reason could have been anticipated in view of the increased occurrence of boundary layer shock wave interactions, and while improvements may be made by development effort it could only be expected that the referance viscous efficiency could be approached and not exceeded. The low bleed recovery of the second bleed stream is basically an engineering problem which was aggravated by the small model scale.

Conclusions

Experiments on a mixed compression intake with a 5° internal cowl angle have shown that, by the choice of a suitable bleed arrangement, stable operation can be secured with an adequate mass flow range at acceptable levels of intake pressure recovery and distortion. An analysis was undertaken to relate payload changes to changes in the pertinent intake parameters (ie intake pressure recovery, bleed flow, bleed recovery, lift and drag). Hence a single figure of merit was assigned to an intake by which means it could be compared with others. In these terms the intake, which was tested at an equivalent flight Mach number of 2.2, offered a payload improvement of 5½ per cent relative to a typical external intake. Deficiencies in the bleed system, caused partly by the small scale of the model but which could probably be eradicated with further development were the main item which prevented the full potential of 7½ per cent payload improvement being achieved.

An analysis on the same basis, but relying on aerodynamic predictions of the pertinent intake variables and conducted for a series of cowl angles, has shown that the internal cowl angle chosen for the intake model was close to the optimum value.

Improvements of this scale are considered by the authors to justify a continuation of this work.

References

1. STREET, P. G. The 12 inch diameter intake test rig at NGTE. NGTE Report R267. October 1965.

2. BURNHAM, J. Progress in Aerospace Sciences. Vol. 2. The Pergamon Press 1970.

3. MASCITTI, V. R. A closed form solution to shock wave properties. Journal of Aircraft. Vol. 6, No. 1. January 1969.

APPENDIX I

Payload Analysis

The variable factors which alone were considered to influence intake performance assessed on a payload basis were:

(1) Intake pressure recovery

(2) Cowl drag and lift

(3) Pre-entry drag and lift

(4) Bleed drag

A combination of theoretical and empirical methods or even direct experimental measurements may be used to evaluate each of the above factors for a given intake geometry at the cruise Mach number. Subsequently performance exchange rates may be used to convert each term into a payload deficit or gain enabling an aggregate effect to be determined.

Intake Pressure Recovery η_I

Intake shock recovery η_S may be derived by successive application of the equations for plane shock waves$^{(3)}$ to the flow regions of the intake, given local flow conditions ahead of the intake. These equations yield shock wave orientation and both static and total pressure ratios across the shock waves. A viscous recovery term η_V may be defined such that

$$\eta_V = \frac{\eta_I}{\eta_S} \qquad \ldots.(2)$$

Since η_I has been experimentally established and η_S may be calculated for the reference intake, η_V may be evaluated and applied to other intakes to predict realistic engine face total pressure recoveries.

Cowl Drag and Lift C_{DC}, C_{LC}

From the external shock pattern of a proposed intake the flow direction and Mach number onto the cowl exterior may be determined. The assumption that the flow is two-dimensional enables the static pressure distribution to be evaluated assuming a Prandtl-Meyer expansion; integration of the resolved pressure forces leads to lift and drag forces associated with the area over which the integration is performed.

At a given intake local Mach number, variations in intake ramp angle have only a minor influence on the static pressure distribution on the cowl exterior provided the cowl shock remains attached. However, the cowl shape does have a significant effect. Figure 8 shows the variation of drag and lift coefficients referred to aircraft conditions for Mach 2.2 flight for a family of cowls described adequately by cowl angle alone and including, at 12 degrees internal angle, a cowl very similar in shape to that of the reference aircraft. The region of pressure force integration extends a distance equal to the intake capture height off from the cowl lip. Pressure forces acting beyond this point have only second order effects on lift and drag. The included wedge angle at the cowl lip was 5°.

Pre-Entry Drag and Lift C_{DPE}, C_{LPE}

The pre-entry drag, and lift coefficients may be derived from the predicted shape of the cowl lip stagnation streamline and the pressure forces acting on that streamline.

Bleed Drag C_{DB}

The fact that the Concorde aircraft discharges the intake bleed flow through a two-stream propulsion nozzle complicates this theoretical study. It is possible that alternative arrangements would be made with an aircraft fitted with a mixed compression intake; for example, direct discharge, overboard could be employed. For the sake of simplicity it has been assumed that the losses in discharging bleed are those associated with the absolute forward momentum supplied to the bleed air due to its passage through the intake and bleed system ducting. Bleed losses were therefore debited against the intake in the form of a bleed drag coefficient. Assuming the bleed air to be expanded to the free stream static pressure and discharged in a rearward direction then

$$C_{DB} = \frac{Q_B\,(V_\infty - V_{BE})}{\frac{1}{2}\rho V_\infty^{2}\,A_H} \qquad \ldots.(3)$$

The bleed mass flow rate Q_B may be calculated in terms of specified bleed flow ratio A_B/A_I and the intake capture flow

$$Q_B = \frac{A_B}{A_I} \times Q_{CAP} \qquad \ldots.(4)$$

The velocity of bleed flow discharge V_{BE} (relative to the aircraft) has been derived by assuming that the bleed total pressure is equal to the local static pressure where the bleed flow divides from the main flow. This static pressure is determined concurrently with the evaluation of shock recovery in theoretical predictions. A velocity coefficient η_{BE} was employed to represent deficiencies in the bleed system.

The complete expression for the bleed drag coefficient, referred to aircraft conditions is

$$C_{DB} = \frac{A_I \; P_{TO}}{\frac{1}{2}\, M_\infty^2 \, P_{S_\infty} \, A_W} \cdot \frac{\left(\frac{A_B}{A_I}\right) M_O}{\left(1 + \frac{\gamma - 1}{2} M_O^2\right)^{\frac{\gamma+1}{2(\gamma-1)}}}$$

$$\times \left[\frac{M_\infty}{\left(1 + \frac{\gamma - 1}{2} M_\infty^2\right)^{\frac{1}{2}}} - \frac{\eta_{BE}\, M_{BE}}{\left(1 + \frac{\gamma - 1}{2} M_{BE}^2\right)^{\frac{1}{2}}} \right] \qquad \ldots.(5)$$

where the inviscid bleed exit Mach number is given by

$$M_{BE} = \sqrt{\left\{\left(\frac{P_{TB}}{P_{S_\infty}}\right)^{\frac{\gamma-1}{\gamma}} - 1\right\} \cdot \frac{2}{\gamma - 1}} \qquad \ldots.(6)$$

For several bleed systems operating at different conditions individual coefficients may be evaluated and then added. Equations (5) and (6) above have been used in the compilation of Figure 9.

Intake Drag and Lift

In the context of this paper intake drag C_{DI} is the sum of pre-entry, cowl and bleed drag coefficients. Similarly, intake lift C_{LI} is the sum of pre-entry and cowl lift coefficients

$$C_{DI} = C_{DPE} + C_{DC} + C_{DB} \qquad \ldots.(7)$$

$$C_{LI} = C_{LPE} + C_{LC} \qquad \ldots.(8)$$

All lift and drag coefficients are referred to aircraft conditions by non-dimensionalising with respect to wing area and aircraft Mach number.

Rationalisation of Recovery, Drag and Lift

In order to express payload as a function of intake pressure recovery, drag and lift, the simplifying assumption that payload is a linear function of these three intake parameters has been made. The accuracy of payload predictions will deteriorate as each of the independent variables deviates from the corresponding values applicable to the reference aircraft because, in reality, the system would not behave linearly. Within these limitations the datum payload P_D, is related to the reference payload P_I by the equation

$$P_D \quad P_R + (1 - \eta_I)\frac{\partial P_R}{\partial \eta_I} + C_{DI}\frac{\partial P_R}{\partial C_D} - C_{LI}\frac{\partial P_R}{\partial C_L} \qquad \ldots.(9)$$

which may be written in the form

$$P_D = P_R \left\{ 1 + \left(\frac{1 - \eta_I}{\eta_I} \right) \cdot \left(\frac{\eta_I}{P_R} \frac{\partial P_R}{\partial \eta_I} \right) + \frac{C_{DI}}{C_D} \cdot \left(\frac{C_D}{P_R} \cdot \frac{\partial P_R}{\partial C_D} \right) - \frac{C_{LI}}{C_L} \cdot \left(\frac{C_L}{P_R} \frac{\partial P_R}{\partial C_L} \right) \right\} \qquad \ldots.(10)$$

$\frac{\eta_I}{P_R} \frac{\partial P_R}{\partial \eta_I} = \phi_{REC}$, $\frac{C_D}{P_R} \frac{\partial P_R}{\partial C_D} = \phi_D$, $\frac{C_L}{P_R} \frac{\partial P_R}{\partial C_L} = \phi_L$ the recovery, drag and lift performance exchange rates respectively.

If it may be allowed that ϕ_{REC}, ϕ_D and ϕ_L do not change when the intake and therefore payload is changed then the payload P_I for an alternative intake will be given by

$$P_I = \frac{P_D}{\left\{ 1 + \left(\frac{1 - \eta_I}{\eta_I} \right) \phi_{REC} + \frac{C_{DI}}{C_D} \phi_D - \frac{C_{LI}}{C_L} \phi_L \right\}} \qquad \ldots.(11)$$

where η_I, $\frac{C_{DI}}{C_D}$ and $\frac{C_{LI}}{C_L}$ are evaluated for the alternative intake.

The performance exchange rates and values for the reference intake parameters used in compiling Figure 10 are:-

$\phi_{REC} = 2.5$ $\qquad C_L = 0.120$

$\phi_D = 6.25$ $\qquad C_{LC} = 0.003366$

$\phi_L = 8.43$ $\qquad C_{LPE} = 0.000627$

$C_D = 0.017$ $\qquad \eta_S = 0.944$

$C_{DC} = 0.000702$ $\qquad \eta_I = 0.918$

$C_{DPE} = 0.000113$ $\qquad \eta_V = 0.972$

$C_{DB} = 0.00027$ $\qquad \eta_B = 0.450$

Assumptions implicit in the derivation of Equation (11) are:-

(1) Intake/airframe interference is unaltered by intake modifications.

(2) Propelling nozzle primary flow performance is unchanged by changes to secondary flow.

(3) Any changes due to lift and drag force alterations can be accommodated to maximum advantage by trim changes.

(4) Possible changes in intake weight due to modifications may be ignored.

NOMENCLATURE

A_B	bleed mass flow area at capture plane
A_E	engine mass flow area at capture plane
A_I	intake capture area
A_S	pre-entry spill mass flow area at capture plane
A_W	wing area
C_D	overall aircraft drag coefficient
C_{DB}	equivalent bleed drag coefficient
C_{DC}	cowl drag coefficient
C_{DI}	intake drag coefficient ($C_{DB} + C_{DC} + C_{DPE}$)

C_{DPE}	pre-entry drag coefficient
C_L	overall aircraft lift coefficient
C_{LC}	cowl lift coefficient
C_{LI}	intake lift coefficient $(C_{LC} + C_{LPE})$
C_{LPE}	pre-entry lift coefficient
DC_{60}	engine face distortion parameter $= \frac{P_{min_{60}} - P_{mean}}{\frac{1}{2}\rho V^2}$
M_∞	aircraft flight Mach number
M_{BE}	inviscid bleed exit Mach number
M_O	Mach number locally ahead of intake
P_{TB}	total pressure of bleed flow
P_{TE}	total pressure at engine face
P_{TO}	total pressure locally ahead of intake
$P_{S\infty}$	ambient pressure
P_D	datum payload
P_R	reference aircraft payload
$P_{min_{60}}$	minimum mean total pressure in any 60° segment
P_{mean}	mean total pressure
$\frac{1}{2}\rho V^2$	mean engine face dynamic head
Q_{CAP}	mass flow crossing A_I
Q_B	bleed mass flow
V_{BE}	inviscid bleed exit velocity
V_∞	aircraft velocity
η_B	bleed press recovery
η_I	intake recovery factor $\frac{P_{TE}}{P_{TO}} \equiv \eta_S \times \eta_V$
η_S	intake shock recovery
η_V	viscous recovery
η_{BE}	velocity coefficient for bleed ejection system
ϕ_{REC}	recovery performance exchange rate
ϕ_L	lift coefficient performance exchange rate
ϕ_D	drag coefficient performance exchange rate

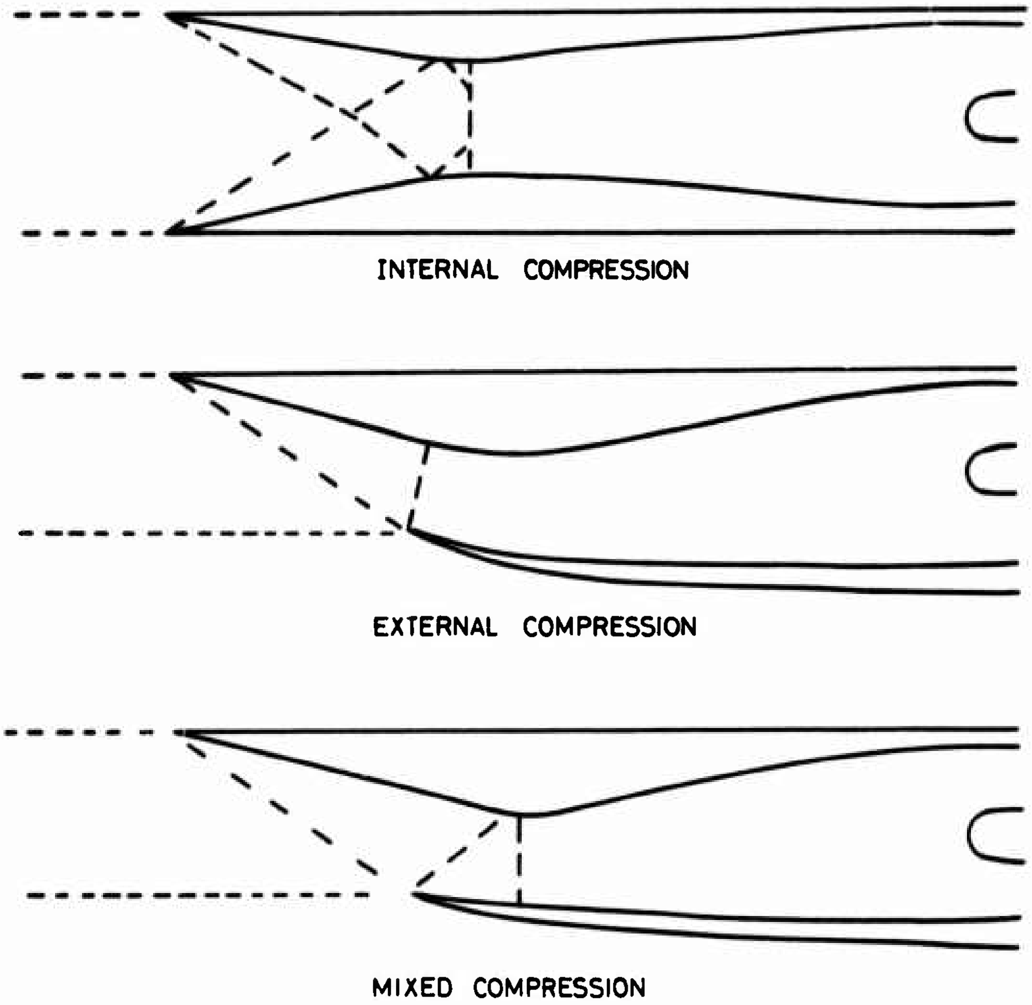
INTERNAL COMPRESSION
EXTERNAL COMPRESSION
MIXED COMPRESSION

Figure 1 Intake types

Figure 2 Model intake mounted on wind tunnel hatch

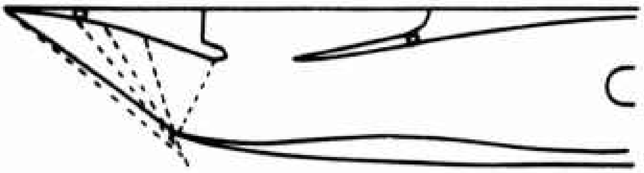

THE CONCORDE INTAKE

CHANGES FROM
THE BUILD ABOVE
ARE SHOWN
IN BLACK

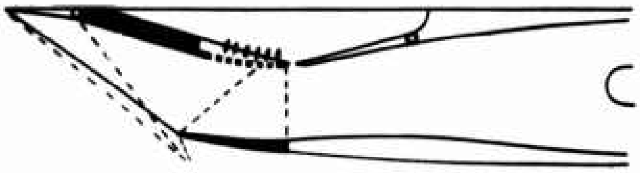

BUILD (a)
MIXED COMPRESSION INTAKE WITH DISTRIBUTED BLEED

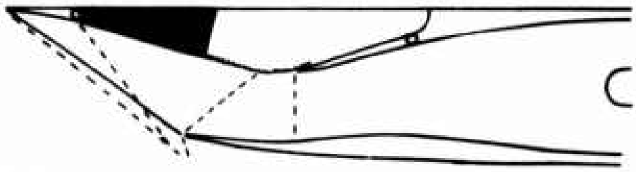

BUILD (b)
MIXED COMPRESSION INTAKE WITH FREE BOUNDARY

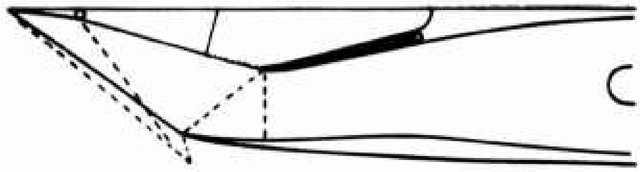

BUILD (c)
AS ABOVE WITH EXTENDED SUBSONIC RAMP

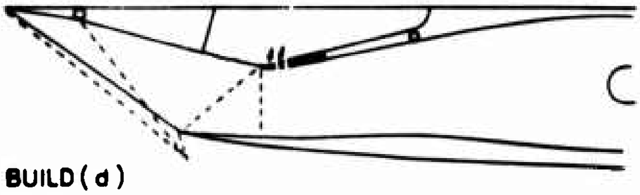

BUILD (d)
AS ABOVE WITH THE ADDITION OF A SMALL REGION OF DIST. BLEED

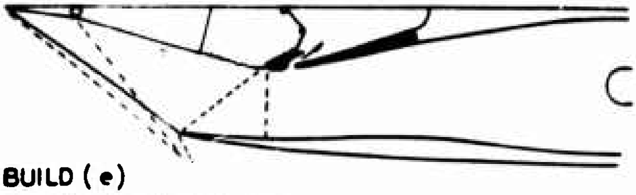

BUILD (e)
DIVIDED BLEED SYSTEM

Figure 3 Range of intakes tested

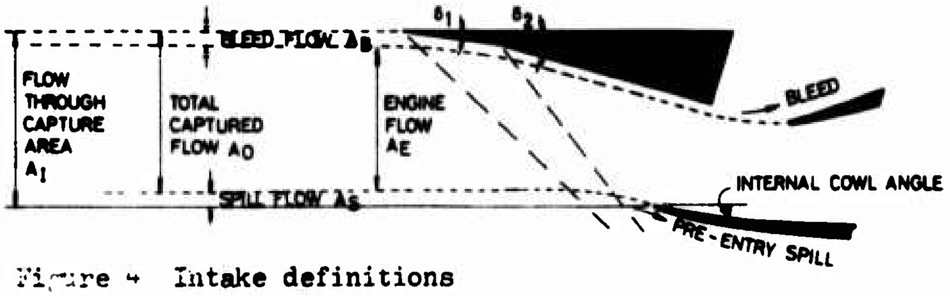
FLOW THROUGH CAPTURE AREA A_I
TOTAL CAPTURED FLOW A_O
BLEED FLOW A_B
ENGINE FLOW A_E
SPILL FLOW A_S
δ_1
δ_2
BLEED
INTERNAL COWL ANGLE
PRE-ENTRY SPILL

Figure 4 Intake definitions

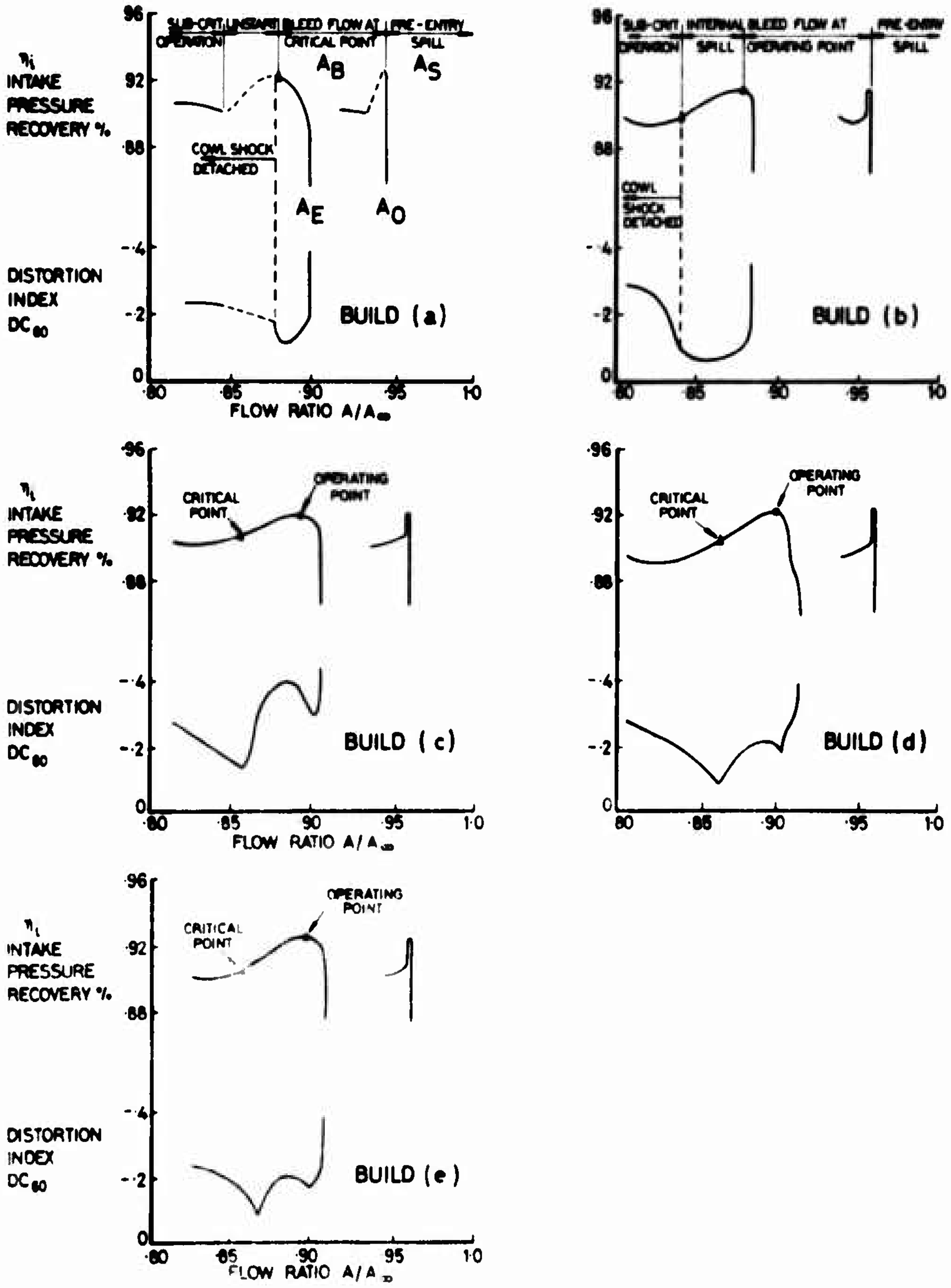

Figure 5 Pressure recovery and flow distortion characteristics for the intakes tested

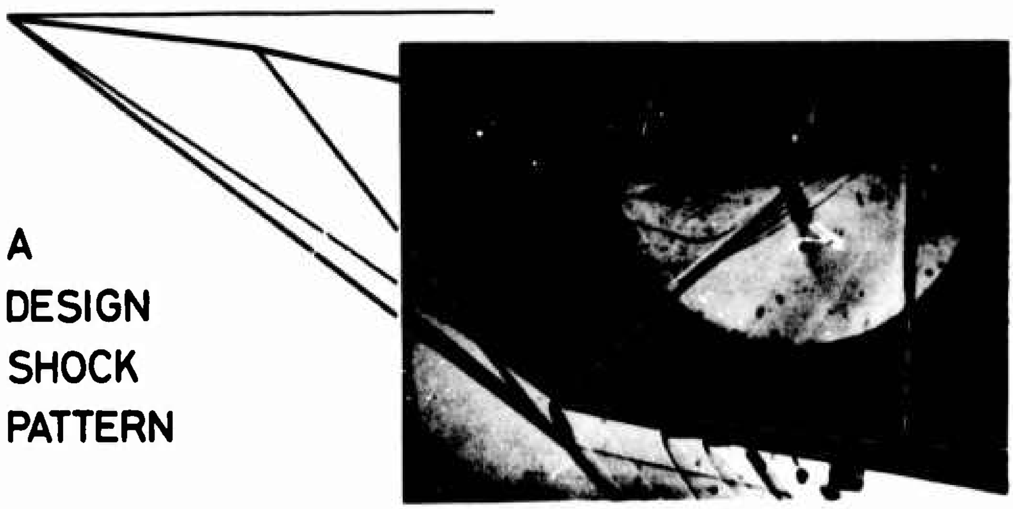
A
DESIGN
SHOCK
PATTERN

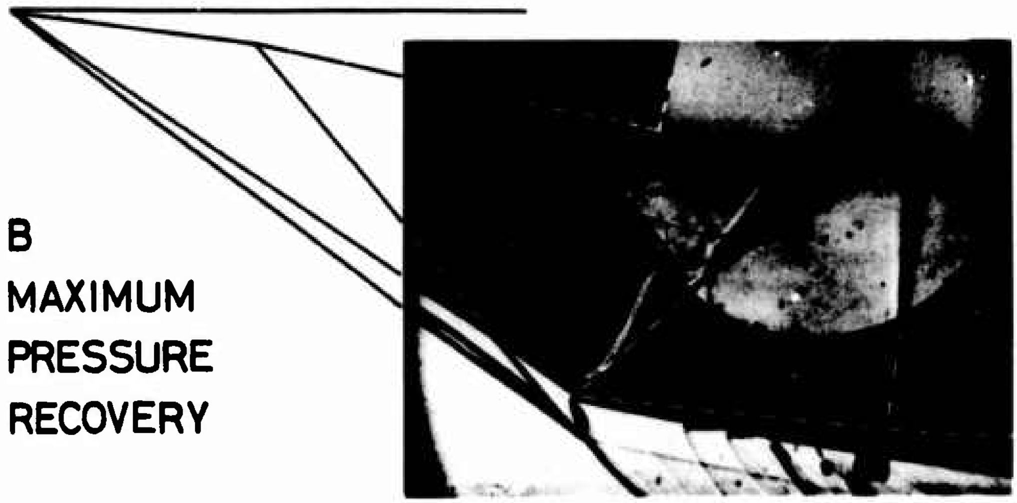
B
MAXIMUM
PRESSURE
RECOVERY

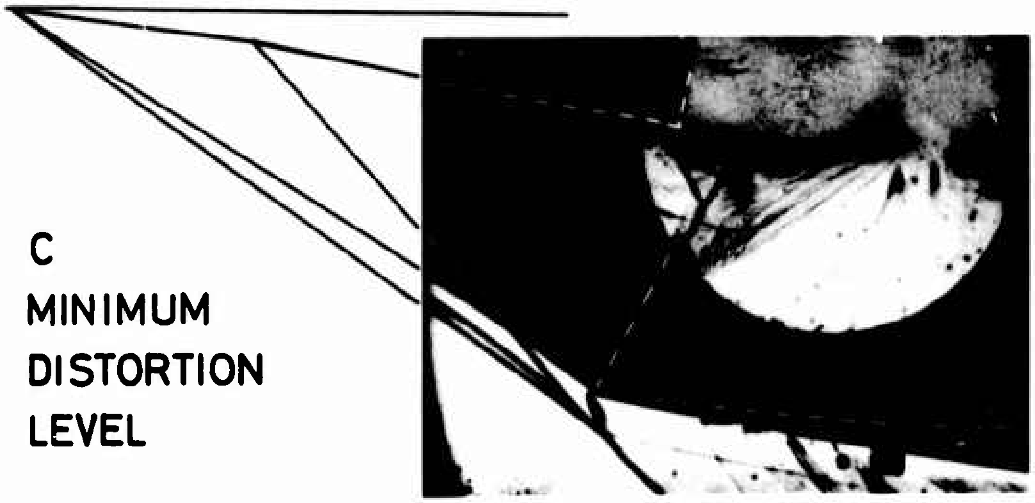
C
MINIMUM
DISTORTION
LEVEL

Figure 6 Schlieren photographs of Build (o) showing shock patterns at different operating conditions.

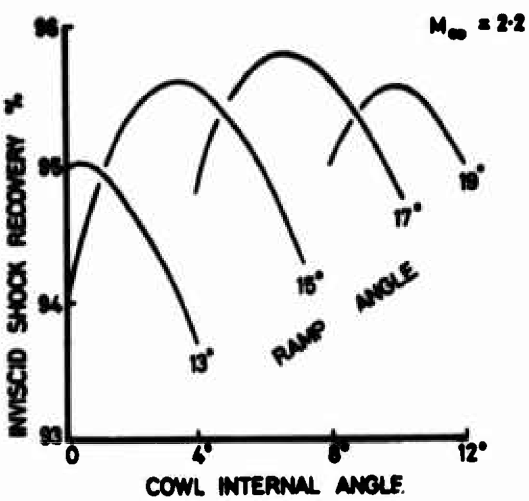

Figure 7 Theoretical shock recovery for a range of cowl and ramp angles

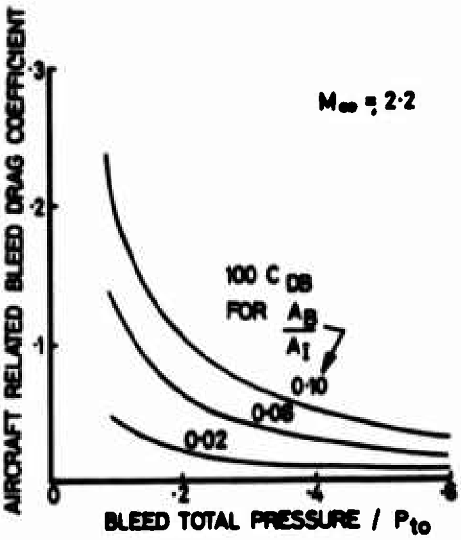

Figure 8 Variation of bleed drag with bleed flow and pressure recovery

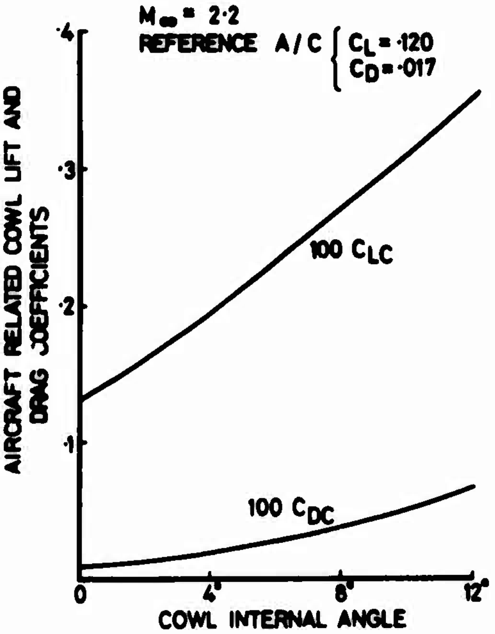

Figure 9 Variation of cowl lift and drag with cowl angle

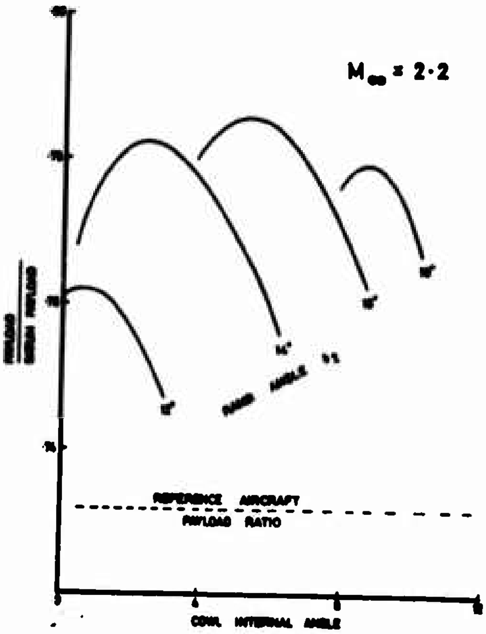

Figure 10 Variation of payload ratio with cowl and ramp angle

RECOMPRESSION PAR CHOCS DANS UNE PRISE D'AIR SUPERSONIQUE EN PRÉSENCE D'UN PIÈGE A COUCHE LIMITE

Georges Meauzé

Office National d'Etudes et de Recherches Aérospatiales (ONERA) - 92320 Châtillon (France)

RÉSUMÉ

Afin de comprendre le fonctionnement du piège à couche limite d'une prise d'air à compression supersonique interne et de connaître l'influence des divers paramètres sur l'efficacité et la stabilité de la recompression, un montage permettant une grande souplesse d'utilisation a été réalisé. A cet effet, le problème particulier du piège à couche limite a été dissocié de l'étude générale de la prise d'air supersonique en recréant dans une tuyère le Mach terminal de recompression supersonique. Tous les phénomènes se passant avant le piège ont ainsi été éliminés. Différentes formes de pièges ont été essayées pour des nombres de Mach de 1,12 - 1,42 - 1,72.

L'expérience a permis de dégager un modèle théorique simple à partir duquel une méthode de calcul a été mise au point. Cette méthode permet d'expliquer et de prévoir les résultats expérimentaux avec une bonne approximation et d'optimiser, pour un écoulement amont donné, la géométrie du piège.

SHOCK RECOMPRESSION IN A SUPERSONIC AIR INTAKE WITH BOUNDARY LAYER BLEED

SUMMARY

In order to have a better understanding of the functioning of the boundary layer bleed of internal supersonic compression air intakes, and a better knowledge of the influence of various parameters on the recompression efficiency and stability, a special experimental set-up, allowing a great operational versatility, was designed and built at ONERA. The particular problem of boundary layer bleed has been dissociated from the general study of supersonic air intakes by supplying a nozzle with a flow whose Mach number is equal to that of the intake at the end of supersonic recompression ; all phenomena taking place before the bleed are thus eliminated. Various bleed shapes were tested at Mach numbers 1.12, 1.42, 1.72.

From the experiments it has been possible to devise a simple theoretical model, from which a calculation method was developed. With this method experimental results can be explained and predicted with a good approximation, and the bleed geometry, for a given upstream flow, can be optimized.

1. INTRODUCTION

L'objet de cette note est de présenter une étude expérimentale de la recompression par choc en présence d'un piège à couche limite, ainsi qu'une méthode de calcul permettant une prévision satisfaisante de l'écoulement, et une optimisation de la configuration du piège pour un écoulement incident donné.

Seuls sont exposés les éléments principaux de l'étude, et les résultats les plus significatifs. Les résultats complets, et certaines précisions sur la méthode de calcul, pourront être trouvés dans le rapport complet de l'étude$^{(1)}$.

2. DESCRIPTION DU MONTAGE RÉALISÉ POUR L'ÉTUDE EXPÉRIMENTALE

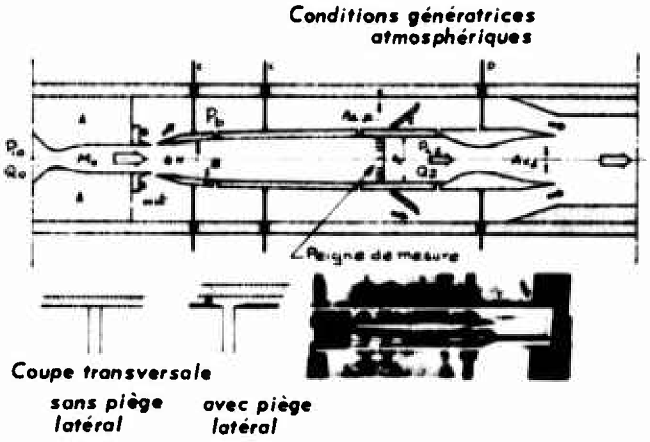

Fig. 1

La partie amont du montage est constituée par une tuyère bidimensionnelle A qui comporte un élément à section constante dans le but d'épaissir la couche limite, et se termine par des becs interchangeables B permettant de faire varier la largeur du piège. La largeur de la tuyère est égale à 3,5 fois sa hauteur. Un jeu de tuyères permet d'obtenir différents nombres de Mach.

La partie aval représente le diffuseur dont chaque moitié est constituée par deux volets reliés entre eux par une tôle souple.

Par l'intermédiaire des deux vérins C, il est possible de régler d'une part l'angle θ et d'autre part l'écart relatif du diffuseur par rapport à la tuyère ΔH.

Le diffuseur est prolongé par un élément à section constante A_2 équipé d'un peigne cruciforme de prises de pressions totales et est terminé par un col sonique réglable A_{c2} permettant d'ajuster la section critique de l'écoulement interne.

La partie aval du col a une forme de tuyère supersonique déterminée en vue de bénéficier d'un effet de trompe pour extraire les débits du piège.

Ces débits de piège, passant de part et d'autre du diffuseur sont contrôlés par les cols soniques Acp dont les volets E permettent de régler les sections.

Le montage permet en outre d'aménager un piège latéral qui s'est avéré indispensable pour assurer la stabilité de l'écoulement. Dans ce cas, des plaques latérales sont disposées contre la tuyère et contre le diffuseur avec une interruption qui constitue le piège latéral. Ce piège, et le piège principal débouchent dans un caisson commun.

3. RELATIONS ÉLÉMENTAIRES

L'étude expérimentale se conduit de la façon suivante : une combinaison des divers paramètres géométriques ayant été fixée (fig. 1), nous ne faisons varier que le second col Ac2 et nous étudions l'évolution corrélative du coefficient de débit primaire $\varepsilon = Q_2/Q_0$ et de l'efficacité $\eta = P_{i2}/P_{i0}$

En admettant que les coefficients de striction des cols soniques soient identiques, nous pouvons écrire, l'écoulement étant supposé adiabatique :

$$\varepsilon = \frac{P_{i2}\,A_{c2}}{P_{i0}\,A_{c0}}$$

P_{i2} étant une pression d'arrêt isentropique moyenne en fin de diffuseur, définie par cette relation, dont on déduit :

(1) $$\eta = \frac{A_{co}}{A_{c2}}\,\varepsilon$$

Nous admettrons de plus que le caisson piège est suffisamment grand devant Acp pour que la pression piège Pb puisse être considérée comme la pression génératrice de l'écoulement secondaire.

D'où, la relation :

(2) $$\varepsilon = 1 - \frac{P_b\,A_{cp}}{P_{io}\,A_{co}}$$

Nous voyons par conséquent que, Acp étant connu par avance, ε est une fonction linéaire de P_b/P_{io} et que la mesure de la pression piège suffit pour déterminer ε ; d'autre part, connaissant la valeur de Ac2 correspondante, nous déterminons η facilement d'après (1).

4. DESCRIPTION DE L'ÉCOULEMENT

Pour cette description, nous supposons une certaine géométrie du piège et du diffuseur fixée ainsi que la section critique Acp et nous donnons à Ac2 des valeurs successivement décroissantes.

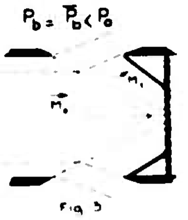

Fig. 2

Pour une valeur de Ac2 suffisamment grande, le diffuseur est en partie amorcé fig. 2. La partie supersonique est terminée par un choc qui fait décoller les couches limites; l'efficacité est évidemment très mauvaise. De plus pour une configuration usuelle, la pression piège Pb est inférieure à la pression statique Po de l'écoulement supersonique Mo.

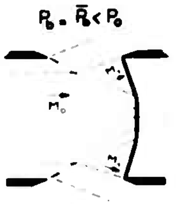

Fig. 3

En refermant Ac2 le choc remonte dans le diffuseur jusqu'à l'entrée. Au niveau du piège, rien ne change tant que l'écoulement d'entrée du diffuseur reste entièrement supersonique (fig. 3).

En particulier, le coefficient de débit ε est constant, $\varepsilon = \bar{\varepsilon}$, mais l'efficacité croît, ce qui se traduit par la partie verticale de la caractéristique η, ε (fig. 4).

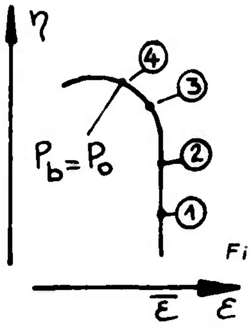

Fig. 4

La pression Pb étant inférieure à Po il y a une détente issue des bords de la tuyère tout au moins en dehors de la couche limite.

Le système de chocs à l'entrée est donc grossièrement constitué d'un choc droit central attaqué au nombre de Mach Mo et de deux chocs obliques extérieurs presque droits attaqués au Mach M1 plus élevé que Mo à cause de la détente (si les faisceaux de détente se croisent sur l'axe, la partie centrale du choc est abordée à M > Mo).

Si l'on continue à fermer Ac2, le choc se détache du diffuseur et un certain débit passe dans le piège derrière le choc (fig. 5). Une description détaillée d'un écoulement comparable dans la prise d'air Concorde est donnée en Ref. 2.

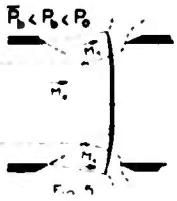

Fig. 5

Ce débit est concentré en un jet très étroit dont la direction est a priori indéterminée ; il a pour effet de faire croître la pression piège (selon la relation 2). Cette pression augmentant, le faisceau de détente s'estompe, le Mach M1 se rapproche de Mo et l'efficacité continue à croître ; par ailleurs, le débit secondaire augmentant, une part plus importante de la couche limite passe maintenant dans le piège (point 3 de la fig. 4) ce qui contribue à l'élévation de l'efficacité.

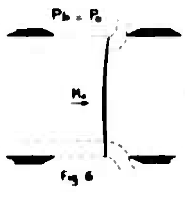

Fig. 6

En poursuivant encore la fermeture de Ac2 le choc se détache de plus en plus, le débit principal diminue et le débit piège augmente d'autant, ainsi que la pression piège qui passe par la valeur de la pression statique (fig. 6).

A cet instant, le faisceau de détente n'existe plus, et nous sommes en présence d'un choc droit au Mach Mo (fig. 4, point 4).

En réalité, le choc n'est pas tout-à-fait droit mais il présente une légère courbure semblable à la courbure d'un choc détaché devant une entrée d'air Pitot en régime subcritique (fig. 6)

Ceci résulte de la divergence de l'écoulement subsonique derrière le choc.

Pour des valeurs de Ac2 plus réduites, le choc émerge toujours davantage et la pression piège prend des valeurs supérieures à po.

Il apparaît alors des chocs obliques issus des becs de la tuyère, qui se combinent avec le choc droit pour former un système en λ . de sorte que l'efficacité moyenne de recompression de l'écoulement est supérieure à l'efficacité du choc droit à Mo.

Si l'écoulement primaire est partiellement intéressé par les deux chocs obliques (fig. 7), son efficacité est améliorée. Mais pendant la fermeture de Ac2 le choc droit se rapprochant du plan de sortie de la tuyère, à un moment donné, l'écoulement primaire cesse d'être influencé par les chocs obliques (fig. 8) et l'efficacité est alors redevenue celle du simple choc droit : la caractéristique présente dans ce cas un maximum.

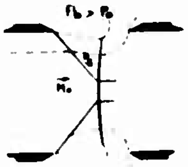

Fig. 7

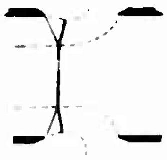

Fig. 8

Pour certaines configurations du piège, dans le cas où l'écoulement primaire est d'abord intéressé par les deux chocs obliques, on constate sur la strioscopie pour une certaine valeur de Ac2 la brusque disparition du système de chocs au niveau du piège associée à une brusque augmentation de la pression piège et du débit secondaire. Nous appellerons ce phénomène : désamorçage du piège

5. MÉTHODE DE CALCUL

Il est possible de calculer pour chaque configuration, l'évolution de l'efficacité en fonction du débit à condition de faire certaines hypothèses que l'expérience semble confirmer.

Une configuration du piège déterminée sera définie par les paramètres géométriques fixés L, ΔH, θ Acp et les paramètres variables x, h et A (fig. 9).

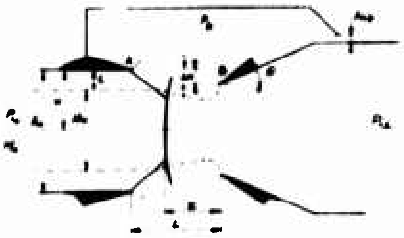

Fig. 9

A chaque valeur de h, hauteur d'écoulement capté par le piège, correspond une épaisseur de perte de débit $\delta_1(h)$, et de quantité de mouvement $\delta_2(h)$ définies par

$$(3)\qquad \delta_1(h) = \int_h^{\delta} \left(1 - \frac{\rho u}{\rho_o u_o}\right) dy$$

et (4)
$$\delta_2(h) = \int_h^{\delta} \frac{\rho u}{\rho_o u_o} \left(1 - \frac{u}{u_o}\right) dy$$

Le coefficient de débit primaire correspondant ε (lié à la pression piège par (2)) est par définition

$$\varepsilon = \frac{H - h - \delta_1(h)}{H - \delta_1(o)}$$

d'où l'on déduit

$$(5)\qquad h = f(\varepsilon)$$

et par conséquent :

$$(6)\qquad \lambda = \frac{H - h}{H} = g(\varepsilon)$$

Il convient tout d'abord d'étudier deux cas particuliers, dont il est indispensable de connaître certains éléments pour appliquer ensuite la méthode de calcul dans le cas général.

5.1. Etude du cas particulier Pb Po

Le coefficient de débit ε désigné alors par εo est donné par $\varepsilon_o = 1 - \frac{P_o Acb}{P_{io} Aco}$. Il est important de connaitre la position du choc repérée par x, ainsi que l'efficacité globale, désignée dans ce cas par $(\eta_{o2})_{Po}$

Position du choc ($P_b = P_o$)

L'écoulement présente un aspect analogue à celui d'une prise d'air Pitot en régime subcritique avec un choc détaché. A condition que l'entrée du diffuseur ne soit pas nettement plus large ($\Delta H < 0$) que la sortie de la tuyère, l'expérience montre que les distances de détachement du choc sont effectivement comparables.

D'après une étude de Moeckel (3) sur les prises d'air en régime subcritique, la distance de détachement du centre de choc est donné en fonction du coefficient de débit ε effectif et du coefficient de débit critique $\bar{\varepsilon}$ par

$$x = 2\,H_e \cdot K \cdot \left(1 - \varepsilon/\bar{\varepsilon}\right)$$

où k est une fonction de Mo (fig. 10).

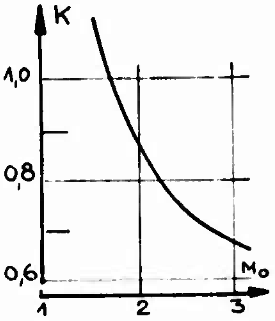

Fig. 10

Nous admettrons que la formule de Moeckel s'applique dans le cas $\varepsilon = \varepsilon_o$ quand on y remplace $\bar{\varepsilon}$ par ε_o, débit critique maximum correspondant à un choc attaché aux lèvres du diffuseur quand $P_b = P_o$ c'est-à-dire d'après (5)

$$\bar{\varepsilon}_o = \frac{H - \Delta H - \delta_1(\Delta H)}{H - \delta_1(o)}$$

Quand $\Delta H = 0$, $\bar{\varepsilon}_o$ est évidemment $= 1$.

Quand $\Delta H \neq 0$ nous conserverons $\bar{\varepsilon}_o = 1$ (on verra que, comme on pouvait s'y attendre, les résultats des calculs sont moins bien confirmés par l'expérience pour ce type de disposition ; les configurations avec $\Delta H \neq 0$ sont d'ailleurs pratiquement moins intéressantes).

La distance du choc associé à $\varepsilon_o < \bar{\varepsilon}_o$ est d'après notre hypothèse:

$$x_o = 2\,H_e\,K\left(1 - \varepsilon_o/\bar{\varepsilon}_o\right) \qquad (7)$$

Calcul de l'efficacité

L'efficacité dans le cas particulier considéré peut s'obtenir, en première approximation, à l'aide de la méthode des écoulements moyens (4).

On obtient ainsi l'efficacité primaire après le choc $(\eta_{o1})_{P_o}$:

$$(\eta_{o1})_P = Q\,\frac{\Sigma(M_m)}{\Sigma(M_o)} \qquad (8)$$

où $\Sigma(M) = \dfrac{1}{M}\left(\dfrac{2}{\gamma+1} + \dfrac{\gamma-1}{\gamma+1}M^2\right)^{\frac{\gamma+1}{2(\gamma-1)}}$

Le Mach Mm est obtenu par la relation

$$\phi(M_m) = \phi(M_o)\,\frac{D}{Q} \qquad (9)$$

dans laquelle

$$Q = 1 - \frac{\delta_1(h)}{H} \qquad (10)$$

et

$$D = 1 - \frac{\gamma M_o^2}{1+\gamma M_o} \cdot \frac{\delta_1(h) + \delta_2(h)}{H} \qquad (11)$$

où $\phi(M) = \bar{\omega}(M)\,\Sigma(M) \cdot (1 + \gamma M^2)$

avec $\bar{\omega}(M) = P/P_i\,(M) = \left(1 + \dfrac{\gamma-1}{2}M^2\right)^{-\gamma/\gamma-1}$

Pour déterminer l'efficacité globale $(\eta_{o2})_{P_o}$ il faut encore connaitre l'efficacité propre du diffuseur η_{e2}, la recompression 1 (face aval du choc) à e (entrée du diffuseur) étant supposée isentropique.

Une expression usuelle de l'efficacité du diffuseur subsonique est :

$$\eta_{e2} = 1 - K_d\,\frac{1}{2}\,\frac{\rho_o U_o^2}{P_i} = 1 - \frac{K_d}{2}\,\gamma\,\bar{\omega}(M_e) \cdot M_e^2 \qquad (12)$$

où Me est le Mach à l'entrée du diffuseur et Kd un coefficient dépendant surtout de la géométrie du diffuseur (c'est-à-dire de ΔH et θ en particulier).

Le Mach d'entrée Me est ici déterminé d'après la loi de recompression isentropique de l'écoulement moyen depuis le choc jusqu'à l'entrée par

(13) $$\Sigma(M_e) = \Sigma(M_m)\, A_e/\lambda A_o$$

Le coefficient Kd peut être obtenu soit par un calcul des couches limites du diffuseur soit par une expérimentation.

Nous avons alors tous les éléments pour tracer sur le diagramme η, ε la courbe

(14) $$(\eta_{o2})_{P_o} = (\eta_{oe})_{P_o} \cdot \eta_{e2}$$

Chaque point correspondant évidemment à une valeur particulière de Acp (fig. 11).

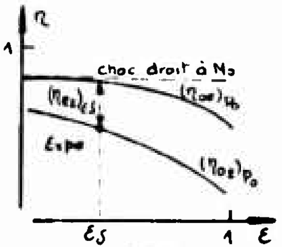

Fig. 11

Dans l'étude présente Kd a été déterminé expérimentalement en se référant au cas particulier où, toute la couche limite passe dans le piège, (εo correspond alors à h = δ). On écrit :

$$\eta_{e2} = \frac{\eta_{o2}\ \text{experimental}}{\eta_o\ \text{théorique}}$$

et, comme dans ce cas, D = Q = 1, le nombre de Mach Mm est le nombre de Mach derrière le choc droit Mo, l'efficacité (η_{oe})po étant celle du choc droit η_o

5.2. Etude du cas particulier où le diffuseur est en régime supercritique

Dans ce cas, le choc est à l'intérieur du diffuseur où, à la limite, juste à l'entrée. Le débit du diffuseur est constant puisque l'écoulement à l'entrée est supersonique.

Il en est de même par conséquent du coefficient de débit désigné par $\bar{\varepsilon}$ et de la pression piège $\overline{Pb}$ qui lui correspond par la relation

(2) $$\bar{\varepsilon} = 1 - \frac{A_{cp}\,\overline{P_b}}{A_{co}\,P_{io}}$$

Pour chaque configuration, il est indispensable de déterminer $\bar{\varepsilon}$ et $\overline{Pb}$ correspondant à une valeur de Acp donnée, $\bar{\varepsilon}$ étant en effet la valeur limite à donner à ε quand on applique la méthode de calcul dans le cas général.

Nous allons, à cet effet, étudier l'écoulement supersonique au niveau du piège et en déduire une deuxième relation entre $\bar{\varepsilon}$ et $\overline{Pb}$, dépendant uniquement des conditions locales du piège. Cette relation, jointe à la relation (2) donnera la solution cherchée.

En l'absence de couche limite, l'écoulement au niveau du piège présenterait l'aspect de la figure 12 avec un faisceau de détente issue de A.

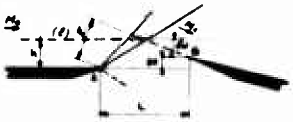

Fig. 12

En réalité, la zone d'écoulement de hauteur h qui nous intéresse est entièrement comprise dans la couche limite, mais nous admettrons que la viscosité est négligeable au niveau du piège, que les lignes de courant restent parallèles entre-elles, et que à l'extérieur de la couche limite l'écoulement subit une détente par ondes simples. Ces diverses hypothèses sont étudiées plus en détails dans$^{(1)}$

Dans ces conditions, la figure 12 permet de déduire h_1 par :

(15) $$h_1 = L \sin \delta\omega + \Delta H \cos \delta\omega$$

où $\delta\omega$ est calculé par la loi de détente de Mayer de Mo à M1 avec $\bar{\omega}(M_1) = P_b/P_{io}$

D'après l'équation de continuité on montre $^{(1)}$ qu'il est justifié d'écrire : (16) $h = h_1 \dfrac{\Sigma(M_o)}{\Sigma(M_1)}$

et en définitive nous obtenons une relation : $\overline{Pb}/P_{io} = f(\bar{\varepsilon})$

5,3. Etude du cas général

Dans le cas général, on se donne Pb ≠ Po.

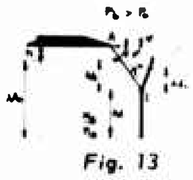

Fig. 13

- Si Pb > Po une onde de choc oblique se forme en A et rencontre le choc droit en I (fig. 13).
- Si Pb < Po nous schématisons le faisceau de détente par une ligne de Mach α_o (fig. 14). Cette simplification est justufiée $^{(1)}$.

  Le Mach M1 et la direction AI sont déterminés par Pb/Pio.

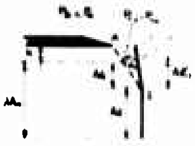

Fig. 14

En aval de ce système d'ondes, l'écoulement cesse d'être uniforme mais étant donné que les directions des diverses parties restent très voisines de la direction de Mo, nous traiterons cet écoulement hétérogène par la méthode des écoulements moyens $^{(4)}$.

Nous faisons alors l'hypothèse que le choc terminal se compose de deux parties :

- une section Ad avec un choc droit dans (Mo),
- une section Ad'$_1$ avec un choc droit dans (M_1).

La loi de conservation des débits permet d'écrire, en supposant pour l'instant que la couche limite passe entièrement par le piège :

(17) $$Ad'_1 = (\lambda A_o - Ad)\,\frac{P_{io}\ \Sigma(M_1)}{P_{i1}\ \Sigma(M_o)}$$

La conservation de la dynalpie permet d'écrire, Mm étant le Mach aval moyen subsonique

(18) $$\phi(M_m) = \phi(M_o)\frac{Ad}{\lambda A_o} + \phi(M_1)\left(1 - \frac{Ad}{\lambda A_o}\right)$$ ainsi que

(19) $$\frac{P_{im}}{P_{io}} = \frac{A_{co}}{A_{cm}} = \frac{\lambda A_o}{Ad + Ad'_1}\ \frac{\Sigma(M_m)}{\Sigma(M_o)}$$

En définitive il vient : (20) $$\eta_m = \frac{\Sigma(M_m)}{\Sigma(M_o)\ Ad/\lambda A_o + P_{io}/P_{i1}\,\Sigma(M_1)(1 - Ad/\lambda A_o)}$$

η_m représente donc l'efficacité moyenne après le système de chocs, pour un écoulement uniforme amont.

En fait, la section λ Ao comporte généralement une partie de la couche limite.

Pour en tenir compte, nous admettrons sous réserve de vérifications expérimentales la relation :

$$\eta_{oe} / \eta_m = (\eta_{oe})_{P_o} / \eta_o$$

Cette relation exprime que le rapport entre l'efficacité effective η_{oe} et l'efficacité η_m de l'écoulement sans couche limite est le même que dans le cas simple Pb = Po discuté au parag. 5.1.

L'efficacité totale en sortie de diffuseur sera donc :

(21) $$\eta_{o2} = \eta_{oe} \cdot \eta_{e2} = \eta_m \cdot \eta_{e2}\left(\frac{(\eta_{oe})_{P_o}}{\eta_o}\right)$$

où η_{e2} est déterminé en fonction de ε par 12 et 13 au paragraphe 6.1.

Pour pouvoir appliquer les calculs précédents, il est indispensable de connaître l'évolution de la section Ad en fonction du coefficient de débit ε c'est-à-dire la position du choc pour chaque valeur de ε.

Nous admettrons que le déplacement se déduit de xo par la loi linéaire

(22) $$x = x_o\,\frac{\bar{\varepsilon} - \varepsilon}{\bar{\varepsilon} - \varepsilon_o}$$

évidemment satisfaite aux limites $\varepsilon = \bar{\varepsilon}\,(x=0)$ et $\varepsilon = \varepsilon_0\,(x = x_v)$

Combinant (7) et (22), il vient alors la loi générale

$$x = 2\,H_e\,K\,\left(1 - \frac{\varepsilon_0}{\bar{\varepsilon}_0}\right)\frac{\bar{\varepsilon} - \varepsilon}{\bar{\varepsilon} - \varepsilon_0} \tag{23}$$

Pour une configuration donnée, toutes les grandeurs du second membre sont maintenant connues, de sorte que à toute valeur de ε, (23) fait correspondre une position x du choc.

En assimilant toujours le faisceau de détente à la ligne de Mach α_0 on a :

$$Ad/A_0 = 1 - \frac{L - x}{H}\,tg\,\alpha_0 \tag{24}$$ et évidemment si $Pb > P_0$

$$Ad/A_0 = 1 - \frac{L - x}{H}\,tg\,\sigma \tag{25}$$

où σ représente l'angle de choc oblique AI.

(23), (24) ou (25) donnent la relation entre Ad et ε et la méthode générale de calcul exposée ci-dessus donne la valeur correspondante de η_{02}

6. DISCUSSION DES RÉSULTATS THÉORIQUES - DÉSAMORÇAGE

6.1. Stabilité de l'écoulement

Si le choc n'est pas à l'entrée de la tuyère et si la partie marginale de l'écoulement primaire est intéressée par les chocs obliques, le calcul de la caractéristique $\eta_{02} = f(\varepsilon)$ est poursuivi au-delà du maximum jusqu'à ce que l'efficacité redevienne celle du choc droit ($Ad/\lambda A_0 = 1$)

Le calcul fait apparaître pour une valeur de Acp, suivant la configuration (L, ΔH) choisie, deux types différents de caractéristiques quand Pb augmente et que par conséquent ε diminue :

1er cas - Le rapport $\eta/\varepsilon = \frac{Ac_0}{Ac_2}$ croît continûment. Dans ce cas, on passe continûment de la configuration de chocs en λ à celle du choc droit.

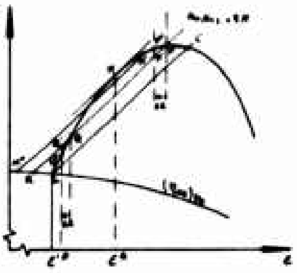

Fig. 15

2e cas - Le rapport $\eta/\varepsilon = \frac{Ac_0}{Ac_2}$ passe par un maximum au point M (fig. 15). ε prend alors la valeur ε^* ; pour $\varepsilon < \varepsilon^*$, η/ε décroît et la caractéristique rejoint la courbe $(\eta_{02})_{b_0}$ en L avec la valeur ε'^* du coefficient de débit.

Il en résulte que dans le domaine LML', il existe trois solutions P, Q, R (fig. 15) pour une configuration $\eta/\varepsilon = Ac_0/Ac_2$ donnée.

On démontre$^{(1)}$ que seules les solutions P et R sont stables. Dans une diminution lente continue de Ac_2/Ac_0, le phénomène sera donc stable jusqu'à la situation (M), ou plus exactement jusqu'à une position M' telle que $\varepsilon(M') - \varepsilon(M)$ soit juste égal à la fluctuation maximale de ε autour de l'équilibre.

Dès que le point figuratif de l'équilibre passera à gauche de M', on voit que sous l'effet des fluctuations, l'écoulement pénètrera dans la zone d'instabilité et le point d'équilibre viendra se fixer en M". Il apparait ainsi un cycle d'hysteresis M'M"LL'.

6.2. Maximum théorique de la pression piège

Indépendamment du phénomène précédent, le désamorçage du piège peut avoir lieu pour d'autres raisons :

6.2.1. - Il existe une limite de fonctionnement liée à une pression piège maximale correspondant à la limite d'existence du point triple I du choc en λ. Henderson$^{(5)}$ montre que pour un Mach Mo, il existe une déviation limite ψ^* au delà de laquelle il n'y a plus de possibilité de point triple, la structure des chocs en λ ne pouvant être conservée, le changement qui intervient conduit à la formation d'un choc unique quasi-droit c'est-à-dire au désamorçage du piège.

Pour un nombre de Mach Mo $<$ 1,27, il n'y a plus du tout de solution de point triple et, par conséquent, on ne pourra espérer bénéficier dans ce domaine d'un effet de choc oblique pour améliorer l'efficacité.

6.2.2. - Le désamorçage peut aussi avoir lieu si le saut de pression à travers le choc oblique est trop intense et provoque le décollement de la couche limite de la tuyère. Nous prendrons comme critère de décollement[(4)] $M_1/M_0 = 0{,}78$.

Pour comparer dans un cas limite les deux derniers types de désamorçage du point de vue de l'efficacité maximale, nous avons représenté fig. 16 l'efficacité η_{oe} calculée en fonction du Mach M_1 pour diverses valeurs de Mo et pour une configuration telle que le choc droit terminal se produise au point de rencontre des chocs obliques sur l'axe, c'est-à-dire avec une section Ad = 0. L'efficacité est alors le produit de celle du choc oblique et de celle du choc droit. La courbe $M_1 = M_0$ représente évidemment l'efficacité du simple choc droit.

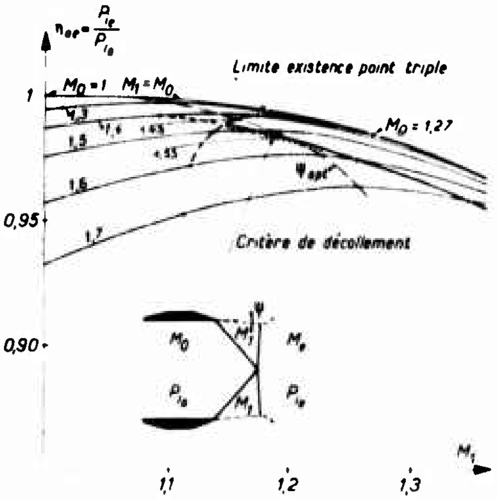

Fig. 16 - Efficacité théorique

Les courbes "iso Mo" révèlent un premier maximum classique η_{opt} pour la déviation Ψ optimum.

Sur la figure 16 sont aussi reportées en coordonnées η_{oe}, M1 les deux courbes correspondant respectivement à la limite d'existence du point triple et au critère de décollement $M_1/M_0 = 0{,}78$.

Les points situés à gauche du critère de décollement sont inaccessibles ; il en est de même des points situés au-dessus de la limite d'existence du point triple et de la courbe $M_1 = M_0$ qui la prolonge.

Dans ces conditions, on constate que :

- pour Mo $<$ 1,43, l'efficacité maximale est fixée par la condition point triple ou simple choc droit,
- pour 1,43 $<$ Mo $<$ 1,53, l'efficacité optimale est identique à l'efficacité maximale,
- pour 1,53 $< M_0$ l'efficacité maximale correspond au critère de décollement.

6.3. Nombre de Mach M_0 optimum

En reportant sur un graphique l'efficacité maximale en fonction du Mach Mo (fig. 17), nous voyons qu'il existe, en dehors du voisinage immédiat de $M_0 = 1$ pratiquement inutilisable pour des raisons de stabilité, un maximum pour $M_0 \simeq 1{,}4$.

Il y aurait donc intérêt dans un projet de prise d'air à obtenir un Mach terminal de recompression supersonique voisin de 1,4 et une configuration du type figure 16 (Ad = 0).

En réalité, il est difficile d'admettre une section Ad strictement nulle (problème de compatibilité de l'écoulement au point de rencontre des chocs obliques et des chocs droits).

La valeur minimum de Ad/Ao qui dépend de M1 et de Mo n'est pas actuellement accessible à la théorie.

Sur la figure 17 sont donc reportées les courbes d'efficacité maximale obtenues suivant lesmêmes principes pour des valeurs échelonnées de Ad/Ao.

A partir de Ad/Ao $>$ 0,5 il n'y a plus de maximum d'efficacité mais le choc en λ offre toujours un gain appréciable par rapport à l'efficacité du choc droit.

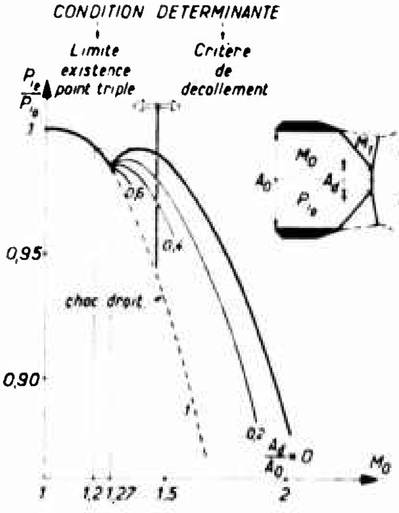

Fig. 17 - Efficacité maximum

7. RÉSULTATS EXPÉRIMENTAUX ET COMPARAISON AVEC LE CALCUL

Seuls quelques résultats expérimentaux significatifs obtenus à $M_0 = 1{,}42$ sont ici présentés ; des essais effectués à d'autres nombres de Mach (1,12 et 1,72) confirment la validité de la méthode de calcul (1).

A Mo = 1,42, en absence du piège sur les parois latérales, les essais ont montré que le choc provoque un décollement de la couche limite sur ces parois. Il en résulte une instabilité de l'écoulement ainsi qu'une mauvaise efficacité. Par contre avec un piège latéral, tous les essais montrent un écoulement remarquablement stable. Le système de chocs avec ou sans détente apparaît très nettement sur les strioscopies (fig. 18).

L'allure générale d'une caractéristique $\eta(\varepsilon)$ est comparée avec celle qui est obtenue sans piège latéral. Le gain d'efficacité est particulièrement important. La comparaison avec le calcul est satisfaisante ; on constate seulement de faibles écarts pour les points voisins de la limite où la pression piège Pb est supérieure à Po.

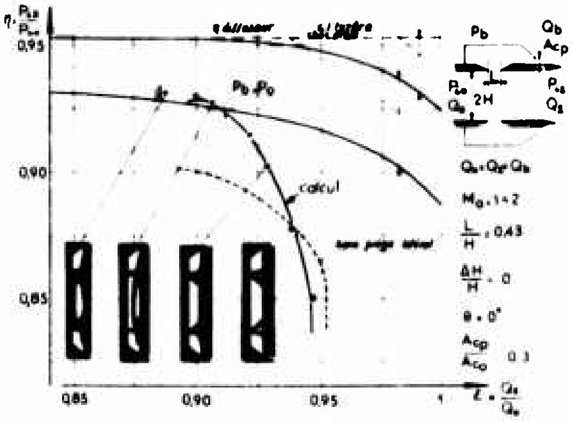

Fig. 18 - Essai avec piège latéral

Ces écarts peuvent provenir de la loi de déplacement retenue pour le choc, qui donne en fait la position du centre du choc.

La courbure progressive du choc vers les parois intervient dans le cas d'une faible largeur de piège et permet de bénéficier plus longtemps de l'effet de chocs obliques. En particulier la limite pour laquelle l'efficacité redevient celle du choc droit est repoussée (fig. 19).

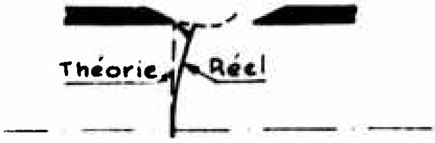

Fig. 19

Influence de l'angle du diffuseur

Le gain d'efficacité est expliqué par l'amélioration de l'efficacité du diffuseur. Toutefois, il y a une légère différence sur la limite de fonctionnement, en faveur de l'angle nul (fig. 20).

Dans le calcul, la loi d'avancement du choc ne dépend pas de l'angle du diffuseur et ne peut donc faire apparaître la différence des limites de fonctionnement. Pour le reste, les caractéristiques sont parfaitement prévues par le calcul.

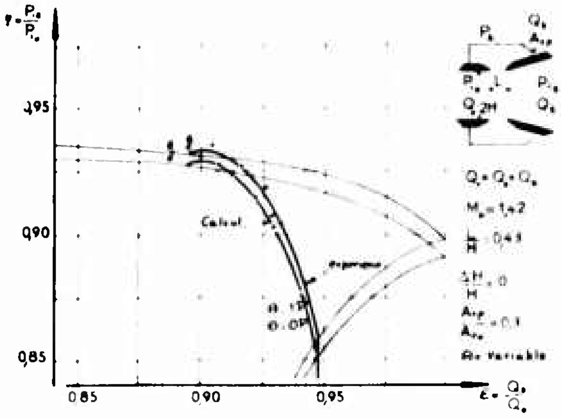

Fig. 20 - Influence de l'angle du diffuseur (avec piège latéral)

Influence de l'écart ΔH du diffuseur

Sur la figure 21 sont représentées deux séries de caractéristiques pour diverses valeurs de $\Delta H/H$ et de Acp/Aco.

Quand le diffuseur est en pitot ($\Delta H > 0$), à débit donné, l'efficacité est plus faible qu'à $\Delta H = 0$ (augmentation du nombre de Mach à l'entrée du diffuseur) mais par contre la marge de stabilité à débit variable est plus grande, car le désamorçage n'intervient que pour un débit plus réduit. Quand le diffuseur est en retrait l'efficacité n'est que très légèrement améliorée mais le désamorçage intervient plus tôt. Le calcul permet bien de prévoir l'influence de ΔH sur l'efficacité et sur la limite de désamorçage avec toutefois un glissement des limites calculées par rapport aux valeurs expérimentales comme précédemment.

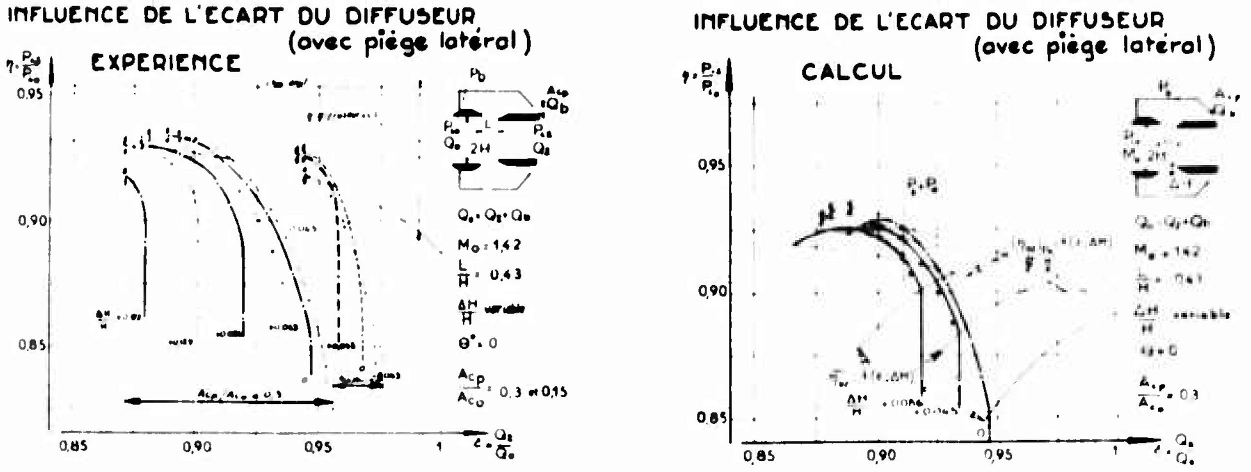

Fig. 21

Influence de la largeur du piège

Pour les points où Pb > Po l'influence du choc oblique augmente naturellement avec la largeur du piège et, par conséquent, l'efficacité croît. Toutefois, à partir du moment où les chocs obliques se croisent sur l'axe l'expérience montre que l'écoulement devient instable et l'efficacité baisse considérablement. Le calcul montre, par ailleurs, que les chocs réfléchis ne sont pas compatibles avec un choc droit (problèmes de points triples).

Pour une largeur encore plus grande, les chocs obliques se réfléchissent sur la ligne de jet en formant des détentes, et l'écoulement est instable comme dans le cas précédent.

Tant que les chocs obliques ne se croisent pas, le calcul (fig. 22) met bien en évidence les divers phénomènes. Pour la largeur de piège L/H 1,2 telle que les chocs obliques atteignent le choc droit près de l'axe, la correspondance est remarquable même pour Pb > Po, car il n'y a plus d'effet de courbure du choc droit central.

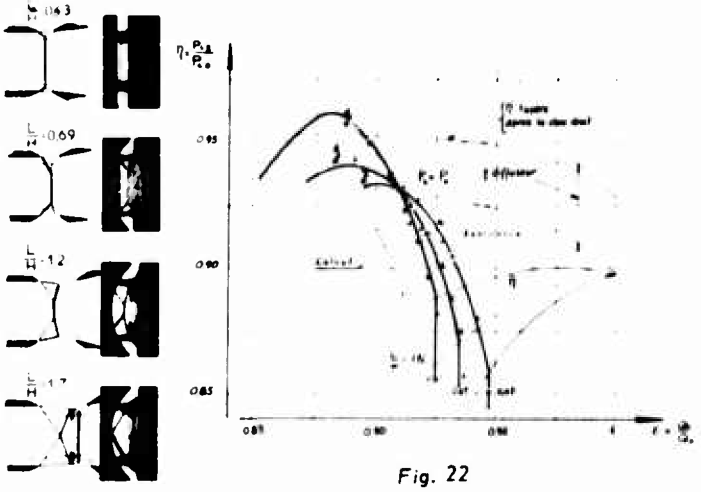

Fig. 22

8. CONCLUSION

Cette étude met en évidence la possibilité et l'utilité du calcul des pièges à couche limite et permet de discuter le choix des différents paramètres en vue d'obtenir la meilleure efficacité.

La méthode de calcul proposée semble bien vérifiée par l'expérience. On notera toutefois que les essais ont été effectués avec une couche limite de faible épaisseur relative et, bien que les calculs en tiennent compte, il se peut que dans le cas d'une couche limite beaucoup plus épaisse comme dans certaines prises d'air hypersoniques, les hypothèses faites précédemment ne permettent plus de prévoir les résultats expérimentaux de façon aussi satisfaisante.

La forme du diffuseur joue évidemment un rôle important et le choix de profils donnant la meilleure efficacité mériterait une étude particulière.

Les essais ont été effectués pour un écoulement amont uniforme et un diffuseur symétrique. Des études complémentaires seraient souhaitables pour couvrir d'autres types de configurations possibles.

9. RÉFÉRENCES

1. MEAUZE, G. Etude de la recompression par chocs d'un écoulement interne supersonique en présence d'un piège à couche limite. Note Technique ONERA (à paraître).

2. LEYNAERT, J. Fonctionnement du piège à couche limite interne d'une prise d'air à compression supersonique externe. Aerodynamics of power plant installations - AGARDograph 103 (1965).

3. MOECKELL, W.E. Approximate method for predicting form and location of detached shock ahead of plane or axially symmetric bodies. NACA TN 1921 (1949).

4. CARRIERE, P. Aérodynamique interne des réacteurs - 1e et 2e parties - Prise d'air. ENSAé Cours de 3e année (1963).

5. HENDERSON, L.F. On the confluence of three shock waves in a perfect gas. Aeronautical Quarterly - vol. XV p. 181 - May 1964.

NOISE GENERATION BY STEADY AND UNSTEADY FLOW DISTORTIONS

J.S.B. Mather and M. J. Fisher
University of Nottingham ISVR, Southampton

1.0 Introduction

The theory of Tyler and Sofrin (Ref. 1) which appeared in 1961 spent many years in abeyance awaiting agreement with a suitably conducted experiment. From 1968 onwards Rolls-Royce and Rolls-Royce (1971) Ltd. began to see this agreement emerging and it is now possible to use the theory, with some simple modifications, to predict the far-field angular distribution of noise radiating from the inlet to a fan or compressor that has mainly rotor-stator interaction tones. It was recognised immediately that the radiation into the rear arc from the by-pass section could not be so easily predicted since jet refraction obviously takes place, and radiation of the non-linear waveform known as 'buzz-saw noise is equally more difficult to predict accurately although generally with low phase velocities the waves tend to radiate the energy at angles greater than 45° to the inlet axis. In 1970, the results from a research compressor rig showed a multiplicity of tones in the far-field at other frequencies than blade passing and its harmonics even when the tip speed of the compressor was well subsonic. A simple extension of the theory (Ref. 2) covered this case and explained the plane waves that appeared on the axis of the fan. The theory essentially extended Tyler and Sofrin's work to the case where all rotor blades were acoustically unequal and this allowed the generation of many more propagating modes at shaft harmonic frequencies.

The work in this paper continues this logical extension and, retaining the blade individuality assumption, produces an expression for the acoustic pressure in the duct caused by the interaction between a rotating inlet distortion and the rotor and stator flow fields. Particular cases are given when the cellular structure of the distortion is not rotating, when the whole system rotates at a value less than that of the rotor, when the system has no circumferential distribution but rotates, and when the rotor passes on the characteristics of the distortion to the stator row.

2.0 Stationary distortions

2.0.1 Applications

These may arise and it is the authors' experience that they do arise in many installations of aero-engines in aircraft. Some of these instances may be common, e.g.

1) inlet at moderate angle of attack on landing where a separation can occur behind the lower lip,

2) rear-engined aircraft where the upwash from the wing enters the inlet and causes a fixed maldistribution of flow,

3) entry into the inlet of the fuselage boundary layer flow perhaps with yaw on the aircraft,

4) S-shaped ducts where the static pressure continuity along the duct gives rise to a distortion pattern

5) poor operation of inlets in cross-flow situations particularly when the forward speed of the aircraft is low,

6) the mixed flow pattern arising from the use of blow-in doors in the wall of the inlet,

7) a maldistribution of the outlet flow in a by-pass unit giving rise to alternating forces on the rotor blades of the fan.

The distortions may be internally generated, e.g.

1) the flow field through the fan rotor when subjected to the potential field of the pylon or some other service-carrying obstacle in the flow path of the duct.

Less common at the moment although under consideration for the future are the V/STOL units which by virtue of their mode of operation subject both the inlet and the outlet to severe aerodynamic conditions. There are many sources of information on these conditions and one of them (reference 3) is given here for completeness. The authors are at this moment unaware of the details of any recirculation of the air flow that might occur but the advent of this situation would obviously create a condition that falls into this category of noise source. It should be noted that the above list can be subdivided into examples where the distortion or maldistribution of the flow is severe and those where the condition can almost be regarded aerodynamically as a secondary effect.

2.0.2 Theory

A general theory has been developed and the details of this are laid out in the Appendix I.

For the case of the interference between stationary distortions and the rotor field, the general formulation can be reduced by putting $\omega = 0$ where ω represents the rotational component of the maldistribution.

Thus the resulting acoustic pressure can be written

$$p(\theta, t) = \tfrac{1}{2} \sum_n \sum_p a_{np} \left\{ \cos\left[(n + p)\theta - n\Omega t + \phi' \right] + \cos\left[(n - p)\theta - n\Omega t + \phi'' \right] \right\}$$

The tonal frequencies produced by this pattern are at the shaft frequency Ω and all of its harmonics (n). It is not possible therefore to determine the effect of this phenomenon simply on a frequency basis. Each of the two terms however represents modal patterns characterised by their circumferential distribution $n \pm p$ and their angular speed

$\dfrac{n\Omega}{n \pm p}$. For a finite value of p, i.e. for the very existence of a

distortion, the two speeds at each frequency will differ. Additionally the critical speeds of the patterns, above which the modes propagate unattenuated along the duct, are determined by their circumferential distributions and are, in consequence, also different. References 1 and 2 show that the spherical radiation of modal patterns from the end of ducts or inlets into the far-field depends essentially on the ratio of the actual pattern speed to the critical speed for that pattern. In general patterns with high ratios radiate acoustic energy at small angles to the duct axis. Since

$$\frac{n\Omega}{n - p} > \frac{n\Omega}{n + p}$$

the patterns may be distinguishable in the far-field acoustic distribution. Methods to determine the modal content of the in-duct pattern by measuring in the inlet flow or in the wall of the inlet duct are being developed (references 10 and 11) and could be applied to this situation.

If the tip speed of the rotor that is experiencing the distortion is subsonic then it can be inferred from the eigenvalues of the modes (Ref. 5) that only the higher speed patterns can propagate unattenuated along the duct and then only if

$$\left| \frac{n\Omega}{n - p} \right| > \Omega_c \quad \text{for each of the modes } n - p$$

and a maximum value of p occurs for each frequency when

$$\frac{n}{p - n}\Omega > \Omega_c$$

Thus

$$p < n\left(1 + \frac{\Omega}{\Omega_c}\right)$$

Therefore at a given frequency ($n\Omega$) the range of p that gives rise to propagating modes follows from

$$n\left(1 + \frac{\Omega}{\Omega_c}\right) > p > n\left(1 - \frac{\Omega}{\Omega_c}\right)$$

A particular case of interest occurs when $p = n$ whence the speed is infinite and the mode is a plane wave which radiates its acoustic energy along the axis of the duct in the far-field.

2.0.3 Conclusions

1) The theory shows that a new family of modes can be generated by the interaction of a stationary inlet distortion and the rotor.

2) With a subsonic tip speed, there is a finite range of distortion patterns (characterised by p) that generate the propagating modes.

3) For a wall supersonic tip speed it is possible that at each frequency there are two families of propagating modes; possibly distinguishable in the far-field by their directional properties.

4) If the rotor has a high subsonic tip speed, the theory shows that propagating modes are generated in the interaction between the rotor and those low order distortion harmonics associated with the more common inlet flow maldistributions.

5) The amplitude of the acoustic energy in any mode is not determined. It should be remembered that it is not necessarily the case that large amplitude distortion harmonics give rise to associated large amplitude acoustic modes.

6) This theory does not take into account the effect of distorted flow on the broad band noise level radiated by the rotor.

2.1 Unsteady cellular distortions

These are characterised by both the discrete nature of the circumferential distribution of pressure and the frequency or rotation .

2.1.1 Applications

There are a number of applications which are aerodynamic in source.

1) It is known that for certain flow conditions in axi-symmetric intakes, the separation at the lip can rotate around the intake in an unstable way.

2) A pre-whirling flow pattern in the duct may be carrying distortions from upstream obstacles or modes.

3) The well-known rotating stall situation where the pattern is known to consist of a number of cells which as a whole rotate in the same direction as the rotor at some fraction of the speed of that rotor.

2.1.2 Theory

From the general formulation in the Appendix it is possible to cover the rotating stall case by retaining ω and p as finite non-zero values but considering only those terms that are generated by a distortion rotating in the same direction as the rotor. Thus

$$p(\theta, t) = \frac{1}{4} \sum_{n} \sum_{l} \sum_{p} a_{npl} \left\{ \cos\left[(n + p)\theta - (n\Omega + l\omega)t + \phi'\right] + \cos\left[(n - p)\theta - (n\Omega - l\omega)t + \phi''\right] \right\}$$

Let $\frac{l\omega}{p} = \Omega_s$, the speed of rotation of the stall pattern.

The frequencies of the two families of modes in the duct are $(n\Omega + l\omega)$ and $(n\Omega - l\omega)$, i.e. sum and difference tones of the shaft harmonic frequency and what might be termed the "cell passing frequency" of the stall pattern. The speed of rotation of these patterns is:

Sum tone, $$\frac{n + p\Omega_s/\Omega}{n + p} \cdot \Omega$$

Difference tone, $$\frac{n - p\Omega_s/\Omega}{n - p} \cdot \Omega$$

Since in a rotating stall the distortion rotates at a speed less than that of the rotor, then

$$\frac{\Omega_s}{\Omega} < 1$$

Thus the speed of the difference tone is greater than the speed of the rotor and the speed of the sum tone is less than that of the rotor. For unattenuated propagation of modes along the duct the modal speed must be supercritical. It will be shown later than from the experimental results the interaction seems to be with blade passing frequency and its harmonics rather than the shaft rotational frequency. Thus

$$\frac{nB - p\Omega_s/\Omega}{nB - p} > \frac{\Omega_c}{\Omega}$$ for the difference tone mode.

This mode will appear at subsonic tip speeds and the sum tone will appear only when the tip speed of the rotor is supersonic. The equation shows that for propagation there must be a minimum value to p, which will decrease as the speed of the rotor increases to a value of Ω_c/Ω equal to unity. This implies that there is a frequency maximum associated with the difference tone, given by

$$B\Omega\left(1 - \frac{p_{min}\,\Omega_s}{B\Omega}\right)$$

If p is associated with the cellular pattern of the rotating stall then there will be a minimum frequency for the modes when p equals B the number of blades.

If the rotating stall pattern is not truly sinusoidal, then p may take on higher values associated with the harmonics of the pattern and this opens up a wider range of acoustic possibilities for the equations briefly outlined above.

2.1.3 Experimental results

The first set of experimental results were obtained from the noise of a 86 cm diameter split stream fan having a by-pass ratio of 5:1. The unit has individually controlled outlet throttles for each of the sections. Unfortunately during the early testing of the rig it was found that the by-pass flow was having a throttling effect on the flow in the engine section giving rise to a stall situation on some parts of the fan blades.

At a tip speed of 220 m/s the spectrum of the noise radiated into the far-field at an angle of 60° to the inlet axis is as shown in Figure 1. The analyser has a constant 20 Hz bandwidth and easily distinguishes the blade passing tone at 2150 Hz and its harmonics. For this work however the interest lies in the broad bands of high amplitude noise adjacent to each of the three tones shown in the spectrum. On close examination these difference peaks lie at a fixed frequency below the tones and this frequency is four times the shaft rotational frequency.

Thus from the theory $\frac{p\Omega_s}{\Omega} = 4$

Since the unit has 25 rotor blades, the equation for propagation reduces to

$$\frac{25-4}{25-p} > \frac{\Omega_c}{\Omega}$$

where Ω_c is the critical speed for a mode with characteristic value

$$25 - p$$

It is possible to combine the two equations, determine an eigenvalue and hence, by iteration, the value of p. From this the far field radiation pattern can be determined. This can then be compared to the experimental patterns shown in Figure 2. Using the inequality criterion the value of p must be greater than 10, but from the radiation patterns it seems that p must take on values nearer to the blade number 25. This value will obviously give a plane wave mode at the difference tone with the first harmonic but it predicts peaks for the difference tones with the second and third harmonics of 50° and 65° respectively. Allowing for deviations in the predicted angle caused by

a) the assumption of an infinite baffle termination to the duct

b) the assumption of a constant area duct with no inlet bellmouth,

the agreement is reasonable.

The second experiment used the identical rig with 33 blades replacing the 25 blades of the original rotor. Although less distinct figure 3 shows that the broad band peaks are again present but at a slightly larger difference frequency. Again the distribution in the far field (Fig. 4) can be matched to the equations by using a value of p equal to 27.

The matching will to some extent depend on the assumptions of propagation and radiation but the equation

$$\frac{B-k}{B-p} > \frac{2B-k}{2B-p} > \frac{3B-k}{3B-p}$$

giving higher cut-off values for modes associated with the lower frequencies is reflected by the trend in the results for the peak of the far-field distributions to move away from the axis for the higher frequency components.

The third experiment is from a different source (Ref. 6), namely from a small diameter, low speed fan run at Perkins Engines Ltd. at Peterborough.

Immediately prior to the onset of stall in the fan, the spectrum showed that the blade passing tone and the second harmonic disappeared leaving two large bands of noise in the regions between the tones (Fig. 5). There are no corresponding results in the far-field but the low tip speed suggests that a value p equal to or close to the blade number will be required for the theory.

2.1.4 Conclusions

1) Experimental results on a large diameter fan rig using two sets of rotor blading show that the theory can predict both the frequency of the difference tone and the far-field directivity pattern.

2) As predicted only the difference tone occurs at subsonic tip speeds.

3) The theory requires the value of the number of cells in the pattern to be equal to the number of blades.

4) This suggests that aerodynamically the rotating stall is at an early stage when the stall system is beginning to propagate around the duct and each blade generates a cell that travels slower than the rotor.

5) At the difference frequency the noise is broad band suggesting that the rotating stall is unstable as the noise from this source has a large turbulent governed component.

6) The compressor continued to run without any deterioration in the condition of the unit nor a significant alteration to the by-pass flow, which suggests that the conclusion four is probably correct.

7) Acoustic measurements may be more sensitive to the flow changes in this early stage than probes and are certainly much easier to obtain with less disturbance to the flow and could prove to be the basis for future work on this aerodynamic phenomenon.

2.2 Correlated fluctuations

Suppose that the inlet distortion is rotating at some speed $\ell\omega$ but the distortion is largely correlated over the whole of the inlet face instead of being divided into a well-formed cellular distribution. This may occur if large scale atmospheric turbulence enters the intake of the engine.

2.2.1 Theory

The theory reduces to the simple case where the circumferential distribution of the distortion is uniform and $p = 0$. In this case the patterns in the duct reduce to two modes associated with a sum tone and a difference tone. The speeds of these modes are such that for subsonic tip speeds only the sum tone mode can propagate unattenuated giving rise to a pressure field

$$p(\theta,\ t) = \frac{1}{2} \sum_{n} \sum_{\ell} a_{n\ell} \cos\left[n\theta - (n\Omega + \ell\omega)t + \phi\right]$$

with the condition that $\frac{n + \frac{\ell\omega}{\Omega}}{n} . \Omega > \Omega_c$ the critical speed of the mode.

At the cut-on condition or point of propagation, the inequality can be replaced by an equality and the minimum frequency is

$$(n\Omega + \ell\omega)_{min} = n\Omega(1 + \frac{\ell\omega}{n\Omega}) = n\Omega_c$$

which is the frequency generated by an n-bladed rotor at sonic tip speed. Note that for higher frequencies, such as blade passing say, the frequencies ($\ell\omega$) associated with the distortion must be an appreciable fraction of the blade passing frequency ($B\Omega$) to promote propagation unless $\frac{\Omega_c}{\Omega}$ is near to unity.

2.2.2 Conclusions

1) For well-correlated input distortions the propagating modes are associated with sum tones of the rotor harmonic and the frequencies of the distortion.

2) There is a minimum frequency for propagation.

3) For low frequencies, which might be expected to be the dominant content of atmospheric turbulence, propagation occurs only if the blade tip speed nears the sonic condition.

2.3 Interaction with stators

The condition envisaged is that where a distortion enters the intake and interacts with the rotor (to produce one of the acoustic situations of section 2.0-2.2). The rotor passes the essential features of the distortion, as well as the normal blade wake systems, to the stator bank which then suffers acoustic changes.

2.3.1 Applications

The applications are obvious and manifold but for advanced technology engines would probably be minimised by moving the stator bank away from the rotor. However in a VSTOL application using powered lift the engines are short in length and rotor-stator spacing is small. Ordinarily the stator number would be chosen to cut-off the modes at the offending frequencies. This theory discusses whether in the presence of distortion that condition is still relevant.

2.3.2 Theory

The details of the theory are not reproduced here. They can be found in reference 7 or they can be easily obtained from a simple extension of the theory in reference 2. The result is that the modal number m, which characterises the circumferential distribution is given by

$$m = n \pm kV \pm p$$

where n is the usual shaft harmonic, $V'$is the number of stators, k is any integer and p is the order of the inflow distortion components and takes any value from 0 to infinity.

2.3.3 Experimental results

The unit used for the experiments is the N.R.C. of Canada fan-in-wing installation. The unit is 25 cm in diameter and can give a tip speed of 200 m/s. There are 18 rotors and 11 stators in the configuration for these tests and the whole unit can be buried in a cross-flow situation. Microphones, measuring a complete semi-circle in the far-field, are also subjected to the cross-flow.

The compressor is not heavily loaded and it is thought that it is for this reason that the fan speed fluctuates. On a percentage bandwidth analysis the filter would be wide enough to contain the frequency change but on a narrow 20 Hz constant bandwidth this would not be possible. The signal therefore was processed by a Federal Scientific UA-7B analyser and the output plotted as frequency against time on a UV recorder. The amplitude of the signal is proportional to the density of the trace on this recorder. Figure 6 shows the result from processing the waveform from the microphone on the fan axis with the unit running at 12000 rpm with no cross-flow. The blade passing fundamental and second harmonic frequencies appear as well as a tone at the twenty-second engine order which is a plane wave mode as explained in reference 2. When cross-flow at a value of 23 m/s is introduced the signal from the same microphone undergoes considerable change (Figure 7). Many more tones appear each as some shaft harmonic and the second harmonic amplitude rises considerably relative to that of the fundamental frequency. From the modal equation, with $k = -3$, then the plane wave mode ($m = 0$) will appear when $n = 34$ $p = -1$

$n = 35$ $p = -2$

$n = 36$ $p = -3$

i.e. at the 34th, 35th and 36th shaft harmonics interacting with the first, second and third orders of the inlet distortion. Other shaft harmonics can be explained in a similar manner using different values of k and p. For each of these modes there will be an associated radiation pattern which will depend on the speed of the mode in the usual way.

2.3.4 Conclusions

1) Additional modes are generated by the multiple interaction of the inlet distortion field, the rotor and the stators of a compressor.

2) The theory predicts these modes and qualitatively agrees with experimental results of a fan in a cross-flow.

3) The multiplicity of modes so generated increases the possibility of the acoustic energy generated by the fan being convected unattenuated to the far-field.

4) Considerably more tonal frequencies are generated.

5) To design to cut-off of these modes, the criterion derived from Tyler-Sofrin's work remains relatively unchanged since the value of p is likely to be small.

6) The large modal content at a given frequency may reduce the effect of absorbent liners in reducing that frequency.

2.4 Tyler and Sofrin

The stator bank of V evenly spaced stators could be said to present to the rotor a "distortion" which can be written in the form

$$p(\theta) = \sum_k a_k \cos(kV\theta + \phi)$$

Thus in the terminology used in the theory p = kV, and at the blade passing frequency and its harmonics

$$n + p = nB + kV$$

Tyler and Sofrin's formulation for the pressure field was

$$p(\theta, t) = \sum_m \sum_n \frac{V}{2} \cos(m\theta - nB\Omega t + \phi_{mn})$$

and thus $m = n + p = nB + kV$ which confirms that the theory is consistent with previous theories.

3.0 Conclusions and Future Work

Individual detailed conclusions are given after each subject within the main text of the paper.

Generally the theory proposes a modal generation process for an interaction between a fan or fan unit and some inlet flow distortion. Special cases of steady state, rotating stall, correlated fluctuations, and interaction with stators are all dealt with and where experimental evidence is available the agreement with theory is qualitatively encouraging.

The work is not intended to be used as a design basis for fans since it is to be hoped that the aerodynamic situations described will be avoided as much as possible during operation of the units. It is however particularly important in the research and development field in noise because

1) the appearance of ancillary tones and broad band peaks must be explained away before the basic noise of the unit can be found,

2) the effect of ensuring that the aerodynamic situation is acceptable can now be quantified enabling a given design procedure to be technically and economically assessed.

From the results on the rotating stall condition it is inferred that the acoustics are probably more sensitive to the aerodynamic situation than the steady state probes are. There is even an advantage over the unsteady probes such as hot wires in that microphones reacting to this effect can be placed in the far-field if the engine is on an outdoor test-bed or the aircraft or at worst in the wall of the inlet/outlet ducting if the engine is mounted in a test cell. In both cases there will be no added interference to the flow. Additionally microphones can be and have been used in the duct walls of an engine in flight where realistic atmospheric conditions arise.

The paper does not deal with effects of distortion on the broad band levels although the authors have found marked increases in this component under many of the conditions described here. The theory has constantly referred to fan or compressor noise since the majority of the experimental evidence comes from that area but the work could equally apply to any rotating flow machine and in particular to the gas turbine where the combustion system exhausts on to it a highly turbulent and distorted flow pattern.

The paper adds a little to the rapidly evolving subject of acoustic diagnosis but much more experimental work is still needed.

4.0 References

1. Tyler, J.M. and Sofrin, T.G. Axial flow compressor noise studies. Trans. Soc. Auto. Engrs. 1961. pp. 309-332.

2. Mather, J.S.B., Fisher, M.J., Savidge, J. New observations on tone generation in fans. J. S. Vib. Vol. 16, No. 3, June 1971.

3. Schaub, U.W. and Bassett, R.W. Flow distortion and performance measurements on a 12 inch fan-in-wing model for a range of forward speeds and angle of attack setting. 38th meeting of the AGARD Propulsion and Energetics Panel. September 1971.

4. Krishnappa, G. Lifting fan noise studies with superimposed cross flows. AIAA Conference. San Diego, January 1972.

5. Snow, D. Cylindrical duct eigenvalues. Rolls-Royce Memorandum INM 90036. November 1970.

6. Hebard, P. Perkins Engines Ltd. Private communication.

7. Mather, J.S.B. A note on the effect of cross flow on the modes generated by Rotor-Stator interaction. Rolls-Royce Report INR 00118, September 1971.

8. Katto, Y. Some fundamental natures of resonant surge. (1st Report, Experimental Results and Analysis of Oscillating Systems). Bulletin of JSME. Vol. 3, No. 12, p. 484, 1960.

9. Ditto. (2nd Report, Theoretical Analysis). Bulletin of JSME. Vol. 3, No. 12, p. 490. 1960.

10. Moore, C.J. In-duct investigation of subsonic fan rotor-stator noise. JASA. Vol. 51, p. 1471-1482, 1972.

11. Yardley, P.D. The application of time-domain averaging techniques to fan noise measurement. Ph.D. Thesis, Southampton 1973.

Appendix I

Reference 2 discussed the effect of the interaction between a rotor having unequal blades in the row and a bank of identical stators. In the theory that follows the individual nature of the blades will be retained. When the experimental results show that the noise produced by the interference between the aeordynamics and the rotor field does not depend on the minor differences between blades then the shaft harmonic number n is replaced by the blade harmonic number nB.

The acoustic pressure field generated by a ducted rotor with unequal blading can be written as

$$p(\theta, t) = \sum_{n} a_n \cos (n\theta - n\Omega t + \phi n)$$

where θ is the circumferential angle, Ω is the shaft speed and n is the shaft harmonic number.

For the experimental case where the rotor is subjected to an unsteady inflow which is distorted, then the coefficient a_n will also depend on θ and t. In general,

$$a_n(\theta, t) = \sum_{l} \sum_{p} a_{nlp} \cos (p\theta + \phi_p) \cos (l\omega t + \phi_l)$$

where ω characterises the unsteadiness of the flow pattern.

Substituting and rearranging

$$\begin{aligned} p(\theta, t) = \tfrac{1}{4} \sum_{l} \sum_{p} \sum_{n} a_{nlp} \Big\{ & \cos\left[(n + p)\theta - (n\Omega - l\omega)t + \phi_1\right] + \\ & \cos\left[(n - p)\theta - (n\Omega + l\omega)t + \phi_2\right] + \\ & \cos\left[(n + p)\theta - (n\Omega + l\omega)t + \phi_3\right] + \\ & \cos\left[(n - p)\theta - (n\Omega - l\omega)t + \phi_4\right] \Big\} \end{aligned}$$

where ϕ_1, ϕ_2, ϕ_3 and ϕ_4 are the 4 combinations of $\phi_n \pm \phi_p \pm \phi_1$.

Terms 1 and 2 in this expression represent the interaction between a n-lobed rotor pattern rotating at an angular speed Ω and a p-lobed distortion pattern rotating at $l\omega/p$ in a direction opposite to that of the rotor. Terms 3 and 4 represent precisely the same interaction where the distortion pattern rotates in the same direction as the rotor. Collectively the four terms represent four different patterns with individual and distinct speeds, Ω_1 to Ω_4 where

$$\Omega_1 = \frac{n - l\omega/\Omega}{n + p} . \Omega$$

$$\Omega_2 = \frac{n + l\omega/\Omega}{n - p} . \Omega$$

$$\Omega_3 = \frac{n + l\omega/\Omega}{n + p} . \Omega$$

$$\Omega_4 = \frac{n - l\omega/\Omega}{n - p} . \Omega$$

From the circumferential distribution of these patterns the critical speed, $\Omega_{ci} (i = 1, 4)$ below which the pattern amplitude will decay with distance along the duct and above which the pattern propagates unattenuated, can be determined in general from the eigenvalues for the excitable duct modes. The acoustic condition of the pattern can then be determined by comparing Ω_{ci} and Ω_i for the four patterns. However certain characteristics appear immediately and they are

a) Ω_1 is always less than Ω

b) Ω_2 is the highest pattern speed.

c) Ω_3 is greater than Ω only if $\frac{\ell\omega}{p}$ is greater than Ω which implies that the distortion pattern is spinning faster than the rotor.

d) Ω_4 is greater than Ω only if $\frac{\ell\omega}{p}$ is less than Ω implying that the distortion is spinning slower than the rotor.

e) As the speed of the rotor is increased the pattern associated with the speed Ω_2 will appear first (if it is generated and carries acoustic energy).

FIGURE 1

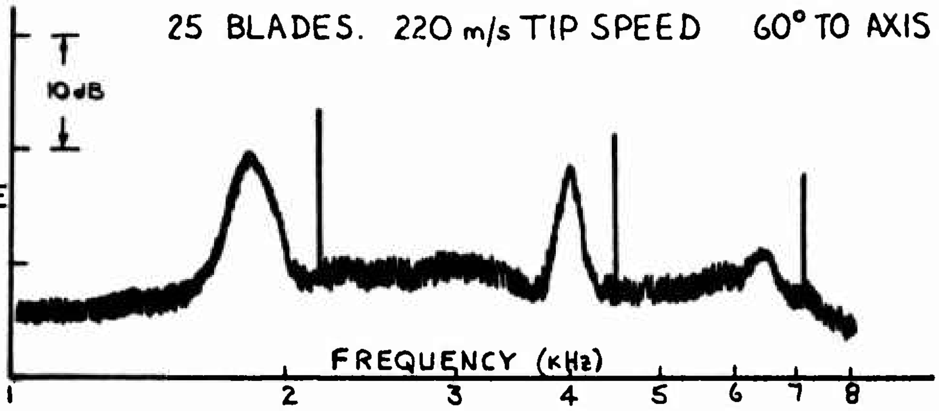
25 BLADES. 220 m/s TIP SPEED 60° TO AXIS

FIGURE 2

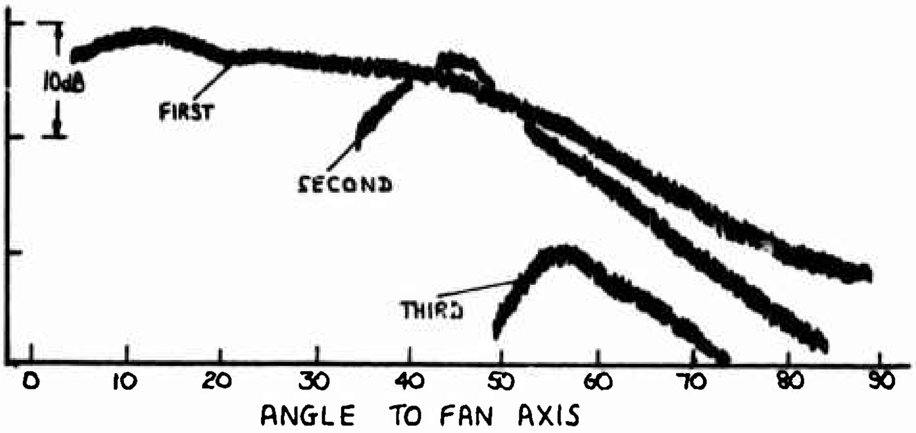

FIGURE 3

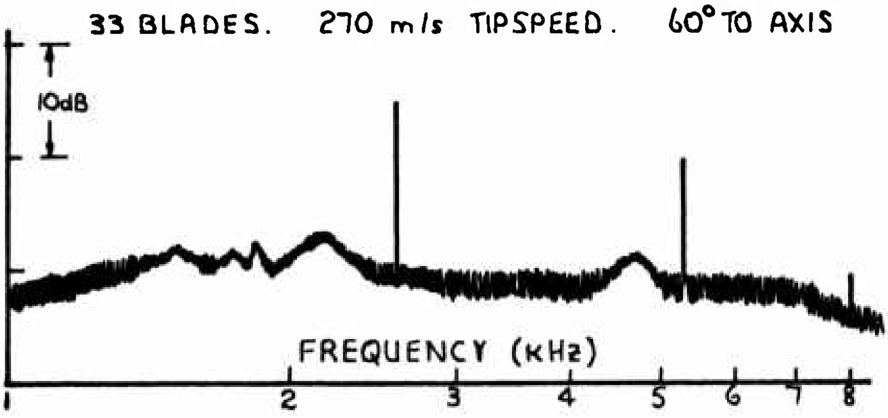
33 BLADES. 270 m/s TIPSPEED. 60° TO AXIS

FIGURE 4

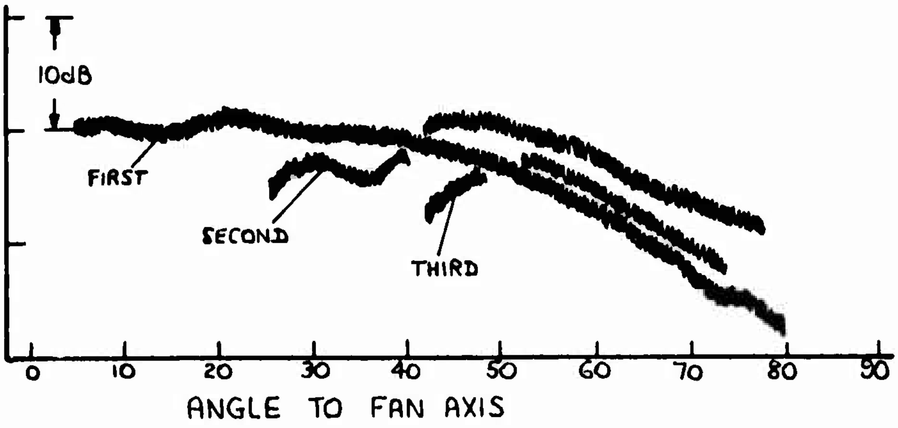

FIGURE 5

PERKINS ENGINES. 19" FAN. 4000 R.P.M.

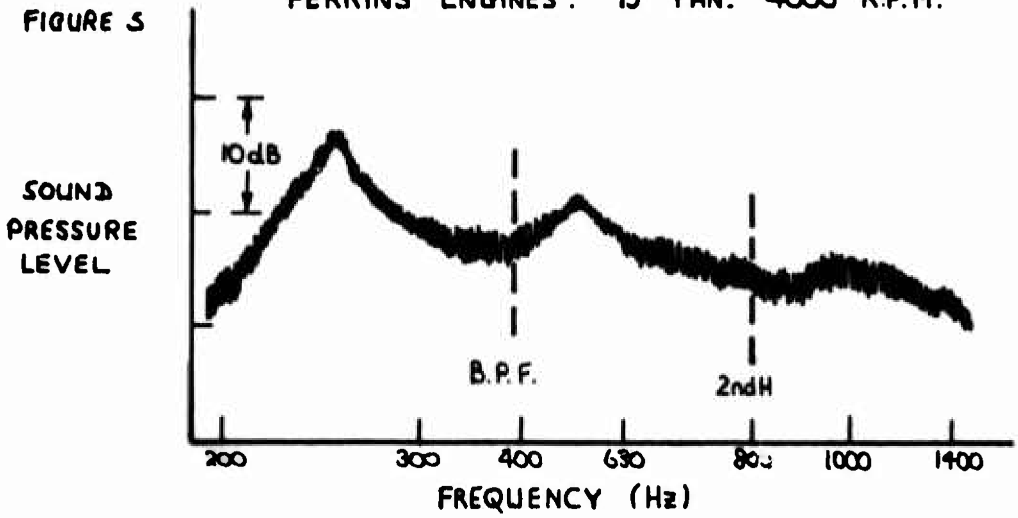

FIGURE 6

NRC TESTS. 12000 R.P.M. NO CROSS FLOW. ON AXIS.

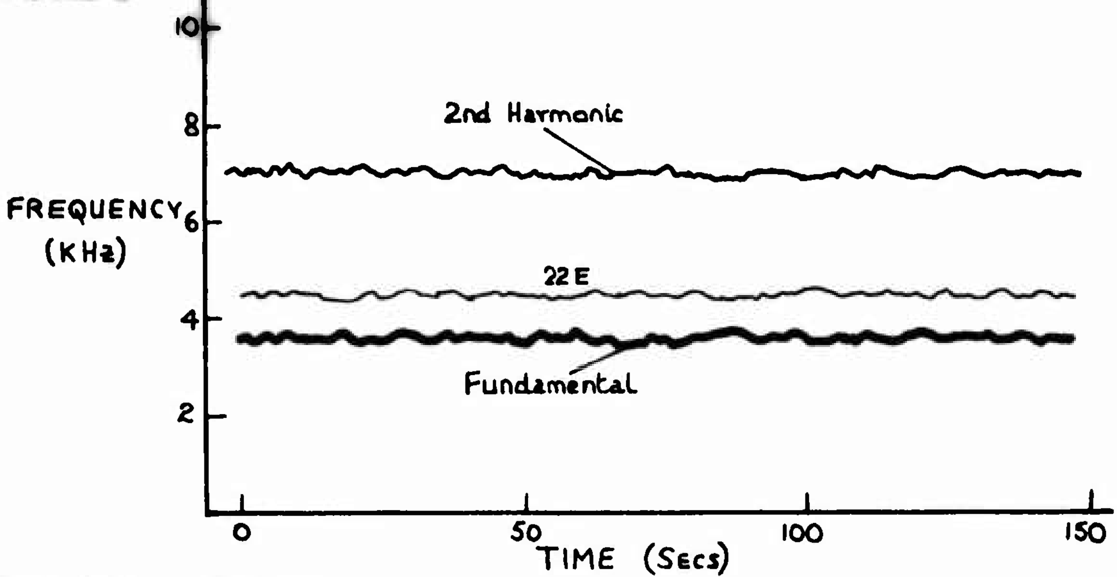

AMPLITUDE ∝ DENSITY

FIGURE 7

12000 R.P.M. 23 m/s CROSS FLOW. ON AXIS.

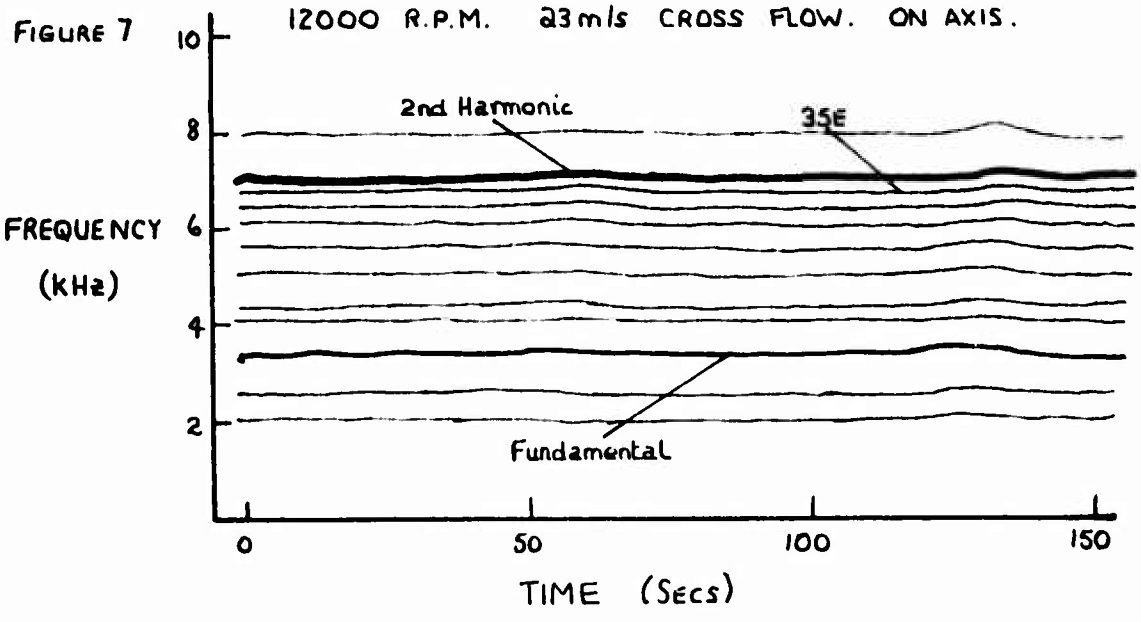

CONTRIBUTION A L'ETUDE DU BRUIT DE JETS EN VOL.

G. RICHTER et C. SCHMIDT

S.N.E.C.M.A.

Dans la mesure où les exigences quant à la limitation de la gêne provoquée par le bruit des avions deviennent de plus en plus astreignantes, les avionneurs et motoristes sont obligés d'accepter les pénalités liées à l'adaptation de la conception des moteurs à une faible émission sonore et à des traitements acoustiques importants. Il est possible, grâce à ces moyens, de réduire le bruit de compresseurs et soufflantes de telle façon que le bruit d'éjection peut constituer une limite pour la réduction possible du bruit global émis par l'avion. Dans le cas des avions supersoniques, les jets dont la vitesse est nécessairement très élevée représentent la source prépondérante de bruit, même en vol à poussée réduite.

Depuis des années, des dispositifs ont été développés qui, d'après des essais sur moteur au point fixe, permettent une atténuation sensible du bruit de jet, essentiellement dans la direction de l'émission maximale. Lorsque ces dispositifs ont été essayés en vol, leur efficacité était dans la plupart des cas fortement réduite, principalement par suite d'une modification de la directivité de l'émission sonore des jets en vol, par rapport à la directivité au point fixe. L'étude de ce phénomène a fait l'objet de nombreuses études expérimentales et théoriques, surtout dans le dernier temps, qui pourtant n'ont pas encore conduit à une explication satisfaisante de ce phénomène. Les mesures du bruit d'avions en vol, qui ont été publiées, montrent une grande dispersion en ce qui concerne les lois de variation de la directivité du bruit avec la vitesse du vol. Il est possible que cette dispersion est due en partie au fait qu'une telle mesure nécessite une grande précision de la détermination de la trajectoire et une parfaite synchronisation entre la mesure de la trajectoire et l'enregistrement du bruit. Une erreur de synchronisation d'une seconde peut conduire à une erreur de l'ordre de 30° dans la détermination de la direction de l'émission sonore maximale de l'avion, aux vitesses pourtant relativement faibles de la montée initiale après décollage ou du vol d'approche à l'atterrissage.

Il semble toutefois possible de déceler quelques tendances générales dans les résultats de mesures, où ces précautions devaient avoir été prises et dont nous avons des connaissances suffisamment détaillées. Dans la fig. 1, sont comparées les répartitions azimutales des niveaux sonores de jets au point fixe et en translation, mesurées pendant des survols de différents avions ou pendant des passages d'un moteur monté sur un véhicule terrestre. Les niveaux sonores sont exprimés en PNdB, c'est-à-dire en dB pondérés d'après la sensibilité de l'oreille qui varie suivant la composition en fréquences du bruit. Les courbes montrent que la vitesse de vol V_o déplace l'angle de l'émission maximale du bruit vers l'amont. Ce changement de directivité joue un rôle important pour l'efficacité de silencieux qui est limitée, dans la plupart des cas, à des angles autour l'angle d'émission maximale au point fixe. Cette directivité de l'atténuation des silencieux ne change pas avec V_o, ce qui a pour conséquence une atténuation plus faible ou même négligeable du bruit maximal en vol, même pour des silencieux bien efficaces au point fixe (fig. 2).

../..

Le changement de directivité est pratiquement le même pour des jets subsoniques et transsoniques, il augmente avec le nombre de Mach de jets supercritiques. On peut supposer que ce phénomène est lié à l'apparition d'ondes de choc dans les jets supercritiques sous-détendus qui constituent des sources de bruit additionnelles rayonnant surtout vers l'amont et, à un moindre degré, vers $\theta \approx 90°$. La puissance des ondes de choc est une fonction du taux de détente du jet qui est plutôt renforcé par la pression dynamique du vol. D'après la théorie, cette émission est amplifiée, vers l'amont, avec le facteur

$$\sqrt{1 + M_o \cos \theta}^{\,-4} \qquad \left[M_o = (V/a)_o = \text{nombre de Mach de vol} \right]$$

Dans ce qui suit, nous nous limitons au cas de jets à vitesses sub- et transsoniques. Fig. 3 montre les champs sonores mesurés au point fixe et en translation, c'est-à-dire - dans le cas des vitesses transsoniques - sur avion en vol et sur moteur monté sur un véhicule en translation (Aérotrain). Les niveaux sonores sont cette fois les niveaux mesurés par le microphone, sans pondération par la sensibilité de l'oreille. Ces mesures ont été comparées avec les champs sonores calculés, en admettant que l'émission sonore d'un jet varie avec la vitesse relative du jet par rapport à l'écoulement ambiant. Sur la base de la théorie de Lighthill, Ffowcs Williams [1] a développé l'expression suivante pour la modification par la vitesse de translation V_o du champ sonore d'un jet subsonique, au point fixe:

$$N_{S\,\text{point fixe}} - N_{S\,\text{vol}} = -70 \operatorname{Log}_{10}\left(1 - \frac{M_o}{M_{jo}}\right)$$
$$- 10 \operatorname{Log}_{10} \left[\frac{\left[(1 - C M_{jo} \cos\theta)^2 + \alpha^2 C^2 M_{jo}^2 (\cos^2\theta + \epsilon^2 \sin^2\theta)\right]^{5/2}}{\left\{\left[1 - C (M_{jo} - M_o) \cos\theta\right]^2 + \alpha^2 C^2 (M_{jo} - M_o)^2 (\cos^2\theta + \epsilon^2 \sin^2\theta)\right\}^{5/2} (1 + M_o \cos\theta)} \right]$$

avec $M_o = V_o/a_o$ nombre de Mach de vol

$M_{jo} = V_j/a_o$ (V_j = vitesse du jet)

C, α, e coefficients se rapportant à la vitesse de convection et la durée de vie des tourbillons dans le jet, et à l'anisotropie de la turbulence.

La formule tient compte de l'effet de V_o sur la forme de la zone de mélange entre le jet et l'écoulement externe d'une part et d'autre part, sur l'amplification de l'émission sonore, en fonction de θ, par la convection des sources par l'écoulement. Par contre, elle suppose que les sources mêmes ne sont pas modifiées par la vitesse de vol.

La comparaison de la courbe théorique avec la mesure met en évidence que l'hypothèse d'une variation du bruit avec la vitesse relative n'est valable que dans l'arc aval, autour de l'angle de l'émission maximale, tandis que l'effet de la vitesse de vol diminue aux angles plus élevés et a pratiquement disparu dans l'arc amont. La fig. 4 montre que l'atténuation, aux faibles angles, est à peu près la même pour toutes les fréquences et qu'aux angles élevés les spectres sont pratiquement confondus. Ceci est valable pour les jets subsoniques aussi bien que transsoniques.

En vue d'examiner, pour un cas particulier, les effets de la vitesse de vol sur les sources de bruit, nous avons entrepris, en étroite collaboration avec l'ONERA, une étude expérimentale sur une maquette de tuyère avec corps central, en simulant le vol par un écoulement secondaire autour du jet, avec un rapport des diamètres d'environ 5. Ces mesures ne représentent pas une recherche systématique de base, néanmoins leurs résultats ../..

permettent des observations dont la validité générale a été vérifiée par quelques mesures comparatives sur une maquette de tuyère convergente simple.

Conditions et méthodes de mesure.

Les mesures ont été effectuées à une vitesse de jet V_j = 570 m/s et une température d'arrêt T_j = 850°K; le nombre de Mach était M_j = 1,09, la vitesse "externe" $V_e \approx$ 80 m/s.

Les grandeurs significatives de la turbulence dans le jet ont été déterminées à l'aide de son émission infrarouge. Cette méthode a été présentée dans plusieurs publications [2] - [5] ; nous nous contentons ici de rappeler que son principe est basé sur l'hypothèse que les fluctuations du rayonnement infrarouge d'un petit volume de l'écoulement turbulent sont comparables aux fluctuations turbulentes supposées être les sources d'émissions acoustiques d'après la théorie de Lighthill. Cette hypothèse devrait être d'autant plus valable que la température du jet est élevée, dans quel cas les fluctuations d'entropie, c'est-à-dire de température, constituent elles-mêmes des sources sonores importantes. L'analyse de mesures acoustiques sur des jets supersoniques [6] a d'ailleurs conduit Tanna, Fisher et Dean à la conclusion d'une forte corrélation entre les fluctuations turbulentes de vitesse et de température.

Les émissions infrarouges sont captées par des radiomètres qui sont insensibles à des émissions à basse température, de l'ordre de la température ambiante, ce qui présente l'avantage, pour l'étude présente, que les signaux ne sont pas perturbés par les fluctuations turbulentes du mélange de l'écoulement "externe" avec le milieu ambiant.

L'investigation du domaine source a été complétée par des mesures de pressions acoustiques par 5 microphones implantés sur une parallèle à l'axe du jet, à une distance qui correspond approximativement à la transition entre les champs sonores proche et lointain (fig. 8).

Mesures préliminaires.

Avant les mesures sur la maquette à corps central, l'ONERA avait effectué des mesures de caractérisation aéro-thermodynamique des écoulements de l'installation d'essais, sur une maquette de tuyère conique sans corps central, à une vitesse subsonique du jet : M_j = 0,7; T_j = 900°K, à des vitesses de l'écoulement externe V_e = 0, 50 et 80 m/s. La fig. 5 montre l'évolution de la vitesse et de la température le long de l'axe du jet, avec et sans écoulement externe, ainsi que les profils radiaux de vitesse et de température, à une distance de 3,75 diamètres de la tuyère. Contrairement à la théorie et à d'autres expériences, le cône d'isovitesse, dans lequel l'écoulement central du jet n'est pas encore mélangé avec le milieu ambiant, n'est pas allongé par l'écoulement externe, mais plutôt raccourci, par suite d'un renforcement de l'épaisseur de la zone de mélange. Nous avons attribué ce renforcement à la turbulence élevée de l'écoulement externe. De tels épaississements, par la turbulence externe ont été observés sur la couche limite sur une plaque plane [7] . Le jet d'un moteur d'avion en vol se trouve en général dans un milieu assez turbulent, dû aux sillages de l'aile et du fuseau moteur, les conditions d'essai présentes devraient par conséquent être plus proche de la réalité qu'avec un écoulement externe à turbulence très faible. Une étude plus systématique de l'effet de la turbulence externe est en préparation à l'ONERA. Un premier résultat obtenu avec un taux de turbulence plus faible confirme cet effet.

../..

D'après les mesures de corrélations spatio-temporelles de l'émission infrarouge du jet, l'écoulement externe turbulent ne modifie pas le rapport de la vitesse relative de convection de la turbulence $(V_c - V_e)/(V_j - V_e)$, avec V_c = vitesse absolue de convection, par contre il réduit l'échelle spatiale de turbulence.

Résultats de mesures sur la maquette à corps central.

Intensité de turbulence

La fig. 6 montre les variations radiales de l'intensité des fluctuations d'émission infrarouge, avec et sans écoulement externe, à une distance axiale d'environ 4 diamètres de la tuyère. A titre de comparaison, les mesures correspondantes sur la tuyère sans corps central sont indiquées également. Les signaux captés par les radiomètres sont une fonction non-linéaire de la température, les courbes ne permettent, par conséquent, qu'une comparaison qualitative. Elles mettent en évidence l'élargissement de la zone de mélange des jets, par l'écoulement externe, et la similitude des profils radiaux des jets sub- et transsoniques. Les allures des profils axiaux sur l'axe (Y/D = 0) et dans la zone de mélange (Y/D = 0,5) correspondent bien aux variations de l'intensité des fluctuations turbulentes de vitesse publiées dans la littérature.

Les spectres de puissance de la turbulence (émission infrarouge) dans la zone de mélange, qui sont représentés dans la fig. 7, ont été déterminés par la transformation de Fourier numérique des fonctions d'autocorrélation des signaux des radiomètres. Les courbes indiquent une forte influence de l'écoulement externe sur la fréquence de l'amplitude maximale des spectres très près de la tuyère, influence qui diminue à des distances plus grandes et s'annule en aval du cône d'isovitesse. Une explication possible pourrait être une modification du caractère de turbulence, par un écoulement externe turbulent. D'après le modèle de Lighthill, on peut discerner deux sortes d'action des conditions locales sur un petit volume de la zone de mélange d'un jet : l'interaction entre les volumes fluctuants ("self noise") d'une part, et d'autre part, un renforcement des tensions turbulentes par le gradient local des vitesses moyennes ("shear noise"). Les émissions acoustiques provenant des interactions turbulence-gradient de vitesse sont principalement orientées vers l'arc aval, tandis que les émissions acoustiques dues à l'interaction turbulence-turbulence sont plus omnidirectionnelles. Toujours d'après la même théorie, la fréquence prépondérante du "self noise" est d'une octave supérieure à la fréquence prépondérante du "shear noise". Le gradient radial de vitesse moyenne est d'autant plus fort que la distance de la tuyère est faible; sa diminution avec la croissance de la largeur de la zone de mélange est accentuée par la diminution de la vitesse sur l'axe, au-delà du cône d'isovitesse, ce qui peut signifier qu'ici les sources du "self noise" sont nettement prépondérantes et la fréquence significative n'est plus modifiée par la turbulence externe, contrairement aux conditions près de la tuyère, où le rapport entre l'énergie des sources peut être modifié par la turbulence externe.

Un tel renforcement relatif de l'interaction turbulence-turbulence devrait contribuer au déplacement de la direction de l'émission maximale du bruit vers des angles plus près de 90°, en vol. Cet effet serait cependant limité du fait que les parties du jet plus proches de la tuyère semblent contribuer moins au bruit mesuré dans le champ lointain que les parties autour de la fin du cône d'isovitesse.

../..

La fig. 8 montre les spectres de puissance du bruit mesuré par les microphones aux emplacements indiqués. La comparaison de ces spectres avec les spectres de la turbulence dans la zone de mélange (fig. 7) fait apparaître une différence importante : à $V_e = 0$, les fréquences de pointe des spectres ne varient pratiquement pas avec la distance axiale de la tuyère; l'influence d'un écoulement externe est peu prononcée.

La prédominance d'une fréquence essentiellement constante sur une longueur dépassant le cône d'isovitesse du jet, dans un plan situé entre les champs proche et lointain, a été observée également par Maestrello [8] .

Le nombre de Strouhal de cette fréquence était $\frac{fD_j}{V_j} \approx 0{,}3$, semblable au résultat de nos mesures (fig. 8). A partir de corrélations dans son plan de mesure, Maestrello détermine les contributions des différentes parties du jet au champ lointain. Il trouve que l'énergie rayonnée vers $\theta \approx 90°$ provient principalement d'émissions à X/D entre 4 et 10 environ, à $\frac{fD_j}{V_j} = 0{,}3$ à 0,6, tandis que pour $\theta \approx 45°$ le nombre de Strouhal prépondérant est plus faible et la longueur du jet, contribuant le plus à cette émission, est plus grande.

Structure ordonnée de la turbulence de jet.

Maestrello mentionne dans le contexte de son étude les travaux sur la structure ordonnée de la turbulence de jet, par Mollo-Christensen [9] , Crow et Champagne [10] et Hardin [11] . La nature de cette structure et la question de sa contribution à la production de bruit ont trouvé un intérêt grandissant dans le dernier temps. D'autres travaux importants sur ce sujet sont par exemple ceux de Fuchs [12] , Laufer et al. [13] et Pfizenmaier [14] . On peut résumer leurs résultats d'essais et leurs conclusions d'une façon très succincte comme suit :

L'examen de l'écoulement d'un jet libre met en évidence l'existence de deux modes de turbulence : la turbulence fine, désordonnée, à laquelle se superposent des fluctuations ordonnées, à symétrie axiale, d'une échelle de 1 à 2 diamètres du jet. Cette structure ordonnée peut être visualisée à partir d'un nombre de Reynolds (basé sur le diamètre) $R_e \approx 10^3$ jusqu'à environ $7 \cdot 10^4$. A des nombres de Reynolds plus élevés, elle subsiste d'une façon latente dans le jet. Une excitation, par exemple par une pulsation périodique du débit, permet d'étudier son évolution et ses propriétés. L'excitation provoque, à une distance de quelques diamètres de la tuyère, une onde dont la vitesse de phase est en accord avec la théorie de l'instabilité temporelle de la couche de cisaillement entre le jet et le milieu ambiant. Son amplitude croît avec l'excitation et, à excitation donnée, avec X/D jusqu'à la formation d'un harmonique; l'onde fondamentale et son harmonique atteignent des niveaux de saturation qui sont indépendants de l'intensité d'excitation mais qui varient avec le nombre de Strouhal. Le niveau maximal de saturation est atteint pour $\frac{f \cdot D_j}{V} \approx 0{,}3$; c'est donc la fréquence, correspondant à ce nombre de Strouhal, qui domine lors d'une excitation aléatoire, par exemple par des fluctuations du débit ou par la turbulence dans la zone de mélange. Des fluctuations de vitesse de l'ordre de 2% de la vitesse moyenne sont suffisantes comme excitation, pour le nombre de Strouhal de 0,3.

La structure ordonnée des fluctuations de pressions et de vitesses n'est pas limitée à la largeur de la zone de mélange, mais elle traverse le cône d'isovitesse et se propage aussi vers l'extérieur de la zone de

../..

mélange. La corrélation des fluctuations dans le cône d'isovitesse avec celles à l'extérieur proche du jet est plus forte que pour le cône d'isovitesse et la zone de mélange, dans laquelle l'énergie de la turbulence fine est plus forte que celle des fluctuations à grande échelle, ce qui explique la difficulté de la mesure de la structure ordonnée dans la zone de mélange.

Plusieurs hypothèses pour la génération de bruit par les fluctuations à grande échelle ont été avancées, basées par exemple sur la variation, avec X/D, de l'extension radiale de ces structures |11| ou sur la variation de leurs distances axiales |13| . Aucune théorie plus complète n'a pu être développée jusqu'ici.

CONCLUSION

Si l'on admet la validité des hypothèses mentionnées ci-dessus, l'émission sonore de ces sources devrait être dirigée principalement vers des angles $\theta > 90°$. Les mesures de bruit dans le champ lointain montrent effectivement que le nombre de Strouhal de pointe des spectres dans cette gamme d'angles est $\frac{f \cdot D_j}{V_j} \approx 0{,}3$. Ceci peut être une coïncidence, mais si l'on admet l'hypothèse que l'émission sonore dans l'arc amont est dominée par des sources liées à la structure ordonnée de turbulence, on peut expliquer l'inefficacité de la vitesse de vol sur le bruit dans cette gamme d'angles. Lorsque l'amplitude de ces fluctuations ordonnées a atteint son niveau de saturation, qui, pour un nombre de Strouhal donné, est fonction de la vitesse V_j, elle ne devrait pas être diminuée par la vitesse de vol. Ceci est évident si l'excitation provient des fluctuations du débit; dans le cas où la turbulence dans la zone de mélange joue un rôle important pour l'apparition de la structure ordonnée, l'amplitude de ces fluctuations ordonnées ne varie que très peu avec cette excitation tant que l'intensité de turbulence dans la zone de mélange n'est pas descendue à des valeurs négligeables. Une diminution de la vitesse relative, à vitesse absolue de jet constante, ne change pas, dans ces conditions, le niveau d'émission acoustique provenant de la structure ordonnée, par contre elle diminue la puissance des sources rayonnant vers l'arc aval.

Ces conclusions ne sont évidemment basées que sur des ressemblances de phénomènes aérodynamiques et acoustiques. Nous pensons, néanmoins, qu'elles ont un degré de probabilité qui justifierait des études plus systématiques et plus approfondies.

REFERENCES

[1] J.E. Ffowcs Williams "Jet noise from moving aircraft". AGARD Conference Proceedings No 42 (Mai 1969).

[2] J. Taillet "Description et mise en oeuvre d'une méthode de caractérisation des sources de bruit dans les jets". L'Aéronautique et L'Astronautique No 40 - 1972-2.

[3] G. Richter "Etude des sources de bruit de jets chauds". Entropie No 51 (Mai-Juin 1973).

[4] J.F. de Belleval et M. Perulli "Représentation de la turbulence d'un jet chaud à partir de son émission infrarouge". ONERA T.P. No 1277 (1973).

[5] J.F. de Belleval, J. Randon, M. Perulli, J.C. Taillefesse "Influence of refraction effects on the interpretation of a hot jet acoustic radiation". AIAA Paper No 73-990.

[6] H.K. Tanna, M.J. Fisher, P.D. Dean "Effect of temperature on supersonic jet noise". AIAA Paper No 73-991.

[7] M. Pichal "Grenzschicht bei hochturbulenter Aussenströmung". ZAMM 52 (1972).

[8] L. Maestrello "On the relationship between acoustic energy density flux near the jet and farfield acoustic intensity". AIAA Paper No 73-988.

[9] E. Mollo-Christensen "Jet noise and shear flow instability seen from an experimenter's viewpoint". Journ. Appl. Mech., Vol. 34 No 1 (Mars 1967).

[10] B.S. Crow et F.H. Champagne "Orderly structure in jet turbulence". Journ. Fluid Mech., Vol. 48, Part 3 (Août 1971).

[11] J.C. Hardin "Analysis of noise produced by an orderly structure of turbulent jets". NASA TN D-7242 (1973).

[12] H. Fuchs "Space correlations of the fluctuating pressure in subsonic turbulent jets". Journ. Sound and Vibration, Vol. 23, No 1 (1972).

[13] J. Laufer, R.E. Kaplan, W.T. Chu "On the generation of jet noise". AGARD - CPP - 131 (1973).

[14] E. Pfizenmaier "Zur Instabilität des schallbeeinflussten Freistrahls". DLR-FB 73-69 (1973).

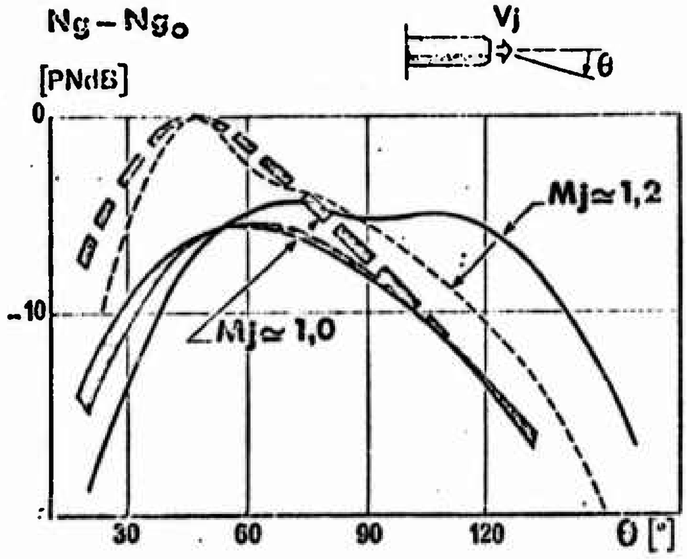

M_j = vitesse du jet V_j/vitesse du son dans le jet a_j.

N_g = niveau global du bruit de jet = f (θ).

N_{g_o} = niveau global maximal du bruit du jet au point fixe.

- - - - - jet au point fixe

——— jet en vol ($M_o \simeq 0,22$)

Fig.1. EFFET DE LA VITESSE DE VOL SUR LE BRUIT "SUBJECTIF" PERÇU AU SOL.

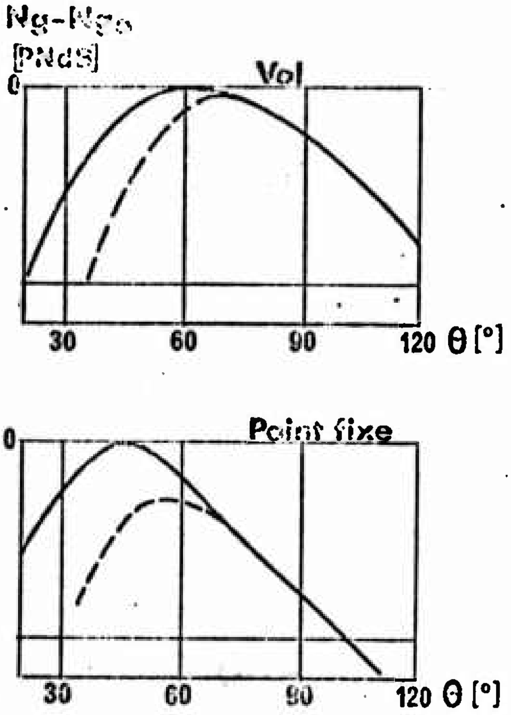

- - - - - avec silencieux

——— sans silencieux

Fig.2 EFFICACITE DE SILENCIEUX AU POINT FIXE ET EN VOL

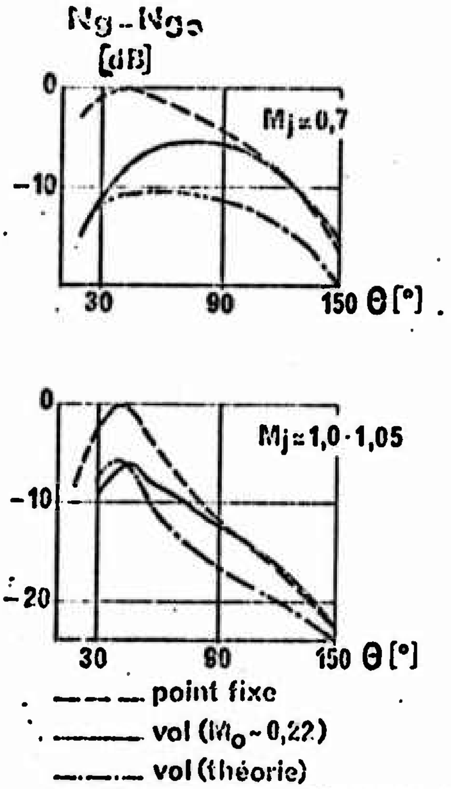

Fig.3 NIVEAUX SONORES DE JETS SUB. ET TRANSONIQUES

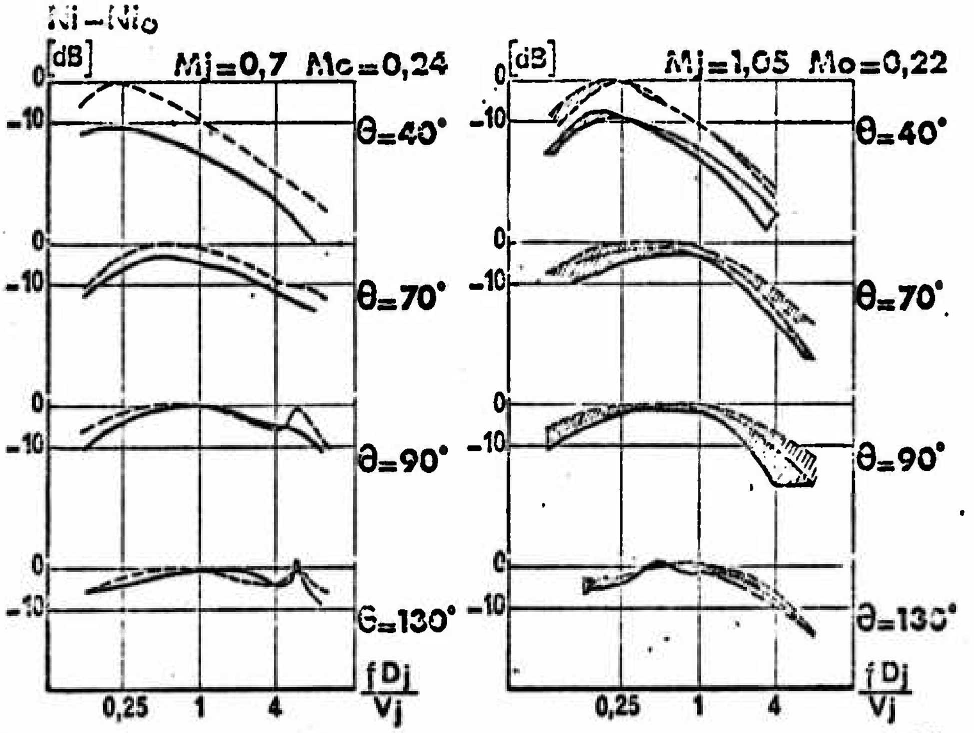

Ni = niveau sonore à la fréquence f.
Ni_o = niveau sonore maximal au point fixe.

---- point fixe
——— vol

Fig.4. REPARTITION SPECTRALE DES NIVEAUX SONORES PAR $\frac{1}{3}$ D'OCTAVES

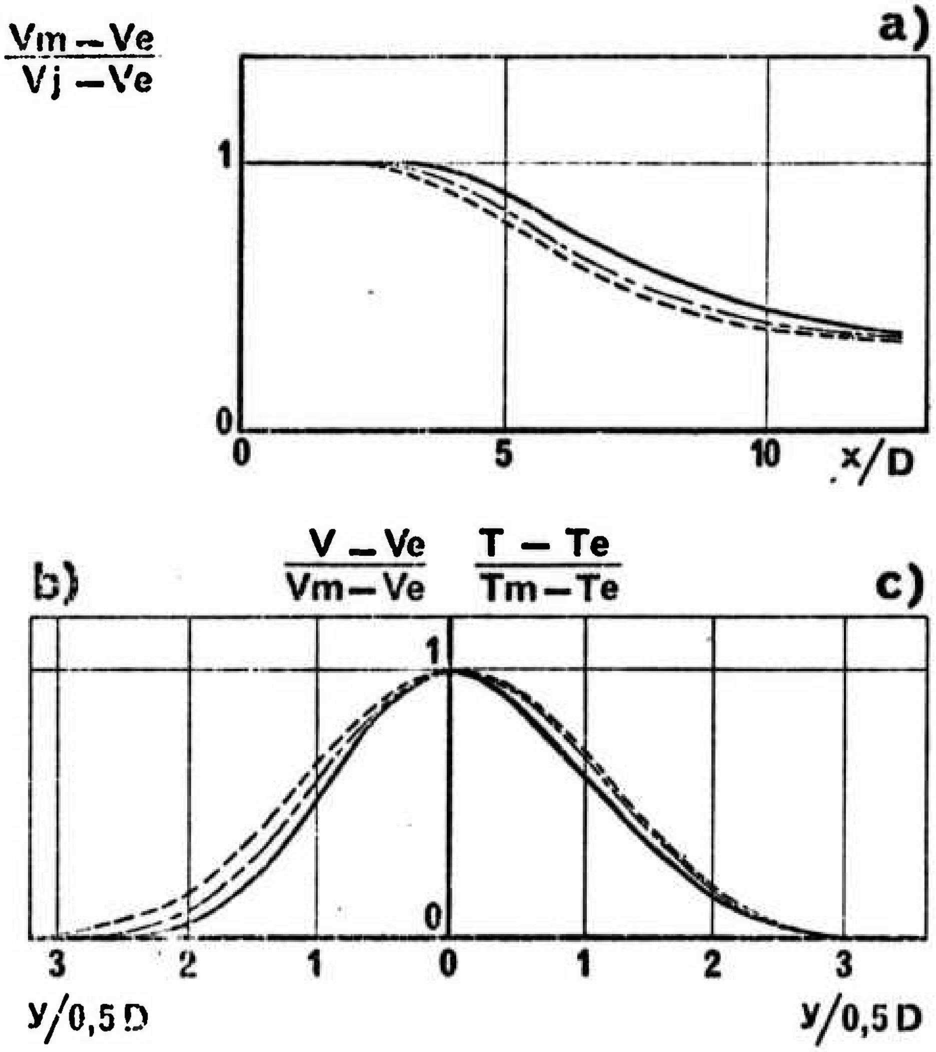

a) Evolution axiale des vitesses maximales.

b) Profil transversal des vitesses à $x/D = 3,75$.

c) Profil transversal des températures totales à $x/D = 3,7$

Indices : j et e jets primaire et secondaire à $x/D = 0$.

m sur l'axe du jet primaire.

—— $V_e = 0$

—·– 50 m/s

– – – – 80 m/s

Fig. 5. TUYERE CONIQUE.

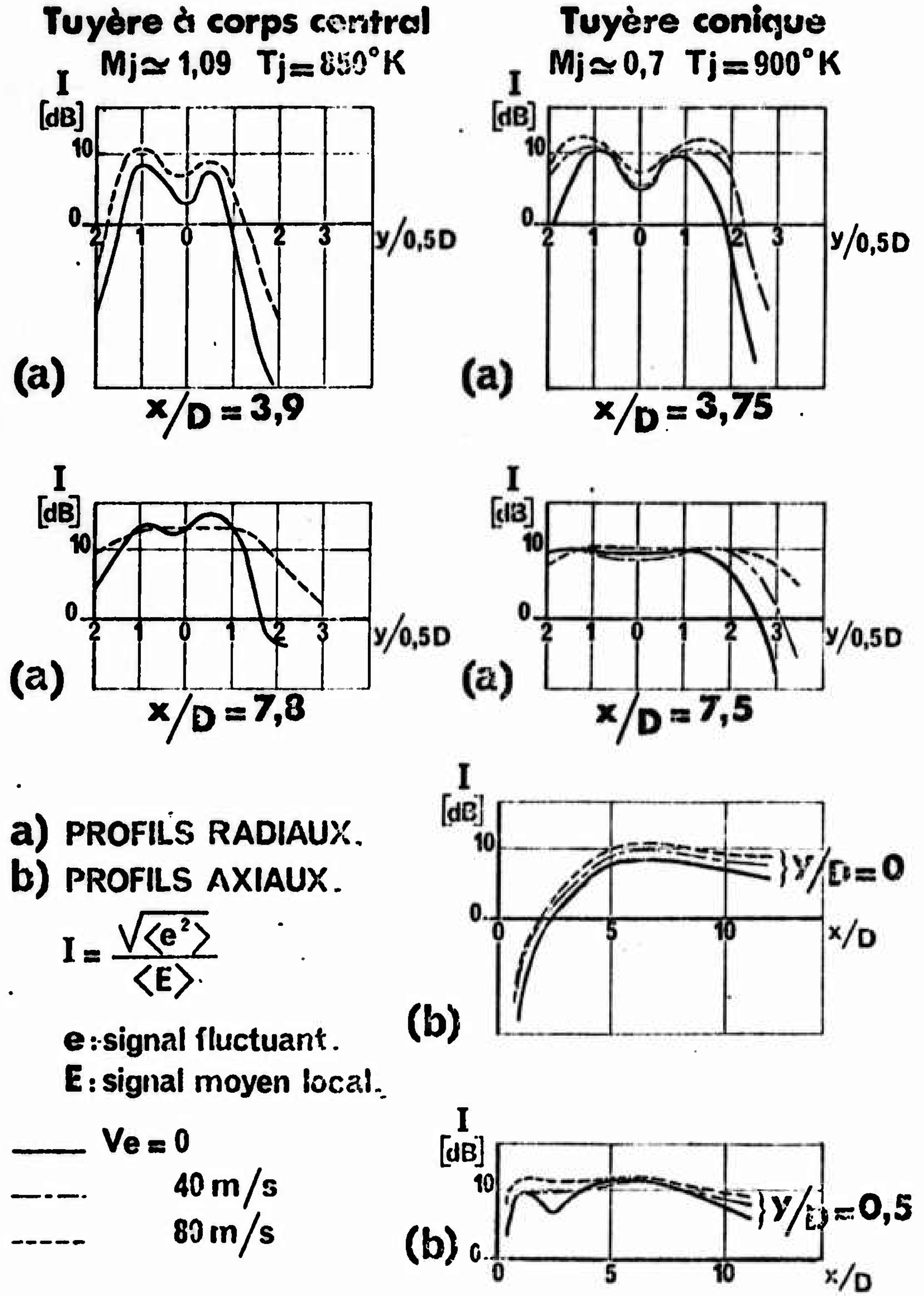

Fig. 6_ INTENSITE DES FLUCTUATIONS TURBULENTES DE L'EMISSION INFRAROUGE_

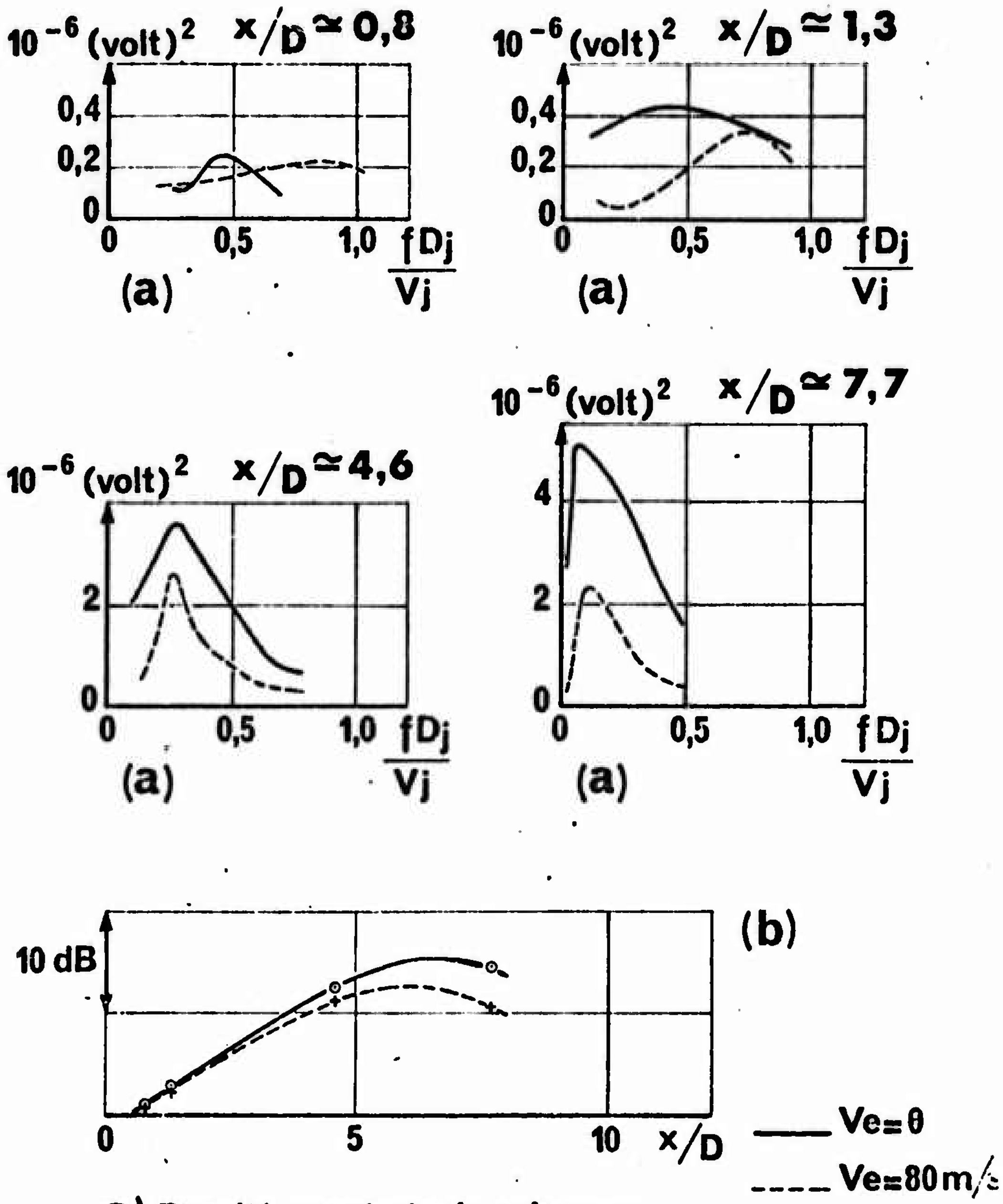

a) Densité spectrale de puissance.

b) Evolution axiale de sa valeur maximale.

Fig. 7.

TUYERE A CORPS CENTRAL. EMISSION INFRAROUGE.

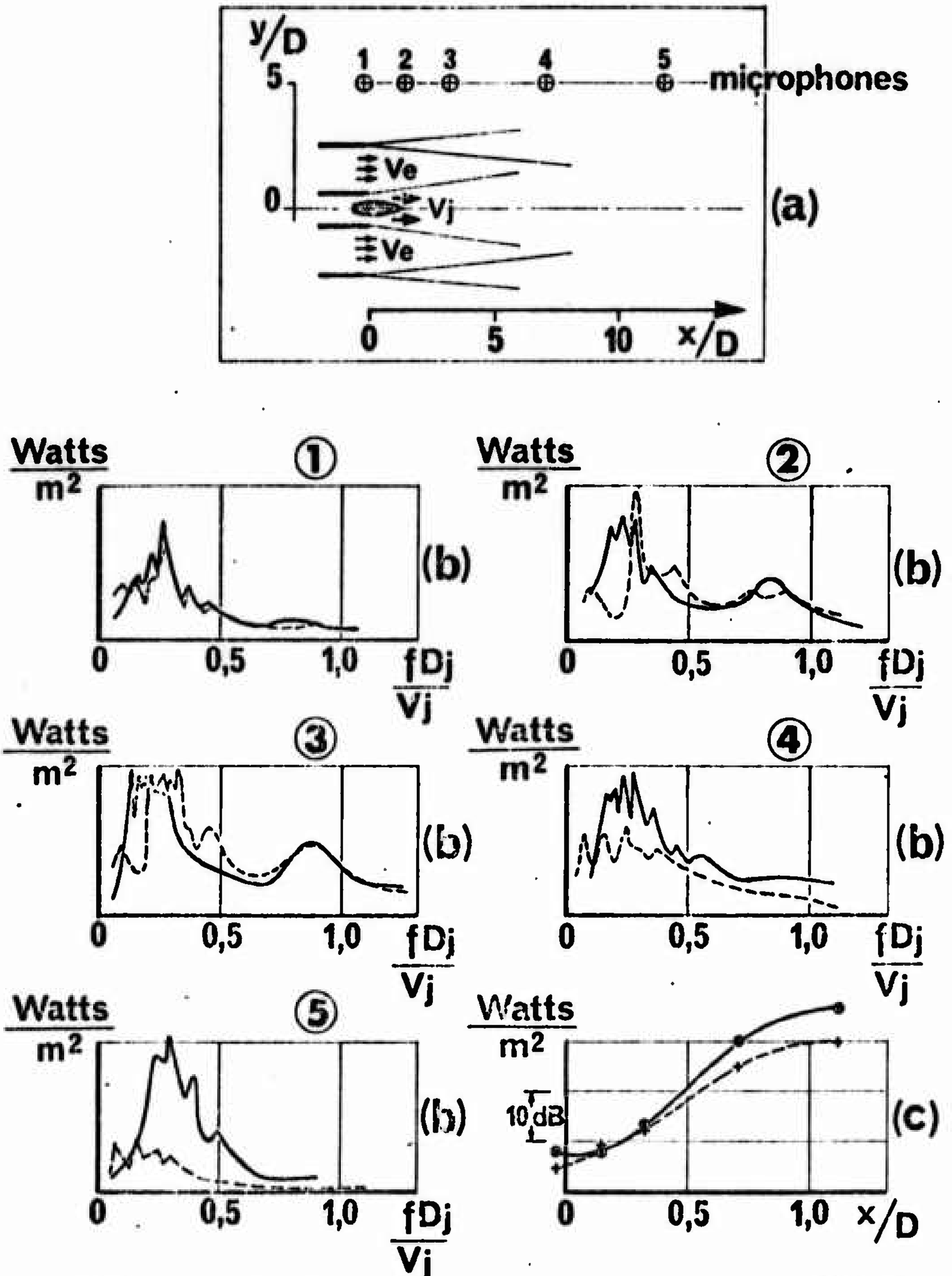

a) Schéma de l'installation. —— Ve = 0

b) Densité spectrale de puissance. ---- Ve = 80m/s

c) Evolution axiale de sa valeur maximale.

Fig. 8_ TUYERE A CORPS CENTRAL_EMISSION SONORE.

INLET DISTORTION AND BLADE VIBRATION IN TURBOMACHINERY

Y. Tanida
Institute of Space and Aeronautical Science, University of Tokyo, Japan

1. Introduction

The blade rows of turbomachine are designed to operate in axisymmetric oncoming flow. In the actual turbomachines, however, inlet airflow may be distorted asymmetrically when the turbomachine is installed in an aircraft with dual intakes, and when the aircraft flies at high angle of attack. The inlet distortions excite rotor blade vibration, sometimes causing blade failures.

For the problem of inlet distortions, an actuator disc type of analysis is most useful, because the concept of actuator disc(a blade row is replaced by a disc of infinitely small axial thickness) can be allowed when the circumferential wave-length of disturbance is much larger than the blade spacing. Ehrich(1), Rannie & Marble(2), and Yeh(3) gave solutions for single two-dimensional blade row, and Dunham(4) presented a more general theory for multi-stage axial compressors. These actuator disc analyses ignore inevitably, however, the inertial effects of fluid inside the rotor blade passages, as pointed out by Takata(5) in his study of rotating stall. Then, on the basis of semi-actuator disc conception(5 to 7)(a blade row is replaced by a cascade of blades of finite chord with infinitely small blade-spacing), the present author gave an analysis for the inlet airflow distortions in a mixed-flow turbomachine with high hub/tip ratio(8).

In this paper, an analysis based on the semi-actuator disc theory is carried out remarking the mutual effects between the inlet airflow distortion and the blade vibration in two-dimensional axial turbomachines.

2. Formulation of the Problem and Assumptions

The non-uniform flow through a turbomachine which consists of two-dimensional linear cascades is considered(Fig.1). The flow is assumed to be stationary in space, being a parallel shear flow in the far upstream region, and its circumferential velocity distortion is a sinusoidal variation of wave-length λ . Then the nonsteady effects will be experienced by a blade of the rotor, which is either rigid or flexible. The outgoing flow far downstream of the outlet stator will also be a parallel shear flow with a sinusoidal distortion of an attenuated amplitude.

The principal assumptions made in this study are as follows;

(a) The flow is incompressible and inviscid, being not accompanied with any energy losses.

(b) The non-uniform flow is superposed as a small perturbation on the two-dimensional average flow. Its wave-length in circumferential direction is much larger than the blade spacing.

(c) The blade row is replaced by a semi-actuator disc, which is defined as a cascade of flat-plate blades of finite chord with infinitely small blade-spacing. When the rotor blades are flexible, a translatory mode of vibration(normal-to-chord) will be considered.

3. Basic Equations

3.1 The Flow outside the Blade Rows

In each flow field outside the blade rows, the origin will be placed just up-or downstream of a blade row. In the present study, non-uniform flow is considered stationary in space, and any circumferential distortion of wave-length λ may be expressed as

$$f(x)e^{-i2\pi y/\lambda} \tag{1}$$

Supposing that the perturbation vorticity is transported downstream at the average flow velocity (U , V), the vorticity at an arbitrary point will be given by

$$\zeta = \zeta_0 e^{i2\pi(x\tan\alpha - y)/\lambda} \quad ; \quad \tan\alpha = V/U \tag{2}$$

Solving the wellknown Poisson's equation concerning a rotational flow field, that is $\nabla^2\psi = -\zeta$, a general expression for the perturbation stream function is then obtained as

$$\psi = Ae^{2\pi(x-iy)/\lambda} + Be^{-2\pi(x+iy)/\lambda} + \left(\frac{\lambda}{2\pi}\cos\alpha\right)^2\zeta_0 e^{i2\pi(x\tan\alpha - y)/\lambda}$$

where A and B are arbitrary constants. The perturbation velocity components in the axial and circumferential directions are then given by

$$\left.\begin{aligned} u &= -i\frac{2\pi}{\lambda}\left\{Ae^{2\pi(x-iy)/\lambda} + Be^{-2\pi(x+iy)/\lambda}\right\} - \left(i\frac{\lambda}{2\pi}\zeta_0\right)\cos^2\alpha \cdot e^{i2\pi(x\tan\alpha - y)/\lambda} \\ v &= \frac{2\pi}{\lambda}\left\{-Ae^{2\pi(x-iy)/\lambda} + Be^{-2\pi(x+iy)/\lambda}\right\} - \left(i\frac{\lambda}{2\pi}\zeta_0\right)\sin\alpha\cos\alpha\, e^{i2\pi(x\tan\alpha - y)/\lambda} \end{aligned}\right\} \tag{3}$$

Now in the case of a single-stage turbomachine shown in Fig. 1, we apply first the above equations to the flow field upstream of the inlet guide vanes, where the origin is indicated by G1. From Eq.(3) and the requirement to keep the perturbations finite everywhere, the perturbation velocity in this region where $-\infty < x < 0$ is given by

$$\left.\begin{aligned} u_1 &= u_{1d} - i\frac{2\pi}{\lambda}Ae^{2\pi(x-iy)/\lambda} \quad ; \quad u_{1d} = -\left(i\frac{\lambda}{2\pi}\zeta_{G1}\right)\cos^2\alpha_1 e^{i2\pi(x\tan\alpha_1 - y)/\lambda} \\ v_1 &= v_{1d} - \frac{2\pi}{\lambda}Ae^{2\pi(x-iy)/\lambda} \quad ; \quad v_{1d} = u_{1d}\tan\alpha_1 \end{aligned}\right\} \tag{4}$$

where (u_{1d}, v_{1d}) is the inlet distortion far upstream of the inlet guide vanes. Eliminating A from Eq.(4), we find

$$u_{G1} - iv_{G1} = -\frac{1}{1 + i\tan\alpha_1}\left(i\frac{\lambda}{2\pi}\zeta_{G1}\right) \tag{5}$$

Similarly, in the field downstream of the outlet stator, where the origin is indicated by S4 and $0 < x < \infty$, the perturbation velocity is

$$\left.\begin{aligned} u_4 &= u_{4d} - i\frac{2\pi}{\lambda}Be^{-2\pi(x+iy)/\lambda} \quad ; \quad u_{4d} = -\left(i\frac{\lambda}{2\pi}\zeta_{S4}\right)\cos^2\alpha_4 e^{i2\pi(x\tan\alpha_4 - y)/\lambda} \\ v_4 &= v_{4d} + \frac{2\pi}{\lambda}Be^{-2\pi(x+iy)/\lambda} \quad ; \quad v_{4d} = u_{4d}\tan\alpha_4 \end{aligned}\right\} \tag{6}$$

where (u_{4d}, v_{4d}) is the outlet distortion far downstream of the outlet stator. Then

$$u_{S4} + i v_{S4} = - \frac{1}{1 - i\tan\alpha_4}\left(i\frac{\lambda}{2\pi}\zeta_{S4}\right) \tag{7}$$

As regards the flow between the inlet guide vanes and the rotor, Eqs.(2) and (3) give

$$\begin{bmatrix} i\frac{\lambda}{2\pi}\zeta_{R2} \\ u_{R2} \\ v_{R2} \end{bmatrix} = M_2 \begin{bmatrix} i\frac{\lambda}{2\pi}\zeta_{G2} \\ u_{G2} \\ v_{G2} \end{bmatrix} \tag{8}$$

where G2 denotes the origin of this field, which is located just downstream of the inlet guide vanes, (0, 0), R2 a point just upstream of the rotor, (L_2 , 0), and

$$M_2 = \begin{bmatrix} e^{iZ_2} & 0 & 0 \\ C_2 & \cosh\hat{L}_2 & i\sinh\hat{L}_2 \\ D_2 & -i\sinh\hat{L}_2 & \cosh\hat{L}_2 \end{bmatrix} \quad ; \quad \hat{L}_2 = \frac{2\pi}{\lambda}L_2$$

$$Z_2 = \hat{L}_2\tan\alpha_2$$
$$C_2 = \cos^2\alpha_2\left(\cosh\hat{L}_2 - e^{iZ_2} + i\tan\alpha_2\sinh\hat{L}_2\right)$$
$$D_2 = -\cos^2\alpha_2\left\{-\tan\alpha_2\left(\cosh\hat{L}_2 - e^{iZ_2}\right) + i\sinh\hat{L}_2\right\}$$

In like manner, for the flow between the rotor and the outlet stator, we derive

$$\begin{bmatrix} i\frac{\lambda}{2\pi}\zeta_{S3} \\ u_{S3} \\ v_{S3} \end{bmatrix} = M_3 \begin{bmatrix} i\frac{\lambda}{2\pi}\zeta_{R3} \\ u_{R3} \\ v_{R3} \end{bmatrix} \tag{9}$$

where

$$M_3 = \begin{bmatrix} e^{iZ_3} & 0 & 0 \\ C_3 & \cosh\hat{L}_3 & i\sinh\hat{L}_3 \\ D_3 & -i\sinh\hat{L}_3 & \cosh\hat{L}_3 \end{bmatrix} \quad ; \quad \hat{L}_3 \equiv \frac{2\pi}{\lambda}L_3$$

$$Z_3 = \hat{L}_3\tan\alpha_3$$
$$C_3 = \cos^2\alpha_3\left(\cosh\hat{L}_3 - e^{iZ_3} + i\tan\alpha_3\sinh\hat{L}_3\right)$$
$$D_3 = -\cos^2\alpha_3\left\{-\tan\alpha_3\left(\cosh\hat{L}_3 - e^{iZ_3}\right) + i\sinh\hat{L}_3\right\}$$

Assuming that the flow angle at the exit of each stationary blade row coincides with the geometric blade angle ,

$$\alpha_2 = \beta_G \quad , \quad \alpha_4 = \beta_S \tag{10}$$

where β_G and β_S are the exit blade angles of inlet guide vanes and outlet stator , respectively.

3.2 The Flow through the Rotor

The flow crossing the rotor will be treated with reference to a relative system of coordinates which moves with the rotor at a circumferential velocity V_R. In the following, asterisk refers to the quantities with respect to the moving relative system. The circumferential distortion in the absolute system, Eq.(1), is transformed onto the relative system as

$$f(x)e^{-i2\pi y/\lambda} = f(x)e^{i\omega^*(t+y^*/V_R)} \quad ; \quad \omega^* = -\frac{2\pi}{\lambda}V_R \tag{1*}$$

We assume that, due to the nonsteady effects of the circumferential velocity distortion, all the rotor blades are forced to oscillate in a direction perpendicular to the blade chord, with the same frequency and amplitude. A rotor blade will then oscillate at a velocity $q e^{i\omega^* t}$ with a phase angle $2\pi s/\lambda$ relative to the neighbouring blade which is at the spacing s apart.

The flow through the rotor will be considered taking into account the effects of the blade vibration, the relative displacement between the blades, and so on. The detailed analysis for the flow through the oscillating blade row are already given by the present author in Refs.(6) and (7), so only the principal procedures will be described in the following.

Continuity and Exit Angle Conditions: Since we are considering the incompressible flow, the condition of mass conservation gives

$$u_{R3}^* = u_{R2}^* - \left\{ \frac{U}{V_R} \sin\beta_R (\tan\alpha_2^* - \tan\alpha_3^*) + i\hat{C}_R \right\} q \quad ; \quad \hat{C}_R = \frac{2\pi}{\lambda} C_R \tag{11}$$

Assuming that the relative flow angle at the exit of the rotor will coincide with the blade angle irrespective of the inlet conditions,

$$v_{R3}^* = -u_{R3}^* \tan\beta_R - q\sec\beta_R \quad , \qquad \alpha_3^* = \beta_R \tag{12}$$

Similar relations are obtained for the flow inside the rotor, where the fluid must move along the blade surface.

Energy Characteristics: For the perturbations of flow, the equations of motion in the chordwise and circumferential directions are, respectively,

$$\frac{\partial w^*}{\partial t} + \frac{\partial}{\partial \xi^*}\left(\frac{p_t^*}{\rho}\right) = 0 \quad ; \quad \vec{w}^* = \vec{u}^* + \vec{v}^* \tag{13a}$$

p_t^*: relative total pressure

$$\frac{\partial v^*}{\partial t} + U\zeta^* = -\frac{\partial}{\partial y^*}\left(\frac{p_t^*}{\rho}\right) \tag{13b}$$

Integrating Eq.(13a) through the rotor, using no-loss condition of the flow relative to the oscillating blades, and applying Eq.(13b) to the flow up-and downstream of the rotor, we find finally

$$\begin{aligned} i\frac{\lambda}{2\pi}\zeta_{R3}^* = i\frac{\lambda}{2\pi}\zeta_{R2}^* &+ \frac{V_R}{U}\left(iu_{R3}^* \hat{C}_R \sec\beta_R + v_{R2}^* - v_{R3}^* \right) \\ &+ q\left\{ (\tan\alpha_2^* - \tan\alpha_3^*)\cos\beta_R - i\hat{C}_R \frac{V_R}{U}\tan\beta_R + \frac{1}{2}\frac{V_R}{U}\hat{C}_R^2 \sec\beta_R \right\} \end{aligned} \tag{14}$$

Now the three equations, Eqs.(11),(12), and (14), permit solution for the flow through the rotor as a function of the inflow conditions, the rotor geometry, and the blade vibrational velocity. All the perturbation quantities in the relative system being directly transfered on the absolute system, the asterisks on them can be dropped. Then, Eqs.(11),(12), and (14) can be arranged in matrix form as

$$\begin{bmatrix} i\frac{\lambda}{2\pi}\zeta_{R3} \\ u_{R3} \\ v_{R3} \end{bmatrix} = M_R \begin{bmatrix} i\frac{\lambda}{2\pi}\zeta_{R2} \\ u_{R2} \\ v_{R2} \end{bmatrix} + q \begin{bmatrix} P \\ Q \\ R \end{bmatrix} \tag{15}$$

where

$$M_R = \begin{bmatrix} 1 & \frac{V_R}{U}(\tan\beta_R - i\hat{C}_R\sec\beta_R) & \frac{V_R}{U} \\ C & 1 & 0 \\ 0 & -\tan\beta_R & 0 \end{bmatrix}$$

$$P = \frac{V_R}{U}\sec\beta_R - \left\{\sin\beta_R(\tan\alpha_2^* - \tan\alpha_3^*) + i\hat{C}_R\frac{V_R}{U}\right\}\tan\beta_R$$
$$+ (\tan\alpha_2^* - \tan\alpha_3^*)\cos\beta_R - i\hat{C}_R\tan\beta_R\left(\frac{V_R}{U} - \tan\alpha_2^* + \tan\alpha_3^*\right) - \frac{1}{2}\frac{V_R}{U}\hat{C}_R^2\sec\beta_R$$
$$Q = -\frac{U}{V_R}\sin\beta_R(\tan\alpha_2^* - \tan\alpha_3^*) - i\hat{C}_R$$
$$R = -\sec\beta_R + \frac{U}{V_R}\sin\beta_R(\tan\alpha_2^* - \tan\alpha_3^*) + i\hat{C}_R\}\tan\beta_R$$

Air Force acting on the Rotor Blades: The unsteady aerodynamic forces acting on a vibrating rotor blade can be deduced from the Momentum Theorem. In the present case, the blade is subject to the exciting force $f_q e^{i\omega^* t}$ per unit length, where

$$\frac{f_q}{\rho U S} = u_{R2}\left(-\sin\beta_R + \tan\alpha_2^*\cos\beta_R + i\hat{C}_R\frac{V_R}{U}\tan\beta_R\right) + u_{R3}\cdot i\hat{C}_R\left(1 + \frac{1}{2}i\hat{C}_R\frac{V_R}{U}\sec\beta_R\right)$$
$$- v_{R2}(\cos\beta_R + \tan\alpha_2^*\sin\beta_R) + v_{R3}\left\{\sec\beta_R + i\hat{C}_R\left(\frac{V_R}{U} - \tan\alpha_3^*\right)\right\} + i\hat{C}_R\left(i\frac{\lambda}{2\pi}\zeta_{R3}\right)$$
$$+ q\Big[-\frac{U}{V_R}\cos\beta_R(\tan\alpha_2^* - \tan\alpha_3^*)\{1 + (\tan\alpha_2^* + \tan\alpha_3^*)\sin\beta_R\}$$
$$+ i\hat{C}_R\left\{\frac{V_R}{U}\sec\beta_R - \sin\beta_R\tan\beta_R(\tan\alpha_2^* - \tan\alpha_3^*)\right\} - \frac{1}{2}\hat{C}_R^2\left(1 + \frac{1}{3}i\hat{C}_R\frac{V_R}{U}\cos\beta_R\right)\sec^2\beta_R\Big] \tag{16}$$

The equation of motion for unit length of blade is

$$m\frac{d}{dt}(q e^{i\omega^* t}) + K\int^t q e^{i\omega^* t}dt = f_q e^{i\omega^* t}$$

where the terms on the left-hand side give the inertial and spring forces, respectively, and the mechanical damping effect is not considered. This can be rewritten as

$$i M\hat{C}_R\cos\beta_R\frac{V_R}{U}\left\{1 - \left(\frac{\omega_n}{\hat{C}_R}\frac{U}{V_R}\right)^2\right\} q = -\frac{f_q}{\rho U S} \tag{17}$$

where $\omega_n = \frac{C_R}{U}\sqrt{\frac{K}{m}}$ is the reduced natural frequency and $M = \frac{m}{\rho C_R S\cos\beta_R}$ is the mass ratio.

3.3 The Flow through the Stationary Blade Rows

The equations for the flow through the stationary blade rows are deduced from those concerning the rotor by letting the rotor speed and the blade vibrational velocity go to zero.

Hence, the following transfer equations are given for the inlet guide vanes and the outlet stator, respectively, when the exit conditions given by Eq.(10) hold.

$$\begin{bmatrix} i\frac{\lambda}{2\pi}\zeta_{G2} \\ u_{G2} \\ v_{G2} \end{bmatrix} = M_G \begin{bmatrix} i\frac{\lambda}{2\pi}\zeta_{G1} \\ u_{G1} \\ v_{G1} \end{bmatrix} \quad ; \quad M_G = \begin{bmatrix} 1 & 0 & 0 \\ 0 & 1 & 0 \\ 0 & \tan\beta_G & 0 \end{bmatrix} \tag{18}$$

$$\begin{bmatrix} i\frac{\lambda}{2\pi}\zeta_{S4} \\ u_{S4} \\ v_{S4} \end{bmatrix} = M_S \begin{bmatrix} i\frac{\lambda}{2\pi}\zeta_{S3} \\ u_{S3} \\ v_{S3} \end{bmatrix} \quad ; \quad M_S = \begin{bmatrix} 1 & 0 & 0 \\ 0 & 1 & 0 \\ 0 & \tan\beta_S & 0 \end{bmatrix} \tag{19}$$

4. Solutions and Results

4.1 Case of the Rigid Rotor

In this case, the velocity of the rotor blade vibration being zero, combination of the transfer equations obtained so far, Eqs.(8),(9),(15),(18), and (19), gives for the single-stage turbomachine of Fig. 1

$$\begin{bmatrix} i\frac{\lambda}{2\pi}\zeta_{S4} \\ u_{S4} \\ v_{S4} \end{bmatrix} = M_S \cdot M_3 \cdot M_R \cdot M_2 \cdot M_G \begin{bmatrix} i\frac{\lambda}{2\pi}\zeta_{G1} \\ u_{G1} \\ v_{G1} \end{bmatrix} \tag{20}$$

The five simultaneous equations, Eqs.(5),(7), and three of Eq.(20), may be solved for the five unknown quantities (u_{G1}, v_{G1} , u_{S4} , v_{S4} , $i\frac{\lambda}{2\pi}\zeta_{S4}$) as a function of the inlet distortion ($i\frac{\lambda}{2\pi}\zeta_{G1}$) and the geometries of the blade rows.

The attenuation of inlet distortion is then given by $|\zeta_{S4}/\zeta_{G1}|$. The vorticity of any fluid may be changed by the action of the rotor and maintained unchanged elsewhere. Therefore, the attenuation of inlet distortion is also given by $|\zeta_{R3}/\zeta_{R2}|$, and its phase shift in the circumferential direction by $\arg(\zeta_{R3}/\zeta_{R2})$.

Simple solutions are obtained in two limiting cases. The first is the case where a single rotor is isolated in an infinite flow field, when letting the row distances , L_2 and L_3 , be infinite gives

$$\frac{\zeta_{R3}}{\zeta_{R2}} = \frac{1 - \frac{V_R}{U}\frac{i}{1 + i\tan\alpha_2}}{1 + \frac{V_R}{U}\frac{\tan\beta_R - i(1 + \hat{C}_R\sec\beta_R)}{(1 - i\tan\beta_R)(1 - i\tan\alpha_3)}} \tag{21}$$

The second is the case where all the blade rows are so closely spaced that all the gaps between them can be neglected. In this case, the transfer matrices concerning the gaps, such as M_2 and M_3 , become unit matrix, and then the above analysis can easily be extended to the case of a multi-stage turbomachine. If a multi-stage axial turbomachine consists of N similar stages in which the stagger angles of the inlet guide vanes and the stators in the intermediate stages are common, the solution is given in a simple form as

$$\frac{\zeta_{out}}{\zeta_{in}} = \frac{1}{1 + N\frac{V_R}{U}\left(\tan\beta_G + \tan\beta_R - i\hat{C}_R \sec\beta_R\right)\cos^2\beta_S} \tag{22}$$

In these particular cases, it is noted that the actuator disc rotor ($\hat{C}_R \rightarrow 0$) achieves only the same attenuation for any wave-number of distortion.

Calculated results for the model of a single-stage turbomachine shown in Fig. 1 will be given when the geometric and flow parameters taken are

$$C_R = 1 \;; \qquad \alpha_1 = 0^\circ, \quad \alpha_2^* = 45^\circ \;; \qquad \beta_G = \beta_R = 30^\circ, \quad \beta_S = 0^\circ$$

Fig. 2 shows the stage attenuation of the inlet velocity distortion when the stationary blade rows are placed at identical axial separations before and behind the rotor, comparing with the results for the actuator disc case. As is seen from Eqs.(8),(9),(15),and as shown in Fig. 2, the attenuation of the inlet distortion intrinsically depends on the ratios of its circumferential wave-length to the blade row distances and the rotor chord. It may be said that the effects of the blade row interference ($\hat{L}^{-1} = \lambda/2\pi L$) and the inertial effects of the fluid inside the rotor ($\hat{C}_R = 2\pi C_R/\lambda$) lead to better attenuation.

Fig. 3 shows the phase shift of the distortion in the circumferential direction. When the blade rows are closely spaced with each other, the phase shift varies in proportion to the wave number ($2\pi/\lambda$), but it becomes less dependent upon the wave number as the row distances increase. This suggests that the inlet distortion of an arbitrary profile may be much deformed in an isolated single rotor, whereas the outlet distortion may have a similar wave form as the inlet one in a closely packed stage.

4.2 Case of the Flexible Rotor

When the rotor blades are flexible, the solution is obtained from the equations governing the motion of fluid, Eqs.(8),(9),(15),(18), and (19), together with the equations concerning the rotor blade vibration, Eqs.(16) and (17).

Calculations are made for the model of a single-stage turbomachine of Fig. 1, when the geometric and flow parameters are the same as in the previous case and the parameters in Eq.(17) for the blade vibration are taken as

$$\omega_n = 1.0 \;, \qquad M = 100$$

Fig. 4 gives the calculated results of the stage attenuation, showing that the rotor blade vibration makes the attenuation of the distortion worse in sub-resonance range, and better in super-resonance range. The attenuation varies remarkably near the resonant condition, that is, the inlet distortion is only slightly attenuated, sometimes amplified, in high sub-resonance range and diminished intensively in low super-resonance range. The blade row interference makes the blade vibration effect less significant, because the closely spaced rows act to suppress the perturbations entering the rotor and make the blade load fluctuations small.

Fig. 5 shows the phase shift of the distortion in the circumferential direction. Near the resonant condition, prominent change of the phase shift is produced by the blade vibration.

A comparison between the interference effects of the up-and downstream blade rows is shown in Fig. 6, when one of them is placed just before or behind the rotor without gap. If the downstream row is located close to the rotor, better attenuation is achieved except in low super-resonance range, but the approach of the upstream one leads to worse attenuation except in high sub-resonance range.

5. Concluding Remarks

The inlet airflow distortion in a turbomachine was studied on the basis of semi-actuator disc approximation when the rotor blades were either rigid or flexible. The results obtained show that (1) the effect of blade row interference and the inertial effect of fluid inside the rotor result in better attenuation of the inlet distortion, and (2) the mutual interactions between the inlet distortion and the blade vibration are rather striking near the resonant condition, although that may be exaggerated by the neglect of mechanical damping effect in the present study. Especially the latter result is noted, which suggests that the blade vibration due to inlet distortion should be examined taking into account the mutual effects between them.

6. References

1. Ehrich, F. Circumferential Inlet Distortions in Axial Flow Turbomachinery. J. Aeronautical Science. Vol. 24, p.413, June 1957.
2. Rannie, W.D. and Marble, F.E. Unsteady Flows in Axial Turbomachines. C. r. des Journees Internationales des Scieces Aeronautiques (ONERA, Paris). Part 2, p. 1, 1957.
3. Yeh, H. An Actuator Disc Analysis of Inlet Distortion and Rotating Stall in Axial Flow Turbomachines. J. Aerospace Science. Vol. 26, p. 739, November 1959.
4. Dunham, J. Non-Axisymmetric Flows in Axial Compressors. Mechanical Engineering Science. Monograph No. 3, October 1965.
5. Takata, H. Rotating Stall in Multistage Axial Compressors. Bulletin of Aeronautical Research Institute, University of Tokyo. Vol. 2, No. 6, p.305, 1961. (in Japanese)
6. Tanida, Y. and Okazaki, T. Stall-Flutter in Cascade, I & II. Bulletin of Japan Society of Mechanical Engineers. Vol. 24, p. 744 & 753, 1963.
7. Tanida, Y. Effect of Blade Row Interference on Cascade Flutter. Trans. Japan Society for Aeronautical & Space Sciences. Vol. 9, p. 100, 1966.
8. Tanida, Y. Inlet Airflow Distortion in Turbomachinery. Z. angewandte Mathematik u. Physik. Vol. 23, p. 645, 1972.

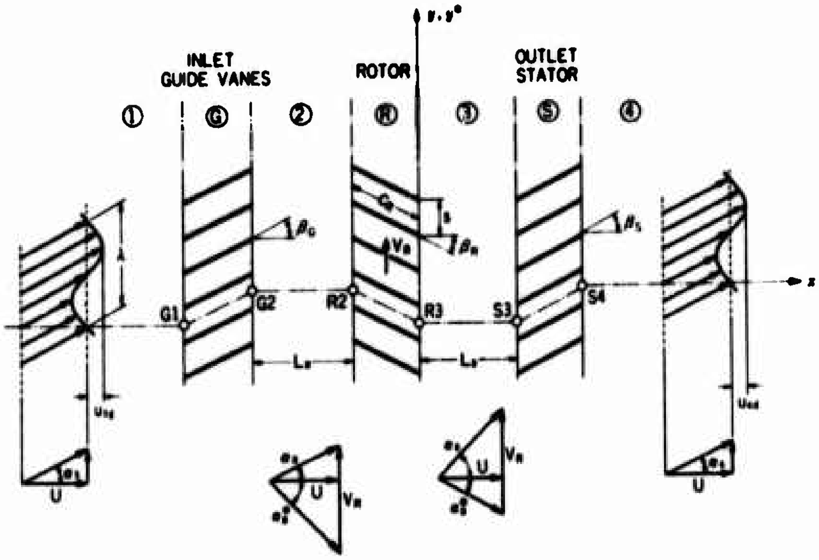
INLET GUIDE VANES
ROTOR
OUTLET STATOR
①
Ⓖ
②
Ⓡ
③
Ⓢ
④
G1
G2
R2
R3
S3
S4
U
V_R
λ
z

Fig. 1 Nomenclature

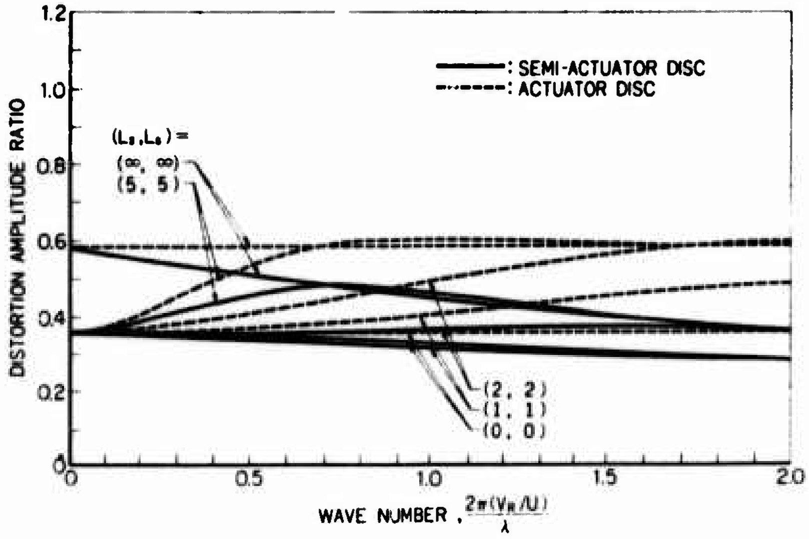

Fig. 2 Distortion amplitude ratio through compressor stage (Rigid rotor)

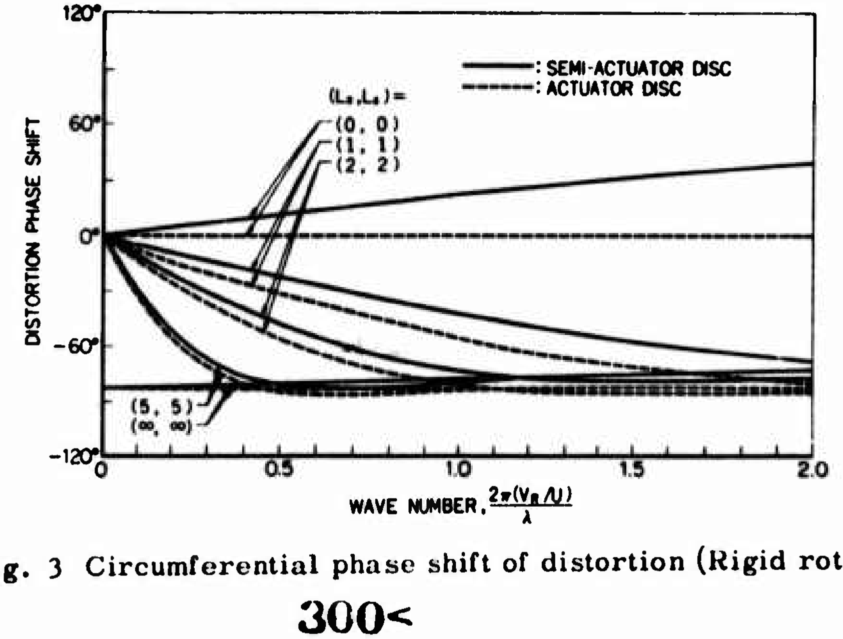

Fig. 3 Circumferential phase shift of distortion (Rigid rotor)

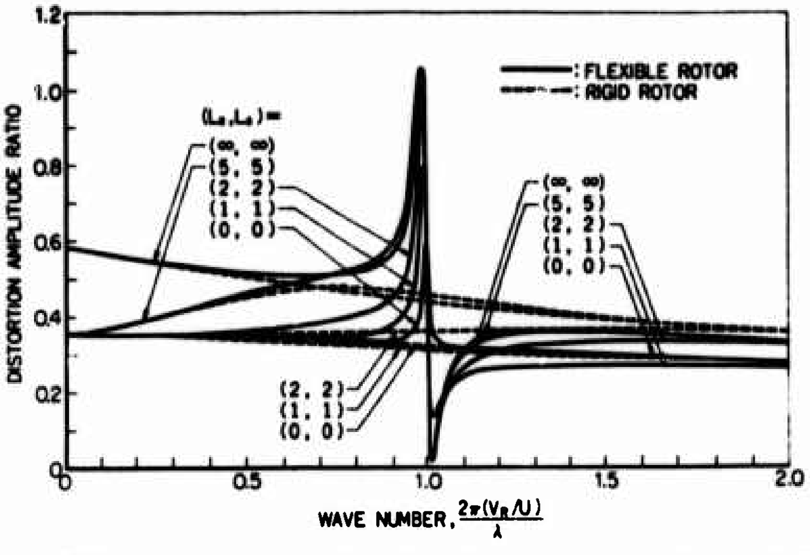

Fig. 4 Effect of rotor blade vibration on stage attenuation

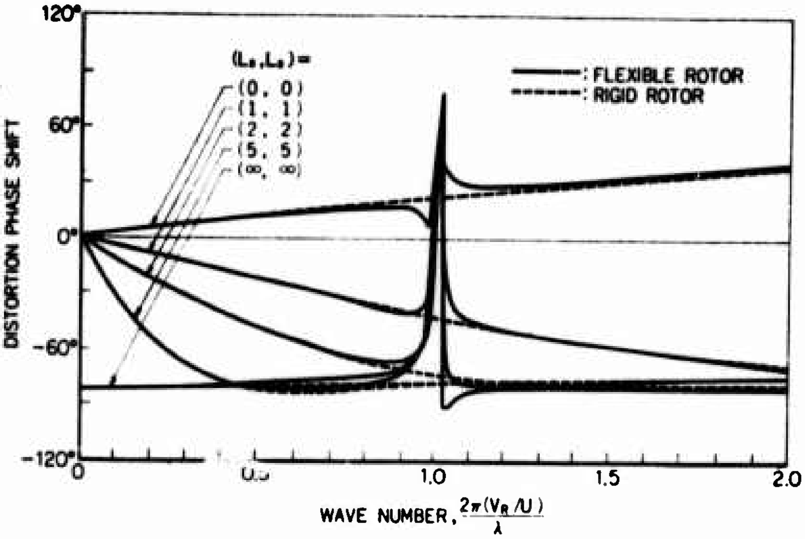

Fig. 5 Effect of rotor blade vibration on distortion phase shift

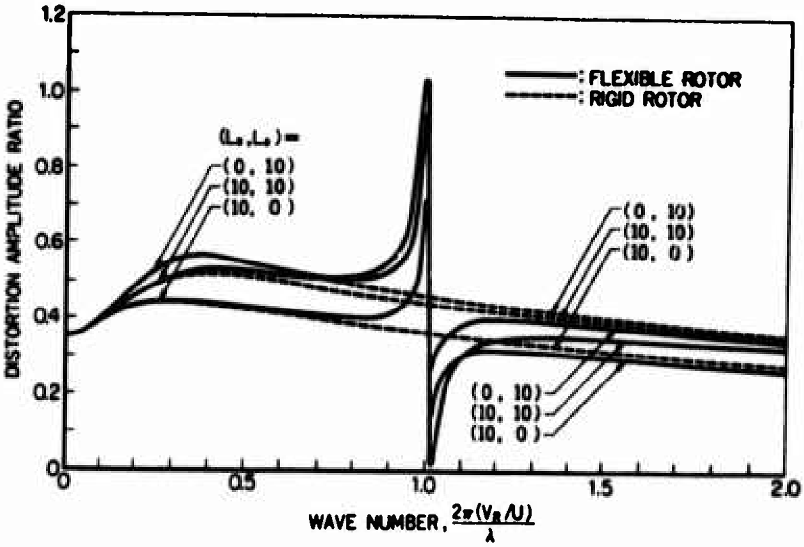

Fig. 6 Comparison of up-and downstream row effects

EXPERIMENTAL INVESTIGATION OF A TRANSONIC AXIAL FLOW COMPRESSOR STAGE WITH STEADY STATE DISTORTED INLET FLOW

M. Lecht, H. Weyer

DFVLR-Institut für Luftstrahlantriebe, Porz-Wahn, Germany

Abstracts

A transonic axial flow compressor stage with a hub to tip ratio of 0.5 and a total pressure ratio of 1.5 is investigated with a 6o° and 12o° circumferential total pressure inlet distortion of different intensity. The selection of distortion screens based on the DC-6o distortion parameter is briefly explained. Different test series have been carried out to get the stage overall performance map and the rotor and stator blade element performance. By traversing the flow in front, between and behind the stage the development of the distortion is followed through the stage and the rotor influence on the upstream flow is shown by the static pressure and the flow direction in front of the rotor. Additionally, the oscillating loading of a rotor blade passing the steady state distorted area is analysed in comparison to that of an oscillating airfoil

Nomenclature

H_{is}	Isentropic total enthalpy
i	Rotor blade incidence angle
$\dot{m}_{red\,3}$	Mass flow corrected to the flow conditions at plane 3 (equivalent to plane 4)
N	Design speed
P	Static pressure
P_{tot}	Total pressure
$\bar{P}_{tot}$	Averaged total pressure
ΔP_{tot}	Screen total pressure loss
q	Dynamic pressure in front of screen
R	Radial position
R_a, R_i	Outer and inner radius
T_{tot}	Total temperature
ΔT_{tot}	Difference between total temperature and inlet total temperature
U	Rotor tangential velocity
U_a	Rotor tip tangential velocity
W_S	Screen mass flow
W_S'	Ideal screen mass flow
α	Absolute flow angle

θ	Temperatur correction $T_{tot,inlet}/288^{o}K$
η_{is}	Isentropic efficiency
π_{tot}	Stage total pressure ratio
φ	Circumferential position
ψ	Work coefficient $2 H_{is}/u_a^2$

Introduction

In modern aircraft jet engine development the engine-inlet compatibility plays a major role. So in compressor design one often assumes that the engine will meet with a uniform, smooth flow at its inlet. This philosophy, however, very often is in contrary to real flight conditions, where complex inlet flow distortion may occur for instance as a steady state dynamic or combined distortion of total pressure, total temperature or flow direction. Inlet flow distortions may rise from different sources as there are flow separation from the inlet lip due to high angles of attack, interference between boundary layer and shock waves leading to pulsating flow seperation or as there is hot gas recirculation.

In order to carry out basic research work the already complex pattern of a steady state distortion in practice makes it necessary to reduce the problem to a single-flow-parameter distortion with simplified shapes of interest. Mainly two kinds of steady state inlet distortion have been the subject of todays investigations; first the so called radial distortion, which is a nonuniform distribution along hub to tip, and second the so called circumferential distortion which is a nonuniform distribution along the circumferential direction. The circumferential distortion type is found to give higher penalty in compressor performance, so the DFVLR Institue for Airbreathing Engines started its mainly experimental work in this field with investigations on the effect of total pressure distortions of the circumferential type.

Test compressor stage

The transonic compressor that has been investigated is a single stage type without inlet guide vanes. The outer diameter at rotor inlet is 4oo mm (15.75 in.) and the hub-to-tip ratio is o.5. The main data at design point are: corrected weight flow 17.3 kg/s (38.13 lbs/sec), total pressure ratio 1.5 and rotor tip speed 425 m/s (1392 ft/sec). The relative Mach number reaches up to about 1.4 at the rotor tip. In the tip region the blade is shaped as a multiple-circular-arc (MCA) and near the hub as a double-circular-arc (DCA) profile. Fig. 1 shows a cross-sectional view through the test compressor.

The casing consists of an outer cage with several internal contour rings carrying the measuring instrumentation. The air is drawn from the atmosphere through a filter house, passing a venturi tube, smoothing screens and a bell-mouth inlet with an area ratio of 6.

Inlet distortion equipment

About one blade height in front of the rotor - between plane 4 and 5 - the spoiling section is located. There is installed a rotatable spoiler support with 72 radial spokes of o,7 mm (o.o31 in.) thickness and lo mm (o.394 in.) axial length, to which distortion screens of various sector angles can be attached. Additionally the screen sector is bordered on each side by splitter plates leading upstream from the spoiling section to avoid the spillage flow around the corners of the screen.In this way a uniform flow just in front of the screen may be approximately achieved.

Instrumentation

Fig. 2 represents the different measuring planes inside the compressor and the instrumentation arrangements. The static pressure was normally measured by twelve hub and twelve casing static taps at plane 4, 5, 6 and 9. At plane 8 there were only six hub and six casing wall taps available.

The compressor inlet total pressure was measured at plane 6 by means of two total pressure traversing probes with a five element circumferential rake (Fig. 3a). The inlet total temperature was taken the same as that measured ahead of the bellmouth inlet. Additionally at plane 6 the flow angle was measured by means of two traversing probes (Fig. 3b).

At the outer casing in plane 7 there were several fast-response pressure pick-ups mounted in direction of the blade chord for determining the fluctuating pressure inside the blade channels. The tip gap between rotor blade and casing was observed by a capacitive gap meter. Behind the rotor in plane 8 three traversing probes for total pressure, flow angle and total temperature respectively were installed closely to each other. Stator exit total pressure and total temperature were obtained from two eight-element radial rakes respectively (Fig. 3c). The contour ring at plane 9 was designed to be rotated over nearly two blade spacings in order to traverse the stator blade wakes. In addition two wedge-type probes were used for the radial traversing of the flow angle between the stator blade wakes (Fig. 3d).

Selection of distortion screens

To simulate a steady state total pressure distortion usually a sector of the compressor inlet annulus is covered by wire screens of different porosity. The screen total pressure loss is a measure for the intensity of the distortion and, in the meantime, a lot of distortion parameters exists all based on the pressure loss. One of them is the so called DC-6o-factor(1) specially defined for a circumferential distortion as the difference between the average total pressure and the minimum average total pressure within any 6o-degree sector related to the inlet dynamic pressure. For the tests described in this paper screens were selected to produce at least a DC-6o-factor of O.5 and O.75 respectively, which are derived from the loss coefficient of the wire screens determined by windtunnel tests (Fig. 4).

To determine the screen losses within a compressor inlet one has to take into account first of all, that the screen covers only a part of the annulus area, leading to a spillage of mass flow according to the inlet Mach number and screen characteristics. Second there is a remarkable influence of the compressor itself on the screen flow and the spillage (2). Third there is an additional loss of the spoiler support that can be added to the screen losses at low Mach numbers and will lead to primature choking of the spoiler. Screens of 58 and 51 percent open area were selected with some estimations on the magnitude of the decrease of the static pressure just behind the screen, which is caused by the effect of the rotor on the upstream flow.

Test procedure

At first overall performance tests were carried out traversing in front of the rotor and behind the stator exit only. The distortion screen was rotated past the instrumentation in a step by step way (18 degrees) so that at least one traversing probe or rake of each type in the two planes (6 and 9) moved through the distorted flow regime. At each circumferential position eight radial traversing points were taken. In addition at the stator exit the radial rakes were moved over one blade spacing in eight discrete steps. The tests were performed at 7o, 85 and loo percent design speed, which agreed with the tests on the undistorted compressor.

After the investigation of the compressor overall performance the flow inside the stage was analysed in detail including measurements of the main flow parameters in plane 6, 8, and 9 at two different mass flow rates - near maximum efficiency and near surge line.

Overall performance

The overall performance of the transonic stage with and without inlet distortion is shown in Fig. 5 for 7o, 85 and loo percent of corrected design speed. The mass flow was corrected to the average total pressure in front of the rotor (plane 6). As was expected a remarkable drop of the total pressure ratio was found at the higher speeds. Simultaneously the stall line retracts to a higher mass flow so that the working range of the compressor is reduced. In contrary to the lower speeds only at loo percent the test results at the different spoiling sector angles and screen porosities can be clearly distinguished. At all speeds, however, the isentropic efficiency shows a sharp drop compared with the undistorted compressor. The scattering of the test points gives rise to the problem of measuring temperatures accurately.

Influence of the total pressure distortion on the stage flow.

At first, the distortion parameter DC-6o as a more or less common definition shall be discussed. This factor is a function of total pressure drop and spoiled sector angle, for instance if the pressure drop remains constant the distortion parameter would rise to its maximum at 6o degrees of spoiled sector and then goes down as the sector is further increased.

During the distortion tests the DC-6o parameter was within the range of 0.5 to 0.9. In Fig. 6 it is plotted versus the mass flow which is corrected to the flow conditions ahead of the screen. The dimensionless total pressure loss $(P_{tot,max} - P_{tot,min})/\bar{P}_{tot}$ over the whole tested massflow range was between o.05 and o.2.

The spillage flow of the screen is shown in Fig. 7 as a function of the inlet mass flow. The screen spillage is defined as the difference between the mass flow facing the screen projection area and the real mass flow through the screen related to the first one as lined out in the picture at the bottom of Fig. 7.

Normally, the spillage should be a smooth function of the inlet mass flow with the spoiled sector angle as a parameter. However, due to the influence of the rotor on the upstream flow each compressor speed line is evident in Fig. 7.

In the following the distorted flow parameters are shown as they develop through the compressor stage. In Fig. 8 for example the total and the static pressure circumferential distribution at medium blade height in the planes 6, 8 and 9 are compared for different mass flow rates at 85 percent design speed. In addition to the original total pressure distortion also a static pressure distortion is induced at the inlet due to the rotor influence. The more the compressor is throttled the more both the pressure distributions become asymmetric. Behind the rotor their original form has changed too, when stall is approached. Behind the stator the static pressure is rather smoothed. The same tendency is revealed in Fig. 9, where the total pressure behind the rotor is plotted against the circumferential direction at three radial positions for different mass flow rates.

The absolute flow angles before and behind the rotor are demonstrated in Fig. 1o. In front of the rotor a positive as well as a negative preswirl occures within the distorted region. This leads to a lower incidence of the rotor blades entering the distorted region and to a higher incidence, when the blades leave. Behind the rotor the absolute flow angle in general is higher within the distorted zone than outside. The distribution of the total temperature rise inside the rotor and the stage respectively is shown in Fig. 11.

According to the flow angle distribution it is evident from Fig. 11 that inside the spoiled area less work is transfered to the fluid by the entering blades than by the leaving blades.

To demonstrate the total pressure distortion throughout the compressor stage the maximum pressure amplitude is related to the circumferentially averaged pressure and plotted in Fig. 12 against the radius for different mass flow rates. Compared with the value in front of the rotor an amplification is observed near the hub at medium mass flow, which becomes larger in its radial extent near stall.

Dynamic rotor response

A rotating blade row perceives a steady state total pressure distortion as a periodic change of pressure, flow angle and flow velocity. During one revolution each rotor blade undergoes a strong variation of its aerodynamic loading. Though measuring in a conventional steady state manner it is possible to analyse the unsteady effects by correlating the circumferential distribution of the flow parameters in front and behind the rotor. However, for this it is neccessary to estimate the streamlines as they pass through the rotor. For this evaluation the following assumptions have been made:

1.) The meridional streamline was assumed to correspond to a constant relative blade height.

2.) The axial velocity remains constant and is taken as an average of the values measured in the plane 6 and 8.

3.) The tangential velocity component increases linearly from the rotor inlet to outlet.

Some results of this analysis are shown in Fig. 13 for the medium mass flow and the near stall point at 85 % design speed. To characterize the dynamic response of the rotor blades the incidence angle and the work coefficient were selected (3). In the upper diagrams the circumferential distribution of the incidence and the work coefficient are plotted for a 6o degree spoiling sector angle. The figure revealed the lower incidence and work coefficient as the blades enter the spoiled area and the increase of the work coefficient together with the incidence inside the spoiled sector. As the blades leave the spoiled region a drop of the incidence as well as of the work coefficient occures. At the near stall point the drop of the work coefficient tends to move opposite the direction of rotor rotation.

To get a better view of the dynamic response, the work coefficient is plotted versus incidence in the diagrams at the bottom of Fig. 13. These plots are similar to those often used for isolated airfoils in oscillatory flow (4). The large circular and triangular symbols represent the steady state compressor operation within the unspoiled area whereas the small open and solid symbols follow the way of a rotor blade through the spoiled area in equal steps of 12 degrees.

These diagrams show a rather hysteresis loop which tends to increase near stall. The time of one hysteresis cycle is about 1.4 milliseconds, that means that the drop of the working coefficient will start about o.5 milliseconds after the incidence starts to rise. Moreover, it should be mentioned that near stall the incidence within the unspoiled sector is nearly of the same magnitude as that for the compressor without inlet distortion. This means that within the spoiled area the incidence exceeds considerably the steady state value. As expected the work coefficient first increases with incidence until values of 18° and 16° respectively. Beyond these angles no further increase of the work coefficient is observed. At 25 % blade height a sudden drop of the work coefficient appears just before the blades are leaving the distorted area and that probably indicates a break-down of the flow in this zone.

In Fig. 14 the results for a 6o and a 12o degree sector are compared (85 percent design speed, near stall, 51 % open screen area).

Near the tip only the 12o degree loop shows a heavy breakdown of the flow after a time of nearly o.5 milliseconds, succeeded by a weak recovery however at a somewhat lower level.
In Fig. 15 the results taken at two different screen porosities and at a constant sector angle of 12o degrees are shown near stall point (85 % speed). Both curves indicate a drop of the work coefficient at nearly the same incidence.

Conclusions

In testing steady state total pressure distortions the influence of the compressor on the upstream flow has to be taken into account. At the exit of the compressor total pressure as well as total temperature distortions occur which are amplified or attenuated depending on the operational conditions. The static pressure distortion created in the front of the stage is rather attenuated at its exit.

Within the undistorted area the rotor works at nearly steady state conditions whereas the distorted area is characterized by dynamic effects like a fluctuating aerodynamic loading of the rotor blades.

References

1. G. Reid. The Response of Axial Flow Compressors to Intake Flow Distortion. ASMS-paper 69-GT-29.

2. G.M. Callahan, A.H. Stenning. Altenuation of Inlet Flow Distortion upstream of Axial Flow Compressors. AIAA 69-485, June 1969, USAF Academy Colorado.

3. C.G. Koch, K.R. Bilwakesh, V.L. Doyle, Evaluation of Range and Distortion Tolerance for High Mach Number Transonic Fan Stages. NASA CR-728o6.

4. J. Liiva. Unsteady Aerodynamik and Stall Effects on Helicopter Rotor Blade Airfoil Sections. Journal of Aircraft, Vol. 6, No. 1, Jan.-Febr. 1969.

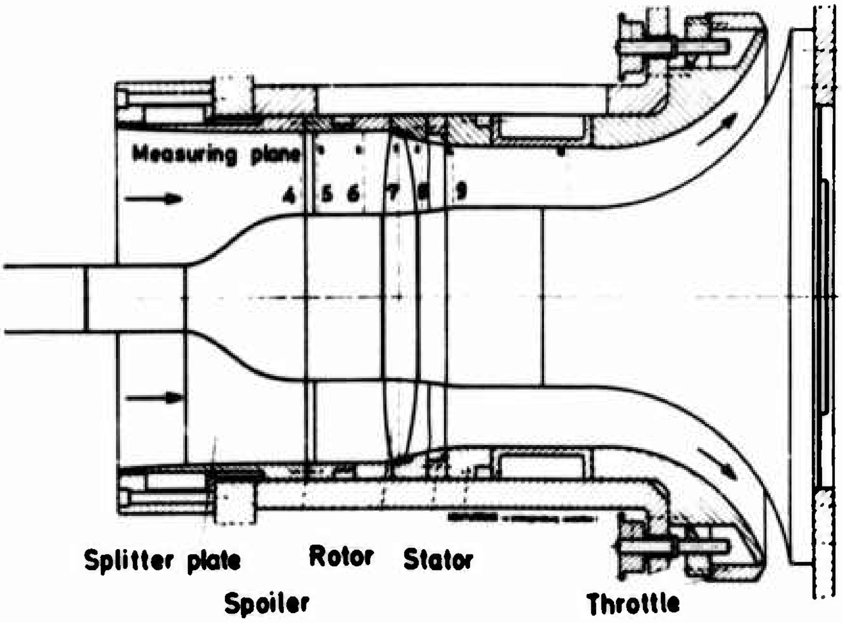
Measuring plane
4
5
6
7
8
9
Splitter plate
Rotor
Stator
Spoiler
Throttle

Fig.1 Cross sectional view of the single stage transonic compressor

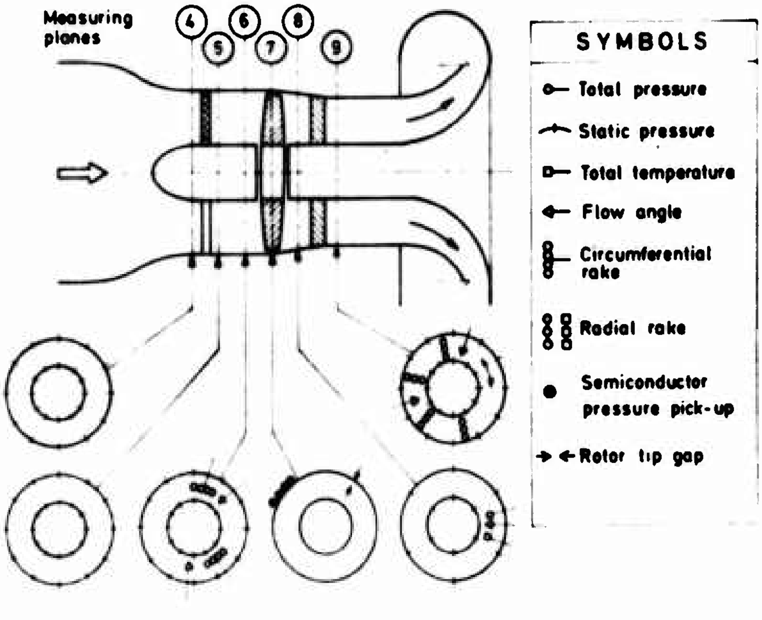
Measuring planes
4
6
8
5
7
9
SYMBOLS
Total pressure
Static pressure
Total temperature
Flow angle
Circumferential rake
Radial rake
Semiconductor pressure pick-up
Rotor tip gap

Fig.2 Meridional view showing instrumentation locations

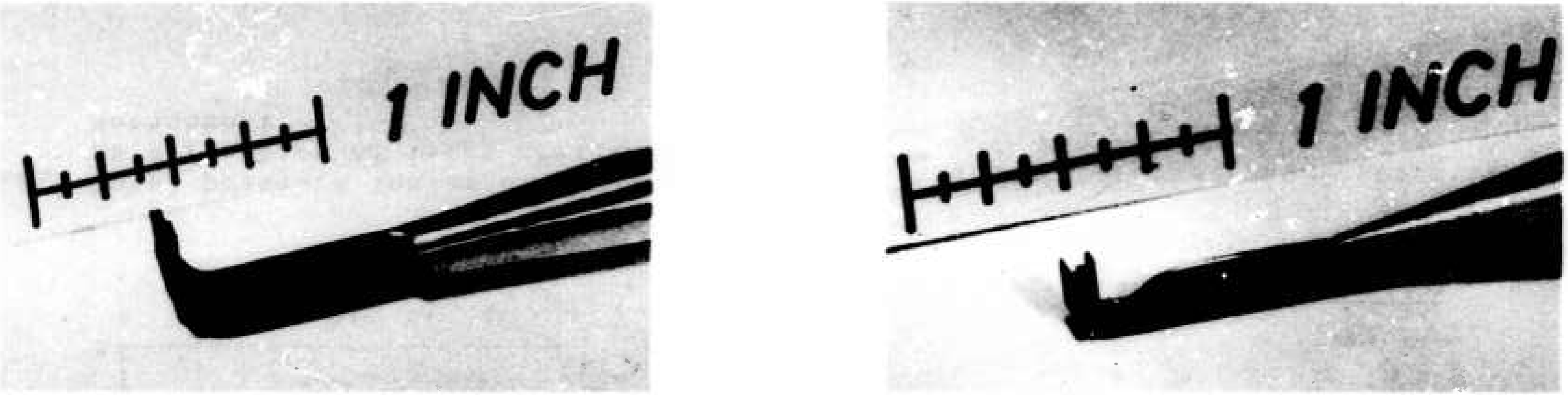
1 INCH
1 INCH

(a) Total pressure radial rake

(b) Flow angle probe

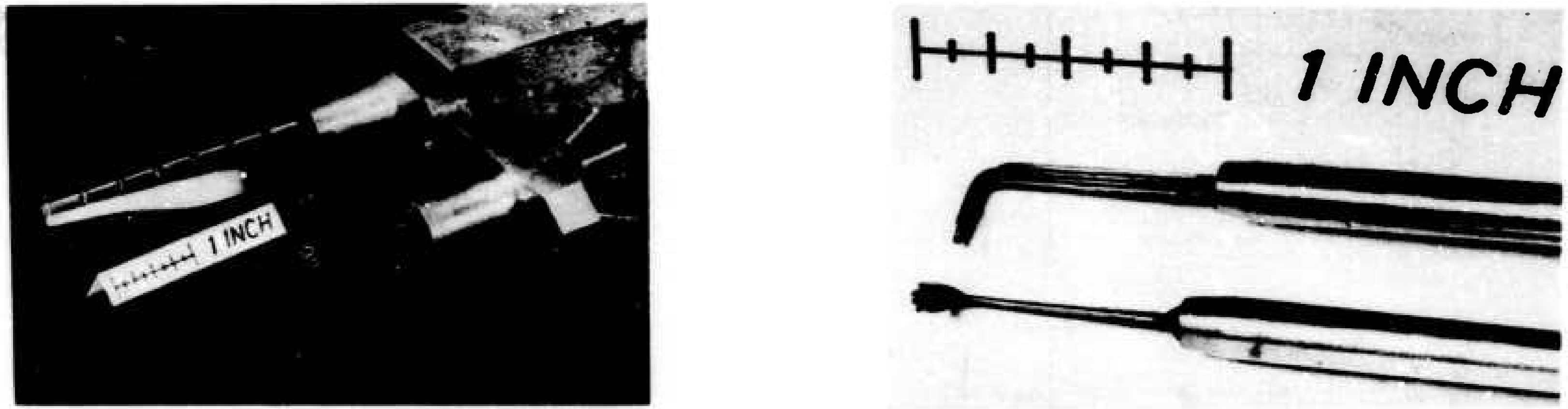
1 INCH
1 INCH

(c) Radial rakes: Total temperatur
Total pressure

(d) Flow angle wedge type probes

Fig. 3 Photographs of instrumentation

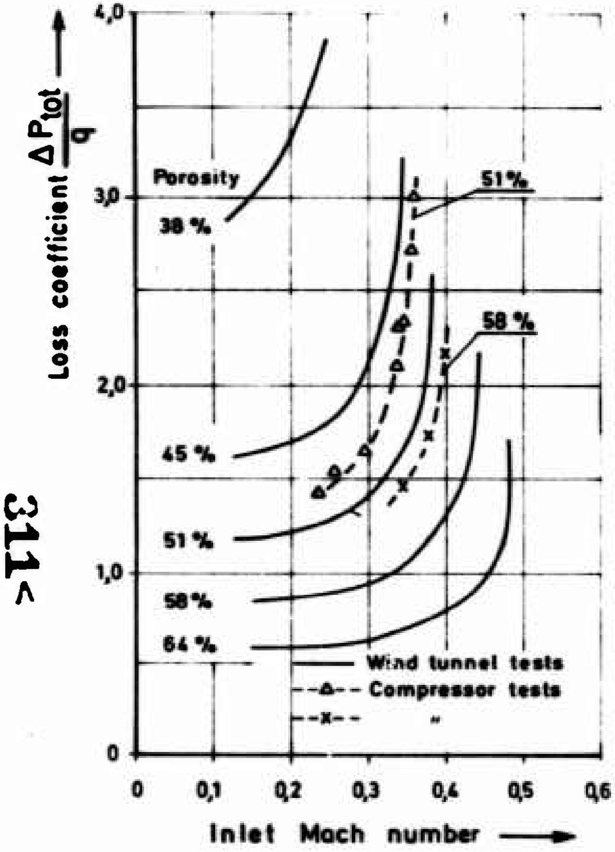

Fig.4 Total pressure losses of screens as a function of inlet critical Machnumber

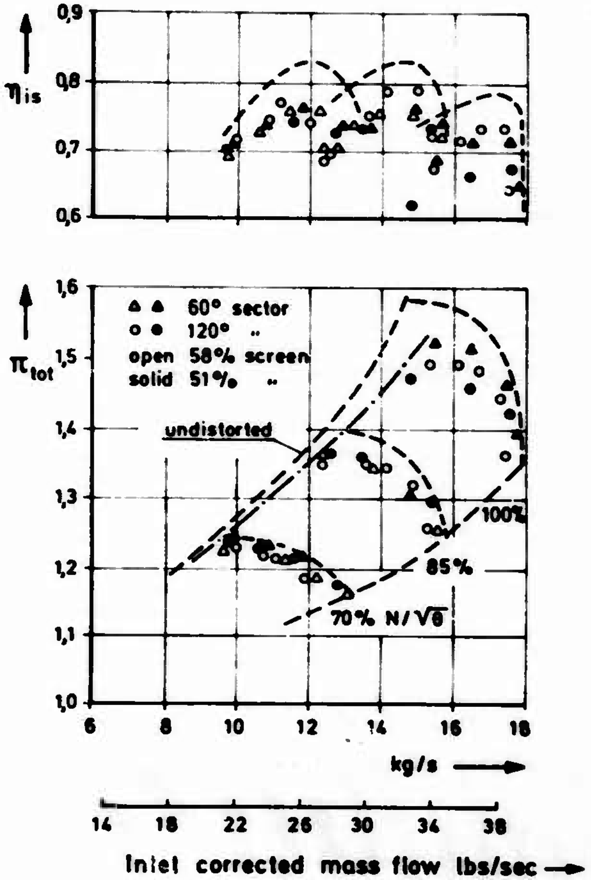

Fig.5 Compressor stage performance map

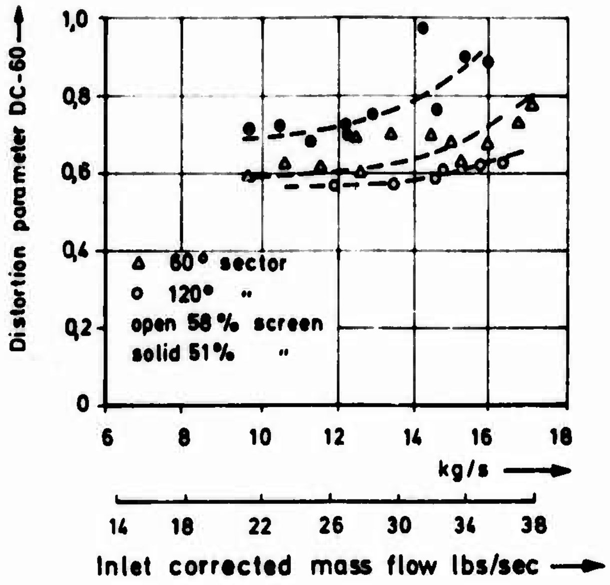

Fig.6 DC-60-distortion parameter as a function of inlet mass flow

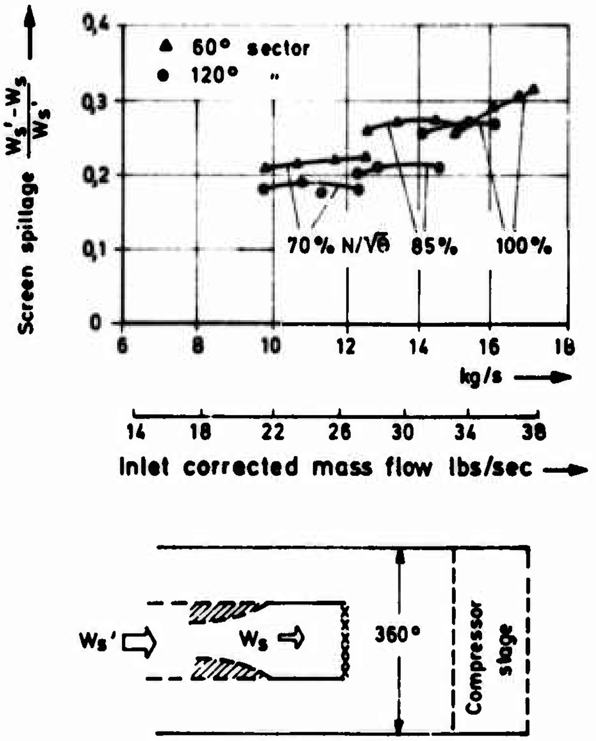

Fig.7 Screen flow spillage as a function of inlet mass flow

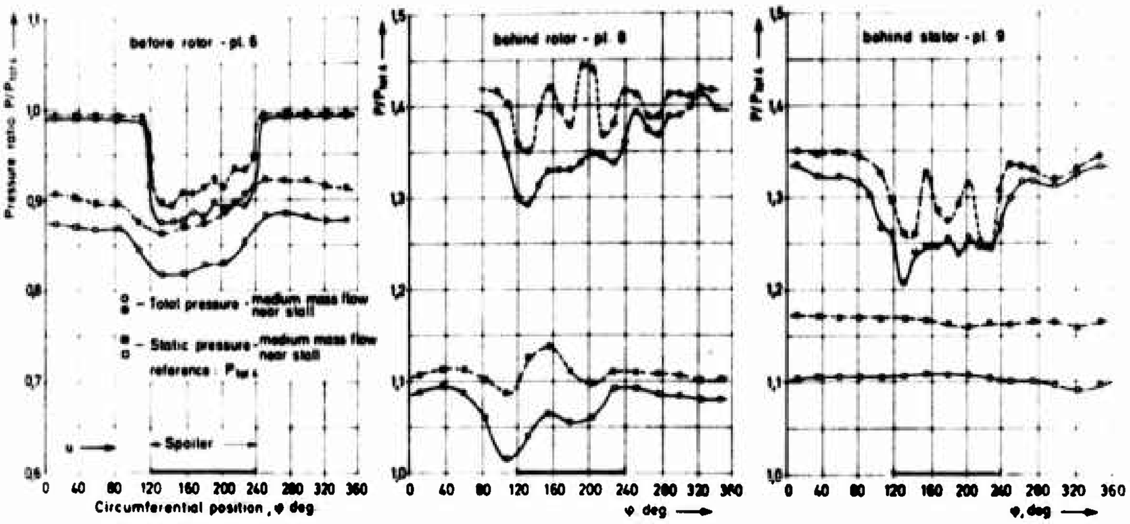

Fig.8 Total and static pressure circumferential distribution at midspan (spoiled sector angle: 120°, screen: 51 % open area, 85% design speed)

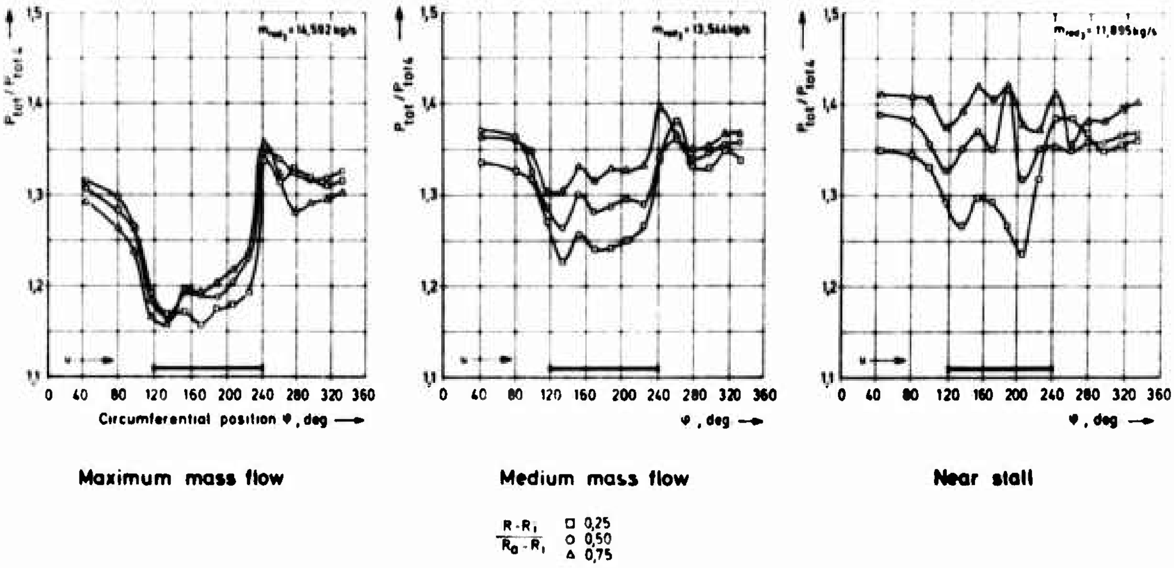

Maximum mass flow

Medium mass flow

Near stall

Fig.9 Total pressure circumferential distribution behind the rotor for different mass flows and radial positions (spoiled sector angle: 120°, screen: 58% open area, 85% design speed)

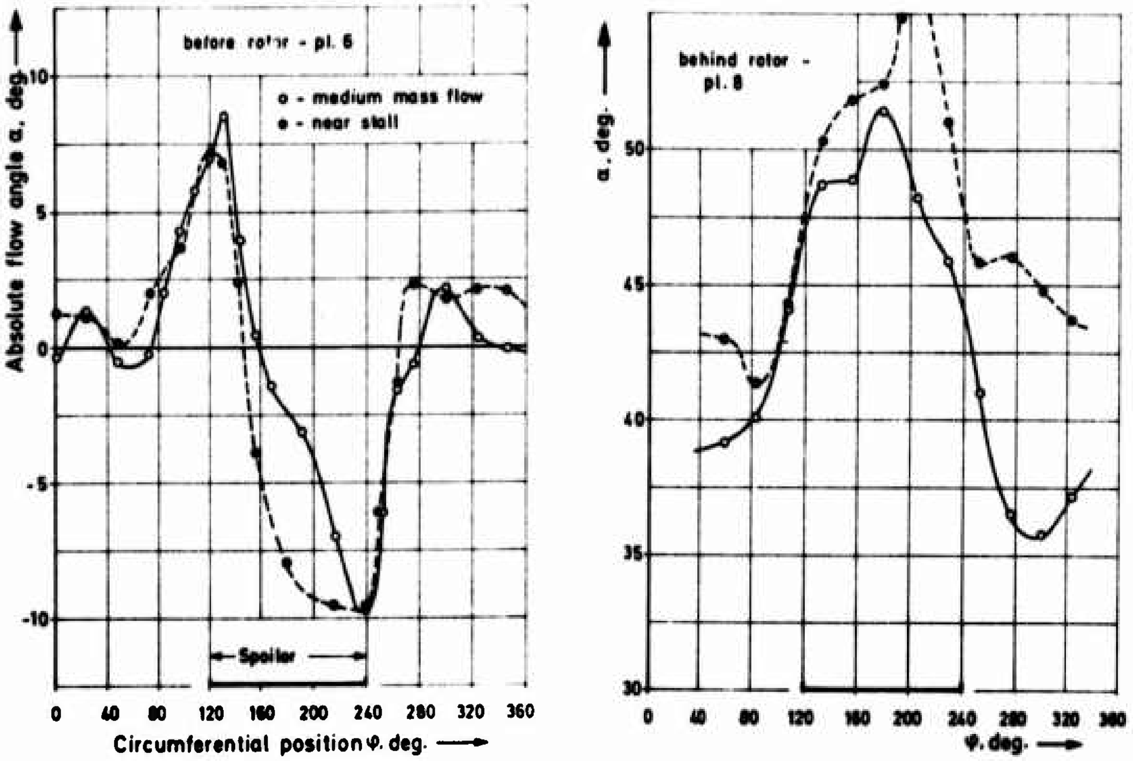

Fig. 1o Circumferential flow angle distribution at midspan (spoiled sector angle: 120°, screen: 51% open area, 85% design speed)

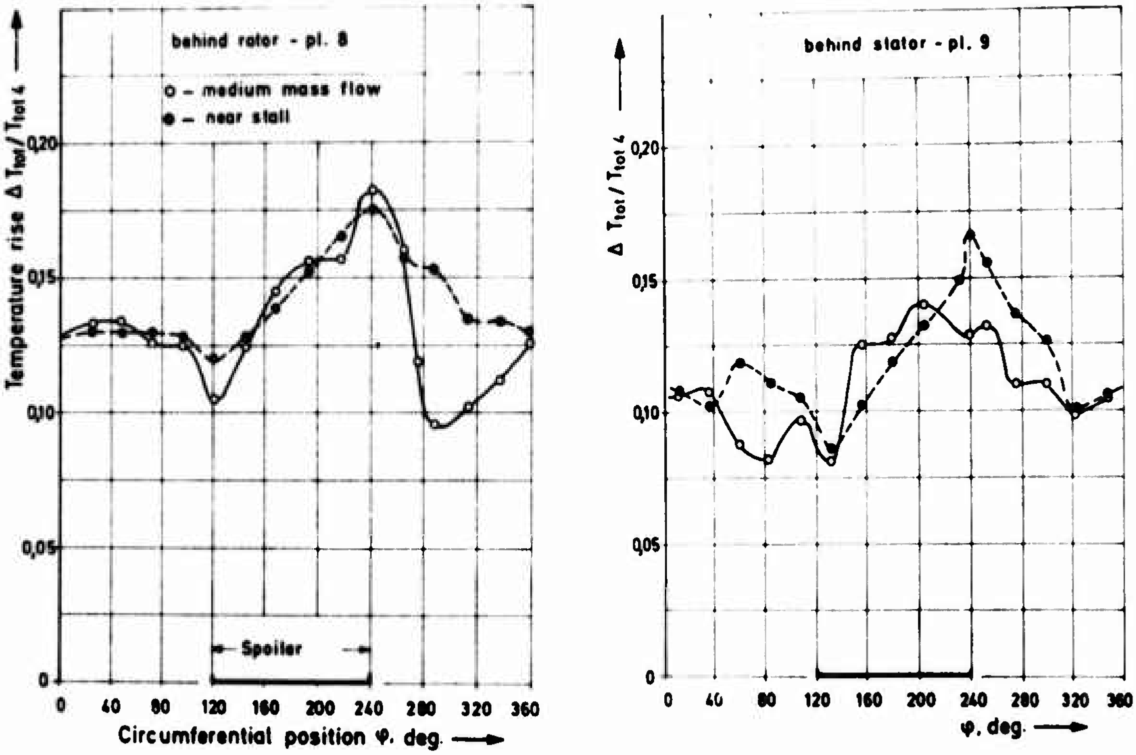

Fig. 11 Circumferential distribution of total temperature rise at midspan (spoiled sectc- are: 120°, screen: 51% open are, 85% design speed)

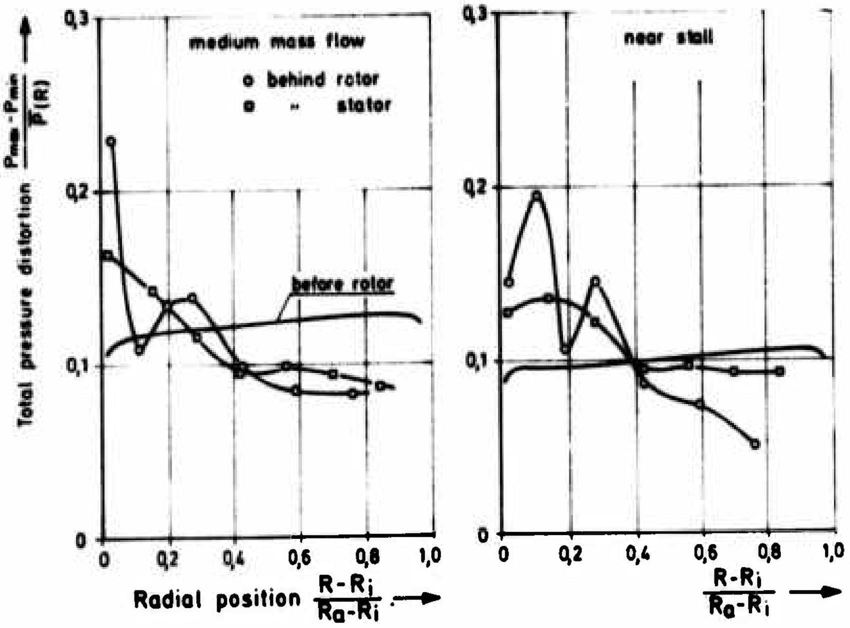

Fig. 12 Radial distribution of distortion(120°sector,51%screen 85% speed)

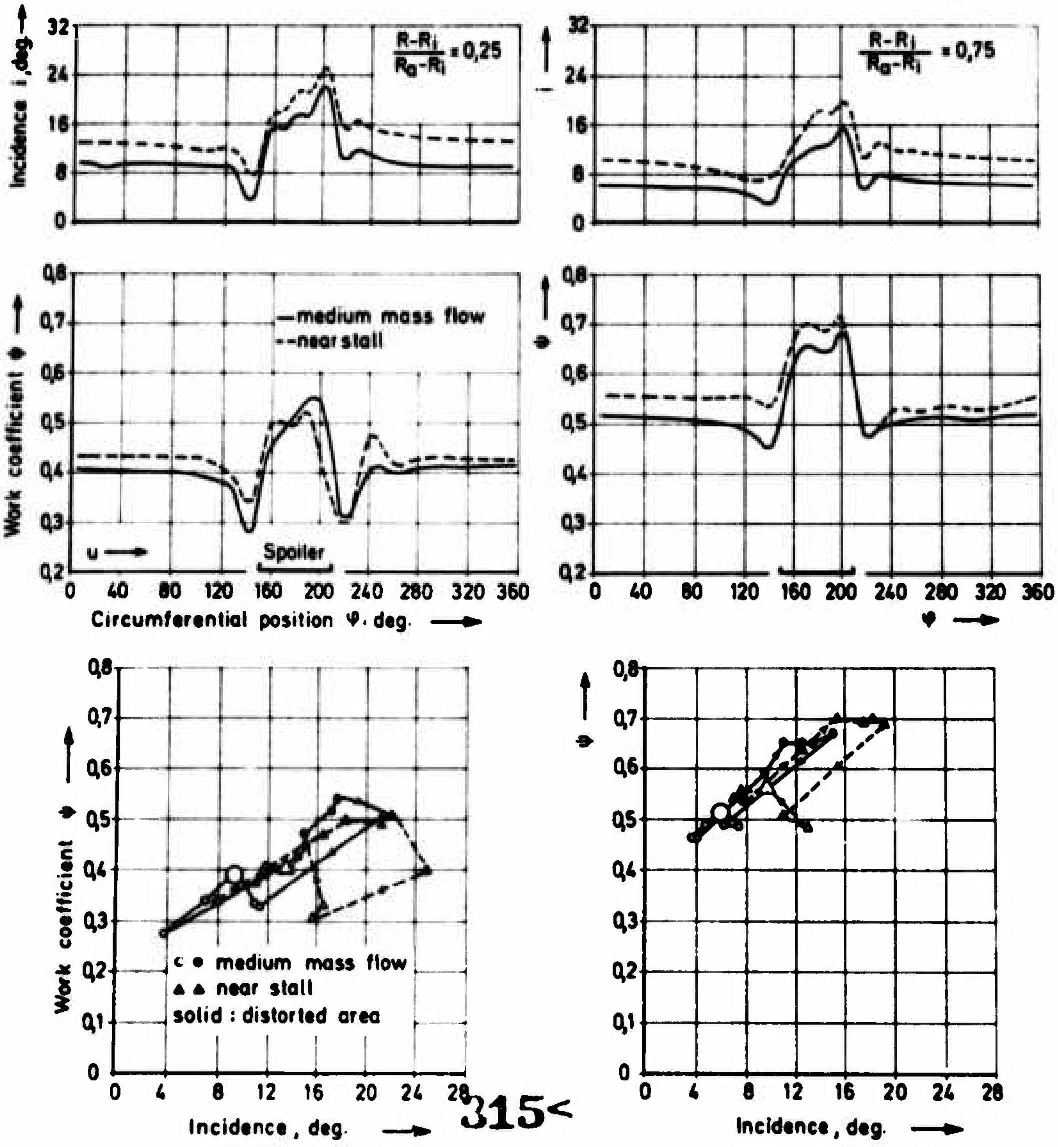

Fig. 13 Dynamic rotor blade response (60°sector,51%screenm85%speed)

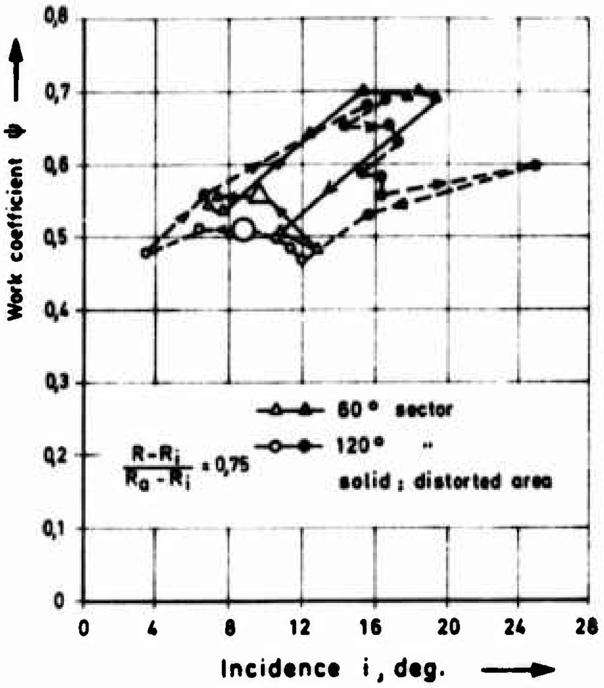

Fig. 14 Dynamic rotor blade response in the tip region near stall (51 % screen, 85 % speed)

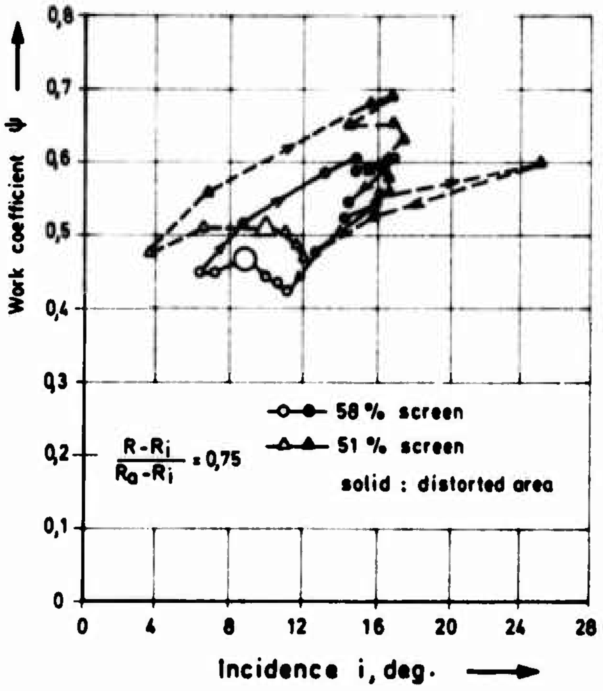

Fig. 15 Dynamic rotor blade response in the tip region near stall (120° sector, 85 % speed)

EXPERIMENTAL INVESTIGATION OF THE PERFORMANCE OF SHORT ANNULAR COMBUSTOR-DUMP DIFFUSERS

A. Klein, K. Katheder and M. Rohlffs

Motoren- und Turbinen-Union München GmbH, Munich

Summary:

Results are presented of an extensive experimental programme which was carried out to determine the losses of short annular combustor-dump-diffuser inlets. Outer to inner flame-tube annulus mass-flow ratio, flame-tube head distance and pre-diffuser opening angle were varied over wide ranges. Tests were run both with and without compressor outlet guide vanes inserted upstream of the inlet. It is found that its wakes cause a substantial rise of losses and also change the geometries which are optimum. Hence entirely wrong conclusions may be drawn from tests were the compressor-wakes are not carefully simulated. Loss coefficients are plotted in such a way that respective optimum configurations are readily obtained.

1. Introduction

Turbojet combustor inlets are designed as diffusers in which the air decelerates from the comparatively high speed behind the compressor to the lower velocity which is required at flame-tube entry in order to avoid unnecessarily high losses, to achieve a short combustion zone and satisfactory ignition conditions. The diffusers of annular combustors divide the air into two main streams that flow along the inner and outer annuli which surround the flame tube, and into a third one of smaller mass rate. The latter enters within the stagnation region of the flame-tube head, where the burners are located. The major portion of the two main streams is fed into the flame tube through its primary and dilution ports and through cooling rings, while a small percentage passes by and serves as cooling medium for the first-stage turbine blades and disc. Conditions are shown schematically in Fig. 1a.

The outer to inner annulus-mass-flow split and hence the respective area ratio, for which the combustor has to be designed, is mainly determined by two conditions. First of all, the primary combustion recirculation zones should be symmetrical with respect to the flame-tube centre line. This requires usually a mass-flow ratio greater than unity. Secondly, the radial temperature profile at the flame tube outlet has to be adjusted to match the requirements of turbine blade and disc cooling. This is achieved by suitably choosing the penetration depths of the inner and outer dilution port jets, and these depend on the annulus-mass-flow ratio. The combustor shown in Fig. 1a is well suited to provide the required air-flow split with low losses, provided it is made long enough. However, this holds only true for one special design condition. The mission of an aircraft includes, however, a large number of various engine working conditions. For them different compressor exit velocity profiles may result, and the dividing lips within the diffusor will become misaligned then with respect to the flow. Therefore separation may occur which produces additional losses, unwanted changes in air-flow split and flow fluctuations, and hence has extremely adverse effects on both combustion and first-stage turbine cooling. In fact intolerable pulsations have sometimes been found to exist in combustors of this type in such a way that the main mass passes alternatively through the outer and inner annuli, respectively. Ehrich (1) proved theoretically that for those branched diffusers indeed such an instability exists under certain conditions. The described flow separation may also occur when the mass-flow ratio is changed during the development of a combustor, e.g. if the turbine cooling concept is altered.

In order to avoid these difficulties, one has developed different kinds of diffusers in recent years. Configurations with a lateral inlet have been successfully investigated by Humenik (2) and Biaglow (3). However, the dump-diffuser concept as sketched in Fig. 1 b seems to be superior, since the required insensitivity with respect to velocity-profile distortions and design changes can be combined with a short length which saves space and weight. Part of the required flow deceleration is achieved in a short pre-diffuser, from which the air is dumped into the adjacent space as a jet which deflects around the flame-tube head. Therefore a second portion of the required diffusion takes place in a flow field that is bounded on one side only by walls. Because of the existence of free streamlines, the flow pattern can adjust itself according to the outer to inner annulus-mass-flow requirements. An especially stable flow will result if one succeeds in producing a stationary vortex by suitably shaping the casing walls (vide Fig. 1 b).

Biaglow (3) tested a two-dimensional model of a combustor-diffuser similar to that of Fig. 1 b. He found that the radial temperature profile at the flame-tube outlet and hence the mass-flow split depend very little on inlet-profile changes. The dump-diffuser concept has hence great advantages over the combustor shown in Fig. 1 a. On the other hand, it produces necessarily higher total pressure losses. They can hardly be theoretically predicted. Therefore an extensive experimental programme was carried out with a simplified short annular dump-diffuser model at the Motoren- und Turbinen-Union München GmbH. Pre-diffuser angle, distance between flame-tube head and pre-diffuser, and annulus-mass-flow ratio were varied over a wide range. Total pressure losses were carefully determined. The main results are reported in this paper.

2. Test Procedure and Data Reduction

The combustor model is sketched in Fig. 2. Important non-dimensional main dimensions are also listed in the figure. The flame tube possessed a hemispherical head. Ports and cooling rings were deleted. Outer to inner annulus area ratio was 1.773, ratio of total annulus area to inlet area 2.135, and outer to inner inlet-diameter ratio 0.911. The pre-diffuser was very short, its length to inlet annulus-height ratio being $l/h_1 = 0.944$ only. Air flow was produced by a compressor, led into a big settling chamber and from there through a smooth contraction into the approach passage which had a length of 22 inlet annulus heights. Flame-tube annulus air-flow split was changed with the help of variable-area orifices at the far downstream end of the annuli. Generally outer to inner annulus-mass-flow-ratios between $0.8 \leq M_o/M_i \leq 2.0$ or 2.5 were investigated. Five different pre-diffusers were tested having included angles $2\Theta = 6^\circ$, 14°, 17°, 21°, and 25°. Flame-tube head distances ranged from $D/h_1 = 0.90$ to 2.50 (definition of D vide Fig.2), in some cases even down to $D/h_1 \approx 0.60$. This wide range of distances has been chosen for two reasons. First of all one wanted of course to establish the dependence of losses on D/h_1. Secondly, the minimum flame-tube head distance that can be accomplished in turbojet combustors depends on the length requirements of the burners used. In this respect $D/h_1 = 0.90$ and 2.50 constitute approximately the lower limits for vaporizers or air spray nozzles, respectively.

In an engine the distance between the diffuser inlet and the exit plane of the compressor is very short. It was felt therefore that the wakes produced by its blades might have an effect on losses because of the velocity profile distortion and/or the turbulence they introduce into the flow. Hence an annular tandem cascade was built which could be inserted in front of the diffuser. It consisted of NACA 65-series blades on circular arc camber lines with 9 % camber and 8 % relative thickness. Mean pitch-chord ratio was 0.565. The arrangement in tandem was necessary in order to retain axial flow direction. Most configurations were tested both with and without the cascade installed, so that the effects of the wakes could be clearly determined. Mass flow rate was measured by an orifice well upstream. During tests without the cascade, radial total pressure distributions were measured for several circumferential positions across the inlet plane 1, the pre-diffuser outlet plane 2 and the outer and inner flame-tube annuli (plane 3, vide Fig. 2). Besides, wall static pressures were recorded in planes 1 and 3 and along the pre-diffusers. "Momentum-weighted" mean values were computed according to the method of Wyatt (4) by fulfilling all the three laws of conservation. From them total pressure losses, referred to inlet dynamic pressure

$$\zeta = \frac{\overline{P}_{t1} - \overline{P}_{t}}{\frac{\overline{\rho}_1}{2}\,\overline{w}_1^{\,2}}$$

were obtained, where the mean velocity $\overline{w}_1$ was determined from mass flow rate M and cross sectional area A_1 by

$$\overline{w}_1 = \frac{M}{\overline{\rho}_1 A_1} .$$

Besides, static pressure recoveries

$$C_{p\ tot} = \frac{\overline{P}_{s3} - \overline{P}_{s1}}{\frac{\overline{\rho}_1}{2}\,\overline{w}_1^{\,2}}$$

were derived from the measured wall pressures by taking the arithmetic mean between the inner and outer values, which differed only slightly. Also the static pressure in plane 2 was determined by extrapolating the pressure distributions along the diffuser walls and taking the arithmetic mean. Thus pressure recovery of the pre-diffuser could be obtained, too.

Diffuser inlet Mach number was $Ma_1 \approx 0.26$ and Reynolds number, based on inlet-annulus height, was $Re_1 \approx 1.0 \cdot 10^5$ throughout the investigation.

During tests with the cascade inserted no measurements were taken in plane 2 due to the existence of the wakes. Also a different procedure was necessary to determine correct mean values in plane 1. To this end a separate experiment was conducted with the combustor detached so that the flow discharged into the ambient air. The total pressure distribution in plane 1 was obtained by carefully traversing the flow over two pitches in 12 radii, and this at two circumferential positions which were displaced by 180° with respect to each other. Momentum-weighted mean values were computed according to Wyatt (4) from which followed, in connection with the pressures recorded in plane 0 (vide Fig. 2), the cascade loss coefficient. This test also provided the ratio of the dynamic pressures in planes 0 and 1. In addition the relationship in plane 0 between the wall and mean total pressures was established. With these informations the total and static pressure mean values in plane 1 could be determined for all the subsequent test runs from the wall pressures alone which were recorded in plane 0.

Fig. 3 shows the diffuser inlet velocity profiles with and without wakes. While the flow was fairly axi-symmetric in the latter case, it was not so in the former. The two radial distributions that were obtained 0.25 chord lengths behind the blades by momentum-weighting circumferentially (vide Fig. 3) have depressions close to the hub and casing due to the secondary flows generated by the cascade. Its presence increases also their blockage factor somewhat. For their arithmetic mean (vide Fig. 3)

$$B_{1\ rad} = 1 - \frac{\bar{\rho}_1\,\bar{w}_1}{\rho_{1\ max}\ w_{1\ max}} = 0.135$$

is obtained, where subscript "max" refers to maximum values, as compared to 0.107 for the naturally developed profile. The true overall blockage factor, however, which includes the circumferential wakes, is substantially larger, viz.

$$B_1 = \frac{1}{A_1}\iint\limits_{(A_1)}\left(1 - \frac{\rho_1}{\rho_{1\ max}}\cdot\frac{w_1}{w_{1\,max}}\right) d\,A_1 = 0.282.$$

The kinetic-energy- and momentum-flux velocity profile parameters

$$\alpha_1 = \frac{1}{A_1}\iint\limits_{(A_1)}\frac{\rho_1}{\bar{\rho}_1}\left(\frac{w_1}{\bar{w}_1}\right)^3 dA_1;\quad \beta_1 = \frac{1}{A_1}\iint\limits_{(A_1)}\frac{\rho_1}{\bar{\rho}_1}\left(\frac{w_1}{\bar{w}_1}\right)^2 dA_1$$

which are also listed in Fig. 3, exhibit a similar increase due to the wakes.

Diffuser performance is known to depend strongly on inlet blockage, vide e.g. Sovran and Klomp (5). For two-dimensional and annular configurations several authors have shown that it deteriorates appreciably if inlet distortions with high blockage are present. This behaviour may hence also be expected for a dump diffuser immediately downstream of a compressor as simulated in the present investigation, since B_1 is found to be very large.

3. Results

As an example for the dependence of loss-coefficients on annulus-mass-flow ratio for different flame-tube head distances, Fig. 4 gives these distributions for the $2\,\Theta = 17^{\circ}$ - pre-diffuser. It is seen from the plot that losses have a minimum at a certain mass-flow ratio. For dump-diffuser flows without wakes its value is about $M_o/M_i = 1.3$, for those with wakes about 1.0. In both cases the minimum depends little only on flame-tube head distance, but as D/h_1 decreases it becomes more pronounced. However, even with rather small flame-tube head distances (D/h_1 = 0.90 and 1.00) losses rise by 15 % to 20 % only as M_o/M_i increases from its minimum value to 2.00, and by just 25 % when M_o/M_i attains 2.50+) . For still smaller flame-tube head distances the change with M_o/M_i becomes more pronounced. Because of the necessity to install the burners it appears unlikely, however, that such small distances could be realized in turbojet engines. The results for the other

---

+) Configurations without wakes were not tested with such large ratios M_o/M_i.

pre-diffuser angles are similar to those of Fig. 4. In addition to the favourably low loss changes with annulus-mass-flow ratio also no fluctuations whatsoever were observed during the tests. These findings mean that dump-diffuser combustor inlets are indeed suitable to cope with a large range of working conditions or design changes. In spite of its shortness, the tested combustor-inlet has losses which, for flows without wakes, exceed those of much longer inlets of the type shown in Fig. 1 a, by 25 % to 30 % only. For the latter $\zeta = 0.30$ to 0.40 is generally taken to be representative (vide Höper (6)). With the compressor blade wakes simulated, however, strikingly high losses are found to exist which are up to about twice as large as those measured with wake-free flow. Even for mass-flow ratios that provide the minimum loss coefficients, values are in the order of $\zeta = 0.65$ as compared to 0.40 without wakes for not too large distances D/h_1.

It appears unlikely that wakes should increase the losses in dump-diffusers only and leave them unaffected in diffusers of the type shown in Fig. 1 a, though the extent of the increase might be different. Since data as those given by Höper (6) have been measured without wakes simulated, one must conclude, that the losses of combustor inlets have generally been underestimated. In this connection one should recall that the cascade-loss coefficient used in the data reduction is a momentum-weighted value. Hence the mixing losses which occur while the wake-type flow is transformed into a uniform profile have been deducted. This is reasonable, because these mixing losses are usually included in the compressor efficiency, so that Fig. 4 represents genuine diffuser loss coefficients. Mass-weighted values would be by at least another 10 % larger.

Fig. 5 presents the dependence of ζ on flame-tube head distance for the 17°-pre-diffuser with fixed mass-flow ratios. For the other angles similar curves were obtained. In case of wake-free flow, losses rise continuously with D/h_1 within the range investigated. This appears to be plausible, because with very large distances D/h_1 the high loss of the sudden expansion to the entire flame-tube casing cross sectional area would result. The curves for flow with wakes, on the other hand, display a minimum at $D/h_1 \approx 1.25$.

They are very similar to those measured by Deich et al. (7), when investigating annular diffusers of turbomachines with a downstream deflector baffle. With these configurations losses started to rise when the baffle distance decreased so much that the cross-sectional area of the two annuli made up by the baffle and the diffuser walls, through which the flow has to pass radially, became smaller than the exit cross-sectional area of the diffuser. A similar phenomenon is to be expected in the present case. It will also happen for flow without wakes, but apparently does so only for D/h_1-values that are smaller than the lowest investigated. The different magnitudes of the values and the behaviour displayed by the curves $\zeta = f\ (D/h_1)$ for flows with and without wakes is confirmed by the static pressure recovery coefficients plotted for $2\ \Theta = 17^\circ$ in Fig. 6+). From their respective distributions for

---

+) For numerical comparisons note that C_p is based on measured static pressures in the entrance plane in one case and on those calculated when momentum-weighting total pressures in the other.

the pre-diffuser alone, which are also given in Fig. 6, follows in addition that with wake-free flow and large D/h_1 nearly the entire static pressure rise takes place in the pre-diffuser. Flow with wakes has very small $C_{p\,tot}$-values, and hence nearly the entire speed reduction between planes 1 and 3 is achieved by losses. Their largest portion seems to occur behind the pre-diffuser, because according to Fig. 7 losses within it amount to 15 up to 25 percent only of the total value (for wake-free flow at least) [+].

Optimum configurations for M_o/M_i = 1.50 can be selected from Fig. 8, where total pressure loss coefficients are plotted versus pre-diffuser angle. It is immediately seen that the wakes not only affect the magnitude of losses but also the geometries for which they are minimum. With wake-free flow losses change gradually and rather little, viz. 7 % at the most, within the range of angles investigated, growing slowly for large values of D/h_1 and decreasing somewhat for small D/h_1. Losses of flow with wakes, on the other hand, have a minimum at $2\Theta \approx 12^\circ$ for any D/h_1. They rise up to 15 % between $2\Theta = 12^\circ$ and 17°. A second minimum is likely to exist for $2\Theta > 25^\circ$. Fig. 9 gives the respective static pressure recoveries. Finally, loss-coefficient distributions vs. 2Θ are presented in Fig. 10 for M_o/M_i = 1.00 and 2.00 and various D/h_1 and in Fig. 11 for D/h_1 = 0.89 and 2.50 with M_o/M_i as the parameter. The same trends are found as in Fig. 8.

4. Conclusions

In the present investigation the total pressure losses of a short annular dump-diffuser combustor inlet have been determined for various values of relevant geometric and aerodynamic parameters. Optimum configurations providing minimum losses have been obtained. The results also suggest that compressor-wake simulation is absolutely necessary when testing the flow in combustor inlets. The compressor-blading introduces viz. distortions which increase losses considerably. They also change the distributions of the losses with outer to inner annulus-mass-flow ratio, with flame-tube head distance and with pre-diffuser opening angle of dump-diffuser inlets. Two main reasons are suggested to explain this behvaiour. First of all it is obvious that wakes become more pronounced as they trail down the pre-diffusor. Hence the distortions which leave at its exit will be larger than those at its entry. It is quite likely then that the wakes may be retarded to an extent where backflow is created locally. This kind of "internal stall" was e.g. described by Wolf and Johnston (8). Secondly, it is known that secondary flows with additional losses are created if directional changes are enforced on shear-flows, vide e.g. Hawthorne (9). The non-uniformities produced by the compressor blading are a shear-type flow. While they are deflected by the presence of the flame-tube head, secondary flows are therefore likely to be generated in a similar way as those found in the wakes of stators in turbomachines. This would also explain the loss-rise with decreasing flame tube head distance displayed by Fig. 5. In spite of these explanations, the phenomenon is, however, not understood in detail.

[+] Note when comparing the curves of Fig. 7 with those of $C_{p\,Diff}$ in Fig. 6 that the latter are the less reliable the smaller D/h_1. They are viz. based on the arithmetic mean of the inner and outer wall static pressures which becomes less representative the more the cross sectional static pressure distribution departs from a constant value as D/h_1 decreases.

List of References

1. Ehrich, F.F. Aerodynamic Stability of Branched Diffusers. ASME-Paper 70-GT-27, 1970.

2. Humenik, F.M. Performance of Short Length Turbojet Combustor Insensitive to Radial Distortion of Inlet Airflow. NASA TN D-5570, 1970.

3. Biaglow, J.A. Effect of Various Diffuser Designs on the Performance of an Experimental Turbojet Combustor Insensitive to Radial Distortion of Inlet Airflow. NASA TM X-2216, 1971.

4. De Wyatt, M.D. Analysis of Errors Introduced by Several Methods of Weighting Nonuniform Duct Flows. NACA T.N. 3400, 1955.

5. Sovran, G. and Klomp, E.D. Experimentally Determined Optimum Geometries for Rectilinear Diffusers with Rectangular, Conical or Annular Cross-Section. Fluid Mechanics of Internal Flow (Ed.: G. Sovran), pp. 271 - 312. Elsevier Publishing Company, Amsterdam-London-New-York, 1967.

6. Höper, H.J. Neuere Gesichtspunkte für die Auslegung von Brennkammern in Luftstrahltriebwerken. Luftfahrtechnik-Raumfahrttechnik, Vol. 16, pp. 143 - 150 and 191 - 194, June/July 1970.

7. Deich, M.E., Zaryankin, A.E. and Zatsepkin, M.F. Results of Testing Turbomachine Exhaust Ducts with Ring Diffusers. Teploenergetika, Vol. 12, pp. 40 - 44, May 1965. English Translation: Thermal Engineering, Vol. 11, pp. 46 - 50, May 1965.

8. Wolf, S. and Johnston, J.P. Effects of Nonuniform Inlet Velocity Profiles on Flow Regimes and Performance in Two-Dimensional Diffusers. Trans. ASME, Vol. 91, Series D (Journal of Basic Engineering), pp. 462 - 473, July 1969.

9. Hawthorne, W.R. The Applicability of Secondary Flow Analyses to the Solution of Internal Flow Problems. Fluid Mechanics of Internal Flow (Ed.: G. Sovran), pp. 238 - 265. Elsevier Publishing Company, Amsterdam-London-New York, 1967.

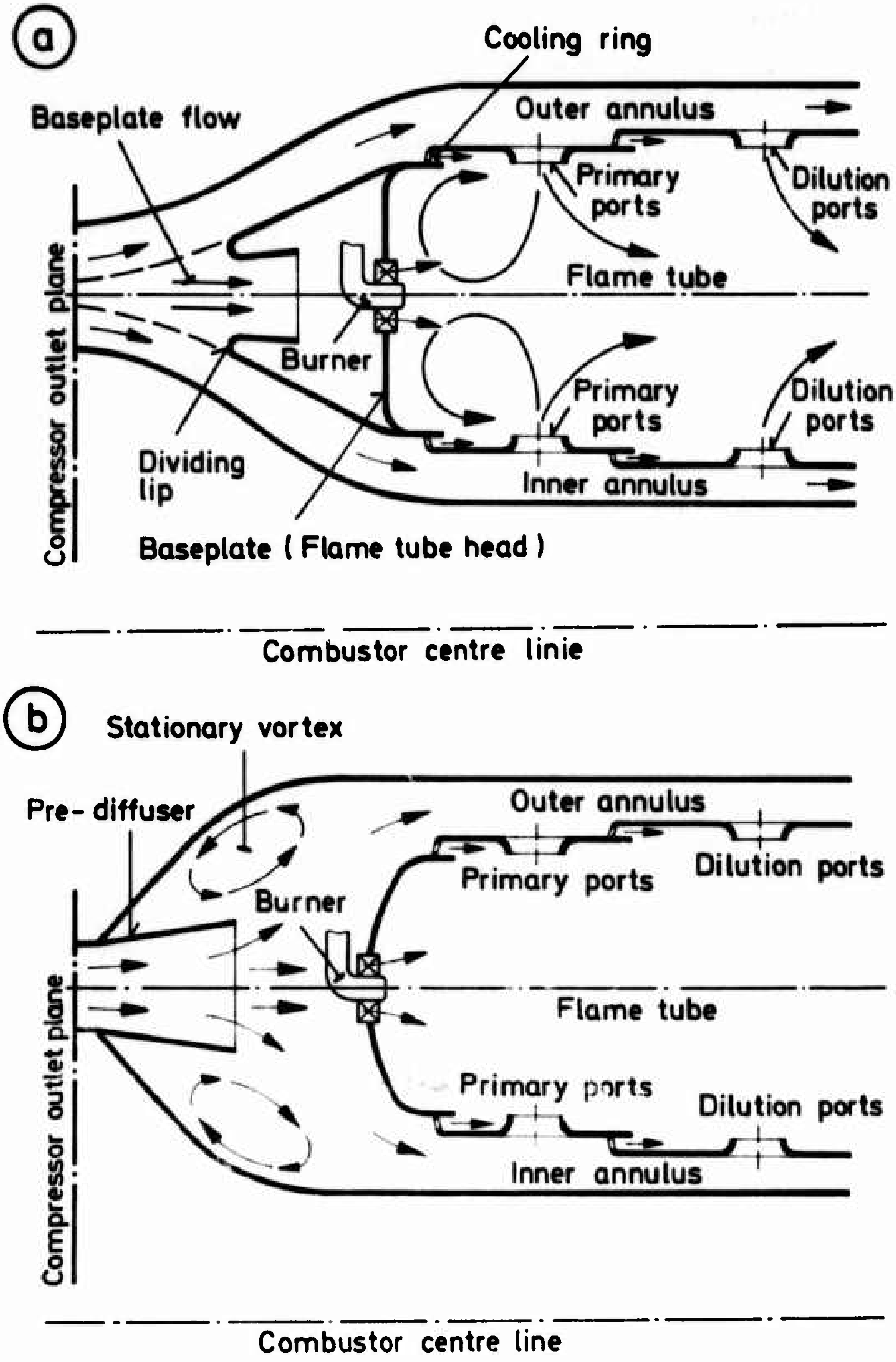
a
Cooling ring
Baseplate flow
Outer annulus
Primary ports
Dilution ports
Flame tube
Burner
Primary ports
Dilution ports
Dividing lip
Inner annulus
Baseplate (Flame tube head)
Compressor outlet plane
Combustor centre linie
b
Stationary vortex
Pre- diffuser
Outer annulus
Primary ports
Dilution ports
Burner
Flame tube
Primary ports
Dilution ports
Inner annulus
Compressor outlet plane
Combustor centre line

Fig. 1: Two different types of turbojet-combustor inlets
a) Conventional type
b) Dump-diffuser type

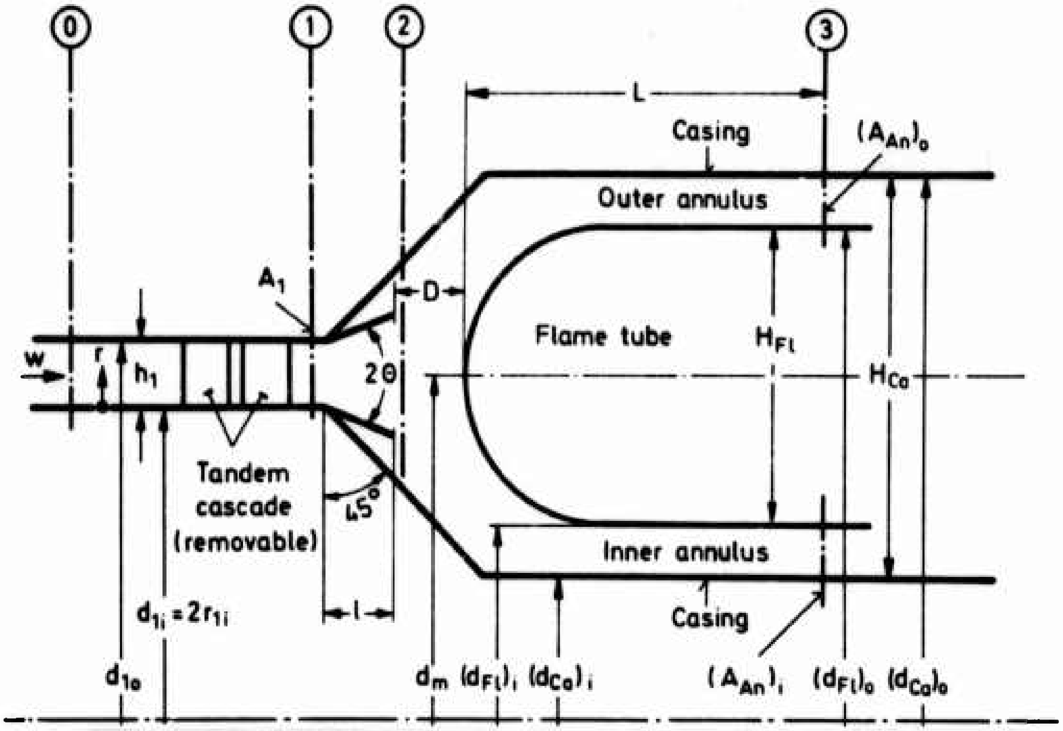
⓪
①
②
③
L
Casing
$(A_{An})_o$
Outer annulus
A_1
D
Flame tube
H_{Fl}
H_{Ca}
w
r
h_1
2θ
Tandem cascade (removable)
45°
Inner annulus
l
Casing
$d_{1i} = 2r_{1i}$
d_{1o}
d_m
$(d_{Fl})_i$
$(d_{Ca})_i$
$(A_{An})_i$
$(d_{Fl})_o$
$(d_{Ca})_o$

$\frac{l}{h_1}$	$\frac{d_{1i}}{d_{1o}}$	$\frac{2h_1}{d_m}$	$\frac{(d_{Fl})_o}{d_m}$	$\left(\frac{d_{Fl}}{d_{Ca}}\right)_o$	$\left(\frac{d_{Fl}}{d_{Ca}}\right)_i$	$\frac{2H_{Fl}}{d_m}$	$\frac{H_{Fl}}{H_{Ca}}$	$\frac{L}{H_{Fl}}$	$\frac{(A_{An})_o}{(A_{An})_i}$	$\frac{(A_{An})_o}{A_1}$	$\frac{(A_{An})_i}{A_1}$	$\frac{(A_{An})_o+(A_{An})_i}{A_1}$
0.944	0.911	0.094	1.245	0.928	1.160	0.490	0.707	1.50	1.773	1.353	0.773	2.135

Fig. 2: Dump-diffuser combustor-inlet test model

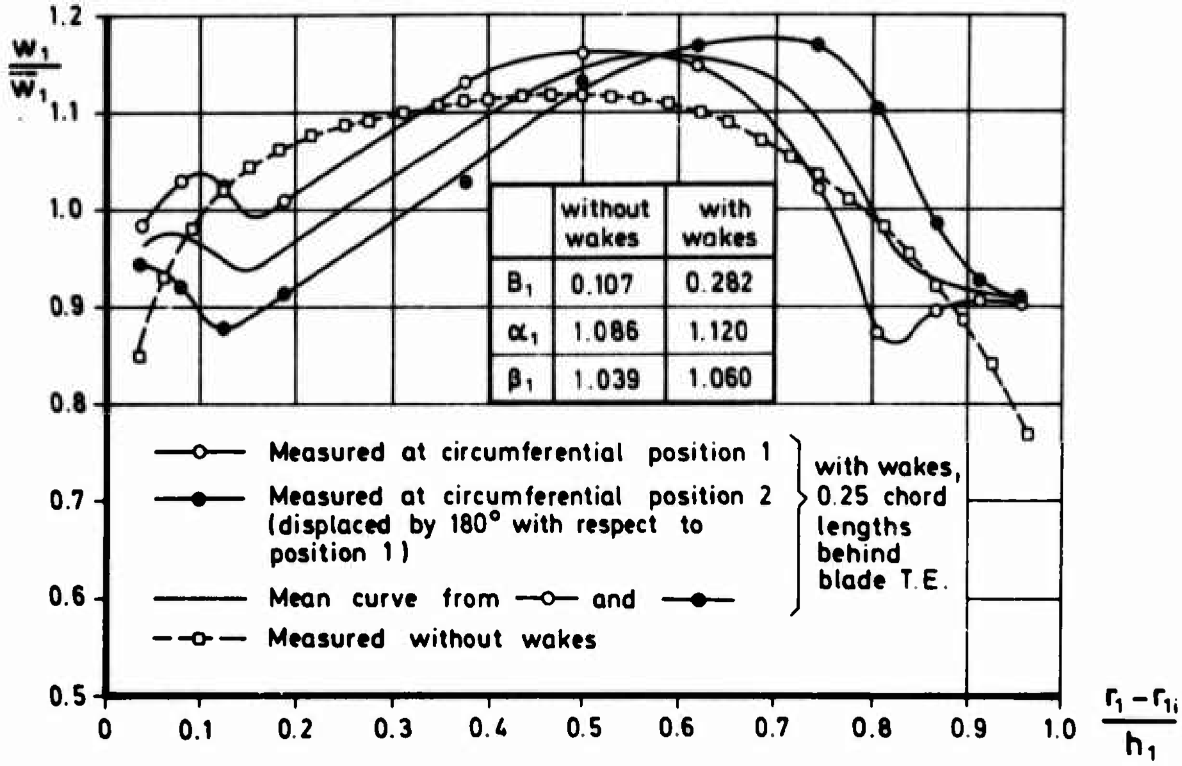

	without wakes	with wakes
B_1	0.107	0.282
α_1	1.086	1.120
β_1	1.039	1.060

Fig. 3: Measured inlet-velocity profiles

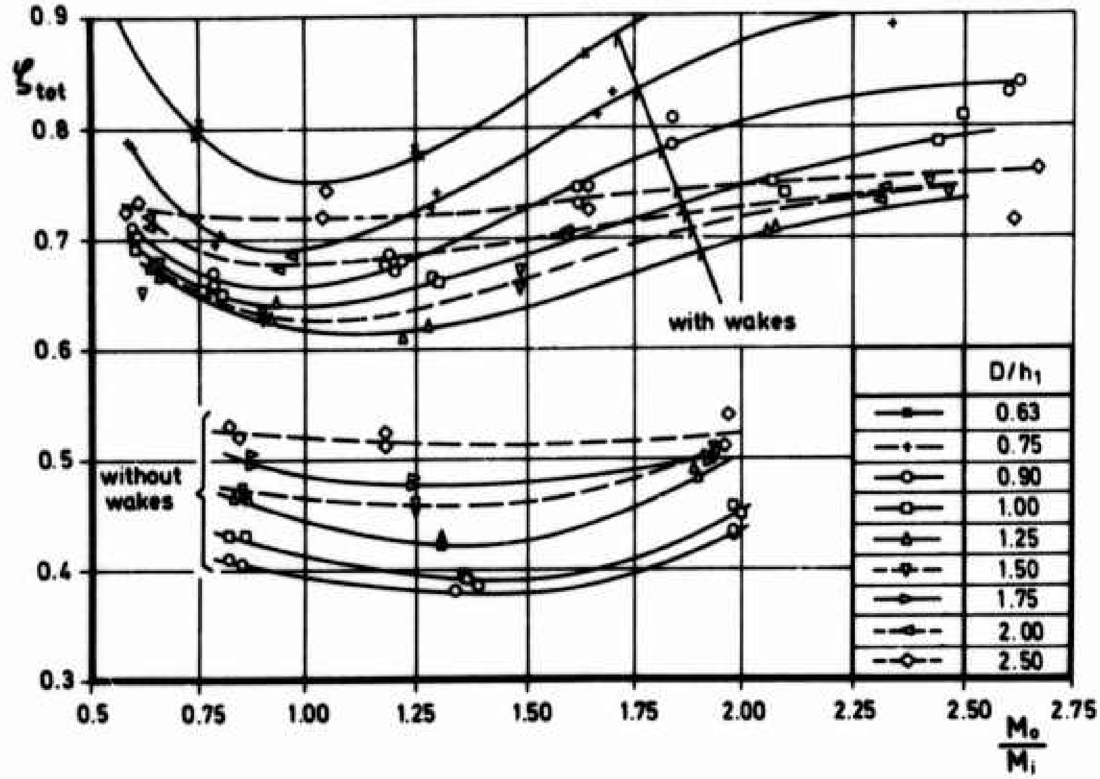

Fig. 4: Dependence of loss coefficient on outer to inner flame-tube annulus-mass flow ratio (17°- pre-diffuser)

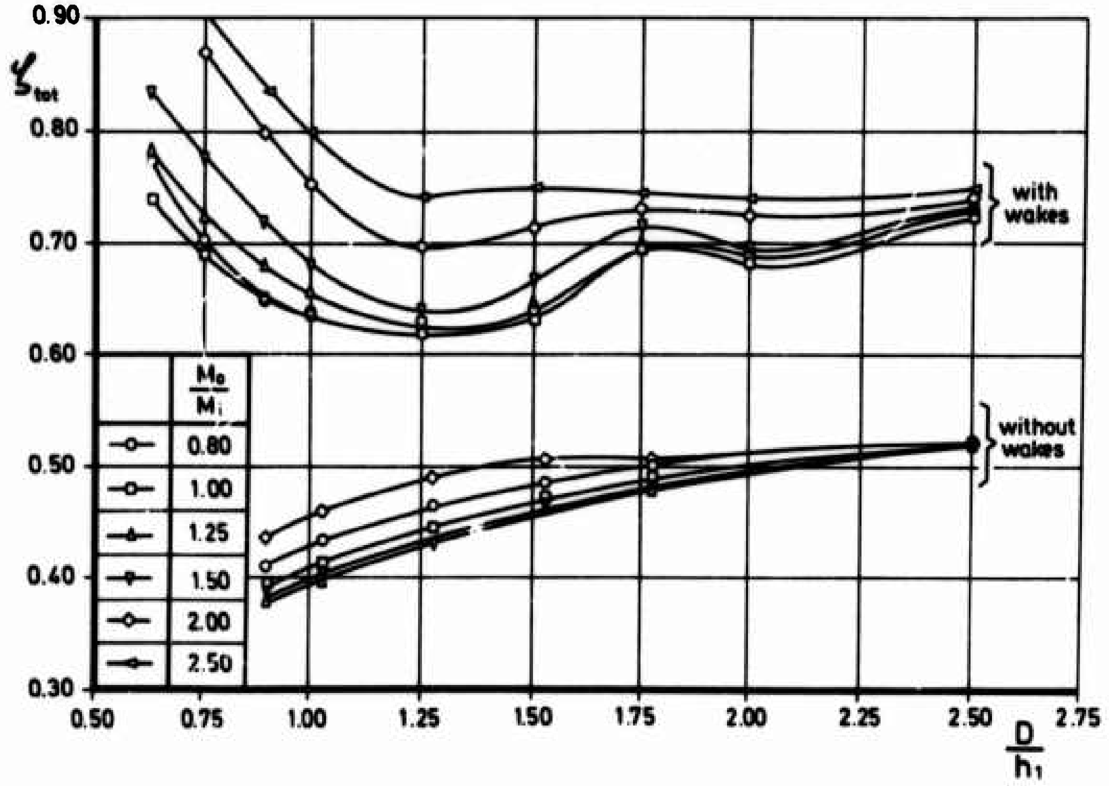

Fig. 5: Dependence of loss coefficient on non-dimensional flame-tube head distance (17°-pre-diffuser)

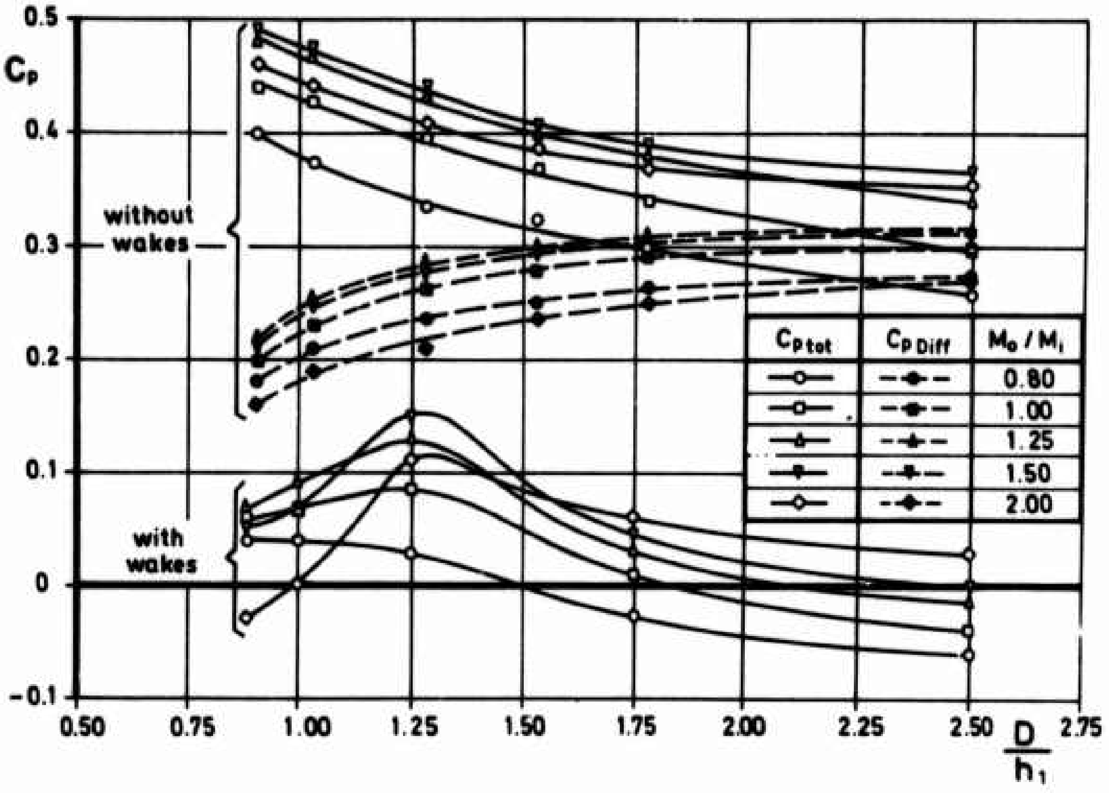

Fig. 6: Static pressure rise coefficient vs. non-dimensional flame-tube head distance (17°-pre-diffuser)

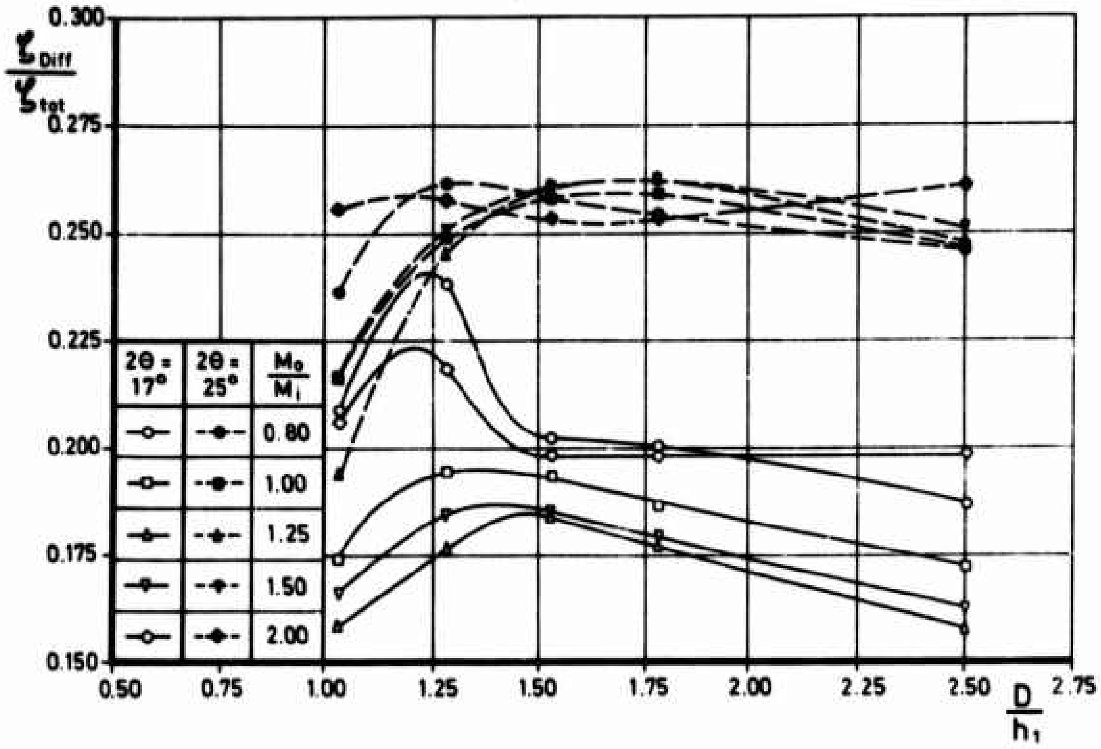

Fig. 7: Pre-diffuser to total loss-coefficient ratio vs. non-dimensional flame-tube head distance (17°- and 25°- pre-diffusers)

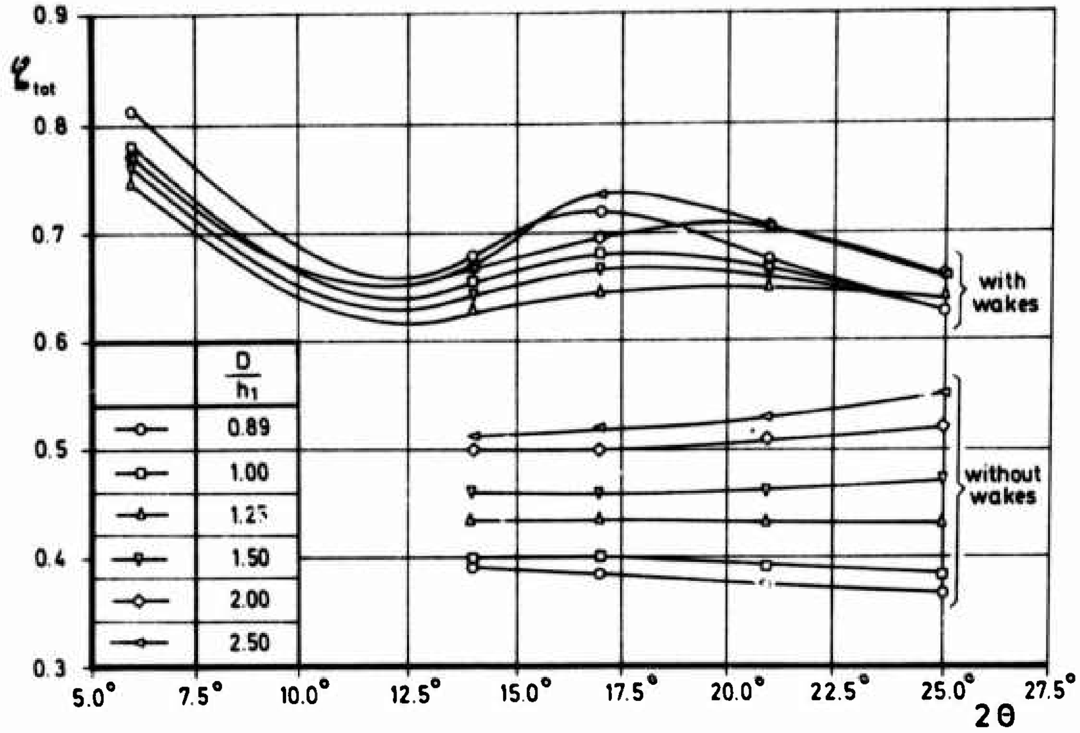

Fig. 8: Variation of loss coefficient with pre-diffuser angle for outer to inner flame-tube annulus mass-flow ratio $M_o/M_1 = 1.50$

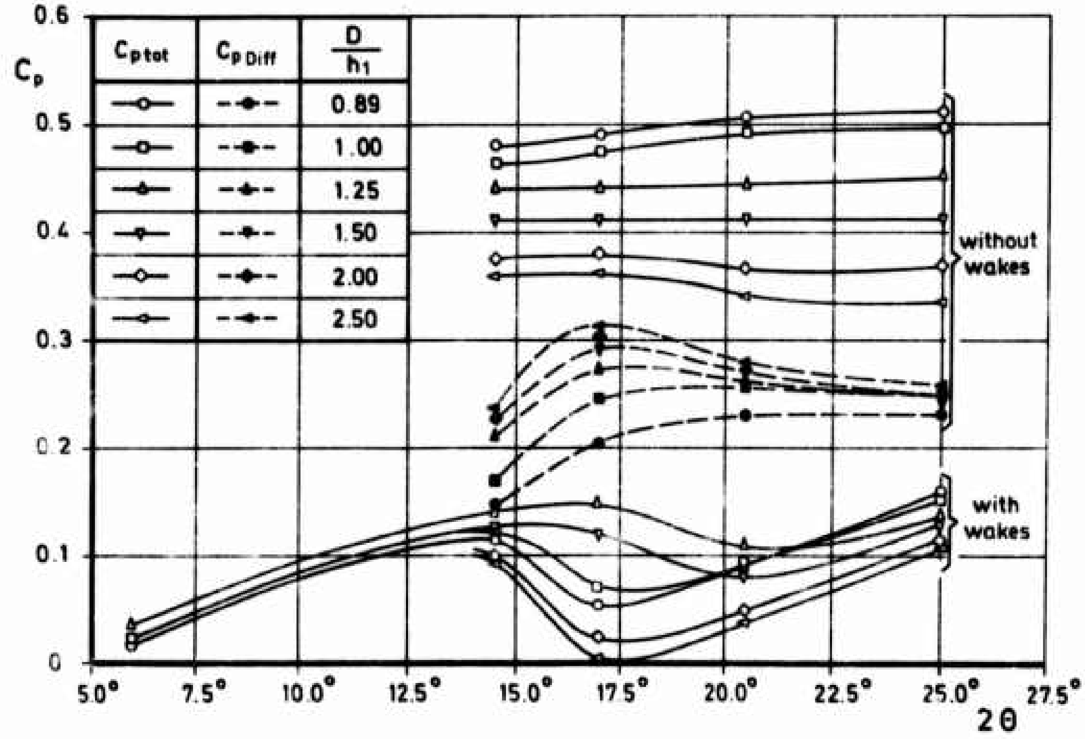

Fig. 9: Variation of static pressure rise coefficient with pre-diffuser angle for $M_o/M_i = 1.50$

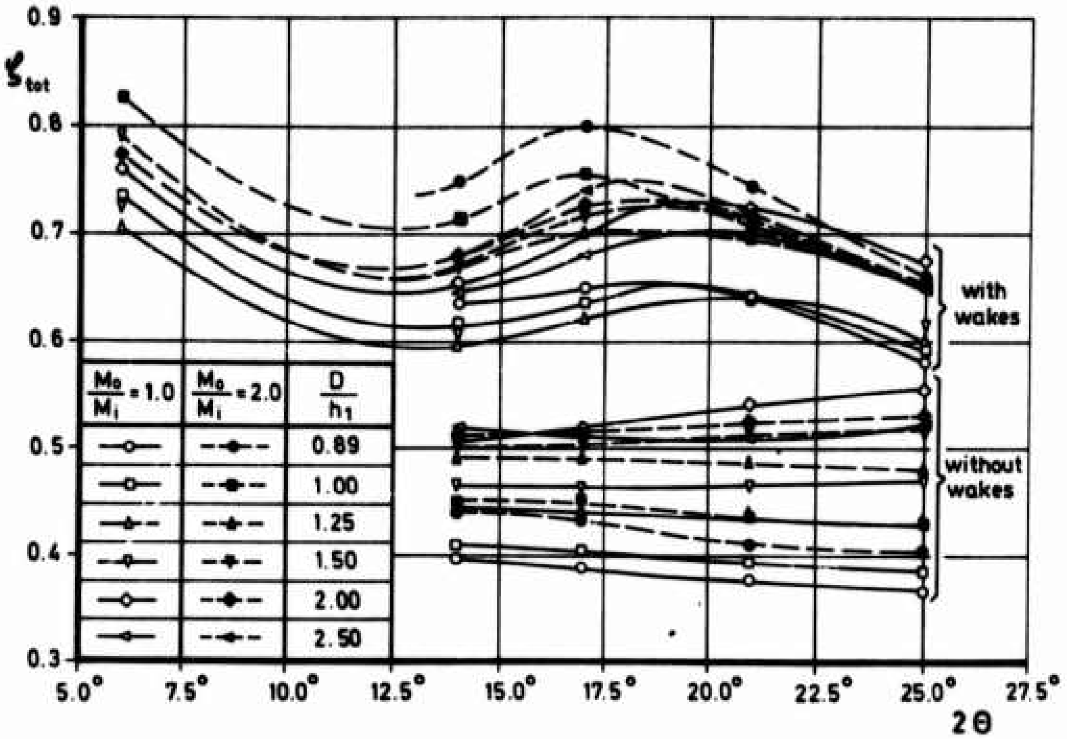

Fig. 10: Variation of loss coefficient with pre-diffuser angle for M_o/M_1= 1.00 and 2.00.

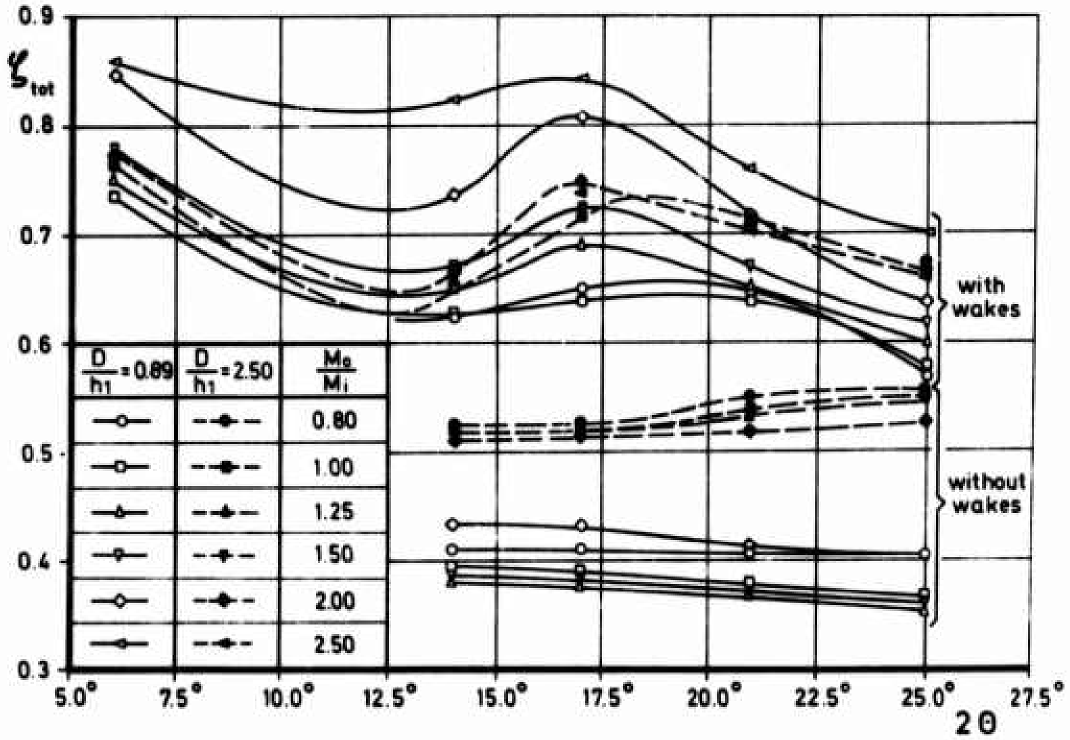

Fig. 11: Variation of loss coefficient with pre-diffuser angle for non-dimensional flame-tube head distances D/h_1 = 0.89 and 2.50

DYNAMIC FLOW DISTORTION IN SUBSONIC AIR INLETS

J. R. Jones and W. M. Douglass, Douglas Aircraft Company, USA

SUMMARY

Subsonic-transport engine-air-inlets were tested in a wind tunnel to measure performance during static operation with cross wind. The models were instrumented so that fluctuating pressure could be measured in addition to steady-state pressures. The principal instrumentation consisted of 36 fluctuating and steady-state total-pressure probes at the end of the inlet.

It was determined that fluctuating pressure data are necessary to detect inlet boundary-layer separations when the separations were intermittent. Also, comparison of steady-state and time-dependent "instantaneous" total-pressure distributions at the end of the inlet showed that the maximum total-pressure losses were two to four times as large as those indicated by the steady-state data, and that the maximum extent of the low total-pressure regions was much larger than that indicated by the steady-state data.

Spectral analysis of the total-pressure fluctuations showed that inlet separation resulted in large fluctuations at low frequencies. Inlet separation was not characterized by high fluctuating-pressure energy levels at any one particular frequency.

INTRODUCTION

Past practice to establish compatibility between an airplane's air inlet and a turbojet or turbofan engine has been to follow a procedure of separate tests of the two components. Inlet distortion was measured in wind-tunnel tests with instrumentation that had slow response capability, that is, the total head probes measured a time averaged or "steady state" pressure. Compatibility of this measured flow with the engine was then demonstrated by simulating the inlet flow with appropriately configured screens that produced an equivalent total pressure distribution.

The concept of component testing is not questioned. Component testing, with proper interpretation, is considered to be most useful. Rather the purpose of this paper is to identify a better description of the inlet flow, in this case for an inlet of a subsonic transport, and to describe a wind-tunnel test and test instrumentation that is appropriate to measure the inlet flow. As will be evident, flow in a subsonic inlet is far from steady and requires appropriate tests and instrumentation to acquire meaningful results.

DISCUSSIONS

The design of an inlet for a subsonic transport is a relatively easy task when compared to that of an inlet for a supersonic airplane or some of the long and contorted inlets of military aircraft. The subsonic-transport air-inlet considered here is the short, nearly axisymmetric inlet of a pod mounted, wing engine.

For the normal range of operation, the inlet provides an airflow with a uniform velocity to the engine. The only flow distortion is an inconsequential boundary layer at the duct perimeter. This uniformity of flow is assured by giving the inlet lip sufficient thickness to maintain attached flow when the airplane is operating at the two conditions where the inlet flow is most likely to separate. These operating conditions are at takeoff when the airplane is at a high angle of attack, and when the airplane is operating on the ground with a crosswind.

Increasing the thickness of the inlet lip reduces the adverse pressure gradients that the inlet boundary layer must traverse. This reduces the tendency for the boundary layer flow to separate and as a consequence extends the region that the airplane can operate without subjecting the engine to an inlet flow distortion. There is, however, a limit to the amount of lip thickness that is prudent for an inlet design because of other considerations. One such consideration is cruise drag. For this reason, the engines of subsonic transport will, at times, be subjected to the flow distortion that results when the boundary layer separates at the inlet lip. Infrequent as this may be, it is important to correctly determine the flow distortion because a consequence of excessive distortion is engine compressor stall or flame-out which in turn affects safety of flight and engine integrity.

Albeit that flow separation has always been known to be an unsteady phenomenon and it is recognized that inlet flow distortion is most frequently a result of flow separation, inlet flow is usually measured with pressure instrumentation incapable of responding to the rapidly varying flow. The error of this method of measuring inlet flow was forcefully demonstrated a few years ago when it was found for some supersonic airplanes that both the inlet flow and the engine's response to that flow had to be considered as dynamic (unsteady) if inlet-engine compatibility were to be achieved. The lesson learned from the supersonic inlet problem suggested that the flow in a subsonic inlet should also be treated as dynamic.

The opportunity to examine the dynamic flow within a subsonic inlet came with the development of the DC-10. The wind-tunnel tests of the air inlet, the special instrumentation, the analysis of the data, and results of the investigation are described in this paper.

DESCRIPTION OF APPARATUS

Test Method

The tests were conducted at the McDonnell-Douglas Aerophysics Laboratory, El Segundo, California. The blowdown wind tunnel with a test section measuring 4 by 4 feet was used. Figure 1 is a schematic diagram of the wind tunnel, the inlet model, and the ducting behind the inlet.

For the crosswind tests, the inlet model and the ducting were installed in the test section through a window blank. The included angle between the inlet centerline and the tunnel centerline was 90 degrees. The main wind-tunnel duct was blocked off at the wind-tunnel supersonic-diffuser throat in such a way that all tunnel flow that did not enter the inlet passed out of the tunnel through the porous walls of the transonic test section installed between the model and the tunnel-diffuser throat. Crosswind speed was controlled by varying the amount of flow allowed to pass through the porous walls with the butterfly valves in the transonic section.

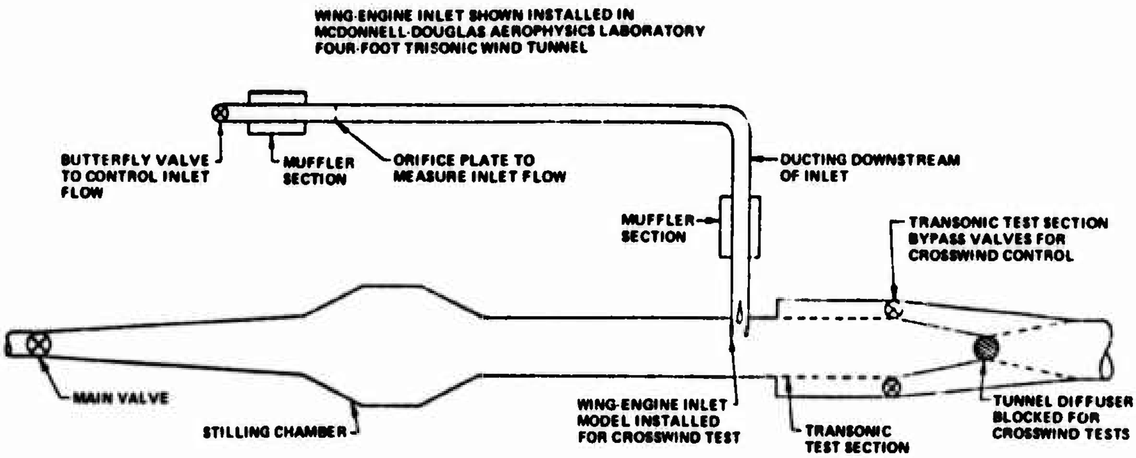
WING-ENGINE INLET SHOWN INSTALLED IN
MCDONNELL-DOUGLAS AEROPHYSICS LABORATORY
FOUR-FOOT TRISONIC WIND TUNNEL
BUTTERFLY VALVE TO CONTROL INLET FLOW
MUFFLER SECTION
ORIFICE PLATE TO MEASURE INLET FLOW
DUCTING DOWNSTREAM OF INLET
MUFFLER SECTION
TRANSONIC TEST SECTION BYPASS VALVES FOR CROSSWIND CONTROL
MAIN VALVE
STILLING CHAMBER
WING-ENGINE INLET MODEL INSTALLED FOR CROSSWIND TEST
TRANSONIC TEST SECTION
TUNNEL DIFFUSER BLOCKED FOR CROSSWIND TESTS

FIGURE 1. SCHEMATIC DIAGRAM OF TEST APPARATUS

The inlet flow was ducted out of the wind tunnel and exhausted into the atmosphere. The wind-tunnel total pressure was between 36 psia and 72 psia, which allowed the inlet mass-flow rate to be controlled by the butterfly valve at the end of the ducting. Just upstream of the butterfly valve was an orifice plate for measuring inlet mass-flow rate. Most of the testing was done at a tunnel total pressure of 36 psia, at which the Reynolds number was approximately 25 percent of full-scale DC-10 inlet Reynolds number.

Pressure Instrumentation

The fluctuating-pressure transducers were located at 1 static-pressure and 1 total-pressure port in the wind-tunnel test section upstream of the model, at 2 static-pressure ports in the ducting downstream of the model, at 6 static-pressure ports on the inlet duct wall at the end of the inlet, at several wall ports upstream of the end of the inlet, at 36 total-pressure ports at the end of the inlet. Steady-state measurements were made with pressure ports adjacent to the fluctuating-pressure transducer ports (except for steady-state pitot measurements in the free-stream) and at additional locations on the inlet duct wall upstream of the end of the inlet. The location of the instrumentation at the end of the inlet is shown in Figure 2.

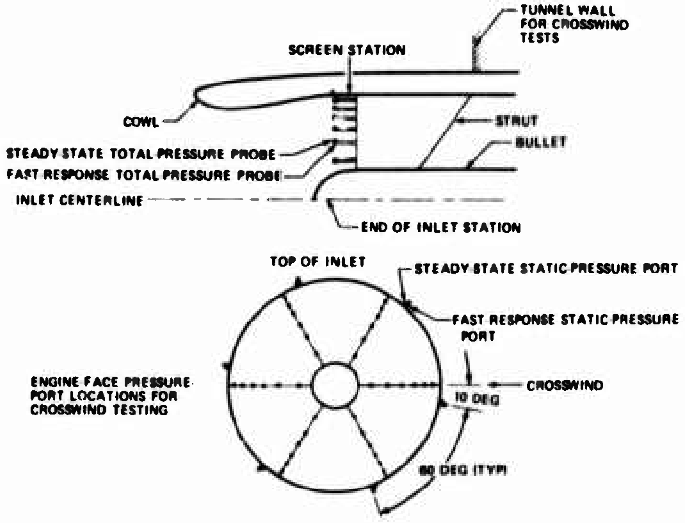
TUNNEL WALL FOR CROSSWIND TESTS
SCREEN STATION
COWL
STRUT
BULLET
STEADY STATE TOTAL PRESSURE PROBE
FAST RESPONSE TOTAL PRESSURE PROBE
INLET CENTERLINE
END OF INLET STATION
TOP OF INLET
STEADY STATE STATIC PRESSURE PORT
FAST RESPONSE STATIC PRESSURE PORT
CROSSWIND
10 DEG
ENGINE FACE PRESSURE PORT LOCATIONS FOR CROSSWIND TESTING
60 DEG (TYP)

FIGURE 2. WING-ENGINE INLET WITH INSTRUMENTATION AT END OF INLET

Fluctuating-Pressure Measurements

Fluctuating pressures in the inlet were measured by the system shown schematically in Figure 3. The fluctuating-pressure transducers were flush-mounted for static-pressure measurements and mounted in the nose of the probe for total-pressure measurements. This arrangement eliminated errors in the measurements caused by finite tube lengths between the pressure transducer and the point where the pressure was to be measured.

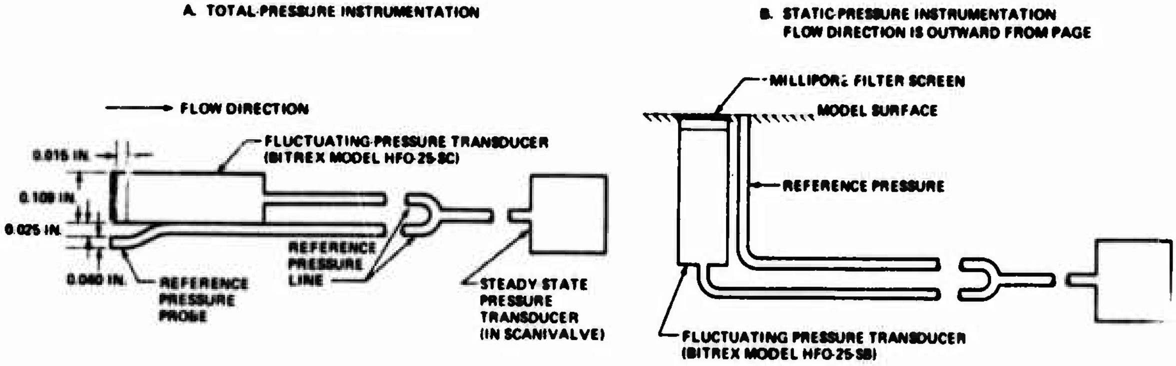
A. TOTAL-PRESSURE INSTRUMENTATION
FLOW DIRECTION
FLUCTUATING-PRESSURE TRANSDUCER (BITREX MODEL HFO-25-SC)
0.015 IN.
0.109 IN.
0.025 IN.
0.060 IN.
REFERENCE PRESSURE PROBE
REFERENCE PRESSURE LINE
STEADY STATE PRESSURE TRANSDUCER (IN SCANIVALVE)
B. STATIC-PRESSURE INSTRUMENTATION
FLOW DIRECTION IS OUTWARD FROM PAGE
MILLIPORE FILTER SCREEN
MODEL SURFACE
REFERENCE PRESSURE
FLUCTUATING PRESSURE TRANSDUCER (BITREX MODEL HFO-25-SB)

FIGURE 3. FLUCTUATING-PRESSURE INSTRUMENTATION

The transducers were Bytrex HFO-25-SC semiconductor strain gage transducers. The dynamic sensitivities of the transducers (volts/psi) were determined by experiment and found to be constant for frequencies between 30 and 3000 Hz. The measured amplitudes of pressures with frequencies below 30 Hz were too low by roughly 5 percent, because of variable transducer sensitivity in this range.

The fluctuating-pressure transducer output was recorded on magnetic tape by the VIDAR High-Frequency Data Acquisition System and a CEC VR 3700 tape recorder described in Reference 1. The fluctuating-pressure transducer signal was filtered by low-pass and high-pass filters before being recorded. The purpose of the low-pass filter is described in later paragraphs. The high-pass filter attenuated frequencies below 0.6 Hz. The high-pass filter modified the transducer output, so that only the fluctuating pressure component would be recorded on tape. The actual time varient pressure was calculated by adding the steady-state pressure component, measured at the adjacent steady-state pressure port, to the fluctuating pressure component measured by the Bytrex transducer.

TEST PROGRAM

The inlet Mach number was varied between approximately 0.20 and 0.85. Crosswind speeds were varied from about 15 to 60 knots. Most of the test was conducted at a free-stream total pressure of 36 psia, which corresponded to 25 percent of full-scale DC-10 inlet Reynolds number at sea-level standard-day conditions. Comparison with data taken at higher Reynolds numbers showed only slight Reynolds number effects.

DATA REDUCTION

The steady-state reduced data included crosswind speed, inlet-throat Mach number, full-scale engine airflow corresponding to the inlet Mach number and inlet total-pressure recovery, total-pressure ratios for each of the total-pressure probes at the end of the inlet, pressure coefficients for duct-wall static-pressure ports, area-average total-pressure recovery, and inlet distortion parameters. The inlet distortion parameters were (1) distortion number $(P_{T_{max}} - P_{T_{min}})/P_{T_2}$; (2) Pratt and Whitney circumferential distortion index; (3) Pratt and Whitney radial distortion index; and (4) Pratt and Whitney total distortion index.

The McAir Analog Computing Editor System used the steady-state pressures and the output from the fluctuating-pressure transducers for the 36 total-pressure probes at the end of the inlet to compute the variation in the distortion parameters with time. The fluctuating-pressure data were taken after the steady-state data had been acquired which allowed the distortion parameters to be computed during the run.

The Analog Computing Editor System was an important aid in on-site monitoring of the test results. The output from the Analog Computing Editor System was displayed on an oscillograph and recorded on magnetic tape by an Ampex FR 1300 tape recorder. Also, the maximum value of each distortion parameter obtained at each test condition was recorded and displayed by the Editor System at the conclusion of each run.

The Editor System was equipped with peak detectors that "marked" the VIDAR tape at the occurrence of maximum distortion at each test condition. This was done so that the instantaneous total-pressure distributions that resulted in maximum Pratt and Whitney distortion index and maximum $(PT_{max} - PT_{min})/PT_2$ could be computed later from digitized data without requiring digitization of the entire run.

The fluctuating total-pressure data recorded on the VIDAR tape were converted into digital format and combined with the steady-state data to enable the instantaneous total-pressure distributions at the end of the inlet to be determined. Distortion indexes as a function of time and standard deviations were also computed from the digital data. The data were digitized for a 0.1-second segment of selected runs. The segment began 0.05 second before the occurrence of maximum distortion as computed by the analog computer.

The distortion indexes computed by the analog computer and the distortion indexes, total-pressure distributions, and standard deviations computed from the digitized data were calculated after filtering the recorded data. The filtering reduced the amplitude of pressure fluctuations with frequencies greater than 1000 Hz. A limited amount of data was reduced by using a 3500 Hz filter. There were two reasons for filtering the data so that frequencies greater than 1000 Hz would be attenuated.

The primary reason was that experimental data (Reference 2) have shown that the occurrence of compressor surge can depend on total-pressure distortion at the engine face due to inlet total-pressure fluctuations. However, the compressor is sensitive only to pressure fluctuations with frequencies below a certain "critical" frequency. The critical frequency probably depends on the specific configuration of the fan or compressor, but was roughly equal to the compressor rotational speed for the case considered in Reference 2, or f_{crit} (Hz) = ω (rps). For the subject test, a more conservative value of critical frequency, $f_{crit} = 2\omega$ was assumed. For the DC-10 engines at takeoff power, twice the fan and low-pressure compressor speed was $2\omega = 100$ rps approximately, or $f_{crit} = 100$ Hz.

The equivalent scale-model critical frequency was determined by using the Strouhal number. Data presented in Reference 3 show that the scale-model power-spectral-density function and the full-scale power-spectral-density function are equivalent if expressed in terms of Strouhal number instead of frequency, as shown in the sketch below.

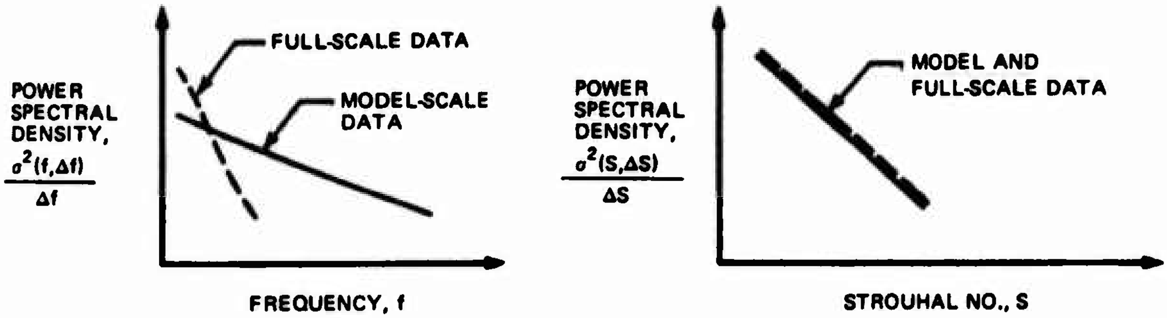

A critical frequency of 1000 Hz for the 10-percent-scale model is equivalent to a full-scale critical frequency of 100 Hz, since the Strouhal numbers for the scale model and for the prototype are the same at these frequencies.

Statistical functions were computed for a limited amount of the fast-response data. The computations included the power-spectral-density function, amplitude-probability-density function, autocorrelation function, and cross-correlation function.

TEST RESULTS, INSTANTANEOUS FLOW DISTORTION

There are two parts to the discussion of the test results: the first part describes the measurement of the "instantaneous" flow distortion and compares it with that measured with "steady-state" instrumentation. It is these data that clearly identify that the flow in subsonic inlet when separated is not steady state and requires high response instrumentation for proper evaluation. For most purposes, these results would be sufficient. However, there is another aspect of unsteady flow that must be considered. This is whether the unsteady flow varies in a random way or whether it has deterministic (natural frequency) characteristics. This aspect of the unsteady flow is the subject of the second part of the discussion of the test results.

Detection of Separation

Figure 4 shows the wing-engine inlet distortion number at the end of the inlet as a function of engine airflow per unit area for various cross-winds. The steady-state distortion number presented in Figure 4A was calculated from the steady-state total-pressure measurements. The peak distortion number, Figure 4B, was determined from the steady-state measurements and the flucturating-pressure measurements. The flagged symbols are the peak distortion numbers calculated from the digitized data. All other peak distortion numbers were calculated by the Analog Computer Editor System.

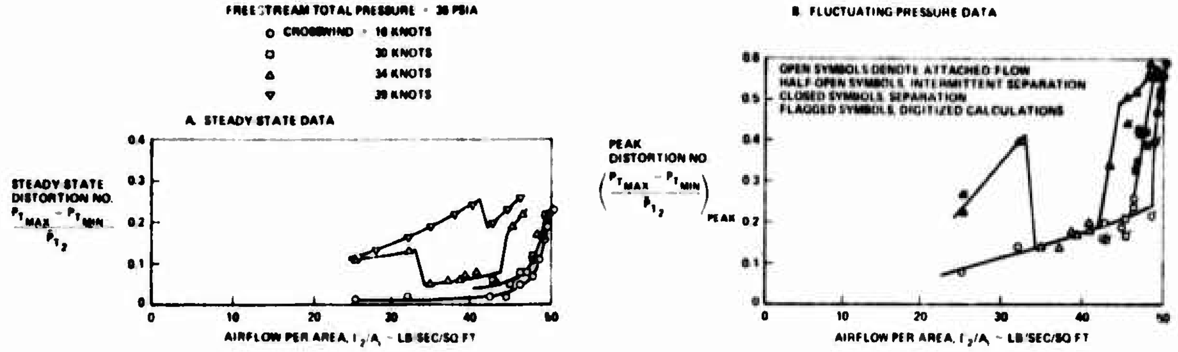

FIGURE 4. WING-ENGINE INLET CROSSWIND PERFORMANCE

The open symbols in Figure 4B are for test conditions that did not result in inlet boundary-layer separation. The half-open symbols indicate test conditions that resulted in intermittent separation. The closed symbols indicate that the boundary layer was separated all of the time. The occurrence of intermittent separation was indicated by

(1) momentary large changes in the pressure levels and/or in the magnitude of the pressure fluctuations within the inlet, such as shown by the pressure time history (oscillograph trace) in Figure 5B;

(2) large increases in the rate of change of peak distortion number with airflow accompanied by only small changes in the rate of change of steady-state distortion number with airflow (Figure 4, intermediate crosswind (square symbols), Γ_2/A_1 = 46 lb/sec/sq ft, for example); and

(3) total-pressure distributions at the end of the inlet that would indicate an attached boundary layer if based on steady-state data, but show very low total pressures on the upwind side of the inlet when the fluctuating-pressure data are used (Figure 6D).

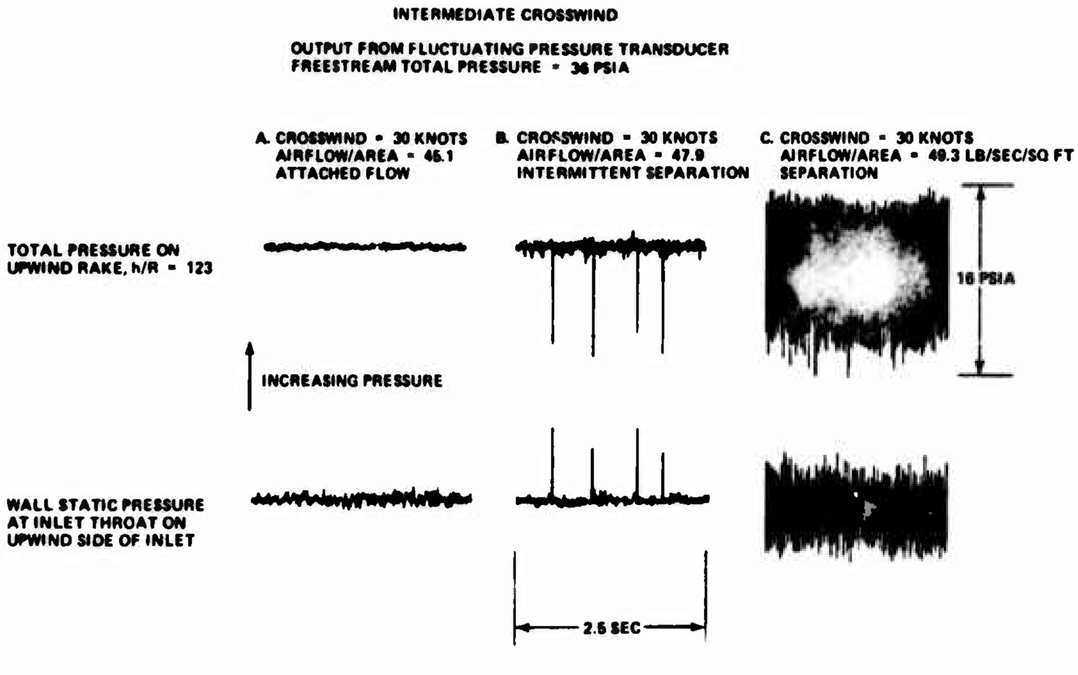

FIGURE 5. OSCILLOGRAPH RECORD OF PRESSURE vs TIME

At a given crosswind, the maximum inlet airflow that could be attained without separation, was estimated from the fluctuating-pressure data, as explained above. Without the fluctuating-pressure data, it would not have been possible to detect intermittent separation. For example, Figure 4B shows that at the intermediate crosswind (square symbols), the maximum obtainable airflow per unit area was 46 lb/sec/sq ft before separation occurred. The steady-state distortion data (Figure 5A) show a gradual increase in the rate of change of distortion with airflow for airflows above about 45 lb/sec/sq ft at this crosswind. Interpretation of the steady-state data with regard to occurrence of separation would have been uncertain if the fluctuating-pressure data had not been available. For example, it would not have been known whether the steady-state data characteristics were indicative of boundary-layer thickening (as occurred with 16 knots crosswind, for example) or of intermittent separation.

Total-Pressure Distributions

A comparison of steady-state total-pressure distributions and the total-pressure distributions corresponding to peak distortion at the end of the inlet is shown in Figure 6. The data are presented for a variety of inlet flow conditions.

1. Figure 6A shows inlet boundary-layer separation at high crosswind with low inlet airflow. The separation resulted from the adverse pressure gradient along the upwind inlet wall. The magnitude of the adverse gradient is decreased as the inlet airflow is increased at a given crosswind.

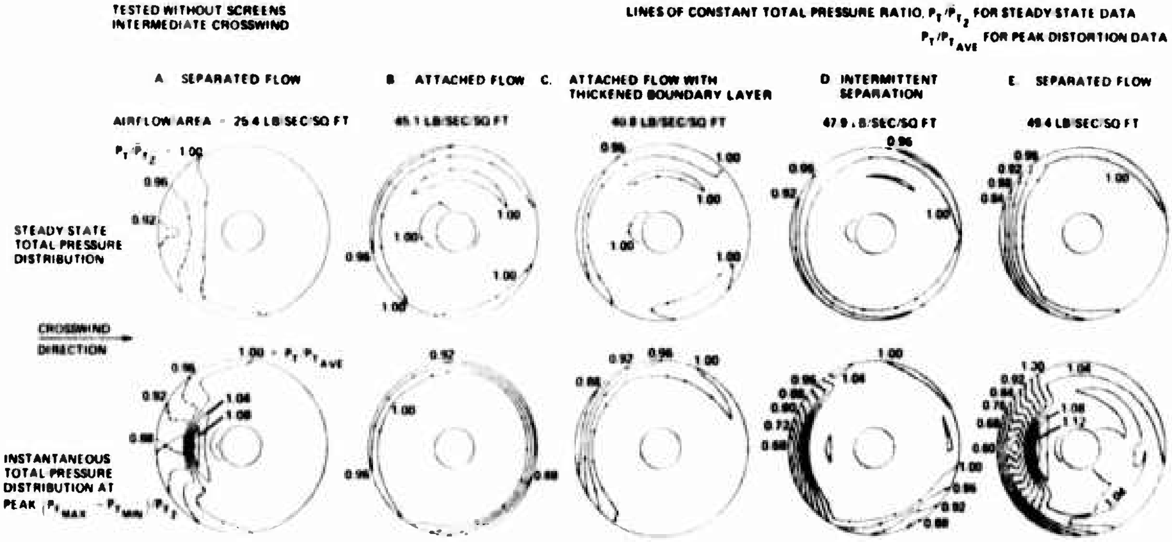

FIGURE 6. TOTAL-PRESSURE DISTRIBUTION AT END OF INLET

2. Figures 6B and 6C show attached flow at intermediate crosswind and high inlet airflows. In Figure 6C the boundary layer on the upwind wall of the inlet is becoming thicker due to increased crosswind speed.

3. Figure 6D shows intermittent inlet separation and Figure 6E is for a constantly separated boundary layer at very high inlet airflows. In this case separation is probably due to a shock-wave boundary-layer interaction near the throat of the inlet.

In every case, the steady-state total-pressure distributions do a poor job of describing the magnitude and extent of the low-pressure region that could influence engine operation.

TEST RESULTS, STATISTICAL ANALYSIS

An unsteady flow can be random, deterministic, or a combination of both. For the flow to be deterministic, it must be cyclic. This is the case of an organ pipe and a Helmholz resonator. There are two reasons to identify that the flow has a deterministic pattern. These reasons are: (1) if the air inlet is in resonance, a change in geometry could largely reduce the amplitude of the resonance and, hence, the flow distortion presented to the engine; (2) the resonance might be caused by the test facility and is, therefore, spurious.

Frequently, the unsteady flow in inlets has both random and deterministic pressure fluctuations where with casual observation, the latter are masked by the random variations. For these reasons, a statistical analysis of the unsteady flow test results is required. In the following paragraphs, the spectral analysis, amplitude probability density function, and the autocorrelation function will be discussed. The cross-correlation can be very useful to find the nature of the resonance. However, the cross-correlation was not required for this test.

Spectral Analysis

The variance, σ^2, is equal to the square of the standard deviation and is proportional to the energy content of the pressure fluctuations. The power spectral density at center frequency, f, is the quotient of the variance of the pressure fluctuations with frequencies between $f - \frac{\Delta f}{2}$ and $f + \frac{\Delta f}{2}$ and the frequency bandwidth Δf.

$$\text{Power Spectral Density} = \frac{\sigma^2 (f,\Delta f)}{\Delta f}$$

Power spectral densities were computed with a bandwidth of one Hz for center frequencies of 3 Hz to 20 Hz; a bandwidth of 5 Hz was used for center frequencies of 25 Hz to 525 Hz; a bandwidth of 25 Hz was used for higher frequencies. The maximum center frequency was 5000 Hz in some cases and 1500 Hz in others.

The power-spectral-density function is the locus of the power-spectral-density-points. Figure 7 shows the power-spectral-density function calculated from the free-stream total-pressure measurement and from 4 of the 36 total-pressure measurements made at the end of the inlet. Three of the total pressures were measured upwind of the bullet and the fourth total pressure was measured downwind of the bullet. The data of Figure 7 are for inlet separation at intermediate crosswind with high inlet airflow.

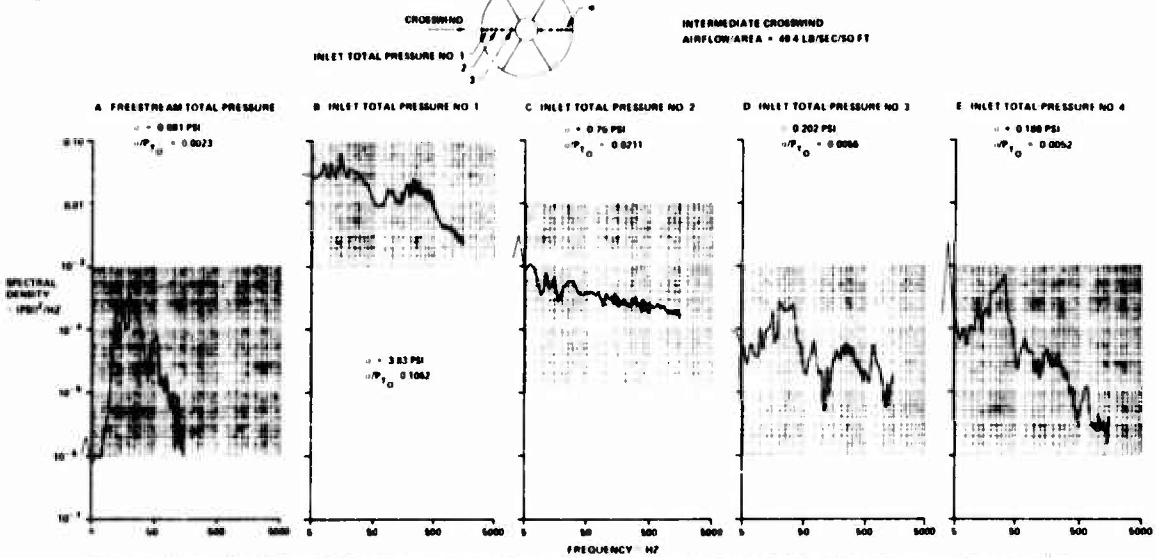

FIGURE 7. POWER-SPECTRAL-DENSITY FUNCTIONS FOR SEPARATED INLET FLOW

Figure 7A shows high energy peaks (high values of power spectral density) in the free-stream total-pressure fluctuations at frequencies of 12, 16, and 20 to 25 Hz. The highest peak occurred at 20 to 25 Hz frequency. This power-spectral-density function is the same, regardless of the type of inlet flow (separated or attached). This indicated that these total-pressure fluctuations were characteristic of the wind tunnel and do not depend in any way on the inlet characteristics.

Reference 4 suggested that these energy peaks were due to longitudinal standing waves in the wind tunnel. The wind tunnel is 145 feet long from the main tunnel valve 120 feet upstream of the inlet model to the blocked wind tunnel supersonic-diffuser throat 25 feet downstream of the inlet model. The first harmonic (fundamental frequency) of the wind tunnel acting as an organ pipe with both ends closed is 4 Hz. Twelve [illegible] Hz, 20 Hz and 25 Hz correspond approximately to the third, fourth, fifth, and sixth harmonic frequencies, respectively.

The power-spectral-density functions for the total pressures at the end of the inlet showed a large influence of the wind-tunnel pressure fluctuations, provided that the inlet measurements were not made in or near the separated wake or in the boundary layer. This influence is shown by high values of power spectral density at 20 Hz and 25 Hz in Figures 7D and 7E.

For inlet total-pressure measurements made in or near the separated wake, the power-spectral-density functions showed little or no effect of the wind-tunnel pressure fluctuations on the measurements (Figures 7B and 7C). For these cases, the high-energy levels of the pressure fluctuations in the wake obscured the wind-tunnel effect. These power-spectral-density functions show highest energy at the lowest frequencies, with no high energy spikes at any particular frequency.

For total-pressure measurements made in the inlet boundary layer where the flow was attached, the total-pressure fluctuations were of much greater magnitude than the free-stream total-pressure fluctuations and were therefore not significantly affected by the free-stream fluctuations.

Since the magnitudes of the wind-tunnel total-pressure fluctuations were not large enough to significantly affect the total-pressure fluctuations in the inlet boundary layer or in the separated wake, it was concluded that the maximum values of the distortion parameters and the corresponding total-pressure distributions were not significantly affected by the free-stream fluctuations for either attached or separated flow.

Amplitude-Probability-Density Function and Autocorrelation Function
Figure 8 shows the amplitude-probability-density function and the autocorrelation function for the free-stream total pressure. These data are shown to describe further the character of the free-stream total-pressure fluctuations and to give an example of a way in which these statistical functions can be used to describe pressure fluctuations.

The amplitude-probability density for a particular value of fluctuating pressure amplitude, y, is defined as the fraction of the total run time that the pressure amplitude is between $y - \frac{\Delta y}{2}$ and $y + \frac{\Delta y}{2}$, divided by Δy, or

$$\text{amplitude probability density} = \frac{1}{\Delta y}\,\frac{\Delta t(y, \Delta y)}{t_2 - t_1}$$

For random pressure fluctuations (pressure fluctuations where the occurrence of a specific pressure amplitude is a random event), the shape of the amplitude-probability-density function is similar to that of a normal or Gaussian probability-density function. For deterministic or non-random pressure fluctuations (a sine wave for example) the shape of the curve is significantly different from that of a Gaussian distribution. The amplitude-probability-density function is therefore useful in determining whether or not the data contain significant deterministic components.

Figure 8A shows the amplitude-probability-density function for the free-stream total-pressure fluctuations. The shape of the curve is practically that of a Gaussian distribution. Therefore, the amplitudes of the pressure fluctuations with 20 Hz to 25 Hz frequency, which dominate the inviscid flow, are not deterministic in nature. This type of pressure fluctuation is called narrowband random noise.

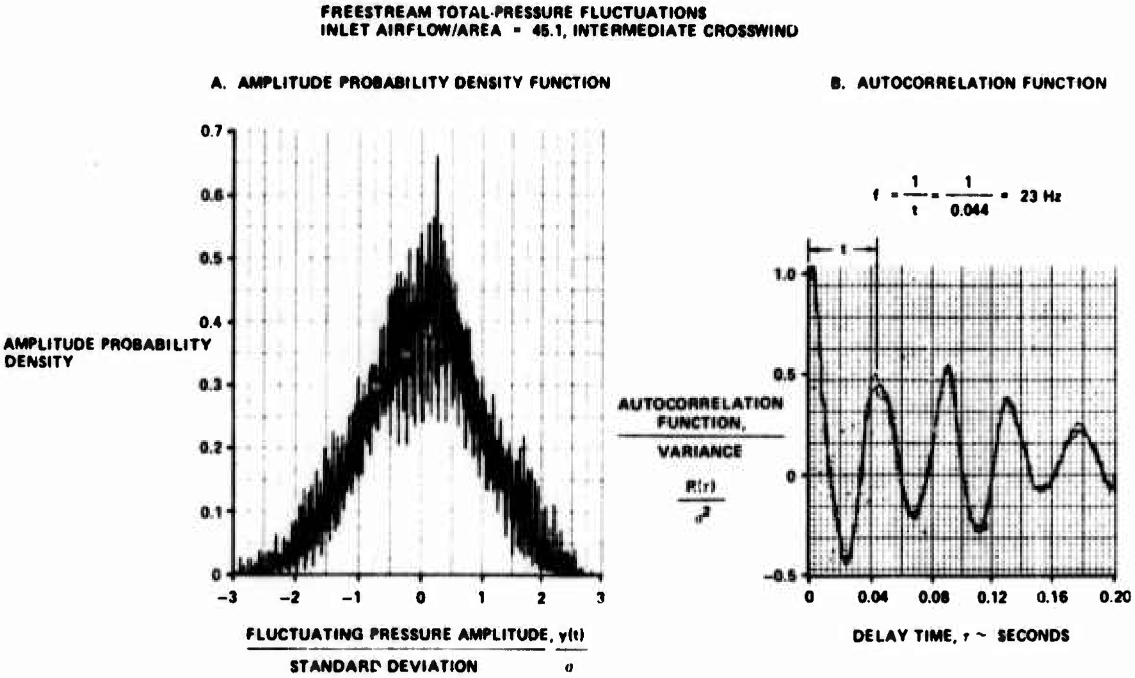

FIGURE 8. AMPLITUDE PROBABILITY DENSITY FUNCTION AND AUTOCORRELATION FUNCTION

The autocorrelation is defined by the equation

$$R(\tau) = \frac{1}{t_2-t_1}\int_{t_1}^{t_2} y(t)\, y(t-\tau)\, dt.$$

The quantity τ is the delay time. The autocorrelation is calculated for various values of delay time, and the locus of the points is the autocorrelation function.

The autocorrelation function for the free-stream total-pressure fluctuations is shown in Figure 8B. The periodic characteristic of the autocorrelation function defines the frequency of the pressure fluctuations that dominate the flow (f = 23 Hz). The damped characteristic of the autocorrelation function is indicative of narrowband random noise. If a sine wave with 23 Hz frequency were dominant, instead of the narrowband random noise, the autocorrelation function would not be damped.

CONCLUSIONS

1. Detection of intermittent boundary-layer separation in an inlet is possible only with fluctuating-pressure data; steady-state data are not adequate.

2. The total-pressure distributions at the end of an air inlet that can affect engine operation are adequately described only through the use of fast response pressure data. In this test peak distortions were measured that were 2 to 4 times as large as the steady-state distortion numbers. Also the maximum extent of the low-total-pressure regions was significantly larger than indicated by the steady-state data.

3. Simulation of the inlet flow for engine compatibility test should represent the real, time-dependent flow-distortion. When this is not possible and screens are used to produce a steady-state flow distortion, the distortion represented should be based on the appropriate "instantaneous" distortion measured in a properly instrumented inlet test.

4. Inlet separation was characterized by high-energy total-pressure fluctuations in the separated wake. Spectral analysis showed highest power spectral density at the lowest frequencies, with no energy spikes at any particular frequency. This would appear to be a random "noise" generation at the flow separation with greater attenuation of the higher frequencies prior to arrival of the disturbance at the measurement location.

5. The wind tunnel produced an energy spike at 20 and 25 hertz. This did not compromise the validity of the inlet distortion measurement.

BIBLIOGRAPHY

1. Lynch, F.R. and Slade, C.J.: Data Acquisition and Automated Editing Techniques for Engine-Inlet Tests. Presented at the AIAA 5th Aerodynamic Testing Conference; Tullahoma, Tennessee, May 1970.

2. Plowde, G.A. and Brimelow, B.: Pressure Fluctuations Cause Compressor Instability. PWA-69-9055, June 1969.

3. Oates, G.C.; Sherman, D.A. and Motycka, D.L.: Experimental Study of Inlet Generated Pressure Fluctuations. PWA-3682, June 1969.

4. Crites, R.C.: The Philosophy of Analog Techniques Applied to the Analysis of High-Speed Screening of Dynamic Data. Presented at the AIAA 5th Aerodynamic Testing Conference; Tullahoma, Tennessee, May 1970.

NOMENCLATURE

A_i	inlet throat area
$P_{T_{ave}}$	time-dependent area-average total pressure computed from the 36 time-dependent total-pressures measured at the end of the inlet
$P_{T_{max}}$	maximum total pressure at engine face
$P_{T_{min}}$	minimum total pressure at engine face
P_{T_0}	free-stream total pressure
P_{T_2}	area-average total pressure at end of inlet computed from steady-state total-pressure and static-pressure data
W_a	inlet airflow
$y(t)$	fluctuating-pressure component
θ_{T_2}	total temperature at end of inlet (°R) divided by 519° R
δ_{T_2}	P_{T_2} (psia) divided by 14.7 psia
Γ_2	engine-face corrected airflow = $W_a \sqrt{\theta_{T_2}/\delta_{T_2}}$

DIRECTIONAL EFFECTS IN 3-D DIFFUSERS

Hermann Viets

Aerospace Research Laboratories/LE, WPAFB, Ohio

1. INTRODUCTION

The diffusion of flows which are not completely mixed (i.e., have a non-uniform velocity profile) is of interest in various fluid dynamic systems. This is particularly true of aircraft applications where the overall length of a system is of primary importance, thus leading to situations where unmixed flows must be diffused. Renewed interest has recently focused on this problem in relation to the development of a highly efficient thrust augmenting ejector[1].

It is the purpose of this paper to examine the effect of direction on the three dimensional diffusion process. Consider an unmixed velocity profile at the inlet to the diffuser. The question then arises: Is there a preferred direction of diffusion? That is, is it more efficient to diffuse the flow in the plane of the velocity profile (Fig. 1a) or in the plane normal to that of the velocity profile (Fig. 1b)? The schematics in Fig. 1 show a square inlet in order to separate the directional effect from that of aspect ratio.

The method of attack is to linearize the governing boundary layer equations about an average streamwise velocity and assume the cross flow velocity component to be small. After some transformation the equations are reduced to a single equation of the form of the classical heat conduction equation for a single variable including both velocity and pressure. The known solutions to the heat conduction equation are then applied and the results for diffusion in different directions are compared.

The linearized attack is an extension of an analysis of rectangular jets in coflowing streams due to Pai and Hsieh[2,3].

2. ANALYSIS

For diffusers of moderate expansion angles, the character of the flow is that the cross flow velocities v and w are small compared to the streamwise velocity component u. Therefore, as in Refs. 2 and 3, the boundary layer assumptions are applied in both the y and z directions. The resulting non-dimensionalized boundary layer equations are

$$u \frac{\partial u}{\partial x} + v \frac{\partial u}{\partial y} + w \frac{\partial u}{\partial z} = - \frac{\partial p}{\partial x} + \frac{1}{R} \left[\frac{\partial^2 u}{\partial y^2} + \frac{\partial^2 u}{\partial z^2} \right] \tag{1a}$$

$$\frac{\partial p}{\partial y} = 0 \tag{1b}$$

$$\frac{\partial p}{\partial z} = 0 \tag{1c}$$

and continuity

$$\frac{\partial u}{\partial x} + \frac{\partial v}{\partial y} + \frac{\partial w}{\partial z} = 0 \qquad (1d)$$

The velocities are non-dimensionalized with respect to the average velocity at the diffuser inlet, U_o; the distances with half the initial wall separation L_o; and the pressures with the dynamic head $\rho\, U_o^2$ (see Fig. 2). Thus R is the Reynolds number, defined as $R = \frac{\rho\, U_o\, L_o}{\mu}$.

Now U(x) is defined as the average non-dimensional velocity in the duct or diffuser. Then from the conservation of mass

$$U(x) = \frac{U(x = 0)}{A(x)} = \frac{1}{A(x)} \qquad (2)$$

where A(x) is the streamwise area distribution.

Consider initial velocity profiles (at x = 0) such that the deviation of the velocity from the average velocity, [u(o,y) - U(x)], is small. If, in addition, the diffuser angles are small, the transverse velocities, v and w, are small. Then the streamwise momentum equation (1a) may be linearized about U(x) by introducing $u' = u - U(x)$, noting that u', v, w and $\frac{\partial U}{\partial x}$ are small and neglecting terms of higher than first order in these variables.

The resulting streamwise momentum equation is

$$U \frac{\partial U}{\partial x} + U \frac{\partial u'}{\partial x} = - \frac{dp}{dx} + \frac{1}{R} \left[\frac{\partial^2 u'}{\partial y^2} + \frac{\partial^2 u'}{\partial z^2}\right] \qquad (3)$$

and from Eq. (2)

$$\frac{1}{A(x)} \left[\frac{d}{dx}\left(\frac{1}{A(x)}\right) + \frac{\partial u'}{\partial x}\right] = - \frac{dp}{dx} + \frac{1}{R} \left[\frac{\partial^2 u'}{\partial y^2} + \frac{\partial^2 u'}{\partial z^2}\right] \qquad (4)$$

In order to simplify this equation, the velocity and pressure may be combined into one variable,

$$Q(x,y,z) = \frac{1}{A(x)} + u'(x,y,z) + A(x)\,[p(x) - p(0)] \qquad (5)$$

then

$$\frac{\partial Q}{\partial x} = \frac{d}{dx}\left(\frac{1}{A}\right) + \frac{\partial u'}{\partial x} + \frac{dA}{dx}\,[p(x) - p(0)] + A \frac{dp}{dx} \qquad (6)$$

Equation (4) becomes

$$\frac{1}{A}\ \frac{\partial Q}{\partial x} = \frac{1}{R}\left[\frac{\partial^2 Q}{\partial y^2} + \frac{\partial^2 Q}{\partial z^2}\right] + \frac{1}{A}\ \frac{dA}{dx}\ [p(x) - p(0)] \tag{7}$$

Now to eliminate the pressure, integrate Eq. (5) over the cross sectional area, A(x),

$$\int_o^g\int_o^h [p(x) - p(0)]\ dydz = \frac{1}{A}\int_o^g\int_o^h Q dydz - \frac{1}{A}\int_o^g\int_o^h u' dydz - \frac{1}{A^2} \tag{8}$$

where g(x) and h(x) are the locations of the walls on the y and z axes, respectively, and A(x) = h(x) g(x). The variable u′ is defined as the deviation from the average velocity; thus

$$\int_o^g\int_o^h u'\ dydz = 0 \tag{9}$$

The pressure is constant over any cross section and

$$A[p(x) - p(0)] - \frac{1}{A}\int_o^g\int_o^h Q\ dydz - \frac{1}{A^2}\int_o^g\int_o^h dA \tag{10}$$

Then the governing Eq. (7) becomes

$$\frac{1}{A}\ \frac{\partial Q}{\partial x} = \frac{1}{R}\left[\frac{\partial^2 Q}{\partial y^2} + \frac{\partial^2 Q}{\partial z^2}\right] + \frac{1}{A^3}\ \frac{dA}{dx}\int_o^g\int_o^h Q\ dydz - \frac{1}{A^3}\ \frac{dA}{dx} \tag{11}$$

The wall contour may be transformed out of the problem by defining

$$\eta = \frac{y}{g(x)} \qquad \text{and} \qquad \zeta = \frac{z}{h(x)} \tag{12}$$

then

$$\frac{1}{gh}\ \frac{\partial Q}{\partial x} = \frac{1}{R}\left[\frac{1}{g^2}\ \frac{\partial^2 Q}{\partial \eta^2} + \frac{1}{h^2}\ \frac{\partial^2 Q}{\partial \zeta^2}\right] + \frac{1}{(gh)^2}\ \frac{d}{dx}\ (gh)\int_o^1\int_o^1 Q\ d\eta d\zeta - \frac{1}{(gh)^3}\ \frac{d}{dx}\ (gh) \tag{13}$$

or multiplying through by the area squared, the governing equation is

$$(gh)\ \frac{\partial Q}{\partial x} = \frac{1}{R}\left[h^2\ \frac{\partial^2 Q}{\partial \eta^2} + g^2\ \frac{\partial^2 Q}{\partial \zeta^2}\right] + \frac{d}{dx}\ (gh)\int_o^1\int_o^1 Q\ d\eta d\zeta - \frac{1}{gh}\ \frac{d}{dx}\ (gh) \tag{14}$$

with the initial condition $Q\ (0,\ \eta,\ \zeta) = F\ (\eta,\zeta)$ (15)

and the boundary conditions at the centerline (from symmetry)

$$\left.\frac{\partial Q}{\partial \eta}\right|_{\eta = 0} = 0 \qquad \text{and} \qquad \left.\frac{\partial Q}{\partial \zeta}\right|_{\zeta = 0} = 0\ . \tag{16}$$

The boundary conditions at the walls are based on an inviscid wall assumption and are derived in the Appendix. They are

$$\left.\frac{\partial Q}{\partial \eta}\right|_{\eta = 1} = 0 \qquad \text{and} \qquad \left.\frac{\partial Q}{\partial \zeta}\right|_{\zeta = 1} = 0\ . \tag{17}$$

The inviscid wall assumption precludes the prediction of separation (and hence stall) in the diffuser, but separation is not permissible anyway under the assumptions previously made to linearize to governing equations.

3. DIFFUSION IN THE PLANE OF THE VELOCITY PROFILE [FIGURE 1a]

Now consider the flow situation illustrated in Fig. 1a. The velocity is not a function of z, and therefore $\frac{\partial^2 Q}{\partial \zeta^2} = 0$. The walls intersecting the z axis are parallel, so h(x) = 1, while the walls intersecting the y axis diverge as g(x). The governing Eq. (14) then reduces to

$$g \frac{\partial Q}{\partial x} = \frac{1}{R} \frac{\partial^2 Q}{\partial \eta^2} + \frac{dg}{dx} \int_0^1 Q\, d\eta - \frac{1}{g} \frac{dg}{dx}\ . \tag{18}$$

By the use of the transformation

$$\xi_1 = \int_0^x \frac{1}{g(s)}\, ds \tag{19}$$

where

$$\frac{\partial}{\partial \xi_1} = \frac{\partial}{\partial x} \frac{\partial x}{\partial \xi_1} = g(x) \frac{\partial}{\partial x}\ . \tag{20}$$

The governing Eq. (18) becomes

$$\frac{\partial Q}{\partial \xi_1} = \frac{1}{R} \frac{\partial^2 Q}{\partial \eta^2} + \frac{1}{g} \frac{dg}{d\xi_1} \int_0^1 Q\, d\eta - \frac{1}{g^2} \frac{dg}{d\xi_1} \tag{21}$$

with the initial condition,

$$Q\ (0,\ \eta) = u'\ (0,\ \eta) + 1 = F_1\ (\eta) \tag{22}$$

and the boundary conditions,

$$\left.\frac{\partial Q}{\partial \eta}\right|_{\eta = 0} = 0 \qquad \text{and} \qquad \left.\frac{\partial Q}{\partial \eta}\right|_{\eta = 1} = 0 \tag{23}$$

The governing equation is now in the form of the well-known unsteady heat conduction equation and will be solved in Section 5.

4. DIFFUSION NORMAL TO THE PLANE OF THE VELOCITY PROFILE [FIGURE 1b]

Consider the flow illustrated in Fig. 1b. Again, the velocity is not a function of z and therefore, $\frac{\partial^2 Q}{\partial \zeta^2} = 0$. The walls intersecting the y axis are parallel, so $g(x) = 1$, while the walls intersecting the z axis diverge as $h(x)$. The governing Eq. (13) then reduces to

$$\frac{1}{h}\frac{\partial Q}{\partial x} = \frac{1}{R}\frac{\partial^2 Q}{\partial \eta^2} + \frac{1}{h^2}\frac{dh}{dx}\int_0^1 Q\, d\eta - \frac{1}{h^3}\frac{dh}{dx} \tag{24}$$

Now by the use of the transformation

$$\xi_2 = \int_0^x h(s)\, ds \tag{25}$$

where

$$\frac{\partial}{\partial \xi_2} = \frac{\partial}{\partial x}\frac{\partial}{\partial \xi_2} = \frac{1}{h(x)}\frac{\partial}{\partial x} \tag{26}$$

Eq. (24) becomes

$$\frac{\partial}{\partial \xi_2} = \frac{1}{R}\frac{\partial^2 Q}{\partial \eta^2} + \frac{1}{h}\frac{dh}{d\xi_2}\int_0^1 Q\, d\eta - \frac{1}{h^2}\frac{dh}{d\xi_2} \tag{27}$$

with the initial and boundary conditions as in Eqs. (22) and (23).

Thus the transformed governing equations and boundary conditions are precisely the same whether the flow is diffused in the plane of the velocity profile or in a plane normal to that of the velocity profile. The difference between the two situations enters through the transformation of the streamwise coordinate. It is now of interest to solve the governing equation and examine the difference between the two transformations of the streamwise coordinate.

5. SOLUTION OF THE GOVERNING EQUATION

The form of the governing equation (21) [or (27)] may be recognized as the unsteady heat conduction equation with a heat generation term. There are several classical techniques available to solve such equations. The method chosen here is to separate the problem into two simpler problems and superimpose the resulting solutions. This approach is justified by the linearity of the governing equation

Let
$$Q\ (\xi,\eta) = G\ (\xi,\eta) + H\ (\xi,\eta) \tag{28}$$

where G and H are solutions to the following problems:

(A)
$$\frac{\partial G}{\partial \xi} = \frac{1}{R}\ \frac{\partial^2 G}{\partial \eta^2} \qquad \text{B.C.} \quad \left.\frac{\partial G}{\partial \eta}\right|_{\eta = 0} = 0 \tag{29}$$

$$\text{I.C.} \quad G(0,\eta) = F(\eta) \qquad \left.\frac{\partial G}{\partial \eta}\right|_{\eta = 1} = 0$$

(B)
$$\frac{\partial H}{\partial \xi} = \frac{1}{R}\ \frac{\partial^2 H}{\partial \eta^2} + \frac{1}{g}\ \frac{dg}{d\xi}\left[\int_0^1 Q\ d\eta - \frac{1}{g(\xi)}\right] \tag{30}$$

$$\text{B.C.} \quad \left.\frac{\partial H}{\partial \eta}\right|_{\eta = 0} = 0$$

$$\text{I.C.} \quad H(0,\eta) = 0 \qquad \left.\frac{\partial H}{\partial \eta}\right|_{\eta = 1} = 0$$

It may be verified, by addition of the two governing equations and by addition of the two sets of boundary conditions, that the governing Eq. (21) is equivalent to the two simpler problems.

The solution to problem (A) has been found (Ref. 4, pg. 101) to be

$$G(\xi,\eta) = \int^1 F(\eta)\ d\eta + \sum_{n=1}^{\infty} 2\ e^{\frac{-n^2\pi^2}{R}\xi}\ [F(\eta)\ \cos n\pi\eta\ d\eta]\ \cos n\pi\eta \tag{31}$$

That the first integral is equal to unity may be seen from the initial condition Eq. (22), and a consequence of the definition of u', Eq. (9).

The solution to problem (B) may be verified by substitution to be

$$H(\xi,\eta) = H(\xi) = \int_0^{\xi} \frac{\frac{dg}{d\tau}}{g(\tau)}\left[\int_0^1 Q\ d\eta - \frac{1}{g(\tau)}\right] d\tau \tag{32}$$

The complete solution for $Q(\xi,\eta)$ is then

$$Q(\xi,\eta) = 1 + 2 \sum_{n=1}^{\infty} e^{\frac{-n^2\pi^2}{R}\xi} \left[\int_0^1 F(\eta) \cos n\pi\eta \, d\eta\right] \cos n\pi\eta$$

$$+ \int_0^{\xi} \frac{\frac{dg}{d\tau}}{g(\tau)} \left[\int_0^1 Q \, d\eta - \frac{1}{g(\tau)}\right] d\tau \qquad (33)$$

This is the solution to Eq. (21). The corresponding solution for diffusion in the opposite plane, Eq. (27), is obtained by replacing $g(\tau)$ by $h(\tau)$. Thus, if the contour of the expanding walls is the same, that is $g(x) = h(x)$, then the mathematical solution, Eq. (33), is independent of the direction of diffusion. However, in transforming the solution back to real coordinates, the effect of the direction of diffusion becomes important since the transformations of the streamwise coordinates, Eqs. (19) and (25), are quite different in the two cases.

6. PRESSURE DISTRIBUTION THROUGH THE DIFFUSER

It should be noted that, in this linearized treatment of the diffuser, the pressure distribution is independent of the inlet velocity profile and depends only on the geometry through the streamwise distribution of average velocity. This may be seen by examining Eq. (10), which indicates that the pressure distribution in the physical streamwise direction depends on the area and the integral of Q over the area. The variable Q is a function of area, pressure and the deviation of velocity from the average velocity, u'. However, the integral of Q is independent of u' by definition (see Eq. 9). Thus the pressure distribution is independent of the inlet velocity profile and may be found by a far simpler method. Returning to Eq. (4) and setting $u' = 0$,

$$\frac{1}{A(x)} \frac{d}{dx}\left(\frac{1}{A(x)}\right) = -\frac{dp}{dx} \qquad (34)$$

or

$$-dp = \frac{1}{A} d\left(\frac{1}{A}\right) \qquad (35)$$

Then integrating

$$p(x) - p(0) = \frac{1}{2}\left(1 - \frac{1}{A^2(x)}\right) \qquad (36)$$

The effect of direction on the diffusion process, therefore, is not evident in terms of the pressure distribution through the diffuser but rather in the degree of mixing found in the velocity profile at the diffuser exit. This effect is discussed in the following section.

7. EFFECT OF DIFFUSION DIRECTION ON THE STREAMWISE COORDINATE TRANSFORMATION

In order to illustrate the effect of direction on the diffusion process, consider the simplest case of a straight walled diffuser. Then, the equation of the expanding walls for diffusion in the plane of the velocity profile, Fig. 1a, is

$$g(x) = ax + 1 \tag{37}$$

where a is the slope of the expanding walls. The transformed streamwise coordinate is

$$\xi_1 = \int_0^x \frac{1}{as + 1}\, ds = \frac{1}{a} \ln (ax + 1) \tag{38}$$

Now for diffusion in a direction normal to the plane of the velocity profile, Fig. 1b, the equation of the expanding walls (for the same area ratio between exit and inlet) is the same as above,

$$h(x) = ax + 1 \tag{39}$$

Then the transformed streamwise coordinate is

$$\xi_2 = \int_0^x (as + 1)\, ds = \frac{ax^2}{2} + x \tag{40}$$

Now the question arises: if there exist two diffusers of equal length but different sets of diverging walls, as illustrated in Figs. 1a and 1b, what will be the difference between their exit velocity profiles? The simplest way to examine this question is to compare the two streamwise coordinate transformations, as shown in Fig. 3. The two transformed coordinates are plotted versus non-dimensionalized physical distance downstream for the case of the wall slope $a = 0.1$. Then at any x position downstream, the corresponding value ξ is directly related to the amount of mixing having taken place up to that streamwise position. Thus it may be seen from the figure that diffusion normal to the plane of the velocity profile always leads to improved mixing in contrast to diffusion in the plane of the velocity profile, since $\xi_2 > \xi_1$ everywhere.

The difference in the degree of mixing indicated above can be substantial. Defining a variable D as the difference between the transformed coordinates at any x position divided by that x position, the value of D is 19% at an x location of two. The difference D grows very rapidly, reaching values of 28% and 44% at x locations of three and five, respectively.

Some insight into the problem of concurrent mixing and diffusion may be obtained by noting that for no diffusion the transformation of the streamwise coordinate degenerates to $\xi = x$. (It should be kept in mind that the walls are assumed inviscid). This situation is depicted in Fig. 3 by the dashed line. Then it can be clearly seen from the figure that diffusion in the plane of the velocity profile (ξ_1) inhibits the mixing process while diffusion normal to the plane of the velocity profile (ξ_2) enhances the mixing process.

8. EFFECT OF ARBITRARY STREAMWISE EDDY VISCOSITY

In the preceding analysis, there is an implicit assumption that the Reynolds number term, R, be constant. This limits the treatment to laminar flows or turbulent flows where a Boussinesq approximation to the eddy viscosity is made, namely, that the eddy viscosity is constant. However, the implications of the preceding results are unaffected by the use of an arbitrary streamwise eddy viscosity, although the numerical values will change, as shown in the following argument:

Let

$$\xi_1 = \int_0^x \frac{1}{Rg(s)} \, ds \tag{41}$$

and

$$\xi_2 = \int_0^x \frac{h(s)}{R} \, ds \tag{42}$$

where R is an arbitrary function of streamwise distance.

Then the governing differential Eqs. (21) and (27) are unchanged except for the disappearance of the Reynolds number, R. The corresponding solution of the governing equation, Eq. (33), is likewise unaffected except for the disappearance of the Reynolds number from the equation. Thus a figure equivalent to Fig. 3 may be generated with the x axis replaced by x/R. The curve for ξ_2 will lie above that for ξ_1, and the same qualitative arguments as those presented with reference to Fig. 3 follow. Thus the basic conclusion holds, that diffusion normal to the plane of the velocity profile is more effective than diffusion in the plane of the velocity profile.

9. SEPARATION OF Q INTO PRESSURE AND VELOCITY

It has previously been argued (Sec. 6) that the streamwise pressure distribution is independent of the velocity distribution. In this section the function Q is separated into its component parts in order to isolate the velocity component for the calculations of some specific examples.

From Eq. (10),

$$p(\xi) - p(0) = \frac{1}{A} \int_0^1 \int_0^1 Q(\xi,\eta) \, d\eta \, d\zeta - \frac{1}{A^2} \tag{43}$$

Now $Q(\xi,\eta)$ has been found (for the case of diffusion in the plane of the velocity profile) in Eq. (33). The integral in Eq. (43) can be easily evaluated by noting that the second term on the right hand side of Eq. (33) drops out upon integration with respect to η. Then

$$p(\xi) - p(0) = \frac{1}{A}\left\{ 1 + \int_0^{\xi_1} \frac{\frac{dg}{d\tau}}{g(\tau)} \left[\int_0^1 Q \, d\eta - \frac{1}{g(\tau)} \right] d\tau \right\} - \frac{1}{A^2} \qquad (44)$$

Now by equating Eq. (33) with the definition of Q Eq. (5), and solving for u' and substituting for $p(\xi) - p(0)$ from Eq. (44),

$$u'(\xi_1,\eta) = 2 \sum_{n=1}^{\infty} e^{\frac{-n^2\pi^2}{R}\xi_1} \left[\int_0^1 F(\eta) \cos n\pi\eta \, d\eta \right] \cos n\pi\eta \qquad (45)$$

The result for diffusion normal to the plane of the velocity profile is identical to the above except that ξ_2 replaces ξ_1.

10. EXAMPLE

As a simple example, consider the deviation from uniformity of the velocity profile at the entrance to the diffuser to be $F(\eta) = b \cos \pi \eta$. Then the coefficient of the Fourier series solution, Eq. (45), is

$$b \int_0^1 \cos \pi\eta \cos n\pi\eta \, d\eta = \begin{cases} b/2 & n = 1 \\ 0 & n \neq 1 \end{cases} \qquad (46)$$

and the solution for u reduces to

$$u'(\xi,\eta) = b\, e^{\frac{-\pi^2}{R}\xi} \cos \pi\eta \qquad (47)$$

Thus the shape of the velocity profile remains qualitatively unchanged while the deviation of the velocity from uniform flow decays as the exponential

$$e^{\frac{-\pi^2\xi}{R}}$$

Now suppose $a = 0.1$, $R = 100$ and the diffuser length is $x_e = 4$ (here R may be viewed as the inverse of an eddy viscosity term). Then the transformed streamwise coordinate is (from Fig. 3) $\xi_1 = 3.36$ for diffusion in the plane of the profile and $\xi_2 = 4.80$ for diffusion normal to the plane. The ratio of the magnitudes of u at the exit of the diffuser in the two cases is

$$\frac{e^{\frac{-\pi^2}{R}\xi_2}}{e^{\frac{-\pi^2}{R}\xi_1}} = 1.153$$

Thus the mixing rate has been improved by approximately 15% by diffusing the flow normal to the plane of the velocity profile rather than in the plane.

11. CONCLUSION

The foregoing analysis indicates the importance of diffusion direction on the linearized mixing process within the diffuser. The same effect may be of even greater importance in the nonlinear case and should therefore be examined both theoretically and experimentally.

12. REFERENCES

1. QUINN, B., Recent Developments in Large Area Ratio Thrust Augmentors, J. of Aircraft, Vol. 10, No. 8, p. 481, October 1973.

2. PAI, S. L., and HSIEH, T. Y., Linearized Theory of Three-Dimensional Jet Mixing With and Without Walls, J. Basic Eng., Vol. 92, No. 1, pp. 93-100, March 1970.

3. PAI, S. L., and HSIEH, T. Y., Three-Dimensional Laminar Jet Mixing, Physics of Fluids, Vol. 12, No. 4, pp. 936-938, April 1969.

4. CARSLAW, H. S., and JAEGER, J. C., Conduction of Heat in Solids, Oxford University Press, 1959.

Special thanks are due to Dr. Brian Quinn of the Energy Conversion Research Lab, and Dr. David Lee of the Applied Mathematics Research Lab for many enlightening conversations and Amn Vito Cedro of the Chemistry Research Lab for several helpful suggestions. Lts Robert Boyle, Jr., and William Fuller also provided several timely comments, which are appreciated, as is the typing of Miss Veronica Grycz.

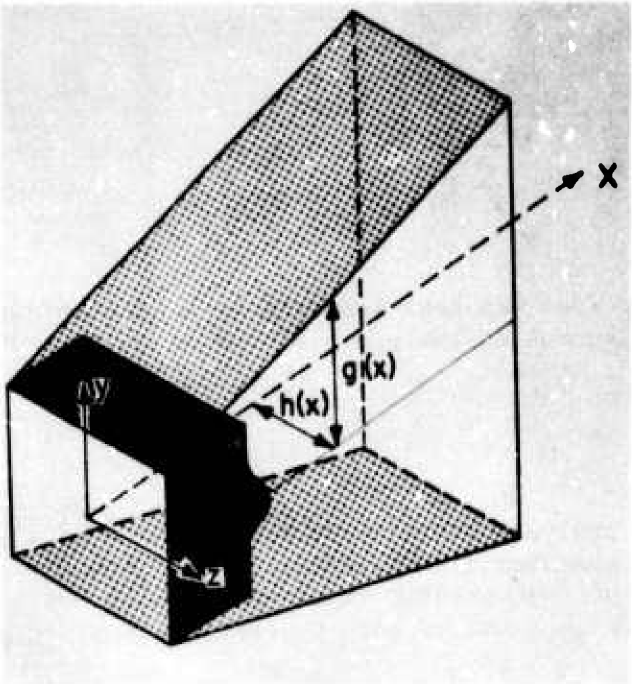

Figure 1a. Square inlet diffuser with diffusion in the plane of the velocity profile.

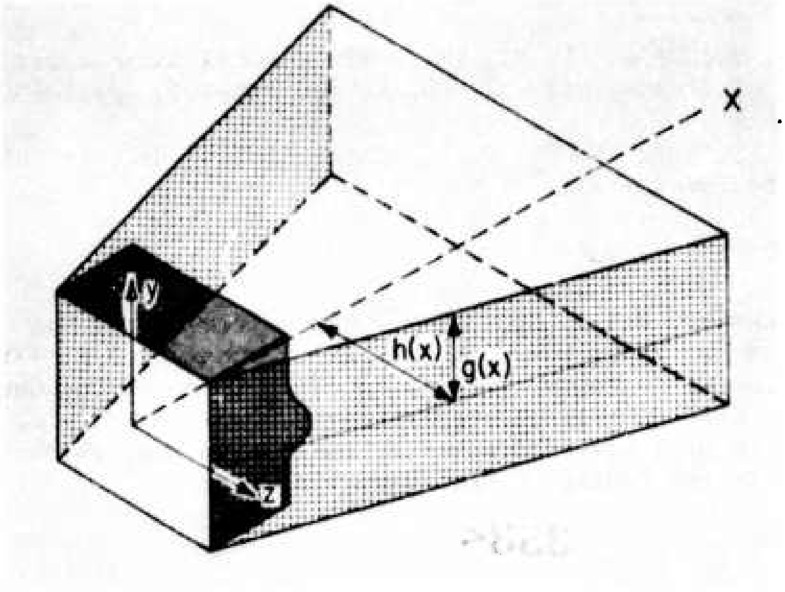

Figure 1b. Square inlet diffuser with diffusion normal to the plane of the velocity profile.

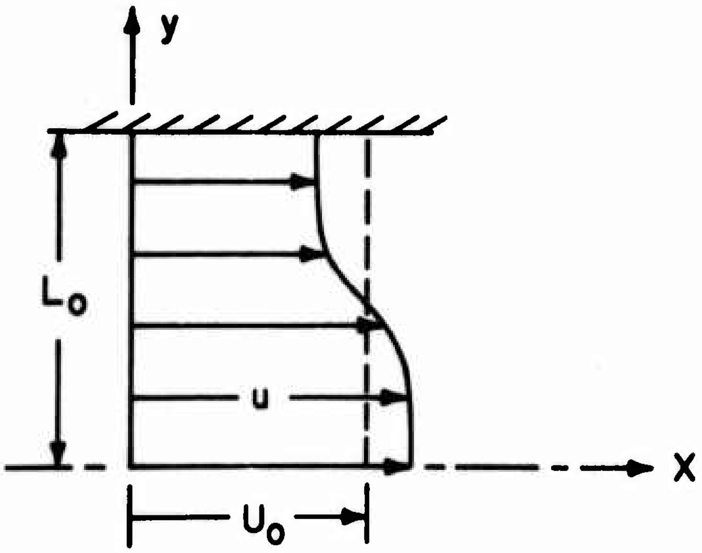

Figure 2. Inlet conditions.

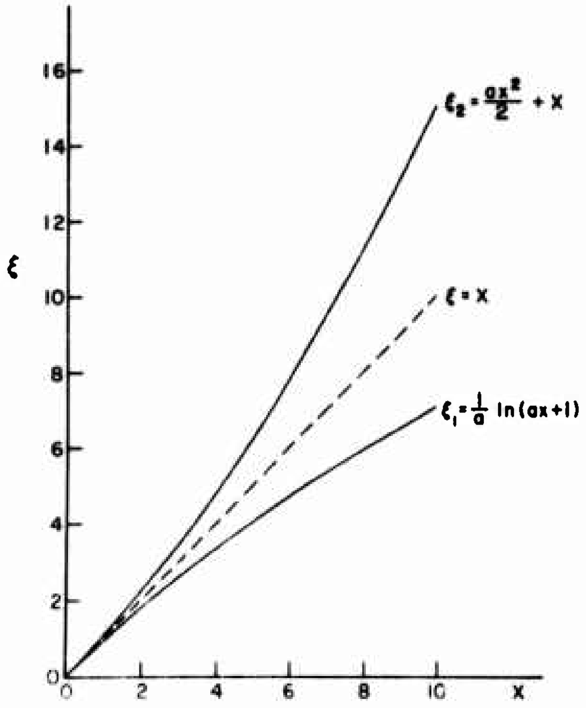

Figure 3. Effect of diffusion on the streamwise coordinate transformation.

APPENDIX DERIVATION OF THE INVISCID WALL BOUNDARY CONDITION

The outer boundary condition is that the wall is inviscid and thus cannot support a shear stress. The boundary condition may be expressed as (see Fig. A1):

$$\left.\frac{\partial w}{\partial \tau}\right|_{\text{wall}} = 0 \qquad \text{(A1)}$$

Expanding by the chain rule

$$\frac{\partial w}{\partial \tau} = \frac{\partial w}{\partial u}\frac{\partial u}{\partial y}\frac{\partial y}{\partial \tau} + \frac{\partial w}{\partial u}\frac{\partial u}{\partial x}\frac{\partial x}{\partial \tau} = 0 \qquad \text{(A2)}$$

or

$$\frac{\partial u}{\partial y} = \frac{-\frac{\partial x}{\partial \tau}}{\frac{\partial y}{\partial \tau}}\frac{\partial u}{\partial x} \qquad \text{(A3)}$$

From Fig. A1,

$$\frac{\partial y}{\partial \tau} = \frac{1}{\sqrt{1 + h'^{2}}}$$

and

$$\frac{\partial x}{\partial \tau} = \frac{h'}{\sqrt{1 + h'^{2}}}$$

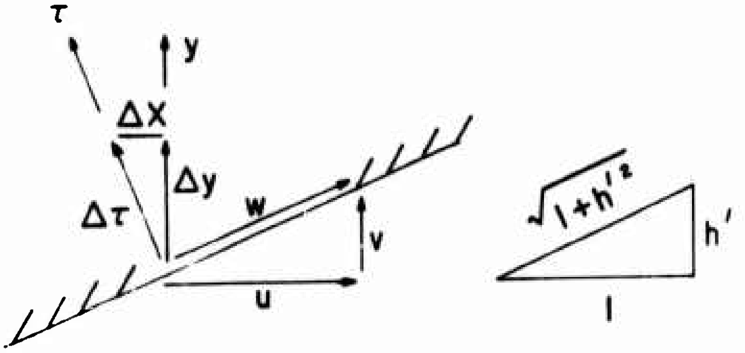

Figure A1. Boundary condition at the wall.

so that

$$\left.\frac{\partial u}{\partial y}\right|_{\text{wall}} = h' \frac{\partial u}{\partial x} \qquad \text{(A5)}$$

or from the definition of u,

$$\left.\frac{\partial u'}{\partial y}\right|_{\text{wall}} = \frac{-h'^{2}}{h^{2}(x)} + h' \frac{\partial u'}{\partial x} \qquad \text{(A6)}$$

It has been previously assumed that the perturbation velocity u and the wall slope h are small, and second order small terms have been neglected in the development of Eq. (12). Thus the velocity derivative at the wall, Eq. (A6), is zero to first order and may be expressed as

$$\left.\frac{\partial Q}{\partial \eta}\right|_{\eta = 1} = 0\ . \qquad \text{(A7)}$$

SOME AERODYNAMIC DESIGN CONSIDERATIONS FOR HIGH BYPASS RATIO FANS

L. H. Smith, Jr.

Group Engineering Div., General Electric Co., Cincinnati, Ohio 45215, USA

Abstract

If the hub/tip radius ratio of a fan is kept low in order to provide high airflow per unit frontal area, it may be necessary to limit the work input at the fan hub to a level substantially lower than that near the fan tip. For some applications, such as the General Electric CF6-6 engine, it is desired to bring the hub energy level up to that of the tip in the fan component through the use of a tandem part-span stage called a quarter stage. The optimum design of such an arrangement involves consideration of special aerodynamic design features and phenomena such as secondary flows due to non-constant blade circulations, diffusion of non-uniform flows, and employment of stator vanes with significant sweep and dihedral. The manner in which these concepts were applied in the design of the CF6-6 fan are discussed, and it is concluded that the employment of the classical aerodynamic design approach to an unusual arrangement can lead to a satisfactory solution.

Introduction

Since the blade speed near the hub of a low hub/tip radius ratio fan is substantially less than near the tip, and since the energy addition process in a turbomachine stage is strongly related to the blade speed, it is natural to consider fan designs that have lower work addition at the hub than at the tip. For aircraft flight speeds in the medium to high subsonic Mach number range, fan bypass stream pressure ratios in the range of 1.5 to 1.8 are required, and these can be obtained satisfactorily over the outer two-thirds of the span of modern single-stage fans that operate with tip speeds of 400 to 500 m/s. It would appear that lower pressure ratios near the fan hub would cause no significant engine penalty, since additional stages in the core stream can be added aft of the fan, either on the fan spool or subsequent spools, to produce the high core-stream pressure ratios employed in modern high-temperature turbofan engines. There are, however, potential problems in fan design for non-constant-energy fans that must be dealt with to obtain an efficient and stable engine compression system. These are best understood through a discussion of the flow patterns that occur in different fan arrangements.

The simplest type of fan arrangement is shown in Figure 1(a). Downstream of the stator vanes, where the flow direction is mainly axial, the static pressure is nearly constant from hub to tip. Therefore, if the fan rotor has added less energy to the flow in the hub region than elsewhere, the lower total pressure near the hub will result in a lower dynamic pressure behind the stator near the hub. This leads to increased velocity diffusion through the stator for this fluid, which could lead to a stalling condition. Because of this tendency for overloading near the stator inner diameter, only small spanwise variations in rotor work input can be used with this type of fan arrangement, with the consequence that either rather large hub/tip radius ratios or rather high tip speeds must be employed.

In the arrangement shown in Figure 1(b), the high loading difficulty at the inner end of the stator when the rotor work input is low there is overcome by the splitter. With it, the annulus area through the inner part of the stator can be contracted, and a reasonable velocity diffusion can be had. High loading on the inner stator does occur with this arrangement, however, for certain engine power settings and transient conditions that cause the bypass ratio to rise and the flow-dividing streamline to appear as shown in the dashed line. And if the splitter nose is close to the trailing edge of the rotor as shown, an increase in rotor hub loading also occurs during such operation. These loading increases may lead to the formation of stable regions of separated flow in the blading, with no discontinuous flow breakdown. Of course, relatively poor flow profiles may be passed on to the core engine at such times.

Figure 1(c) shows an arrangement in which there are several core stream booster stages attached to the fan spool. Substantially reduced fan hub energy levels may be safely employed here because the close-coupled booster rotors can be designed to flatten, or even reverse, the fan rotor work gradient. The increased-bypass-ratio off-design operating modes must now be specially handled, however, to prevent stalling of the booster stages. This can be done by employing a bypass valve (or bleed valve) as shown in Figure 1(c), which can be opened to dispose of the excess flow delivered by the booster stages during high-bypass-ratio off-design operation. Alternatively, the stators in the booster compressor can be made variable, as shown in Figure 1(d), with their angles controlled to match the booster and core compressor flow pumping capacities for all operating conditions. As another alternative, the booster stages can be placed on a separate spool, Figure 1(e), and the individual spool pumping capacities can be matched by spool speed ratio changes.

The schemes shown in Figures 1(c), 1(d) and 1(e) all require an additional degree of engine complexity in one form or another to achieve matching of the compressor components. For some applications it is desired to avoid this complexity, and also to avoid both the increased hub diameter required for the arrangement of Figure 1(a) and the reduced hub pressure ratio and off-design inefficiencies of the arrangement of Figure 1(b). This can be accomplished by employing a fractional-span stage as part of the basic fan. Figures 1(f) and 2 show two means for accomplishing this. In Figure 1(f) the part-span stage is placed ahead of the main rotor. With this arrangement very low values of the ratio of first stage hub radius to second stage tip radius can be obtained, leading to large values of airflow per unit tip-circle area even after an accounting is made of the area blocked by the ring splitter over the first rotor tip. The main disadvantage of this configuration is its acoustics; inlet guide vanes must be employed to support the middle stator, and it is difficult to achieve substantial axial spacings between blade and vane rows without excessive overall length.

In the scheme shown in Figure 2 the fractional-span stage is placed aft of the main rotor. It is obvious that this arrangement is acoustically preferable, and it is this design type that was selected for the General Electric CF6-6 engine. The purpose of this paper is to describe the aerodynamic design features of this fan, to point out the reasons for employing sweep and dihedral in certain of the stator vane rows, and to demonstrate that the classical aerodynamic design approach can be successfully applied to the design of a novel arrangement.

Selection of Levels of Overall Design Parameters For The CF6 Fan

Engine thermodynamic cycle optimization studies carried out to meet the anticipated requirements of the initial CF6 engine led to the selection of a bypass ratio of about 6 and a fan bypass stream pressure ratio of 1.62 for altitude cruise operation. Aerodynamic preliminary design studies aimed at achieving a configuration that would have a good efficiency potential with adequate stall margin resulted in the specification of a tip speed (corrected to $15^{\circ}C$) of 423 m/s, an inlet hub/tip radius ratio of 0.37, and a specific airflow of 202 kg/s m^2 annulus area. Concurrent and interrelated aeromechanical design studies yielded a main fan rotor employing 38 titanium blades having part-span shrouds at the 70% span location.

Further thermodynamic cycle studies indicated that an existing General Electric high performance core engine was well suited to match the 178,000 newton (40,000 lbf) take-off thrust requirement of early CF6 engines if the fan could deliver the same pressure ratio in the core stream as in the bypass stream. This provided an added incentive to use the arrangement of Figure 2, since the hub/tip radius ratio of 0.37 was low enough to prevent the employment of radially-constant work addition in the main fan rotor.

Factors Affecting Design Configuration Details

When designing high performance fluid machinery, the avoidance of boundary layer separation is a major goal. In classical fluid mechanics, such separations are avoided or minimized by shaping the boundary surfaces so that velocity diffusion rates sufficient to separate the boundary layer are avoided. In the field of compressor design these diffusion rate limits are reasonably well known and the problem, then, when designing a novel arrangement like a fan with a fractional-span stage, is to shape the annular boundaries and to select the work distributions so that these limits will be observed.

Early calculations using the circumferential-average (axisymmetric) flow model of Reference (1) to determine meridional streamlines showed that there are two locations in a 1-1/4 stage fan arrangement where careful design control is necessary to obtain acceptable diffusion rates: along the island upper surface near the trailing edge and along the main hub contour aft of the quarter stage. Other items of concern identified during early studies relate to the stability of the ring vortex sheet shed by the quarter stage island, and the ability to properly account for the secondary flows that result from the non-constant circulation distributions in the blading. The manner in which these items affected the design will be taken up in the following sections.

Selection of Spanwise Circulation Distributions

The spanwise distribution of work input for the main fan rotor was affected by the following three considerations. First, there was no point in employing a high loading at the hub because the quarter stage rotor is capable of accepting substantial loading. Also, in the interests of high efficiency, a light loading on the first rotor hub is desirable because it keeps the inner stator hub Mach number low. Second, the loading at the island streamline should be as high as the rotor can safely take in order to minimize the diffusion in the outer outlet guide vanes. The logic here is the same as was described in connection with Figure 1(a); low total pressure at the inner end of a stator vane row leads to high diffusion there. Another reason for keeping the island streamline total pressure up is because this makes the bypass stream total pressure more uniform and reduces the strength of the ring vortex sheet that is shed from the island trailing edge. Although calculations had shown that the loss in propulsive efficiency associated with the employment of a non-uniform jet stream was very slight, there was some concern that the dynamic pressure might approach zero at certain locations in the bypass duct where the static pressure tends to be high if the total pressure were locally too low. There was also some concern that the inherent instability of the ring vortex sheet might lead to turbulence of a moderately large scale and increased losses in the bypass duct. No evidence of this was ever found, however. The third consideration was that it would be best to let the work addition drop off somewhat at the outer wall. This reduces the rotor aerodynamic loading at the location where stalls initiate. It also leads to slightly lower velocities near the outer wall of the bypass duct, which might help reduce duct scrubbing losses.

The distribution of fan rotor exit total pressure that was finally selected based on these considerations is shown in Figure 3, together with the fan discharge distribution. Streamfunction is employed as the display variable rather than radius so that the work distribution of the quarter stage will be more clearly indicated. It is seen that the quarter-stage rotor is designed so that, allowing for anticipated losses in the stator vane rows adjacent to it, a uniform total pressure will be delivered by the quarter stage. The anticipated total-pressure falloffs of the annulus wall and island boundary layers are not shown; the displacement thicknesses of these boundary layers were accounted for in the design process, and the losses that they cause were partially reflected in the design loss coefficient distributions.

The stator circulation distributions resulted from the following considerations.

Both outlet guide vane rows were designed to remove all swirl from the flow. The general level of swirl from the inner stator was chosen to yield a good loading balance between it and the inner outlet guide vanes. This is a secondary, but significant, advantage of the 1-1/4 stage fan arrangement compared with the arrangements of Figures 1(a) and 1(b): the losses in the stator near the hub can be substantially reduced by eliminating the need for the fan stator to remove all, or almost all, of the fan rotor swirl.

The selection of the spanwise distribution of inner stator exit swirl angle was guided by loading and axial velocity distribution considerations. Since the flow leaving the main rotor has a considerably higher total pressure at the island than at the hub, there is a strong tendency for the meridional streamlines to move radially outward when passing through the inner stator. This can be partly offset by allowing the inner stator to discharge the flow with larger swirl at its outboard end than at the hub. Such a swirl distribution is also consistent with the work addition of the rotor that follows; the quarter stage rotor increases the flow swirl much more at its hub than at its tip. In the distribution finally selected, the swirl angle aft of the inner stator varies from 8° at the hub to 18° at the island, measured from the axial direction.

Selection of Outlet Guide Vane Configurations

As previously mentioned, the two regions where the achievement of satisfactory diffusion rates presented the greatest challenge are associated with the outlet guide vanes: (1) the inner end of the outer outlet guide vanes, and (2) the hub surface downstream of the inner outlet guide vanes. The radial distribution of static pressure just aft of the island contributes to both of these difficulties. Although the flow has no swirl at this location, the meridional streamline curvature distribution is such as to cause a high static pressure at the island trailing edge and a low static pressure on the convex hub surface. The high static pressure at the island trailing edge contributes directly to the velocity diffusion required in the outlet guide vanes, and the low static pressure on the hub increases the diffusion required in the transition duct leading to the core compressor.

Various island shapes and locations were studied while attempting to find the best geometry. At this point in the evolution of the design the outer outlet guide vanes were in their final swept position, this having been done to increase their axial distance from the main fan rotor for acoustic reasons, but the inner outlet guide vanes were still radially oriented. These studies showed that the outer outlet guide vane diffusion could be reduced by removing some of the convexity from the upper surface of the island, for this reduced the inlet velocity to the outlet guide vanes. But with the island thickness already reduced to the minimum value consistent with structural integrity, this led to a reduction of the hub radius of the quarter stage rotor, which ultimately led to an undesirable increase in convex hub curvature at the exit of the inner outlet guide vanes. A further outboard placement of the whole island was also studied. The fraction of the total flow that passes through the quarter stage was not a firm design requirement, but it was initially chosen to match that expected to be needed in growth versions of the CF6 engine that would employ the arrangement shown in Figure 1(c). This flow is somewhat larger than the initial CF6-6 core engine flow, a desirable feature because it places the island wake fluid in the bypass stream rather than in the core stream. No advantage was found by the further outboard placement of the island. Apparently, the increased blockage of the annulus area caused by moving an island of fixed thickness to a larger radius is sufficient to nullify the gain of an increased total pressure at the inner end of the outer outlet guide vanes.

No substantial gains were made in overcoming these difficulties until the inner outlet guide vanes were swept and leaned. It had been appreciated from the start that the backward sweep of the outer outlet guide vanes is helpful because their thickness blockage tends to reduce the effective flow area and increase velocities at the island trailing edge. Sweeping of the inner outlet guide vanes has the same effect, but, more importantly, their sweeping places them in a position where they can be used to relieve the radial static pressure gradient that aggravates both difficulties. By leaning them such that their concave surfaces face generally toward the hub, a component of their lift helps to turn the flow radially inward toward the core compressor. Employment of this approach led ultimately to a configuration for which the NACA Diffusion Factor of Reference (2) at the inner end of the outer outlet guide vanes was held to 0.54 and for which the Mach number on the hub aft of the inner outlet guide vanes was kept below 0.60.

Airfoil Design Special Considerations

The same general approach was employed when specifying airfoil shapes for the CF6 fan as has been in use at General Electric since 1959. A detailed circumferential-average (axisymmetric) flow solution was first carried out at the aerodynamic design point using the method of Reference (1). For this solution the calculation grid included several stations inside the main fan rotor and inside the outlet guide vane rows so that their effects upon the meridional streamline pattern would be represented as accurately as possible within the framework of an axisymmetric model. Initially, an island contour was assumed and the forward 90 percent of its chord was specified as a boundary in the flow field. A calculation station extending from the fan hub to the outer casing was placed at the trailing edge of the island; this guaranteed a static pressure match there for the upper and lower island surface streamlines. The island contour and the hub contour were then adjusted slightly until a smooth island resulted. Stations downstream of the island also extended from the hub to the outer casing, matching static pressures across the island vortex sheet. Stations further downstream were interrupted by the main splitter that separates the core flow from the bypass flow. The final meridional streamlines are shown in Figure 2. The radially-inward force component on the flow imparted by the inner outlet guide vanes is reflected in the shapes of the streamlines passing through them.

With the meridional streamlines and swirl velocity distributions thusly established, compatible airfoil shapes were designed. This involved the specification of departure angles* along each meridional streamline at each calculation station in a blade row. For the main fan rotor, the forward parts of the airfoils were shaped so as to keep the suction surface Mach number as low as possible back to the location where the shock from the adjacent blade was expected, consistent with the requirement that no net upstream swirl be induced, and consistent with the attainment of the desired throat area. A program previously conducted under NASA sponsorship on research rotors, reported by Gostelow, Krabacher, and Smith(3), provided data useful for this purpose. Trailing edge angles were selected to match deviation angles calculated from a form of Carter's rule that included an accounting for changes in radius and axial velocity across the blade row, plus an empirical adjustment based on past experience. Calculations of deviation angle perturbations caused by the secondary flow field in the rotor that results from the non-constant circulation distribution employed were made using the method of Reference (4). These showed that the maximum perturbation was a one degree deviation angle reduction, occurring at the hub. This perturbation was not incorporated in the airfoil design, as it was felt to be small and in a favorable direction.

Since the inner stator and quarter-stage rotor operate with moderate subsonic Mach numbers and do not incorporate special features such as sweep, their designs followed conventional lines. Standard airfoil profiles were employed, and incidence and deviation angles were specified according to standard General Electric practice. Secondary flow calculations were also made for these blade rows. For the inner stator the secondary flow caused by the non-constant vane circulation was partially offset by the secondary flow resulting from the entering vorticity generated by the main rotor (circumferentially averaged), with the result that the deviation angle increase at the hub and deviation angle decrease at the island were both less than one degree. For the quarter-stage rotor these effects were additive, and the deviation angle increase at the hub and decrease at the tip were both about 1.5 degrees. Again, these secondary flow perturbations were not included in the original blading designs.

---

*The departure angle is the difference between the circumferential-average flow angle and the airfoil meanline angle. It is equal to the incidence angle at the leading edge and the deviation angle at the trailing edge.

The swept outer and inner outlet guide vanes were designed according to the method presented by Smith and Yeh(5). The blade axes were chosen so as to be approximately parallel to the leading edges of the vanes. For the outer row the blade axis was leaned slightly in the circumferential direction in order to keep the dihedral angle near zero where the vanes intersect the island. The sweep there is 12 degrees. For the inner row the blade axis was leaned substantially so as to accomplish the inward force component described previously. The resulting sweep angles are 27 degrees at the island and -40 degrees at the hub, and the resulting dihedral angles are 23 degrees at the island and -30 degrees at the hub.

Departure angles for the outlet guide vanes were chosen so that the resulting airfoils would approximate standard General Electric subsonic airfoil profiles when viewed parallel to the blade axes. The sweep and dihedral magnitudes in the inner outlet guide vanes were sufficient to justify the calculation and inclusion of the end-effect perturbations of Reference (5). The calculated perturbations were as large as 10 degrees in departure angle at the island and -17 degrees at the hub, both occurring near mid chord. Substantially lower values were calculated at the leading and trailing edges, and since all of the perturbations were calculated to be rather localized near the end walls, the perturbation levels actually used in the blade design were reduced to about 4 degrees at the island and -5 degrees at the hub.

A photograph of the outlet guide vane assembly in a CF6-6 engine is shown in Figure 4.

Performance Demonstrations

The CF6 fan was initially built in 900 mm size for scale model rig testing. The scale model performance program, carried out in the General Electric compressor test facilities at Lynn, Massachusetts, during the spring and early summer of 1968, proved that the 1-1/4 stage concept was sound and demonstrated that the design methods employed were basically satisfactory. Noise tests on a duplicate scale model fan rig at the General Electric Peebles, Ohio, Proving Ground also demonstrated that the fan had excellent acoustic qualities.

Spanwise distributions of total pressure and efficiency measured at fan exit with the fan rig operating at design speed and with a back pressure close to the design value are shown in Figure 5. Each plotted point is based on the average of data taken from sensors mounted in arc rake arrangement, with the sensors spaced across outlet guide vane pitches so as to permit a uniform sampling of a vane passage. The outer seven arc rakes were composed of 12 temperature and 12 pressure elements each. The rakes were constructed such that the odd numbered elements were pressures and the even numbered elements were temperatures. This construction enables pressure and temperature sampling from a common fluid region and minimizes the effects of any gross circumferential variation when computing efficiency. The five outermost rakes spanned three outer outlet guide vane spacings. The remaining two outer panel rakes spanned four spacings. The three arc rakes behind the quarter-stage were of similar construction with six pressure and six temperature elements each. These rakes spanned two inner outlet guide vane spacings.

It is seen in Figure 5 that the desired discharge profiles were closely achieved. Full-scale engine tests carried out later in 1968 generally confirmed these profiles. The engine tests showed, however, that the weakness at the hub of the quarter stage shown in Figure 5 had been eliminated, either as a consequence of small airfoil trim changes, or, more likely, as a consequence of the improved dimensional control that is possible with large hardware.

Total-pressure and swirl-angle profiles measured at the fan rig rotor exit with the fan operating at design speed, but with a slightly increased back pressure, are shown in Figure 6. A cobra-head traversing probe was used to obtain these data. Similar measurements at quarter-stage rotor exit are shown in Figure 7, except that the fan back pressure was slightly less than design when these were taken. The data in Figures 5 and 7 were taken after some trimming changes were made to the original blading. These consisted of an opening of the main fan rotor leading edge near the hub, a closure of the inner stator leading edge at the hub and trailing edge at the island, and an opening of the quarter stage rotor at the hub. Although the need for these modifications was based on tests of the initial configuration, it is interesting to note that the quarter stage blading changes were in the direction indicated by the secondary flow calculations.

The stall line of the fan was found to meet or exceed design predictions at all speeds. Stalls always initiate at the fan rotor tip regardless of speed or bypass ratio. In fact, during the rig test program it was demonstrated that the fan stall line remained essentially unchanged at a bypass ratio of 24, obtained by operating with the core stream throttle nearly closed. Tests with tip radial, one-per-rev, and combination distortion screens indicated that the fan had an adequate tolerance to inlet flow mal-distributions. Because of these favorable results it was possible to safely raise the fan operating line somewhat by closing the bypass nozzle area when trimming the CF6 engine to best meet the needs of McDonnell Douglas DC-10 Aircraft customers.

Acknowledgment

The writer would like to acknowledge the contributions of J. N. Krebs and R. E. Neitzel, who conducted the preliminary design studies and originated the concept of a quarter stage, of R. G. Giffin and G. G. Adkins, who carried out the detailed aerodynamic design calculations, of C. E. Danforth, who directed the aeromechanical design, and of A. P. Adamson and his associates, who were responsible for the detailed mechanical design of the CF6 engine.

References

1. L. H. Smith, Jr., "The Radial-Equilibrium Equation of Turbomachinery," JOURNAL OF ENGINEERING FOR POWER, TRANS. ASME, January 1966, pp. 1-12.

2. S. Lieblein, F. C. Schwenk, and R. L. Broderick, "Diffusion Factor for Estimating Losses and Limiting Blade Loadings in Axial-Flow Compressor Blade Elements," NACA RM E53 D01, 1953.

3. J. P. Gostelow, K. W. Krabacher, and L. H. Smith, Jr., "Performance Comparisons of High Mach Number Compressor Rotor Blading," NASA CR-1256, December 1968.

4. L. H. Smith, Jr., "Secondary Flow in Axial-Flow Turbomachinery," TRANSACTIONS OF THE ASME, October 1955, pp. 1065-1076.

5. L. H. Smith, Jr., and Hsuan Yeh, "Sweep and Dihedral Effects in Axial-Flow Turbomachinery," JOURNAL OF BASIC ENGINEERING, TRANS. ASME, September 1963, pp. 401-416.

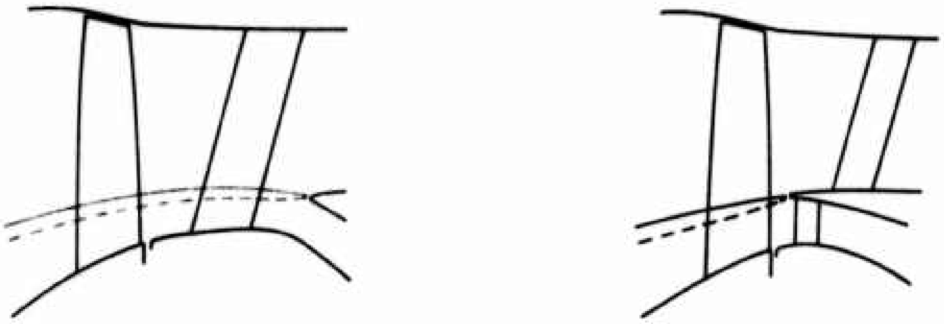

1(a): Fan With Remote Splitter

1(b): Fan With Split Stator

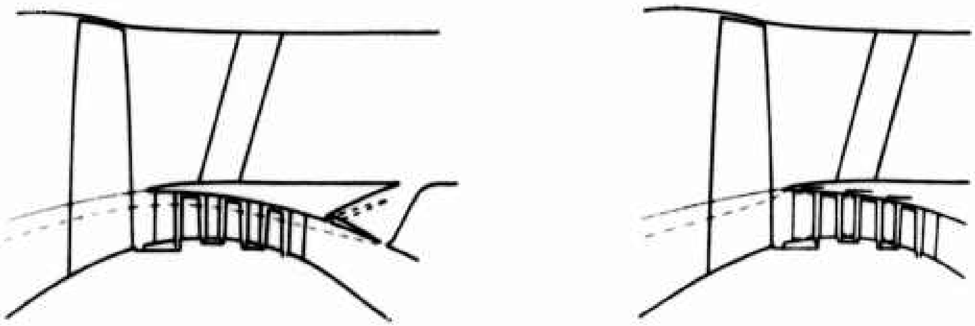

1(c): Fan With Core Boost Stages; Off-Design Matching With Bypass Valve

1(d): Fan With Core Boost Stages; Off-Design Matching With Variable Stators

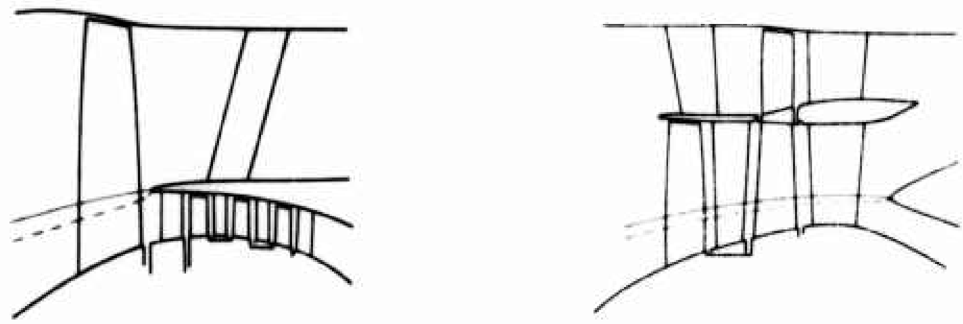

1(e): Fan With Core Boost Stages; Off-Design Matching With Third Spool

1(f): Fractional-Span Fan With Remote Splitter; Short-Span Stage Ahead of Main Rotor

——— **Splitter Streamline, Normal Operation**

- - - - - - - **Splitter Streamline, Off-Design Operation**

FIGURE 1: HIGH BYPASS RATIO FAN ARRANGEMENTS

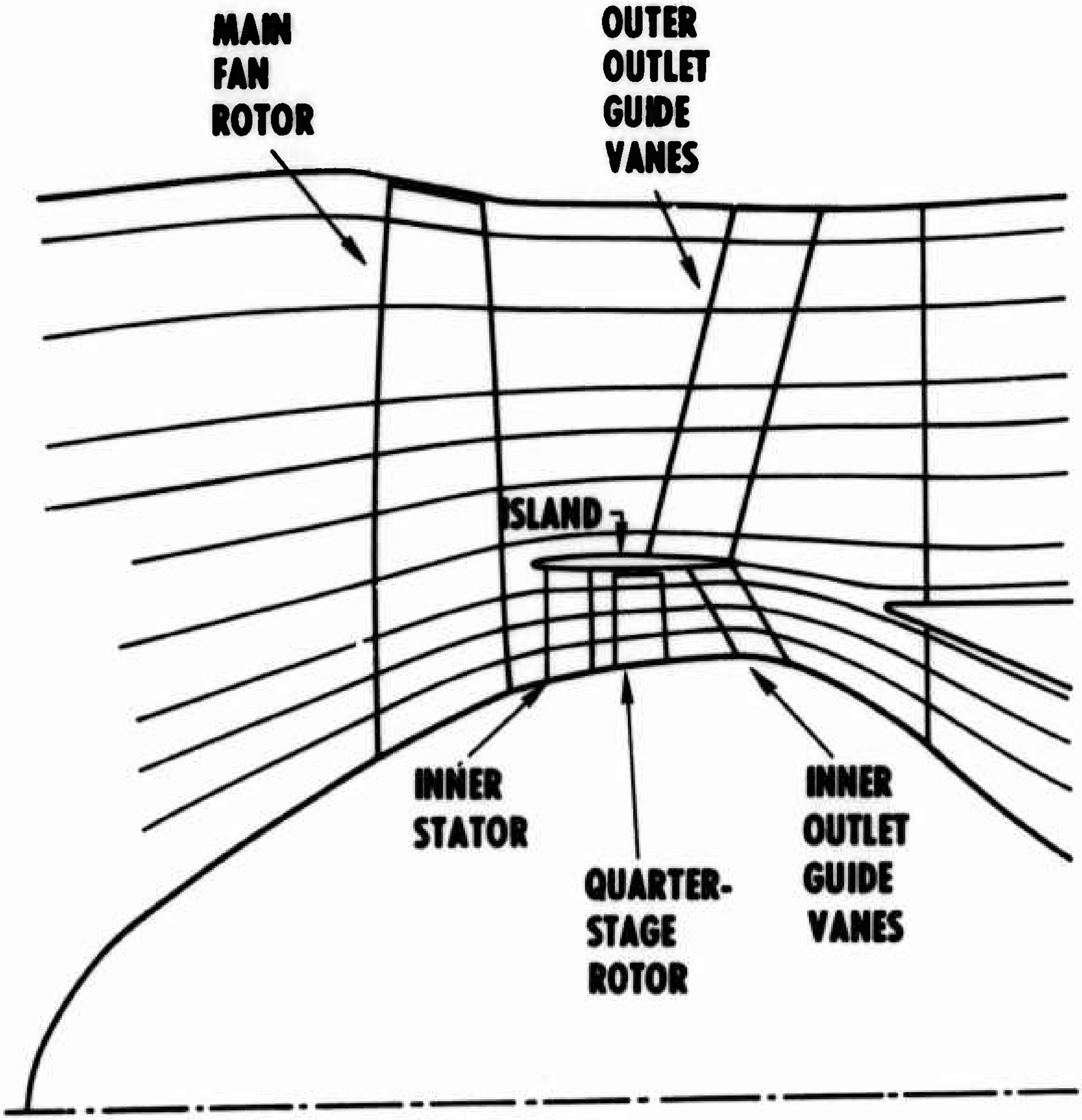
MAIN FAN ROTOR
OUTER OUTLET GUIDE VANES
ISLAND
INNER STATOR
QUARTER-STAGE ROTOR
INNER OUTLET GUIDE VANES

FIGURE 2: CF6-6 1-¼ STAGE FAN

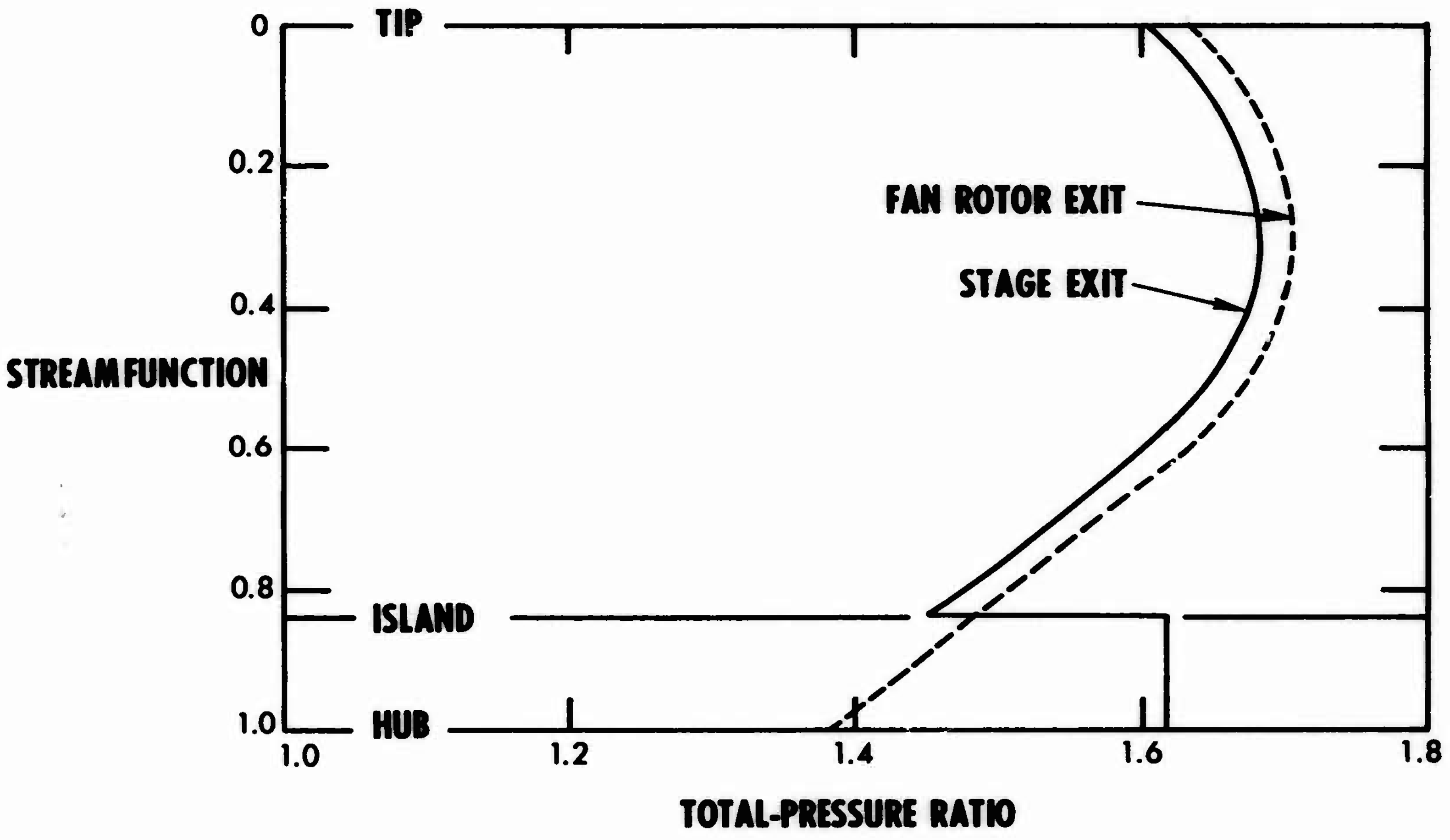

FIGURE 3: CF6-6 FAN DESIGN TOTAL-PRESSURE PROFILES

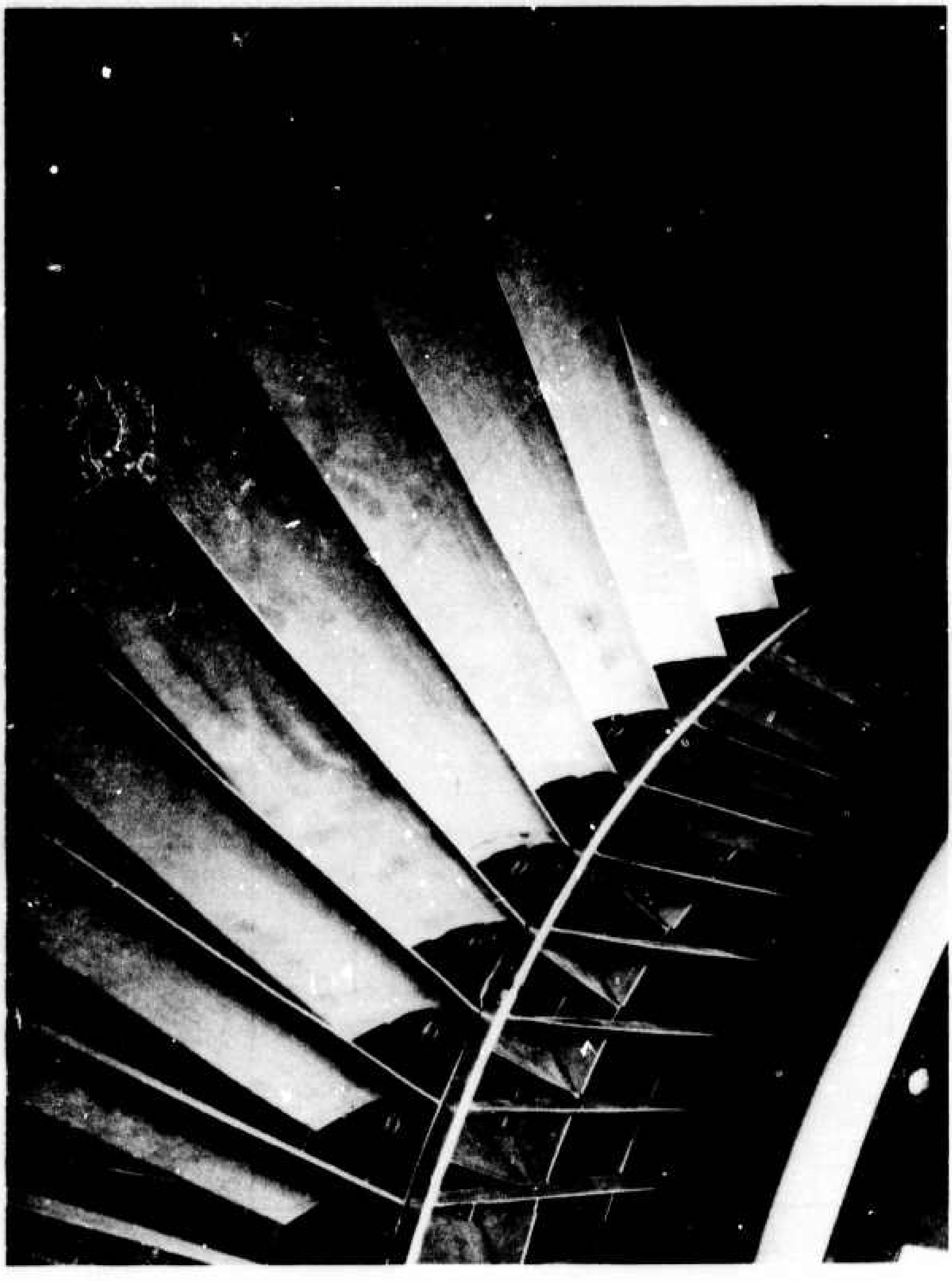

FIGURE 4: CF6-6 FAN OUTLET GUIDE VANES,

VIEWED FROM BYPASS DUCT

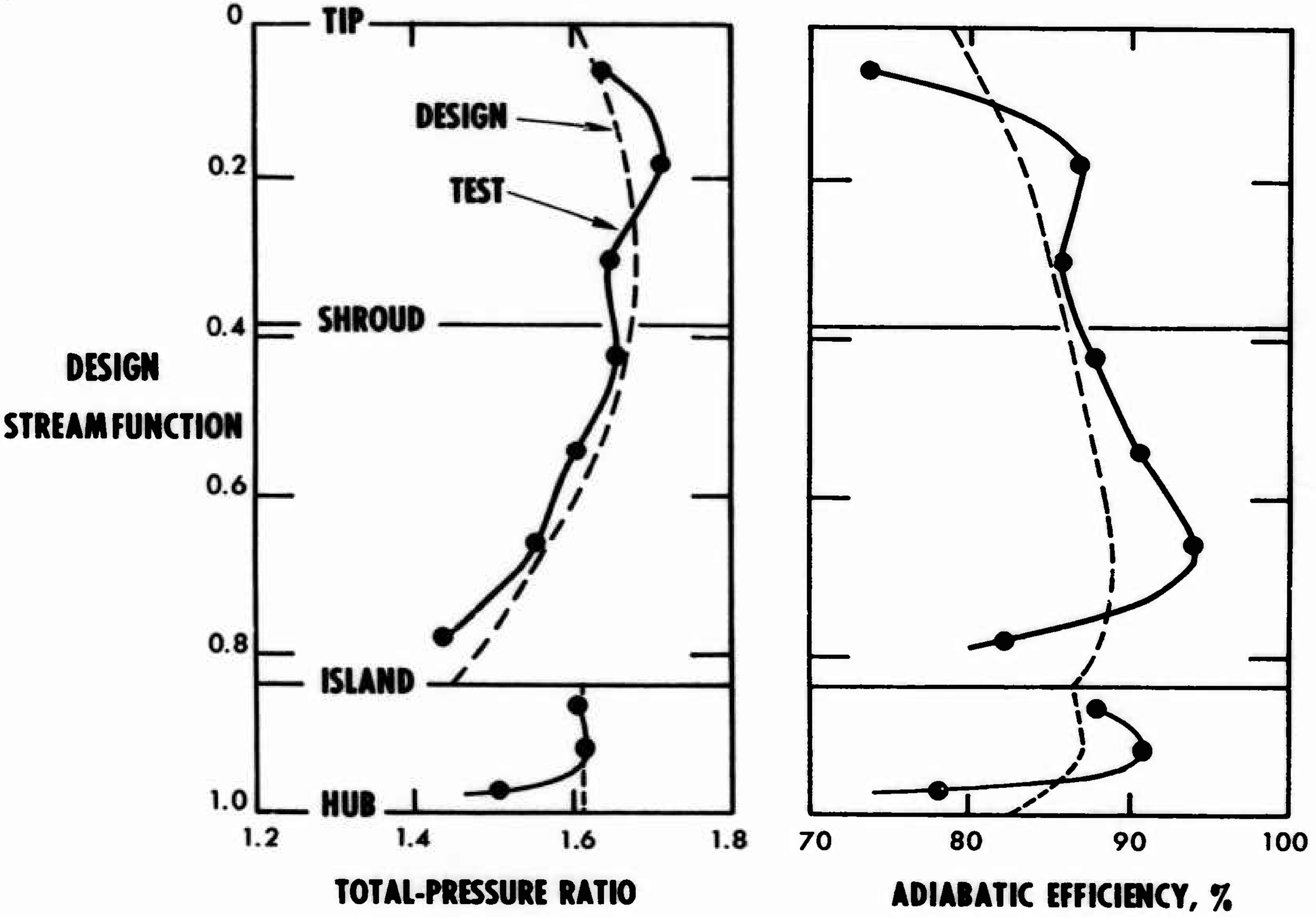

FIGURE 5: CF6-6 FAN RIG EXIT PROFILES

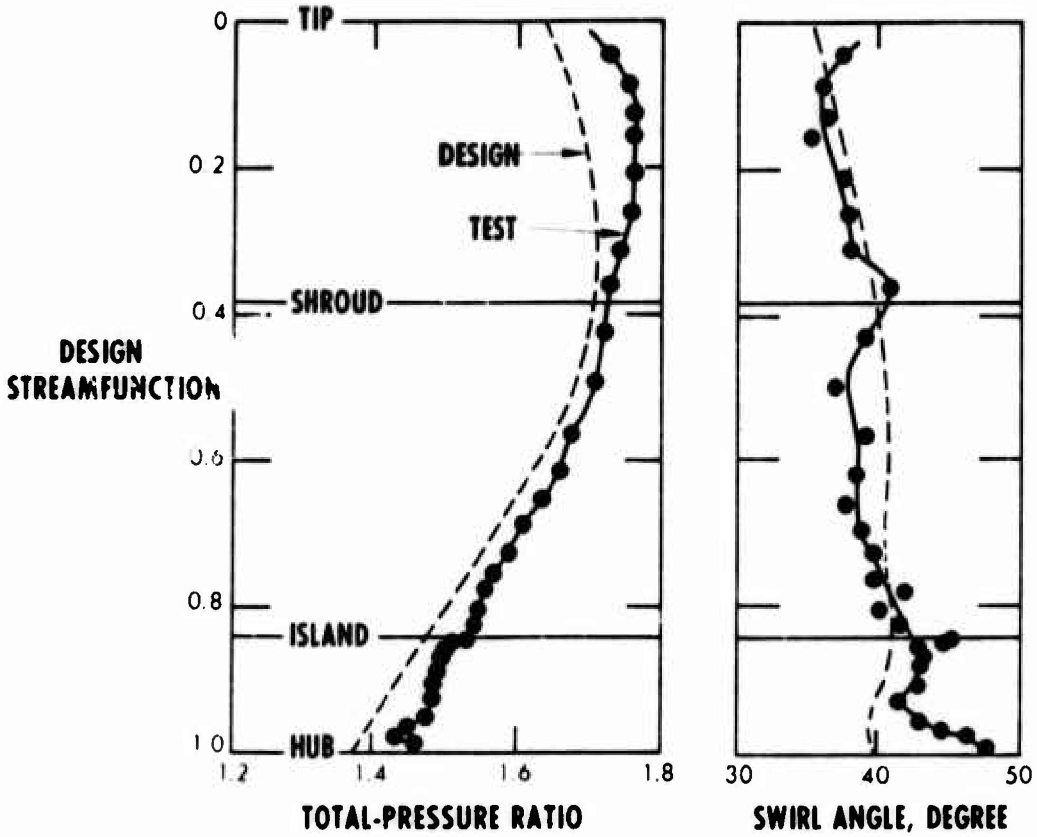

FIGURE 6: CF6-6 FAN RIG MAIN ROTOR EXIT PROFILES

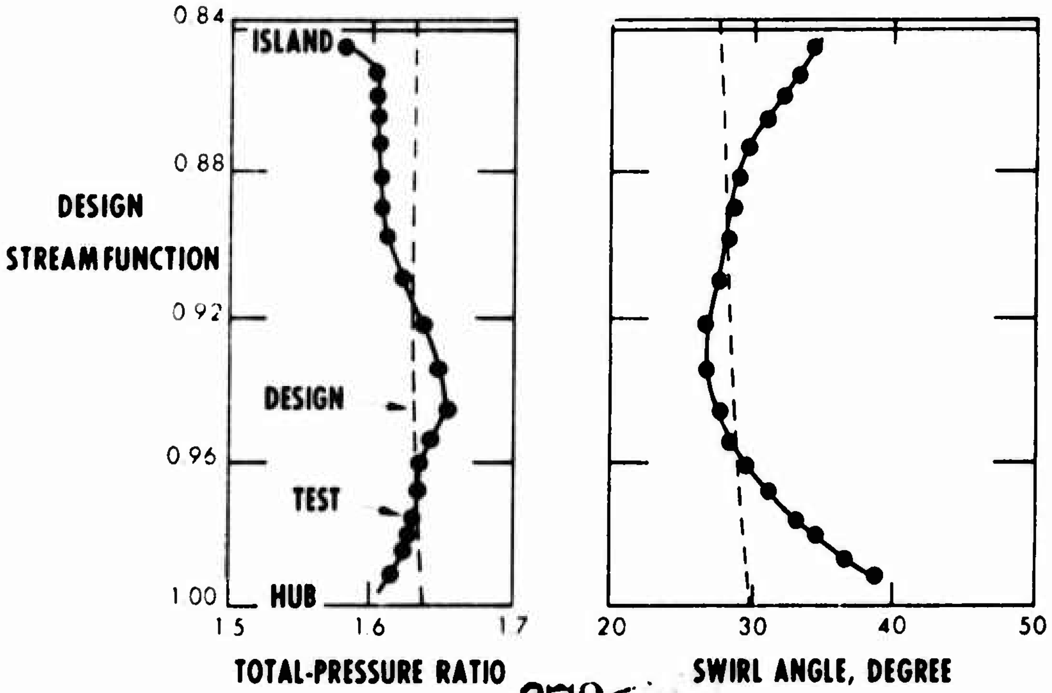

FIGURE 7: CF6-6 FAN RIG QUARTER STAGE ROTOR EXIT PROFILES

A COMPARISON OF THEORETICAL AND EXPERIMENTAL INVESTIGATIONS OF TWO DIFFERENT AXIAL SUPERSONIC COMPRESSORS

H. Simon & D. Bohn, Institute for Jet Propulsion and Turbine Machines, Aachen Technical University. Responsible for this Research Program: Prof. Dr.-Ing. W. Dettmering & Prof. Dr.-Ing. H. Gallus

1. Introduction

According to the conventional definition the supersonic compressor differs from the subsonic or transonic compressor in that the absolute or the relative velocity in at least one of the axial clearances remains supersonic over the entire blade height. Fig. 1 shows different supersonic compressor stages based on this requirement. If we restrict our attention to those stages with especially high load distributions, that is those stages in which rotor and stator have a supersonic upstream flow, there remain three different types (①, ②, ③). All these work with a compression shock in the stator, but differ in the flow of the rotor.

In type ①, the rotor flow is fully supersonic. The static pressure rise takes place essentially in the stator.

Types ② and ③ operate with a shock at the rotor inlet and differ from one another in the stabilisation of the compression shock. In the case of type ②, a minimum of the cross sectional area exists at the rotor blade exit. This reduction in area must be obtained by the hub contour, because deflection causes an additional increase of the cross sectional area. In view of the continuous reduction in the through-flow area from inlet to exit of the rotor blade channel, the supersonic flow cannot get started. In such a rotor type, the shock at the inlet of each blade channel reduces the supersonic velocity to subsonic. The high subsonic flow downstream of the shock is accelerated, reaching ultimately sonic velocity at the rotor exit. The shock at the inlet changes the flow conditions at the inlet and upstream of the rotor, so that the mass flow is reduced in proportion to the through-flow area. Therefore the location of the shock is, within broad limits, determined by channel geometry and the cross section at the rotor exit, but not by the back pressure. This rotor type may be called a rotor with compression shock stabilized by sectional area or, for short, "shock-in-rotor" type.

In the case of the rotor of type ③, the location of the compression shock is determined by the back pressure; the back pressure can at first only influence the shock in the stator, but it seems extremely doubtful whether the shock can be simultaneously stabilized in its optimal position in the rotor. Therefore the investigations were concentrated on the first two stage types.

2. One-dimensional stage calculations

In order to calculate the performance characteristics and estimate the optimal inlet and exit flow conditions for the stages ① and ②, exhaustive stage calculations were made. The following assumptions were maintained:

a) one-dimensional calculations of a representative stream line
b) adiabatic flow ($q = 0$)
c) an ideal gas with constant specific heat ($c_p \neq f(p,T)$)

d) no radial component of velocity in the axial clearances ($c_r = 0$)
e) axial flow upstream and downstream of the stage
f) constant tip radius (r_T = constant)
g) constant stator blade height ($r_{H2} = r_{H3}$)
h) hub-tip-ratio $\nu_1 = r_{H1}/r_T = 0.75$
i) absolute Mach number $M_1 = 0.7 \neq f(r)$

The flow losses in the rotor and stator were estimated after an exhaustive study of literature about investigations of supersonic compressors published up to date, while for the stator the losses were derived from our own tests on supersonic decelerating tandem cascades.

The relative rotor inlet Mach number M_{1r} and the deflection of the fluid in the rotor have a large influence on the energy transfer, and therefore these were chosen as independent variables for the precalculations of the stage design values. In order to get an idea of the possible stage characteristics, the static pressure ratio and the polytropic efficiency of both the stage types have been plotted (Fig. 2 and 3) as a function of the deflection $\Delta\beta$ and of the relative rotor inlet Mach number. The increasing stage pressure ratio with increasing rotor inlet Mach number and deflection can be clearly seen for both the stage types. It is evident that specially high pressure ratios can only be obtained with a strong decrease in efficiency. The curve located on the right in Fig. 2 includes a region of maximum polytropic efficiency ($\eta_{pol} > 0.8$), where pressure ratios between 2.5 and 3.5 were reached. The optimum efficiency shifts with increasing inlet Mach number to smaller deflection angles.

Because of the very flat nature of the efficiency curves in the M_{1r}- and $\Delta\beta$-directions, an optimal point is rather difficult to obtain from Fig. 3. Therefore exhaustive calculations were made to determine for example the influence of the different flow losses in the rotor and stator |2|. Though such studies towards the design of a supersonic compressor stage are mainly qualitative in character, they are nevertheless able to give a clear picture as to the approximate range of design values. In order to make a direct comparison between the two stage types, both the types were designed for a relative inlet Mach number $M_{1r} = 1.4$ and a rotor deflection of $\Delta\beta = 45^\circ$. From these results of the stage calculations, the stage pressure ratio of the shock-in-rotor type (type ②) must be higher in comparison with the values of the supersonic rotor (type ①). Because of the simultaneous existence of subsonic and supersonic regions and of the strong shock-boundary-layer-interactions, the design of the shock-in-rotor type still presents considerable problems.

3. Design of rotors and stators

3.1 Design of the supersonic rotor (type ①)

The aim has been to improve the overall performance of axial flow compressor stages by designing with data obtained from investigations of stationary cascades and from precalculations based on attainments of the flow in rotating blade channels. All experiments on rotating machines being rather costly, the precalculation of the flow through a rotor must take into account, as accurately as possible, the influence of rotations. This permits better interpretation of the subsequent experimental investigations. The supersonic rotor was designed with the help of the characteristic method on stream surfaces |3, 4| and is exhaustively described in |5, 6|. Fig. 4 shows the characteristic networks on mean S_1 and S_2 surfaces. Fig. 5 shows the design of the supersonic rotor.

3.2 Design of the shock-in-rotor type (type ②)

Because of the complexity of the flow in the shock-in-rotor type, no satisfactory calculation method was available, and therefore the design of this rotor has been executed in accordance with the following considerations. In order to enable a direct comparison of the experimental results of both the rotor types, the rotor blade angles of type ② chosen were similar to those of type ①. In determining the blade and hub contours, the following aspects, resulting from cascade and rotor investigations, were especially taken into account:

a) The rotor channel through-flow area should remain constant over a wide range and should have a clear minimum at the exit. The minimum channel area must not come before the exit, as otherwise supersonic flow may occur at the exit and involve other additional losses at the rotor exit. The acceleration of the subsonic flow downstream of the normal shock to sonic values at rotor exit section may be achieved as far as possible in the flow separation region, and this could keep the separation losses to a minimum, perhaps preventing flow separation.

b) To avoid separation in the supersonic region the blade suction surface up to the point of normal shock must have no curvature. An acceleration in this region would be accompanied by higher losses, not only because of the increase of shock losses with higher Mach numbers but also because of the losses arising out of strong shock-boundary layer interaction.

c) To avoid flow separation on the suction surface of the blade profile one must have a very small curvature. On the other hand, a curvature is needed to obtain deflection. Hence, as discussed above, for a given rotor width and deflection a compromise has to be arrived at between the transition region that connects the straight blade inlet and the curvature at the point of maximum camber.

Fig. 6 shows a rotor blade channel based on this concept.

3.3 Design of the stator

One of the main problems in the development of a supersonic compressor stage is the deceleration of the fluid in the stator. Based on the investigations conducted on a supersonic decelerating cascade at this Institute [1, 2], a tandem cascade combination was chosen for the stator. In Fig. 7 a part of the shock-in-rotor type can be seen through the optical window and also the tandem arrangement of the stator.

4. Experimental investigations of the rotors

For the experimental investigations on rotors and stators a supersonic compressor test rig was developed. These have been exhaustively described in [5, 6]. The flow medium was a mixture of Freon (CF_2Cl_2) and air (15 % by volume). Fig. 8 shows schematically the location of the measuring points ahead and behind of the stage. Figs. 9 and 10 show the wall static pressure distributions for different speeds and throttle positions. The distance distribution of the measured length has been represented to scale beneath each diagram. At $n/n_o = 0.38$ it is seen that both the rotors operate subsonically. With increasing speeds the pressure before the rotor also decreases correspondingly. In the supersonic rotor a pressure minimum is established at the rotor inlet. The pressure rise begins first in the region where the characteristic from the hub contour meets the tip. In the region of the rotor, the casing wall pressure distribution calculated according to the characteristic method has been presented in [6]. These pressure distributions show clearly that at design point the flow in the rotor is fully stable and supersonic. In the shock-in-rotor type (Fig. 10), with increasing speeds a compression shock builds up at the rotor inlet which always travels in the rotor channel thereby developing a pressure increase. The characteristic pressure minimum of the supersonic compressor rotor does not occur in this rotor as a result of the compression shock and of the light curvature of the suction side of the blades at inlet.

The bottom-most distributions in the two figures show the casing wall pressure distributions for an unthrottled flow. The values downstream of the rotor are rather low because of the supersonic flow. With increased throttling, a strong compression shock travels upstream, and the pressure distribution upstream of the compression shock remains unaffected. By these measurements it is seen that the condition is the same in both the rotors. The maximum pressures obtained differ from one another only to a small extent.

In order to measure the rotor performance characteristics, tests were conducted at 4 different speeds with different throttle settings and probe measurements made in front of and behind the rotor. The values obtained by probe measurements in the measuring plane S_1 before the rotor indicated very little deviation from design point values because of the undisturbed upstream flow, and hence will not be discussed further.

The following figures 11 to 13 show the values obtained at the measuring plane S_2 behind the rotor with the help of a 5-hole probe. They show a selection of a large number of experimental investigations, which have been exhaustively discussed in [5,6]. In Fig. 11 the diagram on the left shows the radial variation behind the supersonic rotor, and the diagram on the right that for the shock-in-rotor type. The design point values have also been superimposed. Both the rotor types deflect the fluid less than design ($\alpha_2 > \alpha_{2design}$). With increased throttling the measured angle α_2 approximates the design angle α_2. Thereby it has been found that by the supersonic rotor a greater change in angle is obtained than by the shock-in-rotor type. While the fluid in the shock-in-rotor type with strong throttling reaches, on an average, values close to design over the radius, the flow in the supersonic rotor, on the other hand, is strongly deflected. The results of the relative Mach number at the rotor exit are again given in Fig. 12. The supersonic rotor (left) reaches, with unthrottled flow, approximately the design values, while for the shock-in-rotor type (right) the relative Mach numbers are supersonic and not sonic as expected. With increased throttling the relative Mach numbers get reduced. By heavy throttling the design point values are approximately reached in the shock-in-rotor type. Fig. 13 shows the variation of the absolute Mach number M_2 at the rotor exit. In the diagram (left) the values for the supersonic rotor with unthrottled flow lie above the expected values. This implies that the stator, located behind, has an incorrect incidence (see Fig. 11) and also a higher upstream Mach number. Both these effects tend to increase the losses in the stator. In the case of the shock-in-rotor type (Fig. 13, right) it is seen that with unthrottled flow a higher downstream Mach number M_2, than design, is reached. This implies indirectly a higher relative Mach number M_{2r}. By throttling, the exit Mach number in both the rotor types is shifted to less supersonic Mach numbers, corresponding more to the design point. In order to obtain the average values for the rotor performance characteristics the total pressure and efficiency distributions, as well as the mass flows, were integrated from a very large number of probe measurements (Fig. 14). The left diagram shows the performance characteristics of the supersonic rotor. The highest total pressure with the best efficiency at an unthrottled flow is obtained in the vicinity of the design point. The cause of the fall in the total pressure ratio with increased throttling is attributed to the losses arising because of the compression shock. The best values were obtained in the region of the design point with a total pressure ratio of about 3.9 at a total isentropic efficiency of 89 %. The variation of mass flow due to throttling at constant speed was very low. This can perhaps, at high speeds, be attributed to the small variation of the location of the shock waves. At the lowest speed ($n/n_o = 0.72$) a comparably large variation of the mass flow was possible, because of the larger subsonic regions in the rotor. The performance characteristics of the shock-in-rotor type (Fig.14, on the right) show the total pressure ratio variation against mass flow for 4 rotor speeds and 3 or 4 throttle conditions. These values were obtained from calculations based on probe measurements. The average isentropic efficiencies in comparison to the supersonic rotor were somewhat low. These relate to the measured values of deviation from the design point. Besides, somewhat higher losses due to the strong compression shock at inlet and the associated shock-boundary layer interaction are to be expected. At the design speed a total pressure ratio of 3.8 with a total isentropic efficiency of 81 % was reached. As in the supersonic rotor the variation of the mass flow by throttling at constant speed was rather low. But here the shock system at the inlet of the shock-in-rotor type, had a definite influence on the mass rate of flow. At rotor speeds lower than design, the efficiency increased to about 86 %. This is perhaps because of the lower intensity of the shock-boundary layer interaction in the inlet region of the rotor.

7. Experimental results from investigations on a supersonic compressor stage

The described shock-in-rotor type was combined with a supersonic decelerating tandem cascade, which was based on the design of the rotor. This comprised the new supersonic compressor stage. Of the large number of experimental investigations that were made, only a few can be discussed. Fig. 15 shows the blading of the supersonic compressor stage with the rotor on the left and the tandem arrangement on the right. The design of the stator was carried out in accordance with the exhaustively discussed criterion in ref. |2|. At the top edge of the picture are the wall static pressure orifices located along the stage. In comparison to Fig. 10, Fig. 16 shows the static pressure distributions for the different rotor speeds at an unthrottled flow. It shows, that the stator imparts a throttling effect and leads to a strong increase of pressure in the rotor, specially in front of the rotor. The compression shock in the rotor seems to be pushed upstream. This is shown by the earlier increase in the wall static pressures. Comparing the pressure distribution $n/n_o = 1.02$ in Figs. 10 and 16, one finds that because of this retroaction of the stator a pressure increase in the rotor is effected, which would be the same effect when the rotor alone was to be throttled. Because of this retroaction of the stator due to throttling on the rotor, the rotor exit flow angle now matches the stator inlet angle. Within the stator, strong pressure peaks appear because of the possible leading edge and compression shocks in the stator blades. The lower pressure downstream of the stator at higher rotor speeds indicates the possibility of a supersonic flow behind the stator. In Fig. 17 the casing wall pressure distribution for the stage at design speed for different throttle positions has been presented. The bottom-most curve shows the distribution along the stage for unthrottled flow. With increased throttling the strong compression shock shifts upstream, leading to a pressure increase. With maximum throttling the compression shock stabilizes itself in the inlet region of the first row of the tandem cascade, as was expected at design. At the casing a static pressure ratio of 3.7 was attained.

In Fig. 18 the measured static pressures at the hub at design speed for different throttle positions in the stator region have been presented. From the top picture can be seen the location of static pressure orifices at the stator hub. At the bottom of Fig. 18 at the right are presented the measurements obtained from the 13 static pressure measurement points, located near the suction side, while in the figure at the left are the pressure distributions taken of static pressures near the pressure side. With increased throttling, the movement of the compression shock can well be seen. With heaviest throttling, the compression shock reaches its first stable position in the stator. A negligible increase in throttling influences the flow in front of the rotor and leads to an unstable location of the compression shock. In the figures that follow some of the results of the measurement made behind the rotor are presented. Both the diagrams are for the design speed. The presented curves refer to a wear plane and the probe was traversed over one to two blade pitches.

In Fig. 19 the distributions of total pressure, static pressure, Mach number and the total isentropic efficiency for an unthrottled flow are collectively presented. The letters A to E represent the trailing edges of the tandem cascades as represented in the sketch below. The variation of the total pressure ratio (Fig. 19 a) and the Mach number (Fig. 19 c) allow for a clear observation of the wakes. Characteristic for a stator with tandem arrangement are two wakes per pitch, namely the strongly induced wake downstream of the second blade row, and the reduced wake caused by energy exchange with the main stream of the first blade row. In the middle a total pressure ratio $p_{t3}/p_{t1} \simeq 3.4$ is reached. The Mach number M_3 for an unthrottled flow lies in the high supersonic region. This can be explained by the deviation of the flow in the axial direction associated with an area increase. Accompanying this strong acceleration for an unthrottled flow is the low static pressure ratio 1 below (Fig. 19 b). The distribution of the total isentropic efficiency is presented in Fig. 19 d. From the total pressure and Mach number distributions can be seen the associated increased boundary layer losses. The exhaustive probe measurements at different radii helped to determine a final average value of the stage efficiency, hardly over 70 %. In the Figs. 20 a and d the flow parameters for a heavily throttled condition are discussed. By the increase of the pressure behind the stage, the normal compression shock is shifted to the entrance region of the first blade row, where it is stabilised. This curve series of measurements resulted in the hub wall pressure distribution as shown in Curve 2 of Fig. 18 and gives an idea of the position of the compression shock in the stator blades at this throttle setting. The downstream Mach number M_3 lies in the expected range, of about $M_3 \simeq 0.5$. However, the two wakes per blade pitch noticed at the unthrottled flow (Fig. 19 a, c, d) are not perceptible.
The maxima of the stream lines emanating from the suction side of the first blade row practically vanish. This is perhaps the reason for increased losses due to flow separation on the suction side of the first blade row, and this can be very clearly seen from the efficiency distribution of Fig. 20 d. For an average total pressure ratio $p_{t3}/p_{t1} \simeq 3.0$ at a heavily throttled flow a mean value of 70 % was recorded for the total isentropic efficiency. The static pressure ratio p_{t3}/p_{t1} was about 3.2. This value lies somewhat below the static pressure ratio obtained from the wall pressure distributions, $p_3/p_1 \simeq 3.5$ with heavier throttling.

8. Conclusion

In the present paper two different rotor types in combination with a tandem stator cascade, which are practicably suited for a supersonic compressor stage, have been presented. The design of the supersonic rotor was effected with the help of the quasi-three-dimensional characteristic method after ref. |4, 5, 6|. The experimental investigations for these rotor types indicated an overall agreement of the experimental values with the design data.

Because no satisfactory solution for the calculation of the shock-in-rotor type exists, only qualitative aspects were taken into consideration for its design. Both the supersonic and shock-in-rotor type were designed for the same capacity. The experimental values of the shock-in-rotor type showed deviations from the design data. The shock system at the inlet of this rotor as a result of the shock-boundary layer interaction produced an uneconomical boundary layer and the desired reduction in area at the rotor exit was already formed in advance and the flow up to the exit was accelerated to supersonic values. The experimental investigations on the supersonic compressor stage with a shock-in-rotor type and a tandem stator cascade indicated a strong throttling effect of the stator on the rotor. At unthrottled flow, the measured rotor wall pressure distribution was similar to that measured if the rotor alone was heavily throttled. This axial retroaction of the stator resulted in an incidence to the stator approximating design values. For this supersonic compressor stage, a static pressure ratio of about 3.5 was obtained. The total isentropic efficiency at heavily throttled flow was about $\eta_{ts} = 70\%$.

The not entirely satisfactory efficiency values of this supersonic compressor stage are attributed to the flow deviations from design in the rotor. As a result of the thicker boundary layer in the rotor exit region, higher upstream Mach numbers and incorrect incidence angles to the stator were obtained. It therefore follows that with increasing losses in the rotor and stator, the stage efficiency decreases. To increase the stage efficiency, the design of the shock-in-rotor type must be improved and from the experience gained the matching of the stator undertaken. With an improved design of the shock-in-rotor type, which leads to lesser upstream Mach numbers of the stator and a proper matching of the tandem cascade, it is hoped that a better stage efficiency could be reached.

9. References

|1| Dettmering, W. u. B.Becker: Steps in the Development of a Supersonic Compressor Stage. AGARD CP No. 34, 1968

|2| Becker, B.: Untersuchungen an stark umlenkenden Überschallverzögerungsgittern und deren Einsatzmöglichkeiten in der Axialverdichterstufe. Dissertation RWTH Aachen, 1970

|3| Goldstein, A.W.: Axisymmetric Supersonic Flow in Rotating Impellers. NACA Rep. 1083, 1952

|4| Chung-Hua Wu: A General Theory of Three-Dimensional Flow in Subsonic and Supersonic Turbomachines of Axial-, Radial- and Mixed-Flow Types. NACA TN 2604, 1952

|5| Simon, H.: A Contribution to the Theoretical and Experimental Examination of the Flow Through Plane Supersonic Deceleration Cascades and Supersonic Compressor Rotors. Paper No. 73-GT-17, ASME-Gas Turbine Conference, Washington 1973

|6| Simon, H.: Anwendung verschiedener Berechnungsverfahren zur Auslegung eines Überschallverdichter-Laufrades und dessen experimentelle Untersuchung. Dissertation RWTH Aachen, 1973

Figures

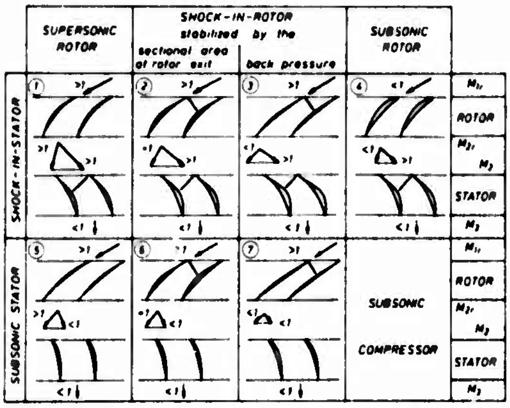
SUPERSONIC ROTOR
SHOCK-IN-ROTOR stabilized by the
sectional area at rotor exit
back pressure
SUBSONIC ROTOR
SHOCK-IN-STATOR
SUBSONIC STATOR
1
2
3
4
5
6
7
>1
<1
SUBSONIC COMPRESSOR
M_{1r}
ROTOR
M_{2r}
M_2
STATOR
M_3

Fig. 1: Supersonic compressor stages

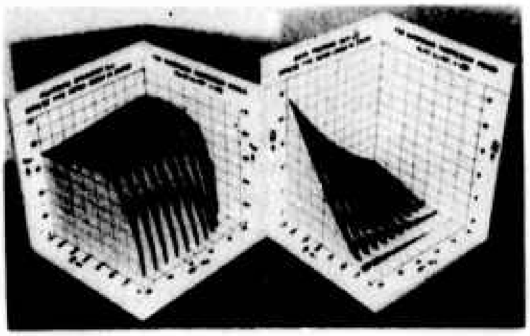

Fig. 2: Calculated performances of the supersonic compressor stage of type 1

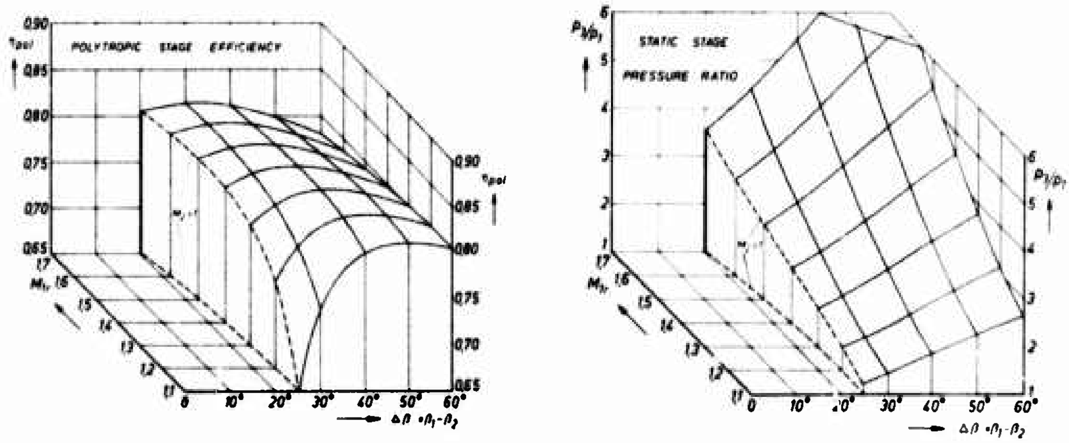

Fig. 3: Calculated performances of the supersonic compressor stage of type 2

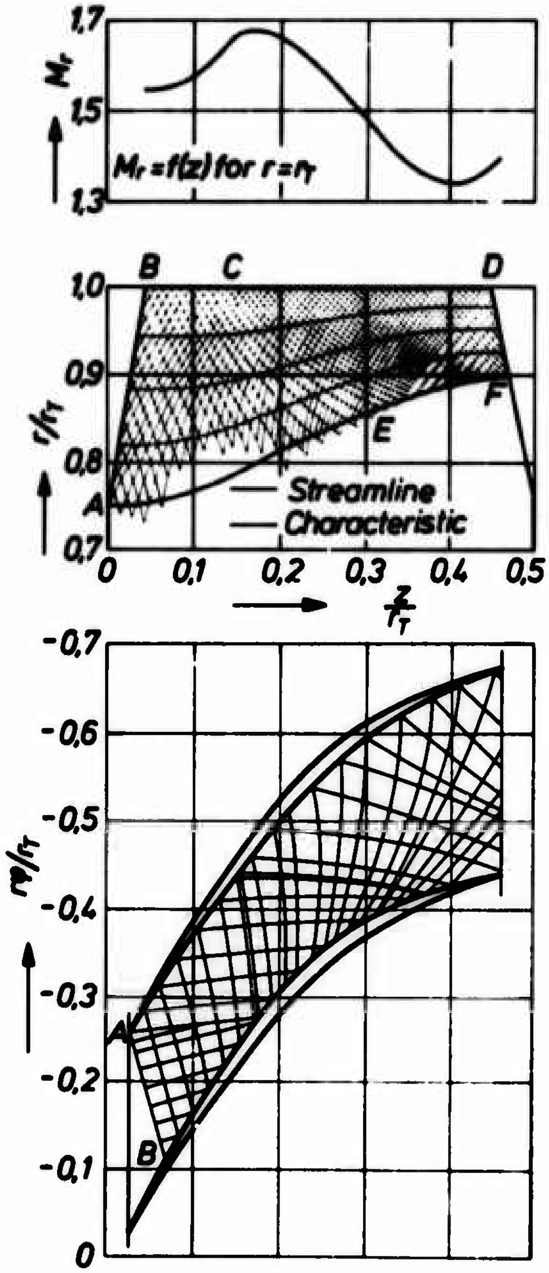

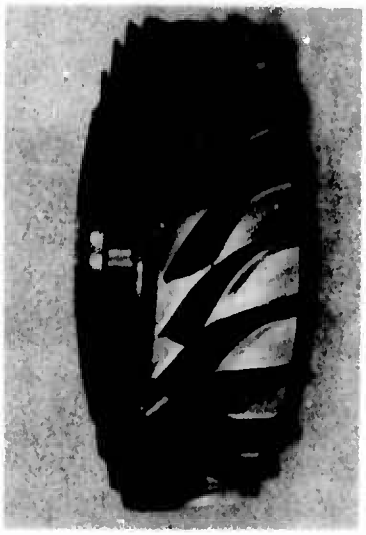

Fig. 5: Supersonic rotor

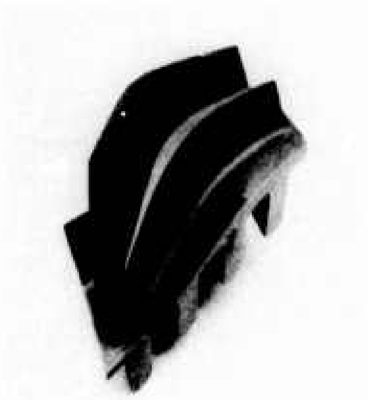

Fig. 4: Characteristic networks on S_1 and S_2 surfaces of the supersonic rotor

Fig. 6: Blade channel of the shock-in-rotor type

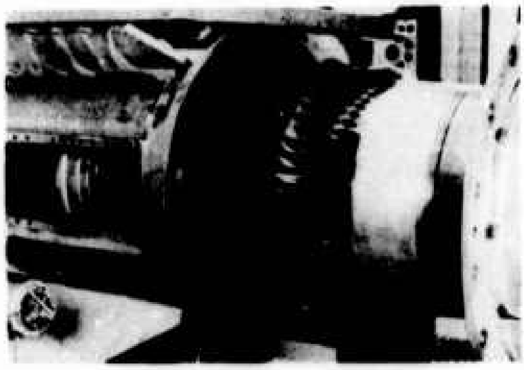

Fig. 7: Supersonic compressor blading (shock-in-rotor type and stator)

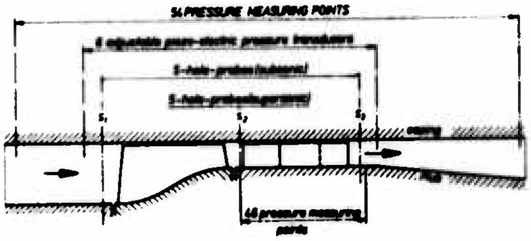
54 PRESSURE MEASURING POINTS
S_1
S_2
S_3
46 pressure measuring points

Fig. 8: Scheme of measuring points

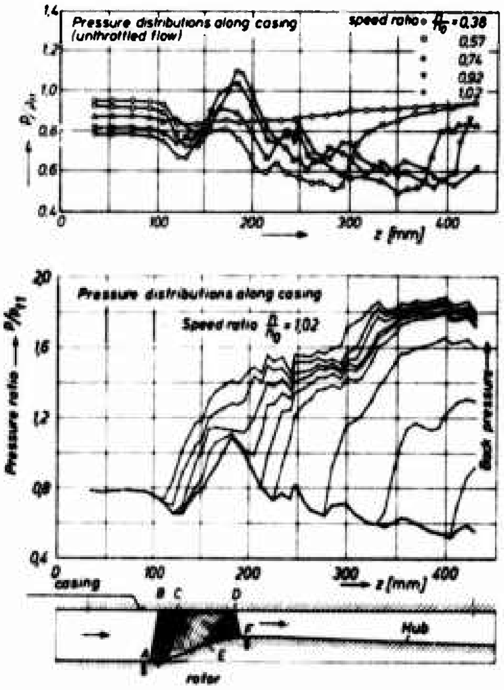

Fig. 9: Pressure distributions at the casing wall (supersonic rotor)

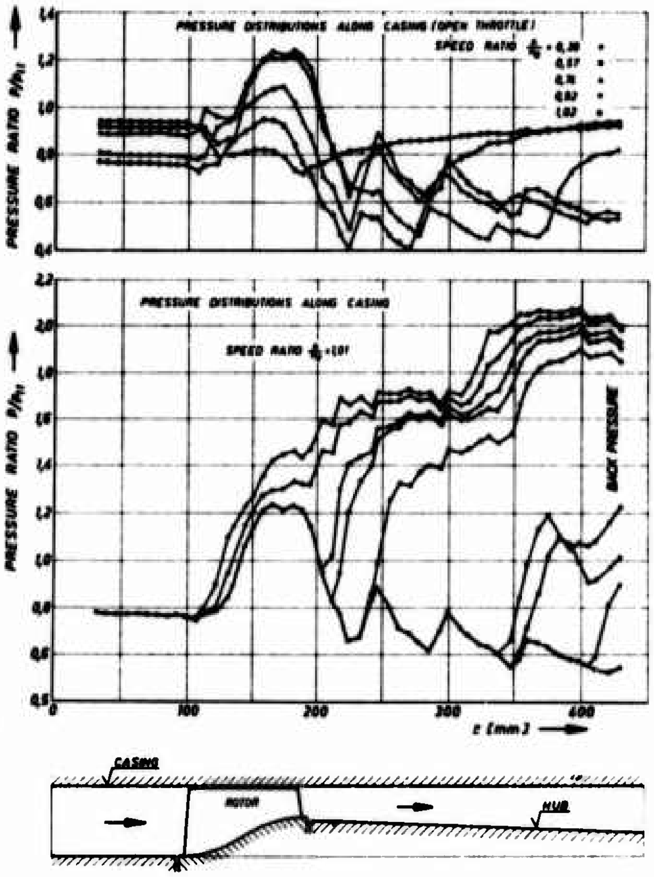

Fig. 10: Pressure distributions at the casing wall (shock-in-rotor type)

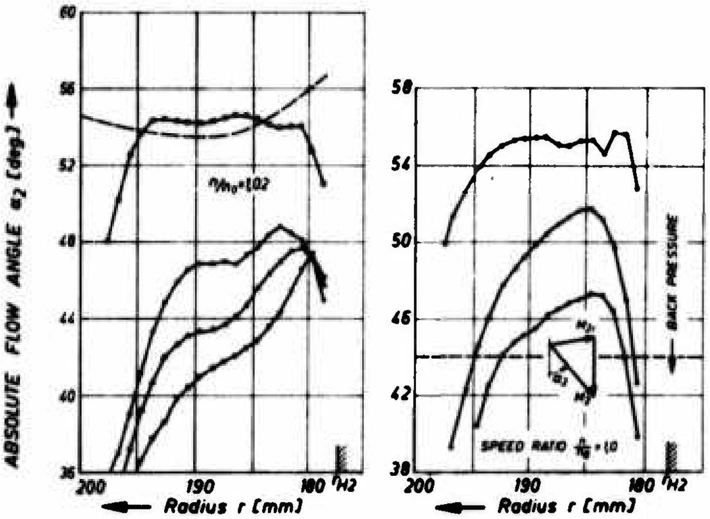

Fig. 11: Radial variation of the absolute flow angle behind the two rotor types at several throttle positions (left diagram: supersonic rotor; right diagram: shock-in-rotor type)

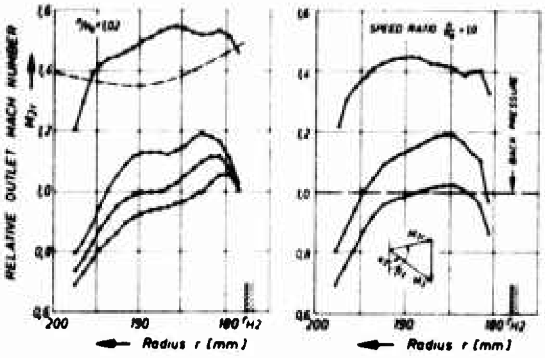

Fig. 12: Radial variation of the relative outlet Mach number behind the two rotor types at several throttle positions (left diagram: supersonic rotor; right diagram: shock-in-rotor type)

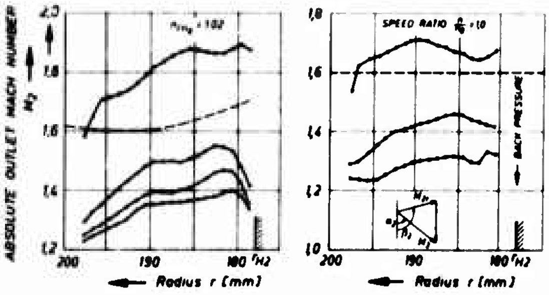

Fig. 13: Radial variation of the absolute outlet Mach number behind the two rotor types at several throttle positions (left diagram: supersonic rotor; right diagram: shock-in-rotor type)

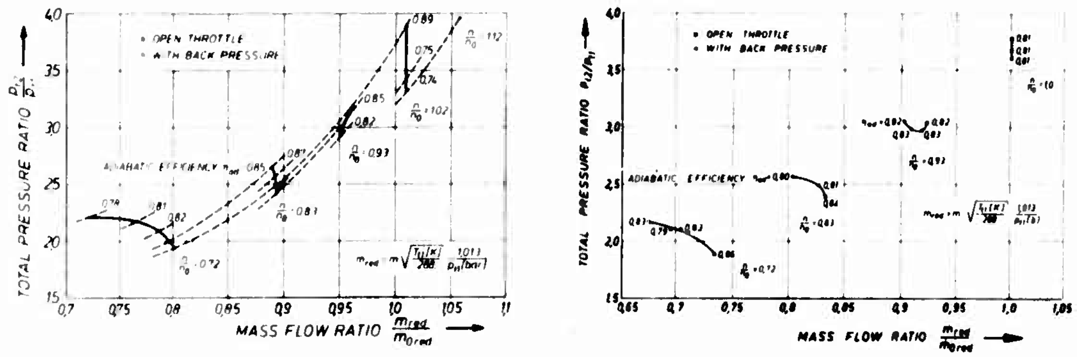

Fig. 14: Performance characteristics of the two rotors alone (left diagram: supersonic rotor; right diagram: shock-in-rotor type)

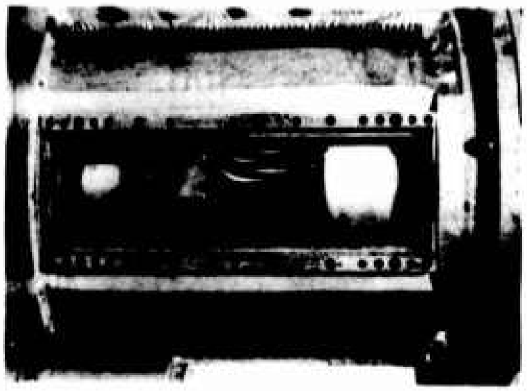

Fig. 15: Supersonic compressor stage

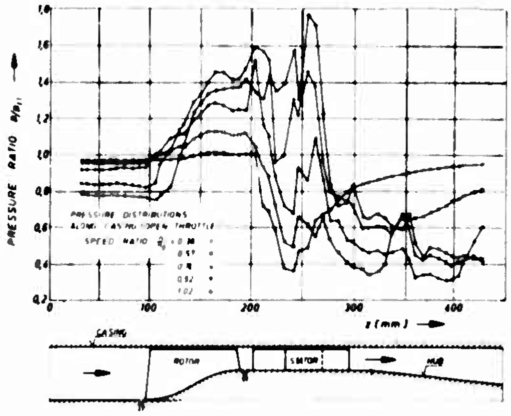

Fig. 16: Pressure distributions at the casing wall at different speeds (stage)

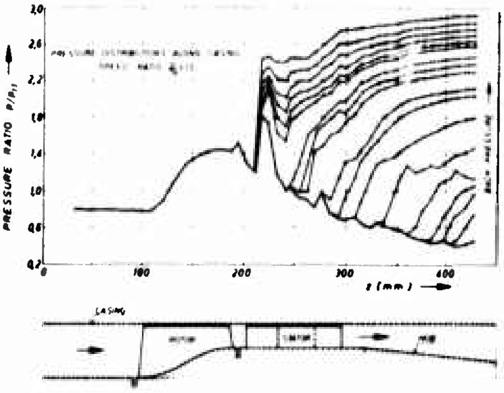

Fig. 17: Pressure distributions at the casing wall at different throttle positions (stage)

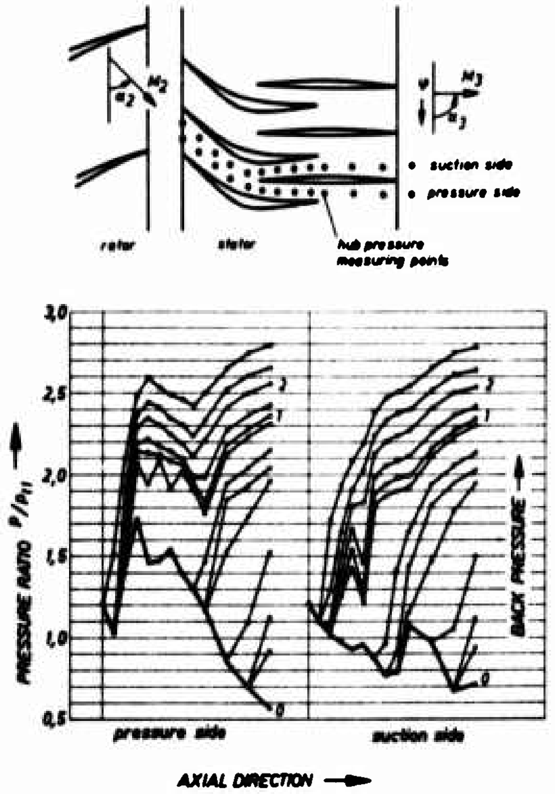

Fig. 18: Pressure distributions at the hub in the region of the stator blades

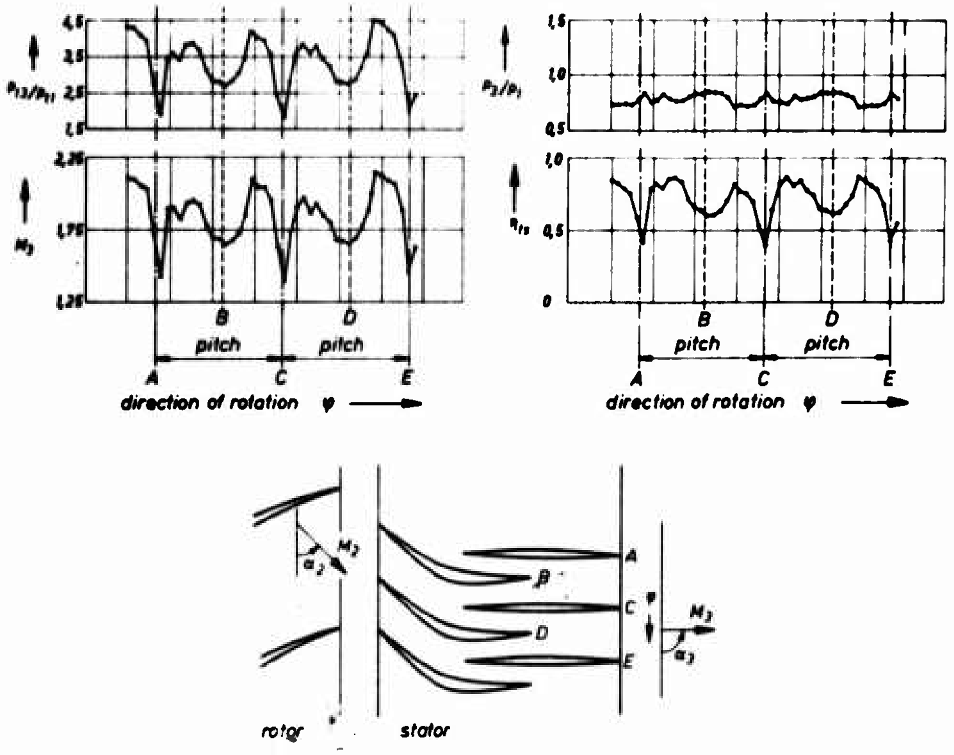

Fig. 19: Flow conditions behind the stator (unthrottled flow)

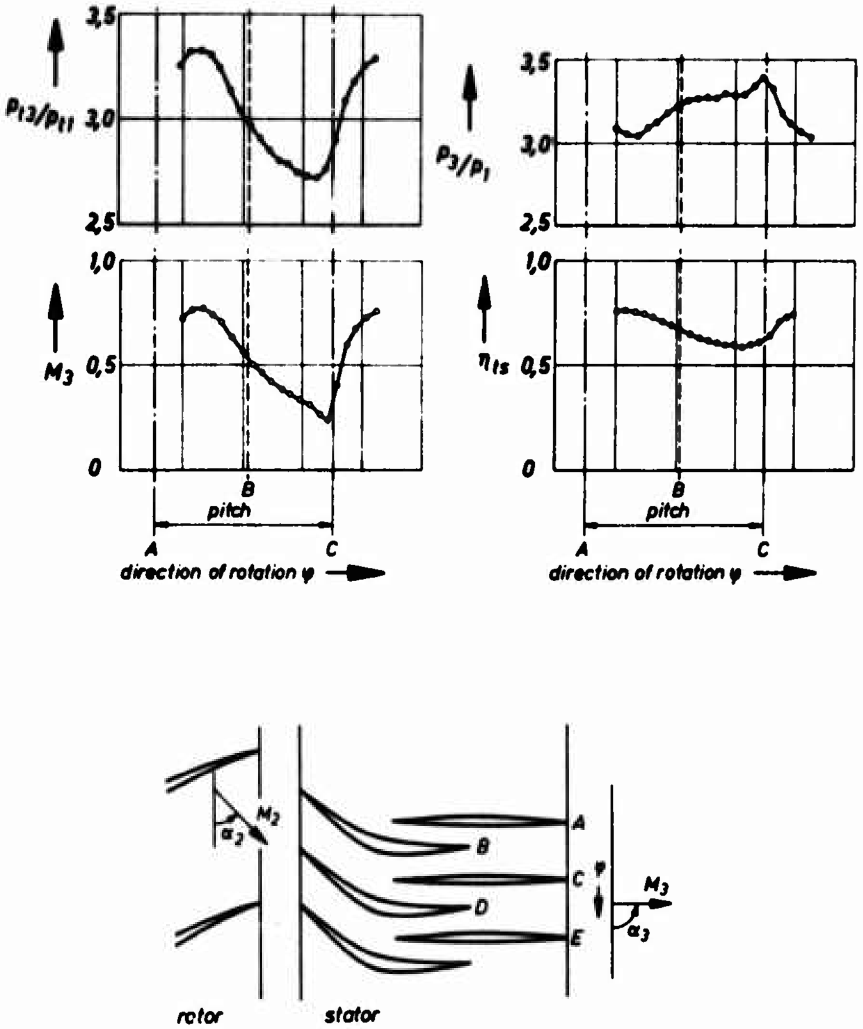

Fig. 20: Flow conditions behind the stator (heavy throttled flow)

THE INFLUENCE OF VISCOUS INTERACTIONS ON THE FLOW DOWNSTREAM OF AN AXIAL COMPRESSOR STAGE

R.C. Lockhart* and G.J. Walker**

*Postgraduate Research Scholar, University of Tasmania
** Senior Lecturer in Fluid Dynamics, University of Tasmania, Hobart, Australia.

ABSTRACT

This paper presents some detailed low-speed observations of the mean and unsteady flow fields downstream of the rotor in a single-stage axial-flow compressor comprising inlet guide vane, rotor and stator rows. Both the mean velocity and the apparent turbulence level are found to vary periodically in the circumferential direction due to interactions between wakes from the inlet guide vane and rotor rows. The rotor wake decay also changes with circumferential position, and cannot be modelled by the wake decay behind an isolated aerofoil or a single cascade as assumed in current blade row interaction theories.

A physical model for the wake-wake interaction process is proposed, and some implications for the design and performance analysis of axial flow turbomachines are discussed.

1. INTRODUCTION

The problem of unsteady flow in axial turbomachines has received an increasing amount of attention in recent years. The reduction of noise and vibration arising from blade row interactions is now one of the most important design considerations, and has a significant bearing on the choice of blade geometry and axial row spacing. There is also greater interest in the effects of periodic flow variations and free stream turbulence on the machine performance, and in predicting the magnitude of unsteady blade forces from measurements of the time-mean flow downstream of a blade row.

Various theoretical analyses have been produced for describing the unsteady response of a blade row to an upstream disturbance, and reviews of these methods can be found in Refs. 1 and 2. But whatever the mathematical model employed, predictions of unsteady effects can be no more accurate than the estimate of the initial disturbance field. It is with the latter problem that this paper is primarily concerned.

For axial row spacings used in practical turbomachines, the viscous wakes of neighbouring upstream blade rows are usually the main source of periodic inlet flow unsteadiness experienced by a following downstream row. Present analytical methods for predicting unsteady blade forces due to these effects rely on experimental data from isolated aerofoil tests to describe the wake decay. This is not an unreasonable model when there is only a single blade row upstream, as Lieblein and Roudebush(3) have found the wakes of isolated aerofoils and single cascades to be generally similar in most respects. Where there are two or more rows upstream, however, the wakes of these rows will interact to produce a viscous flow field which differs markedly from that downstream of a single cascade, and the use of isolated aerofoil data to describe the wake decay is no longer valid.

Consider, for example, the case of an inlet guide vane (IGV) - rotor stage as shown in Fig. 1. Neighbouring rotor blades chop the IGV wakes into segments which are rotated by the effects of blade circulation as they move through the rotor passages. At exit from the rotor row, the initially continuous IGV wakes have been transformed into a street of discontinuous segments. The individual segments are no longer parallel to the local mean flow direction, and they are terminated not by other IGV wake segments but by the wakes of the rotor blades which caused their dispersion. The presence of IGV wakes adjacent to the rotor wakes leads to interactions which can significantly modify the rotor wake decay.

The dispersion of blade wakes in axial machines as outlined above has been described previously by several workers, for example Darrieus (4). Visualisation studies of this phenomenon have been reported by Werlé (5), and observations of the resulting unsteady velocity field have been published by Smith (6). Studies of wake dispersion and related effects undertaken at the University of Tasmania have been described by Boxhall (7), Oliver and Walker (8,9) and Lockhart (10).

The present paper describes some detailed measurements of mean and unsteady flow properties downstream of an axial flow compressor stage. These observations are then used to develop a physical model of the wake-wake interaction phenomenon. In conclusion, some implications for the design and performance analysis of axial turbomachines are discussed.

2. EXPERIMENTAL DETAIL

(a) Research Compressor

The axial flow compressor used in this investigation was designed and built at the Australian Department of Supply's Aeronautical Research Laboratories in Melbourne, and is now operated at the University of Tasmania in Hobart. Only brief details of this machine will be given here: a more complete description can be found in Ref. 11.

Air enters radially through a cylindrical screened inlet 2.13m diameter and 0.61m wide. A flared bend with a $6\frac{1}{4}$ to 1 contraction ratio then turns the flow through 90° into a concentric cylindrical duct with 1.14m outside diameter and 0.69m inside diameter which contains the compressor blade rows. Downstream of the compressor there is an annular diffuser, and a cylindrical sliding throttle at the outlet is used to control the throughflow.

The compressor is a single-stage machine with three blade rows: inlet guide vanes (IGV), rotor and stator. The present tests were conducted with the standard blading configuration of 38 blades in each of the guide vane rows and 37 blades in the rotor, giving a space/chord ratio at mid-blade height of 0.99 and 1.02 respectively; the axial row spacings at mid-blade height were 91mm (1.20c)

IGV-rotor and 80mm (1.05c) rotor-stator. The blades are all 228mm long, with a constant chord of 76mm giving an aspect ratio of 3.0. The blade profile used is the British C4 section (10% chord maximum thickness) on a circular arc camber line. The blade sections were designed to give free vortex flow with 50% reaction at mid-blade height at a flow coefficient (V_i/U_{mb})of 0.76. The blade angles at mid-blade height are as follows:

	β_1 (^{0})	β_2 (^{0})
IGV	0.0	27.8
Rotor	45.0	14.0
Stator	45.0	14.0

Instrument slots in the outer shell of the compressor allow for radial and axial traversing of measuring probes at a fixed circumferential position. The IGV and stator rows are each mounted on rotatable supporting rings to permit circumferential traversing of these blades relative to a stationary probe.

The compressor speed is set by reference to a strobodisc on the end of the rotor shaft, or by a photocell and electronic counter arrangement; timing is by a crystal clock accurate to 1 in 10^6. At 500rpm the speed can be held constant to better than ±1 rpm. The inlet velocity is monitored with a pitot-static tube just upstream of the IGV row and a Betz micromanometer reading velocity head to 0.01mm water.

(b) Measurement Techniques

Hot wire anemometer measurements were obtained with a Disa 55A01 Constant Temperature Anemometer and 55D10 Lineariser; a 55D31 averaging digital voltmeter and 55D35 averaging RMS voltmeter were used to measure the DC and AC components of the lineariser output voltage. The single wire probes (8μm diameter tungsten about 3.5mm long spot-welded to 0.5mm diameter nickel supporting prongs) were aligned with the sensing element along the radial direction of the compressor. The AC component of the lineariser output was displayed on a cathode ray oscilloscope and recorded photographically; the oscilloscope sweep was synchronised with the compressor rotation so that a number of records showing wakes from the same rotor blades could be superimposed. Due allowances for calibration drift and variations in atmospheric conditions were made in reducing the experimental results. The hot wire probes were calibrated in a closed-circuit wind tunnel with a 225mm square by 915mm long working section.

Detailed pressure probe measurements were obtained with a three-hole Conrad-type yawmeter. This instrument was calibrated to allow measurement of total and static pressures, velocity and yaw angle without having to null the difference in side-hole pressures.

All measurements in this investigation were obtained at mid-blade height with a compressor speed of 500 rpm and a flow coefficient (V_i/U_{mb}) of 0.73. The axial and circumferential position of probes relative to the compressor blade rows was measured optically to 0.2mm.

3. FLOW OBSERVATIONS DOWNSTREAM OF THE ROTOR

(a) Nature of Unsteady Velocity Field

Fig. 3 shows some photographic records of velocity fluctuations obtained during a circumferential traverse at an axial distance of 44.5mm downstream of the rotor trailing edge (corresponding to a distance of 0.785 C_R in the mean absolute flow direction, where C_R is the rotor chord). These records illustrate the main features of the unsteady flow field resulting from the dispersion of IGV wakes by the rotor (see Fig. 1) which was discussed previously in Section 1.

Each photograph in Fig. 3 consists of about 30 traces of linearised anemometer bridge voltage fluctuations, which are directly proportional to the local velocity fluctuations; velocity increases upwards. Triggering of the oscilloscope sweep was synchronised with the compressor rotation so that successive traces would show the wakes of the same rotor blades. The temporal variations in fluid velocity shown in these records correspond, to a first approximation, to the spatial variations along the mean streamline passing through the probe position.

Figs. 3(a) - (f) all show marked velocity defects (appearing at intervals of 3.25 ms) which correspond to the passage of rotor wakes. The scatter of traces within these velocity deficient regions is due to turbulent mixing within the rotor wakes. In Figs. 3(b) - (c) the traces outside the rotor wake regions, while showing some vertical scatter, are relatively smooth in nature and give little evidence of turbulent flow: these are essentially regions of potential flow where the temporal variations in ensemble-average velocity are due to the moving potential flow field of the rotor, or to displacement effects and flow curvatures associated with the moving and decaying wake system; the vertical scatter of the traces is due to free stream turbulence or low-frequency unsteadiness from the compressor inlet.

In Figs. 3(d)-(e)-(f)-(a) there are regions outside the rotor wakes in which random velocity fluctuations much larger in amplitude and higher in frequency than the inlet unsteadiness can be seen: these arise from turbulence in the IGV wake segments. In Fig.3(e) the probe is located at the centre of the IGV wake street, and the IGV wake turbulence is continuously evident; but in Figs. 3(f)-(a)-(d) the probe lies toward the side of the IGV wake street and the turbulence is only observed for part of the rotor wake passing period because of the manner in which the IGV wakesegments have been dispersed. Variations in ensemble-average velocity are observed as the IGV wakes pass because of their associated mean velocity deficiency; this is most evident in Figs. 3(e)-(f).

The characteristics of the rotor wake velocity disturbance vary continuously with position relative to the IGV wake street. Moving from Fig. 3(c) to (a), i.e. from the suction to the pressure side of the IGV wakes, there is a continuous decrease in both the width and velocity defect of the rotor wake: the physical process responsible for this change is evidently rather intermittent in nature as the individual velocity traces in Fig. 3(b) appear to fluctuate in shape between those of Figs. 3(a) and (c). The presence of IGV wake fluid adjacent to the rotor wake also seems to modify the shape of the rotor wake velocity disturbance, tending to make the outer edge much more sharply defined. Within the IGV wake street the rotor wake width and velocity defect are both appreciably smaller, being reduced by a factor of about two from their maximum values outside the street.

(b) Mean Velocity and Apparent Turbulence Level Measurements

(i) Introduction

Fig.4 shows the circumferential variation of time-average velocity and apparent turbulence level obtained from hot wire anemometer measurements at five axial stations downstream of the rotor. The measuring positions range from $x^1/C_R = 0.055$ to 1.10, where x^1 is distance from the rotor trailing edge in the mean absolute flow direction and C_R is the rotor chord; the stator leading edge at mid-blade height is at $x^1/C_R = 1.41$. The circumferential position is specified by y^1/s_{IGV}, where y^1 is the distance from the centre of the IGV wake street (measured from the pressure side towards the suction side) and s_{IGV} is the blade spacing in the inlet guide vane row; the origin for y^1 is determined from the unsteady flow records as the position where the IGV wake turbulence component appears to remain nearly uniform with time. The range of y^1/s_{IGV} over which IGV wake turbulence is evident has been marked "IGV wakes" in Fig. 4 and the region external to this where the velocity traces between passing rotor wakes are essentially free of IGV wake turbulence has been marked "pure rotor wakes".

Throughout each traverse, the difference in circumferential settings of the IGV and stator rows was maintained constant to keep each stator blade in the same position relative to the neighbouring IGV wake streets. Traverses were made at all five axial stations with the stator leading edges at mid-blade height lying roughly midway between the neighbouring IGV wake streets ($y^1_S/s_{IGV} = 0.52$); at the station furthest downstream ($x^1/C_R = 1.10$) the measurements were repeated with the stator leading edges at mid-blade height lying near the centre of the IGV wake street ($y^1_S/s_{IGV} = 0.02$).

(ii) Velocity measurements

The curves of time-mean velocity plotted in Fig.4 have been corrected as far as possible for changes in velocity associated with the upstream potential flow field of the stator. This was done by subtracting the velocity variations at the various measuring stations as obtained by Oliver (12) from a potential flow calculation for the stator row; the calculation assumed a steady, two-dimensional, uniform inlet flow and neglected the presence of stator blade boundary layers and wakes. The residual values of velocity (denoted by V) in Fig. 4 have been non-dimensionalised with respect to the circumferential mean velocity $\overline{V}$ to eliminate variations between different traverses arising from wall boundary layer growth and blade wake decay.

The curves of $V/\overline{V}$ in Fig. 4 all vary regularly with y^1/s_{IGV} with a peak-to-peak amplitude of around 2%. The minimum value of $V/\overline{V}$ occurs around $y^1/s_{IGV} = 0.95$, close to the centre of the IGV wake street. The drop in $V/\overline{V}$ on entering the IGV wake street is clearly evident on one side, around $y^1/s_{IGV} = 0.8$, but not on the other: this is partly due to the asymmetrical shape of the dispersed IGV wake segments and partly due to the way in which $V/\overline{V}$ varies outside the wake street.

Even after subtracting the effect of the IGV wake disturbance, the curves of $V/\overline{V}$ would still exhibit a regular variation of roughly sinusoidal form with a maximum around $y^1/s_{IGV} = 0.3$ and a minimum around 0.6. There is a notable tendency for the velocity to increase further around $y^1/s_{IGV} = 0.3$ and decrease further around 0.6 with increasing distance downstream of the rotor.

Changing the relative circumferential settings of the IGV and stator rows by $0.5s_{IGV}$ produces a significant change in the (corrected) distribution of $V/\overline{V}$ at $x^1/C_R = 1.10$, the station closest to the stator leading edge. Part of this change may simply be due to inaccuracies in the correction applied for the stator potential flow field; however, it is considered that the effect is largely a genuine one reflecting changes in the viscous flow field upstream of the stator row produced by the stator pressure field, and vice versa.

(iii) Apparent turbulence level measurements

The apparent turbulence level Tu is defined as the ratio of the RMS velocity fluctuation (measured by the radial hot wire probe) to the local time-mean velocity. The term "apparent" turbulence level has been chosen because the observed velocity fluctuations are actually the sum of a periodic unsteadiness and random turbulent fluctuations. This problem has been discussed by Evans (13) who measured the relative magnitudes of the unsteady and turbulent velocity fluctuations in an axial flow compressor by ensemble averaging techniques.

The variations in Tu shown in Fig. 4 are even more striking than those in $V/\overline{V}$. Nearest the rotor trailing edge (at $x^1/C_R=0.055$) there is already a marked circumferential variation in Tu, with the minimum value occurring within the IGV wake street and the maximum value occurring in the pure rotor wake region. A local minimum in the curve is seen to develop near $y^1/s_{IGV}= 0.2$, and the value of Tu around this position falls very rapidly with increasing x^1/C_R; by $x^1/C_R = 0.225$ this local minimum has become the overall circumferential minimum value. But the most remarkable feature of these measurements is that the maximum value of Tu remains essentially constant with increasing x^1/C_R; the maximum is located within the pure rotor wake region and moves steadily towards the suction side of the IGV wake street with increasing x^1/C_R.

At $x^1/C_R = 1.10$, the circumferential maximum value of Tu is just over twice the minimum value. It should be noted that the minimum value of Tu occurs towards the pressure side of the IGV wake street around $y^1/s_{IGV} =$ 0.2-0.3, where the value of $V/\overline{V}$ is increasing with x^1/C_R and the rotor wake disturbance is at a minimum (see Fig. 3(a)); the maximum value of Tu occurs towards the suction side of the IGV wake street around y^1/s_{IGV} =0.5-0.6, where the value of $V/\overline{V}$ tends to fall as x^1/C_R increases and the rotor wake disturbance is a maximum (see Fig. 3(c)).

Circumferential movement of the stator blades relative to the IGV wake streets can produce changes of several percent in the values of Tu at $x^1/C_R = 1.10$ (about 30% chord streamwise distance in front of the stator leading edge). The apparent turbulence level is increased in the neighbourhood of the stator stagnation streamline and decreased near the centre of the stator passage: a possible explanation is that the velocity defect of an approaching wake is amplified as it enters the region of strong deceleration near the stagnation streamline, and diminished in the region of accelerating flow near mid-passage.

(c) Decay of Apparent Turbulence Level Downstream of the Rotor

Fig. 5 shows the variation of Tu with x^1/C_R for several different values of y^1/s_{IGV}. Changes in the circumferential maximum value of Tu and the local minimum value in the pure rotor wake region around y^1/s_{IGV} = 0.2- 0.3 have also been plotted.

The rate of decay of apparent turbulence level with distance downstream of the rotor is seen to vary widely with position relative to the IGV wake street. The most rapid decay is observed around $y^1/s_{IGV} = 0.33$, where the rotor wake disturbance is at a minimum. At $y^1/s_{IGV} = 0$ the rate of decay is much lower, and at $y^1/s_{IGV} = 0.67$ the value of Tu is actually increasing with distance downstream of the rotor. The latter result is quite the reverse of the normally expected trend for wakes to decay with distance downstream of a body: in these circumstances the use of isolated aerofoil data to describe the rotor wake behaviour is clearly inappropriate.

(d) Flow through the Stator Row

Fig. 6, taken from Lockhart (10) is a typical diagram showing the instantaneous location of the various wake regions through the stator row for a particular blade geometry. This diagram was constructed from photographic records of the unsteady velocity field similar to those of Fig. 3. The flow pattern downstream of the stator is more complex than that downstream of the rotor due to the presence of the stator wakes and the additional viscous interactions which occur through the stator row. The relative flow within the rotor wakes discharges fluid into the stator pressure surface boundary layer and entrains fluid from the stator suction surface boundary layer; the latter phenomenon explains the absence of any discontinuity in the viscous flow region near the suction surface.

Fig. 7, also taken from Ref. 10, shows the circumferential variation in total head at a fixed distance downstream of the stator for several different relative circumferential settings of the IGV and stator rows. Neglecting the total head defect within the stator wakes, the total head is seen to vary in a roughly sinusoidal manner over a range of around 5% of the stage total head rise. The maxima and minima in total head always lie in the same positions relative to the IGV wake street, which correspond respectively to the locations of maximum and minimum time-mean velocity $V/\bar{V}$ plotted in Fig. 4. Changing the relative circumferential settings of the IGV and stator rows alters the amplitude of total head variation outside the stator wakes by less than 20%: evidently the viscous interactions within the stator row contribute relatively little to the variations in time-mean flow properties at the stator outlet. In particular, there is no general tendency for rotor wake fluid to accumulate at the stator pressure surface as observed by Kerrebrock and Mikolajczak (14) in studies of a single rotor-stator stage where wake-wake interactions downstream of the rotor were absent. Although an accumulation of rotor wake fluid at the stator pressure surface can be seen in Fig. 7, this has resulted mainly from wake-wake interactions upstream of the stator.

4. PHYSICAL MODEL OF WAKE-WAKE INTERACTION

The significant streamwise changes in the circumferential distribution of time-mean velocity and apparent turbulence level downstream of the rotor in the research compressor are clearly associated with the tendency of fluid within the rotor wakes to collect near the suction side of the IGV wake street. The measured streamwise changes in $V/\bar{V}$ are similar in magnitude to those expected from the streamwise changes in rotor wake displacement thickness determined from the unsteady flow records.

Two main processes appear to be responsible for the local accumulation of rotor wake fluid. These are:

(i) the flow restriction associated with the reduced width and velocity defect of the rotor wakes within the IGV wake streets, and

(ii) distortions of the rotor wake boundaries produced by relative flows within the adjacent IGV wake segments (see Fig. 2). The magnitude of this effect should depend on the width and velocity defect of the IGV wake, and on the rotor blade lift (which determines the rotor blade circulation and the degree of IGV wake dispersion).

Some of the circumferential variations in rotor wake properties tending to restrict the cross-stream transport of rotor wake fluid could have arisen from viscous interactions within the rotor row itself: IGV wake-rotor blade boundary layer interactions could arise from periodic changes in the instantaneous pressure distribution over the rotor blades, and from changes in shear stress and turbulence level at the outer edge of the boundary layer as the IGV wakes are convected past. The remaining circumferential variations in rotor wake properties must have been due to direct interactions between the IGV wakes and rotor wakes.

The behaviour of a boundary layer growing under a turbulent free stream has been studied by Charnay et al (15) and Evans (13): the turbulence was found to produce a fuller velocity profile with a lower wake component, thus making the boundary layer more resistant to separation. The behaviour of a wake in a uniform turbulent shear flow was examined by Ahmed et al (16) who found that the wake grew slower on the side where the velocity gradient within the wake was opposite in sign to that of the external flow:

a plausible explanation for this behaviour is that large mixing eddies reaching outside the wake experience a reduction in turbulent energy when the local velocity gradient changes sign.

The processes described above provide at least a partial explanation for the observed variations in rotor wake properties near the centre of the IGV wake street. Here the vorticity and velocity gradients in shear layers of the adjacent IGV and rotor wakes are opposite in sign, and mixing of fluid between these layers will tend to reduce the rotor wake width and sharpen the boundary of the rotor wake velocity disturbance. The larger mixing eddies within the adjacent IGV wakes might also enhance the mixing of fluid between shear layers on either side of the rotor wake, and so accelerate the rotor wake decay.

Not all of the variations in mean velocity and apparent turbulence level downstream of the rotor can be explained in terms of viscous interaction effects. The residual variations must be due to potential flow effects associated with fluctuating lift on the rotor blades. Horlock and Daneshyar (17) have shown that lift fluctuations may produce periodic circumferential variations in time-mean flow properties downstream of a rotor row in an axial turbomachine; this result has been confirmed by Henderson (2) who used time-mean total pressure measurements to estimate the magnitude of lift fluctuations on a rotor subjected to periodic inlet flow distortions. In the present investigation, the unsteady flow records obtained close to the rotor trailing edge do show evidence of the rotor circulation varying with circumferential position relative to the IGV wakes, and this is mirrored by the similarity of the mean velocity and apparent turbulence distributions at $x^1/C_R = 0.055$ (see Fig.4).

5. DISCUSSION AND CONCLUSIONS

(a) Performance Measurements

The present study has shown that wake-wake interactions downstream of a low-speed IGV-rotor stage can produce circumferential variations in time-mean velocity and stagnation pressure similar in magnitude to those arising from other effects such as unsteady blade lift. In turbines or high Mach number compressor stages the local accumulation of wake fluid associated with wake-wake interactions should lead to variations in time-mean stagnation temperature as well. It is therefore possible to obtain non-axisymmetric distributions of stagnation pressure and temperature downstream of both rotor and stator rows in a multi-stage machine, and the circumferential variation of these quantities should always be determined if accurate performance measurements are to be obtained.

Kerrebrock and Mikolajczak (14) have developed a method for predicting the viscous losses of rotor blades in a single rotor-stator stage from measurements of the stagnation temperature distribution at the stator outlet. The present study indicates that this analysis will be inapplicable in a multi-stage machine, as the variations in mean flow properties produced by wake-wake interactions upstream of the stator will tend to dominate over those due to intra-stator transport of the rotor wakes.

Viscous interaction effects should also be considered when using the procedure of Henderson (2) to estimate the unsteady lift on a rotor from measurements of the time-mean flow properties downstream of the row. Variations in mean flow properties due to wake-wake interactions may be eliminated by measuring very close to the rotor trailing edge, or by measuring at a number of axial stations and extrapolating back to the trailing edge; but there will still be some uncertainty about the effects of wake-boundary layer interactions within the rotor passages, as has already been noted in Ref. 2.

(b) Machine Design

Circumferential variations in the unsteady flow field produced by wake-wake interactions should significantly influence blade vibration and noise generation in blade rows further downstream, as discussed previously in Ref. 9. Where adjacent pairs of moving or fixed blade rows contain unequal blade numbers, the amplitude of blade vibrations in the downstream row of a pair will also exhibit circumferential variations; blade vibration levels may then locally exceed those predicted from flow models which assume the time-mean disturbance field to be axisymmetric.

It was suggested in Ref.9 that noise and blade vibration and/or axial row spacing could be reduced by choosing equal blade numbers in adjacent pairs of rotor or stator rows, and aligning the rows circumferentially so that the downstream blades were subjected to the minimum disturbance level (which for the case shown in Fig. 4 is obtained at the pressure side of the IGV wake street). The present measurements indicate that row spacing could be limited to a streamwise distance of about 40% chord by this procedure: no practical decreases in disturbance level would be achieved by further separating the blade rows (see Fig.5). Performance could be slightly enhanced by this procedure due to the beneficial effect of upstream wake turbulence on the boundary layers of the downstream blades, and the slightly higher mean velocity in the region of minimum disturbance level.

The circumferential variations in mean flow properties produced by wake-wake interactions could possibly play a useful role in reducing the amplitude of mean flow distortions in an axial machine. The blading configuration suggested above for limiting blade vibration would tend to attenuate flow distortions because of the phase difference between wake-wake interaction effects in alternate rows. Alternatively it might be possible to vary the phase difference between mean flow variations arising from unsteady lift on a blade row and from wake-wake interactions downstream of that row: in the present investigation these two effects were nearly in phase, and this accentuated the flow distortion downstream of the rotor.

ACKNOWLEDGMENTS.

The support of the Australian Department of Supply and the Australian Research Grants Committee is gratefully acknowledged.

REFERENCES

1. HORLOCK, J.H. Unsteady Flow in Turbomachinery. Proc. 3rd. Australasian Conf. on Hydraulics & Fluid Mechanics, Sydney, Australia, 1968, pp. 221-227.

2. HENDERSON, R.E. The Unsteady Response of an Axial Flow Turbomachine to an Upstream Disturbance. Ph.D. Thesis, Uni. of Cambridge, U.K., 1972.
3. LIEBLEIN, S. & ROUDEBUSH W.H., Low-Speed Wake Characteristics of Two-Dimensional Cascade and Isolated Airfoil Sections. U.S.A., N.A.C.A. TN 3771, 1956.
4. DARRIEUS, G. Le flux d'energie en mécanique: Application aux turbomachines. Z. Ang. Math. Phys., Vol. 9b, 1958, pp.225-232.
5. WERLÉ, H. & GALLON,M. Sillages de cheminées, faisceaux tubulaires, grilles et turbomachines. La Houille Blanche No. 4/1973, pp.339-360.
6. SMITH, L.H. Wake Dispersion in Turbomachines. Trans. ASME, Ser. D., Vol. 88, 1966, pp.688-690.
7. BOXHALL, P.J. Unsteady Flow Phenomena in an Axial Flow Compressor. M. Eng. Sci. Thesis, Uni. of Tasmania, Australia, 1971.
8. WALKER, G.J. & OLIVER, A.R. The Effect of Interaction Between Wakes from Blade Rows in an Axial Flow Compressor on the Noise Generated by Blade Interaction. Trans. ASME Ser. A., Vol. 94, 1972, pp.241-248.
9. WALKER, G.J. Effect of Wake-Wake Interactions on the Generation of Noise in Axial-Flow Turbomachinery, Proc. 1st Int. Symposium on Air Breathing Engines, Marseille, France, 1972.
10. LOCKHART, R.C. Some Unsteady Flow Phenomena Downstream of an Axial Compressor Stage. M. Eng. Sci. Thesis, Uni. of Tasmania, Australia, 1973.
11. OLIVER, A.R. Comparison Between Sand Cast and Machined Blades in the Vortex Wind Tunnel. Australian Dept. of Supply, Aero. Res. Labs. Rep. ME 103, 1961.
12. OLIVER, A.R. Uni. of Tasmania, Private Communication.
13. EVANS, R.L. Turbulent Boundary Layers on Axial-Flow Compressor Blades. Ph.D. Thesis, Uni. of Cambridge, U.K., 1973.
14. KERREBROCK, J.L. & MIKOLAJCZAK, A.A. Intra-Stator Transport of Rotor Wakes and Its Effect on Compressor Performance. Trans. ASME, Ser. A, Vol. 92, 1970, pp. 359-368.
15. CHARNAY, G., COMPTE-BELLOT, G., & MATHIEU, J. Development of a Turbulent Boundary Layer on a Flat Plate in an External Turbulent Flow. AGARD CP 93-71, 1971.
16. AHMED, Q.A., LUXTON, R.E. & ANTONIA, R.A. The Behaviour of a Two-Dimensional Wake in a Uniform Turbulent Shear Flow. Mech. Eng. Dept., Uni. of Sydney, Australia, TN F-48 1972.
17. HORLOCK, J.H. & DANESHYAR, H. Stagnation Pressure Changes in Unsteady Flow, Aero. Q., Vol. XXII, 1971, pp.207-224.

NOTATION

s	Circumferential blade spacing
C	Blade chord
x^1	Streamwise distance from rotor trailing edge
y	Circumferential position coordinate
y^1	Position relative to centre of IGV wake street
V	Time mean velocity
$\bar{V}$	Circumferential mean velocity
H	Total head
U_{mb}	Rotor velocity at mid-blade height

Tu	Apparent turbulence level
β_1	Blade angle at inlet (from axial)
β_2	Blade angle at outlet (from axial)

Subscripts.

i	Inlet
IGV	Inlet guide vane
R	Rotor
S	Stator leading edge

FIGURES

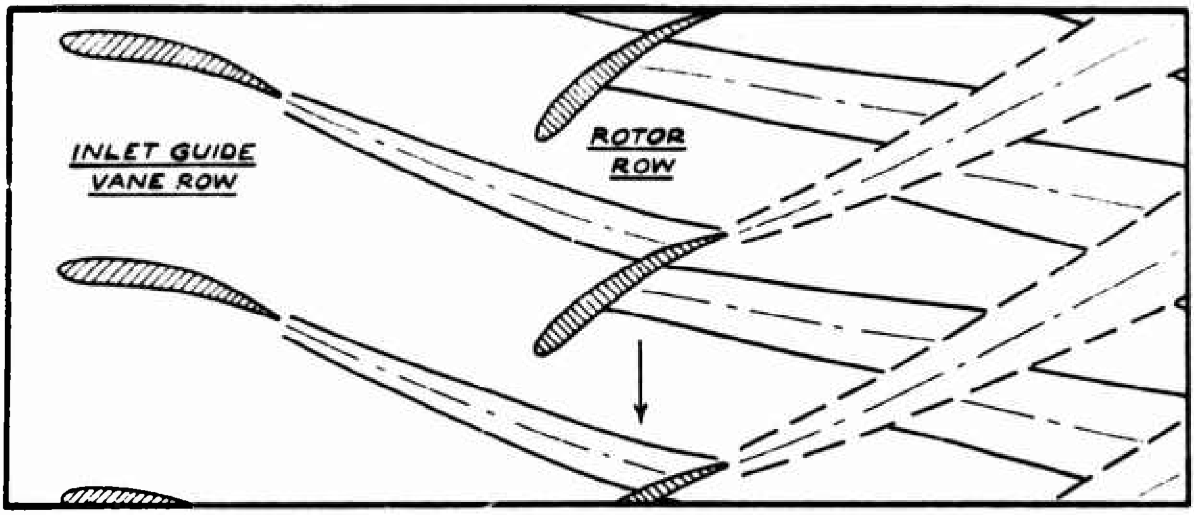
INLET GUIDE VANE ROW
ROTOR ROW

Fig.1. - Dispersion of Inlet Guide Vane Wakes by Rotor Row

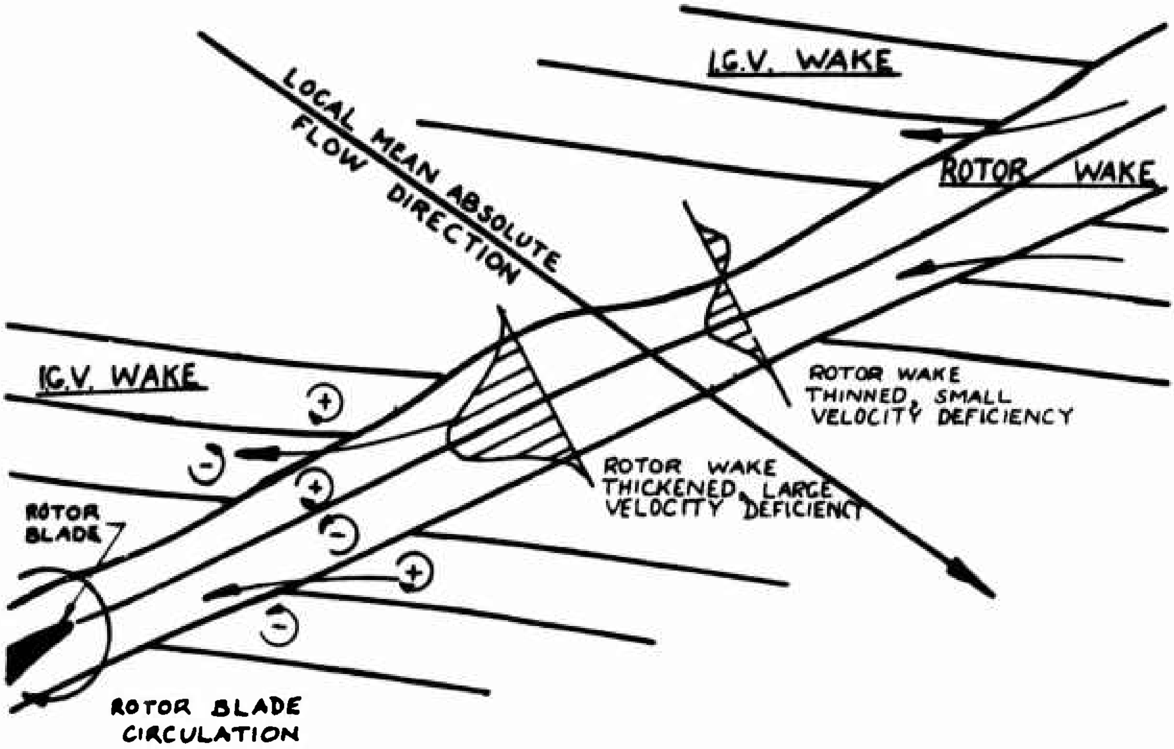
I.G.V. WAKE
LOCAL MEAN ABSOLUTE FLOW DIRECTION
ROTOR WAKE
ROTOR WAKE THINNED, SMALL VELOCITY DEFICIENCY
I.G.V. WAKE
+
-
+
-
+
-
ROTOR WAKE THICKENED, LARGE VELOCITY DEFICIENCY
ROTOR BLADE
ROTOR BLADE CIRCULATION

Fig. 2. - IGV Wake - Rotor Wake Interaction

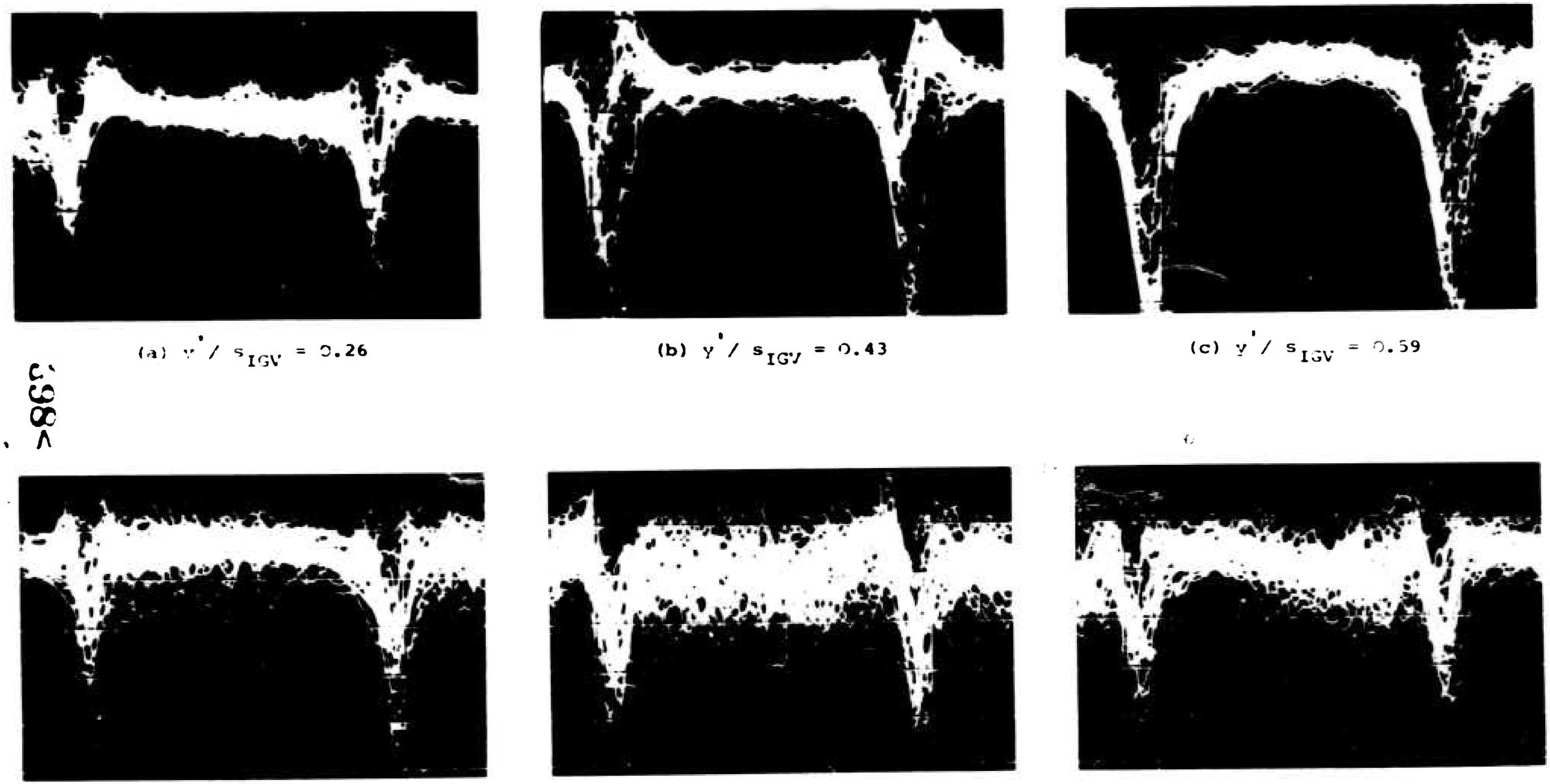

(a) $y'/s_{IGV} = 0.26$

(b) $y'/s_{IGV} = 0.43$

(c) $y'/s_{IGV} = 0.59$

(d) $y'/s_{IGV} = 0.76$

(e) $y'/s_{IGV} = 0.93$

(f) $y'/s_{IGV} = 0.09$

Fig. 3. - Unsteady Velocity Field Downstream of Rotor at $x'/c_R = 0.785$

(Scale: 3.26 $\bar{V}$/div Vert., 0.5ms/div Horiz.)

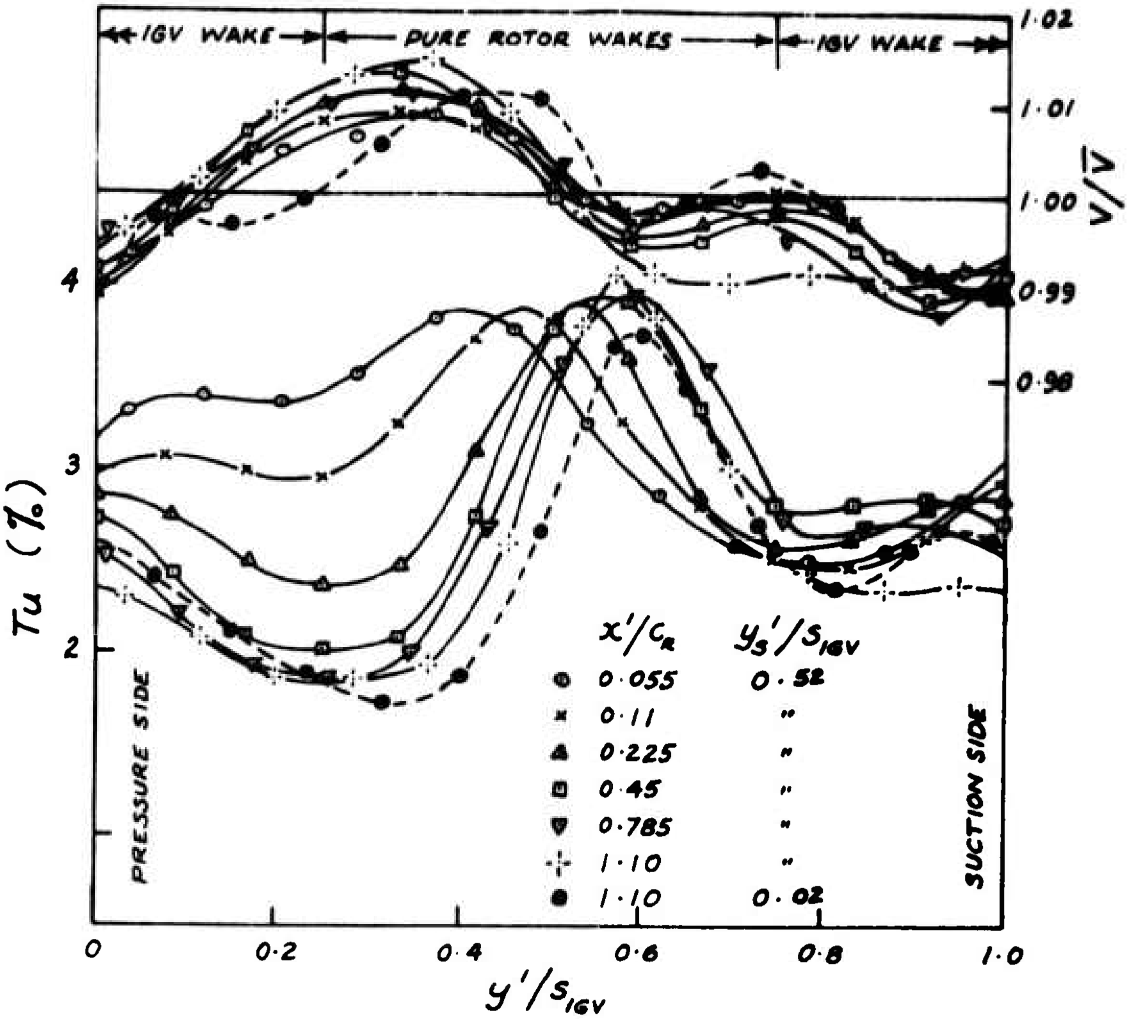

Fig. 4. - Circumferential Variation of Time-Mean Velocity and Apparent Turbulence Level Downstream of Rotor

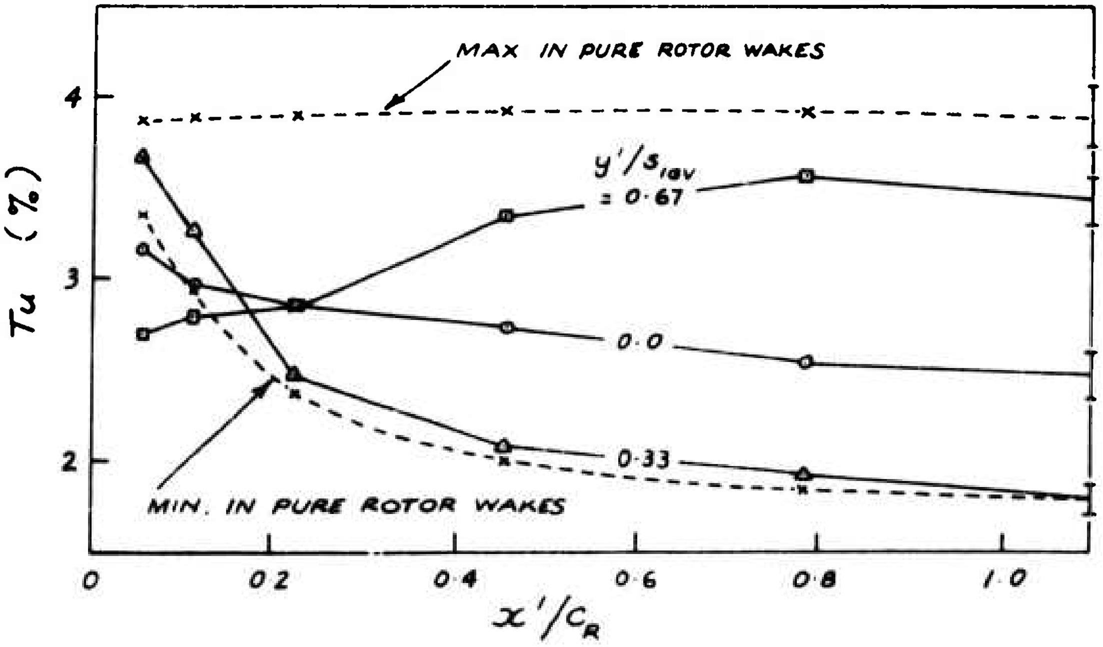

Fig. 5. - Variation of Apparent Turbulence Level Downstream of Rotor along Mean Flow Direction

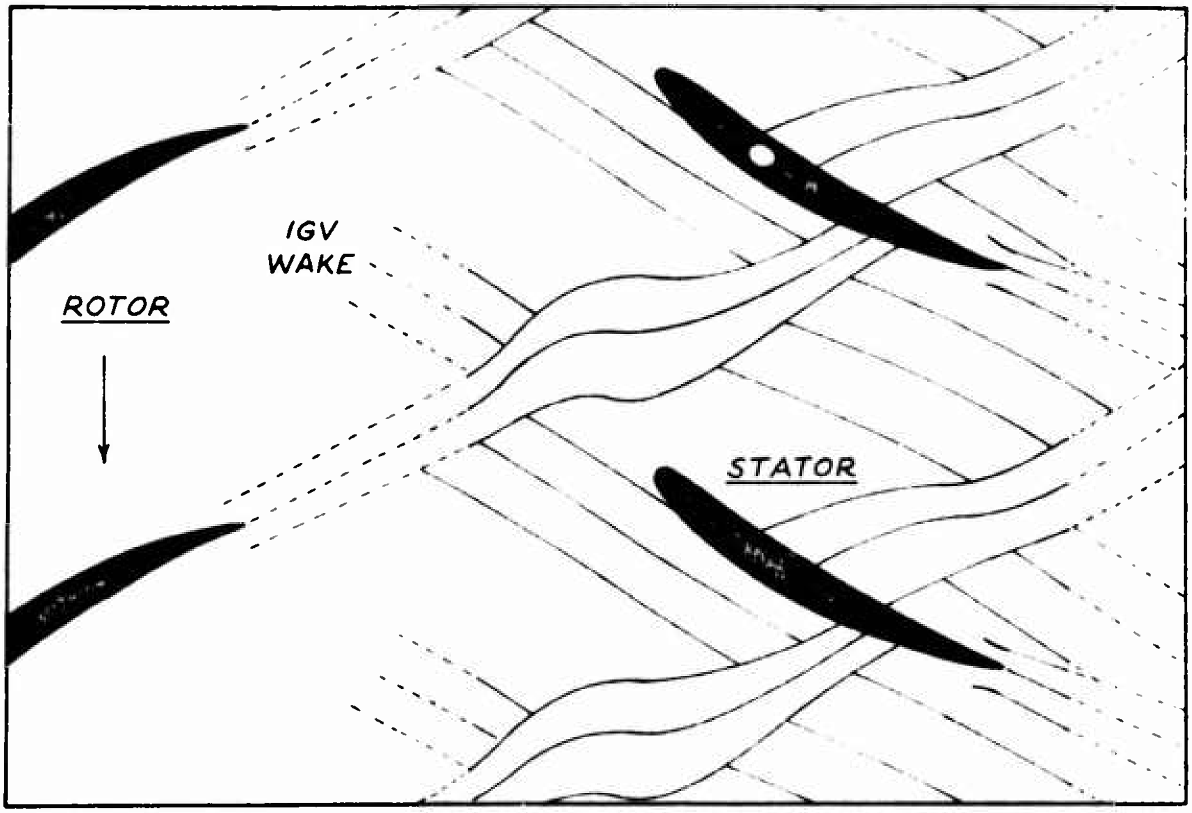

Fig. 6 - Instantaneous Flow Pattern Through Stator Row Showing Location of Blade Wakes

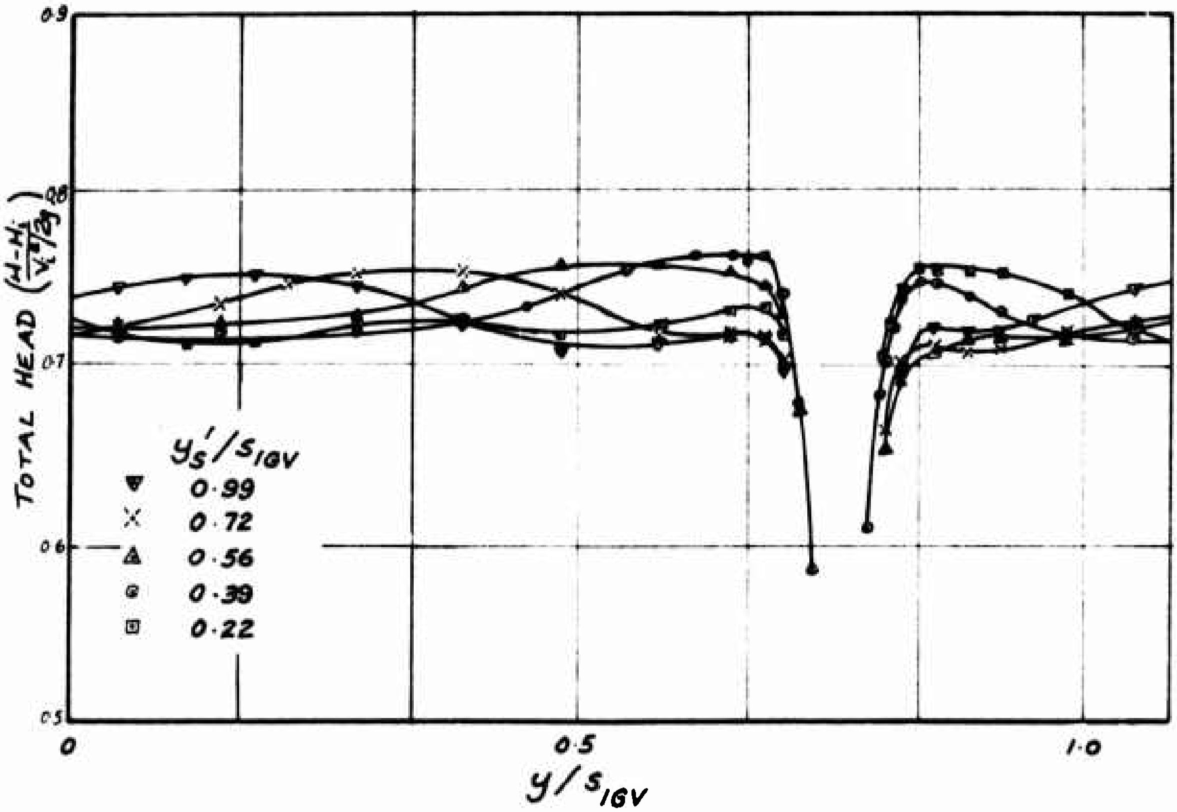

Fig.7. - Circumferential Variation of Total Head $0.17C_S$ Axially Downstream of Stator (for Different Relative Settings of IGV and Stator)

TURBINE COOLING - A REVIEW OF THE VARIOUS INTERFACE PROBLEMS

A. Moore
Rolls-Royce (1971) Ltd., Bristol Engine Division

INTRODUCTION

The object of this paper is to discuss, in very general terms, the relationships between aero engine gas turbine cooling and the various systems and disciplines which interface with it, thus attempting to put turbine cooling into perspective in the overall requirements of a gas turbine power plant.

Initially the paper considers the effect of the present trend in the parameters which dictate the overall thermodynamic efficiency of an aero engine on the turbine cooling requirements, and these are shown to make the cooling problems more difficult.

The paper then summarises each of the turbine cooling interface areas in turn, bearing in mind the requirements imposed on the turbine cooling system by the overall thermodynamic cycle performance considerations.

There are two types of interface considered, namely those concerning adjacent systems, i.e. turbine/ combustor and air systems, and those concerning the inter-relationships between disciplines. These include the relationship between turbine cooling and turbine aerodynamics, failure criteria and manufacturing technology.

THERMODYNAMIC CYCLE CONSIDERATIONS

Perhaps the most significant relationship to be considered when discussing turbine cooling is that with the overall thermodynamic cycle requirements.

This relationship can be inferred from figure 1, which shows the variation in specific fuel consumption (fuel flow/net thrust) and specific thrust (net thrust/ inlet air mass flow) with the compressor pressure ratio and the engine bypass ratio for two values of turbine entry temperature. A typical subsonic aircraft cruise rating has been assumed with realistic cooling flows at each value of turbine entry temperature. This figure shows the advantages, to the overall powerplant performance, of using high values of compressor pressure ratio and bypass ratio, for specific fuel consumption considerations and a high value of turbine entry temperature to give increased specific thrust.

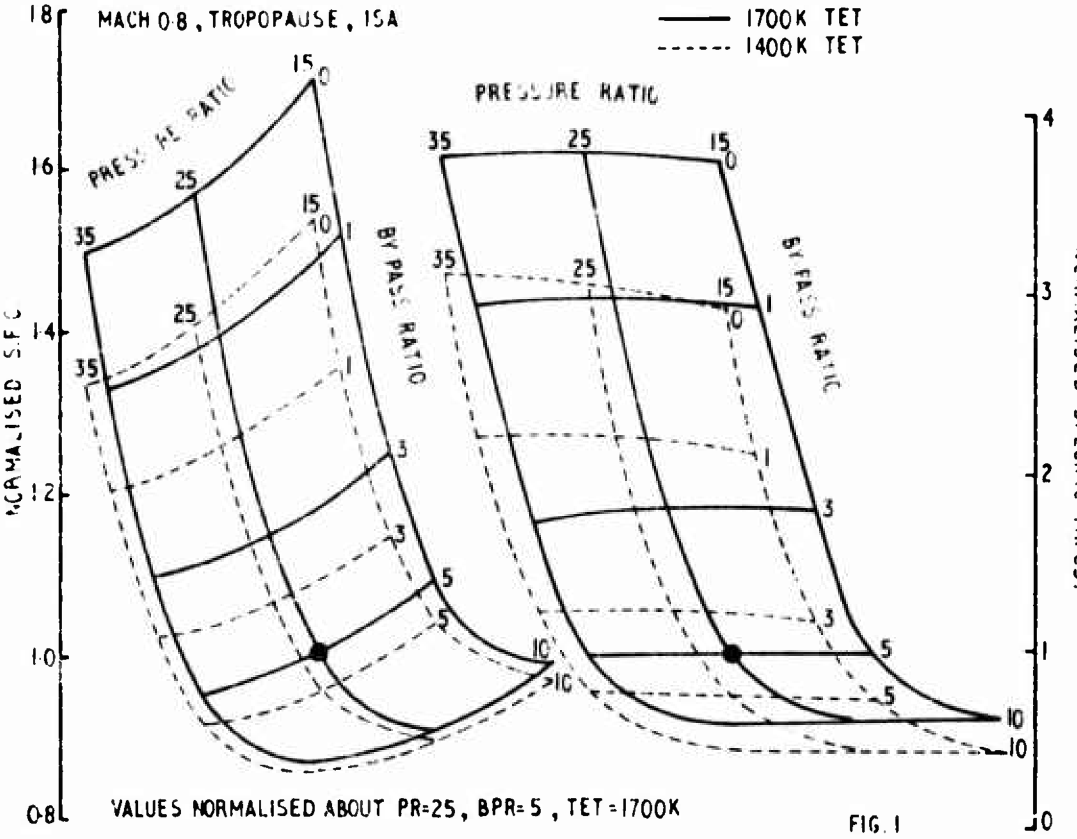

SPECIFIC FUEL CONSUMPTION AND SPECIFIC THRUST VARIATION WITH ENGINE PRESSURE RATIO, BY-PASS RATIO & TURBINE ENTRY TEMPERATURE

FIG. 1

When one considers the implications of these trends on turbine cooling requirements it is apparent that:

a) As the compressor pressure ratio increases, the temperature of the air available for turbine cooling increases which reduces the coolant cooling potential. The increase in pressure also increases the heat flux to be absorbed by the cooling air, for a given value of turbine entry temperature.

b) As the bypass ratio increases, the size of the gas generator decreases making the manufacture of blade and vane cooling systems more difficult. In addition, the number of low pressure turbine stages also increases as the bypass ratio is increased, which increases the cooling requirements.

c) As the turbine temperature increases the required degree of cooling increases.

The thermodynamic performance requirements therefore, create a situation making it more difficult to achieve those requirements, as it creates the need for more turbine cooling, whilst using hotter cooling air, in smaller blades which are more difficult to cool.

This inter-relationship between the various thermodynamic parameters and the turbine cooling requirements and the effect on the powerplant, in terms of thermodynamic efficiency, cost and weight, is shown diagrammatically in figure 2. This diagram, although simplified, shows the complex manner in which the turbine cooling requirements influence the overall powerplant performance, either directly or indirectly by influencing other systems or disciplines which in turn influence the powerplant performance.

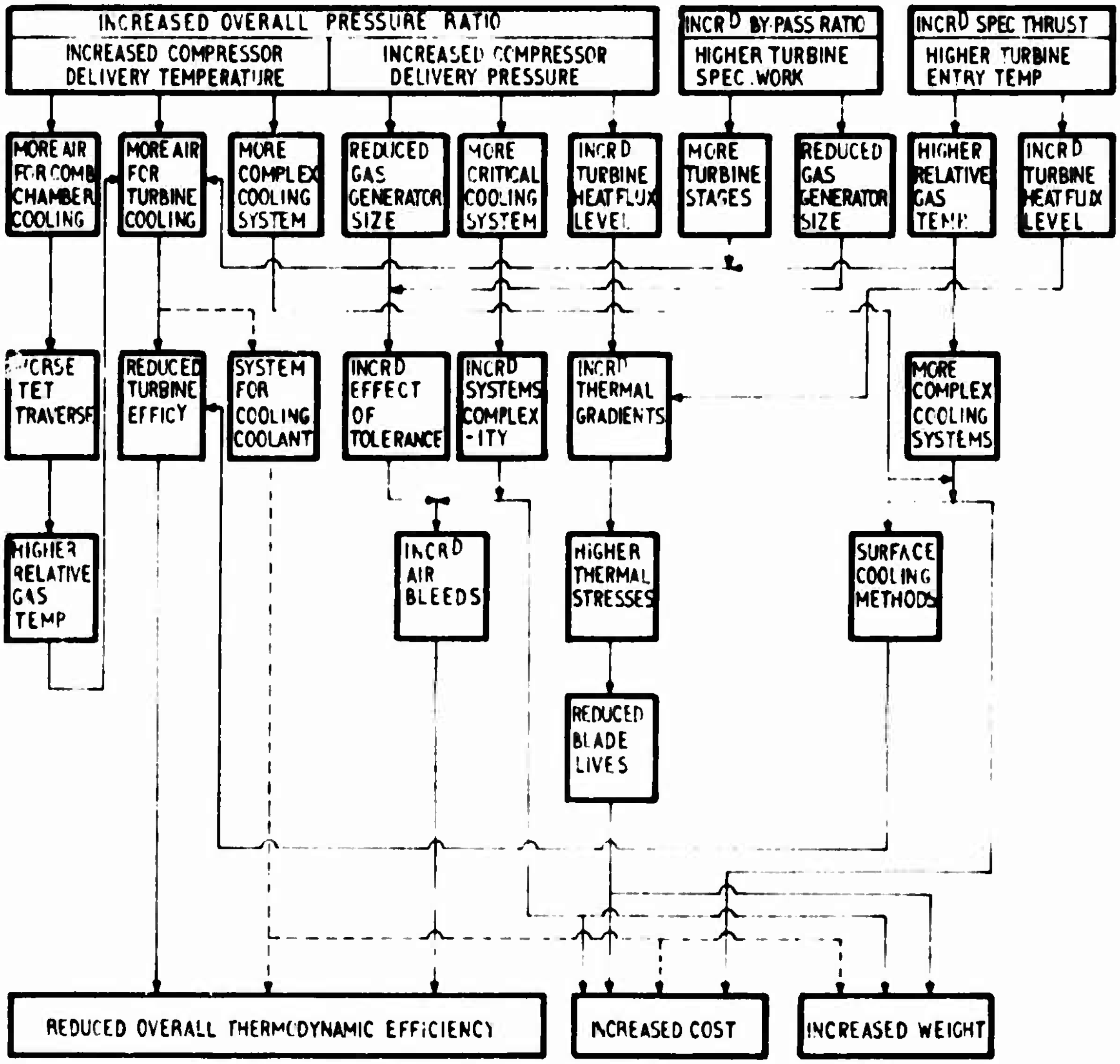
INCREASED OVERALL PRESSURE RATIO
INCREASED COMPRESSOR DELIVERY TEMPERATURE
INCREASED COMPRESSOR DELIVERY PRESSURE
INCRD BY-PASS RATIO
HIGHER TURBINE SPEC. WORK
INCRD SPEC THRUST
HIGHER TURBINE ENTRY TEMP
MORE AIR FOR COMB CHAMBER COOLING
MORE AIR FOR TURBINE COOLING
MORE COMPLEX COOLING SYSTEM
REDUCED GAS GENERATOR SIZE
MORE CRITICAL COOLING SYSTEM
INCRD TURBINE HEAT FLUX LEVEL
MORE TURBINE STAGES
REDUCED GAS GENERATOR SIZE
HIGHER RELATIVE GAS TEMP
INCRD TURBINE HEAT FLUX LEVEL
INCRSE TET TRAVERSE
REDUCED TURBINE EFFICY
SYSTEM FOR COOLING COOLANT
INCRD EFFECT OF TOLERANCE
INCRD SYSTEMS COMPLEX-ITY
INCRD THERMAL GRADIENTS
MORE COMPLEX COOLING SYSTEMS
HIGHER RELATIVE GAS TEMP
INCRD AIR BLEEDS
HIGHER THERMAL STRESSES
SURFACE COOLING METHODS
REDUCED BLADE LIVES
REDUCED OVERALL THERMODYNAMIC EFFICIENCY
INCREASED COST
INCREASED WEIGHT

THE INFLUENCE OF TURBINE COOLING REQUIREMENTS ON THE EFFECT OF ENGINE THERMODYNAMIC PARAMETERS ON THE OVERALL POWER PLANT REQUIREMENTS

FIG 2

It is worth remembering these overall turbine cooling/cycle performance requirements when considering the relatship between turbine cooling and the other relevant interfaces as discussed in the remainder of this paper.

TURBINE COOLING INTERFACES

Turbine cooling is an engine system, which must relate to all of the other systems and disciplines in the engine. For example, a combustor designed to burn fuel efficiently, without regard for the turbine cooling requirements, would impose considerable extra difficulties for the turbine and a combustor designed primarily to minimise the task of the cooling requirements would produce a poor combustion chamber, and engine. Similarly the air systems which supply the turbine cooling air must compromise, and be compromised by, the turbine cooling requirements. The optimum supply requirements for turbine cooling air, for example, is air at the lowest temperature consistent with the pressure requirements. As far as engine air systems design is concerned, it is far more convenient to use a relatively low pressure supply system (dictated by the blade root static pressure) and a relatively high cooling air temperature, namely that at the exit from the high pressure compressor. Alternatively, the overall cycle performance requirements would suggest a coolant supply taken at as low a pressure from the compressor as possible as being the optimum. Thus each system has its own optimum cooling supply point, and a compromise solution must be used. Likewise, there are other compromise situations involving the turbine aerodynamics, blade and nozzle guide vane failure modes and manufacture, all of which must be interfaced to give the 'best overall system'.

With these more general considerations in mind consider now each of the turbine cooling interfaces in turn.

TURBINE COOLING/TURBINE AERODYNAMICS INTERFACE

The purpose of the aero engine turbine is to extract energy from the mainstream flow to drive compressive components in the cycle whilst, at the same time, minimising losses in the expansion side of the engine cycle.

Turbine losses result from viscous dissipation of energy in the blading and annulus boundary layers, growth of secondary flows in the blade passages, blade base drag, shock waves, windage and overtip leakage. In an uncooled turbine these effects are minimised by careful choice of blade and vane aspect ratios and numbers, low wedge angles, thin trailing edges, blade thickness, incidence and cambers which minimise boundary layer growths, and minimal tip clearances. However, cooling requirements are often incompatible with these established non-cooled turbine aerodynamic criteria and result in a partial increase in the inefficiencies the increased temperature is attempting to reduce. This is in addition to the basic loss in cycle performance caused by bypassing the combustion chamber and reducing the energy of the coolant flow

Some of the more important effects of cooling turbine blades and vanes on turbine efficiency are listed below:-

a) Aerofoil shape to accommodate a cooling system.

When significant cooling is introduced into a turbine blade the basic aerofoil shape must be compromised to accept the cooling. Generally this means that the thickness/chord ratio of the blade is increased to give sufficient cross-sectional area for the cooling air passages to be incorporated and the trailing edge wedge angles are increased to enable the cooling passages to be positioned as close as possible to the trailing edge of the blade. It is also usual to increase the trailing edge radius as this reduces the length of the uncooled trailing edge part of the blade, effectively reducing the critical trailing edge temperature. On engines with higher relative gas temperatures, it is necessary to cool the blade trailing edge, more directly. If an internal convection system is used, the coolant is discharged from the blade trailing edge. This increases further the trailing edge thickness and will, with the other cooling air system features already outlined, reduce the efficiency of the turbine.

b) Number of blades.

In an uncooled turbine the number of blades is large (typically 140) and the chord of the blades small, as this, with small thickness/chord ratios and small trailing edge wedge angles and radii gives the best turbine efficiency. When cooling is introduced these parameters increase thus tending to increase the blockage to the gas flow through the turbine and also the base drag of the blade trailing edges. Both of these performance limitations are reduced by decreasing the number of blades, but this must be accompanied by an increase in the blade chord length (blade pitch/blade chord approximately constant) in order to minimise the turbine efficiency loss. This is particularly relevant in small turbines as this effectively increases the size of the blade.

There are two main disadvantages to increasing the chord of a rotor blade, namely that the thickness of the turbine disk rim to accommodate the blade must also increase, which further increases the thickness at the bore of the disk, thus increasing the weight of the disk, and that the corresponding increase in blade pitch will increase the length of the blade shrouds, assuming that a shrouded turbine is being used. As the shroud length is increased both the weight and the stress caused by the bending moment due to the centrifugal forces on the shrouds increase. In order to reduce the bending stress in the fillet radii of the shroud it is often necessary to increase the thickness and hence further increase the weight of the shrouds. This in turn increases the centrifugal stresses in the blades which will, if the original design was stress limited, require increased section blades, and this will add to the increase in the disk stresses. Similarly for a given stress level, the disk thickness will require increasing, thus giving a cumulative increase in the weight of the system.

Further complications are given at higher values of the turbine entry temperature as the rotor blade shroud will itself require cooling and this can again increase the weight producing a cumulative weight effect in the disk and blades.

The various penalties concerning the turbine rotor blade shrouds quoted above, can be eliminated simply by using unshrouded blades, but this involves other compromise situations which must be considered. The first of these is that the overtip leakage on an unshrouded blade cannot be so accurately controlled, as the total perimeter for leakage increases and the degree of sophistication of the sealing arrangement is more limited. This, in turn increases the penalties on turbine aerodynamic efficiency. The second disadvantage of such a system is that the liner, which controls the leakage over the tips of the rotor blades must also be cooled and this is subject to the turbine gas total temperature, not the relative temperature which a shroud rotating with the turbine rotor would feel. The third disadvantage is that shrouds are often made interlocking in order to dampen vibrations in the rotor system. This facility would not be available in an unshrouded turbine.

c) External cooling effects.

As turbine entry temperatures increase the ability to cool the blades and vanes using only internal convection becomes more difficult and eventually it is necessary to use external cooling. The majority of the external cooling systems used at this time are films of air exhausted from the surface through rows of discrete holes, and these cannot be ejected without increasing profile losses both because they inevitably result in transition in a boundary layer and because in regions of high Mach number they are likely to produce shock-boundary layer interactions and separation.

d) Coolant supply system leakages.

The leakage paths, through which cooling air can escape from a supply system into the turbine annulus are numerous and, despite considerable effort to reduce these, some leakage does take place. This not only detracts from the overall cycle performance but also affects the turbine efficiency directly, as these leakages are often normal to the direction of the turbine annulus gas flow.

As the need for external cooling is increased the pressure of the coolant supplies must also increase in order to provide sufficient pressure to enable the coolant to be exhausted against the local gas static pressure. This increased pressure requirement will increase the leakage into the turbine annulus, thus reducing the turbine efficiency.

e) Thermal Boundary Layer Effects

Turbine blades are subject to a very high centrifugal acceleration (circa 40,000 g) thus promoting high natural convection circulations on the cooled thermal boundary layer. This radial flow will presumably affect the aerodynamic characteristics of the turbine blading.

f) Nozzle Guide Vane/Rotor Blade Perturbations.

As the degree of cooling of turbine blades and vanes increases the thickness of the wakes from the aerofoils also increases. The amplitude of the perturbations on both the hydrodynamic and thermal boundary layers of a rotor blade will therefore increase as the cooling of the nozzle guide vane (N.G.V.) upstream of the rotor increases. These perturbations can be expected to influence both the aerodynamic and heat transfer characteristics of the rotor blade.

g) Pumping Work on the Cooling Flow

Work is exerted when coolant is accelerated to the rotor blade velocity. The magnitude of the work is directly proportional to the coolant flow (and consequently a function of the degree of cooling) and is also a function of the method of introducing the coolant to, and exhausting the coolant from, the rotor blades. Typically 1% of coolant flow through a rotor blade will give ½% loss in turbine efficiency but if preswirl nozzles are used, for example, the work requirements can be reduced very considerably and if trailing edge, or pressure side ejection is used this can also reduce the work requirements.

TURBINE COOLING/COMBUSTOR INTERFACE

Turbine cooling is the means whereby turbine blades and vanes are permitted to function in a bostile environment created by the combustion chamber. Although the mean temperature level from the combustor is determined by cycle considerations, the distribution of the combustion chamber exhaust temperature can be influenced to ease the task of the turbine cooling engineer, and this involves optimisation of the combustor dilution and film cooling air flows and geometries. The overall temperature distribution factor (O.T.D.F.) value which specifies the peak temperature for the hottest gas, and is used for nozzle guide vane thermal assessment, is typically 35% and the radial temperature distribution factor (R.T.D.F.) value which specifies the peak value for the circumferentially averaged radial temperature profile will have a value of the order of 10%. This is used for rotor blade cooling studies. In each case the factor takes the form:-

$$\frac{\text{peak gas temp. relative to blade or vane - turbine entry temp.}}{\text{combustion chamber temperature rise}}$$

In general, the requirement, from a N.G.V. cooling point of view, is for as flat an overall temperature distribution as possible as this limits the maximum gas temperature relative to the vanes. An alternative approach which is being considered on engines with a small number of N.G.V.'s is to position the vanes so that the local hot gas streaks pass between them. This entails linking the number of N.G.V.'s directly with the number of combustor primary zone segments and dilution holes. Theoretically an effective gas temperature reduction of up to about 400K could be achieved this way, but a more realistic value would possibly be only 10 or 20% of this value.

The optimum value of radial temperature distribution is not so easily defined as it is a function of the blade radial stress distribution, and the variation in cooling performance up the span of the blade. In an uncooled blade, because the stresses are higher at the root, it is advantageous to use a tip hot profile, but in cooled blades often the optimum position of the peak radial temperature is nearer the blade mid span.

Turbulence level is another factor which is directly influenced by the combustor and which is known to have significant effects on the turbine blade profile loss and heat transfer coefficient. Rolls-Royce (1971) Ltd. has measured turbulence values of between 13% and 22% behind and engine combustor using a laser doppler anemometer compared with 14% without combustion. It is thought that even higher values will be given when combined thermal and velocity turbulence effect are measured.

TURBINE COOLING/AIR SYSTEMS INTERFACE

The obvious air system/turbine interface is the turbine coolant feed system. Ideally, this system supplies air to the turbine blades at the lowest temperature consistent with the pressure requirements and with no loss of air. In practice air is lost from the system to exhaust into the turbine at the root of the rotor blade, causing a loss in turbine efficiency as well as contributing to a loss in the overall thermodynamic efficiency of the cycle. The extent of the leakage is dependent upon the type of system used, for example, a high pressure supply system will affect the turbine efficiency more than a low pressure system, and a system incorporating large diameter seals will be worse than one using split discs or a cover plate.

The actual temperature of the cooling air supplied to the turbine blades is dependent upon the feed system used, which is in turn, influenced by the feed pressure requirement. Such factors as the thermal boundary layer growth in the compressor at the tap off point, heating of the cooling air due to work input from rotating components, the type of coolant transfer system to the cooled blades, (preswirl nozzles, cover plate, split disc) etc., must be considered.

This is further complicated as turbine cooling is only one of a number of functions which must all be accommodated in a restricted space and which are often incompatible. For example the turbine blade cooling air is too hot, because of the pressure requirement, to cool bearings and consequently there is often a conflict requiring involved designs to separate and to ensure, even in a failure situation, that the hot turbine cooling air can never pressurise an adjacent turbine bearing. Other systems functions such as the pressurisation and venting for bearing load optimisation, bearing feed, scavenge and vent systems, shaft, casing and liner cooling and seal thermal matching must also be integrated into the overall engine systems.

The seal thermal matching requirements are becoming particularly important as the trend towards higher bypass ratio, higher compressor pressure ratio and higher turbine entry temperature engines continues, as these are producing engines with small blades, which makes a given increase in tip seal clearance more critical and with larger component temperature ranges, which promotes increased thermal movement. Fortunately the size of the components also decreases which helps to reduce the movements but since such factors as tolerances and minimum build clearances cannot be scaled directly and the mechanical strain due to rotation can even be higher for a smaller engine (the rotational speed increases as the linear size decreases to give a similar value of linear blade speed) then it is apparent that engines with small high pressure systems are at a disadvantage.

The actual value of the turbine overtip seal clearance is the difference of two large numbers, namely the radii of the static and rotor seal members. The movement of each of these members, although small in respect to the dimension of each member is probably the largest component of the radial gap between the two members. Fortunately, since both members move generally in the same direction, i.e. radially outwards during acceleration and inwards during deceleration, the gap tends to remain approximately the same, the variations in the seal gap being due to transient variations in the movement of the two components. This is due to the varying heating and cooling rates of the components which influence the static and rotating seal element movements, caused by differences in air and gas temperatures, heat transfer coefficients and thermal masses.

The transient thermal movement of a turbine rotor during an engine acceleration is made up to parts, firstly the rapid thermal expansion of the rotor blade in perhaps the first ten seconds of the cycle, followed by a much slower radial expansion of the turbine disk. The characteristics of the movement of the outer static member is determined by the geometry of the seal and the associated structure. Three basic arrangements can be used for the static seal member, as follows:-

a) An independent ring dogged to the casing or N.G.V. so that it can move independently. This has the advantage that it does not have the movement constraints of the surrounding structure and can therefore be independently optimised to give the best seal performance. Unfortunately this is only possible for a single engine transient as the temperature parameters, which define the movement of each member, have an independent effect on each member.

The disadvantages of this system include the difficulty of maintaining concentricity with a thin liner mounted independently of the casing and N.G.V.'s, the proneness of such a system to sticking and the increased tolerances due to additional parts.

b) A segmented liner secured to the casing so that it follows the movement of the casing. This is attractive on bypass engines where the casing is cooled with bypass air, as this limits the movement of the casing and hence the static member of the seal. It also has the advantage of having, in general, the smallest tolerance problem of all of the systems.

c) A segmented liner to the N.G.V.'s which are mounted from the inner combustion chamber casing. This has the basic advantage that the movement of this member is subject to the same parameters as the movement of the rotor system (the expansion of N.G.V. is similar to that of the rotor blade) and will therefore, if matched correctly, closely follow the movement of the rotor system. The build up of tolerances will depend upon the continuity paths from each seal member to the turbine location bearing, and this will, in general, be worse than the tolerance situation for a casing mounted seal.

TURBINE COOLING/FAILURE CRITERIA INTERFACE

The basic aim of cooling turbine rotor blades is to prevent failure by reducing the blade metal temperature to a value which gives adequate material properties.

Typical operating metal temperatures to give adequate properties are 1100 and 1150K for civil and military rotor blade mean temperatures respectively and 1250 and 1300K for maximum civil and military blade temperatures respectively. The mean blade temperature influences the creep characteristics of the blade and the maximum temperature relates to the oxidation, corrosion and thermal fatigue characteristics.

Considering these failure modes in turn:-

a) Creep is defined as the continuous increase in permanent deformation under stress and is used, in the context of this paper, with reference to the behaviour of high temperature alloys under tension at elevated temperatures.

In uncooled turbine blades, where there is little variation in metal temperature, creep is the predominant thermal failure mode. As turbine gas temperatures increase and blade cooling becomes necessary then the situation becomes much more complex. One result is that, in practice, considerable variation in metal temperature is given which increases the relative importance of thermal fatigue and oxidation as failure modes. This metal temperature variation is due to the large variation in heat flux rates around the surface of an aerofoil, a factor of perhaps ten from the minimum to the maximum values, which, even with cooling systems designed to attempt to match the heat flux rates, still gives considerable metal temperature variation.

Another effect of introducing cooling into a turbine rotor blade is that the metal cross sectional area is reduced thus increasing the centrifugal stress and hence the creep life. In a design where cooling is introduced into an existing uncooled rotor blade, there is a compromise between cooling rate and metal cross sectional area reduction to give an optimum creep life. In a new design the shape of the aerofoil and the number of blades can be compromised, as discussed in the turbine aerodynamic section, to give a better overall solution.

The relationship between creep life and temperature is exponential, as shown in figure 3. Typically an increase in metal temperature of only 15K halves the creep life of the blade.

b) Thermal fatigue is a failure mode caused by repeated thermally induced strain. The acutal mechanism is very complex involving differential thermal strain in spanwise elements of the blade and subsuequent relaxation, which eventually fails the blade in the worst affected element. This failure mode is therefore most critical in regions which are subject to high temperatures, high cyclic variations in temperature and high metal temperature gradient.

Typical values for these parameters in a turbine rotor blade are 1250K for the maximum metal temperature, 700K to 1250K temperature rise in 5 seconds for the cyclic temperature variation and $50K.mm^{-1}$ for the local metal temperature gradient. The most effective methods for increasing the thermal fatigue life of a blade is to use thin shell blades, with a cooling system designed to match the heat flux rates as defined by the external gas heat transfer coefficients and a constant design value of blade metal temperature. However this solution can increase the centrifugal stress in the blade and can, if thin blade sections are used, reduce the properties of the blade material. Both of these factors will reduce the blade creep life.

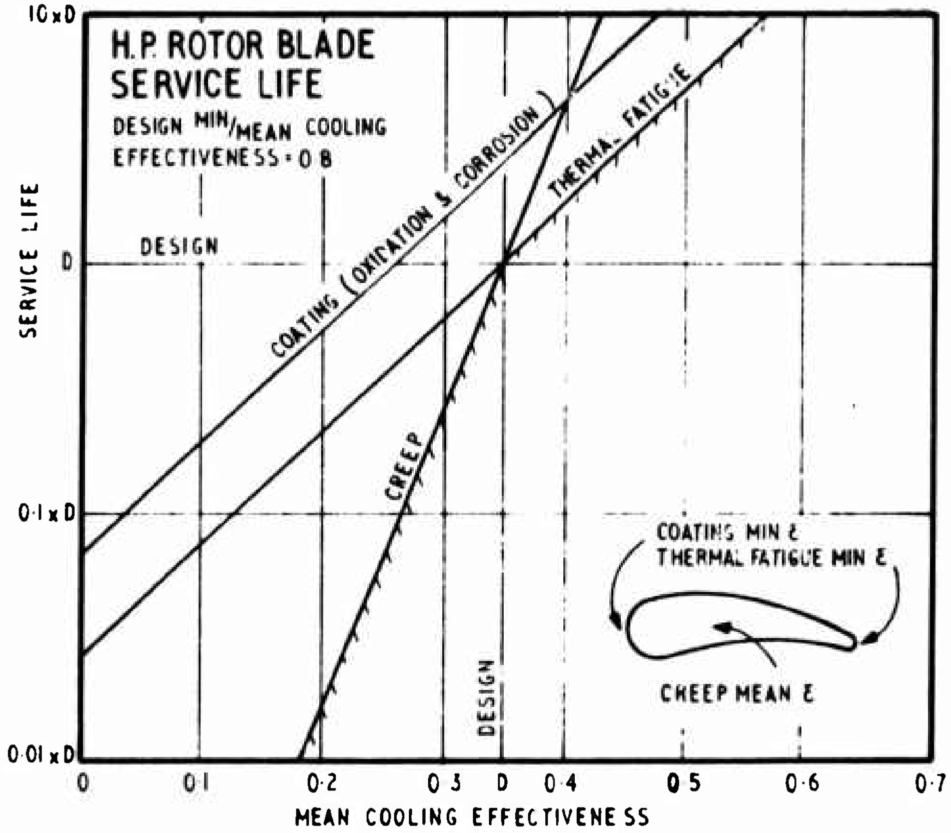

FIG. 3

Thermal matching can be achieved by varying the coolant heat transfer coefficient, perhaps by using impingement cooling at the leading edge of the blade and at the transition regions where high values of heat flux are given or by using external cooling through film cooling holes where internal convection cannot adequately control the local blade temperatures. The situation concerning thermal fatigue is further confused when external cooling is used as, although the temperature of the metal adjacent to the cooling holes is reduced, the local temperature gradients are increased in a plane where the surface is weakened by the presence of the cooling holes. Simple laboratory tests show for example, that the thermal fatigue strength of uncooled blades are reduced by an order of magnitude when drilled to represent blades with film cooling holes.

c) Oxidation/corrosion is caused by oxidation or chemical attack of the surface of the blade at the high gas and blade temperatures experienced in a turbine. Since oxidation rate increases significantly with metal temperature the same cooling techniques are required for this failure mode as for thermal fatigue, i.e. to reduce the maximum temperature of the blade.

The main conflict between cooling and corrosion is given when external surface cooling is used, as an oxide layer thickness which is acceptable on a solid surface may not be acceptable on a porous blade, owing to the increase in surface area of the surface and the tendency to block the surface cooling holes. In addition oxidation is an unstable process since the coolant rate through the surface holes is reduced as the oxide layer thickness increases. This increases the blade surface temperature which accelerates the growth of the oxide layer.

It follows, therefore, that surfaces with small cooling passages must be cooled more than solid surfaces for a given corrosion/oxidation life. Typically 'coarse' transpiration systems (woven wires, etc.) need to be cooled about 100K more than solid surface blades, and 'fine' transpiration systems (powered metallurgy) require about 200K more cooling than solid surface blades. Hence the optimum overall system for a blade, from an oxidation point of view, is a compromise between cooling effectiveness and transpiration or film pore size.

It is usual, in modern aero engines, to use oxidation resistant coatings to increase the oxidation life of blades. This is very straight forward on solid blades but it is difficult to coat the surfaces on the inside of small perforations and this can leave these surfaces, which are particularly critical to oxide layer build up, unprotected. It has been known, for instance, in cooled blades with a number of small diameter holes drilled through the trailing edge of the blade, for the coated external surface of the blade to be relatively free from oxide and the trailing edge cooling passages to be completely blocked with oxide from the surface of the cooling holes.

The cooling design of a blade has therefore to accommodate all of the failure modes and an optimum overall solution established. Figure 3 shows the results of such an exercise, which indicates, at the design value of the blade mean cooling effectiveness (defined as the difference between the local hot gas temperature and the blade temperature divided by the local hot gas temperature minus the coolant inlet temperature), that the design blade life is limited by both the creep and thermal fatigue failure modes. If the design cooling effectiveness is not achieved i.e. the blade is hotter than the design temperature then creep will limit the life of the blade and if the cooling is more than the design value thermal fatigue will be the cause of the failure.

TURBINE COOLING/MANUFACTURING TECHNOLOGY INTERFACE

Over the past five years significant advances have been made in the manufacturing technology associated with cooled turbine blades, particularly in the precision casting and non-mechanical machining processes. Cooled turbine blades for a modern high temperature aero engine probably represent manufacturing technology at its best and yet there are still limitations in this technology which impairs our ability to make the blades capable of withstanding the turbine entry temperatures of modern engines without some compromise to the aerodynamic and thermal efficiency of the turbine. This situation is becoming more critical due, in part to the increase in performance requirements and in part to the reduced size of turbine blades.

Figure 4 shows the variation in size of four turbine blades, the span of the blades ranging from 12mm for the small high pressure turbine rotor blade to 260mm for the Olympus 593 low pressure turbine rotor blade. The manufacturing problems of these two extreme blades are different in nature and each has its own difficulties. The Olympus 593 L.P. blade, for instance, is forged, rather than cast, as this gives the blade better impact strength (necessary because of the large aspect ratio of the blade) and this eliminates the possibility of casting the cooling holes into the blade. Consequently it is necessary to drill, using electro discharge machining techniques, eight holes ranging from 1·9mm to 4·1mm (·075" to 0·165") diameter the full length of the blade (i.e. length/ diameter ratios up to 160) within small tolerance limits and to communicate these radial holes with transfer holes from the blade roots.

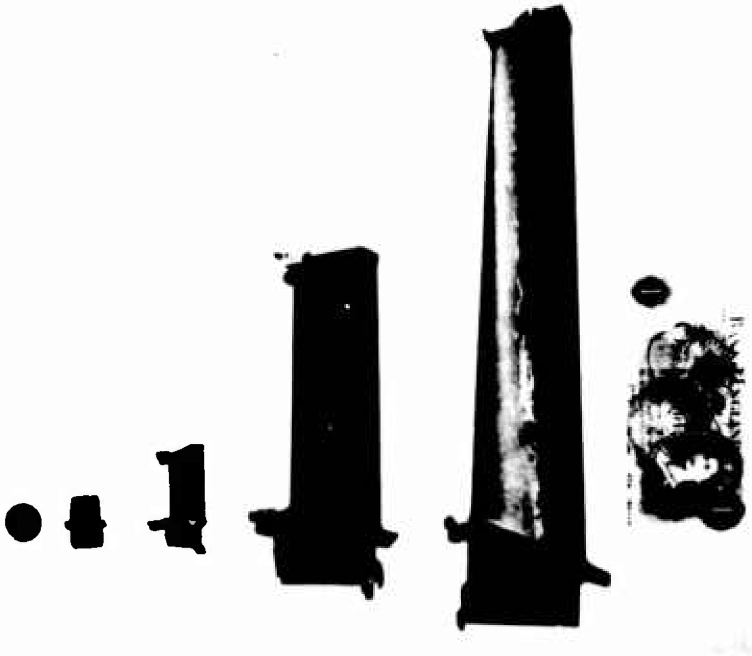

AERO ENGINE GAS TURBINE ROTOR BLADES

FIG. 4

The manufacturing problems associated with the smallest blade are associated with its small size, and also the low cost requirements. For example if the cooling holes used in the Olympus 593 H.P. turbine rotor blade were scaled to this blade size, in order to give the same cooling efficiency the radial holes would be only 0·12mm (·005") diameter.

Manufacturing technology has increased at such a rate over the past few years that the manufacturing limitations of a few years ago are now the limitations of other disciplines. For example the ability to manufacture small holes down to approximately 0·2mm (·008") for film cooling blades can now be achieved. The present limitation to reducing cooling holes less than about 0·3mm (·012") is due to blocking the holes by debris and oxidising the internal surface of the holes. The hole size limitations are therefore now due to the lack of suitable engine clean air bleed designs and the metallurgical properties of high temperature alloys and coating techniques used to prevent oxidation. A similar situation exists with reference to casting thin wall sections for blades. The limitation is not now the ability of the foundries to cast thin sections, but rather the reduction in creep strength which the thin sections exhibit. Again the critical requirement is for improved properties of the alloys.

The limitations on manufacturing technology are not so much the ability to produce a given blade or vane but rather to manufacture the blades consistantly, within small tolerances, with adequate surface finish, in the required time scale, and at low cost. The aerofoil tolerance limits for a large turbine, typically ± 0·12mm (·005") can give significant variations in turbine efficiency in a small turbine for example, and the tolerances on the position of cooling holes, can significantly affect the life of a blade.

The overall limitation on manufacture is cost, and since the manufacture of complex cooled turbine blades ('high technology') is considerably more expensive than that for more modest cooled blades a compromise to be considered in addition to those already discussed in this paper, is the degree of turbine cooling and the increase in the overall cost of the powerplant.

CONCLUSIONS

Turbine cooling is one of the major limitations to the current trend in increased engine performance as the trend in all of the performance parameters is to increase the difficulty of cooling gas turbine aero engines. As a result, in addition to an increase in blade cooling technology, with an appropriate increase in manufacturing technology, being necessary, the various interface components, systems and disciplines can be expected to be further compromised to achieve the necessary cooling performance and blade life requirements.

FILM COOLING OF TURBINE BLADES

M. Saarlas
U. S. Naval Academy, Annapolis, Maryland

1. Introduction

The use of film cooling for practical engineering purposes has been the subject of study during the last thirty years. A great number of investigators have attacked the problem (and the associated Coanda effect) with a rather modest degree of success. The success, and the lack of it, has been founded in experimentation and resulting empirical correlations. The success is evidenced by the fact that the consideration of a simple energy balance sufficiently far downstream from the injection area leads to simple correlation formulas which are capable of correlating a majority of experimental flat wall film cooling data. The lack of success is manifested by the lack of a fluid mechanics-thermodynamic model capable of describing the cooling (effectiveness) for the entire surface. Furthermore, little can be said about film cooling in the more practical cases where its knowledge is now urgently needed, e.g., for turbine blades and buckets where the effect of the pressure gradient (or variable external flow velocity) is an important factor.

Most of the published literature is concerned with the experimental investigation of the problem and serves to extend and to improve the earliest work of Wieghardt in 1943(1) who established the basic (asymptotic) correlation curve. The more recent papers, being essentially variants of the Wieghardt's correlation, seem to correlate - on the average - the published data. Thus, the overall phenomena are partially understood and the data for a given configuration can be correlated locally, but engineering predictions and the design for new configurations cannot yet be approached with any great degree of confidence.

This paper attempts to formulate a more general film cooling equation which can describe the entire flow region downstream from the slot and is capable of handling flows with a pressure gradient. The success of this attempt is demonstrated by combining available boundary layer models, with fluid injection, with the effectiveness equation derived below and comparing with the published flat wall and turbine blade cooling data.

2. The Basic Effectiveness Equation

In order to obtain the film cooling equation the energy equation is written in the total enthalpy form, which by integrating first with respect to y, and then to x direction, yields an energy integral equation. Defining a new variable called effectiveness and considering the flow regions near the slot and far downstream from it two different solutions can be found. Combining these two solutions by evaluating the constants at chosen boundary conditions an equation is obtained, which gives the effectiveness over the entire range of the flow in downstream direction. The effects of a pressure gradient and the heat transfer are also included. The basic parameters involved are the boundary layer thickness - with injection and the enthalpy thickness. Thus, a general equation is available which is valid for only one basic restriction - steady flow. Due to the formulation of the problem that is presented below the effectiveness is defined here as

$$\eta = (H_w - H_e)/(H_c - H_e) \qquad (1)$$

where H stands for the total enthalpy $H = h + U^2/2$. It follows that for slow speed flows the velocity term can be neglected. If one assumes that the coolant and external flows are the same and have constant properties, the previously obtained results can be recovered. In high speed flows the effectiveness will refer to the total temperature.

The general physical model is given in Figure 1 which shows the two basic schemes for injecting the coolant fluid into the main stream. The coolant issues from the slot of height (or width) s and and begins mixing with the external stream and boundary layer. In this process a new and different boundary layer is formed, which the experimental evidence shows to be a turbulent one. The rate of growth of this new layer near the injection slot is larger by an order of magnitude than the initial undisturbed flow. In the vicinity of the slot the velocity profiles vary greatly and are indicated schematically in Figure 2. The velocity profiles are not similar over the entire thickness of the boundary layer. On the other hand, a number of experimental investigations have shown that the temperature profiles can be reduced to a single form given by Wieghardt for a great number of flow situations which fact plays a key role in the developments below by providing an indirect means for separating the energy and the momentum equations.

It is further assumed that the coolant injection represents only a perturbation of the external flow and that the physical model is amenable to analysis by the usual boundary layer techniques. Thus, the momentum, energy, and continuity equations can be written for compressible steady flow as

$$\rho u \frac{\partial u}{\partial x} + \rho v \frac{\partial u}{\partial y} = -\frac{\partial p}{\partial x} + \frac{\partial}{\partial y}\left(\mu \frac{\partial u}{\partial y}\right)$$

$$\rho u \frac{\partial h}{\partial x} + \rho v \frac{\partial h}{\partial y} = u \frac{\partial p}{\partial x} + \frac{\partial}{\partial y}\left(k \frac{\partial T}{\partial y}\right) + \mu \left(\frac{\partial u}{\partial y}\right)^2$$

$$\frac{\partial \rho u}{\partial x} + \frac{\partial \rho v}{\partial y} = 0$$

which are valid for both laminar and turbulent flow time-mean quantities if the symbols are appropriately interpreted.

Thus, the normal barred notation for turbulent flows is omitted.

The momentum equation is now multiplied by u and added to the energy equation which then will be integrated with respect to y from wall (y=0) to the edge of the boundary layer y = δ. Integrating by parts and using the Leibnitz's rule one obtains after some rearrangement

$$\frac{d}{dx}\left[\rho_e u_e \delta_4 (H_e - H_w)\right] - \dot{m}(H_e - H_c) = - q_w$$

where at, and over, the injection area Hw = Hc, and

$$\delta_4 = \int_0^{\delta} \frac{\rho u}{\rho_e u_e}\left[\frac{H_e - H}{H_e - H_w}\right] dy \qquad (2)$$

is the enthalpy thickness, and $\dot{m} = \rho_w V_w = \rho_c u_c$
Integrating with respect to x one obtains

$$\rho_e u_e \delta_4 (H_e - H_w) = \int \dot{m}(H_e - H_c)\,dx - \int q_w\,dx + c \qquad (3)$$

which is the fundamental equation for all further developments below. To obtain a basic equation for film cooling, it is necessary to specialize eq. (3) to two separate regions: one near the slot, and the other the far downstream asymptotic region.

The latter region is the area where similarity of the flow profiles has been found to exist and where all the previous work applies. It follows from eq. (3) that the constant c, for the far region, is either very small as compared to the other terms or even zero depending on the injection configuration. Thus, c will be neglected and eq. (3) can be written as

$$\eta_{as} = \frac{M}{\rho_e u_e \delta_4 + Q'} \qquad (4)$$

where

$$Q' = \frac{\int q_w\,dx}{H_e - H_w} \qquad M = \int \dot{m}\,dx$$

To arrive at the expression that is valid for the region near the injection slot a slightly different approach must be used from the one that led to eq. (4). This is necessary because δ_4 may approach zero near the injection region.

To this end, eq. (3) will be written

$$\rho_e u_e \delta_4 = \frac{M}{\eta} - Q' - \frac{c}{H_e - H_w}$$

Near the slot where the wall temperature changes very little, the last term can be assumed to be constant. Call it C_2. Thus one gets

$$\eta_{near} = \frac{M}{\rho_e u_e \delta_4 - C_2 + Q'} \qquad (5)$$

Since eq. (3) has been specialized now for the near and far regions, it is of interest to investigate if there exists a more general form of the effectiveness equation which would be valid for both near and the downstream asymptotic regions. Comparing equations (4) and (5) the following form is suggested for a general solution

$$\eta = \frac{C_3 M}{\rho_e u_e \delta_4 - C_2 + Q'}$$

with the following boundary conditions:

$x = x_o \quad \delta_4 = \delta_{4_0} \quad \eta = 1$ or η_o

$x \rightarrow \infty \quad \eta \rightarrow \eta_{as} = \dfrac{M}{\rho_e u_e \delta_4 + Q'}$

Thus, at $x = x_o$ $\quad \dfrac{C_3 M}{\eta_o} = \rho_e u_e \delta_{4_o} - C_2 + Q'_o$

and one gets

$$\eta = \frac{M \eta_o (\rho_e u_e \delta_{4_o} + Q'_o - C_2)}{M_o (\rho_e u_e \delta_4 + Q' - C_2)}$$

To satisfy the asymptotic case where $x \rightarrow \infty$ and $\eta \rightarrow \eta_{as}$ the above will be solved for C_2.

$$C_2 \left[M \eta_o - M_o \eta \right] = M \eta_o (\rho_e u_e \delta_{4_o} + Q'_o) - M_o \eta (\rho_e u_e \delta_4 + Q')$$

Upon substituting for the asymptotic value of η one obtains

$$C_2 \left[\frac{\eta_o}{M_o} (\rho_e u_e \delta_4 + Q') - 1 \right] = \frac{\eta_o}{M_o} (\rho_e u_e \delta_4 + Q') \left[\rho_e u_e \delta_{4_o} + Q'_o - \frac{M_o}{\eta_o} \right]$$

Furthermore, for the asymptotic case

$$\frac{\eta_o (\rho_e u_e \delta_4 + Q')}{M_o} \gg 1$$

and one gets finally

$$C_2 = \rho_e u_e \delta_{4_o} + Q'_o - \frac{M_o}{\eta_o}$$

Substituting into the effectiveness equation above η becomes

$$\eta = \frac{\int \dot{m}\, dx}{\rho_e u_e (\delta_4 - \delta_{4_o}) + \dfrac{\int \dot{m}\, dx}{\eta_o} + \dfrac{\int q_w\, dx}{H_e - H_w} + Q'_o} \qquad (6)$$

In general, the last term in the denominator is zero, and $\eta_o = 1$. Equation (6) is the basic equation for film cooling.

3. Applications

Since most of the published data refers to film cooling with an adiabatic wall, eq. (6) can be written as

$$\eta = \left[1 + (\delta_4 - \delta_{4_0})/ms\right]^{-1} \tag{7}$$

where $m = \rho_c u_c / \rho_e u_e$ and s is the slot height (Fig. 1) or an equivalent injection distance (total coolant holes area/ width of the injection area). δ_4 can be obtained from eq. (2) with the assumption that the thermal and velocity boundary layer thicknesses are the same, as

$$\delta_4 = \int_0^\delta \frac{\rho u}{\rho_e u_e}\left[\frac{H_e - H}{H_e - H_w}\right] dy$$
$$\cong \int_0^\delta \frac{\rho u}{\rho_e u_e}\left[\frac{T - T_e}{T_{aw} - T_e} + \frac{u_e^2}{2c_p(T_{aw} - T_e}\left(\left[\frac{u}{u_e}\right]^2 - 1\right)\right] dy \tag{8}$$

Whence $\delta_{4_0} \cong ms(u_c/u_e)^2$. Then the effectiveness becomes

$$\eta = \left[1 + \delta_4/ms - \left(\frac{u_c}{u_e}\right)^2\right]^{-1} = \frac{u_c/u_e}{\frac{\delta_4 \rho_e}{\rho_c s} + \frac{u_c}{u_e}\left(1 - \frac{u_c}{u_e}\right)\left(1 + \frac{u_c}{u_e}\right)} \tag{9}$$

Since $\eta \leq 1$, eq. (9) implies that for optimum cooling $u_c/u_e \lesssim 1$, which is in agreement with similar results of Spalding (2). For practical calculations it remains now to evaluate δ_4 for specific cases. This has been carried out below and compared with the published data for flat wall and turbine blade cooling. The general features and typical results are presented here. For details see Ref. 3.

3.1 Flat Wall Cooling

The simplest method of evaluating δ_4 is to use the turbulent noninjection boundary layer results $u/u_e = (y/\delta)^{1/n}$ and the temperature distribution as obtained by Wieghardt (1)

$$(T - T_e)/(T_{aw} - T_e) = \exp\left[-c_1 (y/\delta)^{\frac{1}{n}+2}\right]$$

where

$$c_1 = \left[\Gamma\left(\frac{1+3n}{1+2n}\right)\right]^{\frac{1}{n}+2} \begin{array}{l} = .768 \ , n = 7 \\ = .775 \ , n = 10 \end{array}$$

Substituting into eq. (7) with $1/n \ll 2$ and $u_e^2/2C_p(T_{aw} - T_e) \ll 1$, one obtains

$$\delta_4 = a\,\delta = a\,c_2\,x\,R_{e_x}^{-.2}$$

where

n	7	10
a	.512	.575
C_2	.37	.514

$R_{e_x} = \rho_e u_e x/\mu_e$

Then the effectiveness becomes with $\delta_{4_0} = a\,\delta_0$

$$\eta = \left[1 + 1/\eta_1\right]^{-1} \tag{10}$$

where

$$\eta_1 = A\left[\frac{x^{.8} - x_0^{.8}}{(ms)^{.8}}\right]^{-1}\left(R_{e_c}\frac{\mu_c}{\mu_e}\right)^{.2}$$

$A = 1/ac_2$

and η_1 can be recognized as the asymptotic film cooling correlation used by previous investigators. Eq. (10) has been applied to the data of References (4), see Fig. 3, and (5) Fig. 4. On the average, eq. (10) represents a fair correlation of the data. Other data cannot be correlated well because this method suffers from the following shortcomings: the boundary layer model does not take into account fluid injection, similar velocity profiles have been assumed with a constant n, and the starting distance x_o has been difficult to determine.

In order to eliminate the most serious shortcoming, lack of the effect of fluid injection, the following approach has been used. The two-layer boundary layer model of Abramovich(6) provides the velocity profiles for evaluating the boundary layer thickness δ from the momentum integral equation

$$d\theta/dx = \tau_w/\rho u_e^2$$

According to the model in Fig. 2 the momentum thickness can be expressed by the following velocity profiles

$$y < \delta_m \qquad u/u_m = (y/\delta_m)^{1/n}$$

$$\delta_m < y < \delta \qquad u/u_e = 1 + (u_w/u_e - 1)(1 - (y/\delta)^{1.5})^2 \qquad (11)$$

as

$$\theta = \int_0^{\delta} \frac{\rho u}{\rho_e u_e}\left(1 - \frac{u}{u_e}\right) dy = Q(\delta_m/\delta, u_w/u_e; n)\ \delta \qquad (12)$$

Integrating, one obtains $\delta = \frac{1}{Q} \int_{x_o}^{x} \tau_w/\rho u_e^2\, dx + \delta_o$

The wall shear, which is essentially determined by u_m and δ_m, can be obtained in similarity to basic turbulent boundary layer development as

$$\frac{\tau_w}{\rho u_m^2} = \frac{.033\, C_3(n)}{\left(\frac{u_m \delta_m}{\nu}\right)^{1/4}}$$

where

$$C_3(n) = \frac{2n^2}{(n+1)(2n+1)}$$

Upon rearranging, one gets

$$\frac{\tau_w}{\rho_e u_e^2} = \left(\frac{u_w}{u_e}\right)^{1.75} \left(\frac{u_m}{u_w}\right)^{1.75} \frac{.033\, C_3}{\left(\frac{u_e \delta_m}{\nu}\right)^{1/4}}$$

Calculations indicate that $1.09 < u_m/u_w < 1.15$, thus an average value of 1.1 is used. Furthermore, experimental evidence indicates (7) that the two layer interface δ_m varies linearly with x. Assuming then $\delta_m \simeq .01x$, and substituting into the integral for δ

$$\delta = \frac{.033\, C_3}{Q(u_e/\nu)^{1/4}} \int_{x_o}^{x} \left(\frac{u_w}{u_e}\right)^{1.75} \frac{dx}{x^{.25}} + \delta_o \qquad (13)$$

Abramovich(6) has calculated the wall velocity u_w variation as an implicit function of x and the coolant velocity ratio u_c/u_e. Since practical turbine coolant velocity ratios tend to be less than unity Abramovich's results were recalculated and the following parametric curve fit obtained for u_w/u_e

$$u_w/u_e = e^{D}(x/s - 19)^{B} - 8 \qquad (14)$$

where $D = 2.16767 - .170965(u_e/u_c) + .1667(u_e/u_c)^2$

$B = .005963 + .02925(u_e/u_c) - .049396(u_e/u_c)^2 + .02057(u_e/u_c)^3$

$.25 < u_c/u_e < .85$

Thus, all the integrations here have been rendered into simple quadratures.

The calculation process requires now the substitution of the velocity profiles, eq. (11), and eq. (14) into eq. (8) and (12), which yields $\delta_4 = a(\delta_m/\delta,\ u_w/u_e; n)\delta$ (15) where δ is evaluated from eq. (13) after calculating Q from eq. (12). Although an iterative procedure is indicated above, since the ratio δ_m/δ is not known initially, the method is very insensitive to this ratio and it can be expressed by means of

$$\frac{\delta_m}{\delta} = \frac{.01\,x}{.37\,x \Big/ \left(\frac{U_e x}{\nu}\right)^{.2}}$$

Thus, the enthalpy thickness δ_4 is obtained as a function of x and u_c/u_e, and the effectiveness can be calculated from eq. (9).

The method outlined above was applied to the cases shown in Fig. 4 and the new results are shown in Fig. 5. Although this approach incorporates a number of assumptions and empirical data, the improvement in the trend and consistency of results is good.

3.2 Turbine Blade Cooling

In practical turbine cooling with a pressure gradient the enthalpy thickness will still be calculated from an equation of the form of eq. (15) if, consistent with the integral method approach, it is assumed that the velocity profiles (11) and the Wieghardt temperature distribution hold. The boundary layer thickness must be calculated from the momentum equation valid for flows with variable external velocity:

$$\frac{d\theta}{dx} + \frac{1}{u_e}\frac{du_e}{dx}(2\theta + \delta^*) = \tau_w/\rho u_e^2 \qquad u_e = u_e(x)$$

Assuming, similarly to eq. (12), that the displacement thickness can be given as

$$\delta^* = \int_0^\delta \left(1 - \frac{\rho u}{\rho_e u_e}\right) dy = P(\delta_m/\delta,\, u_w/u_e; n)\,\delta$$

then the resulting momentum equation

$$\delta \frac{dQ}{dx} + Q\frac{d\delta}{dx} + \frac{1}{u_e}\frac{du_e}{dx}(2Q + P)\,\delta = \tau_w/\rho u_e^2$$

can be integrated to give

$$\delta = \frac{1}{Q u_e^T}\int_{x_0}^{x} \frac{\tau_w}{\rho u_e^2}\, u_e^T\, dx + \delta_0 \qquad (16)$$

where $T = 2 + P/Q$.

Thus, the blade cooling problem is reduced to the same essentials as discussed above. The shear stress will be taken from Bradshaw and Gee$^{(7)}$ results, which yields

$$\frac{\tau_w}{\rho u_w^2} = .013 \left(\frac{u_w \delta_m}{\nu_c}\right)^{-.18}$$

Which, upon substitution into eq. (16) gives

$$\delta = \frac{.013\,(.01)^{-.18}}{Q u_e^T \left(\frac{u_c}{u_{e_s}}\right)^2 \left(\frac{u_c}{\nu_c}\right)^{.18}} \int_{x_o}^{x} u_e^T \frac{dx}{x^{.18}} + \delta_o \tag{17}$$

Eq. (17) is similar to the flat plate equation, eq. (13), with the exception of the variable external blade velocity u_e which, for practical purposes, is available as a polynomial of x calculated by the potential flow methods.

The effectiveness was calculated for the turbine vane data as given in Ref. (8) and the results are compared in Fig. 6. Although the experimental data is obtained on a blade with injection through discrete holes it is expected that the model presented above will give satisfactory results with the possible exception of the near injection region. Calculations were based on an equivalent slot thickness. As Fig. 6 indicates the results are satisfactory.

References

1. Wieghardt, K., Hot Air Discharge for Deicing, AF Transl. Rept. No. F-TS-919-Re, Wright Field, Aug. 1946.
2. Spalding, D. B., Recommendations for the Choice of the Velocity of Injection of a Film Coolant, A.R.C. 25312, Oct. 1963.
3. Saarlas, M., Turbine Blade Film Cooling, U.S. Naval Academy Report EW-8-73, Dec. 1973.
4. Hartnett, J.P., Birkebak, R.C., Eckert, E.R.G., Velocity Distributions, Temperature Distributions, Effectiveness, and Heat Transfer for Air Injected Through a Tangential Slot into a Turbulent Boundary Layer, ASME 60-H-53 April 1960; also J. Heat Transfer, V. 83, Jan. 1961, 293-306.
5. Chin, J.H., Skirvin, S.C., Hayes, L.E., Silver, A.H., Design Data for Single Slot Film Cooling, G.E. Report R58AGT129, June 1958.
6. Abramovich, G.N., The Theory of Turbulent Jets, MIT Press, Cambridge 1963, Section 11.4.
7. Bradshaw, P.A., Gee, M.T., Turbulent Wall Jets with and without an External Stream, R&M No. 3252, 1962.
8. Lander, R.D., Fish, R.W., Suo, M., External Heat Transfer Distribution on Film Cooled Turbine Vanes, J. Aircraft, Vol. 9, No. 10, Oct. 1972.

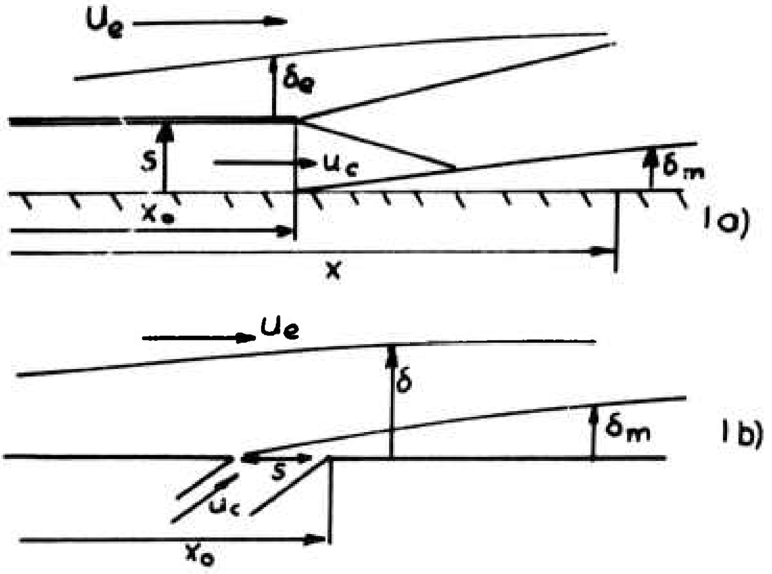
U_e
δ_e
s
u_c
δ_m
x_o
x
1a)
U_e
δ
δ_m
1b)
s
u_c
x_o

Fig. 1 Film cooling configurations

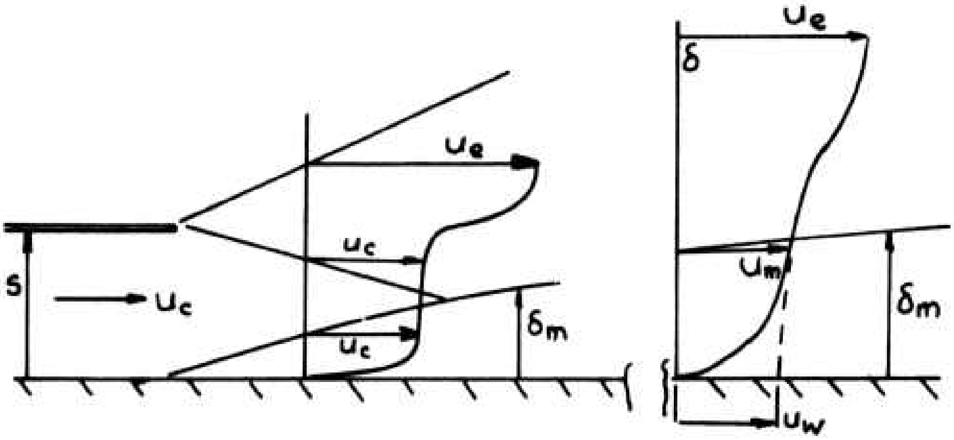
s
u_c
u_e
u_c
u_c
δ_m
u_e
δ
U_m
δ_m
u_w

Fig. 2 The two layer model

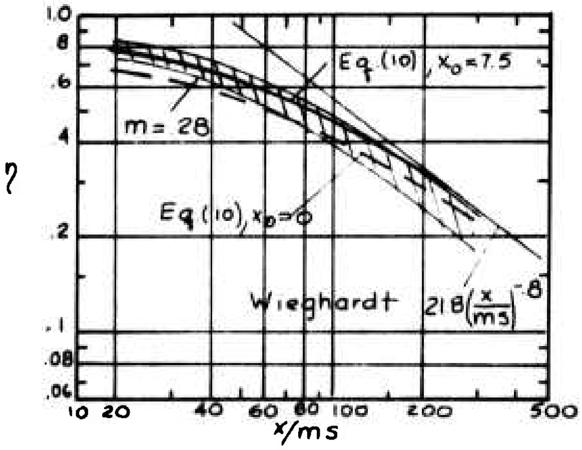

Fig. 3 Effectiveness data from Ref. 4: m =.28, R_{e_c} = 2310, s = .123 in.

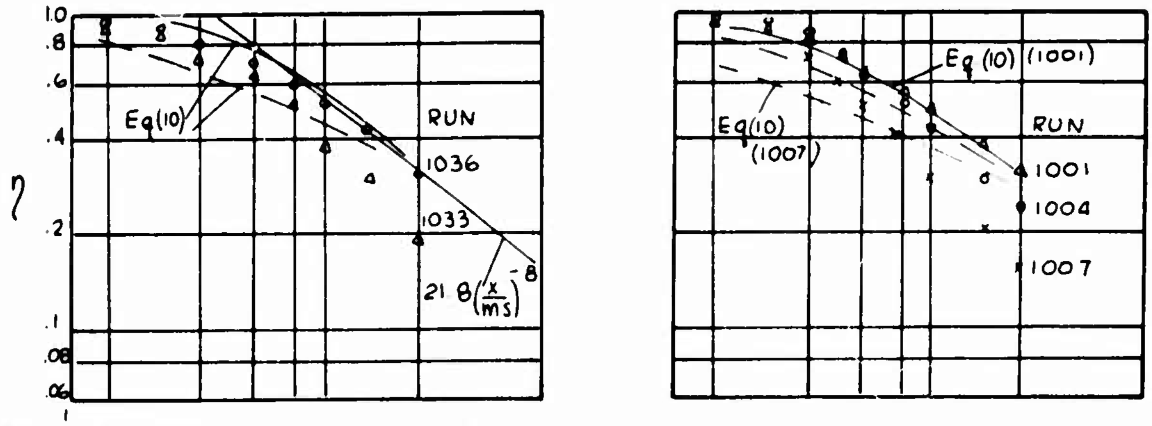

Fig. 4 Effectiveness calculated from eq. (10), data of Ref. 5
s = .106

Run	1036	1033	1001	1004	1007
m	.777	.608	.709	.53	.247
u_c/u_e	.93	.64	.624	.472	.224

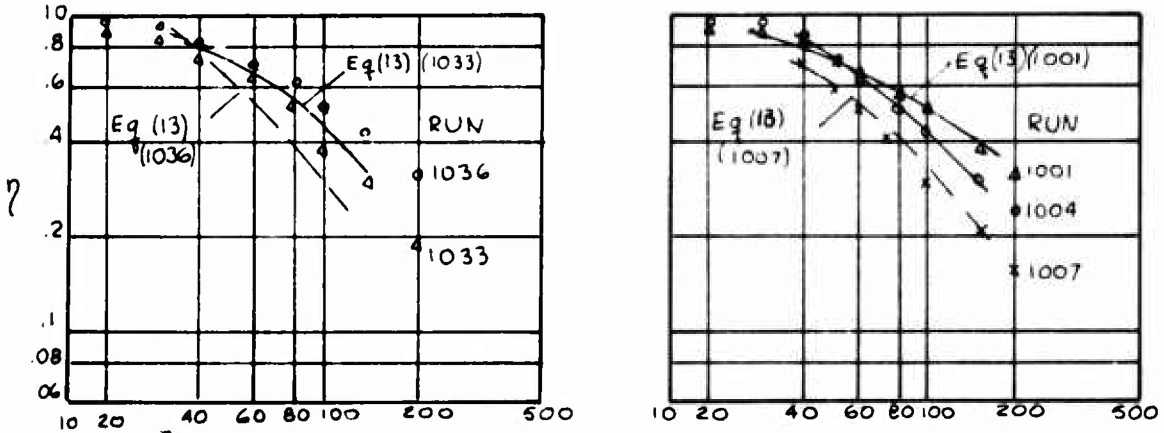

Fig. 5 Effectiveness calculated from eq. (10). Data of Ref. 5
(As in Fig. 4)

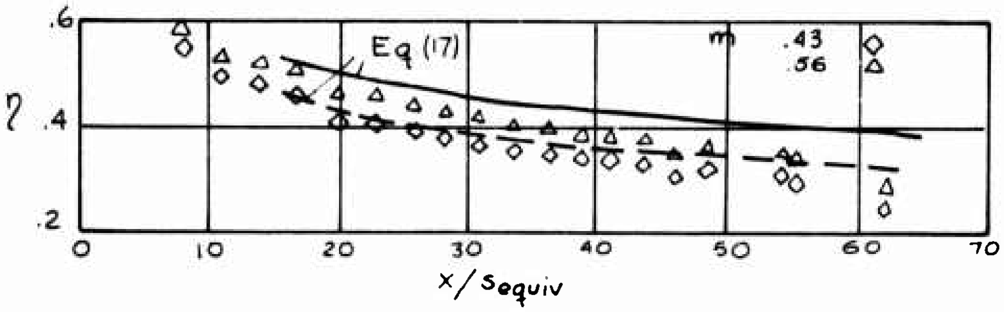

Figure 6 Effectiveness on a turbine vane. Data of Ref. 8, airfoil 1.

AERODYNAMIC AND HEAT TRANSFER INTERACTIONS IN HIGH TEMPERATURE TURBINES

J. R. Fagan, D. J. Helton and D. A. Nealy
Detroit Diesel Allison Division of GMC

INTRODUCTION

The advantages of very high turbine inlet temperatures are readily recognized as offering a great potential for efficient, lightweight, gas turbine engines. To achieve the high temperatures within currently available materials, air is commonly bleed from the compressor discharge and used to cool the turbine. This paper presents the results of a brief parametric study to establish the interaction between cooling air requirements and turbine efficiency in a high temperature turbojet engine. Based upon design experience at Detroit Diesel Allison, blade chord, blade solidity and blade height have been established as the most effective blading parameters available to affect the cooling air requirements. Therefore, these three blade properties were investigated parametrically. The basic question is whether it is useful, in terms of overall engine performance, to bias the turbine blading design toward reductions in cooling air requirements at the expense of some turbine efficiency.

In order to answer this question, a blade heat transfer model was developed to predict the cooling air flow required to meet a fixed stress rupture life as a function of blading geometry and stress levels. A baseline blade was designed and six additional blades were designed having ±20% variations in blade chord, solidity and annulus area, respectively. The design point efficiency for each turbine was predicted by means of the Ainley-Mathieson(1) turbine performance model as modified by Dunham and Came(2) and supplemented by a cooling air loss model developed at Detroit Diesel Allison. The efficiency and cooling air differentials were then evaluated in a cycle analysis of a high temperature turbojet engine to assess the impact on specific thrust.

COOLING PERFORMANCE MODEL

The combination of high stress levels and gas path temperatures characteristic of advanced single stage drive turbines emphasizes the importance of the turbine blade thermal/structural design problem. Consequently, a turbine blade cooling model was developed to evaluate turbine mechanical design feasibility, and to provide realistic estimates of turbine blade cooling air requirements as a function of turbine aerodynamic design. The results of this study serve to establish the impact of turbine aerodynamic design configuration on blade cooling air requirements subject to the following general conditions.

o Fixed turbine rotor inlet temperature

- o Fixed turbine rotor stress rupture life
- o Cooling air supplied from compressor discharge

The turbine airfoil cooling requirements were established on the basis of simple overall energy balance procedures which essentially equate the convective heat load on any cooled structural component to the coolant heat absorption. The latter is strongly influenced by the efficiency of the internal cooling system design. Throughout this study the internal cooling efficiency was held constant at a level representative of current high temperature blading technology.

The convective heat load, Q, imposed on any cooled structure is essentially proportional to the difference between its surface temperature and the gas stream relative total temperature, and is inversely proportional to the thermal resistance of the boundary layer formed along the cooled surface.

Once the heat load for a given airfoil is established, the cooling air flow requirement is obtained by equating the imposed heat load to the coolant energy absorption. If x represents chordwise surface distance (measured from the leading edge), and y represents spanwise surface distance (measured from hub or tip section), then the following overall steady state thermal energy balance must be satisfied,

$$Q = \int\int q_s'' \, dxdy + \int\int q_p'' \, dxdy = W_c C_{pc} \Delta T_c \qquad (1)$$

The left side of Equation (1) represents the integrated convective* heat load for the two surfaces of the airfoil, while the right side represents the coolant heat absorption. For either airfoil surface, the local heat flux, q'', can be expressed as

$$q'' = q''(x, y) = h(T_g - T_w) \qquad (2)$$

where h is the local gas to wall heat transfer coefficient. In general, h, T_g, and T_w may all vary with x and y so q'' is a local heat flux. However, for preliminary coolant flow estimation purposes, it is useful to define average values of T_g and T_w so that

$$Q = (\overline{T}_g - \overline{T}_w) \left[\int\int h_s \, dxdy + \int\int h_p \, dxdy\right] = W_c C_{pc} (\overline{T}_w - T_c) \eta_t \qquad (3)$$

where

$\eta_t = \Delta T_c / (\overline{T}_w - T_c)$ and

T_c = coolant supply temperature.

---

*In general, the radiative contribution to airfoil heat load is negligibly small.

The overall thermal effectiveness, η_t, represents the ratio of the actual coolant temperature rise to the maximum possible coolant temperature rise, $(\overline{T}_W - T_c)$. In cooled airfoil designs, the value of η_t is dependent on the nature of the blade cooling mechanism and as noted above was held constant for this study.

For the case of a fully developed turbulent boundary layer (which can be assumed to exist over the greater portion of the cooled airfoils considered herein), the local surface heat transfer coefficients can be reasonably approximated by the relationship

$$St = h/\rho_g V_g C_{pg} = 0.0296\ (Re_x)^{-1/5}\ (Pr)^{-.4} \qquad (4)$$

Substituting Equation (4) into (3) and carrying out the indicated integrations, then yields the basic relationship from which the cooling air requirements can be determined. Making the further approximation that h is essentially invariant with spanwise distance (y coordinate) and that the effective length, ℓ, of both the suction and pressure surfaces is equal to one-half of the airfoil perimeter, Equations (4) and (5) can be combined and cast into a form which better reflects engine geometric and cycle parameters.

$$W_c/W_g = C1\ C2\ (\phi/\eta_t)\varepsilon\ (A_s/A_g)(\sqrt{T_g}\ /C3\ P_g)^{1/5}\ (\ell)^{-1/5} \qquad (5)$$

The coefficient, C1, accounts for the difference in Stanton number on the blade surface due to coolant injection as shown in Figure 1. Figure 1 also shows the surface velocity distribution coefficient, α.

Inspection of Equation (5) permits several observations to be made relative to the parameters which influence turbine cooling air requirements:

o Percentage coolant flow requirements W_c/W_g are directly proportional to level of cooling (ϕ), and inversely proportional to thermal effectiveness (η_t).

o Percentage coolant requirements are directly proportional to blade surface area/gas flow area ratio. Since for given airfoil settings, A_s/A_g is proportional to solidity, percentage coolant flow requirements tend to increase directly with blade row solidity.

o Percentage coolant requirements decrease slightly as mean airfoil surface length (~true chord) is increased. Other factors being equal, long chord airfoils will require less air (on a percentage basis) than short chord airfoils.

o Airfoils with high exit/inlet relative Mach number ratios will require higher percentage air flows because the parameter α

is increased (see Figure 1).

The relatively simple formulation given as Equation (5) has been shown to provide quite reliable estimates of airfoil cooling requirements. Typical comparisons between detailed analyses and projections obtained from Equation (5) are shown in Table 1, which illustrates the usefulness of the technique.

Table 1. Comparison of Cooling Flow Predictions

Engine Type	Airfoil	Cooling Air Requirement W_c/W_1, %	
		Detail Analysis	Equation 5
Turboshaft	HP1 Vane	3.70	3.85
Turboshaft	HP1 Blade	1.35	1.43
Turbo fan	HP1 Blade	2.60	2.60
Turbo fan	HP2 Blade	0.92	0.82

Cooling performance curves (ϕ vs W_c/W_g) were established for each of the six parametric turbine blade designs by means of Equation 5. The cooling air flows calculated via Equation (5) strictly apply to a relatively small spanwise segment of the airfoil where T_g and T_w can be considered constant. The calculation can be repeated for several spanwise segments each of which is characterized by a different combination of $\bar{T}_g$ and $\bar{T}_w$ values reflecting the radial gas temperature profile and allowable metal temperature distribution. These flows could then be summed to provide the total airfoil cooling flow. Extensive experience has shown that the latter (summed) value is approximately equal to 90% of the value predicted by Equation (5) when it is assumed that the entire airfoil is characterized by the midspan values of $\bar{T}_g$ and $\bar{T}_w$. Thus in the present study, all cooling air flows were taken to be 90% of the value calculated from Equation (5) where $\bar{T}_g$ and $\bar{T}_w$ are taken to be midspan values. Figure 2 shows the resultant cooling air requirements for each of the parametric blade configurations. In order to obtain the specific cooling requirement for each blading configuration, the wall temperature was established at a value which would give the same stress rupture life as the baseline blade. The stress level was obtained by multiplying the untapered stress by an appropriate linear taper factor which reflected the blade geometry and the need to provide an internal coolant flow passage. The internal flow passage was sized to hold the coolant inlet Mach number the same in each of the blade configurations. The resulting coolant flow percentages are indicated by the symbols in Figure 2.

AERODYNAMIC PERFORMANCE MODEL

The prediction of aerodynamic performance of turbines is quite difficult principly because of the importance of three-dimensional effects (commonly referred to as secondary losses) in the highly cambered blade rows of turbines. The importance of blade tip clearance is also accentuated in most high temperature gasifier turbine designs. In addition, in high temperature turbine applications, there is a significant impact on turbine performance or efficiency due to the addition of low momentum cooling air through the blades and vanes. This element is termed cooling losses. There are also parasitic losses due to the addition of low momentum air which has been used to cool the endwalls and wheels of the turbine. These parasitic losses have been assumed independent of the blading changes that are under investigation in this study.

The complexity of the aerodynamic performance prediction problem has lead to extensive use of empirical data as the basis for prediction of turbine efficiency. One commonly accepted model is that proposed by Ainley-Mathieson(1) with a modification of the secondary loss treatment as proposed by Dunham and Came(2). Throughout this work, the aerodynamic performance will be assessed on the basis of the Ainley-Mathieson model augmented by a cooling loss model developed at Detroit Diesel Allison.

The profile loss for zero incidence as proposed by the Ainley-Mathieson model and used in this study is given by

$$Y_p = [\, Y_{p(\beta_1=0)} + (\beta_1/\alpha_2)^2 \, (Y_{p(\beta_1=-\alpha_2)} - Y_{p(\beta_1=0)}) \,] \, (t/c/0.2)^{-\beta_1/\alpha_2} \quad (6)$$

The effect of cooling air mixing on the aerodynamic performance is not accounted for in the basic model of Ainley-Mathieson. DDA has developed a coolant mixing loss model based upon hypothesis that the losses are governed by the momentum mixing of the secondary jet and the primary freestream flow. Following the work of Shapiro(3), the total pressure variation can be written as

$$dP_g/P_g = (-kM_g^{\,2}/2)\,dT_g/T_g - (kM_g^{\,2}/2)\,(2-2\;V_c/V_g \cos \psi_c)\; dM_c/M_g \quad (7)$$

Assuming a constant heat capacity, C_{pg}, and adiabatic flow, the linearized form of the energy equation can be written as

$$dT_g/T_g = (dM_g/M_g)(T_c/T_g - 1) \quad (8)$$

Further, the secondary mass addition is given by

$$dM_c = G\,dA = G\,H_y\,dx \quad (9)$$

Substituting (8) and (9) into (7) and rearranging, the differential equation for the change in total pressure, due to coolant addition is given by

$$dP_g/P_g = (-kM_g^{\,2}/2)\,(1 + T_c/T_g - 2(V_c/V_g)\cos \psi_c)\,GHy/M_g dx \quad (10)$$

or integrating over the length of the coolant injection region, the total pressure recovery is given by

$$P_2/P_1 = e^{-\int_{x_1}^{x_2} (kM^2/2)(1 + T_c/T_g - 2(V_c/V_g)\cos \psi_c) GHy/M_g dx} \qquad (11)$$

Equation (11) can be used to calculate the total pressure change due to transpiration or film cooling of blades by integrating along the suction and pressure surfaces using the blade surface Mach number distribution. Figure 3 shows a comparison of the measured and predicted total pressure losses. Throughout this study, Equation (11) has been used to assess blade cooling losses.

In 1970, Dunham and Came(2) suggested a secondary loss model based upon meanline blade loading parameters given by

$$\begin{aligned} Y_s &= 0.0334\ (C/H)(\cos \alpha_2/\cos \beta_1)\ Z \\ &= 0.1336\ (C/H)(\cos^3 \alpha_2/\cos \beta_1 \cos \alpha_m)(\mathrm{Tan}\ \alpha_1 - \mathrm{Tan}\ \alpha_2)^2 \end{aligned} \qquad (12)$$

Again following the work by Dunham and Came the tip clearance loss for unshrouded blades is given by

$$Y_k = 0.47(C/H)(\delta/c)^{0.78}\ Z \qquad (13)$$

The impact of the blading parameters, namely chord, solidity (or chord to spacing ratio) and blade annulus area (height) have been assessed with respect to their impact on turbine efficiency by means of the models described above. The total change in turbine efficiency is taken as a linear sum of the changes in component efficiencies. Thus,

$$\Delta\eta = \Delta\eta_p + \Delta\eta_c + \Delta\eta_s + \Delta\eta_k \qquad (14)$$

The influence of blade chord, blade solidity and blade height on turbine efficiency are shown in Tables 2, 3, and 4, respectively.

ENGINE PERFORMANCE

The interaction between cooling air requirements and turbine efficiency is illustrated here for the case of a high temperature turbojet engine. The engine cycle analysis assumes that all of the cooling air is provided at compressor discharge conditions with appropriate modifications to total temperature and pressure to deliver the air to the base of the blade. Thus, the burner and turbine vane inlet flow are the difference

Table 2. Blade Chord Effects of Turbine Efficiency

Component Loss	Change in Turbine Efficiency	
	Decreased Chord	Increased Chord
Profile, $\Delta\eta_p$	0.0	-0.04
Cooling, $\Delta\eta_c$	-.07	+0.07
Secondary, $\Delta\eta_s$	+1.12	-1.19
Clearance, $\Delta\eta_k$	+0.24	-0.21
Total	+1.3	-1.4

Table 3. Blade Solidity Effects on Turbine Efficiency

Component Loss	Change in Turbine Efficiency	
	Decreased Solidity	Increased Solidity
Profile, $\Delta\eta_p$	-0.28	+0.20
Cooling, $\Delta\eta_c$	-0.14	+0.04
Secondary, $\Delta\eta_s$	-0.29	+0.17
Clearance, $\Delta\eta_k$	-0.08	+0.05
Total	-0.8	+0.5

Table 4. Blade Height Effects on Turbine Efficiency

Component Loss	Change in Turbine Efficiency	
	Decreased Height	Increased Height
Blade		
Profile, $\Delta\eta_p$	+0.38	-0.38
Cooling, $\Delta\eta_c$	-0.16	-0.07
Secondary, $\Delta\eta_s$	-0.23	+0.23
Clearance, $\Delta\eta_k$	-0.10	+0.20
Total	-0.1	0.0
Vane		
Profile, $\Delta\eta_p$	+0.30	-0.21
Cooling, $\Delta\eta_c$	+0.04	-0.03
Secondary, $\Delta\eta_s$	-0.12	+0.10
Total	+0.2	-0.1
Stage Total	+0.1	-0.1

between the compressor discharge flow and the cooling air flow. Using the engine cycle analysis program a sensitivity analysis was performed to assess the impact of the cooling air and turbine performance on thrust per pound of compressor discharge air. This specific thrust parameter, which affects engine size and weight directly, was used to assess the tradeoff in cooling air and turbine efficiency. Figure 4a shows the change in specific thrust as a function of the change in turbine efficiency and cooling air flow, respectively. Figure 5 shows the change in specific thrust that results from the changes in blade chord, blade solidity and blade height, respectively.

CONCLUSIONS

In drawing real conclusions from a design study of this type, it must be recognized that the results are specific to one engine and that future technology advances will change the quantitative results. Therefore, important general conclusions should reflect only upon the observed basic technology trends.

First, there is a clear trade in specific thrust between cooling air use and turbine efficiency. In all cases, except those involving blade height variations where the predicted efficiency change was nearly zero, the thrust increment due to the change in cooling air was opposite in sign to that due to the turbine efficiency change. That is to say that the higher turbine efficiency blading configurations all required higher coolant flow rates. It must be noted, however, that the specific turbojet engine studied herein was not particularly sensitive to changes in turbine efficiency or cooling air. The observed performance balance indicates the need to quickly and accurately assess a number of blading and flow path configurations with respect to cooling requirements and efficiency within the preliminary design phase of any high temperature turbine. This fact emphasizes the importance of a simple, quantitative cooling flow model such as described herein.

A similarly efficient aerodynamic performance prediction capability is offered by the Ainley-Mathieson model. However, advanced design concepts incorporating controlled radial work distributions and specialized endwall configurations to modify the three-dimensional flow losses cannot be represented by meanline properties such as incorporated in the Ainley-Mathieson model. It is generally accepted that profile losses can be predicted for vane and blade cascades and the coolant loss model described herein has proven to be quite effective. However, secondary loss levels and particularly the radial distribution of secondary losses are not sufficiently well understood to allow accurate predictions based upon the controlling flow physics. Considering the component loss increments shown in Tables 2 through 4, it can be seen that three-dimensional effects represented by the secondary and clearance losses provided a major influence in this study and therefore must be more adequately modeled. Finally, tentative conclusions about high temperature blading can be made. Optimum performance of an air cooled turbine will occur at somewhat lower solidity than for uncooled turbine.

There is apparently an optimum chord blade where increasing turbine efficiency balances the increasing cooling requirements resulting from the reduced taper ratio available as the blade chord is shortened. It also appears that blade annulus height should be made as small as possible to reduce the untapered stress levels without introducing excessive shock losses resulting from the increased Mach numbers and at the same time assuring that limiting loading will not occur within the operating range of the turbine. Further, any annulus reduction must allow growth capability if a practical production engine is to result.

REFERENCES

1. Ainley, D. G. and Mathieson, G. C. R. A Method of Performance Estimation for Axial-Flow Turbines. Aeronautical and Research Council R&M 2974,
2. Dunham, J. and Came, P. M. Improvements to the Ainley-Mathieson Method of Turbine Performance Prediction. ASME Paper No. 70-GT-2, May 1970.
3. Shapiro, A. H. The Dynamics and Thermodynamics of Compressible Fluid Flow. The Ronald Press Co., New York, 1958.

LIST OF SYMBOLS

A_b	Total blade surface area
A_1	Gas stream flow area at rotor inlet
C	Blade chord
C_p	Heat capacity
C_L	Blade loading coefficient $C_L = 2 \frac{S}{C} \cos \alpha_m (\text{Tan } \alpha_1 - \text{Tan } \alpha_2)$
C1	Boundary layer blockage coefficient in cooling flow model (Equation 5) $C_1 = .018\,K = 0.18\ St/St_o$
C2	Fluid transport property coefficient in cooling flow model (Equation 5) $C_2 = (Pr_1)^{-2/3} (u_1)^{1/5} \quad C_{p_1}/C_{p_c}$
C3	Corrected blade inlet flow per unit area $C_3 = \frac{W_1 \sqrt{T_1}}{A_1\ P_1}$

α	Gas angle
β	Blade angle
δ	Blade tip clearance
σ	Surface velocity distribution coefficient in cooling flow model (see Figure 1) $\sigma = \frac{8}{5} \int_0^1 \left(\frac{\rho_1 V_1}{\rho_g V_g}\right)^{-0.8} \left(\frac{x}{\ell}\right)^{-0.2} d\left(\frac{x}{\ell}\right)$
η	Turbine efficiency
η_t	Blade overall thermal effectiveness
μ	Viscosity
ρ	Density
ϕ	Overall cooling performance parameter $\phi = \frac{\overline{T}_1 - \overline{T}_w}{\overline{T}_w - T_c}$
ψ	Coolant injection angle measured from blade surface

Subscripts

c	Coolant
g	Mainstream gas
k	Tip clearance
m	Mean value
p	Profile
s	Secondary
1	Blade inlet station
2	Blade exit station

G	Coolant mass flow per unit area
H	Blade height
h	Blade external film coefficient
K	Boundary layer blockage parameter (see Figure 1)
k	Ratio of specific heats
ℓ	Mean airfoil chordwise surface length (1/2 perimeter)
M	Mach number
P	Total pressure relative to blade row
p	Static pressure
P_r	Prandtl number
Q	Total blade heat load
q''	Blade surface heat flux
Re_x	Reynolds number based upon x
S	Blade meanline spacing
St	Stanton number
T	Total temperature relative to the blade row
t	Blade maximum thickness
V	Fluid velocity
W	Fluid mass flow rate
x, y	Blade surface coordinates in chordwise and spanwise directions, respectively
Y	Aerodynamic loss parameter
Z	Ainley blade loading parameter

$$Z = (C_L / S/C)^2 \; \frac{\text{Cos}^2 \; \alpha_2}{\text{Cos}^3 \; \alpha_m}$$

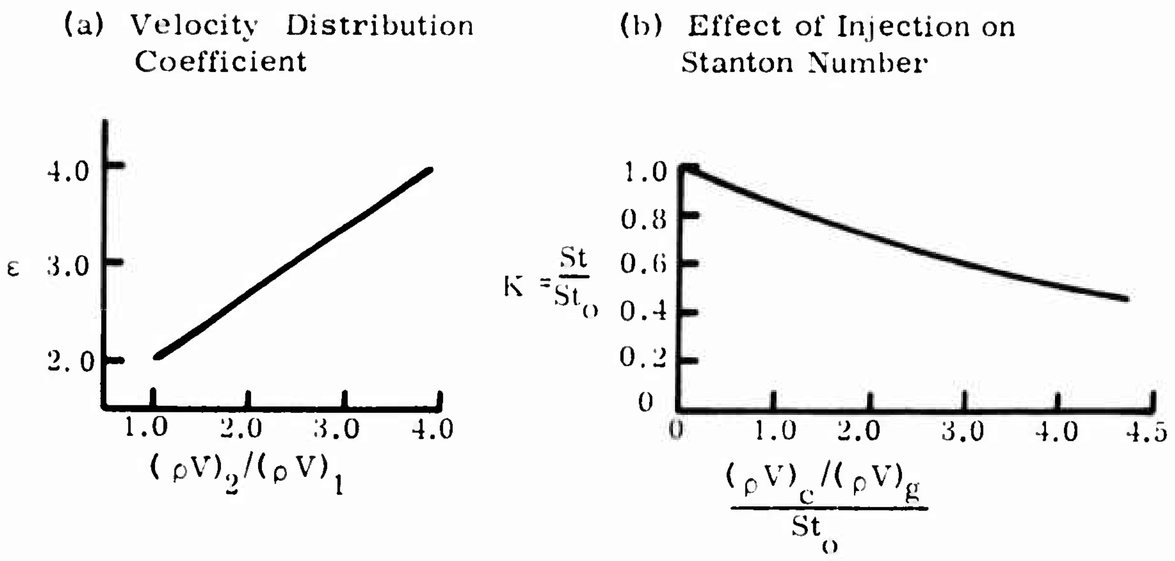
(a) Velocity Distribution Coefficient

(b) Effect of Injection on Stanton Number

Figure 1. Cooling Flow Model Correlations

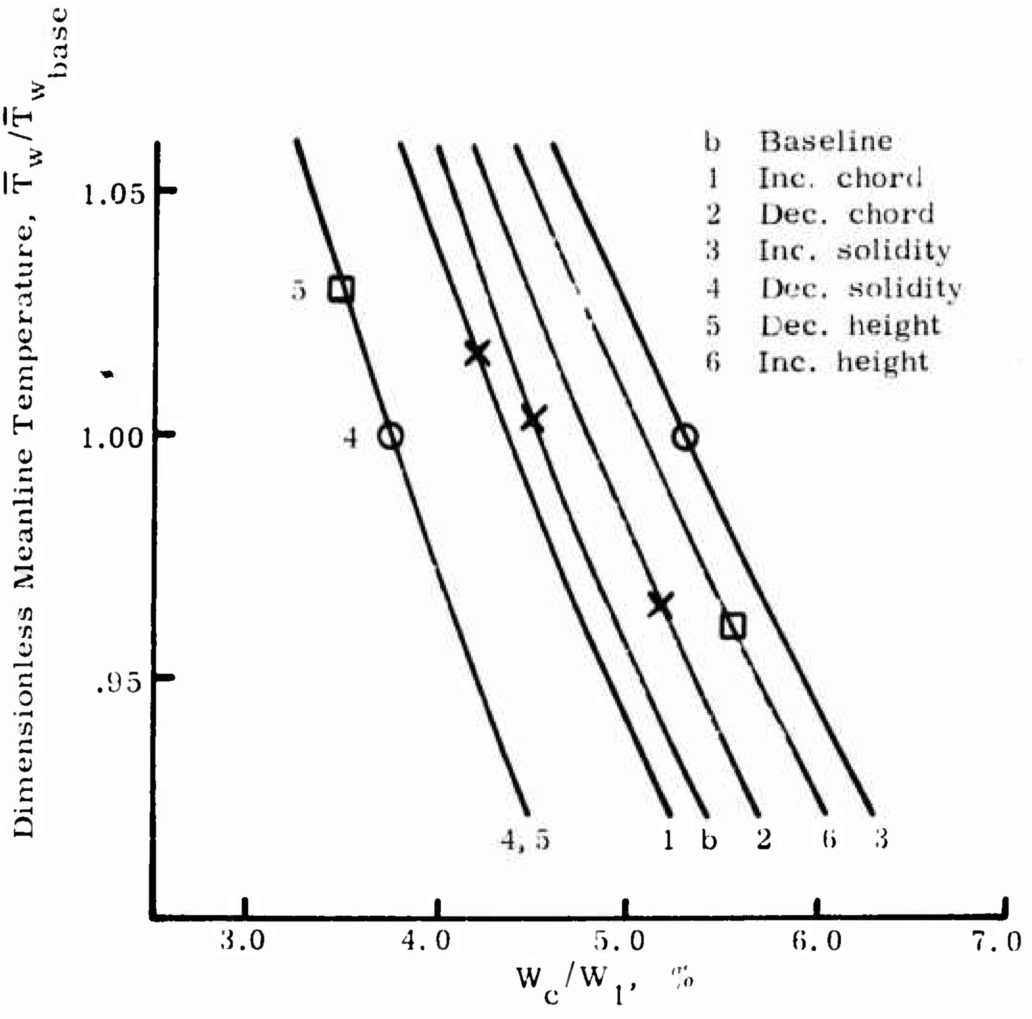

Figure 2. Effect of Meanline Metal Temperature on Required Rotor Blade Coolant Flow Rate

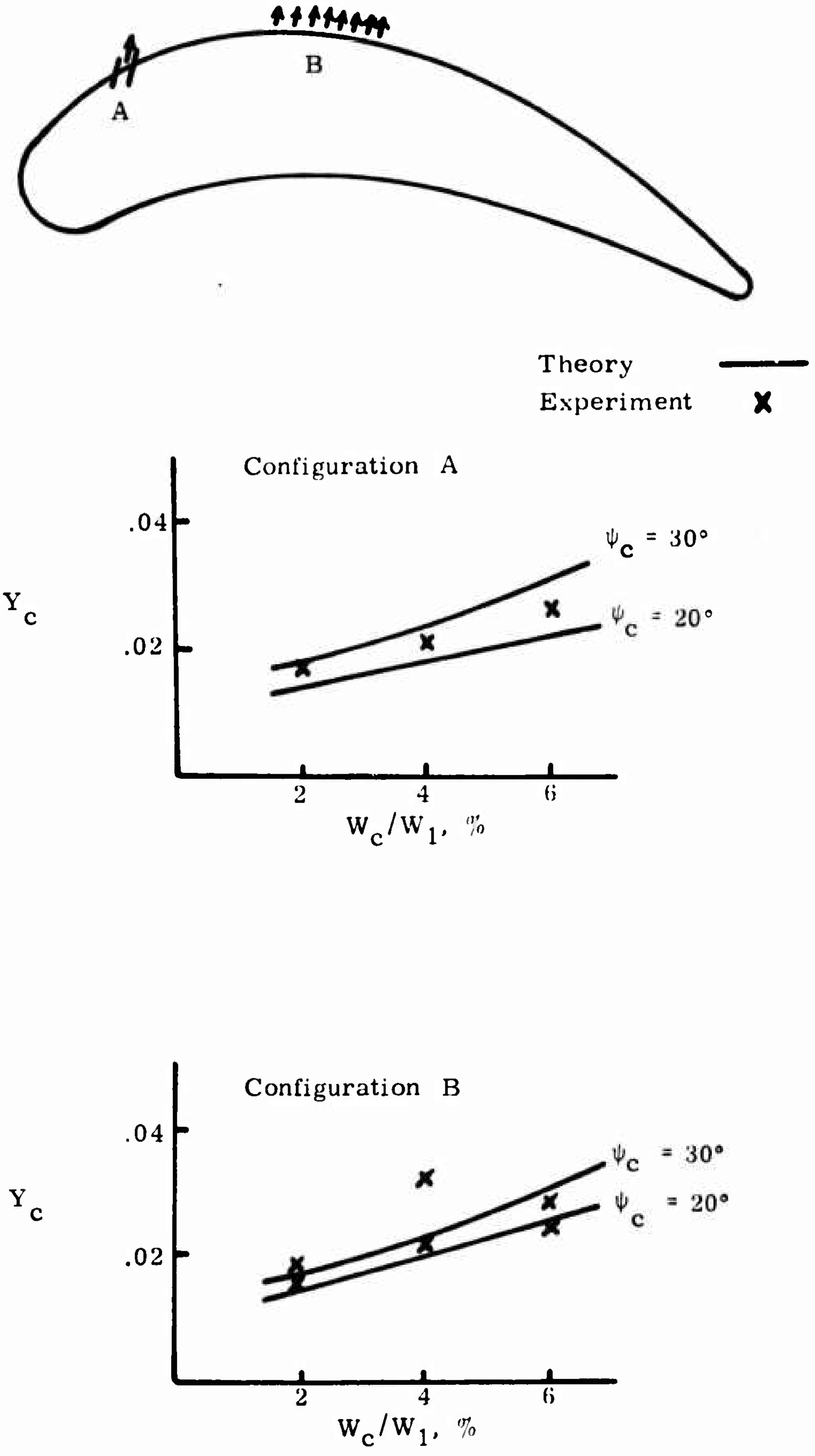

Figure 3. Comparison of Cooling Loss Model With Data

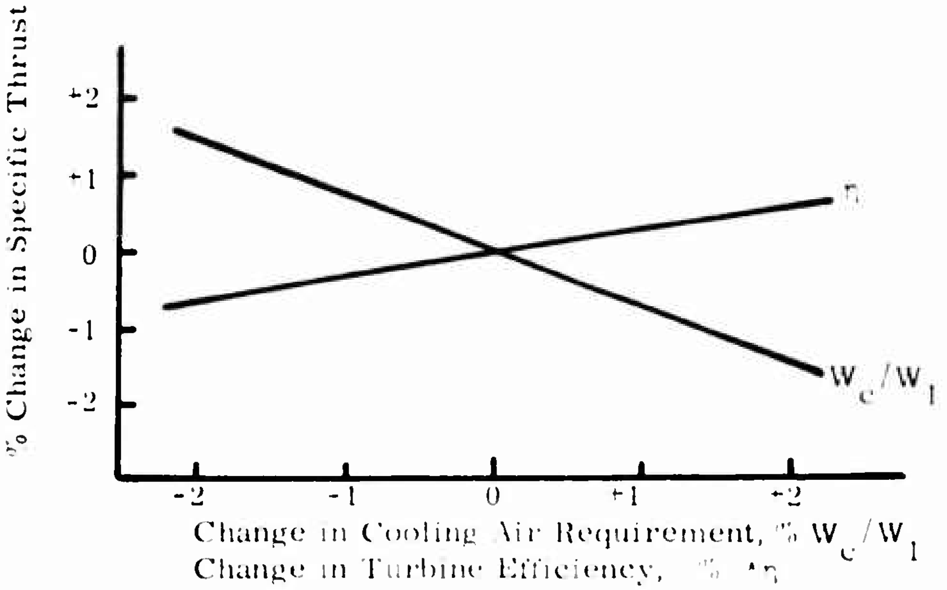

Figure 4. Effect of Cooling Air and Turbine Efficiency on Specific Thrust

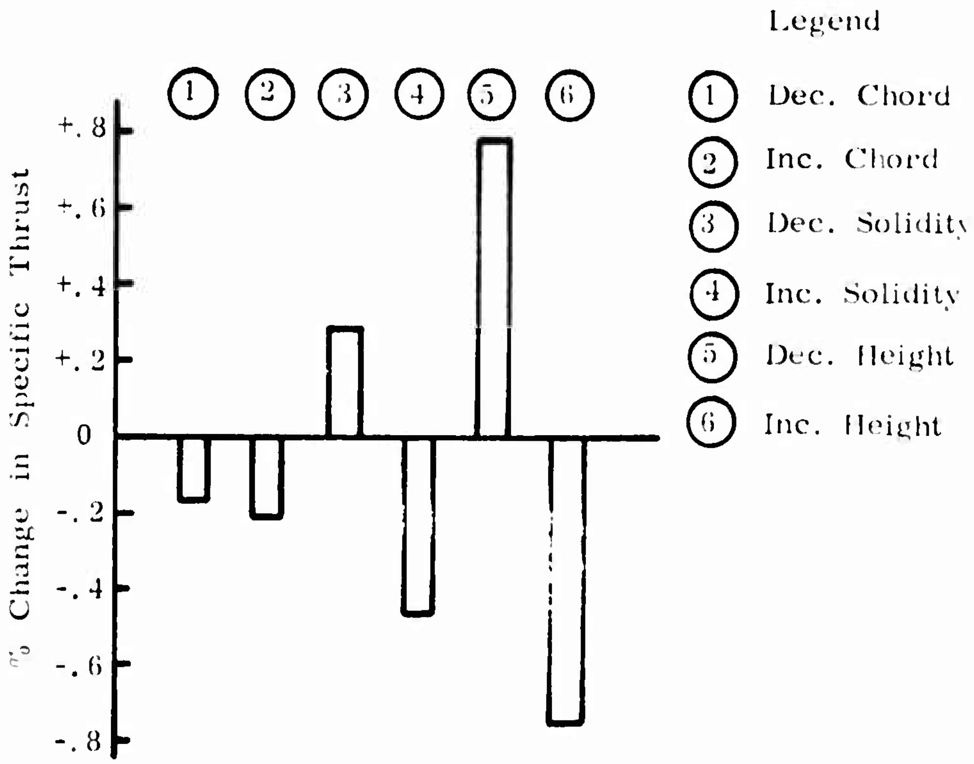

Figure 5. Specific Thrust Variations for Parametric Blades

LINEARIZED THREE-DIMENSIONAL POTENTIAL FLOW THROUGH A RECTILINEAR CASCADE OF BLADES

A. F. de O. Falcão

Instituto Superior Técnico, Universidade Técnica de Lisboa, Portugal

1 - INTRODUCTION

In most of the so-called three-dimensional flow theories for axial turbomachines, the analysis of the flow through a blade row is carried out as the combination of two different approaches. The first one is blade element or strip flow, which supplies two-dimensional performance data for a given profile, isolated or in a two-dimensional cascade, from analytical or experimental investigations with plane flow. The second type is related to the overall flow induced by the whole blade row or rows and allows the aerodynamic interference between the different radii to be taken into account. Due to mathematical difficulties in the full three-dimensional analysis, the classical simplification consists in assuming the flow to be axially symmetric by taking the circumferential average of the flow variables and thus reducing the general flow equations from a three-dimensional to a two-dimensional system.

There are three-dimensional effects that cannot be accounted for by the combination of axially symmetric theory and two-dimensional strip theory. One of these is due to the fact that the vorticity shed by the actual blade row is concentrated in the blade wakes rather than circumferentially uniform. This effect is particularly important for small numbers of blades and large spanwise variation of the blade load, as is the case of screw propellers.

Lifting-line theory no longer assumes circumferential uniformity and it is not surprising that, among all turbomachines, it was first applied to screw propellers and later extended to include the effects of the walls of ducted machines and of compressibility(1). The theory replaces each blade by a bound vortex line or lifting line and is based on the assumption that the velocity and pressure distributions about a blade section in a three-dimensional configuration are equal to the corresponding values for an identical blade section in two-dimensional plane flow, with the direction of the approaching stream modified by the induced downwash angle evaluated at the corresponding point of the lifting-line. Among the most relevant works based on the lifting-line model with compressible flow, we mention the theory developed by Namba and Asanuma(2,3) for linear cascades with shear flow and the papers of Okurounmu and McCune(4) and McCune and Dharwadkar(5) concerning the potential flow through an annular cascade of rotating blades.

It was only recently that some theoretical works have been published allowing an estimate of the range of validity and the errors connected with the quasi-two-dimensional relationship between blade section geometry and aerodynamic performance which underlies lifting-line theory of turbomachines. This is done by using lifting-surface theory, which is free from such quasi-two-dimensional assumptions and replaces each blade by a (usually plane or helical) vortex sheet. The strength of the vortex sheet varies in both spanwise and chordwise directions and the theory relates its distribution to the blade row geometry. This is the approach followed by Namba(6,7) in his analysis of the compressible shear flow through a linear cascade of untwisted blades with constant profile. The compressible potential flow about an annular cascade of rotating blades was delt with by Okurounmu and McCune(8), who presented a method to solve the direct (prescribed load) problem, and by Namba(9,10), who developed a method of solution for the more difficult inverse (prescribed geometry) problem. These authors showed that there is relatively good agreement between the results given by lifting-line and lifting-surface theories for the lift distribution and deflection angle in the case of incompressible or low relative Mach number flow, but lifting line theory is clearly inadequate for high subsonic and transonic relative Mach numbers.

In this paper, we consider the potential flow through a linear cascade of blades with prescribed twist and profile, using the lifting-line and lifting-surface methods. The resulting expressions involve elementary transcendental functions and are considerably easier to compute than those encountered in the analysis of shear and annular flows, making it possible to obtain accurate numerical results and to compare between the different theories without excessive computing time. The paper is based on, and constitutes an extension of, part of an earlier work of the author(11).

2 - RECTILINEAR CASCADE OF LIFTING-LINES

2.1 - Assumptions and Basic Equations. We consider the incompressible inviscid flow through an infinite row of lifting-lines perpendicular to, and spanning, two parallel plane walls, and choose a system of cartesian coordinates x,y,z (with unit vectors $\vec{i},\vec{j},\vec{k}$), which are made dimensionless by taking the distance between the walls equal to unity (Fig. 1). The walls are defined by z=0, z=1, and the lifting-lines by y=0, x=nt (n=0,±1,±2,...), t being the pitch to span ratio. The bound circulation is supposed, in general, to vary along the span and is denoted by Γ(z). The undisturbed flow is uniform, with streamlines forming an angle ε with the x-axis. Following small perturbation theory, we assume the trailing vortex filaments to coincide with streamlines of the undisturbed flow, thus forming a row of vortex sheets defined by x-y tan ε=nt, y>0.

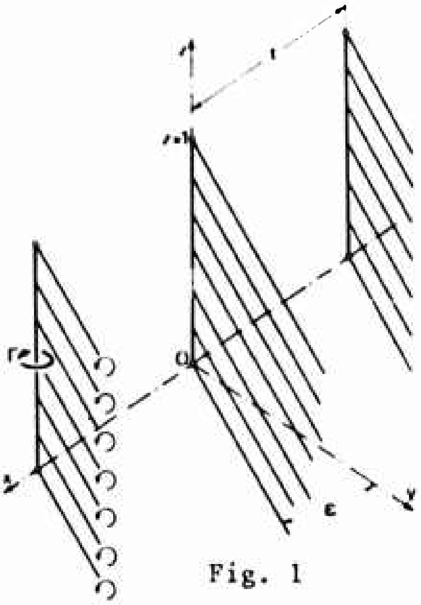

Fig. 1

If, in Eq.(A2) derived in Appendix 1, α is replaced by z, β by u=x-y tan ε, β_0 by nt and σ by y, then the expression of the disturbance velocity $\vec{V}$, induced by the whole vortex system, is found to be

$$\vec{V} = \nabla\phi - (\vec{i}-\vec{j}\tan\varepsilon)H(y)\Gamma(z)\sum_{n=-\infty}^{\infty}\delta(u-nt), \tag{1}$$

where ϕ is a potential function. Introducing the equation of continuity $\nabla.\vec{V}=0$, we obtain the following equation for ϕ

$$\nabla^2\phi = \sec^2\varepsilon\ H(y)\Gamma(z)\sum_{n=-\infty}^{\infty}\delta'(u-nt) - \tan\varepsilon\,\delta(y)\Gamma(z)\sum_{n=-\infty}^{\infty}\delta(u-nt). \tag{2}$$

2.2 - Solution of the Potential Equation. The difficulty due to the discontinuities of the potential function downstream of the cascade ϕ^d across the vortex sheets (see Appendix 1) can be overcome by writing $\phi^d = -\Gamma(z)S(u) + \phi_1^d$, where

$$S(u) = -\frac{1}{2} + \frac{u}{t} - H(u) - \sum_{n=1}^{\infty}\left[H(u-nt)-H(-u-nt)\right]$$

$$= \frac{1}{\pi}\mathrm{Re}\sum_{n=1}^{\infty}\frac{i}{n}\exp(in\omega u),$$

with $\omega=2\pi/t$, is a saw-tooth function of period t, varying linearly between -1/2 and 1/2 in the interval $0<u<t$. Now ϕ_1^d is continuous across the vortex sheets and is found to satisfy

$$\nabla^2\phi_1^d = S(u)\, d^2\Gamma(z)/dz^2. \tag{3}$$

The complete solution of this equation will be obtained as the superposition of three terms

$$\phi_1^d = \phi_2^d + \phi_3^d + Cy, \tag{4}$$

where ϕ_2^d is a solution of the complete equation (3), ϕ_3^d satisfies Laplace's equation and C is a constant to be determined.

A solution of (3), which is a function of z and u alone, is

$$\phi_2^d = \frac{1}{\pi}\,\mathrm{Re}\sum_{n=1}^{\infty}\frac{i}{n}\, f_n(z)\exp(in\omega u), \tag{5}$$

with

$$f_n(z) = \sum_{p=1}^{\infty}\gamma_p\left[1+\left(\frac{2n}{pt\cos\varepsilon}\right)^2\right]^{-1}\cos(p\pi z). \tag{6}$$

The terms γ_p are the Fourier coefficients in the expansion

$$\Gamma(z) = \sum_{p=0}^{\infty}\gamma_p\cos(p\pi z). \tag{7}$$

Expressions for the potentials ϕ^u upstream, and ϕ_3^d downstream, of the cascade plane are obtained as double series of eigensolutions of Laplace's equation

$$\begin{bmatrix}\phi^u\\ \phi_3^d\end{bmatrix} = \mathrm{Re}\sum_{n=0}^{\infty}\sum_{p=0}^{\infty}\begin{bmatrix}A_{np}^u\\ A_{np}^d\end{bmatrix}\cos(p\pi z)\exp(in\omega x-\lambda_{np}|y|), \tag{8}$$

where the eigenvalues λ_{np} are given by $\lambda_{np} = \pi\left[(2n/t)^2+p^2\right]^{1/2}$ and A_{np}^u, A_{np}^d are constants to be determined by the matching conditions at z=0. The constant of Eq.(4) can now be determined by setting equal to zero the disturbance total mass flow rate across a plane y=constant>0 and its value is found to be $C=-(\gamma_0/t)\tan\varepsilon$. If we now introduce the conditions of continuity at y=0 for the potential

$$(\phi^u)_{y=-0} = (\phi^d)_{y=+0},\quad x\neq mt\quad (m=0,\pm1,\pm2,\ldots)$$

and for the y-component of the velocity

$$(\partial\phi^u/\partial y)_{y=-0} = (\partial\phi^d/\partial y)_{y=+0},\quad x\neq mt,$$

we find

$$A_{np}^u = \gamma_p(M_{np}-iN_{np}),\qquad A_{np}^d = \gamma_p(M_{np}+iN_{np}),$$

$$M_{0p} = \frac{\tan\varepsilon}{2p\pi t},\quad p=1,2,\ldots,$$

$$\left.\begin{aligned} M_{np} &= \frac{\tan\varepsilon}{t\lambda_{np}}\left[1+\left(\frac{2n}{pt\cos\varepsilon}\right)^2\right]^{-1},\\ N_{np} &= \frac{2n}{\pi}\left[4n^2+(pt\cos\varepsilon)^2\right]^{-1},\end{aligned}\right\}\quad \begin{aligned}&n=1,2,\ldots\\ &p=0,1,2,\ldots\end{aligned}$$

Only the coefficients A_{00}^u and A_{00}^d are left undetermined, but, as their terms in (8) are constant, we are allowed to write, for convenience, $M_{00}=N_{00}=0$. The expression for the potential then becomes

$$\phi = H(y)\,\chi + \sum_{p=0}^{\infty} \gamma_p \cos(p\pi z) \sum_{n=0}^{\infty} \exp(-\lambda_{np}|y|)\,\big[M_{np}\cos(n\omega x)$$

$$- \operatorname{sign}(y)\, N_{np} \sin(n\omega x)\big], \qquad (9)$$

where sign(y)=2H(y)-1 is equal to 1 for $y>0$ and to -1 for $y<0$, and χ is given by

$$\chi = -\Gamma(z)S(u) + \phi_2^d - \frac{\gamma_0 \tan\varepsilon}{t}\, y, \qquad (10)$$

which, with the help of the expansion$^{(12)}$

$$\frac{\sinh[a(\pi-\alpha)]}{\sinh(a\pi)} = \frac{2}{\pi}\sum_{n=1}^{\infty} \frac{n\sin(n\alpha)}{n^2+a^2} \qquad (0<\alpha<2\pi),$$

can be written

$$\chi = -\frac{\gamma_0 \tan\varepsilon}{t}\, y - \gamma_0 S(u) + \Theta, \qquad (11)$$

with

$$\left.\begin{aligned} \Theta(u,z) &= -\frac{1}{2}\sum_{p=1}^{\infty} \gamma_p \cos(p\pi z)\,\frac{\sinh[p\pi(u-t/2)\cos\varepsilon]}{\sinh(\frac{1}{2}p\pi t\cos\varepsilon)} \qquad (0<u<t) \\ \Theta(u+t,z) &= \Theta(u,z). \end{aligned}\right\} \qquad (12)$$

A difficulty arises if these results are to be used in a lifting-surface theory, due to the singular behaviour at the lifting-lines of the double series, and its x- and y-derivatives, in Eq. (9). This can be overcome in part with the aid of the expansion$^{(12)}$

$$\arctan\frac{\sin\alpha}{e^{\xi}-\cos\alpha} = \sum_{n=1}^{\infty} \frac{1}{n}\, e^{-n\xi}\sin(n\alpha) \qquad (\xi>0)$$

and we obtain

$$\phi = \psi + H(y)\left\{\frac{\Gamma(z)-\gamma_0}{t}\,x + \gamma_0\left[\frac{u}{t} - S(u)\right] + \Theta\right\} + \sum_{p=1}^{\infty} \gamma_p \cos(p\pi z)$$

$$\times\left\{\sum_{n=0}^{\infty} M_{np}\exp(-\lambda_{np}|y|)\cos(n\omega x) - \operatorname{sign}(y)\sum_{n=1}^{\infty}\Big[N_{np}\exp(-\lambda_{np}|y|)\right.$$

$$\left. - \frac{\exp(-n\omega|y|)}{2n\pi}\Big]\sin(n\omega x)\right\}, \qquad (13)$$

where

$$\psi = \Gamma(z)\,\mathrm{Re}\left[-\frac{i}{2\pi}\,\ln\!\left(i\sin\frac{\pi\zeta}{t}\right) - \frac{\zeta}{2t}\right] \qquad (14)$$

$$= -\operatorname{sign}(y)\,\frac{\Gamma(z)}{2\pi}\arctan\frac{\sin(\omega x)}{\exp(\omega|y|)-\cos(\omega x)} - H(y)\frac{\Gamma(z)}{t}x, \qquad (15)$$

with $\zeta=x+iy$. In (14), the expression in square brackets is the complex potential of the plane flow due to an infinite row of vortices of unit strength, along the x-axis, with zero velocity at $y=-\infty$ $^{(13)}$. It follows that ψ is the quasi-two-dimensional potential due to the cascade of lifting-lines of strength $\Gamma(z)$. The remaining terms in the right hand side of (13) represent the three-dimensional effects (i.e. the interference between the different spanwise stations) and their values, as well as those of their derivatives, are everywhere finite.

2.3 - Downwash Velocity and Effective Angle of Attack. The velocity $\vec{v}(z)$ induced at a lifting-line by the vortex system can be obtained with the aid of Eqs. (9) to (15) by writing

$$\vec{v}(z) = \frac{1}{2} \lim_{x,y\to 0} \left[\vec{V}(x,y,z)+\vec{V}(-x,-y,z)\right]. \tag{16}$$

For the x- and y-components, we easily find

$$v_x = \frac{1}{2} V_x(y \tan \varepsilon, y, z), \qquad v_y = \frac{1}{2} V_y(y \tan \varepsilon, y, z), \tag{17}$$

with $y=\infty$. This means that the x- (or y-) component of the induced velocity at a lifting line is one half of the x- (or y-) disturbance velocity component at a corresponding point (with equal coordinates u and z) far downstream. If $\varepsilon=0$, a similar relation is found to hold for any point of the plane $y=0$, in agreement with a more general result given by von Kármán and Burgers(14) for unstaggered lifting systems. Except if $\varepsilon=0$, no simple relation of the same kind can be found for v_z.

If the lifting-line method is to be used to obtain the effective angle of attack of the blades, the downwash velocity $v_1=-v_x\cos\varepsilon+v_y\sin\varepsilon$ is required. Equations (9), (10), (16) and (17) yield

$$v_1(z) = \frac{\gamma_0 \cos \varepsilon}{2t} + \frac{\pi}{4} \sum_{p=1}^{\infty} p\gamma_p \coth(\tfrac{1}{2}p\pi t \cos \varepsilon) \cos(p\pi z). \tag{18}$$

In a similar way, we obtain for the streamwise component $v_2=v_x\sin\varepsilon+v_y\cos\varepsilon$

$$v_2 = -\frac{\gamma_0 \sin \varepsilon}{2t}. \tag{19}$$

The velocity $\vec{v}$ can be splitted into a quasi-two-dimensional contribution $\vec{v}^{2d}$ and a fully three-dimensional term $\vec{v}^{3d}$. For two-dimensional flow it is $v_x^{2d}=-\Gamma/(2t)$, $v_y^{2d}=0$, and thus we obtain

$$v_1^{3d} = -\frac{\Gamma(z)-\gamma_0}{2t}\cos\varepsilon + \frac{\pi}{4} \sum_{p=1}^{\infty} p\gamma_p \coth(\tfrac{1}{2}p\pi t \cos \varepsilon)\cos(p\pi z), \tag{20}$$

$$v_2^{3d} = 0. \tag{21}$$

In order to relate the bound vorticity strength to the cascade geometry, we use an approach similar to classical lifting-line theory of wings with finite span and assume that the lift characteristics of each blade section are identical to those in two-dimensional cascade flow, with the direction of the incoming stream corrected by an angle equal to the three-dimensional downwash angle at the corresponding lifting-line station (Fig. 2)

$$\alpha_i(z) = \arctan\frac{v_1^{3d}}{U} \simeq \frac{v_1^{3d}}{U}, \tag{22}$$

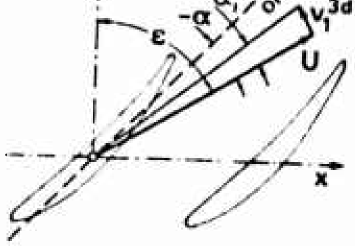

Fig. 2

where U is the indisturbed flow velocity. Let $\alpha(z)$ be the angle between the direction of no lift of the blade section (in two-dimensional cascade flow) and the undisturbed stream direction, and $c(z)$ the blade chord. We assume the lift coefficient of the profile in two-dimensional cascade configuration to be a linear function of the angle of attack and denote by $k(z)$ the corresponding slope. Hence the lift force per unit span can be written

$$L(z) = -\frac{\rho}{2} c(z)\, k(z)\, (\alpha+\alpha_i), \tag{23}$$

where ρ is the fluid density and $\alpha+\alpha_i$ the effective angle of attack. Assuming the two-dimensional relation $L=\rho U\Gamma$ to hold, we obtain, by eliminating L,

$$\Gamma = -\frac{ck}{2}\,(U\alpha+v_1^{3d}). \tag{24}$$

Using (7) for Γ and (20) for v_1^{3d}, we find

$$\sum_{p=0}^{\infty}\gamma_p\,\cos(p\pi z) = -\frac{c(z)k(z)}{2}\left\{U\alpha(z) + \sum_{p=1}^{\infty}\gamma_p\,\cos(p\pi z)\left[\frac{p\pi}{4}\coth\left(\frac{1}{2}p\pi t\cos\varepsilon\right)-\frac{\cos\varepsilon}{2t}\right]\right\}. \tag{25}$$

Assuming the cascade geometry to be known, this equation can be used to obtain the coefficients γ_p. If the product ck is constant, which is in general a good approximation for blades of constant chord, the values of γ_p can easily be found by replacing $\alpha(z)$ by a cosine series of the type of (7) and equating the coefficients of $\cos(p\pi z)$ on both sides of the resulting equation. A numerical method with variable ck was used in(11).

3 - LIFTING-SURFACE THEORY

3.1 - Basic Assumptions.

In this section, a fully three-dimensional theory is developed, based on the use of lifting-surfaces. Small perturbation is still assumed and the analysis is restricted to blades of constant chord and zero thickness.

In lifting-surface theory, the blade is replaced by a bound vortex sheet containing the camber lines of all its sections (camber surface). For small camber, twist and angle of incidence, this surface may be approximated by a plane (chordal plane), in which the bound and trailing vorticity is supposed to lie, and which is not, in general, parallel to the undisturbed stream nor will necessarily contain the leading and trailing edges, particularly in the case of twisted blades. The bound vorticity is then constituted by a plane distribution of lifting-lines, normal to the walls and approximately parallel to the leading and trailing edges, and the free vorticity consists of rectilinear vortex filaments parallel to the walls. The linkage between blade geometry and vorticity distribution is established by setting the condition of resulting velocity tangent to the camber surface. This condition is again simplified by calculating the flow angle at the plane where the singularities lie and neglecting the induced velocity components except the component perpendicular to the plane (downwash velocity).

The system of coordinates x,y,z is chosen as in Sec. 2, but here the z-axis is made to coincide with a blade leading edge or its projection on the chordal plane (Fig. 2). The blades' chordal planes are then defined by $x-y\tan\varepsilon=nt$ $(n=0,\pm1,\pm2,\ldots)$, ε being the angle of stagger as before. In order to analyse the flow about a blade section z=constant, it is convenient to introduce two additional coordinates $\xi=x\sin\varepsilon+y\cos\varepsilon$ and $\eta=-x\cos\varepsilon+y\sin\varepsilon$, which, together with z, constitute another cartesian system of coordinates. The ξ-direction is parallel to the trailing vortex filaments, with $\xi=0$ at the z-axis, and η is measured perpendicularly to, and from, the chordal plane. The projections of the blade leading and trailing edges on the chordal plane are then defined by $\xi=0$ and $\xi=c$, and $\eta=0$, where c is the blade chord.

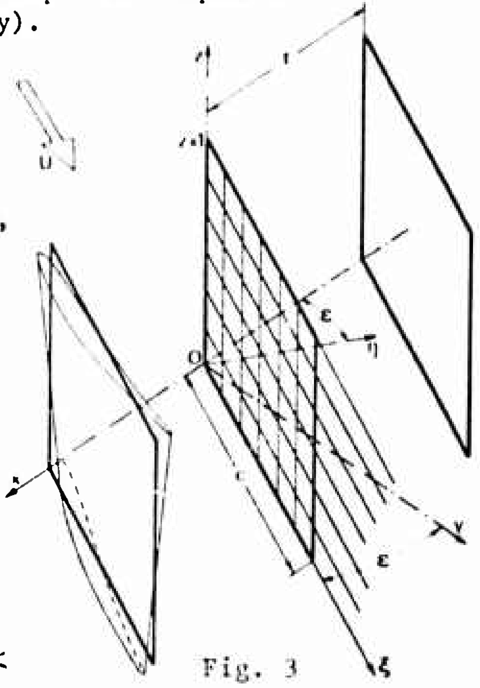

Fig. 3

3.2 - Induced Velocity and Blade Geometry. Let $\vec{q}(\xi,z;\xi')$ be the velocity induced at a point $(\xi,\eta=0,z)$ by an infinite row of lifting-lines of strength $\Gamma(\xi',z)$, the location of which is defined by ξ' and $\eta=nt\cos\epsilon$. Then

$$\vec{q}(\xi,z;\xi') = \vec{V}\left[(\xi-\xi')\cos\epsilon,(\xi-\xi')\sin\epsilon,z)\right], \tag{26}$$

where $\vec{V}(x,y,z)=\nabla\phi$, and ϕ is given by (13) to (15).

We consider now a row of plane lifting-surfaces, i.e. a continuous distribution of lifting-lines at each chordal plane between $\xi'=0$ and $\xi'=c$, with strength $\Gamma(z,\xi')$ per unit length along the chord. The total induced velocity $\vec{Q}(\xi,z)$ at a point of the chordal plane is given by

$$\vec{Q}(\xi,z) = \int_0^c \vec{q}(\xi,z;\xi')d\xi'. \tag{27}$$

Let $\eta=f(\xi,z)$ be the equation of the camber surface of the reference blade $n=0$. With the assumptions of §3.1, the boundary condition at the blade surface can be written

$$\alpha + \frac{Q_\eta}{U} = \frac{\partial f}{\partial\xi}, \tag{28}$$

where Q_η is the downwash component of $\vec{Q}$, perpendicular to the chordal plane, and α is the angle between the undisturbed streamlines and the chordal plane.

If the distribution of the bound vorticity is given, the shape of the camber surface is obtained by integration of the differential equation (28). A more difficult problem arises if the cascade performance is to be determined for a given cascade geometry, for in this case the integrand in Eq. (27) is unknown and the obtention of the vorticity distribution requires solving an integral equation.

Additional difficulties arise from the fact that the integrand in (27) becomes infinite at $\xi'=\xi$ and the bound vorticity is in general infinite at the blade leading edge. A method for overcoming this type of difficulties was given by Glauert(15), in two-dimensional aerofoil theory, by expanding the bound vorticity distribution in a trigonometric series in terms of a variable θ' related to the chordwise coordinate, which replaces the integration variable ξ'. This procedure was later used by Schlichting(16) in two-dimensional cascades and by Namba(6,9,10) in three-dimensional cascade problems. Applying this method to our case, we write

$$\Gamma(z,\xi') = G_0(z)\tan(\theta'/2) + \sum_{m=1}^{\infty} G_m(z)\sin(m\theta'), \tag{29}$$

where

$$G_m(z) = \sum_{p=0}^{\infty} g_{pm}\cos(p\pi z) \qquad (m=0,1,2,\ldots) \tag{30}$$

and $\xi'=c(1+\cos\theta')/2$, with $\theta'=\pi$ and $\theta'=0$ for $\xi'=0$ and $\xi'=c$ respectively. In this way, the Kutta condition at the trailing edge is satisfied and the singularity at the leading edge is suitably represented by the term $\tan(\theta'/2)$.

It is not difficult to conclude that the singularity of the integrand in (27) at $\xi'=\xi$ is introduced by the derivative of the quasi-two-dimensional potential ψ of (14). More precisely, it is due only to the contribution of the reference blade $n=0$. As in Schlichting's method(16) for two-dimensional cascades, the singularity can be discarded from $\vec{q}(\xi,z;\xi')$ by subtracting the contribution $\vec{q}^{(0)}$ due to the quasi-two-dimensional potential concerning the reference blade. Its η-component is

$$q_\eta^{(0)}(\xi,z;\xi') = \frac{\Gamma(z,\xi')}{2\pi(\xi-\xi')}.$$

Then, changing from variables ξ and ξ' to θ and θ' respectively, and performing the integration indicated in (27), we find (see(15))

$$Q_\eta^{(0)}(\xi,z) = \frac{1}{2} \sum_{p=0}^{\infty} \sum_{m=0}^{\infty} g_{pm} \cos(m\theta) \cos(p\pi z). \tag{31}$$

The integration of the remaining terms presents no major difficulties and the final expression for the downwash velocity is found to be

$$Q_\eta(\xi,z) = \sum_{p=0}^{\infty} \sum_{m=0}^{\infty} g_{pm}\Omega_{pm}(\xi) \cos(p\pi z). \tag{32}$$

The expressions of $\Omega_{pm}(\xi)$ are given in Appendix 2.

If a solution is required for the direct problem, the form of the last equation suggests developing the function $f(\xi,z)$ in the following cosine series

$$f(\xi,z) = \sum_{p=0}^{\infty} \beta_p(\xi) \cos(p\pi z). \tag{33}$$

Then Eq. (28), expressing the boundary condition at the blade camber surface, is replaced by as many equations as the number P+1 of terms which are retained in the cosine series of (32) and (33). We obtain

$$\left.\begin{aligned} &\alpha + \frac{1}{U} \sum_{m=0}^{M} g_{0m}\Omega_{0m}(\xi) = \frac{d}{d\xi}\beta_0(\xi), \\ &\frac{1}{U} \sum_{m=0}^{M} g_{pm}\Omega_{pm}(\xi) = \frac{d}{d\xi}\beta_p(\xi) \qquad (p=1,2,\dots,P), \end{aligned}\right\} \tag{34}$$

where finite series with M+1 terms replace the infinite ones. These equations show that the spanwise harmonics p=0,1,2,...,P can be delt with independently from each other. For the harmonic of order p, the unknown coefficients g_{pm} (m=0,1,2,...,M) are determined by writing the corresponding equation (34) at M+1 different points $\xi_1, \xi_2, \dots, \xi_{M+1}$ in the interval $0<\xi<c$. The problem then consists in solving, for each value of p, a set of M+1 linear equations with M+1 unknowns.

4 - COMPARISON OF DIFFERENT THEORIES

4.1 - Cascade Geometry. Numerical results were computed for some test cases, mainly to illustrate the degree of agreement obtained when different theories are used, namely lifting-surface, lifting-line, actuator screen and two-dimensional theories (by order of decreasing approximation). For shortening, in the following text, these will be abbreviated as LS, LL, AS and 2D respectively. The calculations were carried out for twisted compressor blades of prescribed geometry (concave side facing the positive η-direction), with constant chord and (for simplicity) constant parabolic profile (maximum height of parabolic arc h). The undisturbed stream direction was taken tangent to the mid-span section camber line at the trailing edge, the geometric angle of attack (defined, for each value of z, by the unperturbed flow direction and the blade chord) increasing linearly from z=0 to z=1, with total variation Λ.

4.2 - Lifting-surface Calculations. With this geometry, the independent terms in (34) become

$$\frac{d}{d\xi}\beta_0(\xi) - \alpha = \frac{8h\xi}{c^2}, \qquad \frac{d}{d\xi}\beta_p(\xi) = \begin{cases} -\Lambda/(p\pi)^2 & (p=1,3,5,\dots) \\ 0 & (p=2,4,6,\dots) \end{cases}$$

Therefore, only terms of order p=0,1,3,5,... were kept in the calculations.

Results were obtained with several geometric configurations, and curves were plotted for the total load coefficient $C_L(z) = \frac{2\Gamma_{tot}(z)}{Uc} = \frac{2}{Uc}\int_0^c \Gamma(z,\xi)d\xi$ (Fig. 4), the linearized blade surface pressure coefficient

$C_p=2Q_\xi(\xi,z)/U$ (Fig. 5) and the ratio $Q_z(\xi,z)/U$ (Fig. 6). The values $h/c=0.05$ (camber angle 22.61°) and $\Delta=10°$ were kept constant, and several values were given to t, ε and c.

The integrals appearing in Appendix 2 and in the expressions of Q_ξ and Q_z were computed with the aid of Simpson's rule with 15 points. For engineering calculations, it was found that sufficient accuracy is obtained by retaining terms up to p=1 or p=3 (p=5 or p=7 if Q_z is required) in the series expressing variation with z. The number of terms to be kept in the series giving the chordwise load distribution (Glauert's series) depends on the camber line shape. For parabolic shape, terms up to m=3 were found to be sufficient, but additional terms shall possibly be required for other shapes. In the series of circular functions expressing variation with x, the number of required terms increases with the pitch to span ratio t, but terms up to n=1 were found to be enough for t<1. The results shown in this paper were actually computed with larger numbers of terms (up to p=m=n=7), in order to make sure that the, sometimes small, differences between values calculated by different theories were not significantly affected by errors of numerical approximation.

4.3 - Two-dimensional Calculations. Assuming the flow to be two-dimensional at each plane z=constant, it is easy to see that the expression of the velocity component $Q_\eta^{2d}(\xi,z)$ at the chordal plane can be obtained from (32) by discarding the harmonics of order p≥1 and replacing the remaining coefficients g_{0m} by $G_m(z)$. We then find

$$Q_\eta^{2d}(\xi,z) = \sum_{m=0}^{\infty} G_m(z)\Omega_{0m}(\xi) = \sum_{p=0}^{\infty}\sum_{m=0}^{\infty} g_{pm}\Omega_{0m}(\xi)\cos(p\pi z), \tag{35}$$

the double series having been obtained by replacing the coefficients $G_m(z)$ by their developments (30). The way of determining the values of g_{pm} is now identical to that described for LS in §3.2, in the text following Eq. (32), with the difference that, in (34), the coefficients Ω_{pm} are to be replaced, for p≥1, by Ω_{0m}, as follows immediately from the comparison of (32) and (35).

4.4 - Lifting-line Calculations. The theory being based on the assumption of quasi-two-dimensionality, the calculations are similar to those described in §4.3, with the difference that the three-dimensional downwash velocity $v_1^{3d}(z)$ is added to $Q_\eta^{2d}(\xi,z)$. The expression of v_1^{3d} is given by (20), with the Fourier coefficients γ_p, of the total bound circulation distribution, obtained by integration

$$\gamma_p = \int_0^c\Big[g_{p1}\tan(\theta'/2) + \sum_{m=1}^{\infty} g_{pm}\sin(m\theta')\Big]d\xi' = \frac{\pi c}{2}\Big(g_{p0} + \frac{1}{2}g_{p1}\Big). \tag{36}$$

The final equations are then obtained from (34), by replacing, for p≥1, Ω_{p0} by $\Omega_{00}+b_p$, Ω_{p1} by $\Omega_{01}+b_p/2$, and Ω_{pm} by Ω_{0m} (m=2,3,...), with

$$b_p = \frac{\pi c}{8}\Big[p\pi\coth\Big(\frac{1}{2}p\pi t\cos\varepsilon\Big) - \frac{2}{t}\cos\varepsilon\Big].$$

This procedure is in part formally different from, but equivalent to, that described in §2.3, and is more suitable if the object of the calculations is the comparison of different theories.

4.5 - Actuator Screen Calculations. The three-dimensional downwash velocity at the blades is now calculated assuming that the vorticity is uniformly distributed in the x-direction, in such a way that the bound circulation per unit pitchwise length remains equal to $\Gamma_{tot}(z)/t$, with $\Gamma_{tot}(z)$ being the total bound circulation about the actual blade. This is equivalent to replacing the actual cascade by another one with vanishingly small pitch t_ω and blade circulation $\Gamma_{tot,\omega}(z)$, such that $\Gamma_{tot}(z)/t= \Gamma_{tot,\omega}(z)/t_\omega$. Introducing this condition in Eq. (20), the following expression is found

$$v^{3d}_{1\infty}(z) = \frac{\Gamma_{tot}(z)-\gamma_0}{2t}\sin\varepsilon\,\tan\varepsilon\,. \tag{37}$$

The remaining calculations follow as in §4.4, with obvious modifications.

4.6 - Comparison of Numerical Results. The numerical examples were worked out using all four theories and some of the results were plotted together in Figs 4 and 5. In Fig. 4, the scales of C_L were chosen so as to give equal slopes for the straight lines representing two-dimensional results. In this way the influence of cascade geometry upon three-dimensional effects becomes more easily apparent. Figure 4 shows, in all cases, that LL and AS underestimate three-dimensional effects, which, of course, are unaccounted for by 2D. In Fig. 6 only results from LS were plotted, since the other theories are unable to provide an adequate description of the distribution of the spanwise velocity component at the blade surface.

The curves of Figs 4 and 5 show a remarkably good agreement between LS and LL results for the total blade load and blade surface pressure distribution, even with values of the aspect ratio l/c as low as unity. As pointed out in (5), this may be explaned by the fact that the images in the walls of the bound vorticity makes the effective aspect ratio much greater than the actual span to chord ratio.

With constant ε and t/c, both LS and LL show (Fig.4b) three-dimensional effects becoming more important as c increases, while the variation of c does not affect AS and 2D results. Also, in this case, LL is found to give poorer approximation as the aspect ratio l/c decreases.

If t and c are kept constant, three-dimensional effects increase with the angle of stagger ε (which could be explaned by the increasing overlapping of, and decreasing distance between, the trailing vortex sheets), while the results given by LL and AS improve, especially for $\varepsilon>45^o$.

With c and ε unchanged ($c=0.5$ and $\varepsilon=45^o$), the variation of t was found to have little effect upon the shape and relative position of the curves of Fig. 4a,b,c.

Figure 4 shows that, in most cases of practical interest, AS is clearly inadequate to describe the effects due to spanwise gradient of the blade circulation. An easy and general method for comparing AS and LL consists in taking the ratio $\mu=(v^{3d}_1-v^{3d}_{1\infty})/v^{3d}_1$, where v^{3d}_1 and $v^{3d}_{1\infty}$ are the values of the three-dimensional downwash velocity given by LL and AS respectively. Using (20) and (37), and neglecting the harmonics of order $p\geq 2$, we find

$$\mu = \frac{\frac{\pi}{4}\coth(\frac{1}{2}\pi t\cos\varepsilon) - \frac{1}{2t\cos\varepsilon}}{\frac{\pi}{4}\coth(\frac{1}{2}\pi t\cos\varepsilon) - \frac{\cos\varepsilon}{2t}}\,. \tag{38}$$

Figure 7 illustrates the variation of the relative error μ with t and ε, and shows μ decreasing when t decreases and ε increases.

4.7 - The Downwash Velocity at the Walls. In Fig. 4, the curves given by LS and LL show values of $dC_L(z)/dz$ approaching zero at the walls, in contrast with the straight lines obtained from AS and 2D. This is due to the fact that the downwash velocity, induced at the blades by the discrete trailing vortex sheets, is infinite at the walls except if the spanwise derivative of the bound vorticity distribution is zero at z=0 and z=1, as will be shown for LL. The extension to LS is straightforward.

We start by considering (20). Since $1-\coth x\to 0$ exponentially as $x\to\infty$, it follows that

$$v^{3d}_1(z) = F(z) + \frac{\pi}{4}\sum_{p=1}^{\infty} p\,\gamma_p\cos(p\pi z)\,, \tag{39}$$

with F(z) finite for any z. Next, by integrating by parts twice, we find

$$\gamma_p = 2\int_0^1 \Gamma(x)\cos(p\pi x)\,dx = \frac{2}{p^2\pi^2}\left[(-1)^p\Gamma'(1)-\Gamma'(0) - \int_0^1 \Gamma''(x)\cos(p\pi x)\,dx\right]. \tag{40}$$

It can easily be shown that the last integral, which we denote by I_p, is $O(p^{-1})$ if $\Gamma''(z)$ is finite. Then substituting (40) in (39) and using the well known cosine series of the functions $\ln \sin\theta$ $(0<\theta<\pi)$ and $\ln\cos\theta$ $(-\pi/2<\theta<\pi/2)$, we find

$$v_1^{3d}(z) = F(z) + \frac{1}{2\pi}\left[\Gamma'(0)\ \ln(2\sin\frac{\pi z}{2}) - \Gamma'(1)\ \ln(2\cos\frac{\pi z}{2}) - \sum_{p=1}^{\infty}\frac{I_p}{p}\cos(p\pi z)\right].$$

The last Fourier series is uniformly convergent, since its coefficients are $O(p^{-2})$. It follows immediately that v_1^{3d} cannot be finite at $z=0$ and $z=1$ except if $\Gamma'(0)=\Gamma'(1)=0$, as we wanted to prove. These conditions agree with the results obtained, by different ways, in (5) and (11).

5 - CONCLUSION

It has been found that the descriptions given by lifting-surface and lifting-line theories for the three-dimensional effects due to spanwise variation of blade circulation are in remarkably good agreement, at least for the distribution of the blade surface pressure. Such effects can affect the flow field about the blades strongly and the assumption of uniformity of flow along the blade-to-blade direction (actuator screen theory) has been found inadequate to account for them in most configurations of practical interest. The derivations have been based on potential incompressible flow. However, the results can easily be extended to compressible flow with moderate subsonic Mach number with the help of Göthert's rule. It should be pointed out that effects due to large spanwise gradient of relative flow Mach number would not be present in that case. These are known to be inadequately described by lifting-line methods and can arise in shear flow problems and in potential flow about rotating cascades.

Finally, we mention that the results derived here can also be applied, by neglecting small quantities of second order, to those cases where the three-dimensionality is due to spanwise variation of the incoming flow skew angle $\omega(z)$, provided that the vorticity of the undisturbed stream is everywhere small (i.e. $d\omega(z)/dz \ll 1$). The angle α, defined in §3.2, is then a function of z, which, for the direct problem, should be developed in a cosine series, together with $\partial f/\partial\xi$ (see Eq. (28) and (33)).

Acknowledgement. This research was supported by Instituto de Alta Cultura, Lisbon, through Grant NEEM-TLE3.

APPENDIX

1 - Lifting-line Velocity Field with Arbitrary Geometry. Let us consider a cartesian system of coordinates x,y,z, with a lifting-line L lying on a surface $\sigma(x,y,z)=0$ and bounding a vortex sheet S defined by $\beta(x,y,z)=\beta_0$, $\sigma>0$ (Fig. A1). We assume further that the vortex lines of the sheet are the intersections of the surface $\beta=\beta_0$ with a family of surfaces $\alpha(x,y,z)=$ constant. The strength of the lifting-line will be expressed by a function $\Gamma(\alpha)$.

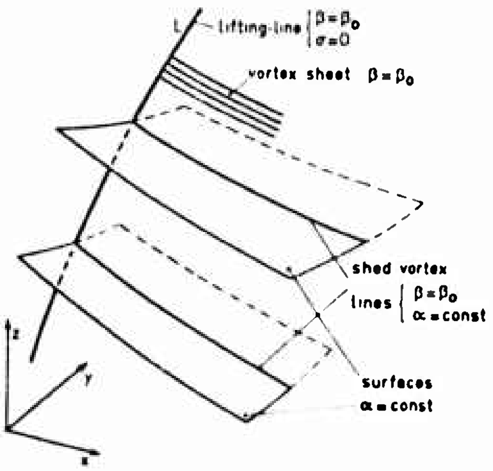
L
lifting-line $\{\beta=\beta_0,\ \sigma=0$
vortex sheet $\beta=\beta_0$
shed vortex lines $\{\beta=\beta_0,\ \alpha=\text{const}$
surfaces $\alpha=\text{const}$
z
y
x

Fig. A1

Let P be a point of L, and Q a point of the sheet's vortex line starting at P. If we assume the flow outside the singularities to be irrotational, then, introducing the potential function ϕ, we can write for the velocity $V=\nabla\phi$ everywhere except at the singularities. Applying Stoke's theorem to a circuit enclosing L and containing Q, with a diaphragm which intersects S along the vortex line PQ, it may easily be shown that $\Delta\phi_Q=\Gamma_P$, which means that the discontinuity of ϕ across the vortex sheet at Q is equal to the strength of the bounding lifting-line at P.

Let s be a coordinate with scale factor equal to unity and measured along the lines of flow of the vector field $\nabla\beta$, with $s=0$ at the vortex sheet. From the result obtained above, it follows that the discontinuity of ϕ can be removed by writing $\phi=\psi+\Gamma(\alpha)H(s)$ $(\sigma>0)$, where ψ is continuous across the vortex sheet and $H(s)$ is Heaviside's unit function. The gradient of ϕ then becomes

$$\nabla\phi = \nabla\psi + H(s)\Gamma'(\alpha)\nabla\alpha + \Gamma(\alpha)\delta(s)\vec{n} \quad (\sigma>0), \tag{A1}$$

where $\delta(s)$ is Dirac's delta function, the prime denotes derivative with respect to the argument, and $\vec{n}$ is the unit vector normal to S, pointing in the positive direction of s. For $s\neq0$ (i.e. $\beta\neq\beta_0$), we have

$$\vec{V} = \nabla\phi = \nabla\psi + H(s)\Gamma'(\alpha)\nabla\alpha.$$

At the vortex sheet, where $s=0$, the last term of (A1) becomes infinite. However, the velocity should remain finite and this condition is satisfied for any s by putting $\vec{V}=\nabla\phi-\Gamma(\alpha)\delta(s)\vec{n}=\nabla\psi+H(s)\Gamma'(\alpha)\nabla\alpha$ $(\sigma>0)$. We can write $\delta(s)\vec{n}=\delta([\beta-\beta_0]/|\nabla\beta|)\nabla\beta/|\nabla\beta|=\delta(\beta-\beta_0)\nabla\beta$, where the relation $\delta(x/a)=a\delta(x)$ was employed. It follows

$$\vec{V} = \nabla\phi - H(\sigma)\Gamma(\alpha)\delta(\beta-\beta_0)\nabla\beta. \tag{A2}$$

That this equation represents the velocity field everywhere will become apparent by taking the curl

$$\nabla\times\vec{V} = \Gamma(\alpha)\delta(\sigma)\delta(\beta-\beta_0)\nabla\beta\times\nabla\sigma + \Gamma'(\alpha)H(\sigma)\delta(\beta-\beta_0)\nabla\beta\times\nabla\alpha. \tag{A3}$$

The first term in the right hand side of (A3) is zero everywhere except at $\beta=\beta_0$, $\sigma=0$, and it is obvious that it describes the vorticity of the lifting-line L. The last term corresponds to a vector field which is different from zero only at the surface $\beta=\beta_0$, $\sigma>0$, where its lines of flow coincide with the trailing vortex lines. Clearly it represents the vortex sheet.

2 - Expressions of the Functions $\Omega_{pm}(\xi)$.

$$\Omega_{00}(\xi) = \frac{1}{2} + \frac{c}{2}\int_0^{\pi}(1-\cos\theta')L(\xi-\xi')d\theta',$$

$$\Omega_{0m}(\xi) = \frac{1}{2}\cos(m\theta) + \frac{c}{2}\int_0^{\pi}\sin\theta'\sin(m\theta')L(\xi-\xi')d\theta' \qquad (m=1,2,\ldots),$$

$$\Omega_{p0}(\xi) = \frac{1}{2} + \frac{c}{2}\int_0^{\pi}(1-\cos\theta')\left[L(\xi-\xi')+T_p(\xi-\xi')\right]d\theta' \qquad (p=1,2,\ldots),$$

$$\Omega_{pm}(\xi) = \frac{1}{2}\cos(m\theta) + \frac{c}{2}\int_0^{\pi}\sin\theta'\sin(m\theta')\left[L(\xi-\xi')+T_p(\xi-\xi')\right]d\theta' \quad \begin{cases} p=1,2,\ldots \\ m=1,2,\ldots, \end{cases}$$

where

$$L(\xi) = \frac{1}{2t}\,\frac{\exp[(2\pi\xi\cos\varepsilon)/t]\cos\varepsilon - \cos[\varepsilon+(2\pi\xi\sin\varepsilon)/t]}{\cosh[(2\pi\xi\cos\varepsilon)/t] - \cos[(2\pi\xi\sin\varepsilon)/t]} - \frac{1}{2\pi\xi},$$

$$\begin{aligned} T_p(\xi) = {} & H(\xi)\left[\frac{1}{2}p\pi\coth\left(\frac{1}{2}p\pi t\cos\varepsilon\right) - \frac{\cos\varepsilon}{t}\right] - \operatorname{sign}(\xi)\frac{\sin\varepsilon\tan\varepsilon}{2t}\exp(-p\pi|\xi|\cos\varepsilon) \\ & + \frac{1}{t}\sum_{n=1}^{\infty}\Big\{\frac{2n\pi}{\cos\varepsilon}\exp(-\lambda_{np}|\xi|\cos\varepsilon)\Big[M_{np}\sin\frac{2n\pi\xi\sin\varepsilon}{t} \\ & + \operatorname{sign}(\xi)\left(N_{np}-\frac{\sin^2\varepsilon}{2n\pi}\right)\cos\frac{2n\pi\xi\sin\varepsilon}{t}\Big] \\ & - \operatorname{sign}(\xi)\exp\left(-\frac{2n\pi|\xi|\cos\varepsilon}{t}\right)\cos\left[\frac{2n\pi\xi\sin\varepsilon}{t} - \operatorname{sign}(\xi)\,\varepsilon\right]\Big\}. \end{aligned}$$

REFERENCES

1. FALCÃO, A. F. de O. Lifting-line Theory of Axial Flow Turbomachines - A Review. *Técnica*. Vol. 34, p. 191-197, 1972.
2. NAMBA, M. and ASANUMA, T. Lifting-line Theory for Cascades of Blades in Subsonic Shear Flow. *Rep. Inst. Space Aeronaut. Sci. Univ. Tokyo*. Vol. 32, p. 133-179, 1967.
3. NAMBA, M. and ASANUMA, T. Theory of Lifting-lines for Cascade of Blades in Subsonic Shear Flow. *Bull. Japan Soc. Mech. Engrs*. Vol. 10, p. 920-938, 1967.
4. OKUROUNMU, O. and McCUNE, J. E. Three-dimensional Vortex Theory of Axial Compressor Blade Rows - Application in Subsonic and Transonic Speeds. *AIAA Journal*. Vol. 8, p. 1275-1283, 1970.
5. McCUNE, J. E. and DHARWADKAR, S. P. Lifting-line Theory for Subsonic Axial Compressor Rotors. *Gas Turbine Lab. Rep*. No. 110, MIT, 1972.
6. NAMBA, M. Lifting-surface Theory for Cascade of Blades in Subsonic Shear Flow. *J. Fluid Mech*. Vol. 36, p. 735-757, 1969.
7. NAMBA, M. Theory of Transonic Shear Flow Past a Thin Aerofoil. *J. Fluid Mech*. Vol. 36, p. 759-783, 1969.
8. OKUROUNMU, O. and McCUNE, J. E. Transonic Lifting Surface Theory for Axial Flow Compressors. *United Aircraft Corp. Res. Labs Rep*. No. K213580-1, East Hartford, Conn., 1971.
9. NAMBA, M. Lifting-surface Theory for a Rotating Blade Row. Part I. Subsonic Blade Row. Part II. Transonic Blade Row. *Cambridge Univ. Engng Dept. Reps* Turbo/TR.35-36, 1972.
10. NAMBA, M. Small Disturbance Theory of Rotating Subsonic and Transonic Cascades. *First Int. Symp. on Air Breathing Engines*, Marseilles, 1972.
11. FALCÃO, A. F. de O. Three-dimensional Flow Analysis in Axial Turbomachines. *Doctoral Dissertation, Cambridge University*, 1970.
12. JOLLEY, L. B. W. *Summation of Series*. 2nd edition, Dover, New York, 1961.
13. MILNE-THOMSON, L. M. *Theoretical Hydrodynamics*. 4th edition, p. 373, Macmillan, London, 1960.
14. KÁRMÁN, Th. v. and BURGERS, J. M. General Aerodynamic Theory - Perfect Fluids. Division E, *Aerodynamic Theory* (Editor: Durand, W. F.). Vol. 2, p. 259, Springer, Berlin, 1935.
15. GLAUERT, H. *The Elements of Aerofoil and Airscrew Theory*. 2nd edition, Cambridge University Press, 1947.
16. SCHLICHTING, H. Berechnung der reibungslosen inkompressiblen Strömung für ein vorgegebenes ebenes Schaufelgitter. *VDI-Forschungsh*. 447, 1955.

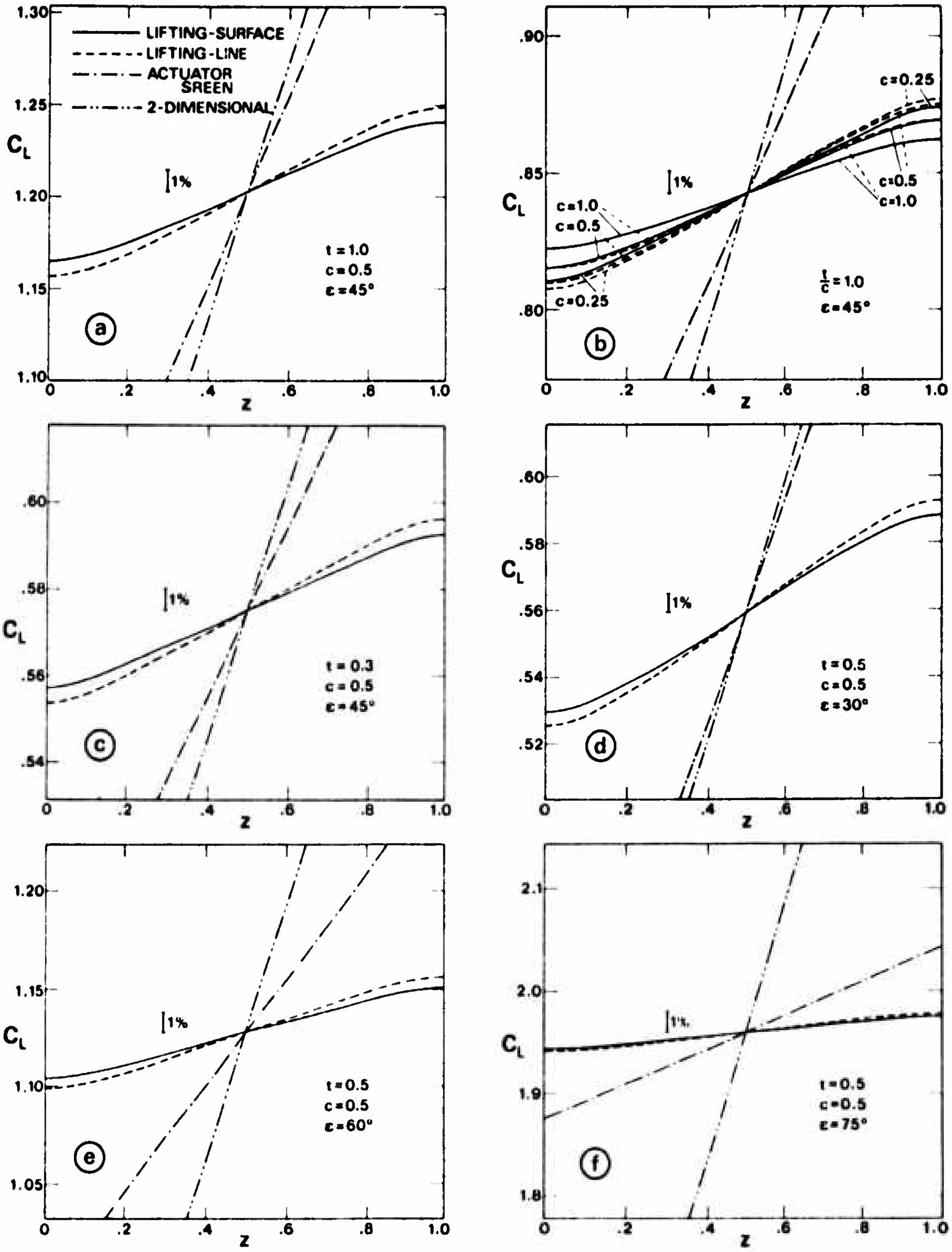

Fig. 4. Variation of total load coefficient with spanwise coordinate.

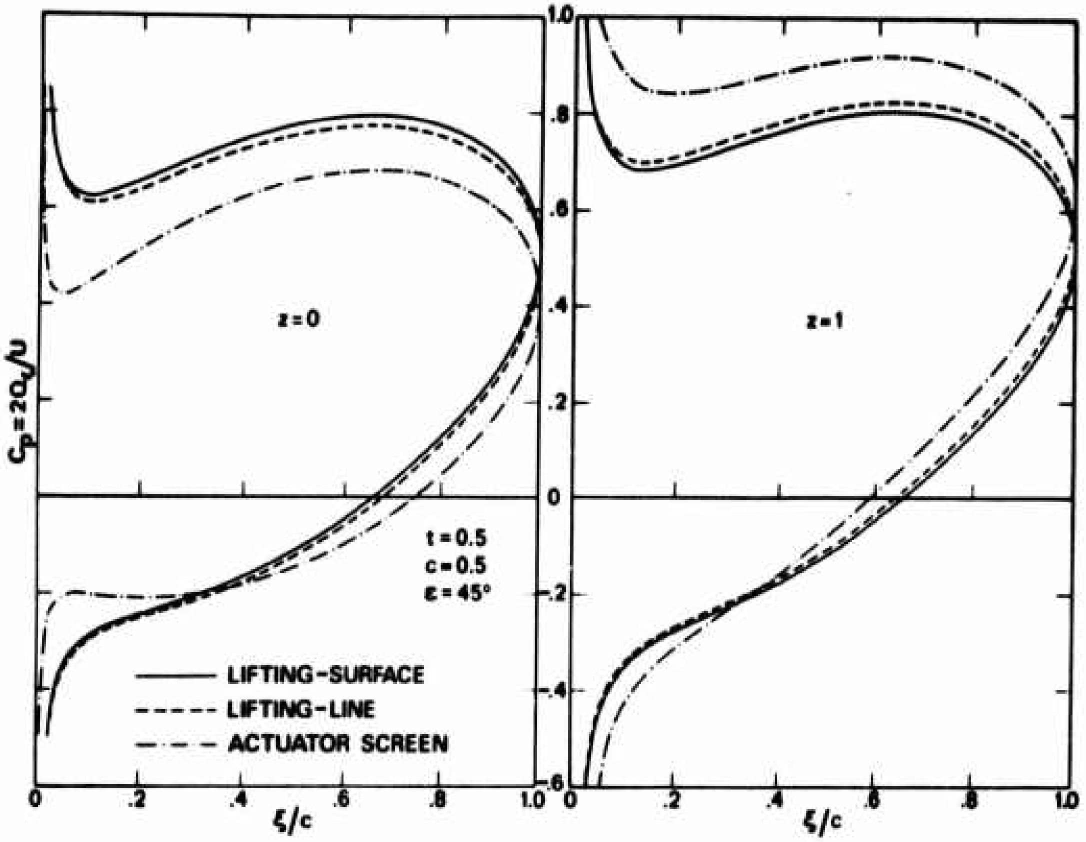

Fig.5. Variation of blade surface pressure coefficient with chodwise coordinate at root and tip.

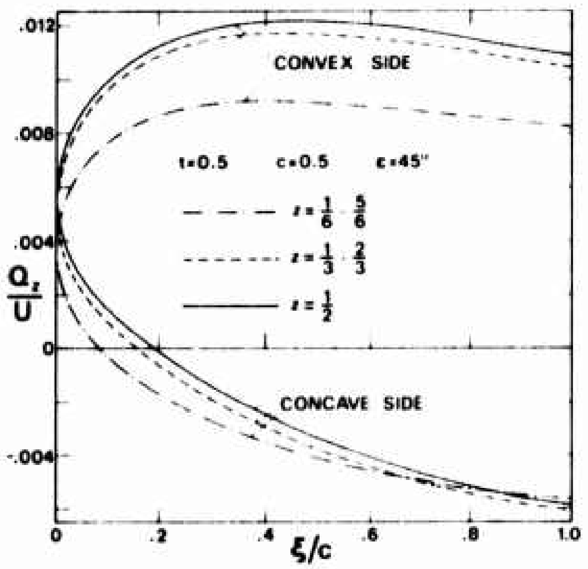

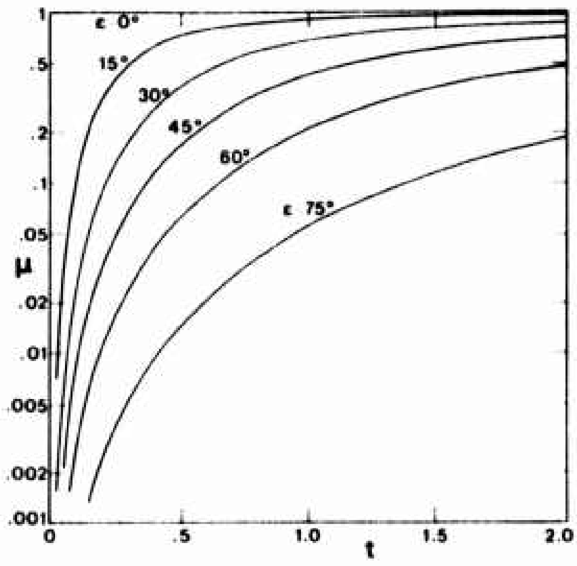

Fig.6. Distribution of spanwise velocity component at blade surface.

Fig.7. Relative value of discrepance between lifting-line and actuator screen.

DESIGN OF BLADE SECTIONS FOR AXIAL-FLOW COMPRESSORS

D.A. Frith, Principal Research Scientist, Mechanical Engineering
Division, Aeronautical Research Laboratories, Melbourne, Aust.

Introduction

The blade sections employed in such axial-flow turbomachinery as the compressors of gas turbine engines play a crucial role in changing the angular momentum across the blade row with low loss.

Accordingly considerable effort has been devoted to the development of means of designing these sections. Yet, even today, the sections employed are generally those developed empirically and shown in application to have a satisfactory level of performance. The term satisfactory is used here because there seems to be no criterion for the achievable performance of such blade sections.

The design methods have been developed around the framework of a model of the flow through the blade row - a model that by necessity is a major simplification of the real flow. In particular the two-dimensional flow through a linear cascade of aerofoils is often taken to represent the flow through the analogous section of a blade row.

Other major simplifications that have been invoked in various design methods include:

(i) regarding the fluid as being incompressible,

(ii) ignoring the effects of viscosity to the extent of regarding the aerofoils as boundaries of the inviscid (potential) model flow with a circulation being defined by a Kutta-Joukowski hypothesis.

Naturally, the weaker the model of the real flow the less likely it is that flow features designed into the model will be present in the real flow.

For example, if a method based upon a two-dimensional, incompressible cascade flow was used to design a section having a prescribed velocity distribution over its suction surface in order to give a specified boundary layer development, it must be expected that the section would have a boundary layer development in real flow only superficially similar to the design one because of the effects of -

(a) three-dimensionality,

(b) compressibility,

(c) cross-flow in the boundary layer and wake,

(d) varying inlet conditions,

in the real flow.

Even with the computational power of the computer, there are limits to the accuracy of practical flow models. It follows that there is a corresponding limit to the flow detail that may be encompassed in any design method.

The development of a practical method of designing blade sections, taking this important factor into account, has been the subject of a programme at the Aeronautical Research Laboratories, Melbourne (1) *.

The broad approach being adopted is discussed in this paper and some of the computational methods developed for its implementation are commented upon.

The Design Problem

The basic objective in designing blade sections is to give them an improved performance over their operating range. This is simply stated but not so simply translated into an effective procedure - as noted by Kuchemann (2) in 1966 in commenting upon the lack of progress in the design of aerofoils since the formulation of the problem by Prandtl some fifty years earlier.

In a more formal manner it may be stated as follows: the performance of a physical system, defined by a set of values (dimensions etc) D, over a range in operating conditions I can be measured by some performance index, P. The objective in designing the system is to specify D, subject to imposed constraints, in such a manner as to optimise P for the specified range in I.

This definition is in a form more suitable for critical appraisal. Specific points in the case of section design are:

(i) it is often not possible to specify an absolute performance index. To obtain an optimum value for an index arbitrarily selected has little value,

(ii) the relationship between P, D and I is generally provided by a model of the system. If the model is relatively inexact, then the performance index calculated may bear little relationship to that for the real system,

(iii) a system is generally a component of some larger system, so the operating environment, I, of the system being designed is only approximately known.

For example, cascade aerofoils are often designed for use as blade sections by prescribing a distribution of velocity over the suction surface for some particular inlet angle (PVD method). This velocity distribution is the design requirement: it is thus a measure of the performance index. It may represent some optimum - such as that having the lowest theoretical drag under particular circumstances, but, as pointed out below, it gives no indication of the performance at other inlet angles.

Further, of course, the inaccuracy of the model used may mean that this prescribed distribution is only roughly replicated in the real situation.

---

* Numbers in brackets designate References at end of the text.

Equally as important is the fact that at the particular design condition for the compressor, the actual inlet angle to the blade row may be somewhat different from the nominal design value used with the PVD method.

It seems, therefore, that the design of blade sections is not amenable to a direct attack: it does not appear possible to specify some input into a design method that will then yield a design that can be accepted as being an optimum.

Instead, it seems necessary to start from a specified section, analyse its performance over the complete range of operation envisaged in the application, then compare this performance with that of others, bearing in mind such other relevant points as the accuracy of the cascade representation of real flow.

In comparing the relative merits of various sections, two approaches can be envisaged, an objective evaluation suitable for mechanisation on the computer and a subjective one, scrutiny by experienced personnel.

The former would be based upon evaluation of a performance index but with special measures to counteract the arbitrariness of the definition of such an index. For example, a number of indices could be specified by different people and a section would then be adjudged as being good for a particular application if it rated well for a high percentage of these indices.

However it seems unlikely, due to the many unknowns implicit in the general approach, that the objective evaluation methods will provide more than an indicator of the better sections.

Synthesis of a Design Method

The design method under consideration (3, 4) is therefore based upon the scheme indicated in figure 1. For a particular application, parameters are to be fed into the scheme in order to yield a section basically suitable to the application, and then to judge it by its calculated performance over the stated operating range. Of necessity, a range of such sections would have to be evaluated with possibly feedback leading to progressively better sections.

There are two major calculating procedures required in this scheme:

(a) a procedure to translate input information into the shape of a blade section,

(b) a procedure to analyse the flow over this section for a range in conditions.

The nature of these procedures depends upon the simplifications used. It seems that, at this stage anyway, the usual simplification of using cascade flow must be retained, mainly for clarity of interpretation rather than for computational reasons.

However, with the availability of the computational power of the computer there is no reason to invoke the assumption of incompressibility, nor is it necessary to completely ignore the effects of viscosity.

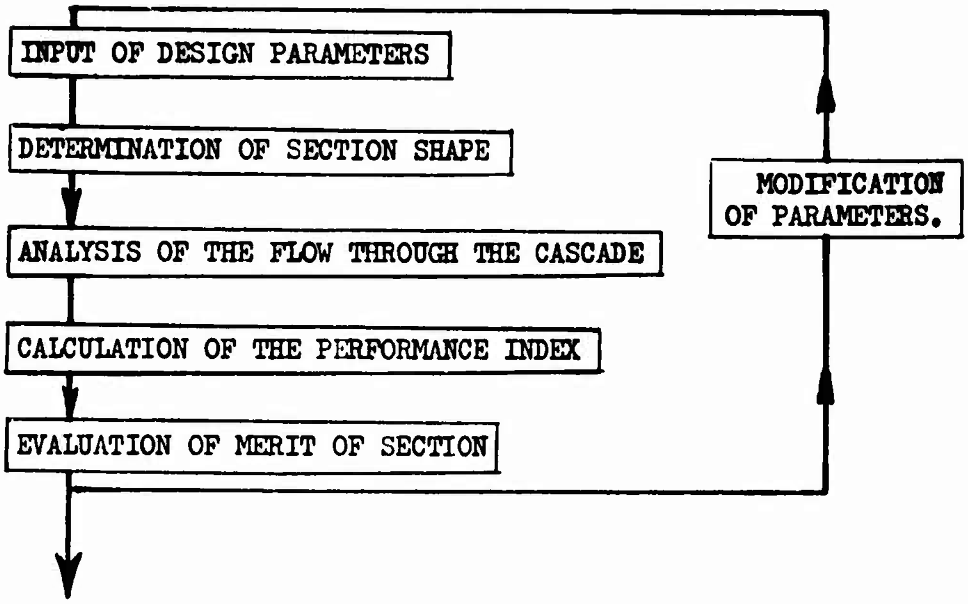
INPUT OF DESIGN PARAMETERS
DETERMINATION OF SECTION SHAPE
ANALYSIS OF THE FLOW THROUGH THE CASCADE
CALCULATION OF THE PERFORMANCE INDEX
EVALUATION OF MERIT OF SECTION
MODIFICATION OF PARAMETERS.

FIGURE 1. CASCADE DESIGN SCHEME.

Turning to the first part of the computational scheme, there are essentially three possibilities:

(i) synthesis - a calculation scheme synthesises the blade section from input flow characteristics,

(ii) specification - the blade section is specified,

(iii) generation - a calculation scheme generates the blade section from input parameters related to both the geometry of the section and the flow characteristics.

The first of these is typified by the prescribed velocity distribution (PVD) method. This take various forms, as indicated by the considerable literature (for example, references 5 to 16), but is essentially based upon the use of either conformal mapping, a representation of the aerofoils by singularities or an adaptation of a channel flow approach. Each of these approaches is characterised by certain computational difficulties which have been overcome to some degree in the published methods.

However, there are a number of fundamental characteristics of all PVD methods that mitigate against their successful application to the problem of design. These fall into two areas - (i) specification of the required velocity distribution so that the overall performance of the section is good, and - (ii) realisation of a practical section for the distribution.

There have been a number of studies (11, 17 to 20) relating to the velocity distribution required to give a boundary layer development that is an optimum within a narrow sense. However, such a distribution relates to one inlet condition and the performance over a range of conditions, including inlet angle, can, until the section has been analysed, only be inferred to follow the trends at the design condition. This consideration is amplified in the Appendices where the difficulties in obtaining a practical section are enlarged upon. The principal point there being that a prescribed velocity distribution generally has to be modified in order to yield a closed section with a smooth contour.

There is therefore little point in using a PVD method to derive a section for analysis and evaluation especially as it entails a complex calculation. On the other hand, there would seem to be even less reason to describe a section on geometrical grounds only, especially as the methods for analysing such sections are also computationally quite complex.

Accordingly, a generation method has been adopted (21).
It is a development of a conformal mapping method (22) in which the mapping function is expressed in a closed form. That is, it is to some extent analogous to the well-known Joukowski for isolated aerofoils but, by virtue of additional parameters defining the section, it is more general in application. The advantages claimed for this generation method are that:

(i) it is numerically simplir and more accurate,

(ii) the section shape is precisely defined and is smooth,

(iii) the parameters defining the section shape may be systematically varied to yield a family of sections with related properties,

(iv) the section shape may be controlled to satisfy mechanical requirements,

(v) the section shape may also be controlled so as to maintain good flow characteristics over a prescribed range of inlet angle,

and (vi) the conformal mapping function of the generation method also serves to define an orthorgonal grid in the cascade plane in which the section lies on grid points (figure 3).
This greatly facilitates the subsequent flow analysis for the section - incompressible or compressible.

The generation method, being based upon conformal mapping, is only applicable to incompressible flow but as the primary purpose is to provide a section shape that can subsequently be analysed, this is not a significant disadvantage so long as a method of analysis for compressible flow is available.

Before turning to this question, it is appropriate to discuss viscous flow effects. Most models are essentially potential (inviscid) flows for which the aerofoils are boundaries and in which the indeterminateness of the circulation is removed by application of the Kutta-Joukowski hypothesis, or the like, to give the trailing-edge stangation point.

This basic flow model has the distinct disadvantage in that, for a particular section, the circulation (or exit flow angle) and the velocity distribution are separately functions of the inlet flow angle and the position of the rear stagnation point.

In order to reconcile measurements with calculations it is then necessary to take positions of this rear stagnation point which produce grave inconsistencies with respect to the velocity distribution near the trailing edge.

Further, for cambered sections the basic flow model gives distribution of velocity over the aft section of the blade that imply a pressure gradient in the viscous flow that just can not exist.

These objections can be eliminated by utilising a potential flow model for which the boundaries are essentially at the displacement flux width of the boundary layers and wake away from the aerofoils. Such a flow can be generated (23) by construction of a cascade potential flow in which within the streamlines representing the aerofoils there is a net source strength, so producing a potential, psuedo wake (figure 2). In such a model the first circulation condition, which positions the stagnation point at the trailing edge, is necessary in order for this psuedo wake to leave the trailing edge smoothly. However, it is also found that a second circulation condition has to be satisfied in order that the curvature of the psuedo wake is continuous. This second circulation condition introduces a slight modification to the usual relation between inlet angle and circulation given by the first condition.

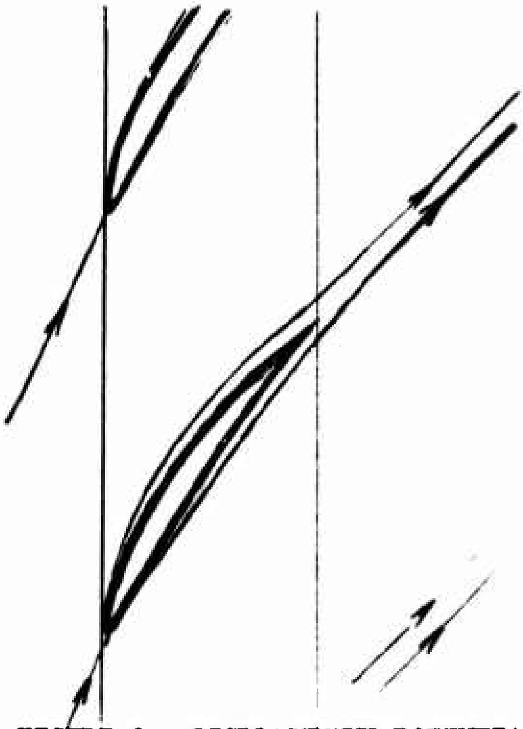

FIGURE 2. DISPLACEMENT POTENTIAL FLOW FOR CASCADE - AEROFOILS NOT STREAMLINES OF THE FLOW.

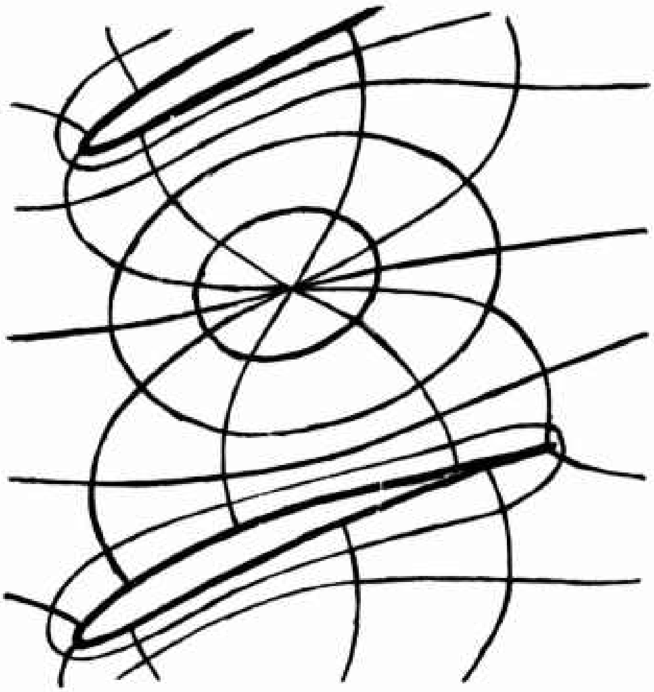

FIGURE 3. ORTHOGONAL GRID IN CASCADE PLANE FOR COMPRESSIBLE FLOW CALCULATIONS.

Turning again to the question of analysis for a compressible flow, Sells (24) developed a method for computing the two-dimensional, subsonic, compressible flow past an aerofoil by using conformal mapping to essentially define an orthogonal grid for calculating numerically the compressible stream function. With the definition of the grid, the aerofoil naturally lies on grid points and application of boundary conditions is thereby materially simplified. Further, the stream function may be divided into analytical and numerical components with the former being dominant in most cases. This simplifies problems of numerical accuracy.

The author has applied this approach to the cascade problem (25) to yield a convenient means of analysing the compressible flow through cascades of aerofoils generated by the method of reference 22.

The orthogonal grid produced in the cascade plane is shown in figure 3.

An Application

Some time ago the author employed a simplified form of this technique in the design of blade sections for a large water pump. Here the requirement was that the blading should be free from cavitation over a specified range in operation. This requirement could be translated to read that the maximum velocity over the surface of the section should not exceed a specified value over the prescribed range in inlet angle.

Sections were generated, using the mapping function of equation 67 in reference 21, in which the pressure rise of the lightly loaded blading was obtained principally over the after region by suitable choice of the parameters of the mapping. An example is shown in figure 4.

These parameters were then varied until an optimum performance was obtained over the operating regime. If the parameters were such as to give thin aerofoils then the maximum velocity over the section was low at the design inlet angle but increased rapidly off-design.

On the other hand, for a thick section this maximum was high at the design angle but only increased slowly off-design.

The optimum section was therefore one of moderate section: the one shown in figure 4.

The important point of this application was that the parameters in the mapping function were chosen to satisfy mechanical requirements for the blading, to satisfy hydrodynamic loading by control of the form of the velocity distribution and then were varied within these limits to give the section that best satisfied the cavitation conditions.

Conclusion

A method for the design of blade sections for axial-flow compressors is discussed. Its structure differs from other design procedures discussed in the literature in order to permit an overall appraisal of the merit of a section.

References

1. FRITH, D.A. and WALKER, G.J. 'Flow through axial compressors - A review of some Australian research', SAE International Gas Turbine Conference, Melbourne, Australia, 1972.

2. KUCHEMANN, D. Prandtl Memorial Lecture, 1966 (Printed in RAE Technical Report 67051, 1967).

3. FRITH, D.A. 'The design of aerofoils in cascade, Part 1 - An examination of present methods.' In course of preparation.

4. FRITH, D.A. 'The design of aerofoils in cascade, Part 11 - An improved method.' In course of preparation.

5. COSTELLO, G.R. 'Method of designing cascade blades with prescribed velocity distributions in compressible potential flows.' NACA Report No. 978, 1950.

6. GOLDSTEIN, A.W. and JERISON, M. 'Isolated and cascade airfoils with prescribed velocity distributions.' NACA Report No.869, 1947.

7. HANSEN, A.G. and YOHNER, P.L. 'A numerical procedure for designing cascade blades with prescribed velocity distributions in incompressible potential flow.' NACA TN No. 2101, 1950.

8. LIGHTHILL, M.J. 'A mathematical method of cascade design.' R. & M. No. 2104, 1945.

9. FRITH, D.A. 'A method for designing cascades of airfoils in two dimensional, incompressible or compressible potential flow.' M. Eng. Sc. Thesis, University of Tasmania, 1963.

10. MUTTERPERL, W. 'A solution of the direct and inverse potential problems for arbitrary cascades of airfoils.' NACA AHR L4K22 b, 1944.

11. PAPAILIOU, K.D. 'Boundary layer optimization for the design of high turning axial flow compressor blades.' ASME Paper 70-GT-88

12. ROSENBLAT, S. and WOODS, L.C. 'A method of cascade design for two-dimensional incompressible flow.' Report ACA-56, 1956.

13. SATO, JUNZO 'An exact two-dimensional incompressible potential flow theory of aerofoil design with specified velocity distributions.' Trans. Japan Soc. Aero. Space Sci, Vol.9, No. 14, 1966, pp11-18

14. SCHWERING, W. 'Design of cascades for incompressible plane potential flows with prescribed velocity distribution. ASME 70-GT-87

15. STANITZ, J.D. 'Approximate design method for high - solidity blade elements in compressors and turbines. NACA TN 2408

16. WILKINSON, D.H. 'A numerical solution of the analysis and design problems for the flow past one or more aerofoils or cascades.'
Part I - The Analysis Problem
Part II - The Design Problem.
R. & M. No. 3545, 1968.

17. WALKER, G.J. Private Communications.

18.PAPAILIOU, K. 'Blade optimisation based on boundary layer concepts,' von Karman Institute, CN60, 1967.

19.SMITH, D.J.L. 'Turbulent boundary layer theory and its application to blade profile design.' ARC CP868, 1966

20.ALLAN, W.K. 'Theoretical analysis of the performance of cascade blades.' ARC 23,061 July 1961

21.FRITH, D.A. 'Inviscid flow through a cascade of thick, cambered airfoils Part I - Incompressible flow.' ASME Paper 73-GT-84

22.FRITH, D.A. 'A method for generating thick, cambered aerofoils in cascade using a closed mapping function.' Report ARL/ME 121, 1968

23.FRITH, D.A. 'A model of two-dimensional, incompressible flow through a cascade of airfoils with allowance for the viscous displacement effect.' ASME Paper 74-GT-126

24.SELLS, C.C.L. 'Plane subcritical flow past a lifting aerofoil.' Proc. Roy. Soc. A.308, 377-401 (1968)

25.FRITH, D.A. 'Inviscid flow through a cascade of thick, cambered airfoils. Part II - Compressible flow.' ASME Paper 73-GT-85

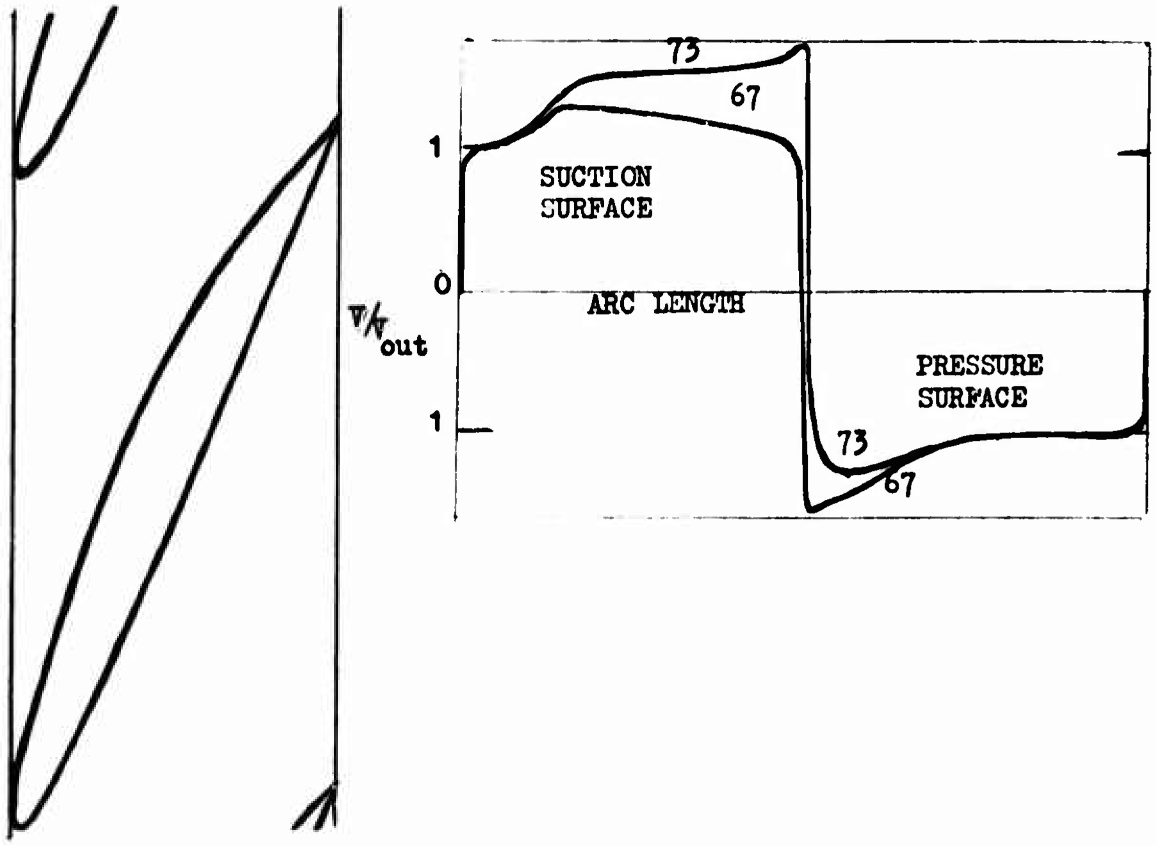

FIGURE 4. AN OPTIMISED PUMP IMPELLOR BLADE SECTION AND ITS CALCULATED VELOCITY DISTRIBUTIONS AT TWO INLET ANGLES.

26. FRITH, D.A. 'Flow around leading edges of aerofoils' 4th Australasian Conference on Hydraulics and Fluid Mechanics, Melbourne, Australia, 1971.

Appendix 1. Practical problems relating to the synthesis approach.

There are a number of fundamental properties of the relation between cascades and the flow through them that have an important influence on the synthesis procedure. Enumerating:

(i) an arbitrarily defined distribution of velocity over the surface of an aerofoil in cascade will not yield a closed aerofoil shape as the compatibility conditions are not satisfied,

(ii) even if closure is ensured, there is no certainty that the resultant aerofoil will have positive thickness along its chord,

(iii) nor is there any control of the thickness of the trailing edge, as may be required for mechanical reasons,

(iv) and neither is there any control over the size of the leading edge and so the response of the aerofoil to varying incidence,

(v) in fact there is little control over the thickness and camber distributions of the aerofoils in the cascades,

and (vi) the form that the prescribed velocity distribution takes up when the incidence is changed to some off-design value is not known until the design has been largely affected.

These six factors greatly reduce the usefulness of the synthesis procedure: they are discussed in further detail in Appendices 2 to 5.

The restrictiveness of (i) may be removed to some extent by introducing parameters into the form of the velocity distribution the values of which have to be determined in ensuring that the aerofoils close. For example, as the suction surface is the most important in the deflecting cascade, prescription of the velocity distribution over this surface to give a controlled boundary layer development can be considered whilst the distribution of the pressure surface is allowed to be determined by the compatibility conditions. However certain precautions are then necessary to ensure that the resulting aerofoil is 'reasonable' namely,

(a) the velocity at the trailing edge on the pressure surface must closely align with that on the suction surface otherwise the section will have a "trailing edge loading" (see Appendix 4) and a spurious hook will result,

(b) the prescribed suction surface velocity distribution should not be taken as far as the stagnation point as the shape of the acceleration region, SM of figure 5, whilst having an insignificant effect on the flow at that incidence, has a profound effect on the shape of the leading edge and so the velocity distributions at other inlet angles (see Appendix 5). If conformal mapping is the basis of the design procedure then this problem can be overcome by ensuring that the mapping function is well behaved in this region, but this increases the complexity of the procedure.

Even with these precautions, the resultant aerofoil may still have negative thickness or other 'unreasonable' attributes. But, even more importantly, its aerodynamic performance may be prejudiced. One of the principal reasons for prescribing a velocity distribution is to control the boundary layer development over the aerofoil to give high lift and/or low drag. Integration of the prescribed suction surface velocity distribution over its arc length leads to a potential for this surface that is indicative of the deflection, hence lift. However, if two different distributions have the same potential but distribution A has a lesser predicted drag than distribution B, it does not follow that after application of these distributions to yield aerofoils, that yielded by A will have a better predicted performance than the one yielded by B. One of the principal reasons for this is that a suction surface velocity distribution only partly determines the shape of the section. Thickness and camber can vary markedly between sections having a particular form of suction surface velocity distribution at some inlet angle, but different pressure surface distributions.

Appendix 2. Cascade aerofoils with negative thickness.

The flow between two aerofoils of a cascade may be considered as analogous to the flow through a channel with walls shaped like the stagnation streamlines, figure 6. Suppose the velocity distributions are prescribed along the walls NPT and NST.

As resultant wall shapes depend upon these distributions, if the prescribed velocity is appreciably greater than the free stream value then the channel will tend to converge over the region NT, as depicted in figure 6 (a). The resultant section will have positive thickness.

However, should the prescribed velocity fall appreciably below free-stream values over part of the arc, then the channel could well bulge over NT with the result that the section has negative thickness over part of the chord, figures 6 (b), 6 (c) and 6 (d).

In the normal case of a deflecting cascade, the levels of velocity producing this effect cannot be simply estimated. As a consequence, calculation of a section shape from a prescribed velocity distribution can often lead to sections having some degree of negative thickness.

Appendix 3. The compatibility condition.

When conformal mapping is used to generate cascades of aerofoils by transformation of the unit circle, e.g. as in reference 21 , two complex conditions have to be satisfied in order that the resultant aerofoils are closed and periodic in id that is, spaced d apart along the imaginary axis.

These conditions may, be application of complex variable theory and Poisson's and Schwarz's Integrals in particular, by reduced to (3)

$$\frac{1}{\pi}\oint_c \ln v(\theta)\,.\,h(\theta)\,d\theta = \ln(\sec\alpha_1 . \sec\alpha_2) \qquad (3.1)$$

$$\frac{1}{\pi}\oint_c \ln v(\theta)\, h(\theta)\frac{\cos\theta}{\cosh k}\,d\theta = \ln(\sec\alpha_1/\sec\alpha_2) \qquad (3.2)$$

$$\frac{1}{\pi}\oint_c \ln v(\theta)\, h(\theta)\frac{\sin\theta}{\sinh k}\,d\theta = \alpha_1 - \alpha_2 \qquad (3.3)$$

$$\frac{1}{\pi}\oint_c \ln v(\theta)\, h(\theta)\frac{\sin 2\theta}{\sinh 2k}\,d\theta = \alpha_1 + \alpha_2 - 2\beta_0 \qquad (3.4)$$

where v is the non-dimensional velocity over the cascade aerofoil, written as a function of the circle angle Θ and

$$\hat{k}(\Theta) = \frac{\sinh 2k}{\cosh 2k - \cos 2\theta} \qquad (3.5)$$

is the cascade function.

These equations may be combined to yield

$$\oint_A v \ln v \; d(s/d) = \alpha_1 - \alpha_2 + \tan\alpha_1 . \ln\sec\alpha_1 - \tan\alpha_2 . \ln\sec\alpha_2 \qquad (3.6)$$

as a necessary, but not sufficient, condition that the conditions of equations (3.1) to (3.4) are satisfied.

The advantage of equation (3.6) lies in the fact that the integral may be evaluated when a velocity distribution is prescribed whereas the integrals of equations (3.1) to (3.4) can only be evaluated after a considerable amount of computational work in relating the prescribed distribution as a function of arc length on the aerofoil to a function of circle angle.

Another way of looking at this question of closure (compatibility) is by reference to the channel flow discussed in Appendix 2 and illustrated in figure 6. For a given inflow condition and arbitrary velocity distributions along the arcs NPT, NST, the width and orientation of the exit from the channel is calculable, that is, it is a function of the values specified. Clearly it will only have the requisite spacing and orientation if the velocity distributions prescribed along NPT, NST satisfy certain conditions.

The circulation about an aerofoil in the cascade is (21)

$$\oint_A v \, d(s/d) = \tan\alpha_1 - \tan\alpha_2 \qquad (3.7)$$

so if a velocity distribution is prescribed, equations (3.6) and (3.7) yield two relations for the $\alpha_1 = \alpha_{1d}, \alpha_2 = \alpha_{2d}$ to be taken with the distribution to define the mapping, hence the required section shape.

These flow angles, α_{1d}, α_{2d} represent the only values compatible with the prescribed velocity distribution. But as equation (3.6) is not a sufficient condition, it is possible that the section will not be closed. In this case the particular prescribed velocity distribution will not yield a cascade of aerofoils.

Alternatively, there is no cascade of aerofoils that will have this flow distribution.

Appendix 4. On loaded trailing edge.

The use of analytical mapping functions to generate aerofoils in cascade (21, 22) is also a convenient method for relating certain aspects of the aerofoil shape and the flow properties, as the nature of these functions simplifies interpretation as compared to numerically defined functions. For example, the relation between leading edge in isolated aerofoils and velocity peaks at incidence is treated by this method in reference 26 .

This mapping function, over the region of the trailing edge, may be separated into two components (3) : (i) that governing the shape of the trailing edge, whether it be cusp, sharp or rounded, and having little or no effect upon the velocity distribution. (ii) that related to the camber of the aerofoil in the region of the trailing edge and so to the gradient of the velocity distribution (aside from the local effect due to the type of trailing edge).

For aerofoils having a physically realistic camber, the gradient of velocity at the trailing edge must be small. Alternatively, if the gradient is not small so that essentially there is a difference between the velocity on the suction and pressure surfaces near the trailing edge, then the section will have excessive camber in this region.

Essentially then, a basic flow model does not admit to a significant trailing edge loading. If such a loading were to be applied in a rigorous synthesis method, the resultant section would have a hook trailing edge.

Appendix 5. On leading edge flows.

Perhaps one of the most cogent disadvantages of the prescribed velocity distribution approach is that there is insufficient control over the form of the velocity distributions at other inlet angles. This is not a practical problem over most of the aerofoil surface as it is known that, aside from non-linear effects due to viscous effects, the velocity increases monotonically with incidence on the suction surface and monotonically decreases on the pressure surface.

However, this does not apply in the region of the leading edge as here an increment of arc may be on the suction surface for a high inlet angle but on the pressure surface for low inlet angles. The behaviour of the velocity distributions in this region will be well-conditioned for a smooth leading edge. However, if the velocity in this region is prescribed then it may be basically ill-conditioned: an example of this is shown in figure 5. The pressure surface distribution near the leading edge looks to be reasonable at the design inlet angle but is not as for a lower inlet angle. The reason is obvious on reference to the shape of the section.

This lack of control is an important factor against prescribing a velocity distribution.

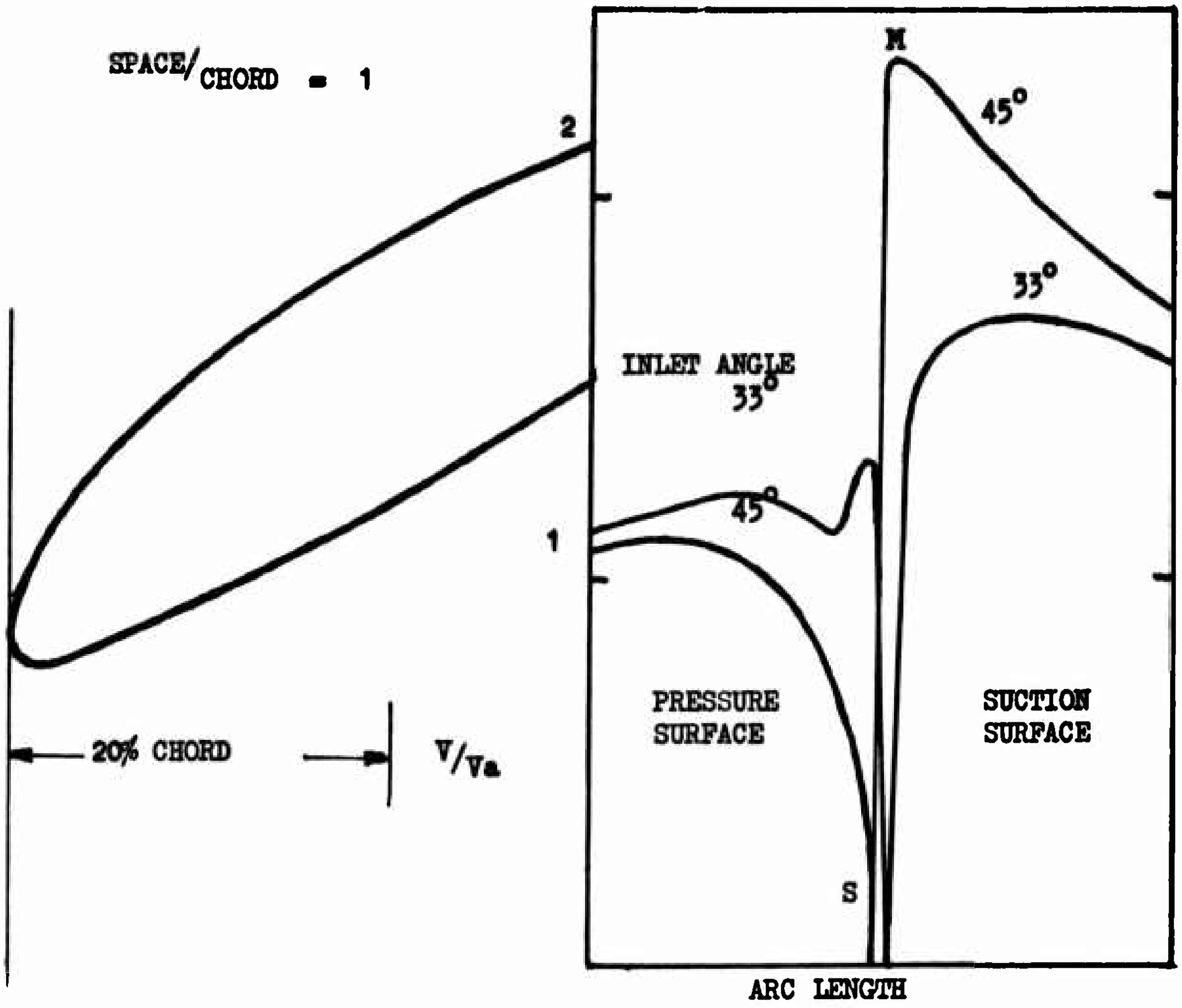

FIGURE 5. VELOCITY DISTRIBUTIONS, FOR TWO INLET ANGLES, OVER A CASCADE AEROFOIL WITH MISSHAPEN LEADING EDGE.

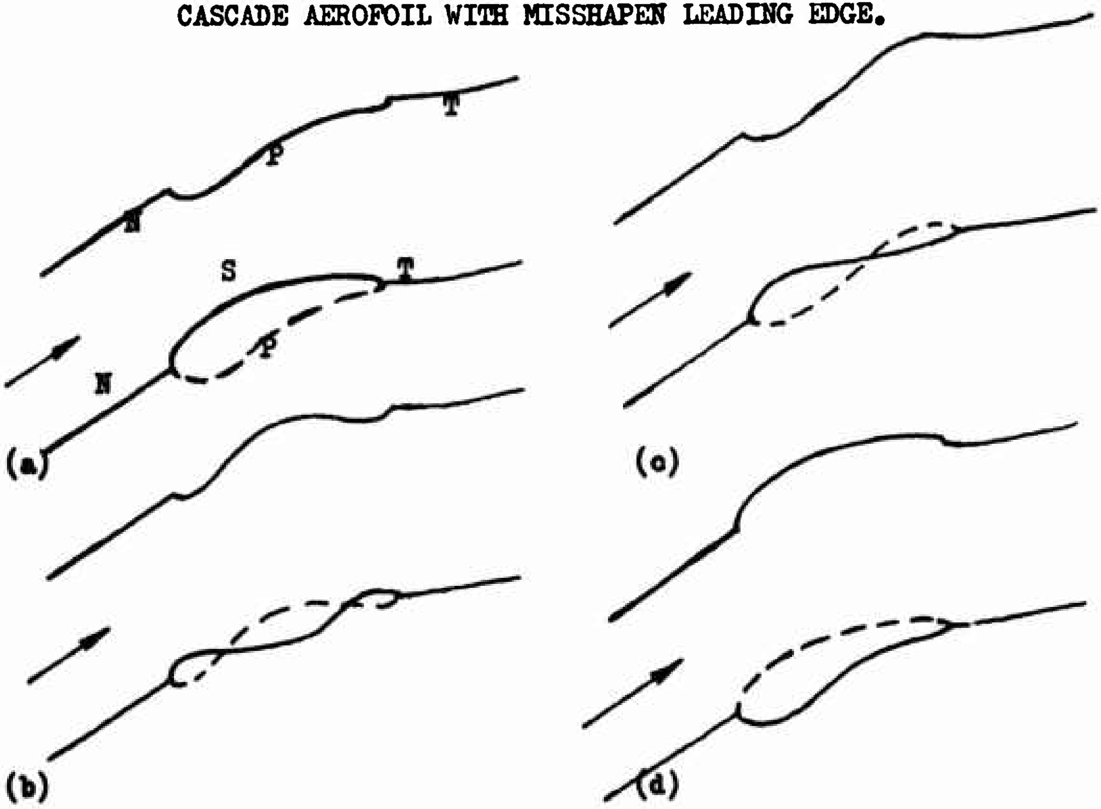

FIGURE 6. VARIOUS CHANNEL FLOWS AND THEIR ANALOGOUS CASCADES.

THE CHORD-WISE PRESSURE DISTRIBUTION ON A ROTATING AXIAL-FLOW COMPRESSOR BLADE

H. L. Moses and W. F. O'Brien, Jr.

Virginia Polytechnic Institute and State University

Abstract

An investigation of the chord-wise pressure distribution at the mean radius of a rotating axial-flow compressor blade is described. Six miniature pressure transducers were spaced along the chord and mounted flush with the surface of the blade. Mean and fluctuating pressure measurements were transmitted from the rotating blade by a frequency modulated, radio telemetry system.

Photographs of the fluctuating pressure waveforms are presented, including those obtained by signal averaging techniques. The signal averaging techniques clarify repetitive components of the signal, such as those due to stator wakes. Mean pressure measurements are compared with the results of two-dimensional cascade tests and with inviscid flow calculations based on simple radial equilibrium.

Introduction

The description of the flow through the rotor of an axial-flow compressor is among the most difficult analytical and experimental problems that are encountered in fluid mechanics. This is particularly true when considering such limiting factors as losses and stall, and unsteady effects due to inlet distortion. Analytical difficulties stem from the fact that the flow is turbulent, three-dimensional, unsteady, usually transonic, and often separated. At best, there is only a qualitative understanding of some of the phenomena involved. Experimental difficulties are associated with the measurement of flow variables on a component rotating at high speeds and transmission of data to a stationary observer.

The need to continue to effectively design new compressors with even more stringent requirements makes a better understanding of the flow extremely important. In particular, there is a need to design for high speeds, perhaps with inlet distortion, and for more heavily loaded blades. To design more heavily loaded blades requires a better understanding of the stall phenomena, especially on the rotor.

Throughout the years of development of the jet engine there has been a great deal of experimental and analytical work in this and related areas. Much of this work was summarized in reference 1. The experimental work has been confined mostly to stationary, two-dimensional cascades and to measurements on the stationary components of compressors. There have been some on-rotor flow studies reported (references 2-7, for example) but this work is definitely limited.

Although there has been a large amount of work in the boundary layer area, most of the analytical work that can be applied directly to the axial-flow compressor has been for non-viscous flow. Two-dimensional techniques (as summarized in reference 8, for example) agree reasonably well with cascade experiments near the design angle of attack. And it is generally believed that existing quasi-three-dimensional methods (as discussed in reference 9) will adequately predict the flow through the rotor near design, but few actual comparisons with experiment have been made.

The purpose of this paper is to report some on-rotor surface pressure measurements and to compare them with analytical predictions as well as cascade data. This work is part of a long-range program involving instrumentation research, experimental studies on both low- and high-speed machines, and analytical methods. The overall program is intended as a contribution toward a better understanding and anaylsis of the flow through the rotor of axial-flow compressors.

Experiment

The experiments were conducted on a relatively low-speed axial flow compressor as shown in Fig. 1. This machine was employed because it was felt that a basic study of this type should be first attempted at low speeds. Thus the difficulties in experiment and analysis associated with high-speed machines were avoided while retaining the essential three-dimensional effects due to rotation.

The compressor has a tip diameter of 45.7 cm and hub diameter of 31.4 cm. It can be operated as a one- or two-stage machine, but only one stage was employed in the present experiments. The rotational speed can be varied from 500 to 3000 rev/min. and the flow rate is adjusted by a valve in the discharge duct. The compressor is directly coupled to a cradled dynamometer for torque measurements.

The stator section has 37 adjustable, thin-plate guide vanes with a total blade twist of 8 degrees. A stator blade angle of 36 degrees at the mean radius, measured from the axial direction, was used for the present study. Thus, the blade angle varied from 40 degrees at the hub to 32 degrees at the outside diameter. The vanes were arranged to give a whirl velocity in the opposite direction from the rotor velocity, as indicated in Fig. 2.

The rotor has 24 adjustable blades with a twist of 4 degrees. The rotor blades have a RAF 6 cross-section (Fig. 3) with a thickness-to-chord ratio of 12 percent. Since the pressure sides of the blades are flat, all angles are measured from these surfaces. The blades have a chord length of 4.28 cm and a nominal tip clearance of 0.038 cm. For the present experiments, the blade angle was set at 65 degrees from the axial direction at the mean radius, 63 degrees at the hub, and 67 degrees at the tip.

Rotor blade surface pressures were measured with 6 miniature transducers spread along the suction surface at the mean radius. The 0.32 cm diameter by 0.080 cm thick transducers and lead wires were inserted in slots milled in the blade such that the diaphram was flush with the surface. The transducers were calibrated under static and rotating conditions as described in reference 10.

Transmission of the data from the rotor to the stationary components was accomplished with a miniature, frequency modulated (FM) telemetry system, which is described in detail in reference 11. Power for the transducers and transmitter was supplied by rechargable batteries. The transmitter and batteries were contained in a small cylindrical housing mounted on the end of the shaft, as shown in Fig. 1. The FM signal was received by a stationary antenna without sliding contact and then demodulated to reconstruct the pressure signals. The six pressure signals were recorded on tape along with a reluctance transducer signal that indicated the circumferential position of the instrumented blade. In addition to separating the mean and fluctuating components, the pressure signals were averaged for a number of revolutions. This procedure showed the repetitive nature of the signals, which was due to the stator wakes.

Since one of the main goals of this research was to determine the effect of rotation on the flow, a small stationary cascade tunnel was constructed for comparison. The cascade blades were identical to those on the compressor rotor, except that the 4-degree twist was removed. Surface pressures were measured on the cascade blades with small static taps and a water manometer. Although the instrumented rotor blade was twisted, it was checked in the cascade before it was mounted on the rotor.

Analysis

Since the present analysis is based on well-known methods, only a brief summary will be presented here. It is essentially a two-dimensional, blade-to-blade, inviscid flow analysis with three-dimensional effects approximated by simple radial equilibrium.

The blade-to-blade calculations were made with an available computer program, "TSONIC", as described in reference 12. The program uses a two-dimensional, inviscid flow technique capable of treating locally supersonic flow. In the present work, the flow is assumed to be incompressible, and the method reduces to a finite difference solution of the stream function equation.

In addition to geometry and flow rate information, the program requires inlet and outlet flow angles. In the present work, the inlet angle was fixed by the stator guide vanes. The outlet angle was found by an iterative process such that the faired pressure distribution for the two surfaces converges at the trailing edge, as suggested in reference 13.

The program also requires the stream channel thickness as input information. For the present analysis, the blade span was divided into five equal increments at the entrance. As a first approximation the channel thickness was assumed constant in the axial direction, assuming that the radial shift in streamlines was negligible. (A better approximation was made after the streamline shift was determined from radial equilibrium, but was not important in the present calculations.)

With the flow angle thus determined at the rotor entrance and exit, the velocity and pressure variation was found from simple radial equilibrium considerations (as discussed in reference 14, for example).

For incompressible flow, (see Fig. 2 for notation)

$$\frac{1}{\rho}\frac{dp_o}{dr} = \frac{C_\theta^2}{r} + C\frac{dC}{dr} \qquad (1)$$

At the entrance to the rotor, the total pressure can be assumed uniform, and equation 1 reduces to

$$\frac{dC_1}{C_1} = -\sin^2 \alpha_1 \frac{dr}{r} \qquad (2)$$

Equation 2 can be integrated when the angle α_1 is specified as a function of the radius and the constant of integration determined by conservation of mass. In the present calculation, α_1 was found experimentally and equation 2 integrated numerically. Since the flow was nearly free vortex, the radial variation of C_x was small.

At the rotor exit, equation 1 can be written in terms of the relative total pressure and velocity,

$$\frac{1}{\rho}\frac{dp_{or}}{dr} = \frac{C_\theta^{\,2}}{r} + W\frac{dW}{dr} \qquad (3)$$

or

$$W_2\frac{dW_2}{dr} = \frac{1}{\rho}\frac{dp_{or2}}{dr} - \frac{(U - W_2 \sin \beta_2)^2}{r} \quad . \qquad (4)$$

The relative total pressure (Por) was assumed constant along a streamline through the blade row. Again, as a first approximation, the radial shift of the streamline was assumed negligible. The radial distribution of the relative total pressure at the rotor exit was then the same as that at the rotor entrance. With the angle β_2 determined from the blade-to-blade solution, equation 4 was integrated numerically and the constant of integration determined from conservation of mass.

The static pressure at any point on the rotor blade surface can be determined from the entrance condition and the blade-to-blade solution for the relative velocity,

$$\frac{P_{or} - P}{\frac{1}{2}\rho W_1^{\,2}} = \left(\frac{W}{W_1}\right)^2 \quad . \qquad (5)$$

The above procedure, in general, required an iteration between the two solutions. In the present calculations, the flow was nearly free vortex flow and a second approximation was not required.

Results

The measured fluctuating pressures at various chord positions are shown in Fig. 4. The complete pressure signal is shown as well as the signal that has been averaged at each circumferential position for a number of revolutions. The averaging technique gives the repetitive nature of the fluctuating pressures due to the upstream stator wakes. It is interesting to note that this repetitive component nearly vanishes at mid-chord and then reappears near the trailing edge. Near design operating conditions, the fluctuating pressures are approximately 5 percent of the mean value.

The experimental mean pressure coefficient on the suction surface of the blade is shown in Fig. 5 and 6 as a function of chord position. Typical values measured on the rotating blades are shown in Fig. 5 for various flow rates (angles of attack). Although there is some experimental uncertainty, the data were quite reproducible. Data from the two-dimensional cascade measured with static pressure taps, the rotating instrumented blade, and the same (twisted) blade in the cascade are compared in Fig. 6. The discrepancy between the static pressure taps and the transducer measurements in the stationary cascade are due to the slight alteration in blade shape caused by the transducers, especially near the leading edge, and to the twist in the instrumented blade. The difference between the cascade and the rotor measurement are due to these same factors and to rotational effects.

The results of the two-dimensional inviscid flow calculations are compared with the surface pressures measured with static taps in the cascade in Fig. 7. Although some difficulties were encountered in the finite-difference calculation, principally with the geometry and the approximation for the Kutta condition, the differences are primarily due to viscous effects. The Reynolds number based on the chord length was relatively low (approximately 1.5×10^5). Transition was caused at a reasonable chord position by large free stream disturbances and a relatively rough blade surface. The low Reynolds number and blade roughness cause the boundary layer to be much thicker than in modern, high-speed compressors. However, the exaggerated viscous effect was not considered a disadvantage in a basic study of this type.

The inviscid flow calculations for the suction surface pressures in the rotor are compared with the experiment in Fig. 8. The effects of rotation were very small in the calculations, so the cascade data should be in agreement except for viscous effects. Again, there is some discrepancy between the static pressure measurements and the on-rotor measurements, which is due in part to the effect of the transducer on the blade shape. Other possible causes for this difference include the combination of rotational and viscous effects.

Conclusions

This investigation is part of a long-range program directed toward a better understanding and analysis of the flow through the rotor of an axial-flow compressor. Although the results are preliminary, the ability to measure both average and high-frequency fluctuating pressures with transducers embedded in the rotor blade is demonstrated. Further work including the improvement of experimental techniques and the addition of viscous effects in the analysis is in progress.

Acknowledgements

This work was sponsored by Project SQUID which is supported by the Office of Naval Research, Department of the Navy, under Contract N00014-67-A-0226-0005. This document has been approved for public release and sale; its distribution is unlimited.

References

1. JOHNSON, I. A., and BULLOCK, R. O., Ed., "Aerodynamic Design of Axial-Flow Compressors", NASA SP-36, 1965.

2. RUNCKEL, R. F., and DAVEY, R. S., "Pressure Distribution Measurements on the Rotating Blades on a Single Stage Axial-Flow Compressor", NACA Tech. Note No. 1189, 1947.

3. WESKE, J. R., "An Investigation of the Aerodynamic Characteristics of a Rotating Axial-Flow Blade Gird", NACA Tech. Note No. 1128, 1947.

4. MICHEL, D. J., MIZISIM, J., and PRIAN, V., "Effect of Changing Passage Configuration on Internal Flow Characteristics of a 48-Inch Centrifugal Compressor; I-Change in Blade Shape", NACA Tech. Note No. 2706, 1952.

5. WESTPHAL, W. R., and GODWIN, W. R., "Comparison of NACA 65-Series Compressor Blade Pressure Distributions and Performance in a Rotor and in a Cascade", NACA Tech. Note No. 3806, 1957.

6. EMETS, P. O., "Comparison of the Results of Pressure Measurements at Rotating Turbine Blades with Computer Calculations of the Flow Past the Blade", Teploenergetiks, Vol. 15, 1968.

7. CARROLL, J. T., "Dynamics Flow Studies by Application of Pressure and Velocity Sensor on Axial Flow Fan Blades", Instrumentation for Air Breathing Propulsion, Vol. 34, AIAA Progress Series in Astronautics and Aeronautics, MIT Press, Cambridge, Massachusetts.

8. GOSTELOW, J. P., "Compressible Flow Theories for Airfoil Cascades," ASME Paper No. 73-GT-9, 1973.

9. KATSANIS, T., "Quasi-Three Dimensional Calculation of Velocities in Turbomachine Blade Rows," ASME Paper No. 72-WA/GT-7, 1972.

10. SEXTON, M. R., O'BRIEN, W. F., and MOSES, H. L., "Pressure Measurements on the Rotating Blades of an Axial-Flow Compressor", ASME Paper No. 73-GT-79, 1973.

11. O'BRIEN, W. F., MOSES, H. L., and CARTER, H. R., "A Multichannel Telemetry System for Flow Research on Turbomachine Rotors" ASME Paper No. 74-GT-112, 1974.

12. KATSANIS, T., "Fortran Program for Calculating Transonic Velocities on a Blade-to-Blade Stream Surface of a Turbomachine", NASA TN D-5427, 1969.

13. DODGE, P. R., "The Use of a Finite Difference Technique to Predict Cascade, Stator, and Rotor Deviation Angles and Optimum Angles of Attack," ASME Paper No. 73-GT-10, 1973.

14. HORLOCK, J. H., Axial Flow Compressors, Butterworths Scientific Publications, London, 1958.

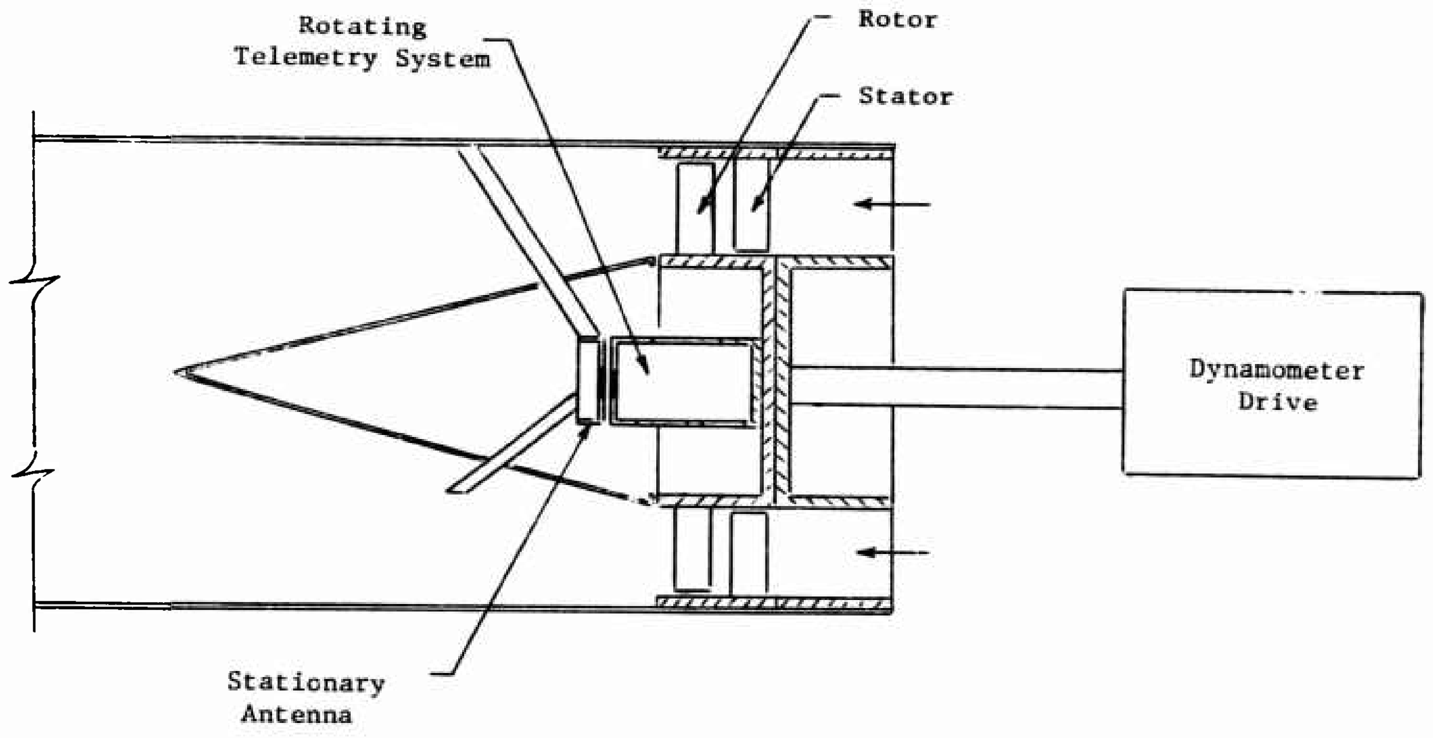
Rotating
Telemetry System
Rotor
Stator
Dynamometer
Drive
Stationary
Antenna

Figure 1. Schematic of Test Compressor

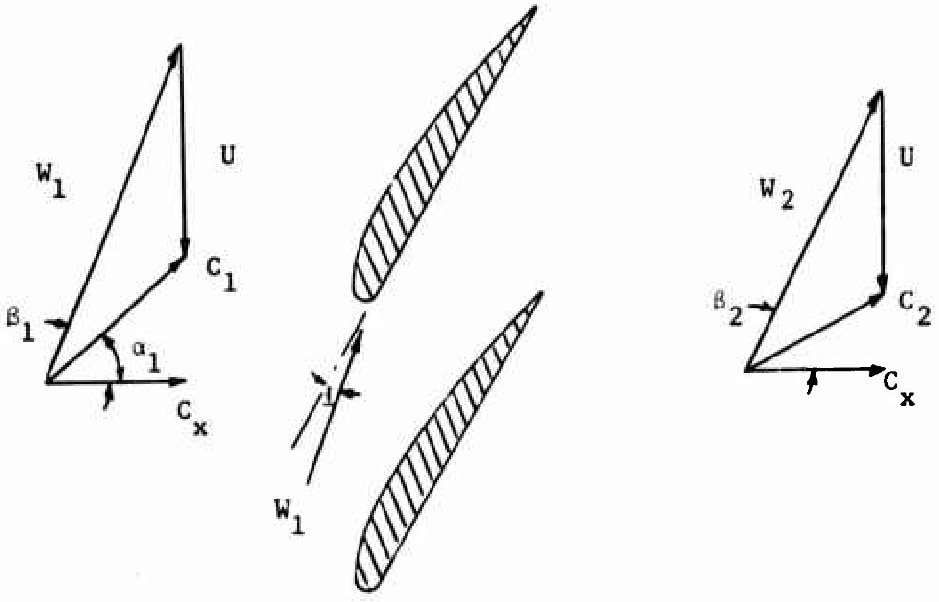
W1
U
C1
β1
α1
Cx
i
W1
W2
U
β2
C2
Cx

Figure 2. Compressor Velocity Triangles

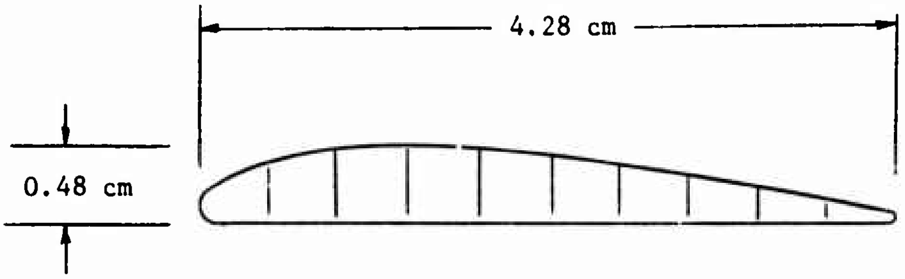
4.28 cm
0.48 cm

Figure 3. Cross Section of RAF 6 Airfoil

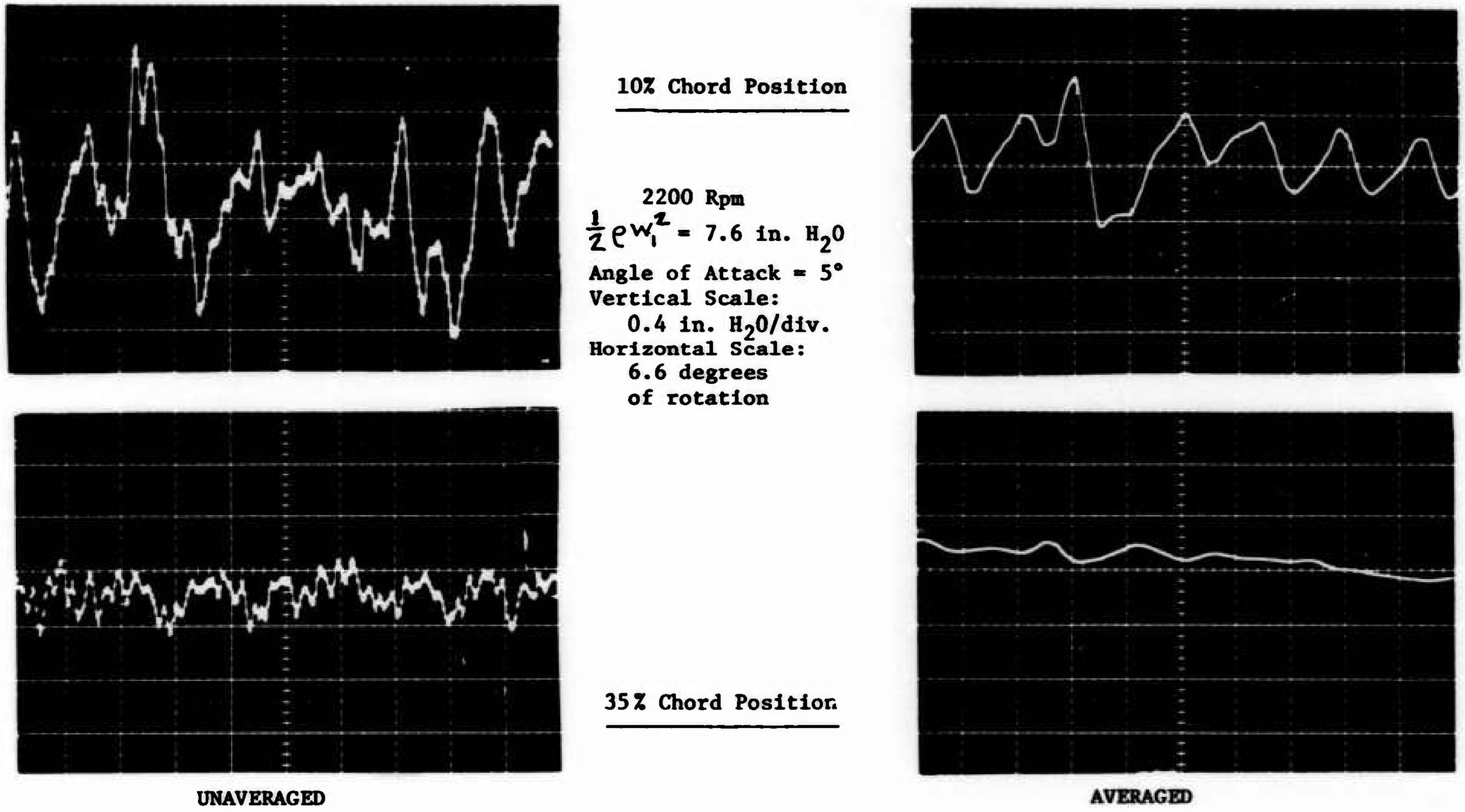

Figure 4. Pressure Fluctuations on Rotor Blade

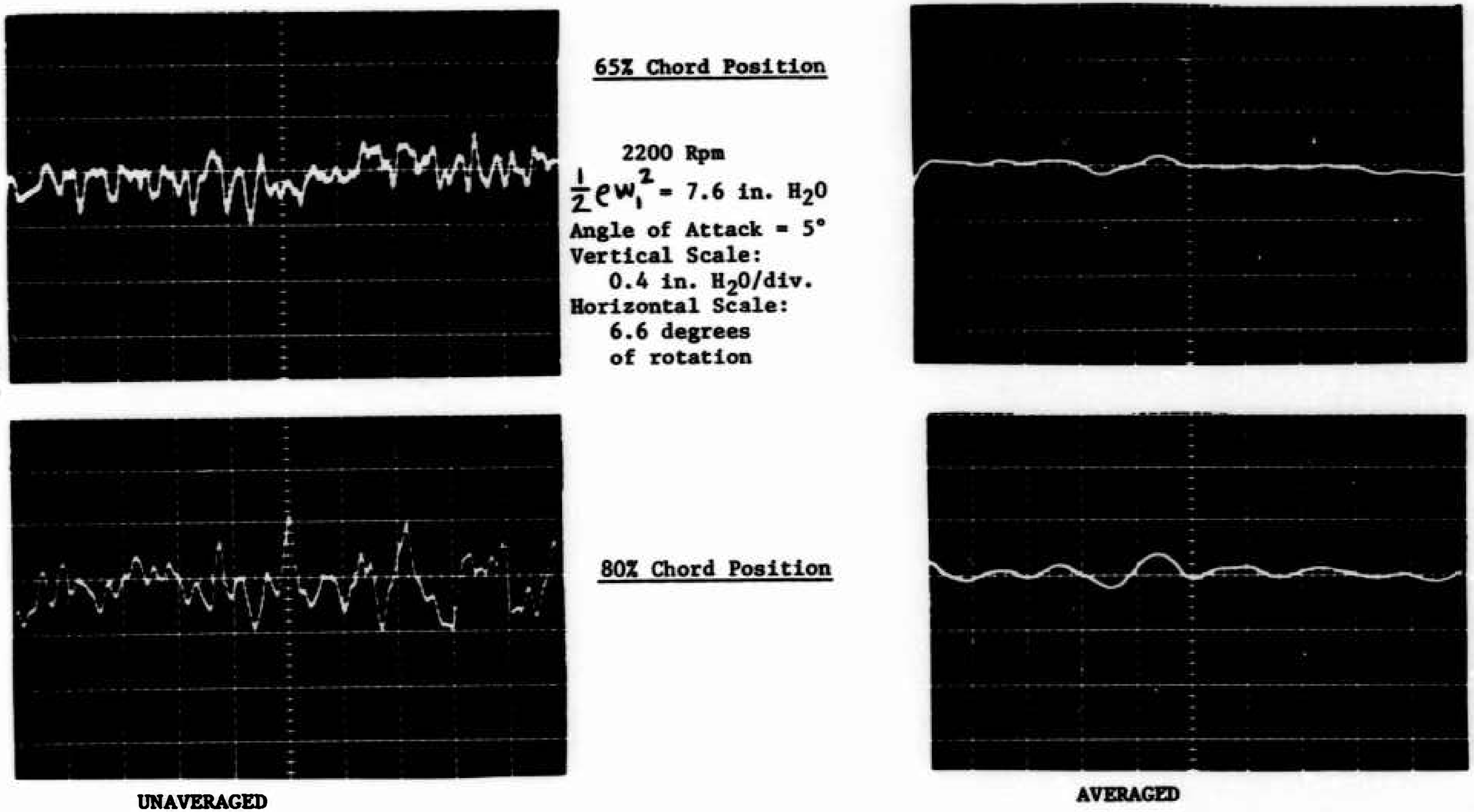

65% Chord Position

2200 Rpm

$\frac{1}{2}\rho w_1^2 = 7.6$ in. H_2O

Angle of Attack = 5°

Vertical Scale:
0.4 in. H_2O/div.

Horizontal Scale:
6.6 degrees
of rotation

80% Chord Position

UNAVERAGED

AVERAGED

Figure 4. (Continued) Pressure Fluctuations on Rotor Blade

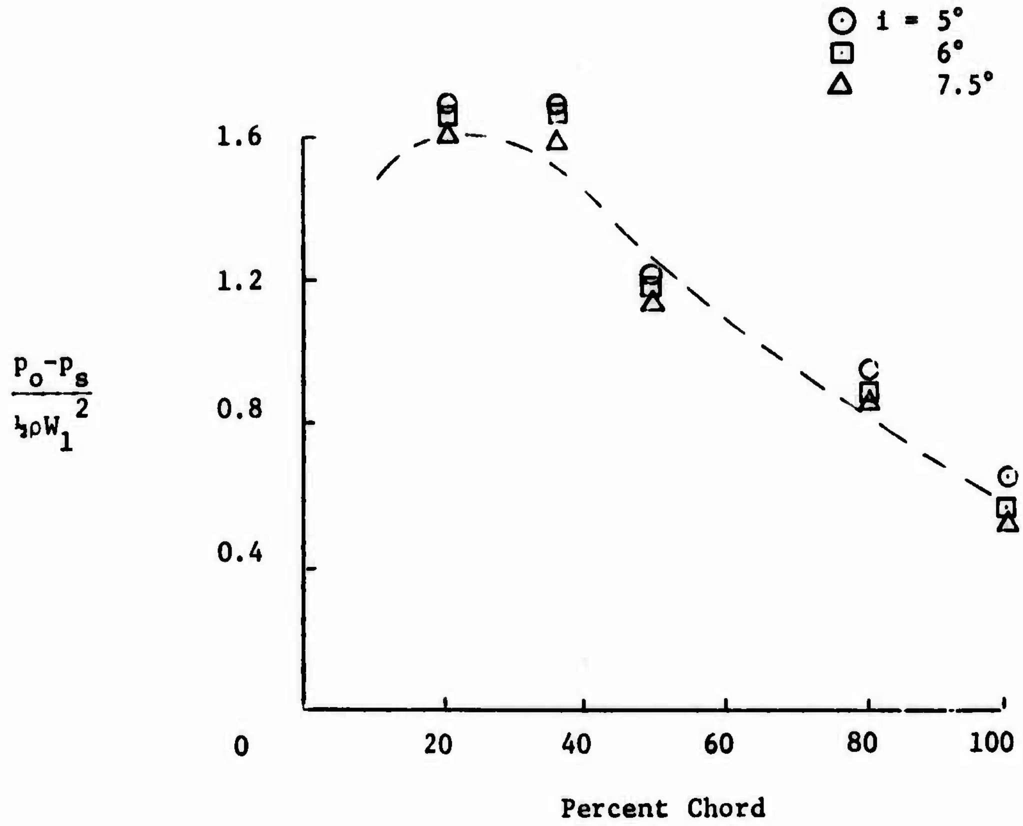

Figure 5. Rotor Suction Side Pressure Coefficient

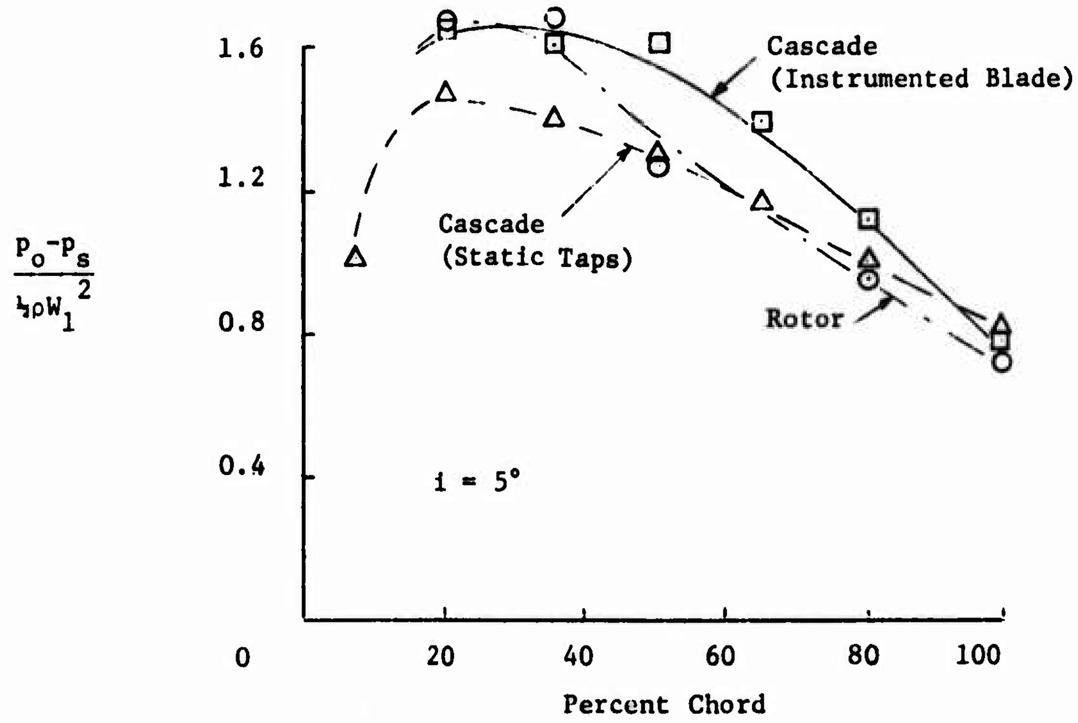

Figure 6. Rotor and Cascade Pressure Coefficient

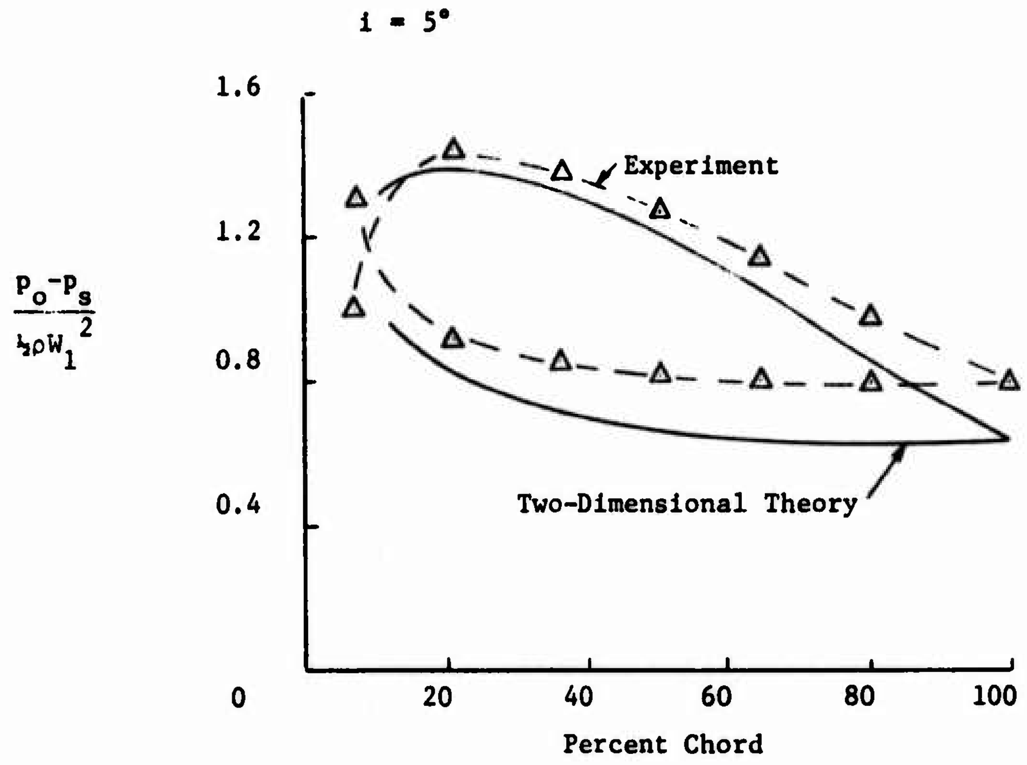

Figure 7. Two-Dimensional Cascade

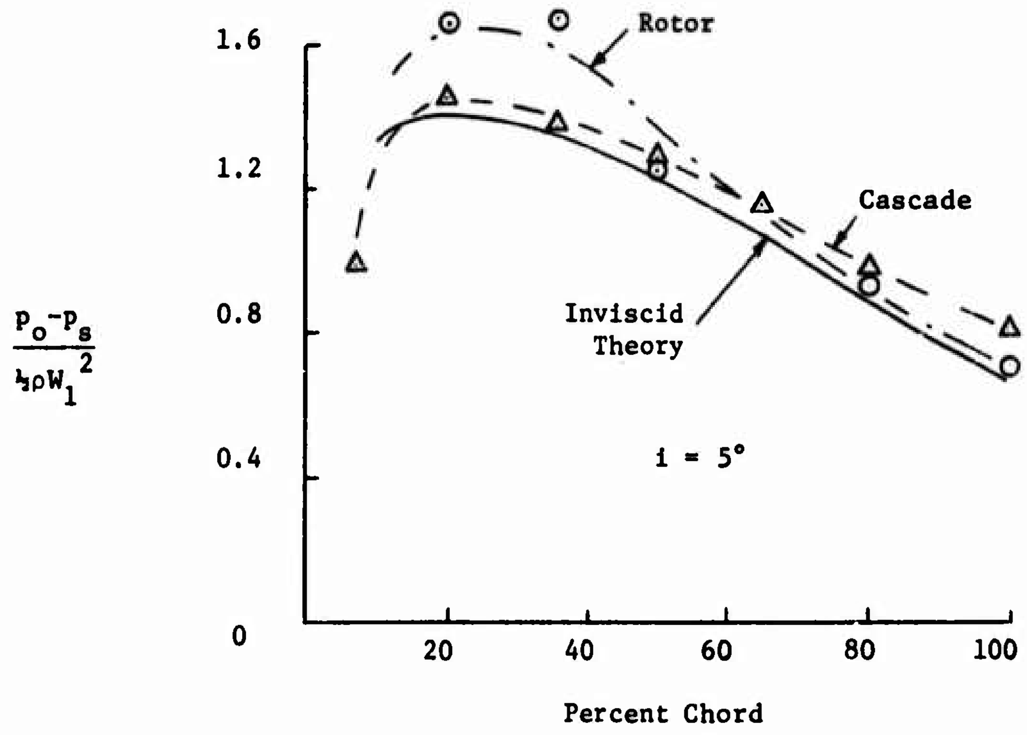

Figure 8. Rotating Airfoil and Cascade

COMBUSTOR MODELLING

I. Poll, R. Payne, J. Swithenbank, M.W. Vincent.

The University of Sheffield, England.

Abstract

A modelling procedure is presented for the prediction of gas turbine combustor performance. The individual processes of fuel-spray evaporation, homogeneous turbulent mixing, and chemical reaction are combined by means of a partially stirred chemical reactor sequence representing the internal mean flow pattern derived from the geometry of a given combustor.

Subsequent tests on the combustor showed satisfactory agreement between experimental and theoretical combustion extinction limits over a wide range of combustor loading. Since the reactor sequence depends on the geometry (and is, for example, independent of fuel/air ratio) these results give confidence that this modelling technique can be applied at all normal operating conditions.

Introduction

Continued interest in the prediction of combustor performance and pollution emission levels has led to the development of mathematical models of the combustion process coupled with aerodynamic and fuel-spray dynamics (1,2).

For the case of high-intensity heterogeneous combustion systems, a particular modelling procedure has been formulated to include the effects of:

(a) Fuel spray evaporation
(b) Turbulent fluid mixing
(c) Chemical reaction

in order to aid in the formation of a general design method for subsonic combustors, and as a diagnostic method for assessing the thrust performance of supersonic and hypersonic systems.

The principal theoretical outputs from the present model may be listed as:

1. Overall combustion intensity
2. The limits of stable operation (i.e. thermal extinction characteristics)
3. Combustion efficiency
4. Potential heat loss to combustor walls

For the primary input parameters:

1. Fuel/air supply rates
2. Fuel nozzle size and operating pressure differential
3. Inlet air temperature and pressure
4. Can geometry and overall pressure loss
5. Full mean composition
6. Inlet air vitiation

The method has been applied to a small-scale test combustor in a recent study investigating the effects of spray evaporation rates on performance. (3) The approach consists of two main stages:

1. Model formation, in terms of a network of stirred - and plug-flow chemical reactors; from a specific input combustor geometry,

turbulent mixing rates, and mean velocity spatial decay rates.

2. Network analysis, incorporating fuel spray evaporation rates, turbulent mixing rates and global reaction kinetics; providing the efficiency, intensity and extinction limits of the combustor.

Model Formation

The principal model units are in the first instance derived as fixed-volume chemical reactors of two characteristic types:

(a) Stirred reactors; denoted by W.S.R. (Well Stirred); in which conditions within the reactor are identical to those in the exit (products) stream. Hence the alternative title of "Zero-dimensional". The processes of fuel evaporation, homogeneous mixing and chemical reaction proceed at rates determined by the reactor inlet conditions and its' volume.

(b) Plug-flow reactors; denoted by P.F.R.; in which no mixing occurs, and hence in which premixed reactants are allowed to burn-out to a mixing-limited extent in one space dimension (usually taken as the mean flow direction). Here the performance of a reactor is governed by kinetic and volume constraints alone, for given feed stream conditions.

These two reactor classifications represent, respectively, broad characteristics observed from combustor sub-zones, viz:

1. The primary flame zone; in which evaporation and mixing rates are comparatively high, and the flame stabilization (continuous ignition) is achieved by recirculation of partially burnt zone products. However, conversion levels, of fuel to products, is relatively low. These characteristics are matched by corresponding WSR operating properties.

2. The secondary/dilution flame zone; downstream, and in series with the primary, in which partially-converted products are allowed to react further, and dissociation losses are made-up such that the final (combustor exit) fuel conversion is high. Sufficient additional air is added to these products in order to reduce the final gas temperature to a level acceptable to the turbine blade materials. This may be modelled as a plug-flow reactor exhibiting good burnout but poor continuous ignition characteristics.

In the formation of an adequate series/parallel reactor network to represent any given combustor design it is necessary, (but not sufficient), to define an effective mixing parameter. That is, given that an individual region of the internal flow may experience high or low levels of turbulent mixing, this may be used to determine the type of reactor to be employed as a model for the region, provided the mixing rate and spacial extent are themselves calculable. Within this study the following working hypothesis will be used to define the turbulent mixing process in any flow region:

Rate of mixing α Rate of turbulence dissipation.

The derivation of a specific mixing time, τ_D, from the above criterion, in conjunction with an overall flow energy balance has been presented previously. (4). Relating this performance variable to that pressure drop across a given flow restriction which contributes directly to turbulence production gives, finally:

$$\tau_{SD} = \frac{\tau_S}{\tau_D} \simeq 50\sqrt{\frac{\Delta P}{3q}} \qquad \text{——————(1)}$$

where τ_S = Mean sub-zone residence time
$= \dfrac{\text{Zone volume}}{\text{Mean volumetric flow-rate}}$
ΔP = Static pressure-drop across stabilizer
q = Dynamic head

The spatial decay rate of turbulence dissipation may be related to the geometric or aerodynamic blockage ratio of the flow restriction by means of a turbulence length scale, l_e, where

$$\lambda \simeq 0.2\, l_e \qquad \text{———(2)}$$

= Characteristic restriction dimension

$l_e \alpha\ 1/k_e$

and: k_e = Characteristic wavenumber of energy containing turbulent eddies.

Giving, finally, the length of the stirred region in the mean flow direction as approximately 10λ (or less for impinging jets). Further the dimension of any individual stirred zone is thereby limited to l_e; thus specifying the maximum number of stirred sub-zones present.

Fig.1. represents schematically the test combustor with stirred and plug-flow regions specified from the above criteria. The resultant reactor network model is shown in Fig.2.

The individual reactor volumes and interconnecting stream mass flow fractions may be calculated from jet entrainment theory (i.e. mean velocity decay). (5)

Network Analysis

A W.S.R. of given volume may be analysed in terms of heat and mass conservation for the exit stream fuel conversion (X) and temperature (T) (6,7) as: (Adiabatic operation):

$$X = \nu\,(T-T_o) \qquad \text{———(3)}$$

and:

$$X = \frac{1}{1+\frac{1}{\tau_{SD}}+\frac{\exp(E/RT)}{\tau_{SK}}} \qquad \text{———(4)}$$

where $\tau_{SD} = \frac{\tau_S}{\tau_K} = \frac{\text{Reactor mean stay-time}}{\text{Specific kinetic time}}$

T_o = Reactor feed stream temperature

and τ_K may be derived from the global reaction data of Kretchmer and Odgers, (8) thus:

Reaction rate per unit volume,r, is defined as:

$$r = \frac{1}{\tau_K}\cdot C_{o_2}\cdot \exp.\left(\frac{-E}{RT}\right) \qquad \text{———(5)}$$

where C_{o_2} = Oxygen concentration within reactor

Hence:

$$\tau_K = \left(\frac{R}{P}\right)^N \cdot \frac{T^{N-0.5}\cdot C_{o_2}}{x_{o_2}^{\ A}\ x_f^{\ N-A}\ k'}\ ,[\text{sec}] \qquad \text{———(6)}$$

where R_1 = Gas constant per mole = 0.08206

P = Absolute pressure in atm

N = Overall reaction order

A = Fractional order in oxygen

x_{O_2} , x_f = Molal concentrations of oxygen and fuel in the reactor

k' = "Collision frequency" constant empirically determined as $1.29.\ 10^{10} \left[\frac{1^N}{K^{0.5}\ \mathrm{gmol}^{N-1} S} \right]$

In addition, the activation energy ratio ($E/_R$) may be found by correlation against Odgers' data as:

$$\frac{E}{R} = f(T_o , \not{0}_o)$$

$\not{0}_o$ = Reactor feed stream equivalence ratio

In the adiabatic heat balance, equation (3), the coefficient represents the inverse of the maximum temperature rise attainable (i.e. at X = 1.0), thus:

$$\nu = 1/(T_{af} - T_o) \qquad \text{———(7)}$$

and the adiabatic flame temperature, T_{af}, may be obtained by correlation against standard data at P, $\not{0}_o$ and T_o; including the effects of dissociation.(9)

Simultaneous solution of equations (3) and (4), including the above global reaction data, provides the reactor exit stream conditions of temperature and conversion at specific input flow rate, and equivalence ratio. A program has been devised to provide this solution for a single WSR, including further the effects of mean flow recirculation - in order to obtain combustion solutions and thermal extinction limits for the model primary zone (see Fig.2.)

Figs. 16 and 17 show representative output information from the program for the first model reactor, WSR_1. In Fig.16 the extinction loading (in gmoles l^{-1} s^{-1} atm^{-N}, where N = the reaction order) of WSR_1 is plotted against reflux ratio,R. Where R is defined as the ratio of the mass flow recirculated to the mass flow through the reactor. Curves at various inlet stream equivalence ratios are included; and for all conditions shown an optimum reflux may be seen which provides a maximum extinction loading. The broken line on the graph represents the locus of this maximum loading with equivalence ratio. The implication of this plot with respect to design work is that in order to obtain the best maximum load characteristics from this type of combustor (dominated by the extinction characteristics of WSR_1) the primary air holes and swirler should be sized such as to provide reflux ratios in the approximate range $0.7 \leqslant \mathbf{R} \leqslant 0.9$ - for stoichiometric or slightly fuel rich primary operation. For lean operation the dilution effects on the reactor due to recirculation of combustion products have a predominant effect over most of the reflux range; and consequently higher reflux ratios are necessary (R = 0.95 for $\not{0}_o$ = 0.85) in order to obtain any advantage in the stability area. (Non-adiabatic operation of the reactor system decreases all peak loadings).

Fig.17 shows a corresponding program output of Carbon monoxide inefficiency vs. WSR_1 loading at various reflux ratios, with the inlet equivalence fixed at stoichiometric. Here the broken line represents the locus of extinction limits with R; and the solid lines the progress of this inefficiency with increased load at fixed R. Carbon monoxide production by WSR_1 is seen to increase with reflux ratio over the entire range; although it should be noted here that the inefficiency characteristics of WSR_1, do not dominate those of the whole combustor. Any series plug-flow reactor in the model will burn-out unburnt products fed to it most efficiently (i.e. in the shortest distance in the mean flow direction) if the carbon monoxide inefficiency level in the PFR feed stream is approximately 0.35. (This follows from consideration of the maximum combustion intensity obtainable from a series stirred-plug-flow model in a manner analogous to that of Beér and Lee (15)).

The inlet equivalence ratio quoted for both Figures 16 and 17 refers to that proportion of fuel spray injected into WSR_1 that is evaporated in the reactor volume. In order to calculate this parameter it is therefore necessary to determine the spray evaporation rate, and extent, in the combustor primary zone reactor, and the variation of these factors with combustor loading.

Evaporation Model

Most evaporation studies have been based on single droplets which are surrounded by diffusion flames. In practical liquid-fuelled combustors a cloud of droplets of various sizes burns with either a yellow flame (as in most industrial furnaces) or a blue flame (as in most gas turbine combustors). The yellow flame indicates that combustion is taking place as a diffusion flame in the wakes of the droplets; whilst the blue flame indicates that conditions are such that the flame has "lifted-off" the droplet. The factors controlling the lift-off (10,11) are principally the concentration of oxygen in the environment of the drops and the differential velocity between the drops and the surrounding gas. In a gas turbine combustor the high recirculation rate of hot products dilutes the oxygen in the incoming air, and the high velocities within the combustor lead to the formation of a blue flame. This is effectively a premixed gas/air flame and has the advantage that radiant heat transfer to the chamber walls is reduced compared to a yellow flame. Nevertheless, the heat transfer to the drop from the hot surrounding gas is in counterflow to the evaporating mass flow, and the actual evaporation model is similar whether yellow or blue flame conditions prevail.

In this study, the evaporation of a cloud of droplets is modelled by first obtaining the droplet size distribution from the known fuel atomizer characteristics, then dividing this distribution into a number (usually greater than 20) of nominally monodisperse droplet size ranges. Since the evaporation time is a strong function of droplet size, the evaporation of each size grouping is evaluated separately. This procedure has the advantage that it is readily adapted to various atomizer characteristics, e.g: pressure atomizers and air-blast atomizers. The evaporation rate is also a function of the relative velocity of the drops, hence the rate depends on the initial relative velocity and the droplet drag. The relative velocities must therefore be evaluated throughout the lifetime of each droplet size grouping.

The above argument is represented mathematically as follows:

The evaporation rate from a droplet (12).

$$\dot{m}_f = \frac{2\pi.k.D}{C_f} . \quad \ln\left\{1 + \frac{C_f \Delta T}{L} + \frac{C_{o_2}}{i}\left(1 + \frac{Q}{L}\right)\right\} \qquad \text{———}(8)$$

Forced convection increases the rate by a large factor:

$$(\dot{m}_f)_F = (\dot{m}_f)_S\left[1 + 0.276.Re^{\frac{1}{2}}\ Pr^{\frac{1}{3}}\right] = (\dot{m}_f)_S\left[1 + 2.3\ Re^{\frac{1}{2}}\right] \qquad \text{———}(9)$$

where the Reynolds number is evaluated at the relative velocity, V_{rel}, between the droplet and gas:

$$Re = V_{rel} \cdot D \cdot \rho_g / \mu_g \tag{10}$$

and:

$$Pr = C_g \cdot \mu_g / K_g \tag{11}$$

The acceleration of the droplet is given by:

$$\frac{d\,V_{rel}}{d\tau} = \frac{3}{4} \cdot \frac{C_D}{D} \cdot \frac{\rho_g}{\rho_L} \cdot V^2_{rel} \tag{12}$$

and:

$$C_D = 0.48 + 28/Re^{0.85} \tag{13}$$

The initial spray velocity is:

$$V_f = C_V \sqrt{(2gP/\rho_L)} \tag{14}$$

Where C_V is a function of droplet size.

The gas velocity in the primary region (13)

$$V_g = 0.45 \cdot \sqrt{(2\,\Delta P/\rho_g)} \tag{15}$$

where the factor 0.45 denotes the ratio between the primary vortex velocity and the air velocity through the primary holes.

The empirical relations determined by Bowen and Joyce (14) were used to specify the droplet size distribution in terms of volume percent oversize (R):

$$R = 100.\ \exp.\left[(-D/\bar{x})^n\right] \tag{16}$$

where the Rosin-Rammler mean diameter $\bar{x}$ is given by:

$$\bar{x} = K/P^{(0.3358 - 0.02427F)} \tag{17}$$

(N.B. here P is in psi units)

$$\log_{10} K = 2.7008 + 0.2162F \tag{18}$$

$$F = (\text{Flow rate in gals/hr})/\sqrt{P} \tag{19}$$

$$SMD = 413.4/P^{(0.3712 - 0.02589F)} \tag{20}$$

$$\bar{x}/SMD = \Gamma\left[(2-1/n)/(1-1/n)\right] \tag{21}$$

From these relations the initial droplet size distributions are shown for various nozzle sizes and fuel pressures in Figs. 3. and 4.

Although oxygen concentration appears as a parameter in the evaporation rate equation, its effect on the evaporation rate was found to be negligible over the range 1 - 20% oxygen. (see Fig.5.) Similarly the effect of ambient temperature within the combustor primary region on evaporation rate was found to be small, as shown in Fig.6. As expected, the theoretical studies also showed that the small drops quickly assume the gas velocity, and evaporate in a short time. On the other hand, larger drops tend to retain their own velocity, and hence the effect of forced convection on their evaporation rate remains high. These features are illustrated quantitatively in Figs. 7 and 8 as a function of time for various drop sizes. Thus by far the largest factor effecting evaporation from the spray cloud was that due to forced convection. This is shown in Fig.9. where it can be seen that a 2 to 3 fold increase in evaporation rate is obtained at a typical combustor operating condition.

The degree of evaporation at the rich and weak limits of combustion for various fuel nozzle sizes was calculated as shown in Figs.10

and 11, and as can be seen, it is predicted that only $\frac{1}{2}$ to $\frac{2}{3}$ of the fuel is evaporated in the primary (flame stabilizing)region. In order to check the burnout of droplets, optical methods may be used, and it is useful to have an estimate of the predicted droplet size distributions at different residence times. This information for a typical operating condition is contained in Fig. 12 where the gradual increase in mean diameter is apparent.

Experimental Studies and Discussion

Experimental verification of the proposed theoretical model is essential to raise it above the level of an academic exercise and demonstrate that the design technique can be applied to complex 3-dimensional combustor geometries.

Moreover, as may be seen from the foregoing sections the method for predicting combustor performance relies on several theoretical stages viz. for given input flow conditions and geometry a reactor sequence model is formed; within each sub-zone a degree of fuel spray evaporation is calculated; and finally, the evaporation - corrected reactor conditions are solved for conversions and temperatures, etc. With this number of stages in the overall calculation it was decided to fix on one principal test of the theory, that is the extinction limits of the test combustor. These limits should correspond to those of the most heavily-loaded stirred reactor in the primary zone, and will be within a few percent of stoichiometric evaporated fuel in this region.

The effect of fitting fuel nozzles giving different spray size distributions (or different spray angle) is therefore predicted to give operation at different overall fuel/air ratios within an overall locus. Qualitatively it may be seen that increasing the flow number of the fuel nozzle will cause the fuel pressure to decrease, leading to larger drop sizes and a smaller proportion of fuel evaporated in the primary region. This means that the stability loop will move to richer mixtures. The first stage in the experimental verification is therefore to demonstrate that the stability loops for different fuel nozzles fall within the predicted locus and vary with fuel nozzle flow number in the manner indicated.

Using the test facility shown in Fig.13 and the test combustor shown schematically in Fig.1. (see also Ref.(4)), the stability loops for a series of fuel nozzles were measured. The results are plotted in Fig.14. In ref (4) the locus of the stability loops had been predicted, and this is also shown on the same graph. The validity of the anticipated locus is well confirmed.

The next point is to determine the validity of the proposed droplet evaporation model. This could be achieved by droplet and/or gas composition measurements throughout the combustor, and these measurements are at present underway. However, the existing stability loop results can also be used to check the evaporation model, since, although the overall mixture ratio may be much weaker than stoichiometric, the primary region should be operating close to stoichiometric. Thus if the evaporation model is correct, it should predict a similar stoichiometric stability loop for the primary region for all the various fuel nozzles. The data plotted in Figs. 10 and 11 as primary fuel evaporation at the combustion limits can therefore be converted to primary air/fuel as shown in Fig.15. Bearing in mind the assumptions made in the evaporation model, the agreement is remarkably good, since it not only verifies that the local mixture ratio at peak loading is stoichiometric, but it also indicates that the expected reduction in τ_{SD} caused by the evaporation delay time broadens the stability loop as predicted (4).

Combustion efficiency for the whole combustor is limited to approximately $\left[1 - 0.02\sqrt{\frac{3}{\xi}} = 1/(1 + {}^{1}/_{\tau_{SD}}) \right]$ by the energy available for turbulent mixing. For this combustor, ξ = dynamic head loss = 28.36, hence the maximum anticipated combustion efficiency is 99.35%. This is reduced by the proportion of fuel unevaporated in the combustor; and, at the combustion limits, Figs. 10 and 11, show that this predicted loss can amount to several percent.

Fig.15, also includes the theoretical stability loop, derived from the reactor theory and network model outlined, of the first, most heavily-loaded stirred reactor in the primary zone. As stated, the limits of this reactor are expected to dominate the extinction characteristics of the whole combustor. It may be seen that at the high turbulent mixing levels experienced in this flow region the theoretical limits are narrower than those measured. However, the effect of an evaporation delay time has not been included at present; only the air/fuel limit imposed on equivalence ratio in the whole reactor by the time available for evaporation to take place. With this further delay included, these theoretical limits are expected to broaden in the same manner as a decrease in τ_{SD} described in ref.(4). The maximum loading point on the predicted stability loop, of course, corresponds to the limit locus at stoichiometric operation, since the locus itself was derived from the same theoretical source.

Conclusions

1. A theoretical model of the combustion process within a gas turbine combustor has been formulated, and extended to include heterogeneous conditions, to a first stage in the development of a design method.

2. An experimental check on the validity of both the droplet size distribution evaporation model, and the reactor sequence model has been shown to provide satisfactory agreement with the predicted operating limits of a small-scale test combustor.

3. Further testing of the predicted combustion efficiencies (as shown, for example, in Fig.17) from the theoretical model is at present under experimental investigation.

Acknowledgments

Various aspects of this research are supported by grants from: Rolls Royce (1971) Ltd., Bristol Engines Division; Lycoming-Creare, National Gas Turbine Establishment, SRC, and USAF European Office of Aerospace Research Grant No.72 - 2248. This support is gratefully acknowledged.

References

1. HAMMOND, D.C.Jnr. and MELLOR, A.M. Analytical Calculations for the Performance and Pollutant Emissions of Gas Turbine Combustors. Comb. Sci. and Tech. Vol.4. p.101. 1971.
2. ROBERTS, R., ACETO, L.D., KOLLRACK, R. and BONNELL, J.M. An Analytical Model for Nitric Oxide Formation in a Gas Turbine Combustion Chamber. AIAA Paper No. 71-715. 1971.
3. VINCENT, M.W. Fuel Spray Evaporation in Gas Turbine Burners. Ph.D. thesis. University of Sheffield, July, 1973.
4. SWITHENBANK, J., POLL, I., VINCENT, M.W. and WRIGHT, D.D. Combustor Design Fundamentals. Fourteenth Symposium (International) on Combustion. The Combustion Institute, p.627. 1972.(see also Ref.16).
5. POLL, I. The Application of Partially Stirred Reactor Modelling to Pollutant Minimisation in Combustors. Part I. University of Sheffield. Dept. of Chemical Engineering Report No. HIC.193. March, 1973.
6. POLL, I. The Application of Partially Stirred Reactor Modelling to

Gas Turbine Combustor Design. Part II. University of Sheffield. Dept. of Chemical Engineering. Report No. HIC.194. December, 1973.

7. VULIS, Lev.A. Thermal Regimes of Combustion, McGraw-Hill, New York, 1963.
8. KRETCHMER, D. and ODGERS, J. Modelling of Gas Turbine Combustors - a convenient Reaction Rate Expression. J. Eng. for Power. p.173.1972.
9. ROBERTS, M.F. Combustion Temperature Rise Calculation, Rolls Royce (1971) Ltd., Ref. CSR99, 1973.
10. SJOGREN, A., Soot Formation by Combustion of an Atomized Liquid Fuel. Fourteenth Symposium (Intl.) on Combustion. The Combustion Institute, p.919. 1972.
11. SUBRAMANYAM, R.G. and BRZUSTOWSKI, T.A. Experimental Studies on the Flame Structure in the Wake of a Burning Droplet. Fourteenth Symp. (Intl.) on Combustion. The Combustion Institute. p.1333. 1972.
12. WISE, H., LOVELL, J. and WOOD, B.J. Effects of Chemical and Physical Parameters on Burning Rate. Fifth Symposium (Intl.) on Combustion.
13. CLARKE, J.S. Joint Conference on Combustion. Institute of Mechanical Engineering/ASME. 1955.
14. BOWEN, I.G. and JOYCE, J.R. Shell Technical Report No. ICF/17. 1948.
15. BEÉR, J.M. and LEE, K.B. Tenth Symposium (Intl.) on Combustion. The Combustion Institute, 1964.
16. OSGERBY, J.T. A Literature Review on Turbine Combustor Modelling and Emissions. Arnold Air Force Station. Tennessee. Report AEDC-TR-73-163 (or: ARO-ETF-TR-73-103), November, 1973.

Nomenclature

A	Fractional reaction order in O_2.
C_f	Specific heat of fuel vapour.
C_g	Specific heat of air.
C_{O_2}	Oxygen mass concentration.
D	Droplet diameter.
E	Activation energy.
F	Nozzle flow number.
i	Stoichiometric mixture ratio(mass).
k	Thermal conductivity of fuel vapour.
k'	"collision frequency" factor.
k_e	Wavenumber of energy-containing eddies.
K	Constant of proportionality.
K_g	Thermal Conductivity of gas.
l_e	Dimension of energy containing eddies.
L	Fuel latent heat of evaporation.
$\dot{m}_f$	Mass evaporation rate of fuel droplet.
n	Distribution constant for spray cloud.
N	Overall reaction order.
P	Can operating pressure; nozzle pressure.
ΔP	Can pressure drop.
q	Dynamic head.
Q	Heat of combustion of fuel.
r	Reaction rate per unit volume.
R	Reflux ratio; Gas Constant; Volume % oversize.
T	Temperature. K.
T_{af}	Adiabatic flame temperature.K.
ΔT =	Droplet to gas temperature difference.
V	Velocity.
x	Molal concentration.
$\bar{x}$	Rosin Rammler mean diameter.
X	Conversion.
λ	Characteristic flow restriction dimension.
τ	Time.
τ_S	Stay-time.
τ_D	Mixing time.
τ_K	Kinetic time.
τ_{SD}	τ_S/τ_D
τ_{SK}	τ_S/τ_K
μ	Viscosity.
ρ	Density.
ξ	Dynamic head loss factor.

Subscripts

f	Fuel.
F	Forced convection.
g	Gas.
L	Liquid.
O	Initial value.
O_2	Oxygen.
rel	Relative.
S	Static.

Abbreviations.

PFR	Plug Flow Reactor.
SMD	Sauter Mean Diameter.
WSR	Well Stirred Reactor.

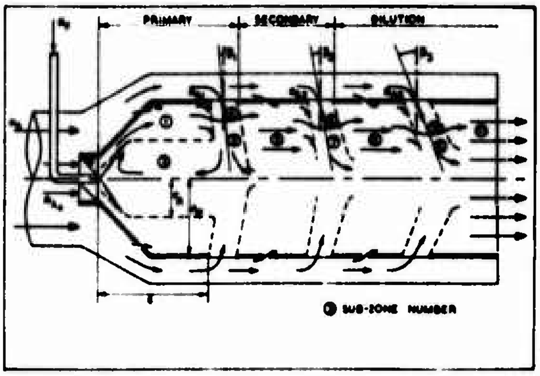
PRIMARY
SECONDARY
DILUTION
SUB-ZONE NUMBER

FIG.1. Idealised Combustor Flow Pattern.

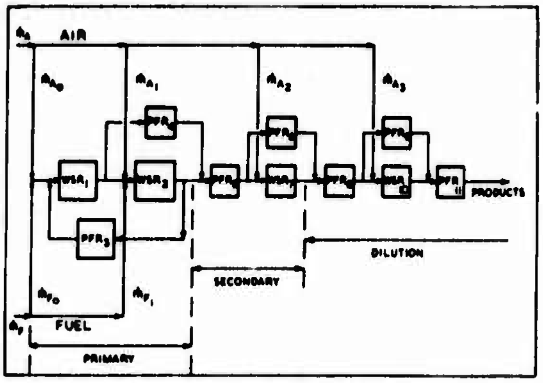
AIR
FUEL
PRODUCTS
PRIMARY
SECONDARY
DILUTION

FIG.2. Reactor Network Model.

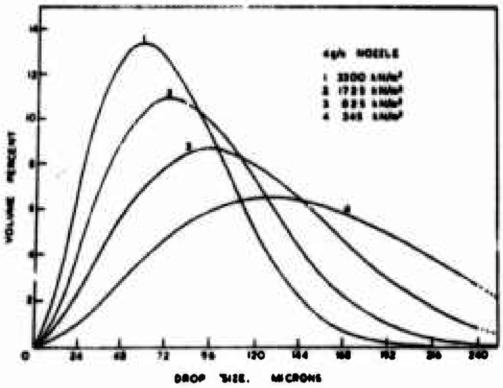

FIG.3. Effect of Nozzle injection pressure on drop size distribution.

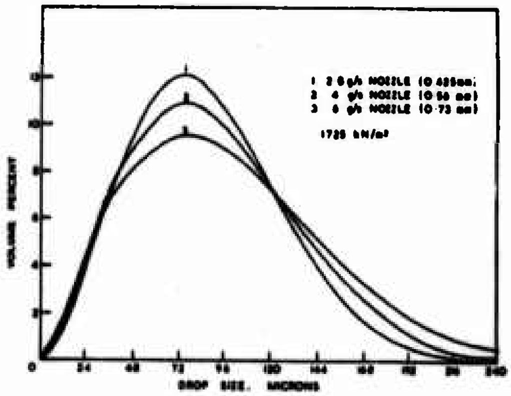

FIG.4. Effect of Nozzle Size on drop size distribution.

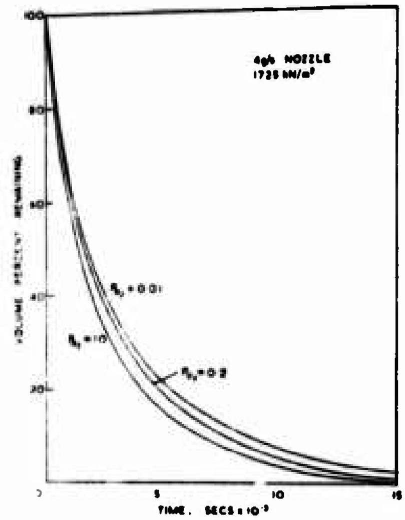

FIG.5. Effect of Oxygen Concentration on evaporation rate.

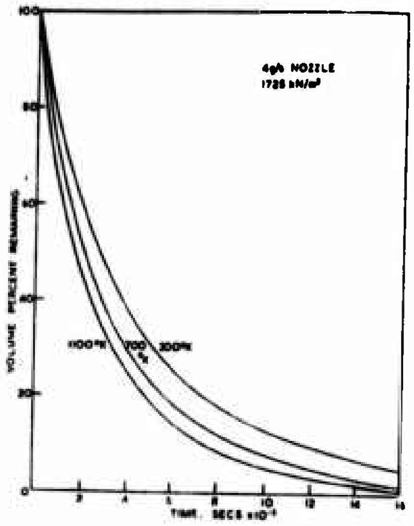

FIG.6. Effect of ambient temperature on evaporation rate.

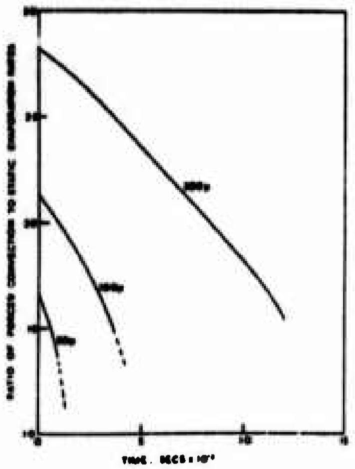

FIG.7. Forced convection evaporation rate with time (Single drops)

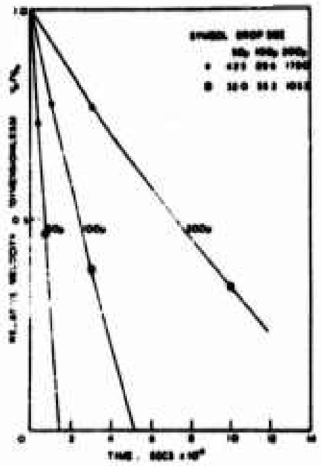

FIG.8. Relative velocity with time (Single drops).

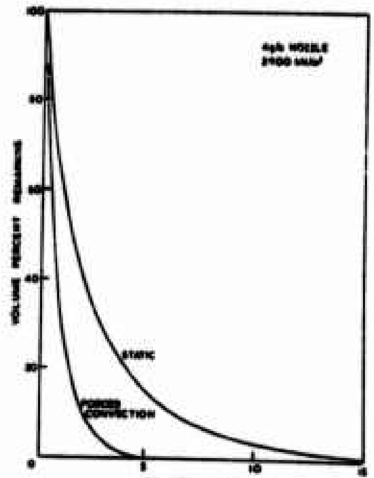

FIG.9. Comparison of forced convection and static evaporation rates.

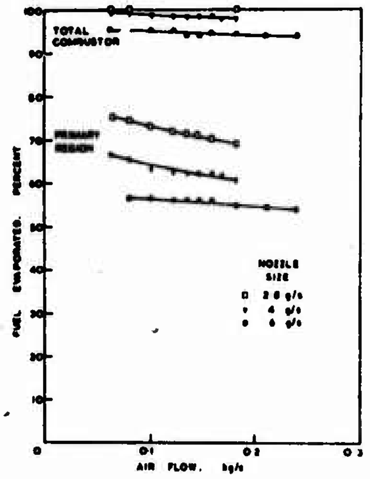

FIG.10. Degree of evaporation achieved versus Air flow - Rich extinction.

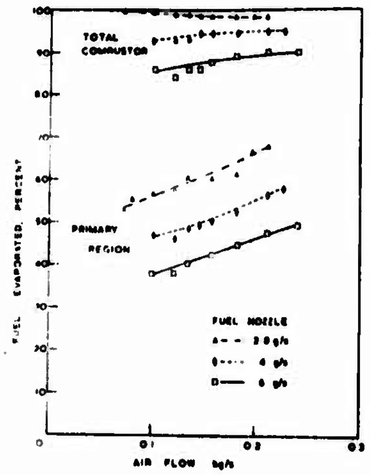

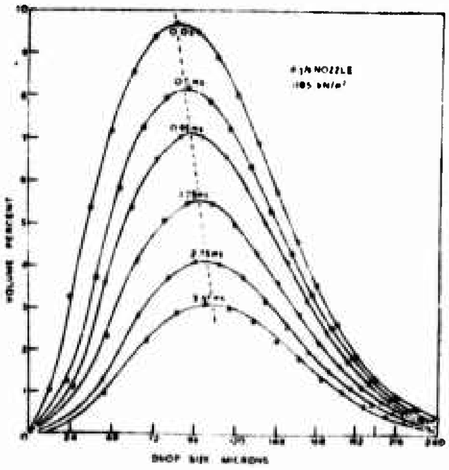

FIG.12. Change of drop size distribution with evaporation.

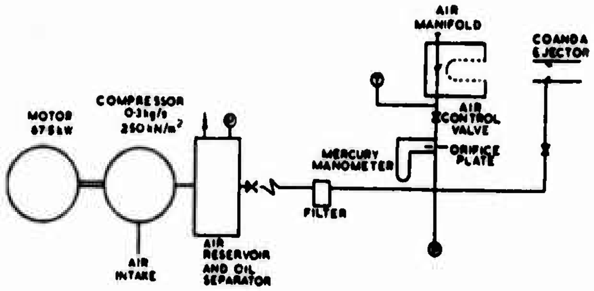
AIR MANIFOLD
COANDA EJECTOR
MOTOR 675kW
COMPRESSOR 0·3kg/s 250kN/m²
AIR CONTROL VALVE
MERCURY MANOMETER
ORIFICE PLATE
FILTER
AIR INTAKE
AIR RESERVOIR AND OIL SEPARATOR

FIG.13. Sketch cf Experimental combustor test rig.

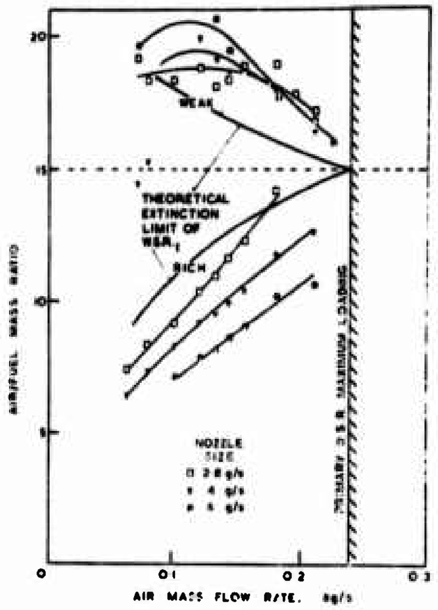

FIG.15. Primary zone measured and calculated extinction limits.

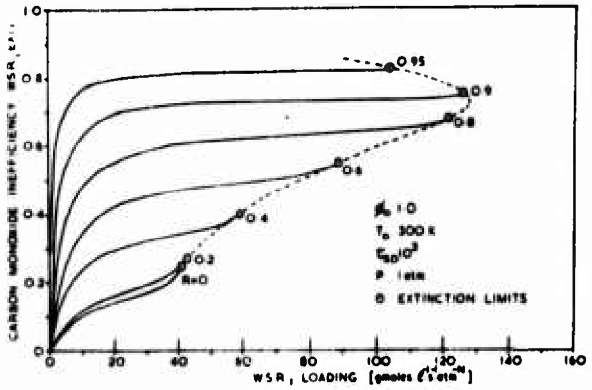

FIG.17. Computed WSR$_1$ Carbon Monoxide inefficiency vs. loading and reflux.

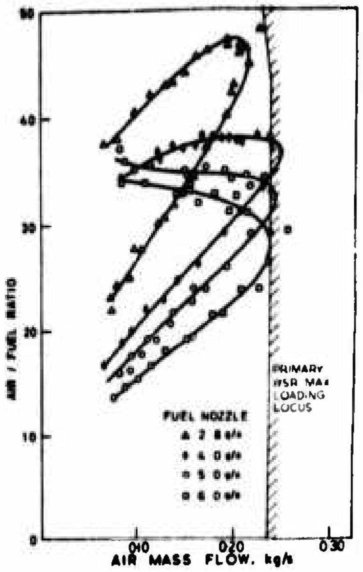

FIG.14. Measured Stability loops.

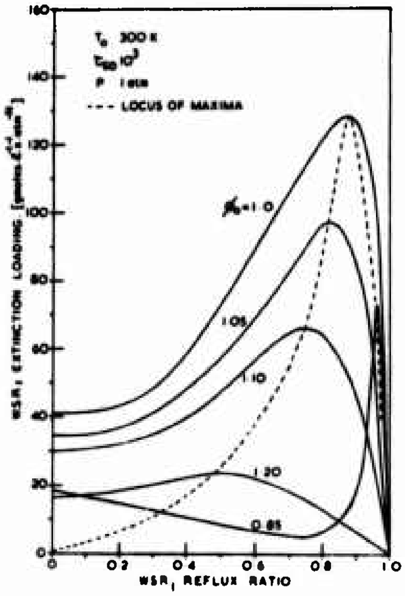

FIG.16. Computed WSR$_1$ extinction characteristics.

HEAT TRANSFER MEASUREMENTS ON
ADVANCED COMBUSTOR LINER COOLING SYSTEMS

D. Wahl, G. Kappler, J. Schmidt
MTU - München G.m.b.H.

Abstract

Measurements of pressure and temperature distribution as well as of wall temperature downstream of film cooling configurations using various pattern of drilled holes and porous material for air penetration are reported. In revision to standard film cooling configurations the advanced combustor liner cooling systems investigated are designed without a film cooling lip to permit cost saving combustor processing. The investigations were performed with the aid of an experimental apparatus specially set up to simulate the range of parameters relevant to gas turbine practice. The measurements demonstrate that the cooling air injection through an array of small holes leads to a more uniform film layer and improves the cooling effectiveness. Correlation of film cooling effectiveness data is presented by considering the blowing rate as important controlling parameter.

Nomenclature

A_n = total step area
A_o = three-dimensional step open area
C_p = specific heat
d = diameter of static holes
D = diameter of main holes
h = step height
l = lip length
M = mass flow
m = $\rho_C \cdot v_C / \rho_G \cdot v_G$ blowing rate
Ma = Mach number
p = pressure
s = slot height
t = thickness
T = temperature
v = velocity

x = distance from cooling air injection point in longitudinal direction
y = distance normal to wall
y_p = pitch in y-direction
z = distance in lateral direction (z = 0 = median plane of the test zone)
z_1 = distance between lateral walls
z_p = pitch in z-direction
α = injection angle
$\delta^* = \int_0^\infty (1 - \frac{v}{v_G})\, dy$ displacement thickness
$\delta_T^* = \int_0^\infty (1 - \frac{T - T_W}{T_G - T_W})\, dy$, thickness of the thermal layer
η = film cooling effectiveness
ρ = density

Subscripts

C = cooling air
F = film
G = main stream
s = static

t = total
W = wall
u = uncooled

Introduction

The cooling of gas turbine combustor liners exposed to hot gases is technically accomplished by film cooling; that is by injecting a cooler gas through an array of discrete holes in a slot from where it expands along the wall surface into the hot gas forming a cooling layer. Due to the rapid increase of gas turbine cycle temperature the need for more efficient combustor liner cooling becomes considerably demanding. Since the thermally most efficient way of cooling a wall by effusion of the coolant through the wall is, with todays technology, not feasible yet for engineering applications, advanced film cooling methods are necessary to yield high cooling effectiveness at a minimum of cooling air flow. Also, for industrial application it is very important that advanced film cooling devices bear to design requirements for cost-saving combustor processing.

As a result of a series of theoretical and experimental (1-9) investigations the physical process of two-dimensional film cooling is qualitatively understood. Basing on simple heat sink models as well as on numerical techniques for predicting two dimensional turbulent layers a number of theoretical correlations and semiempirical prediction formulas have been developed for the film cooling effectiveness. A general survey of this work is given in Reference (1).

Using the results from experimental studies it has been shown that both, geometric and flow parameters, are factors influencing film cooling efficiency. Sivasegaram and Whitelaw (2) considered for instance as geometric parameters the importance of lip thickness and injection angle. The influence of the variation of flow parameters such as velocity ratio, density resp. temperature ratio, mainstream boundary layer thickness and turbulence level has been studied by various authors (4). The papers by Eckert (5) and Eriksen (6) are relevant to three-dimensional film cooling i.e. film cooling with injection through a single hole or a row of holes.

Nina and Whitelaw (7) and Rastogi and Whitelaw (8) investigated the influence of variable slot geometry of various cooling configurations, which are of direct interest to gas turbine practice, but the range of parameters investigated was insufficient to allow for extensive and practically useful conclusions. Accurate theoretical predictions for film cooling with secondary flow through discrete holes and with large temperature differences proved to be very difficult, because the three-dimensional nonuniform flow is yet accessible to anything but simplified analysis.

Therefore, in order to gain more detailed understanding of the effects of large temperature differences and of the interaction of an array of individual jets on the adiabatic wall temperature distribution, which is necessary for the design of actual gas turbine combustors, an experimental facility was set up, and instrumented for the determination of the cooling efficiency of advanced combustor liner cooling systems.

This paper describes the test facility, the design criteria of various film cooling test arrangements and presents typical results. It also covers the work made in attempt to give a more consistent prediction of the cooling effectiveness by considering the blowing rate of the cooling air to the mainstream as an important correlation parameter.

Test Apparatus

The experimental apparatus shown schematically in Fig. 1 (a) employed two separate air supply lines in order to enable a wide range setting of cooling air to mainstream ratios. It consisted basically of a gas turbine combustion chamber which supplied hot air through a settling tract into the test zone.

The main stream air mass flow could be varied between 0,3 kg/s and 1,5 kg/s and the maximum combustion chamber exhaust temperature was 1100 K. The pressure in the test zone at the highest mass flow rate was 1,05 bar.

The cooling air was supplied by a screw compressor and ducted as shown in Fig. 1 (a) following a heat exchanger, a condenser and a settling pressure tank through the test section into the test zone.

The two-dimensional test zone shown enlarged in Fig. 1 (b) had a width of 150 mm and a height of 120 mm. Part of the cooling air was bled in a cooling jacket opposite the test section to ensure equal wall temperatures and hence to avoid any test zone deformations because of thermal expansions.

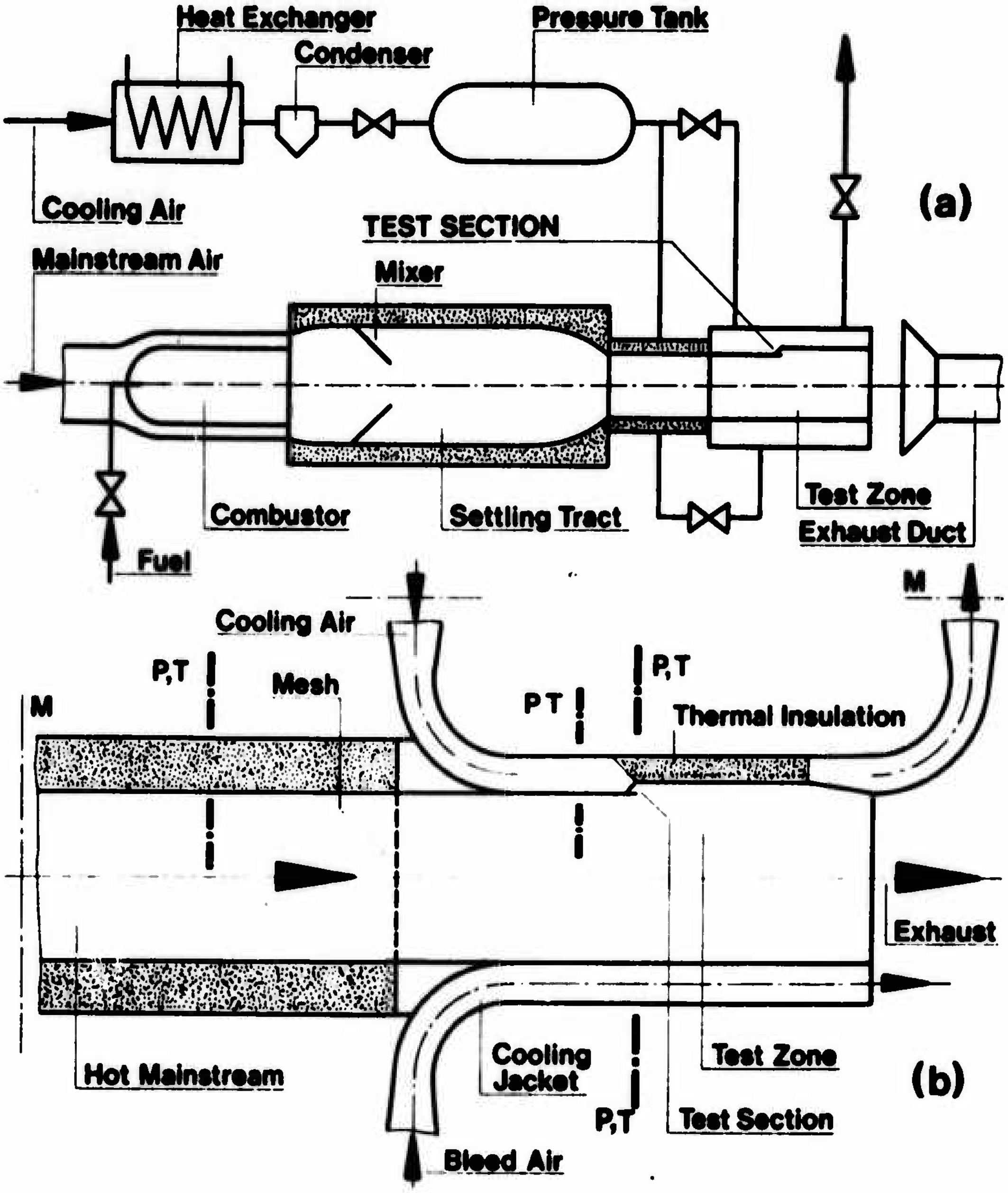
Heat Exchanger
Condenser
Pressure Tank
Cooling Air
(a)
TEST SECTION
Mainstream Air
Mixer
Combustor
Settling Tract
Test Zone
Exhaust Duct
Fuel
Cooling Air
M
P,T
Mesh
M
PT
P,T
Thermal Insulation
Exhaust
Hot Mainstream
Cooling Jacket
Test Zone
(b)
P,T
Test Section
Bleed Air

Fig. 1 Scheme of test apparatus (a) and test zone (b)

The various planes of measurements are indicated in Fig. 1 (b) by the point dotted lines together with the corresponding state parameters measured.

Two basic cooling air ducting arrangements are possible. One arrangement where part of the cooling air does not enter the test zone flowing along the outer film cooled wall and another arrangement where the test wall is insulated with ceramic wool to ensure nearly adiabatic wall conditions. For the experiments reported in this paper the latter arrangement was employed in order to enable comparison of test data with previous work.

The measured velocity and temperature distribution of the main stream in front of the film cooling step is shown for a typical test condition in Fig. 2 (a) resp. Fig. 2 (b). The velocity and temperature distributions as well as the distance normal to the wall y are made dimensionless by referring them to hot gas velocity v_G and the temperature difference $T_G - T_W$ to the boundery layer displacement thickness and the analogous temperature displacement thickness respectively. For comparison the full line in fig. 2 (a) represents the turbulent flow profile computed according to Klebanoff and Diehl (10). The cooling air pressure distribution across the film cooling holes entry plane was also checked and showed a uniform profile.

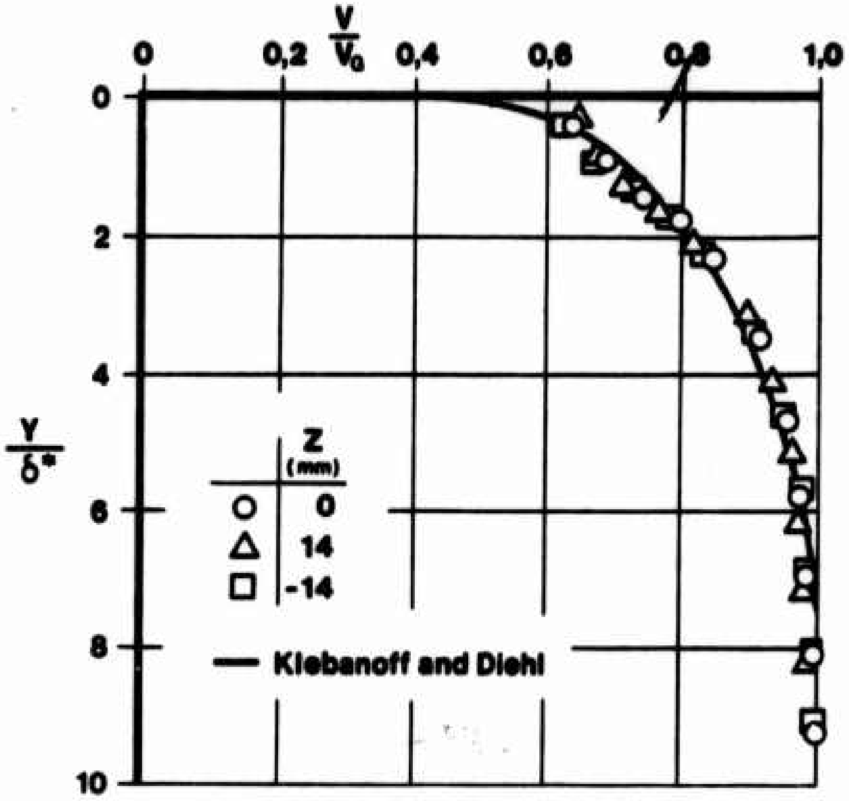

Fig. 2 (a) Mainstream velocity distribution in front of the film cooling step

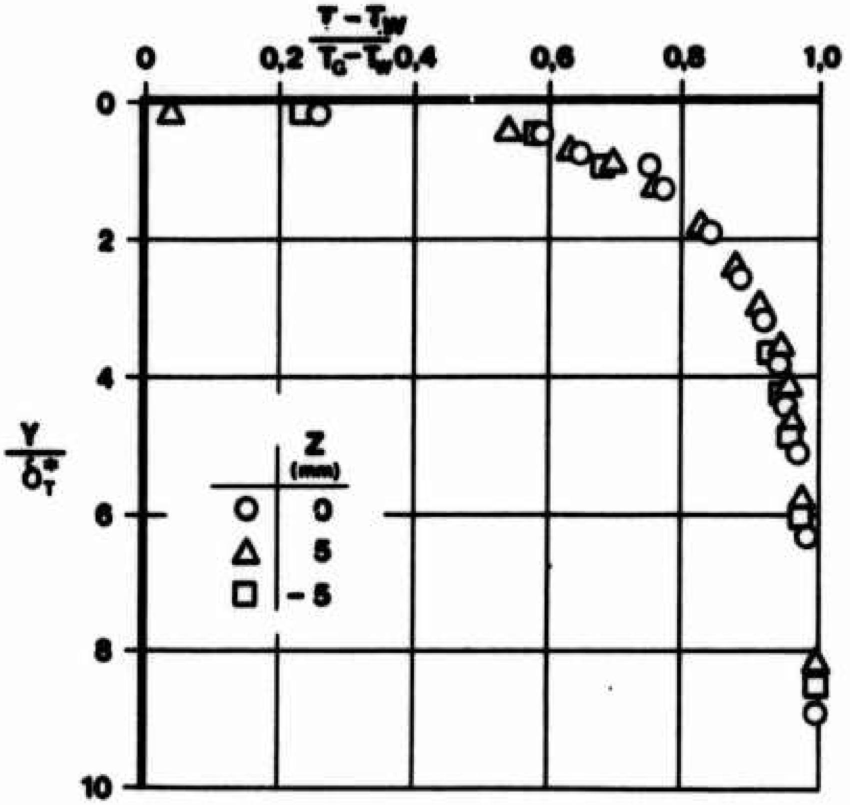

Fig. 2 (b) Mainstream temperature distribution in front of the film cooling step

Test Sections

The two-dimensional film cooling configurations investigated and their characteristic dimensions are listed in Table 1. The geometrical dimensions were chosen to yield the same permeability i.e. the same cooling air mass flow rate at equal pressure losses. The test sections were made of Nimonic 75 and designed for easy exchange in the test channel. Fig. 3 shows the three basic designs. The standard film cooling configurations with main holes and static holes Fig. 3 (a) were investigated first because this configuration is used in combustion chamber design and previous reports on film cooling performance (7) did not account fully for high temperature differences between cooling air and mainstream. Wall temperature measurements of this configuration were therefore necessary to be compared with results from full annular combustor testing with temperature paints spread on the combustor liner.

Also, the accurate determination of their cooling effectiveness was required in order to have a true reference for comparison to the cooling performance of latter designs.

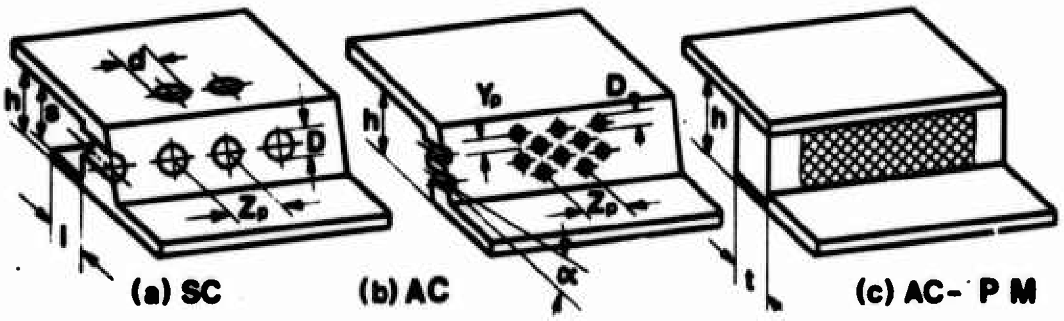

(a) SC (b) AC (c) AC- P M

Fig. 3 Basic design of film cooling configurations

The design criteria of the advanced film cooling configurations Fig. 3 (b) stemmed basically from two considerations. First, the improvement of the cooling performance by replacing the discrete cooling jet holes by an array of holes thus forming a more uniform air cooling layer requiring a lesser amount of cooling air and secondly, to avoid any complicated design parts, like the film cooling lip, to make the configuration more adjustable to cost saving combustor chamber machining.

Taking into account the latest developments of metallic glue techniques, the test section with the porous plate Fig. 3 (c) was fabricated. The application of test sections with porous plates represents the logical interface to effusion wall cooling.

Test configurations

No.	Abbreviation	Test Configuration
1	SC	Standard Film Cooling Configuration with Static holes.
2	SCT	Standard Film Cooling Configuration without Static holes.
3	AC-1	Advanced Film Cooling Configuration.
4	AC-2	Advanced Film Cooling Configuration.
5	AC-PM	Porous Material Cooling Configuration.

Characteristic Dimensions

No.	Abbreviation	s (mm)	h (mm)	l (mm)	D (mm)	d (mm)	Z_p (mm)	$\frac{A_o}{A_h}$
1	SC	4	4,5	4	2	1,6	4	0,279
2	SCT	4	4,5	4	2	-	4	0,172
3	AC-1, $\alpha=10^\circ$	-	4	-	0,7	-	1,2	0,321
4	AC-2, $\alpha=15^\circ$	-	4	-	0,7	-	1,2	0,321
5	AC-PM	-	4	-	-	-	-	-

TABLE 1 Summary of Test Sections

Instrumentation

In order to keep the film cooling region undisturbed the test section was instrumented with chromel-alumel thermo-couples at the test surface facing the insulation. It was checked though, with a special instrumented test section, that thermo-couples placed at the inner surface facing the mainstream gave the same reading as the ones at the outer surface. The accuracy of the measurements was ± 1,5 degrees.

Wall temperatures were measured along the center line of the test zone which is defined as $z = 0$ in a region between $x/s = 0{,}5$ and $17{,}5$. For modern aircraft engine combustion chambers x/s reaches maximum values of 20. Inspite of three dimensional flow effects, special tests had shown that for constant x/s, at normalized distances $x/s > 10$ the wall temperature readings of all cooling configurations where very much the same in a region of $z \pm 14$ mm. This result can be attributed to the small thermal resistance of the thin wall.

For boundary layer measurements small pressure and temperature probes were used. The error of the boundary layer temperature measurements was ± 1,5 degree, the recovery factor being negligible small. The error of the pressure reading was $\pm 10^{-4}$ bar, the probe being insensitive to the flow direction in between an angle of 5 degrees.

For flow visualisation the Schlieren method with a parallel monochromatic light beam through the test zone was used. Schlieren photographs were made to get an integral impression of the flow pattern.

Results and Discussion

The test sections listed in Table 1 were evaluated at main gas stream conditions characterized by $Ma_G = 0.086$, $T_G = 875$ K, $v_G = 50$ m/s and the cooling air to mainstream temperature ratio of $T_C/T_G = 0.4$. The usual test procedure was to determine for each test section the flow field by measuring wall static pressures and the total pressure distribution of the cooling layer and then to proceed with heat transfer measurements consisting of wall and total temperature distribution measurements across the cooling layer.

In order to have immediate indication of the applicability of advanced cooling configuration the measurements were first performed on standard cooling configurations and then compared to the same measurements on advanced cooling systems.

Flow and Heat Transfer Measurements on Standard Cooling Configurations.

Fig. 4 shows a three dimensional representation of the pressure distribution in a plane just behind the film cooling lip $x/s = 0$ and a plane further down-stream $x/s = 17{,}5$. The total pressure measurements reveal the typical flow pattern that consists of cooling air jets which issue from discrete holes and merge to form a coherent cooling layer. From the total pressure measurements two different regions of flow can be discerned. Close to the cooling air entry the jet character of the flow predominates with strong pressure gradients normal to the flow becoming further downstream, because of the equalizing action of the intensive turbulent mixing phenomena, more of the wake flow type.

The strong total pressure decay in Fig. 4 is caused by the cooling air jet entering the boundary layer from the static hole in normal direction to the main stream. Thus, the static holes, which were

arranged in order to increase the total cooling air mass flow and to give a uniform film layer cause the formation of wakes adherent to the test surface thereby diminishing the overall cooling effectiveness.

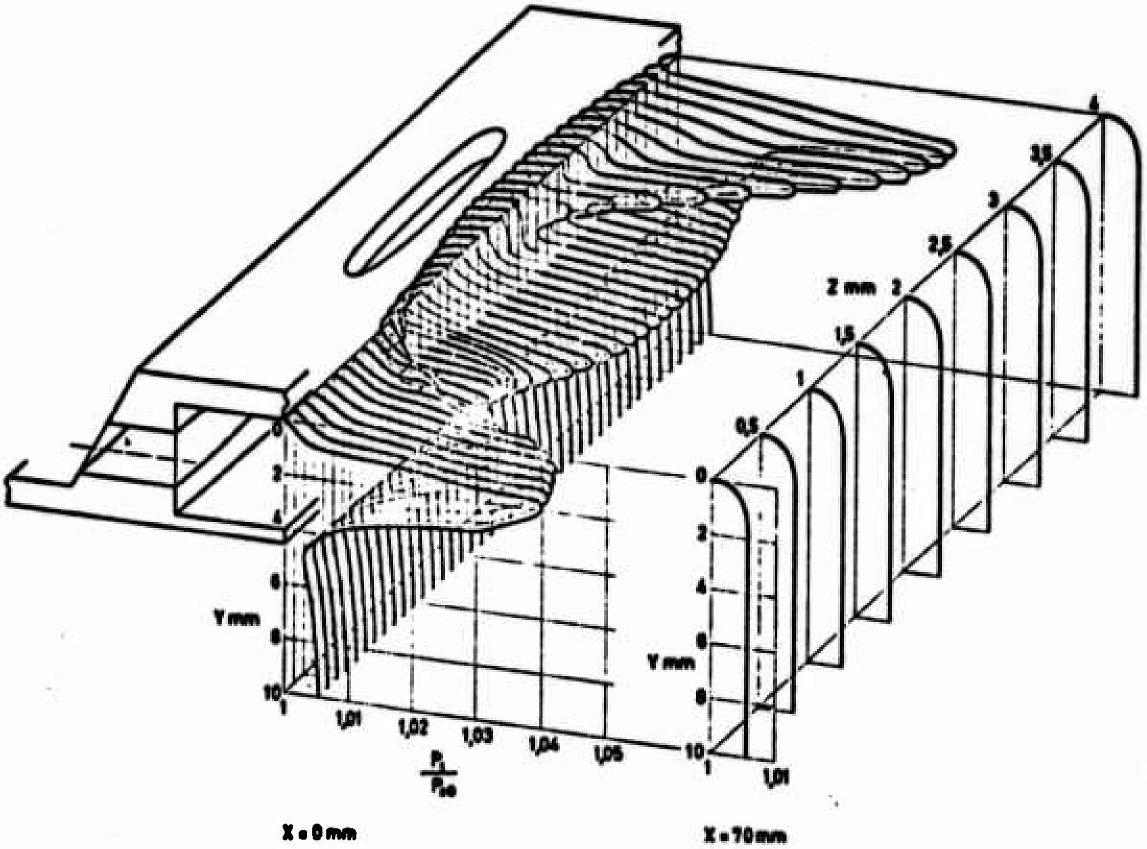

Fig. 4 Total pressure distribution for SC, m = 1,53

The test section wall in front of the cooling air entry was not insulated. Due to the high main stream gas temperature and the heat conduction through the wall from the upstream as well as downstream direction across the cooling step, heat transfer occurred between the wall and the cooling air. This heat transfer led to non-uniform temperature profiles inside the slot region. In order to enable a reasonable comparison of test results the measured wall temperature at x/s = 0,5 immediately downstream of the injection port was defined as the cooling air entry temperature.

Accounting for the main stream temperature gradient close to the wall, shown in Fig. 2 (b), data reduction was made considering the temperature of the uncooled wall as reference temperature instead of the main stream gas temperature T_G. The film cooling effectiveness was defined therefore as:

$$\eta = \frac{T_{Wu} - T_W}{T_{Wu} - T_C} \qquad (1)$$

Computations showed, that the amount of heat transferred by radiation was negligible small and that heat transferred by convection had a low and relatively constant value. Also, it followed from supplemental tests that the heat loss through the insulated wall was minor and could be neglected.

The measurements of temperature profiles across the cooling layer at different distances from the cooling slot, along the centerline of the test zone (z = 0) i.e. downstream of a tangential hole are represented in Fig. 5. In it the local temperature difference

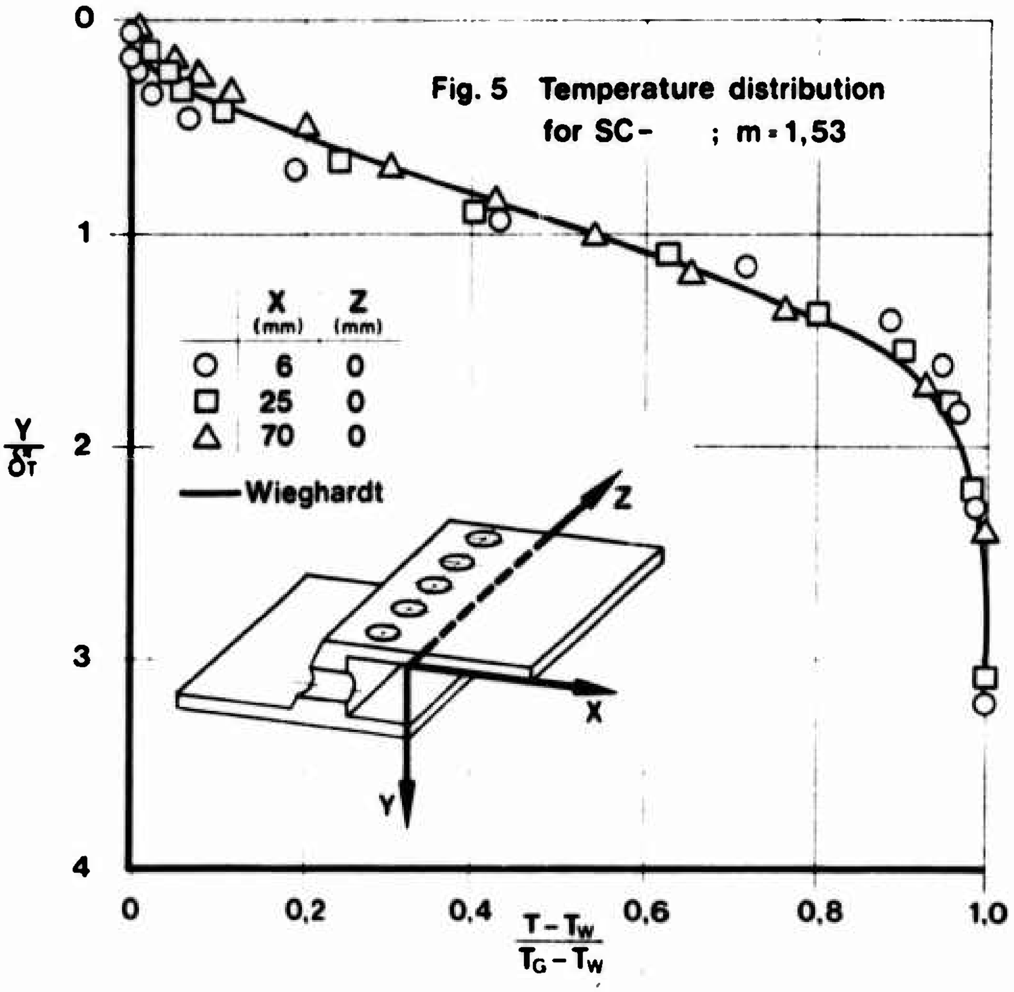

Fig. 5 Temperature distribution for SC- ; m = 1,53

(T-Tw) normalized by the difference between main gas and wall temperature is plotted as a function of the cooling layer depth y reduced by the equivalent temperature boundary layer thickness δ_T^*. The local measurements at three distances x from the slot are separately represented on the plot.

It follows from Fig. 5 that the normalized temperature profiles are very similar except for the ones just behind the cooling air entry region. The full line in Fig. 5 represents the functional relationship deduced by Wieghardt $^{(3)}$.

$$\frac{T - T_w}{T_G - T_w} = 1-\exp\left[-0.768\left(\frac{y}{\delta_T^*}\right)^{\frac{3}{2}}\right] \qquad (2)$$

This relationship is very similar to the one which holds for free jet flows. The good agreement of the function with the test results suggests that for all cooling configurations a similar empirical relationship for the temperature distribution can be deduced.

The cooling efficiency η measured for the standard configuration is represented in Fig. 6 as a function of the blowing rate m. The curve parameter is the distance from the slot x normalized by the slot height s. The local measurements are represented by the symbols given in the legend and the full line represents the best fit curve.

It can be seen that in the potential core region at $0 > x/s > 3$ the cooling effectiveness is only slightly affected by the blowing rate. In the region of wake flow at distances $x/s > 3$ the turbulent mixing of the cool boundary layer with the hot main stream is the heat transfer controlling parameter. The cooling efficiency becomes a function of the velocity ratio v_c/v_G and hence of the blowing rate. At large velocity differences between the cool boundary layer and the main stream, that is at low blowing rates respectively low cooling air mass flows, the turbulent mixing becomes intensive and the cooling effectiveness decreases because the cooling layer is fast absorbed. At high blowing rates $m > 1.2$ the cooling effectiveness tend to a constant value. Blowing rates relevant for practical combustor liner cooling span between $1.0 < m < 1.45$.

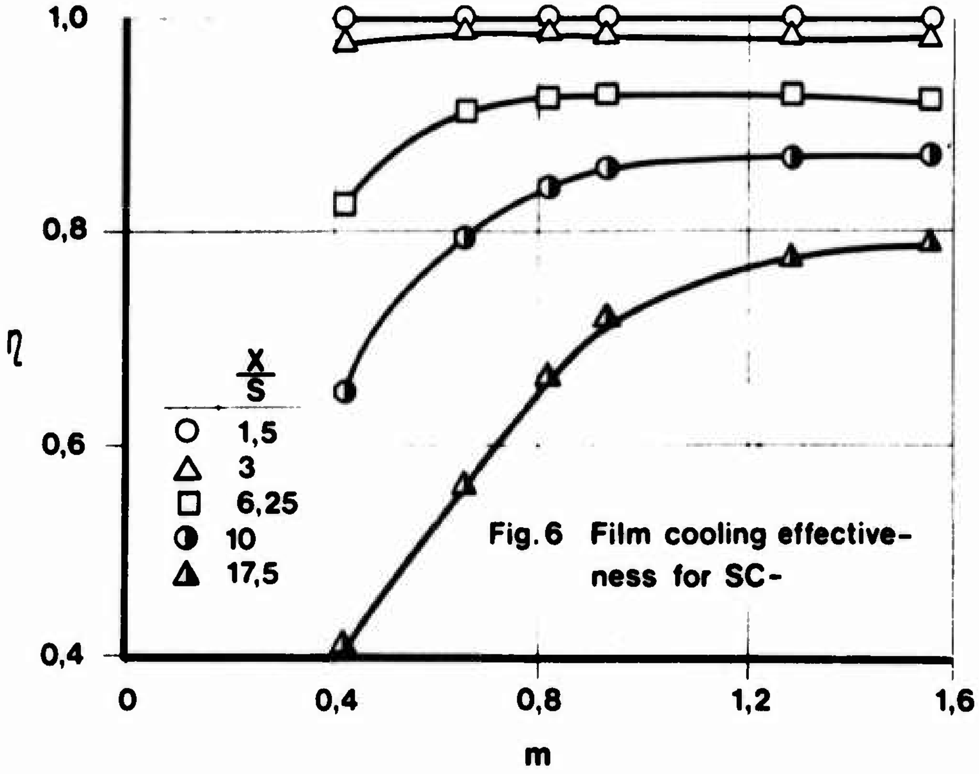

Fig. 6 Film cooling effectiveness for SC-

Flow and Heat Transfer Measurements on Advanced Cooling Configurations.

In analogy to the described test procedure the flow field of the advanced film cooling configurations was determined by measurements of all static and total pressure distributions. Due to the increased number of cooling holes of the advanced versions the number of air jets immediately downstream of the cooling step increased. In contrast to standard configurations this air jets showed only small differences between the highest and lowest pressure level and they integrated fast in a homogeneous film. Similarly it was found for the cooling configuration with porous material that the formation of a continuous film takes place almost at once. At a distance of $x/s = 1.5$ practically no pressure difference could be determined in z direction.

Fig. 7 shows the temperature distribution along the midplane ($z = 0$) of the film for the advanced configurations in comparison to the standard film cooling versions. The measurements represented were made at a normalized distance of $x/s = 6.25$. Inspite of the geometrical differences between the investigated configurations (see Table 1) a strong similarity of the temperature profiles can be observed from Fig. 7. This observation confirms the same statement made with respect to the temperature distribution measured at different locations downstream of the injection holes and plotted in Fig. 5. It must be noted, however, that the representation chosen for Fig. 7 is comparatively insensitive to small changes of temperature distribution and does not fully account for differences of film layer thickness for the various configurations.

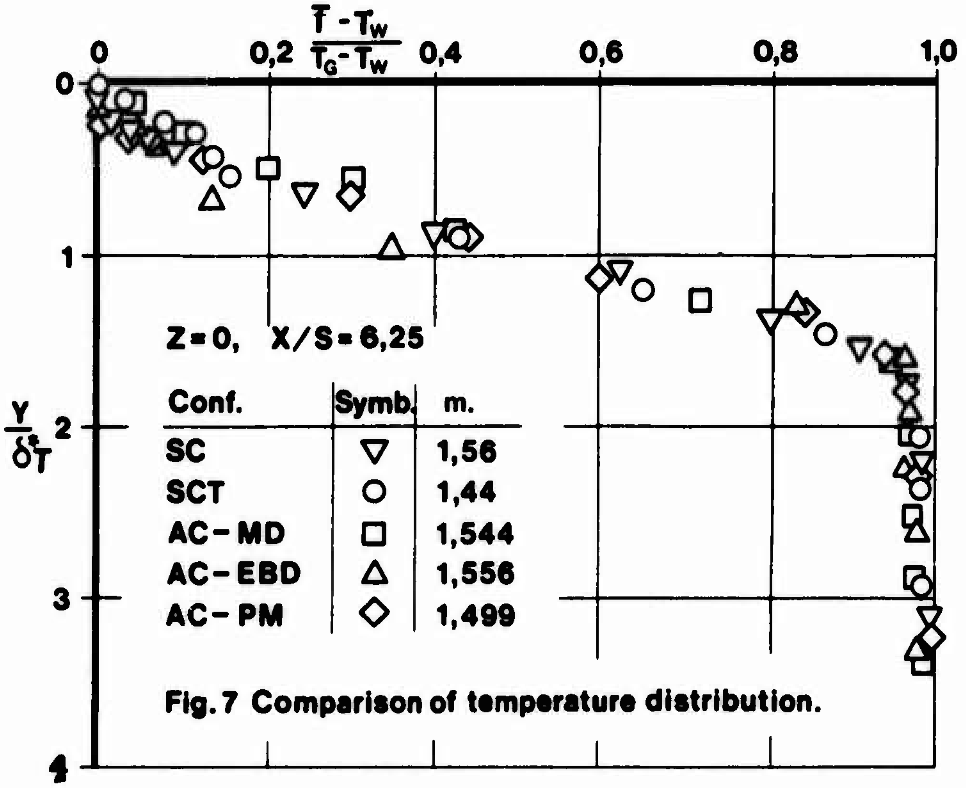

Fig.7 Comparison of temperature distribution.

The film cooling effectiveness of the SCT configuration related to the effectiveness of the standard configuration η/η_{SC} is plotted in Fig. 8 as a function of the blowing rate m. The normalized distance x/s is the curve parameter. It follows from Fig. 8 that for $x/s < 17.5$ the cooling effectiveness of the SCT test configuration is lower than that of the standard configuration.

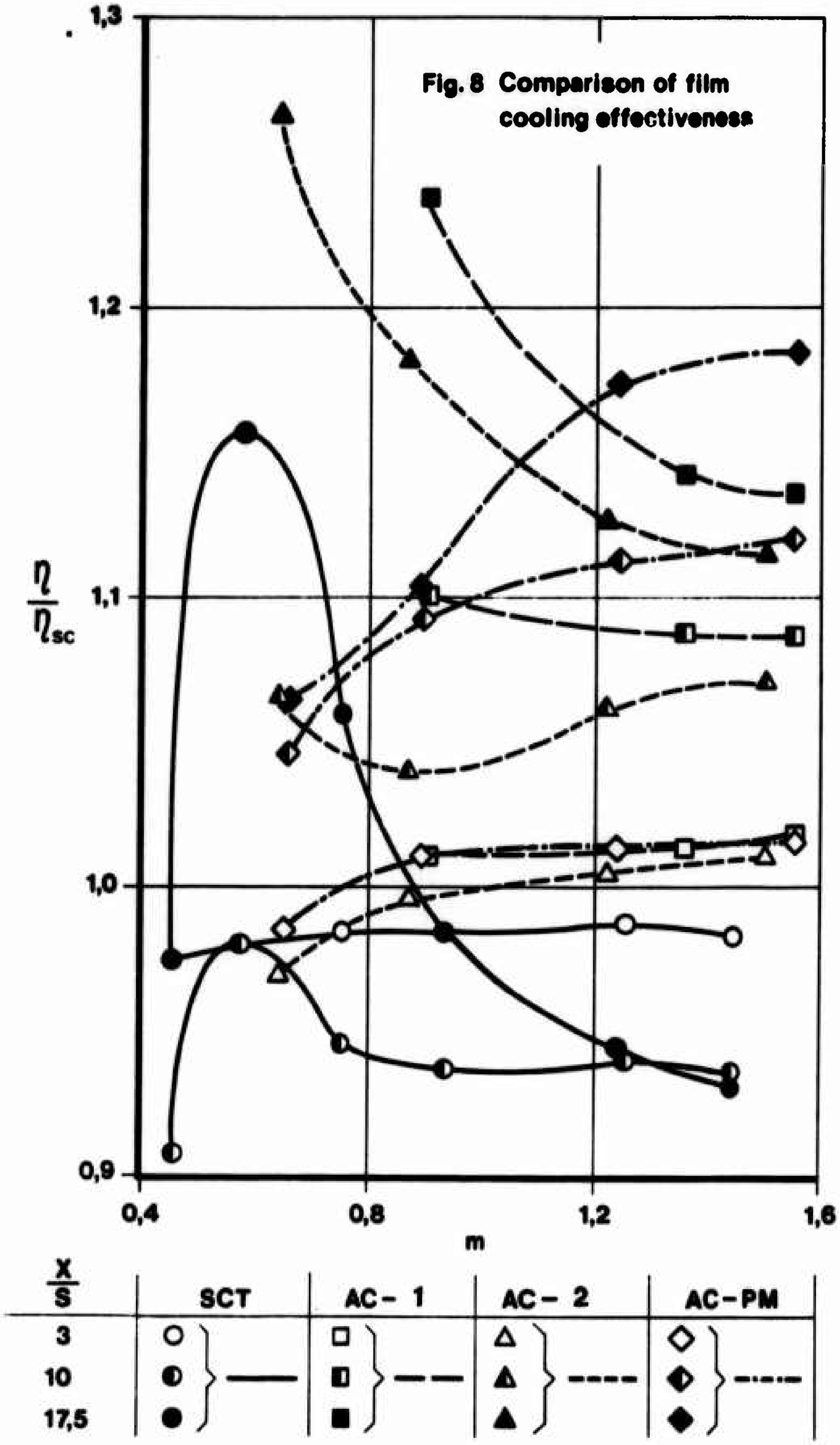

Fig. 8 Comparison of film cooling effectiveness

This observation differs from results reported by Nina and Whitelaw (7) and is attributed mainly to the increased jet action of the SCT cooling film. In order to inject the same amount of cooling air in to the film, the velocity of the penetrating jets increases because of the reduced cooling hole area (the static holes are blanked off). The hot mainstream air penetrates in between the discrete jets to the wall, reducing considerably the cooling effectiveness.

At larger downstream distances $x/s = 17.5$ and low blowing rates $0.47 \leqslant m \leqslant 0.89$ where the jets integrate to a continuous cooling layer the values of η are higher than those of η_{SC}. The peak and the steep decrease of cooling effectiveness shown for the SCT configuration at $x/s = 10$ and $x/s = 17.5$ in Fig. 8 clearly demonstrates the described effect of jet action. An improvement of the cooling effectiveness of the SCT configuration can be obtained therefore, by reducing the cooling jet velocity v_d, that is, by enlarging the hole area, or, by stretching the film cooling lip further downstream in order to stop hot mainstream air penetration to the wall.

The results of heat transfer measurements for the AC - cooling configurations are also represented in Fig. 8.

The figure shows for the AC - 1 and AC - 2 test sections a good qualitative correlation of the cooling effectiveness. Quantitatively there exists however a difference of the effectiveness because their design of cooling hole arrangement was different. The axis of the holes for the AC - 1 version was inclined at an angle of 10° and that of the AC - 2 configuration at an angle of 15° to the mainstream direction. It can be seen from Fig. 8 that an increase of the injection angle causes a reduction of the cooling effectiveness an effect reported also by Sivasegaram and Whitelaw (2).

The highest cooling effectiveness was measured for the test configuration using porous material for cooling air injection. Although the homogenity of the porous material was not fully satisfactory it still gave the most uniform cooling air distribution. Figure 8 shows that the cooling effectiveness continuously increases with the blowing rate and that in the region $3 < x/s < 17.5$ the highest efficiency of all configurations was obtained. For $x/s = 17.5$ the values of the cooling effectiveness are only at $m > 1.2$ higher than those measured for the AC-1 test section.

Correlation of Data

In order to supply practical design criterias for gasturbine combustion chambers, an attempt was made to correlate the cooling effectiveness of the investigated configurations with the aid of an empirical equation taking into account the importance of the blowing parameter m. For blowing rates encountered in combustor liner wall cooling the cooling effectiveness can be described with an equation of polynomial form:

$$\eta = Co + C_1 X + C_2 X^2 + C_3 X^3 \qquad (3)$$

with $X = x/s \cdot m^{-0.25}$ and C_i being empirical coefficients. It should be noted that the velocity of the cooling air which plays a dominant role is related to the slot height s for configurations with a cooling lip and to the step height h, for advanced configurations. The coefficients of equation 3 are listed in Table 2 for the various cooling configurations investigated.

Region of validity $1{,}5 < X < 18$

Configuration	SC	SCT	AC-1	AC-2	AC-PM
Co	1.029	1.065	1.0045	1.019	0.997
C1	-1.77×10^{-2}	-3.4×10^{-2}	-3.74×10^{-3}	-1.23×10^{-2}	8.9×10^{-4}
C2	5.73×10^{-5}	7.91×10^{-4}	-4.56×10^{-4}	1.43×10^{-4}	-4.67×10^{-4}
C3	2.5×10^{-6}	-2.5×10^{-6}	1.4×10^{-5}	1.36×10^{-7}	7.69×10^{-6}

Table 2. Values of the empirical coefficients Ci

In Fig. 9 the cooling efficiency is represented as a function of the variable X. Measured values of cooling efficiencies are denoted by points and the full curves represent the relationships given by equation 3 in connection with the values of Table 2. Figure 9 shows that the measured values are well described by equation 3.

The deviation does not exceed 3.8%. For values of X smaller than 2.5, the cooling effectiveness can be set with sufficient accuracy equal to one.

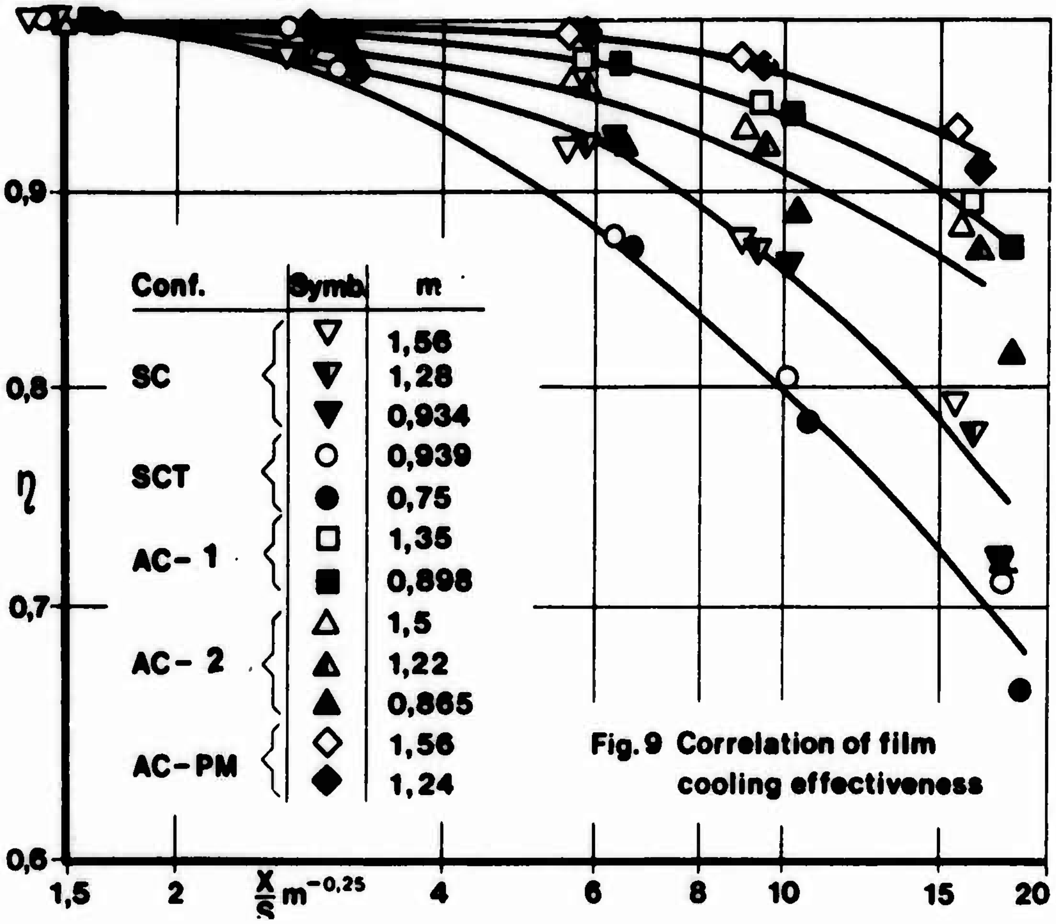

Fig. 9 Correlation of film cooling effectiveness

Conclusions

The detailed measurements described in this paper showed that cooling air injection through an array of holes, instead of a single row of holes, greatly improved the cooling efficiency normally encountered for gas turbine combustor liners.

Advanced film cooling configurations omitting film cooling lips with an array of holes oriented in nearly mainstream direction gave cooling efficiencies close to those of porous materials surpassing efficiencies of standard cooling arrangements.

The highest cooling effectiveness was obtained using porous materials for cooling air penetration. Cooling configurations employing such materials must be designed to take off stresses from the fibre material and to greatly prevent clogging.

The correlation of test data for air cooling rates common in combustion chambers with the aid of the blowing rate as main parameter gave good agreement between measured and analytical values.

For further improvement and better optimization of combustor liner cooling systems more experimental heat transfer investigations are needed. This investigations being performed at aerodynamic and thermodynamic conditions similar to that in actual combustion chambers can give results of immediate practical application.

Acknowledgement

The authors want to express their thanks to Mr. G. Kirschey and Mr. B. Kurpjuhn for their help in carrying out the experiments.

References

1 STOLLERY, J.L., and EL-EHWANY, A.A.M., "A Note on the Use of a Boundary-Layer Model for Correlating Film-Cooling Data", International Journal of Heat and Mass Transfer, Vol. 8, 1965, pp. 55-65.

2 SIVASEGARAM, S., and WHITELAW, J.H., "Film Cooling Slots: The Importance of Lip Thickness and Injection Angle", Journal of Mechanical Engineering Science, Vol. 11, 1969, pp. 22 - 27.

3 WIEGHARDT, K., "Über das Ausblasen von Warmluft für Enteiser", Deutsche Luftfahrtforschung, Forschungsbericht No. 1900, 1943.

4. GOLDSTEIN, R.J., "Film Cooling", Advances in Heat Transfer, Vol. 7, Academic Press, New York and London, 1971, pp. 321-379.

5. ECKERT, E.R.G., "Film Cooling with Injection Through Holes", High Temperature Turbines, AGARD-CP-73-71, 1971, pp.17-1-17-17.

6. ERIKSEN, V.L., "Film Cooling Effectiveness and Heat Transfer with Injection Through Holes", National Aeronautics and Space Administration CR-72991, HTL TR No. 102, 1971.

7. NINA, M.N.R., and WHITELAW, J.H. "The Effectiveness of Film Cooling with Three-Dimensional Slot Geometrics", ASME, Paper No. 71-GT-11.

8. PATANKAR, S.V., RASTOGI, A.K., and WHITELAW, J.H., "The Effectiveness of Three-Dimensional Film Cooling Slots. I. Measurement, II. Predictions". International Journal of Heat and Mass Transfer, Vol. 16, pp. 1665-1681, 1973.

9. KACKER, S.C., and WHITELAW, J.H., "The Turbulence Characteristics of Two-Dimensional Wall-Jet and Wall-Wake Flows", ASME, Paper No. 70-WA/APM-35, 1971.

10. KLEBANOFF, P.S., and DIEHL, Z.W., "Some Features of Artificially Thickened Fully Developed Turbulent Layers with Zero Pressure Gradient", NACA, Report 1110, 1952.

THE DESIGN AND DEVELOPMENT OF AN ADVANCED ANNULAR COMBUSTOR FOR CIVIL APPLICATION.

A B Wassell and J E Bradley.

Derby Engine Division, Rolls-Royce (1971) Ltd.

Summary

One of the requirements of the RB.211 programme from its inception was to produce a short overall engine length. This was, in turn, reflected in all the components including the combustor and led to ambitious performance targets being set in relation to the length made available for the combustion process.

In order to meet these targets several novel features were built into the combustor during its design and initial development phase, especially in the areas of the fuel injection system and liner cooling techniques. The development of new measuring techniques to assess achieved performance constituted a significant part of the total programme. Nevertheless the effort expended in the solution of these problems has enabled a much greater understanding of the whole combustion process to be achieved. A review of these new features and techniques is given and their effectiveness discussed.

A fixed geometry combustor is of necessity designed as a compromise between the conflicting requirements of traverse pattern factor, altitude ignition capability and minimal environmental pollution from exhaust products. This paper discusses some of the compromises that have been adopted for the RB.211 engine and describes the combustion development testing that has been carried out in support of the programme.

Introduction

The advantages that would accrue from the adoption of an annular combustion system in terms of short length and minimum surface area for a given combustor volume were appreciated at a very early stage in the development of the gas turbine engine. These attributes made the annular system ideally suited for use in expendible missile and lift engine applications. In fact Rolls-Royce entered this field in the early 1950's with the production of the RB.82 and RB.93.

This led to the successful development of a line of small annular combustors which powered Europe's first VTOL aircraft like the Short SC1 and the Marcel Dassault Balzac V. In the early 1960's this technology was being applied to military fighter aircraft, but these early proposals were only evaluated on the combustor rigs as the parent engines failed to come to fruition. The data produced, however, was used to formulate the combustor which was subsequently chosen for the joint Rolls-Royce Turbomeca Adour engine (currently powering the SEPCAT Jaguar and the HS Hawk).

All these combustors, however, were for use in low pressure ratio engines of relatively small size (none being greater than 0.7 meters in diameter). The advent of the large high bypass ratio engine required much larger combustors to be developed capable of operating with long life at high pressure ratios (greater than 20 bars). The Company's traditional emphasis on short and compact combustors was reinforced by the need to conserve still further the flame tube cooling air, to reduce engine weight and to minimise the shaft whirling problems that were considered a possibility at the start of the design of three shaft engines.

Description of the RB.211 Combustor Design

(a) Early History

A demonstrator project, the RB.178, was launched in 1966, and the rig testing, in addition to a limited amount of engine testing during 1968 highlighted several problems - notably severe local overheating of the combustor liners - which had not been encountered on the earlier low pressure ratio designs. Two civil projects were launched shortly after the RB.178 incorporating annular combustors based on the experience that had been gathered - the Trent being a 2.5 bypass ratio version of the Adour and the RB.211-06 being derived from the RB.178. In fact the first Trent engine ran in 1968, a few months earlier than the RB.211-06, but was eventually shelved through the lack of a suitable application.

(b) Design Philosophy

The combustor design of necessity lent very heavily on the previous annular experience. Since this was not strictly relevant to the RB.211 operating conditions significant extrapolations of available data had to be made especially in the area of wall cooling. Indeed it required four complete redesigns of the cooling configuration before a satisfactory basis for the future development was achieved.

On the other hand empirical correlations that had been derived for sizing the burning volume of combustor proved exceedingly accurate. Unfortunately the significance of the non-burning portion of the combustor system had not been fully appreciated and it is probably true to say that some of the pattern factor problems described later can be attributed to the shortness of the diffuser section.

Some of these aspects are now discussed in more detail.

(c) Sizing the Combustor

The burning volume was dictated by the need to achieve adequate power output at all conditions of high combustor loading to enable the engine to accelerate from start up or windmilling. The depth of the flame tube was chosen to give a primary zone volume capable of meeting the required altitude relighting requirements and the burning length to be similar to previous annular chamber experience. The emphasis placed on minimum combustor length was not only applied to the burning length, but also to the intake section and this led to a highly loaded diffuser being accepted. Engine length was further minimised by using the combustor entry section as the location of the source of high pressure air for the cabin air bleed off takes - this being achieved by struts which transfer air from the combustor inner annulus to a manifold external to the combustor.

The prime targets for the first RB.211 combustor were to produce an adequate pattern factor (set initially at 40%), at the most a light grey smoke plume from the exhaust, a relight capability up to 9.75 km (32000 ft) and a life of 3000+ hours in service. These targets were set for the RB.211-06 engine which was initially designed for 148 kN (33260 lb) take off thrust and have continued unchanged (except that an invisible smoke requirement has been substituted) up to the 214 kN (48000 lb) RB.211-524 engine - see figure 1.

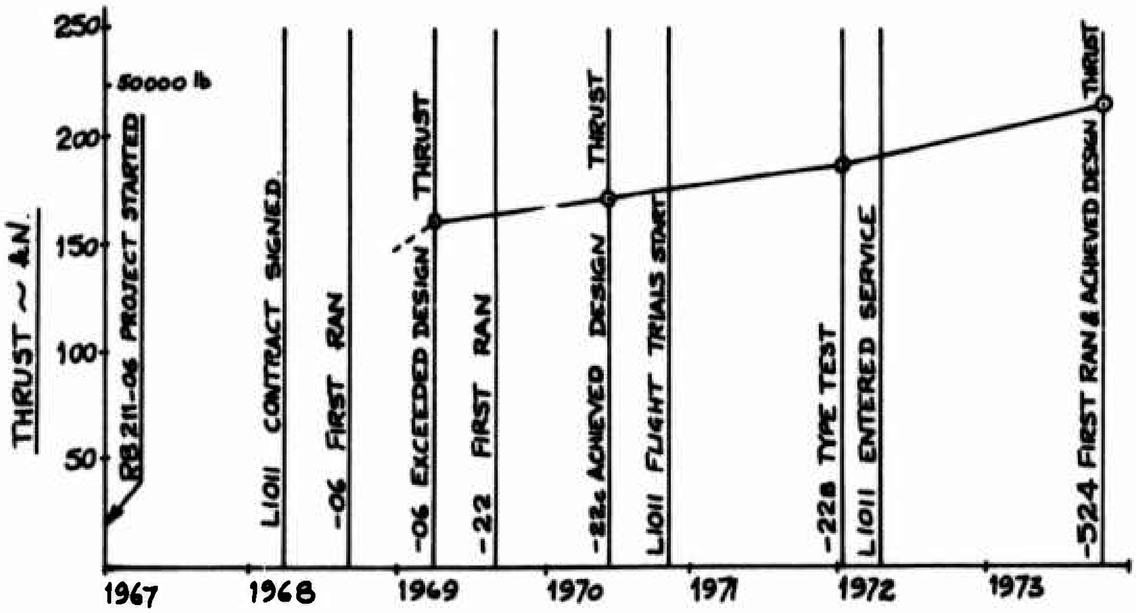

Figure 1 RB.211 Milestones - Thrust Growth.

Throughout this period of engine thrust growth, the combustor remained basically the same, being changed only in the detail of its mechanical configuration (i.e. refinement to the wall cooling processes, alteration to the flow proportions and hole sizes). The combustor length remained unaltered both in its non-burning (or entry diffuser) and burning zones. The short entry diffuser benefitted from a considerable amount of experimental testing performed on aerodynamic models of the RB.178(1). This work continued through the life of the RB.211-06 and further modifications to the strut and fuel injector fuel feed arms were incorporated into the RB.211-22 combustor to minimise the losses due to obstructions present in the outer diffuser.

The extent to which this design departed from previous practice in this respect can be seen from figure 2. This shows the relative lengths of some current engines. The length parameter is corrected for differences in the engine layout to enable a true comparison to be made. The assumptions made are that the combustor length/depth ratio and overall residence time will remain fixed in this scaling process; thus it can be simply shown that

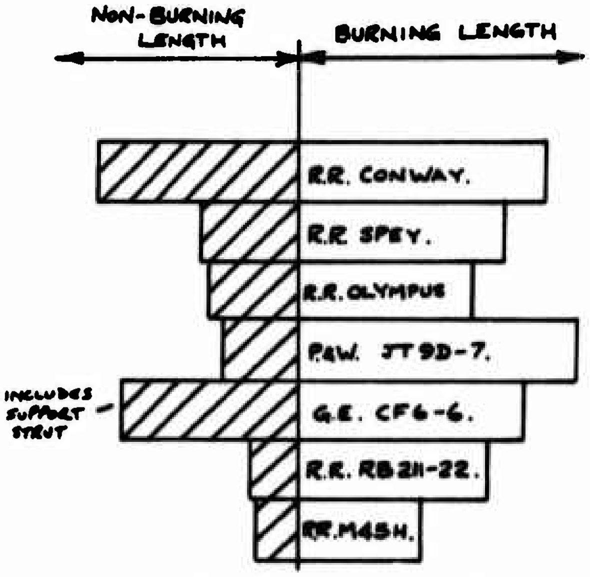

Figure 2 Relative lengths.

$$L_{corrected} = L \cdot \sqrt{\frac{A}{A_{datum}}} \cdot \sqrt{\frac{R_{datum}}{R}}$$

where L = Combustor length.
A = HP vane throat area.
R = Combustor mean radius.

(d) Wall Cooling

Despite the fact that engine pressure ratios (and hence combustor inlet temperatures) and combustor outlet temperatures have been increasing to achieve higher levels of engine performance, the combustor liner temperatures have had to remain constant to maintain the component life. The development of new materials suitable for liner fabrication would ease this problem, but over the last twenty years the materials have not kept pace with the demands of technology.

Thus the designer is forced to improve his knowledge of the heat transfer processes and the methods of cooling that can be applied to combustor liners. Basically film cooling has been adopted as the most efficient internal cooling mechanism with external convective cooling being used in addition on a number of designs. Initially very simple and unsophisticated devices were used to produce a not too circumferentially uniform cooling film. As the task became more demanding technically, the sophistication increased with devices progressing from fabrications to fully machined parts so that the percentage of air used for wall cooling purposes actually dropped despite the general increase in operating temperatures. This is eloquently illustrated by figure 3. The material limitations are shown as the average temperature below which the liner should be kept if a long service life is to be achieved.

This trend must be continued if the designer is to have any chance of scheduling the airflow distribution within the combustor to minimise the production of pollutants, in addition to achieving the desired durability - especially since operating temperatures show no signs of being reduced!

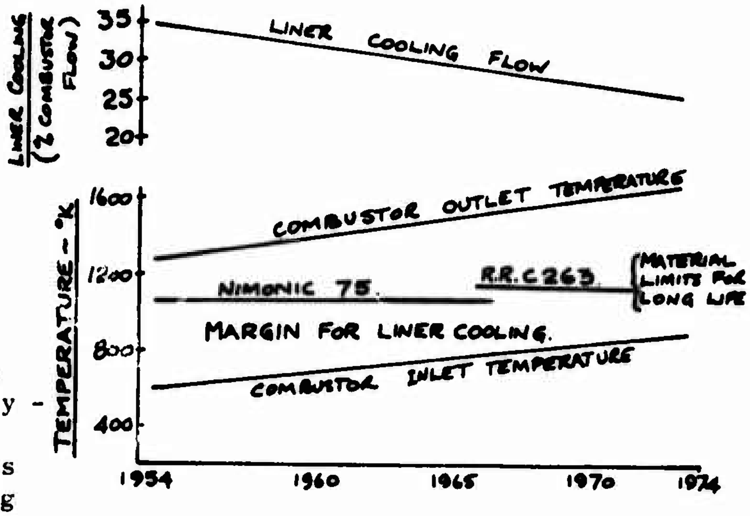

Figure 3 Progress in wall cooling techniques.

(e) Fuel Injector

Rolls-Royce pioneered the development of the air assisted atomiser in the hope that a system simpler and cheaper than the conventional pressure jet system could be produced. First experiments were performed on the RB.108 in the early 1950's, but development continued at a slow pace until this type of fuel injector was selected for the Adour. All previous service experience had been obtained using twin orifice pressure jet atomisers, (including the RB.178) but the Adour has performed successfully using only a single feed system.

A modified version of the air assisted atomiser was adopted for the RB.211. In order to ensure that the smokiness of the exhaust plume was kept to a minimum the incoming cone of fuel was surrounded on both sides by sheets of air. Initially the fuel injector design was of the twin orifice type in which the two concentric fuel tubes fed into one cavity before the fuel was admitted to the swirl chamber. It was soon found that the thickness of the twin feed system caused an unacceptable wake in the outer air sheet resulting in a poor fuel distribution. Since also the lighting performance of the injector did not seem to be improved by the presence of the pilot fuel system, the injector was redesigned on the single feed principle. The current production standard for the RB.211-22 is shown in figure 4.

In general the burner has performed very well. The atomisation achieveable depends strongly on the airflow through the burner: typical fuel droplet sizes at idle would be 100μm whereas, at take-off conditions, this falls to about 25μm. In the early days of the RB.211, fuel placement was somewhat variable comparing different injectors, but close attention to manufacturing procedures has virtually eliminated the problem.

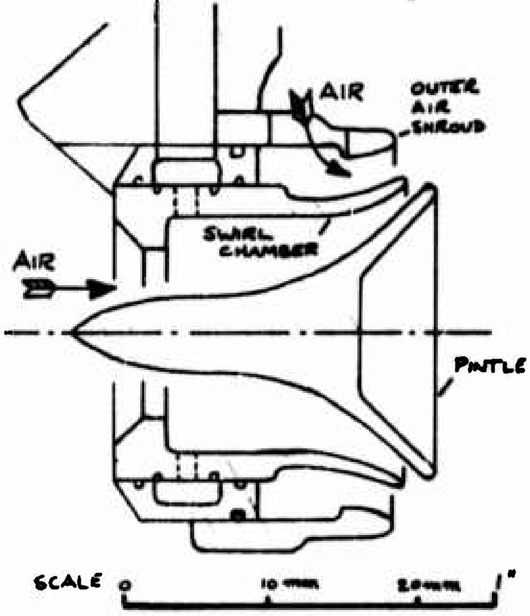

Figure 4 RB.211 Air Assisted Atomiser.

(f) Altitude Relight

As previously mentioned, the volume contained by the flame tube is determined not by the heat release required under the top power condition, but by the need to relight the combustor under windmilling conditions at altitude and to provide sufficient temperature rise to accelerate the engine from these conditions. The size of the primary (or recirculation) zone of the combustor (figure 6) in relati[illegible] the amount of air recirculating controls the relighting abili[illegible]nce this fixes the residence time of the air in the region where the flame can be stabilised. The quantity, distribution and atomisation quality of the fuel and the amount of ignition energy available are the other variables over which the designer exercises control.

At high forward speeds (greater than .6 Mn) the engine will require very little assistance from the combustor to accelerate from the windmilling condition and thus the lighting capability of the combustor will determine the relighting envelope of the engine. At lower speeds, the total volume of the combustor becomes important in determining whether sufficient temperature rise can be achieved to accelerate the engine at the very high combustion loadings that are encountered.

Which of these two volumes (primary or overall) is critical will depend on the layout of any particular design. It is essential, however, to be able to predict the performance of any new combustor at the design stage. This is done at Rolls-Royce by a semi-empirical method based on the prediction of windmilling characteristics for the engine together with correlation of experimental ignition data.

Once the combustor has been manufactured it is possible to evaluate its ignition performance both at sea level and at sub-atmospheric pressures to simulate the conditions encountered under windmilling conditions, The rig data leads to an approximate estimation of the engine relighting characteristics as can be seen from figure 5, but eventually it is necessary to confirm the contractual requirements by full engine tests. This can be done with the engine installed in a production aircraft or in a flying test bed as part of the normal certification procedures or the engine can be tested in an Altitude Test Facility. Figure 5 shows results obtained by both these methods and these indicate that the semi-empirical design method fortunately proved more reliable a guide to relighting performance than did the ignition tests on the rig!

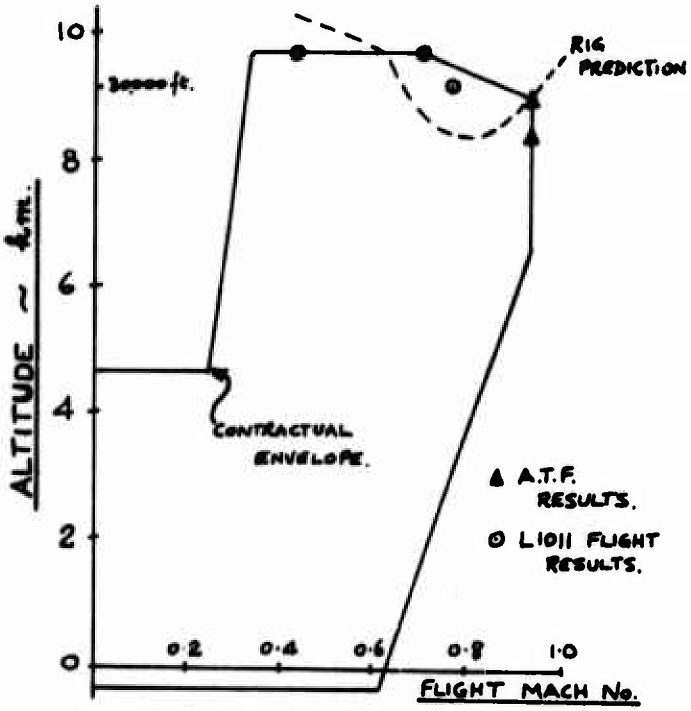

Figure 5 Relight Envelope for RB.211-22 engines.

Experimental Techniques

The preceeding section has discussed the important features designed into an aero-gas turbine combustion system which will determine the ultimate level of achieveable performance. It is certain, however, that because of the still largely unpredictable nature of the combustion process, the first sets of hardware produced from a new design will fall a long way short of the desired targets. The combustion engineer has, therefore, to test this initial hardware, to assess its performance and to carry out modifications based on this analysis repeating the process until the ultimate goals are achieved.

As has been stated already, the combustors for RB.178, and the RB.211 which followed it represented a step change in size and operating pressure in relation to the Company's previous annular combustor experience. This was of course especially true of the test facility equipment necessary to support the combustor development programme. For instance one important performance parameter is the degree of variability of the temperature distribution at exit from the combustor. In addition it is also desirable to determine the fuel air ratio variations both at exit from and at stations actually within the combustor itself. Exit pressure and mass flow variations also provide essential data.

(a) Traversing Equipment

To achieve these data, Rolls-Royce has designed and built its own external traversing equipment for the RB.211 programme based on the operating experience gained on similar, but smaller equipment used

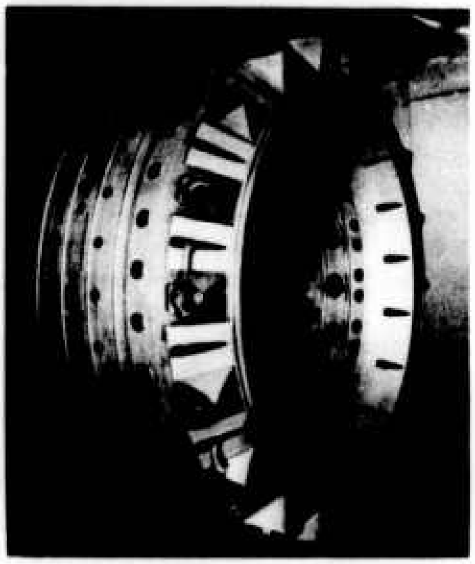

Figure 6 RB.221-22B Production Standard Combustor.

Figure 7 External Traverse Gear.

Figure 8 RB.211 Rig Combustor Unit Installed with Traverse Gear on Test Facility.

in the earlier programmes. The engineering problems can be imagined by reference to figures 7 and 8 which respectively show the traverse gear itself (which weighs c.14 tonnes) and then installed on the test facility behind the RB.211 combustor. This system permits 360°rotation: it is used either swinging through arcs of ± 60° (enabling averaged data to be obtained) or moved in 2.5° intervals (for point sampling). The traverse gear carries individual single point platinum-rhodium thermocouples (double shielded to prevent radiation errors and aspirated to maintain a constant airflow over the bead) and three multi-hole gas sampling probes (for efficiency and pollutant surveys). The exit distribution covering the complete annular chamber requires about 1200 individual readings which can be accomplished in approximately 3/4 hour. The temperature data so obtained from this traversing is used to calculate performance parameters which relate to the lives of the turbine blades and nozzle guide vanes. These are known as the radial and overall pattern factors and are defined in terms of the temperature difference between their respective peak temperatures and the mean temperature non-dimensionalised by the combustor temperature rise.

(b) Pattern Factor Determination

During the development of a combustion chamber, one of the major problems is to minimise the overall pattern factor and to match the radial pattern factor to that required by the turbine blade. The RB.211 programme was no exception in this respect!

All the Company's previous civil engine experience had been gained with tubo-annular combustion systems and it was very quickly found that the advantages expected from the switch to annular systems were going to be difficult to realise because of the greater problems of stabilising the flame in an annular environment. The first liners suffered from severe overheating, especially of the outer wall, despite the better cooling performance and consistency which the fully machined cooling rigs were known to give over the earlier wiggle-strips. Consequently the first priority was to produce a mechanically viable combustor to enable the development of the engine to proceed. This was achieved by overcooling the flame tube walls, but only at the expense of a disastrous deterioration in overall pattern factor.

This can be illustrated by considering part of the history of the traverse development carried out on the -22 combustor. This part relates to the era of low pressure testing (at 2 bars) which was adopted both to speed rig turn round times and as a result of the enormous pattern factors initially measured; for the data suggested that the test pressure level could directly influence the pattern factor level. The other major problem was logistic in that the peak temperatures encountered by the platinum-rhodium couples were high enough (c. 1700°C) to cause frequent failures. To ease this situation, it was decided to operate the combustor at a reduced temperature rise until the pattern factor could be improved substantially. This desperate story is charted on figure 9 from the end of 1969 (just after the first run of the RB.211-22 engine) to August 1970 (the definition date for the prototype combustor for L1011 flight trials).

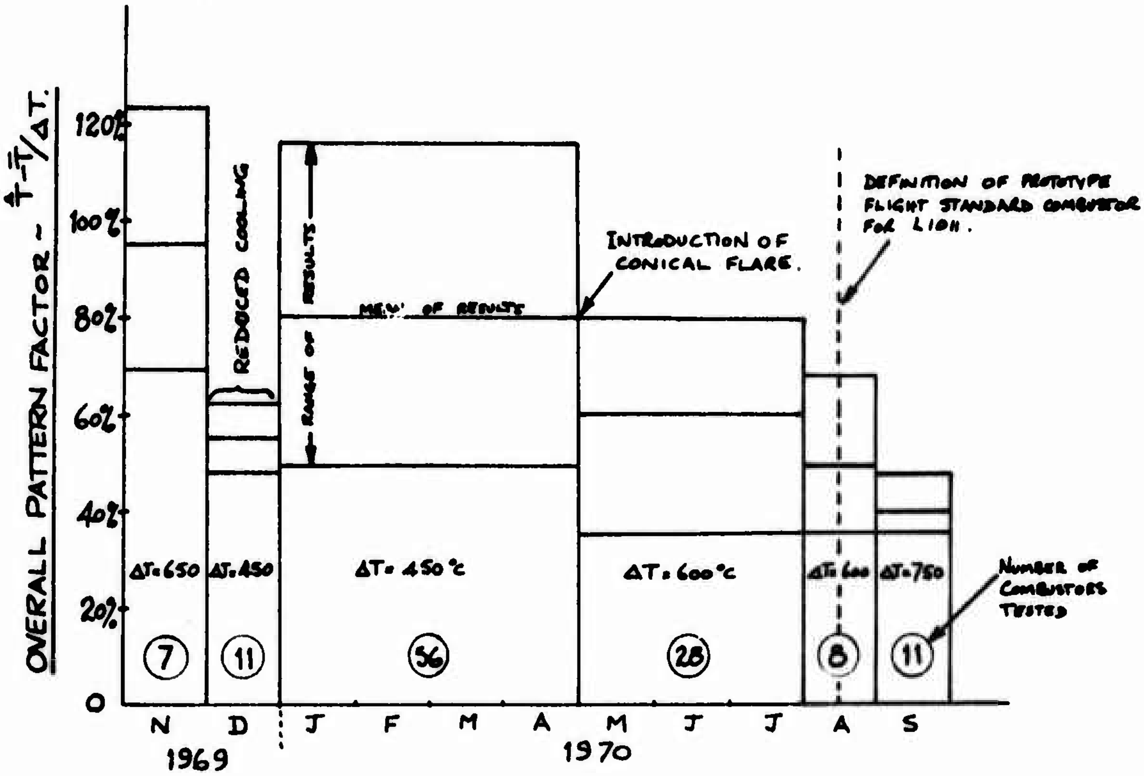

Figure 9 Early Traverse History of RB.211-22 Combustor at 2 bars.

The powerful effect of cooling air quantity on pattern factor is clearly shown in the early tests, but it took some considerable time to arrive at a compromise which would give both an adequate cooling capability and an acceptable traverse quality. The other major milestone in the programme was the introduction of a conical flare around the fuel injector which supplemented the air already surrounding the fuel cone from the injector itself (figure 4). This modification appeared to produce a much more consistent primary zone reversal pattern and the traverse quality responded immediately.

It should be noted, however, that the levels of pattern factors quoted are very dependent on the methods of measurement and the test procedures used. Considerable attention has been paid to this problem at Rolls-Royce and every effort has been made to establish the correct value of the maximum temperature. In particular the design of the thermocouple has been shown to be critical.

Following established practice, during the initial development of the RB.211 combustor the overall pattern factor was defined in terms of the peak temperature measured in each particular temperature survey. It became apparent, however, that this method sometimes gave rise to inconsistent results and occasionally to blatently incorrect conclusions as a result of random sampling errors associated with trying to record the peak temperature. Indeed on occasions it has been shown that temperatures in the vicinity of the peaks can fluctuate by as much as ± 100°C.

In order to overcome this situation, more representative ways of expressing the overall pattern factor were investigated. The outcome of this work was a statistical method to define the peak temperatures for the whole combustor based on data drawn from each sector (a sector being represented by the repeating geometry of the combustor centred on each fuel injector - each 20° for the RB.211). Dryburgh discusses the derivation and operation of this method in his paper(2) also prepared for this symposium. The method has proved itself indispensible in separating the effects of changes which would otherwise have been undetectable.

(c) Primary Zone Sampling

The sector to sector variations that are found to exist in the exit temperature patterns of annular combustors were thought to originate in the combustor's primary reversal zone. In order to investigate this, a system for sampling the fuel air ratio distribution at exit from this zone was devised. A twin headed steam cooled probe already installed in the external traverse gear was inserted through the combustor exit duct. By doing this it was possible to draw samples from this probe at the same time as the exit temperature distribution was being measured. It was soon discovered, however, that at high pressures the primary zone probe became blocked by carbon too quickly to allow a full survey to be completed. Rather than delay the combustor development programme while an effective probe for high pressure operation was produced, it was decided to restrict testing to a pressure of two bars.

The analysis of the sample was performed using a rapid on line system developed by the N.G.T.E.(3) at Pyestock. This enabled the distribution of fuel air ratios to be established for a 120° sector without adding significantly to the time taken to complete the exit temperature survey. A typical plot for the early RB.211-22C engines is shown on figure 10. This clearly shows a considerable variation from sector to sector. In addition the peak levels were high enough to be the probable cause of the visible smoke plume emitted from the engine under take-off conditions, but the worst sector distribution in the primary zone did not, surprisingly, correspond to the worst sector temperature distribution at outlet. Indeed it was subsequently found, using radioactive tracer techniques, that considerable circumferential fuel migration (± 30°) was possible between the point of injection and the combustor exit.

Nevertheless the monitoring of the fuel air distributions at the primary zone outlet has proved to be a very valuable aid in assessing combustor modifications, especially those associated with reducing top speed smoke. This process has led to the production of a smoke free combustor(4) for the RB.211-22B engines. The corresponding primary zone fuel/air ratio plot is shown on figure 11.

(d) Vaporous Emissions during Engine Starting Phase

During the early flight testing of the RB.211 in the Lockheed Tristar, it was found that a white vapour was emitted from the engine exhaust during the starting cycle when the ambient temperature dropped below approximately 20°C. This vapour consists of an aerosol formed by the condensation of fuel vapour which escapes from the combustor under conditions of the high combustor loadings associated with the starting regime.

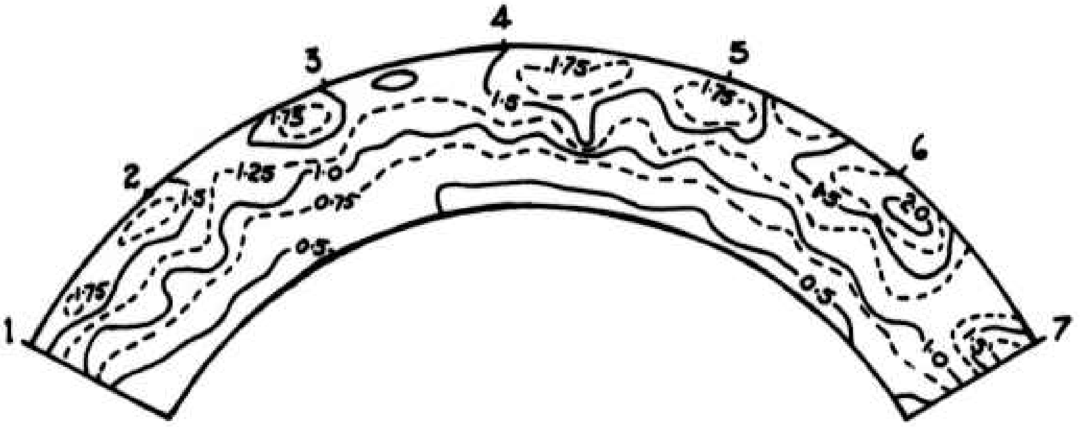

Figure 10 Distribution of Fuel/air Ratio at Exit from the Primary Zone for RB.211-22C (contours of local value/mean value).

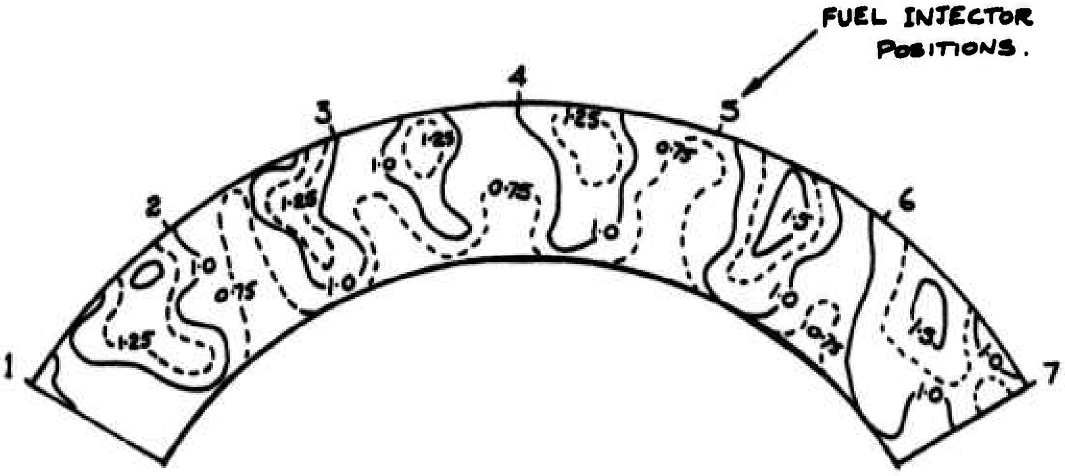

Figure 11 Distribution of Fuel/air Ratio at Exit from the Primary Zone for RB.211-22B. (contours of local value/mean value).

In order to investigate this problem use was made of the atmospheric test facility, since for the starting phase, the combustion chamber pressures are little different from ambient. By so doing, the vapour could be seen leaving the combustor, but it was found preferable to observe the phenomenon at exit from the exhaust stack. The effect of varying the operating fuel/air ratio of the combustor was evaluated under these conditions and it was found that the vapour could be made to disappear by increasing the fuel air above a critical value(5). Although this result was achieved by varying the overall combustor fuel/air ratio it was considered to be as a direct result of the changes being applied to the primary zone. The data is displayed in figure 12 for the initial design.

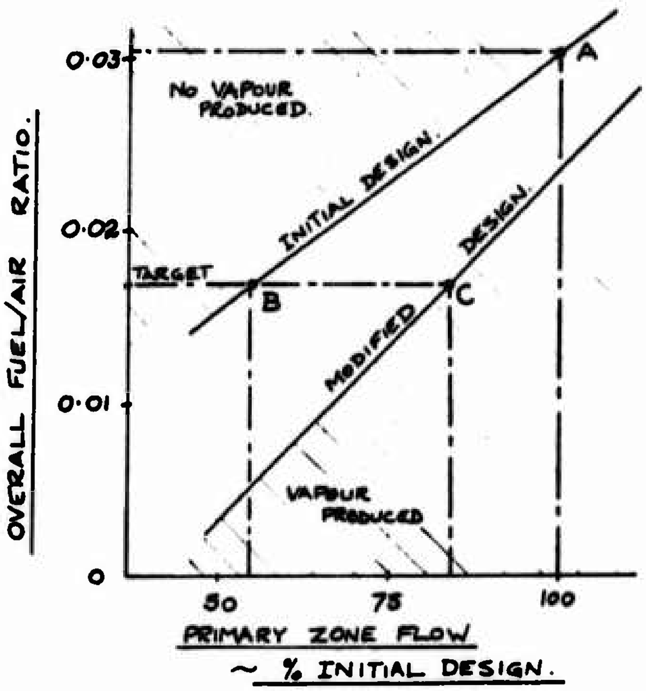

Figure 12 Vapour production during engine starting cycle.

This shows that the vapour problem could be solved if the primary zone airflow could be reduced from A to B. Unfortunately this degree of richening would be unacceptable for other reasons (i.e. the formation of top speed smoke) so that a modified primary zone had to be developed. The results of this programme are also shown on figure 12. It can be seen from this that the target fuel air ratio was successfully met with an acceptable change from the original primary zone airflow (C).

Conclusion

While the combustion designer attempts to produce a concept that will achieve all the known requirements it is unlikely to meet all these goals from the start. If, however, the design has been well executed the combustor will have the necessary potential which will have to be exploited during the development phase. The development will expose new problems which have not previously been encountered and their solutions must be incorporated into the next design concept.

The current in-service performance of the RB.211 combustor has demonstrated that most of the original design targets have been met lending credence to the design methods used. Both the overall and radial pattern factor targets has been substantially achieved; the relight performance has matched predictions; the exhaust smoke plume conforms to the U.S. Environmental Protection Agency's future requirements(6); and finally lives of up to 2000 hours were established within eighteen months from entry into service.

The experience gained developing the RB.211 combustor has shown that the design and development functions are inextricably related. This is especially true when external forces come into play like, for instance, the new pollution control legislation being introduced into the U.S.A. This legislation has already radically changed the established design and development practices and will continue to dominate design trends throughout the next decade.

Acknowledgement

The authors wish to thank the Directors of Rolls-Royce (1971) Ltd. for permission to publish this paper and to thank their colleagues for the assistance received during its preparation. The opinions expressed are those of the authors and do not necessarily represent those of the Company.

References

1. HURD, P.J. Internal Rolls-Royce (1971) Ltd. Report : CRM 27011 March 1967.

2. DRYBURGH, D.C. A Statistical Method for the Analysis of Rig Traverse Measurements on Annular Combustion Chambers. The Royal Aeronautical Society 2nd International Symposium on Air Breathing Engines. March 1974.

3. LANG, J.A. Fuel/Air Ratio Distribution in an Annular Combustor Chamber.Assessment of Preliminary Primary Zone Traverses. N.G.T.E. Report NT 782. March 1970.

4. WASSELL, A.B. The Development of Pollution Controls for the Rolls-Royce RB.211 and Olympus 593 Engines. To be presented at S.A.E. National Air Transportation Meeting, Dallas. April 1974.

5. MANGHAM, J.L. Internal Rolls-Royce (1971) Ltd. Report : CRR 60114 May 1973.

6. Environmental Protection Agency : Control of Air Pollution from Aircraft and Aircraft Engines. U.S. Federal Register Vol 38 Number 136 Part 11. July 1973.

PYROGENIC IGNITION SYSTEM FOR AFTERBURNERS

S. Subrahmanyam, G.K. Murthy and P.A. Paranjpe

Propulsion Division, National Aeronautical Laboratory, Bangalore, India

1. Introduction:

Quick and reliable ignition of kerosene-air mixtures over a broad operating range forms a significant requirement for the operation of afterburners/duct burners of aviation gas turbines. The following three techniques are currently used for igniting the fuel-air mixtures in afterburners. 1) Hot streak ignition 2) Pilot chamber ignition 3) Catalytic ignition. But each of these techniques have certain inadequacies as explained below:

In the hot streak ignition technique, immediately after opening the fuel to the afterburner, additional fuel is injected into the main combustor at a convenient location in sufficient quantity over a very short duration. The injected fuel ignites spontaneously causing a high intensity pencil of flame to shoot through the turbine stages into the afterburner, where it ignites the fuel gas mixture. Obviously this method limits the number of turbine stages in order to reduce the spread of the pencil. In addition the fuel injection process is severely limited in duration because the turbine stators are subjected to excessively high temperatures during this process. Further, in this method, the ignition of the gases takes place first at the gutters located near the outer periphery, thus resulting in a large "dead thrust" zone between maximum dry thrust and minimum afterburner thrust.

In the pilot chamber ignition technique, a small pilot combustion chamber, located ahead of the flame holder, is first ignited by an electrical spark and the hot gases thus generated ignite the afterburner mixture. Sometimes a depression in the turbine exit cone fairing is fitted with a spark plug and a fuel injector so that it works like the pilot combustion chamber described above. This method of pilot ignition is disadvantageous because of the weight of the combustor and a number of parts like spark plugs and ignition unit. Further, the system reliability is likely to be reduced owing to the possible fouling of the spark plug or to the possible failure of high tension electrical insulation on spark plug leads situated in the hot afterburner environment.

Thus for modern engines employing multiple number of turbine stages and requiring fully modulated and part-throttle reheat, both the above methods have their limitations on account of the unfavourable features mentioned earlier. The third technique, catalytic ignition, is fairly of recent origin and it is employed presently only in a limited way. Although catalytic ignition system was found to be quite effective on the basis of experimental work carried out here(1), it has an inherent disadvantage of requiring a highly expensive catalytic element which may become ineffective during service on account of poisoning and deposition of carbon(2). Further it loses effectiveness very rapidly with the decrease in temperature of the catalyst.

In order to overcome the deficiencies and disadvantages of the above described techniques, experimental work was undertaken to evaluate a novel technique of ignition using concentrated hydrazine and a cheap catalyst. This new technique is here-after referred to as "Pyrogenic Ignition System". This paper describes the investigations carried out with this technique and demonstrates its effectiveness and superiority over the established methods.

2. Experimental Set-up:

The experimental set-up used for these investigations was basically similar to that used earlier (1,4) for catalytic ignition studies. It is briefly described below. As shown in Fig.1, it consists of a combustion chamber as a gas generator feeding into a 165mm diameter stainless steel pipe, with flow spreading baffles, which terminates into a model afterburner exhausting to the atmosphere.

2.1 Combustion Chamber

This is a can-type aircraft engine combustor consisting of a nimonic flame tube, a mild steel casing, a fuel atomiser and a spark plug.

2.2 Fuel System

A motor driven, swash plate type aircraft fuel pump supplies fuel from the service tank to the distributor under pressure. Fuel is fed from the distributor to different injectors of the set-up. The surplus fuel is returned to the service tank.

2.3 Automatic Temperature Regulator

Since the fuel is supplied to both the main combustion chamber and the afterburner from the same distributor, any change in the afterburner fuel flow rate alters the through-put to the main combustor. Thus the temperature of the gases entering the afterburner is affected by changes made in the afterburner fuel flow rate. A decoupling of the two flows involves manipulation of the main combustor fuel control valve in accordance with the changes in afterburner fuel flow rate so as to maintain a constant afterburner inlet temperature. A servocontrolled electronic temperature regulator was developed to maintain a constant afterburner inlet temperature.

The regulator system senses the afterburner inlet temperature through a thermocouple, compares the thermocouple output with the reference input fed from a calibrated potentiometer, chops the difference at 50 Hz, amplifies the difference and feeds it to the control winding of the servomotor geared to the fuel control valve of the main combustor.

2.4 Model Afterburner

Model afterburner represents a typical geometry of the afterburner used on aircraft engines. It was made up of three lengths of 232mm diameter stainless steel pipe. The middle portion was fitted with a 24° V - gutter flame holder supported by 3 radial 24° V - shaped struts. This configuration gave a blockage ratio of 35%.

Far upstream of the flame holder, a 12.25 mm diameter fuel ring having a number of 0.5 mm diameter orifices was located at mid-radius at entry to the afterburner. Injection was parallel to the gas stream in the counter-stream direction. This design achieved good penetration, atomization and fuel distribution so that the fuel-gas stream entering the flame holder section was uniform and completely pre-mixed. Thus the uncertain variable of fuel-air ratio distribution was eliminated. The portion downstream of the flame holder was enclosed in a cooling jacket through which high pressure cold air was forced.

2.5 Ignition System

The main combustor was provided with an ignition system consisting of a power supply, a high tension ignition excitor and a high energy discharge type spark plug. A similar system was provided for the afterburner as an auxiliary system. In the afterburner, the spark plug was located just ahead of the flame holder.

2.6 Pyrogenic Ignition System

Fig.2 gives a schematic arrangement of this system. A simple orifice type injector was fitted on the afterburner so that it projects inside the space of the radial supporting strut of the flame holder, so as to spray hydrazine on to a rusted iron baffle plate fitted on the lee-side of the flame holder at the junction between V - gutter ring and the supporting strut. The injector was connected to a hydrazine reservoir situated directly above it. The hydrazine reservoir was provided with two ports, one for replenishment which was connected to the hydrazine storage and transfer system and the other for pressurization during injection. The latter port was connected to a compressed air supply or inert gas cylinder. Highly concentrated hydrazine was not commercially available in India and it was prepared at site from hydrazine hydrate and checked for its concentration(5,6).

2.7 Instrumentation

Air and fuel flow measurements were made with calibrated orifice meters. Static pressures were measured by employing high precision Bourdon gauges. Chromel-alumel thermocouples were used to measure temperatures. Figs. 3 & 4 show the experimental set-up and the model afterburner in operation respectively.

3. Experimental Investigations:

The experiments were carried out in two phases. The first phase included the determination of the stability envelope of the flame holder at two inlet temperatures on the lower side which represents a more difficult case for ignition and stabilization. In the second phase, ignition checks were conducted with the pyrogenic ignition system.

3.1 Stability Limits

During the tests the following procedure was adopted to determine the stability envelope of the flame holder:

1. Air flow rate was set to a desired value and maintained constant

2. Fuel was admitted to the main combustor and ignition switched on.

3. After igniting the main combustor, the electronic temperature regulator was set to give the desired afterburner inlet temperature.

4. Cooling air to the afterburner jacket was admitted.

5. After attaining steady conditions enough fuel was fed to the afterburner and it was ignited by an auxiliary spark ignition system. Ignition at high gas velocities was not possible with a spark ignition. Hence hydrazine was injected on to the baffle plate to achieve ignition.

6. The afterburner fuel flow was gradually reduced or increased until the flame blow-off occured. The fuel flow rates at lean and rich blow-off limits were noted.

The above steps were repeated for different air flow rates and thus stability limits were determined.

3.2 Ignition Limits

The second phase of experiments was conducted to determine the ignition capabilities of the pyrogenic ignition system. The procedure described earlier under steps 1 to 4 of the stability experiments was common to these experiments. After attaining steady conditions at entry of the afterburner, proper amount of fuel was fed into the afterburner so that the fuel-air ratio corresponded to either rich or lean incipient blow-off limit of the flame holder. Hydrazine was then injected on to the rusted iron baffle and the ignition was checked by direct visual observation of the flame. A comprehensive experimental programme was carried out at the lower afterburner inlet temperature of 400° C because a number of spot checks at higher temperatures, right upto 600° C revealed that there is no inadequacy of pyrogenic ignition system at high temperatures and the threshold ignition limits are likely to be even below 400° C as shown by the three spot checks carried out at 350° C, 300° C and 250°C which gave spontaneous ignition. This result is marked as a triangular point in Fig.5.

4. Results and Discussion

4.1 Stability Limits

The full lines in Fig.5 represent the stability characteristics of the flame holder for an entry temperature of 400° C and at the ambient pressure of about 0.9 atm. The abscissa represents the air flow rate in kg/s and the ordinate represents the afterburner fuel-air ratio. The burnt oxygen in the main combustor was not taken into account while calculating the afterburner fuel-air ratio in view of the uncertainty of the main combustor efficiency. It can be seen from Fig.5 that the lean limit fuel-air ratio is nearly half of the stoichiometric ratio and the rich limit fuel-air ratio is 1.5 times the stoichiometric ratio, even for an air flow rate of 3 kg/s which corresponds to an inlet Mach No. of 0.27. Experiments could not be conducted at higher inlet Mach numbers due to the limitation of the available air flow.

4.2 Pyrogenic Ignition

A number of experimental runs were made with hydrazine injection for afterburner mixture conditions close to the lean stability limit of the flame holder for the entry gas temperature of 400° C. In addition a few spot checks were conducted little above the stoichiometric fuel/air ratio to check the effectiveness of ignition. Since these tests did not show any different ignition behaviour than that at lean limit a comprehensive test programme under fuel-rich conditions was found unnecessary. Moreover, ignition studies at rich blow-off limits are of only academic interest since the afterburner would never operate at rich blow-off limits in practice, except for the inadvertent local rich condition. Each time about 100-150 ml of hydrazine was injected on to the rusted iron baffle plate. Successful ignition was achieved with hydrazine of concentration*) 95 percent and above at all the points of the lean stability limit as shown by full points in Fig.3. At lower concentrations of hydrazine it was not possible to achieve sufficient reliability in ignition.

Stability limits were obtained with three successive experiments which gave reproducible results. For each mixture condition ignition with hydrazine was checked consecutively four times and ignition occured every time. The test results were quite reproducible.

The ignition was found to be spontaneous since the total time observed between the opening of the hydrazine cock and the appearance of full flame at the afterburner exit, was less than even 3 seconds.

5. Application Features:

While integrating the pyrogenic ignition technique into the aircraft system the following features would have to be borne in mind on account of the special characteristics of hydrazine.

Since the freezing point of hydrazine is similar to water, it would have to be stored in the aircraft in the appropriate location which is not very cold. It is conceivable that the freezing point can be depressed by some additives such as e.g. UDMH and it would be highly desirable to repeat the above experimental work with such mixtures.

Unless suitable stabilizers can be found for preventing decomposition under prolonged storage, it would be necessary to prepare hydrazine of high concentration fresh on site before actual use on aircraft. The apparatus for preparing hydrazine from hydrazine hydrate is however, very simple. Precaution in handling hydrazine is necessary on account of its toxicity.

---

*) Hydrazine of high concentration right up to 99.7% was prepared in the Propulsion Division facilities for these experiments (5,6)

In order that the afterburner ignition is achieved in the shortest possible time, it might be necessary to have the hydrazine cock close to the afterburner. In this case one of the possible approaches to hold the hydrazine upto the cock would be to provide a concentric tube, in which hydrazine is contained in the inner tube while the fuel flows through the outer concentric tube, thus ensuring appropriate temperature of the hydrazine.

6. Concluding Remarks:

1. Pyrogenic ignition system was found to be very effective since ignition could always be achieved spontaneously at all the points lying within the lean limit and the stoichiometric limit. Since there was no discernible difference between lean stability limit and ignition limit, the effectiveness of this ignition system is particularly noteworthy.

2. Ignition was achieved for gas temperatures as low as 400° C at all the points within the stability envelope. The three spot checks at one fuel-air ratio and at the afterburner turbine entry temperatures of 350, 300 and 250°C have also yielded spontaneous ignition. This shows that the lower threshold limit for pyrogenic ignition system is definitely below 400°C corresponding to that of catalytic ignition system. Thus the pyrogenic system could be applicable to afterburning by-pass or duct burning engines. Moreover this lower temperature limit can be interpreted as having good potential under sub-atmospheric pressures at the usual afterburner entry temperatures.

3. Pyrogenic ignition system offers a special advantage over the catalytic system of ignition in that it does not require any expensive catalyst and there is no danger of soot formation or carbon deposition since hydrazine (N_2H_4) is a carbon-free fuel. The rusted iron was found to remain completely unaffected even after several ignition trials. Moreover, hydrazine is a safe substance, non-detonable and non-corrosive, to carry on an aircraft unlike the pyrophoric substances e.g. tri-ethyl borane which have been employed on experimental scale and under special circumstances.

4. Hydrazine concentration must be above 95% for reliable ignition.

5. Pyrogenic ignition system overcomes the various deficiencies of the other ignition systems and it has significant advantages over the established methods. In view of the very good results demonstrated with this ignition method, serious consideration should be given to its use in actual engines.

7. Acknowledgements:

The authors wish to thank Messrs K. Sivasankaram & K. Sridhara, Scientists of the Division, for the basic experimental set-up and for conducting the actual experiments in the Combustion and Gasdynamics Laboratory of the Propulsion Division.

8. References:

1. SRIDHARA, K & SIVASANKARAM, K. Investigations on a Novel Ignition Method in Afterburners. Paper No. 3-5 of the Symposium on Gas Turbine Technology, held at Gas Turbine Research Establishment, Bangalore in April 1973.

2. GRENLASKI, S.E. & FALK, F. Investigation of Catalytic Ignition of JP-5 and Air Mixtures, Journal of Aircraft, Vol.3, No. 2 p. 141 - 6, 1966.

3. AHLERT, R.C. & PESHIN, R.L. Ignition temperature Vs. Drop Size for Hydrazine and Pentabutane in Air. AIAA Journal, Vol.9, No.10, October 1971.

4. RAO, K.V.L. & PARANJPE, P.A. Catalytic Ignition System for Afterburners. N.A.L. TM.PR.320.2/71, August 1971.

5. SUBRAHMANYAM, S. & MURTHY, G.K. Synthesis of Hydrazine. N.A.L.TM.PR.325.3/73, February 1973.

6. SUBRAHMANYAM, S. MURTHY, G.K. & RAJAGOPALAN, S. Estimation of Hydrazine. N.A.L.TM.PR.325.1/73, January 1973

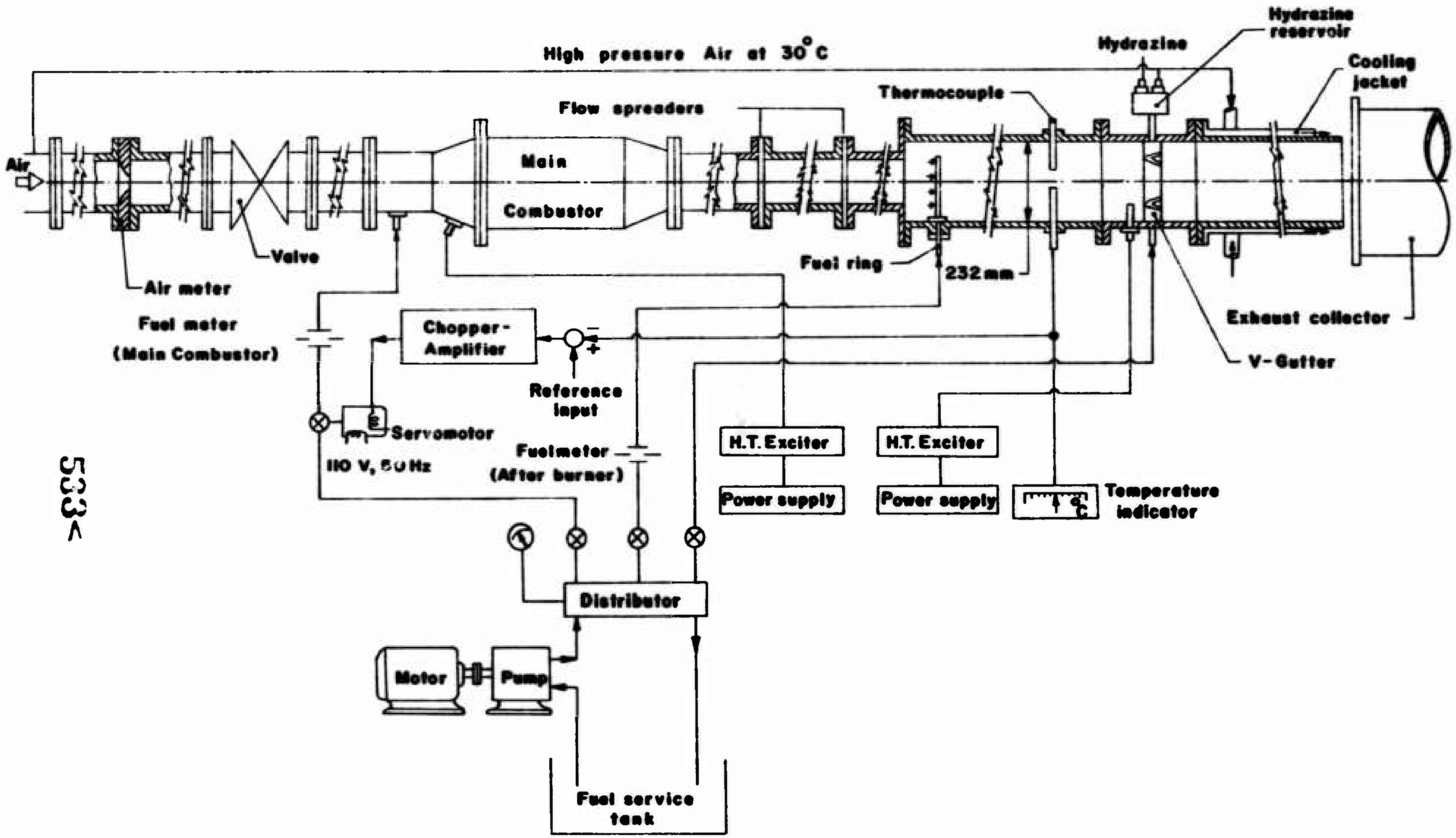
High pressure Air at 30°C
Hydrazine
Hydrazine reservoir
Cooling jacket
Thermocouple
Flow spreaders
Air
Main
Combustor
Valve
Air meter
Fuel meter
(Main Combustor)
Fuel ring
232 mm
Exhaust collector
V-Gutter
Chopper-Amplifier
Reference input
Servomotor
110 V, 50 Hz
Fuelmeter
(After burner)
H.T. Exciter
Power supply
H.T. Exciter
Power supply
°C
Temperature indicator
Distributor
Motor
Pump
Fuel service tank

FIG. I EXPERIMENTAL SETUP (Schematic)

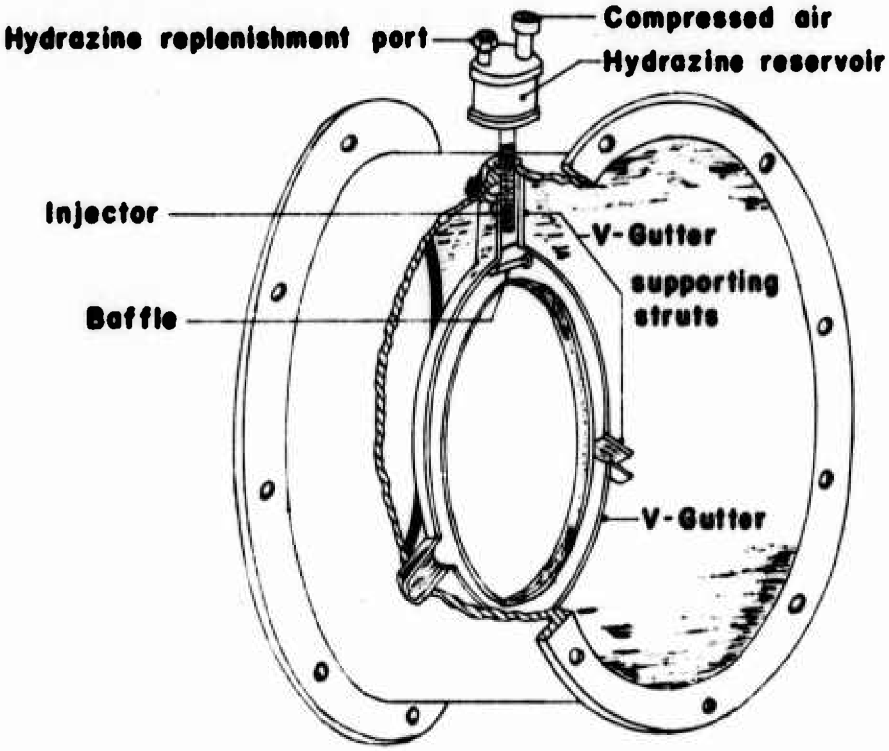
Hydrazine replenishment port
Compressed air
Hydrazine reservoir
Injector
V-Gutter
supporting struts
Baffle
V-Gutter

FIG. 2 FLAME HOLDER WITH BAFFLE AND HYDRAZINE INJECTOR IN POSITION

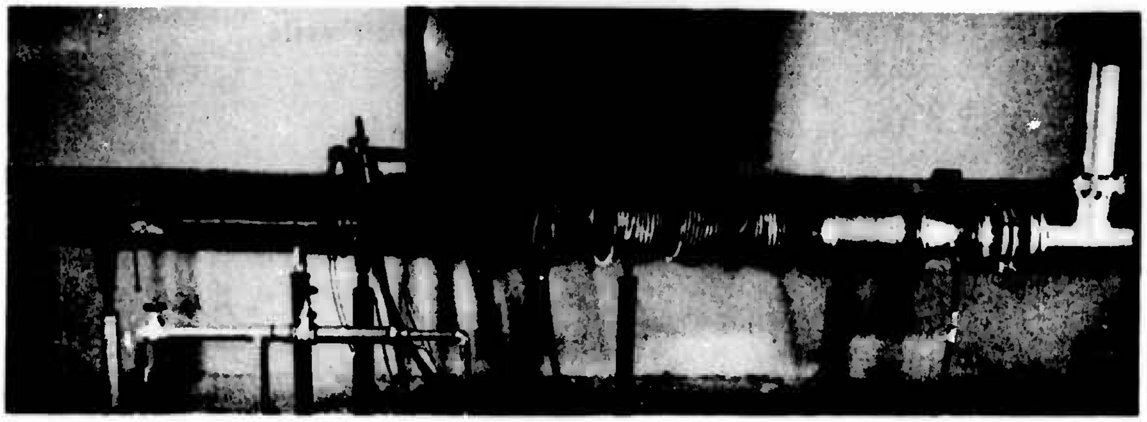

FIG. 3 VIEW OF THE EXPERIMENTAL SET-UP

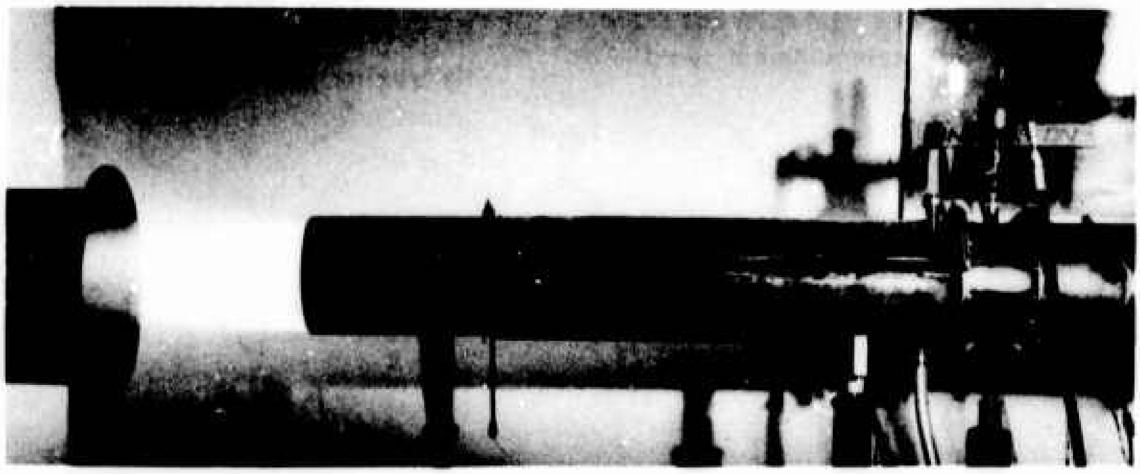

FIG.4 MODEL AFTERBURNER IN OPERATION

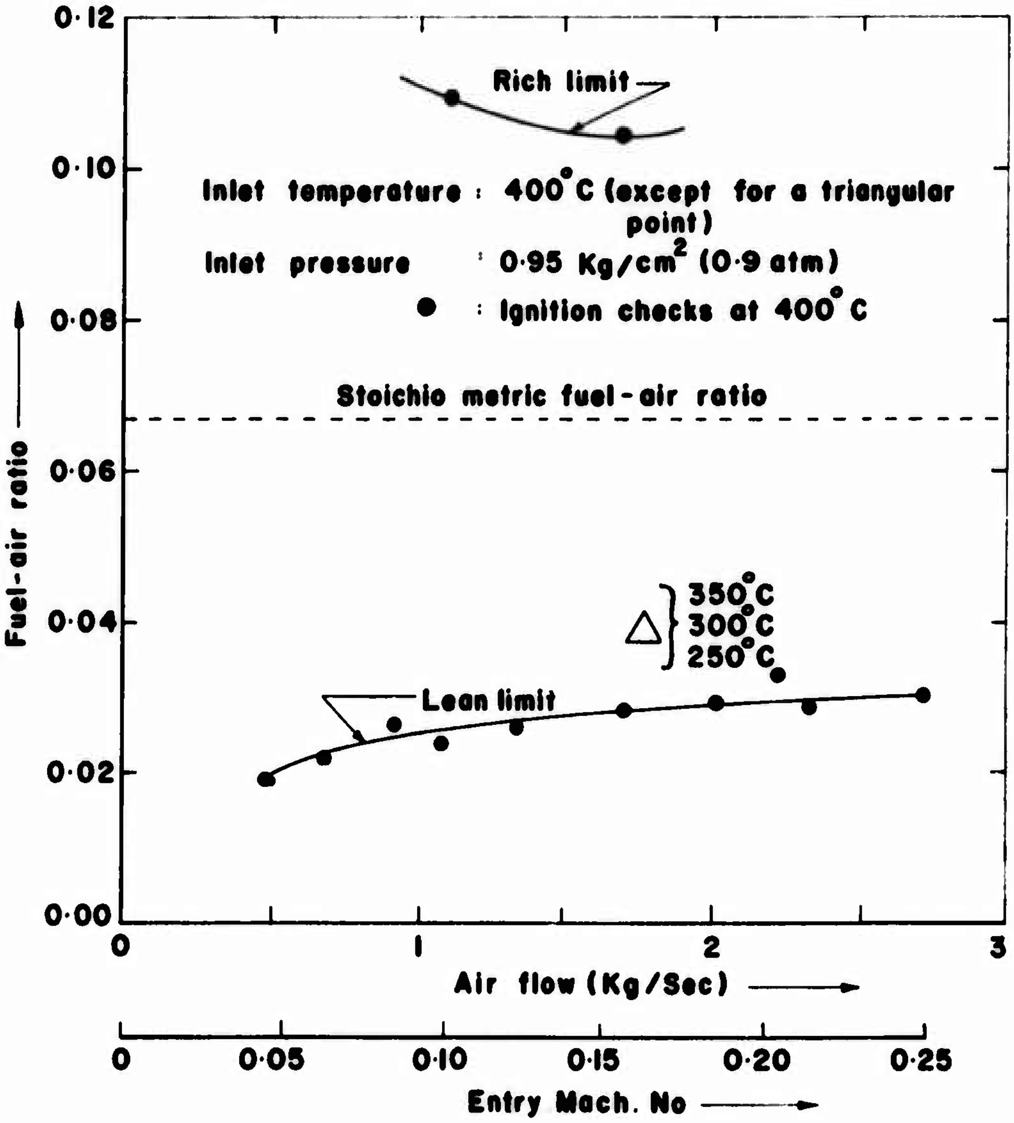

FIG.5 STABILITY LIMITS AND IGNITION CHECKS

VISUALISATION PAR STRIOSCOPIE DANS UN DIFFUSEUR DE COMPRESSEUR CENTRIFUGE SUPERSONIQUE

Yves Ribaud et Patrick Avram

Office National d'Etudes et de Recherches Aérospatiales (ONERA) 92320 Châtillon (France)

RÉSUMÉ

Des expériences de visualisation strioscopiques dans un diffuseur à aubes de compresseur centrifuge supersonique fonctionnant dans le fréon 114 ont permis de préciser les configurations d'ondes rencontrées dans ce type de montage en fonction du vannage et de la vitesse de rotation. Il apparait en particulier que les pseudo-chocs de recompression se réduisent à une onde unique près du pompage. On note également que le diffuseur étudié s'amorce sans difficulté pour des nombres de Mach compris entre 1,24 et 1,4. Enfin lors du pompage apparaissent alternativement deux phases :

- le refoulement durant lequel est mis en évidence un réseau d'ondes générées par les bords de fuite du rotor,
- un fonctionnement sain reconnaissable au système d'ondes classiques liées au diffuseur.

SCHLIEREN VISUALIZATION IN THE DIFFUSER OF A SUPERSONIC CENTRIFUGE COMPRESSOR

SUMMARY

Schlieren visualization experiments performed in a supersonic vaned diffuser for high pressure ratio centrifugal compressor (working fluid used is freon 114) made it possible to define flow wave patterns in this type of machine with different throttlings and rotation speeds. It clearly appears that recompression pseudo-shocks become a single normal schock when surging is approaching. Otherwise throat starting operation is always ensured for a mach number in the range of 1.24 - 1.4. Finally during surge two phases are alternately present :

- backflow during which a wave network generated by rotor trailing edges arises,
- normal operation, demonstrated by the classical diffuser wave pattern.

1. INTRODUCTION

Au cours de ces dernières années, le développement des petites turbines à gaz pour applications terrestres ou aéronautiques a exigé l'étude de compresseurs centrifuges supersoniques de plus en plus poussés, délivrant des taux de compression allant de 5 à 8, voire plus.

Pour sa part, l'ONERA effectue dans ce domaine des recherches tant fondamentales qu'appliquées et dispose à cet effet d'un banc de compresseur équipé notamment pour la visualisation strioscopique de l'écoulement dans les diffuseurs. Si les mesures de pression et de température sont suffisantes pour déterminer les performances, ces informations par contre ne permettent pas toujours de comprendre les phénomènes complexes régissant les écoulements dans les diffuseurs et notamment dans l'espace lisse ainsi qu'au col du diffuseur à aubes. Outre les mesures aérothermodynamiques classiques, la visualisation de l'écoulement a donc été effectuée de façon à améliorer la compréhension des phénomènes et à faciliter la construction de schémas théoriques d'écoulement. Enfin, notons que ce procédé a déjà été employé dans divers laboratoires(1).

2. INSTALLATION D'ESSAIS

Le montage d'essai constitué d'un circuit fermé étanche, comprend essentiellement (fig. 1) :

- une canalisation basse pression amenant l'écoulement à l'entrée du compresseur (1),
- un compresseur centrifuge avec sa pivoterie et un caison de reprise du fluide (2),
- un échangeur (3),
- une vanne de réglage de la contrepression (4).

Le compresseur, expérimenté dans du fréon 114 (fluide permettant de diminuer notablement les problèmes de résistance mécanique) a été défini de façon à délivrer un grand débit spécifique pour un taux de compression de 10, avec un rendement isentropique de 0,8.

- Le rotor, dont le diamètre de sortie est égal à 450 mm comporte un nombre croissant de pales de l'amont vers l'aval (64 en sortie de roue) afin de réduire au maximum les hétérogénéités azimutales à l'entrée du diffuseur. Un moteur asynchrone entraine la roue mobile. Il est alimenté par un groupe convertisseur de fréquence d'une puissance de 50 kW permettant ainsi un réglage de la vitesse de rotation entre 3000 et 12 000 tr/mn.

- Le diffuseur est constitué de canaux bidimensionnels, chaque canal interaube comportant un extrados en forme de spirale dessiné de façon à introduire un minimum de perturbations vers l'amont, un col de courte largeur(2) et un divergent de faible angle d'ouverture(3). Ce diffuseur peut être calé à différents angles afin de rechercher les performances optimales en fonction de la vitesse de rotation choisie.

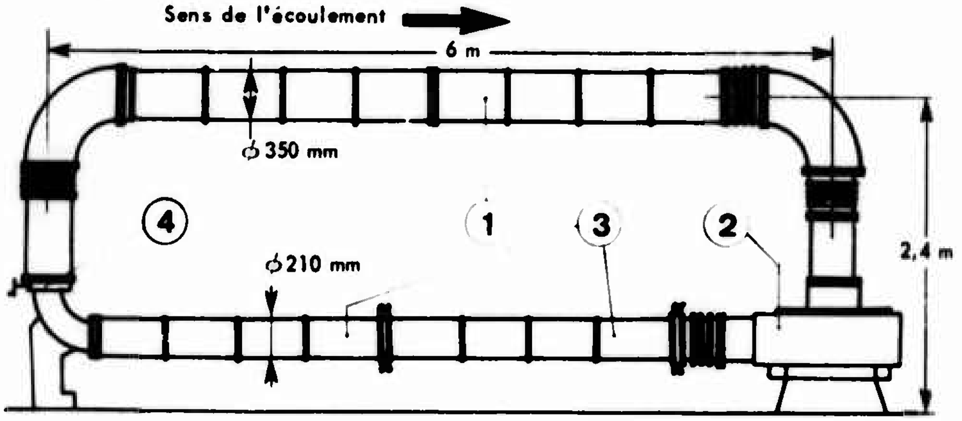

Fig. 1 - Installation d'essais

1 - Canal d'amenée

2 - Caisson de reprise et compresseur centrifuge

3 - Echangeur

4 - Vanne de réglage de la contrepression

3. MONTAGE DE VISUALISATION STRIOSCOPIQUE PAR REFLEXION(4) (fig. 2)

Une fenêtre de verre (1) ménagée dans le carter externe (2) et un miroir plan en acier inox (3) fixé sur le carter interne (4) assurent les trajets des faisceaux lumineux incident et réfléchi à travers la veine étudiée. L'optique de visualisation comprend un miroir collimateur off-axis parabolique (5), suivi d'un miroir plan incliné (6) qui dirige le faisceau parallèle perpendiculairement au plan du diffuseur (7). Une partie du faisceau réfléchi par (3), (5), (6) reprise par une lame semi-transparente (8) focalise ensuite sur une fente (9) et est enfin renvoyée par un prisme spécial vers les appareils d'enregistrement (10) (appareil photographique ou caméra). Lors de l'enregistrement l'éclairement est fourni par un flash de très courte durée (10^{-7} s) assurant ainsi le figeage des phénomènes.

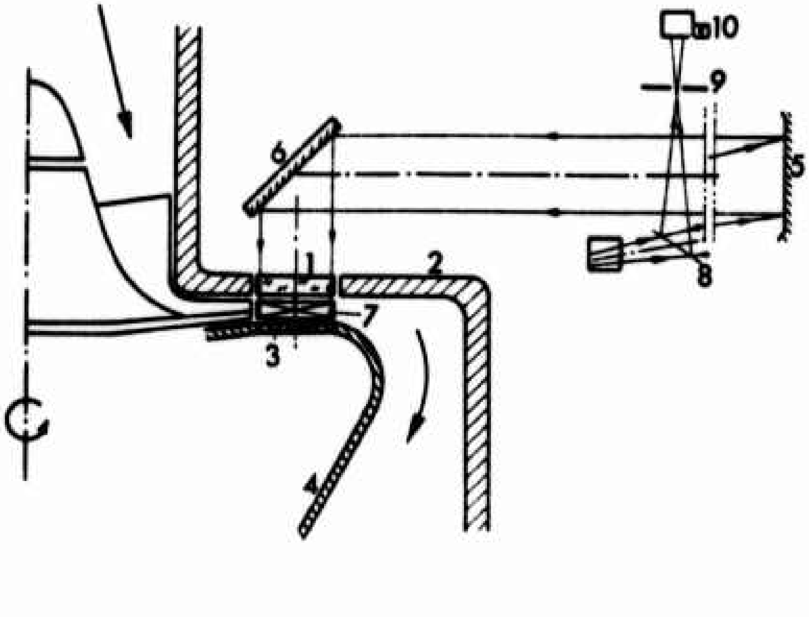

Fig. 2 - Schéma de principe de la visualisation.

4. PRÉSENTATION DES RÉSULTATS

4.1. Influence du vannage

La figure 3 montre, dans un cas d'adaptation entre rotor et diffuseur, l'évolution des configurations dans la partie divergente des canaux du diffuseur en fonction de la contrepression imposée. Les repères portés sur les vues photographiques correspondent au nombre de tours de fermeture de la vanne.

Les taux de compression correspondants apparaissent sur la caractéristique globale portée sur la figure 4, le rapport de compression π, porté en ordonnées étant défini comme le rapport entre la pression statique du caisson et la pression d'arrêt amont, le débit volume étant représenté par le nombre de Mach critique m_{*0} dans la section d'entrée du rotor.

L'extrados des aubes est ici calé à $\alpha_2 = 12°$ par rapport à la direction tangentielle pour une vitesse de rotation de 8000 tr/mn. Le Mach critique sur le cercle d'entrée du diffuseur $m_{*2} = V_2 / a_*$ (où V_2 représente la vitesse absolue de l'écoulement et a_* la vitesse critique du son dans le caisson de reprise), déterminé à partir d'un sondage en pression d'arrêt, est égal à 1,24 en milieu de veine.

On constate tout d'abord que la recompression s'effectue par un système de pseudo-chocs$^{(5)}$ dont l'extension dans le diffuseur est fonction du vannage et plus précisément du nombre de Mach et de la couche limite en amont de la recompression. Ce phénomène a été bien mis en évidence dans les tuyères supersoniques et l'expérience montre$^{(6)}$ que l'efficacité de ce système d'ondes de choc et de faisceaux de détente, compte tenu du décollement des couches limites dans cette zone est comparable à celle d'un choc droit de même intensité à condition que la veine soit cylindrique. Près du pompage, les clichés photographiques indiquent que le système de pseudo-chocs est pratiquement réduit à une onde de choc droite placée au voisinage du col et ceci, dans la gamme des nombres de Mach étudiés (m_{*2} = 1,2 à 1,45). On peut donc en conclure, au moins pour le rotor étudié, que la longueur optimale du col est très faible.

Parallèlement, les mesures des grandeurs aérodynamiques permettent de corroborer les résultats précédents. Ainsi l'exploration axiale en pression d'arrêt de l'écoulement au niveau du cercle d'entrée du diffuseur fait apparaître un développement modéré des couches limites pariétales, dans cette section (fig. 5).

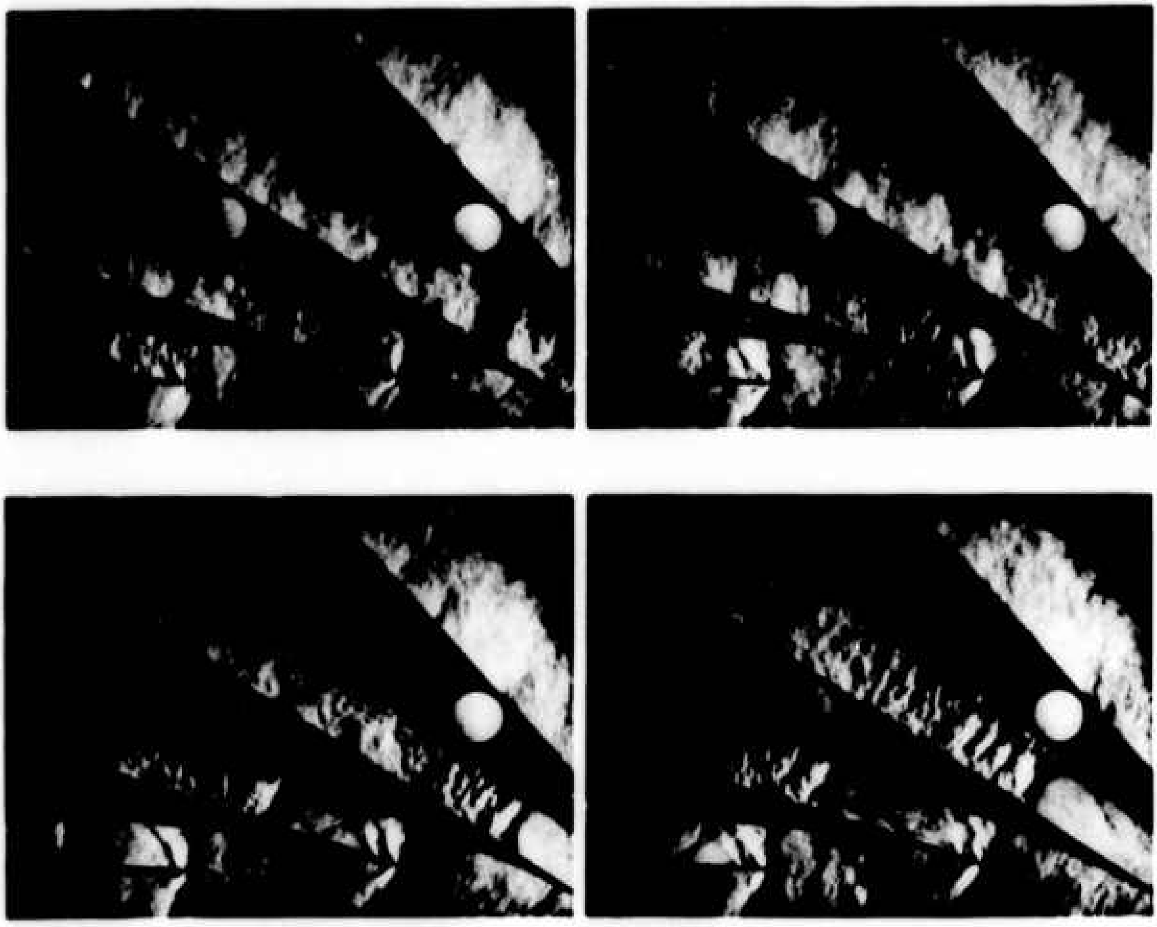

Vannage 8,5

Vannage 8

Vannage 7

Vannage 6

Fig. 3 - Influence du vannage - 8000 tr/mn m_{r2} = 1,24 - α_2 = 12°

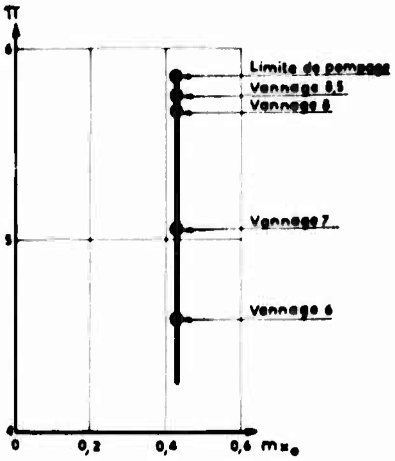

Fig. 4 - Caractéristique débit-pression

8000 tr/mn

m_{r2} = 1,24 - α_2 = 12°

Par ailleurs l'évolution de la pression statique le long de la génératrice moyenne du canal représente tout à fait bien ce que donne la visualisation, au moins dans la partie divergente des canaux. A partir des valeurs du débit, de la température et de la pression statique s'effectue le calcul du nombre de Mach critique moyen M_* dans chaque section et qui est illustré par la figure 6.

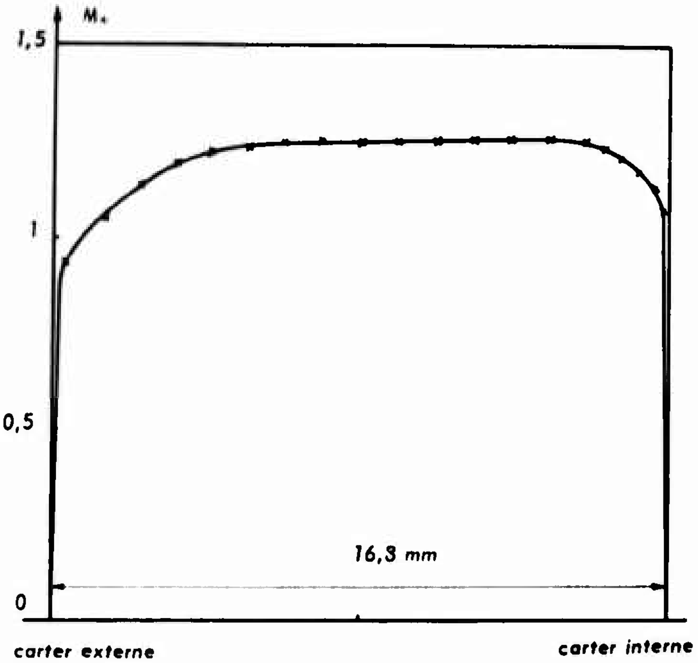

Fig. 5 - Répartition axiale du nombre de Mach critique absolu sur le cercle d'entrée du diffuseur.

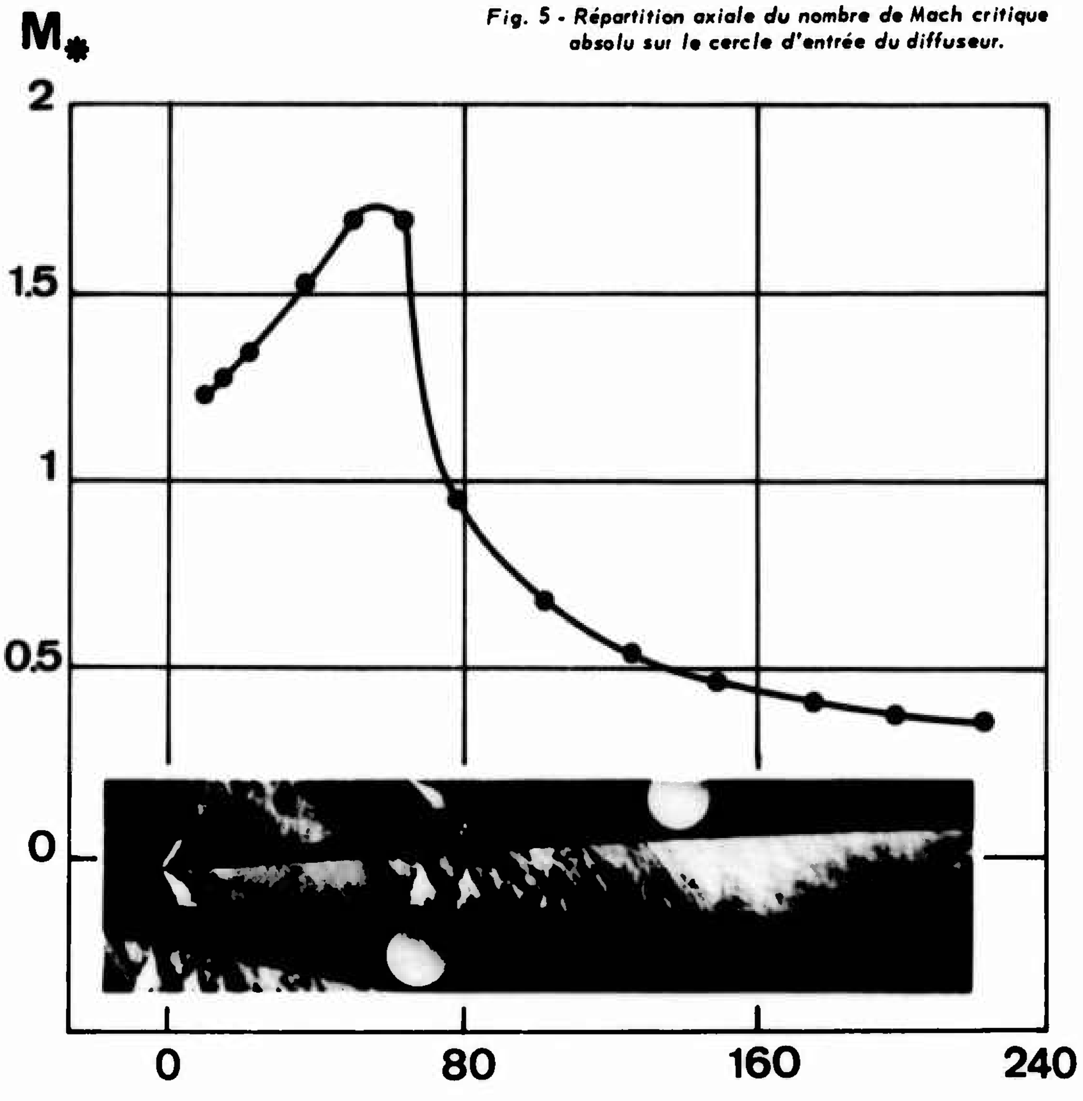

Fig. 6 - Comparaison entre visualisation et répartition du nombre de Mach critique dans le canal interaube - 9500 tr/mn - α_2 = 9° - m_{*2} = 1,38.

4.2. Influence de la vitesse de rotation

L'influence de la vitesse de rotation donc de la vitesse absolue apparait nettement sur les configurations d'ondes à l'entrée du diffuseur, comme le montre la figure 7 sur laquelle on remarque notamment, l'inclinaison plus accentuée des ondes aux plus grandes vitesses. Il est à signaler que, quel que soit le calage utilisé ($9° < \alpha < 12°$) cette grille s'est amorcée, même pour des nombres de Mach faiblement supersoniques.

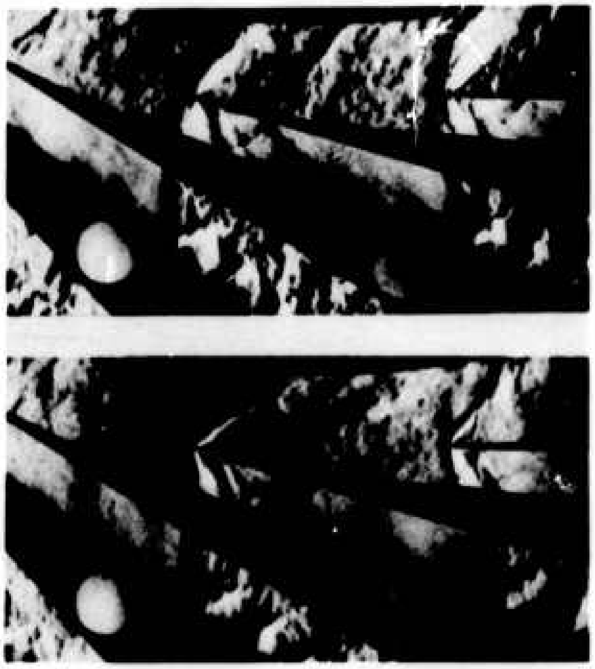

$m_{*2} = 1,24$ Vannage 6

$m_{*2} = 1,38$ Vannage 6

Fig. 7 - Influence de la vitesse de rotation - $\alpha_2 = 9°$

4.3. Nature de l'écoulement au voisinage du col de diffuseur

La schématisation de l'écoulement au voisinage de la section minimale du diffuseur a été grandement facilitée par l'observation de clichés photographiques en couleur dont l'un des avantages est la différenciation nette entre les ondes de choc et les faisceaux de détente. Le cas examiné correspond à $m_{*2} = 1,24$ et $\alpha_2 = 12°$ (fig. 8).

L'onde de choc détachée issue du bord d'attaque (1) de l'aube A rencontre l'aube voisine B, où par suite de son intensité elle crée un décollement très localisé de la couche limite, suivi d'une zone de détente (3). Par ailleurs le contournement du bord d'attaque est le siège d'une forte accélération du fluide (2) et en aval de cette zone de détente se produit un décollement suivi d'un recollement de la couche limite, l'ensemble étant représenté par l'onde de choc en lambda (4). Des points D et F où la divergence des parois est de 3°, naissent des faisceaux de détente (5) et (6) : le premier influe sur l'inclinaison de l'onde de choc (4), tandis que le second sert essentiellement à augmenter la grandeur de la vitesse. Plus en aval, (7) apparait le début du système de pseudo-chocs de recompression qui rend l'écoulement subsonique.

Dans la configuration présentée ici, on s'aperçoit que la section minimale est affectée par un écoulement supersonique. Or, généralement lors de l'établissement du projet, on suppose le nombre de Mach au col égal à l'unité. Cette hypothèse parait justifiée tout au moins lorsque les taux de compression atteints restent modérés et tant que l'épaisseur du bord d'attaque n'est pas négligeable devant les dimensions du col. Mais comme on vient de le noter, le blocage sonique ne peut être considéré dans ce diffuseur. Aussi est-il nécessaire dans le cadre d'un projet de prévoir deux modèles d'écoulement dans le diffuseur :

- l'un correspondant au blocage sonique des canaux,

- l'autre relatif à l'amorçage du diffuseur, de sorte que les conditions moyennes à l'entrée de la grille sont calculées, comme pour les compresseurs axiaux supersoniques, à partir des conditions de périodicité (avec ondes de faible intensité émises par l'extrados) (2) (7).

(Il va sans dire que le cas du diffuseur entièrement subsonique ne fait pas partie de cette étude).

La solution à retenir pour un nombre de Mach de rotation donné est celle qui correspond au débit le plus faible. Aux faibles vitesses de rotation on trouve le blocage sonique et aux grandes vitesses, l'amorçage du diffuseur.

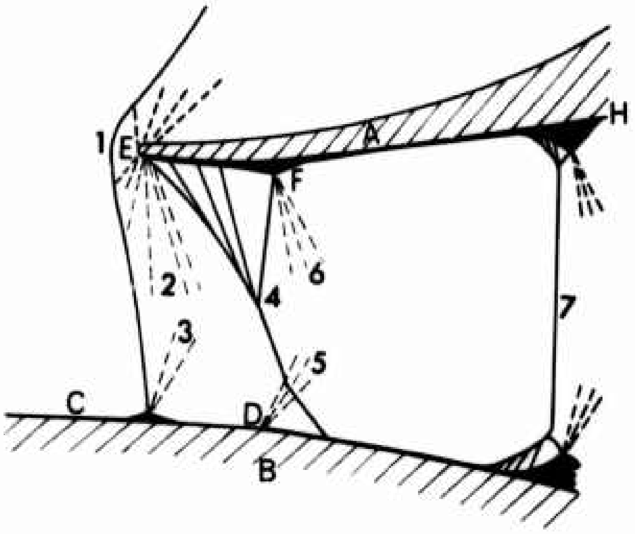

Fig. 8 - Schéma d'ondes au voisinage du col.

8000 tr/mn - $m_{v2} = 1,24$
$\alpha_2 = 12°$ - vannage 7

4.4. Fonctionnement limite - Cas du pompage

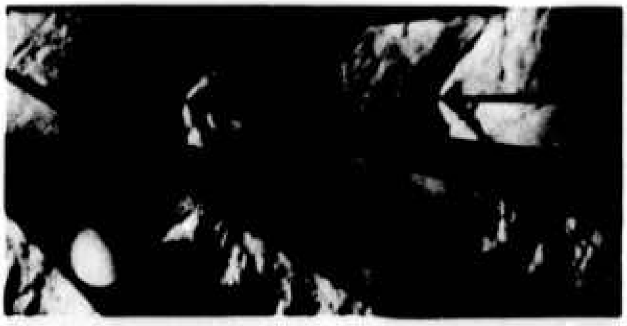

phase d'amorçage

Fig. 9.A

9500 tr/mn
$m_{v2} = 1,38$
$\alpha_2 = 9°$

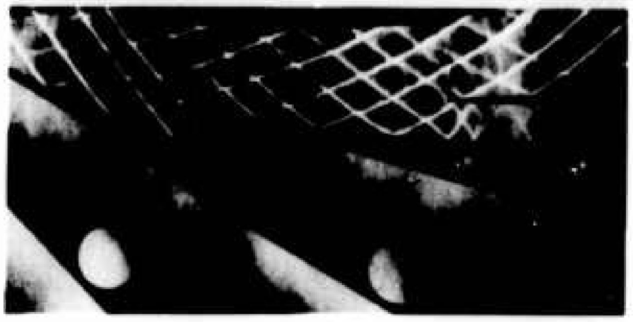

phase de désamorçage

Fig. 9.B

A partir d'un certain niveau de vannage, les ondes de choc de recompression parviennent dans la section minimale et rejoignent aussitôt l'onde de choc de bord d'attaque ; le fonctionnement du diffuseur devient alors instable. Mis en évidence par des prises de vue obtenue par une caméra ultra-rapide (4000 images/ seconde, un flash par image) ce phénomène peut être décomposé en deux phases :

- la première concerne un fonctionnement amorcé (fig. 9.A) comparable au régime sain au cours duquel on voit les pseudo-chocs remonter spontamément vers l'amont, jusqu'à atteindre le choc de bord d'attaque ;

- l'autre, plus fugace a trait au refoulement. Il se caractérise par une remontée rapide de l'onde de bord d'attaque vers l'amont. La disparition des ondes liées au diffuseur est alors suivie par l'apparition d'un deuxième réseau d'ondes (fig. 9.B), dans l'espace rotor-diffuseur, et qui est animé d'un mouvement de rotation. Ces ondes compte tenu de leur nombre et de leur mouvement de rotation sont nécessairement liées au rotor. L'explication de ce phénomène est que le fluide refoulé par le diffuseur est quasiment arrêté par la roue mobile qui possède en bout de pale une vitesse linéaire supersonique par rapport au fluide au repos, en mouvement absolu les bords de fuite des pales du rotor engendrent ainsi des ondes qui se réfléchissent sur les extrados du diffuseur.

5. CONCLUSION

Les techniques expérimentales de visualisation strioscopique constituent un moyen fort utile pour la compréhension des phénomènes existant dans les diffuseurs de compresseurs centrifuges supersoniques. Elles permettent notamment :

- de préciser la structure des configurations d'ondes au voisinage de la section minimale ainsi que dans le divergent aval,
- d'évaluer la longueur des pseudo-chocs de recompression et de définir le comportement des couches limites qui se développent sur les parois des aubes,
- de décrire le phénomène de pompage.

Bien que limitées à l'écoulement dans le diffuseur, les visualisations sont consacrées à un des organes qui dans ce type de machine est le siège de pertes importantes. Associées aux méthodes classiques d'analyse des écoulements elles doivent conduire à une meilleure interprétation des résultats et par voie de conséquence permettre éventuellement une modification du projet initial de façon à améliorer les performances.

RÉFÉRENCES

1. STAHLER, A.F. Transonic flow problems in centrifugal compressors. Centrif. Compressors SAE, Technical Progress Series, vol. 3 (1961).
2. KENNY, D.P. Supersonic radial diffusers. Advanced Compressors. AGARD LS 39-70 (1970).
3. RUNDSTADLER Jr., P.W. et DEAN Jr., R.C. Straight channel diffuser performance at high inlet Mach numbers. Trans. of the ASME Journal of Basic Engin. pp. 397-422, Sept. 1969.
4. PHILBERT, M. et FERTIN, G. Schlieren systems for flow visualization in axial and in radial flow compressors. Communication préparée pour «Gas Turbine Confer. & Products Show», Zurich, March 31-April 4, 1974. (à paraître).
5. CROCCO, L. One-dimensional treatment of steady gas dynamics. Fund. of Gas Dynamics - High Speed Aero. and Jet Propulsion. Vol. III - Ed. H.W. Emmons (1958).
6. NEUMANN, E.P. et LUSTWERK F. J. of Applied Mechanics, 71 - pp. 195-202 (1949).
7. FABRI, J. Mass flow limitations in supersonic compressors. Advanced Compressors. AGARD LS 39-70 (1970).

TRACE DES AUBAGES DE TURBINE TRANSSONIQUES PAR LA METHODE DE L'HODOGRAPHE

G. Karadimas

SNECMA-France

1. INTRODUCTION

Dans les turbines aéronautiques, le travail fourni par étage est limité par le niveau du nombre de Mach et la déviation dans les aubages. C'est surtout le nombre de Mach à l'entrée qui fixe la limite. Son augmentation au-delà d'une certaine valeur fait apparaître des ondes de choc près du bord d'attaque ce qui provoque le blocage amont de l'aubage et conduit par conséquent à une augmentation considérable des pertes.

Il existe néanmoins un autre moyen pour augmenter le travail d'un étage sans dépasser cette limite : c'est l'augmentation du nombre de Mach de sortie en admettant une vitesse périphérique plus grande.

Les progrès réalisés, ces dernières années, en métallurgie, ainsi que le développement des techniques de refroidissement, ont permis d'augmenter considérablement la vitesse périphérique des aubes de turbines. Le nombre de Mach de sortie a pu ainsi passer de 1 à 1, 3, pour un nombre de Mach maximal amont inchangé de l'ordre de 0, 65.

Il faut cependant, pour bénéficier pleinement de cette augmentation, que le rendement des aubages reste inchangé ou qu'il ne chute que de très peu. Aussi l'insensibilité aux variations des conditions de fonctionnement doit rester analogue à celle des grilles subsoniques.

Pour résoudre ce problème nous utiliserons une méthode de résolution découplée, qui permet, moyennant certaines hypothèses, de résoudre d'abord dans la région subsonique un problème de DIRICHLET bien posé et ensuite un problème de CAUCHY pour déterminer la zône supersonique.

Il est à signaler que la méthode proposée ne se limite pas aux seuls écoulements faiblement supersoniques que nous nous proposons de traiter ici, mais qu'elle reste aussi valable pour n'importe quel niveau du nombre de Mach de sortie.

2. DEFINITION DU PROBLEME

Il y a deux types de grilles pour réaliser un écoulement supersonique à la sortie :

- grilles à canal convergent
- grilles à canal convergent-divergent

Les premières sont caractérisées par le fait que l'augmentation nécessaire de section pour établir un écoulement supersonique est obtenue par l'ouverture de l'angle. Les profils sont calculés analytiquement par des méthodes subsoniques (1) pour un nombre de Mach de sortie voisin de 1. Les essais ont montré que jusqu'à ce nombre de Mach les pertes restent très faibles mais au-delà elles augmentent rapidement et il n'est pas possible de les diminuer en modifiant la forme du profil.

Les grilles à canal convergent-divergent par contre sont optimisées pour le nombre de Mach supersonique souhaité. Dans ce cas, c'est en fonctionnement subsonique que les pertes deviennent plus importantes. Toutefois il semble possible, aussi longtemps que le nombre de Mach de sortie reste modéré (1,2 à 1,4), de calculer le profil de façon qu'en subsonique son fonctionnement reste correct.

Les conditions pour obtenir des faibles pertes dans les grilles convergentes-divergentes aussi bien au point nominal qu'autour de celui-ci sont : la maitrise des gradients de vitesse autour des profils et un écoulement uniforme dans le col.

Les méthodes hodographiques se prêtent bien au traitement de ce problème.

Il est connu depuis Tchaplyguine que du point de vue mathématique l'utilisation du module de la vitesse et de son angle d'orientation comme variables de calcul, transforme les équations qui sont non linéaires en variables physiques en équations linéaires dans le plan de l'hodographe.

De nombreux travaux ont été consacrés aux problèmes subsoniques en partant des équations hodographiques. C'est en introduisant la loi de compressibilité approchée (fluide fictif) et une variable σ liée au nombre de Mach par : $\operatorname{ch}\sigma = 1/M$ que R. LEGENDRE (2) a proposé, il y a déjà plusieurs années, les méthodes hodographiques pour le calcul de grilles d'aubes subsoniques. Plusieurs profils de turbine ont été tracés (3) grâce à l'utilisation des montages rhéoélectriques. Plus récemment ces méthodes ont été programmées sur odrinateur et permettent de calculer des profils de turbine ou de compresseur.

Une première tentative de calcul de profils transsoniques par la méthode de l'hodographe a été faite par F. RIGAUT (4) qui a aussi utilisé les réseaux rhéoélectriques.

L'utilisation des réseaux rhéoélectriques étant très lourde et onéreuse, la SNECMA a entrepris de calculer numériquement les profils transsoniques par la méthode de l'hodographe.

Il est connu que dans les grilles à canal convergent-divergent la quasi totalité de la déviation doit s'effectuer dans la partie subsonique. L'expérience montre qu'il est essentiel d'assurer dans la région du col sonique un écoulement homogène et bien orienté. De cette condition dépend essentiellement le bon fonctionnement de la partie divergente du canal, qui a le rôle d'accélérer l'écoulement en évitant l'apparition des ondes de choc.

Lorsqu'on essaye de traiter ce problème par des méthodes directes en se donnant à priori la géométrie du canal, on s'aperçoit rapidement qu'il est très difficile de fixer une ligne sonique en modifiant la partie subsonique du profil.

On simplifie beaucoup le problème en utilisant la méthode de l'hodographe qui est une méthode inverse. Dans ce cas les données du problème sont :

- l'angle et le nombre de Mach en amont de la grille
- l'angle moyen qu'on doit réaliser sur la ligne sonique pour obtenir l'angle de sortie souhaité
- l'évolution de la vitesse en fonction de son orientation sur l'extrados et l'intrados du profil.

De la dernière donnée dépend la géométrie (et le pas relatif) du profil. Il faut une itération sur ces répartitions pour obtenir un profil réaliste, à savoir bien formé et avec une bonne distribution de l'épaisseur. La dernière condition est importante pour la tenue de la pale et son refroidissement éventuel

Pour faciliter l'estimation du premier hodographe et limiter le nombre d'itérations on peut commencer avec un profil tracé à main levée et qui remplit les conditions géométriques souhaitées, ou encore extrapoler à partir d'un profil calculé en subsonique, c'est-à-dire avec un canal convergent-divergent désamorcé.

Il est évident que la meilleure façon de traiter les grilles transsoniques est de disposer parallèlement à la méthode inverse de l'hodographe, d'une méthode directe, qui tient compte éventuellement de la troisième dimension, comme cela se fait déjà pour le calcul des grilles subsoniques.

Signalons également qu'un avantage non négligeable de la méthode de l'hodographe est son temps de calcul très court. Le calcul d'un profil, y compris le calcul de l'écoulement supersonique par la méthode des caractéristiques est de l'ordre de 3 à 4 minutes sur ordinateur IBM 370/145.

3. METHODE DE L'HODOGRAPHE

3.1. Equations de la méthode de l'hodographe

L'écoulement est considéré plan et irrotationnel, le fluide parfait et compressible.

Les conditions d'irrotationnalité et de conservation de débit :

$$\mathrm{rot}\,\vec{V} = 0 \quad ; \quad \mathrm{div}(\rho \vec{V}) = 0$$

permettent de définir un potentiel de vitesse φ et une fonction de courant ψ :

$$d\varphi = u\,dx + v\,dy$$

$$d\psi = -\rho v\,dx + \rho u\,dy$$

qui avec les relations :

$$dz = dx + i\,dy$$

$$u + iv = V e^{i\theta}$$

conduisent à l'équation :

$$dz = \frac{e^{i\theta}}{V}\left(d\varphi + \frac{i}{\rho}\,d\psi\right) \qquad (1)$$

Dans le second membre de cette équation φ et ψ sont fonctions de deux variables indépendantes : l'intensité de la vitesse et son angle d'orientation.

On pose : $\zeta = \dfrac{e^{i\theta}}{V}$; $\ln\zeta = i\theta - \ln V$

et avec : $-\ln V = \sigma$; $\ln\zeta = \sigma + i\theta$

ou encore : $\zeta = e^{\sigma + i\theta}$

Les équations différentielles de l'hodographe logarithmique, reliant φ et ψ à σ et θ, s'obtiendront en écrivant que le second membre de l'équation (1) est une différentielle exacte :

$$\frac{\partial z}{\partial \sigma} = \zeta\left(\frac{\partial \varphi}{\partial \sigma} + \frac{i}{\rho}\frac{\partial \psi}{\partial \sigma}\right)$$

$$\frac{\partial z}{\partial \theta} = \zeta\left(\frac{\partial \varphi}{\partial \theta} + \frac{i}{\rho}\frac{\partial \psi}{\partial \theta}\right)$$

ρ étant fonction de V, c'est-à-dire de σ.
La dérivation et la séparation en parties réelles et imaginaires conduit au système :

$$\begin{aligned} \frac{\partial \varphi}{\partial \theta} &= -\frac{1}{\rho}\frac{\partial \psi}{\partial \sigma} \\ \frac{\partial \varphi}{\partial \sigma} &= \frac{1}{\rho}\left(1 - \frac{d\ln\rho}{\partial \sigma}\right)\frac{\partial \psi}{\partial \theta} \end{aligned} \qquad (2)$$

La relation entre ρ et σ est obtenue à partir de la loi de Bernoulli-Saint-Venant pour un fluide compressible :

$$\frac{d\ln\rho}{d\sigma} = \frac{e^{-2\sigma}}{a^2} = \frac{V^2}{a^2} = M^2$$

On peut alors écrire le système (2) sous la forme :

$$\begin{aligned} \frac{\partial \varphi}{\partial \theta} &= -\frac{1}{\rho}\frac{\partial \psi}{\partial \sigma} \\ \frac{\partial \varphi}{\partial \sigma} &= \frac{1}{\rho}\left(1 - M^2\right)\frac{\partial \psi}{\partial \theta} \end{aligned} \qquad (3)$$

La variable σ qui est liée au module de la vitesse V par $\sigma = -\ln V$ est la variable utilisée pour les hodographes entièrement subsoniques. Pour l'étude des profils transsoniques il est plus intéressant d'introduire comme variable le nombre de Mach critique ou nombre de Laval :

$$M_c = \frac{V}{a_c}$$

En réalité M_c est équivalent à une vitesse, car la vitesse du son critique a_c est une constante.

Nous remplaçons donc σ par M_c dans les équations précédentes :

$$\frac{\partial\varphi}{\partial\theta} = \frac{M_c}{\rho}\frac{\partial\psi}{\partial M_c}$$

$$\frac{\partial\varphi}{\partial M_c} = -\frac{1-M^2}{\rho M_c}\frac{\partial\psi}{\partial\theta} \qquad (4)$$

La masse volumique ρ et le nombre de Mach réel M étant des fonctions connues de M_c, les équations (4) s'écrivent :

$$\frac{\partial\bar{\varphi}}{\partial\theta} = Q\frac{\partial\bar{\psi}}{\partial M_c}$$

$$\frac{\partial\bar{\varphi}}{\partial M_c} = -P\frac{\partial\bar{\psi}}{\partial\theta} \qquad (5)$$

avec :

$$Q = M_c\left(\frac{1-\mu^2}{1-\mu^2 M_c^2}\right)^{\beta} \; ; \quad P = \frac{1}{M_c}\left(\frac{1-\mu^2}{1-\mu^2 M_c^2}\right)^{\beta}\frac{1-M_c^2}{1-\mu^2 M_c^2}$$

$$\mu^2 = \frac{\gamma-1}{\gamma+1} \; ; \; \beta = \frac{1}{\gamma-1} \; ; \; \bar{\varphi} = \rho_c \cdot \varphi \; ; \; \bar{\psi} = \psi \qquad (6)$$

En éliminant $\bar{\varphi}$ dans ces équations, on trouve l'équation de STEICHEN :

$$L(\psi) = (1-M^2)\frac{\partial^2\psi}{\partial\theta^2} + M_c^2\frac{\partial^2\psi}{\partial M_c^2} + (1+M^2)M_c\frac{\partial\psi}{\partial M_c} = 0 \qquad (7)$$

pour la fonction de courant $\psi(\theta, M_c)$.

3.2. Singularités

La définition de l'écoulement dans une grille et l'image du domaine subsonique dans le plan de l'hodographe sont présentées sur la figure 1.

Le caractère périodique de l'écoulement permet de limiter le domaine d'étude, dans la plan physique, à un canal délimité dans sa partie subsonique par :

- 2 lignes de séparation (de l'infini amont I au point d'arrêt A) parallèles, décalées du pas
- les parties subsoniques de l'extrados (A_o S_o) et de l'intrados (A_1 S_1)
- la ligne sonique (S_o S_1)

Le domaine hodographique correspondant comporte deux singularités :

- une du type source-tourbillon qui est l'image de l'infini amont (I)
- une du type point critique, située sur la ligne sonique (S_c)

La périodicité du champ se traduit par l'application sur les feuillets de Riemann de chaque bande $[M_o \; I \; M_1$ (cf. figure 1)$]$. Ces feuillets sont raccordés par une coupure supportant un saut de la fonction de courant égal à la différence entre les valeurs de ψ sur l'extrados et l'intrados.

Pour simplifier nous supposerons qu'il n'y a pas de recouvrement dans le plan d'hodographe ce qui est le cas, le plus souvent, pour les profils de turbine. Un recouvrement ne représente d'ailleurs une difficulté que pour le calcul numérique.

Examinons d'abord la singularité image de l'infini amont. Celle-ci a été étudiée par M. FENAIN de l'ONERA qui a travaillé sur les méthodes hodographiques des profils d'ailes isolés (6).

A l'infini amont les équations (4) s'écrivent :

$$\begin{aligned} \frac{\partial\varphi}{\partial\theta} &= \frac{M_{c\infty}}{\rho_\infty}\frac{\partial\psi}{\partial M_c} \\ \frac{\partial\varphi}{\partial M_c} &= -\frac{1-M_\infty^2}{\rho_\infty M_{c\infty}}\frac{\partial\psi}{\partial\theta} \end{aligned} \qquad (8)$$

Pour étudier le voisinage du point $M_c = M_{c\infty}$ et $\theta = \theta_\infty$ où nous avons la singularité du type source-tourbillon nous introduisons de nouvelles variables :

$$\begin{aligned} \xi &= \frac{\theta-\theta_\infty}{\sqrt{1-M_\infty^2}} = R\cos\omega \\ \eta &= \frac{M_c-M_{c\infty}}{M_{c\infty}} = R\sin\omega \end{aligned} \qquad (9)$$

R et ω étant des coordonnées polaires définies sur la figure 2.

Ce changement des variables conduit au système :

$$\begin{aligned} \frac{\partial\varphi}{\partial\xi} &= \frac{\sqrt{1-M_\infty^2}}{\rho_\infty}\frac{\partial\psi}{\partial\eta} \\ \frac{\partial\varphi}{\partial\eta} &= -\frac{\sqrt{1-M_\infty^2}}{\rho_\infty}\frac{\partial\psi}{\partial\xi} \end{aligned} \qquad (10)$$

On peut poser maintenant $\tilde{\varphi} = \frac{\rho_\infty}{\sqrt{1-M_\infty^2}}\cdot\varphi$; et $\tilde{\varphi}$ et ψ deviennent solutions, en première approximation, du système de Cauchy :

$$\begin{aligned} \frac{\partial\tilde{\varphi}}{\partial\xi} &= \frac{\partial\psi}{\partial\eta} \\ \frac{\partial\tilde{\varphi}}{\partial\eta} &= -\frac{\partial\psi}{\partial\xi} \end{aligned} \qquad (11)$$

Par conséquent les équations qui relient φ et ψ aux variables ξ et η, c'est-à-dire à θ et M_c sont celles qui déterminent une fonction analytique comme pour l'écoulement d'un fluide incompressible, ce qui montre que la singularité introduite est bien du type source-tourbillon.

En coordonnées polaires $\tilde{\varphi}$ et ψ, qui sont des fonctions harmoniques conjuguées, peuvent s'écrire :

$$\begin{aligned} \psi &= A\omega + B\log R + Cte \\ \tilde{\varphi} &= A\log R - B\omega + Cte \end{aligned} \qquad (12)$$

avec : $$R^2 = \left(\frac{M_c - M_{c\infty}}{M_{c\infty}}\right)^2 + \left(\frac{\theta - \theta_\infty}{\theta_\infty}\right)^2$$

$$tg\,\omega = \frac{M_c - M_{c\infty}}{\theta - \theta_\infty} \; \frac{\sqrt{1-M_\infty^2}}{M_{c\infty}}$$

La condition de périodicité :

$$\int_0^{2\pi} \frac{\partial z}{\partial \omega}\, d\omega = z(2\pi) - z(0) = ih$$

dans laquelle h représente le pas, permet de calculer les constantes A et B.

Ceci permet de définir ψ au voisinage du point I :

$$\psi = \psi_\infty = \rho_\infty V_\infty h \cos\theta_\infty \left[\frac{\omega}{2\pi} - \frac{tg\,\theta_\infty}{2\pi\sqrt{1-M_\infty^2}} \log R + Cte \right] \qquad (13)$$

Pour rendre ψ sans dimension nous divisons par le débit $\Delta\psi$:

$$\psi^* = \frac{\psi}{\Delta\psi} = \frac{\psi}{\rho_\infty V_\infty h \cos\theta_\infty} \qquad (14)$$

de façon que ψ^* prenne les valeurs O et 1 sur le contour de l'hodographe.

Au voisinage de la singularité image de l'infini amont on a alors :

$$\psi^* = \psi^*_\infty = \frac{\omega}{2\pi} - \frac{tg\,\theta_\infty}{2\pi\sqrt{1-M_\infty^2}} \log R + Cte \qquad (15)$$

La singularité col en S_c vient du choix de la fonction $\psi = f(\theta)$ sur la ligne sonique. La nécessité de construire un col conduit à choisir dans la zone transsonique une solution particulière de l'équation de type mixte qui soit une solution-tuyère (7) . Cette solution est trivalente dans le demi plan de l'hodographe ($M_c > 1$) et possède une singularité critique au point col.

Le problème elliptique que nous nous proposons de résoudre est donc bien posé en complétant la donnée de ψ^* sur la frontière, $M_c = 1$, par :

$$\psi^* = f(\theta) = A(\theta - \theta_c)^{1/3} + B \qquad (16)$$

θ_c étant la valeur de l'angle au point col.

3.3. Conditions aux limites

Le problème est de trouver la fonction de courant ψ^* qui satisfait à :

$$L(\psi^*) = (1-M^2)\frac{\partial^2\psi^*}{\partial\theta^2} + M_c^2 \frac{\partial^2\psi^*}{\partial M_c^2} + (1+M^2) M_c \frac{\partial\psi^*}{\partial M_c} = 0$$

avec les conditions aux limites suivantes :

$\psi^* = 0$ sur l'extrados

$\psi^* = 1$ sur l'intrados

$\psi^* = f(\theta)$ sur la ligne sonique

$\Delta\psi^* = 1$ à travers la coupure

On enlève la singularité amont dans tout le plan en utilisant une fonction de courant régularisée ψ_{reg} telle que :

$$\psi^* = \psi_{reg} + \psi_\infty^* \qquad (17)$$

avec :

$$\psi_\infty^* = \frac{\omega}{2\pi} - \frac{tg\,\theta_\infty}{2\pi\sqrt{1-M_\infty^2}} \log R + C \qquad (18)$$

on a :

$$L(\psi_{reg}) = - L(\psi_\infty^*)$$

avec les conditions aux limites :

$\psi_{reg} = 1 - \psi_\infty^*$ sur l'intrados

$\psi_{reg} = - \psi_\infty^*$ sur l'extrados

$\psi_{reg} = f(\theta) - \psi_\infty^*$ sur la ligne sonique

Le rôle de la constante C est le suivant :
Sur la ligne M_c = O de l'hodographe (fig. 1) ψ^* saute de O à 1 au milieu du segment A_o A_1 image du point d'arrêt. On choisit la constante C de manière que ψ_{reg} soit continue sur la frontière.

Nous relions les points I et M (fig. 3) par une droite et nous désignons l'angle polaire de cette droite par ω_A, de sorte que :

pour $\psi^* = 1$: $\omega = \omega_A$; pour $\psi^* = 0$: $\omega = \omega_A - 2\pi$

Ceci permet de définir la constante C et ensuite la fonction de courant à l'infini amont :

$$\psi_\infty^* = \frac{\omega - \omega_A}{2\pi} - \frac{tg\,\theta_\infty}{2\pi\sqrt{1-M_\infty^2}} \log R \qquad (19)$$

ce qui revient à choisir l'origine des ω selon la direction IM.

3.4. Résolution numérique et retour au plan physique

Pour la résolution numérique nous écrivons l'équation de STEICHEN (7) sous la forme :

$$L(\psi_{reg}) = \left[\frac{\partial}{\partial\theta}\left(P\frac{\partial\psi_{reg}}{\partial\theta}\right) + \frac{\partial}{\partial M_c}\left(Q\frac{\partial\psi_{reg}}{\partial M_c}\right)\right] \cdot f(M_c) \qquad (20)$$

dans laquelle P et Q sont définis par les équations (6).

Le coefficient de $\frac{\partial^2\psi_{reg}}{\partial M_c^2}$ étant M_c^2 dans l'équation (7) nous avons :

$$Q \cdot f(M_c) = M_c^2$$

d'où :

$$f(M_c) = \frac{M_c^2}{Q}$$

L'équation à résoudre s'écrit alors :

$$\frac{\partial}{\partial\theta}\left(P\frac{\partial\psi}{\partial\theta}\right) + \frac{\partial}{\partial M_c}\left(Q\frac{\partial\psi}{\partial M_c}\right) = -\frac{Q}{M_c^2}\,L(\psi_\infty^*) = F(M_c, R, \omega) \tag{21}$$

Elle est résolue par la méthode des différences finies en utilisant les techniques classiques de surrelaxation.

Le retour au plan physique se fait par intégration de dz sur le contour de l'hodographe.

Rappelons l'équation (1) :

$$dz = \frac{e^{i\theta}}{V}\left(d\varphi + \frac{i}{\rho}\,d\psi\right)$$

dans laquelle $d\varphi$ et $d\psi$ seront définis à l'aide des équations (5) :

$$\begin{aligned} d\varphi &= \frac{d\bar\varphi}{\rho_c} = \frac{1}{\rho_c}\left(Q\frac{\partial\bar\Psi}{\partial M_c}\,d\theta - P\frac{\partial\bar\Psi}{\partial\theta}\,dM_c\right) \\ d\psi &= d\bar\Psi = \frac{\partial\bar\Psi}{\partial\theta}\,d\theta + \frac{\partial\bar\Psi}{\partial M_c}\,dM_c \end{aligned} \tag{22}$$

Sur l'extrados et l'intrados on a $d\psi = 0$; ce qui donne :

$$\frac{\partial\bar\Psi}{\partial M_c} = -\frac{\partial\bar\Psi}{\partial\theta}\,\frac{d\theta}{dM_c}$$

où $\frac{d\theta}{dM_c}$ est la pente de l'hodographe donné.

On déduit :

$$d\varphi = -\frac{1}{\rho_c}\left[Q\left(\frac{d\theta}{dM_c}\right)^2 + P\right]\frac{\partial\bar\Psi}{\partial\theta}\,dM_c$$

et

$$dz = \frac{e^{i\theta}}{V}\,d\varphi = -\frac{e^{i\theta}}{V\rho_c}\left[Q\left(\frac{d\theta}{dM_c}\right)^2 + P\right]\frac{\partial\bar\Psi}{\partial\theta}\,dM_c = dx + i\,dy$$

En séparant les parties réelles et imaginaires nous déduisons les coordonnées :

$$\begin{aligned} \frac{dx}{h} &= \frac{\rho_\infty}{\rho_c}\,M_{c\infty}\cos\theta_\infty\left[\frac{\partial\psi^*}{\partial M_c}\cos\theta - \frac{\partial\psi^*}{\partial\theta}\sin\theta\right]d\theta \\ \frac{dy}{h} &= \frac{\rho_\infty}{\rho_c}\,M_{c\infty}\cos\theta_\infty\left[\frac{\partial\psi^*}{\partial M_c}\sin\theta + \frac{\partial\psi^*}{\partial\theta}\cos\theta\right]d\theta \end{aligned} \tag{23}$$

4. PARTIE SUPERSONIQUE DU PROFIL

La partie supersonique est calculée de façon à établir un écoulement uniforme et parallèle à la sortie avec une longueur minimale de tuyère.

Le calcul est effectué dans le plan physique par la méthode des caractéristiques. Les données initiales pour ce calcul sont la frontière transsonique et une ligne de courant.

La définition de la frontière transsonique a été traitée de façon détaillée par P. GERMAIN (7) et nous n'en parlerons ici que très succinctement.

La figure 4 présente l'écoulement transsonique au voisinage du col d'une tuyère symétrique et son image dans le plan hodographique. La répartition de ψ étant connue sur la ligne sonique il est possible de calculer l'écoulement jusqu'à la frontière transsonique (problème de Cauchy). En effet si l'on donne les valeurs de ψ et de l'une de ses dérivées le long d'un segment sur la ligne sonique on peut déterminer la solution de l'équation dans un triangle curviligne limité par ce segment et les deux caractéristiques issues du point S_c.

Sur la figure 5 nous avons présenté trois cas différents suivant le choix de la ligne de courant.

Le premier cas est celui d'une tuyère symétrique avec une ligne de courant rectiligne issue du point S_c. Dans ce cas nous avons dans le plan d'hodographe deux triangles caractéristiques limités aux segments S_1 S_c et S_c S_o, S_c étant le point où l'on a affiché la singularité.

On construit les parois de la tuyère de proche en proche à l'aide des caractéristiques à partir d'une distribution de Mach sur une ligne de courant et en respectant la conservation de débit. La tuyère étant symétrique il suffit en fait de calculer une demi-tuyère. La tuyère finit du côté extrados par une partie droite DF_o (cf. fig. 5a) dont la direction est en rapport avec l'angle de sortie souhaité.

Ce type de canal convient bien pour des nombres de Mach de sortie élevés ($M > 2$). On peut obtenir des pertes faibles au point nominal mais inévitablement les pertes augmentent rapidement en fonctionnement partiel.

Les deuxième et troisième cas sont des tuyères dont l'une des parois respectivement extrados ou intrados, est rectiligne (fig. 5b et 5c).

Dans ce cas S_c se place en S_o (ou S_1) et on calcule par le problème de Cauchy tout le triangle caractéristique issu de S_o S_1. On donnera un hodographe à frontière perpendiculaire à la ligne sonique en S_c et une répartition de ψ ayant la singularité col en S_c.

Ce type de canal semble être mieux adapté pour des faibles nombres de Mach ($M < 2$) mais il se désadapte aussi rapidement en fonctionnement partiel.

Un cas plus général est celui où on donne une forme quelconque à l'une des parois. Ce cas est intéressant pour des nombres de Mach faiblement supersoniques ($M \approx 1.3$). On peut définir alors un canal convergent-divergent qui en fonctionnement partiel (nombre de Mach plus faible) ne présente pas de décollement de couche limite.

5. EXEMPLE DE CALCUL

Un profil, calculé à l'aide de cette méthode, est présenté à titre d'exemple (fig. 6). Il a été calculé dans le but de réaliser une grille annulaire destinée à établir un écoulement supersonique devant une grille annulaire fixe d'aubes de compresseur supersoniques ($M = 2$; $\alpha = 45°$). L'extrados après le col a été choisi rectiligne. L'épaisseur du bord de fuite a une valeur très faible pour limiter les sillages devant la grille de compresseur.

Des essais effectués au banc de grille annulaire de l'ONERA (8) ont montré que le profil donne bien les résultats escomptés. Des prises de pression statique sur les parois latérales ont permis de tracer les lignes iso-Mach dans la partie divergente du canal. On constate un écoulement uniforme après le col, et une évolution bien régulière jusqu'à la sortie où on trouve bien le nombre de Mach de 2 en moyenne.

6. REMARQUES - CONCLUSIONS

Les grilles transsoniques qu'on rencontrait jusqu'à maintenant surtout dans les derniers étages des turbines à vapeur, se présentent désormais aussi dans l'étage HP des turbines aéronautiques.

Quoi que le nombre de Mach de sortie de telles turbines n'est pas très élevé (1.2 à 1.4) il parait préférable de dessiner leurs aubages avec un canal convergent-divergent.

Le choix de la méthode de l'hodographe que nous avons fait pour la définition des profils, donne des avantages appréciables du point de vue mathématique. Outre qu'il permet d'utiliser des équations linéaires pour la partie subsonique, il rend également possible le découplage du problème, c'est-à-dire, le traitement séparé des parties subsonique, transsonique et supersonique de l'écoulement.

Le fait que la méthode de l'hodographe est une méthode inverse, est à considérer plutôt comme un avantage car il permet d'optimiser l'évolution de vitesse autour du profil et d'imposer un écoulement uniforme et bien orienté dans la région de la ligne sonique. L'inconvénient d'avoir à choisir à priori l'hodographe peut vite être pallié avec l'expérience acquise en cours d'utilisation.

Un autre inconvénient de cette méthode est le fait qu'elle est bidimensielle. Il est préférable pour cela de l'utiliser conjointement avec une méthode directe qui tient compte de la divergence de la veine. On pourra ainsi définir plus rapidement des aubages optimisés, car contrairement aux méthodes directes qui ont des temps de calcul très longs, la méthode de l'hodographe est rapide.

L'utilisation d'une console graphique facilite davantage son usage. Elle permet aussi de poursuivre plus aisément le dessin de la partie supersonique par la méthode des caractéristiques.

REFERENCES

1. G. KARADIMAS "Increasing the Aerodynamic Loading of Axial Flow Turbines".
   ASME Publication 72 - GT - 78
   San Francisco, March 1972

2. R. LEGENDRE "Calcul d'un profil pour ailette de turbine à partir d'un hodographe"
   La Recherche Aéronautique N° 84 (1961)

3. R. HOUARD et G. KARADIMAS "Catalogue de onze profils pour ailettes de turbines".
   Revue Française des Mécaniciens N° 33 (1970)

4. F. RIGAUT "Détermination analogique de profils d'aile en régime transsonique"
   Groupe mécanique des Fluides de l'AGARD
   Paris, Sept. 1968

5. G. WORMS "Calcul de profils d'aubes de turbine transsoniques par la méthode de l'hodographe"
   Compte-rendu SNECMA YK N° 619 (non publié)

6. M. FENAIN "Méthodes numériques de résolution des problèmes d'écoulement mixte autour de profils.
   N.T. ONERA 4/1285 AN - Juillet 1969

7. P. GERMAIN "Recherches sur une équation du type mixte"
   La recherche Aéronautique N° 22 (1951)

8. G. JANSSENS et J.P. GUYOT "Amorçage des grilles d'aubes supersoniques".
   La Recherche Aérospatiale N° 1973-1

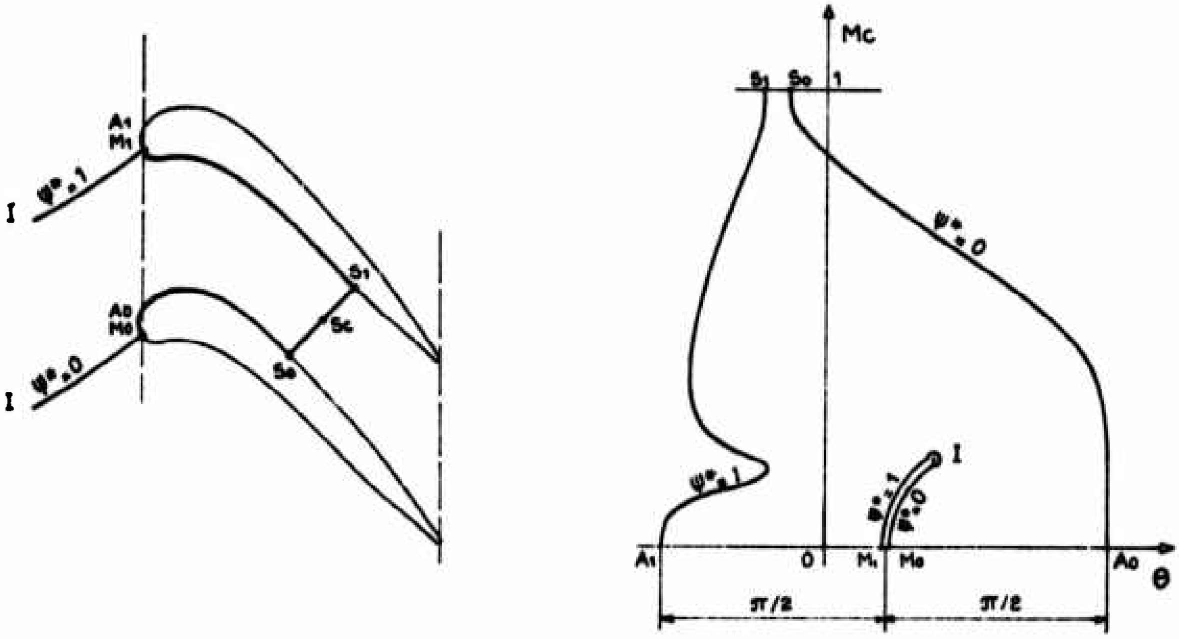
A1
M1
ψ* = 1
I
A0
M0
ψ* = 0
I
S1
Sc
S0
Mc
S1
S0
1
ψ* = 0
ψ* = 1
I
ψ* = 1
ψ* = 0
A1
O
M1
M0
A0
θ
π/2
π/2

1. Ecoulement dans une grille et son image dans le plan de l'hodographe

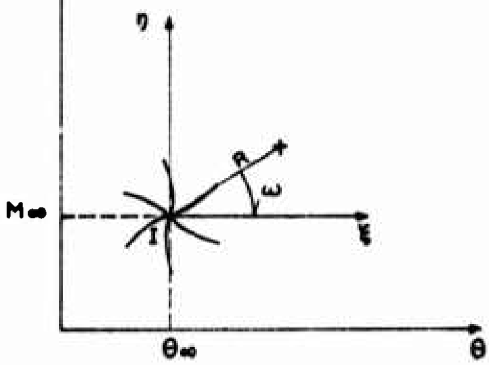
Mc
η
R
ω
M∞
I
ξ
θ∞
θ

2. Singularité infini amont

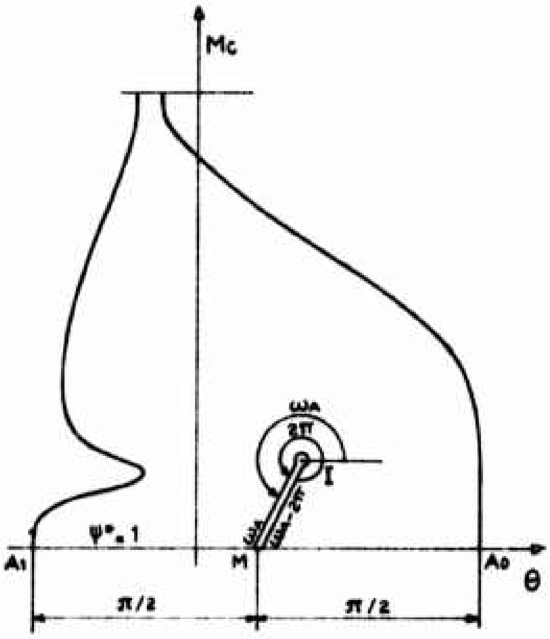
Mc
ωA
2π
I
ψ* = 1
A1
M
A0
θ
π/2
π/2

3. Coupure dans l'hodographe

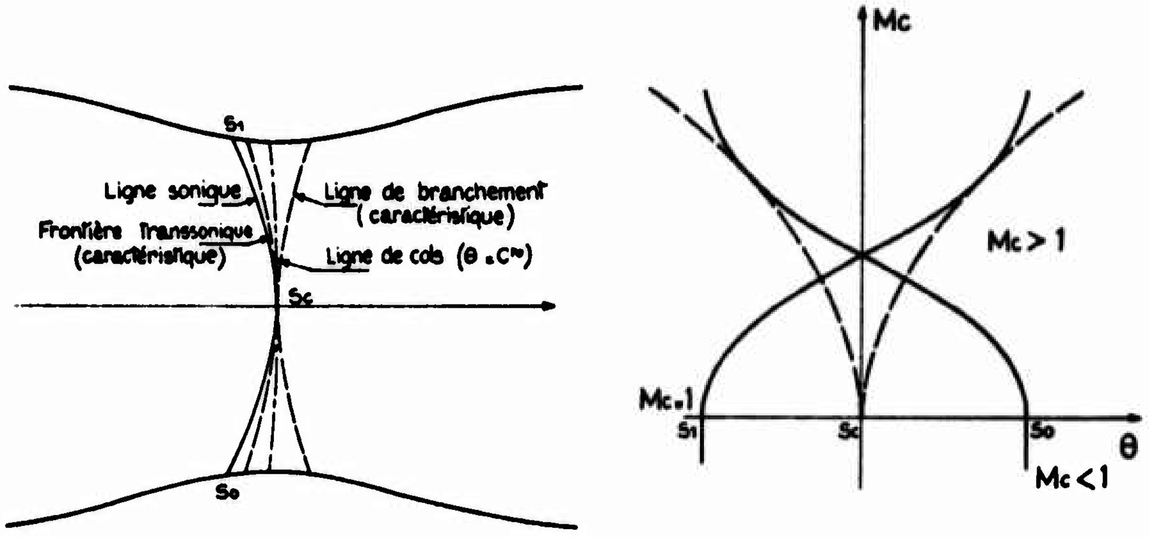
S1
Ligne sonique
Frontière transsonique (caractéristique)
Ligne de branchement (caractéristique)
Ligne de cols (θ = Cte)
Sc
So
Mc
Mc > 1
Mc = 1
S1
Sc
So
θ
Mc < 1

4. Ecoulement transsonique au voisinage du col

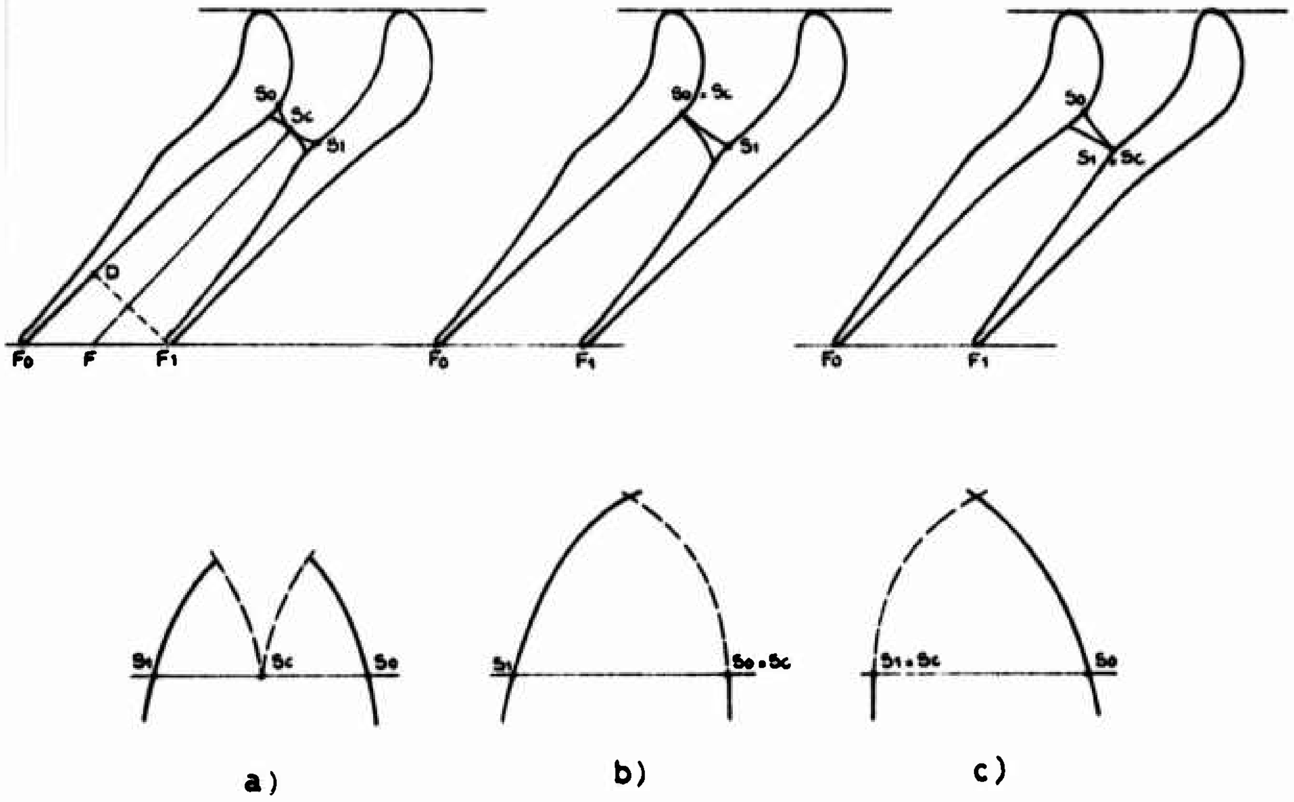
So
Sc
S1
D
Fo
F
F1
So = Sc
S1
Fo
F1
So
S1 = Sc
Fo
F1
S1
Sc
So
S1
So = Sc
S1 = Sc
So
a)
b)
c)

5. Différents types de tuyères convergentes-divergentes

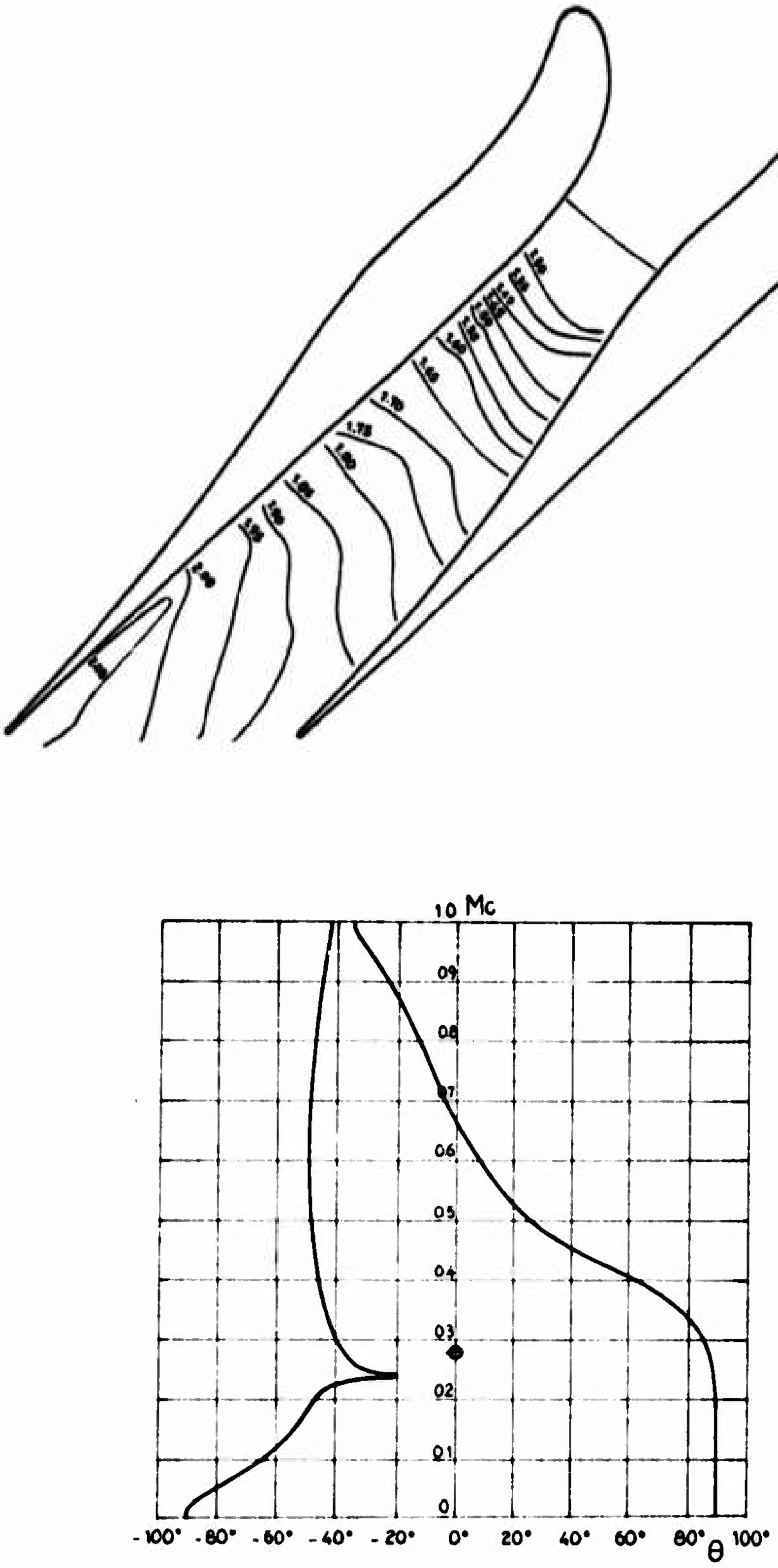

6. Profil et hodographe de distributeur (M = 2)

A STATISTICAL METHOD FOR THE ANALYSIS OF RIG TRAVERSE MEASUREMENTS ON ANNULAR COMBUSTION CHAMBERS.

D.C. Dryburgh

Derby Engine Division, Rolls-Royce (1971) Ltd.

1. Summary.

The method of analysis described gives a very detailed picture of the temperature traverse results obtained by the rig testing of annular combustors. Many new aspects of the temperature distribution are brought out, and the variability from sector to sector plays a central part in the theory. One of the most important traverse parameters is replaced by a more reliable statistical estimate, and tests of significance can be used to assess the results of development changes. The method has been developed as a tool for the combustion engineer and applications of its use and proofs of some of the basic assumptions are included.

2. Introduction.

This paper describes a new method of analysing the exit temperature traverses of annular combustion chambers in a way which makes more effective use of the measured data. The temperature distribution at the chamber exit must be made as flat as possible to permit a high mean temperature, and hence a high thrust, to be achieved without exceeding the limiting peak temperature for the nozzle guide vanes and the turbine blades. For this purpose, chambers are tested in a traverse rig where the operating conditions are well defined and the exit temperature can be measured accurately and in detail. The traverse development programme covers a series of representative operating conditions and many variations on the basic design, since there is no method of predicting the traverse in sufficient detail.

In the past, only three aspects of the traverse have been analysed. The mean radial profile is important because of its effect on the turbine blade life. The temperature distribution in the average sector gives the mean conditions experienced by the HP nozzle guide vanes and yields a wealth of information on the behaviour of the chamber. The peak temperature over the whole traverse gives the extreme conditions for the nozzle guide vanes and the difference between it and the peak of the average sector gives a measure of the sector variability.

Detailed examination of an exit temperature traverse shows that the sectors differ appreciably from each other in many respects. This 'random effect', as it is often called, has been known for a long time. It varies in an unpredictable way from chamber to chamber, and no causative mechanism has yet been found; its magnitude, however, is much greater than can be accounted for simply in terms of manufacturing tolerances. There is thus a powerful incentive to understand and control the random processes as a possible method of improving the traverse quality.

The new method of analysis is based on very simple statistical ideas. The emphasis is placed on the individual sectors, and for each a number of parameters are calculated, representing different aspects of the temperature distribution in that sector. For each parameter, the mean gives the most likely estimate of the sector performance, while the standard deviation gives a measure of the variability between sectors. Statistical projections can be made to give traverse guarantees which apply to all chambers similar to the one tested.

The technique, as described in the following sections, is not limited to the analysis of temperatures, nor to the exit plane of the chamber. It forms a useful framework for relating one parameter, measured in one plane, to a different one in, perhaps, another plane. Complete 360° coverage of the annulus is not needed, although the fewer the sectors available, the greater the range of uncertainty will be. A useful by-product of the analysis is the detection of rogue sectors, i.e. sectors which differ by a large amount, in one or more respects, from the others. Such sectors may be excluded from the analysis, even though it is not always possible to find the cause of the trouble by examining the chamber and the rig equipment.

3. Partitioning of the Traverse.

The first step in the analysis of the traverse is to divide the annulus into sectors, a sector being the smallest geometrical unit which repeats round the chamber. The number of sectors is usually equal to the number of fuel injectors or to half that number. Figure 1 below is a schematic illustration of a partitioned temperature distribution. The separate sectors on the right show the average sector distribution and a typical spacing of the grid on which the temperatures are measured. Some minor practical difficulties can be avoided by choosing the sector boundaries away from the peak temperatures, but apart from this, the location of the boundaries relative to prominent features is not important.

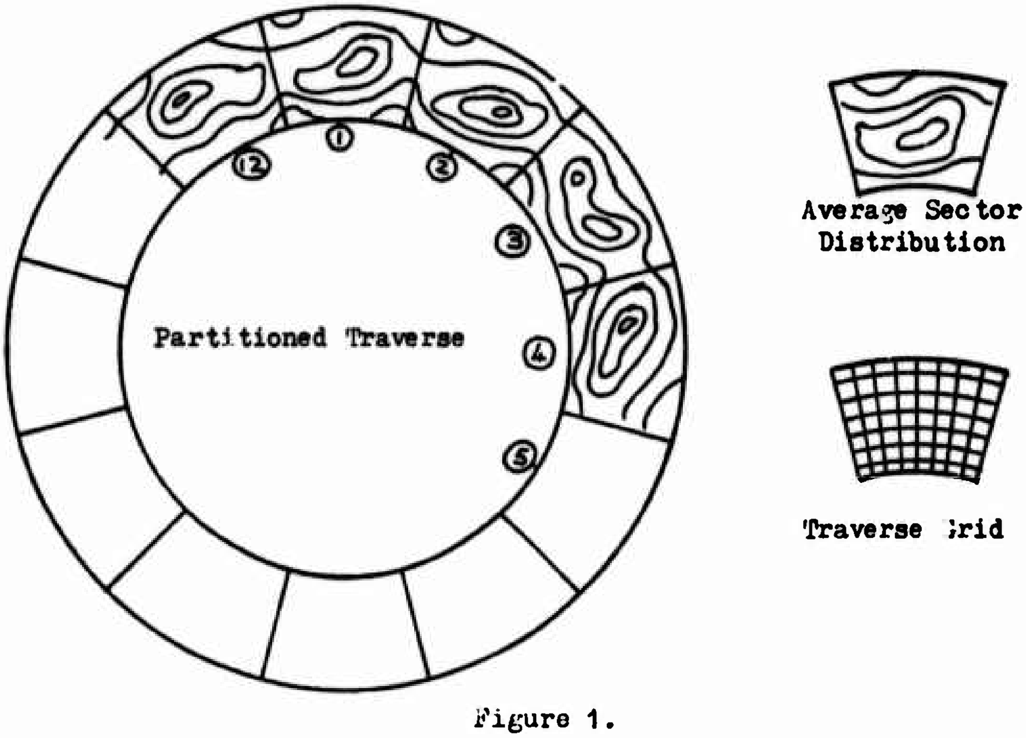

Figure 1.

The annular chambers under development at the Derby Engine Division have 18 fuel injectors giving rise to a traverse with 18 or 36 hot spots. Circumferentially, the spacing of the traverse positions is $2\frac{1}{2}^\circ$, that is 144 points round the annulus and 8 intervals spanning each sector. There are between 6 and 8 radial immersions, depending on the size of the combustor.

On large chambers the ratio of annulus height to mean radius is sufficiently small for equal radial increments to correspond to equal area sampling. Corrections to give true equal area or mass weighting can be applied to the measurements in the partitioned array if desired, before proceeding to the rest of the analysis.

4. x,y, and z Parameters.

A non-dimensional representation of temperature is used to compensate for differences in operating conditions between tests. The z-parameter corresponding to a temperature, T, is defined as

$$z = (T - \bar{T})/(\bar{T} - T_{in})$$

where $\bar{T}$ is the overall mean temperature and T_{in} the inlet value. It has proved very useful to split z into two parts, x and y. x represents the mean rise of the sector while y relates the temperature to this mean:

$$x_k = (T^k - \bar{T})/(\bar{T} - T_{in}) \; : \; y_k = (T - T^k)/(T^k - T_{in})$$

T^k is the mean of sector k. When corresponding temperatures of different sectors are compared, we can see how much of the difference is due to a shift in the sector mean and how much to a change relative to the mean. The difference between the y and z representations is a subtle one and it may be helpful to think of y as being z corrected for the difference between the sector mean rise and the overall mean rise. This notation is applied to individual temperatures in the sector, for example the peak temperature or that at the (i,j) point, and to averages such as the mean at radius i. Those which have been found most useful are defined in Appendix 1.

Since y and z are alternative ways of expressing the same temperature they are not independent. An algebraic relation between x, y and z is obtained in Appendix 2 and some other expressions are deduced. It is shown that the means of y and z, taken over all sectors, are, for all practical purposes, equal: the standard deviations however, depend on whether the y or z form is used.

The first step in the analysis is to obtain the x,y and z values for each sector and then to calculate the means and standard deviations. The quantities which summarise the traverse are $\bar{y}$ (or $\bar{z}$), the mean peak, and σ_x, σ_y and σ_z which express various aspects of the random variability. In the next section the relation to the conventional traverse parameters will be studied in greater depth.

The Pattern Deviation Factor, d, has been introduced quite recently and is defined in Appendix 1. It expresses the difference between the temperature distribution in each sector and the average sector, but, whereas y only looks at the peak, d takes account of the whole sector. It is always positive and sectors with low values have a temperature pattern similar to that of the average sector, while those with high values can be flatter than average, more peaked, or perhaps just peaked in a different place. The mean of d, or, preferably, its root mean square value, is a useful measure of the degree of variability of the whole traverse about the average sector distribution.

5. The Relation Between the New and the Conventional Traverse Quality Parameters.

The Overall Temperature Distribution Factor (OTDF).

This parameter, also known as the Pattern Factor, is the one most in need of reformulation. It is simply z_{max} corresponding to the highest sector peak and is the most commonly quoted of all the quality parameters. It has never been regarded as satisfactory to rely on a single extreme measurement in a situation with so much variability, and now z_{max} has been replaced by a statistical projection based on all the sector peaks. The new parameter, the OTDF(50), gives a value,

z_{50}, which will be greater than z_{max} on 50% of a series of traverses on the same or similar combustors. An OTDF(95) can also be quoted.

There are two possible ways of deriving the OTDF(50): the first is an estimate based on the sector peaks, while the other takes the peak value from an array of estimates.

Method 1.

Here we consider the sector peaks $\hat{z}_k$ which are assumed to follow a Normal probability distribution (this is justified in Appendix 3). On Figure 2 below, the top curve, labelled N = 1, gives the probability that a single sector peak, chosen at random, will be less than the abcissa, z. The other two curves, labelled N = 9 and N = 18, are the Nth powers of the first and they show the probability that every one of a sample of N peaks, chosen at random, will be less than z.

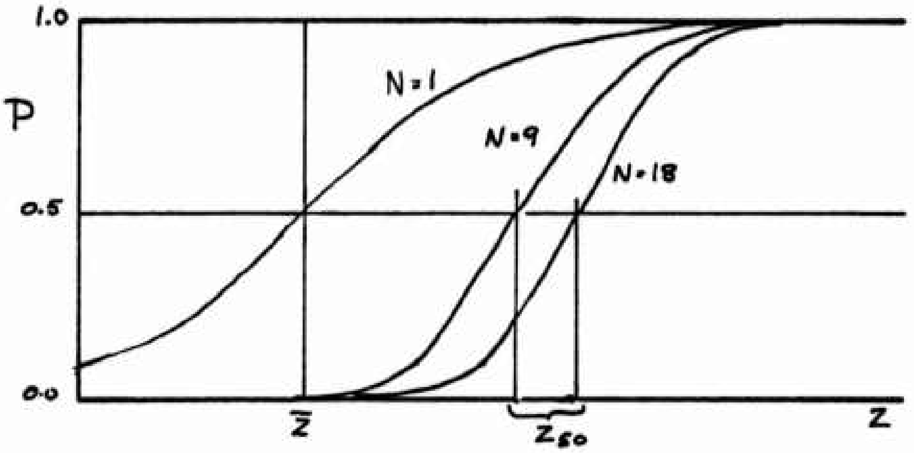

Figure 2.

These curves can be expressed in the form $z(P,N) = z + a(P,N)\ \sigma_z$ where there is a probability P that all of a random sample of N will be less than z(P,N). Tables of the coefficients a(P,N) are easily constructed.

Method 2.

Here, instead of working with sector peaks, we apply the same reasoning to each point of the sector and produce an array corresponding to the chosen probability level:

$$z_{ij}(P,N) = z_{ij} + a(P,N)\ \sigma_{z,ij}$$

Finally the peak value is taken.

In general the two methods give similar results but they will only be identical if all the sector peaks have the same position in the sector. There is a danger in the first method that, if the peaks lie on or near the sector boundaries, temperatures from the neighbourhood of a dominant peak will be counted twice and hence the OTDF(50) will not be based on an unbiased distribution. In such circumstances, the second method is preferred.

In practice, the OTDF(50) has proved to be a stable estimate and it shows much less variation than z_{max} when a series of traverses of similar chambers are compared. A meaningful estimate of the OTDF(50) can still be made with only partial coverage of the annulus, though with rather greater uncertainty. Conversely, subject to the conditions described later in Section 7 being satisfied, the results from a number of traverses can be combined to give an enhanced precision for the OTDF(50).

Mean Radial Profile.

The radial profile for each sector is obtained and averaged to give an overall mean for the whole chamber. This two-step process enables the uniformity of the sectors to be checked since it is possible to obtain an acceptable overall profile from widely varying sector ones. The difference between y and z parameter representations for the individual sectors is illustrated in Table 1 below, which is for a typical traverse with $\sigma_x = 5.25\%$.

Rad (i)	1	2	3	4	5	6	7	8
y_i (%)	-14.27	-1.10	4.33	7.27	9.41	9.40	3.26	-18.32
z_i (%)	-14.18	-1.03	4.32	7.19	9.32	9.34	3.25	-18.21
$\sigma_{y,i}$ (%)	6.26	3.82	2.57	2.67	2.65	2.60	3.50	8.41
$\sigma_{z,i}$ (%)	8.69	7.39	5.80	4.52	4.23	4.98	6.30	10.35

Table 1.

The increased scatter in the z formulation is due to the inclusion of the x variability. Guarantees for the radial profile should thus be based on σ_z, but σ_y gives a more sensitive test for changes between traverses.

The radial profile is often summarised by quoting the peak value (RTDF) and its position. In the table above it is 9.41% at about 60% height.

Mean Sector Distribution.

This array is usually expressed in y-parameter form, though numerically $y_{ij} = z_{ij}$. The peak value is the Block Temperature Distribution Factor (BTDF) and the difference between this and RTDF is sometimes called the 'regular' variation. The BTDF is normally less than $\bar{z}$, the mean peak, though the two are equal if all the sector peaks occur at the same point of the sector. Too large a difference between them indicates poor control over the position of the sector peaks, perhaps as a result of aerodynamic factors. The relation between changes in the chamber geometry and in the mean sector pattern yields much practical information on the internal combustion mechanisms and is invaluable in the development of the traverse.

6. Detection of Rogue Sectors.

Occasionally one or more of the x, y, z or d parameters are found to lie well away from the mean. The Student's t-Test can be used to find the probability that such a value could arise by chance in a sample of N drawn at random from a Normal population. A low probability suggests that some other factors have influenced these sectors, and that they should be excluded from the analysis. The chamber and the test unit should always be examined and, in crucial cases, a repeat test may be necessary. Some defects, such as blocked fuel injectors, may affect more than one sector.

If the kth sector is suspect on the basis of, say, $\hat{y}$, t is evaluated as

$$t = (\hat{y}_k - \bar{y})/\sigma_y$$

and the associated probability can be found from tables of Student's t for N-1 degrees of freedom, which can be found in any standard textbook on statistics. The test may be made rather more sensitive by recalculating the mean and standard deviation without the dubious sectors.

7. Comparison of Traverses.

The statistical method of analysis has many advantages when changes in the traverse results come to be assessed. Each aspect of the temperature distribution can be examined in turn to see whether there is a significant difference, a probable difference, or no likely difference. Each traverse test is regarded as giving a random sample of the various parameters, x, y, z and d, drawn from parent populations characteristic of each chamber, and the problem is to establish whether the difference in the sample means and standard deviations reflects a real change in the populations. The F-test for the variance ratio gives the probability that the population standard deviation has changed, while the Student's t-test obtains the corresponding probability for a shift in the mean. Most textbooks on statistics contain instructions on how to apply both tests and the tables needed to interpret the results.

A high probability in either test points to a real difference between the traverses. The more sectors there are in each sample, the more sensitive the tests are and the smaller the value of F or t required for a given level of significance. When a number of tests carried out on similar chambers are found not to differ appreciably in any of their aspects, the results can be aggregated to give a single large sample which can then be used for further, more sensitive comparisons. In this way a datum standard of traverse for a particular design of chamber can be established with a high degree of precision.

The importance of changes in the average sector pattern has already been pointed out, and the differences can be highlighted in a number of ways. The simplest is to express each array in y-parameter form and subtract to show which areas have become hotter and which colder. Alternatively the differences can be expressed as an array of Student's t values by using the standard deviations $\sigma_{y,ij}$ associated with each point of the sector. This can produce a rather different picture, especially if there are high standard deviations in places like the cooling films, and lower values elsewhere. A strict interpretation of the Student's t array in terms of significance levels should not be attempted because neighbouring points cannot be regarded as statistically independent, but nevertheless this array can be used to show where the more important changes in the sector distribution, if any, have occurred.

The preceding description of the new technique has included many references to the results that can be produced for single traverses, and any attempt to pursue these topics further would lead to a detailed account of the development of a particular chamber, a subject which has already been covered briefly at this Symposium in the paper by Wassell and Bradley(1). Two rather different applications of the method will be sketched out, the first showing how the effects of the test unit and other associated equipment can be isolated from the results, and the second describing some numerical experiments on the variation of the circumferential sampling interval.

8. Example 1: the Isolation of Constant Features.

In a development programme the same chamber will normally be tested a number of times at differing operating conditions and with geometrical modifications. If each traverse is compared with the previous one, certain strong resemblances are found. The correlation coefficient between the x arrays is very high, often exceeding 0.9, for the z arrays it is slightly lower, while for the y's it drops to 0.5 or 0.6. It is not surprising that the x arrays should agree so well, for they depend on the total amounts of fuel and air finding their way into the sector. y depends much more on the way in which the fuel and air are distributed within the sector and may well be the target for development modifications. If each new traverse is compared with the original one, it is found that, with time, the correlations decrease. Figure 3 has been produced to illustrate this effect on a chamber which had a particularly long development history. Each traverse test has been allocated an age, and two tests carried out one after the other at, perhaps, different

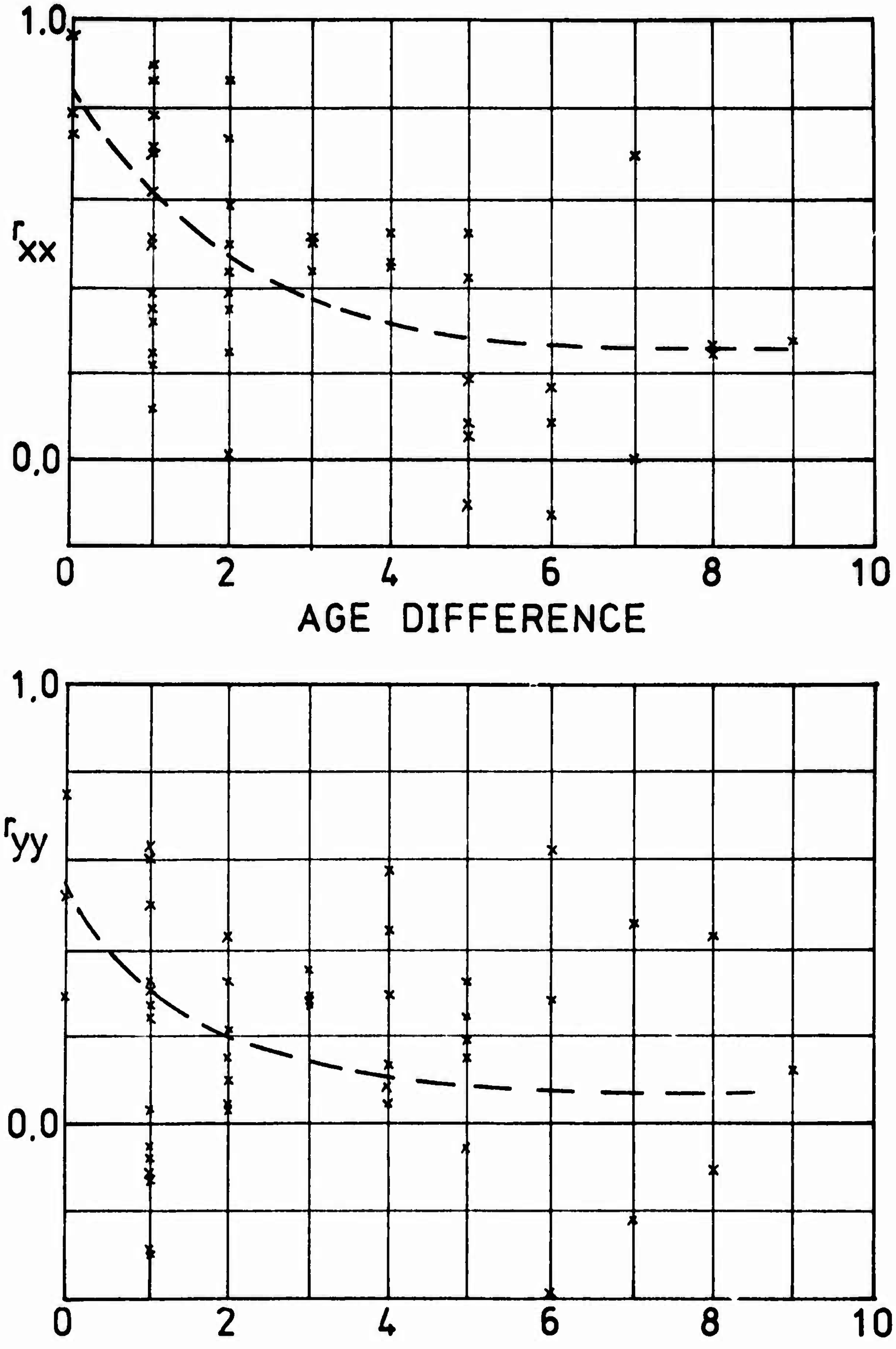

Figure 3. Decay of xx and yy correlations with interval between tests.

temperature rises or pressures, have the same age. Tests are compared in pairs and r_{xx} and r_{yy} are the correlation coefficients between the two x arrays and the two y arrays. The abcissa in Figure 3 is the age difference. The decay of both correlation coefficients is very obvious, with r_{xx} tending asymptotically towards 0.3 and r_{yy} tending more rapidly to zero. Similar behaviour is demonstrated by other chambers, and may indicate long-term changes in the characteristics of the chamber due, perhaps, to a combination of exposure to high temperatures, reworking to change the port geometry, and the strains of installing the chamber in a tightly fitting test unit.

These results open up other avenues of exploration. The asymptotic value of 0.3 for r_{xx} might not be due to the chamber at all, but could have its origin in some permanent feature of the test stand, the fuel injectors or the traverse thermocouples. It is our practice to replace thermocouples singly as they fail and they seldom occupy constant positions in the traverse gear so that any thermocouple effect would rapidly average out over a number of tests. Burner sets are changed less frequently, but they are checked prior to each test and are always installed in the same positions. An estimate of any permanent features could be made by averaging over a large number of tests covering as many different chambers, sets of fuel injectors and thermocouples as possible. What we would be left with is everything that has not changed in the series of tests. This residue could be treated as a correction to be applied to all the tests and comparison of the corrected traverses could show up differences which were previously indetectable. Other types of test series can be considered to extract the effects of the test unit and the fuel injectors: these would require clocking the chamber round in the test unit one sector at a time, and interchanging the fuel injectors according to a pattern.

Traversing on this scale will be expensive but it may become necessary if the contribution of the chamber on its own is no longer the dominant random effect. Suppose, for example, that $\sigma_x = 5.6\%$, and that the effects of the chamber and test unit are uncorrelated and equal: each will be 4% $(5.6 = \sqrt{(4^2 + 4^2)})$. If the chamber contribution is halved to 2%, the measured value will only fall to $\sqrt{(4^2 + 2^2)} = 4.5\%$. The effect of greatest interest is masked by the other variables.

9. Example 2: Variation of the Circumferential Sampling Interval.

The greater the angular interval between adjacent points, the greater is the risk of missing some of the sector peaks, though possibly they could be restored by an interpolation procedure. Questions of the trade-off between the test time saved and the loss of information have been studied by a simulation procedure.

A special method of 'interpolation' was used for this investigation and its rather unconventional properties will first be described. A Fourier method was adopted because it was thought that the periodic properties derived from the whole annulus would give the most accurate method of restoring the sector peaks lying between the traverse points. It exploits the Fast Fourier Transform technique which has made possible the rapid and accurate determination of all the Fourier coefficients of a large array. Each radius is treated in turn.

To increase the number of points round the annulus from, say 72 to 144, the 72 Fourier coefficients are obtained covering all frequencies up to 36. A further 72 zero coefficients are added to give 144 in all, and the expanded series is inverted to give a traverse of 144 equally spaced points. The first, and every second point thereafter, will be one of the original 72, apart from small computer rounding errors, and the resulting curve will pass through all the original points.

To decrease the number of points from, say, 144 to 108, the proced-

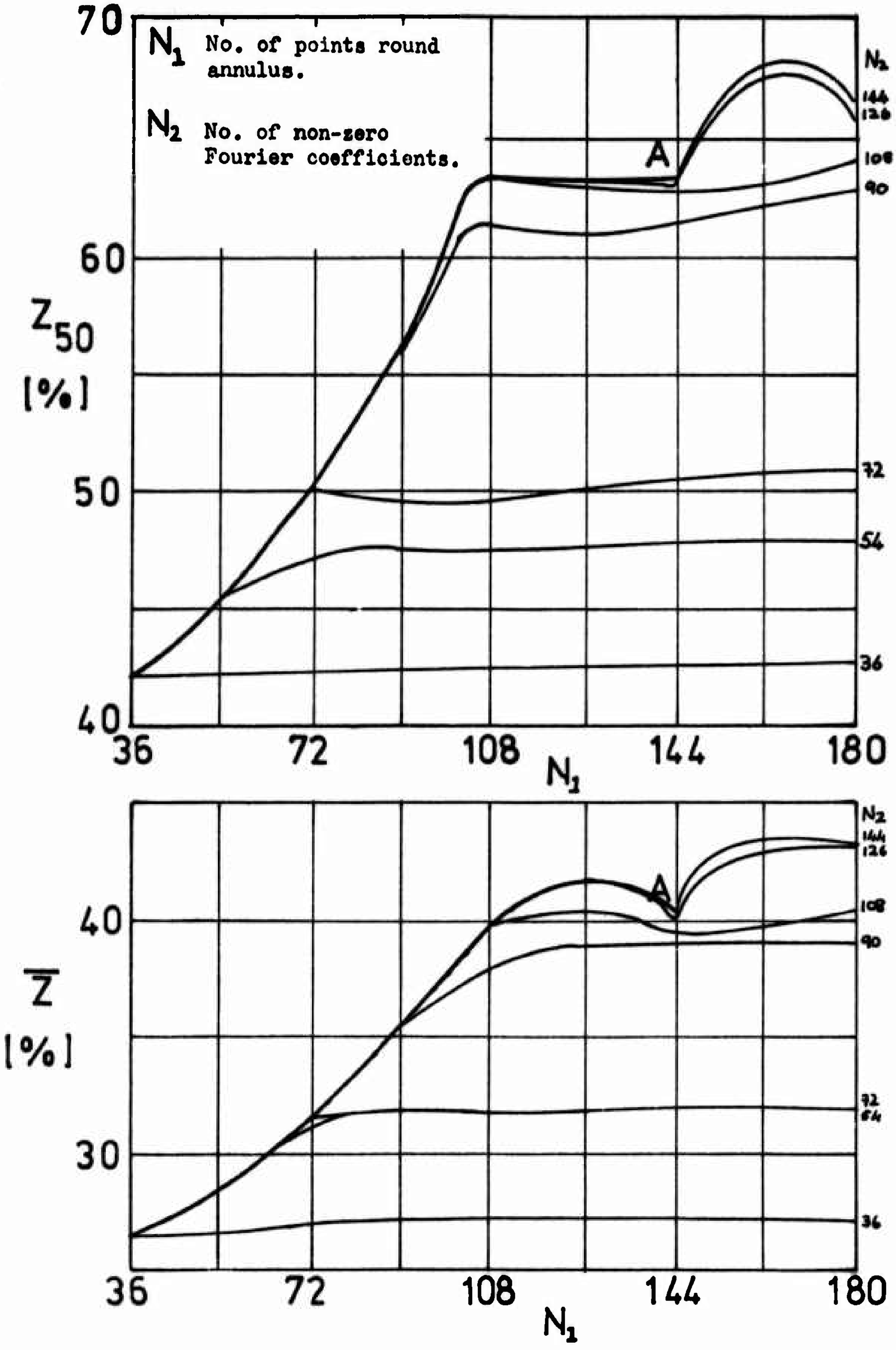

Figure 4. Effect of interpolation procedure on OTDF(50) and mean peak.

ure is similar but the result a little different. The 36 highest order Fourier coefficients are discarded before inversion. The new curve is a least squares fit to the 144 original points but will not in general pass through any except the first. There is a loss of information when the number of points is decreased and this cannot be regained by interpolating back to the original number.

For the numerical experiments to investigate the consequences of the interpolation technique, a rather poor quality 144 point traverse was chosen. Figure 4 shows the effect on the OTDF(50) and the mean peak, $\bar{z}$, as the number of points round the annulus is decreased. The point A indicates the initial values of both parameters and the heavy curve shows that both decrease as the number of circumferential points decreases from 144 in steps of 18 to 36. The lighter curves running to the right show the effect of subsequently increasing the number of points again. There is a certain amount of statistical noise on these curves and small deviations should be disregarded. Initially, the OTDF(50) and $\bar{z}$ are 63.4% and 40.3% at the point A. At 72 points these have fallen to 50.0% and 31.5% and if we then interpolate back to 144 points they are only slightly changed to 50.3% and 30.8%.

Figure 4 shows that the number of circumferential points could be decreased to about 108 (an angular spacing of 3.33°) without sacrificing too much accuracy, but beyond this point both parameters decrease rapidly, and most of the fine structure has been lost by 72 points.

An interesting consequence of this result is that, if a traverse is measured on an engine where a small interval is impracticable, the traverse will always appear to be better than on the rig. To give a fair comparison, the information content of the rig traverse should first be reduced by interpolating to the engine spacing.

Another possible use for this interpolation technique arises when the traverse gear cannot conveniently give an integral number of points round each sector. For example, if the combustor has 20 sectors but the traverse gear can only index round in increments of $2\frac{1}{2}^{\circ}$, the 144 point traverse can be interpolated to 140 or 160 points before analysis.

10. Conclusions.

This completes the present account of the new method of analysis and of some of its applications. It was developed from the start as a practical tool for the combustion engineer and its ultimate success will depend on the extent to which it manages to sweep aside the veil of mystery which surrounds so many aspects of combustion chamber behaviour.

The concept of the OTDF(50) has proved itself in practice as a stable criterion of chamber performance, and the added ability to detect and eliminate rogue sectors further improves the consistency of the estimate. It must be stressed however, that, if rogue sectors occur too often, corrective action should be taken in the manufacturing process or in the traverse procedure to prevent a high incidence of such sectors in service combustors.

The many new aspects of the traverse exposed for inspection and the availability of tests of significance for changes in these parameters make it rather more difficult for the development engineer to be misled by insignificant changes in traverse quality. The introduction of parameters measuring traverse variability makes it possible for its reduction to become one of the stated objectives of a traverse development programme.

Most of our experience with the new method has been gained on annular chambers under development at the Derby Engine Division of Rolls-

Royce (1971) Ltd. The evolutionary nature of their design leads to a strong family resemblance in some aspects of their behaviour. A few chambers of radically different design have been analysed and there are indications that these traverses behave in a rather different way. The application, to different designs of combustor, of standard methods of measurement and analysis of rig traverse data would be a most revealing exercise and would enable the advantages and disadvantages of the different types to be compared. This might not lead immediately to a combustor incorporating all the best features, but it could lead to the formulation of the correct questions and to the design of the correct experiments to discriminate between rival design practices.

From the computational point of view, the combustion chamber is the Cinderella of the gas turbine. The internal processes are much less amenable to calculation than are those in turbomachinery, and a fluid-mechanical model of a practical combustor is still a long way into the future. Such a model would only describe the average sector and would tell us nothing about the random effects.

Traversing is likely to become more important as the combustion engineer rises to the challenges of even higher performance and the legislative controls on emissions. There will be pressure for more refined interpretation of the results; traverses of different parameters and in different planes will have to be considered together, to build the necessary picture of the combustor. The techniques described here should enable a start to be made on these problems.

Finally, it must be remembered that traverse analysis is not a static art. Like all other topics in the interpretation of experimental data, it tries to answer the questions asked of it. As the questions change, so will the methods of analysis.

11. Acknowledgements.

The permission of Rolls-Royce (1971) Ltd to present this paper is gratefully acknowledged. Many members of the Combustion Department of the Derby Engine Division have contributed to the development of the method and their interest and encouragement has been indispensable. The contents of this paper and the opinions expressed are the sole responsibility of the author.

12. References.

1). WASSEL, A.B. and BRADLEY, J.E. The Development of an Advanced Annular Combustor for Civil Application. Paper 37, Second International Symposium on Air Breathing Engines, March 1974.

2). PEARSON, E.S. and HARTLEY, H.O. Biometrika Tables for Statisticians, Vol. 1. Cambridge University Press, 1966.

Appendix 1. Notation and definition of parameters.

The parameters required in the method are introduced in their logical sequence. In many cases the meaning will be obvious from the definition but all the important ones are described in the main text.

T_{in}	inlet temperature.
T^k_{ij}	traverse parameter measured at i,j point of sector k.
i	radial index.
j	circumferential index within sector.
$\bar{\bar{T}}$	mean exit temperature over whole traverse.

Sector parameters.

T^k		mean of T^k_{ij} over sector k.
$\hat{T}^k$		peak value of T^k_{ij} over sector k.
x_k	$\dfrac{T^k - \bar{T}}{\bar{T} - T_{in}}$	non-dimensional parameter for sector mean rise.
$\hat{y}_k$	$\dfrac{\hat{T}^k - T^k}{T^k - T_{in}}$	non-dimensional representation of peak temperature in sector k.
$\hat{z}_k$	$\dfrac{\hat{T}^k - \bar{T}}{\bar{T} - T_{in}}$	alternative non-dimensional representation of peak temperature in sector k.
σ_x		standard deviation of x_k about mean $\bar{x}$ ($\bar{x} = 0$ by definition).
$\bar{y}, \sigma_y$		mean and standard deviation of $\hat{y}_k$.
$\bar{z}, \sigma_z$		mean and standard deviation of $\hat{z}_k$.

Average sector distribution.

y^k_{ij}	$\dfrac{T^k_{ij} - T^k}{T^k - T_{in}}$	non-dimensional representation of individual traverse measurement.
z^k_{ij}	$\dfrac{T^k_{ij} - \bar{T}}{\bar{T} - T_{in}}$	alternative non-dimensional representation.
y_{ij}, z_{ij}		mean of y^k_{ij} (z^k_{ij}) taken over all sectors: refers to i,j, point of average sector.
$\sigma_{y,ij}, \sigma_{z,ij}$		corresponding standard deviations at i,j point.
$z_{max,ij}$		maximum value of z^k_{ij} found at i,j point of all sectors.
d_k		sector pattern deviation parameter - the root-mean-square difference between the kth sector temperature distribution y^k_{ij}, and the mean sector distribution, y_{ij}. $d_k^2 = \sum_{i=1}^{N_i} \sum_{j=1}^{N_j} \left(y^k_{ij} - y_{ij}\right)^2 \Big/ N_i N_j$
$\bar{d}, \sigma_d$		mean and standard deviation of d_k.

Appendix 2. Relations Between the x, y and z Parameters.

The required relation follows immediately from the definition of these quantities in Appendix 1. It may be written

$$(1 + z) = (1 + x)(1 + y) \quad \text{or as}$$

$$z = x + y + xy$$

Two further expressions can be obtained from the second equation, one between the means of z and y (the mean of x is zero, by definition) and the other between the standard deviations.

By averaging over the N sectors we obtain

$$\frac{1}{N}\sum z = \frac{1}{N}\sum x + \frac{1}{N}\sum y + \frac{1}{N}\sum xy$$

or $$\bar{z} = \bar{x} + \bar{y} + \sum xy/N$$

and it should be noted that $\bar{x} = 0$ by definition. The final term on the right can be written

$$\frac{1}{N}\sum x(y - \bar{y}) = \frac{N-1}{N} r_{xy}\, \sigma_x\, \sigma_y$$

where r_{xy} is the correlation coefficient between the x,y arrays. Thus

$$\bar{z} = \bar{y} + \frac{N-1}{N} r_{xy}\, \sigma_x\, \sigma_y$$

In a typical case, $y = 0.40$, $N = 18$, $\sigma_x = 0.05$, $\sigma_y = 0.10$ and r_{xy} is limited to the range -1 to +1 by definition. Thus the second term on the right is always small compared with the first, and for all practical purposes we can take $\bar{z} = \bar{y}$. Assuming this result, the second form of the basic relation can be written

$$z - \bar{z} = y - \bar{y} + x(1 + y)$$

and by squaring and averaging over the sectors a further expression for the standard deviations can be obtained:

$$\frac{1}{N-1}\sum (z-\bar{z})^2 = \frac{1}{N-1}\sum (y-\bar{y})^2 + \frac{1}{N-1}\sum x^2(1+y)^2 + \frac{2}{N-1}\sum x(1+y)(y-\bar{y})$$

or $$\sigma_z^2 = \sigma_y^2 + \frac{1}{N-1}\sum x^2(1+\bar{y}+y-\bar{y})^2 + \frac{2}{N-1}\sum x(1+\bar{y}+y-\bar{y})(y-\bar{y})$$

When the last two terms on the right are expanded, only terms of the second order in x, $y - y$ need be retained as all the other terms are much smaller. Thus

$$\sigma_z^2 = \sigma_y^2 + (1+\bar{y})^2\sigma_x^2 + 2r_{xy}(1+\bar{y})\,\sigma_x\,\sigma_y + \text{terms of third and higher order in } x,\ y - \bar{y}.$$

At the two extremes, $r_{xy} = \pm 1$ and so $\sigma_z = |\sigma_y \pm (1 + \bar{y})\sigma_x|$

Appendix 3. Tests for a Normal Distribution.

The Normal distribution plays such an essential part in statistical applications, and so many of the common tests are based on it, that it is usually taken for granted. The calculation of the OTDF estimates will be sensitive to the shape of the distribution near the extremes and so it is important to establish how well the x, y, z and d parameters obey the Normal law. It would be possible though time-consuming and laborious to work with an empirical distribution.

There are a number of standard tests to show whether the members of a sample could have been drawn from a Normal distribution, but most of them require a large sample while we usually have 18 or less. One test which can be used, is based on the ratio of the mean to the standard deviation: for any array, say, z, we calculate a_z

$$a_z = \frac{1}{N}\sum |z - \bar{z}| \Bigg/ \sqrt{\frac{1}{N}\sum (z - \bar{z})^2}$$

Tables of the significance levels for sample sizes down to 11 are published in the Biometrika Tables for Statisticians.(2)

This test has been applied to 15 assorted rig traverses, all with 18 sectors, and Table 2 below summarises the results.

Parameter	x	y	z	d	N-distr
Mean of'a'	0.8021	0.8082	0.7982	0.7939	0.8096
St dev.of'a'	0.0659	0.0481	0.0696	0.0694	0.0473
No. in upper/lower 10%	4	3	4	7	3

Table 2. Test for Normal distribution.

x, y, and z appear to conform well to the Normal distribution though d is more doubtful. Its mean & standard deviations are not very different from z, but a large proportion of the results lie in the wings of the 'a' distribution.

As a special test of the z-distribution, the observed OTDF, z_{max} has been compared with the predicted OTDF(50), z_{50}, for these 15 rig traverses. Since each has a different value of z_{max} and z_{50}, the parameter 'a' has been deduced from the expression

$$z_{max} = \bar{z} + a\sigma_z$$

and compared with the value 1.778 based on the normal distribution for 18 sectors. The mean of the 15 estimates of 'a' was 2.05, with a standard deviation of 0.609 and is in poor agreement with the expected value. However, on 5 of the traverses the peak sector was found to be a rogue. Using the next hottest peak and recalculating $\bar{z}$, σ_z, gave a revised mean of 1.720 for 'a' and a standard deviation of 0.272. This is acceptably near 1.778 and gives further confirmation of the Normality of the z-distribution and of the validity of the OTDF concept.

OPTICAL TEMPERATURE MEASUREMENTS IN A CONTINUOUS FLOW COMBUSTION CHAMBER

A. Coghe, U. Ghezzi, S. Pasini

Istituto di Macchine, Politecnico di Milano, Italy

1. INTRODUCTION

Many reasons suggest to employ, at least from a theoretical point of view, optical methods for temperature measurements in gas turbine combustion chambers. First of all, in the highest temperature zones, the use of more traditional methods (for instance thermocouples) becomes problematic both for realization and meaning of results, owing to remarkable corrections needed and not well known corrective factors. Second, probe introduction may perturbate the phenomena inside the combustion chamber; moreover, the own inertia of the measuring system impeds to follow with sufficient precision swiftly variable situations.

In the present paper are examined the possibilities of employing the optical method of line reversal for temperature measurements inside a gas turbine combustion chamber. The obtained measures are naturally mean values along certain optical paths; it is then necessary to apply to auxiliary systems of investigation, for instance thermocouples, if the local values are desired. Optical methods require available transparent windows, perfect optical alignments (peculiar for the precision of measurements), practical solutions for test repeatability, and so on. All these circumstances bring to the conclusion that the measure obtained is affected by a certain number of errors; for some of them the entity can be evaluated with good precision, but for the others there is only the possibility of knowing their interval of variation.

2. MEANING OF TEMPERATURE IN GAS TURBINE COMBUSTION CHAMBERS

In this paper a discussion will not be risen whether inside a combustor the different temperatures (of vibrational, translational, rotational, or electronic nature) are coincident, thus deriving a meaning for the concept of temperature as an index of a certain equilibrium situation; this will be taken as an assumption, verified in the average. The work is rather concerned with the examination of the temperature field inside the combustion chamber and particularly with the temperature behavior versus space and time.

Fuel is injected into the primary zone as a spray, mixes with air and burns: combustion occurs according to not well clarified modalities. One theory states each drop of fuel burns singularly with a diffusion flame; another theory says more drops, or even the whole spray, concur to form a diffusive flame front. This second alternative seems to agree better with experimental results. It is anyway clear that a frozen situation in the primary zone, at a certain instant, will show very sharp local temperature gradients, implying therefore a problematic definition of a significative temperature. Besides that, the situation does not keep locally stationary, because turbulence and mixing phenomena make local conditions function of time too.

The so-called secondary zone sees fuel drops almost completely burned, also if oxidation reactions of unburned hydrocarbons (like oxidation of CO to CO_2) still take place. In such a region, very sharp local temperature gradients are not expected, also if local conditions cannot be assumed stationary; hence, punctual temperature values should not be considered constant.

What above said makes clear that the meaning of the term temperature, in situations analogous to those before illustrated, depends mainly upon the modalities followed while measuring or, at least, upon the criteria adopted for the interpretation of results. If the system were in fact stationary and uniform, ambiguity for temperature definition could not exist, on condition that a correct measuring device was adopted; on the contrary, for the system under examination, the knowledge of an unequivocal temperature value would require a device able to feel very strong gradients (whose dimensions were therefore infinitesimal) and with a very small inertia: device which is not available at present (at least for the temperature levels concerned with this work).

Usually, for gas turbine combustion chambers, local temperature values can be obtained either by measurements with thermocouples or by an energetic balance from local compositions. In the primary zone it is clear that thermocouples give only mean spatial temperature values, because big gradients can be found within dimensions comparable with their diameter; moreover, their thermal inertia is with no doubt an obstacle if very swift local fluctuations should be followed. On the other hand, also when temperature measurements obtained through a thermal balance from gas samples are considered, it becomes evident that a mean value, both spatial and temporal, is the only available, because of the relatively large quantity of sample needed for a meaningful analysis (in respect of dimensions for which a change in conditions may become significative), and the time required for gas sampling. In fact, following this procedure, temperature measurements in combustion zones brought to values lower than those logically expected in primary zones, also in relation to chemical compounds here formed (for instance NO); the incongruity can be solved by considering measures as basically mean temperatures, not responsable for many of the phenomena involved. The situation improves a little in the secondary zone of dilution, both for the lower thermal levels and the smaller temperature gradients here found. Apart these considerations, the introduction of sampling probes perturbates remarkably the phenomenon, mainly in zones of larger gradients.

At this point it should be asked whether an optical method, like the one presented, may improve the reliability of results and when its application may be justifiable. The main characteristic of the line reversal method is the capability of giving only temperature values averaged along certain optical paths (assumed an uniform seeding). As a consequence, even under the most favorable conditions, the method cannot take directly into account the temperature gradients encountered inside combustors. The system is on the contrary able to feel, with no perturbations, also the highest temperature zones, through the contribute they give to the total radiancy emitted by the flame. Therefore, if the seeding atoms can be assumed uniformly distributed, the assumption follows the mean temperature measured is the true value, within the limits of errors and experimental uncertainties. In relation to the capability to follow very fast fluctuations, the method must be said much better than others based on probes introduction. It should be emphasized, however, instantaneous values are related to conditions of certain spatial regions, thus being indicative of sources of macroscopic and not local fluctuations.

3.1 EXPERIMENTAL DEVICE

The experimental device, including the combustion chamber with its air and fuel feeding systems, has been illustrated in previous papers (see Ref (1), (2), and (3)). Here are shown only the schematical map of the plant (see Fig (1)) and some constructive details of the combustion chamber (see Fig (2)). Fig (2) shows also the seeding injection system of a sodium solution, essential for the optical measurements. The external wall of the combustion chamber was transparent (Pyrex as material), to allow the optical measurements for all the positions determined by the liner holes center-lines.

Tests were run at different air/fuel ratios (AFR = 70, 90, 110, and 130), with a fuel mass flow rate equal to 3 g/s (kerosene as fuel) and an air flow at atmospheric pressure.

3.2 OPTICAL MEASUREMENTS

Temperature measurements inside the combustion chamber were obtained following optical methods based on the analysis of emission and absorption of radiations from the combustion gases. Plank's and Kirchhoff's laws are employed; their validity requires equilibrium conditions, independently of the chemical or phisical nature of the radiant emitters. Moreover, emitters are assumed in thermal equilibrium with flame gases, deriving from that their electronic population obeys Boltzmann's distribution and equilibrium among electronic and translational states exists. These conditions are better verified if, instead of the whole radiation emitted by the hot gases, only a monochromatic radiation (corresponding to the resonance line given by the transition from an exited state to the fundamental one) is considered. Combustion gases do not present always resonance lines, but the obstacle is easily overcome by introducing from the outside an opportune seeding, producing thermically excitable atoms. Among resonance lines, the most used one is the sodium D-line, because populations of alcaline metals atomic levels assume easily Boltzmann's distribution and equilibrium condition with combustion gases. For the present work, a sodium chloride solution (containing 400 ppm of sodium) was sucked by capillarity and injected into the combustion chamber by a secondary flow of air with a very low mass flow rate (about 10 l/min). Atomization was by air-blast.

The optical-electronic apparatus used for temperature measurements is schematically shown in Fig (3). A tungsten strip filament lamp with a quartz window (G.E.C. 20 A/ 6 V) was used as a reference standard. The image of the tungsten filament was focused on the flame through lens L_1 and then on the slot of the monochromator by lens L_2, giving a one to one magnification. Lens L_2 was stopped down by diaphragm D to ensure the monochromator (Hilger-Watts D-330 equipped with a 1200 lines/mm grating blazed for 5000 Å) receives the radiancy R_g emitted by gas and the filament lamp radiancy R_s, under the same solid angle. A slit large 0.02 mm and high 2mm gave a precise determination of the region of the flame analyzed.

Hot gases temperature measurements were both by sodium D-line reversal method and by the same technique modified to allow rapid measurements, with a temporal resolution around one hundredth of second. The line reversal method requires manual regulation of the current of the lamp until, by a trial and error method, the following condition is achieved:

$$R_s(\lambda,T) = R_{s+g}(\lambda,T) \qquad (1)$$

where:

$$R_{s+g}(\lambda,T) = (1 - \alpha_g)\, R_s(\lambda,T) + \varepsilon_g\, R_g(\lambda,T) \qquad (2)$$

being:

$\alpha_g = \alpha_g(\lambda,T)$ = gas absorptivity for incident radiation at wavelength λ and temperature T

$\varepsilon_g = \varepsilon_g(\lambda,T)$ = gas emissivity at the same conditions.

In equilibrium conditions can be used the Kirchhoff's law:

$$\varepsilon_g(\lambda,T) = \alpha_g(\lambda,T) \qquad (3)$$

eq (1) gives therefore:

$$R_g = R_s \qquad (4)$$

and

$$T_g = T_s^b \qquad (5)$$

where:

T_g = true gas temperature

T_s^b = black body brightness strip lamp temperature at λ.

Namely, the background monochromatic intensity, at match, equals that of a black body at gas temperature. The lamp calibration curve gives the temperature T_s^b versus the feeding current. The insertion of a standard resistor type Reinchsanstolt (resistance: 0.01 ohm; uncertainty of the value: 0.001%), in series with the lamp, allowed an accurate determination of the current by measuring the potential difference across the resistance by a digital voltmeter. The lamp was calibrated by comparison with a monochromatic electronic pyrometer at the Institute of Metrology "G. Colonnetti" of Turin.

The line reversal is a null method (hence very simple and accurate), but each measurement requires a long time, during which gas conditions must be kept constant. Actually, a great number of high frequency casual fluctuations characterize the radiancy emitted by hot gases and low frequency oscillations may be caused by the own pulsations of the system. The photomultiplier converts luminous signals into current, but does not change sensibly the characteristics; therefore, to determine the point of reversal ($R_s = R_{s+g}$) an integration of the signal is needed for a given time. For the present work the time was chosen equal to 1 sec.

It is however extremely interesting to analyze continuously the temperature behavior in a combustion chamber for times sensibly less longer than one second. A simple method was developed, based on the assumption the variation law of the standard lamp radiancy R_s versus the feeding current i can, with good approximation, be considered linear on a logarithmic scale, at least within the temperature interval tested (1800 to 2200 °K). An analogous relationship, valid in the same temperature interval, has been found experimentally for the total radiancy R_{s+g} versus the current. At this point, once drawn the straight line representing R_s, it becomes evident the possibility to draw also the line relative to R_{s+g}, close to the expected point of reversal, by the determination of only two points (see Fig (4)). These points were obtained by keeping constant the lamp current (at the value i_1) and by employing a slightly modified chopper, presenting one window completely transparent (transmissivity $\tau = 1$) to the lamp radiation and the other with a transmissivity $\tau = \tau_o < 1$ (usually a chopper is employed as a shutter, inserted between the standard lamp and the flame). Practically, the following procedure was adopted: before, the line corresponding to $R^o_s(i)$ was drawn from experimental points by varying the current i, with no lenses and combustion chamber; then, a second line $R_s(i)$ was drawn in operative conditions, with lens L_1 and the entrance chamber window alone, to determine the transmissivity τ_1, utilized to correct the measures, as it will be explained later on; at last, the line relative to $R_{s+g}(i)$ was determined by two points obtained in corrispondence to $\tau_1 \cdot R^o_s(i_1)$ and $\tau_0 \cdot \tau_1 \cdot R^o_s(i_1)$, where $R^o_s(i_1)$ is the prefixed value of the lamp radiancy.

A continuous registration of the signals was made by a photoregistrator and allowed not only instantaneous temperature values, but also the temperature behavior in function of time, the amplitude of oscillations, and the indetermination of the single measurements. In Fig (5) a typical behavior of R_{s+g} corresponding to $\tau_1 \cdot R^o_s(i_1)$ and $\tau_0 \cdot \tau_1 \cdot R^o_s(i_1)$ is shown, as it appeared on an oscilloscope: for a certain step, each couple of values allows to determine, by interpolation, the flame temperature, averaged for a time interval defined by the angular velocity of the chopper.

3.3 MEASUREMENTS BY THERMOCOUPLES

Temperature measurements by thermocouples were obtained by employing Pt/Pt-10%Rh thermocouples, accomplished as shown in Fig (6). No way was tried to shield the hot junction to reduce radiation, nor a forced suction was created to augment the heat transfer coefficient. The thermocouple support was mounted in such a manner to move radially inside the liner of the combustion chamber. The different positions of the hot junction gave therefore the temperature profile.

4.1 ANALYSIS OF EXPERIMENTAL RESULTS

The basic problem to be solved for the interpretation of the results is evidently the evaluation of the errors of the entire system. As well known, the line reversal method is mainly based on flame application of Planck's and Kirchhoff's laws. Naturally such laws are verified in thermodynamic equilibrium conditions; for real cases this circumstance may not be verified, also if the differences involved (at least for the experimental conditions of the present work) do not usually cause big temperature errors. Following this point of view, the major cause of error should be given to the non-radiant equilibrium, which induces a depopulation of the excited states; but for flames at atmospheric pressure (being the collisional effects the main ones) only an error equal to few degrees is observed. When the seeding atoms can be supposed homogeneously distributed, also if the temperature profile is not uniform, the measured temperature can be assumed, if local equilibrium conditions are ensured, the mean value along the optical path interested by the beam. Difficulties for the interpretation of results may arise when the seeding atoms can not be assumed uniformly distributed; in fact, zones at different temperatures would be considered with different weights and therefore the mean value would become altered. For the present work, the injection system ensured a sufficiently uniform seeding distribution. The seeding injector was experimentally proved by adopting different configurations (particularly by varying the injector position); an absence of differences in the signal was considered enough to prove a good distribution of the injected substance.

At any rate, it seems the main source of errors, for the system employed, should be the radiation, which crosses absorbing and diffusing media (independently from Kirchhoff's law), as lenses and transparent walls of the combustion chamber. It should be then taken into account the flame too can absorb and spread independently from the presence of the seeding; moreover, the flame can behave in different ways in respect of the lamp light or the flame light emitted on the same wavelength of the lamp (radiation due to the seeding). The phenomenon is better explained by referring to Fig (7), which reproduces schematically the test system. α_1 and α_3 are the absorptivities (o) of optical components, before and after the flame; α_g is the absorptivity and ε_g the emissivity of gas, due to sodium atoms; α_2 is the absorptivity of R_s, when no sodium is present; radiancy R_g of gas is subjected to an auto-absorptivity $\overline{\alpha}_2$. All these magnitudes are referred to the operative wavelength λ. In reversal conditions, for eq (1) and (2), the lamp radiancy absorbed by the gas is equal to its radiancy, and therefore:

$$\alpha_g\cdot(1-\alpha_1)\cdot(1-\alpha_2)\cdot R_s = \varepsilon_g\cdot(1-\overline{\alpha}_2)\cdot R_g \qquad (6)$$

for eq (3) it follows:

$$\frac{R_s}{R_g} = \frac{1-\overline{\alpha}_2}{(1-\alpha_1)\cdot(1-\alpha_2)} \qquad (7)$$

To achieve the flame temperature it is therefore necessary to know (besides naturally R_s) also α_1, α_2, and $\overline{\alpha}_2$. The values of α_1 and α_2 can be experimentally determined while calibrating; thus their errors are known too. On the contrary, $\overline{\alpha}_2$ is not as easy to determine, from a quantitative point of

(o) Absorptivity refers here to phenomena reducing radiation intensity, without specifying any nature.

view; therefore, only the maximum possible error due to flame absorptivity can be determined. Eq (7) says that, if $\alpha_2 = \overline{\alpha}_2$, the presence of absorptivity does not introduce errors for the temperature evaluation. Errors are then depending upon the possible difference between $\overline{\alpha}_2$ and α_2; hence the convenience to calculate the maximum span. Evidently, this difference is due to the fact that while the whole radiation of the lamp crosses the flame (naturally less by the factor $(1 - \alpha_1)$), the flame radiation is emitted along the flame itself and therefore the radiation absorptivity decreases as decreases the flame thickness to be crossed. A certain temperature distribution would give the possibility to calculate the value of $\overline{\alpha}_2$; but mainly here the maximum possible error is searched and this procedure will thus not be followed (also because not easily verifiable hypotheses should be introduced).

First of all, it will be shown that $\alpha_2 > \overline{\alpha}_2$. In fact, it would be $\alpha_2 = \overline{\alpha}_2$ in the extreme hypothesis of the seeding atoms concentrated in that part of the flame opposite to the monochromator (and then the whole flame radiation would cross the flame). If the seeding substance were on the contrary completely in that part of the flame facing the monochromator, the flame radiation could reach it with no absorptivity by the flame itself; thus it would result $\overline{\alpha}_2 = 0$. Being therefore $0 \leqslant \overline{\alpha}_2 \leqslant \alpha_2$, the maximum and minimum values of the error will be known. The minimum value is found when $\alpha_2 = \overline{\alpha}_2$, so eq (7) becomes:

$$\frac{R_s}{R_g} = \frac{1}{1 - \alpha_1} \qquad (8)$$

while the maximum value correspondes to $\overline{\alpha}_2 = 0$, and therefore:

$$\frac{R_s}{R_g} = \frac{1}{(1 - \alpha_1)\cdot(1 - \alpha_2)} \ . \qquad (9)$$

Because $(1 - \overline{\alpha}_2) \geqslant (1 - \alpha_1)$, it comes from eq (7) that $R_s > R_g$; thus, in reversal conditions, the lamp temperature is higher than the flame temperature.

4.2 EXPERIMENTAL RESULTS

Temperature measurements by line reversal method were taken along the optical paths corresponding to positions 1 through 12 of Fig (8). As it can be seen, positions 5 through 8 correspond to measurements taken along the major diameter and are the most significative ones, mainly if compared to thermocouples measurements. Along optical paths not crossing the liner center-line (positions 1 through 4 and 9 through 12) were taken other measurements only as a verification. Values of τ_1 and τ_2 maximum and minimum found during tests are given in Tab (I). As already said, it has been evaluated only the maximum error due the difference of τ_2 from $\overline{\tau}_2$. Such an error, while calibrating, varied from 10 to 100 °K. As far as τ_2 is concerned, its variation was from 40 to about 140 °K, dependingly upon the position (it is clear the necessity to calibrate at each position, because of the different behaviors in relation to the optical paths considered). The minimum correction to be introduced, owing to the evaluation of τ_1 and τ_2, were within the interval 30 to 140 °K, while the maximum ones which take into account that $\tau_2 \neq \bar{\tau}_2$), were from 40 to 220 °K.

The interpretation of the experimental results is related to the temperature field in which the line reversal method is meaningful. To accomplish optical measurements atoms should be present in an excited state, namely sodium atoms in the electronic condition 3^2p (from which radiates the D-resonance line). If a Boltzmann's distribution can be hypotesized, it can be shown that at 3000 °K only a fraction of sodium atoms (about 10^{-3}) is in an excited state and therefore can emit; on the contrary, at 1500 °K this fraction abates to about 10^{-7}. Experience shows that, for the seeding concentrations normally used (and also here employed), such a percentage of excited atoms is not enough to be detected by an electronic instrumentation like the one here used (o). In fact, with a seeding of 1000 ppm, 10^{-4} excited atoms per million will be found, that is a ratio of particle present to atoms excited equal to 10^{10}. It can therefore be assumed the mean temperature is referred only to that zone (among those crossed by the optical beam) where temperature is higher than 1500 °K. However, at this temperature level, measurements by thermocouples are very reliable and so particular problems are not expected.

Tab (II) shows, as an example, the results of the measurements taken in correspondence to positions 5 through 8 and for the only value AFR = 90; besides the measured values T_M are also given the temperature values corrected by the maximum (T_{MAX}) and minimum (T_{MIN}) errors. As it can be seen, for position 5 a measurement by the line reversal method was not allowed, owing to the low temperature level of the zone, as the temperature profile obtained by thermocouples and shown (not corrected) in Fig (9) can confirm.

A mean temperature measurement, already very meaningful if taken alone, may become of higher utility if coupled to local measurements by thermocouples. In the present work, radial temperature profiles were taken by thermocouples of the kind before illustrated, for numerous stations (including stations 5 through 8), corresponding to different cross sections of the combustion chamber. Optical measurements, together with

---

(o) For instance, by employing photon counting techniques, the above limit could be lessen much more, but problems would arise for the interpretation of results, because much longer observation times are required.

measurements taken by thermocouples, allowed to achieve the (true) local temperature profile. The procedure followed is very simple and is here briefly recalled.

By hypothesis, the error due to conduction through the thermocouple wiring (calculated around 20 to 30 °K) will be neglected and the radiation will be toward the absolute zero; therefore, if T_g is the true temperature of gas and T_p the temperature given by the thermocouple, it follows:

$$h \cdot (T_g - T_p) = \sigma \cdot \varepsilon_p \cdot T_p{}^4 \qquad (10)$$

where:

h = heat transfer coefficient between gas and thermocouple

σ = Stefan-Boltzmann constant

ε_p = thermocouple emissivity;

from eq (10) it comes:

$$T_g = \frac{\sigma \cdot \varepsilon p}{h} T_p{}^4 + T_p. \qquad (11)$$

But along a certain optical path the mean value of T_g (which is a function of the radius r) is known (see for instance Tab (II)), so:

$$\int T_g \, dr = \int \left(\frac{\sigma \cdot \varepsilon p}{h} T_p{}^4 + T_p\right) dr = \overline{T_g}. \qquad (12)$$

Eq (12) makes clear that, being known both $\overline{T_g}$ (which for the calculations was assumed equal to the average between T_{MAX} and T_{MIN}) and T_p (given by thermocouples as a function of the radius r), the behavior of the group $(\sigma \cdot \varepsilon_p/h)$ versus the radius r can be calculated and so eq (11) will give the punctual value of T_g. Searching for an approximate solution and assuming $(\sigma \cdot \varepsilon_p/h)$ is about constant along a diameter, eq (12) will give:

$$\overline{T_g} = \left(\frac{\sigma \cdot \varepsilon p}{h}\right) \overline{T_p{}^4} + \overline{T_p} \qquad (13)$$

which allows a very easy calculation of $(\sigma \cdot \varepsilon_p/h)$. The value of the group $(\sigma \cdot \varepsilon_p/h)$ was found, for the cases here considered, comprised between $3.5 \; 10^{-11}$ and $4.5 \; 10^{-11}$ $°K^{-3}$.

Fig (10) through (15) show temperature profiles taken by thermocouples. The profiles of Fig (11) through (15) were corrected by means of factor $(\sigma \cdot \varepsilon_p/h)$ calculated as said; also interpolated values were used for intermediate positions. For the temperature values of Fig (10), corrections were not introduced because considered not very meaningful (at least from the point of view of optical measurements), owing to the remarkable asymmetry of the temperature profile, caused by the presence of the ignitor. As soon as the ignition zone is left, the graphs show that the temperature profiles become symmetrical again.

As it was said, very fast temperature measurements were taken too (with a period very close to one hundredth of second), to allow both the evaluation of the mean fluctuations of temperature and an idea of the period of the fluctuations themselves. It is clear that an optical measurement gives only a resultant signal sum of the behavior of single points which are on the optical path considered, but nevertheless the informations available are very interesting. As far as the fluctuations of the signal are concerned, it was already observed their amplitude is about 20% of the mean value of the signal (± 10% around it; see Fig (5)). Remembering the exponential relationship between temperature and signal, the fluctuations of the mean temperature value stay within 2%. The conclusion may therefore be drawn the mean temperature value keeps constant in time and fluctuations are much less important than how may be expected at first sight.

In relation to the period of oscillation, a low frequency oscillation (with period around 0.5 sec) was observed, attributable to the responce of the feeding line, to which oscillations at much higher frequency are superposed. As above said, measurements were taken at intervals around one hundredth of second; the registration of the signal showed the oscillation period is much less than the interval between two subsequent measurements.

This paper will not deepen into the study of connections between period and intensity of the fluctuations, and the behavior of the system, also if it seems intuitive that interesting informations may be drawn from such an analysis. A research program in this direction is anyway under development at the Institute of Machine of the Polytechnic of Milan. The main purpose of this work was in fact to emphasize the extreme sensibility of the optical method to explain the characteristics of the mean fluctuations, related to absorption and emission of a radiation.

5. CONCLUSIONS

The application of the line reversal method to combustion chambers allows to determine mean temperatures with a margin of error around few tens of degrees; in fact, with an accurate calibration of the system, quite a precise analysis of errors is possible, also if, under certain aspects, it is a laborious one. The utility of the system is more appreciated in the higher temperature field, where simpler methods, like for instance those based on thermocouples, show deep uncertainties. Moreover, the method is particularly suitable for the evaluation of temperature fluctuations along the optical paths considered and for an analysis of the oscillation period.

On the other hand, the method is rather complicated to set in, expecially for systems not to be tested in laboratory, such for instance real scale gas turbine burners, requiring in fact the employment of quite a sophisticated instrumentation, a good optical alignment, absence of vibrations, the predisposition of a seeding system, and transparent windows (or transparent walls, as for the present case). This last requisite sometimes makes difficult a realization; besides, the optical windows may change while testing their transmissivity (for instance, because of dirt deposit which may form), varying as a consequence the calibration of the system, which should therefore be repeated frequently. It must then be remembered that the measurements obtained are the mean ones along certain optical paths, thus a limitation for the informations available directly.

At last, by coupling this system to punctual measurements by thermocouples, the temperature profiles can be known with good approximation. From this it appears that the method can be utilized as a calibration system for thermocouples working under particularly unfavorable conditions. Its application as a routine method is in fact rather onerous, as it was previously said, if measurements affected by controlled errors are to be taken.

6. REFERENCES

1. U. Ghezzi, et alii. An experimental research on the behavior of a continuous flow combustion chamber. Agard meeting on atmospheric pollution. London, April 1973.
2. S. Pasini, et alii. Un impianto per lo studio sperimentale della combustione a flusso continuo. Internal Report of C.N.R. (National Research Council), 1972.
3. A. Coghe, et alii. Nota sulla misura di temperatura in fiamme mediante termocoppie. XXVIII Congresso Nazionale A.T.I., Torino, September 1973.
4. A. Moutet. Méthode de mesure et d'enregistrement rapide des températures des flammes. La Recherche Aéronautique, no 27 and 28, 1952.
5. G. W. Bauserman, et alii. Determination of transient flame temperatures. The Review of Scient. Instr., vol 25, no 7, July 1954.
6. J. G. Closton, et alii. Temperature measurements of shock waves by the spectrum line reversal method. Nature, vol 248, p 429, December 1958.

$\tau_{1\ \mathrm{MIN}} = 0.3$
$\tau_{1\ \mathrm{MAX}} = 0.7$

$\tau_{2\ \mathrm{MIN}} = 0.5$
$\tau_{2\ \mathrm{MAX}} = 0.7$

Tab (I)

POS	STA	T_M	T_{MAX}	T_{MIN}
5	A	--	--	--
5/6	B	2300	2080	2160
6/7	D	2140	1960	2090
8	G	2190	2000	2140

Tab (II)

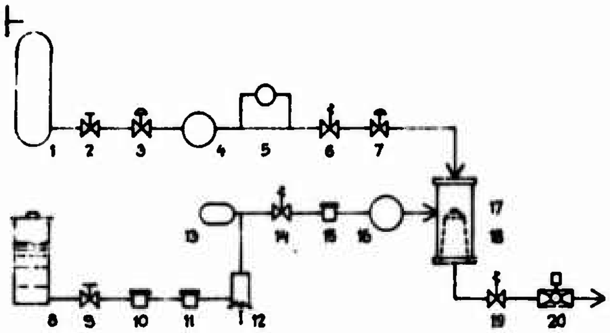
1
2
3
4
5
6
7
8
9
10
11
12
13
14
15
16
17
18
19
20

1 AIR PRESSURE TANK
2 MANUAL VALVE
3 PRESSURE REDUCING VALVE
4 AIR FLOW METER
5 AIR DENSITY METER
6 SAFETY VALVE
7 AUXILIARY VALVE
8 FUEL TANK
9 MANUAL VALVE
10 COARSE STRAINER
11 FINE STRAINER
12 PLUNGER-TYPE FUEL PUMP
13 HYDRAULIC COMPENSATOR
14 SAFETY VALVE
15 COARSE STRAINER
16 FUEL FLOW METER
17 FUEL INJECTOR
18 COMBUSTION CHAMBER
19 SAFETY VALVE
20 BUTTERFLY VALVE

FIG (1)

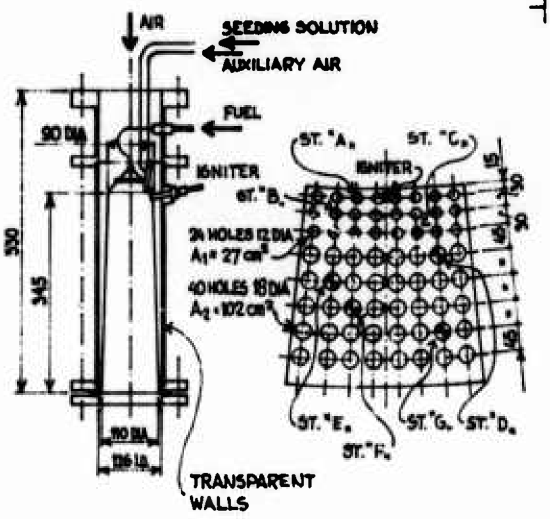
AIR
SEEDING SOLUTION
AUXILIARY AIR
FUEL
90 DIA
IGNITER
330
345
ST. "A"
ST. "C"
IGNITER
ST. "B"
24 HOLES 12 DIA
$A_1 = 27\ cm^2$
40 HOLES 18 DIA
$A_2 = 102\ cm^2$
ST. "E"
ST. "F"
ST. "G"
ST. "D"
110 DIA
126 I.D.
TRANSPARENT WALLS

FIG (2)

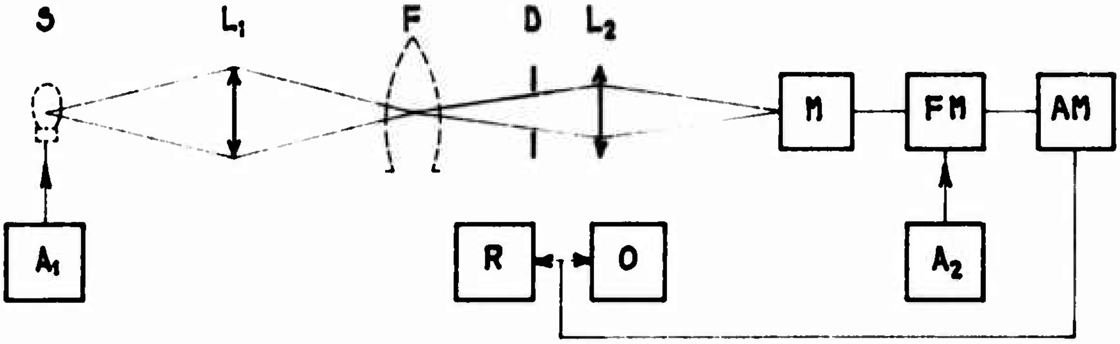
S
L_1
F
D
L_2
M
FM
AM
A_1
R
O
A_2

A_1 - POWER SUPPLY
S - STANDARD TUNGSTEN STRIP LAMP
L_1, L_2 - LENSES
F - FLAME
D - DIAPHRAGM
M - MONOCHROMATOR
FM - PHOTOMULTIPLIER
A_2 - HIGH VOLTAGE POWER SUPPLY
AM - OPERATIONAL AMPLIFIER
R - PHOTOREGISTRATOR
O - OSCILLOSCOPE

FIG (3)

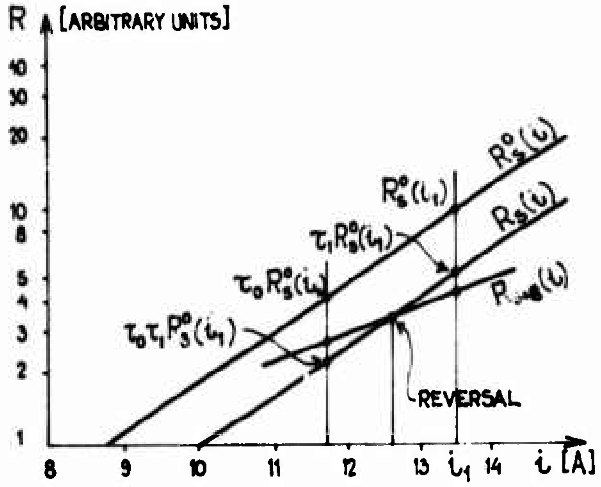

FIG (4)

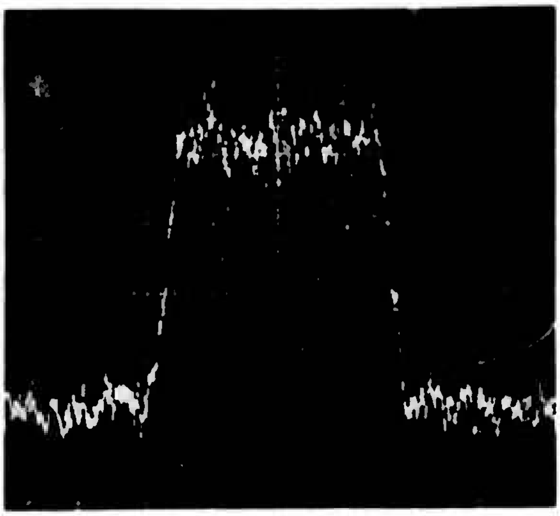

FIG (5)

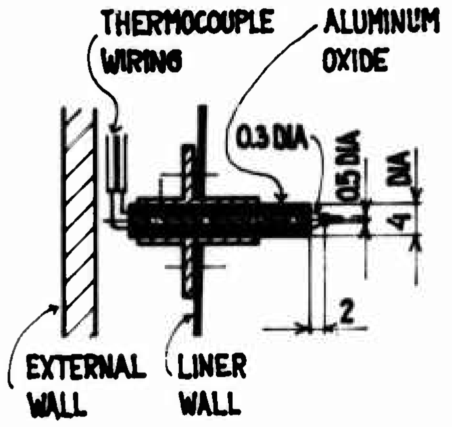
THERMOCOUPLE WIRING
ALUMINUM OXIDE
0.3 DIA
0.5 DIA
DIA
4
2
EXTERNAL WALL
LINER WALL

FIG (6)

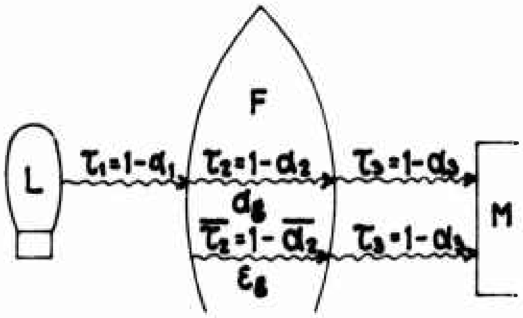
L
τ1=1-α1
F
τ2=1-α2
αg
τ̄2=1-ᾱ2
εg
τ3=1-α3
τ3=1-α3
M

FIG (7)

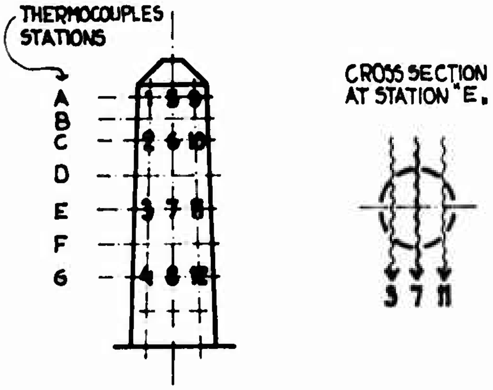
THERMOCOUPLES STATIONS
A
B
C
D
E
F
G
1
5
9
2
6
10
3
7
11
4
8
12
CROSS SECTION AT STATION "E"
3
7
11

FIG (8)

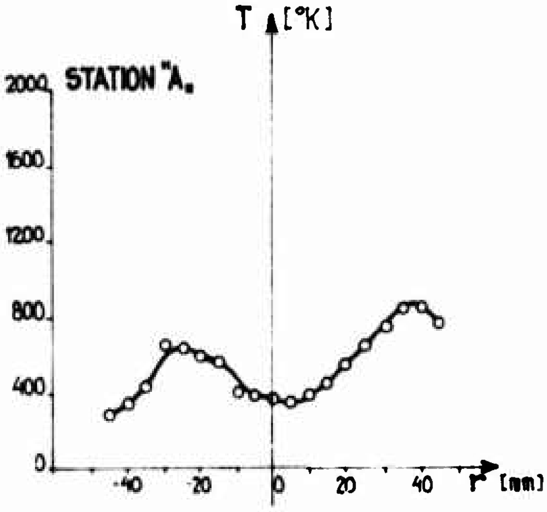

FIG (9)

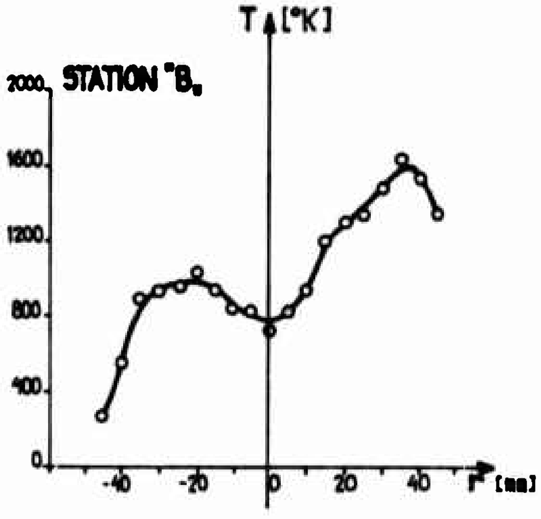

FIG (10)

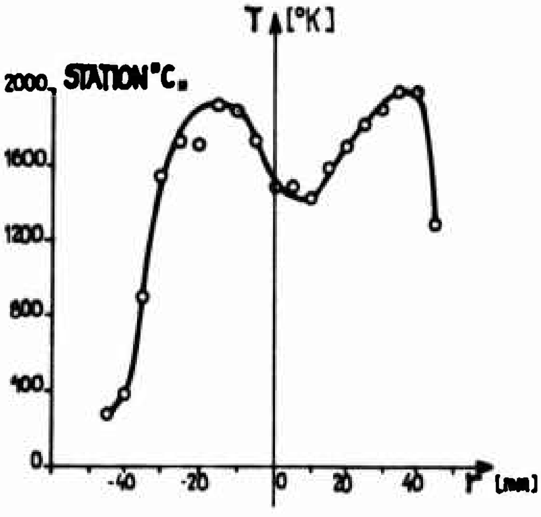

FIG (11)

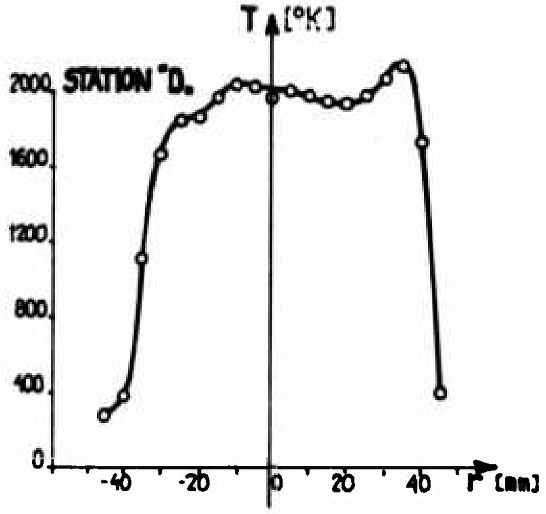

FIG (12)

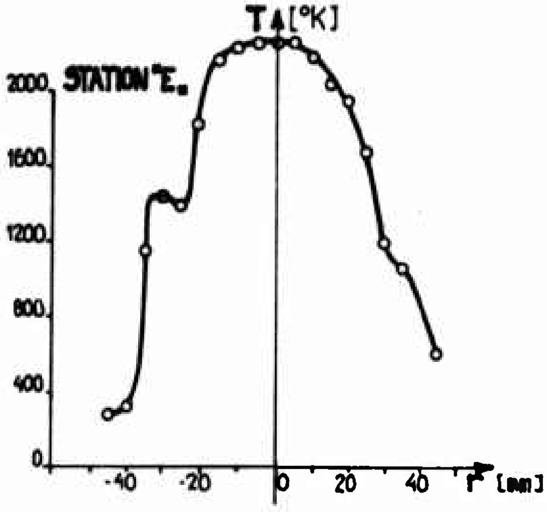

FIG (13)

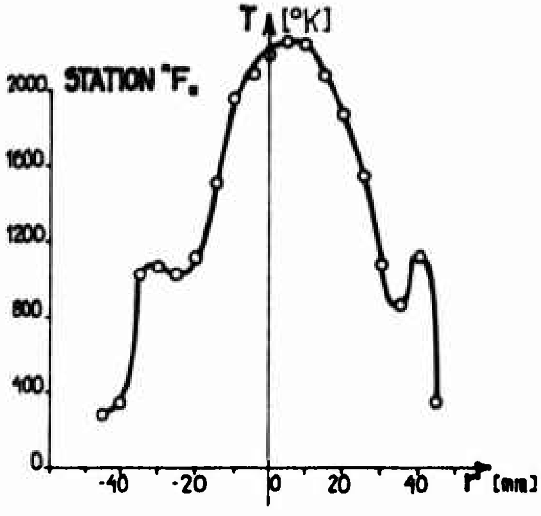

FIG (14)

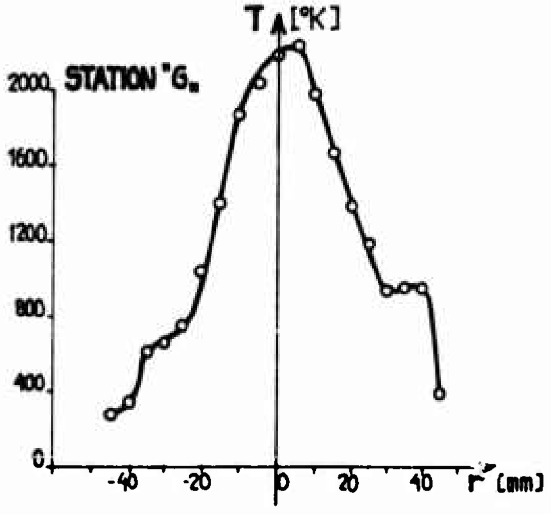

FIG (15)

SOME ASPECTS OF DIGITAL CONTROL SYSTEMS APPLIED TO AIRCRAFT POWERPLANTS.

J. McNamara E. Roberts C.G. Legge

Rolls-Royce (1971) Limited, Bristol U.K.

INTRODUCTION

Gas Turbine Powerplants have been intensively developed to produce improved performance and operating economy. This has been achieved substantially by development of the powerplant itself, and also to a considerable extent by increasing the sophistication of the powerplant control system. The control system has been required to run the powerplant accurately and safely ever closer to its peak of performance.

This constant object of realising as much as possible of the potential performance over a wide range of operational conditions has resulted in the control system becoming much more complex.

Powerplants featuring multiple spools with modulated reheat systems, variable-geometry intakes and variable-area nozzles are now common. In these cases the control laws have reached a degree of complexity where it is doubtful if they could be implemented practicably by hydromechanical means alone, and recourse has been made to electronic control systems. These have the advantage of making it possible to perform the required complicated control functions within a system of acceptable size and weight, and also are much more easily modified during the course of development.

Their attendant problems of reliability and environmental tolerance have been the subject of much study and acceptable operational systems are now being produced.

Even with electronic control systems, with their comparative ease of modification, development of the powerplant control in terms of time and cost has become an appreciable proportion of the overall powerplant development process.

This occurs mainly because of development problems in the powerplant, as its operating envelope is progressively extended from sea-level running in the test bed to its full flight envelope in the flying test-bed and/or prototype aircraft. This gives rise to frequent and quite extensive changes in the control functions required. In some cases the greater ease with which the electronics can be altered to accommodate these requirements enables improvements in powerplant performance to be effected by altering the electronic control system rather than by modifying the mechanical parts of the system.

A need for ease of modification during development has led to an increased interest in the possibilities of digital control systems. In such systems the control function is specified by the digital computer program, which can be easily and rapidly changed. The system hardware consists essentially of a digital computing facility and its communications path with the powerplant transducers and actuators as shown in Fig.1. This communications path consists of elements such as signal conditioning circuits, multiplexers, analogue-digital converters etc., which once developed, can in principle be used on other control systems. Therefore, the digital system lends itself to modular construction, offering the possibility of reduction of development costs of new systems.

These factors, together with other considerations such as a more systematic approach to monitoring and safety, indicate that digital control systems may be used increasingly in the future, particularly for complex powerplants.

However, although in the last decade research and development has been pursued in the United Kingdom on direct digital control of aircraft powerplants, the work has yet to materialise into a fully flightworthy controller for a civil or a military application.

The task has not been made easier by the fact that since the introduction of electrical analogue control systems on the Proteus(1) engines in the Britannia, extensive development of the electrical analogue controller for other engine/aircraft projects has occurred.

Such projects as the Olympus 320 in TSR.2 (before cancellation), Olympus 593 in Concorde and R.B.199 in MRCA have electrical analogue controllers for the powerplants. Here, micro-miniaturisation and new electronic packaging techniques are greatly reducing the size and weight of the controller compared with systems originally produced with discrete components.

It is interesting to note that in Concorde and MRCA, the use of digital elements to provide some of the necessary control functions is now common practice. Thus we are, in fact, in the "hybrid" stage of the evolution of electronic controllers for aircraft powerplants.

The introduction of direct digital control techniques to complex powerplant control must be shown to produce a system which is comparable in size, weight and cost with current electronic analogue controllers. Apart from these basic criteria there are many other aspects of digital control systems applied to aircraft powerplants that must be considered. It is the purpose of this paper to highlight those aspects which are important in the operational use of digital controllers.

SYSTEM CONFIGURATION

The system configuration for full-authority electronic control systems is basically dictated by the reliability and safety requirements. Fundamentally the reliability requirements for operational cost effectiveness are determined by the presently-achieved engine in-flight shut down rate. This rate should not be greater than 1.10^{-4} per engine hour from all causes. In some applications only a very small proportion of this is available for the electronics, and therefore the in-flight shut-down rate due to electronics control system failure should not be greater than 10^{-6} per engine hour. In existing hydromechanical full-authority fuel-control systems the low shut down rate is achieved by very high reliability with mean-time-between-failures (MTBF) of tens of thousands of hours. Within existing technology it is not practicable to produce simplex electronic systems (either analogue or digital), of the required complexity, with MTBF's of this order. Thus some form a redundancy is essential, but to what level of multiplicity this can be taken is limited by practical considerations. In general the weight, size and cost penalties are the limiting factors not only of the electronic equipment but their associated engine transducers. Furthermore pilot instrumentation and crash recorder parameters demand independent and isolated engine transducers. Thus engine instrumentation alone dictates a restriction to twin-lane configuration for the engine control system.

A twin-lane configuration can be obtained by using either duplicated self-monitored lanes, where only one lane at a time is switched on (Fig.2), or by cross-monitoring two lanes (duplex) and reverting to single-lane operation after the first fault (Fig.3).

The basic system configuration should be applicable to general powerplant control for either military or civil application. It should not be necessary to go back to a fundamental redesign in order to meet new powerplant applications or new operational requirements.

The introduction of an overall centralised aircraft powerplant control system, where triplicated or quadruplicated configurations can be employed (Fig.4), is futuristic and serious practical work is very unlikely until digital controllers have proved their worth as an integrated control system for a total power-plant (intake, main engine and reheat; Fig.5). Systems currently being developed in the U.K. incorporate main engine and reheat control as a first step towards a fully-integrated system.

RELIABILITY AND SAFETY REQUIREMENTS

Having established a basic system configuration, its operational modes are determined by the safety requirements.

The catastrophic failure rate for a civil aircraft from all causes must not exceed 1.10^{-7} per aircraft hour. This basic requirement results in a design figure for engine hazardous effects from any particular mode of failure of 1.10^{-8} per engine hour.

Although the definition of what constitutes a hazardous engine condition will vary from one application to another, some obvious hazards can be identified, viz;

i) overspeeding the engine

ii) rapid run-down of the engine during a critical period of flight

iii) loss of three engines in a four-engined aircraft

iv) the loss of thrust while jet-borne in a single engine VSTOL military aircraft (Harrier).

In civil applications it is normal practice to provide an independent overspeed governor to reduce the probability of a control system fault overspeeding the engine. Taking this into account the probability of a fault in the electronics of the control system causing an uncontrolled 'run-up' of the engine must not exceed 1.10^{-6} per engine hour. It can be shown that a figure of 1.10^{-6} uncontrolled electronics failures per engine hour also satisfies the other requirements for most applications.

Since complex control systems (either digital or analogue) will probably have an MTBF not much better than 1000 hours per lane on entry into service, it is essential for such systems to fail operational on the first fault.

While crew intervention to deal with faults which result in slow drifts is considered reasonable, any fault which would cause gross mishandling of the engine, and which demands immediate remedial action, should be detected by the system monitoring. Furthermore, since crew action should be based on unambiguous information the system itself should identify the faulty lane, and thus should be capable of automatic reconfiguration (i.e. switching out a faulty lane, or lane changeover).

Hence, in practice the individual lanes in any twin-lane system must be provided with some form of fault detection capability.

An important consideration is the situation existing after a failure in one of the control lanes. Inevitably, for the remainder of the flight, there will be a higher-than-normal probability of engine shut-down due to electronic failure. Depending on the design of the system there may also be a higher-than-normal probability of hazardous effects. It is suggested that after a first failure the risk of a catastrophe from the system should not exceed 1.10^{-6} for the rest of the flight. Thus in the final failure case the system must fail safely (freeze to the last good operational condition) and then it is acceptable for the crew to depower the control system, and either revert to some "get-you-home" back-up system or close the engine down.

The 'fail-safe' requirement implies that the last surviving lane will contain virtually the same self-monitoring capability regardless of the original system configuration.

Finally, it would be commercially desirable for the aircraft to be capable of being despatched with one lane inoperative on one of the engines. For this to be permitted, the overall safety requirements of the aircraft must still be met. The criterion proposed is that for the control system to have 'GO' capability with one lane inoperative on one engine, it must be acceptable, from a safety viewpoint, for all flights to be despatched in this condition.

It is believed that if digital control systems are designed to meet these reliability and safety requirements, then there will be no important shortcoming in the system when applied to any future complex powerplant control.

SOFTWARE INTEGRITY

The computer program within the digital controller defines the system's functional capabilities. It has several different aspects such as monitoring safety procedures, control functions and automatic tests.

A large amount of attention has to be devoted to the detailed programming of the computer to ensure that the functions and operations required achieve a high degree of integrity. For this reason it is important to consider very carefully which of the various programming techniques should be employed. The choice ranges from "machine-code" to "high-level" languages.

In a machine-code program the programmer uses the basic instructions of the computer, which are directly related to the operation of the machine. Although potentially the most efficient in terms of speed and storage space, the technique requires specialised personnel to achieve satisfactory results. There is a further difficulty in ensuring that a program which appears to be fault-free does not in fact contain, despite extensive testing, some dormant fault which will manifest itself during operation of the control system. Finally if the same task is required to be performed by another computer, virtually the whole of the programming work has to be repeated, as there is no interchangeability of machine code programs between computers.

In attempts to alleviate some of these difficulties various user-oriented languages have been developed. The principle aim of such languages is that the user need not concern himself with the intricacies of the computer's machine code, but can concentrate on the actual engineering task. Also programs once having been written in this way should be transferable between computers provided the language is available for the computers.

The inevitable disadvantage of such languages is that the resulting machine-code or translated version of the program is not so efficient as regards speed and storage space as a skilled programmer could have produced directly in machine-code.

Testing programs in a higher level language can actually become more difficult than in machine-code, as the programmer cannot directly monitor the step-by-step operation of his program. This arises because there is no direct relationship between his written program and its appearance within the store of the computer. Furthermore, with some high level languages he will not even know whereabouts data is stored in the memory.

Thus the problem of dormant faults is no way alleviated by the use of a programming language. The remoteness of the programmer from the finished program in the computer may well cause him to overlook possible faults.

It is concluded that from the point of view of the control engineer, who is not necessarily a computer programming expert, writing programs can be difficult for complex power-plant control, leading to operational failures and degrading system integrity.

One solution to this problem is the method of using the available expert programming resources to provide a "library" of subroutines which between them perform all the necessary functions and operations for engine purposes, and which are written in such a way that the finished program consists entirely of these subroutines, there being no separate linking structure or "Master program".

These subroutines can be written and thoroughly tested individually to a very high degree of confidence because of their relative simplicity. Moreover, since the sub-routines correspond directly to the control engineer's block diagram, programs are very easy to write even for complex powerplant control. Thus the overall program is unlikely to contain dormant errors. It is believed that this kind of modular approach to programming is the most effective means of producing high-integrity software.

MONITORING

The system monitoring depends on the configuration; a cross-monitored system detects a fault by inter-lane comparison and must then locate the faulty lane, while a self-monitored system simultaneously detects and locates the fault.

For either configuration the function-shared nature of the digital controller, in which the same circuitry is used for many different functions, enables it to do a lot towards the testing of its own operation. However, the final test must be performed by circuits independent of the computer because of the possibility of self-compensating faults.

For the self-monitored system, faults in a digital computer may conveniently be divided into two categories :-

a) faults which disrupt the sequential operation of the computer

b) faults which cause incorrect numeric outputs

Faults in the first category are easier to detect as they alter the time taken for the program to run or may prevent it being run at all. This type of fault can be detected by a timing check independent of the computer.

Faults in the second category require further measures for their detection, as in the presence of such a fault, the program may appear to run quite normally.

Such faults can be caused by minor corruptions of the program stored in the computer memory or by faults in the arithmetic circuitry of the Central Processor Unit (C.P.U.). Although major corruptions in these areas would generally result in both types of fault, some form of C.P.U. and store monitoring is required.

The computer works on a "program cycle" basis; that is, during each control cycle the computer generates a set of discontinuous outputs. To minimise the computing power required, the duration of the control cycle should be as long as possible, but has an upper limit governed by the dynamics of the controlled system (eg. actuators). The control cycle duration thus becomes equal to the longest time for which a faulty control system can be allowed to continue operation, so as not to cause serious mishandling of the engine. It follows that the system must be checked for faults in every single control cycle.

The C.P.U. may be checked by having the computer carry out a series of test operations so designed that any fault existing in the C.P.U. while the check is performed will produce an incorrect test result. The contents and operation of the computer memory can be checked by methods based on sum-checking, due attention being paid to the different requirements of the parts of the store containing various types of information, whether program or constants, long-term or short-term data etc.

It is also necessary to organise the program architecture so as to provide for the detection of intermittent faults as well as faults which persist for most of a sample period or longer.

The use of the computer to test the other parts of the system minimises the inclusion of monitoring circuits, the integrity of which would have to be separately considered.

System monitoring is based on the fact that correct sensor readings within the computer require a fault-free path from sensor to computer. Thus system monitoring reduces to sensor monitoring. Various methods have been employed including direct comparison, rate of change, out of limit, inter-parameter comparison, sign correlation and time comparison - these are all programming techniques. Hardware monitoring is used only where it provides an advantage over computer program methods.

The action to be taken by the control system as a whole when a fault is detected depends on the application, but certain generalisations can be made. When a fault occurs immediate action must be taken to prevent a hazardous condition developing. However because of the possible presence of noise in the system, detection of intermittent faults, whether real or apparent, may occur frequently during a flight; if every such incident were invested with permanent significance the entire control system could be depowered in quite a short time. Whenever a fault is detected, therefore, final action must be delayed until it can be established that the fault is either persistent or occurring sufficiently frequently to seriously degrade the control function.

Considerable effort has been devoted to these various aspects of computer and system monitoring, and there is a high degree of confidence that the required fault detection can be achieved without incurring a large penalty in computing time and additional circuitry. However, the final stage of proving that the integrity of digital controllers are to flight standard has yet to be accomplished. In the case of the civil application the Civil Aviation Authority have to be convinced, but many people believe that final confirmation of airworthiness will be achieved only via a military application.

CONTROL FUNCTION

Over the last decade a few dedicated groups in the U.K. engine controls industry have demonstrated direct digital control of engines, including modulated reheat, on such powerplants as Olympus, Spey, Gyron Junior engines and the Pegasus vectored thrust engine. Various full range digital control systems have been evaluated on sea-level static test-beds.

This work has shown that digital systems are capable of performing successfully all the functions necessary for control of a complex powerplant. The ability of digital systems to control an engine in several different ways using the same physical hardware has also been demonstrated. This flexibility is one of the major advantages of digital control and should greatly ease the development process when applied to a new engine project. Modifications to the control functions can be performed rapidly and, provided the computer has a re-programmable store, at no extra direct cost.

The flexibility can be retained in service, if required, for updating the control functions when later marks of engine are fitted, or in response to new operational requirements (e.g. noise-abatement). Alternatively, when the control functions are finalised, the store can be replaced by a permanent "read-only" memory.

The advantages of control flexibility in the development stage, which digital systems provide, is already being exploited. Digital systems are used to obtain engine characteristics, and also enable early running of the engine in any particular manner to provide information for development and specification of the eventual control system. Thus the versatility of control has been shown for digital methods.

One way in which this feature of the digital system could be used more extensively is in "Powerplant Management" or "Multi-Mode Control". These terms are applied to a system philosophy which recognises that ideally, the powerplant should be controlled differently according to the immediate circumstances of the flight. At take-off, for example, the control system may be required to give maximum thrust, whereas during the climb-out phase, the control function may have to be modified to meet noise abatement criteria. During cruise, performance optimisation relative to fuel consumption may be required, while maximum acceleration may be of over-riding importance during approach and landing.

The control function requirements for these various modes may be quite different from each other. In a digital system, however, this simply means that several different control programs must be stored in the computer. The programs would simply be called-up by mode-selector switches by the pilot or flight engineer as required. (See Fig.5).

As far as the pilot is concerned, selecting a particular mode merely changes slightly the range of engine power obtainable over the full travel of his throttle lever.

SUPPLEMENTARY FUNCTIONS

No digital control system would be complete without some form of fully automatic pre-flight checkout.(2)

If dormant faults can occur in safety and monitoring circuits, then in order to maintain the integrity of a system such circuits must frequently be checked. In addition it is desirable to check the whole system prior to engine start-up so as to avoid the consequences of an aborted start.

It is relatively easy for the computer in a digital system to simulate faults which cause monitoring circuits to trip, and safety circuits to operate. It should be noted that if this is done, it is necessary to ensure that the circuits recover if the simulated fault is of short duration (to avoid nuisance disconnects).

It is also fairly easy for the computer to check itself and most of the remainder of the system (with minimal additional hardware).

There are, however, a few tests and calibrations which cannot readily be done by the computer alone, but which may need to be carried out from time to time to maintain system integrity.

Thus it is convenient to provide two levels of test. The first is fully automatic, and rapidly tests all the safety and monitoring circuits and most of the system, and would be performed prior to every flight (the Pre-Flight or Line A test). The second is semi-automatic, takes rather longer to check all the system and would be performed perhaps once per day (Line B test). An automatic pre-flight test of this nature could well reduce turn-round time, since the total test time is in the region of 1 minute (at least half of the lanes can be tested simultaneously) as well as dispensing with a ground-test unit.

A further easily-provided function is that of fault-logging; the computer can store details of the nature and number of occurrances of most types of fault for later analysis. This facility should prove useful, especially in the case of intermittent faults where tests on the ground are unlikely to reveal the fault.

SUPPLEMENTARY FUNCTIONS

Recently the comprehensive techniques of Engine Health Monitoring (E.H.M.) have received much attention. These techniques have included vibration measurement, trend analysis and engine life recording. At present the majority of these techniques are still the subjects of various different studies. In the U.K., at least for military applications, there appears to be a trend towards the better-defined Engine Life Recording (E.L.R.) approach.

The aim of a complete E.H.M. system is to establish "on condition" servicing of powerplants by the continuous evaluation of engine performance.

A system which could use the control parameters already within the digital controller to provide some useful indication of the state or elapsed "life" of the engine is considered a worthwhile objective.

Although included as a sub-section of a complete E.H.M. system, the E.L.R. is based on the principle that an engine is assigned an overall life between overhauls from past experience..

The main E.L.R. parameters recorded are cycle fatigue, thermal shock, creep and over-temperature. Studies on this aspect of digital controllers indicate that additional program and memory requirements are extremely small and by the use of a post-flight readout facility this facility can be readily provided.

REFERENCES

1. HUNT A.J. Electrical Control of Engine Power - Proteus and Supersonic Engines. Joint IEE/RAS conference on the importance of electricity in the control of aircraft. Session 5 Paper 3 February 1962.

2. ROBERTS E. Digital Control Systems Self-Check. AGARD Conference Proceeding No.51. Testing of Airborne Avionic Systems. October 1969.

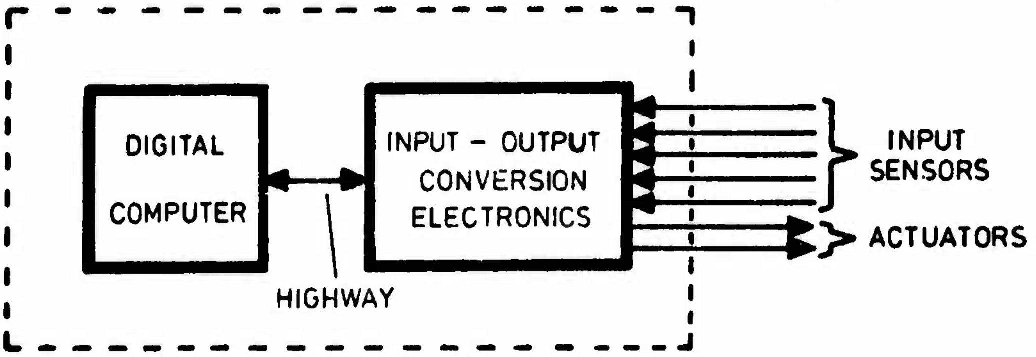
DIGITAL COMPUTER
INPUT - OUTPUT CONVERSION ELECTRONICS
HIGHWAY
INPUT SENSORS
ACTUATORS

Fig 1 BASIC DIGITAL CONTROL LANE.

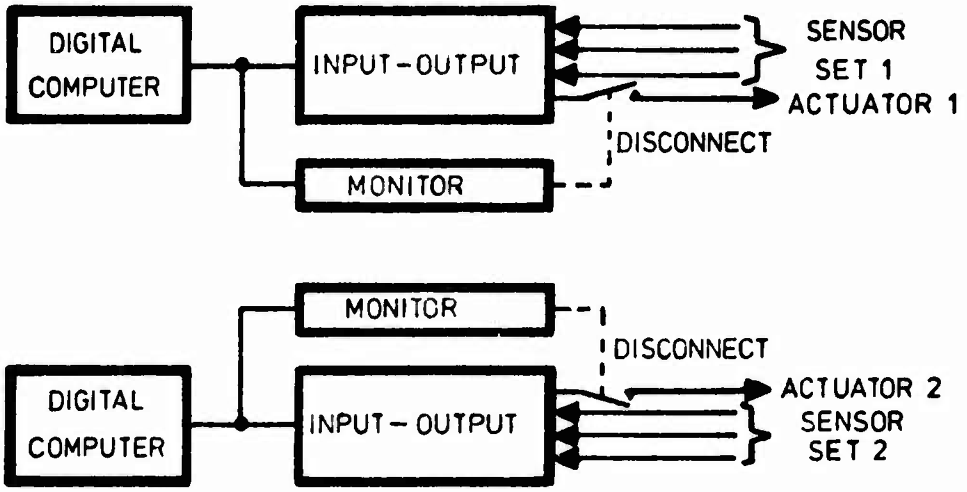
DIGITAL COMPUTER
INPUT-OUTPUT
MONITOR
DISCONNECT
SENSOR SET 1
ACTUATOR 1
MONITOR
DISCONNECT
DIGITAL COMPUTER
INPUT-OUTPUT
ACTUATOR 2
SENSOR SET 2

Fig 2 DUPLICATED SELF-MONITORED CONTROL SYSTEM

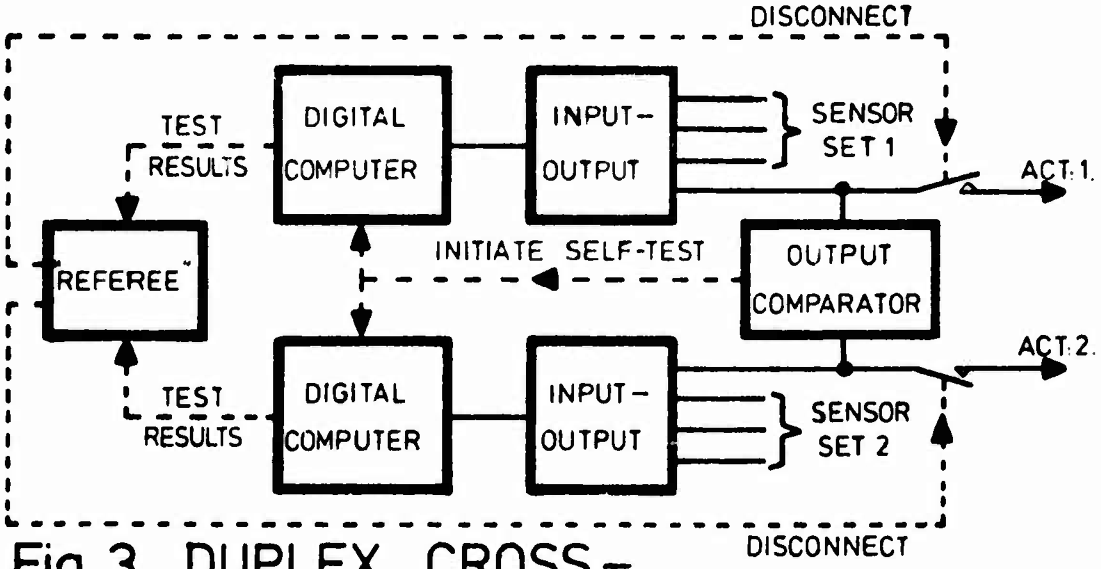
DISCONNECT
TEST RESULTS
DIGITAL COMPUTER
INPUT-OUTPUT
SENSOR SET 1
ACT. 1.
REFEREE
INITIATE SELF-TEST
OUTPUT COMPARATOR
ACT. 2.
TEST RESULTS
DIGITAL COMPUTER
INPUT-OUTPUT
SENSOR SET 2
DISCONNECT

Fig 3 DUPLEX CROSS-MONITORED CONTROL SYSTEM

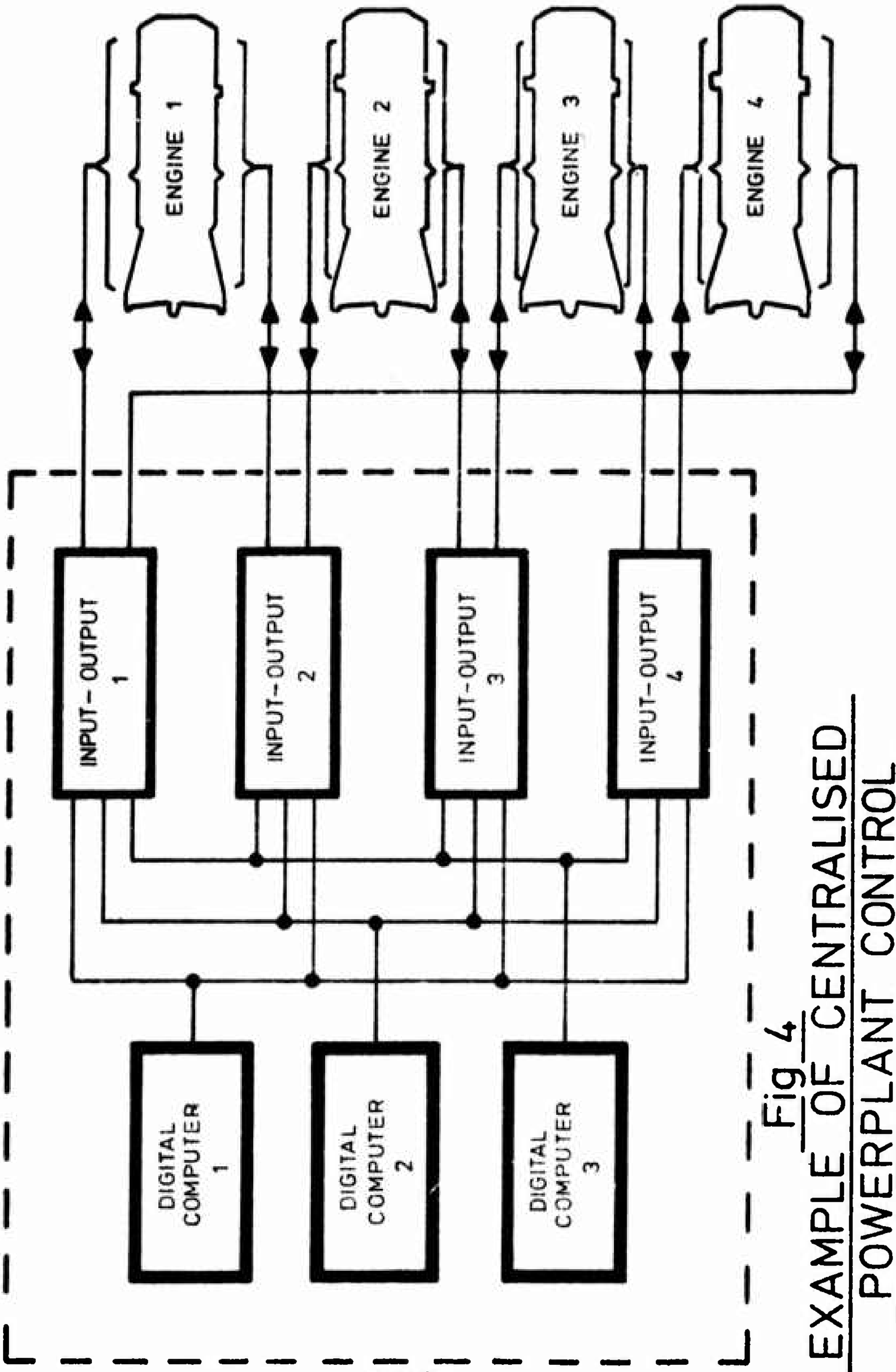
ENGINE 1
ENGINE 2
ENGINE 3
ENGINE 4
INPUT-OUTPUT 1
INPUT-OUTPUT 2
INPUT-OUTPUT 3
INPUT-OUTPUT 4
DIGITAL COMPUTER 1
DIGITAL COMPUTER 2
DIGITAL COMPUTER 3

Fig 4
EXAMPLE OF CENTRALISED POWERPLANT CONTROL

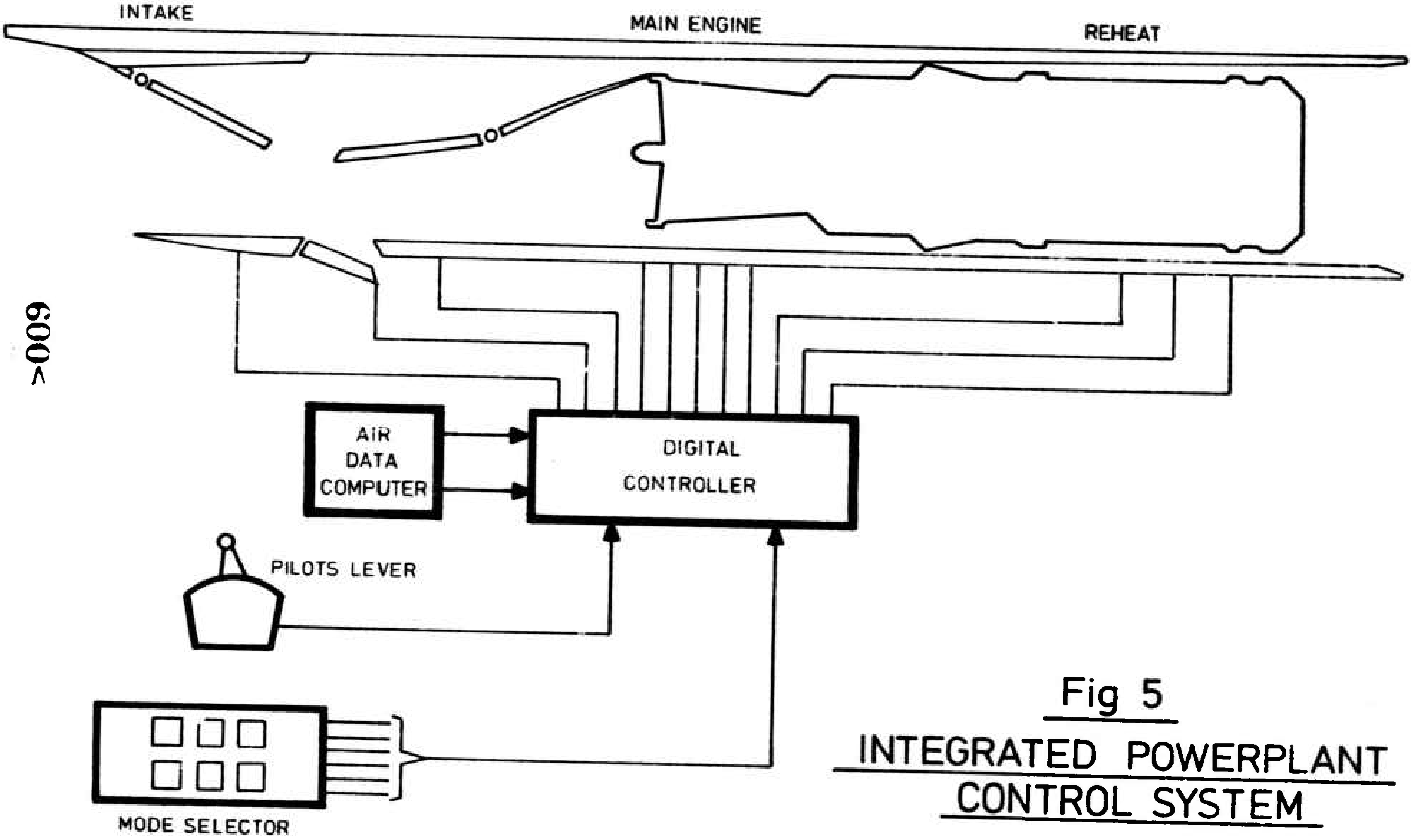
INTAKE
MAIN ENGINE
REHEAT
AIR DATA COMPUTER
DIGITAL CONTROLLER
PILOTS LEVER
MODE SELECTOR

Fig 5

INTEGRATED POWERPLANT CONTROL SYSTEM

TELEMETRY OF ENGINE ROTOR TEST DATA

A.J.S. Pratt

Rolls-Royce (1971) Limited., Derby, U.K.

1.0 Introduction

The measurement of rotor parameters is a fundamental requirement in the development of the modern aero gas turbine engine. Information about rotor stresses and temperature can often only be obtained by installing transducers on the rotating assemblies and transmitting electrical signals to the stationary parts of the engine. With single spool engines conventional contacting slip rings can be used but on multi-spool engines, shaft ends are not always accessible and the combination of large shaft diameters and high rotational speeds produces rubbing speeds far too high for contacting slip ring systems to be practical. Also, the demand for more and more data channels per test has stimulated the development of non-contacting data telemetry systems which avoid the limitation of contacting slip rings. This paper discusses several such systems currently in use at Rolls-Royce in the course of engine and rig development.

2.0 'Non-electronic' Telemetry

The greatest demand in engine development is for dynamic strain measurement using strain gauges. In this case the frequency and relative amplitudes of strain gauges signals are required and provided that only a limited number of channels are needed, a simple amplitude modulated system with no rotor-borne electronics can be used. Referring to Fig. (1).

In this system the transducer (strain gauge) is in one arm of an AC bridge which is supplied with a fixed amplitude, fixed frequency A.C signal by means of an inductive rotor-stator coupling in the form of a pair of concentric coils positioned at one end of the rotor.

Changes of gauge resistance modulate the bridge output and this is transmitted from the rotor back to the stator by a second pair of concentric coils. The strain signal is extracted by a phase sensitive detector.

The system has the advantages of simple rotating components which still make it attractive for some applications but it also has severe limitations such as:- limited channel capacity . (maximum of about 12), poor signal to noise performance, lack of in situ calibration and a complicated setting up and operating procedure.

2.0 'Non-electronic' Telemetry ... continued ...

Many of these limitations can be avoided by using rotor borne electronics to polarise transducers, condition and switch the output and transmit it from the rotor to the outside world, and 'radio telemetry' as it is known has become a standard method of obtaining many channels of data from multi-spool engines.

3.0 System Specification

The standard radio telemetry system currently in use at Derby has the following specification :-

3.1 Capacity : up to 48 channels of dynamic stress or temperature, in blocks of 8 channels. Mixed systems (i.e. temperature and stress are possible).

3.2 Accuracy : a total system error not greater than ±1% full scale for temperature and not greater than ±3% for dynamic stress.

3.3 Calibration : There is provision for in situ calibration of the whole system - transducer to final data output - at any time during a test.

3.4 Environment : The system will operate up to temperatures of +125°C under centrifugal accelerations of up to 30,000 'g'.

4.0 Description of Radio Telemetry System

4.1 The system, whether used for temperature or stress data, has three main sub systems :

Power Supply
Control
Data Conditioning and Transmission.

Each sub-system consists of engine borne electronic circuits together with a rotor to stator non-contacting coupling and test bed electronics outside the engine (Fig.2). The power supply system is common to temperature and stress versions but Control and Data Conditioning differs in some respects.

4.2 The Power Supply System

A fundamental problem with rotor borne electronics is to provide reliable, continuous power to the electronics under all variations in speed and temperature.

4.2 The Power Supply System ... continued ...

Several techniques have been used including batteries, but for most applications the inductive couplings transmitting R.F. power has been found to be most convenient. Concentric windings, one on the rotor, one on a stationary part of the engine as described in (2.0) are used to transmit up to 50 watts of power at 485kHz onto the rotor. This R.F. power is fed to several rectifiers, smoothing and stabilising circuits giving the various dc voltages needed.

4.3 Control

In order to obtain a large number of data channels with a minimum of separate transmitting channels some switching is required. Currently eight data channels per transmitter are used with up to 6 transmitters, giving a maximum capacity of 48 channels. The primary functions, therefore, of the control system is to control this switching process from outside the engine. In addition, calibration circuits can be operated and in the case of the stress system, gauge polarisation can be switched on and off to assist in diagnosing spurious signals.

4.4 Transducer Selection

Up to 8 separate transducer outputs can be switched, one at a time, in any order, through a single transmitter channel. A three bit binary word is generated at the ground station equipment as three fixed frequencies; these being mixed by a set of push buttons, each button corresponding to a particular selection. The selected mixed frequencies are amplified and transferred to the rotor by means of a second inductive coupling similar to the power coupling. The rotor electronics separate the three frequencies using tuned amplifiers and the rectified amplifier outputs correspond to the 3 'bits' of the binary word. A binary to decimal converter drives the transducer selection switches allowing any transducer to be selected from the ground station equipment.

The operation of this switching system is monitored by a 'selection check' facility whereby a 3 bit binary word is transmitted from the rotor as 3 frequencies and these are decoded to indicate that the required selection has been made and that the electronics are functioning correctly.

With the system described a total of eight strain gauges per transmitter channel can be used giving a total of 48 channels of strain gauge for 6 transmitters.

4.4 Transducer Selection ... continued ...

When the system is used for temperature measurement 7 of the 8 selections are used for active transducers; the other is used for a fixed value calibration resistor so that in-situ calibration can be selected at any time. Thus a 6 transmitter system gives 42 temperature channels.

4.5 Stress Transducer Calibration

Strain gauge transducers are calibrated in-situ by switching known high value resistors across all strain gauges simultaneously, giving a known percentage change in the effective gauge resistance. These resistors are switched in and out at several frequencies produced by adding another sinusoidal frequency to the other selection frequencies. Calibration can be selected at any time with any gauge selection at any one of several frequencies covering the operating frequency range of the system (5Hz to 27kHz).

A further frequency control signal is used to switch off the strain gauge polarising supply to allow spurious signals in the transducer wiring to be identified and isolated. This signal is detected and rectified in the same way as the selection signals.

4.6 Data Conditioning and Transmission

The transducers in both the stress and temperature systems are resistive devices supplied with a constant DC current, and the transducer output is directly proportional to the transducer's resistance change. In the stress system the switched output from each transducer is fed to an a.c. amplifier and the amplifier output is used to modulate an F.M. transmitter. The transmitter output is capacitively coupled from rotor to stator via a pair of 'aerial' rings and is received by an FM receiver which is tunable over a range of 5MHz. A maximum of 6 transmitter channels can be used simultaneously with requencies ranging from 40 to 75 MHz.

When temperature transducers are used the d.c. output of the switched transducer is used to control a voltage to frequency converter, with an output in the audio range and a frequency directly proportional to the temperature being measured. The output from the V to f converters modulate the FM transmitters and the same FM receivers are used as for the stress system.

4.7 Data Recording and Analysis

The output from the Stress system is up to six simultaneous analogue signals proportional to the strain imposed on the strain gauges.

4.7 Data Recording and Analysis ... continued ...

At any time the strain gauge selection can be changed on the 6 output channels up to a maximum of 8 selections. The analogue outputs are monitored and recorded on FM tape or U-V system.

In the case of the temperature system there are several options. Again up to six simultaneous frequency outputs proportional to temperature are available with manual control of the selection up to 7 alternative transducer selections. Alternatively, the selection can be automatic with all available channels continuously switched to a set of frequency to analogue converters followed by serial to parallel converters the outputs of which are continuous analogue signals equivalent to temperature recorded on U-V film or FM tape. More recently the temperature system has been linked directly to a small digital computer by land line and automatic calibration and multiplexing of the temperature signals is carried out. The data is then available as a fully computed print-out in calibrated engineering units or as a time/temperature graph as the test proceeds.

4.8 Construction

The operational environment of the rotor-borne electronics is severe: + 125°C and accelerations of 30,000 'g' and so considerable attention has to be paid to the mechanical as well as electronic design of the electronic packages. The separate functions of the rotor electronics are divided between a number of discrete packages each 32mm square by 16 mm deep with lead out wires on one of the square faces. This configuration is considered to be optimum from the point of view of economy of space, mechanical strength and ease of manufacture. Sets of modules are cemented into an annular metal carrier with all the module connections on the inner circumferential face. Figures 3 and 4 illustrate the modules and carriers.

The electronic circuits are hybrid in form being built of a mixture of discrete components, off-the-shelf linear and digital integrated circuits and special thick film monolithic circuits. Components are mounted on small printed circuit boards, tested and then encapsulated in a high density epoxy resin.

The development of a typical module is a lengthy process involving exhaustive environmental tests on each type of component and on the electronic circuits at each stage of manufacture. After final encapsulation, the module is temperature tested at full 'g' loading on a spinning rig and only after passing these tests can it be built into an engine assembly.

4.8 Construction ... continued ...

The need to ensure complete reliability under extreme operating conditions has resulted in a rather conservative electronic design : older components with known performance under these conditions rather than up-to-date but unknown components are used to avoid unexpected problems.

4.9 Installation in Engine

The carrier containing the electronic and power and aerial coils is mounted at one end of the rotor adjacent to a bearing. The proximity to a bearing ensures the good radial and axial locations necessary for efficient operation of the inductive and capacitive couplings.

Where the ambient temperature of the electronics unit is above 125°C, which is generally the case, cooling air has to be supplied to the unit from a source which is independent of the engine. The electronics carrier and its stator assembly have labyrinth seals so that cooling air can be injected, passed over the electronics modules and coils and then dumped into the bearing scavenge chambers where it is removed together with the normal bearing sealing air.

In some cases the cooling air has to be pre-cooled to achieve the required cooling effect without excessive airflow. At all times the temperature of the stator coils is monitored as a measure of the general temperature of the electronics package and this is used to control the cooling air flow. This varies from almost zero at start-up to a maximum of 0.25 Kg/sec. at maximum speeds on the largest diameter units.

The transducer wiring is brought through on the inside of the rotor assembly to a terminal ring adjacent to the electronics carrier and from there short connecting wires are attached to terminal posts on the carrier itself. Figures 5 and 6 illustrate a typical engine installation.

4.10 Operational Experience

The stress and temperature system described above has been used some 25 or so times in the last 3 years on four engine types including the HP and IP rotors of the RB211. The reliability of the rotating electronics package has been good; the only failures directly attributable to the electronics were caused by severe overheating when cooling air supplies failed. The main problems have been in obtaining good reliability in the transducer to electronics wiring runs. One minor problem with the temperature system, since cured, has been RF interference in the v-f converter resulting in a reduced accuracy. The majority of tests, however, have been trouble free and it has been possible to acquire data which it would have been impossible to acquire by any other means.

5.0 Recent Developments

5.1 Use of Large Scale Integrated Circuits

With the telemetry system described above 21 modules are required for a 42 channel (6 x 7) temperature system and 23 for a 48 channel (6 x 8) stress system. Despite the component construction of the modules, the space required for up to 23 of them is embarrassing in some applications.

Also a large number of modules requires a correspondingly large number of interconnecting wires. Many of the modules are used in the switching function of the system and so a recent development has been to design a special large-scale metal-oxide semi-conductor integrated circuit to replace a number of separate modules. In the one circuit the functions of transducer selection, selection checking and calibration are combined. The circuit is all contained in a single package and was designed at the outset to be capable of switching low level signals making it suitable for steady state as well as dynamic strain gauge and also thermocouples.

Environmental tests have demonstrated that it is capable of operation at 160°C with a comfortable margin. Figure 7 shows a typical circuit.

5.2 The Radio Telemetry Slip Ring

Paradoxically the first applications of the circuit described in 5.1 was not in a normal telemetry system but a single spool engine where it replaces a conventional contacting slip ring unit. In this particular application a large number of turbine temperatures have to be measured using thermocouples on the turbine blades and the poor reliability and limited capacity of the slip ring system was an embarrassment. The basic mechanical arrangement of the slip ring unit was retained but a three transmitter telemetry system was built into the existing shaft giving a capacity of 40 channels of thermocouple data plus 16 channels of dynamic strain gauge. The rotating electronics comprises power supplies, radio frequency transmitters, transducer switching and signal conditioning circuits. The Ground Station contains a power oscillator, radio frequency receivers and transducer switching circuitry. Inductive and capacitive co uplings are used to transfer power, control and output signals between rotating and stationary parts of the system. Figure 8 is a photograph of the unit partially assembled.

The thermocouples are multiplexed by a 48 way electronic switching circuit made from the Rolls-Royce designed integrated circuit described in 5.1. The output from this circuit is a histogram of thermocouple output voltages which is amplified and used to modulate the frequency of the transmitter. Known calibration levels are applied to three of the 48 channels, while four are devoted to the

5.2 The Radio Telemetry Slip Ring ... continued ...

measurement of thermocouple cold junction temperatures. All thermocouple cold junctions are brought to an aluminium disc which is used as a thermal plane whose temperature is measured using resistance mat transducers.

Thermocouples are scanned at a rate of 5 every 3 seconds, a complete scan being completed in about 20 seconds. This rate is determined by the logging equipment in the ground station.

Paper tape is used as the recording medium and a computer program corrects for cold junction temperature variations, thermocouple calibration and non-linearity, giving an output in engineering units.

Strain gauges are selected in pairs by manual control at the ground station. Eight pairs are available but only 1 pair can be monitored at a time. The selected strain gauges are polarised and the outputs amplified and used to modulate the frequency of two transmitters. As with the original system, each strain gauge may be depolarised in situ to check for interference. Also a calibration signal may be superimposed on each strain gauge output, if required, by ground station control.

6.0 Concluding Remarks

The demand for engine rotor data will continue to increase and the possible applications of telemetry are by no means exhausted. This paper has been limited to techniques used by Rolls-Royce at Derby and Bristol: other manufacturers are using equivalent techniques and there is still considerable scope for ingenuity in methods of transmitting the data from engine rotors.

7.0 Acknowledgments

The author would like to thank his colleagues Mr. E.N. Jones, Mr. H.W. Redhead and Dr. J.G.B. Worthy for their help in preparing this paper.

Fig.1 'non-electronic' Telemetry

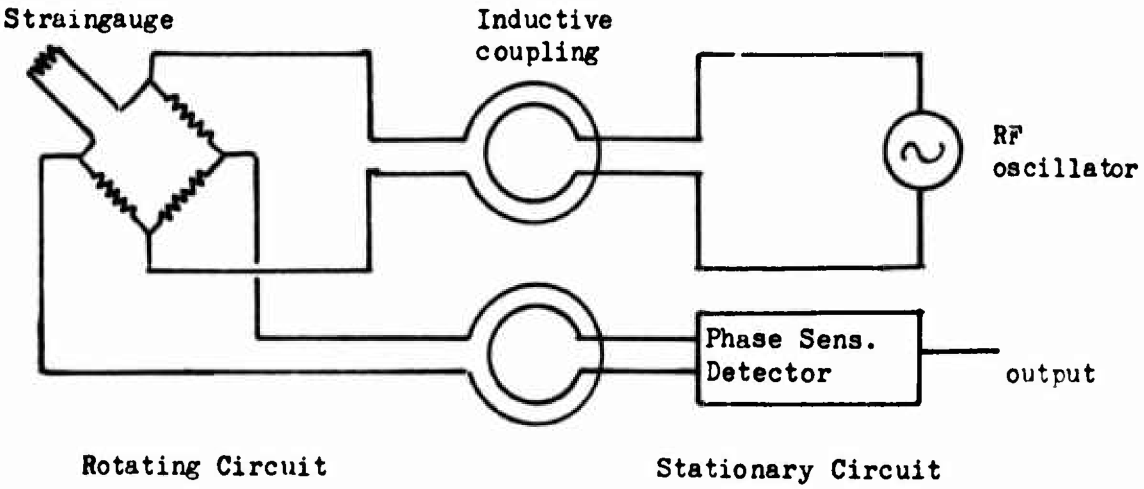
Straingauge
Inductive coupling
RF oscillator
Phase Sens. Detector
output
Rotating Circuit
Stationary Circuit

Fig.2 Radio Telemetry System

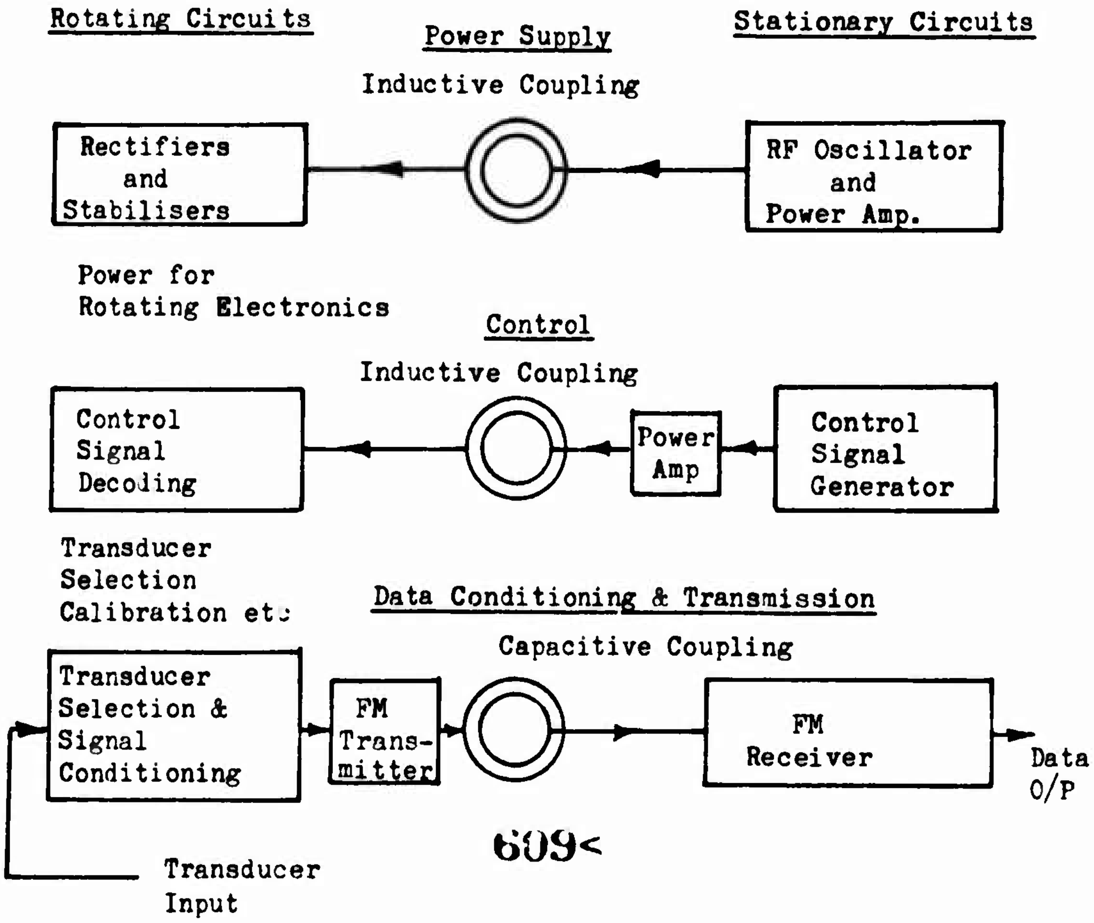
Rotating Circuits
Power Supply
Stationary Circuits
Inductive Coupling
Rectifiers and Stabilisers
RF Oscillator and Power Amp.
Power for Rotating Electronics
Control
Inductive Coupling
Control Signal Decoding
Power Amp
Control Signal Generator
Transducer Selection Calibration etc
Data Conditioning & Transmission
Capacitive Coupling
Transducer Selection & Signal Conditioning
FM Transmitter
FM Receiver
Data O/P
Transducer Input

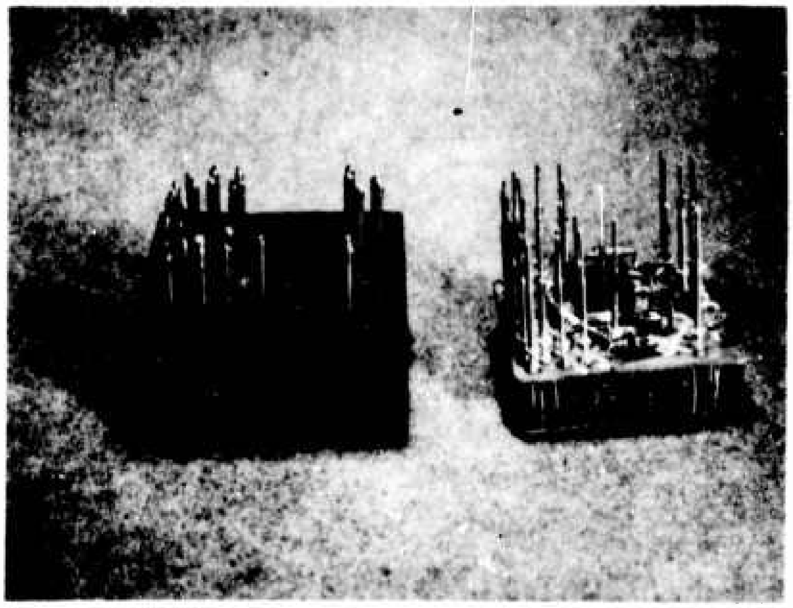

Fig.3 Photograph of Modules

Fig.4 Photograph of Carrier

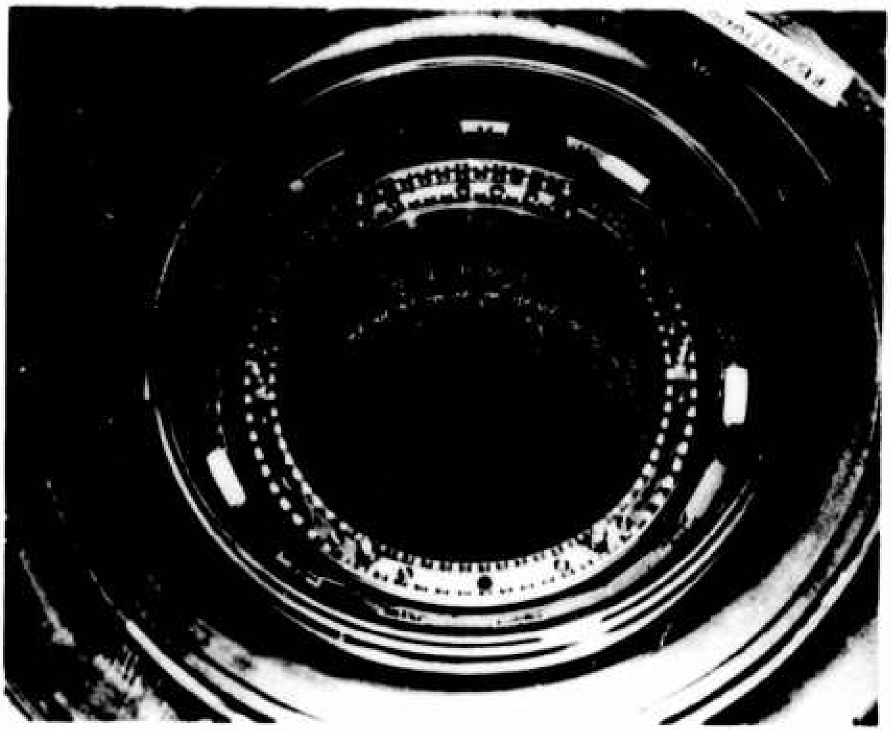

Fig.5 Photograph of Installation in a RB211 HP Rotor

Fig.6 Diagram of Typical Installation

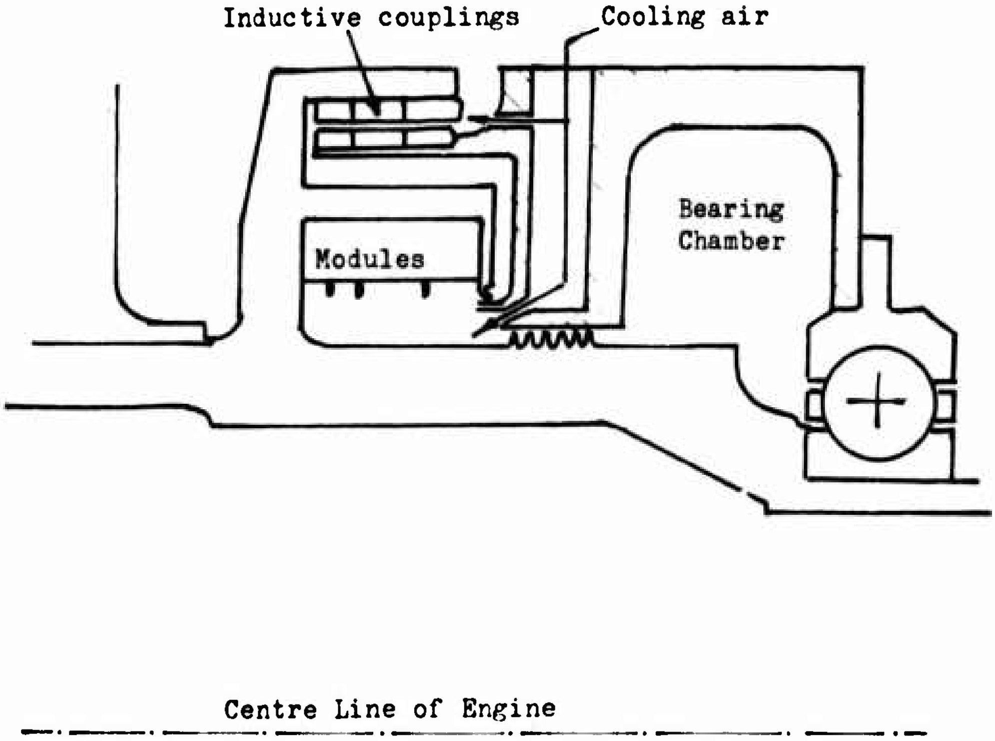
Inductive couplings
Cooling air
Bearing Chamber
Modules
Centre Line of Engine

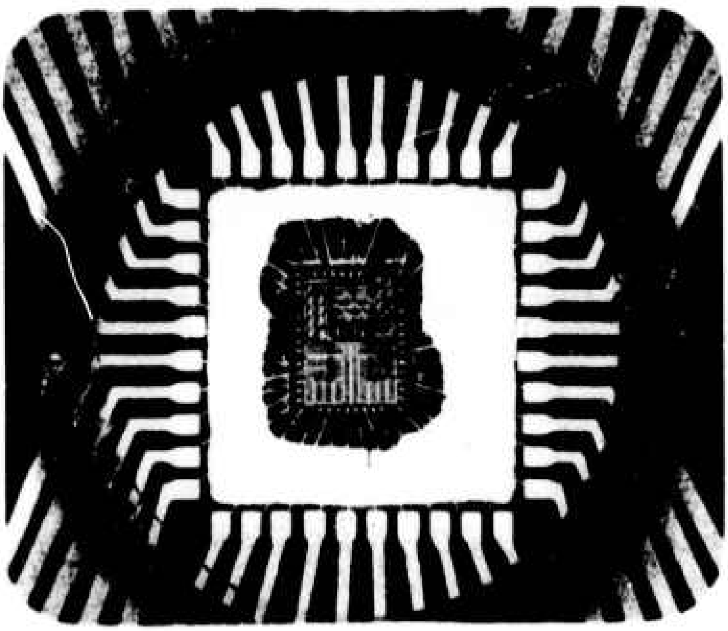

Fig.7 Photograph of Large Scale Integrated Circuit

Fig.8 Photograph of Radio Telemetry Slip Ring Unit

UTILISATION DE LA METHODE DES ANALOGIES HYDRAULIQUES POUR L'ETUDE D'UN DIFFUSEUR SUPERSONIQUE POUR COMPRESSEUR CENTRIFUGE

H. MITON J. VALENSI J. PLOTKOWIAK
I.M.F. de Marseille (France) Hispano-Suiza Div. SNECMA (France)

NOMENCLATURE

M_1	: nombre de Mach périphérique à la sortie de la roue
K_p	: coefficient de pression
$\bar{r}$	: distance radiale du bord d'attaque des aubes à l'axe de rotation rapportée au rayon de la roue
Indice 1	: sortie de la roue
Indice 2	: sortie du diffuseur

INTRODUCTION

Une étude expérimentale a été entreprise avec pour objet de vérifier la validité de l'emploi du bassin d'analogies hydrauliques en vue d'observer le fonctionnement des diffuseurs supersoniques à aubes de compresseurs centrifuges. Les travaux ont comporté deux phases : la première a été réalisée sur une boucle à fréon comportant un compresseur centrifuge muni d'un diffuseur à aubes ; la deuxième phase a été réalisée au bassin d'analogies hydrauliques sur un modèle tendant à simuler l'écoulement à la sortie de la roue du compresseur centrifuge ainsi qu'à travers les aubes du diffuseur. L'étude expérimentale effectuée à l'aide des deux moyens d'essais a comporté principalement l'observation de l'écoulement par la méthode des stries dans les divers régimes de fonctionnement, avec la mise en évidence des phénomènes instationnaires ; elle a comporté également, d'une part, dans le compresseur, des mesures de pression sur les parois latérales du diffuseur, d'autre part des mesures locales du niveau de la surface libre, dans le bassin d'analogies. Ces deux séries de mesures ont permis d'évaluer et de comparer les performances du diffuseur dans les deux types d'écoulement.

2 DESCRIPTION DES MOYENS D'ESSAIS

2,1 Boucle à fréon

Le compresseur utilisé est une machine prototype centrifuge (Fig.1

Il constitue l'organe moteur de la boucle à fréon. Le fluide utilisé est le Fréon R 114. L'installation permet de mesurer le débit gazeux, la température à l'admission et à la sortie du compresseur, la vitesse de rotation, la célérité du son, dans les conditions d'arrêt à l'admission (composition du gaz d'essais), enfin la pression en différents points de la machine.

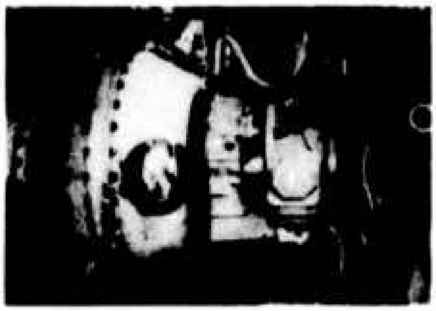

fig.1 Compresseur d'essais

Le diffuseur étudié est constitué par des aubes orientables disposées sur une couronne circulaire entre deux flasques planes et parallèles ; des prises de pression au nombre de 46, ont été pratiquées à travers les flasques. En outre un hublot comportant une glace à faces parallèles a été installé sur l'une des flasques, de façon à offrir un large champ d'observation englobant la sortie de la roue et un certain nombre d'aubes du diffuseur. En face de ce hublot encastré dans la flasque opposée, est placé un miroir plan d'un diamètre égal à celui de la glace du hublot. Ce montage, représenté sur la figure 2, permet les observations de l'écoulement par la méthode bien connue des stries en réflexion.

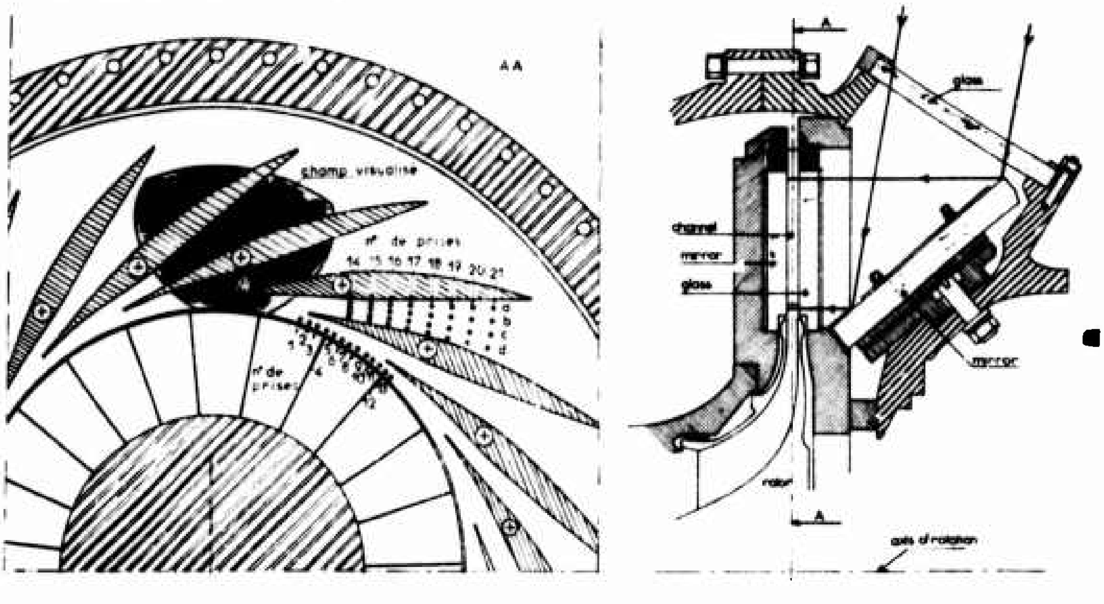

fig. 2 Dispositif de visualisation

2,2 Bassin d'analogies

Le bassin d'analogies hydrauliques se compose essentiellement d'un plateau horizontal rectifié, en forme de couronne. Ce plateau est porteur d'aubes formant diffuseur d'une épaisseur supérieure à l'épaisseur de la nappe en écoulement dans le bassin. Dans l'axe du bassin, l'eau est distribuée radialement par l'intermédiaire d'une roue axiale dont la vitesse de rotation permet de fixer la valeur de la circulation en amont des aubes du diffuseur. Un dispositif à déversoir permet de régler la contrepression en aval tandis que le débit d'eau à travers la roue est réglé indépendemment de sa rotation par le vannage d'un orifice d'alimentation.

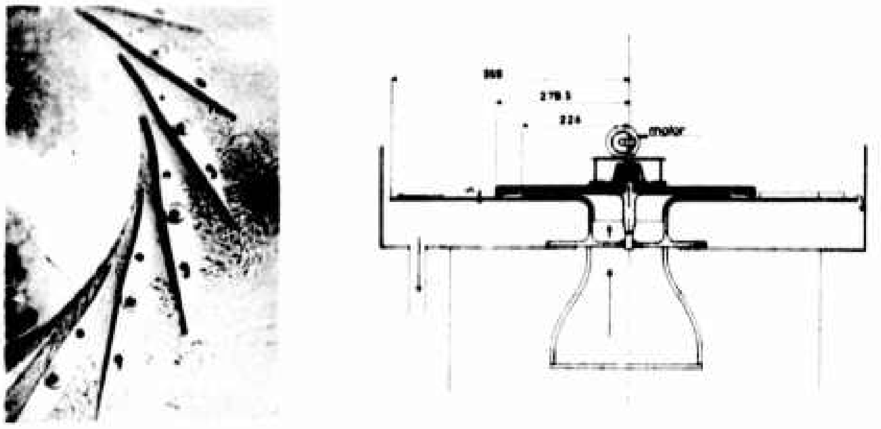

fig.3 Bassin d'analogies hydrauliques

3 RESULTATS OBTENUS

3,1 Boucle à fréon

Les essais ont été effectués, le compresseur étant équipé d'un diffuseur dont les aubes dessinées par la SNECMA-HISPANO SUIZA sont identiques à celles équipant certains compresseurs habituellement livrés par cette firme. Quatre configurations géométriques différentes ont été utilisées en faisant varier l'orientation des aubes et, par conséquent, la largeur du col, entre 19,8 mm et 7,2 mm ainsi que la distance radiale du bord d'attaque des aubes à la périphérie de la roue de $\bar{r} = 1{,}03$ à $\bar{r} = 1{,}09$ en prenant comme unité de longueur le rayon de la roue (280 mm).

Pour chacune de ces ouvertures, les essais ont été conduits pour six valeurs différentes de la vitesse de rotation de la roue s'échelonnant entre 3000 tours/minute et 8500 tours/minute correspondant à des nombres de Mach (vitesse périphérique / célérité du son à l'admission) égaux à 0,6 et 1,75 respectivement. Les essais, dont les résultats sont présentés ici, ont été réalisés au voisinage du maximum de pression sur la caractéristique débit-pression correspondant à la vitesse du rotor et au calage des aubes. Dans un tel régime de fonctionnement l'onde de choc de recompression, dans le diffuseur, se situe tout près de l'entrée du canal inter-aubes.

3,1,1 Répartition de la pression observée à la sortie du rotor

La figure suivante, (fig. 4), présente le rapport de la pression statique locale à la pression moyenne observé dans cette région. Les résultats obtenus ne paraissent pas nettement influencés par la configuration géométrique du diffuseur. Dans tous les cas, le bord d'attaque des aubes provoque une onde de choc suivie par une détente, ce qui prouve que la périphérie de la roue se comporte vis à vis des ondes incidentes, comme une surface isobare. On remarquera, en particulier que l'intensité du premier choc ne diminue que peu lorsque le bord d'attaque des aubes s'éloigne de

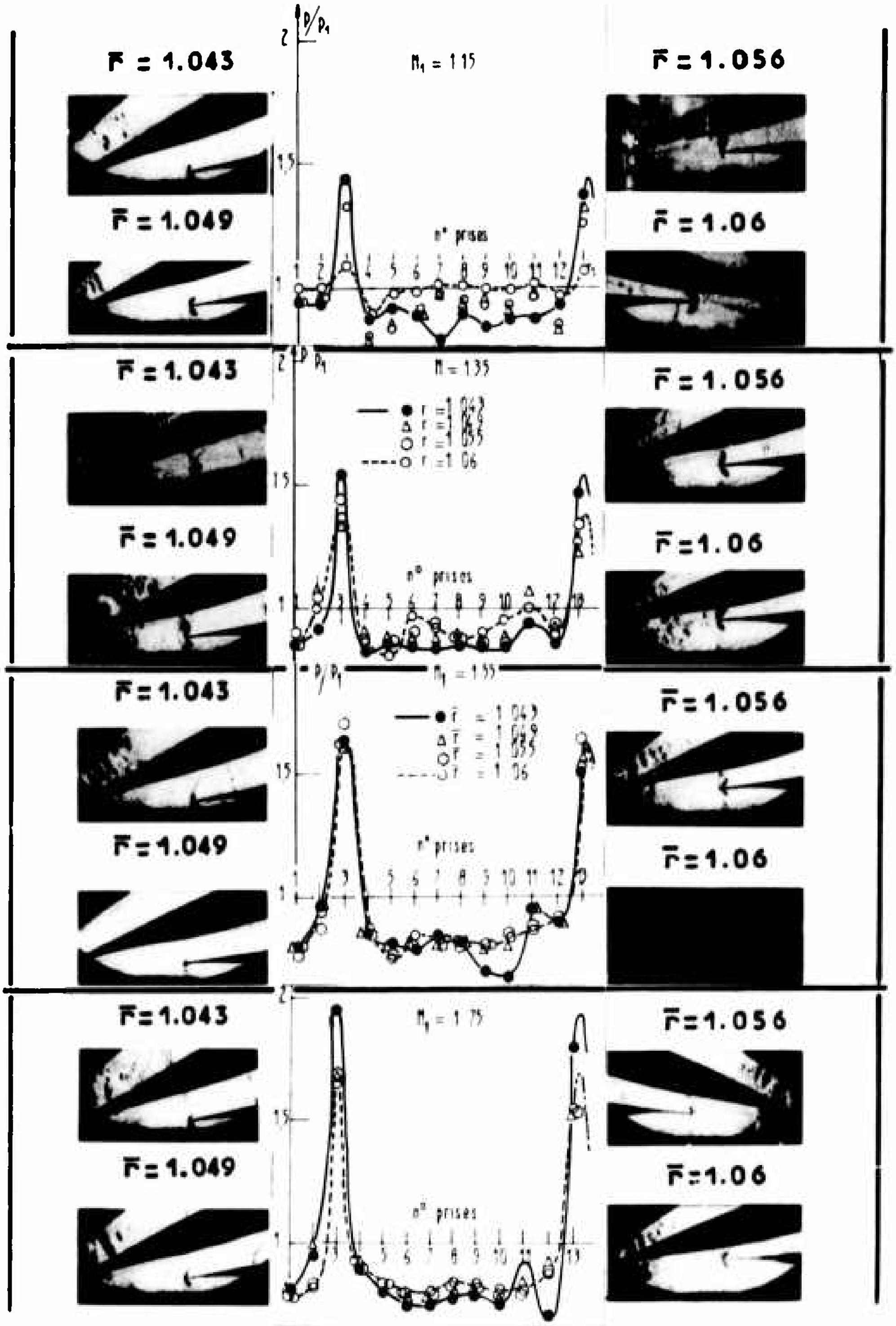

fig 4 Ecoulement à la sortie de la roue

la périphérie de la roue ($\bar{r}$ croissant). Par contre, pour une configuration géométrique donnée des aubes du diffuseur cette intensité croît très nettement avec le nombre de Mach périphérique, particulièrement à partir de $M_1 = 1,35$. Entre deux maximum de pression, l'importantes fluctuations peuvent être observées. Elles peuvent correspondre à des réflexions multiples d'ondes le long du profil des aubes, mais plus vraisemblablement à des perturbations de la couche limite le long des parois latérales du diffuseur.

3,1.2 Ecoulement au voisinage du col

Dans cette région, l'écoulement n'a pu être étudié qu'au moyen des photographies strioscopiques.

La photographie de la figure 5 montre que lorsque le nombre de Mach périphérique atteint 0,6, une onde de choc oblique apparait au bord d'attaque des aubes et se réfléchit dans le canal.

fig. 5 Ecoulement dans le col du diffuseur ($M_1 = 0.6$)

L'écoulement est donc soumis à une très forte accélération entre la sortie de la roue et l'entrée des canaux inter-aubes.

Lorsque le nombre de Mach périphérique est supérieur à 1, on observe une séparation de la couche limite le long des parois latérales, quelle que soit la configuration géométrique du diffuseur. Cette séparation ne parait pas très importante tant que le nombre de Mach reste inférieur à environ 1,40 : elle se présente alors sous la forme de rides un peu en avant du bord d'attaque des aubes (fig. 4). Lorsque le nombre de Mach atteint environ 1,5, ces ondes se rapprochent pour former un choc détaché à l'entrée du canal. Ce blocage parait ainsi être dû, davantage au comportement de la couche limite le long des parois latérales qu'au tracé du profil des aubages.

3,1.3 Ecoulement dans les canaux inter-aubes

En aval du col, la compression de l'écoulement se réalise généralement à travers un système d'ondes de choc multiples (pseudo-choc). Cette configuration bien connue est due au comportement de la couche limite. Cette compression ne se produit à travers un choc droit que lorsque le nombre de Mach est faible (fig. 5), et lorsque le rapport de pression est élevé.

La répartition moyenne de la pression dans les canaux inter-aubes a été calculée dans huit sections différentes du canal, à partir des résultats fournis par quatre prises de pression statiques placées dans ces sections. Ces résultats sont représentés sur la figure 6 . On peut voir qu'àprès un court intervalle dans lequel est situé le système d'onde de choc, l'augmentation de pression est pratiquement nulle. Ceci confirme que l'écoulement est séparé des parois, en raison, certainement, de la valeur élevée (environ 20 °) de l'angle du cône équivalent à l'espace inter-aube dans la région de sortie des canaux.

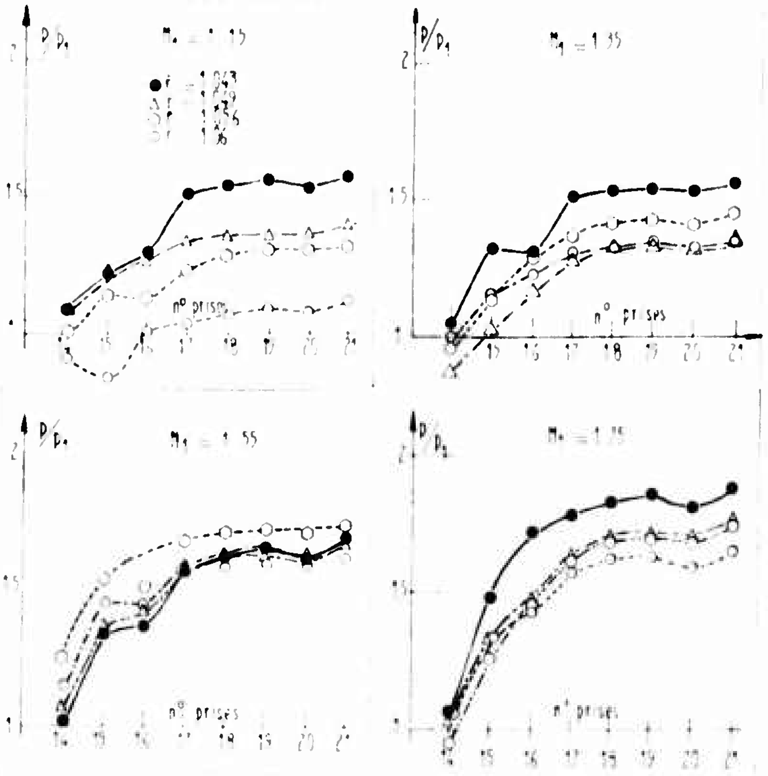

fig.6 Profils de pression dans les canaux inter-aubes

D'autre part, la configuration des courbes isobares dans ces canaux parait très tourmentée. Les résultats obtenus pour $\overline{r}$ = 1,043 représentés sur la figure 7 montrent que l'accroissement de pression est toujours plus rapide dans l'axe du canal que le long des parois des aubes. Des résultats analogues ont été observées pour les trois autres positions des aubes.

3,1.4 Phénomènes instationnaire. Influence du sillage des pales du rotor sur l'écoulement dans les canaux inter-aubes

Le montage de capteurs à réponse rapide n'ayant pu être envisagé lors de ces essais, l'étude des photographies strioscopiques a cependant permis d'obtenir des renseignements intéressants sur les phénomènes instationnaires.

D'abord l'amplitude des fluctuations de l'écoulement à l'entrée des canaux inter-aubes a été examinée en fonction de la distance séparant

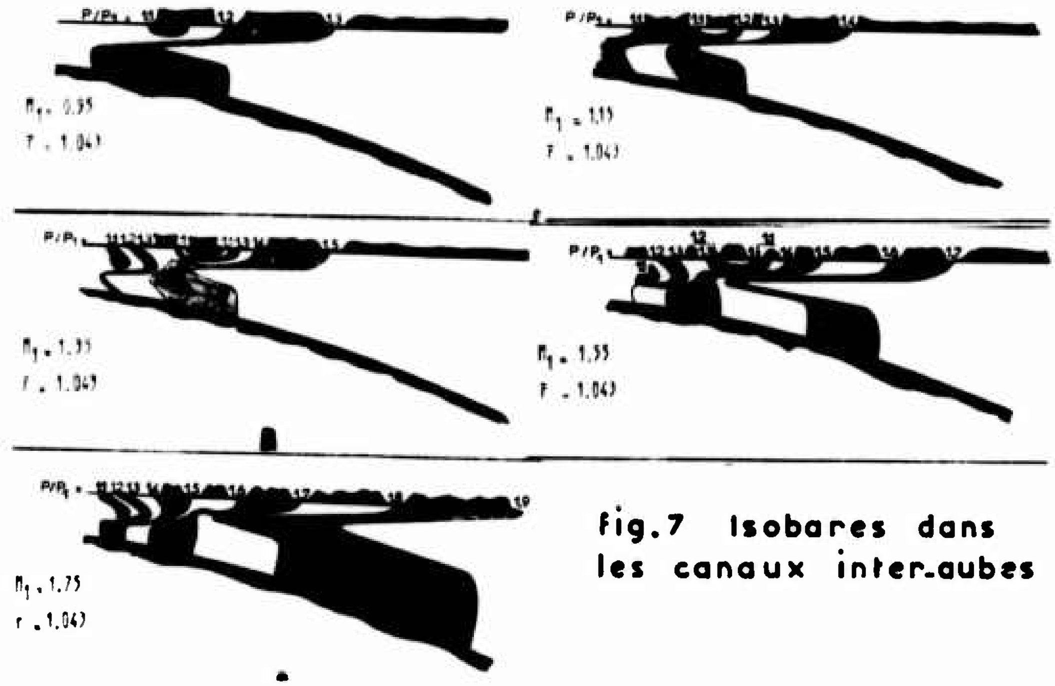

fig.7 Isobares dans les canaux inter-aubes

le bord d'attaque des aubes de la périphérie du rotor.

Les deux séries de photographies (fig. 8) correspondent respectivement à $\bar{r}$ = 1,043 et $\bar{r}$ = 1,055 .

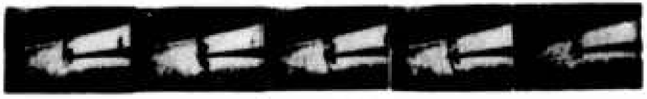

$\bar{r}$ = 1.056

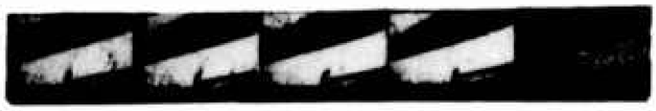

$\bar{r}$ = 1.043

fig.8 Oscillations des ondes au bord d'attaque des aubages

Elles présentent une reconstitution des différentes configurations d'ondes observées au cours du passage d'une pale de la roue devant l'entrée du canal.

Pour r = 1,043, les ondes paraissent animées de mouvements de très forte amplitude alors que pour $\bar{r}$ = 1,055 l'écoulement parait déjà beaucoup plus uniforme. En conséquence, il apparait que la distance optimum entre la périphérie de la roue et le bord d'attaque des aubes, distance qui doit être conservée aussi faible que possible pour limiter les pertes le long des parois latérales, se situe, pour le compresseur étudié, aux alentours de $\bar{r}$ = 1,05 .

D'autre part, les pulsations de l'écoulement dans le diffuseur ne semblent pas être exactement périodiques comme on aurait pu s'y attendre. Ce phénomène a été constaté en comparant différentes photographies instantanées correspondant à des positions déterminées d'une pale de la roue par rapport aux aubes du diffuseur. C'est l'examen image par image d'un film réalisé à l'aide d'une caméra ultra rapide qui a prouvé que les fluctuations de l'écoulement étaient bien reliées directement au passage des pales.

Ceci prouve qu'il existe des différences importantes et aléatoires entre les écoulements dans les différents canaux du rotor.

La figure 9 montre des ondes de compression attachées au bord de fuite des pales du rotor, visibles dans la région subsonique des canaux du diffuseur.

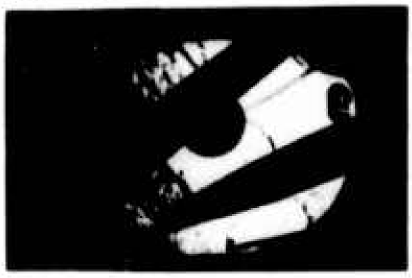

Fig.9 Sillages des pales de la roue dans les canaux inter-aubes

En effet, ces ondes, dont le profil n'est que peu déformé tant que l'écoulement dans les canaux est supersonique (la vitesse absolue de l'écoulement étant alors approximativement égale à celle de ces ondes), se concentrent, suivant le principe de la formation d'un choc, vers la sortie du diffuseur où l'écoulement est devenu subsonique. On peut voir ces ondes, qui ne provoquent pas d'interaction avec la couche limite le long du profil des aubages, se réfléchir sur une aube auxiliaire placée à la sortie du diffuseur, (Fig. 9).

3,1.5 Performances globales du diffuseur

La figure 10 représente le taux de compression statique du diffuseur en fonction du nombre de Mach périphérique. Ce taux de compression augmente à peu près linéairement avec le nombre de Mach et très légèrement avec l'inverse de la distance séparant le bord d'attaque des aubes de la périphérie de la roue.

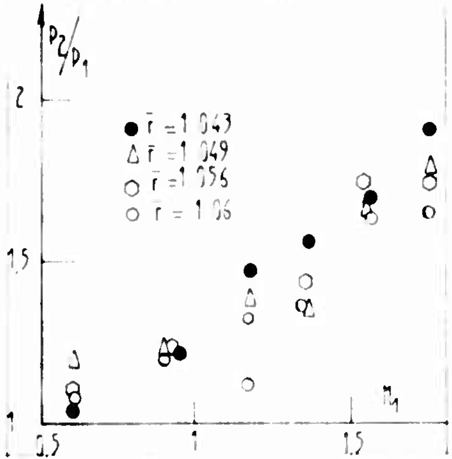

Fig.10 Performances globales du diffuseur

3,2 Essais au bassin d'analogies hydrauliques

Les aubages utilisés au bassin d'analogies sont semblables en tous points, (forme, dimensions), à ceux installés dans le compresseur à fréon. Ces essais ont été effectués pour les même nombres de Mach périphériques, (i . e . nombre de Froude pour l'analogie), les mêmes configurations géométriques que les précédents et également, au voisinage du taux de compression statique maximum du diffuseur, avant désamorçage.

Cependant, l'écoulement dans le rotor n'est pas reproduit ici, le diffuseur étant, en principe, alimenté par un écoulement uniforme.

En réalité, il existe bien des pulsations engendrées par la rotation des pales de la roue assurant le mouvement du liquide, sans toutefois que, sur ce point, la similitude avec l'écoulement dans le compresseur à fréon puisse être assurée.

3,2.1 Ecoulement entre la périphérie de la roue et le col

La répartition du niveau de la surface de l'écoulement (représentant la distribution de la densité pour le "gaz hydraulique") n'a pu être mesurée aux mêmes endroits que dans la boucle à fréon. Dans le cas présent les mesures ont été réalisées le long de la paroi de l'aube faisant face à la périphérie du rotor.

La répartition de la pression locale rapportée à la pression à l'entrée du diffuseur (rapport correspondant pour l'analogie hydraulique à celui des carrés des hauteurs d'eau aux points correspondants) ont été mesurés dans cette région et tracés sur la figure 11 pour $\bar{r} = 1{,}043$.

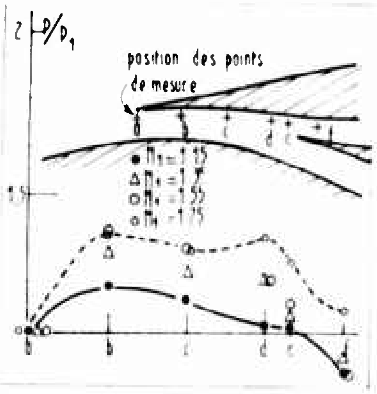

fig.11 Profils de pression à l'entrée du diffuseur ($\bar{r} = 1.043$)

Ces courbes montrent qu'une compression se produit le long de l'aubage en partant du bord d'attaque, suivie par une détente qui se poursuit dans le canal et entre en interaction avec l'onde de choc issue du bord d'attaque de l'aube suivante dont, dans ces conditions on n'observe pas la réflexion sur la paroi, (fig. 12).

Des phénomènes analogues ont été observés pour les autres configurations géométriques du diffuseur.

fig.12 Visualisation de l'écoulement à l'entrée du diffuseur

3,2.3 Ecoulement dans les canaux inter-aubes

Dans la première partie du canal, on observe des oscillations suivies par une augmentation rapide de la pression (fig. 13).

L'accroissement de pression enregistré à travers ce ressaut est représenté sur la figure 14 en fonction du nombre de Mach juste en amont. Il est clair que l'on a affaire à un système d'ondes analogue à celui déjà observé dans l'écoulement de fréon, plutôt qu'à un ressaut représentant une onde de choc droite. Ceci est confirmé par la photographie de la figure 14, qui montre que le passage de l'écoulement supersonique au subsonique

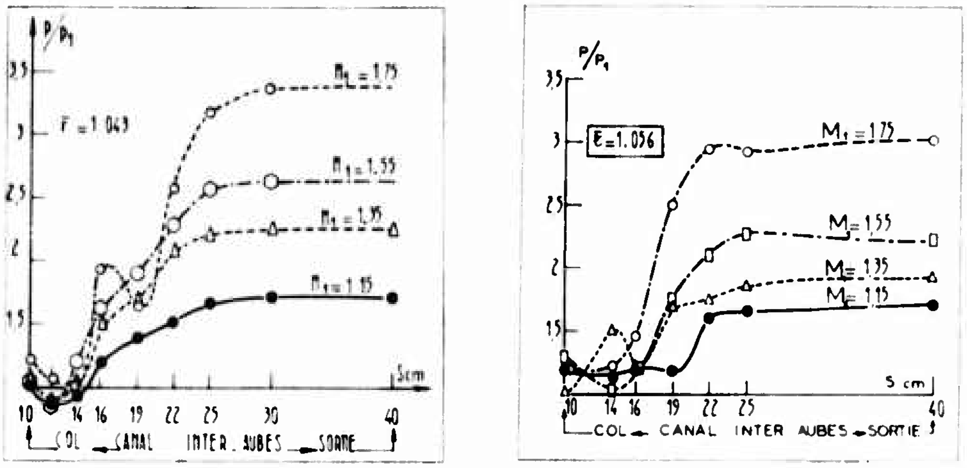

fig. 13 Evolution du rapport de pression dans les canaux inter-aubes

s'effectue à travers une série d'ondes visibles dans le canal un peu en aval du col.

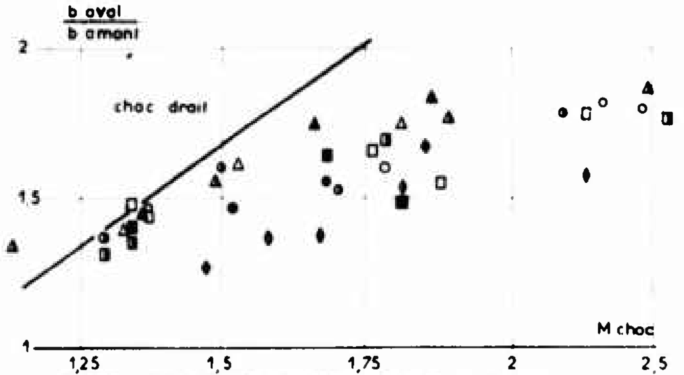

Variations de la densité du gaz hydraulique à travers l'onde de choc dans le canal de diffusion

fig. 14

Derrière ce ressaut, la pression demeure pratiquement constante quelles que soient les conditions d'essais, ce qui prouve que l'écoulement est séparé des parois. Cette séparation a pu être mise en évidence en introduisant un liquide coloré le long des parois des aubages (fig. 15).

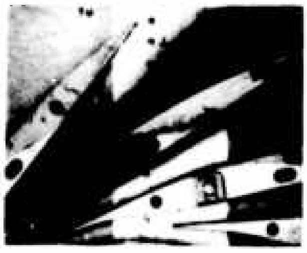

fig. 15

Aucun écoulement secondaire ou phénomène tridimensionnel n'a été observé. Quelles que soient les conditions d'essais le niveau de la surface libre est resté uniforme dans les sections normales à l'axe du canal derrière les ondes de compression.

4 COMPARAISON DES RESULTATS OBTENUS DANS LES DEUX SERIES D'ESSAIS

Deux différences importantes existent entre les écoulements dans la boucle à fréon et dans le bassin d'analogies hydrauliques.

Il y a d'abord la différence entre les deux gaz. Le fréon 114 a un rapport de chaleurs spécifiques de l'ordre de 1,088 , alors qu'il est égal à 2 pour le "gaz hydraulique". Les viscosités du fréon et de l'eau sont également différentes. De plus, dans le bassin d'analogies hydrauliques le sillage des pales de la roue n'était pas représenté correctement, et en conséquence aucune similitude n'a pu être réalisée en ce qui concerne les phénomènes instationnaires.

Cependant des observations semblables ont pu être effectuées, concernant la configuration générale des deux écoulements. En particulier l'existence d'une forte détente (d'ailleurs destinée à faciliter l'amorçage du diffuseur) à travers le col, a pu être mise en évidence par l'observation des photographies strioscopiques dans la boucle à fréon, par les mesures du niveau de la surface libre dans l'analogie hydraulique.
De plus, la configuration des ondes de compression dans les canaux inter-aubes a été trouvée identique dans les deux types d'écoulement (du type "pseudo-choc"). Enfin, la séparation de l'écoulement dans ces canaux a pu être prévue à l'aide de l'analogie hydraulique.

Cependant, ce moyen d'essais n'a permis de mettre en évidence aucun phénomène tridimensionnel dans les canaux inter-aubes, phénomènes qui paraissent exister dans la boucle à fréon, (fig. 7).
Cette première comparaison étant relativement satisfaisante, on a pu rapprocher les résultats des mesures de pression effectuées sur la boucle à fréon et le bassin d'analogies. Afin de s'affranchir de la différence entre les chaleurs spécifiques des deux gaz, le coefficient suivant, indiqué dans la référence 1 , a été utilisé :

$$Kp = \left\{ \frac{2}{\gamma - 1} \left[\left(\frac{p}{p_1} \right)^{\frac{\gamma - 1}{\gamma}} - 1 \right] \right\}^{\frac{1}{2}}$$

où γ représente le rapport des chaleurs spécifiques du gaz considéré, p la pression statique locale, p_1 la pression statique moyenne à l'entrée du diffuseur.

On a représenté, d'autre part, sur la figure 16, les nombres de Reynolds / unité de longueur, dans l'écoulement à l'entrée du diffuseur en fonction du nombre de Mach à la sortie de la roue.
Les valeurs obtenues sont très différentes dans les deux cas et ne peuvent être comparées.

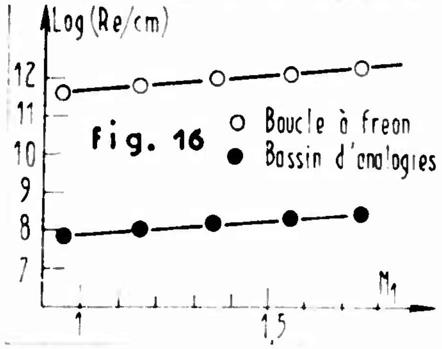
Fig. 16

L'évolution du coefficient de pression dans les canaux inter-aubes est représentée sur la figure 17 dans deux configurations géométriques du diffuseur, pour les deux écoulements. On peut observer une évolution semblable dans les deux cas.

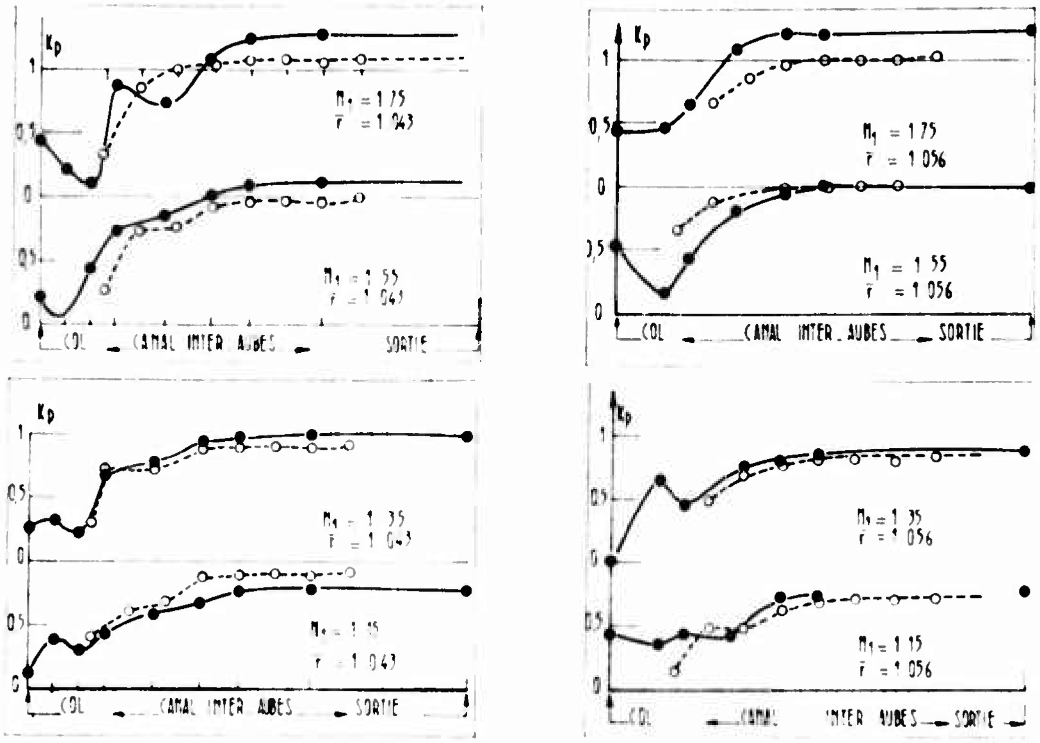

fig.17 Comparaison des repartitions du coefficient de pression dans les canaux inter-aubes.
O : eclt. de freon - ● : eclt. d'eau

De la même façon, le taux de compression statique Kp 12 entre l'entrée et la sortie du diffuseur est représenté sur la figure 18. Ici également l'accord entre les deux écoulements est assez satisfaisant.

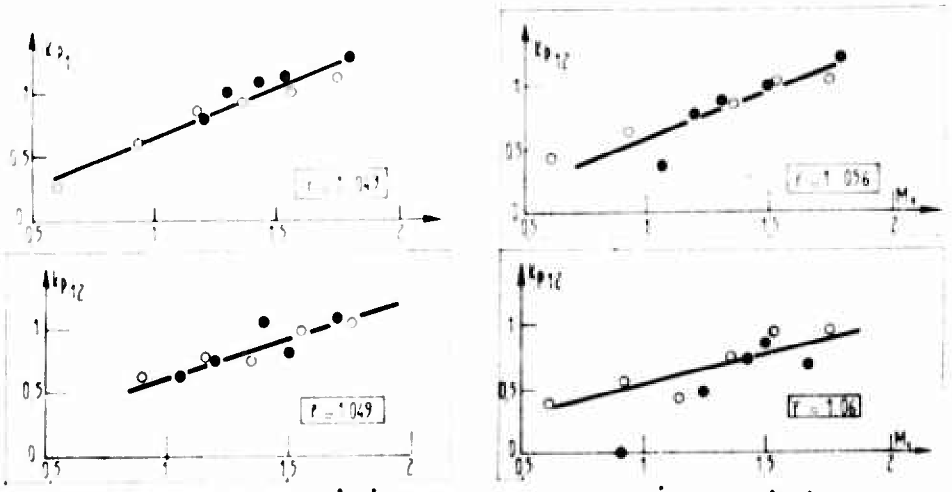

fig. 18 Coefficients de pression globaux
O : eclt de freon - ● : eclt d'eau

5 CONCLUSION

Le rapprochement des observations et mesures effectuées au bassin d'analogies hydrauliques, des observations et mesures effectuées sur la boucle à fréon, montre que le bassin d'analogies hydrauliques peut constituer un moyen d'essais satisfaisant au moins pour l'étude systématique préliminaire d'aubes de diffuseurs supersoniques de compresseurs centrifuges. La boucle à fréon apparait cependant comme un moyen d'essais indispensable pour la mise au point définitive du diffuseur, une fois effectuée au bassin d'analogies une présélection parmi les configurations proposées, qu'elles soient empiriques ou calculées suivant des théories simplifiées.

REFERENCES

1 H.E. SHEETS
Non dimensional compressor performances for a range of Mach number and molecular weights
ASME Transactions, January 1952 .

2 P. PAPON
Application de la méthode des analogies hydrauliques à l'étude de la diffusion supersonique (cas des compresseurs centrifuges)
Thèse de Doctorat, Université d'Aix-Marseille, 1966 .

3 J. FABRI
La visualisation de l'écoulement dans un compresseur axial supersonique
L'Aéronautique et l'Astronautique n° 32 171 - 8 .

4 F. HORTOBAGYI
Quelques résultats d'essais sur un compresseur centrifuge à hautes performances
Entropie n° 20 , Mars - Avril 1968 .

THE DESIGN AND DEVELOPMENT OF THE GEM ENGINE

R.M.Heathcote

C.E.Payne

BASIC CONCEPT

During 1966 the Bristol Siddeley Small Engine Division began to study in depth, the sort of gas turbine engine of about 1000 HP size, which would prove an appropriate power plant for helicopters likely to enter service in the late 1970s. The survey was extensive and included such possibilities as a recuperative cycle or the use of inter-stage reheat in the expansion side. On the grounds of avoiding excessive weight, complexity and technical risk, it was soon decided to revert to the traditional thermodynamic cycle.

There followed a detailed examination of the effect of choice of cycle temperature and pressure ratio on specific fuel consumption, engine weight (specific power) and complexity. Making certain assumptions as regards compressor efficiency, combustion chamber and mechanical losses, cooling and leakage air flows, the relationship between specific fuel consumption and specific output power was evaluated over a range of pressure ratio and turbine entry temperature (Figure 1). The range of turbine inlet temperature considered was that associated with uncooled turbine blades - it being argued that turbine blade cooling should not appear in an engine at the start of its life, but should be reserved as a means for developing its power potential thereafter. In combination with this study of alternative cycles possible configurations were evaluated on the drawing board.

The design based on the simplest cycle (6:1 pressure ratio) was the BS 360-03 (Figure 2). As compared with engines of higher pressure ratio, the BS 360-03 is relatively cheap and light, but of course, suffers on fuel consumption. The impact of this higher fuel consumption is shown on Figure 3 where the influence on total installed engine plus fuel weight is shown in terms of the aircraft sortie duration. For flight durations in excess of two hours it will be seen that in terms of permissible payload, it pays to equip the helicopter with a heavier, more sophisticated and more efficient engine (typified by the BS 360-07).

Further engine configurations were studied therefore based on higher pressure ratio cycles. The alternatives of an axial or centrifugal compressor system were examined, the use of a reverse flow combustion system in place of a conventional straight through system and the alternatives of single and twin-spool gas generators.

Figure 4 shows some examples. The BS 360-05 has a single-spool gas generator, a wholly axial compressor system and a straight-through combustion system. It is a very long engine and having one spool and therefore a limited pressure ratio to avoid over-complex variable geometry in the compressor system, it has an intermediate level of efficiency. Retaining a single-spool gas generator, the BS 360-06 represents the other extreme in configuration. The compressor system is wholly centrifugal and a reverse flow combustion system is used. The increase in diameter results in the engine being 40 per cent heavier than the BS 360-05. Again the use of a single-spool gas generator limits the pressure ratio of the engine and moreover, the compressor system, being centrifugal, is significantly less efficient than the equivalent axial. As a consequence, the engine has a very indifferent efficiency. The final configuration - BS 360-07, was that eventually adopted for the engine. It has a two-shaft gas generator and this allows elevation of the cycle pressure ratio. The use of a centrifugal compressor for the second stage equates well to the introduction of the reverse flow type of combustion system and avoids the problem with an axial of very small blades in the last stages. The engine is both short and light for the pressure ratio involved. The improvement in the thermodynamic cycle gives it the highest efficiency of all.

The Anglo-French Helicopter agreement of 1967 gave impetus to these studies the outcome of which is the RS 360 or Gem as it is now called which powers the Westland Lynx helicopter. This helicopter is planned to fulfil several roles and will be used by all of the Armed Services. It will eventually replace the Army Scout and the Naval Wasp and be used by the R.A.F. for transport and training (Figure 5).

The design concept ground rules (Figure 6) that were laid down for the engine are :

1 Reliability and Safety

2 Ease of maintenance

3 Good mission performance

Additional to the considerations of cycle thermodynamics these requirements resulted in the incorporation of a number of basic design features as follows:

1 A two-spool gas generator - to provide a good overall surge margin and hence the flexibility and good handling qualities required. At the same time the potential unreliability of variable geometry or blow-off was avoided.

2 A two-stage power turbine - for high efficiency and to provide scope for further development.

3 A mechanical arrangement making use of a reverse flow combustion system to give short shafts thus avoiding whirling problems which might otherwise arise as a result of the small diameter and high rotational speeds.

4 A front-drive arrangement to provide an adequate field of view for the crew, the engines being mounted aft of the rotor.

5 An arrangement which allows the engines to be plugged directly into the rotor gearbox so bringing the engine C.G. as near as possible to the helicopter rotor.

6 Modular construction - to facilitate repair by replacement of modules and the direct substitution of factory tested modules in the field.

GENERAL DESCRIPTION

The Gem engine (Figure 8) comprises a two-spool gas generator and a two-stage free power turbine with a through shaft giving a front drive via a step down reduction gear with a shaft output speed of 6000 RPM. The engine ratings are as shown on Figure 7.

The two-spool gas generator comprises a low pressure set with an axial compressor and a single-stage axial turbine and a high pressure set with a single-stage centrifugal compressor, a reverse flow combustion chamber and a single-stage axial turbine.

The four-stage LP compressor is related to a series of compressors which formed the basis of a research programme at Rolls-Royce. This research dealt with the problems of high stage loading studying the levels of efficiency and adequacy of surge margin in such compressors.

However during the development of the engine the surge margin at the lower end of the speed range was seen to be adequate partially due it is thought to a size effect. The choice before us was to introduce variables with the consequential extra cost and complexity or to rematch the compressor to improve the low speed surge line. This latter was done at the expense of mass flow and efficiency at high speeds (Figure 9) and the power was restored by increasing the flame temperature but still within the design objective concerning the requirement to retain un-cooled turbine rotor blading.

The centrifugal compressor began life in the engine as a radial vaned impeller but later in the programme it was found that a quicker development path lay in obtaining the required efficiency by using impellers with swept back vanes (Figure 10).

The turbines feature high hub/tip ratios and short blade lengths. Consequently low aspect ratios, particularly in the first two stages, have resulted. The possibility of high tip leakage losses resulted in the original design featuring shrouded blades. The shroud was subsequently removed from the HP stage because the compressor change required a higher rotation speed and the problem of sealing on this stage, which will be described later, has been on of the major development tasks. The HP turbine driving the centrifugal impeller has a cooled nozzle blade but uncooled rotor blades.

The single-stage LP turbine, driving the axial compressor is relatively lightly loaded. This is for reasons of future growth when a front stage can be added to the axial compressor to increase throughput and still have satisfactory LP turbine loading.

For the power turbine the expansion ratio is about 2.5:1. By using a two-stage design in preference to a single-stage there is a gain of about four per cent in efficiency plus scope for future growth.

In common with most helicopter engines as much energy as possible is taken out of the gas stream before the final exhaust and the jet pipe is designed for an exit velocity of 350 ft/sec.

GENERAL MECHANICAL AND INSTALLATION FEATURES

It has already been stated that reliability, safety and ease of maintenance are prime requirements in the basic design. In order to achieve this, great reliance has been placed on the feed across of experience from the civil propulsion engine market. The engine features all the modern diagnostic or health monitoring techniques that have been proven in service (Figure 11). Vibration monitoring points are available and most of the engine can be inspected internally while in an installed position through specially provided borescope ports. Magnetic chip detectors are placed in each scavenge line and spectrographic oil analysis may be carried out by sampling through the dipstick hole in the oil tank.

The design of the engine is also such that it has the potential to be fully modular (Figure 12). Already it has been established that the engine can be broken down easily into its major assemblies. These are all self-contained in that rotating members are mounted on their own bearings within the module assembly thus enabling them to be individually balanced, replacement therefore can be carried out without the need for further balancing procedures. A programme is in hand to establish the permissible aerodynamic margins and when completed spare engines will become a thing of the past and in-line replacements can be considered a reasonable proposition.

Because the Gem has been conceived to power the Lynx helicopter it has been possible to develop the installation in close collaboration with Westland Helicopters Limited right from the start and a tightly cowled but readily accessible installation has resulted from this very close collaboration (Figure 13). This close collaboration has been extended to include the Armed Forces and great attention has been paid to accessibility and the replacement of accessories which are mainly grouped on top of the engine. An assessment of the removal times has been made and they compare very favourably with previous installations (Figure 14). The assessments have been carried out as far as possible under representative conditions including the use of Arctic gloves and although the servicing tool kit is more extensive. Figure 15 shows the 'desert island' tool kit that would suffice.

The conventional two fire-zone approach has been abandoned and instead the engine is double skinned where necessary to keep the carcass temperature within the required limits (Figure 16).

A further point to note is that is has been regarded as a fundamental concept that the engine is completely self-contained requiring only an LP supply of fuel, a 28 volt supply of electrical power and two mechanical linkages to the aircraft controls. The oil system and tank are attached to the engine as is the fuel and control system, ignition system and, if required, torquemeter.

The Plessey control system is tailored to the concept of two-engine reliability. It gives fully automatic rotor speed governing under all modes of flight to maintain a substantially constant helicopter rotor speed, with an inherent capability for load sharing by means of closely matching individual free turbine governor droop characteristic. Basically hydro-mechanical, but with pneumatic actuation and electric overrides for T_6 N_L and N_f, the system is contained within two units both of which are engine mounted. The system is constructed on the module principle, each module containing complete and replaceable control functions.

Simple concepts have led to a compact, lightweight and potentially highly reliable control system, the reset mode of free turbine governing leads to extremely stable and precise speed holding with excellent response; the protective measures assure full compliance with civil airworthy safety standards and the modular construction allows easy fault diagnosis and ready maintenance away from base.

Turning now to some of the more general overall design features (Figure 17), it should be noted that because of its Naval application great attention has been paid to the corrosion problem. The engine does not feature any magnesium although the weight advantage was a great temptation. The LP compressor blading is made of corrosion resistant materials.

It would have been very easy to decide to aim for the lightest construction and let the carcass outline follow the outer annulus of the aerodynamic passages. Because of the use of a centrifugal impeller this would have led to at least two flat diaphragms in the carcass line and the distinct possibility of a carcass resonance. Additionally there would have been the problem associated with stiffening flat plates against end loading. The engine features a separate carcass leaving the annulus to be formed by casings which are not required to carry mounting loads. This obviously eases the problem of rotor tip sealing. The double skinning also has another beneficial effect in that the containment ability of the engine is much improved.

The Gem uses a multi-shaft arrangement but it should be observed that all the bearings transmit their loads direct into the main casings and not via the intermediary of intershaft bearings. There are some steadies between the power turbine and LP shaft systems but these bearings carry no loads. All main line journal bearings are carried on an oil cushion or squeeze film and this has undoubtedly led to a smooth engine.

MECHANICAL DETAILS AND SOME DEVELOPMENT PROBLEMS

Main Reduction Gearbox

The power take-off is through a 4½:1 reduction gearbox module housed in the air intake hub. It is designed to transmit 900 SHP for an output drive speed of 6000 RPM. This unit is extremely compact and can conveniently be handled by one man during assembly (Figure 18).

The gearing is a simple epicyclic of the double helical type which transmits the load smoothly through the train with less vibratory excitation at speed than that associated with straight spur gearing. Input is by the sunwheel assembly which is fully floating and centred by three planets. Output is through a robust one-piece planet carrier. The three planets rotate on white metal faced steel spindles and these also mesh with a divided annulus which locates the train axially. The annulus is fixed in such a manner as to provide torsional restraint while allowing limited independent radial freedom.(Figure 19)

The floating features ensure uniform division of the load between both helices and in particular on the sunwheel eliminates bearings completely from a high speed rotating member. The provision of good facilities for timing enables the back-lash of sun and planet teeth to be kept to a small magnitude. This is a deliberate policy in order to limit the sun gear radial excursion and thus the possible out-of-balance forces carried by the flanks of the teeth to a minimum.

The advantage of the double helical arrangement over the single is that the end thrust component of the load is reacted internally and therefore thrust bearings are not required.

The two halves of the double helical train are closely spaced axially providing a compact arrangement. The planets are the space limiting components and they are produced by electron beam welding two finish ground single helical gears of opposite hand at their hub diameter, leaving only the bore to be hone-finished. Using this technique concentricity tolerances between the teeth and the bore are maintained well within 0.0006 in. limit in production.

This arrangement is one that has been arrived at during the development of the gear (Figure 20). Originally the planets were dowelled and bolted together and this arrangement although satisfactory was heavy and expensive. Electron beam welding produces an article that meets all the accuracy requirements but is much lighter thus reducing the loading on the planet pins. As it also costs much less to produce this seems to be one case where no penalties have been paid in one direction for advantages in another.

Gear stresses are conservative and are based on the extensive experience gained from the development of the Dart and Tyne engines. Lubrication of the reduction gearing,is by oil,fed through the power turbine shaft via a transfer tube to the planet carrier. Each of the handed gear meshes are separately lubricated by jets. The feed to the planet spindles is via a fine thread filter in each line and sludge traps are incorporated in both the carrier and the spindles themselves. Development of the reduction gear is progressing satisfactory and the successful completion of a 12 hour 40 per cent overtorque test augurs well for stretch potential in the future.

COMPRESSORS

Air is delivered to the low pressure compressor through an aluminium alloy casting having five radial spokes which support the hub containing the rotor front bearing (Figure 21).

Bolted to the air intake casing is the LP compressor stator casing which supports the rotor rear bearing through the outlet guide vanes. The rotative assembly after being balanced in its own bearings can be built into the stator casing, which is split along the engine axis on stages, 1, 2 and 3. The tendency that split casings have for going out-of-round has been prevented by careful attention to the detail design and by the manufacturing technique employed. The split casing is dowel located and rigidly clamped to a continuous ring at both ends; the intake at the front and the 4th stage stator at the rear. The salient points in the manufacturing technique are - to make the casing as a continuous cylinder and to carry out all brazing operations on stator blades and reaming of the split line clamping bolt holes prior to splitting by sawcutting, thereby ensuring true mating. The metal removed by the sawcutting operation is replaced by bonding a shim to each half to form two similar half casings. A wearaway coating on the bore and end faces of the plastic inter-stage inner seals, allowing close running clearance, contribute significantly to the high efficiency of this component. Similarly the accuracy achievable in the roundness of the stator casing allows close rotor tip clearances. This technique although its validity has now been established nevertheless took a considerable amount of manufacturing development to get right because the thinness of the casing makes it slightly unstable during the brazing and heat treatment processes. The placement of the dowels at 45° was also not ideal to prevent horning-in of the casing and they have now been moved to the split end.

The rotor consists of a one-piece titanium drum having four rows of detachable blades. The drum comprises four discs connected just below the blade roots by cylindrical rings carrying the interstage seal fins. The discs are supported at the front and rear by stub shafts stemming outwards from the inner two discs, the outer discs each being overhung. This arrangement leaves room under the outer discs for the bearing housings, providing close spaced bearings free from whirling problems. The drum is fabricated from four finish machined pieces which are electron beam welded at the cylindrical ring-abutment faces. Concentricity within 0.001 in. is achieved with this technique. The construction is light and compact and is free from the balance maintainability problems associated with bolted assemblies. However once again development was necessary because the original choice of material resulted in the electron beam process inducing high residual stresses leading to cracking. The necessary heat treatment to eliminate this led to such a reduction in physical properties that a change to IMI.318 Titanium was made and the problem has been eliminated.

The air delivery to the HP compressor is through a cast aluminium alloy annular duct having four radial spokes which support the hub containing the HP compressor front bearing and accessory spiral bevel drive gears, the drive being taken from the HP shaft. The hub also provides support for the LP compressor rear bearings. The outer wall of the cast duct is supported from the outer casing of the engine which connects the air intake to the combustion chamber outer casing. The outer casing forms a stiff coned low temperature connecting skin providing blade containment for low weight penalty and a rigid attachment for the rear engine mounting and accessory gearbox. The outer casing and interduct support flange also carries the impeller shroud which has a wearaway coating allowing close running clearances between it and the Titanium impeller. This contributes significantly to high component efficiency.

At the same time as the residual stress problem was discovered on the LP compressor drum is was also seen that the close forging process on the impeller was producing similar effects. A similar change of material was made and this has proved satisfactory. More arduous sortie pattern requirements have led to a further step being taken now to IMI.550 Titanium materials. As this is an air tempered material also, the residual stress problem is unlikely to reveal itself again.

COMBUSTION SYSTEM

A reverse flow combustion chamber has several advantages in a small gas turbine. The air flow path of this type of chamber renders the combustion system insensitive to compressor exit velocity profile. Furthermore, the large volume conferred by this layout gives light combustion loading and the downstream situtation of the fuel injectors simplifies design of the combustion chamber entry section making the fuel injectors readily accessible. The combustion chamber is formed by the annular space between the flanged drum of the main engine structure and the lightly stressed inner casing surrounding the gas generator turbine. The outer casing incorporates bosses for torch ignitors, fuel drains and borescope inspection ports. The front face of the chamber is formed by a curved wall which connects the axial diffuser and the HP nozzle support flange. The flame tube and discharge bend are fabricated separately. The two parts are bolted together at the outer wall and this assembly is supported in the engine by bolting to the HP nozzle support flange and is located circumferentially on dogs at the rearmost part of the flame tube dome. A sliding joint seals the inner wall at its junction with the inner discharge bend which is part of the HP nozzle unit.

Fuel is introduced into the flame tube through seventeen 'vaporiser' tubes where it is mixed with, and atomised by, some of the air entering the combustor primary zone. This system ensures that low fuel pressure is acceptable at idling conditions so that very small metering holes are not essential; a low pressure fuel system can be used; metering orifices can be placed in a cool region upstream and are less prone to blockages; the system is simple and cheap to manufacture and exhaust smoke is negligible.

The combustion system was developed from experience on one of similar configuration and size used in a small auxiliary unit. The main development problem (Figure 22) was that with the high surface area to volume ratio, high wall temperatures were experienced on the early running. Attention to the detailed cooling arrangements has brought them down to acceptable values. Light round has also been a problem and has resulted in the number of spray torches being doubled and spaced round the can.

TURBINES

Small engine turbines pose particular problems in selecting the optimum compromise between mechanical and aerodynamic requirements. Low aspect ratios (and consequently higher secondary losses) are unavoidable if blades are to be sufficiently robust and manufacturing problems kept within bounds. Trailing edge blockage effects are also proportionally greater and these factors must be taken into account in assessing the level of performance that can be achieved in a small turbine.

The HP and LP spools are driven by single-stage axial turbines of aerodynamically conventional design, employing moderate blade speeds and loadings. The power turbine work is such that two-stages are required to achieve efficient operation and an axial exit flow direction to minimise exhaust system losses. All blades and vanes are uncooled with the exception of the HP nozzles which employ a simple form of leading edge impingement cooling together with a pressure surface film cooling slot near the trailing edge.

The HP rotor blades which are cast in MAR 246 material are unshrouded, the advantages of the higher T.E.T. possible without shrouds more than offsetting the increased tip leakage. All other rotor blades are shrouded to ensure minimum overtip losses. These blades are cast in SEL material. The blades are attached to the forged high temperature alloy discs by conventional fir-tree serrations. In the case of the two-stage power turbine the discs are electron beam welded together after broaching of the fir-tree serrations.

Particular attention has been paid to eliminating possible leakage paths which by-pass the turbines and to the mechanics of the HP turbine segmented shroud so that hot tip clearance is a minimum. The perfection of the means to achieve this requirement has been a major development task and the illustration shows the difference between the initial and final designs (Figure 23).

All turbine nozzles with the exception of the stage two power turbine which is cast, are fabrications. In the case of the LP and stage one power turbine these fabrications also carry the turbine bearing housings.

OIL SYSTEM

The oil system is conventional in concept and the only unusual feature is the gear pump which uses three gear elements instead of four to scavenge a pair of oil lines. However, as always, a major development problem has been oil consumption. There are more than 20 air labyrinths in the engine (Figure 24) and these are very sensitive to incorrect air pressure balance. The situation was aggravated by the change in pressure levels throughout the engine when the pressure split between the LP and HP systems was changed.

The problem can be split into three main divisions, viz:

1 Chamber unbalance

2 Chamber isolation

3 Leakage paths

As is normal in such cases each of these has been solved by a large number of small detail changes, the major ones of which were:

1 Replacement of the HP turbine bearing ring seal by an air labyrinth because of wear problems at the high rubbing speeds encountered in this location.

2 Opening up the volumes around the bearings to avoid bad pressure distributions across the seal.

3 Eliminating the weir effects of features such as oil jets in the bearing chambers.

4 Introducing large scavenge funnels in the bearing chambers to give a better collecting effect.

5 Increased size of scavenge pipes.

6 Small tanks in the scavenge line to absorb the shutdown leak.

7 Integral end caps on one side of the bearing chambers.

8 Improved balance across the bearing chamber seals.

9 Venting some chambers back to the oil tank.

10 Improved breather performance by shielding the inlet.

11 Taking the seal balance air from a common source on the reduction gear rather than bringing the rear seal supply through the shaft from the centre bearing.

12 Introduction of a hydraulic seal between the centre bearing chamber and the HP turbine bearing chamber.

13 Venting the centre bearing chamber through the auxiliary gearbox drive to the auxiliary gearbox and then to the breather.

An engine built to the latest modification standard incorporating these changes will be run at consumption figures well under the specification requirement of 0.5 pints/hour.

AIR SYSTEM

Another consequence of the change of pressure split between the compressors was that the cooling air flows had to be revised (Figure 25). The LP delivery air was no longer adequate and as a result gas re-circulation occurred which resulted in blade shedding both on the LP and power turbine first-stage discs all of which were contained. Improvements were made to the size and number of the transfer pipes to cut down the pressure drops in the supply line. Leakage paths were blocked up at the turbine end and the air was directed more positively to where it was most needed. At the same time the air was tapped off from a higher source. These changes have had the desired effect and restored the effectiveness of the turbine cooling air.

It has only been possible in this paper to deal briefly with a few of the many aspects of the design and development of the Gem engine, Many people have contributed to its progress over the last six years and those of us who have had the rewarding experience of working together on it look forward with confidence to its entry into Service in 1976.

In conclusion I should like to express my thanks to Rolls-Royce (1971) Limited for allowing me to use Company data in preparing this paper, but wish to point out that any views expressed are my own and not necessarily those of Rolls-Royce. I would also like to express my indebtedness to H.Purvis and M.R.Harper for their help in the preparation of this paper.

SMALL
ENGINE
DIVISION

Parameter variations in BS360 design cycles

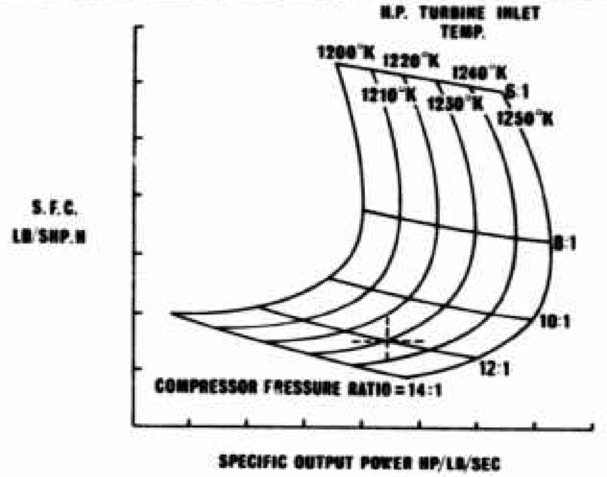

Figure 1

SMALL
ENGINE
DIVISION

8000 lb A.U.W. Helicopter Payload – Duration Comparison

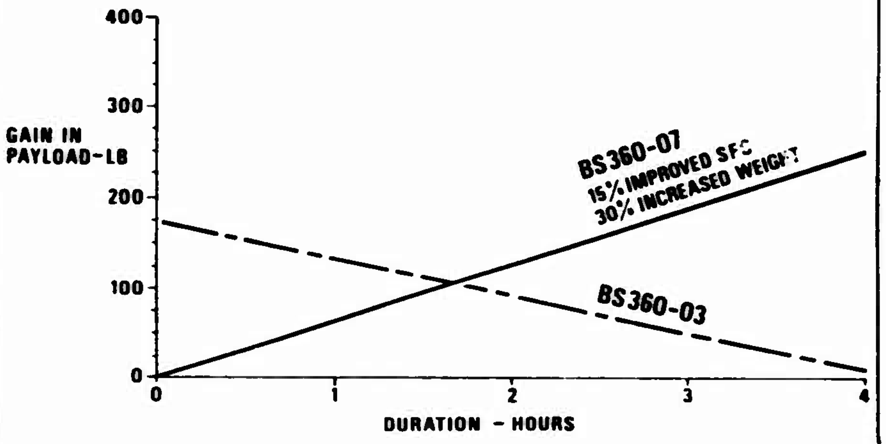

Figure 3

SMALL
ENGINE
DIVISION

BS360-03 Engine

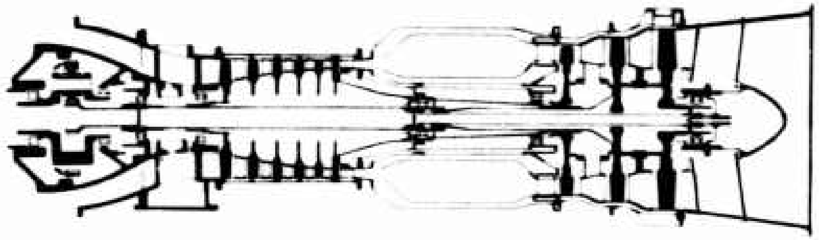

Figure 2

SMALL
ENGINE
DIVISION

BS360 Design Comparisons

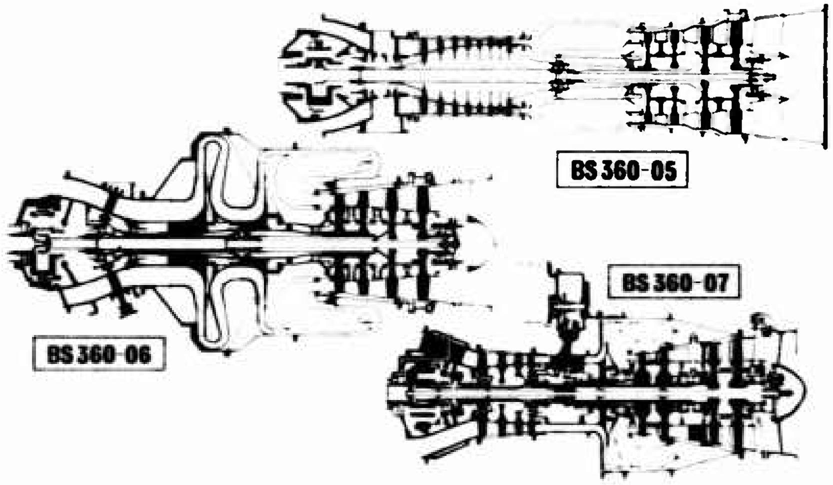

Figure 4

SMALL ENGINE DIVISION

W.H.L. Lynx—Army & Navy Versions

Figure 5

SMALL ENGINE DIVISION

Gem Turboshaft Engine

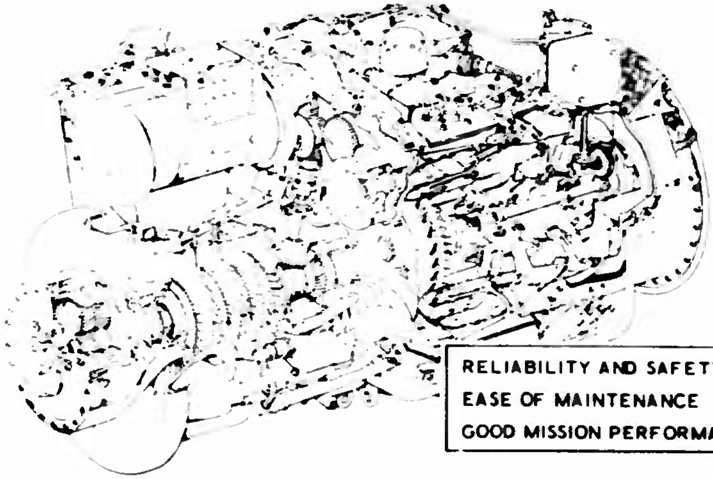

RELIABILITY AND SAFETY
EASE OF MAINTENANCE
GOOD MISSION PERFORMANCE

Figure 6

SMALL ENGINE DIVISION

Performance at S.L., I.S.A.

RATING	S.H.P.	S.F.C. lb/shp-hr	OUTPUT SPEED R.P.M.
MAX. CONTINGENCY (2½ Minutes)	900	-	6000
INTER. CONTINGENCY (1 Hour) & MAXIMUM POWER (5 Minutes)	830	0·52	6000
MAX. CONTINUOUS	750	-	6000
TYPICAL CRUISE	415	0·66	6000

Figure 7

SMALL ENGINE DIVISION

Mechanical Features

BLADE CONTAINMENT
SQUEEZE-FILM MOUNTED BEARINGS
NO VARIABLE GEOMETRY

CORROSION-RESISTANT L P COMPRESSOR
NO MAGNESIUM
STIFF CARCASE

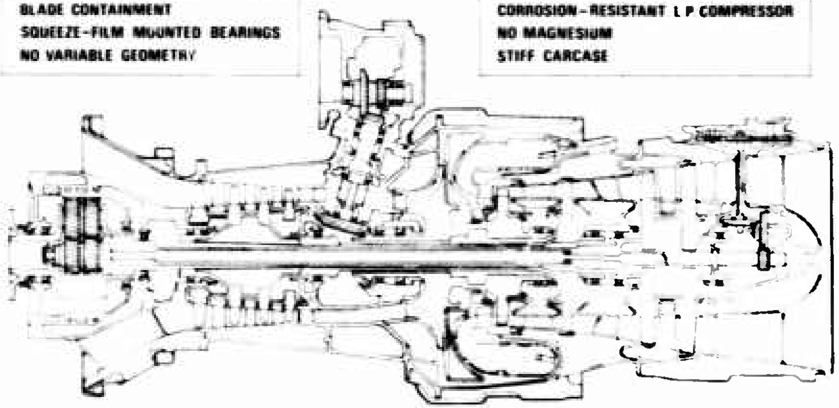

Figure 8 and 17

SMALL ENGINE DIVISION

BS 360 L.P. Compressor–Effect of Re-Matching

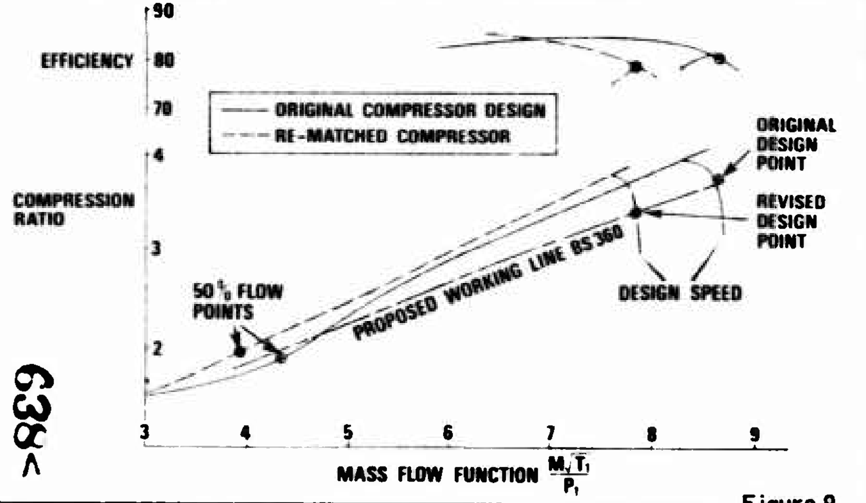

638<

Figure 9

SMALL ENGINE DIVISION

Condition Monitoring

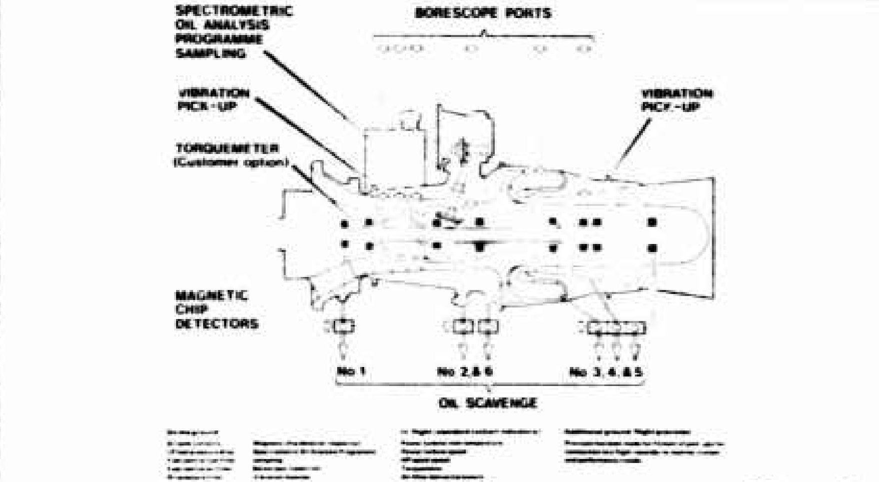
SPECTROMETRIC OIL ANALYSIS PROGRAMME SAMPLING
BORESCOPE PORTS
VIBRATION PICK-UP
VIBRATION PICK-UP
TORQUEMETER (Customer option)
MAGNETIC CHIP DETECTORS
No 1
No 2 & 6
No 3, 4, & 5
OIL SCAVENGE

Figure 11

SMALL ENGINE DIVISION

Types of H.P. Impeller

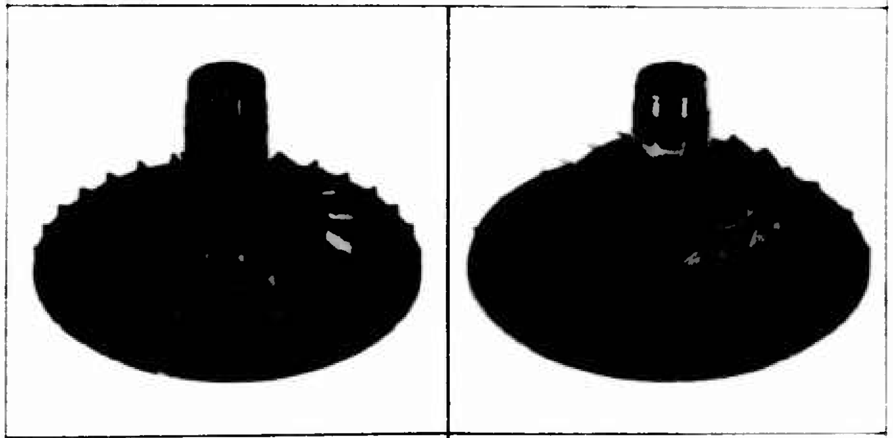

INITIAL DESIGN

CURRENT DESIGN

Figure 10

SMALL ENGINE DIVISION

Basic Modules–Hardware

Figure 12

SMALL ENGINE DIVISION

Accessibility

SINGLE FIRE ZONE

NO CENTRAL FIREWALL

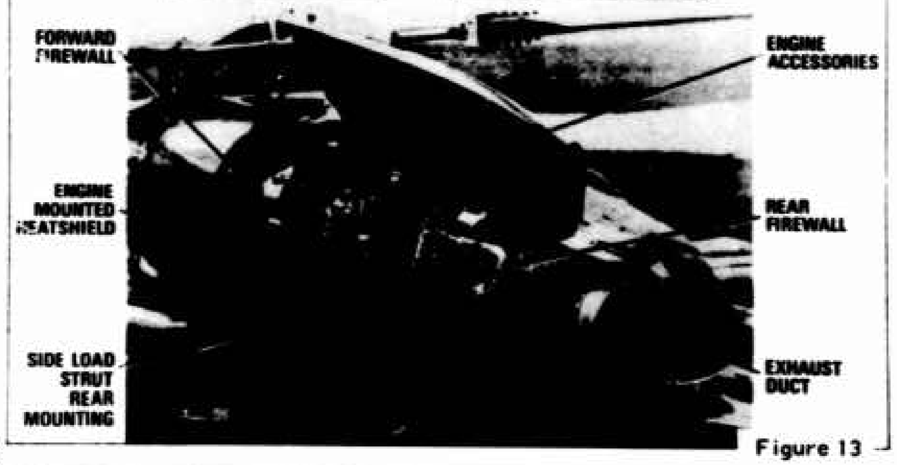
FORWARD FIREWALL
ENGINE MOUNTED HEATSHIELD
SIDE LOAD STRUT REAR MOUNTING
ENGINE ACCESSORIES
REAR FIREWALL
EXHAUST DUCT

Figure 13

SMALL ENGINE DIVISION

Engine & Accessory Replacement Times

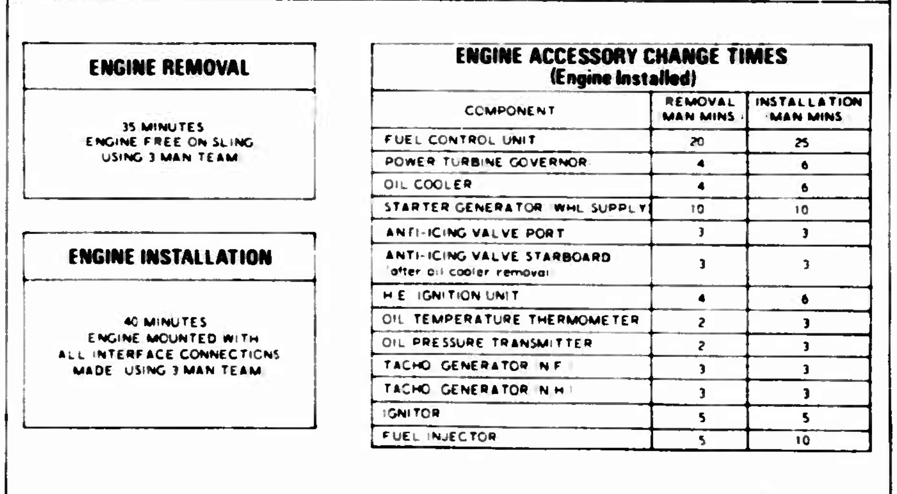

ENGINE REMOVAL

35 MINUTES
ENGINE FREE ON SLING
USING 3 MAN TEAM

ENGINE INSTALLATION

40 MINUTES
ENGINE MOUNTED WITH
ALL INTERFACE CONNECTIONS
MADE USING 3 MAN TEAM

ENGINE ACCESSORY CHANGE TIMES
(Engine Installed)

COMPONENT	REMOVAL MAN MINS	INSTALLATION MAN MINS
FUEL CONTROL UNIT	20	25
POWER TURBINE GOVERNOR	4	6
OIL COOLER	4	6
STARTER GENERATOR (WHL SUPPLY)	10	10
ANTI-ICING VALVE PORT	3	3
ANTI-ICING VALVE STARBOARD (after oil cooler removal)	3	3
H.E. IGNITION UNIT	4	6
OIL TEMPERATURE THERMOMETER	2	3
OIL PRESSURE TRANSMITTER	2	3
TACHO GENERATOR (N F)	3	3
TACHO GENERATOR (N H)	3	3
IGNITOR	5	5
FUEL INJECTOR	5	10

Figure 14

SMALL ENGINE DIVISION

Tool Kit

ENGINE ACCESSORY CHANGE EQUIPMENT

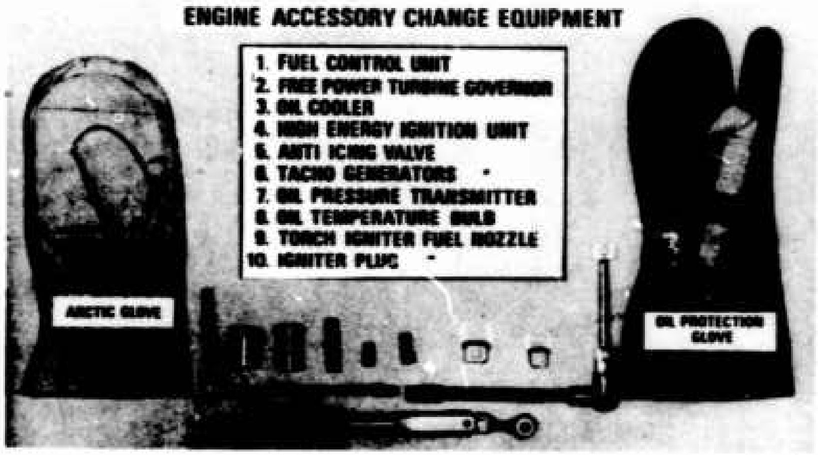

1. FUEL CONTROL UNIT
2. FREE POWER TURBINE GOVERNOR
3. OIL COOLER
4. HIGH ENERGY IGNITION UNIT
5. ANTI ICING VALVE
6. TACHO GENERATORS
7. OIL PRESSURE TRANSMITTER
8. OIL TEMPERATURE BULB
9. TORCH IGNITER FUEL NOZZLE
10. IGNITER PLUG

ARCTIC GLOVE
OIL PROTECTION GLOVE

Figure 15

SMALL ENGINE DIVISION

Heat Shields

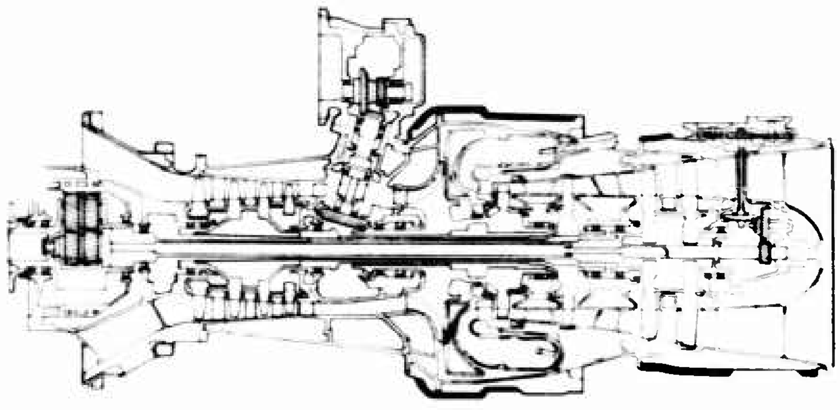

Figure 16

(For Figure 17 see Figure 8)

SMALL
ENGINE
DIVISION

Gearbox Module Assembly

Figure 18

SMALL
ENGINE
DIVISION

Planet Pin Construction

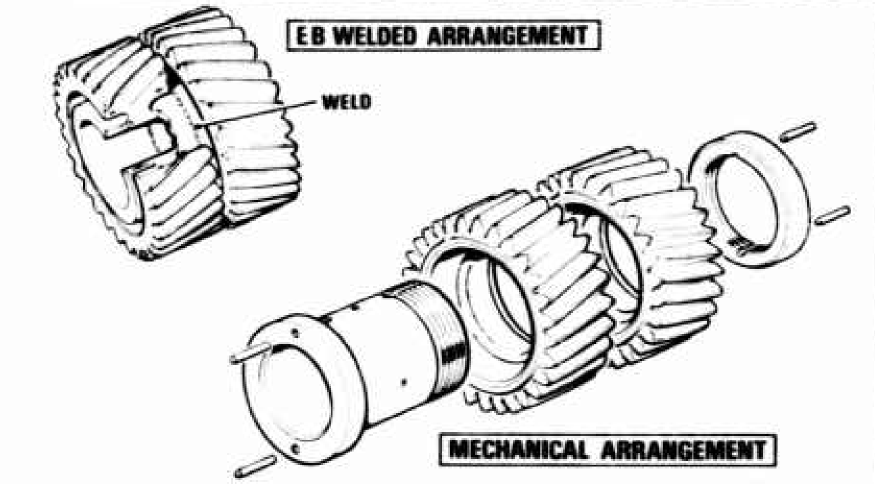
EB WELDED ARRANGEMENT
WELD
MECHANICAL ARRANGEMENT

Figure 20

SMALL
ENGINE
DIVISION

Main Reduction Gearbox

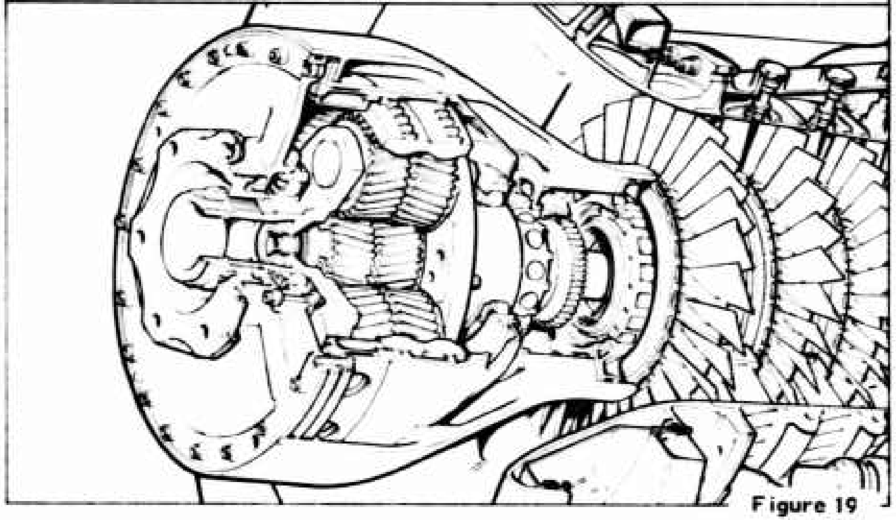

Figure 19

SMALL
ENGINE
DIVISION

L.P. Compressor

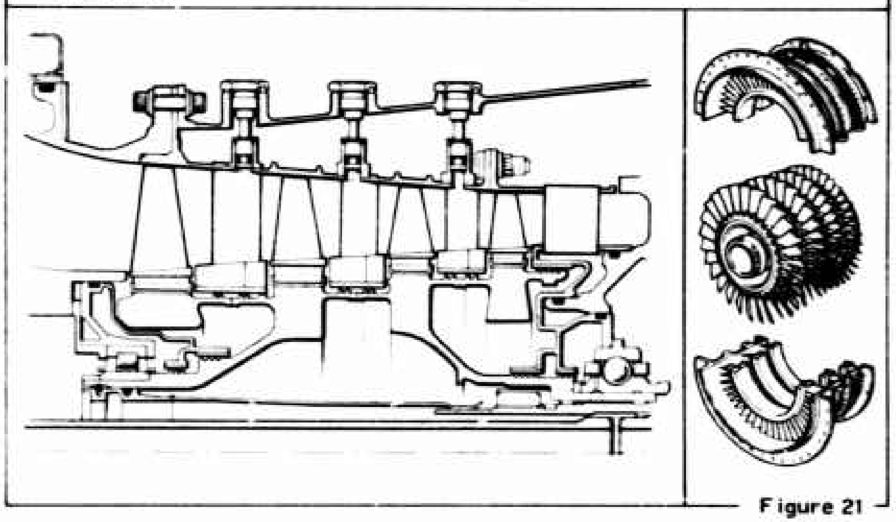

Figure 21

SMALL ENGINE DIVISION

Combustion Chamber

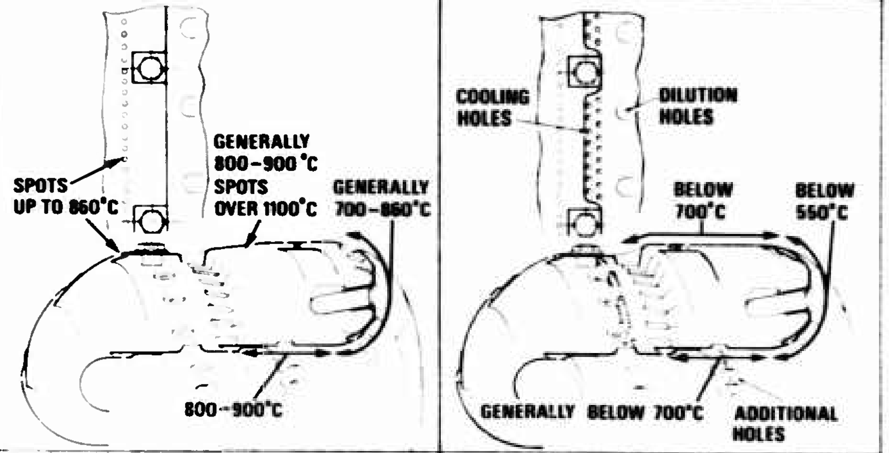
SPOTS UP TO 860°C
GENERALLY 800-900°C SPOTS OVER 1100°C
GENERALLY 700-860°C
800-900°C
COOLING HOLES
DILUTION HOLES
BELOW 700°C
BELOW 550°C
GENERALLY BELOW 700°C
ADDITIONAL HOLES

INITIAL DESIGN

CURRENT DESIGN

Figure 22

SMALL ENGINE DIVISION

Turbine Blades and Shrouds

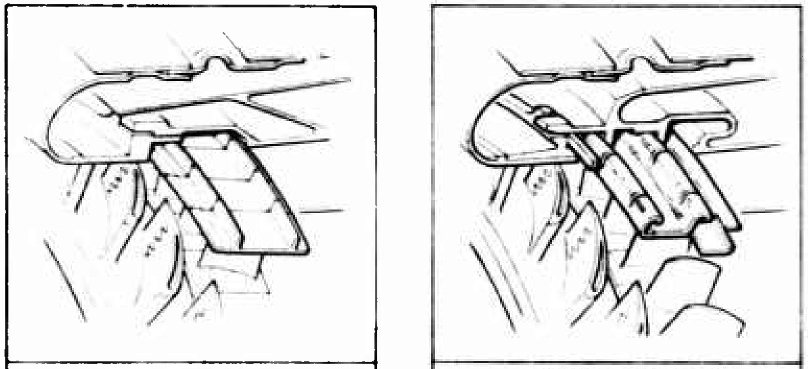

INITIAL DESIGN

CURRENT DESIGN

Figure 23

SMALL ENGINE DIVISION

Air Sealing

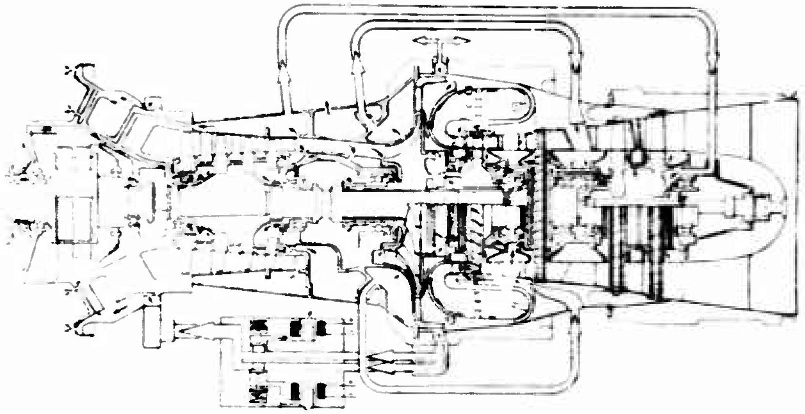

Figure 24

SMALL ENGINE DIVISION

Turbine Cooling Air

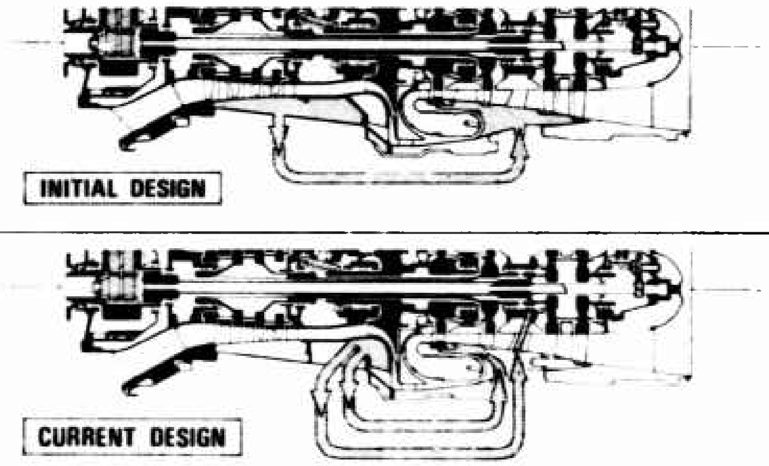
INITIAL DESIGN
CURRENT DESIGN

Figure 25